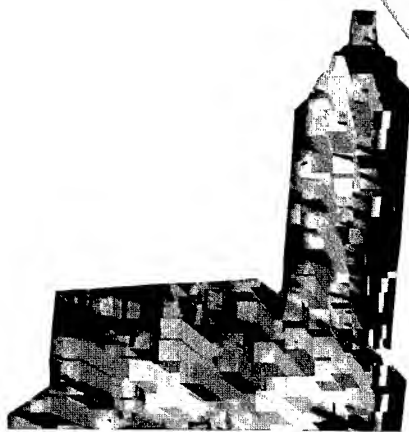


27TH EUROPEAN MICROWAVE 97

CONFERENCE + EXHIBITION

Bridging the Gap Between Industry and Academia

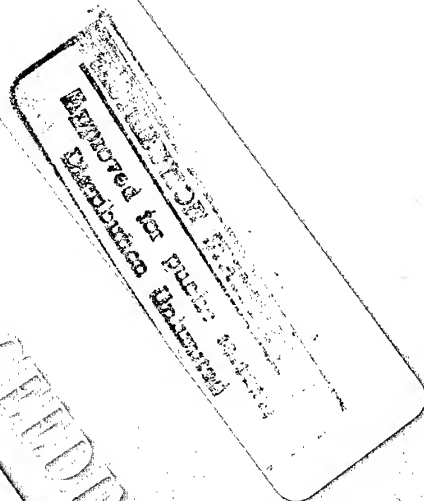


Reproduced From
Best Available Copy

19980408125

Convention Center

September 8-12, 1997



CONFERENCE PROCEEDINGS - VOLUME 1

IEEE Catalog Number 97TH8317

ISBN: 0-7803-4202-X (Microfiche)

FOREWORD



The European Microwave Conference dates back almost 30 years. This year, for the first time, EuMC is coming to Jerusalem. We in Israel are honoured and privileged to host this prestigious Conference. We are working hard to make it a memorable event, both scientifically and culturally.

Jerusalem is a very unique city with a history of 3000 years, breathtaking beauty and numerous points of interest. A visit in Jerusalem is a visit in history and religion. Keeping this in mind, we are offering various tour packages in addition to the excellent scientific program. In fact, we have devoted Tuesday afternoon to a visit of the old city and a reception by the Mayor in the famous Israel Museum.

The scientific program is of high standard, as is customary in EuMC. We are accommodating around 250 papers in 4 parallel sessions and three poster sessions. Following the decision of the Management Committee to encourage and increase industry participation, we have introduced this year for the first time a new category of application-oriented papers. We were very glad to see that this new category was very successful, and comprises about 25% of the accepted papers. I am sure that industry experts will find interest in them.

An exhibition of microwave products will run in parallel to the Conference. We expect the exhibition to be very successful. In Israel we have both a strong microwave industry and a large need for microwave systems, both military and commercial. Therefore exhibition booths were rented by both Israeli industry and foreign companies.

The Conference program includes, in addition to the submitted papers: 5 focused sessions featuring invited talks on important issues, such as wireless communications, packaging, commercial applications, millimeter waves and active filters. Also, 14 invited speakers, some of the best microwave experts in the world, have agreed to share their knowledge with us on a variety of topics. On Friday, 4 workshops and a short course will take place. These involve interesting and timely topics, and I am sure that many of you will find them worth attending.

Thanks to the importance and prestige of the Conference, we were able to raise substantial sponsorship from Israeli industry, representatives of foreign companies, Israeli government and the USA Army. These donations are very important, and enable us to organize a respectable Conference, and strengthen the social activities, which are an important part of the event.

I wish to express sincere thanks to many individuals who have helped to make this event a reality. In particular, I am grateful to the TPC members and members of the Review Board, who devoted their time to evaluate the submitted papers and enabled the construction of our strong scientific program. Special thanks to the Conference Secretary, Shmuel Auster, who carried with me the burden, and to members of the Local Committee, who were very helpful in promoting the Conference. I am greatly indebted to the organizers of the focused sessions and workshops, who put together an excellent program, and of course, I thank all the authors who have submitted papers.

I warmly welcome you to Jerusalem and hope you brought your spouses. I can assure you they will not be bored ...A great scientific, as well as cultural, historical and touristic experience is awaiting you.

Asher Madjar
Conference Chairman

DTIC QUALITY INSPECTED 8

TECHNICAL PROGRAM COMMITTEE

Chairman

A. Madjar, RAFAEL
PO Box 2250 (code 87), Haifa, Israel
Tel: 972-4-8794128 Fax: 972-4-8792037
e-mail: asher@ee.technion.ac.il

Secretary

S. Auster, ELISRA Electronic Systems Ltd., Israel

Members

T. Berceli, Technical University of Budapest, Hungary
T. J. Brazil, University College Dublin, Ireland
A. Costanzo, University of Bologna, Italy
W.K. Gwarek, Warsaw University of Technology, Poland
I. Koffman, Orbit, Israel
Y. Leviatan, Technion, Israel
L.P. Ligthart, Delft University of Technology, The Netherlands
J. Machac, Czech Technical University, Czech Republic
H. H. Meinel, Daimler Benz Aerospace AG, Germany
R.D. Pollard, University of Leeds, UK
P. Russer, Technische Universität München, Germany
M. Salazar-Palma, Polytechnic University, Spain
G. Salmer, IEMN, France
R. Shavit, Ben Gurion University, Israel
S. Shonbach, ELTA, Israel
R. Sorrentino, Inst. of Electronics University of Perugia, Italy
O.G. Vendik, St. Petersburg Electrotechnical University, Russia
D. Vanhoenacker, Université Catholique de Louvain, Belgium

EuMC STEERING COMMITTEE

R. Sorrentino, Inst. of Electronics University of Perugia, Perugia, Italy (Chairman)
R.H. Jansen, Dept. of Electrical Engineering RWTH Aachen Technical University, Aachen, Germany
L.P. Ligthart, Fac. of Electrical Engineering, Delft University of Technology, Delft, The Netherlands
A. Madjar, RAFAEL, Israel
H.H. Meinel, Deutsche Aerospace AG, Munich, Germany
S.J. Nightingale, UK

EuMC MANAGEMENT COMMITTEE *

Chairman

R. Sorrentino, Italy

Vice Chairman

J. Zehentner, Czech Republic

A. Madjar, Israel

L.P. Ligthart, The Netherlands

Ordinary Members

S. Auster, Israel, Group 5

C. Costa-Freire, Portugal, Group 6

G.N. Goltsman, Russia, Group 7

P.Y. Guillon, France

R.H. Jansen, Germany

J.S. Joshi, UK

I. Kasa, Hungary, Group 3

F.M. Landstorfer, Germany

H.H. Meinel, Germany

J. Modelski, Poland, Group 4

S.J. Nightingale, UK

M. Orefice, Italy

A. Räsänen, Finland, Group 2

A. Vander Vorst, Belgium

D. Vanhoenacker, Belgium, Group 1

Honorary Secretary

A.F. Wilson, UK

*** COUNTRIES REPRESENTED**

Each member in the Management Committee represents a country or a group of countries as follows:

Group 1: Belgium, The Netherlands, Luxemburg, Ireland

Group 2: Denmark, Faroes, Finland, Greenland, Iceland, Norway, Sweden

Group 3: Albania, Bulgaria, Hungary, Romania

Group 4: Czech Republic, Estonia, Latvia, Lithuania, Poland, Slovakia, Ukraine

Group 5: Croatia, Cyprus, Greece, Israel, Slovenia, Turkey, Yugoslavia

Group 6: Andorra, Austria, Lichtenstein, Portugal, Spain, Switzerland

Group 7: Belarus, Moldova, Russia

SPONSORS

Hewlett-Packard

Elisra Electronic Systems, Israel

Elta Electronic Systems, Israel

Eyal Microwave, Israel

General Microwave Israel

Gilat Satellite Systems, Israel

Israel Ministry of Commerce & Industry

Israel Ministry of Science

Motorola Communications, Israel

ORMIC Components, Israel

Rafael, Israel

Ravon / Mini Circuits, Israel / USA

RDT - Components, Israel

Rhode & Schwarz, Germany

Siemens, Germany

Spinner, Germany

US Army European Office

CONFERENCE SECRETARIAT

ORTRA LTD.

1 Nirim St., P.O. Box 9352

Tel Aviv 61092, Israel

Tel: 972-3-6384444

Fax: 972-3-6384455

E-mail: info@ortra.co.il

PAPER REVIEW BOARD

Adelseck	B.	Germany	Galwas	B.	Poland
Aitchison	C. S.	U.K.	Ghione	G.	Italy
Alinikula	P.	Finland	Goblik	V.V.	Ukraine
Angelov	I.	Sweden	Godor	E.	Hungary
Armenise	M.- N.	Italy	Goltsman	G.N.	Russia
Arndt	F.	Germany	Gomez-Martin	R.	Spain
Artal	E.	Spain	Grabow	W.	Germany
Asenov	A.	Scotland	Guettich	U.	Germany
Back	I.	Sweden	Guglielmi	M.	Netherlands
Baechtold	W.	Switzerland	Guillon	P.	France
Barbosa	A.	Portugal	Hansen	R. H.	Germany
Bartolic	J.	Croatia	Heemskerck	H.J.M.	Netherlands
Bartolucci	G.	Italy	Heide	P.	Germany
Baudrand	H.	France	Heinrich	W.	Germany
Baumann	G.	Germany	Heymann	P.	Germany
Beaumont	S. P.	U.K.	Hodisan	A.	Israel
Beyer	A.	Germany	Hoffmann	K.	Czech Rep.
Bois	J.-R.	France	Horno	M.	Spain
Bolomey	J.Ch.	France	Iezekiel	S.	U.K.
Bonek	E.	Austria	Ivanov	K.P.	Bulgaria
Briere	P.	France	Ivanov	S. A.	Hungary
Brockert Hoff	W.	Germany	Jacob	A. F.	Germany
Brussard	G.	Netherlands	Jaeger	D.	Germany
Bucci	O.-M.	Italy	Jansen	R. H.	Germany
Camacho-	C.	Spain	Jastrzebski	A. K.	U.K.
Penalosa			Jelenski	A.	Poland
Cappy	A.	France	Jelinek	F.	Czech Rep.
Catedra	M. F.	Spain	Jerzy	M.	Poland
Cazaux	J.- L.	France	Joachim	W.	Germany
Cernohorsky	D.	Czech Rep.	Jofre	L.	Spain
Chramiec	J.	Poland	Johansson	U.	Sweden
Citerne	J.	France	Kasa	I.	Hungary
Collier	R.J.	Uk	Kasal	M.	Czech Rep.
Conciauro	G.	Italy	Kellner	W.	Germany
Costa Freire	J.	Portugal	Kenderessy	M.	Hungary
Corbella	I.	Spain	Kitlinski	M.	Poland
Crosnier	Y.	France	Klamka	J.	Poland
Davies	R.	U.K.	Kohn	E.	Germany
De Zutter	D.	Belgium	Kollberg	Erik	Sweden
Delage	S.	France	Kompa	G.	Germany
Delhay	E.	France	Landstorfer	F.	Germany
Detlefsen	J.	Germany	Lemorton	J.	France
Dobrowolski	J. A.	Poland	Leroy	Y.	France
Donzelli	G.	Italy	Levine	E.	Israel
Duret	G.	France	Lioubtchenko	V.	Russia
Ferrando	M.	Spain	Loele	H.	Germany
Foster	P.	U.K.	Machusky	E. A.	Ukraine
Fouad Hanna	V.	France	Martens	L.	Belgium
Fricke	K.	Germany	Mazanek	F. M.	Czech Rep.
Frigyes	I.	Hungary	Mediavilla	A.	Spain
Frullone	M.	Italy	Medina	F.	Spain
Funck	R.	France	Meinel	H. H.	Germany
Fusco	V.F.	U.K.	Menzel	W.	Germany

Milovanovic	B.D.	Yugoslavia	Schuenemann	K.	Germany
Mongiardo	M.	Italy	Schumacher	H.	Germany
Mrozowski	M.	Poland	Schweeger	G.	France
Narhi	T.	Netherlands	Seoane	A.	Spain
Neri	A.	Italy	Shapir	I.	Israel
Nosich	A. I.	Ukraine	Sharir	V.	Israel
Obregon	J.	France	Shugurov	V.	Lithuania
Olver	D.	U.K.	Sierra	M.	Spain
Orefice	M.	Italy	Snowden	C. M.	U.K.
Page	J. E.	Spain	Sombrin	J.	France
Paraboni	A.	Italy	Splitt	G.	Germany
Pelosi	G.	Italy	Starsi	P.	Sweden
Pinto	G.	Italy	Stavrov	I.	U.K.
Pregla	R.	Germany	Stec	B.	Poland
Priou	A.	France	Stewart	J.A.C.	N.Ireland
Profirescu	M. D.	Romania	Taklaja	A.	Estonia
Pulliainen	J.	Finland	Trifunovic	V.	Yugoslavia
Quere	R.	France	Vahldieck	R.	Switzerland
Raisanen	A.	Finland	Vainikainen	P.	Finland
Reyes-Zavo	E.	Spain	Valentin	R.	Germany
Rizzoli	V.	Italy	Van De Capelle	A. R.	Belgium
Robertson	I.	U.K.	Van De Roer	Th. G.	Netherlands
Rocchi	M.	France	Vander Vorst	A.	Belgium
Rosloniec	S.	Poland	Vegni	L.	Italy
Roux	P.	France	Vilcot	J.-P.	France
Rozzi	T.	Italy	Vokurka	J.	Czech Rep.
Rumelhard	C.	France	Vugrinec	J.	Slovenia
Sabban	A.	Israel	Wenger	J.	Germany
Sannino	M.	Italy	Withington	S.	U.K.
Sautereau	J.-F.	France	Zehentner	J.	Czech Rep.
Schiek	B.	Germany	Zoboli	M.	Italy
Schmidt	L.-P.	Germany	Zurcher	J.-F.	Switzerland

AUTHORS' INDEX

Abbas	F.	518	Bruck	Y.M.	238, 243, 249
Abe	S.	1098	Buchali	F.	26
Aglietti	M.	1175	Buoli	C.	1058
Ahlonsou	L.	709	Burgosgarcia	M.	767
Ahn	D.	501	Buslov	O.Y.	1020
Aikawa	M.	14	Caddemi	A.	109
Akaishi	M.	454	Caliumi	A.	1175
Akpinar	M.	93	Caorsi	S.	733
Ala-Laurinaho	J.	681, 880	Capmany	J.	1228
Alam	T.A.	687	Carlsson	E.F.	196, 886
Alessandri	F.	676, 490	Catena	S.	810
Alimenti	F.	773	Caverly	R.H.	1046
Alinikula	P.	219, 409	Cazal	A.	146
Alonso Montes	J.I.	279, 385, 767	Cazaux	J.-L.	7, 146
Alves Torres	J.	1164	Celuch-Marcysiak	M.	1246
Amann	M.C.	375	Cervi	L.A.	1058
Amari	S.	490	Chakalov	R.A.	196
Avitabile	G.	354	Chartier	E.	1026
Bader	B.	848	Chenakin	A.V.	838
Baets	R.G.F.	749	Cherednichenko	S.	972
Balbastre	J.V.	523	Chramiec	J.	697
Barbancho-Pérez	I.	297	Christ	J.	556
Barnard	J.	331	Christensen	S.B.	1175
Barth	H.	832	Chuang	J.C.P.	1014
Bartle	D.	442, 1041	Chung	M.H.	501
Basu	S.	481	Ciampolini	P.	810
Baudrand	H.	506, 854	Ciceres-Armendariz	H.	767
Baumann	G.	26	Cidronali	A.	354
Behar	D.	671	Citerne	J.	866
Belous	A.G.	544	Cole	M.J.	1228
Bengtsson	L.	1228, 1234	Colinge	J.P.	1008
Berceli	T.	168, 1222	Collier	R.J.	631, 891
Betser	Y.	1240	Comparini	M.C.	1198
Beyer	A.	721	Contarino	V.M.	1222
Bianconi	P.G.G.	631	Conti	G.	949
Biernat	A.	601	Corral	J.L.	1228
Blanck	H.	1026	Costa-Freire	J.	761, 1159, 1164
Blaunstein	N.	124, 153	Costanzo	A.	826
Bogan	Z.	442	Daly	M.	442
Boglione	L.	1052	Dank	Z.	153
Bogod	L.	341	De Barros	L.A.	1240
Bolioli	S.	909	De Carvalho	N.B.	820
Bolomey	J.Ch.	709	De Kok	M.	749
Bornemann	J.	496, 676	De la Fuente	J.G.	104-108
Bort	M.	523	De los Reyes	E.	523
Brsch	R.	20, 448	De Maagt	P.J.I.	605
Bouquet	Ph.	745	De Ponti	E.	130
Bratherton	J.R.	1003	Degli-Esposti	V.	130
Brilliant	A.	347	Delage	S.L.	745, 1026
Briso	C.	279	Delconte	J.	442
Britebard	A.	1186	Demir	S.	56
Bronner	W.	1030			

Demmler	M.	1030	Gipsman	A.	860
Desclos	L.	437	Gismero	J.	190.
Detlefsen	J.	39	Glaser	C.	254
Detlefsen	W.	139	Goh	C.S.L.	550
Dinu	A.	596	Gol'tsman	G.	972
Dirassen	B.	909	Gomez	J.M.	385
Djebari	M.	324	Gonzalez	E.	190
Do Ky	H.	254	Grabow	W.	139
Do Rosario	M.J.	1159	Grajal	J.	190
Domingues	P.G.	739	Gregoris	G.	7
Dortu	J.M.	1070	Grindrod	E.	119
Dovgan	D.	909	Gubina	M.	318
Duncan	H.	1276	Guillouard	K.	866
Elad	D.	804	Gura	K.	838
El-Ghazaly	S.M.	870, 1014	Gusev	G.S.	792
Engheta	N.	978	Guseva	M.N.	927
Ermutlu	M.	203	Gutierrez	P.M.	745
Felgentreff	T.	428	Gwarek	W.K.	1246
Felson	L.B.	949	Gühl	R.	933
Ferling	D.	26	Güttich	U.	933
Ferrero	A.	692	Habermajaer	I.	309
Ferrucci	L.	130	Hajian	M.	470
Filicori	F.	422	Hall	P.S.	1181
Fillerbock	M.	933	Hammadi	S.M.	870
Fink	T.	1030	Hammoudeh	A.	119
Fischer	S.	1030	Hanke	G.	365
Floriot	D.	745, 1026	Hao	Y.	715
Follmann	R.	930, 1360	Hartnagel	H.L.	104
Fortes	F.	1159	Hasegawa	M.	903
Fouad-Hanna	V.	506, 854, 866	Hasegawa	T.	903
Freire	M.J.	1142	Hashimoto	O.	589
Frigyes	I.	309	Hattori	J.	1098
Fruechting	H.	624	Haydl	W.H.	448, 532
Fu	W.	181	Heide	P.	1127
Fuerst	R.	1289	Heimark	J.	877
Fukuda	T.	215	Heinrich	W.	26
Fusco	V.F.	81, 87	Henze	N.	624
Fuster	J.M.	285	Herben	M.H.A.J.	605
Fuziwara	E.	1192	Herblot	J.L.	32
Gabbay	D.	273	Herczfeld	P.	642, 1222, 1240
Gaidukov	M.M.	909, 1080	Hershtig	R.	784
Gallego	J.D.	114	Hiller	G.	1046
Gallop	J.C.	518	Hilt	A.G.	915
Garcia	J.L.	617	Hilton	G.S.	175
Garcia	M.	1234	Hirvonen	T.	681, 880
Garcia Castillo	L.E.	767	Hizal	A.	56
Gardner	P.	1181	Hollmann	E.K.	792, 1020
Garzon	M.	273	Hong	H.J.	501
Gavan	J.	1207	Horno	M.	1142
Geck	B.	476	Hosny	E.A.	1301
Gershenzon	E.	972	Hudek	P.	375
Gevorgian	S.	196, 886	Hulsmann	A.	1030
Ghannouchi	F.M.	336	Humphrey	D.E.J.	87
Giannini	F.	1309	Hunscher	C.	75
Giavarini	A.	1086	Huret	F.	379, 485, 1136
Gillon	R.	1008	Huynen	I.	303, 1008
Ginestet	P.	146			

Hyrylainen	J.	341	Koepf	G.	1020
Iezekiel	S.	1003	Kohler	K.	1030
Ilchenko	M.Y.	927	Koivunen	K.	662
Ilchenko	M.E.	842	Kollberg	E.	886
Ion	R.	596	Komatsu	N.	1192
Isasa	M.V.	573	Kompa	G.	324, 328, 375, 601
Ishida	M.	1192	Kondratier	V.	318
Ishida	O.	1316	Konno	K.	150
Ishikawa	Y.	1098	Koral	Y.	959
Isota	Y.	1316	Korban	V.K.	157
Itoh	T.	181, 992	Koshikawa	S.	150
Ivanov	Z.	196	Kovacs	E.	596
Ivanov	K.P.	229	Kozyrev	A.B.	792, 909, 1020, 1080
Jackson	P.	1276	Krausz	S.	1169
Jacob	A.F.	1258	Kristensson	G.	1252
Jang	D.P.	501	Krozer	V.	104, 190
Jeckeln	E.G.	336	Kubo	H.	1098
Jenu	M.	662	Kumura	M.	1192
Jongh	R.V.	470	Kutscheid	T.	75
Jorke	J.	1035	Kwon	Y.	798
Jovanovic	S.	185	Ladvanszky	J.	915
Jöstingmeier	A.	561, 1270	Lahteenmaki	J.	232
Kadosh	A.	225	Laming	R.	1228
Kadri	L.	379, 1136	Landstorfer	F.M.	556
Kahmen	G.	1035	Langham	C.D.	518
Kalinichenko	Y.V.	927	Langlois	P.	371
Kaneko	T.	454	Ledain	B.	32
Kangaslahti	P.	219	Leijon	R.	359
Kangasmaa	S.	341	Leistner	D.	1122
Kaparkov	D.	318	Leung	L.	1041
Kapilevich	B.	397	Leuzzi	G.	1309
Kapitan	L.	1041	Levin	M.	124
Kapur	S.	727	Levin	G.Ya.	209
Karode	S.L.	81	Levin	R.	755
Kassing	R.	375	Levin	I.	269, 655
Kaunisto	R.	409	Levy	R.	784
Kawaguti	D.	1192	Lieke	M.	75
Kazuhara	M.	437	Ligthart	L.P.	470
Kellner	W.	1070	Limiti	E.	1309
Kenmei	L.B.	1136	Lin	C.I.	190
Kennis	P.	379, 485, 1136	Lindell	I.	1252
Keys	V.N.	792	Lindenborn	H.	624
Khazov	M.L.	792	Lindenmeier	S.	848, 937
Kildal	P.S.	359	Loginov	V.E.	1020
Kim	Y.S.	97, 415	Long	D.E.	727
Kim	B.	97, 415	Loukkola	J.	1092
Kim	I.S.	501	Lupo	G.	755
Kim	C.S.	501	Luy	F.	1035
Kinoshita	N.	779	Macchiarella	G.	1086
Kishimoto	K.	903	Machac	J.	1264
Kivinen	J.	464	Madani	K.	1295
Klaiber	M.	1148	Madihian	M.	437
Klapproth	L.	1070	Madjar	A.	668, 671, 804, 1240
Kleindienst	T.	1030	Madonna	G.L.	692
Knöchel	R.	1103	Mahlev	U.	1207
Kobayashi	Y.	703			
Kobayashi	K.	1154			

Maldonado	F.	190
Males-Ilic	N.	966
Manes	G.	354
Mangold	T.	538
Maricevic	Z.A.	1133
Markovic	V.	966
Marquardt	J.	476
Marrocolo	F.	810
Marsetz	W.	1030
Marti	J.	285
Maruhashi	K.	437
Masini	L.	1175
Massa	A.	733
Massler	H.	448
Matarasso	S.	225
Maurin	Ph.	745
Meerovich	V.	1080
Menzel	W.	391, 649, 676, 1148
Mesa	F.	1142
Meshy	J.	69
Meyer	R.	375
Mezzanotte	P.	773
Migliozzi	M.	1264
Mikhnev	V.A.	584
Milano	A.	266, 269
Milanovic	B.	966
Milcho	M.V.	209
Miranda	J.M.	114
Mitchell	D.	1041
Molina-Fernández	I.	297
Molnar	B.	309
Mongiardo	M.	949
Montanucci	P.	1076
Mora	G.	1058
Motamedi	A.	1216
Mueller	K.	1020
Munoz	S.	114
Musch	T.	62
Müller	U.	26, 721
Nam	S.	798
Nasser	A.A.A.	1301
Nativ	Z.	225
Nauwelaers	B.	921
Neef	H.	832
Negev	M.	69
Nemirovsky	Y.	460
Neri	A.	826
Nesic	A.	185
Nieuwkerk	L.R.	45
Nishiyama	T.	1098
Nishizawa	S.	589
Nohr	W.D.	365
Noweck	M.	1122
Nunes	A.C.	761
Nussbaumer	P.	481
Nuño	L.	523

Nüchter	P.	933
Oberschmidt	G.	1258
Obregon	J.	745
Ohtomo	I.	215
Okubo	N.	432
Olbrich	G.R.	428, 943
Omar	A.S.	561
Omar	A.S.	1270
Onda	K.	437
Ono	K.	1154
Osadchy	V.N.	1080
Otto	J.	1113
Ovchar	O.V.	544
Pérez-Vega	C.	617
Pałeczny	E.	379, 485
Pannier	P.	379, 485, 1136
Papa	E.	130
Pastorino	M.	733
Pavlov	A.S.	1080
Pearson	L.W.	260
Pedro	J.C.	739, 820
Peixeiro	C.	579
Pejanovic	M.	135
Pereverzeva	L.	838
Perez	S.	745
Perez-Vega	C.	617
Petrov	P.K.	196
Pezo	D.	347
Picard	D.	709
Pierantoni	L.	937
Pino	A.G.	573
Piotrowski	J.K.	697
Pisoni	U.	692
Plattner	A.	676
Poisson	M.A.	1026
Pollard	R.D.	687, 1003, 1052
Polo	V.	285
Poplavko	Y.	838
Popovich	R.	755
Porra	V.	219
Postoyalko	V.	1052
Pouysegur	M.	7
Pregla	R.	229
Prokopenko	Y.	838
Prudan	A.M.	1020
Pugh	E.N.	978
Puska	P.P.	512
Qian	Y.	181
Railton	C.J.	175, 550, 715
Ramirez-Garcia	R.	767
Rangelow	I.W.	375
Ranieri	P.	1076
Raskin	J.P.	1008
Ravanelli	R.	1086
Raisainen	A.V.	681, 880

Reiter	G.	168	Seo	M.K.	798
Richalot	E.	506, 854	Serres	M.	303
Richter	H.	26	Shafai	L.	254
Rieckmann	C.	561, 1270	Shafir	I.	668, 671
Ritter	D.	1240	Shavit	R.	273
Riva	G.	130	Shemesh	Y.	1186
Rivkin	T.	1020	Sherman	V.	909
Rizzoli	V.	826	Shi	F.	375
Roh	T.M.	97, 415	Shigesawa	H.	779
Rojansky	V.	567	Shin	J.	97
Rosario	M.J.	761	Shirakawa	K.	432
Roselli	L.	773, 810	Shtrikman	I.	624
Rosen	A.	984	Sierra	M.C.	573, 1201
Rosen	H.	984	Sihvola	A.	203, 1252
Rosenbaum	L.B.	792	Singh	P.	727, 1181
Rowe	M.P.	978	Sinnesbichler	F.	428
Ruoss	H.O.	556	Sipus	Z.	359
Russer	P.	538, 848, 937, 943, 949	Snowden	C.M.	687
			Sobhy	M.	1301
Rutkowski	A.	51, 579	Sokolovsky	V.	1080
Sabban	A.	163, 671, 1186	Som	F.	309
			Sordi	S.	773
Sahuc	C.	146	Sorrentino	R.	490
Sajin	G.	596	Spiegel	S.J.	460
Sajin	M.	596	Sporkmann	T.	93, 1360
Sakuno	K.	903	Stec	B.	51
Salazar-Palma	M.	767, 1133	Stiebler	W.	1070
Salvador	C.	354	Stolze	A.	324
Samaniego	J.	1295	Stotz	M.	832, 1064, 1122
Sanchez	M.G.	119		G.B.	1086
Santarelli	A.	422	Stracca	E.	481
Sarkar	T.K.	1133	Strid	M.G.	254
Saryo	T.	454	Stubbs	Y.D.	544
Sato	H.	903	Stupin	E.	903
Savopol	T.	596	Suematsu	Y.S.	97, 415
Sawan	M.	336	Suh	Y.	749
Schaefer	A.	1070	Sun	A.	1076, 1198
Scheck	H.O.	341	Suriani	V.	909
Schiek	B.	62	Svishchev	P.J.F.	45
Schlechtweg	M.	1030	Swart	Y.A.	1041
Schmale	I.	328, 375	Takchenko	J.L.	749
Schmegner	K.E.	933	Tauritz	R.	1360
Schmidt-Szalowsk	M.	897	Tempel	Y.	877
Schneider	J.	448, 832	Thodesen	M.J.	1003
Scholz	W.	375	Thornton	C.	56
Schreurs	D.	721, 921	Toker	T.	14
Schwab	W.	391	Tokumitsu	C.	949
Schübler	M.	104	Tomassi	I.	14
Scott Tyo	J.	978	Toyoda	T.	39
Sebastian	J.L.	114	Troll	G.	1122
Seeds	A.	309	Trummer	M.	779
Segall	E.	998	Tsuji	V.G.	544
Seghettini	M.	1198	Tsykalov	J.K.	903
Segovia	D.	1201	Twynam	S.	1192
Seguinot	C.	379, 485, 1136	Ueda	K.	1192
			Umez	C.M.H.	157
Sehm	T.	880	Unal	T.	1092
			Uusitupa		

Vahldieck	R.	496, 1216	Wiatr	W.	897
Vainikainen	P.	464, 584	Wight	J.S.	254
Van der Vorst	M.J.M.	605	Winebrand	M.	567
Van Raay	F.	375	Wolff	I.	93, 1360
Van Rossum	M.	921	Wong	M.F.	506, 854, 866
VanderVorst	A.	984, 303	Wordenweber	R.	909
Vanhoenacker	D.	1008	Yaginuma	T.	215
Vannini	G.	422	Yagoubov	P.	972
Veljovic	Z.	135	Yagura	M.	903
Vendik	O.G.	196, 318	Yakover	I.M.	955
Vendik	I.	318, 1347	Yakuwa	N.	454
Vered	M.	269	Yamada	A.	903
Verspecht	J.	921	Yamaguchi	T.	215
Verver	C.J.	254	Yanovsky	F.J.	157
Veszely	G.	168	Yefimov	B.P.	209
Vieira	J.C.	1222	Ylamurto	T.	341
Viitanen	A. J.	512	Yoshikawa	H.	703
Volgyi	F.	168	Young	L.	891
Vossiek	M.	1127	Young	P.R.	1, 631
Vountesmeri	V.	838	Yushchenko	A.	838
Wada	K.	1192	Zaitzer	A.	909
Wakabayashi	T.	1154	Zaki	K.	784
Walter	M.	721	Ze'evi	E.	75
Wang	W.	260	Zehentner	J.	1264
Wanielik	G.	832	Zhang	W.	232
Wasige	E.	375	Zhang	Y.H.	1014
Weigel	R.	1323	Zhu	Y.	903
Weiss	M.	1103	Zilbershtein	M.	153
Wenger	J.	832, 1064, 1122	Zirath	H.	1234
Wettergren	J.	611	Zoref	S.	668
Whitefield	D.	442	Züfle	K.	448

1996 EuMC MICROWAVE PRIZE

Each year the EuMC Management Committee awards the EuMC Microwave Prize for the best paper presented at the Conference. Selection is based on originality, value and method and was judged on the quality of both written and oral presentation.

The 1996 prize was awarded to the following paper:

"Novel FMCW Radar System Concept with Adaptive Compensation of Phase Errors"

by M. Vossiek, P. Heide, M. Nalezinski and V. Mágori

SIEMENS AG - Corporate Technology

Dept. ZT KM 1, D-81730 Munich / Germany.



Martin Vossiek

Martin Vossiek was born in Dortmund, Germany, in 1964. He received the Dipl.-Ing. degree in 1991 and the Dr.-Ing. degree in 1996 from the Ruhr University Bochum. From 1989 to 1990 he worked on ultrasound imaging systems for dermatology.

Since 1990 he is with Siemens Corporate Technology in Munich. From 1990 to 1996 he was mainly engaged in ultrasonic sensor systems for industrial automation. In 1996, Dr. Vossiek joined the microwave and surface acoustic wave group, where he is developing advanced concepts and algorithms for commercial microwave and SAW sensor systems.



Patric Heide

Patric Heide, was born in Siegen, Germany in 1966 and received his Dipl.-Ing. and Dr.-Ing. degrees in electrical engineering from the University Siegen in 1991 and 1994, respectively.

He is involved in the sensor development at Siemens Corporate Technology in Munich since 1991, where he has built up substantial experience on microwave and millimeterwave technology.

Dr. Heide is the head of the 'microwave sensor group' at Siemens ZT, where he is responsible for the Siemens' R&D activities in the field of microwave sensor systems for industrial, vehicular and domestic applications.



Martin Nalezinski

Martin Nalezinski was born in Heidelberg, Germany in 1966. He received his Dipl.-Ing. degree in electrical engineering from the Technical University of Munich in 1992.

After this, he worked in the surface acoustic wave production facility at Siemens Matsushita, Munich.

In 1994, he started his dissertation project at Siemens Corporate Technology in Munich, where he is developing 24 GHz sensor components for a high-precision distance measurement system for industrial process automation.



Valentin Mágori

Valentin Mágori was born in Bratislava, Czechoslovakia in 1938. He received the Dipl.-Phys. degree in 1968 from the Ludwig-Maximilian University, Munich. From 1968 to 1970 he worked on neurophysical experiments at the 'Gesellschaft für Strahlen- und Umweltforschung' in Neuherberg. He joined Siemens Corporate Technology in Munich in 1970, where he has worked on ultrasonic systems for more than 20 years. Since 1980 he has managed the development of ultrasonic, microwave and surface acoustic wave sensors. In 1996, he received the Dr.-Ing. h.c. degree from the 'Universität der Bundeswehr' in Munich.

CONTENTS - VOLUME I

	<u>PAGE</u>
OPENING SESSION.....	1-13
FOCUSED SESSION A1	14-38
SESSION B1.....	39-68
SESSION C1.....	69-92
SESSION D1	93-118
SESSION A2	119-145
SESSION B2	146-162
SESSION C2	163-189
SESSION P1 (POSTERS)	190-335
SESSION A3	336-364
SESSION B3	365-390
FOCUSED SESSION C3	391-414
SESSION D3	415-436
SESSION A4	437-463
SESSION B4	464-484
SESSION C4	485-500
SESSION P2 (POSTERS)	501-635
PLENARY SESSION I	636-661

OPENING SESSION

	<u>Page</u>
OP.1 Microwaves in Your Future	
L. Young, USA.....	1-6
OP.2 How MMIC Technologies Are Improving Satellite Transponders	
J.-L. Cazaux, G. Gregoris, M. Pouysegur, France.....	7-13

FOCUSED SESSION A1 - MULTILAYER, MCM & PACKAGING TECHNOLOGY

A1.1 A Basic Concept of Microwave Design Automation Based on Three-Dimensional Masterslice MMIC Technology	
I. Toyoda, T. Tokomitsu, M. Aikawa, Japan.....	14-19
A1.2 T/R Module Packaging - A Challenge for Future System Design	
W. Bösch, Germany.....	20-25
A1.3 Evaluation of Glob Top and Underfill Encapsulated Active and Passive Structures for Millimeter Wave Applications	
G. Baumann, E. Müller, F. Buchali, D. Ferling, H. Richter, W. Heinrich, Germany.....	26-31
A1.4 Innovative Multilayer Technologies for Active Phased Array Antennas	
B. Ledain, J. L. Herblot France.....	32-38

SESSION B1 - RADAR SYSTEMS & CIRCUITS

	<u>Page</u>
B1.1 Motion Monitoring With a Millimeter Wave Radar Sensor	
T. Troll, J. Detlefsen, Germany.....	39-44
B1.2 Collision Avoidance Radar Able to Differentiate Objects	
P.J.F. Swart, L.R. Nieuwkerk, The Netherlands.....	45-50
B1.3 A Planar Microwave Phase Discriminator	
B. Stec, A. Rutkowski, Poland.....	51-55
B1.4 A Novel Low Noise Active Circuit Replacement Criteria for Parallel Fed Large Scale Active Antenna Arrays	
S. Demir, C. Toker, A. Hizal, Turkey.....	56-61
B1.5 A High Precision Analog Frequency-Ramp Generator Using a Phase-Locked-Loop Structure	
T. Musch, B. Schiek, Germany.....	62-68

SESSION C1 - ANTENNA APPLICATIONS

C1.1 Dual Shaped Reflector Antenna for Airport CW Radar	
J. Meshy, M. Negev, Israel.....	69-74
C1.2 Electrical and Mechanical Design of the Amos Communication Antenna Subsystem	
M. Lieke, C. Hunscher, T. Kutscheid, E. Ze'evi, Germany.....	75-80
C1.3 Novel Retrodirective Beam Formation Techniques	
S.L. Karode, V.F. Fusco, UK.....	81-86
C1.4 Lumped Coupled Ring Antenna Array	
D.E.J. Humphrey, V.F. Fusco, UK.....	87-92

SESSION D1 - THERMAL & NOISE MODELLING OF DEVICES

	<u>Page</u>
D1.1 Nonlinear Modeling Including the Self Heating Effect and Load-Pull Measurements of GaIn P/GaAs Power HBTs M. Akpinar, R. Follmann, T. Sporkmann, I. Wolff, Germany.....	93-96
D1.2 A Novel Extraction Method for Temperature Dependent Large Signal Equivalent Circuit Model of HBT Y.S. Suh, T.M. Roh, Y. Kim, J. Shin, B. Kim, South Korea.....	97-103
D1.3 Thermal Coupling in Multi-finger Heterojunction Bipolar Devices M. Schübler, V. Krozer, H.L. Hartnagel, Germany, J.G. De La Fuente, Spain.....	104-108
D1.4 Influence of the Model Parameters on the Noise Performance of Double-Polysilicon BJTs for Microwave LNA's A. Caddemi, M. Sannino, Italy.....	109-113
D1.5 Drain Temperature Dependence on Ambient Temperature for a Cryogenic Low Noise C-Band Amplifier S. Munoz, J.D. Gallego, J.L. Sebastián, J.M. Miranda, Spain.....	114-118

SESSION A2 - MOBILE & WIRELESS SYSTEMS

A2.1 Modeling of Propagation in Outdoor Microcells at 62.4 GHz A. Hammoudeh, E. Grindrod, UK, M.G. Sanchez, Spain.....	119-123
A2.2 Unified Approach to Predict Los Characteristics in the Urban Microcellular Environments N. Blaunstein, M. Levin, Israel.....	124-129
A2.3 Characterization of Mm-Wave Indoor Propagation With Directive Antennas G. Riva, V. Degli-Esposti, E. De Ponti, L. Ferrucci, E. Papa, Italy.....	130-134
A2.4 A New Technique for Performance Improvement of Mobile Radio Systems M. Pejanovic, Z. Veljovic, Yugoslavia.....	135-138
A2.5 Interoperable 5.8 GHz DSRC Systems as Basis for Europeanwide ETC Implementation W. Grabow, W. Dettlfsen, Germany.....	139-145

SESSION B2 - RADAR APPLICATIONS

B2.1 Design and Performance of the Transmit/Receive Module and the Tile Subsystem of Advanced Synthetic Aperture Radar (ASAR) for ENVISAT Satellite A. Cazal, J.L. Cazaux, C. Sahuc, P. Ginestet, France.....	146-149
B2.2 A Headway Control System Concept Using Dual-Mode Millimeter-Wave Radar K. Konno, S. Koshikawa, Japan.....	150-152
B2.3 Wave Pattern of a Buried Leaky Coaxial Cable Under Local Inhomogeneous Conditions N. Blaunstein, Z. Dank, M. Zilbershtein, Israel.....	153-156
B2.4 Radar Study of Polarization Structure of Precipitation F.J. Yanovsky, C.M.H. Unal, The Netherlands, V.K. Korban, Ukraine.....	157-162

SESSION C2 - ANTENNA STRUCTURES

	<u>Page</u>
C2.1 A Comprehensive Study of Losses in Mm-Wave Microstrip Antenna Arrays A. Sabban, Israel.....	163-167
C2.2 A Whispering Gallery Mode Transducer Using Microstrip-Slot Antenna Exciter F. Vylgyi, G. Reiter, T. Berceli, G. Veszely, Hungary.....	168-174
C2.3 The Analysis of Medium Sized Arrays of Complex Elements Using a Combination of FDTD and Reaction Matching C.J. Railton, G.S. Hilton, UK.....	175-180
C2.4 A Ring-Laser Type Quasi-Optical Oscillator Using Leaky-Wave Antenna W. Fu, Y. Qian, T. Itoh, USA.....	181-184
C2.5 Active Wideband Antenna With Circular Polarization A. Nesic, S. Jovanovic, Yugoslavia.....	185-189

SESSION P1 (POSTERS)

P1.1 Characterisation of Schottky Diode Performance by Numerical Simulation Couples With Harmonic Balance J. Grajal, J. Gismero, F. Maldonado, E. Gonzalez, Spain; V. Krozer, C.I. Lin, Germany.....	190-195
P1.2 HTS/Ferroelectric CPW Structures for Voltage Tuneable Phase Shifters O.G. Vendik, P.K. Petrov, Russia; R.A. Chakalov, S. Gevorgian, Z. Ivanov, E.F. Carlsson, Sweden.....	196-202
P1.3 Electromagnetic Shielding Effects Using Chiral and Other Complex Materials A. Sihvola, M. Ermutlu, Finland.....	203-208
P1.4 Multifrequency Modes and Output Signal Modulation-Type BWTs B.P. Yefimov, M.V. Milcho, G.Ya. Levin, Ukraine.....	209-214
P1.5 Channel Dropping and Branching Filters Using NRD-Guide for Millimeter - Wave Integrated Circuits T. Yaginuma, T. Yamaguchi, T. Fukuda, I. Ohtomo, Japan.....	215-218
P1.6 Monolithic Artificial Transmission Line Balanced Frequency Doublers P. Kangaslahti, P. Alinikula, V. Porra, Finland.....	219-224
P1.7 Ka-Band FET Frequency Quadrupler With Low Group Delay Variation Z. Nativ, A. Kadosh, S. Matarasso, Israel.....	225-228
P1.8 Analysis of Circular Waveguides With Azimuthally Magnetized Ferrite K.P. Ivanov, R. Pregla, Germany.....	229-231
P1.9 UTD-Based Path Loss Prediction With Experimental Validations for Micro-Cellular Mobile Radio Communications W. Zhang, J. Lahtenmaki, Finland.....	232-237
P1.10 Regular Linearization Principle for Nonlinear Circuits Y.M. Bruck, Israel.....	238-242
P1.11 Linearization of P-N Junctions by the Same P-N Junctions Y.M. Bruck, Israel.....	243-248
P1.12 Linearization of P-N Junctions by Linear Elements Y.M. Bruck, Israel.....	249-253
P1.13 Development of a 30 GHz, Wireless LAN Transmit/Receive Module M.G. Stubbs, C. Glaser, H. Do Ky, C.J. Verver, L. Shafai, J.S. Wight, Canada.....	254-259
P1.14 Frequency Tunable MESFET Active Patch Antenna/Oscillators W. Wang, L.W. Pearson, USA.....	260-265
P1.15 2 to 18 GHz Triple Balanced Mixer for MMIC Implementation A. Milano, Israel.....	266-268
P1.16 6 to 18 GHz Phase Shifter: A New High Performance Switch MESFET A. Milano, I. Levin, M. Vered, Israel.....	269-272

	<u>Page</u>
P1.17 Summation Topologies for High Power Amplifier Based on MMIC Technology	
R. Shavit, D. Gabbay, M. Garzon, Israel.....	273-278
P1.18 An Automated Emulator of Mobile Satellite Link	
C. Briso, J.I. Alonso, Spain.....	279-284
P1.19 Non-Linear Photonic Mixers for Up and Down-Converting Links Based on Mach-Zehnder Intensity Modulators	
J.M. Fuster, J. Marti, V. Polo, Spain.....	285-296
P1.20 Efficient Determination of Nonlinear Microwave Circuits Operating Regions	
I. Barbancho-Pérez, I. Molina-Fernández, Spain.....	297-302
P1.21 Wideband Analytical Model of an Open-Ended Microstrip Line Under Illumination	
M. Serres, I. Huynen, A. VanderVorst, Belgium.....	303-308
P1.22 Noise and Loss Characteristics of Microwave Direct Modulated Optical Links	
I. Frigyes, I. Habermajaer, B. Molnar, F. Som, Hungary; A. Seeds, UK.....	309-317
P1.23 Simulation of Linear and Non-Linear Characteristics of High-Tc Superconducting Resonators and Filters	
O.G. Vendik, I. Vendik, Sweden; D. Kaparkov, M. Gubina V. Kondratiev, Russia.....	318-323
P1.24 A Simplified Physics-Based Quasi-Static MSM Photodiode Model	
M. Djebbari, G. Kompa, A. Stolze, Germany.....	324-327
P1.25 An Improved Physics-Based Nonquasi-Static FET-Model	
I. Schmale, G. Kompa, Germany.....	328-330
P1.26 Simulation of High Bit Rate Optical Fibre Communications Link Using a Physics Based Laser Diode Model	
J. Barnard, UK.....	331-335

SESSION A3: MOBILE & WIRELESS CIRCUITS

A3.1 Linearization of Microwave Emitters Using an Adaptive Digital Predistorter	
E.G. Jeckeln, F.M. Ghannouchi, M. Sawan, Canada.....	336-340
A3.2 Six-Port Direct Conversion Receiver	
J. Hyrylainen, L. Bogod, S. Kangasmaa, H.O. Scheck, T. Ylamurto, Finland.....	341-346
A3.3 Modulation Imperfections in IS54 Dual Mode Cellular Radio	
A. Brilliant, D. Pezo, Israel.....	347-353
A3.4 A GaAs MMIC Digital Phase Modulator	
G. Avitabile, A. Cidronali, C. Salvador, G. Manes, Italy.....	354-358
A3.5 Radiation from Directive Antennas Close to Human Tissue	
R. Leijon, Z. Sipus, P.S. Kildal, Sweden.....	359-364

SESSION B3: PACKAGING & INTERCONNECTION TECHNIQUES

	<u>Page</u>
B3.1	Improving of High-Speed Modules by an Advanced Chip-In Board Assembly
	G. Hanke, W.D. Nohr, Germany..... 365-370
B3.2	RF and DC Multilayer: The Multi Function Concept
	P. Langlois, The Netherlands..... 371-374
B3.3	Air Bridge Based Planar Hybrid Technology for Microwave and Millimeter Wave Applications
	E. Wasige, G. Kompa, F. Van Raay, I. Schmale, I.W. Rangelow, W. Scholz, F. Shi, R. Kassing, R. Meyer, M.C. Amann, P. Hudek, Germany..... 375-378
B3.4	Scattering Parameters and Mode Conversion in Asymmetric CPW-Microstrip Overlap Transitions
	L. Kadri, P. Pannier, F. Huret, P. Paleczny, C. Seguinot, P. Kennis, France..... 379-384
B3.5	Analysis of Transients in Coupled Tapered Lossy and Frequency-Dependent Transmission Lines Using SPICE
	J.I. Alonso, J.M. Gomez, Spain..... 385-390

FOCUSED SESSION C3: MICROWAVE ACTIVE FILTERS

C3.1	Low-Noise Microwave Active Filters in Planar Realizations
	W. Menzel, W. Schwab, Germany..... 391-396
C3.2	Variety of Approaches to Designing Microwave Active Filters
	B. Kapilevich, Russia..... 397-408
C3.3	Microwave Active Filters For Wireless Applications: Systems Approach
	P. Alinikula, R. Kaunisto, Finland..... 409-414

SESSION D3: NON-LINEAR DEVICE MODELLING

D3.1	A New Simple Extraction Method for Higher Order Components of Channel Current in GAAs MESFET
	T.M. Roh, Y.S. Kim, Y.S. Suh, B. Kim, South Korea..... 415-421
D3.2	A Finite-Memory Nonlinear Model for Microwave Electron Devices
	F. Filicori, G. Vannini, A. Santarelli, Italy..... 422-427
D3.3	Large Signal and Noise Modeling of HEMT Devices Including Frequency and Temperature Effects
	F. Sinnesbichler, T. Felgentreff, G.R. Olbrich, Germany..... 428-431
D3.4	Genetic Determination of Large-Signal HEMT Model
	K. Shirakawa, N. Okubo, Japan..... 432-436

SESSION A4: MILLIMETER-WAVE INTEGRATED CIRCUITS

	<u>Page</u>
A4.1	Monolithic Up/Down Converters for Millimeter-Wave Wireless Networks
	M. Madihian, L. Desclos, K. Maruhashi, K. Onda, M. Kazuhara, Japan..... 437-441
A4.2	Low-Loss High-Power Ka-Band Multipole Multithrow MMIC PIN Switch
	M. Daly, D. Whitefield, Z. Bogan, D. Bartle, J. Delconte, USA..... 442-447
A4.3	Coplanar Switches in PHEMT Technology from X- to W-Band
	K. Zölle, W.H. Haydl, H. Massler, R. Bysch, J. Schneider, Germany..... 448-453
A4.4	A Novel MultiChip Module Unifying Transmitter and Receiver at 51 GHz
	N. Yakuwa, M. Akaishi, T. Kaneko, T. Saryo, Japan..... 454-459
A4.5	Micro-Machined GCPW Resonators and Filters for Applications at Millimetric Wave Frequencies
	S.J. Spiegel, Y. Nemirovsky, Israel..... 460-463

SESSION B4: MICROWAVE MEASUREMENTS APPLICATIONS

B4.1	Wideband Indoor Radio Channel Measurements at 5.3 GHz
	J. Kivinen, P. Vainikainen, Finland..... 464-469
B4.2	Time Domain Antenna Measurements: Implementation and Verification of a Novel Technique
	R.V. Jongh, M. Hajian, L.P. Ligthart, The Netherlands..... 470-475
B4.3	A Millimeter-Wave Frequency Extender for Microwave Network-Analyzers
	B. Geck, J. Marquardt, Germany..... 476-480
B4.4	A Membrane Probe for Testing High Power Amplifiers at mm-Wave Frequencies
	S. Basu, P. Nussbaumer, E. Strid, USA..... 481-484

SESSION C4: WAVEGUIDE DISCONTINUITIES

C4.1	Analytical and Full-Wave Characterization of Multimode Waveguide Discontinuities
	P. Pannier, E. Paleczny, C. Seguinot, F. Huret, P. Kennis, France..... 485-489
C4.2	A Matrix Decomposition Technique for the Efficient Analysis of Complex Waveguide Networks
	F. Alessandri, R. Sorrentino, Italy..... 490-495
C4.3	Scattering of TE₁₁ Mode from Two Asymmetric Ridges of Finite Thickness in a Circular Waveguide
	S. Amari, J. Bornemann, Canada, R. Vahldieck, Switzerland..... 496-500

SESSION P2 (POSTERS)

	<u>Page</u>
P2.1	Design of Multilayer 2-Pole Band Pass Filter With Additional Poles Using Closed Loop Resonator
	H.J. Hong, D.P. Jang, I.S. Kim, C.S. Kim, M.H. Chung, D. Ahn, Korea..... 501-505
P2.2	Antennas Analysis Using Edge Elements and Spherical Modes Expansion
	E. Richalot, M.F. Wong, V. Fouad-Hanna, H. Baudrand, France..... 506-511
P2.3	Polarization Transformer Constructed from Chiral Slab and Soft and Hard Surface
	P. P. Puska, A. J. Viitanen, Finland..... 512-517
P2.4	Microwave Ferroelectric Superconducting Phase Shifter
	F. Abbas, J.C. Gallop, C.D. Langham, UK..... 518-522
P2.5	Susceptibility Analysis of Arbitrarily Shaped 2-D Dielectric Screens Using the Generalized Scattering Matrix Method
	J.V. Balbastre, L. Nuno, M. Bort, E. de los Reyes, Spain..... 523-531
P2.6	Conductive Substrate Losses in Coplanar and Microstrip Transmission Lines
	W.H. Haydl, Germany..... 532-537
P2.7	Modelling of Multichip module Interconnections by the TLM Method and System Identification
	T. Mangold, P. Russer, Germany..... 538-543
P2.8	Monolithic Filters and Frequency-Separation Devices Based on the Ceramic Resonators
	V.G. Tsykalov, A.G. Belous, O.V. Ovchar, Y.D. Stupin, Ukraine..... 544-549
P2.9	Transient Analysis of Printed Circuit Board Layouts Using a Time Domain Solution of Kirchhoff's Network Equations
	C.S.L. Goh, C.J. Railton, UK..... 550-555
P2.10	Multiple Probe Nearfield Scanning for EMC-Investigations
	H.O. Ruoss, J. Christ, F.M. Landstorfer, Germany..... 556-560
P2.11	TEM-Modes in Slot-Coupled Waveguides
	A.S. Omar, C. Rieckmann, A. Jöstingmeier, Germany..... 561-566
P2.12	Enhanced Gain Patch Antennas at Millimeter Waves
	V. Rojansky, M. Winebrand, Israel..... 567-572
P2.13	Synthesis of Circularly Polarised Radial Line Slot Array
	M. Sierra, M.V. Isasa, A.G. Pino, M.C. Sierra, Spain..... 573-578
P2.14	Microstrip Patch Array for the Mobile Terminal Antenna of a Mobile Communication System
	T. Rutkowski, Poland, C. Peixeiro, Portugal..... 579-583
P2.15	Profile Inversion of Stratified Dielectric Media Using the Two-Step Reconstruction
	V.A. Mikhnev, P. Vainikainen, Finland..... 584-588
P2.16	The Shielding Effects of Lossy Dielectric Material for Three Layered Elliptical Human Model
	S. Nishizawa, O. Hashimoto, Japan..... 589-595
P2.17	Low Power Microwave Effects on Erythrocyte Membranes
	G. Sajin, R. Ion, E. Kovacs, T. Savopol, A. Dinu, M. Sajin, Romania..... 596-600
P2.18	A Laser Radar for Precise 2D- and 3D-Object Imaging
	A. Biernat, G. Kompa, Germany..... 601-604
P2.19	Scan-Optimized Integrated Lens Antennas
	M.J.M. Van der Vorst, P.J.I. De Maagt, M.H.A.J. Herben, The Netherlands..... 605-610
P2.20	Mutual Coupling Between Transverse Slots in Cylindrical Structures
	J. Wettergren, Sweden..... 611-616

	<u>Page</u>
P2.21 A Simple Approach to a Statistical Path-Loss Model for Indoor Communications	
C. Pérez-Vega, J.L. Garcia, Spain.....	617-623
P2.22 Analytical Analysis of Antennas in the Presence of a Multilayered Dielectric Sphere With Application to Hand Held Terminals	
I. Shtrikman, N. Henze, H. Fruechting, H. Lindenborn, Germany.....	624-630
P2.23 A Low Loss Phase Shifter for Dielectric Waveguide Using Asymmetrical Guides	
P.R Young, R.J. Collier, P.G.G. Bianconi, UK.....	631-635

PLENARY INVITED SESSION I

Pl.1 Optical Synthesis Of Microwave Signals	
A.J. Seeds, UK.....	636-641
Pl.2 Millimeter Wave Fiberoptic Links	
P. Herczfeld, USA.....	642-648
Pl.3 Interconnects and Packaging For MMIC's	
W. Menzel, Germany.....	649-654
Pl.4 The Israeli GaAs Foundry	
I. Levin , Elta Ltd., Ashdod, Israel.....	655-661

VOLUME I

MICROWAVES IN YOUR FUTURE

Leo Young
Filtronic-Comtek,
31901 Comtek Lane
Salisbury, MD 21801, USA

SUMMARY

The microwave scene is changing rapidly. The main conclusions may be summarized as follows: 1. Wireless communications rivals Defense applications as the main driver of microwave technology, 2. The internationalization of microwave technology continues, 3. Technology-wise the distinctions between microwaves and other RF are beginning to blur, 4. U.S. factory sales of microwave components have not shared in the growth of electronics products sales generally (but this may not be so when microwave and RF are taken together), 5. To be successful, the microwave engineer must complement his specialized knowledge with a broader understanding of related areas of technology, 6. There will be plenty of work to do for microwave engineers in the foreseeable future.

LIST OF CONTENTS

1. INTRODUCTION
2. MICROWAVES AFTER WORLD WAR II
3. FROM SLUMP TO UPTURN
4. THE INTERNATIONALIZATION OF MICROWAVE TECHNOLOGY
5. SOME U.S. INDUSTRY NUMBERS
6. WHERE ARE THE OPPORTUNITIES?
7. CONCLUSION

1. INTRODUCTION

Microwaves have been known for more than a century, mostly as electromagnetic waves. Originally scientific and experimental, they were developed and applied rapidly during World War II. Now another phase of rapid development has set in because of developments in wireless communications. New semiconductor devices, high-Q ceramic resonators, high-temperature superconductors, nanomechanics, and other previously undreamed-of developments are constantly enhancing our ability to design more capable microwave systems. Here is one person's view, seen from the other side of the Atlantic.

2. MICROWAVES AFTER WORLD WAR II

Radar, discovered just before World War II, probably did more than any other scientific development to win the Battle of Britain. During the "Cold War" that followed, the

momentum of microwave R&D was kept up by Defense funding, especially in the United States. With the end of the Cold War a decade or so ago, the U.S. government sharply reduced its Defense budget, including funding of microwave R&D. Students, seeing the writing on the wall, shunned microwave courses and voted with their feet in favor of software and other courses where they saw better job opportunities. To quantify these impressions somewhat, I shall attempt to relate them to the rise and fall and rise (again) in membership of the Institute of Electrical and Electronics Engineers (IEEE), in particular its Microwave Theory and Techniques Society (MTT-S).

The Institute of Radio Engineers (which merged with the American Institute of Electrical Engineers in 1962 to become IEEE) approved the formation of the MTT-S on March 7, 1952. In that year only one Transactions was published, consisting of 48 pages. The first national symposium was held in New York City on November 7, 1952, attended by 210 people. Ten papers were presented in one day. In January 1953 MTT-S paid-up membership stood at 471. Today MTT-S membership stands at 9,200 (up from 6,400 in 1980) and comes from all over the world. The 1996 annual international symposium in San Francisco, California, attracted some 9,000 people to the exhibition (up from 2,000 in 1980) and about 2,500 persons to the technical sessions (up from 1,000 in 1980). This year, the 1997 Symposium in Denver, Colorado, had 24 workshops associated with the main Symposium (in parallel sessions), spread over 6 days. Attendees had more than 500 papers to choose from. Whereas Symposium digests had remained pocket size until about the mid 1960's, the 1997 Digest and workshop proceedings were too heavy to carry away, and a special mailing service was opened at the convention site.

3. FROM SLUMP TO UPTURN

The slump in microwave fortunes between the end of the cold war and today's communications upsurge has a tail: *Student* membership is still down. Bottoming at 1,000 in 1982, and topping out at 1,600 in 1988, *student* membership has declined since 1989, dipping to 1,100 in 1996, showing that the stigma of job shortages still attaches to microwave engineering in young people's minds. (Numbers are rounded off to the nearest 100). By contrast, the corresponding numbers for *student* membership in the IEEE Communications Society are 2,900 (in 1980), 2,800 (in 1982, also a minimum), and rising steadily from there to 4,900 (in 1996). New courses at universities have been broadened from *Microwave* to *RF*. MTT-S *student* membership trends may still not have caught up with industry realities. Thus, with the pipeline not filled, it seems that (at least in the U.S.) young microwave engineers should have no difficulty finding interesting job opportunities in the foreseeable future.

THE INTERNATIONALIZATION OF MICROWAVE TECHNOLOGY

International IEEE student membership numbers are enlightening. *U.S. student* membership in 1980 was 26,700, peaked in 1985 at 37,100, and declined almost

constantly every year down to 20,400 in 1996. This is in stark contrast to *non-U.S. student* membership, which rose from 8,100 in 1980 to 20,400 in 1996, when it reached parity with U.S. student membership for the first time. IEEE *total (all grades) U.S. membership* in 1980 was 176,400, peaked in 1990 at 243,500, and in 1996 stands at 217,200; the corresponding *total non-U.S. membership* shows a steady rise every year from 37,500 in 1980 to 94,400 in 1996, going from 17-1/2 percent in 1980 to 30 percent in 1996, of the total IEEE membership of 311,500. I don't have the corresponding numbers for MTT, but I believe the trend is similar.

The internationalization of microwaves is reflected in the top leadership of the MTT-S as well. Its Administrative Committee (more or less equivalent to a Board of Directors) has had increasing numbers of international members for about 30 years, but its first non-American President was elected only this year. He is Professor Roger Pollard of Leeds University, England, who will take office in 1998.

Furthermore, a quick look at the MTT Transactions and Symposia Digests shows that the percentage of non-American contributors keeps rising both in the Transactions and at the Symposia. Microwaves have become an international activity with strong interactions from all over the world. Part of this is due to better communications, which itself is facilitated through microwaves.

5. SOME U.S. INDUSTRY NUMBERS

In the U.S. the trend in total factory sales of microwave components has not kept up with total factory sales of electronics products, according to figures published by the Electronics Industries Association and the Department of Commerce. To summarize the key features, whereas the dollars for microwave components have remained virtually constant from 1986 to 1994 (averaging \$1.25 billion +/- 10 percent, and showing no trend up or down), the corresponding dollars for all of electronics has been rising steadily in the same period from \$218 billion to \$321 billion, an increase of 48 percent in 8 years.

6. WHERE DO THE OPPORTUNITIES LIE?

Thus, forty years of mostly good times for microwave engineers were followed by roughly a decade of uncertainty, which has now been replaced by a period of great opportunity. However the current emphasis is more on development and application under commercial sponsorship than on R&D under government auspices. Hence there is less emphasis on basic research (which also trains engineers and builds up infrastructure, a major government concern), and more emphasis on commercial applications of microwaves (that depend heavily on yesterday's government spending on R&D). As the wheel turns, where will it stop next? Just as there are business cycles, so there are technology cycles, some random, some greatly influenced by outside events not controlled by engineers, such as the Cold War, which encouraged microwave technology.

Today the situation is very much in a state of flux. Commercial systems abound and compete, especially in communications; the outcome is often not clear.

Microwave technology narrowly defined is too small an area to detect trends. I shall therefore consider also 1) RF so long as the *techniques* are similar (mainly frequencies from 100 MHz to 100 GHz), 2) areas where the *theory* owes much to microwaves (such as optics, electro-optics, fiber optics, acoustics), and 3) technologies critical to microwave work (such as communications, or certain components or materials).

One area stands out: *Communications*. In fact, many of the other areas listed below contribute to communications technology, or depend on it, or use it, in some way.

- Communications, both Wireline and Wireless
 - o Fixed Installations/Satellite Broadcasts
 - ◆ Point-to-Point Communications
 - ◆ Point-to-Multipoint Communications
 - ◆ Multi-Channel Video Distribution Systems
 - ◆ Millimeter Waves carried over Optical Fibers
 - ◆ RF-to-Optics and Optics-to-RF conversion
 - ◆ Direct Broadcast Satellites
 - ◆ Wireless Local Area Nets (LAN), Wide Area Nets (WAN)
 - ◆ Multiple Access Methods(FDMA, TDMA, GSM, CDMA)
 - ◆ Digital Signal Processing
 - ◆ RF Circuits and Filters
 - ◆ Antennas (Phased Arrays, Adaptive Antennas, etc.)
 - ◆ Propagation of Radio Waves
 - o Mobile Telecommunications
 - ◆ Cellular Telephones
 - ◆ Personal Communication Systems
 - ◆ Small, Light-Weight Devices
 - ◆ Light-Weight, Long-Life Batteries
- Transportation/Intelligent Vehicles & Highways
 - o Traffic Safety
 - ◆ Anti-Collision Radar
 - ◆ Instantaneous up-to-date Information (Road conditions, Weather)
 - ◆ Communications (between Mobile and Station; Mobile to Mobile)
 - ◆ Emergency Calls with Automatic Vehicle Location

-
- o Navigation Aids
 - ◆ Using the Global Positioning System (GPS)
 - ◆ Using Cellular Phone Base Stations
 - o Tagging, Tracking, Identification
 - ◆ Tracking, ID (of people, cars, trucks, railroad cars)
 - ◆ Automatic Toll Collection
 - ◆ Data Cards (as for Service Records)
 - Sensors and Sensing
 - o Radiometric Sensing from Satellites (Crops, Water, Snow)
 - o Millimeter Wave Radar
 - o Environmental Monitoring (for Pollution, e.g., by Propagation Attenuation)
 - o Medical Diagnostics (Imaging, Infrared Sensing)
 - o Security Systems/Perimeter Guarding
 - Medical Applications
 - o Communications (as with distant Experts to guide Emergency Surgery)
 - o Knowledge Bases connected by Microwave Links
 - o Imaging (MRI, ultrasonic)
 - o Heating Biological Tissue for:
 - ◆ Ablation (removing harmful growth), Necrosis (killing harmful tissue)
 - ◆ Anastomosis (rejoining tissue cut by surgery)
 - ◆ Angioplasty (widening obstructed arteries to increase blood flow)
 - Defense
 - o Electronic Warfare
 - o Radar, Sonar, Radiometers
 - o Detection/Recognition/Identification Techniques
 - o Tracking and Guidance
 - o High-speed Coding/Computing
 - Digital Computers
 - o Microwave Circuits and Phenomena in Digital Computing
 - o Gigahertz Clock Rates
 - o Software
 - o Computer Aided Design (including design of complex IC's from the physics)

- Special Materials, Devices, Components, and Techniques
 - o Optics/Electro-Optics
 - o Surface Acoustic Waves and other *Non*-Electromagnetic Waves
 - o Emerging Electronic Materials (Semiconductors, High-Q Ceramics)
 - o Microwave Circuits and Filters
 - o Microwave Lumped-Circuit Elements
 - o Receivers (Low-Noise, Linear, Constant Time Delay)
 - o High-Power Amplifiers
 - o Optical Amplifiers
 - o Antennas
 - o Non-reciprocal Devices
 - o High-Temperature Superconductors
 - o Nanomechanics
 - o Metrology
 - o Packaging
 - o International Standards

This list is far from complete. Some particulars could be listed under more than one heading. Several of the areas listed are not microwave devices, but are critical to the acceptance of microwave systems. Every engineer needs to make his or her own list.

7. CONCLUSION

Successful engineers must be aware of all technologies relating to their own area of specialization, and should be ready to find out more whenever the need arises. They must not only keep up with developments in their own technology area, but they should also understand how competing technologies compare with their own.

That is the double challenge which makes being an engineer so interesting.

ACKNOWLEDGMENT

I wish to thank the many people and organizations who helped me collect information, among them IEEE staff, members of the MTT-S Administrative Committee; and in particular, Ferdo Ivanek and Don Cox for up-dating me on modern communications; Arye Rosen for explaining medical applications; Ted Saad for providing historical background; as well as Steve Adam, Bert Berson, Erich Bloch, Eliot Cohen, Jim Crescenzi, David Messerschmitt, Howard Ellowitz, Harlan Howe, Tatsuo Itoh, Irwin Jacobs, Keith Kennedy, Don Parker, Harold Sobol, Dick Sparks, Peter Staecker, Frank Sullivan, and many others who gave me valuable insights for the paper.

HOW MMIC TECHNOLOGY IS IMPROVING SATELLITE TRANSPONDERS

Jean-Louis CAZAUX, Guy GREGORIS, Michel POUYSEGUR and Michel SOULARD*

ALCATEL-ESPACE, 26, Avenue J.F. Champollion, 31037 TOULOUSE, FRANCE

Tel: 33-(0)5-61-19-57-59; Fax: 33-(0)5-61-19-52-74

LEMNAC, 5 rue N. Pons, 92734 NANTERRE, FRANCE

Abstract: Fifteen years after their first demonstration, MMICs are now rapidly conquering the world of space electronics. The driving force behind MMIC development have been miniaturization, cost reduction and higher reliability. MMICs have first been introduced into GEO Telecommunication satellites with a new generation of compact equipment. After these first convincing demonstrations, MMICs have now become an absolute necessity for turning into reality future satellites with active antennas, observation radars or future systems such as LEO constellations. The paper presents several major achievements for space programs and discusses about procedures to fly these advanced microelectronics.

1. INTRODUCTION

Systems designers realize better nowadays that MMICs can fit the demanding trends of the very competitive space business: manufacturing of payload equipment must be faster, cheaper and more reliable when changing from one generation to another [1].

The advantages of MMICs are:

- ⇒ an obvious size decrease leading to a mass reduction of the equipment
- ⇒ low cost and a good uniformity for the production of large series of identical circuits
- ⇒ low cost for the equipment manufacturing due to the quasi-absence of tuning
- ⇒ reduction of parts count and interconnects which improves reliability

However, the advantages of MMIC insertion could only be drawn after a large amount of work has been carried out to improve design techniques, manufacturing yield in foundries and packaging methods.

The purpose of this paper is to present several major achievements for space-borne MMIC-based equipment.

2. MMIC INSERTION INTO SPACE-BORNE EQUIPMENT

A classical telecom payload includes several units where MMICs can be inserted:

- Receivers transposing the input frequencies down to the output frequencies.
- Channel Amplifiers (CAMP) adjusting the gain of each channel of the repeaters and operating at the output frequencies. The CAMP may include an ALC (Automatic Level Control). Also, the CAMP may be followed by a Linearizer in order to limit the effects of non-linearity.
- Solid State Power Amplifiers (SSPA) mostly up to C-Band where they fairly compete with Traveling Wave Tube Amplifiers (TWTAs). The latter is more used at Ku-Band and higher.
- TTC (Telemetry, Tracking and Command) Receivers and Transmitters.

Only the two first functions are discussed in this section because they well represent the evolution with these microelectronics.

2.1 CAMPs and Linearizers

In most space companies, MMICs have been first applied in CAMPs. This was prompted by the fact that this equipment is most commonly used in rather large numbers for commercial satellites. Another

motivation for this choice is the use of simple low level circuits, mainly amplifiers and gain controllers. Ku-Band CAMPs were the firsts to be designed and manufactured with MMICs. Three types of circuits were used: Low Level Amplifier, Variable Attenuator and Flatness Corrector [2]. At this occasion, a MMIC process has been formally space-qualified for the first time [3] following the methodology proposed by the French Administration [4].

As an illustration, the Ku-Band CAMP on-board AMOS includes 7 MMICs. Its gain is adjustable from 51 dB to 16 dB, with 0.5 dB step resolution. The flatness is better than 0.5 dBpp from 10.9 to 11.7 GHz and the DC consumption is 2 W. This CAMP has permitted a mass and cost reduction by a factor 2.5 from the previously employed discrete FETs hybrid families in satellites EUTELSAT 2 while keeping the same performance rating (Figure 1).

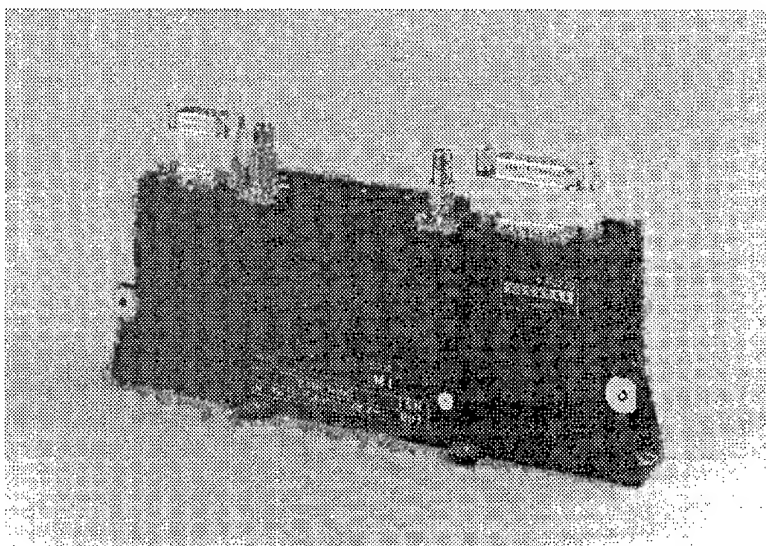


Figure 1: First flight model of MMIC CAMP (Alcatel-Espace)

AMOS has been the first to be launched in May 1996 and has been quickly followed by several other programs which make also use of Ku-Band MMIC CAMP.

Summary of Satellites equipped with MMIC CAMPs.

Program	Band	Number of MMIC per CAMP	Number of CAMP per satellite
AMOS	Ku	7	9
ARABSAT 2	C / Ku	14 / 7	24 / 34
TURKSAT 1C	Ku	7	24
TELECOM 2D	Ku	5	15
HOTBIRD 2 Plus, 3, 4, 5	Ku	10	4 x 28
MABUHAY	C / Ku	5 / 10	38 / 32
SINOSAT	Ku	10	18
NILESAT	Ku	10	32
ST1	C / Ku	5 / 9	20 / 24
M2A	C / X	5, 15 / 16	16, 54 / 4
ASTRA 2 B	Ku	9	40

C-Band CAMPs usually go along with pre-distortion linearizers to improve the power budget of the repeater. Then they need a typical number of 12 MMICs chips including a Phase-Shifter as

supplementary function. ARABSAT 2 has been the first program to incorporate such a sub-system. Its launch date is planned for 1996. For currently designed CAMPs, MMICs have become common in C, X or Ku-Bands. Such experience for Alcatel-Espace is summarized on Table 2.

2.2 Telecom Receivers

The next step was to introduce MMICs in Telecom Receivers. The receiver is a more complicated RF sub-system and it can be considered as the core of the repeater. It consists of:

- a low noise amplifier (LNA) at the uplink frequency,
- a frequency converter which is a microwave mixer,
- a local oscillator (LO) generating a reference frequency. It is generally stabilized by a phase-locked loop (PLL)
- an amplification chain at the downlink frequency.

Due to very demanding performance, not all microwave functions use MMIC technology. The first stage of LNA, for instance, is still based on discrete PHEMT hybrids. However the situation is changing rapidly with the progress of monolithic technology and MMIC have already conquered functions as frequency conversion and linear output amplifier.

An MMIC receiver incorporates about 10 MMIC chips. The needed MMIC chips are : LNA and/or Low Level Amplifiers at input frequency, Balanced Mixers for frequency conversion [5], so-called « Negatrons » (Negative resistance circuit for the VCO), Multipliers when necessary for the LO [6], Attenuators, Low Level, Medium Level and High Linearity Amplifiers at output frequency. Two or three different foundries or processes might be used in order to optimize every function:

- Standard low level 0.5 μm MESFET process (same as for CAMPs),
- High level process: 0.5 μm Power MESFET or HFET, (or PHEMT or HBT in future)
- Very low noise process if necessary like 0.25 μm PHEMT.

Some MMICs have been already inserted in receivers for programs like TELECOM 2D, MABUHAY and NILESAT in Ku-Band, and receiver with complete set of MMICs are now implemented in coming programs in C-Band (ST1-1), Ku-Band (ASTRA-2) and Ku+ (18/12 GHz) for DBS application. Again for comparable performance, the weight of the monolithic version of the receivers is about 50 % to 60 % lower than the hybrid version.

2.3 Satellite Constellations

The telecommunication satellite market is quite exploding with spectacular announcements of several satellite clusters for the end of the century. LEO constellations like IRIDIUM, 66 satellites and GLOBALSTAR, 48 satellites (plus 8 spares) represent a first « generation » devoted to worldwide cellular personal communication services. Both programs are expected to start their services in 1998. Each IRIDIUM satellite will use more than 1600 MMIC chips [7]. For GLOBALSTAR, Alcatel-Espace has manufactured C/S downconverters (16 per payload, shown on Figure 2), 2 telemetry transmitters and 2 telemetry receivers which give a total of 94 MMICs per satellite (Low level amps, Mixers, VCOs, Multipliers and Power amps).

The total number of MMICs assembled in this program by Alcatel-Espace comes to 5264. Such high numbers represent a real break in the work organization of the production of space-borne equipment.

With sub-systems from other partners, the count part number of MMICs will exceed 800 per GLOBALSTAR satellite. The total number of chips necessary for those two major mobile telephone programs exceed 150 000 chips.

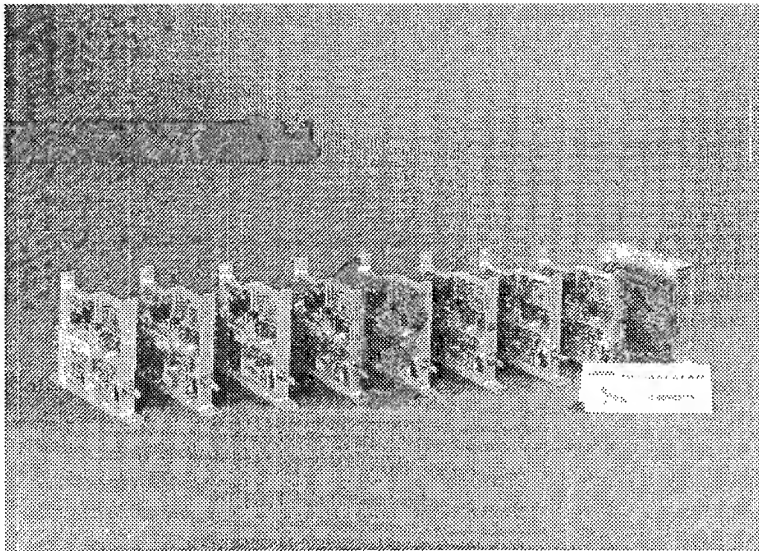


Figure 2: C/S Converter for GLOBALSTAR (Alcatel-Espace)

A second « generation » of satellite constellations is making the headlines nowadays. They are systems which plan to offer interactive video and multimedia communications services beginning in 2001 or 2002 (See Table 4).

First to be announced has been the astonishing system of TELEDESIC with 840 active in orbit (700 km)! Recently this number has been revised to a more realistic, but still impressive 288 satellites.

Its competitor systems in Low Earth Orbit (LEO) are M-STAR from Motorola and SKYBRIDGE promoted by Alcatel-Telecom. The latter consists in a 60-satellite constellation operating at Ku-Band (14/12 GHz) [8]. With higher orbit (geostationary), other systems are less demanding in term of satellite quantity. For these constellation programs, the most applied frequency is Ka-Band (30/20 GHz). Performance at such high frequencies is made possible by the emerging of commercial 0.25 μm PHEMT foundry. Such a process is currently under a space-qualification program managed by the French Administration (CNET/CNES/DGA).

Table 4: Satellite constellation systems announced for multi-media applications.

System	Spaceway	Cyberstar	Astrolink	Teledesic	M-Star	Skybridge
Companies	Hughes	SS/Loral	Lockheed Martin	B.Gates C.Mc Caw Boeing	Motorola	Alcatel
Orbit	GEO	GEO	GEO	LEO (700 Km)	LEO	LEO (1450 Km)
Frequencies	Ka	Ka	Ka	Ka	50 GHz	Ku/Ka
I.S.L.	60 GHz	60 GHz	60 GHz	Ka	Optical	No
Satellites	20	3	9	288	72	64
Starting Date	1998	1999	T0+ 3 Y	2001	2001	2001

Those concepts will be based on steerable active antennas having very large numbers of microwave modules. It is most likely that those will be extremely compact, demanding a lot of efforts for higher integration at MMIC design and, above all, at packaging level. All these programs impose severe cost restraints and, therefore, give a real opportunity for MMIC technology.

2.4 T/R Modules

Another area of concern for MMIC's space application is Earth observation. MMIC technology with increasing manufacturing yield has made possible to consider active antennas with large number of Transmit/Receive modules for synthetic aperture radar (SAR).

Three main programs have been recently conducted at Alcatel-Espace: the SPOT RADAR demonstrator in X-Band supported by the CNES [9], a military radar program and ASAR. The later is the second generation of SAR instrument promoted by ESA. The first generation was ERS1 (launched in 1991) and ERS2 (launched in 1995). Offering additional advantages (as dual polarization, wide swath capability, greater coverage,...). ASAR will be the C-Band (5.331 GHz) radar of the ENVISAT payload of ESA. It will be launched in 2000 and will be the first space-borne SAR with active T/R modules in Europe. The ASAR active antenna will incorporate 320 T/R modules (TRM) which make use of 15 MMICs each, designed by either Alcatel-Espace or Matra Marconi Space. The microwave component technologies are discrete PHEMTs for the LNAs, power MESFETs for the SSPAs and MESFET MMICs for all other functions. All manufacturer sources are European. Each TRM weights 170 gr. Their main performance is about 10 W Output Power with 0 to 40 dB Transmit Gain and about 3 dB Noise Figure with -10 to 30 dB Receive Gain. The mean consumption (with 6% Tx and 60% Rx duty factors) is 3.2 W [10].

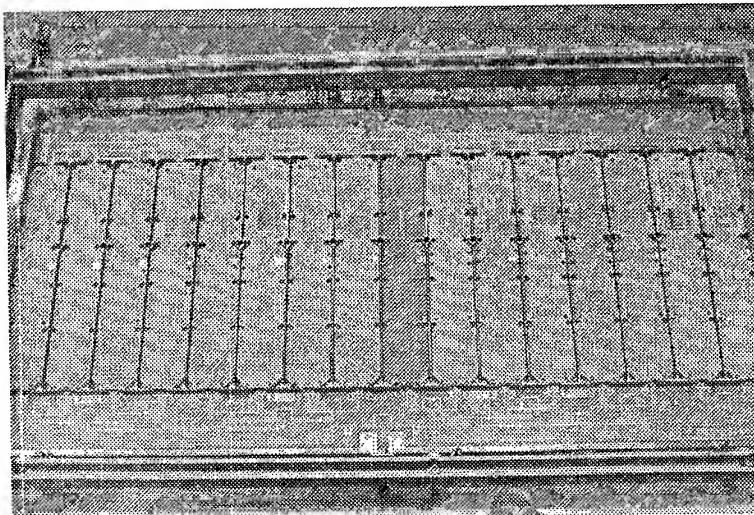


Figure 3: Photograph of an ASAR Tile. ASAR will employ 20 tiles, each embedding 16 T/R Modules. (Alcatel-Espace)

3. PROCESS EVALUATION AND SPACE QUALIFICATION

The space industry experiences a strong industrial and technological transition from the yesterday private market with proven technologies to the tomorrow competitive market with advanced technologies and reduced cycles. In this situation various contradictions are revealed like the addition of margins against performance, long duration life test evaluations against short time to market, strict procedures against continuous improvement, specific packages against low cost.

The extensive introduction of MMICs in space-borne electronics is a response to the market evolution. MMIC designs may not be considered as isolated tasks and the equipment supplier has to implement a methodology which covers from the feasibility evaluation phase to the production and procurement phases.

The component evaluation, qualification and procurement procedures for space are specified in the ESA/SCC and MIL standards for Europe and the United States, respectively. Apart from the detailed requirements, one of the particularities for space is the Lot Acceptance Test required along with the screening. When MMICs are considered, compared to standard ICs, the relevance of the product qualification approach is questioned and process line qualification approaches are preferred. This because the GaAs technology is new, the failure mechanisms are not fully understood and the equipment supplier usually procures dice for hybrids production.

The first MMIC flown in space were qualified in the product qualification approach but a worldwide approved procedure was rapidly needed to avoid prohibitive acceptance testing efforts. A major advance in this direction has been made by the French industries and administrations [4]. This methodology has been applied by Alcatel-Espace to qualify the HAV process of TriQuint [3]. The TriQuint evaluation program consisted in two phases. Phase 1 was the evaluation of the technology via the life test of a Technological Characterization Vehicle. Phase 2 was the evaluation of a functional domain via the life test of a Representative IC. The evaluation of Alcatel-Espace hybrid line was conducted in parallel on the same MMIC modules. Out of this evaluation, it was possible to procure new MMIC functions with limited acceptance tests, based on the verification of the degradation kinetics after a short burn-in.

European manufacturers have initiated similar efforts with the support of European Space Agency or National French Agencies and discussions have been initiated in the United States by the NASA, JPL and DoD with an international participation to issue a GaAs MMIC reliability and qualification guide [11].

4. PROSPECTIVE AND CONCLUSION

MMICs are now clearly unavoidable for space-borne equipment design. When used on classical equipment they have demonstrated that mass and cost can be divided by a factor 2.5.

As an illustration, the Ku-Band CAMP of Telecom 2D weights 210g where the one of EUTELSAT 2 was about 550g for a comparable performance. The miniaturization is continuing, the next generation will be the MCM (Multi Chip Module) technology which employs multilayer RF substrates to interconnect ASICs and MMICs into a single housing. A MCM CAMP has been developed and is under industrialization. Its weight has been reduced to 95g for the same functionality. A comparison of size between the three generations is shown on Figure 4.

Also of importance is the fact that MMICs have allowed the emerging of new concepts which require very large numbers of compact, reproducible and reliable circuits at the least cost. This type of production is already a reality with satellite constellation for mobile communication as for GLOBALSTAR or radar active antenna as for ENVISAT/ASAR. In telecommunication also, active antennas represent the natural evolution to respond to the increasing demand of operational flexibility. Power-sharing among the beams, reconfigurability, steerability, beam-hopping, beam-scanning are some of the new possibilities offered with the active antennas.

Multimedia projects like TELEDESIC or SKYBRIDGE will marry large number of satellites and active antenna leading to the need of a tremendous number of MMIC modules. For those, it is clear that one of the most important challenge of the coming years is to demonstrate and produce very advanced high density packaging.



Figure 4: Three generations of CAMP: « Hybrid » with 550g, « MMIC » with 210g and « MCM » with 95g. This represents about 10 years of evolution.

Also, the Hi-Rel methodologies will have to be less normative and more driven by physics principles to account for actual needs and requirements. Then, we are convinced that MMICs have just entered the world of space electronics and that their future is undoubtedly bright in this field.

Acknowledgment

The support of France-Télécom, the CNES and the European Space Agency for telecom studies and radar developments with MMIC technology is gratefully acknowledged.

References

- [1] J.L.Cazaux, « MMIC's for space-borne systems: status and prospective », GaAs IC Symp. Philadelphia, USA, Oct 1994, also in *Microwave Engineering Europe*, Dec-Jan 1995, p 43-51.
- [2] F.Labarre, J.L.Cazaux, C.Goldztein, N.Pichon, M.Soulard, « A new concept: an electronically tunable MMIC flatness corrector », IEEE-MTT-Symp., Boston, USA, Jun 1991.
- [3] A. Bensoussan, P. Coval, WJ Roesch and T. Rubalcava, « Reliability of a GaAs MMIC process based on 0.5 μm Au/Pd/Ti gate MESFETs », IEEE Int. Reliability physics symposium, San Jose, CA, April 12-14 1994.
- [4] M.Bellfort et al., « A methodology for the space qualification of GaAs MMICs », CNES/DGA/France Telecom CNET, Ref: CNES/QFT/RC-013. See also in GaAs 92, ESTEC, The Netherlands.
- [5] J.F.Villemaire, M.Soulard, « A statistical load pull for mixer design using a commercial circuit simulator », To be presented at MTT-S Int. Microwave Symp., San Francisco, USA, June 1996
- [6] B.Rattay, J.M.Vanestenvorde, M.Hübner, J.L.Foucher, « A novel design method for frequency doublers and quadruplers illustrated on C and Ku-band telemetry, command and control space applications », 25 th European Microwave Conf., Bologna, Italy, Sept. 4-7, 1995.
- [7] D.Polsky Werner, « MMICs gain commercial space market ground », in *Space News*, Oct 3-9, 1994.
- [8] P.B. de Selding, « Alcatel plans competitor to Teledesic's system », in *Space News*, Apr 1-7, 1996.
- [9] C.Mangenot, J.L.Cazaux, G.Caille, D.Carbonne, E.Luvisutto, « Demonstration model of an active SAR subpanel », IEEE-AP-S-Symp., Ann Arbor, Michigan, USA, June 1993.
- [10] A.Cazal, A.Jude, J.L.Cazaux, M.Clement, « Design and performance of the Transmit / Receive module of Advanced Synthetic Aperture Radar (ASAR) for ENVISAT satellite », 25 th European Microwave Conf., Bologna, Italy, Sept. 4-7, 1995.
- [11] S.Kayali, G.Ponchak, and R.S.Shaw « GaAs MMIC reliability assurance guideline for space qualification » JPL Publication 96-25. See also in IEEE M and MW monolithic circuits symposium, San Diego, CA, May 1994.

A Basic Concept of Microwave Design Automation based on Three-Dimensional Masterslice MMIC Technology

**Ichihiko TOYODA, Tsuneo TOKUMITSU,
and Masayoshi AIKAWA.**

NTT Wireless systems Laboratories,
1-1 Hikari-no-oka, Yokosuka-shi, Kanagawa, 239
Japan.

Tel: +81-468-59-2554
Fax: +81-468-55-2106
E-mail: toyoda@nhosun.wslab.ntt.co.jp

Abstract

Three dimensional (3-D) MMMC technology effectively increases the integration levels of multifunctional MMICs and achieves masterslice MMICs. The 3-D masterslice MMIC technology can be used as an advanced design method of MMICs as well as high integration levels. This paper discusses the feasibility of microwave design automation software based on the 3-D masterslice MMIC technology.

1. Introduction

The forthcoming multimedia era requires highly integrated and cost-effective multifunctional MMIC's for mobile communications, satellite communications, wireless LAN etc. The rapid growth of these applications also require short time to market. In meeting these objectives, it is important designers to be more productive as well as cut down fabrication turn and cycle time. The design process of digital LSI is almost totally automated, but MMIC design is still manual with the designer creating each element individually. This requires much knowledge and experience. The reason is that MMIC performance is strongly related to pattern layout because MMIC is an analog high frequency circuit and parasitic components strongly degrade performance. Another reason is that circuit components are not effectively reused due to the lack of effective concepts such as macro and core. MMIC design tools must be created that eliminate high level design skill and increase design productivity.

In this paper, the feasibility of 3-D masterslice MMIC-base microwave design automation software that makes designers more productive is discussed.

2. Three-Dimensional MMIC and Masterslice MMIC

We have been proposing a three-dimensional (3-D) MMIC technology [1]-[10] which effectively enhances the integration levels of multifunctional MMICs. Figure 1 shows the calculated characteristics of TFMS lines which are the basic elements of the 3-D MMIC. The characteristic impedances of single TFMS lines are

shown in (a) as a function of strip width w . A wide range of characteristic impedances from 10 to 100 Ω is obtained with very narrow line widths under 30 μm . Figure 1 (b) shows the maximum coupling between two identical TFMS lines located side by side with line spacing s . Better than 25 dB isolation can be obtained when line spacing s wider than $3h$. Thus, TFMS lines offer very dense layouts.

Figure 2 shows a microphotograph of an X-band image-rejection mixer [4] constructed with a miniaturized quadrature hybrid [2], Wilkinson divider, and two unit mixers. The 3-D MMIC technology effectively reduces the passive circuits. The areas occupied by both passive circuits and active circuits are almost same, around 0.1-0.4 mm^2 .

Figure 3 shows C-, X-, and K-band amplifiers. The intrinsic areas of the amplifiers are only 0.5 x 0.7 mm. As shown in this figure, similar performance can be obtained with same circuit topology and same small circuit size regardless of their operation frequency.

The technology also achieves masterslice MMICs that offer shorter development TAT and lower cost. The masterslice MMIC is constructed with a master array and 3-D passive circuit on a wafer as shown in Fig. 4. The unit cells, each of which includes active devices, resistors, and lower electrodes of MIM capacitors, are arranged in matrix on a wafer to form a master array. Ground metal 'GND1, which creates enough space for 3-D transmission lines. Since GND1 also isolates the wafer properties, such as conduction, from the 3-D passive circuits, this technology allows us to design circuits uniformly regardless of wafer material [8].

Figure 5 shows a design and fabrication flow of the 3-D masterslice MMIC. The designer selects a masterslice wafer suitable for his specification, and designs 3-D passive circuits using the information offered by masterslice vendors. Complete 3-D multifunctional MMICs can be fabricated using foundries. Circuit design can be easily reused. Thus the 3-D masterslice MMIC technology achieves semi-custom design similar to LSI gate-arrays, and allows the MMIC users to design their own MMICs.

3. Application to Microwave Design Automation

The features of the 3-D masterslice MMIC technology are as follows:

- 1) Active devices are arranged in advance.
- 2) Many unit cells are arranged in a matrix.
- 3) Similar performance is obtained with same circuit topology over wide frequency range.
- 4) Circuit performance can be modified by changing transmission line parameters.
- 5) 3-D structure offers parasitic free layout and high density circuits.
- 6) The technology is suitable for frequencies from several GHz to the millimeter band.
- 7) Circuits on several kinds of wafers (GaAs or Si) can be designed in the same way.

for circuit synthesis. Features (3) and (4) may be effectively used for circuit synthesis. Features (6) and (7) show that this technology can be used for wide variety of applications. Thus, the 3-D masterslice MMIC technology takes us one step closer to MMIC design automation.

4. Conclusion

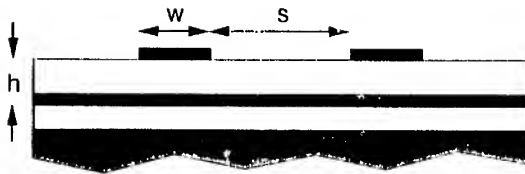
Since the 3-D MMIC has high degree of freedom in transmission line routing, the design flexibility of the 3-D MMIC is not degraded even when active devices are placed in advance. Accordingly, we can use the 3-D masterslice MMIC technology as an advanced MMIC design method. The technology effectively eliminates the need for high level design skill and increases MMIC design productivity. The technology promises to achieve microwave design automation software and allow MMIC users to design their own MMICs.

Acknowledgment

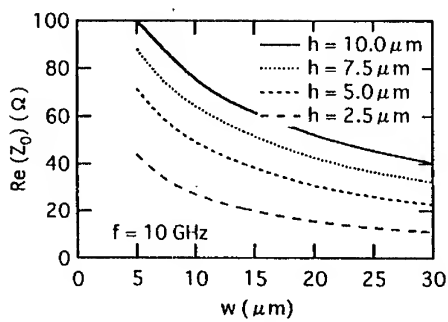
The authors would like to thank Drs. Suichi Samejima and Kenji Kohohiyama for their suggestions and encouragement. They also thank Drs. Kimiyoshi Yamasaki, Makoto Hirano and many other colleagues at NTT Wireless Systems Laboratories and NTT System Electronics Laboratories for their fruitful discussions.

References

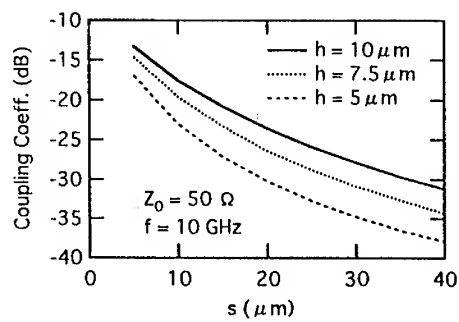
- 1 T. Tokumitsu, T. Hiraoka, H. Nakamoto and M. Aikawa, "Multilayer MMIC using a 3 μm x 3-layer dielectric film structure," in 1990 *IEEE MTT-S Int. Microwave Symp. Dig.*, pp. 831-834, May 1990.
- 2 I. Toyoda, T. Hirota, T. Hiraoka, and T. Tokumitsu, "Multilayer MMIC branch-line coupler and broad-side coupler," in 1992 *IEEE Microwave and Millimeter-Wave Monolithic Circuits Symp. Dig.*, pp. 79-82, June 1992.
- 3 I. Toyoda, M. Hirano, and T. Tokumitsu, "Three dimensional MMIC and its application: An ultra-wideband miniature balun," *IEICE Trans. Electron.*, vol. E78-C, no. 8, pp. 919-924, Aug 1995.
- 4 I. Toyoda, T. Tokumitsu, and M. Aikawa, "Highly integrated three-dimensional MMIC single-chip receiver and transmitter," *IEEE Trans. Electron.*, vol. 44, no. 12, pp. 2340-2346.
- 5 T. Tokumitsu, M. Aikawa, and K. Kohiyama, "Three dimension 1 MMIC technology: A possible solution to masterslice MMIC's on GaAs and Si," *IEEE Microwave Guided Wave Lett.*, vol. 5, no. 11, pp. 411-413, Nov. 1995.
- 6 T. Tokumitsu, K. Nishikawa, K. Kamogawa, I. Toyoda, and M. Aikawa, "Three-dimensional MMIC technology for multifunction integration and its possible application to master-slice MMIC," in 1996 *IEEE Microwave and Millimeter-Wave Monolithic Circuits Symp. Dig.*, pp. 85-88, June 1996.
- 7 M. Aikawa, T. Tokumitsu, and K. Nishikawa, "Advanced MMIC technology for the next generation-3D MMIC's and master-slice technology," in *Proc. 26th European Microwave Conf.* Pp. 748-753, Sep. 1996.
- 8 I. Toyoda, K. Nishikawa, T. Tokumitsu, C. Yamaguchi, M. Hirano, and M. Aikawa, "Three-dimensional master-slice MMIC on Si substrate," in 1997 *IEEE Radio Frequency Integrated Circuits Symp. Dig.*, June, 1997.
- 9 M. Hirano, K. Nishikawa, I. Toyoda, S. Aoyama, S. Sugitani, and K. Yamasaki, "Three-dimensional passive circuit technology for ultra-compact MMIC's," *IEEE Trans. Microwave Theory Tech.*, vol. MTT-43, no. 12, pp. 2845-2850, Dec 1995.
- 10 K. Onodera, M. Hirano, M. Tokumitsu, I. Toyoda, and T. Tokumitsu, "Folded U-shaped microwire technology for ultra-compact 3D MMICs," *IEEE Trans. Microwave Theory Tech.*, vol. MTT-44, no. 12, pp. 2347-2353, Dec. 1996.



(a) Cross-sectional view



(b) Characteristic impedance



(c) Coupling coefficient

Fig. 1: Calculated characteristics of TFMS lines.

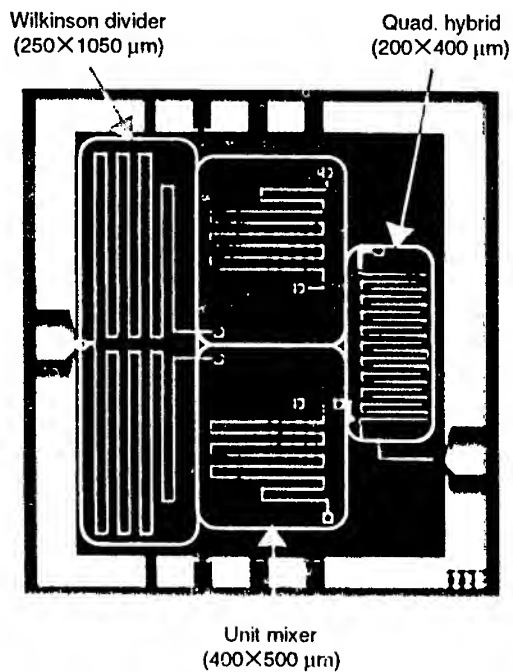
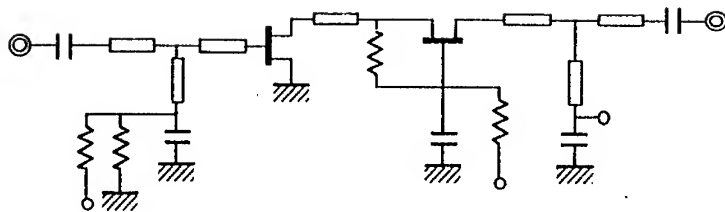
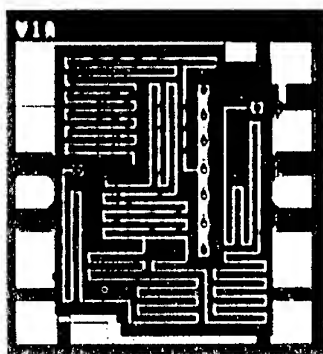


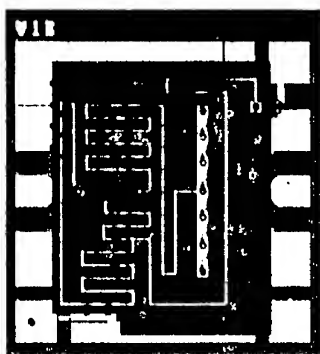
Fig. 2: Microphotograph of an X-band image-rejection mixer. (Chip size: 1.2 × 1.28 mm)



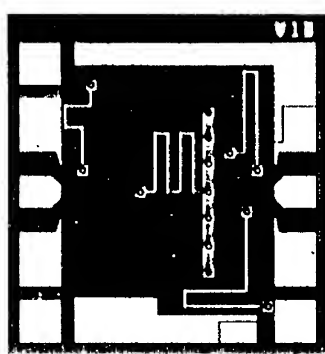
(a) Circuit topology



C-Band

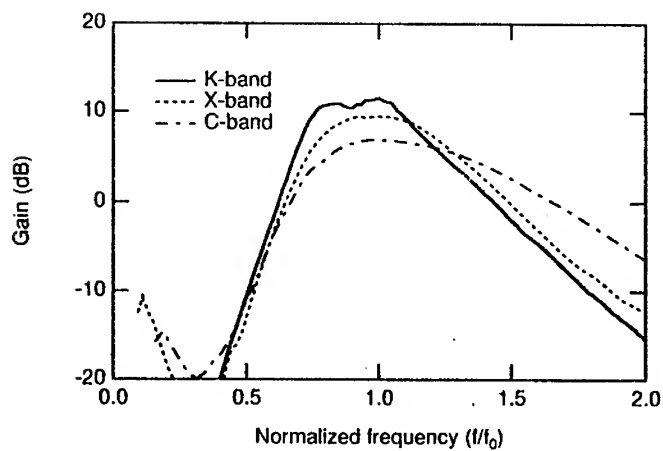


X-Band



K-Band

(b) Microphotograph (Chip size: 0.5×0.7 mm)



(c) Measured performance

Fig. 3: Three-dimensional MMIC amplifiers for C-, X-, and K-band.

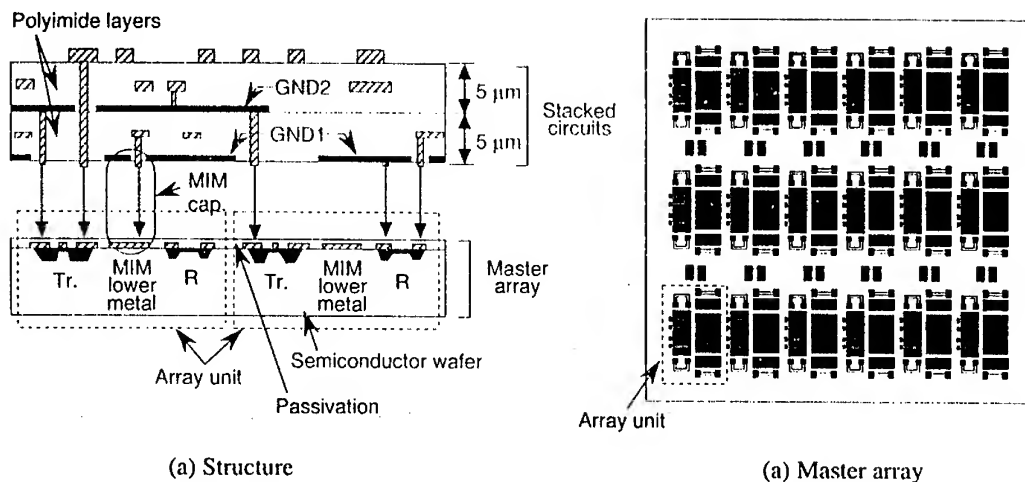


Fig. 4: Three-dimensional masterslice MMIC.

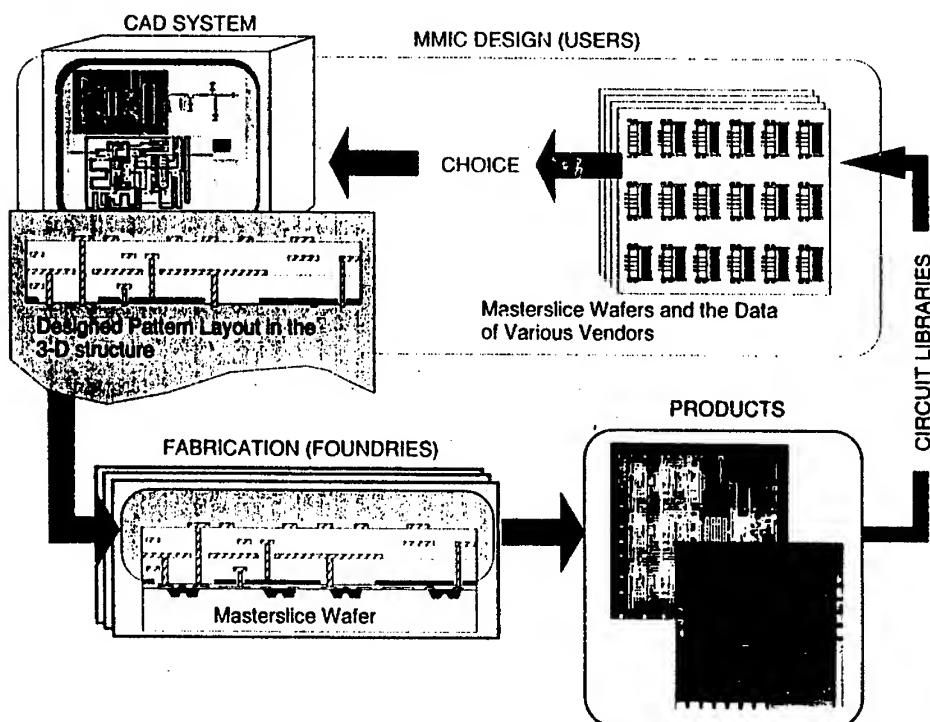


Fig. 5: 3-D masterslice MMIC design/fabrication flow.

T/R Module Packaging - a Challenge for Future System Design

Wolfgang Bösch
Daimler Benz Aerospace AG
Defense and Civil Systems – Airborne Systems
wbosch@vs.dasa.de

ABSTRACT

Future packaging technology is driven by key parameters, such as volume and mass of the T/R module, interconnect technology and overall efficiency. These parameters and their effects on the radar system are discussed. Further, enabling technologies to achieve performance and cost objectives are listed, an overview of European T/R module technology is given and some examples of advanced packaging technologies are presented.

1. INTRODUCTION

Active phased array antennas have three major applications areas. First there is a growing demand for active arrays in communication satellite systems. The volume of required T/R modules in this market segment is considerably high. Secondly there are the space based radar instruments, which have shown their usefulness for a large number of applications in the recent years. Especially the Synthetic Aperture Radar (SAR) instruments are utilized widely for civil and military earth observation and global economic monitoring applications. The third important application for active phased array antennas are the ground based, naval and airborne military radar systems. The utilization of the active antenna technology offers significant advantages compared to traditional radar system designs. Adaptive beamforming, improved target detection, missile defense, increased system performance and multimode operation besides better reliability and efficiency are the major benefits. Common to all T/R module applications in active phased arrays is, that the available prime power, the thermal management (heat dissipation), the mass and the size are the most limiting and hence demanding factors for future T/R module technology developments.

2. REQUIREMENTS AND FUTURE TRENDS

Comparing the typical performance specifications given in Table 1 for space and airborne radar systems, the T/R module requirements are very similar for both applications. These requirements are also applicable for future naval radar systems. Some of the driving factors are directly related to future packaging technologies, such as antenna size, volume and mass, others are only indirectly related and not so obvious as overall efficiency, RF losses or life time of the module. The most important common requirements, driving factors and trends for the future are discussed in the next paragraphs.

Volume and Size

The operating frequency and the antenna grid (i.e. distance between the individual radiating elements which is typically $\lambda/2$ at the highest operating frequency) determine the foot print of T/R modules. For space applications one T/R module typically drives several antenna radiators located in one subarray [Zahn, 1]. Therefore only one dimension of the module has to be compatible with the element spacing of the antenna. In addition, for some satellite systems (e.g. RADAR SAIL proposed by CNES, [Aguttes et al, 2]) the thickness of the antenna panel is of great concern and limits the height of the T/R modules. In airborne radar systems every radiating element is controlled by a separate T/R module. Hence a 'stick type' assembly for the radar antenna has to be chosen and two dimensions of the module have to be compliant to the antenna grid. Figure 1 shows a typical arrangement of T/R modules in an airborne radar taken from the AMSAR (Airborne Multirole Solid-state Active array Radar) program of GTDAR (GEC Thomson DASA Airborne Radar EEIG) [Albarel et al, 3]. For future conformal antennas the integration depth is important and hence all 3 dimensions, i.e. the volume of the T/R module has to be minimized.

Mass

Concerning the mass, a rule of thumb for airborne radar's is, that for every kg in mass for the active radar antenna the gross aircraft take off weight will increase by 3.5 kg. The maximum allowed mass for a nose radar is roughly 200 kg and will not increase in the future, hence is a real challenge for the T/R module designers. For satellite systems every kg that has to be lifted into space translates into US\$ 100.000 additional cost. Of course there is an absolute upper limit in mass for radar instruments carried on satellite platforms too, broken down to the T/R module level the short term goal for

space based systems is about 70 g per module, for airborne radars the goal is less than 50 g. These requirements to reduce volume and mass mainly will drive future packaging technology.

Thermal Management and Cooling

Modern technologies, such as multilayer substrates, 3D assembly structures, core chip MMICs and ASICs enable a higher integration level of the T/R modules and hence cause a higher power density of the active radar antenna. For airborne radars with about 2500 T/R modules assembled in a 90 cm diameter radar antenna and an average dissipated power of 10kW to 20kW, it becomes evident that efficient cooling is a major issue and a technological challenge. In space the active radar antennas are exposed to steep temperature gradients. Therefore new efficient heat sinking techniques (e.g. diamond structures) have to be developed. The integration of highly dissipative MMICs and power devices in a very densely packed environment will be the challenge for future packaging technology.

Overall Efficiency

Overall power added efficiency of a T/R module is not only a question of the device (drain-) efficiency of the power amplifier, but is also strongly related to a number of other components and their operating mode in the module. The module overall efficiency is defined as the ratio of the RF output power to the supplied DC input power to the module (the RF input power is neglected for the time being), averaged over time. Assuming a typical duty cycle of 10%, the T/R module is in the transmitting mode only 10% of the time, hence the efficiency of the transmit power amplifier contributes only 10% to the overall efficiency, although with the highest DC power consumption. Whereas the receiving components, the switches and the digital control circuits are switched on 90% to 100% of the time. Their contribution is a significant portion of the overall efficiency. The use of low power consumption technologies and a stand-by mode for analog and digital components, a smart architectural design and the optimization of the Tx and Rx components timing will further enhance overall efficiency.

Looking at the transmit path of the radar module, the RF signal is conditioned in amplitude and phase, amplified by driver amplifiers and the power amplifier and finally routed to the radiating antenna elements. Several components after the power amplifier contribute to the overall losses, these are mainly the transitions inside the package, the losses of the interconnecting lines, the losses of the circulator and if required the T/R switch, the transition to the connector, the connector itself and finally the distribution network to the antenna radiators. Assuming a power added efficiency of the isolated power amplifier of 50% and 2.5dB overall losses along the output path, the overall module transmit efficiency is reduced to 26%. If the output network is redesigned and the losses improved to 1.5dB, the overall efficiency becomes 34%. This is an improvement of 8 points which has a significant impact on the system design. It is easy to show that when the RF output power is kept constant an improvement of 8 points in efficiency translates to a reduction of one third (factor 0.68) in overall dissipated heat. If the thermal conductivity of the assembly and package remains unchanged, the device temperature typically would drop by more than 30°C, which would increase the life time by a factor of magnitude! A reduction of the losses in the transmit path will of course also reduce the inherent losses in the receive mode and hence significantly improve the noise figure of the T/R module. An improved noise figure has a direct impact on the system design (e.g. RF output power can be reduced to achieve the same system performance).

The overall radar antenna and supporting system equipment mass is also strictly related to the T/R module overall efficiency. McQuiddy [4] has shown that for a typical airborne radar (5kW radiated RF power) an increase in efficiency from 15% to 20% would reduce the gross overall take-off weight from 1250 lbs to 500 lbs, a factor of 2.5. Similar numbers are true for space applications.

The above paragraphs have shown that the overall efficiency is strongly related to most of the important radar parameters. Therefore, besides mass and volume constraints, the overall efficiency is a crucial design parameter for space and airborne radar systems.

Clever high efficiency design techniques (harmonic matching, class E operation, etc.) and the rapidly emerging technologies for solid state devices will soon enable power amplifier designs in X-band with 10W output power and 50% power added efficiency. New materials and device technologies, such as SiGe, InP, SiC and GaN will further increase the RF output power and the operating frequency, but it will be very difficult to reach amplifier efficiencies in excess of 60%. This number will significantly be reduced by external circuit and interconnect losses. Because there is a predictable upper limit in amplifier efficiency it is even more important to emphasize other areas of efficiency improvement. Especially new module architectures, low power digital technologies and low loss transitions, interconnects and assembly technologies have a high potential. Optimizing the module efficiency has an immense impact on the radar system and is a big challenge for future packaging and integration technology.

Interconnects and Connectors

In the future more and more functions will be integrated onto a single ASIC or MMIC chip. Mixed analog and digital signal chips will be the standard for new developments. This higher integration level leads to multiple and even denser spaced interconnects. Hence modern assembly technology has to address complex mixed technology chips and very densely spaced, low loss interconnecting lines on multilayered substrates. But not only interconnects inside the microwave package, but also the interface to the outside world on the digital, control and analog RF side is very demanding in view of the necessary volume and size reduction. The newest trends are pressure contacts or connectorless RF interfaces, based on electromagnetic coupling, to the distribution and/or radiating elements. Besides other advantages this technique significantly eases the integration of active antennas holding several thousands of T/R modules. It also provides a good reparability of the active arrays. Unfortunately these new interconnecting techniques are not space-qualified yet.

The increasing demand for bandwidth, the immunity towards electromagnetic interference, size and low weight are factors that are well addressed by modern fiberoptic technology [see Banerje et. al. 6]. The distribution of RF and digital signals by fiberoptics will also affect future T/R module packaging technology.

3. MARKET IMPOSED CONSTRAINTS (COST & AFFORDABILITY)

Although new civil and military radar systems that are based on active antenna array technology offer an increased radar system performance, the potential customer will not accept a significant increase in price compared to the already existing traditional systems. Hence there is a firm price limit for future radar systems that has to be reached within the next few years. The major cost factor of an active radar system are the T/R modules [McQuiddy et al, 5]. Reducing the cost of the T/R modules is the main driving factor for semiconductor device, new packaging and manufacturing technologies. The cost is mainly a factor of performance (efficiency, output power and noise figure), complexity and quantities of modules produced [Funck et al, 7].

4. ENABLING TECHNOLOGIES TO ACHIEVE PERFORMANCE AND COST OBJECTIVES

Microwave Integrated Circuits (MMIC) Technology

Without the current, batch process oriented, MMIC manufacturing technology the realization of active phased array radar and communication systems would not be possible. Especially the reproducibility, the consistent amplitude and phase tracking and the high integration level guarantee a proper operation of the active array. In the future improved semiconductor materials, a better understanding of physical long term effects related to reliability issues, and an improved manufacturing yield will enhance the performance and reduce the costs of the T/R modules. In addition, better circuit design techniques that consider production related parameters, more efficient software to perform sensitivity analysis and the use of electromagnetic simulators are important factors to be considered. On the MMIC manufacturing side, automated RF on wafer probing and the standardization of probe patterns reduce overall module testing costs. Furthermore, modern statistical probing techniques (Known Good Die) and database sampling strategies [M/A-COM, North, 8] as well as data and chip tracking are essential for high volume low cost T/R module production.

Assembly and Packaging Technology

Traditionally T/R modules were manufactured utilizing microwave hybrid technology where the substrates are mounted on carriers and integrated into milled metallic boxes, hermetically sealed with ceramic coaxial feedthroughs. As a result of the maturing MMIC technology and the emerging market for T/R modules an increased emphasis is put on assembly and packaging technologies. The driving factors are performance, size, mass and cost [Midford 10], [Funck 7], [Wein 11].

The package of a T/R module must serve several interrelated electrical, mechanical and thermal functions. Individual functions, such as mechanical stiffness and stability, thermal conductivity and heat spreading, hermetically sealed feedthroughs and RF signal distribution are traditionally accomplished by separate materials and particular components forming the package. Modern material technology can combine some of these functions and even take over tasks that were not attributed to the package in the past.

A first example is the 'direct die attach' technology, where naked MMICs and digital chips directly are assembled onto the substrate, which is CTE matched to the GaAs chips. It provides thermal heat spreading and is an integral part of the package. Hence the number of parts and consequently the assembly costs are reduced. Utilizing the 'known good die' concept only one final test of the T/R module is performed and no intermediate RF testing is necessary. Figure 2

illustrates an RF signal processor with integrated logic on a 7 layer polyimide substrate [Feldle, 9]. An advanced C-Band T/R module is shown in Figure 3.

Secondly there are single- and multilayer LTCC and HTCC substrates combined with MCM-D technologies possibly embedded in metal matrix composite materials. The ceramic and polyimide substrates provide multilayer RF and digital interconnects and signal distribution. Planar, hermetically sealed feedthroughs for RF and digital signals replace the costly coaxial solutions. Figure 4 shows an advanced technology proposed by Dasa Ulm.

A third example are the metal coated plastic packages manufactured by injection molding technology with metal inserts which provide sufficient heat spreading. These packages are cost-effectively fabricated in complex geometric shapes, thus connectors, radiating elements, diplexers, filters, distribution networks, and mode suppressing structures are an integral part of the package. Figure 5 shows an automotive sensor package with integral radiating elements.

Design and Process Related Issues to Reduce Cost (Microwave Factory)

In a yield and cost driven T/R module design, both RF and digital chip design and package design should be a joint, coordinated effort within one team, and not run through independent teams as it is often the case [Wein, 11]. An integrated CAD design tool should enable the design engineer to analyze the effects of module fabrication tolerances on yield and module performance. A 3D analysis of electromagnetic coupling and the simulation of thermal effects under pulsed conditions are additional future CAD requirements.

The mature statistical methods developed to control and qualify an MMIC production process should be extended within a 'Microwave Factory Line' to the fabrication of T/R modules. Automated testing, binning and matching of components will enhance the overall module performance. The traceability of all parts, guaranteed by a common database, helps to qualify the fabrication process to MIL or space standards.

One of the biggest cost saving forces is the batch oriented ('wafer scale') processing of T/R modules. Standardization of components and parts, automated assembly (pick and place, automated wire bond and/or flip-chip), automated inspection procedures and automated testing and probing capabilities are obligatory for a reproducible, high volume, low cost fabrication process. Most of the fabrication cost reduction in the near future will be based on automatization and standardization. Only the dual use for military and civil applications, for radar and communication systems will leverage the capital expenses necessary for a fully automated microwave module fabrication line.

5. EUROPEAN T/R MODULE TECHNOLOGIES

An overview of current European T/R module technologies and the expected future evolution is given in Table 2. The information summarized in this table was contributed by several European companies. Dassault Electronique is involved in microwave remote sensing activities of CNES and has engineered in collaboration with Alcatel Espace an X-Band T/R module. They are also developing packaging technologies based on multilayer ceramic and organic substrates, and T/R module packages which provide a high integration density and interconnect capabilities. Alcatel Espace has a long experience in T/R module design. Currently C-Band T/R modules are fabricated (jointly with MMS) for a European space based SAR project (ASAR) to be launched in the year 1999. In collaboration with Thomson CSF, Alcatel Espace has also designed and successfully manufactured several T/R modules for the military demonstrator project OSIRIS. They are also engaged in flip-chip and future 3D packaging technology studies. Besides other radar projects GEC Marconi is involved in the airborne radar project AMSAR and is evaluating new assembly and interconnect technologies (e.g. flip-chip and connectorless interconnects). Daimler Benz Aerospace is currently developing C-Band and X-Band T/R modules for airborne, space based and ground based active radar systems. They are also working on advanced packaging technologies based on metalized plastic or metal matrix composite packages, multilayer ceramic substrates and high density interconnects. They are setting up a qualified pilot line for T/R module volume production. Their thin film technology is in the process of being space qualified by ESA. The semiconductor company UMS, a joint venture between Thomson, Daimler Benz Aerospace and Temic is delivering most of the MMICs.

6. ACKNOWLEDGEMENT

I would like to thank Mr. Sombrin from CNES, Dr. J.-L. Cazaux from Alcatel Espace, Mr. R. Funck from Dassault Electronique, Mr. G.D. Morrison from GEC Marconi, Dr. R. Zahn from Dasa Dornier and Dr. H.-P. Feldle from Dasa Ulm for their helpful discussions and the provided information.

7. CONCLUSIONS

The requirements of T/R modules related to future packaging technologies for space, airborne, naval and ground based radar systems are very similar. Mass, volume and interconnect technology are directly related and important parameters to be considered. Radar system performance is strongly affected by the overall module efficiency, which is also related to the applied packaging and assembly technology. A big challenge for future packaging technology is the cost reduction of the T/R module fabrication. Only a higher level of integration when utilizing multifunction MMICs and ASICs, multilayer substrates, automated assembly and test procedures, and newly engineered packaging materials, will guarantee a low cost production of advanced T/R modules.

REFERENCES

- [1] R. W. Zahn, 'The Design of a Future X-Band Synthetic Aperture Radar', AEÜ Int. J. Electron. Commun. Vol. 50 (1996), No. 2, pp. 85 - 91
- [2] J.-P. Aguttes, J. Sombrin, E. Conde, 'Radar "SAIL" Satellite Concept', to be published in ACTA Astronautica
- [3] G. J. Albarel, J. S. Tanner, M. Uhlmann, 'AMSAR Antenna Architecture and Predicted Performance', IEEE International Symposium on Phased Array Systems and Technology, Boston, 18. Oct. 1996
- [4] D. N. McQuiddy, 'Solid-State Phased Array Radar Technology', Tutorial Session on Solid State Phased Arrays, IEEE International Symposium on Phased Array Systems and Technology, Boston, 18. Oct. 1996
- [5] D. N. McQuiddy et. al., 'Transmit/Receive Module Technology for X-Band Active Array Radar, Proceedings of the IEEE, Vol. 79, No. 3, March 1991, pp. 308 - 341
- [6] S. Banerjee, G. Zimmer, H.-P. Feldle, P. Marten, 'A X-Band Phased Array Microwave / Photonic Beamforming Network', IEEE MTT-S, June 14-18, 1993, Atlanta, pp. 505 - 508
- [7] J.-L. Fouré, A. Dravet, J.-P. Cazenave, R. Funck, 'Mixed Technologies for Microwave Multichip Module (MMCM) Applications - a Review', IEEE NTC 95, The Microwave Syst. Conf., Orlando, 17.-19. May 1995
- [8] R. North, D. Kennedy, M. Murphy, 'Database Sampling: A Real-World Solution to MMIC Yield Sensitivity Analysis', Microwave Journal April 1997, pp. 106 - 115
- [9] H.-P. Feldle, 'Transmit / Receive Module Technology for Active Array Radar', Microwaves & RF, Oct. 1996, pp. 215 - 220
- [10] T. A. Midford, J. J. Wooldridge, R. L. Sturdivant, 'The Evolution of Packages for Monolithic Microwave and Millimeter-Wave Circuits', IEEE Trans. on Ant. and Propagation, Vol. 43, No. 9, Sept. 1995, 983 - 991
- [11] D. S. Wein, 'Advanced Ceramic Packaging for Microwave and Millimeter Wave Applications', IEEE Trans. On Antennas and Propagation, Vol. 43, No. 9, Sept. 1995, pp. 940 - 948

Subject	Current Technology	Future Evolution
T/R Module RF control circuits	Single chip functions (6) MESFET Process (6) Multifunction demonstrators	Multifunction core chip (2)(4)(5) Optical phase shifting (4) RF / LF MCMs (1)(2)
LNA technology	0.25µm HEMT technology (6)	0.1µm InP P-HEMTs (1), HBTs (4)
Limiter technology	Reflective and non-reflective limiters using discrete diodes (6)	MMIC limiter (4)
Power Amplifier	MESFETs, HFETs, P-HEMT (1)	HBTs (2)(4) and HFETs
Substrates	Thick and thin film on alumina (6) Multilayer polyimide for logic Multilayer organic substrates (1)(3)	LTCC and HTCC substrates (3) Increased exploitation of AlN (1)(4) Substrate integral part of the package (6) 2½ and 3D packaging (6)
Assembly Technology	Automated pick & place Chip & wire (6) Semi automated test	Flip-chip (1)(4) Fully automated Test
Packaging & Housing	Milled alloys Hermetic coaxial feed-throughs Metallic micropackages (1)	Metal Matrix Composites (AISC) (6) Planar feed-throughs (6) LTCC with integrated cavities Metal coated plastic packages (2)
Interfaces & Connectors	Coaxial connectors Optical distribution demonstrator (2)(4)	Planar connections Vertical interconnects Pressure contacts and RF field coupling (2)(4)
Size (for X-Band)	35mm x 160mm x 15mm (2)	13mm x 13mm x 50mm (2)
Mass / Channel	70g (2)	30g (2)

- (1) Alcatel Espace
(2) Daimler Benz Aerospace
(3) Dassault Electronique
(4) GEC Marconi
(5) Thomson CSF
(6) all

Table 2: Overview of European T/R Module Technology

	Space based SAR Radar	Airborne Nose Radar
Centre Frequency	9.6 GHz	X-Band
Bandwidth	100 MHz	100 MHz - 2 GHz
RF Output Power	5 - 10 W	5 - 10 W
Duty Cycle	5 - 10 %	up to 35%
Overall Power Added Efficiency	better 25 %	better 25 %
Tx / Rx Path Gain	30 dB	30 - 40 dB
Rx Gain Control (Range & Resolution)	20 dB, 5 or 6 bits	20 dB, 5 or 6 bits
Rx / Tx Phase Control (Range & Resolution)	0 - 360°, 6 bits	0 - 360°, 6 bits
Operation Temperature Range	-20°C ... +60°C	-20°C ... +80°C
Size per Rx / Tx Channel	35 x 160 x 15 mm ³	15 x 15 x 60 mm ³
Mass	<70 g	<50 g
T/R Modules / System	900	1000 - 2500
Active Antenna Area	8 - 12 m ²	0.3 - 0.65 m ²
Active antenna mass	650 kg	200 kg
Average radiated RF Power	400 - 800 W	3 - 6 kW
Available prime power	2 - 4 kW	15 - 30 kW

Table 1: Typical T/R Module and active antenna related requirements

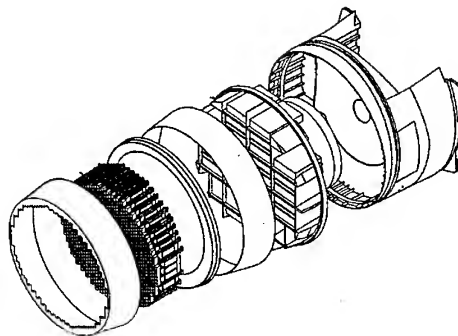


Figure 1: Airborne active array antenna and supporting units (courtesy of GTDAR)

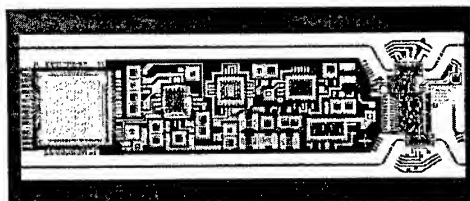


Figure 2: RF signal processor on a ceramic substrate with multilayer polyimide structure on top (courtesy of Dasa)

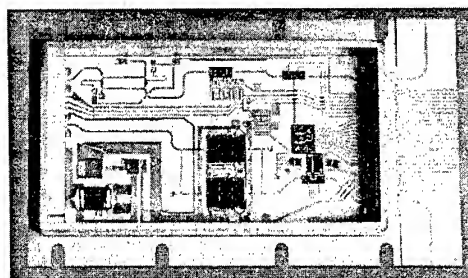


Figure 3: Advanced C-Band T/R Module with planar hermetic feed-throughs (courtesy of Dasa)

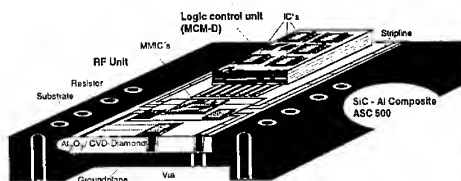


Figure 4: Metal matrix package with ceramic substrate and multilayer polyimide (courtesy of Dasa)

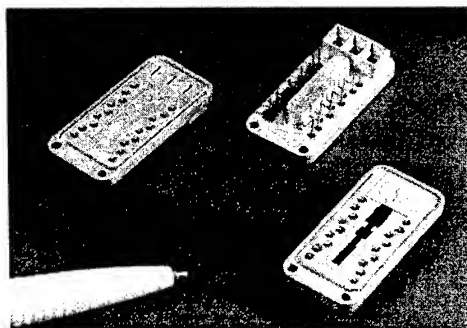


Figure 5: Plastic package for automotive radar module with integrated radiators (courtesy of Dasa)

Evaluation of Glob Top and Underfill Encapsulated Active and Passive Structures for Millimeter Wave Applications

G. Baumann¹, E. Müller¹, F. Buchali², D. Ferling², H. Richter², W. Heinrich³

¹Alcatel Telecom, Mannheimerstr. 22b, D-75179 Pforzheim, Germany

²Alcatel Telecom, Lorenzstr. 10, D-70435 Stuttgart, Germany

³Ferdinand-Braun-Institut für Höchstfrequenztechnik
Rudower Chaussee 5, D-12489 Berlin, Germany

Abstract

The protection of active devices against mechanical and environmental influences is necessary to guarantee a proper performance and life time. Packaging of the devices however is a very cost intensive factor and therefore it is very important to search for more economical packaging methods for RF-applications, too.

In order to investigate the influence of epoxy encapsulation material we have characterized active and passive devices, which are wire bonded with subsequent glob top encapsulation as well as flip chip bonded with underfill encapsulation. The devices have been measured up to 70 GHz in order to evaluate the change of RF-transmission line characteristics and device parameters due to mounting and encapsulation. With a parameter extraction method the elements of an equivalent electrical circuit for the inner active device and the parasitics are determined. A change of impedance for encapsulated transmission lines of about 3Ω for a 50Ω line was found. Wire bonded devices exhibit a stronger variation of parasitics due to encapsulation in comparison to flip chip bonded devices, a reduction in G_{\max} of 1.2 dB and 0.2 dB at 20 GHz were found, respectively. For both HEMT and MESFET the inner device was unchanged. For MMIC and hybrid circuit packaging epoxy encapsulation is suitable even for mmwave range. For circuit design modified parameters should be considered.

Introduction

Glob top encapsulation as a low cost packaging method is well known for silicon devices die- and wire bonded as well as underfilling and subsequent glob top encapsulation for flip chip mounted devices. For GaAs high frequency components traditionally hermetic packages based on metal or ceramic housings are used, which are fairly expensive. The increased application of RF-modules in radiolinks for telecom and computer applications demands a reduction of costs especially for packaging. One approach to reduce costs is to use glob top encapsulation for environmental protection of GaAs wire bonded transistors or even to use flip chip mounted devices with underfilling. MMICs are usually designed for air with a permittivity of $\epsilon_r = 1$ as the medium above the circuit. If the permittivity of the surrounding medium is increased due to encapsulation material the line and device characteristics as well as the parasitics have to be proved. The line impedance and electrical length as well as the device parameters including parasitics are considered in MMIC and hybrid circuit development. These values determine essentially gain and bandwidth of amplifiers. Therefore a detailed analysis of these parameters including the changes due to mounting and encapsulation is necessary to adapt the MMIC design rules. Whereas the design of lines should be adapted to the permittivity of encapsulation material, the change of parasitics and the inner device has to be considered for RF-design.

Realization of device structures

To compare the RF-performance of different chip connection methods wire bond assemblies, Fig. 1, as well as flip chip assemblies, Fig. 2, were prepared using the same active and passive devices with subsequent encapsulation by glob top and underfilling, respectively. Passive coplanar lines on alumina ceramics (chip), Fig. 1c, flip chip bonded on an alumina submount are used to investigate line and interconnection characteristics. A reference line with the same length was used to investigate the influence of flip chip bonding. The lines on the substrate and on the chip are designed as 50Ω coplanar waveguides. As active devices the MESFET, JS8830, with $0.25 \mu\text{m}$ gatelength and $220 \mu\text{m}$ gatewidth, and the HEMT, JS8910, with $0.1 \mu\text{m}$ gatelength and $120 \mu\text{m}$ gatewidth, from Toshiba were used. MESFET and HEMT were mounted die and wire bonded as well as flip chip bonded on an alumina submount.

The wire bond assemblies were realized by die attachment with an epoxy glue and bonding with a 17 μm thick Au wire. Flip chip bonding is a well established technology for standard IC with an increasing application also for RF devices with extremely small bump dimensions, Fig. 3, /Ferling (3)/. The realization of the flip chip assemblies is based on the formation of galvanic Au-microbumps on the substrate and flip chip mounting by Au/Au thermocompression bonding onto the submount, /Richter (2)/. The formation of Au-microbumps is integrated in the standard thin film process flow for substrate manufacturing, whereas the GaAs device is used "as processed" without any additional preparation step prior to flip chip bonding. An Au pad metallization is required, but it is usual applied for RF devices to enable Au wire bonding. The applied bumping method enables the formation of bumps with heights up to 40 μm and diameters down to 25 μm . With this method GaAs semiconductors with contact pad sizes down to e.g. 30 x 40 μm (gate contact pad of Toshiba MESFET JS 8830) could be bonded in a reliable way. Flip chip bonding was performed with a commercially available flip chip bonder at a temperature of 275°C and a bond pressure of 110 N/mm².

For epoxy encapsulation two materials have been applied. The first is a glob top encapsulation as shown in Fig. 1b. Wire bonded devices were encapsulated with a standard glob top material in a two step process. First a dam was placed with a high viscosity epoxy material around the chip edges with subsequent second step with the same encapsulant but with a modified viscosity. Application of the encapsulants was done wet in wet followed by a common curing operation. Another important issue is the dielectric constant of the underfill material, which should be as low as possible to avoid deterioration of RF-performance at millimeter wave frequencies. The dielectric constant of glob top material was 3.2.

In a second way the flip chip assemblies have been encapsulated with an epoxy underfiller, Fig. 2c. Using this method, one has to take into account a very low height between the semiconductor and substrate surface (app. 20 μm) and often very close spacings between the bond studs (e.g. 30 μm). For single chips the area to underfill is very small (e.g. 300 x 400 μm). These applications require an underfill material with low viscosity and very small sized filler particles to fill all spacings reliable. For these small dimensions a very carefully adapted dispense technique and equipment are needed in the case of tiny chips. For our investigations we have used an epoxy material with particle size of 1 - 5 μm and a dielectric constant of 3.2. The cross section of the flip chip assembly in Fig. 4 shows the good underfill result in the narrow gap between chip and substrate.

As a reference flip chip assemblies with glob top encapsulation /Sturdivant (1)/ were prepared according to Fig. 2b. In this variant however air is enclosed between the chip and the substrate.

Passive device structures

The RF-measurements were performed on a wafer prober with coplanar probes. Scattering parameters are measured in the frequency range up to 70 GHz with a HP 8510C and HP8510B network analyzer.

Fig. 5 shows the return loss S_{11} of the reference coplanar waveguide. A return loss of less than -20 dB is due to a good adaptation of the 50 Ω impedance. The flip chip bonded coplanar waveguide with the same design and length has an increased return loss especially at frequencies above 20 GHz. The flip chip bonded device has the additional bump interconnect between submount and the waveguide on chip is detuned due to the submounts permittivity /Tsunetsugu (4)/. The influence of flip chip bonding and detuning on insertion loss, Fig. 6, is negligible.

Figs. 7 and 8 present data for glob top and underfill encapsulated flip chip bonded waveguides with the non encapsulated line as reference. For the underfilled line the return loss deteriorates as a result of change of permittivity. This can be explained by detuning of the CPW line on the chip. Simulations indicate that characteristic impedance decreases by 11%, which causes the higher level of reflection. Also phase constant and attenuation increases by 12% resulting in shorter intervals between the resonance peaks in Fig. 7. On the other hand, the dielectric underfill improves the microwave properties of the bumps by reducing the characteristic impedance mismatch. As a consequence, the increase in reflection with frequency is only weak and at frequencies above 40 GHz all versions exhibit the same return loss level. The calculated parameters of the flip chip bonded and underfilled coplanar waveguides are listed in Table 1. For the glob top variant a characteristic comparable to the underfilled line was found, /Sturdivant,(1)/. The insertion loss of encapsulated waveguides, both glob topped and underfilled, is increased due to waveguide detuning and increased losses of the line, Fig. 8. Measurements have shown that the line impedance of a coplanar line is only detuned of about 3 Ohms at 50 GHz, if there is a glob top encapsulation over the line. For a CPW transmission line an additional loss of 0.6 dB/cm has been extracted.

Active Devices

The MESFET devices were measured after mounting and after encapsulation. Initial on wafer measurements were not possible due to absence of coplanar contact pads. The measured RF-performance after wire bonding and after glob top encapsulation for the wire bonded versions is shown in Fig. 9. The transit frequency f_t goes down from 32 GHz to 23 GHz due to encapsulation. The reduction of G_{\max} caused by the glob top material lies in the range of about 1.2 dB at 20 GHz, with decreasing difference in G_{\max} for higher frequencies.

The measurements of flip chip mounted devices after device mounting and after underfilling are shown in Fig. 10. The transit frequency f_t for the flip chip version goes down from 31 GHz to 25 GHz, without and with underfiller, respectively. The reduction in G_{\max} lies in the range of 0.2 dB at 20 GHz.

For the flip chip devices we have found a reduced influence of encapsulation on RF-characteristics. In the case of flip chip bonding, Fig. 2c, only the chip is encapsulated, whereas in the case of wire bonding a 500 μm long line is glob topped to protect the whole bond wire, Fig. 1b. The influence of encapsulation on the passive feed lines at input and output is increased for the wire bond version.

In order to determine the parasitics of an electrical circuit we have applied a parameter extraction method /Anhold, (5), (6), Dambrine, (7)/. Measurements of the "cold" transistor without amplification as well as of the "hot" active transistor were performed to evaluate the parasitics and the circuit elements of the inner device. With "cold" measurements at $V_{ds}=0\text{ V}$, V_{gs} at pinch off and V_{gs} forward biased, the pad capacitances C_{pg} and C_{pd} , the inductivities L_g , L_s , L_d , and the resistors R_g , R_s , R_d are determined. With a "hot" measurement all the intrinsic elements, as C_{gs} , R_i , C_{gd} , C_{ds} , g_m and τ are determined, Fig. 12. The evaluated elements are listed in Tables 2 and 3 for MESFET and HEMT, respectively.

For the MESFET, Fig. 11, due to glob top encapsulation the pad capacitances are increased drastically to about 70 %. The resistances are increased by about 30% due to the losses of glob top material, whereas the inductances are nearly unchanged as well as the transconductance.

In the flip chip version the underfiller increases the pad capacitances C_{pg} and C_{pd} of about 50 %. The increase of resistances was about 15 % and the inductances and the transconductance are nearly unchanged.

For the HEMT versions we have found a behavior similar to the MESFET. Even for the HEMT the inner device is nearly unchanged due to encapsulation. The parasitics show a similar behavior for the flip chip and wire bonded HEMT in comparison to the MESFET. The pad capacitances increase in both cases, the increase of resistances is not so high compared to the MESFET and the inductances are nearly unchanged.

Comparing flip chip and wire bonding, flip chip bonding leads to drastic reduced inductances, a reduction of 65 % was found. The pad capacitances are of the same order for both variants, but the resistances are increased for flip chip mounting by 13 %.

Conclusions

In conclusion both types of low cost packaging are viable, glob top encapsulation for wire bonded devices as well as underfilling for flip chip mounted devices. We have found an influence of encapsulation material on transmission line characteristics, the characteristic impedance was reduced by 6 % and the loss was increased by about 0.6 dB/cm. For the first time a parameter extraction method was applied to extract the parasitic elements of encapsulated RF-transistors. For the active devices an increase of pad capacitances and resistances due to the permittivity and losses of the encapsulation material was found. Similar results were achieved for MESFET and HEMT devices. The inner active device is not influenced by encapsulation. Glob top encapsulation of wire bonded devices and flip chip mounted components with underfilling exhibit a reduction of transit frequency by 28 % and 19 %, respectively. For wire bonded devices with encapsulation a higher variation of parasitics compared to flip chip assemblies has to be considered.

Acknowledgement

The authors would like to thank A.Gutu-Nelle, M.Worbs, K.Hägele, W.Heck, T.Schleeh, E.Schoeller and G.Zickwolf for the experimental work as well as H.Robin for RF-measurements and evaluation. The work has been supported partly by the German Ministry of Education and Science (BMBF) under contract 16 SV 163/5.

References

- (1) R.Sturdivant, et. al: "Investigation of MMIC Flip Chips with Sealants for improved Reliability without Hermeticity". 1996, Proc. IEEE MTT-S International Microwave Symposium, pp.239 - 242.
- (2) H.Richter, A.Baumgärtner, G.Baumann, D.Ferling "Flip Chip Attach of GaAs-Devices and Applications to Millimeter Wave Transmission Systems," Proc. Microsystem Technologies '94 Conference, pp. 535-543, VDE-Verlag GmbH
- (3) D.Ferling, G.Baumann, H.Richter, A.Baumgärtner, U.Meier: "Multichip Modules with Integrated Planar Antenna for mm-Wave Radio Communication". Proceedings 25th European Microwave Conference, p. 111-116, Bologna, Italy, Sept. 4-8, 1995.
- (4) H. Tsunetsugu, T. Hayashi, K. Katsura, M. Hosoya, N. Sato, N. Kukutsu, "Accurate, stable, high-speed interconnections using 20- to 30- μm microsoldier bumps, IEEE TCPM, Vol. 20, No.1, March 1997, pp.76-82.
- (5) R. Anhold, S. Swirhun, "Equivalent-Circuit Parameter Extraction for Cold GaAs MESFET's", IEEE MTT, Vol.39, No.7, July 1991, pp.1243 - 1251.
- (6) E. Arnold, et.al: "Direct Extraction of GaAs MESFET intrinsic element and parasitic inductance values", 1990, Proc. IEEE MTT-S International Microwave Symposium, pp. 359 -362.
- (7) G. Dambrine, et al: "A new method for determining the FET small-signal equivalent circuit", IEEE MTT, Vol.36, No.7, July 1988, pp.1151 - 1159.

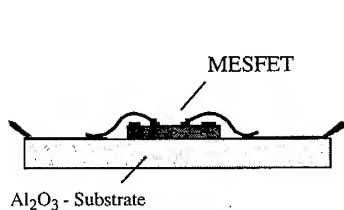


Fig. 1a: Wire bonded chip

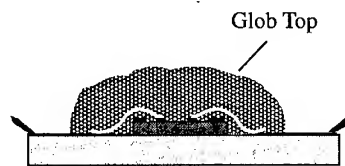


Fig. 1b: Wire bonded chip with glob top encapsulation.

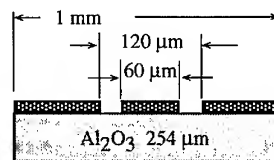


Fig. 1c: Dimensions of the CPW line.

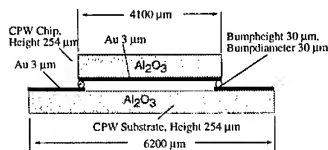


Fig.2a: Flip chip bonded chip.

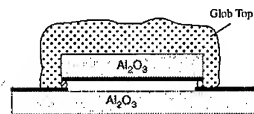


Fig. 2b: Flip chip bonded chip with glob top encapsulation.

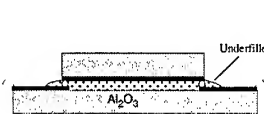


Fig. 2c: Flip chip bonded chip with underfill.

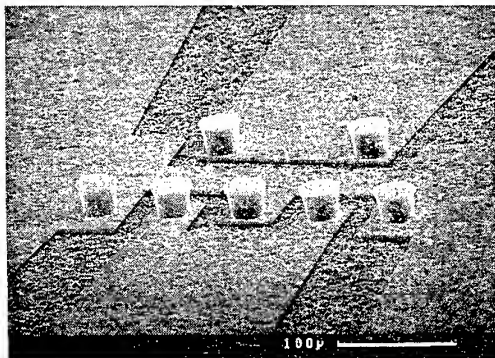


Fig. 3: Substrate with Au-bumped chip interconnect sites (Bump height / diameter 25 / 35 μm)

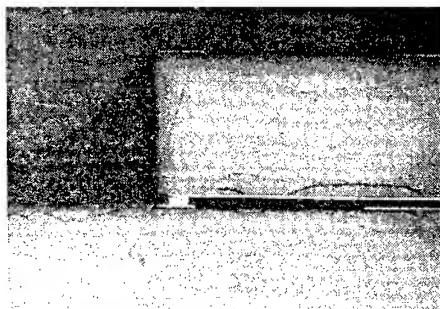


Fig. 4: Crosssection of a flip chip mounted device with epoxy underfill

	without underfill	with underfill $\tan(\delta\epsilon)=0$	with underfill $\tan(\delta\epsilon)=0.005$
β/β_0 @ 1 GHz	2.380	2.676	
α (dB/mm) @ 1 GHz	0.026	0.029	
Real(Z) [Ω] @ 1 GHz	49.8	44.2	
β/β_0 @ 50 GHz	2.309	2.593	2.593
α (dB/mm) @ 50 GHz	0.146	0.165	0.181
Real(Z) [Ω] @ 50 GHz	47.9	42.8	42.8

Table 1: Calculated parameters of flip chip bonded coplanar structure, see Fig. 2a and Fig. 2c.

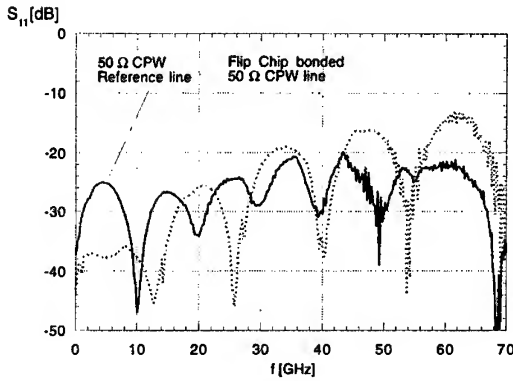


Fig. 5: Measured return loss of flip chip bonded chip in comparison with a coplanar waveguide of identical line length, acc. Fig. 1a, c.

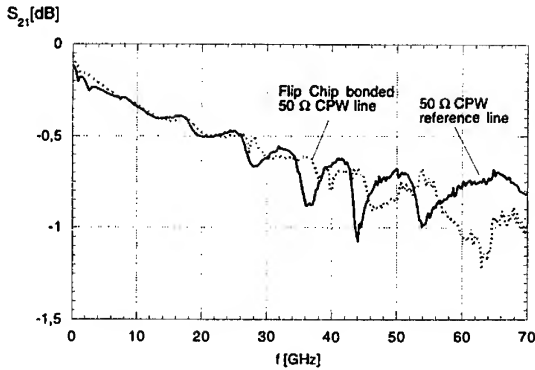


Fig. 6: Measured insertion loss of a flip chip bonded chip in comparison with a reference line of identical line length.

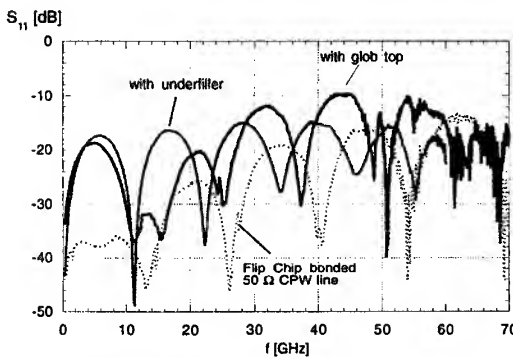


Fig. 7: Measured return loss of a flip chip bonded CPW transmission line, acc. Fig. 2 with glob top and underfiller.

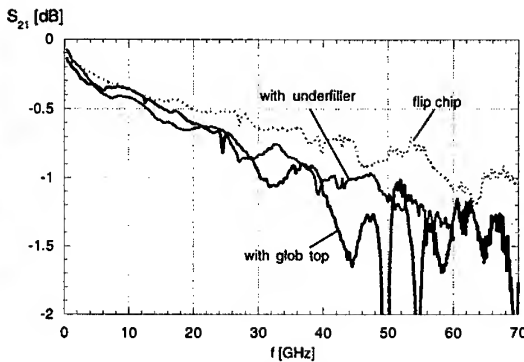


Fig. 8: Measured insertion loss of a flip chip bonded CPW transmission line, acc. Fig. 2 with glob top and underfiller.

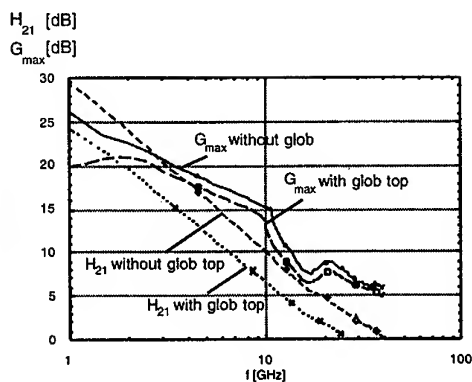


Fig. 9: Measured G_{\max} and H_{21} of the MESFET JS8830 in wire bond version, with and without glob top.

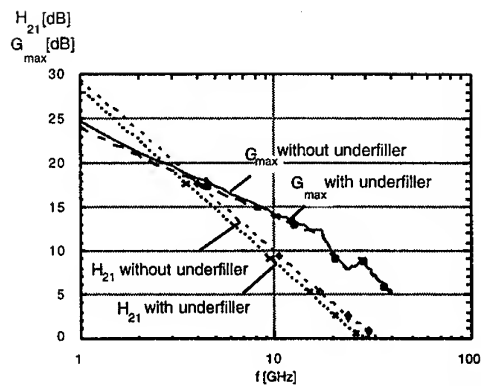


Fig. 10: Measured G_{\max} and H_{21} of the MESFET JS8830 in flip chip version, with and without underfiller.

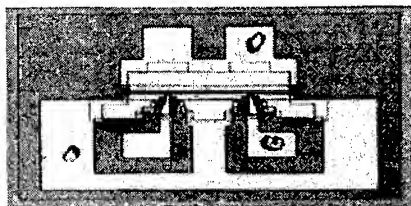


Fig. 11: Layout of the MESFET JS8830.

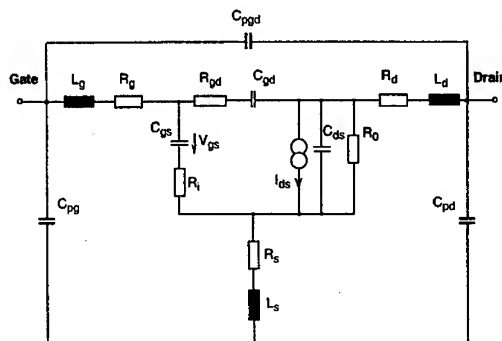


Fig. 12: Equivalent circuit model

	Wire bond	Wire bond with glob top	Flip chip	Flip chip with underfiller
C_{pg}/fF	88	124	90	112
C_{pd}/fF	55	105	41	70
R_g/Ω	3.2	4.8	3.66	5.05
R_s/Ω	3.5	4.5	3.75	3.78
R_d/Ω	3.4	4.2	4.28	4.4
L_g/nH	0.11	0.12	0.043	0.047
L_s/nH	0.030	0.037	0.013	0.014
L_d/nH	0.13	0.118	0.018	0.0163
g_m/mS	62.5	56	62	63

Table 2: Elements of equivalent circuit for a MESFET JS8830.

Wire bond	Wire bond with glob top	Flip chip	Flip chip with underfiller
58	98	124	150
40	50	62	47
3.5	4.6	5.6	6.8
2.1	2.1	3.0	3.7
3.8	4.5	5	5.6
0.079	0.1	0.029	0.03
0.016	0.021	0.04	0.011
0.10	0.12	0.029	0.028
53	56	74.1	75.8

Table 3: Elements of equivalent circuit of a HEMT JS9810.

INNOVATIVE MULTILAYER TECHNOLOGIES FOR ACTIVE PHASED ARRAY ANTENNAS

**Bernard LEDAIN, packaging Research and Development Manager
Jean Luc HERBLOT, Microwave Senior Engineer
DASSAULT ELECTRONIQUE
55, Quai Marcel Dassault, 92214 SAINT-CLOUD, FRANCE**

ABSTRACT

A high performance organic multilayer structure has been developed and manufactured for an active phased array antenna. The driving factors were cost reduction and high integration. To satisfy these requirements, the same multilayer structure mixing aluminum and Teflon® laminates is used as a mechanical support of microwave functions, RF and DC interconnects, power divider including planar resistors, thermal dissipator, ASIC's and MMIC packages. Key technological developments that have been realized are planar resistors in stripline configuration using Ohmega® Foil technology with 10% tolerance, fusion bonding multilayer technology, starting with thick aluminum backed laminates (plated through holes connected to aluminum, plated through holes unconnected to aluminum) and MMIC's and ASIC's integration (chips or ceramics).

This approach has proved to be efficient in terms of cost and performances by reducing RF discontinuities, reducing bonding and wiring, minimizing interface parasitic, eliminating parasitic resonance and reducing coaxial connectors.

Further developments are in progress: passive function integration such as filters, couplers, ... or dielectric loss reduction using suspended stripline propagation.

INTRODUCTION

Dassault electronique has developed a technological and electrical test vehicle of a wide band active phased array antenna.

A new technology for power splitter has been developed to:

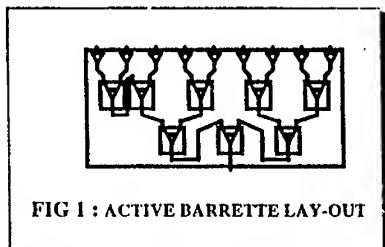
- minimize weight and volume
- minimize the number of electrical discontinuities (change in microwave propagation modes)
- minimize thermal gradient to keep accurate phase and amplitude balance of the different microwave channels in the temperature range
- minimize recurring costs
- maximize testability, modularity, reworkability.

To satisfy these constraints it was decided to integrate on the same multilayer structure the low noise amplifiers and the power divider. This structure was called «active barrette».

Technical requirements, technological developments and results of this «active barrette» will be described further on in this article.

«ACTIVE BARRETTE» DEVELOPMENT

Electrical requirements



Each «active barrette» (fig. 1) has 9 inputs and one microwave output. It integrates :

- 9 low noise amplifiers (MMIC and chip capacitors mounted on a ceramic substrate) as close as possible to the radiating element,
- the 9 ports unbalanced power divider
- one layer for power supply of amplifiers (multivoltage)
- one filter to control power supplies stability.

The standard solution for this type of packaging in Dassault Electronique is a double sided aluminum chassis:

- one being the microwave side : bare chips on ceramic substrates are interconnected by microstrip lines printed on Teflon boards and buried into the mechanical housing.
- the other being the DC side : surface mount components are soldered on a standard printed circuit board. This side provides microwave side with power and commands.

The hermeticity is accomplished by soldered gals beads, and by a laser welded lid that is used for grounding between microwave channels.

This well known solution is not compatible with interconnection density, antenna pitch, weight and cost, needed by this new application.

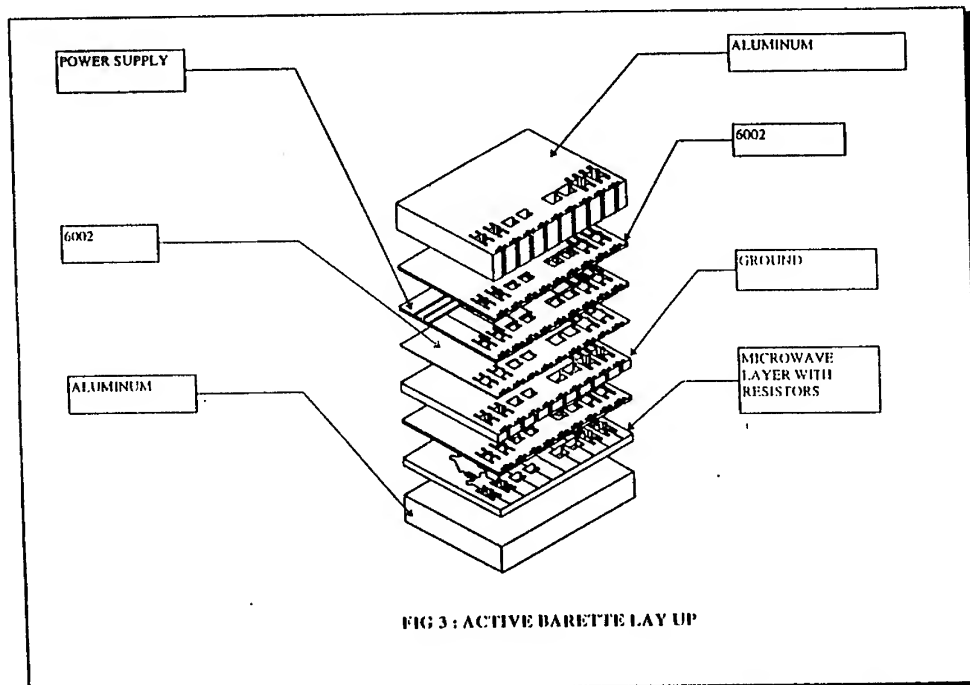
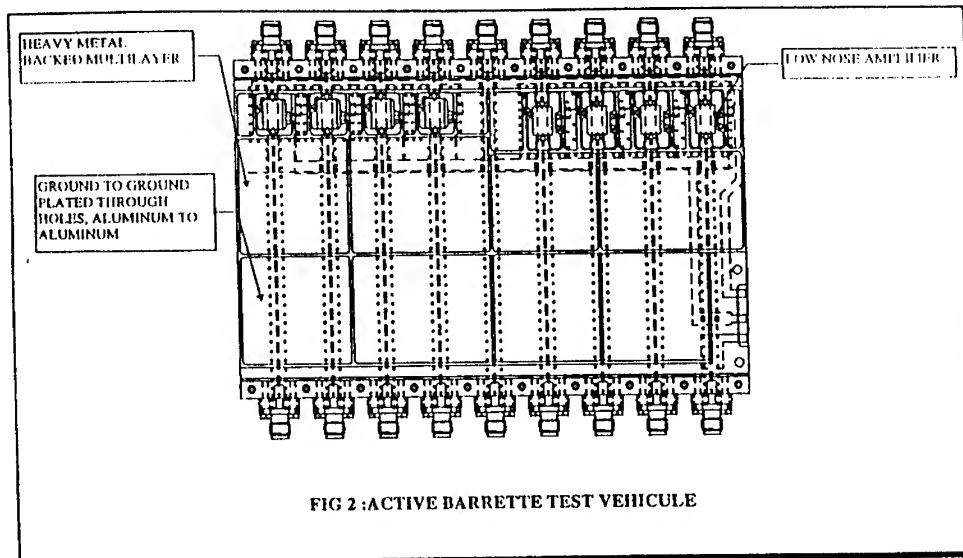
One answer to the technical problem is :

- *the development of a multilayer structure used as simultaneously :*
 - * mechanical support
 - * electromagnetic grounding
 - * thermal dissipator
 - * electrical interconnection between microwave functions (RF, DC)
 - * hermetic enclosure for MMIC's
 - * power divider
- *the direct connection of functions by removing standard coaxial connectors.*

The proposed solution is based on a multilayer heavy metal backed structure with milled cavities for amplifiers integration. The microwave layer is in stripline configuration to minimize losses with ground to ground plated through holes. The power divider is a resistive Wilkinson type. A picture of the finished test vehicle and the lay up of the corresponding structure are described in the next two figures (2-3).

RT Duroid® 6002 with fusion bonding has been selected because it combines excellent microwave properties with a Z axis coefficient of thermal expansion similar to copper that allows very high reliability of plated through holes. In order to minimize size and losses of the power divider, stripline technology has been chosen.

Three major technological problems had to be solved for the manufacture of these «active barrettes»; **integrated resistors in stripline configuration, plated through holes in aluminum heavy metal backed multilayers, integration of low noise amplifiers.**



RESISTORS IN STRIPLINE CONFIGURATION

The nine ports power divider has been designed using 8 two ports unbalanced power dividers with 3 cells each. Consequently, each « barrette » requires 24 resistors within the range of 100 to 300 Ω . /a tolerance of $\pm 10\%$ is needed on each resistor. Different technical solutions have been studied:

- *chip resistors soldered in milled cavities in the multilayer structure*

Chip resistors have been vapor phase soldered in such cavities and have been submitted to 500 thermal shocks (-55°C to 125°C) and 500 hours storage at 125°C without any degradation. This was a convenient solution in terms of reliability. It has several advantages : 100% control of resistor values, easy reworkability, wide range of resistors possible on the same board. However, it has many disadvantages : expansive milling, reducing the connectivity of the multilayer ; many soldered connections, reducing global reliability; parasitic radiation; local discontinuity of line impedance due to the size of the chip resistor bonding pads which are wider than the size of the divider conductive lines.

- *screen printing of polymer inks*

Extensive study has been made. Results have been disappointing. Resistors values are not reproducible :

- . After screening, tolerance is $\pm 40\%$.
- . After laser trimming, less than 1%
- . Thermal coefficient of resistance 0.3%
- . Variation after 100 thermal cycles in microstrip configuration +3%
- . Variation after 100 thermal cycles in stripline configuration + 14%. This clearly indicates a chemical degradation of the ink during lamination.

In conclusion, polymer inks can be used only in microstrip configuration with laser trimming.

- *Ohmega® Foil technology*

A two years study sponsored by the D.G.A. has been carried out, the results of which are the following:

- etching tolerance : $\pm 5\%$
- minimum resistor width : 200 μm
- tolerance after fusion bonding : $\pm 7\%$
- no influence of the Ohmega ® foil layer on microwave properties
- shift of resistor values after 500 thermal cycles (-55°C , $+125^{\circ}\text{C}$):
 - . microstrip : +2%
 - . stripline : + 3%
- thermal coefficient of resistance within the range (-55°C , $+125^{\circ}\text{C}$)
 - . microstrip : $\pm 6\%$
 - . stripline : $\pm 7\%$
- power handling : 300mW

No shift in microwave performance of tested two ports power divider- (chip resistors, Ohmega ® Foil technology) has been noticed following :

- 500 thermal cycles (-55°C , $+125^{\circ}\text{C}$)
- 500 hours at 125°C
- 40 days 40% C , 95%HR
- 48 hours salt spray

All results clearly show that with a -3% correction of the drawings, high reliability Ohmega® Foil resistor with $\pm 10\%$ can be produced in stripline configuration.

Key points for manufacture are the following ones:

- chip shape and orientation
- over etching compensation
- resin protection of resistors after etching : a polyimide resin was selected.

According to these results Ohmega® Foil technology has been selected to produce the power divider. Today, with the established process, we have 100% resistors in the 10% tolerance. (24 test resistors with the same values as the functional resistors are manufactured and tested on the same sheet of material).

PLATED THROUGH HOLES IN ALUMINUM HEAVY METALBACKED MULTILAYERS

The second technological problem that had to be solved to produce these boards was to realize high reliability plated through holes in aluminum and Teflon® for ground to ground connections. The following parameters have been optimized :

• *drilling*

Drilling Diameter (mm)	Spindle Speed (RPM)	Infeed Rate (mm/mn)	Retract Rate (mm/mn)
0.4	70 000	1.5	0.5
0.55	50 000	0.1	0.1
0.65	50 000	0.1	0.1
0.75	48 000	0.1	0.1
0.85	44 000	0.1	0.1
1.05	40 000	0.1	0.1
1.25	35 000	1	5
1.55	35 000	2	9

• *Adhesion improvement between aluminum and 6002 material :*

The best results are obtained by a chemical activation of aluminum and an ammonium persulfate etching of copper on the Teflon® raw material.

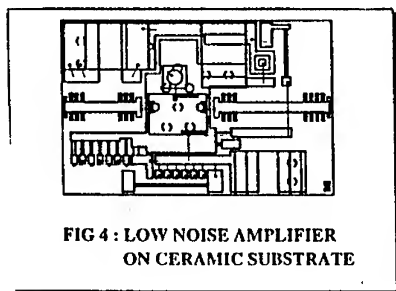
• *Metallisation of plated through holes :*

Two standard commercial lines of metallisation based on double zincate process have proved to be efficient. A precise control of operating conditions is essential (for example, the water rinse between different bathes must be very efficient to obtain good results).

Plated through holes in contact with or isolated from aluminum have been produced and proved to be very reliable (500 thermal cycles -55°C, +125°C)

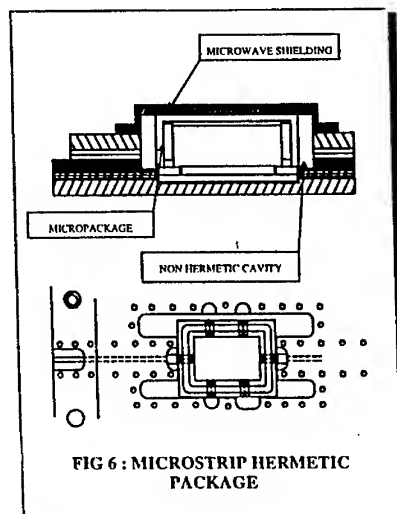
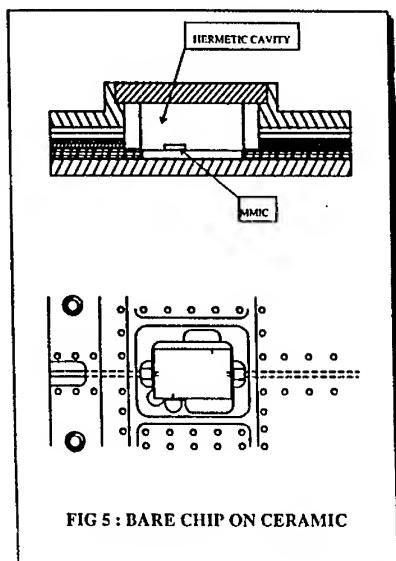
LOW NOISE AMPLIFIERS INTEGRATION

The amplifier of the «active barrette» is a thin film ceramic substrate that integrates the MMIC chip, microstrip lines for I/O's connections and tuning of the MMIC, circuits for polarization, decoupling and protection (fig. 4).



Two types of integration have been tested : bare chip on ceramic (fig. 5), and ceramic in a microstrip hermetic micropackage (cofired ceramic or metallic with ceramic feedthrough) (fig. 6). In both cases, good results have been obtained , up to X band.

For this test vehicle, integration of amplifiers in metallic micropackages with microstrip feedthrough was finally selected as the most appropriate (no problem of hermeticity, good electrical results, efficient surface ratio between the ceramic and the finished package). For commercial applications, bare chip should be more effective as regards to cost consideration (micropackages are very expensive).



CONCLUSION FURTHER DEVELOPMENTS

This concept of integration, patented by DASSAULT ELECTRONIQUE has proved to be very efficient. A 30% save in weight and price has been found compared with the more traditional packaging technology (buried microstrip lines).

The active power splitter is convenient for many applications (space, aircraft, civilian...). The concept has been developed for X band applications. It is possible to imagine higher frequencies configurations for this process.

Further developments are in progress allow the use of this concept of packaging to more sophisticated functions.

- Integration of passive components such as filters, couplers
- suspended air lines or filters for dielectric losses reduction

ACKNOWLEDGMENTS

D.G.A. for sponsoring studies.

G.DANTAN for mechanical study.

S.SECHER and V.RANANJASON for technological developments.

Motion Monitoring with a Millimeter Wave Radar Sensor

Thomas Troll, Jürgen Detlefsen

Technische Universität München
Lehrstuhl für Hochfrequenztechnik
Arcisstr. 21, D-80333 München, Germany

Phone/Fax: +49-89-289-23395/23397
e-mail: {troll|det}@hfs.e-technik.tu-muenchen.de

ABSTRACT

An existing 94 GHz pulse radar system for autonomous mobile robots has been extended by a CW Doppler unit for fast motion monitoring. The extension is set up with low cost components and works independently from the pulse system. Until now the capabilities for motion detection has been validated in several environments.

1 INTRODUCTION

This work is part of a special research programme towards the development of autonomous mobile robots which can fulfil service and transport tasks in structured environments like office buildings and industrial plants.

Though a radar sensor in the field of robotics seems to be very uncommon, there are a lot of benefits using millimeter waves for perception tasks like collision avoidance, localization and exploration [6]. Since the propagation of microwaves is nearly independent of atmospheric conditions and coherent signal processing allows high sensitivity, it is possible to cover distances up to 100 m at reasonable transmitted power. Combined with the direct access to the object's velocity, this feature lets a microwave radar usefully enhance the sensing capabilities of an autonomous system, as other self-illuminating sensors like laser scanners and ultrasonic sensors hardly exceed a detection range of 15 m.

This paper is organized as follows: Starting with a brief description of the existing radar system in section 2, an overview over the problem of motion monitoring radar system follows in section 3. There the contribution focusses on an extension for fast motion detection, which is based on a continuous wave Doppler unit. Finally the signal and information processing of the Doppler data is validated in various examples shown in section 4.

2 SYSTEM DESCRIPTION

We have developed and evaluated an experimental 94 GHz sensor for the use on autonomous vehicles (figure 1). It is designed to measure distances as well as velocities of objects. The distances are determined via the time of flight of single pulses in a detection range of 80 m. A very short pulse width of 2 ns results in a radial resolution of 25 cm. The distance of resolved objects can be measured with an accuracy of 2 cm. The velocity is directly accessible via the Doppler effect. This effect requires a coherent signal source to guarantee a fixed relation between transmitted and reflected signal. In our case an IMPATT

oscillator, phase-locked by a Gunn oscillator, guarantees high phase stability at sufficient peak power. The carrier frequency of 94 GHz yields corresponding Doppler frequencies of 625 Hz per 1 m/s, which permit accurate velocity measurement within a short observation time.

For the angular resolution of 2.1° the radar beam is focussed by a Fresnel type lens, 110 mm in diameter. This sharp beam is deflected by a mirror for three-dimensional imaging of the surroundings. The implementation of the sensor is described in detail in [2], the most important system parameters are shown in table 1. Based on this system various applications like navigation and observation, which correspond to typical perception tasks of an autonomous robot, have been implemented in the last years [4][5].

Even if the object's velocity can be extracted out of the pulse Doppler signal as well, the result refers to only one range gate at a time. Scanning the range of sight by this method would be a very time consuming approach and is not practicable for fast motion detection. Since a pure motion monitoring does not need a range resolution, the system has been extended by a continuous wave (CW) Doppler unit. This unit is completely independent of the pulse system and, in contrast to it, it requires much less and cheaper components.

Figure 2 shows the system extension. The motion detector uses the quadrature demodulator like the pulse unit to yield amplitude and phase of the motion signal. The Doppler signal of typical objects in indoor environments hardly exceeds a bandwidth of 10 kHz. Therefore a standard signal processing unit can be used. To switch the operating mode between pulse and CW, a simple digital signal has to be generated by the control unit. A concurrent use of both modes seems possible, since the CW signal is not entirely suppressed by the ultra fast PIN switch.

3 MOTION MONITORING

In principle there are two methods for motion detection: directly via the Doppler effect and by tracking the object's location. The latter method requires a sensor system with a high radial resolution and sufficient signal-to-noise ratio, since the objects have to be detected for a longer time. Experiments with laser and millimeter wave sensors for intelligent cruise control have shown that this method is not robust enough for industrial applications.

Unlike that the direct access to the velocity is a very efficient way to obtain velocity information. However, to exploit the Doppler effect a coherent measurement system is needed. Millimeter wave sensors offer a high carrier frequency which yield conveniently high Doppler frequencies of about 500 Hz per 1 m/s. In addition to a quantitative evaluation of the signal, an analysis of the spectral distribution may allow a classification of movements e.g. a man/machine distinction.

The Doppler signal of an object within the detection range of a coherent system, as shown in figure 2, can be described as follows.

$$u_a(t) = A e^{j2\pi f_d t}.$$

The amplitude A only depends on the distance and the reflectivity of the illuminated object. The object's velocity causes a range independent frequency, the well-known Doppler frequency

$$f_d = 2 \frac{v_r}{\lambda_0}.$$

To obtain the motion information, data processing is performed using either a fast fourier transform (FFT) or a phase evaluation of the convolution term (PACF). The latter is much faster, but it fails, if there is more than one object in the radar beam at a time.

4 EXPERIMENTS AND RESULTS

Stationary deflection mirror To validate the capabilities of the CW Doppler unit, it is tested in various environments. Figures 3 and 4 show the Doppler signal of a corner reflector mounted on a motor driven linear axis. The velocity is nearly constant and the spectrum is only limited by the system's resolution. In contrast to it a moving person causes a signal as shown in figure 5. According to its varying velocity it yields a spread spectrum in the frequency domain (figure 6). In addition to a quantitative evaluation of the signal, an analysis of the spectral distribution may allow a classification of movements e.g. a man/machine distinction. This would be a very useful feature for busy environments.

Rotating deflection mirror With regard to the moving objects there is no difference in the received signal between a non rotating and a rotating deflection mirror. As long as the object remains in the scanning radar beam, its velocity information can be determined. In the rotating case the immobile scene causes an additionally slow varying signal, since amplitude and phase of the reflected signal vary while the beam is scanning the surroundings (figure 7). This signal is periodic with one revolution of the mirror and therefore it can easily be calibrated. Thus the sensor is able to detect small variations of the environment (moving and stationary objects) with an extremely high sensitivity, since an object shift of 1.5 mm causes a phase-shift of 360° (figure 8).

5 CONCLUSION

An existing 94 GHz pulse radar system has been extended by a CW Doppler unit for fast motion monitoring. The extension is set up with low cost components and works independently from the pulse system. Until now the capabilities for motion detection are validated in several environments. In addition to the motion monitoring especially the experiments with a rotating mirror let expect a operation of the system for self-localization on natural landmarks [1][3].

6 REFERENCES

- [1] U. D. Hanebeck and G. Schmidt. Absolute Localization of Fast Mobile Robots Based on an Angle Measurement Technique. In *IFAC Workshop on Intelligent Components for Autonomous and Semi-Autonomous Vehicles*, Toulouse, France, 1995.
- [2] M. Lange and J. Detlefsen. 94 Ghz Three-Dimensional Imaging Radar Sensor for Autonomous Vehicles. *IEEE Trans. Microwave Theory Tech.*, 39(8):819–827, 1991.
- [3] T. Röfer. Navigation mit eindimensionalen 360° -Bildern. In R. Dillmann, U. Rembold, and T. Lüth (Hrsg.), editors, *Autonome Mobile Systeme*, Informatik aktuell. Springer-Verlag, 1996.
- [4] M. Rožmann and J. Detlefsen. Environmental Exploration based on a Three-Dimensional Imaging Radar. In *Proceedings of the IEEE/RSJ International Conference on Intelligent Robots and Systems*, pages 422–429, Raleigh (NC), 1992.
- [5] M. Rožmann and J. Detlefsen. Standortbestimmung in Innenräumen mit einem hochauflösenden 94-GHz-Radarsensor. In *8. Radarsymposium*, pages 43–50. Deutsche Gesellschaft für Ortung und Navigation, Verlag TÜV Rheinland, Köln, 1993.
- [6] N. O. Stöffler and T. Troll. Model-update by Radar- and Video-based Perceptions of Environmental Variations. In *International Symposium on Robotics and Manufacturing*, pages 751–756, New York, 1996. ASME Press.

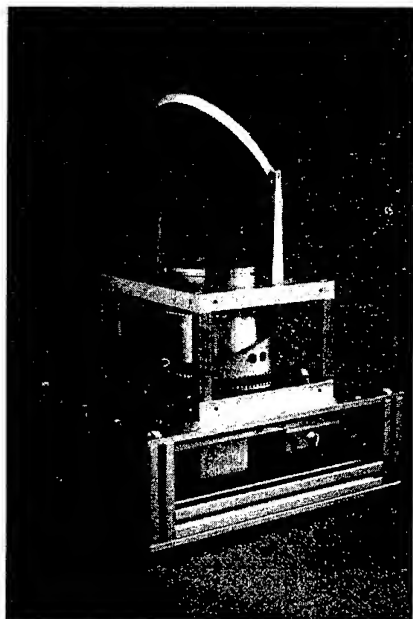


Fig. 1 Photograph of the 94 Ghz Radar Sensor.
Dimensions: 28 cm×33 cm×45 cm.

System Parameters

Frequency	94 GHz
Wavelength	3.2 mm
PRF	1 MHz
Pulse width	1.7 ns
Pulse bandwidth	700 MHz
Pulse peak power	10 mW
Radiated mean power	20 μ W
Detection range	0 ... 80 m
Radial resolution	25 cm
Distance accuracy	2 cm
Angular resolution	1.5°
Angular accuracy	0.15°
Velocity range	± 8 m/s
Velocity accuracy	10 mm/s
Deflecting system	stepper mot.
Deflection angles:	
Azimuth	360°
Elevation	$\pm 18^\circ$

Table 1

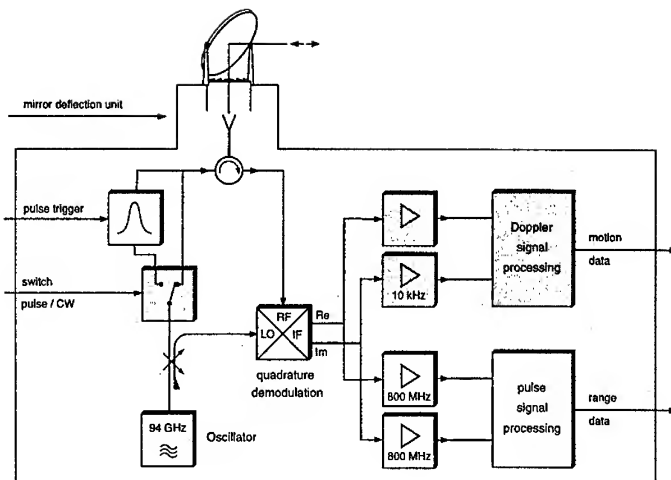


Fig. 2 Extension of the existing system by a continuous wave Doppler unit

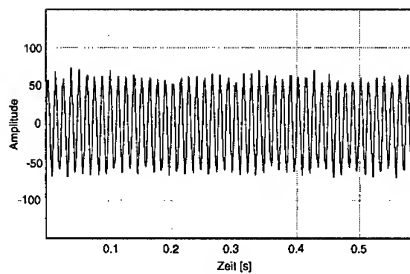


Fig. 3 Stationary deflection mirror: Time domain signal of a moving corner reflector

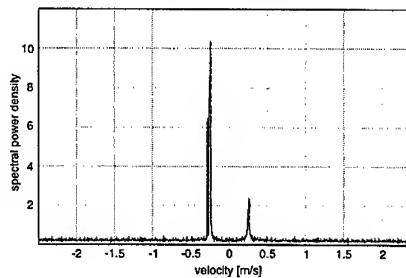


Fig. 4 Stationary deflection mirror: Doppler spectrum of a moving corner reflector

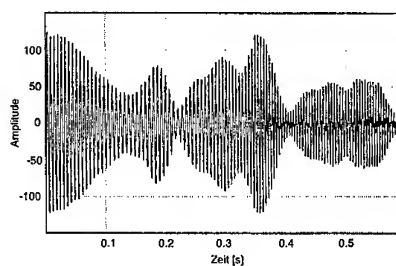


Fig. 5 Stationary deflection mirror: Time domain signal of a moving person

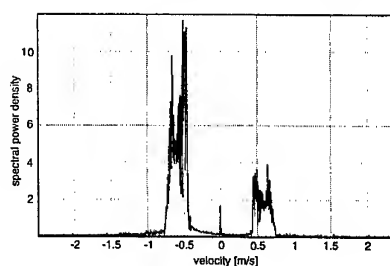


Fig. 6 Stationary deflection mirror: Doppler spectrum of a moving person

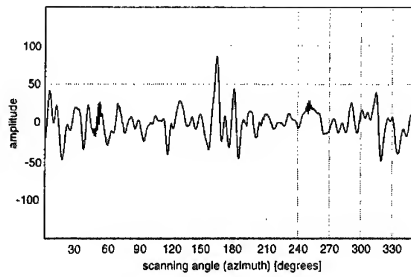


Fig. 7 Rotating mirror: The signal is caused by the stationary scene and is periodic with one revolution of the deflection mirror.

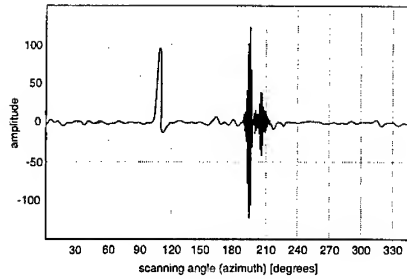


Fig. 8 Rotating mirror: The response of the stationary scene (fig. 7) is calibrated. Detection of two environmental variations. At 100° a new stationary object and at 190° a moving object.

COLLISION AVOIDANCE RADAR ABLE TO DIFFERENTIATE OBJECTS

P.J.F. Swart and L.R. Nieuwkerk

IRCTR, Delft University of Technology, P.O. Box 5031, 2600 GA Delft, The Netherlands

Tel.: +31 15 278 1023, Fax: +31 15 278 4046

e-mail: swart@irctr.et.tudelft.nl

ABSTRACT

The Collision Avoidance Radar *Colarado* (Collision Avoidance Radar Able to Discriminate Objects) is a multistatic frequency modulated continuous wave (FMCW) radar system developed for use in the control system of an autonomous vehicle. The aim of the system is to detect the presence of obstacles (targets) in the surrounding area and in addition to determine their positions and ultimately follow their movements. The advantage of using radar for this purpose is that unlike the sensors based on other physical principles (optical, ultrasound), its performance is insensitive to the illumination level, atmospheric disturbances (like fog) or acoustic noise in the environment. In the next a laboratory prototype system version, the demonstrator, is described and first results are presented.

1. INTRODUCTION

The Colarado project aims are the realisation and demonstration of a very flexible advanced anti-collision radar (Obstacle Warning Radar, OWR) with real-time FMCW radar signal processing. The Delft collision avoidance radar is designed for use on automatic guided vehicles, Jacobs (1) and Staaldunin (2). The radar is developed at the International Research Centre for Telecommunications-transmission and Radar, IRCTR. The RF and LF parts are made by the Telecommunication and Teleobservation Technology group, the real-time radar signal processing development is carried out in co-operation with the laboratory of Computer Architecture and Digital Techniques, both at the department of electrical engineering of Delft University. Project funding is provided by the Netherlands Technology Foundation.

The realised demonstrator is one of the experimental radar facilities at IRCTR. The FMCW radar system has a rather high spatial resolution that is needed because of the multistatic antenna configuration on a relatively small base to achieve three-dimensional 'imaging' of the target area. The chosen strategy and original concept puts a large demand on real-time signal processing. The demonstrator validates the system concept and forms the instrument to arrive at systems of practical use. The parallel multi-processor development system allows for reconfigurable prototyping.

Spin-off are mobile collision-avoidance systems (road, rail, shipping and aviation) based on initial use on automatically guided -container- vehicles for the European Combined Terminals company in the Rotterdam harbor area. The real-time signal processing algorithms are another important Colarado spin-off.

2. COLARADO SYSTEM

The radar is of the FMCW type and uses a multistatic antenna system consisting of two transmit and three receive antennas. The transmit signal is produced by a voltage controlled oscillator that is sawtooth steered over a 1.5 GHz bandwidth around 9.75 GHz, resulting in 10 cm range resolution, in 256 μ s sweep time followed by an idle time of 32 μ s. The RF signal to the two transmit antennas is time-multiplexed on a per sweep basis. The three receiver channels work in parallel. Thus with 5 antennas 6 propagation paths of different length are obtained to enable the location of objects in 3-D space.

The antennas are located in the vertical plane on a support of 2.5 m width and 1 m height on the front of the automatically guided vehicle. The bottom of the antenna frame is 0.5 m above the ground. The antennas are MLA (microstrip like waveguide antennas) small open-ended dielectric filled waveguides, Tian et al (3). The azimuth opening angle of the transmit antennas is 108°, the elevation 3 dB beamwidth is 80°. The antenna directivity is 7 dB. The effective isotropically radiated power is 10 mW. Specifications are listed in Table 1, the system block diagram is given in Fig.1.

The real-time signal processing tracking and tracing algorithms, scene display and collision avoidance signal are implemented on a parallel PowerPC's computer. The processing aims at real-time reconstruction of 3-D scenes

as sensed by the system. After sampling and FFT processing of the FMCW radar beatsignal into 128 range bins, i.e., a maximum range at 12.8 m, the beatfrequency spectra are scanned for peaks corresponding with individual objects (Peak Tracking and Tracing). The results from the three receiver channels are then used to reconstruct the spatial coordinates of each object as located in the scene (Object Tracking and Tracing). Switching between the two transmit antennas results in two complete target maps that are finally matched to eliminate false targets resulting from combinations of spectral peaks belonging to different true targets, Schier et al (4).

The signal source is one single VCO (Radian type 2829A) with 20 dBm output power that is within 0.5 dB constant from 9 to 10.5 GHz. Phase noise is specified as -85 dBc/Hz at 100 kHz. The VCO non-linearity amounts to only 0.5 percent which however was found still to result in a spectral leakage, i.e., resolution degradation, that is too large with respect to the Colarado system requirements. After correction using a RAM table input to the sawtooth steering generator overall linearity is within 0.025 percent with a good long term stability. The 1.5 GHz bandwidth gives a range resolution of 10 cm and depending on the placement of the antennas on the 2.5 by 1 m mounting frame this results in azimuth and elevation angle resolutions around 10 respectively 20 degrees. This may be improved by using the spectral phase information.

The transmit antenna inputs and the receiver antenna external mixer LO inputs are connected with 3 m length SMA cables to the VCO output signal. The cable attenuation is around 1 dB/m at 10 GHz. The RF level at the transmit antenna input is 3 dBm. The mixer LO input is about 6 dBm. The mixer down-converts the received RF signal to the beatsignal frequency band of 35 to 535 kHz. The minimum received signal based on the RCS of a human at the maximum range distance of 12.8 m equals -101 dBm. Without the use of low-noise RF preamplifiers the noise level at the output of the receive antenna is -118 dBm. Since in practice a S/N ratio of 17 dB was not reached (mixer isolation, reflections, VCO phase noise, AM, LF-amplifier, 12 dB/oct dynamic range compression) RF pre-amplifiers are placed at the receive antenna outputs (20 dB gain, 4 dB noise figure).

The dynamic range in object RCS is set to 30 dB. An extra 20 dB is needed for maximally 10 objects in the scene. Accounting furthermore for the antenna diagram and the deviation from 12 dB/oct spatial spreading loss due to the multistatic antenna configuration the total dynamic range is 60 dB. The minimum S/N ratio is 20 dB.

3. CURRENT STATUS

The Colarado anti-collision radar demonstrator is operational since begin 1997, a photograph is shown in Fig. 2. The radar (X-band) RF-part, LF-part, analog to digital conversion, FFT, interfacing and processing hardware (Arcobel 4x transputer-PowerPC) are complete and function within the imposed specifications (real-time). The RF-part and the (one of three identical, cyclic phase-locked printed circuit boards) receiver digital part are shown in Figs. 3 and 4. The radar was linearised, system-parameters were measured followed by modifications mainly to reach the required system sensitivity (detection of a human being). A full calibration of the radar (amplitude and phase over the complete range) remains to be done. Digitalisation, FFT spectrum determination, data transport to the processing part for the three parallel receiver channels with optional windowing and complex or polar format output are in every detail working properly (6 Mbyte/s). For the demonstrator processing (parallel processor) and simulator (sequential, workstation(s)) a uniform software environment has been developed in such a way that algorithms designed for and tested on the simulator can directly be used also in the demonstrator and vice versa so that radar data recorded with the demonstrator can be played back on the simulator where results on the same data with various algorithms can be intercompared.

Thus, a very flexible advanced anti-collision radar (Obstacle Warning Radar, OWR) and data processing system is available. The system offers three-dimensional multi-target scene information of which the geometric resolution can be improved by additional phase processing, and possible velocity measurement.

4. MEASUREMENTS

To verify the system specifications and to provide data sets for further processing algorithm development, test measurements are performed. Extensive testing of the system is partly carried out in-door in a room of 9 x 6.5 x 3 m. The actual system coverage area of 12.8 x 10 x 5 m exceeds the available space and as a consequence many large reflections from the walls and ceiling as well as multi-path signals severely mask the contributions of targets under test. To partly overcome this problem and yet to remain in a very well controllable laboratory situation a transponder is used in stead. The in-door measurement setup of the system and some early results are given in Fig. 5. From these in-door experiment results it is concluded that the detection algorithms based on only amplitude range data gives already reasonable results.

An initial out-door test showed that the system sensitivity is well above the RCS of a human being (0.4 m^2), more exact quantification will be based on a recently acquired large in-door (sports hall) data set for various multi-target scenes including reflectors, persons and transponder. First qualitative results are given in Fig. 6.

5. FUTURE PLANS

In the coming year the demonstrator is intended to be shown to work at the ECT (European Combined Terminals) terrain at the Rotterdam harbor area mounted on an AGV (automatic guided -container- vehicle).

As stated previously up to now only spectral amplitude data is used in the transformation of range to angular information. Although the system has a 10 cm range resolution the obtained angular resolutions of 10 and 20 degrees in azimuth and elevation respectively are rather poor. This is due to the relatively small distances between the antennas by the size limitation of the available mounting area of 2.5 by 1 m. Resolution improvement is therefore required and maybe obtained by additional processing of the spectral phase data that is available also. To this aim the phase change caused by distance changes between target and radar may be used in a first angular resolution refinement step, i.e., SAR-processing, although this requires a priori knowledge of the velocity of the target with respect to the radar. Then a further resolution improvement is possible based on phase differences in the same way as using beatfrequency differences. The latter method suffers however from the 2π phase ambiguity and this is the reason for preceeding this by the mentioned first step to avoid resulting angle ambiguity. The angle ambiguity may also be reduced by decreasing antenna spacing (wavefront reconstruction, inverse phased array) whereas the antenna spacing should be large for the resolution based on beatfrequency. The use of a multistatic antenna configuration allows for both large and small spacings.

The current X-band Colarado system was needed to show the principle of high resolution multistatic sparse array radar being able to differentiate objects. Now that the soundness of the concept is proved, the used frequency has to be shifted to the bands allocated to automotive application. Based on this and other considerations Colarado is going to be upgraded to 35 and 77 GHz. Two follow-up co-operation projects between IRCTR and the universities of Aachen and Leeds were started this year with a duration of three years. In these projects millimeter wave radar modules will be developed, radar system integration will be carried out at IRCTR. For the 35 GHz radar front-end monolithically integrated circuits, maybe single-chip, and for the 77 GHz modules hybrid technology will be used.

The real-time signal processing algorithms are in the demonstrator implemented in software. In a next project the large and costly parallel transputer-PowerPC computer used for this aim is to be replaced by small and likely low-cost Application Specific Processing integrated circuits.

6. CONCLUSIONS

Multistatic wideband radar used in the described way can provide three-dimensional position and velocity information of a multi-target scene with a high repetition frequency. This approach relies on the real-time processing of large amounts of data. A demonstrator system version is operational and first results are obtained. Future versions of the system include upgrades of the RF-part to Ka-band and W-band, and development of Application Specific Processing circuits to improve on real-time performance versus costs.

REFERENCES

1. J.J. Jacobs, Feasibility study on bistatic anti-collision radar, Technical Report TVS A-318 TUD/ET, Delft, June 1990. (In Dutch)
2. K.J. v.Staalduinen, System design of a multistatic FMCW anti-collision radar for unmanned vehicles, IRCTR Report S-006.95, Delft, November 1995. (In Dutch)
3. M. Tian, P.D. Tran, M. Hajian, L.P. Ligthart, "Air-gap Technique for Matching the Aperture of Miniature Waveguide Antennas", in Proc. IEEE Instrumentation and Measurement Techn., California, IEEE Catalog No. 93CH3292-0, May 1993, pp. 197-201.
4. J. Schier, H.J. Agterkamp, A.J.C. van Gemund and G.L. Reijns, "Object Tracking and Tracing - Incremental Approach", in Proc. of the 2nd Eur. IEEE Workshop on Computer-Intensive Methods Control and Signal Processing, Prague, August 1996, pp. 151-154.

Table 1. Specifications

application	anti-collision radar system on AGV, 3D-imaging
frequency	9.0 – 10.5 GHz
modulation	FM-CW sawtooth PRF 3.47 kHz
signal source	VCO Radian type 2829A
EIRP	10 mW
location	Delft University, electrotechn. eng., in / out-door
antenna type	MLA 2 step air-gap, directivity 7 dB
antenna height	multistatic, between 0.5 and 1.5 m above ground
maximum range	12.8 m
radar cross section range	0.4 – 400 m ² (30 dB)
maximum number of targets	10 (dynamic range max. +20 = 50 dB)
maximum target velocity	10 m/s
resolution (based on amplitude data only)	range 0.1 m; azimuth 9°; elevation 22°

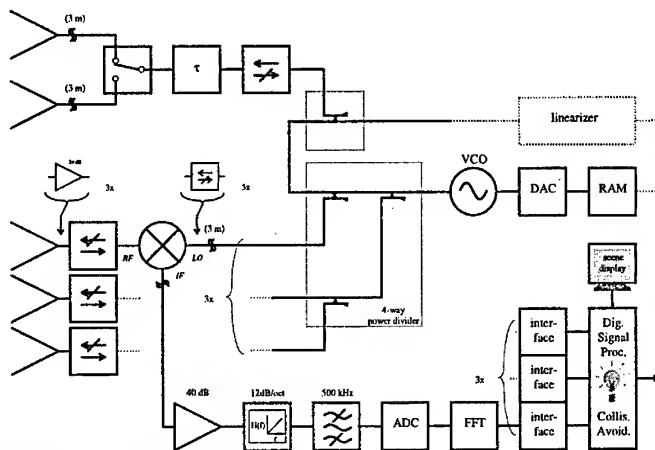


Figure 1. System block diagram

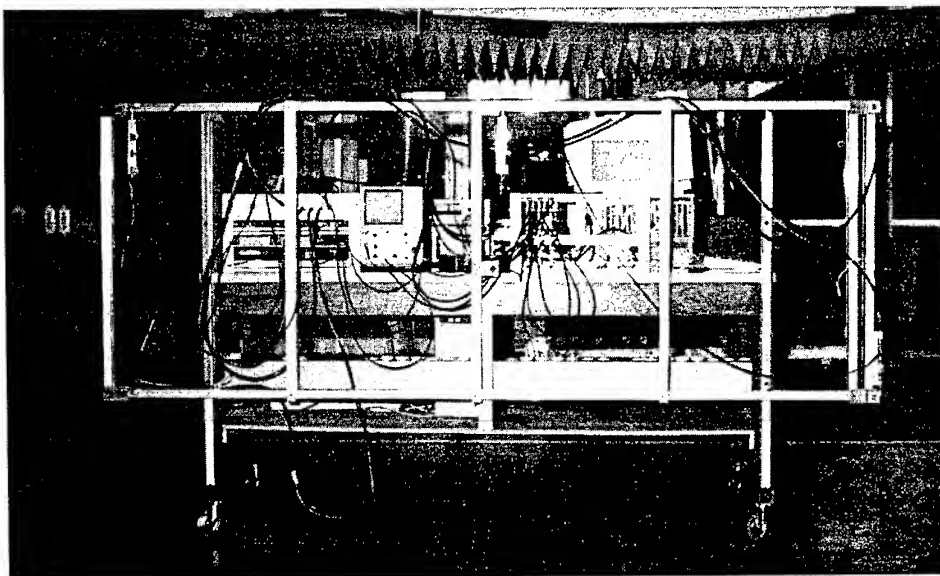


Figure 2. Colarado demonstrator

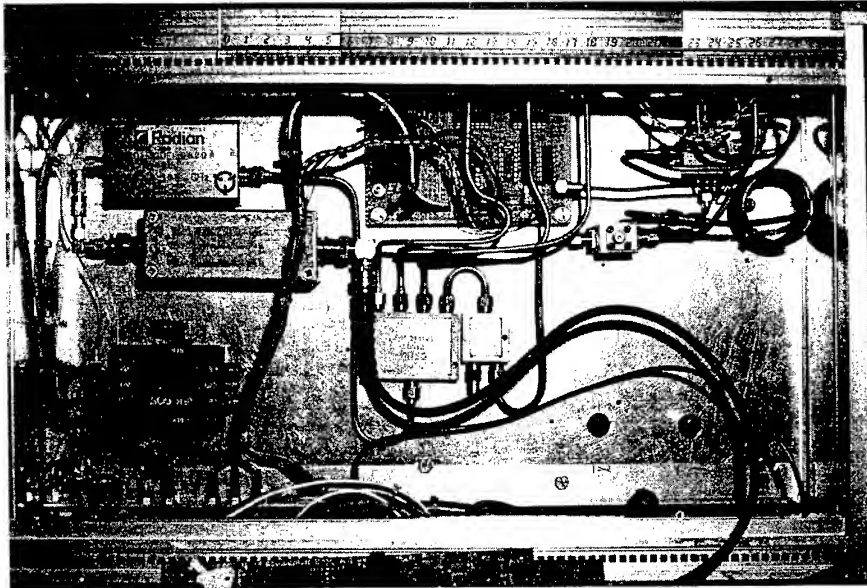


Figure 3. RF-part of the Colorado system (X-band)

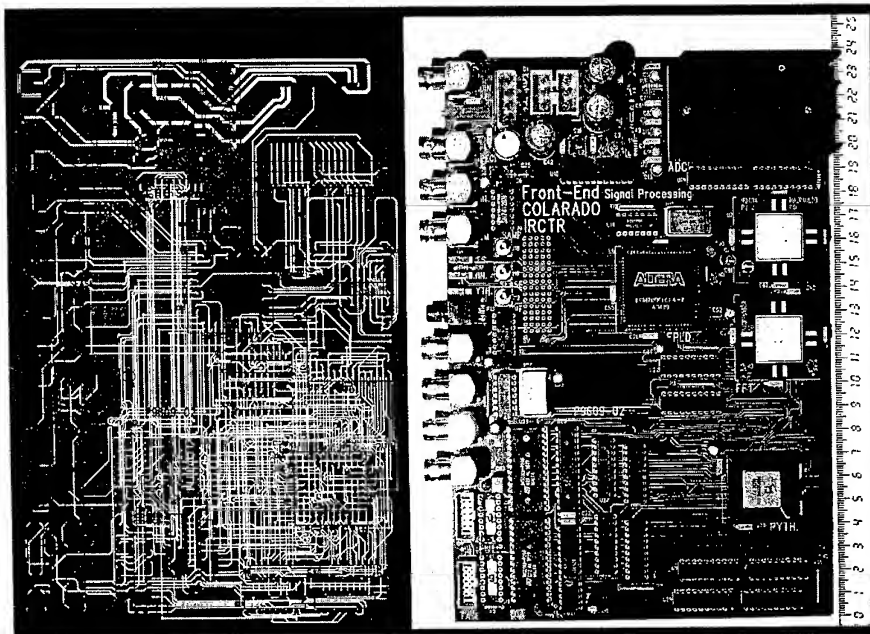


Figure 4. Analog to Digital Converter, FFT and computer interface printed circuit board

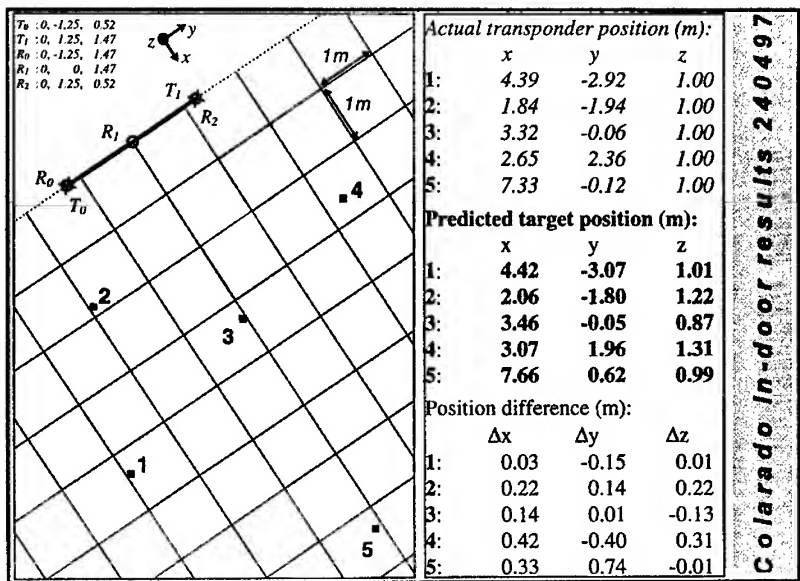


Figure 5. Colorado in-door test set up and object detection results

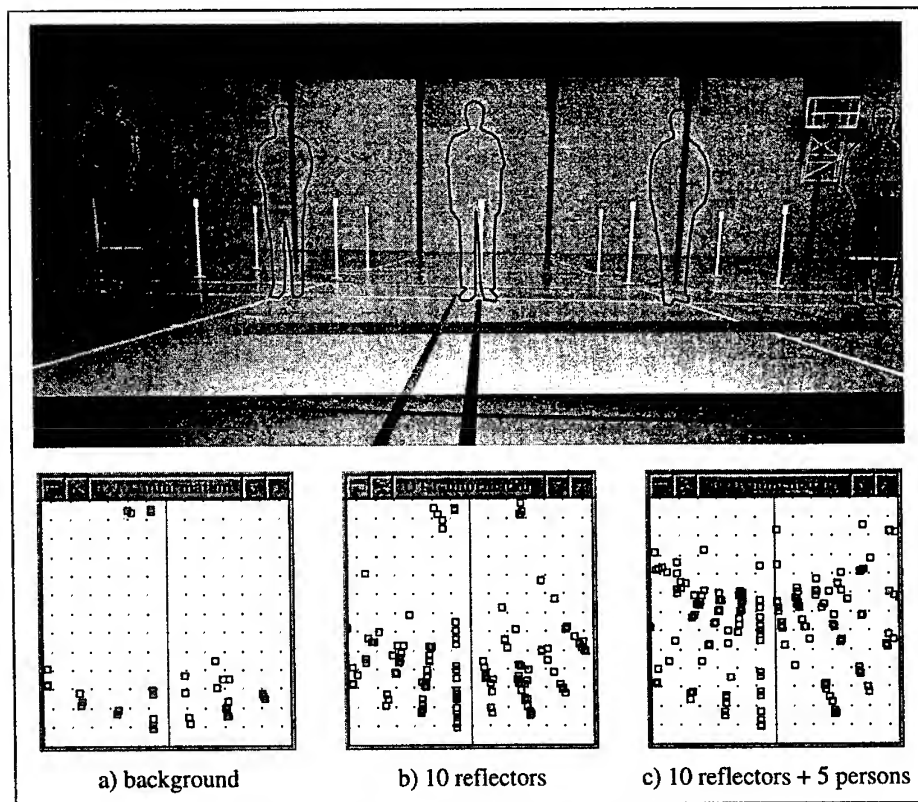


Figure 6. Colorado large in-door (sports hall) test results

A PLANAR MICROWAVE PHASE DISCRIMINATOR

Bronisław Stec, Adam Rutkowski

Institute of Radar Technology
Faculty of Electronics
Military University of Technology
Kaliskiego Str. 2
01-489 Warsaw, Poland
tel. :+48/22/ 685 95 50 ; fax. :+48/22/ 685 94 44

ABSTRACT:

The topology of proposed phase discriminator circuit involves the elements of one type in the form of quadrature couplers. The structure is symmetric and does not include either transmission line crossings or phase shifters, typically required under such circumstances. The complete phase discriminator can be made as one planar IC. Such a structure of the microwave phase discriminator is introduced for the first time.

INTRODUCTION

The microwave phase discriminator (MPD) is a device intended for measurements of the phase difference Φ of the two microwave signals. In a general case the MPD consists of an interferometer and a block of microwave detectors. Depending on the interferometer structure various ranges of unambiguous phase measurement within the interval $\pm 90^\circ$ or $\pm 180^\circ$ may be achieved.

An important feature of interferometers intended for use in up-to-date radar and measuring devices is their ability to be implemented on a single substrate in the form of microwave integrated circuits (MIC). All the known MPD versions (e.g. [2, 3, 4, 5, 6]) have crossing connections. In results in that they have to be constructed as some spatial structures. Furthermore, the crossing of connection lines requires a suitable number of auxiliary connectors between the microstrip line and the coaxial cable. Such connections insert into a circuit some unwanted reactances worsening discriminator parameters.

The circuit shown in Fig.1 has been made on a single substrate as a MIC, using the microstrip line technology. The microwave interferometer consists of six identical directional couplers. The couplers are Lange type proximity couplers with two pairs of coupled lines. The interferometer utilises the properties of two quadrature couplers in tandem connection with coupling factor equal to 3dB.

CHARACTERISTICS OF THE CROSSING

The tandem connection of directional couplers is used, amid the other applications, in case where the strong coupling is not possible (not obtainable) with only one coupler. For example, to obtain 3dB coupling one may connect two 8.34dB couplers. Connection of two 3dB couplers in tandem way, however forms so called 'cross connection'.

The circuit of such type (Fig.2.) has ports 10-14, 10-11, 15-14, 15-11 isolated, and the modulus of the transmittance between the ports on diagonals (i.e., 10-15, 11-14) equals 1. An additional important feature of the circuit is that its relative (differential) phase shift equals about 45° for wide band of frequency. It makes possible to use tandem connection of the 3dB/90° couplers at the same time as a planar connection of two microstriplines and as a wideband $+45^\circ$ phase shifter. Therefore the couplers QC1 and QC2, together with properly selected transmission lines TL1 and TL2, replace jointly line crossing and -45° phase shifters (Fig.2b.)[1].

Measured values of the transmittance modulus and the relative phase shift for the tandem connection of the 3dB/90° couplers are shown in Fig.3.

THE MPD PRINCIPLE OF OPERATION

The observed signal u_s and reference signal u_r can be connected to any pair of ports 1-4 (Fig.1.). Depending on the selected pair of input ports an algorithm for calculations phase difference of compared signals is changed. If the observed signal is connected to ports 1-3, 2-4, 2-3 or 1-4 the range of an unambiguous phase measurement covers $\pm 180^\circ$. In other cases the range of an unambiguous phase measurement decreases to $\pm 90^\circ$.

Assuming identical transmittance moduli to coupled ports and direct ports of quadrature couplers, the signal u_s and u_r are given to the ports 2 and 3, respectively:

$$\begin{aligned} u_r &= U \cdot \sin(\omega t + \varphi_r) \\ u_s &= U \cdot \sin(\omega t + \varphi_s) \end{aligned} \quad (1)$$

On the microwave detectors' inputs D1÷D4 arrive voltages:

$$\begin{aligned} u_1 &= U_1 \cdot \sin(\omega t + \psi_1) \\ u_2 &= U_2 \cdot \sin(\omega t + \psi_2) \\ u_3 &= U_3 \cdot \sin(\omega t + \psi_3) \\ u_4 &= U_4 \cdot \sin(\omega t + \psi_4) \end{aligned} \quad (2)$$

where:

$$\begin{aligned} U_1 &= \sqrt{0.5 \cdot U^2 + 0.5 \cdot U^2 \cdot \cos(\varphi_r - \varphi_s - \frac{\pi}{4})} \\ U_2 &= \sqrt{0.5 \cdot U^2 + 0.5 \cdot U^2 \cdot \cos(\varphi_r - \varphi_s - \frac{5}{4}\pi)} \\ U_3 &= \sqrt{0.5 \cdot U^2 + 0.5 \cdot U^2 \cdot \cos(\varphi_r - \varphi_s + \frac{5}{4}\pi)} \\ U_4 &= \sqrt{0.5 \cdot U^2 + 0.5 \cdot U^2 \cdot \cos(\varphi_r - \varphi_s + \frac{\pi}{4})} \end{aligned} \quad (3)$$

ψ_i - denotes signal phases at output ports of the interferometer

At the detectors' outputs, after square-law detection, the voltages proportional to the amplitudes and phases of the input signal arrive:

$$\begin{aligned} U_{d1} &= k \cdot U_1 = 0.5 \cdot k \cdot U^2 + 0.5 \cdot k \cdot U^2 \cdot \cos(\varphi_r - \varphi_s - \frac{\pi}{4}) \\ U_{d2} &= k \cdot U_2 = 0.5 \cdot k \cdot U^2 + 0.5 \cdot k \cdot U^2 \cdot \cos(\varphi_r - \varphi_s - \frac{5}{4}\pi) \\ U_{d3} &= k \cdot U_3 = 0.5 \cdot k \cdot U^2 + 0.5 \cdot k \cdot U^2 \cdot \cos(\varphi_r - \varphi_s + \frac{5}{4}\pi) \\ U_{d4} &= k \cdot U_4 = 0.5 \cdot k \cdot U^2 + 0.5 \cdot k \cdot U^2 \cdot \cos(\varphi_r - \varphi_s + \frac{\pi}{4}) \end{aligned} \quad (4)$$

where: k - proportionality factor, depending on detectors parameters

Subtracting in pairs the detector output voltages results in getting voltages with sine and cosine dependency on measured phase difference.

$$\begin{aligned} U_y &= U_{d1} - U_{d2} = k \cdot U^2 \cdot \sin(\varphi_r - \varphi_s - \frac{\pi}{4}) \\ U_x &= U_{d4} - U_{d3} = k \cdot U^2 \cdot \cos(\varphi_r - \varphi_s - \frac{\pi}{4}) \end{aligned} \quad (5)$$

Taking the ratio of these voltages, the input signals phase difference Φ can be obtained as:

$$\Phi = \varphi_r - \varphi_s = \arctg \frac{U_y}{U_x} + \frac{\pi}{4} \quad (6)$$

The constant factor $\pi/4$ is an attribute of the crossing realised with couplers QC1 and QC2.

THE PARAMETERS OF THE PLANAR MPD

The accuracy of the microwave interferometer depends on the phase relations between its outputs and inputs. The experimental results of phase measurements between input ports 1, 2, and output ports 5, 6, 7, 8, are given in Fig. 4. The monotony of the phase change confirms proper behaviour of the circuit.

The phase measurement error of the described MPD is a function of frequency and measured phase difference (see Fig. 5.), much the same as in other known version of phase discriminators.

The bigger are differences of transmittance moduli to direct ports and coupled directional couplers, the more significant are measurement errors. It means that near to the centre frequency of couplers' bandwidth measurement errors are close to zero and do not depend on measured phase difference. However, as frequency comes near to the lower or upper limit of the bandwidth, the error goes up.

The measured phase difference error for the built model of the circuit over one octave bandwidth did not exceed $\pm 1.5^\circ$ (Fig. 6.). This error may be furthermore decreased by proper calibration of the circuit and application of extended algorithms for processing output voltages of the detectors.

CONCLUSIONS:

The presented MPD can be constructed in an integrated form what makes possible its application in miniature radar devices, communication systems and measuring sets. The device may measure phase of continuous and pulsed signals. It may be also used in the radioelectronic war systems as a part of microwave frequency discriminator or as a wideband phase meter in phased direction bearing circuits.

REFERENCES:

1. Joseph A. Mosko, An Introduction to Wideband, Two-Channel Direction-Finding Systems. Microwave Journal, February 1984, pp. 91-106
2. Stephen E. Lipsky, Microwave passive direction finding, John Wiley & Sons, Inc., New York 1987
3. Bao-Yen Tsui, Digital Microwave Receivers, Theory and Concepts, Artech House, Dedham 1989.
4. Ray J. King. Microwave homodyne systems, Institution of Electrical Engineers. England 1978
5. B. Stec, Microwave phase discriminator, Bulletin of the Military University of Technology (in Polish) No. 4(392), Warsaw, April 1985
6. A. Rutkowski, B. Stec. Passive wide-band phase shifter, Elektronika (in Polish), No. 3, Warsaw, March 1996

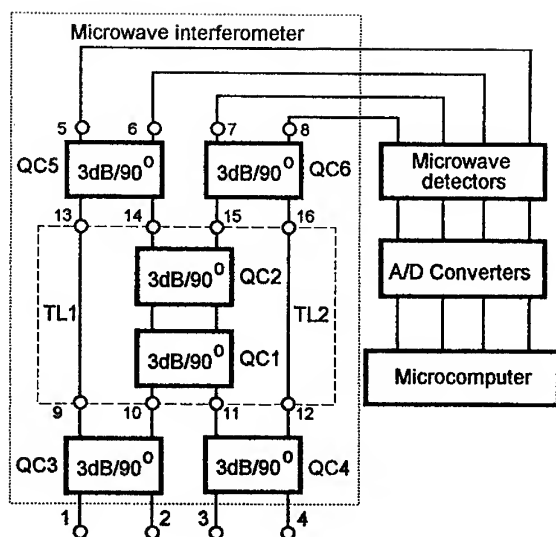


Fig. 1. An integrated version of the microwave phase discriminator

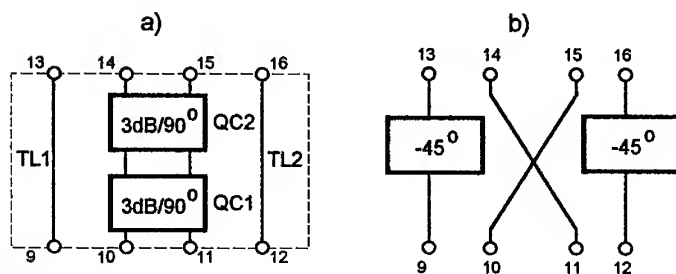


Fig.2. The tandem connection of 3dB/90° couplers and its schematic diagram

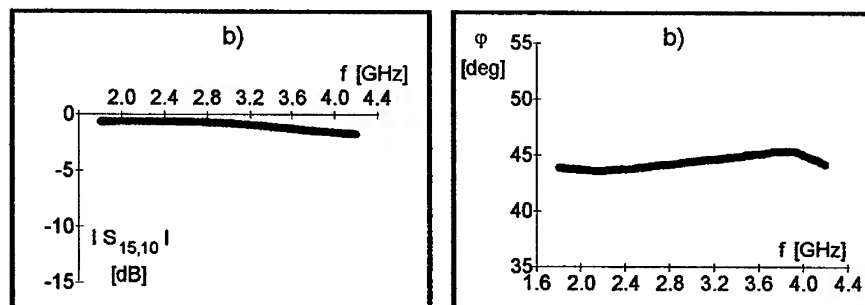


Fig.3. Characteristics of the tandem connection of the 3dB/90° couplers

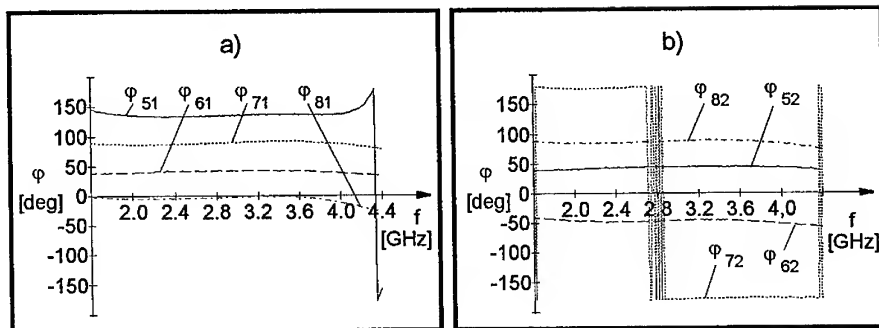


Fig. 4. Relative phase shift between interferometer ports as a function of frequency (measurement results)

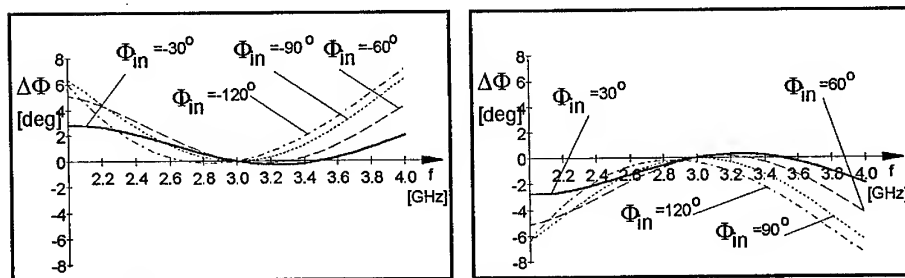


Fig. 5. Estimated measurement error for various phase difference values Φ_{in} versus frequency

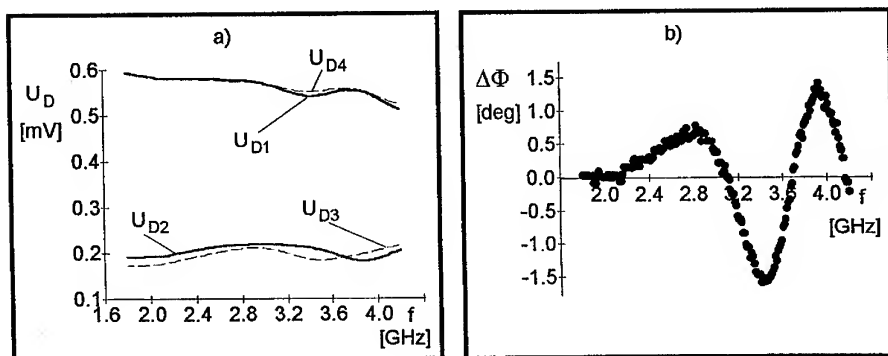


Fig. 6. Output voltages (measured) for detectors D1÷D4 and the phase measurement error versus frequency

A NOVEL LOW NOISE ACTIVE CIRCUIT REPLACEMENT CRITERIA FOR PARALLEL FED LARGE SCALE ACTIVE ANTENNA ARRAYS

SIMSEK DEMIR, CANAN TOKER, ALTUNKAN HIZAL

Middle East Technical University, Electrical and Electronics Eng. Dept.

06531, Ankara, TURKEY

Abstract: In this work noise analysis of parallel feed structures for active antenna arrays are presented. Signal and noise behaviour of the feed structures are signified by the newly introduced concepts of "coherent" and "incoherent" impedance match of power combining structures. It is also shown that a feed structure can be re-designed for low noise operation without affecting its radiation characteristics. Optimum design of parallel feed structures for low noise operation is explained. Also an optimum use of active elements in such structures is investigated to have a low overall noise temperature of the antenna array with minimum number of active elements. In the analysis a new method is introduced where a "noise equivalent line length" is defined. This definition which unifies the contribution of noise from different array elements, is used in the design of a parallel feed structure and as an active circuit replacement criteria in passive arrays.

I. INTRODUCTION

An important figure of merit for receive antennas is noise performance. Since 1960's antenna arrays have been investigated for better signal-to-noise ratios, Lo et al. (1), including the recent active antenna structures, Grabherr and Menzel (2). However, in these analysis, feed lines are not studied for their noise performance. Moreover, explicit methods for low noise design of feed structures do not appear in the literature.

Receive antenna array design for certain radiation characteristics is related to the case where all elements receive coherent signal. Feed structure designs that are appearing in the literature are mainly concerned with impedance matching for coherent excitation. However, impedance matching for coherent excitation does not imply the incoherent impedance matching which is the case where the signal that are combined in the structure are incoherent. The response of a feed structure to excitations from incoherent sources such as internal noise of the antenna array, is totally different and such a concept is not considered previously. In our work, incoherent matching of the feed structures is accounted for the first time. Moreover, a novel concept, 'noise equivalent line length', is introduced and utilized for noise analysis of feed structures. Without loss of generality, feed structures that are constructed by transmission lines are investigated.

Using analysis above a low noise large scale antenna array design guide is presented where the critical point to insert a low noise gain element for improved noise performance is identified. In our analysis, it is also shown that insertion of low noise active elements in an antenna array improves the noise performance, however where to insert the active elements is a design problem from point of view of labor, cost and improvement in performance. We defined node, branch, virtual node, virtual branch, and level concepts for parallel feed structures. A weighted equivalent line length function is introduced. This novel function which carefully combines the analysis results of the previous works, stands for the noise contribution of a line segment in a parallel feed structure to the output noise power and utilized for comparing different feed network structures of large scale antenna arrays.

II. PARALLEL FEED STRUCTURE NOISE ANALYSIS

The noise analysis of feed structures is based on the noise analysis of a low loss transmission line, Collin (3). Characteristic impedance, Z_{ch} , attenuation per unit length, α , and length of the line, l , and the ambient temperature, T , determine the generated noise power. The attenuation factor of the line introduces an imaginary part to the Z_{ch} but it is assumed that line is low loss and therefore, Z_{ch} remains, practically, real. The source and load reflection coefficients are defined with respect to the characteristic impedance of the line. Available noise power of a low loss transmission line is obtained for $Z_L = Z_{out}^*$, where $L = e^{2\alpha l}$:

$$P_{n,available} = kT\Delta f \frac{L - |\Gamma_g|^2/L - 1 + |\Gamma_g|^2}{(1 - |\Gamma_g/L|^2)L} \quad (1)$$

Available noise power of a low loss transmission line is a function of source mismatch and loss factor. This power increases with increasing magnitude of source reflection coefficient. The upper limit of this available power is:

$$P_{n,available,max} = kT\Delta f \quad (2)$$

This means that in the limit of mismatch, a low loss transmission line introduces an available noise power equal to the available noise power of a resistor. Therefore matching is of ultimate importance from point of view of noise

generation which corresponds to incoherent impedance matching of the feed structure of the antenna array.

Above noise analysis is used towards the definition of a noise equivalent line length which simplifies the noise performance evaluation of the feed structures considerably. In doing so, the noise contributions from different elements of a feed structure to the output noise power is expressed in terms of a single parameter which puts explicitly the strength of the contribution relative to the theoretical minimum. Simple addition of these equivalent line lengths is a good comparison criteria for the overall noise performance of the feed structure. Moreover, this uncomplicated parameter, is used as a replacement criteria of active circuits in an antenna array for the optimum noise performance.

Let L be the loss factor of the line under investigation which has a source reflection coefficient, Γ_g , and loss coefficient, α , then its available noise power, P_{ine} , is given by (1). Let L_{neqv} be the loss factor of a line which has a line length l_{neqv} and has the same loss coefficient, α . Furthermore let this line be impedance matched at its source side, then its available noise power is given by:

$$P_{eqv} = k T \Delta f \frac{L_{neqv} - 1}{L_{neqv}} \quad (3)$$

For the line under investigation, let us define an equivalent line which is matched and therefore has the available noise power in (3). If L_{neqv} is obtained such that $P_{eqv} = P_{ine}$, then L_{neqv} turns out to be:

$$L_{neqv} = \frac{L^2 - |\Gamma_g|^2}{(L^2 - |\Gamma_g|^2) - (L - 1)(L + |\Gamma_g|^2)} \quad (4)$$

Consequently, noise equivalent line length, l_{neqv} , of the line turns out to be:

$$l_{neqv} = \frac{1}{2\alpha} \ln \left(\frac{L^2 - |\Gamma_g|^2}{(L^2 - |\Gamma_g|^2) - (L - 1)(L + |\Gamma_g|^2)} \right) \quad (5)$$

Using the equivalent line length, output noise temperature can be obtained through (3). Noise equivalent length of a mismatched line is longer than its physical length where minimum noise equivalent length which corresponds to matched case is equal to its physical length. Without comparing the actual noise temperatures, one can deduce the effect of mismatch on noise generation by comparing the noise equivalent and physical lengths. In Fig. 1, noise equivalent line length normalized with its physical line length is given as a function of the source reflection coefficient.

Noise contributions of different segments can be superposed in terms of their noise equivalent line lengths to give an approximate value for the total noise equivalent length. Let us consider two line segments with noise equivalent line length, loss factor and noise power which are represented with l_1 , L_1 and P_1 and l_2 , L_2 and P_2 , respectively. Noise power of the first line section will be attenuated in the second one and the resultant noise power of cascaded connection is given by:

$$\begin{aligned} P_{total} &= kT\Delta f \frac{L_1 - 1}{L_1 \cdot L_2} + kT\Delta f \frac{L_2 - 1}{L_2} \\ &= kT\Delta f \frac{L_{eqv} - 1}{L_{eqv}} \end{aligned} \quad (6)$$

That is:

$$\begin{aligned} L_{eqv} &= L_1 \cdot L_2 \\ l_{eqv} &= l_1 + l_2 \end{aligned} \quad (7)$$

A parallel feed structure is composed of a number of transmission line sections which sometimes function as impedance transformers, and junction points of line sections which function as power combiners. Noise equivalent line lengths of these individual structures can be added to find the overall noise equivalent line length of the feed structure. For a $1 : q^2$ double section quarter wave impedance transformer, noise equivalent line length is obtained through the generated noise power by the line segments:

$$P_{n_1} = kT\Delta f \left(1 - \frac{L((Z_g - Z_1)^2 - (Z_g + Z_1)^2)}{(Z_g - Z_1)^2 - L^2(Z_g + Z_1)^2} \right)$$

$$P_{n_2} = kT\Delta f \left(1 - \frac{L((Z_g - qZ_1)^2 - (Z_g + qZ_1)^2)}{(Z_g - qZ_1)^2 - L^2(Z_g + qZ_1)^2} \right) \quad (8)$$

The total noise power at the output is:

$$P_{Total} = \frac{P_{n_1}}{L_2} + P_{n_2} \quad (9)$$

and noise equivalent line length of the impedance transformer is given by:

$$l_{neqv,tr} = \frac{1}{2\alpha} \ln \left(\frac{1}{1 - P_{Total}/kT\Delta f} \right) \quad (10)$$

For a $1:p^2$ power combiner structure, the equivalent line length is calculated based on the noise power at the output port. For a transmission line power combiner, the output power is the sum of the available power at the input ports if the input signals are coherent and have the proper power ratio Parad and Moynihan (4). Otherwise, if the signals are incoherent, the output power is the weighted summation of the input powers where the weights are the power combination ratios. The following is the noise equivalent line length of the power combiner where port 1 is the output arm, and port 2 and 3 are the input arms:

$$l_{neqv,comb} = l_{neqv,1} + \frac{1}{1+p^2} l_{neqv,2} + \frac{p^2}{1+p^2} l_{neqv,3} \quad (11)$$

For the case, where the thermal noise powers of the two arms are equal, the noise equivalent line length is given by:

$$l_{neqv,comb} = l_{neqv,1} + l_{arm} \quad (12)$$

These individual structures are used to construct a parallel feed structure. The main frame of a parallel feed structure is a parallel arm where sub arrays are connected to form an array. The sub arrays might be antenna elements and the formed array might be a sub array to be used in the successive level of the parallel feed network. The line segment between the sub array and the parallel arm is named as a *Branch* (Br). The junction point of a branch and the parallel arm is the *Connection Point* (CP) of the sub array and a *Virtual Connection Point* (VCP) of the parallel arm. The sections of the parallel arm between consecutive VCPs are named as *Virtual Branches* (VBr). A parallel arm array has a single branch and a single connection point at its output side, but, have more than one VCP and VBr depending on the number of antenna elements connected to the arm. In a parallel feed structure, all the antenna elements are virtually connected to the same point, output of the array, with complex weights to create the required radiation pattern. The Br's are used to obtain the necessary complex weight of the antenna element (sub array) and VBr are usually of $n\lambda/2$ length and used to supply the connectivity of the antenna elements. VBr's can be used to create a tapered feed by means of quarter-wave-length impedance transformers.

Contribution of available noise power of a lossy line segment, P_{line} , to the output noise power depends on signal power contribution weight factor of the line, w , to the output signal power. Hence, the noise contribution of a line to the noise power at the output is:

$$P_{out,line} = w \times P_{line} \quad (13)$$

For this noise power at the output, a weighted noise equivalent line length $^w l_{neqv}$, is defined similar to the noise equivalent line length definition as:

$$^w l_{neqv} = \frac{1}{2\alpha} \ln \left(\frac{L^2 - |\Gamma_g|^2}{(L^2 - |\Gamma_g|^2) - w(L-1)(L + |\Gamma_g|^2)} \right) \quad (14)$$

By this definition weighted equivalent length of each line segment in a structure can be calculated. These weighted equivalent lengths explicitly give the strength of each noise source in the structure, which enables the designer to see the relatively noisy parts of the feed structure. Summation of noise temperatures corresponding to these noise equivalent line lengths will give the overall noise temperature. On the otherhand, the sum of the individual noise equivalent lengths yields the noise equivalent line length of the feed structure.

The impedance at the output of the array decreases rapidly with the increasing number of parallel connected antenna elements, which makes it difficult to match for coherent and incoherent operation. This situation is prevented by

implementing impedance transformers at the connection points of sub arrays. In a corporate feed the number of these connection points is a maximum. Therefore, coherent and incoherent matching is solved with less problem in a corporate feed structure. Weighted noise equivalent line length formulation is applied to a $N = 2^n$ element uniform corporate fed microstrip rectangular patch antenna array which is incoherent impedance matched. The following is the noise equivalent line length for this structure based on (7):

$$\begin{aligned} l_{total, n \text{ even}} &= \sum_{k=1}^{n/2} \lambda \cdot 2^{k-1} - \lambda/4 \\ &= \lambda \cdot 2^{n/2} - \frac{5}{4} \lambda \\ l_{total, n \text{ odd}} &= l_{total, n-1} + \frac{1}{2} \lambda \cdot 2^{(n-1)/2} \end{aligned} \quad (15)$$

Because of spurious radiation losses and conductor losses, realizable microstrip transmission lines widths are limited. Consequently, characteristic impedances required for incoherent impedance match in parallel arm structures are impractical and incoherent mismatch is unavoidable. Such a structure may be coherent impedance matched but because of incoherent impedance mismatch its noise equivalent line length will be much worse than minimum attainable length. Weighted noise equivalent line length of a $2 \times p$ element uniform fed parallel arm structure has the following approximate noise equivalent line length, including the incoherent mismatch:

$$l_{total} = \sum_{k=1}^{p/2-1} \frac{1}{2\alpha} \ln \left(\frac{L^2 - |\Gamma_{g,k}|^2}{L^2 - |\Gamma_{g,k}|^2 - w(L-1)(L + |\Gamma_{g,k}|^2)} \right) \quad (16)$$

where,

$$\begin{aligned} w &= \frac{2k}{p} \\ \Gamma_{g,k} &= \frac{Z_{ant}/2k - Z_{ch,k}}{Z_{ant}/2k + Z_{ch,k}} \end{aligned} \quad (17)$$

A two level parallel arm structure has the shortest physical line length but because of the incoherent mismatch, the noise equivalent line length might be several times longer than the physical line length. For a corporate feed structure, the total physical line length is a maximum, but because of easy integration of impedance transformers, incoherent impedance can be attained, and noise equivalent line length can be made a minimum. The noise equivalent line length is a measure to decide the structure of the array for low noise operation from this point of view.

III. ACTIVE ANTENNA ARRAY DESIGN

For the line segments in the structure, line lengths are determined with phasing requirements and characteristic impedances should be chosen for the incoherent impedance match. However, in the cases where incoherent impedance match is not attained, noise performance will be degraded. For a large antenna array, active circuit integration might be a solution for low noise operation. In that case l_{neqv} will be a design guide to determine the insertion level of the active devices in the feed structure. This level will depend on the noise figure and gain of the active circuit and the loss of the line segments. Fig. 2 shows schematically, levels in a corporate feed structure where active elements are placed at one of them. Replacing active devices at level 1 is the best for lowest noise performance at the expense of large number of active circuits, i.e., 2^n . However, there will be a level in the structure where noise improvement is just achieved with decreased number of active elements compared to a passive antenna array.

In order to see this fact let us consider the two cases given in Fig. 3. In this figure the connection point, A, of two successive levels, k and $k+1$ are shown with noise equivalent length l_{neqv1} corresponding to levels 1 to k of the structure shown in Fig. 2, and noise equivalent length l_{neqv2} corresponding to levels $k+1$ to n . A feed structure with noise temperature, T_f and efficiency, η_f , can be partitioned into two consecutive sections with noise temperatures and efficiencies, T_1, η_1 and T_2, η_2 , respectively, where $T_f = T_1 \times \eta_2 + T_2$ and $\eta_f = \eta_1 \times \eta_2$, and to improve the performance, an LNA can be placed between these two partitions as shown in the Fig. 3.b. Depending on η_2 and T_2 distributed amplification may yield even a better G/T compared to $(G/T)_{passive}$. Notice that, when comparing noise powers of these two systems, active system's noise power should be normalized since signal power of active system is G times more than the passive system's. Distributed amplification yields a better G/T than the passive case when the following equation yields a result greater than zero :

$$\begin{aligned}
P_{out,passive} - \frac{P_{out,dist}}{G} &= T_f - \eta_2(T_{LNA} + T_1) - \frac{T_2}{G} \\
&= T_2(1 - \frac{1}{G}) - \eta_2 T_{LNA}
\end{aligned} \tag{18}$$

To satisfy this condition, high G and low T_{LNA} are required. This equation also implies that active circuit integration is necessary for low efficiency systems. Using this calculation maximum length of noise equivalent line of the second partition of the feed structure can be determined, where an active circuit with a certain G and T_{LNA} should be inserted for better noise performance. This point will be the optimum point where the number of required LNAs is a minimum and the noise performance of the passive array is improved.

IV. ACTIVE ARRAY

A 16×16 corporate fed microstrip antenna array on a RT-DUROID 5880 substrate is designed. Quarter-wave-line impedance transformers are placed according to the results of section III, to the feed structure to decrease the noise generation by the lossy feed lines. The rectangular patch antennas are resonant at 10 GHz having a 276Ω resistive input impedance. The uniform fed antennas are equi-separated by a distance, d , which is determined by radiation pattern considerations. The total weighted equivalent line length of this 16×16 patch array is calculated to be about 14.8λ which corresponds to $T = 101^\circ K$ for $T_{amb} = 290^\circ K$. Using microstrip matching elements and an ultra low noise pHEMT, NEC 32484A, a low noise amplifier is designed. The noise figure of the amplifier is 0.6dB and gain is 14dB. It is assumed, and shown that appropriate matching circuits whose total physical length will be about $\lambda/2$ can be designed independent of wherever the amplifier is inserted in the feed structure, Demir et al. (5). In case, this amplifier is connected to the output of the 16×16 passive array, noise temperature at the output of the amplifier turns out to be $T = 35.6 dB-K$. Using weighted equivalent line length method and the results of section V, the noise temperatures corresponding to different amplifier placement levels are calculated and presented in Table 1. The improvement of noise performance with the added number of amplifiers is clearly seen from this table.

Using Table 1, above equations yield that active antenna has a better G/T than the passive antenna for connection level 7 which is also implied by (18). It can be said that for this structure and the amplifiers concerned, the level where the improvement is just achieved is level 7 where four active elements are required. Further improvements can be achieved using more active elements at the different levels as can be seen from Table 1.

Level	1	2	3	4	5	6	7	8	output
# of amp.	256	128	64	32	16	8	4	2	1
T_{level} (dB-K)	30.7	30.9	31.1	31.7	32.1	32.9	33.6	34.7	35.6

Table 1: Number of amplifiers and the output noise temperature for different levels as connection points of amplifiers.

V. CONCLUSION

Noise analysis of feed structures of antenna arrays are not considered in detail, previously. In this work, noise analysis of low loss transmission lines are given and a new concept named as "noise equivalent line length" is introduced. Through the signification of coherent and incoherent impedance matching concepts, noise sources in a parallel feed antenna array are identified and strength of these sources are expressed in terms of their noise equivalent line lengths. This provided the means to apply the noise equivalent line length as a low noise parallel feed structure design guide. Coherent impedance matching which is important for efficient radiation characteristics does not imply incoherent impedance matching which is important for noise generation of the feed structure. Moreover, noise equivalent line length is also utilized as an active circuit replacement criteria in antenna arrays which showed that G/T performance of a passive antenna array may be improved by inserting active circuits to certain levels in the feed structure.

References

- [1] Y. T. Lo, S. W. Lee and Q.H. Lee, 'Optimization of directivity and signal-to-noise ratio of an arbitrary antenna array', Aug. 1966, Proc. IEEE, vol. 54, pp 1033-1045.
- [2] W. Grabherr and W. Menzel, 'Broadband, low noise active receiving microstrip antenna', in Proc. 24th European Microwave Conf., Sep. 1994, pp 1785-1790.
- [3] R. E. Collin, Antennas and Radiowave Propagation, New York, McGraw Hill Int. Ed., 1985.
- [4] L. I. Parad and R. L. Moynihan, 'Split-Tee power divider', Jan. 1965, IEEE Trans. Microwave Theory Tech., vol. MTT-13, no. 1, pp 91-95.
- [5] S. Demir, C. Toker and A. Hizal, 'Design of an active microstrip array using a microwave circuit simulator', in Proc. IEEE MTT-S Top. Symp. on Tech. for Wireless Appl., Vancouver, Canada, Feb. 1997, pp 103-106.

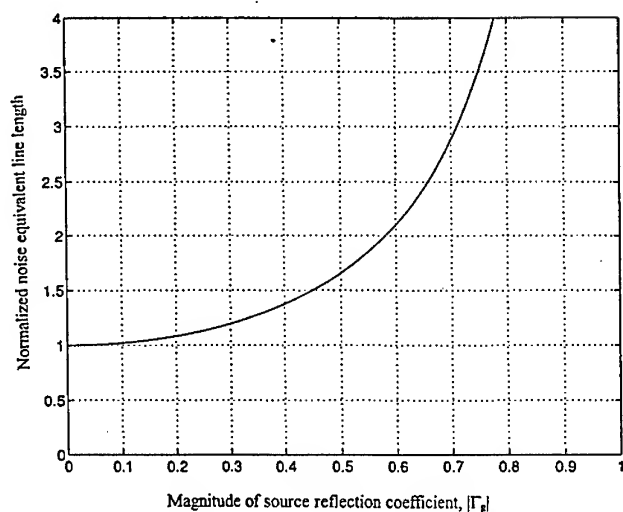


Fig. 1. Variation of noise equivalent line length with the source reflection coefficient, normalized with its physical line length.

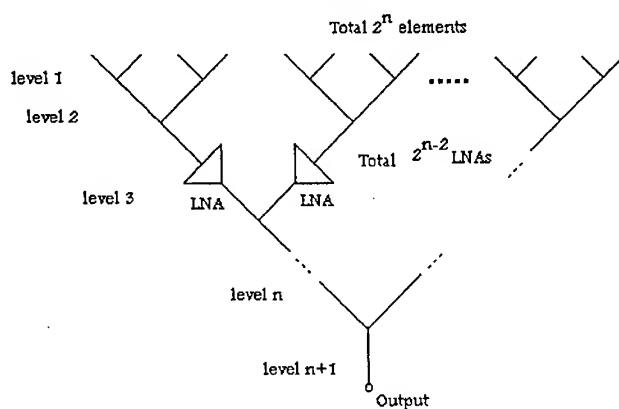


Fig. 2. Schematic representation of a $N=2^n$ element corporate feed structure.

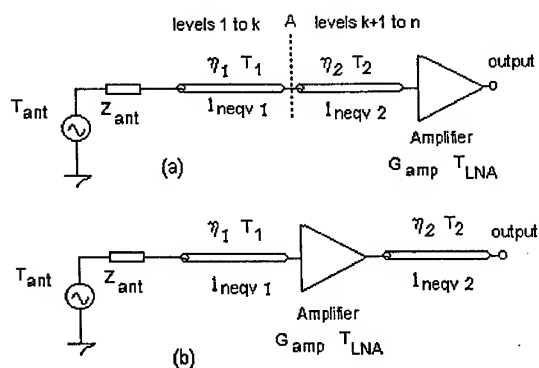


Fig. 3. Active circuit integration with antenna arrays: (a) LNA connected to level $n+1$ (b) LNAs connected to level $k+1$.

A High Precision Analog Frequency-Ramp Generator Using a Phase-Locked-Loop Structure

Thomas Musch and Burkhard Schiek

Ruhr Universität Bochum

Institut für Hochfrequenztechnik

Universitätsstraße 150

D-44780 Bochum, Germany

ABSTRACT

A high precision analog frequency-ramp-generator has been developed. The highly linear frequency-ramp is generated using a Phase-Locked-Loop (PLL) circuit design. It features a smooth analog ramp without any step behaviour normally expected of a PLL-system. In order to obtain such an analog ramp exact timing conditions have to be ensured when programming the variable divider. A synchronizing circuit is used to obtain this precise timing. As the ramp generator works well only if all parts are designed carefully, simulations are required.

The ramp linearity was determined indirectly using a modified FMCW-system (Frequency Modulated Continuous Wave) especially built for these measurements and additionally by examining the synchronism of two PLL-linearization circuits with different VCOs which have significantly different tuning curves.

INTRODUCTION

Various applications need fast linear frequency ramps. Such analog frequency ramps are often the only way to obtain very short measurement times when stepped synthesizers are not fast enough and conventionally linearized oscillators do not reach the required high level of linearity. For example if a ramp-time of 100 μ s and 1000 measuring points are required the settling time of a stepped ramp generator has to be less than 100ns. Such short settling times can only be obtained with a very complex synthesizer structure. Furthermore in some applications an analog ramp can be the better choice. An important example for the advantageous use of such a linear analog frequency ramp is in the field of measurement systems based on the FMCW principle. The FMCW principle is primarily used in RADAR-systems and also many industrial applications like moisture measurements and tank level control rely on this method.

The implementation of an analog ramp generator in a FMCW-system allows the easy use of a spatial filter in the IF-path to compensate for the free field attenuation. The spatial filter has the effect of equalizing the different signal levels of targets at different distances so that the resolution of the analog to digital converter which digitizes the IF-signal can be reduced. With a stepped frequency generator this filter cannot be employed resulting in the necessity of a high resolution analog to digital converter. As the frequency of the IF-signal in a fast FMCW-system can be quite high the analog to digital converter has to have a high sample rate. This can be a problem because a high sample rate and a high resolution of an analog to digital converter are conflicting parameters.

One possible way of generating the analog frequency ramp is to drive a VCO with an analog voltage ramp. As VCOs normally show quite a nonlinear tuning behaviour, an analog linearization circuit is necessary. This is the common way of generating an analog frequency ramp but the linearity achievable will sometimes not be good enough for a high precision measurement system where the ultimate linearity is desirable. Using a PLL to linearize the VCO can fulfill the requirements.

DESCRIPTION OF THE PLL-RAMP-GENERATOR

The PLL-ramp-system uses a crystal oscillator for generating the reference frequency. Therefore the ramp frequency is determined very accurately and drift effects in the analog parts of the circuit do not affect the ramp-frequency. The block diagram in figure (1) shows the simplified structure of a single loop PLL (Phase-Locked-Loop) linearization circuit.

The division factor N of the frequency divider is increased or decreased in integer unity steps at equidistant time intervals. The division ratio of the frequency divider is determined by the micro-controller μP . As the programming of the frequency divider needs a precise timing, a synchronizing circuit is implemented to provide the divider with a new division value just in time. If the strict timing conditions are violated, the ramp linearity will be clearly deteriorated. The divider is programmed synchronously with the reference frequency so that the following equations (1) can be derived, describing the dependence of the reference frequency f_{ref} and the number of division ratios Z on the frequency ramp, the VCO sweep bandwidth $B = f_{max} - f_{min}$ (f_{max} , f_{min} maximum and minimum VCO frequency) and the sweep time T of the ramp. With N_{max} and N_{min} being the maximum and minimum division factors, $Z = N_{max} - N_{min}$, one can obtain

$$\begin{aligned} Z &= \sqrt{B \cdot T} \\ f_{ref} &= \sqrt{\frac{B}{T}} \end{aligned} \quad (1)$$

Normally the ramp time T and the bandwidth B are given by the system application. Then the number of division ratios Z and the reference frequency f_{ref} are clearly fixed and there is no degree of freedom in the choice of these values.

If the loop filter $F(s)$ in the loop feedback is designed correctly a smooth analog ramp will be obtained. The loop filter should have at least a single integral behaviour because otherwise the phase-error at the Phase-Frequency-Discriminator (PFD) could exceed its limits.

DESCRIPTION OF THE MEASUREMENT-SYSTEM

One way to proof the good linearity of the analog frequency ramp is the use of a modified FMCW-system. The PLL-ramp-generator is feeding a FMCW-radar using a low dispersion delay-line as the device under test. The IF-spectrum of such a test assembly is a good indicator of the linearity since every nonlinearity causes an expansion of the spectral peak. Figure (2) shows the FMCW-system.

To get a realistic result the frequency response of the circuit should be flat with the delay-line being as long as possible and having low dispersion. Then the shape of the IF-spectral peak gives a good idea of the ramp linearity. The mechanical length of the delay-line used in this system is 100m. This kind of measurement does not deliver a precise value of the nonlinearities. On the other hand the FMCW-measurement is close to an important application usually requiring highly linear frequency ramps so that the results derived by this system give a good guess about the usefulness within a FMCW-radar system.

In order to measure the frequency deviation from an ideal ramp more sensitively than with the FMCW-method we used a system with two identical ramp PLL-circuits having different VCOs with different tuning characteristics. These two linearisation circuits are synchronized using a single cristal reference oscillator. The block diagramm of this measurement-system is shown in figure (3).

The two PLLs produce identical ramps which start with a very small time offset, so that in the case of perfectly linear analog ramps the IF-signal given to the DSO (Digital Storage Qscilloscope) should have a constant frequency while both ramps are running parallel. The IF-frequency f_{if} is determined by the difference frequency between the two ramps. This difference frequency can be calculated from the ramp slope \dot{f} and the delay τ_d between the ramps using a mixer. With $B = 320\text{MHz}$, $T = 204.8\mu\text{s}$ and $\tau_d = 700\text{ns}$ one gets:

$$\dot{f} = \frac{B}{T} = 1.5625 \cdot 10^{12} \text{Hz/s} \Rightarrow f_{if} = \dot{f} \tau_d = 1.09375 \text{MHz} \quad (2)$$

Equation (1) determines the values for the number of points on the ramp $Z = 256$ and the referency frequency $f_{ref} = 1.25\text{MHz}$.

If the two ramps are not perfectly linear the IF-frequency varies depending on the difference frequency between VCO₁ and VCO₂. To get an idea of this variation the IF-signal is transformed into the frequency domain using a FFT (Fast Fourier Transform). By inspecting the peak in the IF-spectrum one gets a good information of the IF-frequency stability. In the measurements section the results derived by this method are shown.

SIMULATIONS

Several simulations have been made in order to obtain a good circuit behaviour and to estimate the improvement in linearity using such a PLL-linearization. The first simulation shown in figure (4) compares the frequency deviation from the ideal ramp when giving a simple analog voltage ramp to the VCO input (upper figure) to the frequency deviation in the closed loop (lower figure).

The upper figure is based on a measured tuning curve of one VCO used within the linearisation PLL. The frequency deviation is quite large reaching 80MHz in its maximum. Using the PLL to control the same VCO the simulation shows that the frequency linearity error is much smaller compared to the "free running" case. This simulation shows the potentials of such PLL-linearisation circuits.

The results are not so impressive if the tuning characteristic of the VCO shows a slight oscillating behavior. In this case the PLL has to generate a VCO tuning signal which is changing quickly. Because of the finite bandwidth the PLL can not perfectly control such a fast tuning signal with the result of a larger frequency deviation. The VCOs used in the two-loop measurement-system show such a slight oscillatory tuning behaviour resulting in a varying difference frequency between the two VCOs. To simulate this difference frequency within the closed PLL the two tuning curves were measured and the resulting difference frequency with and without a PLL-linearisation is shown in figure (5).

The frequency deviation between the two oscillators f_{if} is measured with the two-loop system. Without the PLL-loops the oscillators have quite a large difference frequency because their tuning curves have significantly different shapes. Within the closed loops on the other hand the difference frequency is quite small, but slightly higher than with the VCO having a flat tuning characteristic.

MEASUREMENTS

To prove the high linearity predicted by the simulations some laboratory prototypes of the PLL circuit have been built. These circuits have been tested using different principles of measurement to determine the ramp linearity. An exact direct linearity measurement is hard to perform since the predicted linearity error is extremely small. As described before two measurement principles were used to test the ramp quality. Figure (6) shows the IF-spectrum of the FMCW-measurement. A simulation with a nonlinearity of 1% is printed as a dashed line together with the measured curve to get an impression of the effect that a small nonlinearity can cause.

The other measurement method uses two identical PLL-circuits that linearize two VCOs with *different* tuning characteristics which are shown in figure (8). The curves show the tuning voltage of the VCOs versus the oscillating frequency. Obviously their tuning characteristic is different producing a difference frequency between the two oscillators that has to be corrected by the ramp-PLLs.

The mixer in figure (3) produces an IF-signal which is the difference frequency of the two VCOs. The IF-signal has been digitized and transformed into the frequency domain. The predicted IF-frequency is 1.09375MHz. Looking at the measured IF-spectrum in figure (8) it is quite obvious that the spectral purity of the IF-signal is very good. The result of a precise IF-frequency measurement is a deviation of the predicted (equation (2)) and the measured IF-frequency of less than 20kHz which is in the range of the simulated deviation. The measured linearity error between the two ramps is in the order of 10^{-4} related to the bandwidth of 320MHz. The more precise two-loop method proves again the excellent linearity of the PLL-linearized VCOs which by themselves have quite a poor linearity.

CONCLUSION

A PLL-linearization circuit for generating an extremely linear frequency ramp has been developed. In order to reach an optimum in circuit performance and to estimate the frequency error several simulations have been made. The results of these simulations have been proofed by various measurements. One of these measurements is close to a useful application since it employs a modified FMCW-radar-system. The other method uses two PLL-circuits leading to more sensitive results. All the simulations and measurements underline the good performance of such a PLL-linearization circuit.

REFERENCES

- [1] B. Schiek and H. Siweris: Rauschen in Hochfrequenzschaltungen, Hüthig Verlag, Ch. 7, pp. 255-260, 1990
- [2] T. Musch and B. Schiek: "Ein rauscharmer und kostengünstiger YIG-Oszillator im Frequenzbereich von 2,2 bis 6,4 GHz", Kleinheubacher Berichte, Vol. 39, pp. 479-488, 1996

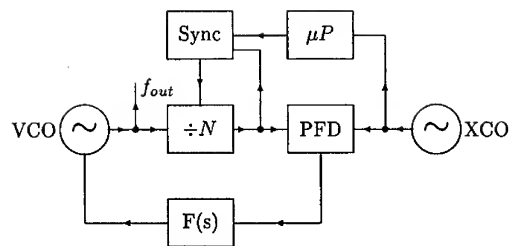


Figure 1: Simplified block diagram of a single loop PLL-system

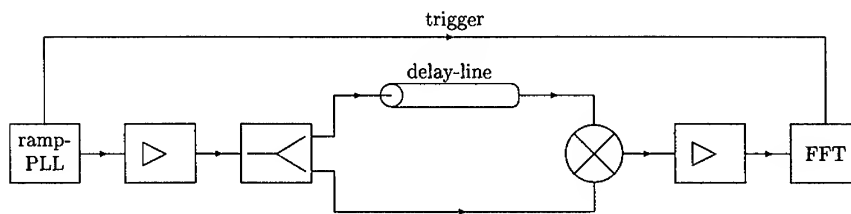


Figure 2: Block diagram of the FMCW-system

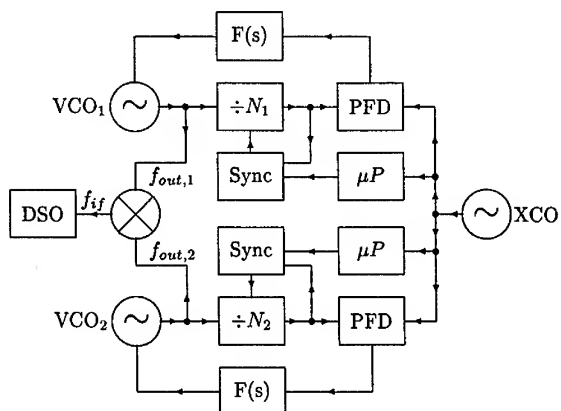


Figure 3: Simplified block diagram of the two loop measurement-system

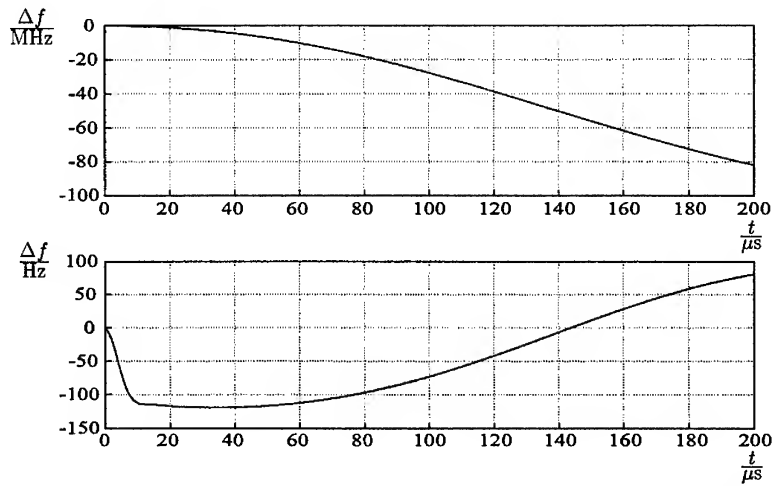


Figure 4: Nonlinearity without (upper figure) and with (lower figure) PLL-circuit

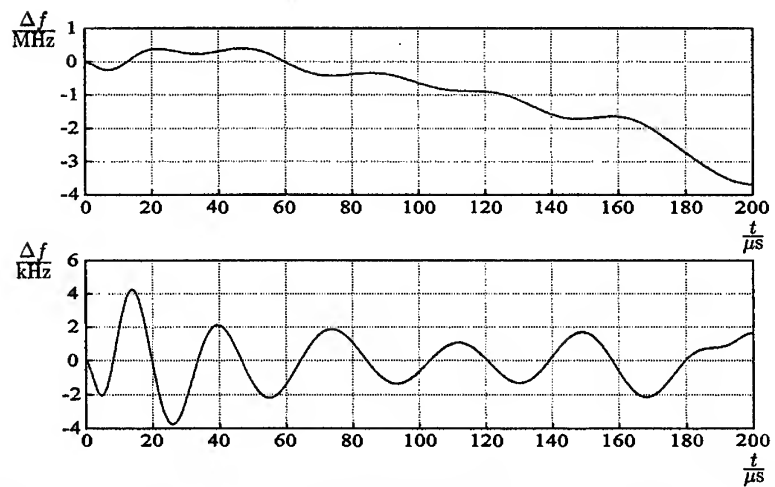


Figure 5: Two-loop IF-frequency without (upper figure) and with (lower figure) PLL-circuit

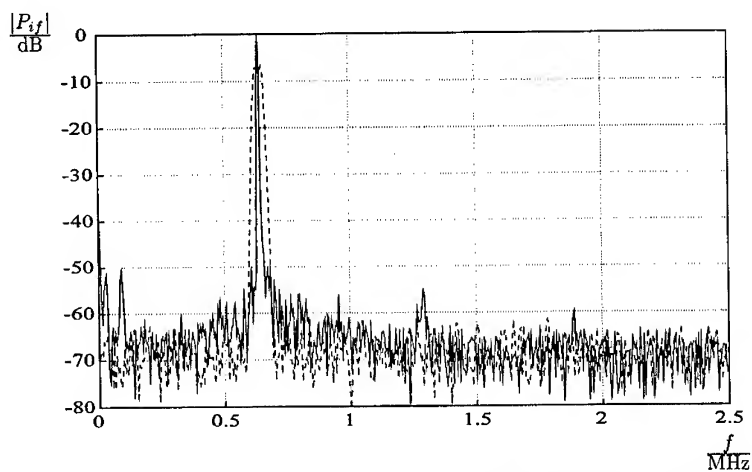


Figure 6: Measured IF-spectrum (solid curve) compared to a simulated IF-spectrum (dashed curve) caused by a nonlinearity of 1%

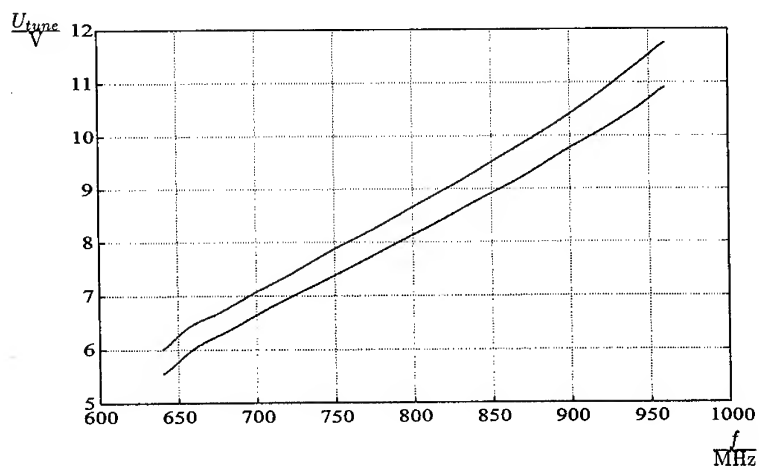


Figure 7: Tuning curves of both VCOs

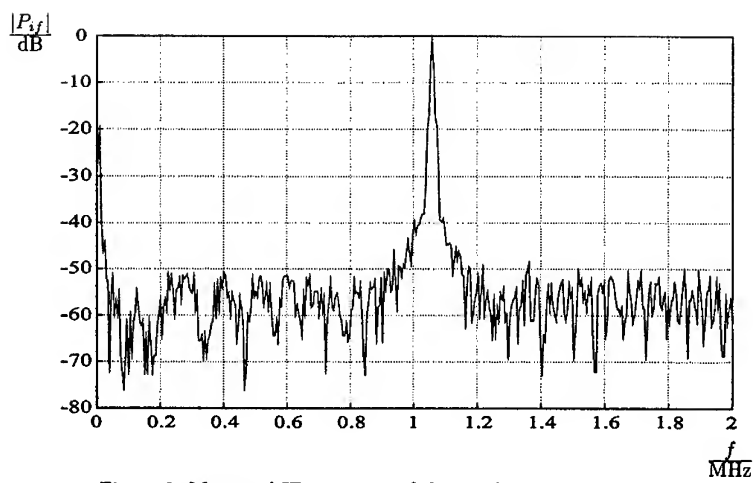


Figure 8: Measured IF-spectrum of the two-loop test circuit

Dual Shaped Reflector Antenna for Airport CW radar

Jacob Meshy, Michael Negev - Antenna Dept. ELTA

Abstract

Modern airports require an accurate search radar to control the ground traffic in an airfield environment. The radar uses the CW mode to help operate in a high clutter area, covered with buildings and other obstacles. Two collinear, separate antennas are used for transmit and receive, requiring high isolation between them.

The following article describes an approach to design of a low cost, dual inverted COSEC reflector antenna. The method combines manual design with heavy graphical display and accurate analysis program. This approach was used to develop the antenna for the Elta ASDR EL-M2125 radar, which was tested at the Salt Lake City airport. The article describes the design procedure and the test results.

Main requirements

The dual reflector antenna should meet the following requirements:

- Inverted, (below the horizon) specially defined coverage shape in elevation with a steep slope at the end of the elevation pattern.
- Constant azimuth beamwidth in elevation angles, to keep the radar resolution at all distances.
- High isolation between the two adjacent antennas, better than -85dB.
- Circular Polarized with low ellipticity.
- Low level Sidelobes.
- Low cost production.

Design concept and tools

Shaped reflector antennas, mostly COSEC², are well known for many years, with good results. The main interest in this work is the way and tools we used. It was needed to accomplish the task in short time, as well as to maintain tight requirements and flexibility of the design to fit to new requirements.

The design method was based on two concepts:

- Manually design of most parts, including extensive use of graphical display.
- Using accurate and reliable analysis program. This helps to conceive to an accurate solution.

In this work we used two computer programs:

- a. GRASPC/7 - reflector analysis software from TICRA, Denmark.
- b. MATLAB - powerful mathematical software with strong graphical capabilities.

Design procedure

The shaped reflector is designed in two steps - the central curve and the surface based on it.

There are several methods based on Geometrical Optics to design the central curve. In this work, we used the method of Thorel [1]. The result of this step is regarded as raw output. We implemented various mathematical smoothing methods in combination with GRASP analysis program. This approach accelerates the design and helps control the contribution of each part of the reflector.

The reflector surface is calculated analytically, directly from the central curve. For a shaped reflector, there are many available surfaces, depending on the definition of the equi-phase planes, [2].

In this part, we used a combined manual design, using a very powerful graphical display and analysis program.

It can be seen, in the following figures, the various views and the simplicity of identifying unusual result, and obtaining the limits of each solution.

The main effect of the surface shape is on the azimuth cuts in elevation. Since this antenna contains two different surfaces, as well as it is inverted COSEC, it was important to analyze the results carefully. The conclusion of this work was a different type for reflector. The results show different radiation pattern characteristics, but the azimuth beamwidth in elevation was kept quite constant for both reflectors.

Antenna structure

The design of two offset reflectors, one above the other, was chosen to meet the low level side lobes requirement. This arrangement is compact, and fit to be covered with a radome, but it increases the coupling between the antennas.

The direct radiation of the feeds is the main contributor to the coupling, so they were separated by an isolation plate. The size and materials of the plate were chosen to reduce the coupling to -90dB.

The asymmetric solution led to the design and manufacture of two different reflectors, see fig. 5.

The reflectors were designed by using the GRASPC7/GRASPC - reflector pattern analysis programs of TICRA, Denmark, and they manufactured were from epoxyglass sandwich.

Two cylindrical circular polarizers are attached to the feeds. They consist of 4 meanderline layers.

Results

The electrical characteristics of the antenna were tested on the outdoor Elta antenna test-range.

The measured results show a very good fit to the specifications:

- Elevation coverage of both reflectors are very similar and close to the requirements.
- Horizontal cuts in elevation are almost constant, and even slightly shortened.
- Ellipticity is below 1dB at all frequencies.
- Isolation is better than -90dB.

Figures

The attached figures show a few examples of the many drawings of the design. The drawings represent the extensive use of graphical aids.

Fig. 1.x shows some aspects of the design of the central curve, the GO design and mathematical smoothness. Various views of the control of several geometrical parameters of the surface in fig. 1.3 and the contribution on the pattern in fig. 1.2.

Fig. 2.x show some views of the various surface characteristics and limitations. A "twist" is shown in several views. The view of radius of curvature was very effective to analyze the regularity of the surface.

Fig. 3.x are calculated patterns of both antennas in Elevation and Azimuth. Different surface type influence the elevation pattern. The most important control is in the beginning and the end of the shaped beam, in fig. 3.1. Azimuth cuts in elevation in "UP" reflector are much more sensitive to the surface type, fig.3.2.

Fig. 4 includes final measured patterns of UP and DOWN antennas.

Fig. 5 is a photograph of the complete antenna system at the radar evaluation site in Salt Lake City airport.

Summary

In this work we introduced a unique design and measurements of an accurate, circularly polarized, dual shaped reflector antenna system. The isolation between the two antennas is around -90dB to enable CW operation. The antenna is circularly polarized with an A.R better than 1dB.

We introduced a design method based on a combination of manual/ mathematical design, with extensive use of graphical views, and accurate, reliable analysis program. This method was proved as fast, giving good results and flexible.

Two different reflectors were designed from scratch in a short time which gave very similar coverage, inverted COSEC with a constant azimuth beamwidth in elevation.

Two prototypes of the antenna assembly were built and integrated with the Elta ASDR EL-M2125 radar which was tested at the Salt Lake City airport.

References

1. L. THOUREL "Les Antennes", 1971 edition, chapter 10.5.2
2. A. Brunner, "Possibilities of Dimensioning Doubly Curved Reflectors for Azimuth Search Radar Antennas", IEEE Transactions on antennas and propagation, vol. AP-19, NO. 1, January 1971, pp. 52-57

Figures

1. Central curve design

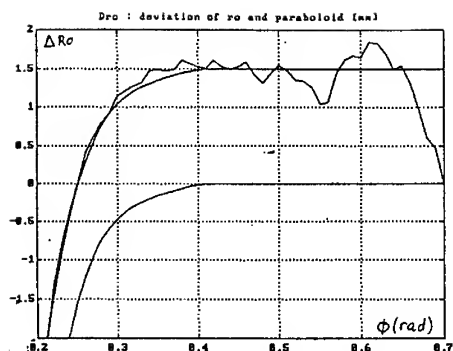


Fig. 1.1 Central curve by GO synthesis and smoothing

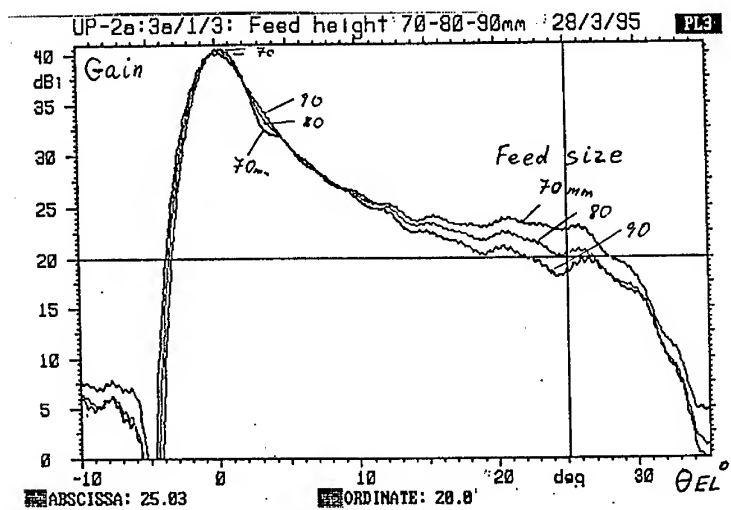


Fig. 1.2 Control of Elevation coverage synthesis

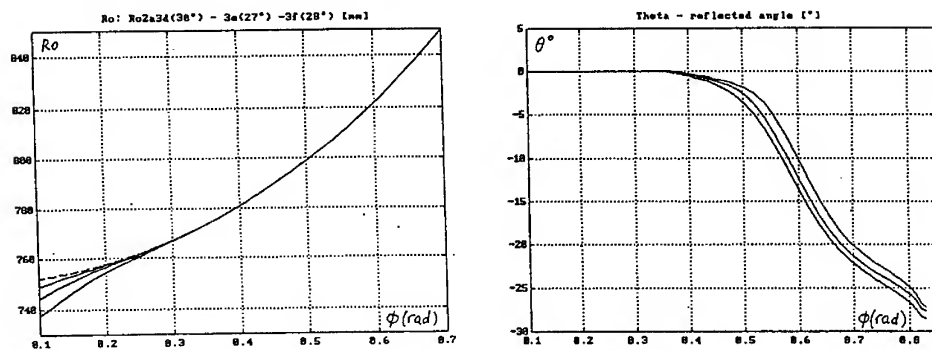


Fig. 1.3 Various display of the central curve: a. radius-vector variations- Δp b. reflected angle- θ

2. Surface design

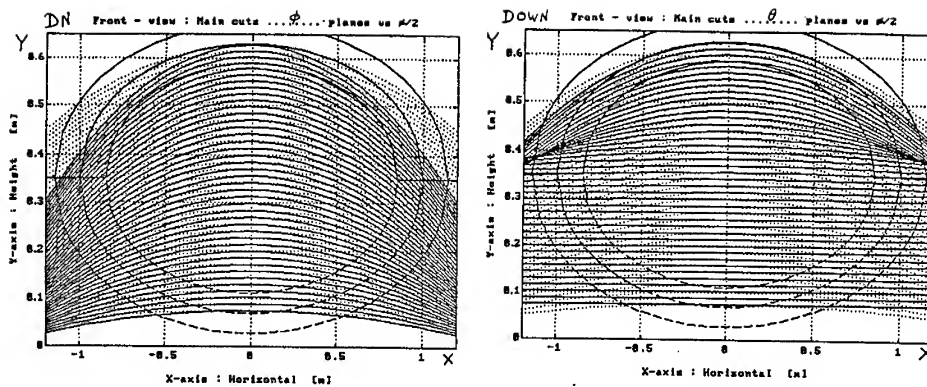


Fig. 2.1 Surface different shapes and limits - Front view

Fig. 2.2 Deformations of the surface edge
- Side cuts and "twist"

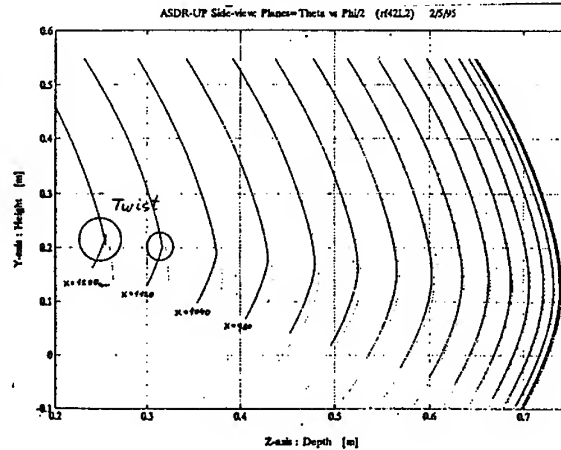
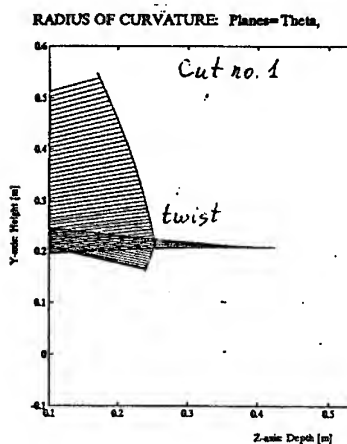
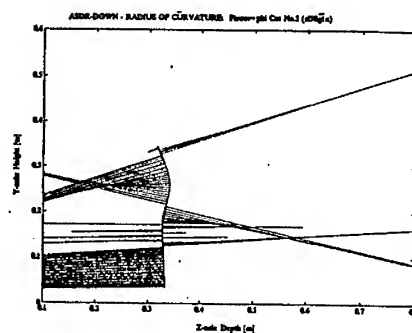


Fig. 2.3 Radius of curvature display



a. "twist" in cut no. 1



b. changes in surface curvature

3. Pattern analysis

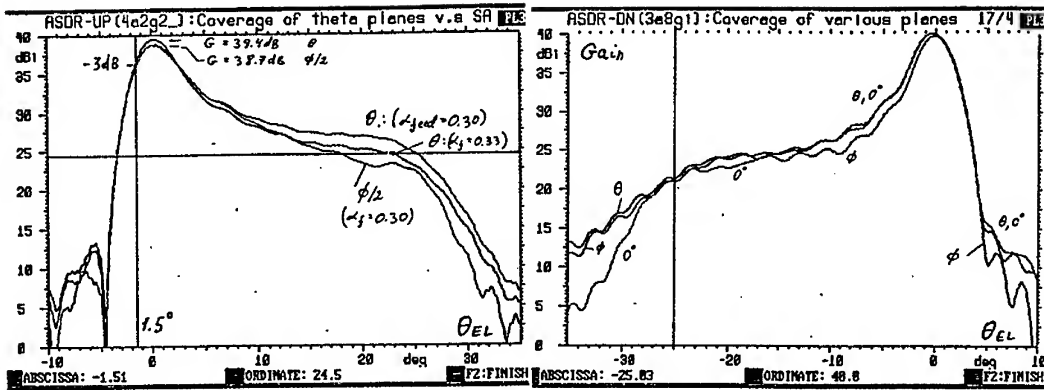


Fig. 3.1 Control of Elevation coverage with surface type - a. UP b. DOWN reflectors

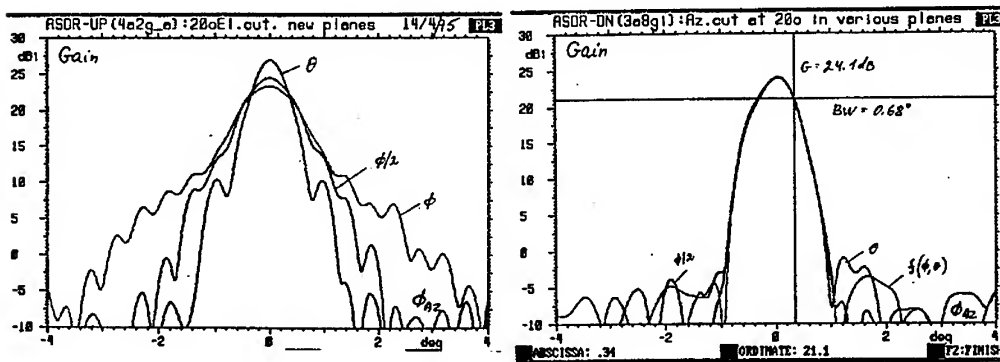


Fig. 3.2 Improvement of Azimuth cuts with surface type - a. UP b. DOWN reflectors

4. Actual antenna

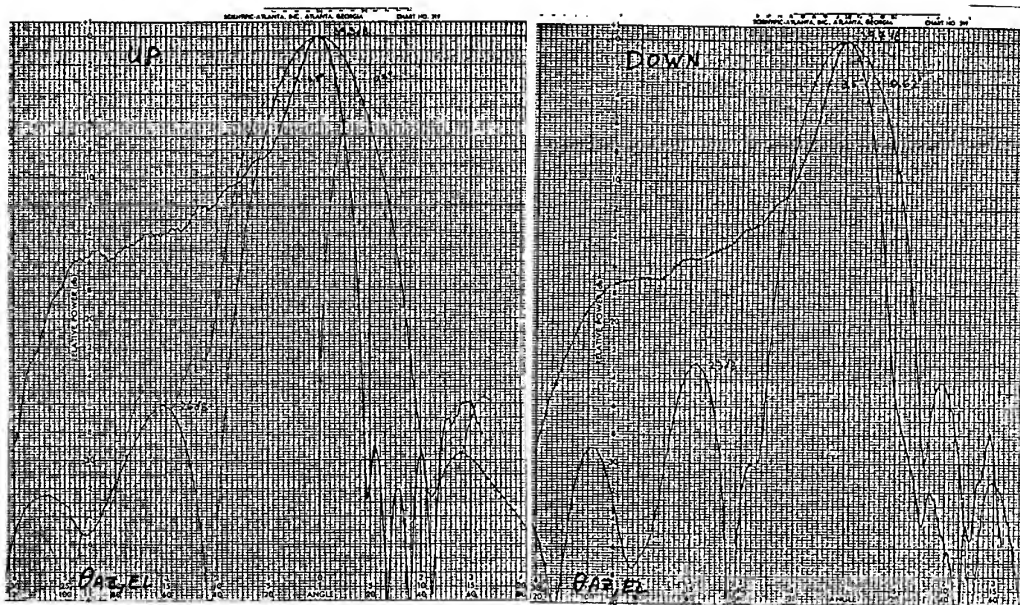


Fig. 4 Antenna measured patterns - a. UP b. DOWN antennas

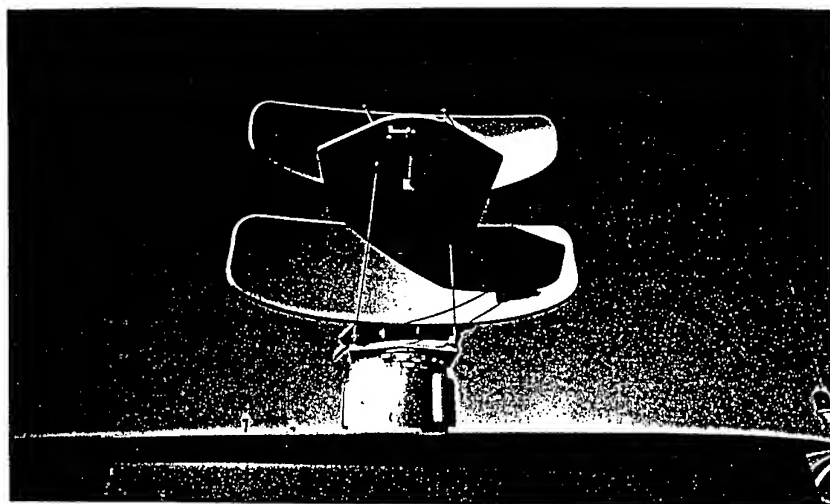


Fig. 5 Antenna at Salt Lake City airport

Electrical and Mechanical Design of the AMOS Communication Antenna Subsystem

M. Lieke*, C. Hunscher*, T. Kutscheid*, E. Ze'evi**

*Dornier Satellitensysteme GmbH

**IAI/MBT

*Summary of a paper for session C1 of the 27th European Microwave
Conference*

Point of Contact:

Manfred Lieke

Dornier Satellitensysteme GmbH

PO Box 80 11 69, 81663 Munich, Germany

Tel: +49-89-607-2 85 68 Fax: +49-89-607-2 33 84

E-mail address: manfred.lieke@dss.dornier.dasa.de

Abstract

The design, development and test activities performed on the Ku-band antenna subsystem for the Israeli communication satellite AMOS are presented. Starting from AMOS mission requirements like service areas and EIRP in conjunction with mechanical constraints imposed by the ARIANE 44 MINI SPELDA, the different steps of both electrical and mechanical antenna design optimizations during the development phase are summarized. The antenna gain, reflector diameter and focal length are the results of the trade-off analyses, done during the design phase.

The antenna subsystem has been designed, manufactured and qualified by Dornier Satellitensysteme GmbH (DSS), Germany, between 1992 and 1995. Its design has been verified by a number of qualification/acceptance tests starting at component level with tests demonstrating the performance of the mechanisms at different temperatures or with RF-tests of feed system components. Finally the test sequence culminated in overall subsystem tests, e.g. RF-pattern measurements in a Compact Test Range and hot/cold deployment tests of the reflector under thermal vacuum conditions.

1 Introduction

Since the launch by Ariane 44L in May 1996 the Israeli communication satellite AMOS is operating successfully at the geostationary orbital position 4° West. With a total mass of less than 1000kg offering seven Ku-band transponders of 35 Watt this new spacecraft type will be an interesting alternative especially for customers from developing countries. AMOS provides diversifying communication and broadcasting services over the Israeli territory while its coverage area enables Israel's neighbouring countries to take advantage of its high performance. Moreover a second spot beam can be switched either to Hungary or to Portugal. Basically the AMOS communication antenna provides services in the middle East and Eastern Europe with an EIRP of some 55dBW.

2 AMOS Mission Requirements

The antenna subsystem of AMOS has to perform telecommunication services in the 11/14 GHz frequency bands from the geostationary arc at 4° West. Three high gain spot beams have to be provided, one pointing to Israel/Middle East, one to East Europe/Hungary and one to Portugal. Only two beams shall be operated simultaneously, the Israel/Middle East beam and either that to Hungary or that to Portugal. The selection of the active beam shall be done by RF-switching within the antenna subsystem. Dual linear polarisation has been required. The requirements are summarised in Tab. 1.

3 Electrical Antenna Design

The design of the combined transmit (10.95-11.70 GHz) / receive (14.0-14.5 GHz) antenna (Fig. 1) has been driven by the main requirements of 41.1/42.2 dBi (Tx/Rx) gain over Israel and 39.9 dBi (Tx and Rx) over Hungary. Therefore an offset parabolic reflector of 1.70m diameter and 1.20m focal length has been chosen. The feed assembly (Fig. 2) has been composed of three individual feed systems, each one consisting of a conical corrugated horn (aperture diameter 70mm), a square to circular waveguide

Frequency band	Ku-Band
Uplink:	14.00 to 14.50 GHz
Downlink:	10.95 to 11.70 GHz
Service areas	1. Israel and the Middle East 2. East Europe with the beam center over Hungary
Antenna polarisation	linear
Uplink:	Vertical (European Beam) & Horizontal (Middle East beam)
Downlink:	Horizontal (European Beam) & Vertical (Middle East beam)
No. of Transponders:	7 active, out of 9 up to 6 active in the Middle East beam up to 4 active in the European beam
Transponder Bandwidth:	72 MHz
EIRP:	55 dBW at beam center
G/T:	14 dB/K at beam center
Antenna gain	
Uplink:	41.5 dBi over Israel/Middle East, 41.0 dBi over Hungary
Downlink:	41.7 dBi over Israel/Middle East, 40.4 dBi over Hungary
Antenna beam isolation:	23 dB (sidelobes, cross-polarization)

Tab. 1 AMOS Technical Specifications

transition and an orthomode transducer to separate the two senses of linear polarisation. The feed systems dedicated to the Hungary and the Portugal beams can be selected via two waveguide switches (Tx and Rx).

During the running program a widening of the Israeli beam has been requested by the customer to adapt the coverage to the political changes in the middle East in the mid nineties. In the frame of this action the Hungarian beam has been widened, too. For the beam widening the two conical corrugated horns of Israel and Europe have been replaced by rectangular horns (Fig. 3). The new feeds have been designed, manufactured and qualified within less than six months and exchanged at the integrated spacecraft.

The antenna electrical design optimisations have been performed using high standard and well proven computer routines. Sophisticated horn software has been applied for the optimization of the feed horns. The antenna radiation pattern have been computed using the GRASP 7 program package, developed by TICRA, Copenhagen.

The feed systems were designed to be compatible with the cross-polar specifications, to provide low insertion and return losses and to handle the power levels required. As far as possible components were applied, which have been qualified and used for similar space missions, or which could be adapted to the AMOS mission with minor modifications. This held for the corrugated horn(s) and the orthomode transducers, which were direct derivations of feed system components for the Ku-band antenna of the German Communication Satellite DFS Kopernikus.

4 Mechanical Antenna Design

The mechanical design of the antenna was based on the heritage gained by DSS during several space programs in the scientific as well as the communication business.

In order to comply with the volume constraints given by the use of the Ariane 4 Mini Spelda shroud the reflector had to be stowed for launch and deployed in orbit into its operational configuration. This was accomplished by a pyrotechnical release of the two hold-down points and a subsequent reflector rotation driven by a spring actuated mechanism.

Both the stowed and the deployed configuration are depicted in Fig. 4 and Fig. 5 together with the associated S/C panel.

4.1 Reflector Dish

The offset reflector shown in Fig. 6 with a circular aperture and a parabolic contour consists of a thin sandwich shell stiffened by horizontal and longitudinal sandwich ribs.

The main geometrical characteristics of the reflector are:

- Aperture diameter: $D = 1700 \text{ mm}$
- Offset $d = 170 \text{ mm}$
- Focal length $f = 1200 \text{ mm}$

Both shell and ribs are made from ultra-high modulus GY70/Epoxy skins on an aluminium honeycomb core. Whereas the dish skin lay-up is a four layer orthotropic one the rib skin laminate is made from six layers $[0^\circ/\pm 60^\circ]_s$. In combination with an appropriate adjustment of the aluminium core thickness and density the CTE's of both sandwich types was adjusted to the range between $0.6 \times 10^{-6} \text{ K}^{-1}$ and $0.8 \times 10^{-6} \text{ K}^{-1}$ depending on the direction.

The connection between shell and ribs is performed by continuous CFRP wedges which are laminated and cured in place. The rib crossings are reinforced by CFRP nodal plates which asserts a high strength load path. At the extending ends of the two longitudinal ribs Titanium brackets are spliced in which build the interface to the Deployment and Latch Mechanism (DLM).

In order to provide a strong and stiff interface the two housings of the Hold-Down and Release Mechanism (HRM) are installed at the central rib crossings. The optical alignment of the dish in deployed configuration is performed with reference to a mirror cube being glued onto the side face of the longitudinal rib close to the outer rib intersection.

The thermal control of the reflector is achieved by white paint on the front side and a single layer of a VDA Kapton® blanket reinforced by a scrim on the rear side. The attachment of the blanket relies on stand-offs along the rim and additional Velcro® patches along the ribs.

The electrical grounding is performed by connecting all elements via straps and conductive glue to the aluminium honeycomb core of both shell and ribs.

4.2 Reflector Release and Deployment Mechanism

As is visible in Fig. 4 and Fig. 5 the Reflector Release and Deployment Mechanism consists of

- a Deployment and Latch Mechanism (DLM)
- two Hold Down and Release Mechanisms (HRM's)

4.2.1 Deployment and Latch Mechanism

The Deployment and Latch Mechanism (DLM) is a spring driven mechanism deploying the reflector from the stowed into the deployed configuration by a rotation of some 65° about its hinge axis. As depicted in Fig. 7 it consists of a Drive & Latch Hinge (DLH) and a Support Hinge (SH) being attached to the reflector interface brackets on the antenna side and to the west panel interface bracket on the satellite side. Both DLH and SH are equipped with two angular contact bearings being pre-stressed for high stiffness and zero backlash.

The rotation is actuated by two helical springs located on the DLH - see Fig. 7 and Fig. 8. Full redundancy is provided since one spring alone can safely perform the deployment under worst case friction conditions. At the completion of deployment the reflector is latched in an end stop in the DLH the position of which can be adjusted during antenna alignment. Contrary to most of the deployment mechanisms used in space constructions the AMOS DLM has no dedicated damping element. The deployment energy of the reflector is solely dissipated by structural damping in the mechanism and the reflector as well. This philosophy leads to a comparably high end shock during latching which - once the drive torque is defined with appropriate margins - is determined by the eigenfrequency of the deployed reflector. It has the advantage of making the mechanism simple and lightweight and to increase its reliability since a damper not being present is not subject to failure.

The Support Hinge carries two redundant micro switches monitoring the latched configuration.

Four flat Copper flexleads connect the Aluminium base bracket of each hinge to the S/C. Apart from acting as a multiply redundant grounding path these flexleads couple the DLM temperatures to those of the West Panel. In addition the Titanium reflector brackets are connected by two flexleads each to the associated base brackets and the individual hinges are entirely covered by a thermal insulation box. This combination of measures keeps the temperature range as well as the temperature gradients small resulting in a maximum thermoelastic stability of the deployed configuration.

4.2.2 Hold Down and Release Mechanism

The fixation of the stowed reflector and its release at begin of deployment is accomplished by two Hold Down and Release Mechanisms the design of which can be seen in Fig. 9.

The interface between reflector and satellite is designed as a cone mating a cup which allows to transfer both axial and transversal loads. The reflector is held by pre-tensioned bolts mounted in separation devices which can pyrotechnically open a segmented nut. Supported by a helical spring the bolt is ejected and captured by a cap on top of the housing which is mounted on the reflector. The two HRM's are ignited sequentially in order to guarantee a safe release.

4.3 Feed Assembly

The conical corrugated horn as well as the two rectangular horns are made from aluminium using standard milling and eroding techniques. Inner and outer surfaces are alodyne treated, the flange areas are silver plated to reduce the risk of passive intermodulation products (PIMP). The apertures are covered by white painted Kapton sunshields. The waveguide transition and the ortho-mode transducers are also made from aluminium, standard milling and eroding processes have been applied. A complex aluminium structure interfacing with the S/C West panel supports the three feed systems in the focal plane. Each feed system is defocused w.r.t. the reflector's focal point such that the corresponding beam meets its dedicated coverage area. The output ports of the ortho-

mode transducers are connected via tailor made waveguide runs to the waveguide switches and to the repeater I/F on the spacecraft North panel, respectively.

5 Antenna S/S Qualification

The qualification program of the antenna subsystem comprised a mechanical and electrical verification of the feed assembly and reflector assembly performance taking into account the environmental conditions during launch and in orbit. Apart from the geometrical measurements and alignments this included thermal vacuum tests for the feeds (+81°C to -35°C) and the reflector (+90°C to -180°C), sine and random vibration of the DLM, the HRM, the feed assembly. The reflector assembly had to undergo a sine vibration test along with several deployment tests in air as well as in vacuum. An acoustic test was performed on S/C level since the interaction of the antenna S/S with the S/C panel can hardly be simulated properly on S/S level.

Extensive measurements of the RF-parameters have been performed, starting with radiation pattern tests on feed system level such as measurements of insertion loss, return loss and decoupling/isolation between the neighbouring feeds. The feed assembly has been tested to be free of generating passive intermodulation products in thermal vacuum within the qualification temperature range from -35°C to +81°C. For the antenna subsystem, integrated on the spacecraft West panel, radiation pattern, gain, VSWR and the isolation between the three beams have been measured in the antenna compact test range of Dornier Satellitensysteme GmbH at Ottobrunn. After exchange of the feed systems on spacecraft level for the beam widening the RF acceptance tests have been repeated at the far-field test range of Alcatel Espace, Toulouse.

6 Performance

The EIRP contours of the Middle East and European beams are shown in Fig. 10 and Fig. 11. The main electrical and mechanical performance parameters of the antenna elements are summarised in Tab. 2 and Tab. 3, respectively. All requirements have been fulfilled, partly with a considerable margin.

Parameter	Middle East Beam uplink/downlink	European Beam uplink/downlink
Min. gain	41.8 dBi/42.1 dBi	41.9 dBi/41.8 dBi
Min. X-polar discrimination	23.5 dB/27.2 dB	33.1 dB/25.6 dB
Co-polar beam isolation	45 dB/35 dB	32 dB/35 dB
X-polar beam isolation	52 dB/46 dB	45 dB/43 dB

Tab. 2 Electrical Performance of the AMOS Communication Antenna

Parameter	Reflector Dish incl. HRM	DLM	Feed Assembly
Mass w/o thermal blankets	8.42 kg	3.76 kg	5.23 kg
Contour accuracy at 20°C	0.05 mm rms (best fit)	N/A	N/A
Ir-Orbit thermal distortions	0.05 mm rms (best fit)	0.0001 deg/°C	N/A
Reproducibility of deployed angle	0.001 deg		N/A
Fundamental eigenfrequency	76 Hz (stowed) / 5.5 Hz (deployed)		153 Hz
Functional temperature range	-180°C to +90°C	-40°C to +50°C	-35°C to +81°C

Tab. 3 Mechanical Performance of the AMOS Communication Antenna

7 Concluding Remarks

The design and qualification procedures for the AMOS antenna subsystem have been described. Test results exceeded the contractual requirements. All that ensured AMOS successful operation in orbit.

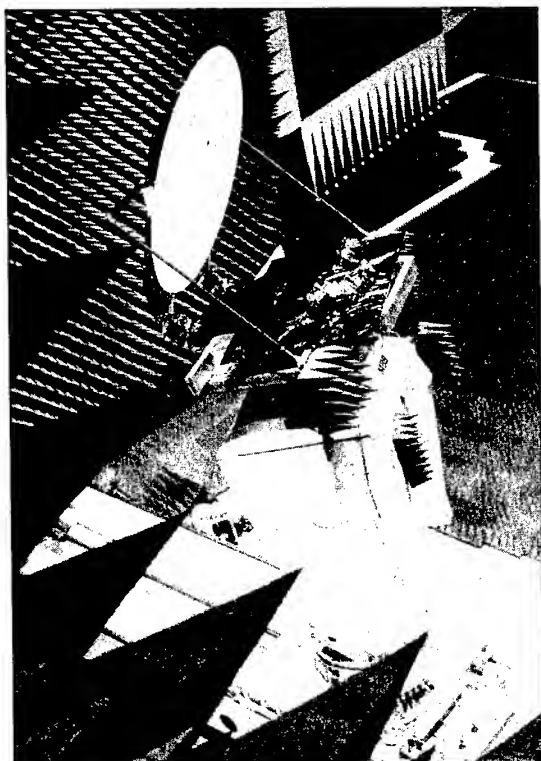


Fig. 1 AMOS Antenna Subsystem in Dornier Compact Range

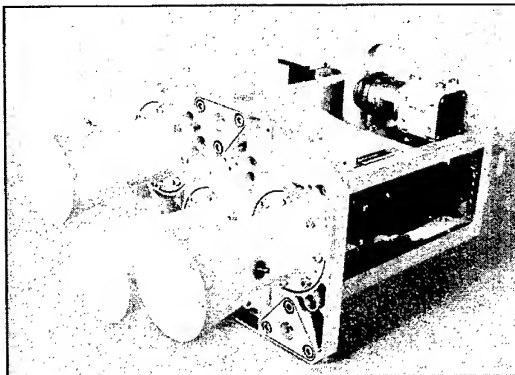


Fig. 2 AMOS Feed Assembly, Configuration Before Beam Widening

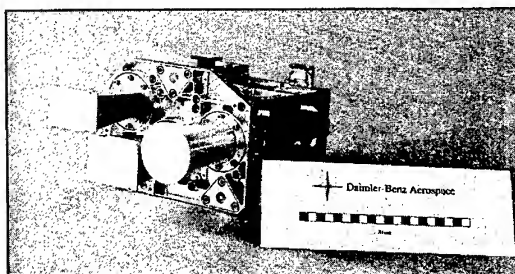


Fig. 3 AMOS Feed Assembly, Flight Configuration

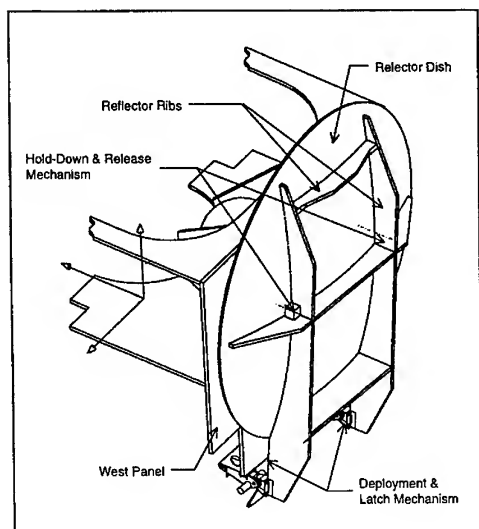


Fig. 4 AMOS Ku Antenna, Stowed Configuration

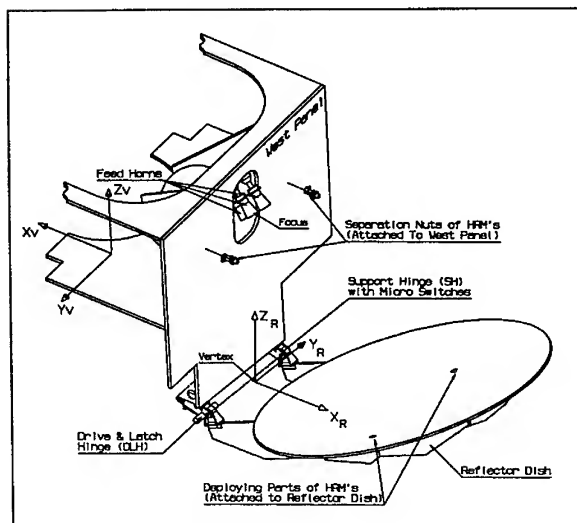


Fig. 5 AMOS Ku Antenna, Deployed Configuration

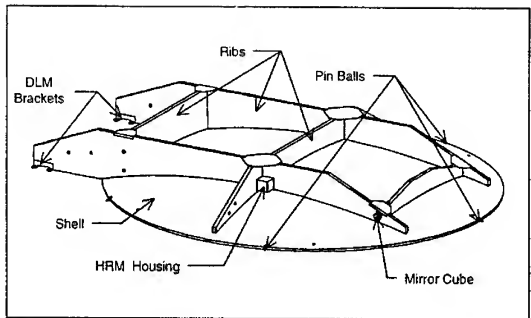


Fig.6 Rib Stiffened CFRP/Al Sandwich Reflector

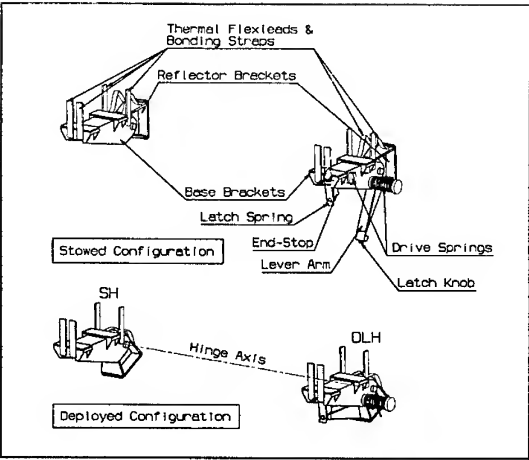


Fig. 7 Deployment and Latch Mechanism (DLM)

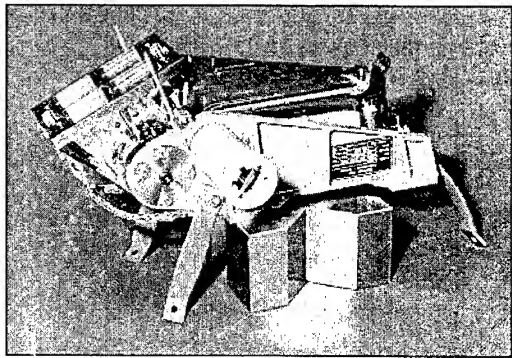


Fig. 8 Drive and Latch Hinge (DLH), Deployed Configuration

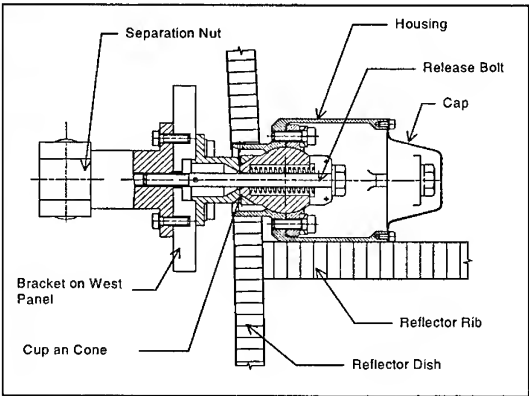


Fig. 9 Hold-Down and Release Mechanism (HRM)

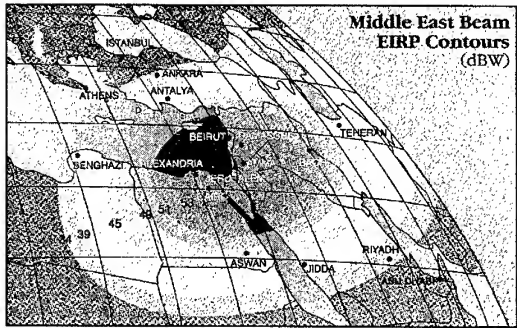


Fig.10 Middle East Beam EIRP Contours

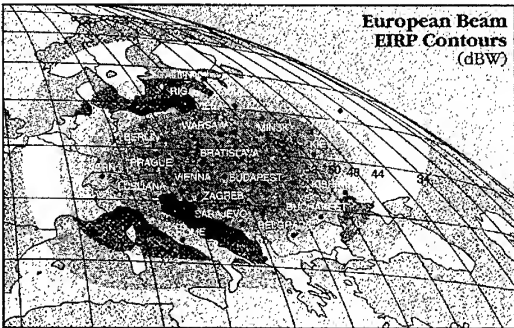


Fig. 11 European Beam EIRP Contours

Novel retrodirective beam formation techniques

S. L. Karode, V. F. Fusco

High Frequency Electronics Laboratory
Department of Electrical and Electronic Eng.
The Queen's University of Belfast, Ashby Building
Stranmillis Road, Belfast, BT9 5AH, N. Ireland
Tel +44 01232 245133 Ext. 4089, Fax. +44 01232 667023
e-mail s.karode@ee.qub.ac.uk/ v.fusco@ee.qub.ac.uk

ABSTRACT

This paper presents two novel active antenna architectures for retrodirective beam formation which rely on heterodyne phase techniques for their operation. Both the methods use the phase conjugate properties of a mixer driven with f_0 and $2f_0$ signals for retrodirective beam formation. In the first approach frequency diversity, coupled with power divider circuits is used as a quasi circulator to provide isolation between incident and retransmitted signals. In the second method a dual linearly polarised microstrip patch antenna provides the complementary function of radiator and isolation element by virtue of its polarisation diversity response. Two element arrays using both approaches were made for 1 GHz operation. Results and theoretical performance figures for the retrodirective antenna architectures are presented in the paper and are compared to a passive 2 element array which is used as a reference for discussion.

INTRODUCTION

A retrodirective antenna array reflects any incident signal back in the direction from which it was sourced. The most well known retrodirective antenna is the corner reflector where the geometry of the structure results in retrodirective beam formation [1]. The planar equivalent of the corner reflector is the Van Atta array [2, 3]. A modification to the Van Atta Array, called the bilateral Van Atta retrodirective array makes use of amplifier gain introduced in the transmission line paths interconnecting the antenna elements[4]. Retrodirective antenna arrays find applications in various commercial and military systems where limited tracking without a priori knowledge of the source is required. Electronic traffic and toll management, freight management and channel markers are to name but a few.

Retrodirective beam formation is a result of phase conjugancy of an incident wavefront i.e. each element in the array delivers an outgoing wavefront component which is phase shifted with respect to a reference phase by exactly as much as the incoming wavefront was advanced. In this case the total path length from the source to the array element and back to the source is constant for all of the elements in the array resulting in maximum field retransmission in the direction of the source. The array factor for this class of antenna can be stated as in equation 1.

$$E_{rt} \approx e^{j(\omega t + \phi)} \sum_{i=-\frac{N}{2}}^{\frac{N}{2}} e^{j\left(\frac{2\pi x_i}{\lambda_r} \sin \theta_i - \frac{2\pi x_i}{\lambda_r} \sin \theta_r\right)} \quad 1$$

where,

- N - number of elements in the array,
- θ_t - Position of the transmitter measured from the broadside,
- θ_r - Position of the receiver measured from the broadside, and
- λ_r - Wavelength of the received signal,
- λ_t - Wavelength of the transmitted signal, and
- x_i - Distance of i_{th} element from array phase centre.

Both the methods presented here use microstrip patch antenna for transmitting and receiving the signal. In both the approaches a mixer along with a local oscillator operating at approximately twice the incident frequency is used to get the required phase conjugate signal necessary for retrodirective operation [5]. In practice a small frequency offset between incident and retransmitted waveforms is introduced to facilitate frequency discrimination incoming and outgoing signals at the detection apparatus.

SCHEME 1 : RETRODIRECTIVE ANTENNA ARRAY USING POWER DIVIDERS

In the proposed scheme shown in figure 1, phase conjugancy is obtained by mixing the received signal with a reference signal at approximately twice the incident frequency (i.e. 1.99GHz). The mixer output signal at 1GHz is then amplified and retransmitted by the patch antenna after passing through a power divider. Due to the narrow bandwidth of the microstrip patch antenna ($\approx 5\%$) only the difference product of the mixer, which bears the phase conjugate relationship with respect to the incident signal, is retransmitted, this results in retrodirective beam formation. The power divider, at the expense of a 3dB path loss, acts as a quasi-circulator [6] to provide isolation between incident and retransmitted signal pathways. Using equation(1) the theoretical azimuthal response of the retrodirective antenna array was constructed This is plotted in figure 6, the agreement obtain shows that the model used in the equation(1) represents clearly the actual behaviour of the antenna.

SCHEME 2: RETRODIRECTIVE ANTENNA USING A DUAL POLARISED PATCH

This scheme, shown in figure 2, works on a similar principle as scheme 1. Here the combination of microstrip patch antenna and power divider is replaced with a dual polarised patch antenna. The dual polarised microstrip patch antenna used in this application is designed to operate in two linear orthogonal modes, TM_{10} and TM_{01} , at approximately the same frequency. Isolation between the polarisation diverse signals ensures minimum interference between received and transmitted signals, hence low cross polar levels are important. For the dual polarised microstrip patch antenna used in this scheme , E and H field cross polarisation levels are better than that 21 dB, (figure 3) while the port isolation over the frequency range of interest is better than 22dB as shown in figure 4.

This arrangement of retrodirective beam formation has lower path loss, but also slightly poorer isolation between retransmitted and incident signals when compared to the first scheme. This manifest itself in terms of the decreased azimuthal flatness response of the system, figure 7, as

compared to that in figure 6. Another difference in this scheme is that it uses two different linear orthogonal polarisations for receiving and retransmission of the signal. This means the transmit/receive antenna must have capability to operate in two orthogonal modes for transmission of the signal and reception of the retransmitted signal from the retrodirective antenna array.

TEST AND MEASUREMENT

Each of the schemes described above were tested at 1GHz using a two element microstrip patch antenna array as the transmit/receive sensor, figure 5 shows the measurement set-up. Here a Transmit/Receive antenna makes an azimuthal cut from -90 to 90 degrees, a circulator is used to extract the received signal from the transmitted one. The small frequency offset between transmit and receive frequencies provides additional isolation for the architecture in figure 1 and for the arrangement in figure 2 additionally enhances isolation. Results shown in figure 6 and 7 present normalised comparative performance of a simple array and retrodirective array using scheme 1 and 2 respectively. As evident from these figures, for a simple in-phase passive array the peak occur at broadside (0°) irrespective of the position of the transmitting antenna, whereas in the case of the retrodirective arrays the maximum response peak occurs at different positions aligned with the transmitter position due to the return beam being redirected towards the transmitter. This results in the flatter overall antenna pattern compared to the pattern of the simple two element array, the 3dB beamwidth for the passive array is $\pm 30^\circ$. Whereas with the power divider retrodirective array of figure 1 $\pm 50^\circ$ of retrodirection can be achieved before the beam strength decreases by 3 dB. For the dual polarised patch retrodirective antenna array shown in figure 2, $\pm 45^\circ$ beam width can be achieved for the same condition.

CONCLUSION

Two new types of retrodirective antenna architectures using heterodyne phase technique were designed, tested and modelled at 1GHz. The results obtained for these prototypes shows that the schemes proposed here are capable of retrodirective beam formation. The architecture described here are compact, and suitable for monolithic integration. In addition, although not described here, suitable encoding can be easily added to the return path signal making the antenna types shown here suitable for vehicle tracking and other transponder type applications.

ACKNOWLEDGEMENT

This work has been carried out with the support of Commonwealth Scholarship Commission, Association of Commonwealth Universities, London and by the Engineering and Physical Science Research Council.

REFERENCES

1. Kraus, J. D., "Antennas", McGraw-Hill Book Company, 1950.
2. Van Atta L. C., "Electromagnetic reflector", U.S. patent No. 2,908,002, Oct. 6, 1959.
3. Sharp E. D. and Diab M. A., "Van Atta reflector array", *IRE trans. on Antenna and Propagation*, vol. AP-8, pp, 436-438.
4. Andre S. N. and Leonard D. J., "An active retrodirective array for satellite communications", *IEEE trans. on Antenna and Propagation*, Mar 1964, pp, 181-186.

5. Pon, C. Y., "Retrodirective array using the heterodyne technique", *IEEE trans. on Antenna and Propagation*", Mar 1964, pp, 176-180
6. Kother, D, Hopf, B., Sporkmann, T., Wolff, I., Koslowski, S., MMIC Circulators Covering the Frequency range from L W -Band, *1995 European Microwave Conference*, Bologna, pp 1186-1190

FIGURES

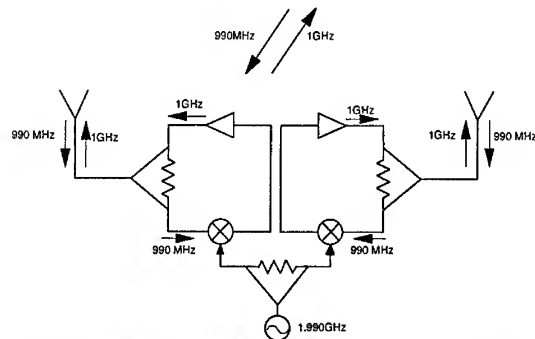


Figure 1- Retrodirective antenna using power divider.

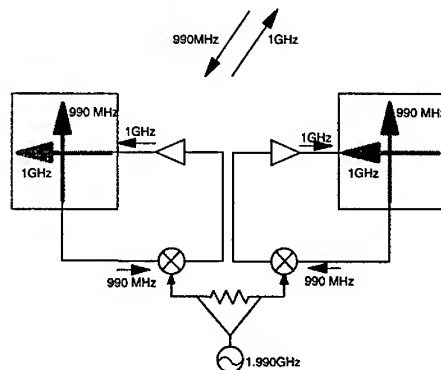


Figure 2 - Retrodirective antenna using Dual Polarised Patch antenna

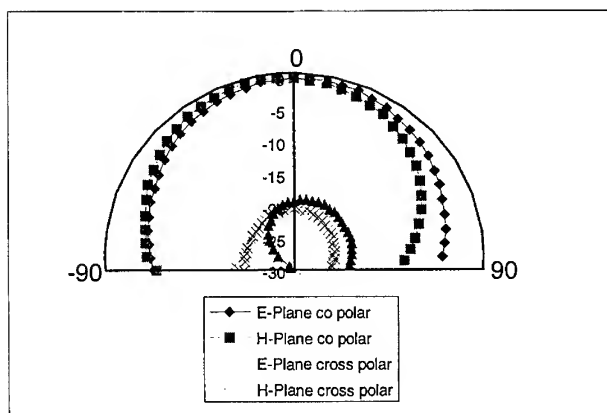


Figure 3 - E and H field radiation patterns of dual polarised patch antenna

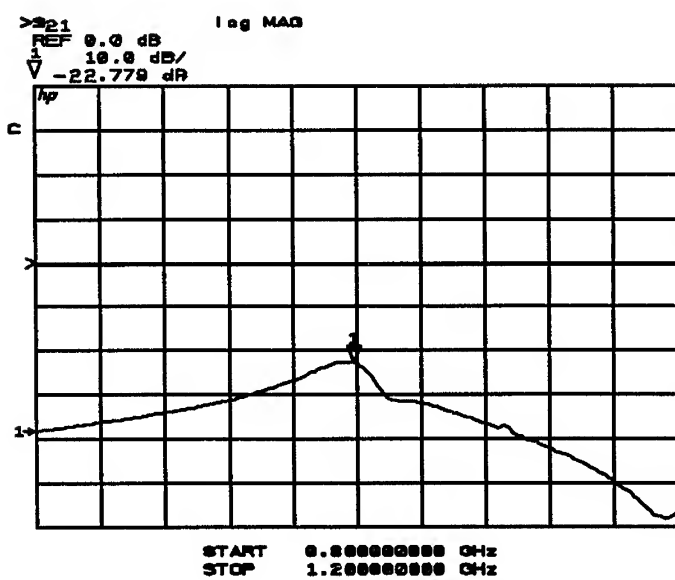


Figure 4 - Isolation measurement of dual polarised patch antenna

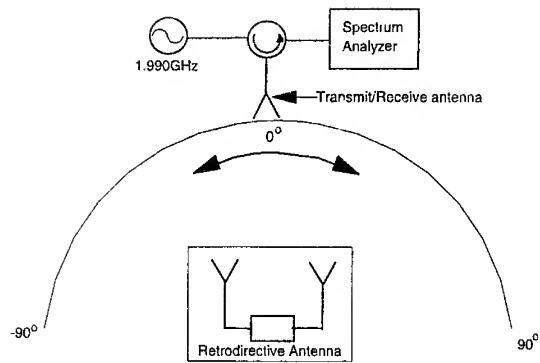


Figure 5 - Test Set-up

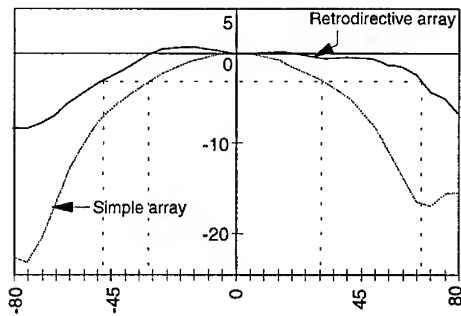


Figure 6 -Antenna pattern for Retrodirective antenna using Power Divider

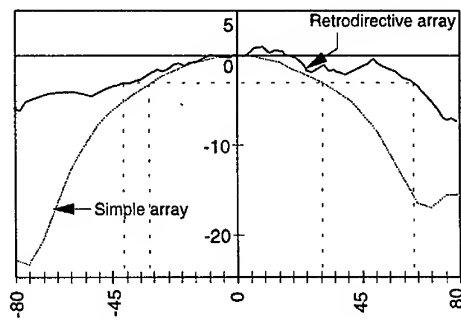


Figure 7- Antenna pattern for Retrodirective antenna using Dual Polarised Patch antenna

LUMPED COUPLED RING ANTENNA ARRAY

D.E.J. Humphrey, V.F. Fusco

High Frequency Electronics Laboratory
Department of Electrical and Electronic Engineering,
The Queen's University of Belfast, Ashby Buildings,
Stranmillis Road, Belfast, BT9 5AH, N.Ireland, United Kingdom.
Tel: +44 (0)1232 274087, Fax: +44 (0)1232 667023
e-mail: d.humphrey@ee.qub.ac.uk / v.fusco@ee.qub.ac.uk

ABSTRACT

Arrays of coupled active antenna oscillators are used for power-combining at microwave and millimetre-wave frequencies. The mutual coupling between array elements determines the operational mode of the array and hence its far-field radiation pattern. Separately it is known that enhanced oscillator modal stability can be achieved by coupling oscillators through lumped capacitive elements. In this paper lumped element and mutual element coupling are employed concurrently. The arrangement takes the form of a ring coupled oscillator used to excite a 2x2 array whose sources are coupled by capacitive elements and whose loads, the actual microstrip patch antenna elements, are mutually coupled. In this paper the effect of these couplings are evaluated using a time domain analysis. Experimental results for a 2x2 array are presented which validate the theoretical predictions made.

INTRODUCTION

The quest for high power, high efficiency solid state devices for mobile wireless communication basestation applications is ever increasing with the consequence that the output from many devices can be now spatially power combined using quasi-optical techniques [1]-[2]. Such a system can be configured from active antenna elements where the mutual coupling between elements induces mutual injection-locking [3]. In this paper a novel array arrangement is presented where coupling not only takes place in the air space above the patch antenna elements, but also the actual oscillator elements are coupled using lumped capacitive elements [4]. By this method two forms of coupling are simultaneously employed to help stabilise a locked entrained array frequency. A time domain simulation algorithm has been developed whereby a time delayed and attenuated coupled signal can be applied to the other capacitively coupled oscillators in the array i.e. representing free space mutual coupling. Thus the array can be simulated in the time domain. In addition, the reactively coupled oscillator dynamics are computed independently using an analytical formulation.

THEORETICAL CONSIDERATIONS

The non-linear circuits for the individual elements in a 4-element ring antenna array configuration can be shown to be modelled by the following equations [5] which have been adapted from the separated peak amplitude and phase components of a parallel resonant circuit

Van der Pol [6] equivalent model of the oscillator, where the non-linear device $G(v)$ is fitted from the simulated oscillator model according to the expression:-

$$i = -av + bv^3 \quad (1)$$

From Kirchoff's laws and after the approach used in [7] to decouple amplitude and phase dynamics has been applied, the individual peak amplitude and phase expressions for the arrangement in Figure 1 in the absence of the time delayed mutual coupling artefact become:-

$$\begin{aligned} \frac{dA_i}{dt} + \frac{\omega_i}{2Q_i} A_i [1 + R_{Li}(-a_i + b_i A_i^2)] = \\ \frac{1}{2C_i} \left[D_i \cos(\theta_i - \phi_i) - \sum_{k=1}^N A_k [G_{ik} \cos(\phi_k - \phi_i) - B_{ik} \sin(\phi_k - \phi_i)] \right] \end{aligned} \quad (2)$$

$$\begin{aligned} \frac{d\phi_i}{dt} + \omega_L - \omega_i = \\ \frac{1}{2A_i C_i} \left[D_i \sin(\theta_i - \phi_i) - \sum_{k=1}^N A_k [G_{ik} \sin(\phi_k - \phi_i) + B_{ik} \cos(\phi_k - \phi_i)] \right] \end{aligned} \quad (3)$$

where $D_i e^{j(\omega_i t + \theta_i)}$ represents the injection-locking element at radian frequency ω_L from an external source to the i th oscillator. A_i is the oscillator peak amplitude, ϕ_i the oscillator phase and the lumped element coupling admittance Y_{ik} , is equal to $G_{ik} + jB_{ik}$. The radian frequency ω_i is equal to $\frac{1}{\sqrt{L_i C_i}}$ of the equivalent oscillator model. The inclusion of the terms in D_i

enables a single oscillator (or several oscillators) to be injection-locked and this effect on the ring oscillator arrangement evaluated. It is noted that for the condition examined here the terms in D_i will all be zero. Equations (2) and (3) are also seen to be valid for non-identical oscillators in the array.

From equations (2) and (3), two numerical methods can be applied whereby the ring oscillator arrangement can be estimated. The first method is to numerically solve the differential equations (2) and (3) using Runge-Kutta methods [8]. This yields useful start up information. The second method can be used to determine only the steady-state array output behaviour of the system, since in this condition:-

$$\frac{dA_i}{dt} = 0 \quad (4)$$

and:-

$$\frac{d\phi_i}{dt} = 0 \quad (5)$$

Thus in the steady state case the entrained frequency ω_L , the individual peak amplitudes A_i and the relative phases (to the first oscillator) ϕ_i , can be calculated by least squares optimisation. Results obtained by direct integration of equations (2) and (3) and the steady state solution found after imposing equations (4) and (5) are seen to be self consistent with the full time domain circuit simulation results all of which predict identical start-up times and steady-state operation, Figure 2.

The time domain Van der Pol circuit model [6] has been further developed to include a Richards model [9] of a patch antenna designed to operate at the Van der Pol circuit resonant frequency. In addition the time delayed and attenuated coupling signal [10] is applied to each antenna across the ring array, Figure 1.

In order to confirm the theoretical predictions, four of the 1 GHz MIC oscillators in reference [4] were used to drive a 2x2 array of 0.5 wavelength spaced microstrip patch antennas constructed on $\epsilon_r = 4.55$, 1.5 mm thick substrate, with each antenna matched for 50 Ω operation. This frequency was selected for ease of experimental confirmation. The normalised E-Plane predicted and measured patterns are shown in Figure 3. The predicted pattern is obtained by measuring the individual power levels of each oscillator in the ring coupled arrangement separately, then as different oscillator pairs and finally with all four oscillators power combined. For each arrangement a vector diagram was constructed using the appropriate pairs of resultant power measurements. From these considerations the amplitudes and phase relationships between each oscillator in the coupled network can be derived, Table 1. These are compared to those predicted by the analytical solution described by equations (2) and (3) and to Van der Pol model time domain simulation results for a system modelling the experimental procedure. Oscillator 3 was detuned relative to the other oscillators so that a maximum phase error was introduced at frequency entrainment in order to establish a worst case entrained frequency result. The resulting experimentally derived amplitudes and phases are then used as unbalanced excitation signals in a conventional passive array factor calculation algorithm. Here the antenna pattern for an actual patch antenna was used to construct the array group pattern. The resultant pattern match illustrates that in-phase power combining is occurring and that apart from edge diffraction effects the maximum observed difference between the measured and theoretical radiation patterns is less than 2 dB. It was noted that without the presence of the capacitive ring coupling network structure the array presented here could not be stabilised for spatial power combining on the basis of mutual free space coupling alone.

The time domain simulation results for the non identical oscillators calibrated to the experimental arrangement used in the previous experiment are compared to a simulated array with identical oscillators in Figure 4. Here it is noted that the use of identical oscillators results in a perfect *in-phase* condition whereas the non-identical oscillators deviate from this condition. In addition the non-identical arrangement shows good correlation to that observed

experimentally, Table 1. When the distributed mutual coupling algorithms are removed from the Time Domain simulation, similar results occur. Thus it can be concluded that the free-space coupling has little effect on the overall operation of the lumped coupled array. From these results the presence of the lumped capacitive coupling elements appear to ensure that the active array always stays in an approximately *in-phase* power combining mode.

CONCLUSIONS

It is seen that array stability is introduced when individual oscillators are placed in a ring coupled network. With this condition a current is introduced across the lumped element impedances (8 pF capacitances in this case) causing an in-phase condition to be invoked. The time domain simulation and the analytical model presented here are seen to consistently predict *in-phase* array mode operation. Experiments carried out on a frequency scaled array at 1 GHz confirm the predictions even though the 4 coupled oscillators are non-identical and have maximum static phase error introduced at the frequency entrainment condition.

REFERENCES

- [1] J.D. Mink, "Quasi-optical power combining of solid-state millimetre-wave sources," Feb. 1986, *IEEE Trans. Microwave Theory Tech.*, vol. MTT-34, pp.273 - 279.
- [2] J.C. Wiltse, J.D. Mink, "Quasi-optical power combining of solid-state sources," Feb. 1992, *Microwave Journal*, pp.144 - 156.
- [3] D.E.J. Humphrey, V.F. Fusco, S. Drew, "Active Antenna Array Behaviour," Aug. 1995, *IEEE Trans. Microwave Theory Tech.*, vol. 43, no. 8 pp. 1819 - 1825.
- [4] D.E.J. Humphrey, V.F. Fusco, "Capacitively Coupled Oscillator Array Behaviour," April 1996, *IEEE Proc. Circuits, Devices and Systems*, vol. 143 no. 3 pp. 167 - 170.
- [5] K.D. Stephan, W.A. Morgan, "Analysis of Interinjection-Locked Oscillators for Integrated Phased Arrays," July 1987, *IEEE Trans. on Antennas and Propagation*, vol. AP-35, no. 7, pp. 771 - 781.
- [6] B. Van der Pol, "The Non-linear Theory of Electric Oscillations," Sept. 1934, *Proc. IRE*, vol. 22, pp. 1051 - 1085.
- [7] R.A. York, "Nonlinear Analysis of Phase Relationships in Quasi-Optical Oscillator Arrays," Oct. 1993, *IEEE Trans. Microwave Theory Tech.* vol. 41, No. 10, pp. 1799 - 1809.
- [8] R.L. Burden, J.D. Faires, "Numerical Analysis," 1989, *PWS-Kent Publishing Company*, Boston.
- [9] W.F. Richards, Y.T. Lo, D.D. Harrison, "An Improved Theory from Microstrip Antennas and Applications," Jan 1981, *IEEE Trans. Antennas and Prop.*, vol. AP-29, no. 1, pp.38 - 46.
- [10] R.A. York, R.C. Compton, "Measurement and Modelling of Radiative Coupling in Oscillator Arrays," March 1993, *IEEE Trans. Microwave Theory Tech.*, vol. 41, no. 3 pp.438 - 444.

	Oscillator 1	Oscillator 2	Oscillator 3	Oscillator 4
<i>Measured</i>	7.71 dBm, 0 deg	7.57 dBm, 8.1 deg	7.91 dBm, 52.4 deg	9.2 dBm, 9 deg
<i>Time Domain</i>	7.71 dBm, 0 deg	7.58 dBm, -2 deg	7.91 dBm, 53 deg	9.22 dBm, 0 deg
<i>Analytical</i>	8.81 dBm, 0 deg	9.15 dBm, 5 deg	8.98 dBm, 62 deg	10.449 dBm, -3 deg
<i>a</i>	21.8962	21.8962	19.3624	20.9657
<i>b</i>	49.4249	50.7411	41.9262	34.8669

Table 1

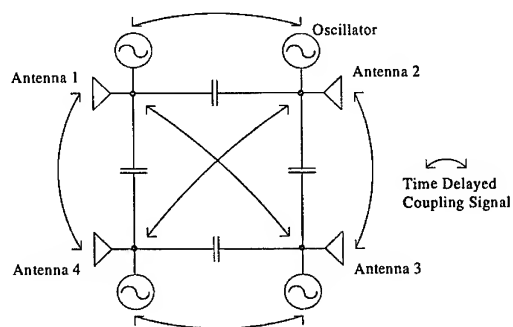


Figure 1:- Ring Coupled System

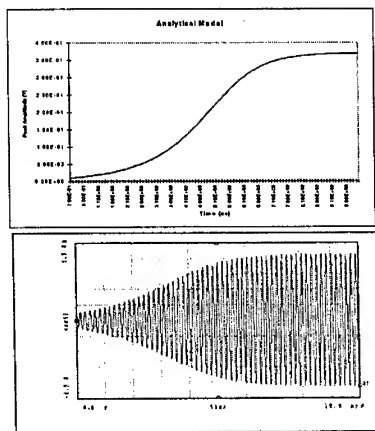


Figure 2:- Ring Coupled Oscillator Model Start-Up

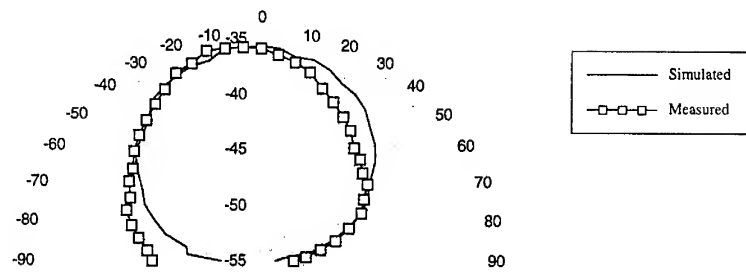


Figure 3:- E-Plane Far-Field Prediction and Measurement

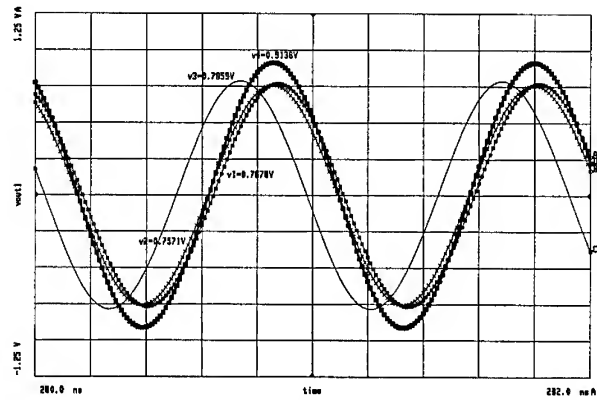


Figure 4a:- Non-Identical Oscillators: Time Domain Simulation

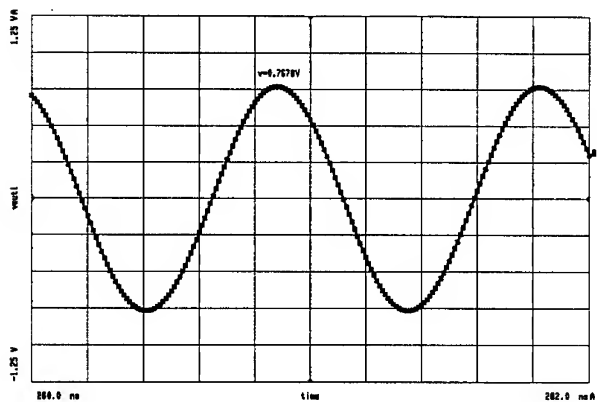


Figure 4b:- Identical Oscillators: Time Domain Simulation

NONLINEAR MODELING INCLUDING THE SELF HEATING EFFECT AND LOAD-PULL MEASUREMENTS OF GaInP/GaAs POWER HBTs

M. Akpinar, R. Follmann, T. Sporkmann and I. Wolff
 Institut für Mobil- und Satellitenfunktechnik
 Carl-Friedrich-Gauß-Straße 2, D-47475 Kamp-Lintfort, Germany
 Tel: +49-2842-981-200, Fax: +49-2842-981-299

Abstract

A practical method to model HBTs including the self-heating effect has been developed and implemented in the utilized software package LIBRA as a simple test bench. This method is based on a practical thermal feedback circuit, which is combined with the standard BJT Gummel-Poon model to account for the self-heating effect. The Self-Heating Effect has a remarkable influence on the large signal behaviour of the device especially at high power conditions. This fact has been demonstrated with power and load-pull measurements and verified with the developed model. Excellent agreement between the modeled and the measured power performance has been achieved.

Summary

Thermal effects in GaAs HBTs, like self-heating and thermal runaway play a significant role in the prediction of the device's large signal behaviour, because of the low conductivity of GaAs and high power density of HBT. The existing bipolar transistor models do not take into account these thermal effects. Several approaches to include the self-heating effect in the large signal model have been reported in the past. Many of these methods are based on the modification or extension of the standard Gummel-Poon model to account for several effects, which are common in HBTs [2], [3], [4].

The modifications in LIBRA's built-in bipolar transistor model, which is based on the Gummel-Poon model, require some modifications in the extensive source code, which can be done only by senior LIBRA users.

From the practical point of view, there is a demand to develop a LIBRA test bench, which can easily be

implemented by each LIBRA user to model HBTs including Self-Heating Effect by using the existing built-in Gummel-Poon model.

A practical test bench to do this has been developed and implemented in LIBRA as shown in Fig.1. It consists of the standard BJT Gummel-Poon model and a feedback circuitry to realize the coupling between the thermal and electrical circuit.

First, the standard Gummel-Poon model is used to model the idealized DC- and microwave performance of the device. The idealized IV-curves with zero slope (base width modulation is ignored) can be modeled by making the Forward Early Voltage (model parameter V_a) very large [5].

The device's total dissipated power P_{DC} will be calculated by multiplying the external supply voltages V_{CS} and V_{BS} with the bias currents I_C and I_B as can be seen in Fig. 1:

$$P_{DC} = I_C V_{CS} + I_B V_{BS}$$

P_{DC} is then converted to a thermal current I_p , which represents the power flow in the thermal circuit and which is supplied to the known thermal resistance R_{TH} . The voltage across R_{TH} gives the temperature rise ΔT in the device. The temperature rise ΔT (thermal voltage) will be multiplied with a weighting factor w , which is dependent on the base current I_B and the collector-emitter voltage V_{CE} and transformed to an electrical current source I_F through a transformation factor δ :

$$I_F = \delta w \Delta T$$

The direction of the feedback current I_F is opposite to the direction of the base bias current I_B , reducing the total base current flow in the transistor. The reduced base current with increased temperature causes a reduction in the collector current, thereby giving rise to a negative slope of the device's I_C - V_{CE} characteristics.

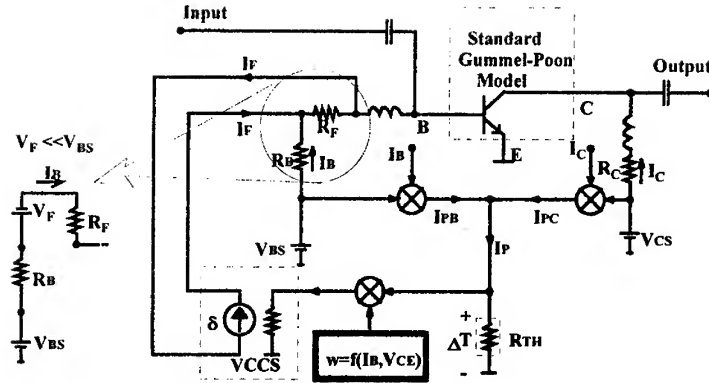


Fig. 1 : Modeling the HBT Self-Heating

If V_F is the thevenin equivalent voltage corresponding to the feedback current I_F , so that

$$V_F = \delta w \Delta T R_F,$$

the total base current flowing into the transistor and the collector current are given as:

$$I_B = \frac{V_{BS} - V_F}{R_B},$$

$$I_C = B_F I_B.$$

It is assumed that

$$R_F \ll R_B$$

where, B_F is the model parameter, which represents the forward current gain of the device.

The multiplication factor w can be separated into two parts: the base current dependent part (base current correction), and the collector voltage dependent part (collector voltage correction).

The HBT's I_C - V_{CE} characteristics exhibit a higher negative slope as the base current becomes higher, which is a phenomenon caused by the Self-Heating effect and which is commonly observed in DC-measurements. We have found that the dependency of the slope of the I_C - V_{CE} characteristics on the base current can be empirically approximated as

$$-\Delta I_C \sim w_1 I_B^2,$$

where $-\Delta I_C$ is the negative slope of I-V curves and w_1 is a fitting parameter.

Furthermore the HBT's I_C - V_{CE} characteristics exhibit a negative slope only in the saturation

region ($V_{CE} > V_K$), where V_K is the knee voltage of the I_C - V_{CE} characteristics.

This fact can be modeled by a piecewise-linear diode element, which is supplied by the collector-emitter voltage and whose built-in potential V_0 is equal to the knee voltage V_K of the measured DC-characteristics. The collector voltage correction factor w_2 can be defined as the current, which flows through this diode:

$$w_2 = 0, \quad \text{if } V_{CE} \leq V_0,$$

$$w_2 = I_{diode} = f(V_{CE}), \quad \text{if } V_{CE} > V_0.$$

For the case $V_{CE} < V_0$, it will be assumed that no self heating occurs and therefore $I_F=0$. For $V_{CE} > V_K$, the w_2 is equal to the diode current, which is a linear function of the collector-emitter voltage.

The above temperature dependent HBT model is verified by comparison with measured I-V curves of an GaInP/GaAs HBT, with an emitter area of $2 \times 60 \mu\text{m}^2$ processed with the UMS HBT process.

This device is modelled initially with the standard Gummel-Poon Model ignoring the Self-Heating Effect (with the parameter V_A very large). The model is then replaced into the test bench shown in fig. 1 to fit the negative slopes of the measured I-V curves.

Fig. 2 shows the measured and simulated I_C - V_{CE} characteristics of the device. An excellent agreement between the measured and simulated results is achieved.

The measured and the simulated S-Parameters of the device at a bias point of $V_{CE}=3\text{V}$ and $I_C=55\text{mA}$ are shown in Fig. 3. The model exhibits also a good agreement with the measured microwave performance up to 20 GHz. The maximum discrepancy between the measured and the simulated gain S_{21} is less than 1dB.

Fig. 4 shows the measured and simulated fundamental power and power gain at 1.8 GHz. Good agreement between the measured and simulated power performance is achieved. In order to show the influence of the self-heating effect at high power conditions, another HBT device with an emitter area of $12 \times 40 \mu\text{m}^2$ also processed by UMS was measured and modeled.

In Table 1, the values of the extracted Gummel-Poon model parameters and the additional fitting parameters 'DELTA', 'RF' and 'W1' are listed. An excellent agreement between measured and modeled I_C - V_{CE} characteristics has also been achieved for this device as can be seen in fig. 5.

A series of load pull measurements at various bias points and at 1.8 GHz have been done on this device by means of the load-pull measurement stand at IMST. The developed model including the self-heating effect is verified at high power levels by comparing the results of load pull simulation and the load pull measurement at 1.8 GHz.

In Fig. 6, the measured and modeled constant output power contours at 1.8 GHz and an available input power of 6 dBm are compared at a bias point of $U_{CE}=3\text{V}$, $I_C=185\text{mA}$.

The measured maximum delivered output power to the load is 21.7 dBm at an output reflection factor of $\Gamma=0.64/175^\circ$. The simulated maximum output power by using the model including the self-heating effect is 21.68 dBm at an output reflection coefficient of $\Gamma=0.61/164^\circ$. The simulated maximum output power by using the model ignoring the self heating effect is 22.54 dBm at an output reflection coefficient of $\Gamma=0.62/163^\circ$. The developed model including the self-heating effect is able to predict the maximum output power and the optimal output reflection coefficient with great accuracy. The discrepancy between the measured and estimated maximum output power is only 0.02 dB. The model ignoring the self-heating effect estimates the maximum output power 0.84 dB higher than the measured value. This discrepancy is not very big but remarkable. At higher collector currents the Self-Heating Effect will be greater and its influence on the power performance of the device also greater.

Conclusion

A thermal feedback circuitry, which is combined with the standard Gummel-Poon model is used to model the HBT Self-Heating Effect. This method is implemented as a LIBRA test bench, without any attempt to change the extensive source code.

Good agreement between measurements and simulations are demonstrated for the DC, microwave and power characteristics.

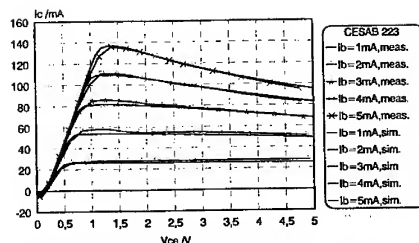


Fig.2 : Measured and simulated I-V Characteristics (2 Finger HBT)

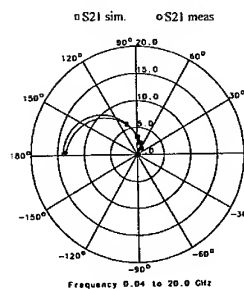
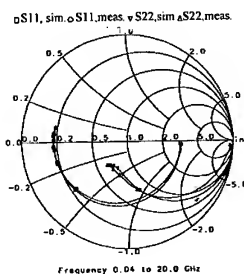


Fig.3 : Measured and Simulated S-Parameters (2 Finger HBT)

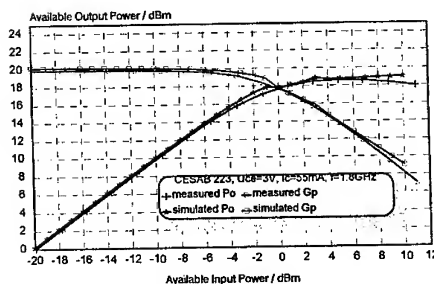


Fig. 4 : Measured and Simulated Power Performance (2 Finger HBT)

PAR.	VALUE	PAR.	VALUE
IS	1.91e-23 A	ITF	1.82e-2 A
ISE	2.61e-14 A	XTF	0.21
ISC	2.57e-13 A	VTF	0.31 V
BF	27.37	FCC	0.58
BR	0.8	VJE	0.72 V
NF	1.34	MJE	0.4
NE	2.78	VJC	0.87
NR	1.27	MJC	0.32
NC	3.14	CJC	4.61e-13 F
VA	100000 V	CJE	1.96e-15 F
VB	1000 V	XCJC	6.43e-2
IKF	0.85 A	RC	0.44
IKR	7.03e-4 A	RE	0.88
RBM	0.8 Ohm	DELTA	10
RB	3.19 Ohm	RTH	150 K/W
IRB	6.45e-5 A	RBEX	10000 Ohm
TF	3.15e-12 S	RF	1e-3 Ohm
TR	1.45e-09 S	WI	0.25

Tab. 1 : Values of the Model Parameters
(12 Finger HBT)

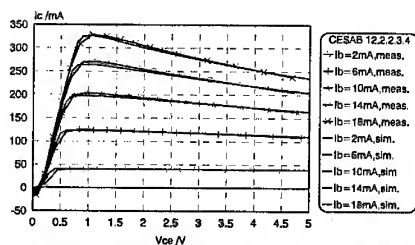


Fig. 5 : Measured and Simulated I-V Characteristics
(12 Finger HBT)

The developed model is also verified at high power and low output impedance conditions by comparison with the in house load-pull measurements. At high power conditions the self-heating effect has a remarkable influence on the power performance of HBTs and hence must be taken into account.

References

- [1] : P.C. Grossman, J. Choma Jr., "Large Signal Modeling of HBTs Including Self-Heating and Transit Time Effects", *IEEE Trans. on Microwave Theory and Tech.*, pp. 449-464 March 1992.
- [2] : F.S. Correria and S. Tadayan, "A modified Gummel-Poon model applied to HBTs", in: *Proc. European Microwave Conf.*, pp. 96-98, 1993.
- [3] : A. Samelis, D. Pavlidis, "A Heterojunction Bipolar Transistor Large signal Model for High Power Applications", *IEEE MIT-S Digest*, pp. 1231-1234, 1995.
- [4] : A. Samelis, D. Pavlidis, "Modeling HBT Self-Heating", *Applied Microwave & Wireless*, pp. 108-112, 1996.
- [5] : P. Antognetti, G. Massobrio, *Semiconductor Device Modeling with SPICE*, New York, London, Hamburg, McGraw Hill 1987.

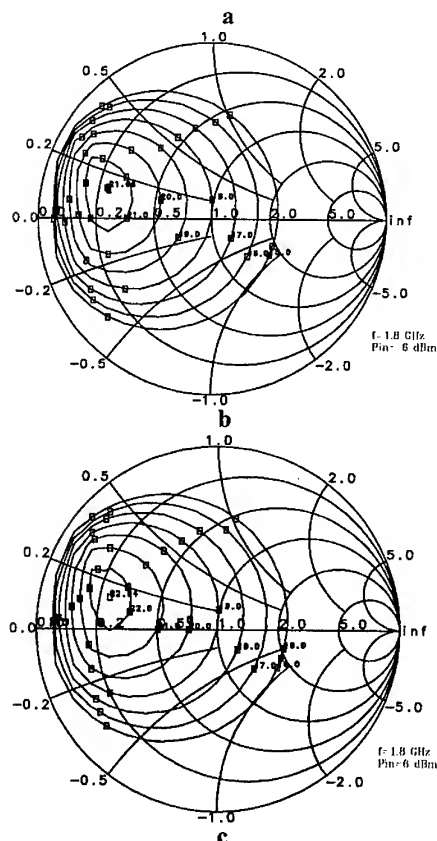
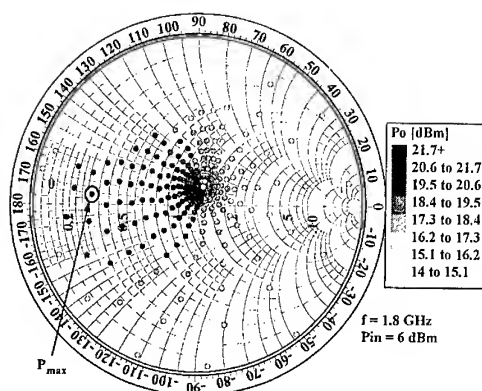


Fig. 6 : Measured and Simulated Constant Output Power Contours of the 12 Finger HBT
a) measured; b) simulated including Self-Heating; c) simulated ignoring Self-Heating.

A Novel Extraction Method for Temperature Dependent Large Signal Equivalent Circuit Model of HBT

Young-Suk Suh, Tai Moon Roh*,
Youngsik Kim*, Jinho Shin*, and
Bumman Kim*

Affiliation:

Dept. of Electronics Eng., Yeungnam University,

* Dept. off E.E, POSTECH,

Address:

Dept. Of Electronics Eng.,

Yeungnam University,

Kyong-San, Kyong-Buk, 712-749,

South Korea.

Abstract

A new equivalent circuit parameter extraction method for HBT is proposed. An accurate analytical expression for thermal capacitance (C_{th}) is derived. This equation shows the previous expression for C_{th} is deprived. This equation shows the previous expression for C_{th} is erroneous. And a direct extraction scheme for the current source model parameter, without any trimming process, is proposed. This scheme uses the Gummel-plot in which the thermal effect and voltage drop in parasitic resistance are removed.

Introduction

An accurate HBT large signal model is very important for the design of nonlinear circuits such as microwave power amplifiers. Hetrojunction bipolar transistors have very sensitive characteristics to the junction temperature, and many models and parameter extraction procedures, considering the thermal effects, have been developed. We propose a new extraction method for thermal capacitance and current source model parameters which is more accurate, reliable, and consistent to the measured DC, S-parameter, and thermal data.

Model description

The extended Ebers-Moll model for HBT, shown in fig.1, is widely used, and the corresponding current models are represented in the fig.1. The most important temperature dependent static electrical characteristics of an HBT are the base (I_{b2}) and collector current (I_{cc}). These characteristics are modeled by the three temperature dependent parameters $V_{bex}(T_j)$, $V_{bcx}(T_j)$ and $I_{sen}(T_j)$ as shown in the fig. 1. The junction voltage drop by the temperature is considered through the parameter $\alpha_{be} = dV_{be}/dT_j$ and $\alpha_{bc} = dV_{bc}/dT_j$. We introduce a model parameter extraction method step by step.

Thermal Parameters

The thermal resistance (R_{th}) and the junction voltage degradation rate to temperature (α_{be} and α_{bc}) are extracted by the previously reported methods [1]. The thermal time constant is an important parameter for the inter-modulation analysis of HBT and can influence the IM_3 value strongly[2]. The constant base current pulse method under the constant collector DC bias voltage is widely used for the thermal capacitance parameter (C_{th}) extraction [1]. We have measured a typical shape of collector current as shown in fig. 2 for 2x10 um-AlGaAs/GaAs HBT. The collector current decays exponentially from the state I_{ci} to I_{cf} . The time constant of collector current can be measured, and the previous method adopts this time constant as a thermal time constant. However, collector current time constant is not thermal time constant, as a thermal time constant. However, collector current time constant is not thermal time constant, because the internal power dissipation is not constant and varies with the collector current levels. We analyzed this switching problem and derived a new expression for thermal capacitance and thermal time constant. The thermal-electrical differential is

$$\begin{aligned} T_j(t) &= T_{am} + R_{th}P(t) - R_{th}C_{th} \frac{d(T_j(t) - T_{am})}{dt} \\ P(t) &\approx I_c(t)V_{ce} \end{aligned} \quad (1)$$

The collector current decreases with junction (T_j) temperature increment ($\Delta T = T_j(t) - T_{am}$) from the ambient temperature (T_{am}) under the constant base current (I_{bo}). Using the first order approximation of current gain degradation, $\beta(T_j) = \beta_o - \beta_1 \Delta T$, the time evolution of collector current in this switching problem is

$$I_c(t) = I_{bo}u(t)(\beta_o - \beta_1(T_j - T_{am})) \quad (2)$$

where $u(t)$ is unit step function. The solution of equation (1) and (2) is

$$T_j(t) = T_{am} + T_s(1 - e^{-t/\tau}) \quad (3)$$

$$\tau = \frac{R_{th}C_{th}}{1 + R_{th}\beta_1V_{ce}I_{bo}}, \quad T_s = \beta_oV_{ce}I_{bo}\tau / C_{th}$$

where T_s is steady state junction temperature increment and τ is collector current time constant. Thermal capacitance is

$$C_{th} = \frac{\tau}{R_{th}}(1 + R_{th}\beta_1V_{ce}I_{bo}) \quad (4)$$

If we neglect the second term of Eq. (4), the widely used simple form $\tau = R_{th}C_{th}$ is obtained. However, in many cases the second term of eq. (4) can not be negligible. A simple calculation of β_1 shows these characteristics very well.

$$\beta_1 = -\frac{\Delta\beta}{\Delta T} = \frac{(I_{ci} - I_{cf})/I_{bo}}{T_j - T_{am}} = \frac{(I_{ci} - I_{cf})/I_{bo}}{R_{th}V_{ce}I_{cf}} \quad (5)$$

Where I_{ci} is initial collector current before self heating under unit step base current and I_{cf} is steady state (final collector current as shown in fig.2. Putting Eq. (5) into Eq. (4), C_{th} and τ_{th} become

$$C_{th} = \frac{\tau}{R_{th}} \left(1 + \frac{I_{ci} - I_{cf}}{I_{cf}}\right) \quad (6)$$

$$\tau_{th} \equiv R_{th}C_{th} = \tau \left(1 + \frac{I_{ci} - I_{cf}}{I_{cf}}\right) \quad (7)$$

where τ_{th} thermal time constant. The second terms of Eq. (6) and (7) are the current degradation ratio due to the thermal effect under the constant base pulse. If the degradation ratio is 0.3, the simple calculation ($C_{th}=\tau/R_{th}$) underestimates the real thermal capacitance with 30% error.

Parasitic Resistance, Inductance and Pad Capacity

Emitter, Base, and collector resistance are extracted from the measured S-Parameters using the analytical expression for the low frequency simple equivalent circuit of HBT [3,4]. The parasitic inductances and pad capacitances can be extracted using the cold S-parameter measurements [4,5].

Voltage Controlled Sources

Current source parameters (I_{sen} , n_{cn} , I_{seo} , XA , n_{en} , I_{scl} , n_{cl} , I_{sel} , n_{el} , I_{sf} , n_f , I_{sr} , n_r) can be extracted from the measured Gummel-Plot. Two major existing methods are direct extraction using the slop and magnitude of currents in the ideal exponential region (region II in fig. 3) of Gummel-Plot, and optimization or numerical fitting process up to the high current region (region III in fig. 3). However, the direct extraction method can generate small errors of the extracted values due to the finite thermal resistance and electrical resistance which cause the non-ideal exponential current curve. The optimization methods can also generate various values of errors depending on the different fitting processes, optimization regions, or optimization goals. A small error of extracted n_f and I_{sf} by these methods is not shown in the semi-log scaled Gummel plot. However, in the linear scaled plot, the modeled I_c 's based on the similar I_f 's or n 's shows quite different values, especially in high current region. The sensitivities of the modeled I_c to n_f and I_{sf} are very high. These errors make a bad prediction of base-emitter voltage (under the constant base current mode) and the terminal current (under the constant base-emitter voltage mode). The best current model parameters are the parameters which are extracted from the measured data in the actual and high current levels of HBTs operating as amplifiers. The voltage and current relationship in forward bias Gummel-Plot is

$$\begin{aligned} \frac{\eta_f k T_{am}}{q} \ln(I_c) &= V_{bet} - \left((R_e + \frac{R_b}{1+\beta}) + \alpha_{be} R_T V_{ce} \right) I_e \\ &+ \frac{\eta_f k T_{am}}{q} \ln(I_{sf}) \\ &= V_{bet} - (R_{bet} + R_{eq}) I_e + \frac{\eta_f k T_{am}}{q} \ln(I_{sf}) \\ &= V_{be} + \frac{\eta_f k T_{am}}{q} \ln(I_{sf}) \end{aligned} \quad (8)$$

where V_{bet} is applied base-emitter external voltage, R_{bet} is resistance between base and emitter, looking into the emitter port, and R_{eq} is effective negative electrical resistance due to the thermal effect. Using Eq. (8) de-embedding the electrical resistance and thermal resistance effect in Gummel-plot, an ideal exponential curve up to the high current level can be plotted. Figure 4-a shows the measured data (collector current vs. Base-emitter terminal voltage) from the region II and III of fig. 3. Figure 4-b shows the measured collector current vs. $V_{bet} - R_{bet} \times I_e$. In the figure, the thermal effect by the non-zero thermal resistance is removed. The collector current fly-forward is due to the electrical resistance effect only. Finally, a Gummel plot, removing the electrical

resistance and thermal resistance effects, is shown in the fig. 4-d. This figure shows ideal exponential behaviors (a straight line) up to the high and actual current level. The parameter I_{sf} and n_f can be directly extracted from the fig. 4-d. The best parameters n_f and I_{sf} , which can predict the measured I-V curve range from 1mA to resistance and thermal resistance effects, is shown in the fig. 4-d. This figure shows ideal exponential behaviors (a straight line) up to the high and actual current level. The parameter I_{sf} and n_f can be directly extracted from the fig. 4-d. The best parameters n_f and I_{sf} , which can predict the measured I-V curve range from 1mA to 10mA of collector current as shown in fig. 4-d, are the parameters, extracted from the straight line, connecting the two points of collector current (1mA and 10mA) in the Gummel-plot fig. 4-d. From the higher point (I_{cA} , V_{beA}) and the lower point (I_{cB} , V_{beB}) in fig. 4-d, n_f and I_{sf} can be directly extracted.

$$n_f = \frac{q}{kT_{am}} \frac{\ln(I_{cA}) - \ln(I_{cB})}{V_{beA} - V_{beB}},$$

$$I_{sf} = \exp \left[\ln(I_{cA}) - \frac{q}{n_f k T_{am}} V_{beA} \right] \quad (9)$$

The other current parameters can be extracted by similar procedures from the measured reverse and forward Gummel plot. Next, we introduce a method for the extraction of parameter XA. At one ambient temperature ($T_{am,1}$), from the base current of fig. 4-d (this figure implies Gummel-plot under $T_{j,1}=T_{am,1}$), I_{sen} is calculated ($I_{sen,1}$). The calculated $I_{sen,1}$ implies I_{seo} i.e. $I_{sen,1}=I_{seo,1}$. At different ambient temperature ($T_{am,2}$), the value of $I_{sen,2}$ should be predicted with the parameter XA and $I_{seo,1}$.

$$I_{sen,2} = I_{seo,1} \left(\frac{T_{am,2}}{T_{am,1}} \right)^{XA} \exp \left[\frac{q\Delta E}{k} \left(\frac{1}{T_{am,1}} - \frac{1}{T_{am,2}} \right) \right] \quad (10)$$

The parameter XA is calculated from Eq. (10), where ΔE is a constant representing the band gap difference between emitter and base layer. The modeled currents predict the measured data exactly as shown in fig. 5 in the linear scale and predict well the measured constant current mode DC-IV data in fig. 6.

Internal Capacitance

After de-embedding the parasitic inductances, pad capacitances, emitter, and collector resistances we make a small signal equivalent circuit with transconductance g_m from (I_{co}) and junction dynamic resistance r_x (from I_{D2}). Using this small signal model and the net S-parameters without parasitic components (de-embedded from the measured S-parameters), the unknown parameter C_{bcx} , C_{bc} and C_{bc} can be extracted at all measured bias points using some optimization. The full model constructed by our method predicts the measured AC and DC data very well. This model was applied to the 1-stage power amplifier at 1.8GHz. The simulation result predict well the measured output harmonics.

Conclusion

We proposed the temperature dependent nonlinear current source model of HBT, which has the three temperature dependent parameters, and a novel extraction method. The main distinctive features of our work are ; (1) an accurate first order analytical thermal capacitance equation and a thermal time constant equation are derived. (2) A systematic procedure for the current source model parameters (I_s 's and n 's) is proposed. The parameters can be extracted from the measured data without any optimization or trimming processes.

Reference

- [1] D.S. Whitefield et al., "Temperature-Dependent Large signal Model of Heterojunction bipolar Transistors", 1992 GaAs IC Symposium, pp.221-224
- [2] Ke. Lu et al., "Low-Frequency dispersion and it's influence on the The Intermodulation Performance of AlGaAs/GaAs HBTs", 1996 IEEE MTT-s Digest, pp. 1373-1376.
- [3] D. Wu, et al., "A Novel Extraction Method for Accurate Determination of HBT Large-Signal Model Parameters", 1995 IEEE MTT-s Digest, pp. 1235-1238.
- [4] S.A. Mass et al., "Parameter-Extraction Method for Hetrojunction Bipolar Transistors", IEEE Microwave and guided Wave Lett., 1992, vol. 2, No. 12, pp. 502-504.
- [5] P. Baureis et al., "Parameter Extraction for HBT's Temperature Dependent Large signal Equivalent Circuit Model", 1993 GaAs IC symposium, pp. 263-266.

Figure Caption

Figure 1. Large signal Model of HBT

Figure 2. Time evolution of collector current pulse ($I_{bo}=350\mu A$, $V_{cc}=6V$)

Figure 3. The measured Gummel-Plot of $2 \times 10 \mu m$ AlGaAs/GaAs HBT

Figure 4. The measured collector current is plotted in four independent axis (a) measured terminal voltage V_{be1} , (b) $V_{be1} = V_{be1} - R_{be1} + I_e$, (c) $V_{be2} = V_{be1} - R_{eq1} I_e$ and (d) net junction voltage $V_{bej} = V_{be1} - R_{eq1} I_e$

Figure 5. The measured (point and modeled (line base and collector currents in linear scale.

Figure 6. Measured (point and modeled (line collector current (I_{ce}), $I_b=50\mu A \sim 350\mu A$ with $50\mu A$ step.

Figure 7. Measured (point and modeled (line) S-parameter from 0.5~18 GHz at $V_{ce}=5V$, $I_b=250\mu A$.

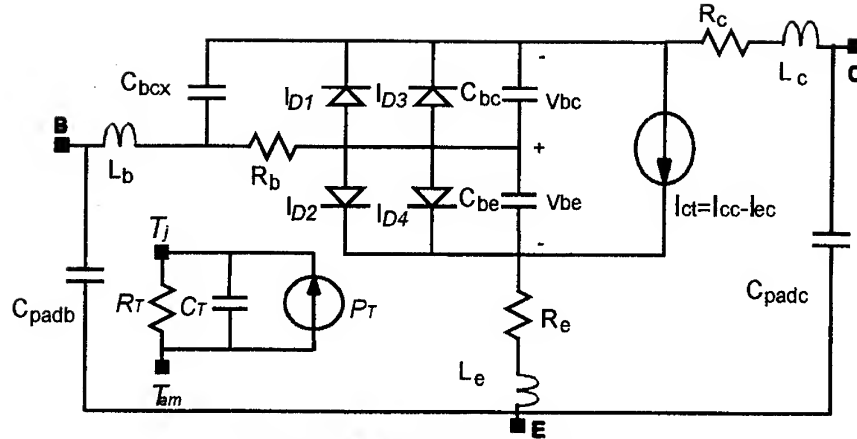


Fig. 1 Large signal Model of HBT

<Nonlinear Current Source Model>

$$I_{D1} = I_{scn} \left[\exp \left(\frac{qV_{bcx}}{n_{cn}kT_{am}} \right) - 1 \right], I_{D2} = I_{sen} \left[\exp \left(\frac{qV_{bcx}}{n_{en}kT_{am}} \right) - 1 \right], I_{D3} = I_{scl} \left[\exp \left(\frac{qV_{bcx}}{n_{cl}kT_{am}} \right) - 1 \right]$$

$$I_{D4} = I_{sel} \left[\exp \left(\frac{qV_{bcx}}{n_{el}kT_{am}} \right) - 1 \right], I_{cc} = I_{sf} \left[\exp \left(\frac{qV_{bcx}}{n_{f}kT_{am}} \right) \right], I_{ec} = I_{sr} \left[\exp \left(\frac{qV_{bcx}}{n_{r}kT_{am}} \right) \right]$$

<Temperature Dependent Parameters> **<Thermal Equivalent Circuit Model>**

$$V_{bcx} = V_{be} - \alpha_{be}(T_j - T_{am}), V_{bcx} = V_{bc} - \alpha_{bc}(T_j - T_{am})$$

$$I_{sen} = I_{seo} \left(\frac{T_j}{T_{am}} \right)^{XA} \exp \left[\frac{q\Delta E}{k} \left(\frac{1}{T_{am}} - \frac{1}{T_j} \right) \right]$$

$$P_T = V_{ce}I_c + V_{be}I_b$$

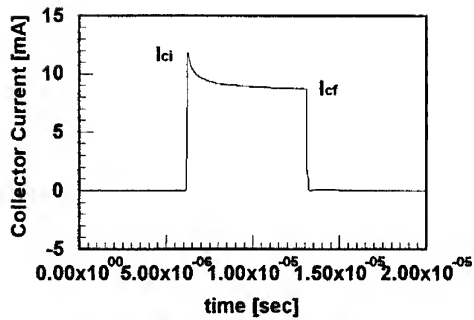


Fig. 2 Time evolution of collector current pulse ($I_{bo}=350\mu A$, $V_{ce}=6V$)

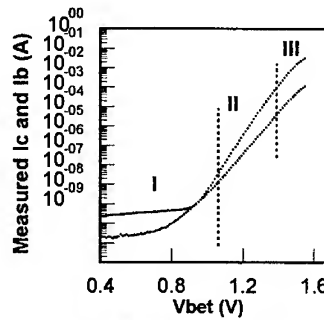


Fig. 3 The measured Gummel-Plot of $2 \times 10 \mu m$ AlGaAs/GaAs HBT

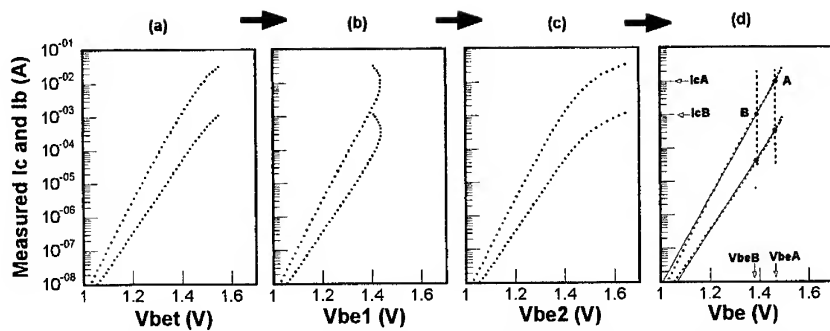


Fig. 4 The measured collector current is plotted in four different independent axis (a) measured terminal voltage V_{bet} , (b) $V_{be1}=V_{bet}-R_{bet} I_e$, (c) $V_{be2}=V_{bet}-R_{eqt} I_e$, and (d) net junction voltage $V_{bej}=V_{bet}-(R_{bet}-R_{eqt}) I_e$

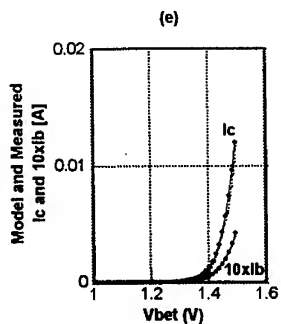


Fig. 5 The measured (point) and modeled (line) base and collector currents in linear scale

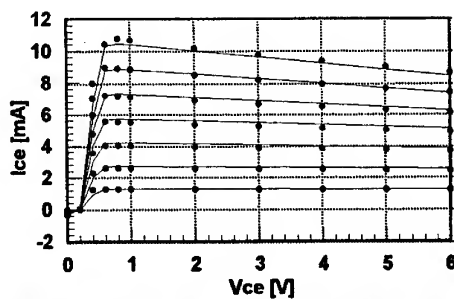


Fig. 6 Measured (Point) and Modeled (Line) Collector Current (I_c), $I_b=50\mu A \sim 350\mu A$ with 50 μA Step

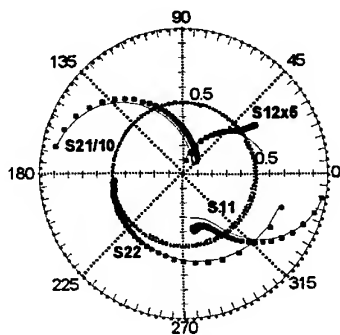


Fig. 7 Measured (point) and Modeled (line) S-Parameter from 0.5~18 GHz at $V_{ce}=5V$, $I_b=250 \mu A$

Thermal Coupling in Multi-finger Heterojunction Bipolar Devices

Martin Schüßler*, Viktor Krozer⁺, Jesús Grajal de la Fuente**, Hans L. Hartnagel*

* TH Darmstadt, Institut für Hochfrequenztechnik,
Merckstr. 25, D-64283 Darmstadt, Germany, email: hfmwe008@hrzpub.th-darmstadt.de

⁺ TU Chemnitz-Zwickau, Lehrstuhl für Hochfrequenztechnik,
Reichenhainerstr. 70, D-09126 Chemnitz, Germany, email: vkrozer@infotech.tu-chemnitz.de

** Univ. Polit. Madrid, ETSIT, Ciudad Universitaria,
28040 Madrid, Spain. email: grajal@gmr.sse.upm.es

July 9, 1997

Abstract

The thermal characteristics of power HBT devices are considered. The analysis includes emitter finger coupling and limitation in power operation due to selfheating. An essential part of the generated heat is dissipated through the top device layers and metal contacts. A strongly uneven temperature distribution in the emitter finger of multi-finger devices is the result of not sufficient temperature drain through the emitter air-bridge. Sufficient thermal dissipation can be additionally obtained by temperature drain through the base and collector metallised areas on top of the device. An optimum distance between individual emitter fingers exists for maximum thermal coupling. This yields better thermal homogeneity.

Introduction

Heterojunction Bipolar Transistors (HBT) are considered to be especially useful for microwave power amplification, because of their high theoretical power density operation and high microwave gain, which yield a high power-added efficiency in power amplifiers. However, this advantage can not be fully utilised because of the heat generation of HBT devices, which considerably degrades the high power performance of the devices and circuits [1, 2, 3, 4, 5, 6]. A particularly severe problem is the inhomogeneous temperature distribution ultimately leading to current breakdown observed in HBT power devices. The inhomogeneous temperature distribution originates from self heating in the device, which can be studied with appropriate device models.

Previously a DC and AC physical analytical HBT model has been developed [4, 7, 8], which has been successfully implemented into the commercial simu-

lation environment LIBRA. The model includes temperature effects such as thermal coupling between different emitter fingers and selfheating and temperature dependent material parameters for GaAs, AlGaAs, and InGaP. Currently the HBT model considers only Joule heating generation, although it is foreseen to upgrade the model for further heat sources such as carrier transients etc. [9]. Results for the power operation of HBT devices have been demonstrated in [4]. Based on these simulations an analytical HBT model has been developed, which is capable of simulating double heterojunction bipolar transistors (DHBT). It is based on the Ebers-Moll model and incorporates additional current sources for temperature dependent operation as indicated in fig. 1. The added current sources and resistances I_{Av} , I_{Th} ,

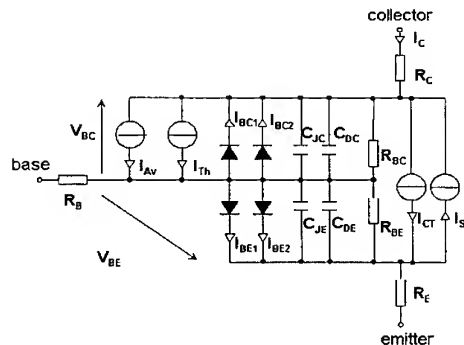


Figure 1: Large-signal equivalent circuit for the HBT model.

I_{Sp} , R_{BC} , and R_{BE} are the avalanche current, thermally generated current, base-collector heterojunction current, and base-emitter and base-collector leakage resistances, respectively.

The avalanche current is defined as $I_{Av} =$

$I_C(M(V_{CE}) - 1)$ where the multiplication factor M can be evaluated using an approximating function according to

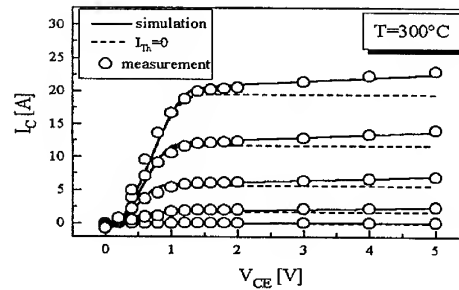
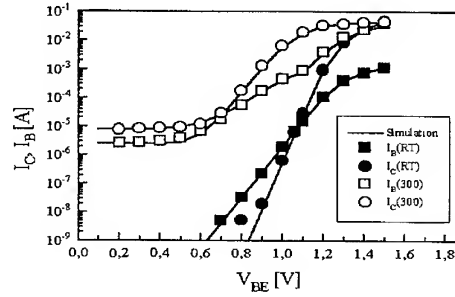
$$M = M_0 \exp\left(\frac{V_{CE}}{V_0}\right) \quad (1)$$

with M_0 and V_0 being model constants. The avalanche current of HBT devices exhibits a negative temperature coefficient for the breakdown voltage of approximately $\sim 1V/100 K$ up to $200^\circ C$. At higher temperatures carrier multiplication increases at low base-collector voltages due to thermal carrier generation. A heterojunction base-collector junction is modelled by the current source I_{Sp} according to

$$I_{Sp} = C_1 I_{CT} \ln\left(\frac{2}{1 + \exp\left(\frac{V_{BC}}{C_2}\right)}\right), \quad (2)$$

where C_1 and C_2 are model parameters and thermionic emission has been assumed as the current mechanism at the heterojunction.

Comparison of the experimental and simulated results for an InGaP DHBT are provided in fig.2 at room temperature and $300^\circ C$ ambient operating temperatures. A good agreement has been achieved between experimental and simulated results. At higher operating temperatures thermal generation of carriers becomes important as indicated in fig.2.



Temperature characterisation of individual emitter fingers

The HBT model described above together with a thermal model have been used to determine the temperature distribution across and along an individual emitter finger. The intrinsic temperature has been determined by measuring the base current of the device. The thermal runaway can be explained by a local shift of the turn-on voltage of the base-emitter junction with increasing local temperature. The voltage shift is alleviated by an increase in the thermal resistance of approximately a factor of 4 with a temperature increase from room temperature to $200^\circ C$. This is essentially due to an increase in the specific thermal conductance of the material with temperature. The value at room temperature for GaAs is $\sigma_{th} \approx 0.45 W/cm \cdot K$ and at $200^\circ C$ $\sigma_{th} \approx 0.19 W/cm \cdot K$.

Thermo-electrical simulations have been performed by dividing the HBT top layer structure into 40 HBTs with $1 \times 1 \mu m^2$ area connected in parallel according to fig. 3 and using the thermal model indicated in fig. 4. The simulations consider a two emitter fin-

Figure 2: Output I/V characteristic and Gummel plot for a DHBT.

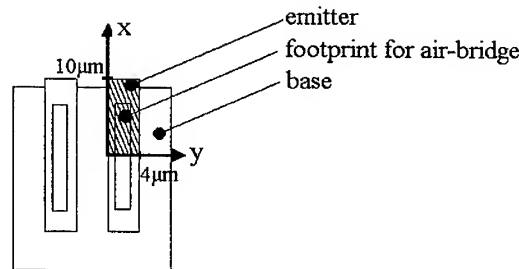


Figure 3: Schematic drawing of the discretisation used in thermal simulation. The simulated region is indicated by the hatched area.

ger device with an air-bridge. A two finger configuration obeys an uneven distribution of the thermal resistance R_4 due to asymmetry in the structure. A comparison between the measured temperature and the simulated maximum and minimum temperatures within the emitter finger is demonstrated in fig. 5 At

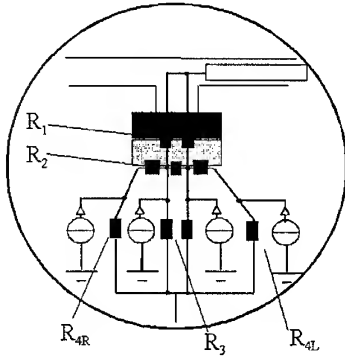
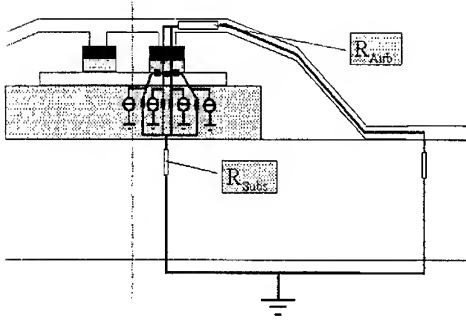


Figure 4: Cross-sectional view indicating the thermal model. The shaded resistors are calculated for the overall HBT structure.

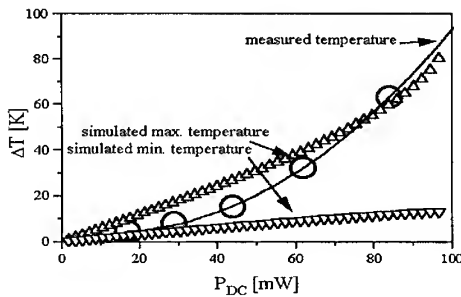


Figure 5: Measured and simulated temperatures for an InGaP DHBT as a function of dissipated DC power. The maximum and minimum temperatures indicate the respective temperatures determined from simulations across an emitter finger.

lower power levels the temperature is homogeneously distributed in the emitter and agrees well with the measured temperature. At large power levels the

measured temperature resembles the simulated maximum emitter temperature because the major part of the emitter current flows through the high temperature region. The difference between the minimum and maximum values for the temperature becomes large. At very high power levels the measured temperature is higher than the simulated maximum temperature because the temperature dependence of the material thermal conductivity has been ignored in the simulations. The temperature profile and the normalised current distribution are provided in fig. 6 for a power dissipation of 80 mW. In these simula-

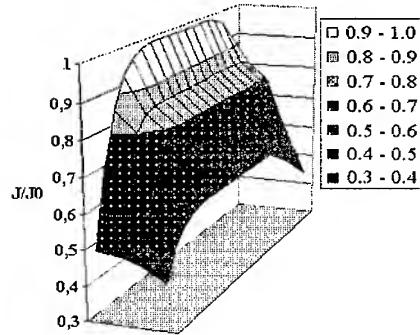
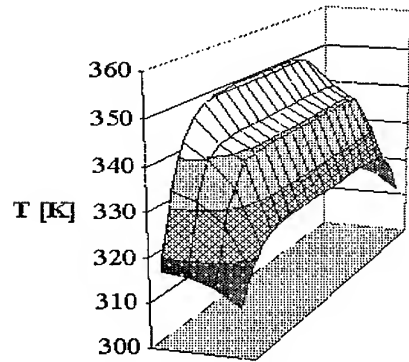


Figure 6: Simulated temperature and current distribution in an emitter finger of a two emitter finger HBT as a function of the geometrical dimensions. The current is normalised to the maximum current. The dissipated power is 80 mW.

tions the thermal conduction through the air-bridge has been assumed negligible. A temperature difference of 40°C can be observed in fig. 6. This determines the inhomogeneity in the current distribution due to the temperature dependence of the diode characteristic. The dominating contribution to the total emitter current is located near the emitter side facing the second emitter finger.

Heat dissipation in the emitter is restricted to heat drain through the air-bridge footprint. However, the air-bridge footprint should be smaller than the metallised emitter area, resulting in a small cross-section and poor thermal properties. The poor thermal conductivity gives rise to the inhomogeneous temperature distribution. The impact of air-bridge thermal conduction on the device performance can be depicted from fig. 7, where the temperature distribution is illustrated for emitter fingers with and without thermal conduction through the air-bridge. When

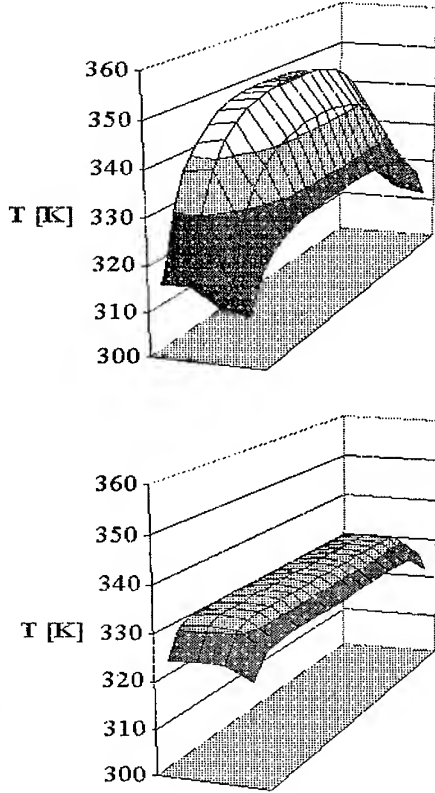


Figure 7: Simulated temperature in an emitter finger of a two emitter finger HBT as a function of the geometrical dimensions. In the left figure it is assumed that no heat flows through the air-bridge. The dissipated power is 80 mW.

the air-bridge thermal conductance is poor, then the temperature rise is high because the heat can not escape from the emitter. However, if an air-bridge footprint covering the entire emitter contact can be realised the temperature distribution is homogeneous and the temperature increase is 30°C in contrast to 50°C for the poorly conducting air-bridge.

Calculation of the thermal coupling of emitter fingers

It has been shown above that thermal coupling is responsible for the thermal runaway in HBT devices. It is therefore important to obtain an optimised design of the HBT device with respect thermal coupling. The thermal resistance of a HBT device can be obtained from calculations of the electrical capacitance of an equivalent electrical structure. The geometrical structure of multi-finger HBT devices resembles that of multiple coupled striplines with inhomogeneous layered dielectric. The thermal resistance is then the inverse of the electrical capacitance $R_{th} \rightarrow 1/C$ if the substitution $\epsilon \rightarrow 1/\rho_{th}$ is made in the capacitance formula. This equivalence can be utilised for the determination of the coupling coefficient between adjacent emitter fingers.

The calculation presented in [10] assume perfectly conducting top and bottom metallisations with an inhomogeneous dielectric filling of the structure as indicated in fig. 8. Assuming that both emitter fin-

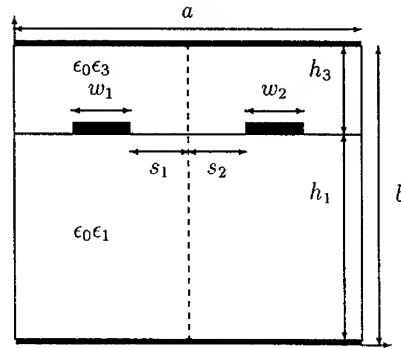


Figure 8: Schematic drawing of the coupling structure used in simulations.

gers have equal widths $w_1 = w_2$ the formulas for the thermal coupling are given by [10]:

$$k_c = \frac{1}{1 + K(\rho_{th})} \quad (3)$$

$$K(\rho_{th}) = \frac{1}{R^2} \sum_{n=1}^{\infty} \frac{J_0^2(X) \sin(Y) \sin(T)}{n(\Delta_n)^2} R_m \quad (4)$$

$$R_m = \kappa_{th1}^2 \sinh^2\left(\frac{n\pi h_1}{a}\right) \sinh\left(\frac{2n\pi h_3}{a}\right)$$

$$X = \frac{n\pi w_1}{2a}$$

$$Y = \frac{n\pi}{a} \left(\frac{a}{2} - s_1 - w_1 \right)$$

$$T = \frac{n\pi}{a} \left(\frac{a}{2} + s_2 + w_2 \right)$$

$$\begin{aligned}
R^2 &= \sum_{n=1}^{\infty} \frac{J_0^2(X) \sin^2(Y)}{n(\Delta_n)^2} \kappa_{th1}^2 \cdot R_1 \quad (5) \\
R_1 &= \sinh^2\left(\frac{n\pi h_3}{a}\right) \sinh\left(\frac{2n\pi h_1}{a}\right) \\
&+ \sinh^2\left(\frac{n\pi h_1}{a}\right) \sinh\left(\frac{2n\pi h_3}{a}\right) \\
\Delta_n^2 &= \kappa_{th1}^2 A + \kappa_{th1} \kappa_{th3} B \\
A &= \cosh\left(\frac{n\pi h_1}{a}\right) \sinh\left(\frac{n\pi h_3}{a}\right) \\
B &= \cosh\left(\frac{n\pi h_3}{a}\right) \sinh\left(\frac{n\pi h_1}{a}\right)
\end{aligned}$$

The coupling coefficient k_c indicates the fraction of temperature from the neighbouring emitter fingers coupled to the emitter finger under consideration. A factor of $k_c = 1$ results in complete coupling. The above formula can be used for determination of the optimum spacing between adjacent emitter fingers. As indicated in the discussion the optimum spacing is a trade-off between minimum coupling and maximum thermal conductance of the structure.

Conclusions

Results for the temperature distribution across and along emitter fingers of multi-finger HBT devices have been discussed. The simulations have been performed with an improved HBT model coupled to a thermal circuit. It could be shown that heat dissipation through the air-bridge is essential for low operating temperatures as well as homogeneous distribution of temperature in the emitter finger. Thermal runaway can be explained by the nonhomogeneous temperature and current distribution.

Thermal coupling to neighbouring fingers creates an uneven distribution of thermal resistances and hence temperature and should therefore be avoided in device design. Formulas for the calculation of the thermal coupling of individual emitter fingers have been provided.

REFERENCES

- [1] W. Liu, S.-K. Fan, T. Henderson and D. Davito. Temperature dependence of current gains in *GaInP/GaAs* and *AlGaAs/GaAs* heterojunction bipolar transistors. *IEEE Trans. Electron Devices*, ED-40:1351-3, 1993.
- [2] A. Marty, T. Campy, J. Tasselli, D.L. Pulfrey and J.P. Bailbe. A self-consistent DC-AC two-dimensional electrothermal model for *GaAlAs/GaAs* microwave power HBT's. *IEEE Trans. Electron Devices*, ED-40:1202-1210, 1993.
- [3] M.E. Hafizi, W. E. Stachina, R. A. Metzger, P. A. McDonald and F. Williams Jr. Temperature Dependence of DC and RF Characteristics of *AlInAs/GaInAs* HBT's. *IEEE Trans. Electron Devices*, ED-40(9):1583-7, 1993.
- [4] V. Krozer, M. Ruppert, M. Schüßler, K. Fricke, W.-Y. Lee and H.L. Hartnagel. Calculation of the Power Capabilities of HBT Amplifiers Based on a New Physical HBT Model. *J. Microwave and Millimeter-Wave Computer-Aided Eng.*, 6(4):270-280, 1996.
- [5] J. Dupuis, R. Hajji, F. M. Ghannouchi, K. Saab and S. Lavallée. A New DC Model of HBT's Including Self-Heating Effects Suitable for Circuit Simulation. *IEEE Trans. Electron Devices*, ED-42(12):2036-2042, 1995.
- [6] B. Bayraktaroglu, J. Barrette, L. Kehias, C.I. Huang, R. Fitch, R. Neidhard and R. Scherer. Very High-Power-Density CW Operation of *GaAs/AlGaAs* Microwave Heterojunction Bipolar Devices. *IEEE Electronic Device Letters*, EDL-14:493-5, 1993.
- [7] M. Schüßler, V. Krozer, J. Pfeiffer, W. Statzner, W.-Y. Lee and H.L. Hartnagel. *AlGaAs/GaAs* and *GaInP/GaAs* HBT for High Temperature Microwave Operation. In *ISSSE 1995, Intern. Symp. on Signals, Systems and Electron.*, San Francisco, USA, Oct. 25-27 1995.
- [8] V. Krozer, M. Ruppert, W.Y. Lee, J. Grajal, A. Goldhorn, M. Schüßler, K. Fricke and H.L. Hartnagel. A Physics-Based Temperature-Dependent SPICE Model for the Simulation of High Temperature Microwave Performance of HBT's and Experimental Results. In *1994 IEEE MTT-S, Intern. Microwave Symp. Dig.*, San Diego, USA, Mai 23-27, 1994.
- [9] O. Tornblad, U. Lindefelt and B. Breitholtz. Heat Generation in Si bipolar power devices: the relative importance of various contributions. *Solid-State Electronics*, 39(10):1463-1471, 1996.
- [10] B. N. Das and K.V.S.V.R. Prasad. A Generalized Formulation of the Electromagnetically Coupled Striplines. *IEEE Trans. Microwave Theory & Technique*, MTT-32(11):1427-1433, 1984.

INFLUENCE OF THE MODEL PARAMETERS ON THE NOISE PERFORMANCE OF DOUBLE-POLYSILICON BJT's FOR MICROWAVE LNA's

A. Caddemi and M. Sannino

Dipartimento di Ingegneria Elettrica, Università di Palermo,
Viale delle Scienze, 90128, Palermo, ITALY, Tel/Fax ++39-91-6566 275

ABSTRACT

In the recent past we have measured the noise and the scattering parameters of several series of double polysilicon BJT's over the 2-6 GHz frequency range at different collector current values, according to their emitter finger number. From the experimental data, a noisy circuit model has been extracted based on a T-equivalent network. By means of the correlation matrix techniques, novel analytical expressions of the noise parameters have been derived. As a second step, a sensitivity analysis has been performed for evaluating the influence of each model element on the noise performance. The results show how to improve the characteristics of such devices for a better performance when employed in microwave low-noise amplifiers.

INTRODUCTION

The double-polysilicon self-aligned (PSA) process has definitively emerged as the most effective technique for the realization of high speed silicon devices. The PSA bipolar transistors offer remarkable improvements in the gain-bandwidth product, maximum oscillation frequency, low-noise performance and component integration level in VLSI application. Such components are also being increasingly used in wireless communication systems at microwave frequencies.

As far as the noise performance is concerned, we refer to the representation in terms of the noise parameters which appear in the following relationship

$$F(\Gamma_s) = F_0 + 4 r_n \frac{|\Gamma_s - \Gamma_0|^2}{|1 + \Gamma_0|^2 (1 - |\Gamma_s|^2)}$$

where F and Γ_s are the noise figure and the source reflection coefficient of the device under test, respectively, and F_0 (minimum noise figure), Γ_0 (value of the complex source reflection coefficient Γ_s at which F_0 occurs) and r_n (noise resistance normalized with respect to 50 Ω) are the four noise parameters.

We have recently performed the complete characterization in terms of scattering and noise parameters of several PSA transistors having different emitter finger number n_e over the 2-6 GHz frequency range at different low-voltage bias conditions, as suggested by the manufacturer [1].

We here refer to the results relevant to the Q_2 family (4 emitter fingers) tested at the fixed voltage condition of $V_{CE}=2.8$ V and at the collector current values of $I_C=2$ and 8 mA. After measurements, a T-equivalent circuit including noise sources has been extracted by minimizing the difference between measured and computed performance on the basis of a decomposition approach [2].

The circuit model has then been employed for determining new analytical expressions of the noise parameters F_0 , $|\Gamma_0|$ and r_n as a function of the model elements.

Such expressions are here exploited in a sensitivity analysis aimed at determining the influence of the model elements on the noise performance of the device. The effects attributable to variations of the polysilicon resistance lead to some interesting remarks which may help in "tailoring" a transistor structure optimized for use in microwave low-noise amplifiers (LNA).

This work was supported by Italian Space Agency (ASI), National Research Council (CNR) and a European Scientific Project (POP).

MODEL EXTRACTION FROM MEASUREMENTS

By means of a fully automated system whose measuring procedure has been extensively described in several papers we perform the complete characterization of the device by noise figure measurements only ([3] and references therein). From the noise data we derive all the noise, gain and scattering parameters thus acquiring a complete knowledge of the device performance at microwave frequencies.

As a general result concerning the present investigation, we have observed that F_O takes on very low values as compared to conventional bipolar transistors, i.e. less than 1 dB at 2 GHz for the Q_3 series (8 emitters) and about 2 dB up to 5 GHz for all families with a typical cutoff frequency of 10 GHz (at the lower bias current).

Since the measured data for each family exhibited reduced spread, by use of simple statistics we determined the performance of a *typical* device to be employed during the modeling step.

As far as the equivalent circuit is concerned, we decided to employ the Hawkins noise model and, as a first step, we analyzed the performance of the simple T-structure reported in [4]. However, we found that such a model failed in reproducing both the small-signal and the noise behavior of the measured devices since it neglects some important high-frequency effects. This is mainly due to the absence of either the emitter resistance generated by the polysilicon layer and the collector-to-base capacitance which has a profound influence on the S_{12} and S_{21} scattering parameters of the *chip* device.

A more suitable structure has been found to be that reported in Fig.1, including two uncorrelated noise current generators i_{n1} and i_{n2} and the thermal noise voltages associated to the base resistance R_b and to the polysilicon layer resistance R_{ee} . The model element at the lower bias current ($I_C=2$ mA) are reported in Tab.1.

The model performance has been optimized using a decomposition approach for either the scattering and the noise parameters with respect to the statistically averaged measurement data. The values of the emitter resistance R and the noise current sources i_{n1} and i_{n2} have been fixed by use of well-known physical relationships, while the values of the remaining circuit elements have been varied during the separated optimization cycles.

Furtherly, we were interested in deriving closed-form expressions of the noise parameters showing the influence of the circuit elements on each of them. This has been accomplished by use of the correlation matrix technique which is a rigorous mathematical procedure for noise parameter computation [5].

We analyzed the behavior of F_O , $|\Gamma_O|$ and R_n by using our modified T-model and derived the relevant expressions. Note that $R_n = r_n \cdot 50 \Omega$. We here report the relationships derived for $|\Gamma_O|$ and R_n :

$$|\Gamma_O| = \left(\frac{0.2 + \left[(-R^3 - R_{ee}^3 - R_b^3 - 4\pi f C_c R R_b R_{ee}^2) \cdot (R^2 + 2R R_{ee} + R_{ee}^2 + 4R_b^2 R^2 \pi^2 C_c^2 f^2) \right] / K_1}{0.2 - \left[(-R^3 - R_{ee}^3 - R_b^3 - 4\pi f C_c R R_b R_{ee}^2) \cdot (R^2 + 2R R_{ee} + R_{ee}^2 + 4R_b^2 R^2 \pi^2 C_c^2 f^2) \right] / K_2} \right)$$

$$R_n = \frac{\alpha}{2R} \frac{R_b^2 + R^2 + R_{ee}^2}{\left[\alpha + 4\pi^2 f^2 C_c C_e R (R_b + R_{ee}) \right]^2 + 4\pi^2 f^2 C_c^2 (R + R_{ee})^2}$$

where K is the Boltzmann constant, T is the temperature expressed in [K], α is the common base current gain and $K_1, K_2 [\Omega]^2$ have constant values approaching unity. In Fig.2 a,b we show the agreement between measured (**meas**) and calculated (**calc**) values of F_O and $|\Gamma_O|$.

INFLUENCE OF THE MODEL ELEMENTS ON THE TRANSISTOR NOISE PERFORMANCE

The relationships so derived have been employed in a sensitivity analysis to gain information on the role played by the model elements upon the device noise performance, with special concern for the resistance R_{ce} associated with the polysilicon layer.

We also analyzed the sensitivity of the optimum source reflection coefficient $|\Gamma_{og}|$ relevant to the maximum available gain for evaluating its dependence on the model elements.

The aim of such a study was that of pointing out how to improve the performance of a PSA transistor for its use in a low-noise stage of wireless front-ends at microwave frequencies. When designing such circuits, a trade-off condition between noise and gain has always to be obtained for ensuring either a low noise contribution from the first stage by approaching F_O and a small noise contribution from the cascaded stages which is inversely proportional to the available gain of the first stage (see Friis' formula in radio receivers).

The desired targets are therefore : 1) low values of F_O and r_n for a better low-noise performance over a wider range of matching conditions and frequencies; 2) values of $|\Gamma_O|$ and $|\Gamma_{og}|$ close to each other for an easier achievement of the optimum trade-off condition between noise and gain.

The sample bar diagrams reported in Fig.3 show the dependence of F_O , $|\Gamma_O|$ and R_n on a $\pm 10\%$ variation of the circuit element values as evaluated at the central frequency of 4 GHz. As it clearly seen, upon diminishing R_{ce} we get a decrease of F_O and an increase of $|\Gamma_O|$ without sensibly affecting R_n since the contribution due to the low value of R_{ce} is masked by R_b and R_c . On the contrary, the influence of R_{ce} upon F_O is amplified by a factor R_{ce}^4 with respect to the base resistance weighting as R_b^3 .

By employing the scattering parameters, we then analyzed the sensitivity of the gain reflection coefficient $|\Gamma_{og}|$ with respect to the circuit elements since the link between such parameter and the model elements cannot be extracted directly in form of a closed-form expression.

We observed that the influence of $|\Gamma_{og}|$ to variations of R_{ce} is negligible, whereas a decrease of R_{ce} makes the values of $|\Gamma_O|$ vs. frequency closer to $|\Gamma_{og}|$ as reported in the plot of Fig.4 and also lowers the values of F_O .

Therefore, by acting on a given PSA process in such a way to obtain an acceptable decrease (10-15 %) of the polysilicon layer resistance we get an improvement of the noise performance and allow for an easier trade-off condition in the design of low-noise amplifiers by having values of $|\Gamma_O|$ closer to $|\Gamma_{og}|$ over the low-microwave frequency range.

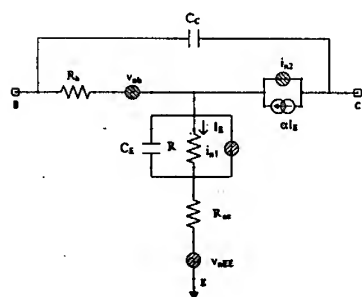
CONCLUSIONS

Different series of double polysilicon bipolar transistors have been characterized in terms of noise and scattering parameters over the 2-6 GHz frequency range at different collector current values, according to their emitter finger number. A circuit model has been extracted for the Q_2 series (4 emitters) series based on an improved T-equivalent circuit including noise sources. By such a model, novel analytical expressions for the noise parameters F_O , $|\Gamma_O|$ and r_n have been derived for this polysilicon self-aligned structure. Following that, a sensitivity analysis has been performed for evaluating the influence of the device model elements upon the noise parameters. We found that by decreasing the polysilicon layer resistance the noise performance of the PSA transistor may be improved for "tailoring" a device to be specifically used in low-noise amplifiers at microwave frequencies.

REFERENCES

- [1] A. Caddemi, M. Sannino and C. Sclafani (student), "Noise and gain performance of PSA transistor series for personal communication systems vs. emitter number and operating conditions", *Proceedings of the 25th European Microwave Conference*, pp. 1181-1185, Bologna, Italy, Sept. 1995.

- [2] A. Caddemi, M. Sannino and M. Tarantola (student) "On the equivalent noise resistance of advanced poly-emitter BJTs at microwave frequencies", *Proceedings of the XI International Microwave Conference MIKON 96*, Warsaw, Poland, May 1996.
- [3] G. Martines and M. Sannino, "The determination of the noise, gain and scattering parameters of microwave transistors (HEMTs) using only an automatic noise figure test-set", *IEEE Trans. Microwave Theory Tech.*, vol. MTT-42, pp. 1008-1013, July 1994.
- [4] R. Pucel, U. Rohde, "An exact expression for the noise resistance R_n for the Hawkins bipolar noise model", *IEEE Microwave and Guided Wave Letters*, vol.3, N.2, pp.35-37, Feb.1993.
- [5] H. Hillbrand and P. Russer, "An efficient method for computer aided noise analysis of linear amplifier networks", *IEEE Trans. Circuits Systems*, vol. CAS-23, pp.235-238, Apr. 1976.



$R_{be} (\Omega)$	36.1	$v_{nb} (nV^2/Hz)$	$58 \cdot 10^{-3}$
$R_{ce} (\Omega)$	12.6	$v_{nre} (nV^2/Hz)$	0.57
$R_{xx} (\Omega)$	3.5	$Re (corr)$	0.99
$C_x (pF)$	0.41	$Im (corr)$	0.065
$C_c (pF)$	0.22	α	0.998
$i_{n1}^2 (pA^2/Hz)$	552		
$i_{n2}^2 (pA^2/Hz)$	681	$\tau (psec)$	6.5

Fig.1 - Improved T-noise model adopted for the double-poly BJT series

Tab.1 - Values of the circuit elements for the Q_2 series at low-noise bias ($I_C=2$ mA)

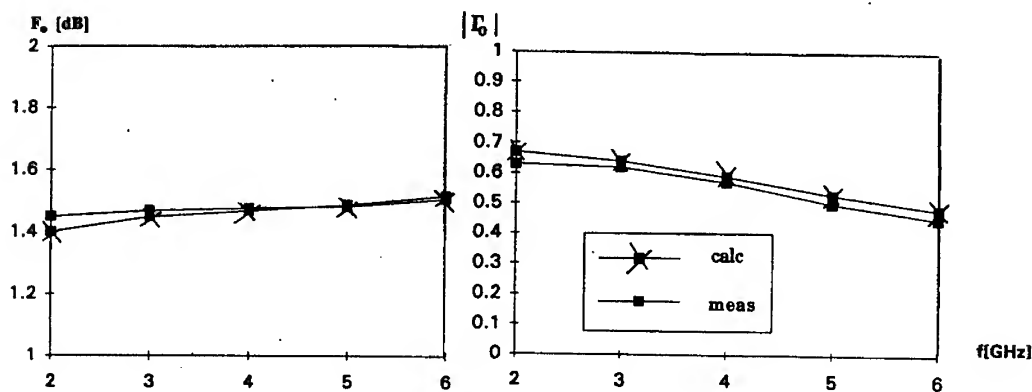


Fig.2 - Comparison between measured (meas) and calculated (calc) values of: (a) minimum noise figure F_0 ; (b) optimum noise source reflection coefficient $|\Gamma_0|$.

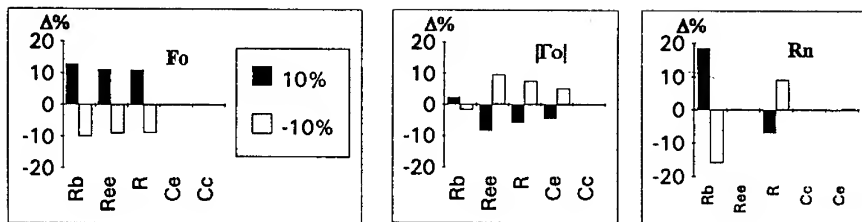


Fig. 3 - Bar diagrams relevant to the analysis performed at 4 GHz on the noise parameters F_o , R_n and $|\Gamma_o|$ for a 10% variation of the element values shown in Tab.1

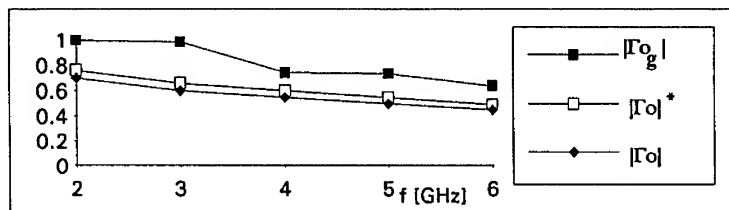


Fig.4 - Comparison among the values of $|\Gamma_{og}|$ (which is not affected by a 10% variation of the element values), $|\Gamma_o|$ evaluated by the original model and $|\Gamma_o|^*$ evaluated by considering a $\pm 10\%$ of the model element values

Drain Temperature Dependence on Ambient Temperature for a Cryogenic Low Noise C-Band Amplifier.

S. Muñoz, J. D. Gallego*, J. L. Sebastián and J.M. Miranda.

Dpt. Física Aplicada III
Facultad de Ciencias Físicas. U. C. M.
28040 Madrid (Spain).

* Centro Astronómico de Yebes.
Aptdo. 148. E19080 Guadalajara (Spain).

ABSTRACT

A comparison between predicted and measured noise temperatures for cryogenic HEMT amplifiers is presented by using the Pospieszalski's noise model. A good agreement between predicted and measured amplifier's noise performance is obtained both at room and cryogenic temperatures. However, the predicted values overestimate noise temperature in the center part of the measured temperature range (50K - 230K). A parabolic dependence for the drain temperature with ambient temperature is proposed to obtain a better fitting to the experimental results.

INTRODUCTION

In order to reduce the number of measurements needed to obtain noise figure predictions the analysis of the FETs' (MODFETs) noise performance has become a subject of primary interest. It has already been shown (1) that a complete noise analysis can be performed using a simple noise measurement and an equivalent circuit model. More recently (2,3), other models have been described that further simplify the measurement requirements while improving the noise figure predictions. These models predict the four noise parameters at any frequency provided that two frequency independent constants and the transistor's equivalent circuit are known. These two constants are the equivalent temperatures of the intrinsic gate resistance and drain conductance, T_g and T_d respectively.

Verifications of these models have already been carried out with noise and S-parameters data taken for different active devices at a single operating bias point and as a function of operating bias (4). The validity of a simplified noisy model has recently been checked for packaged pseudomorphic devices by comparison between the measured noise parameters with those obtained from a computer analysis of the simplified noisy model of the device (5).

The values of T_d and T_g are known for typical HEMT devices (6) at room and cryogenic temperatures. Our previous simulations assumed that T_g was very close to the transistor's physical temperature and that T_d could be obtained from linear interpolation of the values known at room and cryogenic temperatures (297K and 14K respectively) (7).

This work shows a comparison between predicted and measured noise temperature for cryogenic HEMT amplifiers designed over the frequency range 3.2GHz - 4.7GHz. The noise temperature is simulated by using the model proposed by Pospieszalski (3). The experimental results suggest a non linear dependence of T_d on ambient temperature since a linear interpolation overestimates T_n at ambient temperatures in the range 50K - 230K.

NOISE TEMPERATURE MEASUREMENTS

Four cryogenic C-band amplifiers have been designed and built with transistors from different manufactures and batches. Each amplifier consists of three stages as shown in Figure 1.

The source inductance and loading resistor values were selected for each stage so that both unconditional stability and low power dissipation across the full band were achieved. Therefore, no oscillation was produced for any combination of passive input and output impedances at any operating temperature. The input matching circuit was optimized for minimum cryogenic noise and the output matching circuit for low reflection. The two interstage coupling networks provide flat gain of approximately 34 dB for the amplifier.

The noise temperature was measured with a fully automated system in the range 15K - 275K. Cryogenic measurements were taken with the "cold attenuator" method by using a calibrated noise diode at room temperature, a 15dB attenuator and a DC-block cooled at cryogenic temperatures. Room temperature data were obtained with the noise diode. The accuracy of measured noise temperature is estimated in $\pm 9\text{K}$ for the room temperature and $\pm 1\text{K}$ for the lowest cryogenic temperature, in the worst case (8).

All the amplifiers were biased for minimum noise operation at room temperature ($V_{ds} = 2\text{V}$; $I_{ds} = 10\text{mA}$). When the amplifiers were cooled below 100K, the bias was changed to a new value of $V_{ds} = 1.5\text{V}$; $I_{ds} = 5\text{mA}$ which corresponds to the optimum noise for $T_{amb} = 15\text{K}$.

Figure 2 shows the measured mean noise temperature for the four amplifiers as a function of ambient temperature in the range 15K - 270K.

As is observed, amplifiers 1 and 2 show the best performance with a mean noise temperature of approximately 10K @ $T_{amb} = 60\text{K}$ with a ripple of $\pm 0.5\text{K}$ in the band.

Amplifiers 3 and 4 had an anomalous performance showing a bump around 125K that may be due to trap effects at cryogenic temperatures.

MODELING NOISE TEMPERATURE

The amplifiers were simulated with MMICAD (9) by using the Pospieszalski's noise model and a HEMT equivalent circuit obtained from DC and S parameters measurements of the active device at room temperature. Capacitors were modeled as RCL circuits and resistors as RL circuits. In order to obtain unconditional stability and an acceptable input reflection across the full band, an inductive feedback was used at the source and the drain was resistively loaded. The noise added by the drain loading resistors to the total noise of the amplifiers is 0.4K for $T_{amb} = 15\text{K}$ and 10K for $T_{amb} = 300\text{K}$. This noise represents about 10% of the total noise at cryogenic temperature and 20% at room temperature.

In the Pospieszalski's noise model, the HEMT's noise properties are only determined by the values of the equivalent gate and drain temperatures T_g and T_d . The equivalent gate temperature is considered to be equal to the ambient temperature as typically shown by HEMT devices (3). In order to model the noise temperature of the amplifiers at any ambient temperature, T_d is obtained as a first approximation by using a linear interpolation from the temperature values originally proposed by Pospieszalski (4,6). However, the linear interpolation does not predict the experimental data accurately and therefore another approach has been considered. The experimentally observed deviation from linearity and the overestimation of the noise at high temperatures suggested us that a non linear dependence of T_d with

T_{amb} may improve the predictions. The parabolic dependence shown in Fig. 3 may be easily included in MMICAD.

Figure 4 shows a comparison between predicted (with linear and non linear dependence) and measured noise temperature for all amplifiers as a function of ambient temperature in the range 15K - 270K.

As is observed, the non linear drain temperature dependence on ambient temperature predicts the best fitting to measured mean noise temperature in the center part of temperature range. A better value for amplifiers noise performance at room temperature is also provided by the non linear dependence.

CONCLUSIONS

As observed in Figure 4, a parabolic dependence of T_d predicts a good fitting of the noise temperature in the ambient temperature range 15K to 300K. Pospieszalski's values were correct for $T_{amb} = 15K$ but they overestimate the noise at room temperature. This may be due to the improvement of the devices presently available. The results shown in Figure 4 suggest that the new proposed T_d function leads to a more accurate prediction of the noise temperature of cryogenic amplifiers in a broad ambient temperature range, modeling the nonlinear dependence of T_n with T_{amb} .

REFERENCES

- (1) A. F. Podell. "A Functional GaAs FET Noise Model". May 1981, IEEE Trans on ED, Vol. 28, pp. 511-517.
- (2) M. S. Gupta and P. T. Greiling. "Microwave Noise Characterization of GaAs MESFET's: Determination of Extrinsic Noise Parameters". Apr. 1988, IEEE Trans. on MTT, Vol. 36, pp. 745-751.
- (3) M. Pospieszalski. "Model of Noise Parameters of MESFETs and MODFETs and their Frequency and Temperature Dependence". Sept. 1989, IEEE Trans. on MMT, Vol. 37, pp. 1340-1350.
- (4) M. W. Pospieszalski and A. C. Niedzwiecki. "FET Noise Model and On-Wafer Measurement of Noise Parameters". Proc. of 1991 Int. Microwave Symp.
- (5) A. Caddemi, A. di Paola and M. Sanino. "Full Characterization of Microwave Low-Noise Packaged HEMT's: Measurements Versus Modeling". Apr. 1997, IEEE Trans. Instrum. Meas. Vol. 42, n° 2, pp. 490-494.
- (6) M. Pospieszalski. "Cryogenically-Cooled HFET Amplifiers and Receivers: State of the Art and Future Trends". 1992, IEEE MTT-S Digest. pp. 1369-1372.
- (7) M. Pospieszalski et al. "Very Low Noise and Low Power Operation of Cryogenic AlInAs/GaInAs/InP HFET's". 1994, IEEE MTT-S Digest. pp. 1345-1346.
- (8) J. D. Gallego. "Cryogenic C-Band HEMT Amplifier Prototypes For IRAM". Technical Report CAY 1.
- (9) MMICAD Ver. 5.20. Monolithic and Microwave Integrated Circuit Analysis and Design, 1991, Optotek Ltd., 62 Steacie Drive, Kanata, Ontario K2K2A9, Canada.

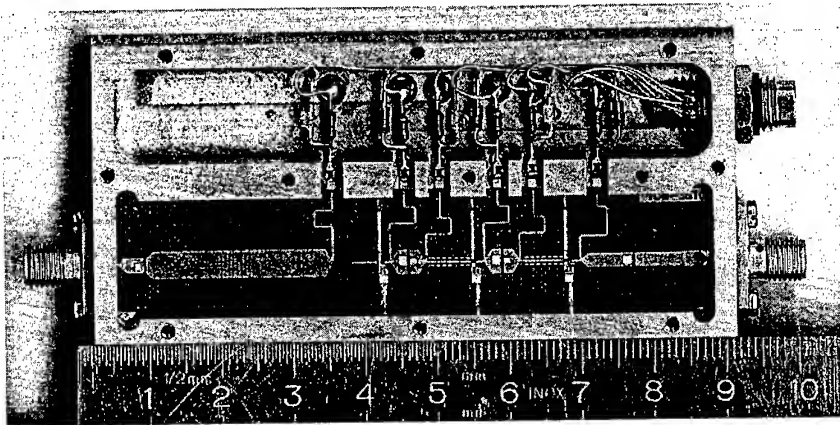


Fig. 1. A three stage cryogenic C-band amplifier.

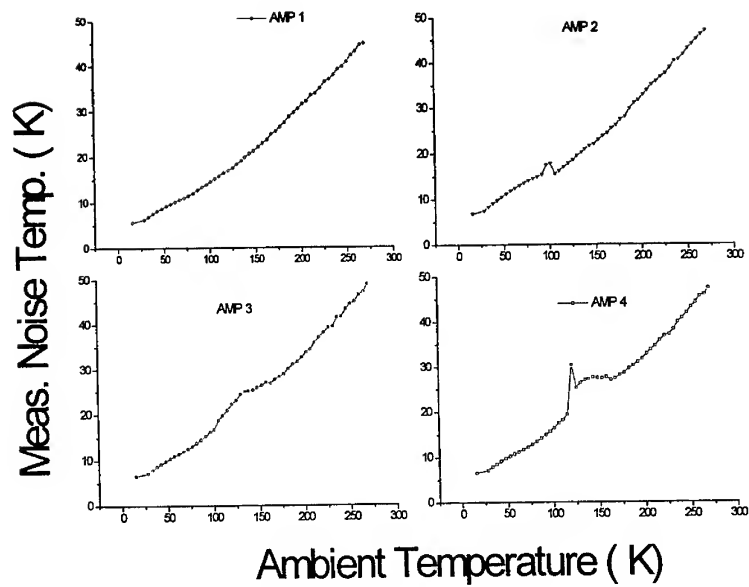


Fig 2. Noise temperature of different cryogenic C-band amplifiers.

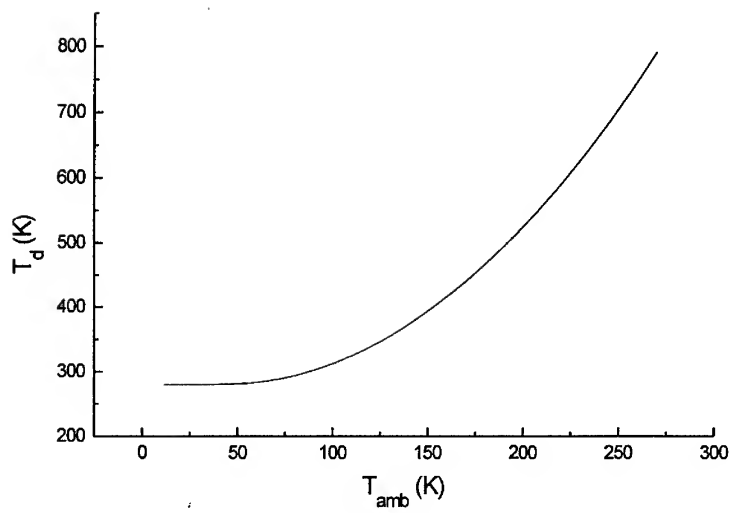


Fig. 3. Drain temperature non linear dependence on ambient temperature.

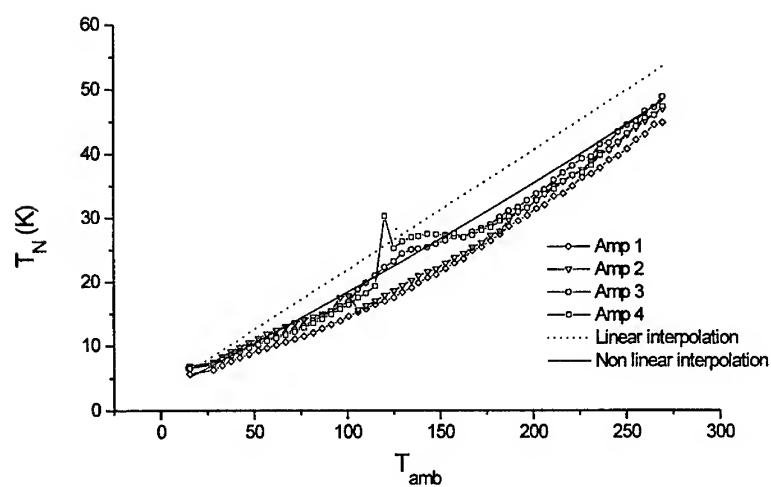


Fig. 4. A comparison between predicted and measured noise temperatures for cryogenic HEMT amplifiers.

MODELLING OF PROPAGATION IN OUTDOOR MICROCELLS AT 62.4GHz

A.Hammoudeh, M.G.Sanchez*, and E.Grindrod**

o University of Glamorgan, Department of Electronics and IT, Pontypridd CF37 1DL, UK

*** Universidad de Vigo, Dpto. Tecnologias de las Comunicaciones, 36204 Vigo-Spain

+ Defence Research Agency, St Andrews Road, Worcs. WR14 3PS, UK

Abstract

Results of Line-of-Sight (LOS) and Non Line-of-Sight (NLOS) mobile radio propagation experiments made to characterise 62 GHz sub-urban microcell channels employing omnidirectional antennas are presented. Experimental results are compared with theoretical predictions obtained from an exhaustive ray tracing algorithm. NLOS results show a sharp drop in the mean signal level when the direct component is blocked. The model is found not to be able to predict the signal with accuracy in the shadow region, where reflections do have a major influence, and are responsible for any coverage in there.

Introduction

The use of millimetre wave frequencies, where large signal bandwidths are available [1-3], has been proposed for future cellular mobile radio communication systems employing many low powered base stations with antennas which are elevated by only several metres above the ground [4-5]. In particular, the frequencies around the 60 GHz have been suggested for urban microcellular structures [6-7]. The quasi optical nature of radio waves at this frequency inhibits illumination of shadow regions to a certain extent. The strong oxygen absorption predominant at 60 GHz limits the operational range of the system. These two factors allow greater frequency re-use within a cellular system thus increasing network capacity.

This paper reports experiments made to measure NLOS propagation characteristics at 62 GHz in a sub-urban microcellular environment. Measurements were conducted in a street with houses, located at both sides, made primarily of stones. Building surfaces had a large number of windows and wooden doors. There were also a number of lamp posts, parked cars and other objects present at both sides of the street. In addition, the work describes a ray tracing algorithm which has been developed to model the environment and the propagation mechanisms exhibited at this frequency. The model, due to the small size of the wavelength, takes into account the effect of surface roughness.

Measurements Geometry

Measurements were made by transmitting a continuous wave signal from a fixed base station to a mobile receiver and recording the signal envelope variation as a function of mobile position. The microcell base antenna, set at a height of 3.1 metres above the ground, was placed horizontally at one end of the street at a distance of 2.35 metres from the nearest building surface. It was oriented along the street. The receive antenna was also mounted horizontally on the roof of a transit van at a height of 2.8 metres above the ground.

The mobile receiver was moved 57 metres along a road which crosses the main street at right angles as is shown in Fig. 1. The receiver was driven at an almost constant speed of 10 miles per hour (4.47 metres per second). Distance markers to provide a measure of the distance travelled were also recorded.

Measurement Hardware

The 62.4 GHz transmitter is housed in a box mounted on a pneumatic mast. The transmitter is composed of a 100 mW phase locked oscillator. The output of the oscillator is fed to the base antenna via an isolator. The receiver is a simple balanced mixer followed by a low noise pre-amplifier. The received signal is down

converted to an IF of 600 MHz, and its amplitude is measured using a logarithmic amplifier centred at 600 MHz. The receiver, with a noise floor of -74 dBm, is also housed in a box and is mounted upon the roof of a transit van.

Measurements were conducted using a vertically polarised omnidirectional receive antenna. The antenna has full azimuthal coverage with a 3 dB elevation beamwidth of 6.5° and a gain of 6 dB. A 10 dBi standard horn antenna was used at the base station. The E and H plane beamwidths being 69° and 55° respectively. The logarithmic amplifier output voltage is fed into channel 1 of the data storage and acquisition unit, with channel 2 being used to record distance markers. Both channels are digitised simultaneously via 12-b A/D converters at a rate of 20k sample per second. The data is then transferred to a computer for subsequent analysis.

Multiray and diffraction model

A simulation programme, based on the image technique, has been developed to predict the signal characteristics and to assist in interpreting experimental results. Buildings at both sides of the street are assumed to have uniform reflecting surfaces with diffracting edges, whose geometry is specified. The ground is also assumed to be a flat uniform reflecting surface. The effects of other objects, such as lamp posts, pedestrians and cars, have not been considered.

The tool is originally developed to aid characterisation of UHF microcell propagation where diffraction is a significant contributor to the received signal strength. The diffracted field by a building edge is calculated using the exact solution developed by Maliuzhinets [8] instead of the more usual empirical approach proposed by Luebbers [9]. The order of diffraction a ray can experience is specified by the user and is used as an input to the model. At 62 GHz however, the diffraction phenomenon can be neglected in mobile scenarios.

The model also considers polarisation mismatches and the E and H plane patterns of the transmit and receive antennas. In the modelling presented here however, the E and H planes of the base antenna are approximated so that all rays within the 3 dB beamwidth of the main lobe are assumed to have a constant gain. Rays outside the main beam are not included in the calculations. This assumption is justified since the most significant sidelobes in the E and H planes are 13 dB and 17 dB below the main beam respectively. Consideration of reflections up to any order can be specified by the user. The reflected electric fields from dielectric planar surfaces are calculated using the Fresnel coefficients. However, when roughness is taken into account the scattered electric field, assuming a Gaussian distributed surface roughness with a standard deviation of α_s , is computed using a simplified formulation of the solution proposed in [10]. The scattering factor is given by:

$$|\rho_s| = |F| e^{-\frac{g}{2}} \quad 1$$

where F is the Fresnel reflection coefficient and g is a measure of the roughness of the surface which is expressed by:

$$g = \left(\frac{4\pi\alpha_s \cos \theta}{\lambda} \right)^2 \quad 2$$

where θ is the incident angle measured from the normal to the surface, and λ is the wavelength.

When the surface is smooth, $\alpha_s = 0$, the value of the scattering factor given in (1) becomes identical to that of the Fresnel coefficient. Although the expression given in (1) is valid for values of $g < 1$, it has been successfully used to model scattering when the value of g is significantly larger than one [11]. Calculations

presented here also use the same approximation for simplicity. Predictions given in this paper assume building surfaces to be made of stone with $\epsilon_r = 6.81$, and $\sigma = 0.95$ siemens per metre [12]. The dielectric parameters for the ground are $\epsilon_r = 10$, and $\sigma = 0.005$ siemens per metre [13]. A value of $\sigma_s = 6.2$ millimetres has been obtained from 100 samples measured in the main street for walls A and B (refer to Fig. 1). The other walls C and D, are smooth.

Measured Signal Envelope

The signal envelope measured as the mobile receiver travelled a distance of 57 metres along the cross road is shown in Fig. 2. The mobile receiver route (refer to Fig. 1) consists of three distinctive sections. In the range 0-28 metres along the road (section 1), the mobile receiver is in the shadow region of the base station. The line-of-sight prevails for the next 11 metres (section 2), before being blocked again over the last 18 metres (section 3).

When the receiver is in clear view of the base station (section 2 from 28-39 metres) the signal envelope exhibits severe multipath fading. This is primarily due to interference between the direct ray and reflections from Walls A and B in the main street. Reflections from the ground do not contribute to the signal strength at such distances from the station because of the narrow elevation beamwidth of the receive antenna and the heights of both the transmit and receive antennas above the ground. The signal strength drops significantly when the direct ray is obscured and any coverage in the shadow region is mainly due to reflections.

Theoretical Predictions

The mean signal level of the measured and predicted envelopes are obtained by computing the moving average. The average was calculated over a window length of 150A which is being moved by 40A. Fig. 3 shows a comparison between experimental and theoretical results obtained by considering reflections up to the second order and no diffractions from building edges. It can be clearly seen that the measured mean signal level drops initially by about 9 dB and 14 dB below the line-of-sight when it is being blocked as the mobile receiver moves small distances into the shadow regions. At larger distances, it reaches the noise floor of the measuring system. Theoretical predictions show almost similar initial drop, and it is in good agreement with the measured values.

The propagation mechanism between the base station and the mobile receiver is best explained with the assistance of Fig. 4. This figure shows the electric field strength of reflected rays computed as a function of the receiver position along the road assuming an ideal transmitter radiating 0 dBW isotropically. As is evident in Fig. 4, when the receiver approaches the end of section 1, where the LOS is still being blocked, the major contributors to the received signal strength are single reflections from wall C. This yields an increase in the mean signal level of 13 dB above the noise floor of the receiver which was measured at beginning of section 1. When the receiver is in clear view of the base station (section 2), propagation is dominated by the LOS, and the mean signal level increases by 9 dB. When the direct path is blocked again as the receiver moves into section 3 the mean signal level falls by 14 dB at small distances into this shadow region. At this range the main contributors to the received signal are single reflections on wall D. When those reflections disappear, the mean signal level drops again to the noise floor.

In such microcell geometry it was noted that second order reflections are much weaker contributors to the received signal strength. Fig. 5 shows the measured and predicted mean signal level obtained by considering single reflections only with no diffractions from building edges. It can be clearly seen that the elimination of second order reflections has no effect on the mean signal level predicted in the shadow regions. However, the range over which the mean signal level remains at a high value in the shadow region, particularly over section 3, becomes smaller. This is mainly due to the exclusion of double reflections from walls AD. Predicted results shown in Fig. 5 are in better agreement with the measured ones than those given in Fig. 3.

Further predictions were also made by taking diffraction into account. It has been noted that the addition of

diffraction at this frequency has no effect on changing the mean signal level in the shadow region.

Conclusions

Experimental results of measurements made at 62.4 GHz between a fixed base station and a mobile receiver in an outdoor microcell where the line-of-sight component prevailed for a short distance and was then blocked are presented. The complex propagation mechanism is represented by a ray tracing model based on geometric optics and diffraction. A reasonably good agreement has been achieved between the measured and predicted mean signal levels by considering single reflections only and no diffractions.

When the mobile receiver is in clear view of the base station, propagation at 62.4 GHz is dominated by the direct component. At small distances into the shadow region, the propagation mode between the base and the mobile receiver is primarily by single reflections from building surfaces. At large distances, however, higher order reflections are weak, and unable to provide coverage deep inside the shadow region. The mean signal level drops sharply to the noise floor of the receiver.

Results have shown that the coverage area is limited to the LOS region and to a few metres into the shadow region where single reflections from building surfaces keep contributing to the signal strength.

References

1. Steele, R., and Prabhu, V. 1985, "Higher-User-Density Digital Cellular Mobile Radio Systems", Proc. IEE, pt. F, vol. 132, no. 5, pp. 396-404.
2. Steele, R., 1985, "Towards a High-Capacity Digital Cellular Mobile Radio System", Proc. IEE, pt. F, vol. 132, no. 5, pp. 405-415.
3. Huish, P.W., Johnson, T.A., and Nicholls, M.J., 1985, "MM-Wavelength Microcellular Mobile Radio Systems-A Solution to Spectrum Congestion for High User Densities?", Int. Conf. Land Mobile Radio, pp. 47-53, Cambridge, UK.
4. McGeehan, J.P., and Yates, K.W., 1986, "High-Capacity 60 GHz Microcellular Mobile Radio Systems", Telecommunications, vol. 20, no. 9, pp. 58-92.
5. Hammoudeh, A., and Allen, G., 1995, "Millimetric Wavelengths Radiowave Propagation for Line-Of-Sight Indoor Microcellular Mobile Communications", IEEE Trans. Vehicular Technology, vol. 44, no. 3, pp. 449-461.
6. Correia, L.M., and Lovues, G., 1994, "Outdoor Propagation Modelling and Measurements in COST231 at the Millimetre Wave Band", Report TD(094)073, Joint COST231/235 workshop, Prague, Czech Republic.
7. Thomas, H.J., Cole, R.S., and Siqueira, G.L., 1994, "An Experimental Study of the Propagation of 55 GHz Millimetre Waves in an Urban Mobile Radio Environment", IEEE Trans. on Vehicular Technology, vol. 43, no. 1, pp. 140-146.
8. Maliuzhinets, G.D., 1958, "Excitation Reflection and Emission of Surface Waves from a Wedge with a Given Impedance Faces", Sov. Phys. Dokl., vol. 3, no. 4, pp. 752-755.
9. Luebbers, R.J., 1984, "Finite Conductivity Uniform GTD Versus Knife Edge Diffraction in Prediction of Path Loss", IEEE Trans. Antennas and Propagation, vol. 32, no. 1, pp. 70-76.
10. Beckmann, P. and Spizzichino, A., 1987, The Scattering of Electromagnetic Waves from Rough Surfaces. Artech House Inc., Norwood, MA.
11. Landron, O., Feuerstein, M.J., and Rappaport, T.S., 1996, "A Comparison of Theoretical and Empirical Reflection Coefficients for Typical Exterior Wall Surfaces in a Mobile Radio Environment", IEEE Trans. Antennas and Propagation, vol. 44, no. 3, pp. 341-351.
12. Correia, L.M., and Frances, P.O., 1994, "Estimation of Materials Characteristics from Power Measurements at 60 GHz", PIMRC'94-5th IEEE Int. Symp. on Personal, Indoor, and Mobile Radio Communications, pp. 510-513. The Hague, Netherlands.
13. Jakes, Jr., W.C., 1974, Microwave Mobile Communications. New York: John Wiley & Sons, Inc.

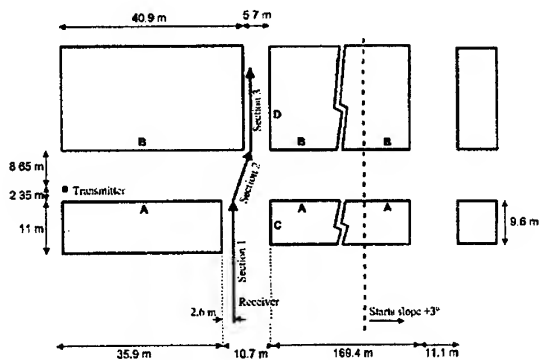


Figure 1: Measurement geometry.

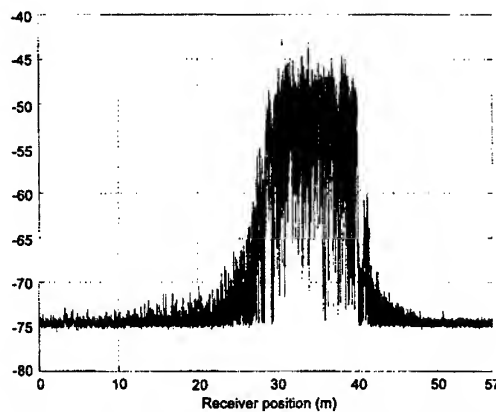


Figure 2: Received signal envelope measured when the mobile receiver travelled 57 metres along the cross road: 0-28 metres section 1: Shadow region, 28-39 metres section 2: Line-of-sight propagation, 39-57 metres section 3: Shadow region.

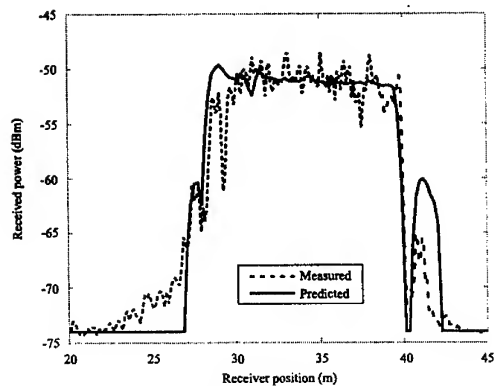


Figure 3: LOS and NLOS mean signal level as a function of receiver position. Predictions are made considering rough surfaces with $\sigma_h = 6.2$ millimetre for buildings in the main street (wall A and B). Wall C and D are assumed to be smooth. Reflections up to the second order are considered with no diffractions.

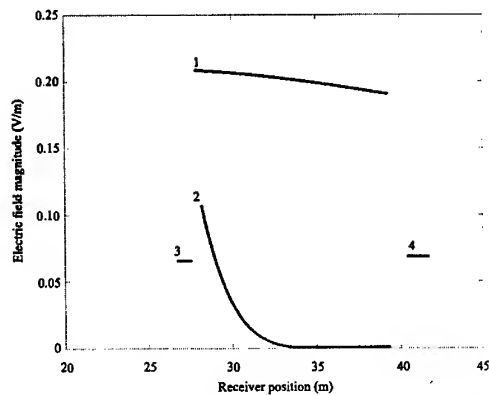


Figure 4: The electric field of the various rays as a function of receiver position. Rough building surfaces with $\sigma_h = 6.2$ millimetre are assumed for buildings in the main street (wall A and B). Wall C and D are assumed to be smooth.

- 1: Direct ray,
- 2: Single reflection on wall A,
- 3: Single reflection on wall C,
- 4: Single reflection on wall D.

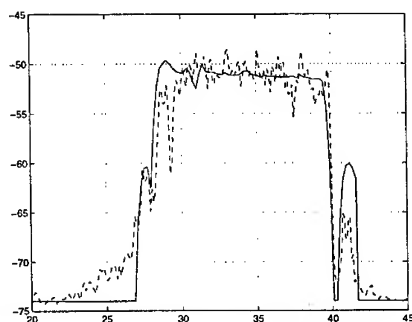


Figure 5: LOS and NLOS mean signal level as a function of receiver position. Predictions are made considering rough surfaces with $\sigma_h = 6.2$ millimetre for buildings in the main street (wall A and B). Wall C and D are assumed to be smooth. Single reflections up to the second order are considered with no diffractions.

UNIFIED APPROACH TO PREDICT OF LOS CHARACTERISTICS IN THE URBAN MICROCELLULAR ENVIRONMENTS

N. Blaunstein

Department of Electrical and Computer Engineering,
Ben-Gurion University of the Negev, P.O. Box 653
Beer Sheva 84105, Israel

M. Levin

Tadiran Communication Ltd., P.O. Box 500,
Petakh-Tikva 49104, Israel

Abstract

This work presents experimental results carried out by the communication group of Tadiran Ltd., as well as, theoretical predictions obtained both by Bertoni et al. [1, 2] and Tadiran's group [3, 4] for the estimation of the effectiveness of the MultiGain Wireless Local Loop (MWLL) system developed by Tadiran for use in urban areas with regularly distributed rectangular rows of buildings, when both base station antenna and the radio port antenna are at the street level below the rooftops. The experiments are examined in different propagation conditions: Line-of-Sight (LOS) along the street level, and obstructed ("clutter") conditions, when both the antennas are placed in the environment with strong shadowing surrounding them. To predict these experimental conditions, in the *first case* a model of 3D-multislit impedance waveguide (earlier developed for the 2D and 3D case of perfectly conductive waveguide in [3]) is proposed to estimate the path loss at the street level and at the street intersections [4], respectively. For the *second case* the 2D-model of multi-diffraction from the building roofs according to [1, 2] is used in conjunction with actual variations of building heights, the distances between them and the actual base station antenna height variations. The contributions in path loss is obtained to predict the experimentally observed coverage effects and the microcell shape for MGWLL systems in urban and suburban areas with regularly distributed rows of buildings and rectangularly crossing streets.

1. Principle of theoretical prediction

1.1. LOS propagation along the street

Instead the usually used "two-ray" model, consisting of the direct and the reflected-from-the-ground rays [1], in the conditions when both antennas were placed at the street level in LOS conditions, a new multislit waveguide model were proposed in [3, 4] for describing wave propagation in urban areas with straight streets and with randomly distributed walls of buildings and gaps between them as exhibited in Fig. 1.

Waveguide model. Let us consider that the buildings on the street are replaced by randomly distributed non-transparent screens with scales L_n , the electrical properties of which are defined by surface impedance Z_{EM} ; the distances between the buildings (slits) we define as l_n , $n=1, 2, 3...$ (see Fig. 1). The laws of their differential distribution are postulated as independent and exponential with mean values $\langle L \rangle$ and $\langle l \rangle$ respectively, the probability density functions being given by

$$\langle L \rangle^{-1} \exp\{-L_n/\langle L \rangle\}, \quad \langle L \rangle^{-1} \exp\{-L_n/\langle L \rangle\}, \quad n=1, 2, 3... \quad (1)$$

The impedance parallel plane waveguide with randomly distributed buildings along the street models a city street with receiver and transmitter at street level below the rooftops. One waveguide plane is placed at the waveguide side $z=0$, and the second one at $z=a$ ("a" is the street width, see Fig. 1). We also assume that a vertical electric dipole as a real transmitter is placed in the xz -plane with coordinates $x=h_T$; $y=0$; $z=d$, where $0 < d < a$ on the z -axis; $0 < h_T < h_b$ on the x -axis; h_T is the transmitter height; h_b is the average building height. We present the full field as a superposition of a direct wave field from the source, fields reflected from the road and then from the walls, and fields diffracted from the building edges [3, 4]. Alternatively, the resulting field can be considered as a sum of the field arriving at the receiver, placed at height h_R , from the virtual image sources as schematically presented in Fig. 1. According to the approach proposed in [3, 4] we also introduce here the "telegraph signal" functions, $f_1(y)$ and $f_2(y)$, which equal 1 when reflection or diffraction from the walls (screens) takes place and zero when rays pass through the spaces between the buildings, i.e. fall into the slits of the waveguide. Thus segments with $f_{1,2}(y)=1$ represent screens including their edges, but segments with $f_{1,2}(y)=0$ represent slits (see Fig. 1). The real electric properties of screens (walls) are defined by the surface electric impedance $Z_{EM} \sim \epsilon^{-1/2}$, $\epsilon = \epsilon_0 - i4\pi\sigma/\omega$, where ϵ is the dielectric permittivity of the wall surface; ϵ_0 is the dielectric constant of vacuum; σ is the electric conductivity of the wall surface; ω is the angular frequency of the radiated wave, $\omega = 2\pi f$, f is the frequency of the radiated wave.

The full field inside the street waveguide can be presented as a sum of the direct field from the source and rays reflected and diffracted from the building walls and corners. In order to calculate the full field from the source we substitute for each reflection from the walls an image source Π_n^+ (for the first reflection from the left-hand walls of the street waveguide) and Π_n^- (for the first reflection from the right-hand walls), where n is the number of the reflections (see Fig. 1).

Average field intensity along the street. To calculate the average total field along the street waveguide we, as in [3, 4], take into account the exponential screens and slits distributions (1), the transmitter antenna as a vertical electric dipole with field $\sim |D| \exp\{ikR\}/4\pi R$, and the simple evaluations from the GTD, in which the formulations of diffracted waves are similar with those obtained for reflected waves and in which the reflection coefficient Γ_n of each reflected wave from the screen (wall) is simply replaced with a diffraction coefficient D_{nm} for each diffracted ray from the wall's edge [3, 4]. Here $R=|r|$ is distance from the source; $D=(4\pi i/\omega)p_z$; p_z is the electric momentum of a vertical electric dipole; $k=2\pi/\lambda$ is the wave number, and λ is the wavelength ($\lambda \ll a, l_n, L_n$). Using the procedure of averaging arbitrary order moments of "telegraph signal" functions $f(y)$, presented in [3, 4] and combining the reflected and diffracted waves with the direct wave (LOS component) from the source, we obtain the total average field in the broken impedance waveguide:

$$\begin{aligned} \langle I \rangle \approx & C^2 \Gamma_g^2 [|\Gamma_n| + |D_{nm}|]^2 r^{-1} \exp\{-|\ln M[\Gamma_n]|[(\pi n - \varphi_n)/a]r/\rho_n^{(0)}a\} + \\ & + D^2 \Gamma_g^2 [1 - (M[\Gamma_n])^2]/[1 + (M[\Gamma_n])^2]^2 r^{-2} \end{aligned} \quad (2)$$

Here $M = \langle L \rangle / (\langle L \rangle + \langle l \rangle)$ is the parameter of brokenness; $C = \{(D)^{1/2} \lambda / (2h_T h_R)^{1/2}\} [h_T h_R / a^2 + h_b / a + 1]^{-1/2}$; $D = |D|$; the coefficient of reflection for each reflected waveguide mode, Γ_n , can be presented as: $\Gamma_n = (K_n - kZ_{EM}) / (K_n + kZ_{EM})$, $K_n = (\pi n + i|\ln M|) / a = \text{Re}K_n + i\text{Im}K_n$; $n=0, 1, 2, \dots$. We do not present here the expression of the reflection coefficient Γ_g , because it is sufficiently fully described in the literature for different kinds of radiated field polarization. Let us now examine expression (2) for various actual experimental situations in the urban street scene.

Wide Avenues. Let us consider that the street width is larger than the average building heights and both antenna heights, that is, $a > h_b, h_T, h_R$. In this case at distances less than the "break point" in the approximate formula (2) the second term, which describes the direct wave and the waves reflected from the ground and which attenuates as a spherical wave $\sim r^{-2}$, is larger than the first term, which describes the attenuation of the normal reflecting modes along the multislit street waveguide. Beyond the "break point", conversely, the first term in (2) is larger, and field intensity attenuates exponentially. This law of attenuation is close to that obtained experimentally in most measurements, where the attenuation mode of field intensity beyond the "break point" was $\sim r^{-q}$, $q=5-7$. This law cannot be explained using the "two-ray" model [1]. Moreover no clear physical explanation of such "sharp" field intensity attenuation in the farthest zones from the transmitter existed until now. This effect can be clearly understood using the waveguide street model and following from it the exponential attenuation of field intensity (which is close to mode $\sim r^{-q}$, $q=5-7$) at the distances beyond the "break point". Moreover, the waveguide model, as was shown in [3, 4], continuously tends to the "two-rays" model in the case of wide streets. We can also show that the "break point" range obtained in [1], $r_b = 4h_T h_R / \lambda$, is valid only for urban areas with wide streets and that our model continuously limits to this approximate formula only for the case of $a > h_b, h_T, h_R$. In fact, let us determine the "break point" range as the range at which the first term in (2) is equal to the second one. From this condition using formula (2) we can easily obtain the range of break point:

$$r_b = (4h_T h_R / \lambda) [1 + h_b / a + h_T h_R / a^2] / [|\Gamma_n| + |D_{mn}|]^2, \quad (3)$$

which continuously (with constant $\sim [|\Gamma_n| + |D_{mn}|]^2$ in order with one for $0 < |\Gamma_n| < 1$ and $0 < |D_{mn}| < 1$) tends to $r_b = 4h_T h_R / \lambda$, obtained by [1] for the case when $a > h_b$ and $a^2 > h_T h_R$, i.e. for the case of wide streets.

Narrow Streets. In the inverse case of urban areas with the narrow streets ($a < h_b$) the approximate waveguide model (2) can be successfully used to describe the field intensity attenuation along the street in LOS conditions. As was obtained from straightforward calculations the 3D-model predicts two modes of field intensity attenuation, from r^{-2} to exponential, and the existence of a break point. But for the case of narrow streets the range of the break point is farther from the transmitter, than in the case of wide street. In fact, for the wide street we observe the break point (according to (3)) at the range of 200-220 m for $f=900-950$ MHz. At the same time for the narrow street the break point was not observed at the investigated propagation path $r < 500$ m ($r_b = 950-1000$ m for $f=900-950$ MHz according to (3)). Thus, as can be seen from estimations, following from formula (3), for $a \ll h_b$ and $a^2 < h_T h_R$, the range of "break point" tends to infinity for the observed wavelength band, $\lambda = 0.01-0.3$ m with a decreasing street width or with an increasing building height. In the inverse case of a wide street the 3D-model (2) tends to the "two-rays" model and formula (3)

transforms into that obtained in [1]. So we have a good transition from the waveguide model to the "two-ray" model in the particular case of wide avenues or canyons with building heights less than the street width. On the other hand, the waveguide multislit model, more generally than "two-ray" model, predicts the propagation characteristics in LOS conditions along straight streets.

1.2. Propagation in the obstructive conditions

In obstructive (or clutter) conditions the receiver or transmitter antennas (or both of them) are placed in the shadow zones, when there are many non-transparent buildings surrounding them. In this case the role of diffraction from the roofs of buildings increases and the total fields depend not only on the reflected, but mostly on the diffracted waves [2].

2D-model of multi-diffraction. Let us consider that an elevated antenna (base station) radiates a field that propagates in an environment with regular distributed non-transparent buildings with various heights h_i and different separation distances d_i ($i=1,2,3,\dots$) between them. The height of the base station antenna, H , can be greater or smaller than the first (near the antenna) building height, h_1 .

We here consider that $H > h_1$ (see Fig. 2), because this condition is closed to our experiments in "clutter" conditions of both receiving and transmitting antennas. In this case when the base antenna is higher than the first building, the radiating field propagates over the rooftops by a process of multiple diffraction past rows of buildings (Fig. 2). The field reaching street level results from diffraction of the fields incident on the rooftops in the vicinity of the receiving antenna.

Contributions in path loss. Treating the base station as a transmitter and assuming that the receiver is at street level, we can obtain the path loss in dB as the sum of the free space path loss $L_0 = -10 \log_{10}\{(1/4\pi R)^2\}$, and excess loss L_{ex} , i.e., $L_{Total} = L_0 + L_{ex}$. For the case of our experiments (see below) when angle α_N (see Fig. 2) is small, $\alpha_N = \tan^{-1}\{(H-h_N)/R\} \approx [H - h_N]/R$, we can present expression for L_{ex} in the case of various parameters h_N and d_i (see Fig. 3) according [2] as:

$$L_{ex} = 57.1 + 5 \log_{10}[x^2 + (h_N - h_r)^2] - 9 \log_{10}[\sum d_i/N] + \\ + 20 \log_{10}\{\tan^{-1}[(h_N - h_r)/x]\} - 18 \log_{10} H + \log_{10} f + 18 \log_{10} R. \quad (4)$$

Here the total distance between the base station and radio port, R , is in km; the radio wave frequency, f , is in MHz.

2. Comparison with experimental data

The first series of measurements were taken in the small town of Kefar-Yona, Israel, where the MGWLL system of Tadiran was under trial in conditions of direct visibility along the street (LOS conditions, position I of the moving radio port in Fig. 3), and in the obstructed conditions of existing shadow zones between receiver and transmitter (positions II, III, ... of the moving radio port in Fig. 3). The omnidirectional base station antenna was located at the same (or lower) level than the buildings' roofs, at a distance of 4-5 m from the corner building surface as depicted schematically in Fig. 3. The mobile omnidirectional radio port antenna changed its position along the street in the middle of the road in LOS conditions (Fig. 3). The tested MGWLL system was operated in the frequency band $f=902-928$ MHz. The tested environment is a typical

small urban or suburban region of two- and three-storied brick buildings with approximately uniform heights $h=7-8$ m and with a right-angle crossing straight street plan (as schematically presented in Fig. 3). The base station transmitter antenna was installed at the height $h_T=8$ m; the moving radio port antenna was lower than rooftop level ($h_R=2-3$ m). The tested cell radius of such an area estimated from measurements was approximately 1-2 km. Field intensity measurements in dB relative to intensity in free space at the range $r=100$ m were obtained to estimate the path loss and the field intensity attenuation in LOS conditions along the street, taking into account actual dielectric properties of the brick walls of buildings and the real distribution of buildings along the street level.

Let us compare the theoretically obtained formulas, both for LOS and "clutter" conditions, with Tadiran's experimentally measured received signal power's spatial distribution in the urban area investigated. Taking into account that the angle α_N from the base station antenna at the top of the N -th building (see Fig. 3) is small in the real conditions of the experiment, we used expression (4) to estimate the path loss in obstructive conditions for the moving radio port. For the LOS conditions in our calculations we used formula (2). From the net of measurements the "diamond"-shape of coverage curves of field intensity attenuation in the suburban area was obtained (the base station is located in its center, as pointed in Fig. 4). In this picture the values of intensity loss near the each curve obtained experimentally and the values in circles, calculated according to formulas (2) and (4), are also presented. As can be seen from picture presented in Fig. 4, the coverage curves are elongated along the main road, where the base station is located. We also can notice from comparison between experimentally and theoretically obtained values of signal power loss that for urban areas with a sufficient shadowing between receiver and transmitter when the transmitter antenna is near the rooftops level (the angle α_N from the transmitter at the top of last building near the receiver is small), we can use formula (4) with great accuracy. Comparison between measurements in the LOS conditions and values obtained from 3D-multislit impedance waveguide model showed that formula (2) can be used for the estimation of path loss along the straight streets at ranges less than 500-1000 m from the transmitter.

Conclusions

In the propagation of radio waves in urban and suburban areas with regular distributed low-storied buildings and with the transmitter antenna below the rooftops or at their level, the common theoretical approach developed by Bertoni et al. [2] can be successfully used for estimations of field intensity attenuation in obstructive conditions taking into account the real distribution of their heights and distances between them. In LOS conditions, the 2D- and 3D-waveguide models (which depends on the geometry of the street and the distribution of buildings along the street level), proposed in [3, 4] and generalized in this work, give a good explanation of the field intensity attenuation along the street level for urban conditions, when the average streets' width is smaller ("works" 2D-model) and larger ("works" 3D-model) than the average buildings' height, and when the range from the transmitter antenna does not exceeds 500-700 m. These two approaches can be successfully used for the prediction of personal and mobile communication channels in urban and suburban environments with grid-plan of crossing straight streets for the microcells with effective sizes not more than 1 km, using the real distribution of building heights and the distances between them.

References

1. H.H. Xia, H.L. Bertoni, L.R. Maciel et al., IEEE Trans. Anten. and Propag., vol. 41, no. 10, pp. 1439-1447, Oct. 1993.
2. L.R. Maciel, H.L. Bertoni, and H.H. Xia, IEEE Trans. Vehic. Technol., vol. 42, no. 1, pp. 41-45, Feb. 1993.
3. Blaunstein, N and M. Levin, Radio Sci., vol. 31, pp. 313-323, March-Aprile 1996.
4. Blaunstein, N and M. Levin, Radio Sci., vol. 32, pp. 115-131, Jan.-Feb., 1997.

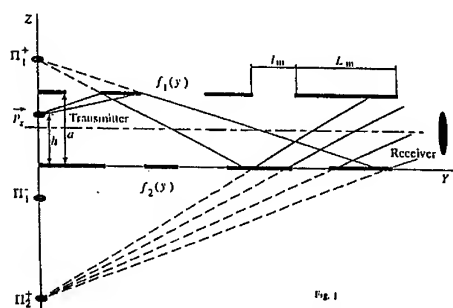


Fig. 1

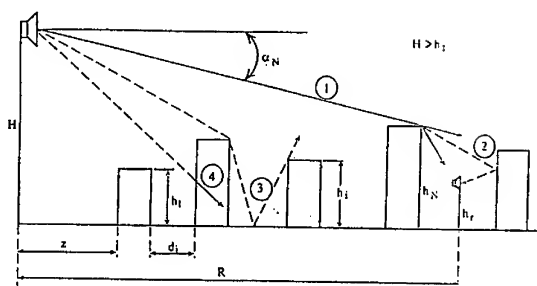


Fig. 2

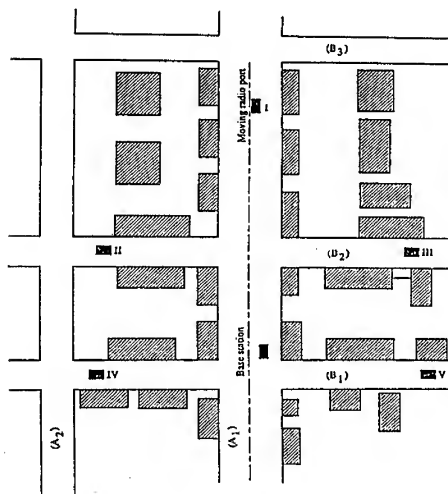


Fig. 3

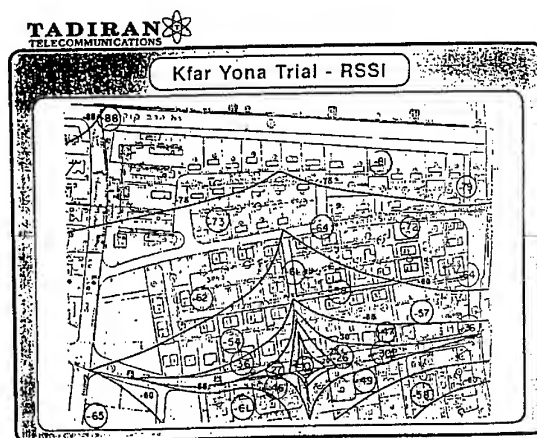


Fig. 4

CHARACTERIZATION OF mm-wave INDOOR PROPAGATION WITH DIRECTIVE ANTENNAS

Guido RIVA*, Vittorio DEGLI-ESPOSTI**, E. DE PONTI***, L. FERRUCCI***, E. PAPA***

* Fondazione Ugo Bordoni, Bologna

** Università degli studi di Bologna

*** ITALTEL spa a Stet and Siemens Company (Cassina de' Pecchi - Milan)

Villa Griffone, I-40044 Pontecchio Marconi, Bologna

Tel: +39 51 846854; Fax: +39 51 845758; e-mail: griva,vdegliespsti@deis.unibo.it

Topic #2, scientific paper

Abstract

The rapid and widespread demand for new services, as high-speed data and multimedia services, which are very demanding in terms of bitrate and thus bandwidth, are increasing the interest toward broadband applications. The aim of the work is to study if and when the selective fading can be effectively coped with by the adoption of directive antennas, so exploiting the inherent angular diversity of the communication channel. The achievable improvements are highlighted and some suggestions for the design of future millimeter wave wireless LANs are provided. The investigation is accomplished by means of an electromagnetic computer model, based on a fully 3D ray tracing approach. The adopted algorithm has been validated by comparison with some test measurements both at 30 and 60 GHz, whereas the adopted electromagnetic parameters have been estimated by means of specific measurements of the materials characteristics.

Introduction

The high flexibility of radio communication networks is greatly encouraging the use of indoor wireless transmission for many applications. Earlier solutions dealt with voice and/or low rate data applications; recently, the importance of new services, as high-speed data and multimedia services, which are very demanding in terms of bitrate and thus bandwidth, has raised up and an increasing interest has been devoted to broadband applications.

Among possible frequency bands for WLANs, millimeter wave bands, and particularly the 30 GHz and the 60 GHz bands, are two of the most suited candidates, as they offer a large amount of free bandwidth [1-4]. A number of interesting studies have been devoted to the latter [6-8], as it provides some well known advantages, such as the oxygen attenuation peak and large allocated bands, whereas the former is still quite unexplored, both from an electromagnetic characterization point of view and indoor WLAN potential applications. They are both very attractive due to the strong wall attenuation, which could contribute to minimising the interference between adjacent LANs, whereas the small involved wavelengths allows reduced antenna size. Correspondingly, suitable wideband measurement campaigns have to be carried out, in order to get some deeper insight on the propagation mechanism at those frequencies and in order to validate the adopted RT program at both millimeter frequencies.

In order to ensure a reliable and error free radio transmission at 100 Mbit/s or more in an adverse multipath propagation environment such as the indoor one, a possible solution, among the others, might consist in the adoption of directive antennas, taking advantage both of the increased antenna gains and of the rejected multipath components arriving at

the receiver outside the main beam [2,10-12]. This technique can be eventually viewed as the exploitation of a spatial (angular) diversity.

In order to investigate the potential improvements from the usage of directive antennas, which is the aim of this paper, an accurate propagation channel characterisation is highly recommended. Since experimental sounding is very expensive and time-consuming, computer models and above all ray tracing tools represent a valid alternative. On the other hand, the candidate ray tracing (RT) program has to be appropriately validated at millimeter frequencies by comparison with measurement results, both in terms of narrowband and wideband statistics [5]. We will show that the adherence is quite satisfactory, even in the case of coarse RT environment description, allowing to conveniently characterize multipath fading and extracting the most important propagation parameters.

Ray tracing program

Ray models have been recently acknowledged as the most suitable tools for indoor microwave radio propagation modelling. The validity of the ray approach could be put into question when the wavelength is comparable with the size of the environment and/or of its disomogeneities (i.e.: walls, furniture, etc.), which is the case of UHF radio. On the contrary, in the millimeter wave case the ray approach is certainly appropriate.

The starting point is the representation of the electromagnetic field generated by an antenna. In the ray approach, the associated spherical wave is represented as a set of straight rays having their origin in the antenna site. Each ray can be associated a *local plane wave* which is the local approximation of the spherical wave. Rays can experience reflection, transmission, diffraction and diffuse scattering actions due to the presence of obstacles. Since diffraction contribution at millimeter wave frequencies is very small it has been neglected here. In the present work we take into account walls, floors, ceilings, doors, windows, columns, etc. Every obstacle is modelled as a set of basic plane walls producing reflection and transmission. Each wall is a slab described by its electromagnetic properties (dielectric constant, magnetic permeability, conductivity) and is assumed to have a smooth surface. Thanks to the high frequency involved, multiple reflection effects into the slab have been neglected [7].

Due to reflections, transmissions or diffractions a ray-tree is produced in which each node is a wall (or the receiver), each branch a sub-ray and the root is the transmitter [9]. All the rays whose paths reach the receiver location should be considered when calculating the received signal, and all the corresponding field contributions at the receiver must be weighted with the receiving antenna's radiation characteristics and added according to their relative amplitudes and phases at the Rx point. The depth of the tree is truncated to three in our case, which has been found to give stable results in all cases.

Measurements

The 30 GHz measurement campaign has been performed inside the laboratories of ITALTEL in Cassina de' Pecchi (Italy). A wideband coherent measurement procedure has been followed using an HP85107A network analyser in order to provide reliable amplitude+phase channel measurements. The frequency response of the channel has been sounded over 801 equi-spaced points in the band [29.5,31] GHz thus achieving a time resolution of about 1 ns and an aliasing-free time range of 530 ns. Both Tx and Rx are linearly polarized reference horns with a 3dB beamwidth of about 8° and a gain of 27 dB.

We aimed at suitably characterizing the materials and to compare the measured channel impulse response with the outputs of the RT simulation program. The former issue has been accomplished within an anechoic room in this way: a transmitting horn antenna is directed toward a slab of the considered material; the maximum gain direction of the receiving antenna, equal to the transmitting one, is adjusted in order to accurately receive the reflected wave; then the field reflected by the slab is measured by means of the network analyzer (S₁₂ mode), with port 1 connected to the Tx input and port 2 to the Rx output.

The measurements have been repeated for five incidence angles (10° to 50° at 10° steps) and the corresponding values have been recorded. In case of normal incidence, the Rx is located on the other side of the slab and the transmitted power is measured. The corresponding dielectric constant ϵ and conductivity σ have been estimated by means of a best fit of the reflection and transmission coefficients to a theoretical model with multiple reflections into the slab. In figure 1 it has been reported a sample of the results from this procedure. At 60 GHz, some information on the electromagnetic parameters of the materials are already available in literature [6].

In figure 2, the thicknesses providing 20 or 40 dB of attenuation have been compared at 30 and 60 GHz and for different materials. It is quite evident that the signals are severely attenuated by thin slabs of materials and thus at millimeter frequencies we can assume that walls provide a good isolation between different rooms. This is not completely true for those materials, as glass or plywood, which are usually present with comparable or smaller thickness.

In order to validate the RT program, some wideband measurements have been performed in a simple environment (an empty room, 5.8 x 10.6 x 5 m wide) and in a more complex one (an office with furnitures, 5.7 x 10.4 x 2.7 m wide). Both vertical and horizontal polarizations have been adopted as well as cross-polarized reception. The measurements have been repeated with a fixed Rx site and different Tx locations, as shown in figure 3.

In figure 4, we have reported a comparison between measured and simulated delay spreads, for different polarizations and for the two environments. It is evident that the agreement is quite good for both the environments and both polarizations (slightly better in case of horizontal polarization). In figure 5 it is shown that in case of cross-polarization the delay spread values are sensibly higher than in case of polarization, due to the absence of a strong direct path between TX and Rx; in addition, a greater variability with the location site (reported in abscissa as 1...6) comes out, with respect to the case of copolarization.

Conclusions

The potential benefits stemming from the use of directive antennas has been shown by measurement campaign [10][11]; some simplified evaluation based on geometric optics have been performed at 19 GHz [12]; here it has been accomplished by means of a more refined RT program. Figure 6 shows the impact of the antenna directivity on the average delay spread in a typical office room and in case of ideal directional antenna. It is evident that when the main lobe aperture decreases, the delay spread decreases accordingly. It could be shown that even in case of spatial diversity, the diversity gain could benefit from the presence of directive antennas and it can take advantage from an appropriate choice of the Base Station location: the corresponding results are not reported here for sake of brevity.

References

- [1] P.F.M. Smulders, "Broadband wireless LANs: a feasibility study," Ph.D. Thesis, Eindhoven University of Technology, The Netherlands, 1995
- [2] M. J. Gans, R. A. Valenzuela, J. H. Winters, M. J. Carloni. High data rate indoor wireless communications using antenna arrays. The sixth IEEE PIMRC, Toronto, Canada, September 27-29, 1995.
- [3] A. M. Hammoudeh and G. Allen, "Millimetric wavelengths radiowave propagation for line-of-sight indoor microcellular mobile communications," IEEE Trans. Veh. Tech., vol. 44, No. 3, pp. 449 - 460, August 1995.
- [4] K. Uehara, T. Seki, K. Kagoshima, "New indoor high-speed communication system," 45th IEEE Vehicular Technology Conference, pp. 996 - 1000, Chicago, IL, July 1995.
- [5] G. E. Corazza, V. Degli Esposti, M. Frullone, G. Riva, "A Characterization of Indoor Space and Frequency Diversity by Ray-Tracing Modelling," IEEE Journal on Selected Areas in Communications, Vol. 14, No. 3, pp.411-419, April 1996.
- [6] L. Correia and P. O. Frances, "Estimation of material characteristics from power measurements at 60 GHz," IEEE PIMRC'94, The Hague, The Netherlands, Sept. 1994.
- [7] L. Correia and P. O. Frances, "Transmission and isolation of signals in buildings at 60 GHz," The sixth IEEE PIMRC, Toronto, Canada, September 27-29, 1995.
- [8] V. Degli-Esposti, G. Falciasacca, M. Frullone, G. Riva, "Narrowband characterization of 60 GHz radio propagation in indoor environment," Annals of telecommunications, special issue on millimeter waves, 1997. To be published.
- [9] - Pietro Daniele, Vittorio Degli-Esposti, Gabriele Falciasacca, Guido Riva, "Field prediction tools for wireless communications in outdoor and indoor environments," IEEE MTT-S European Topical Congress "Technologies for Wireless Applications", Turin, Italy, November 2-4, 1994.
- [10] -P.F.M. SMulders and A.G.Wagemans "Wide-band measurements of mm-wave indoor radio channels" PIRMC '92, Boston, MA, Oct.92, pp.329-333.
- [11] -R. Khayata and C.-C. Huang "Characterizing wireless indoor communications: measurements in the ISM band with a directional antenna" PIRMC '92, Boston, MA, Oct.92, pp.315-319.
- [12] -P.F.Driessen. "Gigabit/s indoor wireless systems with directional antennas". IEEE Trans. Comm. (1996), vol. 44, No. 8, August 1996, pp. 1034- 1043.

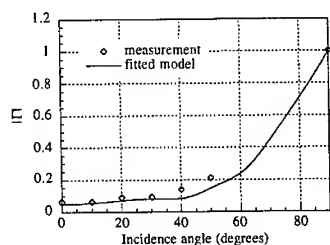


Figure 1 - Fitting of reflection coefficient amplitude for plywood to measured values.

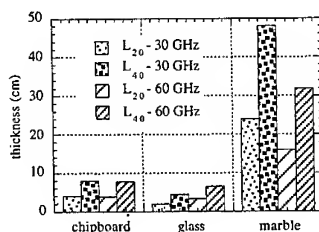


Figure 2 - Thickness providing an isolation of 20 (L_{20}) and 40 (L_{40}) dB for the three reported materials at both 30 GHz and 60 GHz [7].

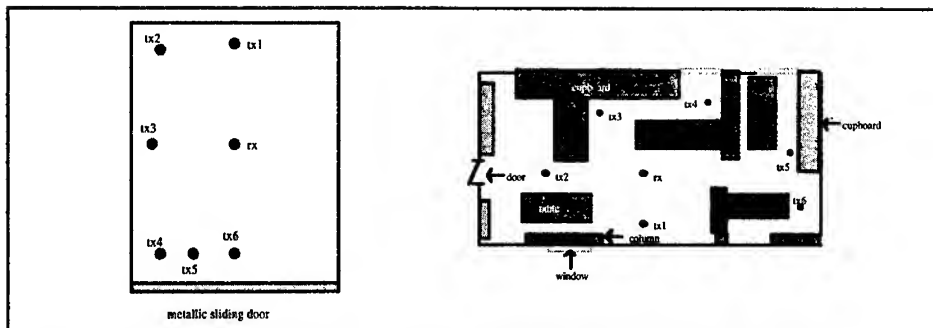


Figure 3 - The two considered environment: an empty room (5.8 x 10.6 x 5 m) and a furnished office (5.7 x 10.4 x 2.7 m), with the corresponding Tx and Rx locations.

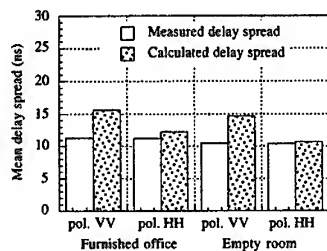


Figure 4 - Comparison between measured and calculated delay spreads in the two considered environments and for two orthogonal linear polarizations.

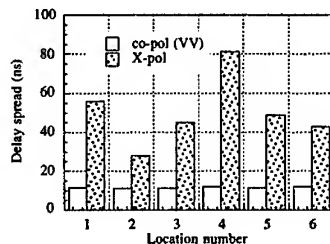


Figure 5 - Comparison between delay spread values in case of co- and cross-polarized antennas, at different locations in the furnished office (refer to figure 3 for the exact positions).

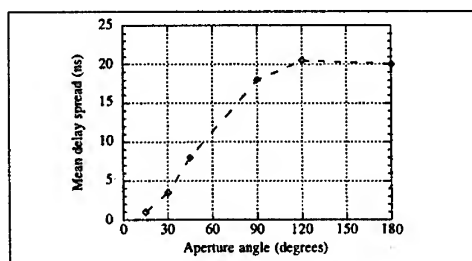


Figure 6 - Impact of main lobe beamwidth on the mean delay spread at the receiver.

A NEW TECHNIQUE FOR PERFORMANCE IMPROVEMENT OF MOBILE RADIO SYSTEMS

Milica Pejanović, Zoran Veljović

Faculty of Electrical Engineering, University of Montenegro, 81000 Podgorica, Yugoslavia

ABSTRACT: In this paper a new technique for improving quality of signal transmission over mobile radio channels with flat fading of Rayleigh statistics, is suggested. It is the technique based on implementation of 16QAM trellis modulation. After an original analytical model for such signal processing scheme is defined, the mobile radio system performance are determined through calculation of bit error rate at the system output. It is shown that the technique proposed in this paper enables better received signal quality in comparison with other known techniques such as diversity reception with various combination methods or trellis coding with phase-shift keying modulations.

I INTRODUCTION

Generally, when signal transmission over mobile radio channel is considered, the main problem causing its poor quality is fading. For land mobile radio systems that fading is flat (time and frequency non-selective) and has Rayleigh statistics. In counteracting its impact, various solutions are used. One of the well known techniques are diversity reception systems with different combining methods (maximal ratio, selection, equal gain). Nowadays, another very attractive possibility occurs. It is the implementation of trellis coding together with different modulation schemes (PSK, DPSK, QAM) in the transmitted signal.

In our previously published papers, Pejanović et al (1)-(2), we have analysed the effects of trellis coding (TC) in combination with 8PSK, DPSK and PSK with pilot tone. We have derived a general model for mobile radio system performance determination through bit error rate calculations which could be used for fading of various statistics as well as for different modulation methods combined with trellis coding. Also, we have shown that analysed trellis modulation methods enable significant performance improvement. However, we have proved that their efficiency in comparison with diversity receiving systems with reasonable number of branches (2 or 3) is not much better. Despite the thing that TCM schemes are much easier for physical implementation than diversity systems, we have thought that even better effects could be obtained through their modifications. That is why we have decided to analyse further and find a technique which could obtain considerably better signal quality than solutions already analysed by us or by other authors.

In this paper, we suggest a technique based on two very attractive elements for use in channels with Rayleigh fading: trellis coding and 16QAM. The way of implementation these elements presented here is original and haven't been encountered in literature.

II SYSTEM OVERVIEW

Fig.1 gives generalized block diagram of the mobile radio system with trellis coded 16QAM. An input binary sequence a produces at the output of the trellis coder+16QAM circuit sequence $C_i = (c_{i1}, \dots, c_{ik}, \dots)$, with C_i being i th codeword of the TCM scheme. At the interleaver output, the codeword $C_i' = (c'_{i1}, \dots, c'_{ik}, \dots)$ is obtained having the symbol duration T . Codewords C_i' gives transmitted signal $s(t)$ after passing the pulse shaping filter whose complex impulse $p(t)$ satisfies Nyquist criteria for zero intersymbol interference. $s(t)$ is subjected to flat Rayleigh fading as well as white Gaussian noise. Rayleigh fading is introduced by multiplicative factor $g(t)$ defined as zero mean, complex Gaussian process with variance σ_g^2 . Gaussian additive noise is described with its complex envelope $n_w(t)$ having zero mean, double-sided power spectral density N_0 and variance $\sigma_n^2 = 1$.

At the receiver end, output of the matched filter is sampled every T seconds and samples values at the deinterleaver output are given with r_k . At the other side, at the output of the channel estimator/deinterleaver samples values v_k appear. Further on, MLS estimation is performed for received sequences r and v , giving at the decoder output the sequence $C_j = (c_{j1}, \dots, c_{jk}, \dots)$. Assuming optimum decoder, the codeword C_j with the largest a posteriori probability $P(C_j | r, v)$ is selected, Divsalar and Simon (3).

In this analysis the realization of 16-state trellis encoder is specially focused. In literature, Proakis (4), some solutions could be found based on 8-state trellis encoder with another added input bit and delay circuit. However, our analyses show that such type of coder causes parallel transitions in trellis diagram which further on significantly degrade performance of the mobile radio system considered. Thus, a new structure for 16-state trellis encoder is given (Fig.2). It could be noticed that the proposed coder has an additional delay circuit as well as adder so that the complete Ungerboeck's mapping of 16QAM symbols is performed. In that way elimination of all parallel transitions that appears in trellis diagrams of the known coders is obtained. Fig.3 shows trellis diagram for the proposed coder structure.

III SYSTEM PERFORMANCE DETERMINATION

Using the general analytical model for bit error determination, precisely described in Pejanović et al (1), the following closed form expression for probability of error is obtained:

$$P_b \approx \frac{1}{n} \sum_i m_{ij} P(C_i \rightarrow C_j) \quad (1)$$

where: n is the number of input bits per encoding interval, m_{ij} is the number of errors for every error event, $P(C_i \rightarrow C_j)$ is the probability of confusing codeword C_i with codeword C_j . In implementing above general expression when 16QAM is considered, it is very important to notice that $P(C_i \rightarrow C_j) \neq P(C_j \rightarrow C_i)$ (for 8PSK these probabilities are equal). The reason for this could be seen from signal constellations (Fig.4), i.e. for 16QAM magnitudes aren't the same for all signal points. Actually, three groups of signal points

could be identified as it could be seen from the given signal constellation diagram. First group with magnitude $\sqrt{2}\varepsilon$ (and signalling probability 1/4) is denoted with "o", the second group with magnitude $3\sqrt{2}\varepsilon$ (and signalling probability 1/4) is denoted with "+" and the third group with magnitude $\sqrt{10}\varepsilon$ (and signalling probability 1/2) is denoted with "**". For every of these three groups with signalling probabilities p_1, p_2 and p_3 , probabilities of confusing two codewords could be found and then an appropriate bit error rates at the output of the considered mobile radio system are calculated. If the symbols from the group "o" are transmitted, bit error rate is P_{b1} . For the symbols from the group "+" bit error rate is P_{b2} , while for the symbols from the group "**" bit error rate is P_{b3} . These bit error rates P_{bh} ($h=1,2,3$) are defined with relation (1), where:

$$P_h(C_i \rightarrow C_j) = \begin{cases} -\sum \text{Residue} \left[e^{s\delta_h} \frac{\Phi_h(s)}{s} \right]_{RP}, & \delta_h \leq 0 \\ \sum \text{Residue} \left[e^{s\delta_h} \frac{\Phi_h(s)}{s} \right]_{LP}, & \delta_h > 0 \end{cases} \quad (2)$$

$$\Phi_h(s) = \left(\prod_k \frac{1 + |c_{jk}|^2 (1 - |\mu_h|^2) \gamma_{sh}}{|\mu_h|^2 d_k^2 \gamma_{sh}} \right) \cdot \left(\prod_k \frac{-1}{(s - p_{1k})(s - p_{2k})} \right) \quad (3)$$

In the above relations s is complex variable, μ_h is correlation coefficient between random variables $Ag_k c_{ikh}/(N_0)^{1/2}$ and v_k , where A is constant, g_k is sample of random process $g(t)$ and v_k are signal samples at the output of channel estimator/deinterleaver which are Gaussian random variables with zero mean and variance σ_v^2 . δ_h is given with the relation:

$$\delta_h = \ln \left(\prod_k \frac{|c_{ik}|^2 (1 - |\mu_h|^2) \gamma_{sh} + 1}{|c_{jk}|^2 (1 - |\mu_h|^2) \gamma_{sh} + 1} \right) \quad (4)$$

In the relation (3) d_k^2 is the squared Euclidean distance between c_{ik} and c_{jk} , while p_{1k} and p_{2k} are the left plane and right plane poles of the complex function $\Phi_h(s)$, respectively.

In the relations (3) and (4), variables γ_{sh} are defined as: $\gamma_{s1}=18\varepsilon/N_0$, $\gamma_{s2}=2\varepsilon/N_0$ and $\gamma_{s3}=10\varepsilon/N_0$. Also, the parameters $|c_{ik}|_h^2$ have

the following values: $|c_{ik}|_1^2 = 18$, $|c_{ik}|_2^2 = 2$ and $|c_{ik}|_3^2 = 10$.

Finally, bit error rate at the output of the considered mobile radio system with implemented trellis coded 16QAM, could be found using the general approach for total probability:

$$P_b = \sum_{h=1}^3 P_h \cdot P_{bh} \quad (5)$$

When ideal coherent detection in the receiver is used then the coefficient $|\mu_h| = 1$ for every value of h and δ_h is equal zero, so that:

$$P_h(C_i \rightarrow C_j) = -\sum \text{Residue} \left[\frac{\Phi_h(s)}{s} \right]_{RP} \quad (6)$$

with:

$$\Phi_h(s) = \left(\prod_k \frac{1}{d_k^2 \gamma_{sh}} \right) \cdot \left(\prod_k \frac{-1}{(s - p_{1k})(s - p_{2k})} \right) \quad (7)$$

Some of the obtained results for bit error rate versus signal-to-noise ratio per bit $\gamma_b = \varepsilon/(nN_0)$, at the output of the mobile radio system with trellis coded 16QAM realized by means of the proposed 16-state coder, are given in Fig.5. The same diagram presents the bit error rate values not only for the proposed 16-state coder structure but for other 8-state coder solution usually used in transmitting data over voice channels. The results shown clearly prove advantages of the suggested 16-state coder structure from the point of the system performance.

In Fig.6 comparison of bit error rates for the considered trellis coded 16QAM scheme and other known and previously analysed techniques for performance improvement is given. It is obvious that TCM 16QAM technique with an appropriate designed 16-state trellis encoder, gives significant improvement of the mobile radio signal quality. Also, the comparisons show that it is not only easier for physical realization, but it is more efficient than diversity receiving systems or trellis coding with phase modulations.

IV CONCLUSION

A new technique for obtaining better received signal quality in mobile radio systems is suggested. It is the technique based on 16 QAM trellis coded modulation implemented on transmitted signal corrupted by Rayleigh fading. A structure of the overall system is given. Problem of right design for 16-state trellis encoder is also investigated and an original solution is given. Modifying general,

previously derived analytical model, bit error rate at the considered system output is determined. Comparing the results obtained for the TCM 16QAM technique with the results for other known techniques, its advantages are clearly shown.

V REFERENCES

- (1) M.Pejanović-Đurišić, Z.Veljović, Z. Petrović, "Error rates for trellis coded PSK modulation with pilot tone in time-selective fading channel", 1996, Proceedings of the International Conference on Communication Technology ICCT'96 - Beijing, China, vol. I, pp. 540-543.
- (2) M.Pejanović-Đurišić, Z.Veljović, Z. Petrović, "Evaluation of trellis coded modulation effects in time-selective fading mobile radio channel", 1996, Proceedings of the 26th European Microwave Conference - Prague, Czech Republic, vol. I, pp. 55-58.
- (3) D.Divsalar and M.K.Simon, "The design of trellis coded MPSK for fading channels: Performance criteria", 1995, Trans. on Comm., vol.46, pp. 1004-1012.
- (4) J.G.Proakis, "Digital Communications", 1989, McGraw-Hill, New York.

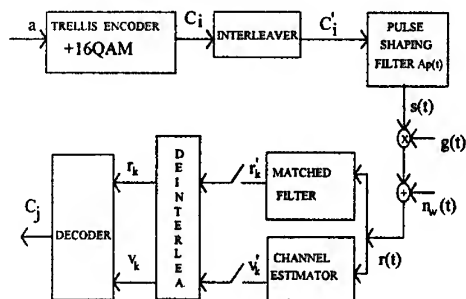


Fig.1. Generalized block diagram

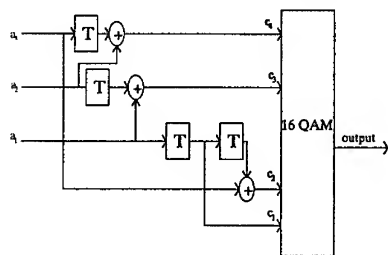


Fig.2. Structure of the proposed 16-state coder

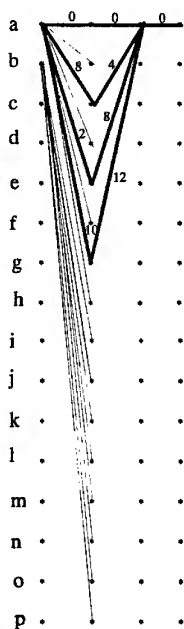


Fig.3. Trellis diagram for the proposed 16-state coder

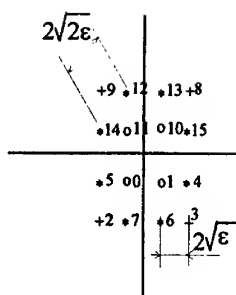


Fig.4. 16QAM signal constellation

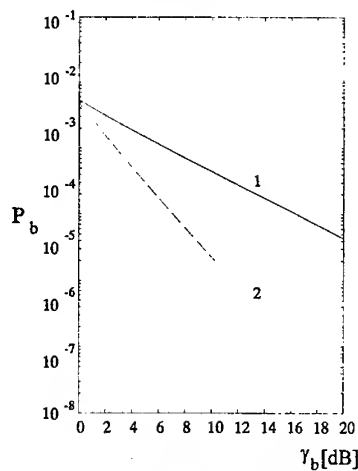


Fig. 5. Bit error rates for TCM 16QAM
1- for trellis coder with 8 states
2- for trellis coder with 16 states

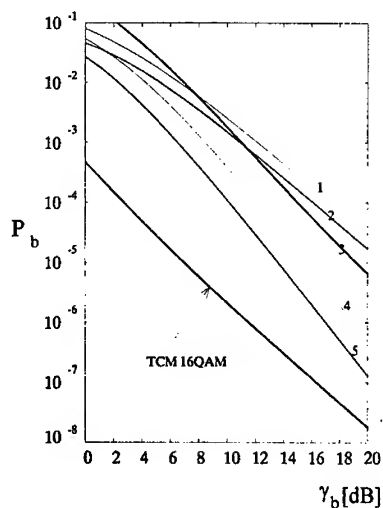


Fig.6. Bit error rates for suggested technique, and other known solutions:

- 1- diversity with selection, $M=2$
- 2- diversity with max. ratio, $M=2$
- 3- TCM 8PSK
- 4- diversity with selection, $M=3$
- 5- diversity with max. ratio, $M=3$

Interoperable 5.8 GHz DSRC Systems as Basis for Europeanwide ETC Implementation

Wolfgang Detlefsen, Wilhelm Grabow

Robert Bosch GmbH, Advanced Development Communications,
FV/SLH, Robert Bosch Str. 200, D-31139 Hildesheim, Germany

Phone: +49 5121 493903, Fax: +49 5121 492538, email: wolfgang.detlefsen@fr.bosch.de

INTRODUCTION

Among the most requested new services in the field of Intelligent Transport Systems (ITS) are Electronic Toll Collection (ETC) on highways and automatic access control to restricted areas, e.g. parking lots. They provide financing of new roads, tunnels and bridges and their maintenance, higher driver comfort, fluent traffic, reduction of manual operations and reduction of toll plaza sizes. Several field trials such as on the German A555 in 1994 and 1995 have been carried out to prove the reliability of different technical solutions. The majority of road operators in Europe demand interoperable 5.8 GHz Dedicated Short Range Communication (DSRC) systems for these road traffic applications. All existing 5.8 GHz systems use the same general principle for data transmission and work with transponders on the vehicle side. Although major parameters especially for the RF-part are identical, there are some essential differences between the existing solutions of electronic suppliers concerning type of uplink modulation, polarization of waves, data rates and protocols. Furthermore, there are only little common structures in the specified ETC applications and related data contents of the money transactions respectively. Since 1991, European electronic suppliers, car manufacturers, road operators, authorities, universities and institutions are working intensively on standardization. This paper gives an overview about DSRC standardization, technical concept of the physical layer of 5.8 GHz DSRC, examples of roadside and vehicle equipment and advanced solutions for future multilane ETC.

STATUS OF DSRC STANDARDIZATION

The European standardization body CEN TC 278 WG 9 is responsible for the overall system design of DSRC. CEN (Comité Européen de Normalisation) has the leading position within ISO DSRC standardization as well. Since 1995 most of the technical work is finalized and documents on draft standards are available for physical (1), (2), data link (3) and application layers (4). Although an infrared solution is specified for the physical layer as well, an interoperable approach for Europe is seen for the 5.8 GHz medium only. Major manufacturers of DSRC systems have started the development of vehicle and infrastructure equipment for the 5.8 GHz frequency band based on these draft standards. Despite the failure of the first national voting procedure in spring 1996 (due to some countries with interests in already existing systems), interoperability according to the draft CEN documents as a de facto standard is prescriptive in recent call for tenders e.g. the eco point system in Austria. Special DSRC sessions and demonstrations on interoperability (5) at the ITS World Congress 1996 in Orlando, Florida have pushed the possible adoption of at least some parts of the CEN proposals for the US. Furthermore, there is a good chance that the future ETC system in Korea and Australia are based on DSRC compliant to CEN draft standards. At present, members of the CEN

standard supporting group include Amtech, AT/Comm, Bosch, Cegelec, CS Route, Combitech Traffic Systems, Hyundai and Texas Instruments. A new voting on DSRC draft standards has been initiated in April 1997 by CEN and results for all layers are expected in July 1997. The layer 2 has already been approved in June 97.

In Europe, ETSI (European Telecommunication Standards Institute) is responsible for type approval of equipment and specifies mainly RF parameters and relevant methods of measurements. Currently, a draft ETSI standard (6) is in revision and will start with the voting procedure in mid 1997.

TECHNICAL CONCEPT OF DSRC

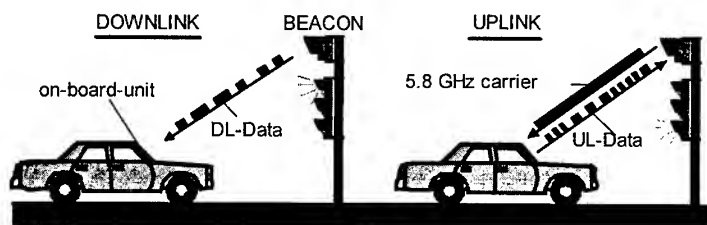


Figure 1: 5.8 GHz Dedicated Short Range Communication (DSRC)

DSRC is well suited for a bi-directional data communication between beacons located in close vicinity to a road and on board units (OBUs) behind the windshields of vehicles. Beacons can be installed in cities at poles of traffic lights or under bridges in the case of highways. Figure 1 shows a typical example for a single lane access control application. OBUs need to be available at low costs and thus from the technical point of view must be realized with little circuitry. Consequently it is necessary to apply more technical effort to the infrastructure side. In the CEN standardization process special attention was given on robustness against interference and frequency reuse distances. As a result there are different classes for spectrum parameters defined. Class C guarantees minimum frequency reuse distances. Major parameters of class C are shown in figure 2.

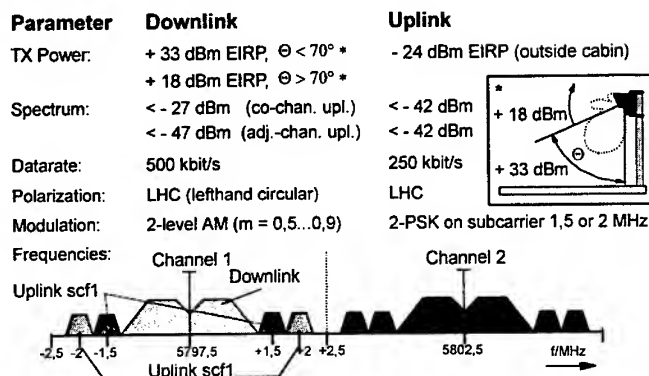


Figure 2: RF-parameter overview for class C

In downlink mode, the beacon transmits data with a rate of 500 kbit/s via amplitude modulation of a 5.8 GHz carrier to the OBU. In the simplest case the receiving part of the OBU consists of a microstrip antenna with a detector diode and a baseband amplifier. In the uplink mode (see figure 3) the OBU receives an unmodulated carrier from the beacon. The 5.8 GHz carrier is modulated with a sub-carrier at 1.5 MHz or 2.0 MHz which itself is phase modulated with the uplink data stream (250 kbit/s). By this type of modulation, two side bands appear with each containing the same information. After transmission back to the beacon, this signal is downconverted to the baseband and demodulated. The advantage of the transponder principle is very low circuit complexity on the OBU side, which does not need any frequency generating or converting components and therefore is well suited for low-cost products. Circular polarization and diversity techniques improve the communication link (7). An overview about DSRC data link layer and application layer is given in (8).

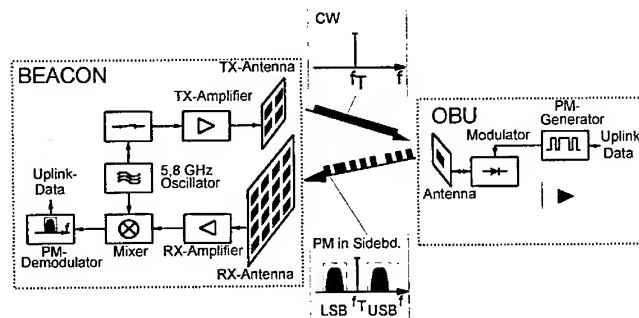


Figure 3: Block diagram of uplink communication

EXAMPLES OF DSRC EQUIPMENT

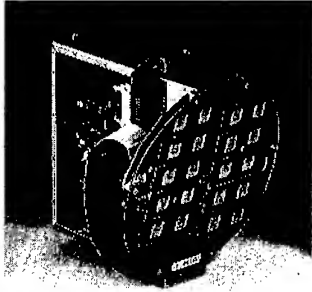


Figure 4: 5.8 GHz beacon module

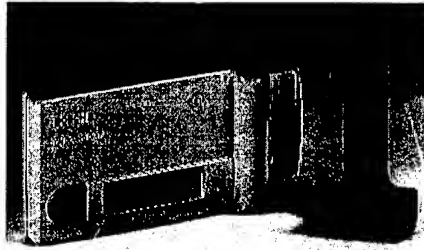


Figure 5: OBU for electronic toll collection

Complete systems for interoperable DSRC based on CEN draft standards will be available on the market by the end of 1997. Some typical examples of upcoming products are shown in this chapter. Figure 4 shows a roadside beacon module that includes all necessary functions for DSRC physical layers, data link layer and application layer. It can be installed in a traffic light housing and work as a stand-alone system as well as part of a beacon network for extended applications. It is well suited for road access control and can store up to 20,000 different IDs depending on the number bytes per ID. The security of the access control system is scaleable on request of the customer. The lowest level is identification by a fixed ID number. This will be even more secure than magnetic stripe cards because monitoring the communication link is extremely difficult due to passive operation and small communication zones. Higher safety demands are realized by an optional chip card allowing authentication in both directions and encryption of data. A further application of this beacon module is single lane or multilane ETC, where narrow communication zones are not required. Figure 5 shows an OBU with chip card reader, display and internal battery. A wake-up circuitry controls a sleep-mode and an operation-mode of the OBU which guarantees a battery life-time of approximately five years under the assumption of two transactions per day.

ADVANCED ETC SYSTEM WITH PHASED ARRAY ANTENNAS

In automatic toll collection and access control systems an exact allocation between the transmitted data and the position of the communicating vehicles is important for an enforcement of unauthorized ones. Existing solutions realize the localization of vehicles by several receiving antennas with spot beams for each lane (see figure 6a). Within the field trial on the A555 in Germany, an installation based on that principal achieved the best performance among the 5.8 GHz systems. Furthermore, these small beams guarantee robustness against possible multipath interference. But to achieve this high technical performance, considerable installation expenditure with many antennas and receivers is necessary. Therefore, it is reasonable to search for an advanced solution, which may in future replace the well proved system with fixed antennas at the same stage of quality. A phased array antenna may be more flexible and well suited to substitute several fixed beam antennas (see figure 6b). An appropriate phased array antenna has been realized as an experimental system. Nowadays, phased array antennas for 5.8 GHz can be realized at reasonable cost because the high volume market of 12 GHz satellite TV-sets has reduced component cost essentially.

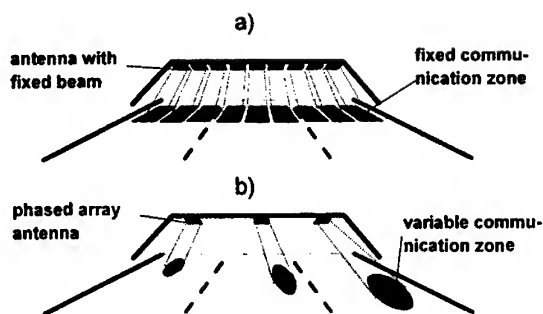


Figure 6: Principles of a) existing system with fixed communication zones and b) new approach with phased array antenna

The experimental system consists of a phased array receiving antenna with a steerable narrow main-lobe and a transmitting antenna with a fixed radiation pattern shaped to cover one lane as shown in figure 7. Both antennas are planar microstrip patch arrays for left-handed circular polarization. Side-lobe suppression is attained by a fixed amplitude tapering of the element weighting factors. Phase shifter modules containing low-noise amplifiers, 4-bit phase shifters and a 4-way power combiner are connected to each column of the receiving antenna. These modules have been developed in microstrip technique utilizing surface mount components to ensure a simple and low cost production. An 8-way power combiner summarizes the output signals of eight phase shifter modules. Figure 8 shows the realization of the phased array antenna. Data communication with OBUs and a host computer is managed by a beacon controller. A separate antenna controller adjusts the 4-bit phase shifters and thus can steer the main lobe to different communication zones on the lane. System parameters are dimensioned such that these communication zones overlap and cover a scan area and a tracking area on the lane (see figure 7). While no vehicle is detected the antenna scans the main lobe through the scan area. By measuring the power level of the received signal for different main lobe configurations and detecting a correct data transmission with an OBU, the antenna is able to locate the position of a vehicle entering the scan area. The Doppler shift of the received signal can be measured and the velocity of the vehicle can be retrieved. This information is used to calculate an estimate position of the vehicle over communication time and to track the main lobe according to the vehicle motion. The antenna is able to handle data transmission protocols for electronic toll collection up to a speed of 250 km/h.

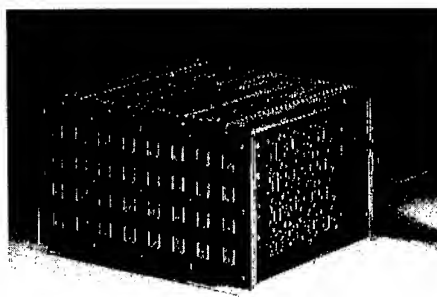
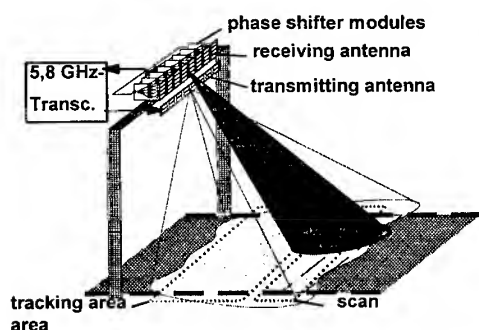


Figure 7: System setup of the phased array antenna

Figure 8: Realized antenna system

To evaluate the performance of the phased array the radiation patterns have been measured in an anechoic chamber as a first step. Beam steering and sidelobe suppression performed as expected. More relevant for the overall system behavior is the forming and the size of the communication zones on the lane. The antenna has been set up according to figure 7 in a height of 5.5 meters above the lane. Power levels of the uplink signal at the beacon for different OBU positions in a plane one meter

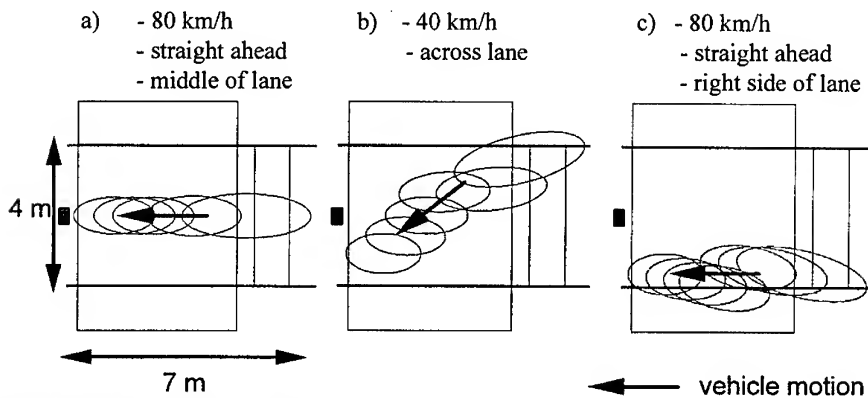


Figure 9: Test drives for tracking behavior above and parallel to the lane have been measured.

The main lobe has been steered towards different directions in the azimuth. It can be seen that the power levels are high only in a small zone in the center and descend with a steep slope towards the sides of the lane. This is important for a reliable localization of OBU signals in presence of interfering signals from other OBUs. Furthermore, the beam steering algorithm has been proved at a test site with complete ETC transactions and full protocol according to draft DSRC standards. Figure 9 shows typical examples of the tracking behavior for different measurement drives. By appropriate interpretation of the displayed communication zones (curves refer to 3 dB below maximum level) an exact localization of the vehicle for enforcement purposes is given each time the OBU transmits data.

CONCLUSION

With the finalized standardization of DSRC by CEN TC 278 WG9 a long time demanded precondition for a widespread implementation of interoperable systems is now fulfilled. Electronic industry can now take the opportunity to supply vehicle and roadside into a worldwide growing DSRC market. Road operators can expect advanced ETC systems based on DSRC for multilane applications including high performance localization for enforcement in the very near future.

REFERENCES

- (1) CEN, prENV 12253, Road Transport and Traffic Telematics (RTTT) - Dedicated Short Range Communication (DSRC) - Physical Layer using Microwave at 5.8 GHz
- (2) CEN, prENV 278/9/#63, Road Transport and Traffic Telematics (RTTT) - Dedicated Short Range Communication (DSRC) - Physical Layer using Infrared at 850 nm
- (3) CEN, prENV 278/9/#64, Road Transport and Traffic Telematics (RTTT) - Dedicated Short Range Communication (DSRC) - Data Link Layer: Medium Access and Logical Link Control
- (4) CEN, prENV 278/9/#65, Road Transport and Traffic Telematics (RTTT) - Dedicated Short Range Communication (DSRC) - Application Layer
- (5) "5.8 GHz Toll Collection Standard Proposal Gains US Support After Demo", The Intelligent Highway, Volume 7, Issue 15, October 28, 1996, Transport Technology Publishing LLC
- (6) ETSI, prI-ETS 300 674, Radio Equipment and Systems (RES); Road Transport and Traffic Telematics (RTTT); Technical Characteristics and Test Methods for Data Transmission Equipment Operating in the 5.8 GHz Industrial, Scientific and Medical (ISM) Band
- (7) W. Detlefsen, W. Grabow, U. Kersken, R. Schmedding, "Reliability of 5.8 GHz Short Range Links in Vehicle-Roadside Communication", Vehicle Navigation and Information Systems Conference, Ottawa, October 1993
- (8) J. D. Büchs, W. Detlefsen, W. Grabow, R. Schmedding, "Development of Standards and Equipment for 5.8 GHz Communication Systems Used for Electronic Access Control and Fee Collection ", 3rd Annual World Congress on Intelligent Transport Systems 1996, Orlando, Florida, October 1996
- (9) F. Dobias, W. Grabow, "Adaptive Array Antenna for 5.8 GHz Vehicle to Roadside Communication", 1994 IEEE 44th Vehicular Technology Conference, Stockholm, June 1994

Design and performance of the Transmit/Receive Module and the Tile Sub-System of Advanced Synthetic Aperture Radar (ASAR) for ENVISAT satellite.

A. Cazal, J.L. Cazaux, C. Sahuc, Ph. Ginestet.

ALCATEL ESPACE, 26 Av J.F. Champollion 31037 Toulouse, FRANCE.
Tel: 33 61 19 62 29, Fax: 33 61 19 52 74

ABSTRACT:

A major space-borne radar program is on-going in Europe : the Advanced Synthetic Aperture Radar supported by the European Space Agency.

ASAR makes use of an active antenna composed of 20 RF Tile Sub-systems. Each Tile embeds 16 C-Band Transmit/Receive Modules, 1 Control Interface Unit, 4 Power Supply Units and 1 Radiating Panel. It is clear that the overall 320 T/R Module is the key element of the radar performance.

Emphasis is put on the T/R Module design which is dual H/V polarization, 10 W transmit power, 3 dB receive noise figure and use both discrete FETs (P. HEMTs and Power GaAs FETs) and GaAs MMICs. Commands and DC supply switching are controlled with an integrated ASIC. Overall size is 213x38.4x22 mm³ and weight is 200 gr. In order to succeed the electrical challenge, new miniaturizing technics and technologies were qualified at space level as integrated MMIC functions, new RF substrate and connections and a lot of assembling processes.

Due to the high volume production (more than 320 T/R Modules and 8000 hybrids) the design has been put through a very exhaustive industrialization procedure which is detailed below.

INTRODUCTION:

The Advanced Synthetic Aperture Radar project is the second generation of SAR instrument promoted by ESA. The first generation was ERS1 (launched in 1991) and ERS2 (launched in the beginning of 1995). Offering additional advantages (as dual polarization, wide swath capability, greater coverage,...) the ASAR will be part of the ENVISAT payload (launch foreseen in 1999). ALCATEL ESPACE has been chosen as main contractor for the Tile Sub-System of the active antenna and as design authority for the Transmit/Receive Module. See Tile Sub-System Architecture in Figure 1

Tile Sub-System manufacturing is performed by ALCATEL ESPACE (Toulouse) and T/R Module production is equally shared between ALCATEL ESPACE and MATRA MARCONI SPACE (Portsmouth, UK). In 1995 the work was focused on the industrialization of the Engineering Models (EM). 64 EM T/R modules are fabricated in 1996 and is followed in 1997 by 320 FM (Flight Model).

T/R MODULE GENERAL DESCRIPTION:

The RF antenna electronic is based on T/R modules of 213 x 38.4 x 22 mm³ operating at 5.331 ± 8 MHz. Each module weights 200 gr. The T/R module operates between a RF port, 2 radiators and a calibration port. The sliding connectors are directly connected to the radiated panel which minimizes the losses.

The T/R Module RF side view is shown in Fig 3. Switching between the two polarizations is done at low level to minimize the RF losses between the power amplification and the radiators in Tx mode and between the radiators and the low noise amplification in Rx mode.

The T/R module lies on a gold-plated aluminum baseplate with RF parts on the upper face and a command card on the lower face.

European manufacturers have been preferred for all main parts and components likes MMIC's, FETs and PHEMTs, micro-packages, circulator-isolator-limiter, ASIC, DC switch hybrids, etc..

T/R MODULE MAIN PERFORMANCE :

All measurements have been performed with an automatic test bench providing a full characterization (pulsed S-parameters, peak power, noise figure, gain and phase profile within pulse, AM/AM, AM/PM...) within 20 minutes.

The following table summarizes the mean performances measured at 5.331 GHz and at 25°C on the first 32 EM modules.

Parameters	Measured	Remarks
Rx Gain /Tx Gain	30 dB / 40 dB	with 40 dB of dynamic range
Rx Noise Figure	3 dB	
Tx Output Power	P1dB = 39.5 dBm	Psat = 40 dBm
Mean Consumption	2.4 W	Duty Cycle: 6% Tx and 60% Rx

T/R MODULE INDUSTRIALIZATION AT DESIGN AND FABRICATION LEVELS

The EM module has been optimized in terms of manufacturing, assembling and performance. Some examples are : Integration of Circulator, Isolator and Limiter, Use of TMM10 RF substrate, Uniformization of the RF and DC connections, ect

All technologies and processes used are under space qualification procedure or already space qualified.

T/R MODULE INTEGRATION INTO THE RF STRUCTURAL FRAME :

The T/R modules are integrated into a RF structural frame (alodine plated aluminum) which embeds 16 modules RF fed by 1/16 dividers (2 Duroid microstrip corporate feeds for each T/R and CAL port). The 16 modules lies lengthwise and are all parallel each other as shown in Figure 2.

TILE SUBSYSTEM GENERAL DESCRIPTION:

The TILE Sub-System receive RF signal and Calibration signals from the ASAR RF Sub-System. Within the TILE Sub-System the RF signal are distributed to the 16 T/R Modules by the Corporate Feed. The T/R Modules apply phase and gain changes to form the antenna beam excitations. The signals are then power amplified prior to being fed to the Radiator Panel for radiation.

A highly attenuated return echo signal will be received from the earth using the same Radiator Panel. The signal is routed to the T/R Modules receive path, where it is amplified in the low noise amplifier. Phase and gain shifts individually within each module provide the excitations for the receive beam forming. The

outputs from all modules are routed at RF to the Signal Corporate Feed, which now acts as a combiner effectively adding signals inputs coherently and noise input incoherently.
See TILE SubSystem Schematic in Fig 3.

The TILE SubSystem is divided into four major parts :

- **RF STRUCTURAL FRAME** embedding 16 T/R Modules and 2 RF Coporate Feeds.
- **Tile Control and Interface Unit (TCIU)**
There are 20 TCIU's which form the control element of the ASAR antenna, each one directly controls 16 TR Modules for the purpose of modifying the antenna RF characteristics.
- **Four Power Supply Units (PSUs).**
These equipment's are manufactured by ALCATEL ETCA located in Belgium. ETCA has more than 30 years experience in power supplies to be used for space application. The PSU's are intended to power the T/R Modules and the TCIU.
- **Radiating Panel.**
The radiating panel performs the following two functions :
 - Receive transmit power from the T/R Modules and pass return echo power to them.
 - Radiate antenna patterns in accordance with the gain and phase commands.

TILE SUBSYSTEM MAIN PERFORMANCES :

Parameter	Measured @ ambient	Remarks
Noise Figure in Rx	4.2 dB	
Output Signal level in Tx	75 W	Peak level
Mean Consumption	50 W	Radar Mode 2.5% Tx; 60% Rx
Mass	16 Kg	Safe supporting structure
Dimension	996 x 663 x 70 mm3	

CONCLUSION

After a successful pre-EM phase the design optimization and the performance of the selected European components has been validated by ALCATEL ESPACE. The industrialization is now terminated and the production of EM T/R Modules (68 units) is nearly finished. The manufacture of the 20 FM TILE Sub-System (320 T/R Modules, 80 PSUs and 20 TCIUs) is scheduled for this year. The first EM Tile Sub-System is assembled and tested at ALCATEL ESPACE. The electrical results are very satisfactory.

ACKNOWLEDGMENT

The authors want to deeply thank the technical staff from ALCATEL ESPACE, MATRA MARCONI SPACE, DORNIER for their fruitfully collaboration and ESA/ ESTEC for their support.

Fig 1 : TILE SubSystem

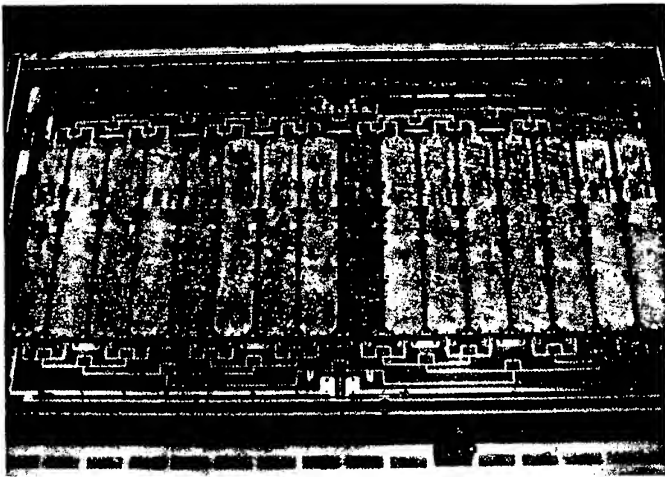
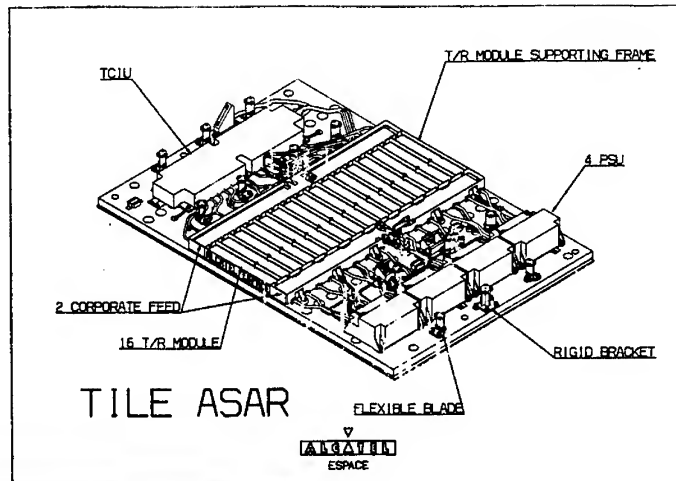


Fig 2 : Transmit Receive Module and Corporate Feed Integrated into the Supporting Frame

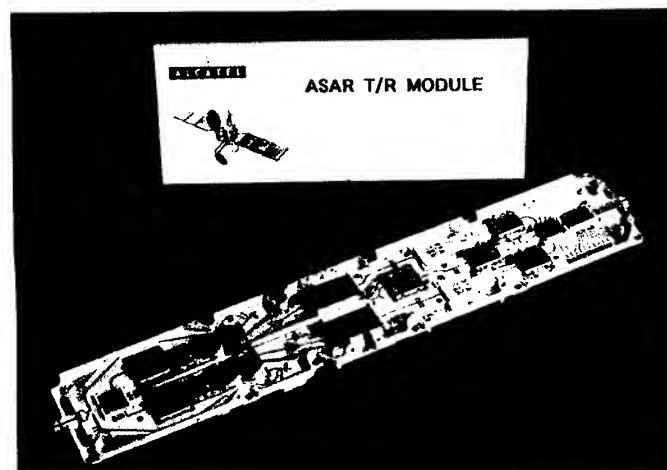


Fig 3 : Transmit Receive Module - RF side view

A Headway Control System Concept Using Dual-mode Millimeter-wave Radar

Kenichi Konno and Shoichi Koshikawa

Antenna Giken Co., Ltd., 4-72 Miyagayato, Ohmiya 330, JAPAN

Phone: +81-48-685-1300; Fax: +81-48-684-4144

The topic number: 19. Millimeter-wave Application

The type of paper: Application-oriented

Abstract

In the future, headway control systems for consumer use must be cheap and capable of operating in all environmental conditions. To enable such systems to be built, a headway control system using dual-mode millimeter-wave radar has been proposed. The radar would be able to operate in both radar mode, in which it would measure the distance to the leading vehicle, and in communication mode, in which it would exchange data with a vehicle ahead of it. By operating in two modes alternately, the dual-mode radar can provide the headway control system with all the data needed to control the distances to the leading vehicles, and because the proposed dual-mode radar system can be use the radar sensor as communication equipment, lower costs will result. By steering the radar's antenna, it can recognize the leading vehicle's ID code, direction, and distance. This information is very useful for locating the position of the leading vehicles. By using these information, a map is produced which can then be used for stable control of the vehicles. This paper describes the concept of the dual-mode radar system, the headway control system using the radar, and the results of the dual-mode radar experiments undertaken.

1. Introduction

In typical headway control systems, radar sensors have usually been used. Inter-vehicle or roadside-vehicle communication systems or vision systems with image processing have also been used for more stable vehicle control. This is needed because of the problems involved in recognizing the lane separation or positioning of leading vehicles.

In the future, headway control systems for consumer use in IVHS must be cheap and capable of operating in all environmental conditions. To enable such equipment to be built, a headway control system using a dual-mode millimeter-wave radar has been proposed. The radar would be able to operate in both radar mode, in which it would measure the distance to the leading vehicle, and in communication mode, in which it would exchange data including the leading vehicle's ID code with a vehicle ahead if that vehicle were installed with a millimeter-wave tag or ID card at the rear side. The tag system is very simple and, since it has no RF source, it is also very cheap. By operating in two modes alternately, the dual-mode radar can provide the headway control system with all the data needed to control the distance to the leading vehicles: their speeds, acceleration conditions, and (for more stable platoon driving control) the leading vehicle's steering angle and break signal. By steering the radar's antenna, it can obtain each leading vehicle's ID code, direction and distance. This information is very useful for stable headway control.

2. The Concept of a Dual-mode Radar System

Figure 1 shows a basic block diagram of the proposed dual-mode radar. It consists of a base station and a tag. The base station comprises a VCO with ASK modulator, a transmitting antenna, a receiving antenna, a homodyne mixer, and two video amplifiers, one of which is used in communication mode and the other in radar mode. The tag consists of a receiving antenna, a detector, a video amplifier, a reflection-type PSK modulator, and a receiving/transmitting antenna. It has no RF power source, and so can be manufactured at a lower price. By automatically choosing the mode-select signal, it operates alternately in communication and radar mode.

3. The Concept of a Headway Control System Using Dual-mode Radar

By steering the radar's antenna, this system can obtain information from the leading vehicles as explained above, and by using this information, each vehicle's position and its speed vector can be determined at any time, as shown in Fig. 2. This vector map of vehicles is very useful for stable headway control.

4. Dual-mode Radar test

Figure 3 shows the field test system for both modes of the dual-mode radar. In radar mode, the FM-CW method is used. The VCO of the dual-mode radar generates FM-CW and CW RF signal alternately. In radar mode, linear ramp voltage is chosen and in communication mode, constant voltage is chosen for the varactor voltage of the VCO. This mode select signal is shown in Fig. 4.

In communication mode, tests were performed with an 8-bit transmission signal. When downlinked, the signal was inserted into dual-mode radar (base station) and the 60 GHz RF signal generated by the VCO was modulated to the ASK with the 8-bit signal. This modulated RF signal was transmitted through the transmitting antenna to the tag. At the tag the modulated ASK RF signal was received and detected. The 8-bit signal that was detected was amplified and regenerated to clear pulse. When uplinked, the regenerated signal was delayed 16 bits and then inserted into the PSK modulator with a 450 kHz subcarrier. The CW RF signal radiated from the radar and received by the receiving and transmitting antenna of tag was modulated by the 8-bit signal with a 450 kHz subcarrier and retransmitted through the same antenna to the base station. At the base station the received phase modulated RF signal was detected by the homodyne mixer and passed through a 450 kHz narrow band pass filter, then regenerated to a clear pulse signal.

In radar mode, FMCW RF signal was transmitted through the transmitting antenna. The obstacle (with a tag installed) reflected the FMCW RF signal then it was received by dual-mode radar through the receiving antenna and detected by the same homodyne mixer.

5. Test results

Figure 4 shows the envelope wave form of the detected signal on communication mode, and the detected signal in radar mode. The dual-mode operation has been successfully tested. The results indicate that it is possible to use the proposed dual-mode radar for communication and range measurement between leading vehicle and following vehicle.

6. Conclusion

A dual mode-radar and a headway driving control system using dual-mode radar was proposed. This radar would be able to communicate and measure the distances between leading and following vehicles in all environmental conditions. This capability is very useful for stable headway driving control in IVHS, and because the proposed communication system can use the radar sensor as communications equipment, lower costs will result.

A headway control system using dual-mode radar with higher bit rates is now being investigated and the authors are looking forward to reporting on the results at the earliest opportunity.

Table 1. Specification of test equipment

Base station	Frequency (GHz)		59.5
	RF power (mW)		10.0
	Tx & Rx antenna gain (dBi)		29.5
	Modulation	Radar mode	FMCW
		Comm. mode	ASK (downlink) CW (uplink)
	Transmission rate (kbps)		10.0
tag	Tx & Rx antenna gain (dBi)		24.0
	Modulation (uplink)	Reflection type PSK with 450 kHz subcarrier	

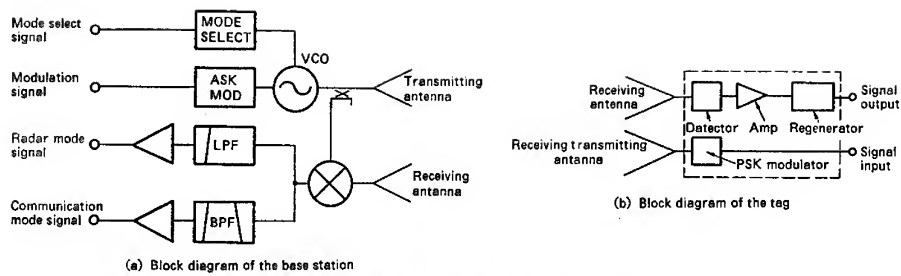


Fig. 1 Block diagram of the dual-mode radar

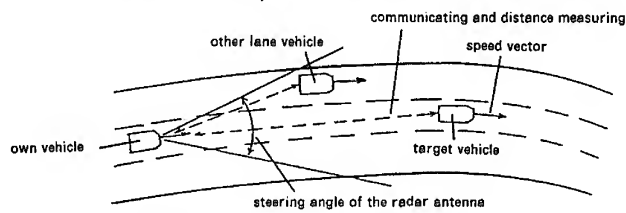


Fig. 2 Operation of the dual-mode radar

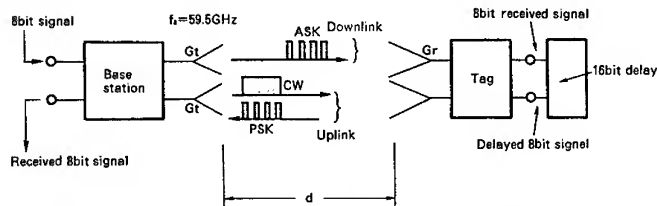
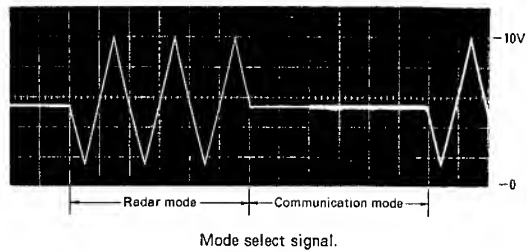


Fig. 3 Field test of the dual-mode radar



The detected signal in radar mode.



The detected signal in communication mode.

Fig. 4 Mode-select signal and the detected signals

WAVE PATTERN OF A BURIED LEAKY COAXIAL CABLE UNDER LOCAL INHOMOGENEOUS CONDITIONS

N. Blaunstein⁽¹⁾, Z. Dank⁽²⁾, and M. Zilbershtein⁽²⁾

⁽¹⁾Department of Electrical and Computer Engineering,
Ben-Gurion University of the Negev, Beer-Sheva, Israel

⁽²⁾Magal Security Systems Ltd.

Abstract

The theoretical and experimental investigations of radiation properties of a buried leaky coaxial cable, as a guiding radar system, are presented for various artificial and natural local inhomogeneous conditions along the cable system. The possibilities of generation of complicated interference picture of such a radar pattern caused by different kinds of local inhomogeneities are discussed theoretically and studied experimentally.

Wave Pattern of Guiding Radar System Under Local Inhomogeneous Conditions

During the recent decades, leaky coaxial cables are generating increasing interest as a tools of intrusion detection in guided radar systems [1-3]. As it is known, a buried leaky coaxial cable can support two TEM-like modes [4-7]. The first, internal mode, is the perturbed transmission line mode which has the main part of its energy confined under the cable shield but with some leakage outside it. The second mode is the external mode which uses the cable shield and the earth as conductors. Such construction enables the signals to be coupled into immediately adjacent objects and the temporal variations of these signals can be used in the intrusion detection systems. The radiation properties of leaky coaxial cables were investigated in a number of works, see e.g. a review in [4], but in most of them, with exception of [2,3], only the open installation of the cable was considered. At the same time, it is known that the radiation pattern of the buried cable differs essentially from that in the open installation. This is caused mainly by the losses in the earth, inhomogeneities, and the presence of the earth-air interface. In such situation the exact theoretical analysis of the radiation properties of the cable is very complicated. In this work we report some results of experimental investigations of the near field radiation pattern and their comparison with our theoretical predictions.

The propagation of internal mode can be considered in a standard manner. It is important that the extinction suppress the voltage and current oscillations at the input of the line. The propagation of the external mode can be considered as for an insulated single wire cable buried at some depth in a homogeneous lossy earth. The simple estimates show that the propagation constant is found near the wave number of the insulating layer, perturbed by losses in the earth and by the presence of the interface. The propagation constant does not vary greatly with the burial depth. The main property of this mode is the very large value of the attenuation constant.

The two main parameters affecting the performance of leaky coaxial cables in guiding radar systems are attenuation, which limits the longitudinal range, and coupling, which determines the overall sensitivity. Attenuation is relatively easy to measure by simple insertion loss techniques although the accurate prediction of losses in an actual working environment is much

more difficult. Coupling is the measure of the signal accessibility at a given radial distance outside the cable and, being very dependent on the particular installation and environmental aspects, is very difficult to assess. Some attempts have been made to predict it based on transfer impedance concept [4].

The internal and external modes interact with each other. For us it is important that the internal mode, excited in the cable by the generator, is the source of the external mode. The leakage effect can be modeled by a transfer inductance. The specific transfer inductance is only a shield parameter and not by itself give full information on the intensity of the leakage fields. The relevant parameters are the coupling coefficients [4]. They also depend on the internal and external parameters. In particular, a value of velocity ratio of the two modes close to unity may have more influence on the leakage intensity than a high transfer inductance.

In the experiments we used the loop of the leaky coaxial cable buried at the depth 10-15 cm. The length of the cable is equal to 144 m. The carrier frequency is ~40 MHz. The measurement of the characteristic impedance of the cable gave 51Ω at the frequency used.

In the first test we studied the distribution of the external mode radiation along the cable. The electric field intensity was measured each 1.5 m along the cable at the height ~0.8 m above the ground. The results for the matched load $Z_L = 51 \Omega$ are presented in Fig. 1. We see that even for the matched load the radiation of the external mode exceeds some oscillations at the input of the cable. This effect can be caused by the fact that the two modes travel with different phase velocities and are successively in phase and in anti phase [4].

In the next test we investigated the influence of screening objects (metallic sheets) located near the transmitting cable above the ground surface. Six sheets of zinc iron (1.5×2.0 m each) were used for the measurements. The sheets were put consecutively on one side of the cable (90-102 m from the input of the cable), and also on both sides of the cable (90-96 m from the input). The distance between the cable and solid iron strip (90-102 m) is equal to 0.2 m, and aperture's width between right and left strips (90-96 m) is 0.4 m. The results of the measurements are presented in Figs. 2 (one side screening) and 3 (two side screening).

The experimental results are supported by a vast theoretical investigation. We consider an idealized situation, modeling the discontinuity of the coupling coefficient along the infinite line by the following function: $c(z) = c_0$, if $0 \leq z \leq d$, and $c(z) = c$, otherwise.

Assuming that the propagation constant does not depend on the distance and introducing the parameter $q = c_0/c$ as the relative value of coupling inhomogeneity, we after some straightforward derivations obtain that the discontinuity comparable with the wavelength, can result in strong interference fading of the outer mode signal distribution along the cable (Figs. 4 and 5). The results of simulations are similar to that obtained in the experimental investigation at the distance ~30 m from the input of the cable (see Fig. 1). A similar treatment was applied to the case when $c = \text{const}$ and the distribution of the propagation constant has some discontinuity. We discuss also some possibilities to eliminate the strong oscillations in the radiation pattern.

Conclusion

The possibilities of creation of a very complicated picture of radiation pattern distribution caused by the local underground inhomogeneities and their influence on the radiation properties of a buried H-field leaky cable system, as a guiding radar, were examined both theoretically and experimentally. The existing possibilities to eliminate such disturbances in the radiation pattern of the guiding radar system were discussed.

References

- [1] R. E. Patterson and N. A. M. Mackay, IEEE Trans. **IM-26**, 137 (1977).
- [2] J. H. Richmond, N. N. Wang, and H. B. Tran, IEEE Trans. **EMC-23**, 139 (1981).
- [3] J. H. Richmond, IEEE Trans. **EMC-27**, 70 (1985).
- [4] P. Delogne, *Leaky Feeders and Subsurface Radio Communications* (London, Peter Peregrinus, 1982).
- [5] P. Delogne, Radio Sci., **22**, 1179 (1987).
- [6] D. J. Gale and J. C. Beal, IEEE Trans. **MTT-28**, 1006 (1980).
- [7] R. W. P. King and G. S. Smith, *Antennas in Matter* (MIT Press, Cambridge, 1981).

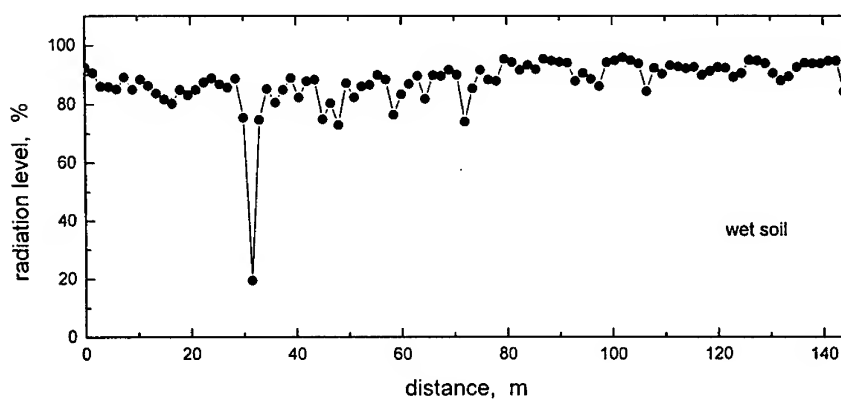


Fig. 1

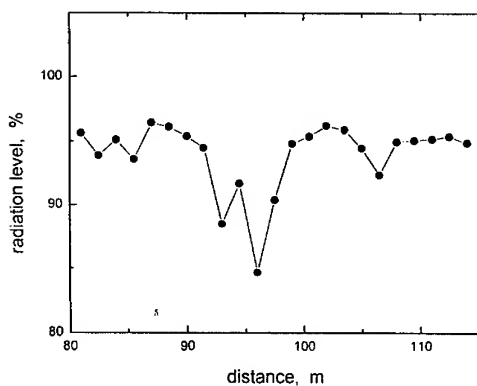


Fig. 2

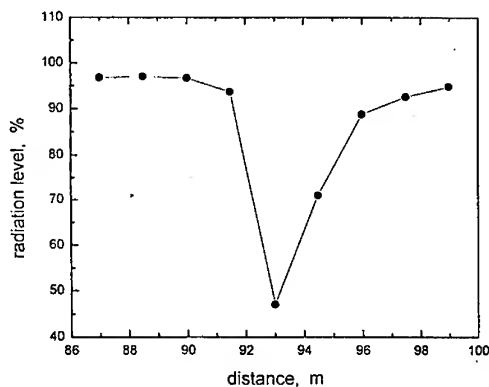


Fig. 3

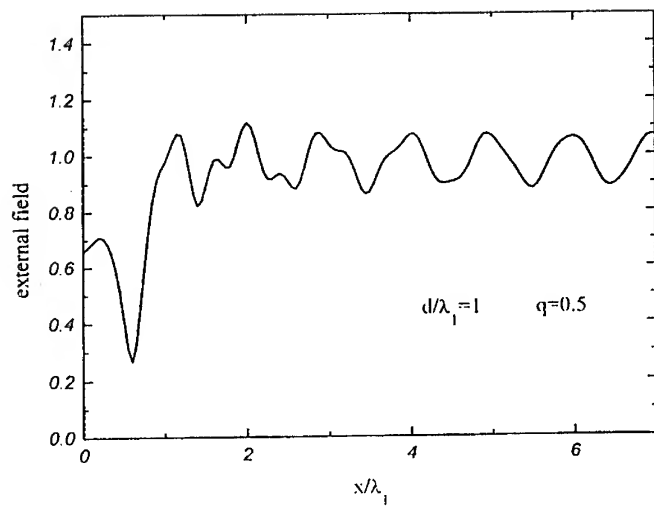


Fig. 4

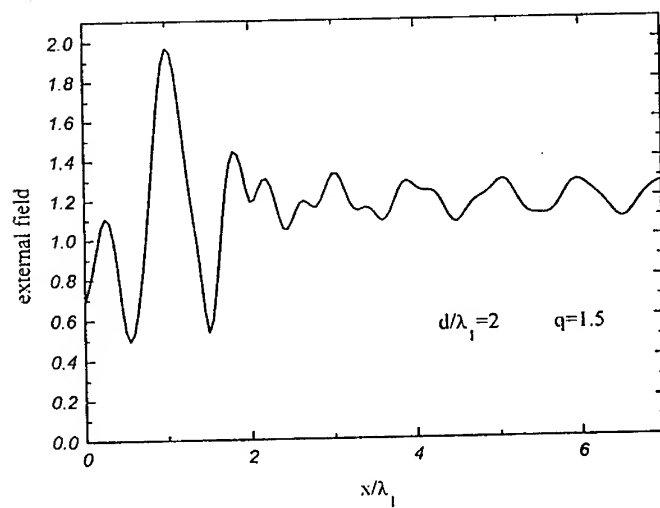


Fig. 5

RADAR STUDY OF POLARIZATION STRUCTURE OF PRECIPITATION

F. J. Yanovsky (*) (**), L. P. Ligthart (*), C. M. H. Unal (*), V. H. Korban (***)

(*) IRCTR, Delft University of Technology, P.O. Box 5031, 2600 GA, Delft, The Netherlands

(**) Kiev Int'l University of Civil Aviation, Komarova, 1, 252180, Kiev, Ukraine

(***) Odessa Hydrometeorological Institute, Odessa, Ukraine

Fax: +31 15 2784046, +38 044 4883027; Phone: +31 15 278 6292, +38 044 4849445

e-mail: <F.Yanovsky@et.tudelft.nl>, <C.M.H.Unal@et.tudelft.nl>, <yanovsky@kmuga.freenet.kiev.ua>

ABSTRACT

Polarization structures of different kinds of precipitation are experimentally studied with ground-based radars. The behavior and characteristic values of the differential reflectivity, depolarization ratio and Stokes parameters for different weather objects are discussed. Statistical data corresponding to the polarization parameters are given. The possibility to classify weather objects with statistical procedures is shown. In particular, a method to detect hail based on radar polarimetry is confirmed experimentally, and the reliability of the procedure is assessed.

1. INTRODUCTION

The study of clouds and precipitation with a radar is based on the analysis of reflected signals. The amplitude, Doppler spectrum, polarization characteristics bear a lot of information about the microstructure, phase state, liquid water content, and dynamic processes in a weather object. Certainly, the features of the radar and the mode of sounding must be taken into account for the correct extraction of useful information. It is known for a long time that the use of polarimetry increases the radar potentiality for classification and physical interpretation of the observations. Nevertheless polarization characteristics are quite recently used in practice in radar meteorology, Doviak and Zmic (1). Therefore experimental results, new data processing methods and their interpretation are important for this topic.

One of the facilities to obtain experimental data is the Delft Atmospheric Research Radar (DARR). Experience in this field is acquired in IRCTR (International Research Centre for Telecommunications-transmission and Radar) using this radar system. DARR is located in Delft, The Netherlands, on the roof of a 23 floors building, 15 km away from the Northern Sea. This radar is used for vertical and slope sounding of clouds and precipitation. Continuous clouds and widespread precipitation are typical weather objects to be observed in this region. Because they often have comparatively similar structures in different directions, these objects give very good conditions for the development of different measuring techniques as well as for the interpretation of the measured and processed results. However there are very seldom weather objects like cumulonimbus, thunderstorm, hail, strong air turbulence, etc...

The Odessa Polarization Radar (OPR) is another facility, which also was used for experimental observation. This ground-based weather radar is situated in the South part of the Odessa region in Ukraine, close to the Black Sea. Cumulonimbus clouds with rain- and hail-showers quite often occur in this region of Ukraine. The hailstones cause significant damage to the agriculture. Therefore there is a special service to detect hail zones in clouds and to prevent the falling out of hailstones in Ukraine. Because OPR is not so sensitive as DARR, clouds and light precipitation are not considered to be objects for observation with OPR.

Examples of DARR measurements and OPR measurement results are given in this paper for a more complete view of polarization structure of different kinds of precipitation. Statistical characteristics of the differential reflectivity, linear depolarization ratio, Stokes parameters for different kinds of weather objects can be used as informative parameters to implement an automatic weather object classification. This possibility is discussed in more details using as an example the procedure for hail zone detection based on the OPR measurements.

2. FEATURES OF THE RADAR SYSTEMS

The DARR is a frequency modulated continuous wave Doppler polarimetric radar with a central frequency of 3.315 GHz and is described by Lighthart (2). The frequency excursion can be changed from 1 until 50 MHz, providing a range resolution from 150 m up to 3 m. The maximum transmitted power is 100 W. Both DARR antennas are steered by means of a Hewlett-Packard A600 computer but they do not scan. Their measured equivalent beamwidth is 1.5°. Electrically switched linear polarizations with different orientation angles can be selected. The output of DARR is the time-dependent scattering matrix per range and Doppler cell. Data are acquired by the Concurrent 8400 computer system which is the real-time processing facility of the DARR. For precipitation, the differential reflectivity and the linear depolarization ratio are retrieved.

The OPR is a pulse polarimetric X-band radar which is able to scan the weather objects in a vertical and horizontal plane. The transmitted power and the length of the pulse is respectively 65 kW and 1 μ s. The transmitting antenna system is designed to emit 9.375 GHz sounding radio-waves with different polarizations, including linear (vertical, horizontal, and forty-five degrees) and circular polarizations. The state of polarization can be electrically switched from one period to another. A two-channel receiver with a divisor of polarization is capable to receive both co- and cross-polar waves simultaneously. The reflectivity, differential reflectivity Z_{dr} , depolarization ratios, and Stokes parameters can be measured in real time. The accuracy of the measured polarization parameters is: 0.15 dB for Z_{dr} and for the second Stokes parameter, and about 1 dB for the other polarization parameters.

Concerning OPR both transmitted (index t) and received (index r) waves are described with the four-dimensional Stokes vector:

$$\bar{S}_t = \begin{bmatrix} I_t \\ Q_t \\ U_t \\ V_t \end{bmatrix} \quad \bar{S}_r = \begin{bmatrix} I_r \\ Q_r \\ U_r \\ V_r \end{bmatrix} \quad \text{where} \quad \begin{aligned} I &= I_x + I_y \\ Q &= I_x - I_y \\ U &= I_x I_y \cos \Phi_{xy} \\ V &= I_x I_y \sin \Phi_{xy} \end{aligned} \quad (1)$$

where I_x and I_y are the intensities of the orthogonal components of the electromagnetic wave, and Φ_{xy} is the phase difference between the orthogonal components.

In this case, we can obtain the scattering matrix by measuring the Stokes parameters. The degree of polarization, the ellipticity, orientation angle of the polarization ellipse of the completely polarized component of the wave, as well as the differential reflectivity, linear and circular depolarization ratio, and other polarization parameters, which are often used in weather radar polarimetry, can be expressed in terms of the Stokes parameters.

3. EXPERIMENTAL DATA

Widespread precipitation have been measured with DARR during November 1996. The main value of these data is that they combine simultaneously polarimetric and Doppler measurements. This feature opens new possibilities to interpret the microstructure and dynamics of weather objects. However the Doppler-polarimetric aspect of this experiment is out of the scope of this article. The large Doppler-polarimetric data set is still being analyzed. First results have given the profiles of differential reflectivity and linear depolarization ratio when sounding widespread precipitation at 30° and 90° of radar elevation. Fig. 1 shows a differential reflectivity profile for a light rain event (about 1 mm/h). The radar elevation angle equals 30°.

The differential reflectivity Z_{dr} is sensitive to the shape and orientation of the reflecting particles. The peak value of Z_{dr} indicates an oblate mean shape around 2 km of range. Since the reflectivity is also showing a peak at this range, there is a melting layer. This gives the possibility to analyze separately data above, inside and below the melting layer.

Zones of hailstones inside cumulonimbus, rain and hail precipitation were analyzed with the OPR data.

According to Stepanenko (3), the following classification is made. When the mean L_{dr} is larger than -9 dB, the reflecting object consists mainly of non-spherical ice particles (crystal clouds). A mean L_{dr} smaller than -17.5 dB corresponds to liquid-drop clouds. Clouds have the mixed structure if intermediate values of the mean L_{dr} occur. Shupiaty et al. (4) pointed out that this area of ambiguity may even be narrower, from -12 to -14 dB for the mean value of L_{dr} when the reflectivity is above 32 dBZ. Our assessment for the statistical characteristics of the linear depolarization ratio L_{dr} and reflectivity Z for hail zones and rain showers is presented in Table 1.

The OPR measurements give the possibility to analyze distributions of the Stokes parameters for different meteorological objects. The distributions of the first two Stokes parameters are presented in Figs. 2 and 3. They are based on 1654 measurements of hail and 958 measurements of rain showers. The first histogram shows larger values of the first Stokes parameter for hail events. The second Stokes parameter has the same physical meaning as the differential reflectivity. Both negative and positive values of the second Stokes parameter were observed. Larger values of Q were expected for the rain showers. The obtained histogram in Fig. 3 confirms this prognosis.

The distribution of the parameter Q for hail appears to be bimodal. This bimodal nature of the second Stokes parameter distribution for hail can be explained quite simply. Usually a hail event is observed in the background of a rain shower. Therefore this distribution shows the presence of both hailstones and raindrops. This is also confirmed with the distribution of Q for showers since it has a weak bimodality.

Due to the limitation of pages, we do not give the histograms for the two last Stokes parameters. Summarizing, the distribution of the third as well as the fourth Stokes parameter brings the possibility to recognize a rain shower from a hail event. Large values of the third Stokes parameter U are more found for hail. The fourth Stokes parameter is measured with circular (right and left) polarization. There is more difference between right- and left-circular polarized reflection for hail. This is due to the more irregular shape of the hailstones in comparison with raindrops.

Thus, recognition of hail and rain shower zones is possible using different polarization parameters or their set including the Stokes parameters.

4. STATISTICAL PROCEDURES

The obtained results using polarization characteristics can be used to discriminate different types of precipitation. An algorithm to recognize hail from a rain shower was implemented using the reflectivity and linear depolarization ratio measurements.

Let us assume that we have a two-dimensional density distribution, $p_H(Z, L_{dr} / H)$ and $p_R(Z, L_{dr} / R)$ for hail and shower events. The indexes H and R mean "hail" and "rain" respectively. A Gaussian two-dimensional distribution $p(L_{dr}, \lg Z)$ using the statistical parameters given in Table 1 and the correlation between $\lg Z$ and L_{dr} , $\rho=0.15$, is calculated. The logarithm of the likelihood ratio, $F(\bar{X})$, is taken as the discriminant function with $\bar{X} = \{\lg Z, L_{dr}\}$.

$$F(\bar{X}) = \ln \frac{p(\bar{X}/H)}{p(\bar{X}/R)} \quad (2)$$

Then, from equation (2), we get:

$$F(\lg Z, L_{dr}) = \alpha \left[(\lg Z)^2 + (L_{dr})^2 \right] + \beta \lg Z \cdot L_{dr} + \gamma \lg Z + \delta L_{dr} + \epsilon \quad (3)$$

where α , β , γ , δ and ϵ are the actual functions of the parameters of the distributions $p_H(Z, L_{dr} / H)$ and $p_R(Z, L_{dr} / R)$. Hence, the "making decision" algorithm is the following:

$$\begin{aligned} F(\bar{X}) &\geq \text{THRESHOLD} \Rightarrow \text{HAIL} \\ F(\bar{X}) &< \text{THRESHOLD} \Rightarrow \text{RAIN} \end{aligned} \quad (4)$$

Models of the discriminant function density $p(F)$ for rain showers and hail are shown in Fig. 4. The Probabilities of right and erroneous decision, which characterize the reliability of the distinction between hail and shower zones, are shown in Fig. 5. Series 1 corresponds to the false alarm probability F_a of hail detection, and series 2 shows the summarized probability P_o of the error versus threshold.

$$P_o = F_a + (1 - D_r) \quad (5)$$

where D_r is the probability of right hail detection.

According to this result the minimum summarized probability of erroneous decision P_o can be less than 0.01. This value can be used as a first assessment of hail detection reliability for a radar which measures the reflectivity and linear depolarization ratio.

5. CONCLUSIONS

The data obtained give new knowledge about the polarization structure of precipitation, especially concerning the statistical characteristics of the Stokes parameters for different kinds of precipitation. Methods for researching the microstructure and dynamics of weather objects or for detecting, locating and recognizing thunderstorms, hail, heavy rain and other dangerous meteorological phenomena, can be developed using the polarization properties of clouds and precipitation.

It is not possible to make a completely correct comparison of polarization results from different weather objects, measured with polarimetric radars operating at different wavebands. On the other hand, it is very interesting to observe the same object with different radar frequencies, because that gives the possibility to measure the scattering matrix coefficients as a function of frequency. The large technical possibilities of DARR, as a tool for atmospheric remote sensing, can not be used completely because of the immobility of the system. In this context the use of a new Transportable Atmospheric Radar (TARA), which is currently under development in IRCTR, in different geographic regions, can bring fruitful results.

The use of parameters like the differential reflectivity and linear depolarization ratio does not require absolute values of the received signal but only their ratios. Some meteorological problems can be already successfully solved with relative calibration. When the measurement of the reflectivity is needed, the absolute calibration of the radar must be performed as well.

There are a lot of possibilities to recognize hail zones. However the optimum way of radar measurement and signal processing is not yet established. This must be done using a research Doppler-polarimetric weather radar like the future TARA system. Comparison of the reliability of statistical methods using different polarimetric parameters to recognize different meteorological phenomena can be done using the procedure described in this paper. The research of the polarization characteristics of hail zones in different regions and accumulation of statistical data must give the possibility to synthesize an optimum algorithm for hail detection.

REFERENCES

1. Doviak R.J. and D. S. Zrnic, Doppler Radar and Weather Observation, Academic Press, Inc., 1993.
2. Ligthart L.P., FM-CW Delft Atmospheric Research Radar, IEE Proceedings, Vol 127, Pt F, No 6, 1980.
3. Stepanenko V.D., Radar Meteorology, Gidrometeoizdat, Leningrad, 1973 (in Russian).
4. Shupiaty A.B., L.A. Dinevich and R.V. Tychina, Remote indication of hail in clouds with polarization characteristics of radar signal, Trudy CAO, Issue 121, 1975 (in Russian).

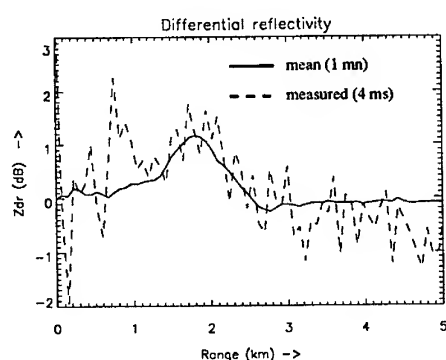


Fig.1. Profile of the radar differential reflectivity in dB.

Table 1. Statistical characteristics of radar parameters for rain showers and hail.

Parameters	Mean, $M\{*\}$		Variance, $\sigma^2\{*\}$	
	Shower	Hail	Shower	Hail
Reflectivity Z (mm^6/m^3)	$M\{\lg Z\}=3.2$	$M\{\lg Z\}=4.6$	$\sigma^2\{\lg Z\}=1.15$	$\sigma^2\{\lg Z\}=1.0$
L_{dr} (dB) ($10 \lg Z_{xy}/Z_{xx}$)	$M\{L_{dr}\}=-17$	$M\{L_{dr}\}=-10$	$\sigma^2\{L_{dr}\}=1.8$	$\sigma^2\{L_{dr}\}=2.2$

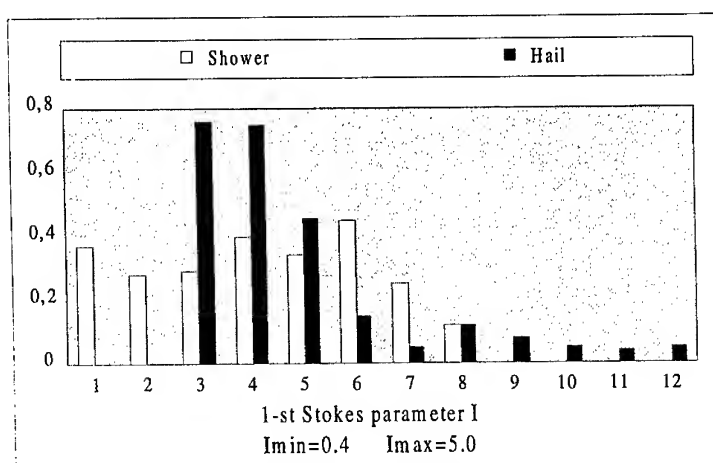


Fig. 2. Histograms of the first Stokes parameter for shower and hail

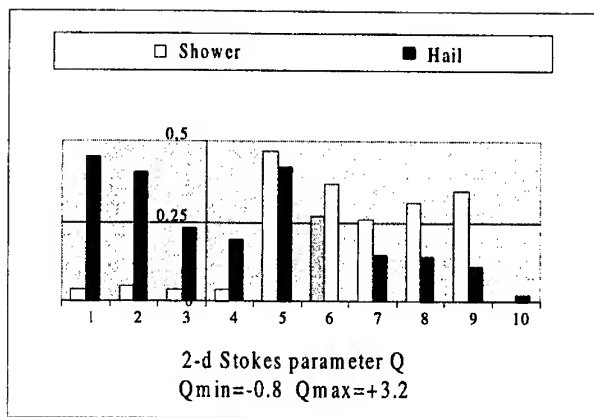


Fig. 3. Histograms of the second Stokes parameter for shower and hail

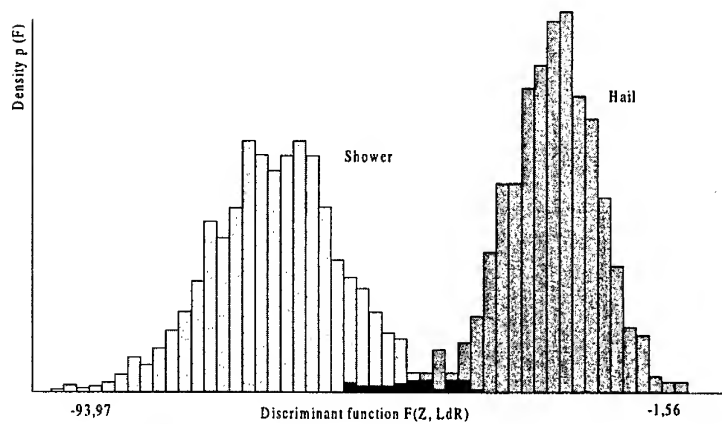


Fig. 4. Histograms of the discriminant function $F(lgZ, L_{dr})$ versus the threshold value

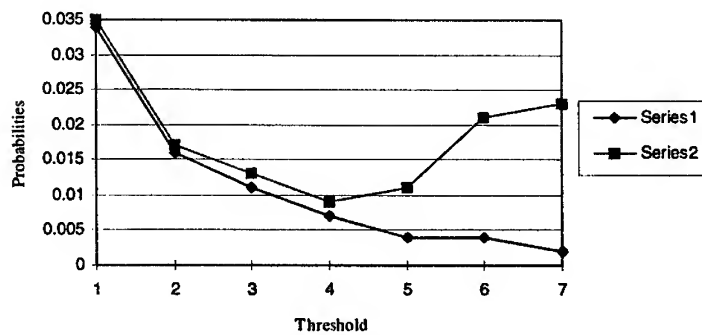


Fig. 5. Characteristics of the reliability of hail-shower distinction

A COMPREHENSIVE STUDY OF LOSSES IN MM-WAVE MICROSTRIP ANTENNA ARRAYS

A. SABBAN

Rafael, P.O.Box 2250 Haifa, 31021, Israel, Tel. 972-4-8794360, Fax 972-4-8792037

ABSTRACT

This paper presents a study of losses in mm-wave microstrip antenna arrays. Methods to reduce losses in mm-wave microstrip antenna arrays are described in this paper.

Microstrip antennas possess attractive features such as low profile, light weight, small volume and low production cost. In addition, the benefit of a compact low cost feed network is attained by integrating the microstrip feed structure with the radiating elements on the same substrate. However, losses in the microstrip feed network forms a significant limit to the achievable gain in microstrip antenna arrays.

Conductor, dielectric and radiation losses are the major components of loss in mm-wave microstrip antenna arrays. Surface wave losses in thin microstrip substrates (compare to wavelength) are usually negligible. At frequencies ranging from 30 to 40 GHz conductor losses are around 0.15 to 0.2 dB per wavelength, dielectric losses are around 0.04 to 0.05 dB per wavelength for a 50 ohm line on a 10 mil duroid substrate with $\epsilon_r=2.2$. The open nature of the microstrip configuration suffers from radiation originating at various geometrical discontinuities. This radiation phenomenon causes additional signal loss in the microstrip antenna feed network. These phenomena become significant in mm-wave microstrip antenna arrays, more bends, T-junctions and other discontinuities are introduced in the feed network and radiation loss increases considerably. As an example radiation loss of a right angle bend in a 50 ohm line on a 10 mil duroid substrate with $\epsilon_r=2.2$, is 0.1 dB at 30GHz and 0.17 dB at 40GHz.

In this paper losses in a 64 and 256 patches array at 35GHz are evaluated and methods to minimize these losses are presented. A planar multiport network model and the segmentation methods are used to evaluate radiation loss.

Design considerations of the arrays and computational results are presented.

INTRODUCTION

This paper summarizes a study of losses in mm-wave microstrip antenna arrays. Methods to reduce losses in mm-wave microstrip antenna arrays are presented. A planar multiport network model and the segmentation method are used in this paper to evaluate losses in microstrip antenna array feed networks.

Gain limitation in microstrip antenna arrays due to conductor loss and equations to calculate conductor loss and dielectric loss in microstrip lines are given in [1].

However, this discussion is limited to a 12GHz plane slot array and radiation loss and dielectric loss are neglected. A planar multiport network model and the segmentation method are used to evaluate radiation loss from microstrip discontinuities as presented in [2]. As an example radiation loss of a right angle bend in a 50 ohm line on a 10 mil duroid substrate with $\epsilon_r=2.2$, is 0.1 dB at 30GHz and 0.17 dB at 40GHz. These results

point out that radiation loss need to be taken into account for accurate microstrip antenna array design at mm wave frequencies. In this paper losses in a 64 and 256 patch antenna array at 35GHz are evaluated. Methods to minimize these losses are presented.

The multiport network modeling approach is a convenient method for analyzing microstrip patches and microstrip feed networks [2]-[3]. This analysis includes dielectric loss, conductor loss, radiation loss and radiation effects.

MULTIPORT MODELING OF MICROSTRIP LINES AND PATCHES

The multiport network model is based on the parallel-plate wave-guide model [4] for microstrip lines. A similar network modeling approach has been used for analysis of microstrip discontinuities [2] and microstrip antennas [3]. The planar waveguide model consists of two parallel conductors bounded by magnetic walls in the transverse directions. In this modeling approach for microstrip structures, fields underneath the microstrip configuration, the external fields (radiated fields, surface waves) are modeled separately in terms of multiports subnetworks by adding an equivalent edge admittance network connected to the edges of the microstrip configuration. These subnetworks are characterized in terms of Z-matrices which are evaluated by using the Green's function approach. The sub-networks are combined using the segmentation technique to obtain circuit characteristics such as scattering parameters. Equations to compute the sub-networks Z-matrices are given in [5].

EVALUATION OF MICROSTRIP FEED NETWORK LOSSES

Equations to calculate conductor loss and dielectric loss in microstrip lines are given in [1]. Dielectric loss is incorporated in the multiport network analysis by considering a complex dielectric constant. Conductor losses are included in the analysis by defining an equivalent loss tangent δ_c , given by $\delta_c = \sqrt{2}/\omega\mu\sigma/h$, where σ is the strip conductivity, h is the substrate height and μ is the free space permeability.

The multiport network model is employed to evaluate radiation loss from microstrip feed networks by adding a number of open ports at the edges of the planar model for the discontinuity structure. The multiport network model is used to evaluate the voltage distributions at the open ports, voltages at the discontinuity edges are represented by equivalent magnetic current sources, as described in [2]. The amplitude M of the magnetic current elements is twice that of the edge voltage at that location and the phase of the magnetic current is equal to the phase of the corresponding voltage. The total radiation is computed using the superposition of the far-field radiated by each section. Equations to calculate radiation loss are given in [2]. Examples of computed results of feed network losses at 30GHz on a 10 mil duroid substrate with $\epsilon_r=2.2$ are listed in Table 1.

Table 1: Computed results of feed network losses at 30 GHz

Loss Mechanism	Loss(dB)
Conductor Loss Per wavelength	0.15
Dielectric Loss Per wavelength	0.04
Radiation Loss for a 50Ω Bend	0.1
Radiation Loss for a 20Ω Bend	0.17
Radiation Loss for a Step 50Ω to 70.7Ω	0.015
Radiation Loss for a T-Junction 50Ω to 70.7Ω	0.09

DESIGN CONSIDERATIONS AND EVALUATION OF LOSSES IN 64 AND 256 MICROSTRIP ANTENNA ARRAYS

One of the major advantages of microstrip antennas is the simplicity of array construction [6]-[9]. The radiating elements may be etched jointly with the feed network as an integrated structure leading to a very compact lightweight and low cost design. Although the technique for designing feed networks is well established, several difficulties are encountered while implementing it at mm wave frequencies. Conductor loss increases considerably at mm wave frequencies. Conductor loss may be minimized by designing the feed network length per wavelength as short as possible. By using a multilayer feed network design, the feed network length per wavelength is minimized considerably. Gold plating of the microstrip lines decrease conductor losses. Dielectric loss can be reduced by using substrates with a low dielectric loss. In order to minimize the radiation loss, the number of discontinuities, such as bends and T-Junctions, should be made as small as possible. Radiation from a curved microstrip line is much smaller compared to radiation from right angled bend. Moreover in order to reduce the radiation from the feed network, the width of the microstrip line is designed to be less than 0.12λ and the substrate thickness is 0.25mm with $\epsilon_r=2.2$.

Microstrip antenna arrays with integral feed networks may be broadly divided into arrays fed by parallel feeds and series fed arrays. Usually series fed arrays are more efficient than parallel fed arrays. However, parallel fed arrays have a well controlled aperture distribution and the bandwidth and polarization are determined by the microstrip antenna used.

Two microstrip antenna arrays which consists of 64 radiating elements has been designed. The first array uses a parallel feed network and the second uses a parallel-series feed network. Comparison of the performance of the arrays is given in Table 2. Results given in Table 2 verifies that the parallel series fed array is more efficient than the parallel fed array due to minimization of the number of discontinuities in the parallel series feed network.

Two microstrip antennas array which consists of 256 radiating elements has been designed. In the first array, Type A, the numbers of microstrip discontinuities have been minimized. The Type A array feed network incorporates one bend discontinuity. The second array, Type B, incorporates nine bend discontinuities in the array feeding network. Comparison of the performance of the arrays is given in Table 3.

The measured gain results are very close to the computed gain results and verifies the loss computation presented in this paper.

Table 2: Performance of 64 Elements Microstrip Antenna arrays

PARAMETER	Corporate feed	Parallel feed
Number of elements	64	64
Beamwidth(deg.)	8.5	8.5
Computed gain(dBi)	26.3	26.3
Microstrip line loss(dB)	1.1	1.2
Radiation loss T-J.(dB)	0.27	0.54
Radiation loss bends(dB)	0.4	0.8
Radiation loss steps(dB)	0.007	-
Mismatch Loss (dB)	0.5	0.5
Expected Gain(dBi)	24.0	23.2

Table 3: Performance of 256 Elements Microstrip Antenna arrays

PARAMETER	Type A (1 bend)	Type B (9 bends)
Number of elements	256	256
Beamwidth(deg.)	4.2	4.2
Computed gain(dBi)	32	32
Microstrip line loss(dB)	3.1	3.1
Radiation loss T-J.(dB)	0.72	0.72
Radiation loss bends(dB)	0.13	1.17
Radiation loss steps(dB)	0.015	-
Mismatch Loss (dB)	0.5	0.5
Expected Gain(dBi)	27.5	26.5

Results given in Table 3 verifies that the Type A array is more efficient than the Type B array due to minimization of the number of bend discontinuities in the Type A array feed network.

CONCLUDING REMARKS

This paper summarizes a study of losses in mm-wave microstrip antenna arrays. Methods to reduce losses in mm-wave microstrip antenna arrays have been presented. A planar multiport network model and the segmentation method are used in this paper to evaluate losses in microstrip antenna array feed networks. Results presented in this paper point out that radiation loss need to be taken into account for accurate microstrip antenna array design at mm wave frequencies. By minimizing the number of bend discontinuities the gain of the 256 elements microstrip antenna array, Type A, is higher by 1dB than the gain of Type B array.

REFERENCES

1. J.R. James, P.S Hall and C. Wood, "Microstrip Antenna Theory and Design", 1981.
2. A. Sabban and K.C. Gupta, "Characterization of Radiation Loss from Microstrip Discontinuities Using a Multiport Network Modeling Approach", I.E.E.E Trans. on M.T.T, Vol. 39, No. 4, April 1991, pp. 705-712.
3. A. Benalla and K.C. Gupta, "Multiport network model and transmission characteristics of two port rectangular microstrip antennas" IEEE Trans. A.P vol. 36, pp. 1337-1342, Oct. 1988.
4. G. Kompa and R. Mehran, "Planar waveguide model for computing microstrip components," Electron Lett., vol. 11, no. 9, pp. 459-460, 1975.
5. A. Sabban, Ph.D Thesis, "Multiport Network Model for Evaluating Radiation Loss and Coupling Among Discontinuities in Microstrip Circuits", University of Colorado at Boulder, January 1991.
6. A. Sabban, "A New Wideband Stacked Microstrip Antenna", I.E.E.E Antenna and Propagation Symp., Huston, Texas, U.S.A., June 1983.
7. A. Sabban, E. Navon "A MM-Waves Microstrip Antenna Array", I.E.E.E Symposium, Tel-Aviv, March 1983.
8. A. Sabban, "Wideband Microstrip Antenna Arrays", I.E.E.E Antenna and Propagation Symposium MELCOM, Tel-Aviv, 1981.
9. A. Sabban, "Microstrip Antenna and Antenna Array", U.S Patent, Patent Number 4,623,893, Nov. 18, 1986.

A whispering gallery mode transducer using microstrip-slot antenna exciter

F.Völgyi, G.Reiter, T.Berceli, G.Veszely

Technical University of Budapest, Dept. of Microwave Telecomm.
H-1111 Budapest, Goldmann-tér 3, H U N G A R Y
Phone: 36-1-463-1559, Fax: 36-1-463-3289, E-mail: t-volgyi@nov.mht.bme.hu

ABSTRACT

A mode transducer is described which generates a whispering gallery mode output with a coaxial TEM mode input. The low-power device will be used for cold-test measurements of a high power gyrotron at 140 GHz. The basic idea, design, experimental model measurement data at 15 GHz, and the design of a new model for 38 GHz are given for the $TE_{16,2}$ transducer using microstrip-slot antenna (MSSA) exciter.

INTRODUCTION

It is necessary to operate the high power gyrotrons in high order TE modes (whispering gallery mode: WGM) to keep the cavity ohmic losses at an acceptable level, Kreischer et al [1]. A WGM is defined as a $TE_{m,n}$ mode with its azimuthal index (m) much greater than its radial index (n). For R&D of gyrotrons, the study of the WGM-fields are sometimes needed (cold-test measurements). Different mode transducers and converters are used for this purposes, Moeller [2], Reiter [3], Völgyi [4] and Völgyi et al [5].

Microstrip antenna arrays draw increasing interest due to their flat profile, low weight, ease of fabrication and low cost. Planar configurations are used for microwave heating at Völgyi [6], in automatic process control at Völgyi [7], and for WLAN-systems at Völgyi [8]. Before the realization of a mm-wave array, scaled models are designed and measured at lower frequencies. Two of these models will be introduced, which are microstrip-slot antenna (MSSA) structures and they are used for exciting of WGM in an overmoded circular waveguide, the first at 15 GHz, and the second at 38 GHz.

The paper is organized as follows: the equations of electric field components for $TE_{16,2}$ circular mode are reviewed in the first section, after showing the mechanical structure of the transducer the network model and experimental results for the 15 GHz model are presented in the next section, followed by the design of a new model for 38 GHz and concluding remarks are given in the last section.

ELECTRIC FIELD COMPONENTS OF $TE_{16,2}$ CIRCULAR MODE

Assuming a circular-cylindrical coordinate system described by (r, ϕ, z) then the transversal electric components of the field of a $TE_{16,2}$ WGM (neglecting the $\exp(j\omega t)$ time dependence) may be written as:

$$E_{\phi} = C_1 J'_{16}(a'_{16,2} r / r_0) \cos(16\phi) \exp(-j\beta z) \quad (1);$$

$$E_r = C_2 \frac{J_{16}(a'_{16,2} r / r_0)}{r / r_0} \sin(16\phi) \exp(-j\beta z) \quad (2)$$

where: C_1 and C_2 are constants, $J_{16}(\)$ and $J'_{16}(\)$ are the Bessel function and the derivative of Bessel function, $\beta = 2\pi/\lambda'$ and λ' is the wavelength in $TE_{16,2}$ mode. The value of $a'_{16,2} = 23.264$ is the second root of the $J'_{16}(a'_{16,2}) = 0$ equation. With the cutoff-wavelength of λ'_c , the desired radius of circular-waveguide is:

$$r_0 = a'_{16,2} \frac{\lambda'_c}{2\pi} \quad (3)$$

Figure 1 shows the $J_{16}(23.26r/r_0)$ and $J'_{16}(23.26r/r_0)$ Bessel functions versus r/r_0 . Using equations (1) and (2), from Figure 1 we can establish:

$E_{\phi} = 0$ at $r/r_0 = 1$ and $r/r_0 = 0.77$, and $\phi = \pi/32$ and $3\pi/32$, where E_r have maxima with opposite signs,

$E_r = 0$ at $\phi = 0; \pi/16$ and $\pi/8$, where E_{ϕ} have maxima.

At last we establish, that we can split the cross-section of circular waveguide to sixteen uniform sectors with the same values of tangential electric components, viz. inside of a $\pi/8$ sector the relative phases are opposites (positive and negative) in radial (r) direction and in azimuthal (ϕ) direction, too. This is shown in Figure 2.

TEM - $TE_{16,2}$ MODE CONVERTER USING MSSA

The schematic of the 15 GHz model of our mode converter is shown in Figure 3, where $\lambda_m (= 15.4 \text{ mm})$ is the wavelength in the $Z_0=140 \Omega$ microstrip line, $\lambda_0 (= 20 \text{ mm})$ is the freespace wavelength and $\lambda' (= 26.85 \text{ mm})$ is the guided-wavelength in $TE_{16,2}$ circular-waveguide mode with $r_0=111 \text{ mm}$.

The inner conductor of the coaxial-input SMA-connector is soldered to the center point of MSSA-exciter, which is realized on Duroid-5880 substrate, having a thickness of 0.794 mm.

The radiating slots of this antenna are cut on the ground-plane side, exciting the whispering-gallery mode of the circular-cylindrical waveguide in which this mode can propagate. Slot dimensions: $1.4 \times 7.1 \text{ mm}$ and $2.5 \times 6.0 \text{ mm}$ are, respectively. Transfer characteristic and the so called mode purity requirements are satisfied by using diaphragms with coupling-slots: 1.8° (Figure 4) and 3.6° .

The half-photomask of the microstrip circuitry of MSSA is shown in Figure 2. The input power is directed to 32 microstrip-slot antenna sections using a microstrip power splitter, in which the line impedances are (from center to the open circuited end): $157' - 96' - 76 - 63.9' - 45.2' - 38 - 76 - 63.9' - 45.2' - 38 - 76 - 73' - 140 \text{ Ohms}$, respectively, where the upper mark (') means the transformer section with the length of quarter wavelength ($\lambda_m/4$). Appropriate relative phases between slots are set by the designated phase shifters.

THE NETWORK MODEL

Perfect symmetry of the microstrip-slot antenna is supposed, i.e. only the modes of 16k azimuthal mode number (k is odd) will be excited. The waveguide is dimensioned so, that only the modes with the suffices $m=16; n=1,2,3$ can propagate.

Using the results of Reiter [9], [10], [11] the network model of the transducer can be constructed (Fig. 5.). The voltage generator on the left side models the source coupled to the coaxial input. The distributor network symbolizes the mode converter effect of the microstrip-slot antenna: it transforms the voltage into the transmission lines corresponding to the propagating modes and into the lumped reactances corresponding to the cut-off modes respectively. The coupling circuit parts model the mode-coupling effect of the irises. If we use the irises of Fig. 4, then according to the orthogonality relations no mode coupling occurs between the modes of the same azimuthal mode suffix. Consequently the upper part of the coupling circuit (belonging to the $TE_{16,2}$ mode) is separated from the lower one.

The transmission lines attached to the other propagating modes can be found in the lower branch, the lengths of these are strongly differ from the half wavelength. The experiences of network calculations show the networks containing transmission lines of lengths differ strongly from the half wavelength are not suitable for signal transmission and their input impedance is pure reactive. Thus through the distributor network the reactances of the lower branch can be drawn into the first two-pole created at the input of the upper branch. Similarly the coupling networks loaded by reactances in the upper branch can be transformed to reactive two-poles. Finally a network is given as the equivalent network of the transducer in which the reactive two-poles are connected to each other by transmission lines attached to the $TE_{16,2}$ mode and of length approximately of half wavelength.

If the transmission and reflection measurements are in accordance to this model, then the transducer is mode-pure.

EXPERIMENTAL RESULTS

Near-field probing, which is done at distances of millimetres from the MSSA, served as a diagnostic tool in the design and the prototype production stages of the mode converter. Single-element rectangular microstrip patch, miniature dipole with split-coaxial balun made from semi-rigid cable and a small loop for magnetic-field probing were used for these purposes. Radial and azimuthal scanning of E_z component are shown in Figures 6 and 7. The measured result is in good agreement with the theoretical curve, given in Figure 1. At the radius $r < 55 \text{ mm}$, the measured value is lower than 22 dB (0.63 %) for the suppressed mode with the index of $n = 1$. Using an absorber phenolic rod less than half the waveguide diameter, this would be vanished, according to the results of Moeller [2].

Figure 8 shows the transmission characteristic of closed structure using two mode-transducers (dotted line) and diaphragms (continuous line). The effectiveness of the mode filtering element is 12 - 20 dB, in the frequency range of 13.5 - 16 GHz.

Figure 9 shows the far field radiation characteristic (E_θ -pattern) of the mode transducer, along with cross-polarization characteristic (dotted line). This figure indicates the absence of other radial modes having $m = 16$. In addition, there is evidence of an $m = 1$ component at the -30 (-25) dB level. The measured cross-polarization level is about -15 dB.

SUPPLEMENTARY MEASUREMENTS OF THE 15 GHZ MODEL

The motivation of our supplementary measurement was: to increase the mode purity using absorber material (mentioned at Moeller [2]) and making a more correct filter-section according to Reiter [3] using the methods of network theory.

All these experiences were utilized in our new design at 38 GHz. The complete microstrip-slot antenna exciter has been designed with the aid of microwave CADs (MMICAD from Optotek Ltd. and the software of Sainati [12]).

Microwave absorber materials (with the radius of 50 mm) were taken into the circular waveguide having a radius $r_0=111 \text{ mm}$. Referring to Figure 1, these absorbers don't affect the used $TE_{16,2}$ mode, only the parasitic modes with lower mode-indices are influenced. Nearfield radial scanning data are given in Figure 10 where the measured relative value of E_θ -component at the range of $r < 50 \text{ mm}$ is much smaller than our earlier limit (see Figure 6). The input return loss (L_R) also was improved. The expected

improvement in transmission loss is 1.4 dB at the frequency of 15.1 GHz. For the open structure of input MSSA, the measured and calculated radiation patterns show small differences, because of the measurement was carried out in the Fresnel zone and in the reflective laboratory-environment, and there are supposed positioning errors.

Transmission versus frequency measurement between two MSSA-s, separated by the length of 3x13 mm circular waveguide section is shown in Figure 11. The expected modes are also designated, supposing that $\lambda_g = 26.3$ mm at all frequencies for the different modes. We can conclude: the microstrip-slot antenna type exciter is a relatively broadband structure, having significant coupling not only for the desired $TE_{16,2}$ mode, but at other frequencies for the unwanted $TE_{16,1}$ and $TE_{16,3}$ mode, too.

Using two irices with opening of 1.8° , and a length of 3x13 mm waveguide section between them, the effectiveness of mode filtering is shown in Figure 12. Better suppression of unwanted modes is possible, using an additional iris with the opening of 3.6° (see Figure 13).

To gain equivalent circuit parameters from Reiter [13] of our structure, we have measured transmission characteristic with expanded frequency scale. Figure 14 shows the measured diagram for the closed structure of two MSSA-s and one iris (1.8°). The parameters (calculated from measurement) are also given. Figure 15 shows the transmission versus frequency characteristic of the closed structure having two MSSA-s, two irices (1.8°) and a waveguide section with the length of 3x13 mm.

DESIGN OF A NEW MODEL FOR 38 GHz

Starting from our basic MSSA-exciter shown in Figure 2, we have changed:

- the impedance level of microstrip lines exciting two slots for $Z_0 = 110 \Omega$,
- the length of these lines, shortening them, having the phaseshift of 180° directly between slots, using equation: $3\lambda_m/2 = r_0(1-0.77)$, where $r_0 = 39.09$ mm is the radius of our new highly overmoded circular waveguide,
- the input section of the microstrip power-splitter, having impedances of 100Ω , so the input impedance is $100/4 = 25 \Omega$, which is transformed to 50Ω inside of the coaxial input section.

In our new design, the impedances from center to the open end:

[50-35.3'-25]-100-87.2'-76-53.7'-76-64.7'-110 Ω are, respectively, where the upper mark (') means the transformer section with the length of quarter wavelength ($\lambda_m/4$). The selected substrate material was D-5880-10 mil.

Figures 16 and 17 show the microstrip power-splitter and radiating-slot side of the substrate used for MSSA-exciter at 38 GHz. Slot dimensions: 0.4×2.86 mm and 0.7×2.54 mm are, respectively. The mode purity requirements of the converter is satisfied by using irices with coupling slots 1.8° and 3.6° . To optimize the input section of power splitter a control circuit is designed and will be measured.

The calculated loss (dielectric and copper loss only) versus frequency characteristic is shown in Figure 18. The dotted line shows the calculated values with $\text{tg}\delta = 0.0012$, the continuous line is calculated with a more realistic $\text{tg}\delta = 0.0045$. There are other components of the total loss, too. With approximate values, there are given below:

- extra loss from rough surface of microstrip lines (etching!):	0.8-1.2 dB
- surface waves of substrate:	0.5-1 dB
- radiating loss of discontinuities:	≈ 1 dB
- loss of: input coaxial connector, coaxial-microstrip transition, circular waveguide section, contact at irices, radiating slots, etc.	2.5-3 dB
- calculated loss of the feed network	0.8 dB

So the total loss, to be expected:

$$\Sigma L = 5.6-7.0 \text{ dB}$$

Turning to the circular waveguide section, the first question is: where are the resonances of different modes on the frequency scale?

Supposing that resonators bordered by irices are having $\lambda_g/2$ -length at the used $TE_{16,2}$ mode, the calculated resonant frequencies versus inner radius of circular waveguide are shown in Figure 19. The used equations are also given in the Figure.

CONCLUSIONS

We have developed the model of a MSSA-type exciter to obtain a TEM to $TE_{16,2}$ converter for the cold-test measurements of a gyrotron at 140 GHz. The basic idea, i.e. to simulate the field of the useful mode by a MSSA and to filter out the unwanted modes by a circular waveguide-cavity filter is proved to be realizable. Antenna measurement methods were applied to control the amplitude and phase distributions of radiating slots, and the far-field characteristic of the open structure. Using the network model, a network-like measurement was carried out on the closed device. Design considerations and experimental results of mode converters were given in the paper. In this experiments students were also involved. The modular design concepts of MSSA and microstrip power splitter can be well exploited in the education and in the laboratory practice of students.

ACKNOWLEDGEMENT

This work was supported by the US-Hungarian Joint Fund. We would like to thank Dr. R. Temkin and Kenneth E. Kreischer of the MIT Plasma Fusion Center, for the useful technical discussions. The authors wish to acknowledge the help of their students, Z.Varga and T.Gyuricza at Technical University of Budapest.

REFERENCES

[1] K.E.Kreischer, B.G.Danly, J.P.Hogge, T.Kimura, R.J.Temkin and M.E.Read: "The Development of High Frequency, Megawatt Gyrotrons for ITER" 1995 IEDM Meeting, Washington D.C.

[2] Ch.Moeller: "A Coupled Cavity Whispering Gallery Mode Transducer" 17th Int.Conf. on Infrared and Millimeter Waves, Pasadena, CA, 1992, pp.42-43

[3] G.Reiter: "A Proposal for the Implementation of Coaxial TEM to TE_{16,2} Circular Waveguide Mode Converter" (in Hungarian) Research Study, TUB/DMT-1995

[4] F.Völgyi: "Microstrip-Slot Antenna used as a Whispering-Gallery Mode Converter" Design and Measurement Report, TUB/DMT- May 1996.

[5] F.Völgyi, Gy.Reiter, Gy.Veszely and T.Berceli: "Experimental Results of a Coaxial TEM-Circular TE_{16,2} Mode Transducer" 22nd Int. Conf. on Infrared and Millimeter Waves, Wintergreen, Virginia, USA, July 20-25, 1997.

[6] F.Völgyi: "Microstrip Antenna Array Applicator for Microwave Heating" 23rd European Microwave Conference, Madrid, Spain, September 1993, pp.412-415

[7] F.Völgyi: "Integrated Microwave Moisture Sensors for Automatic Process Control" Ch.15 in book: "Microwave Aquametry" (edited by: A.Kraszewski), IEEE Press, New York, 1996 ISBN 0-7803-1146-9 pp.223-238

[8] F.Völgyi: "Microstrip Antennas Used for WLAN Systems" ISAP'96 Int.Symp. on Antennas and Propag., September 24-27, 1996, Chiba, Japan, Proc.Vol.3 pp.837-840

[9] G.Reiter: "Solution of Field Equations for Strongly Coupled Cavity Systems", Electromagnetic Wave Theory, Proc. of Symposium held in Delft, the Netherlands, Sept 1965. pp. 357-367

[10] G.Reiter: "Single Mode Coupling Between Cylindrical TE₀₁₁ Resonators", URSI Int. Symposium on Electromagnetic Theory, August 25-29, Budapest, Hungary, Part b pp. 500-502

[11] G.Reiter et al: "A Coaxial TEM-Circular TE_{16,2} Mode Transducer for Cold Test of Gyrotrons Output Converters", 21st Int. Conf. on Infrared and Millimeter Waves, Berlin, 1996 AT4

[12] Robert A.Sainati: "CAD of Microstrip Antennas for Wireless Applications" Artech House, Boston-London, 1996, ISBN 0-89006-562-4

[13] G.Reiter: "A Proposal for the Measurement of Inverter-Admittances Used in Microstrip-Slot Antenna Type Mode Converter" (in Hungarian), Research Study, TUB/DMT, April 1997.

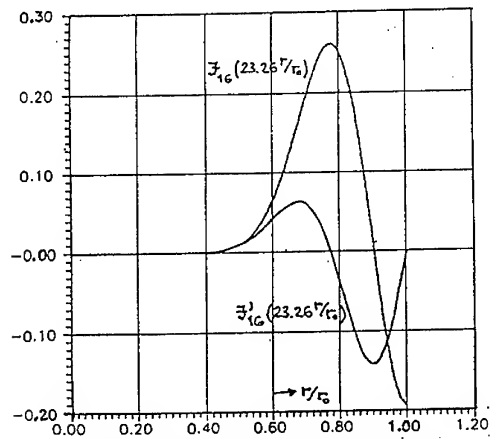


Figure 1. Bessel functions in eq. (1) and (2)

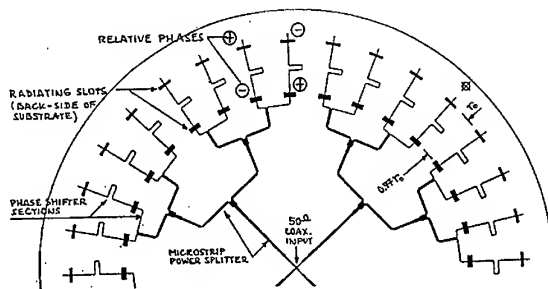


Figure 2. The half-photomask of the microstrip circuitry of MSSA

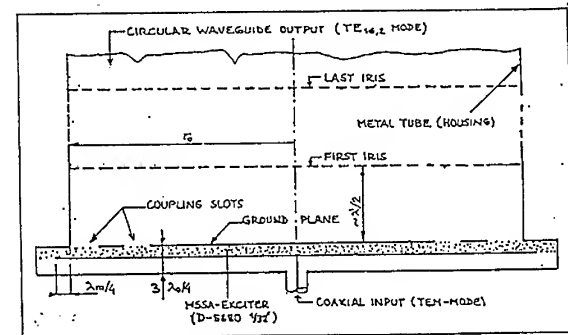


Figure 3. Schematic of the MSSA-excited mode converter

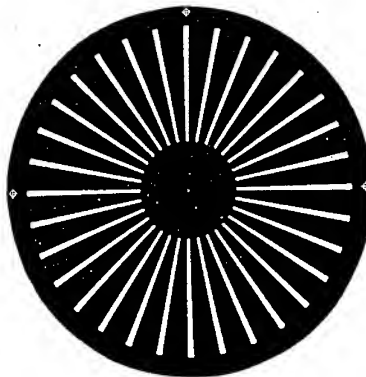


Figure 4. Iris with the openings of 1.8 deg.

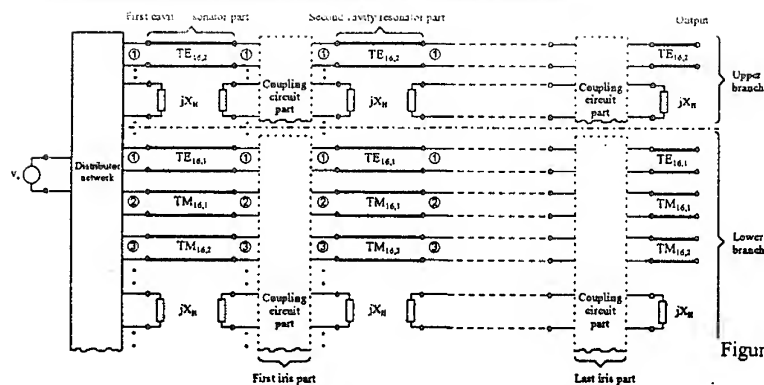


Figure 5. The network model of the transducer

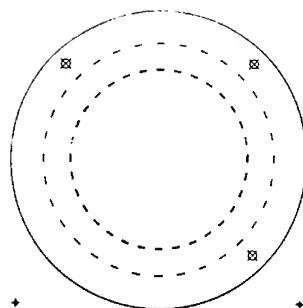


Figure 7. Slot radiators of the 38 GHz converter (metallization is white)

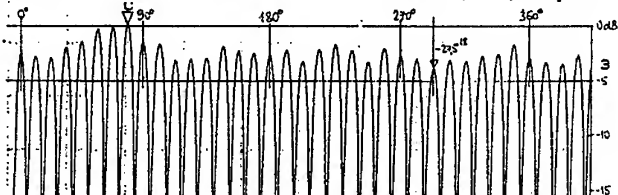
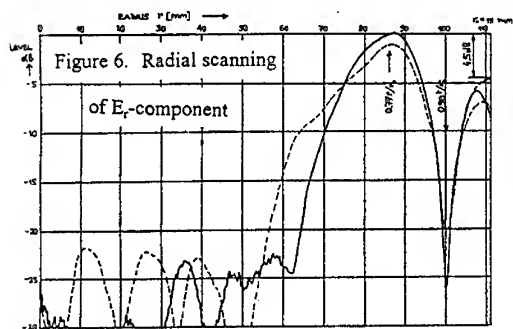


Figure 7. Azimuthal scanning of E_r -component

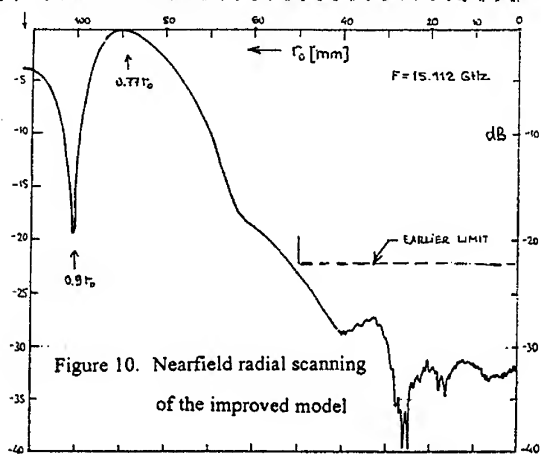
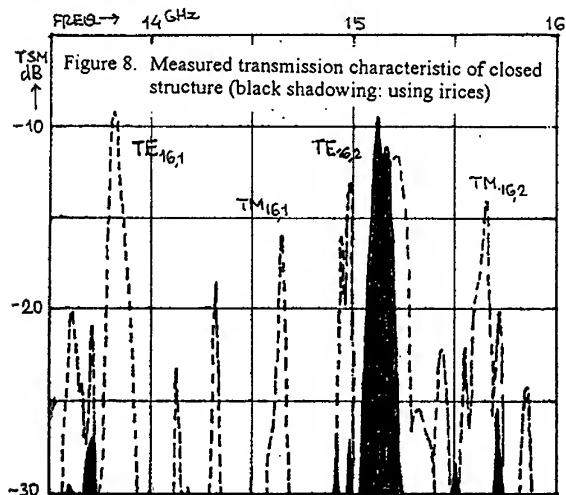
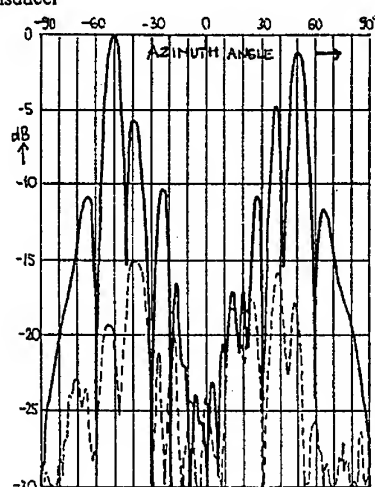
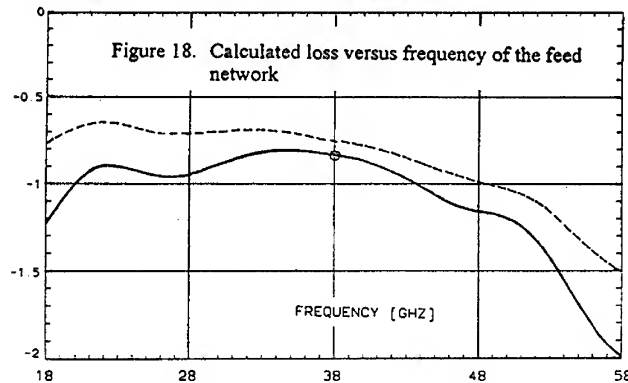


Figure 9. Measured far-field radiation pattern of the mode transducer



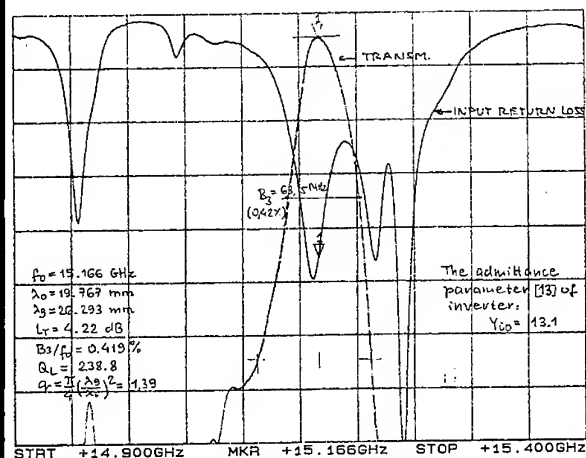


Figure 14. Input return loss and transmission measurements

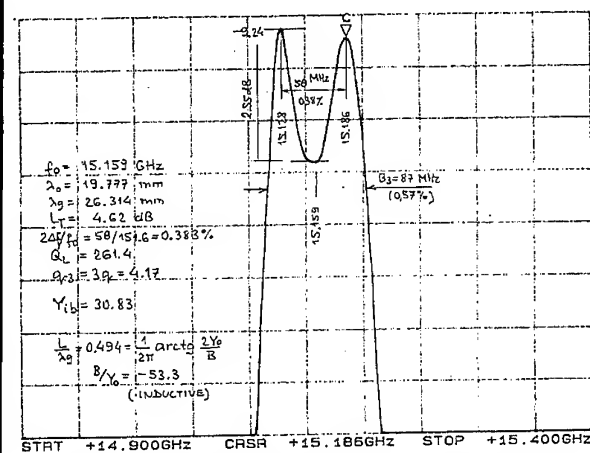


Figure 15. Measured transmission loss vs. freq. characteristic using $2 \times 1.8^\circ$ irises

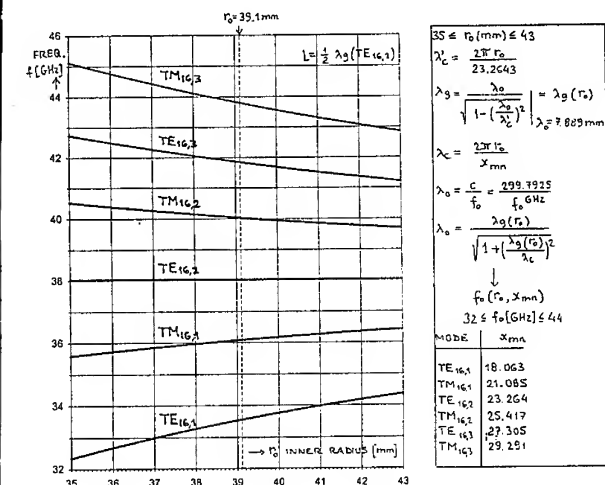


Figure 19. Calculated resonant frequencies vs. inner radius of CWG

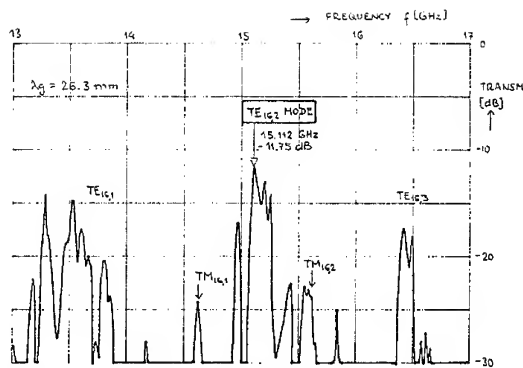


Figure 11. Measured transmission loss vs. freq. characteristic for closed structure of two MSSAs and a circular-waveguide section with a length of 39 mm

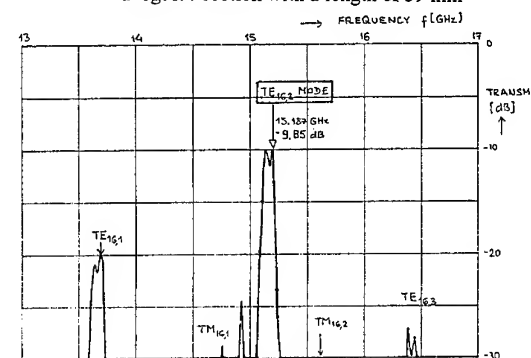


Figure 12. Mode filtering using $2 \times 1.8^\circ$ irises & 39 mm CWG

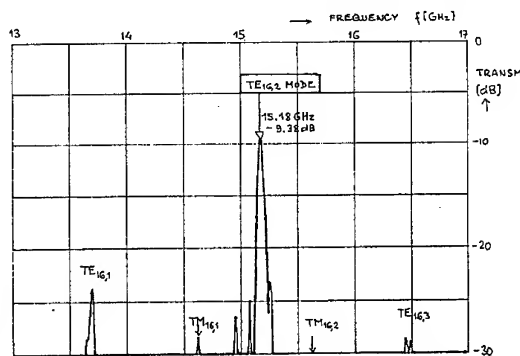


Figure 13. Mode filtering using irises: $1.8^\circ-1.8^\circ-3.6^\circ$

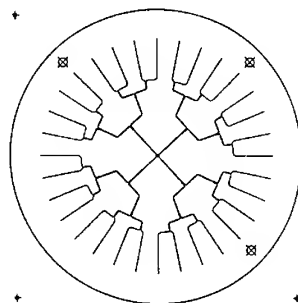


Figure 16. Microstrip power-splitter for MSSA exciter at 38 GHz (metallization is black)

References (Microstrip Antennas)

1. Völgyi, F.: "High-Gain Microstrip Antennas" (in Hungarian) *Híradástechnika*, Vol. 36, No. 6. 1985. pp. 266-281. (A Pollak-Virag awarded paper)
2. Völgyi, F.: "Development of Microstrip Antennas" (in Hungarian) Research Report, TUB/DMT, 1985., OKKFT-A/5-C/e2, p. 157.
3. Völgyi, F.: "High Efficiency Microstrip Antenna Array" Proc. of the 17th EuMC., 7-11th September 1987., Rome, Italy, pp. 747-752.
4. Völgyi, F., Denk, A., Somogyi, A., Tamasi, S. and Babits, L.: "Broadbanded Microstrip Antenna" Hungarian Patent, 30th June 1989., No. 205 816 B (Int.Cl. H 01 Q 1/38)
5. Völgyi, F.: "Versatile Microwave Moisture Sensor" SBMO'89 Int. Microwave Symposium/Brazil, Sao Paulo, 24-27 July 1989. Proc. Vol-II pp. 456-462.
6. Mernyei, F. and Völgyi, F.: "Simple Methods for Testing Temperature Dependence of Microstrip Antenna Arrays" 20th EuMC, Budapest, September 1990. pp. 365-370.
7. Völgyi, F.: "Flying Decibels - Extremely Lightweight Microstrip Antennas" ICOMM'90 Int. Conf. on Millimeter Wave and Microwave, Dehra Dun, India, December 1990. pp. 343-348.
8. Mernyei, F. and Völgyi, F.: "Planar Antenna Array for Airborne Radiometer Applications" ICOMM'90, Dehra Dun, India, December 1990. pp. 393-396.
9. Mernyei, F., Völgyi, F., Heidrich, E., Kehrbeck, J. and Lebherz, M.: "Microstrip Antenna Applications" *Periodica Polytechnica (Hungary) Ser. El. Eng.*, Vol. 36. No. 1., 1992. pp. 273-283.
10. Völgyi, F.: "Integrated Microwave Moisture Sensors for Automatic Process Control" IEEE/MTT-S'93 WSMJ-Workshop, Atlanta, GA, USA, Proc. 14th June 1993. pp. 39-44.
11. Völgyi, F.: "Microstrip Antenna Array Applicator for Microwave Heating" 23rd EuMC, Madrid, Spain, September 1993. pp. 412-415.
12. Völgyi, F.: "Upper S-Band Microstrip Antennas with Polarization Diversity and Frequency Agility" MILCON'95 Int. Defence Conf. 19-23 March 1995., Abu Dhabi, United Arab Emirates, Conf. Proc. pp. 200-207.
13. Völgyi, F.: "Integrated Microwave Moisture Sensors for Automatic Process Control" Ch. 15. in book: "Microwave Aquametry" (edited by A. Kraszewski), IEEE Press, New York, 1996., ISBN 0-7803-1146-9 pp. 223-238.
14. Völgyi, F. and Zombori, B.: "A New Application of WLAN-Concept: Complex Permittivity Monitoring of Large-Sized Composite Boards" IEEE MTT-S, WMFB-Workshop, 17th June 1996., San Francisco, USA, pp. 119-122.
15. Völgyi, F.: "Microstrip Antennas Used for WLAN Systems" ISAP'96 Int. Symp. on Antennas and Propagation, 24-27 September 1996., Chiba, Japan, Proc., Vol. 3. pp. 837-840.
16. Beke, J. and Völgyi, F.: "Interactions of Kernel Features and Field Parameters in Microwave Drying of Corn" Asia Pacific Microwave Conference, 17-20 December 1996., Hotel Ashok, New Delhi, India, Conf. Proc. Vol. 2. pp. 383-386.
17. Völgyi, F., Reiter, G., Berceli, T. and Veszely, G.: "A Whispering Gallery Mode Transducer Using Microstrip-Slot Antenna Exciter" Suggested Paper for the 27th EuMC, Jerusalem, Israel, 8-12 September 1997. Accepted

The analysis of medium sized arrays of complex elements using a combination of FDTD and reaction matching

by: C. J. Railton and G. S. Hilton
Centre for Communications Research
Faculty of Engineering, University of Bristol
Bristol, BS8 1TR
England

ABSTRACT

The analysis of medium sized arrays of complex antenna elements by means of a full-wave numerical modelling technique often requires impractical amounts of computer power. Nevertheless, it is essential that all the mutual couplings between elements are taken into account. In this contribution, a technique is presented in which the individual element is characterised using the FDTD method and, using the information this provides, the behaviour of the complete array is predicted using a method based on reaction matching. Results using this method are compared to measurement and to results obtained using a complete full-wave analysis for three and five element arrays of printed dipoles and are shown to be in good agreement. For arrays of between 10 and 50 elements, savings in computer time of several orders of magnitude can be achieved and, in addition, changes in array geometry do not always necessitate all the results being recalculated.

INTRODUCTION

The prediction of the far field radiation patterns and return losses for antenna arrays comprising a finite number of complicated elements, such as microstrip patches, printed dipoles and the like, with modest computer resources is doubly problematic. Firstly, even the analysis of a single element may be difficult and secondly calculation of the interaction between array elements, which may be placed in close proximity, increases the scale of the problem enormously. This is true both with techniques such as FDTD [1] for which the computational effort is only linearly dependent on the size of the computational space but which requires the discretisation of the total space occupied by the array and for the Method of Moments [2] for which the effort is proportional to some power of the number of unknowns. For medium sized arrays of between five and fifty closely spaced complicated elements where infinite array approximations are inadequate but where mutual impedance effects cannot be ignored, the situation using either technique rapidly becomes impracticable. In this contribution, a methodology is presented which allows accurate results to be obtained for problems of this type using just a medium power workstation such as the HP9000/730.

A general method for drastically reducing the amount of computer resources required for this type of problem was recently presented [3] where its effectiveness was demonstrated for the case of an array of wire dipoles. In this contribution the method is extended to allow the analysis of the much more complicated case of an array of printed dipoles of the type described in [4] and illustrated in Figures 1 and 2. The individual element

consists of a printed dipole with a microstrip feed and balun. The dimensions are given in Figure 1. The array is based on arranging the elements in the pattern of an equilateral triangle as illustrated in Figure 2. Each element protrudes through an aperture in a reflecting back plane which is considered to have infinite area. Comparison of the results obtained using the new method with those produced using a full FDTD analysis and with measurement show good agreement.

THEORY

An example of the general problem to be solved is shown in Figure 3, where three elements of an array are shown. The actual element which will be used as an example in this paper is shown in Figure 1. Around each element a fictitious surface is drawn, shown as a dashed line, on which the scattered field patterns of that element in isolation are calculated. Each element with its surrounding surface is represented as a 2 port network. Because the response of the element to an incident signal at the feedline is different from its response to an incident field from a distant source, each element is characterised for both situations.

In order to get the information which is required, several different test signals are applied to the isolated element. The choice of these test signals is discussed below. In each case the resulting scattered field at the surrounding surface and the strength of the signal emanating from the feedline is calculated. The procedure may be summarised as follows:

Test 1. Response to a signal at the feedline. Apply a signal having a voltage of u^i to the feed line. Calculate the reflected voltage, v^i , and the distribution of the tangential field components on the surrounding surface, $\{E^i, H^i\}$. It can be seen that v^i/u^i is the reflection coefficient of the isolated element. The mode of the antenna which is excited by this test is referred to as the **transmit mode**.

Tests 2. Response to incident test fields. Apply a number of incident test fields having distributions $\{E^p, H^p\}$ at the surrounding surface. In each case calculate the strength of the signal emanating from the feed line, v^p , and the distribution of the scattered field at the surrounding surface, $\{E^p, H^p\}$. It is noted that this requires P separate FDTD runs where P is the number of test fields used.

In [3], a single incident test field is applied and the approximation is made that the form of the scattered field resulting from the actual incident field will be the same as that resulting from the incident test field. This corresponds to the assumption that the induced current distribution on the antenna is independent of the form of the incident signal. For the wire dipole treated in [3] this is indeed very nearly the case. However for the more complicated case of the printed dipoles, it has been found that the direction from which the incident field arrives can make a considerable difference to the form of the scattered field. This behaviour is illustrated in Figure 5 which shows the scattered fields in the E plane and the H plane of the element resulting from incident fields impinging from three different directions corresponding to the positions of three different neighbours in the array. It can be seen that, whereas in the H plane, the scattered field is indeed virtually independent of the direction of the incident field, this is definitely not the case for the E plane. In particular, it can be seen that the characteristic null in the radiation pattern which exists at around 70° from boresight when the feedline is excited, changes position depending on the direction of the incident excitation.

In view of this behaviour, it is necessary to extend the basic method described in [3] in order to allow the inclusion of several test fields so that the effects of the direction of arrival of the incident fields could be accounted for. Since the basic method does not directly lend itself to multiple test functions, a different way forward was sought. Rather than using all the available test fields at once, each test field is used individually to provide separate estimates of the array S matrix. Thus if six test fields were used, there would be six estimates of the S matrix of the complete array, each estimate corresponding to a chosen test field.

The test fields are chosen to be the incident field on a specified element caused by feedline excitation of a neighbouring element. For instance, consider dipole 1 in the three element array shown in Figure 4. Ignoring for the moment the fields scattered by the elements which are not excited at the feedline, there are two different possible field patterns incident on dipole 1 depending on whether dipole 2 or dipole 3 is excited. Similarly there are two possible field patterns associated with the other two dipoles leading to six functions in all. Any or all of these may be used as test functions to provide estimates of the array S matrix. If the mutual coupling between elements is small (about -20dB in this case) then the actual incident field, including all scattering effects will be only slightly perturbed from the test functions and, thus, accurate results may be expected.

As has previously been discussed, the incident field at, for instance, element 1 resulting from excitation of element 2 may be quite different from that resulting from excitation of element 3. If the value of S_{12} for the array is calculated using test field 1 and the value of S_{13} is calculated using test field 2, then accurate results would be obtained for both. In general, the final array S matrix is made up by selecting components from the set of estimated S matrices such that the test function used for the chosen estimate is closest in form to that of the expected actual incident field.

In the case where less than six test functions are used, whether because of symmetry or simply to reduce the computational requirement, then for each component of the array S matrix, the test function which is considered the closest approximation to the actual incident field will be used. For instance, consider the case where only three test functions are used as shown by the solid lines in Figure 4 which are derived as follows:

Function 1	source element 1	target element 2
Function 2	source element 1	target element 3
Function 3	source element 2	target element 1

We may use any of these functions to approximate the field arriving at a specified element resulting from excitation at a different specified element. For the example described here, test function 2 has been used in place of test functions 4-6. Clearly, other choices are possible.

For the results presented here, three test functions were used which are illustrated by the solid lines in Figure 3 and the isolated element is analysed using the FDTD method [5]. It is possible that more accuracy would be obtained if all six near-neighbour incident fields were used and work is continuing to establish the optimum number of test fields.

RESULTS

In Figure 6, the co-polar and cross-polar far field radiation patterns, calculated using this method are shown and compared to results obtained using the full FDTD method and to measurement. The results are taken at a frequency of 9.3GHz, the centre of the operating bandwidth of the antenna. It can be seen that, for the co-polar patterns, agreement is generally better than ± 1 dB. For the cross-polar results the same general levels are obtained but the actual shape is different, mainly due to measurement uncertainties. However, agreement with measurement is as good as with the full FDTD method.

CONCLUSIONS AND DISCUSSION

It has been shown that accurate results can be obtained using the combination of FDTD and reaction matching described in this contribution for an array of complex elements. In order to completely characterise the array using full FDTD required 14 days of computer cpu time on an HP700 workstation, using the new method this was reduced to about 8 days. For larger arrays the savings are much greater. For instance for an array an order of magnitude larger the estimated time required for FDTD is about 2 years on an HP700 whereas for this method the estimated time is about 72 days. Moreover, if it were required to change the geometry of the array, it would be necessary to completely repeat the FDTD analysis in order to characterise the new structure. With this method, however, only some of the results would need to be recalculated. Thus the optimisation of the geometry of an array which is impractical using full FDTD or MoM, becomes more viable using this type of modelling.

ACKNOWLEDGEMENT

This work was supported by Defence Evaluation and Research Agency, UK.

© British crown copyright 1997/DERA

Published with the permission of the controller of Her Britannic Majesty's Stationery Office.

References

1. K. S. Kunz and R. J. Leubbers "The Finite Difference Time Domain for Electromagnetics" CRC Press 1993
2. R. F. Harrington "Field Computation by Moment Methods" IEEE press 1993
3. C. J. Railton, S. A. Meade and G. S. Hilton "New Methodology for the Analysis of Finite Arrays of Complex Antenna Elements", Electronics Letters Vol. 32, No. 9, pp 784-785, April 1996.
4. G. S. Hilton and C. J. Railton, "Finite-Difference Time-Domain Analysis of a Printed Dipole Antenna", IEE 9th Int Conf on Antennas and Propagation, April 1995, Eindhoven, The Netherlands. vol 1, p72-75.
5. I. J. Craddock and C. J. Railton "Application of the FDTD method and a full time-domain near-field transform to the problem of radiation from a PCB" Electronics Letters, Vol 29, No. 23 November 1993, pp. 2017-2018

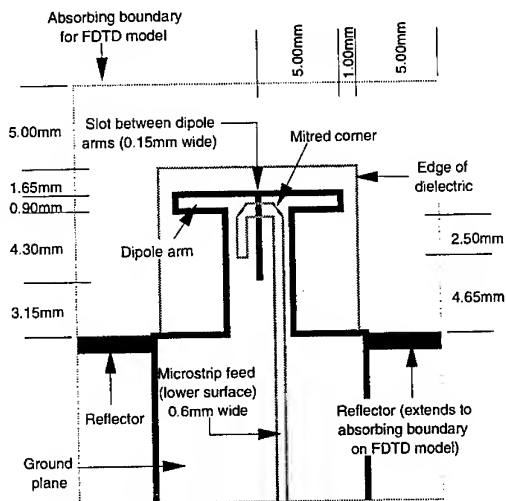


Figure 1 - Surface view of the printed dipole antenna with reflector mounting

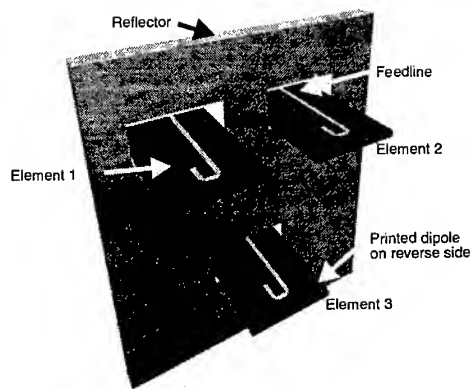


Figure 2 - 3D view of the three element array arranged on an equilateral triangle of side 18mm

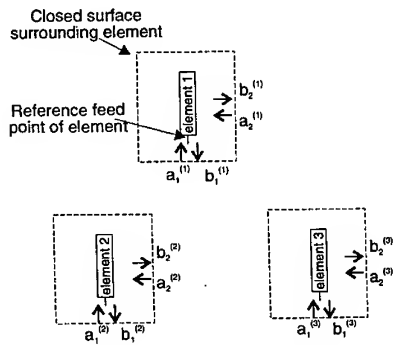


Figure 3 - Outline of the basic problem to be solved

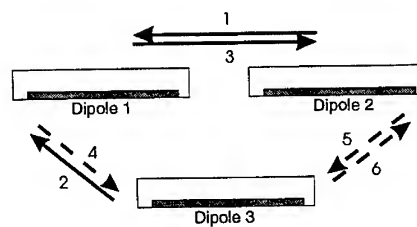


Figure 4 - The set of nearest neighbour test functions

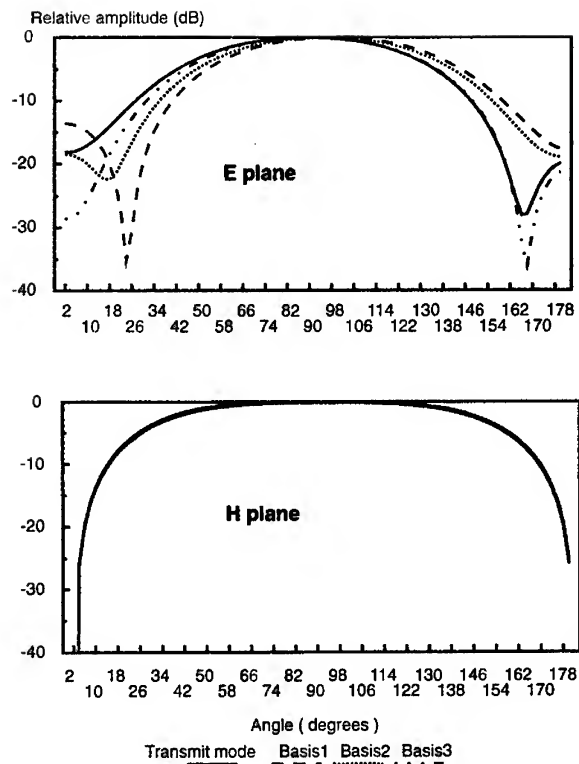


Figure 5 - The scattered field pattern in response to different incident fields

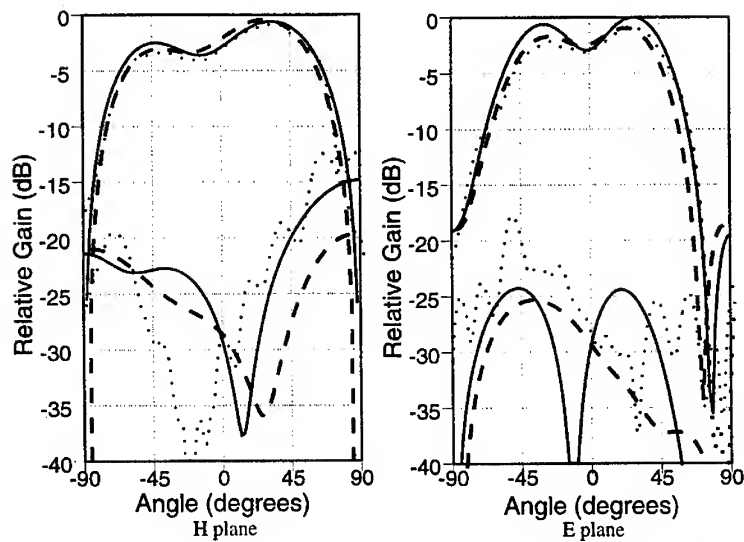


Figure 6 - Co-polar and cross-polar radiation patterns for the three element array element 1 excited

— FDTD - - - This research Measured

A Ring-Laser Type Quasi-Optical Oscillator Using Leaky-Wave Antenna

Wei Fu, Yongxi Qian and Tatsuo Itoh

Electrical Engineering Department
University of California, Los Angeles
Los Angeles, CA 90095

ABSTRACT

This paper presents a novel ring-laser type quasi-optical oscillator based on leaky-wave antenna, which can be used as an alternative to conventional configurations employing VCOs. It consists of a gain-control amplifier, a phase-shifter and a microstrip leaky-wave antenna. The feature of this structure is that the leaky-wave antenna not only serves as a radiation element, but also provides oscillation feedback. The beam-scanning capability of this quasi-optical oscillator is also demonstrated experimentally.

INTRODUCTION

The leaky-wave antenna is often used in frequency scanned radar systems[1], where the beam-scanning capability is realized by changing the operation frequency. Usually voltage-control oscillators (VCOs) can be employed to achieve frequency scanning. However, in this traditional approach where VCOs is terminated by the leaky-wave antenna, the oscillator and antenna are designed separately, which usually results in an inefficient circuit. VCOs circuit design will become further complicated if one tries to achieve wide oscillation range and good frequency stability simultaneously[2].

In this paper, we present a new ring laser type of quasi-optical oscillator using leaky-wave antenna (Fig.1) as an alternative implementation to the conventional configuration using VCOs. It is simply formed by a gain-control amplifier, a phase-shifter and a leaky-wave antenna. In this structure, the leaky-wave antenna not only serves as a radiation element, but also provides oscillation feedback. It is a multiple longitudinal mode oscillator, and appropriate oscillation mode can be selected by changing the gain of the amplifier. To achieve beam-scanning, the oscillation frequency can be easily shifted by changing the phase of the phase-shifter.

THEORY AND RESULTS

The passive leaky-wave antenna, as shown in Fig. 1, is made of microstrip line with periodic step discontinuities. According to Floquet's theorem[3], the guided wave can be expressed as an infinite number of traveling waves with propagation constant $\beta_n = \beta_0 + 2n\pi/d$, where β_0 is the propagation constant in the microstrip line. Radiation is induced by appropriately choosing the length d of one period, such that the β_{-1}

traveling wave resides in the fast-wave region. Beam-scanning of the periodic leaky-wave antenna is achieved by changing the operating frequency, and the main beam angle is determined by,

$$\theta = \arcsin\left(\frac{\phi_{element} - 2\pi}{k_0 d}\right) \quad (1)$$

where k_0 is the free-space wave-number. $\phi_{element}$ is the phase delay for one period, and is frequency dependent.

A leaky-wave antenna[4], a gain-control amplifier, and a phase-shifter are used to form a quasi-optical oscillator. Since the leaky-wave antenna resides within the loop, it will provide a feedback for the oscillation in addition to being the radiation element. Oscillation will occur when the loop gain is larger than unity, and the oscillation frequencies are determined by

$$\phi_{antenna} + \phi_{amplifier} + \phi_{phase-shifter} = 2n\pi \quad (2)$$

where $\phi_{amplifier}$ and $\phi_{phase-shifter}$ are the phases of the gain-control amplifier and the phase shifter, respectively. $\phi_{antenna}$ is the phase shift of the leaky-wave antenna. The S-parameters of each antenna element is calculated by the FDTD method, and the phase of the whole leaky-wave antenna is obtained by cascading each element. The principle of this oscillator is similar to a multiple mode ring-laser oscillator. The frequency of each oscillation mode is determined by (2). The specific longitudinal mode can be selected by changing the gain of the gain-control amplifier or by adjusting the phase of the loop. The purpose of the phase shifter is to change the oscillating frequency in order to realize beam-scanning capability.

The leaky-wave antenna is fabricated on low-cost PC-board substrate($\epsilon_r=4.4$, thickness=20mil). The S-parameters of the leaky-wave antenna, as shown in Fig.2, indicates a good agreement between simulation and experimental results. Fig.3 shows far-field patterns of this quasi-optical oscillator at 8.07GHz, 8.226GHz, and 8.5GHz, respectively. A scanning range of 12° is obtained when oscillation frequency changes from 8.07GHz to 8.5GHz.

CONCLUSION

A new ring laser type quasi-optical oscillator, which can be considered as a simple alternative to conventional designs employing VCOs, is proposed in this paper. Its oscillation frequency is easily shifted by changing the phase of the phase-shifter. The resultant beam-scanning capability should make this new type quasi-optical oscillator useful in frequency scanned radar systems.

ACKNOWLEDGMENTS

The authors would like to thank Mr. Carl Pobanz for his helpful discussions. This work was supported by AFOSR under JSEP.

REFERENCE

1. M. I. Skolnik (Ed.), Radar Handbook, McGraw-Hill, New York, 1970.
2. D. Fisher and I. Bahl, Gallium Arsenide IC Applications Handbook vol.1 Chapter5.
3. R. E. Collin and F. J. Zucker, Antenna Theory. John Wiley and Sons, New York, 1969
4. H.Z. Chang , M. Chen, B. Houshand and T. Itoh, "Characterization of leaky-wave Antennas and Active Gain Enhancement." Presented at 26th European Microwave Conference, 1996

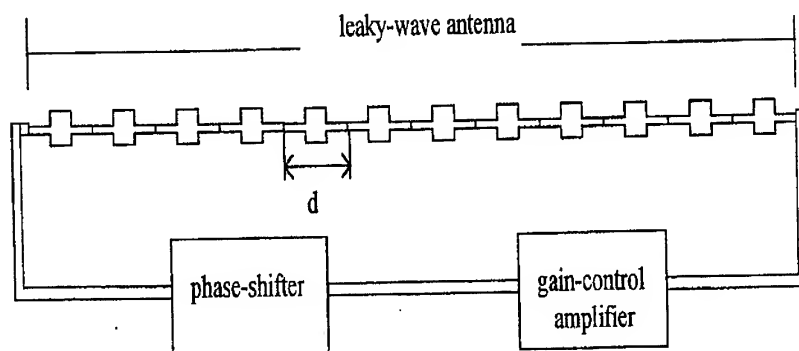


Fig.1 New Type Quasi-Optical Oscillator

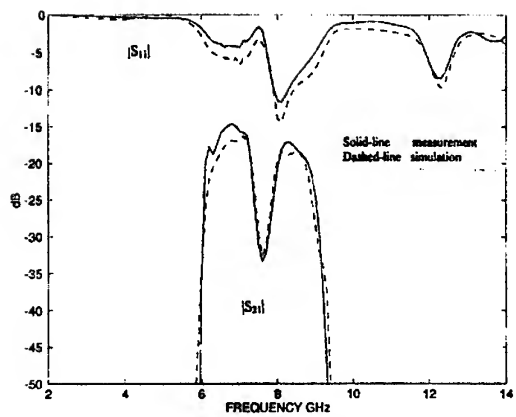


Fig.2 S-parameters of Passive Leaky-wave Antenna

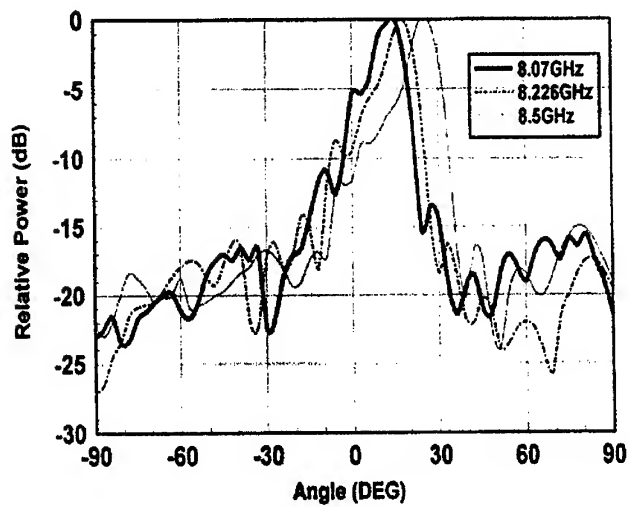


Fig.3 Quasi-Optical Oscillator Radiation Pattern

ACTIVE WIDEBAND ANTENNA WITH CIRCULAR POLARIZATION

Aleksandar Nešić and Siniša Jovanović

Institute of Microwave Techniques and Electronics
Lenjinov bulevar 165b, 11070 Belgrade, Yugoslavia

Tel.: +381 11 222 1215. fax: +381 11 138 826, e-mail: aca@imtel.co.yu

Abstract

The paper presents analysis, design and realization of the novel active wideband circular polarization antenna integrated with FM transmitter of about 20 dBm radiated power operating in the frequency range from 4.6 GHz to 5.8 GHz, which is realized on dielectric substrate placed perpendicularly to the antenna plate. Axial ratio (AR) < 6 dB in the frequency range of 13% and AR < 3 dB in the range of 6% is obtained.

Introduction

Printed antennas with circular polarization are practically unavoidable in numerous mobile and satellite radio systems. Active printed antennas are also becoming essential components due to their low cost and small size. In [1] and [2] a new type of single-feed printed antenna with circular polarization is presented, which has more than ten times wider band than most frequently used patch antennas with circular polarization. It consists of two orthogonal dipoles with parallel feeding, whose impedances are complexly conjugated. In this manner, quadrature feeding current is obtained. Integration of this type of antenna with an oscillator-transmitter is realized through balanced microstrip line standing perpendicularly on the antenna plate in order to avoid parasitic coupling with orthogonal dipoles resulting in degradation of AR.

This paper presents design, analysis and optimization of a printed antenna with circular polarization integrated in the drain circuit of an oscillator-transmitter. The paper also presents design and optimization of an oscillator-transmitter which has the possibility of frequency change in the bandwidth of 23% in which AR is less than 10 dB as well as the possibility of frequency modulation. All important theoretical results are in good agreement with those obtained experimentally on the realized model.

Design, analysis and optimization

Two orthogonal strip dipoles printed on dielectric substrate are designed to provide that the impedance of the first is $Z_1 = (50 - j50) \Omega$ and the impedance of the second is $Z_2 = (50 + j50) \Omega$. In such a manner, when the dipoles are fed in parallel, their currents will be in phase-quadrature and the total impedance becomes $Z \approx (50 + j0) \Omega$, fig. 1.

Dipoles are designed assuming a conducting reflector plate at a distance of $\lambda_0/4$. The analysis and optimization are realized using the IE3D software package [3].

Both orthogonal dipoles are printed on the same side of dielectric substrate and connection with transmitter (fig. 2) is performed through the symmetrical (balanced) microstrip line which is placed perpendicularly to the dielectric substrate, fig. 3. The symmetrical microstrip line penetrates through holes in reflector and antenna plate, fig. 3.

For designing the FET oscillator configuration small signal S-parameters are used. The analysis is performed using Eesof's Touchstone program package [4]. Oscillation condition is accomplished by optimization of the impedance in the source circuit, i.e. open-circuited microstrip line and impedance in the gate circuit. In the gate circuit, there is also a tuning diode. By changing its capacitance, necessary tuning as well as FM or FSK modulation is achieved. Optimization was conditioned by the requirement to obtain the oscillation condition in the range between 4.6 and 5.8 GHz, i.e. in the range where AR of the antenna is less than 10dB.

Realization

Orthogonal dipoles are realized on a very thin dielectric substrate of Teflon-fiberglass ($\epsilon_r=1.17$, $h=0.127\text{mm}$), fig. 1. Under the antenna plate, at the distance of $\lambda_0/4$, there is a reflector plate and polyurethane foam between them ($\epsilon_r=1.03$), fig. 3. Oscillator-transmitter is also realized on dielectric substrate of the same characteristics as the orthogonal dipoles, fig. 2. FET drain circuit is extended to the BAL-UN and then to the symmetrical (balanced) microstrip by which orthogonal dipoles are fed. In drain circuit a high-pass filter is realized to avoid parasitic modulation of the oscillator by low frequency signal received by antenna. Through coupling with the microstrip line a sample of transmitting signal is obtained, which is used for measuring as well as for coupling with phase discriminator in case the frequency is stabilized with phase lock loop, fig. 2 and 3.

Obtained results

Fig. 4 shows change of frequency and output power of the transmitter versus tuning diode polarization. These measurements are performed on the test SMA port.

Fig. 5 shows AR versus frequency for $\theta=0^\circ$. As reference antennas, linearly polarized standard gain horn (Scientific Atlanta) as well as a receiving antenna of the same type as measured antenna were used. Minimum AR is obtained at $f=4.9$ GHz.

Fig. 6 features radiation pattern at $f=4.9$ GHz versus θ . Curves "min" and "max" represent maximum and minimum values of the level obtained upon spinning of the measured antenna.

Conclusion

This paper presents a novel type of active wideband printed antenna with circular polarization with an oscillator-transmitter whose frequency changes in 23% range within which $AR < 10\text{dB}$. The transmitter is modulated by FM or FSK signals. There is also the possibility of stabilization of the oscillator-transmitter via phase lock loop. AR in the range of 13% is less than 6 dB and in the range of 6% is less than 3 dB. The antenna bandwidth order of magnitude is higher than that of most frequently used patch antennas with circular polarization.

Acknowledgment

This work is supported by the Serbian Science Foundation. The authors also thank Ms. Ivana Radnović, Ms. M. Marjanović and Mr. M. Tasić for their help in realization of the model as well as Ms. N. Španović for her assistance in translation of this paper into English.

References

- [1] Nešić, A., Radnović, I., Mikavica M.: "Printed antenna and array with circular polarization", Electronics Letters, 25th April 1996, Vol. 32, No. 9., pp. 785-786.
- [2] Nešić, A. and all: "New printed antenna with circular polarization", 26th EuMC, September 1996, Prague, pp. 569-575.
- [3] IE3D User's Manual, ver. 3.0, Zeland Software, Inc., Fremont, CA, 1995.
- [4] Touchstone and Libra Reference (Ver. 2), Westlake Village, Eesof, Inc., 1990.

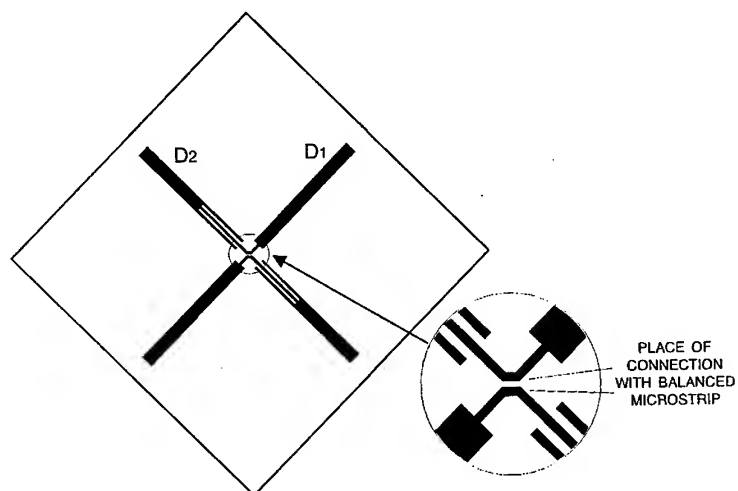


Fig. 1. Two orthogonal dipoles with complexly conjugated impedances

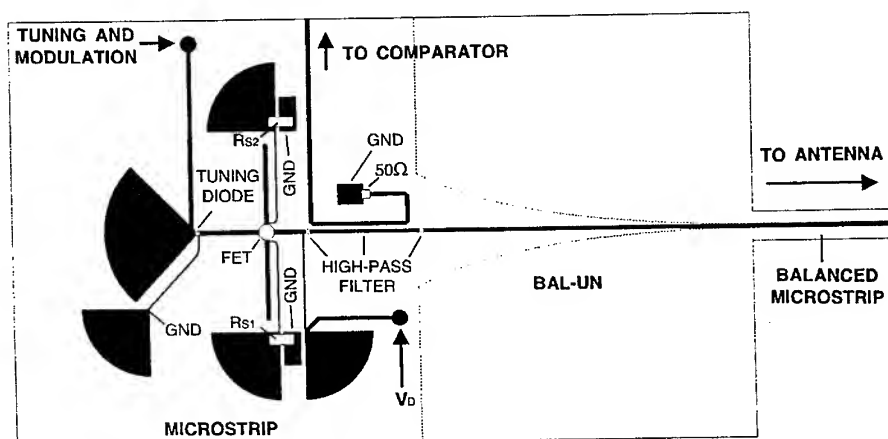


Fig. 2. Transmitter with unbalanced to balanced microstrip transition

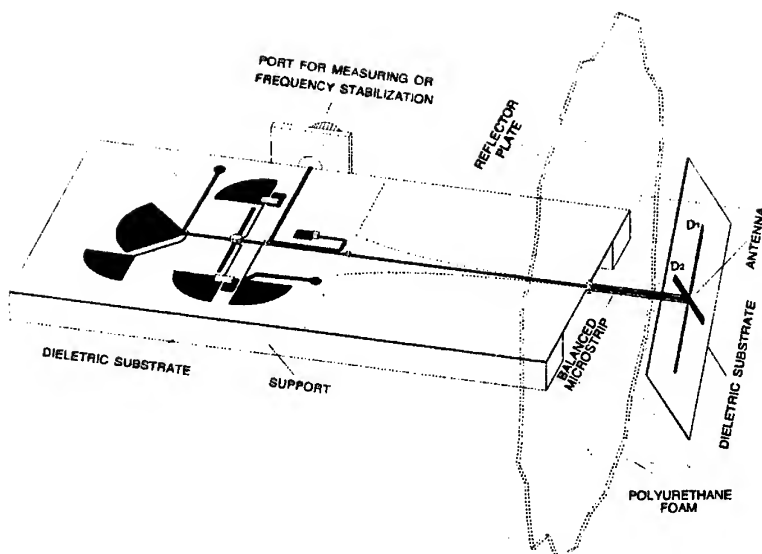


Fig. 3. Circular polarization antenna integrated with transmitter

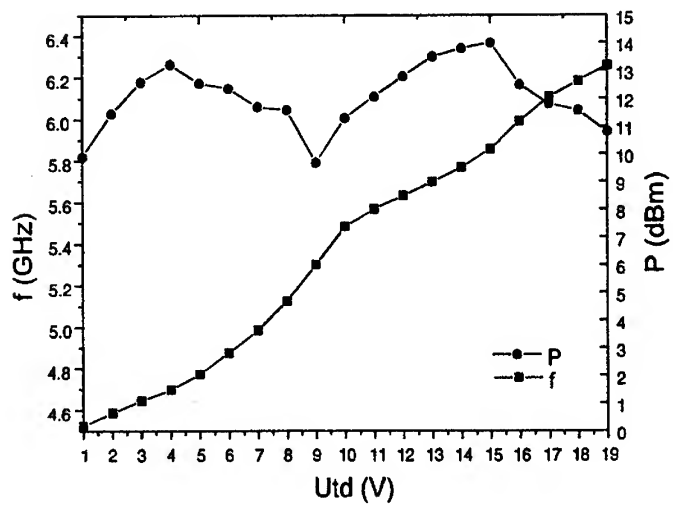


Fig. 4. Frequency and output power of the transmitter vs. tuning diode polarization

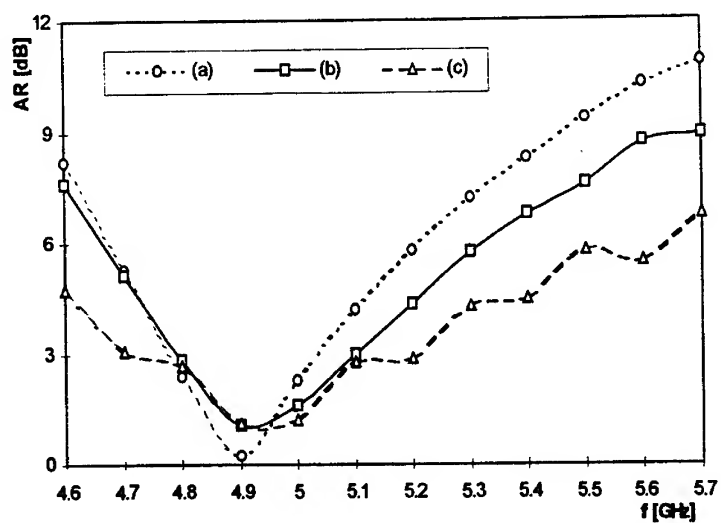


Fig. 5. Axial ratio at $\theta=0^\circ$ vs. frequency. (a) simulated by IE3D, (b) measured by standard gain horn, (c) measured by receiving antenna of the same type as tested antenna

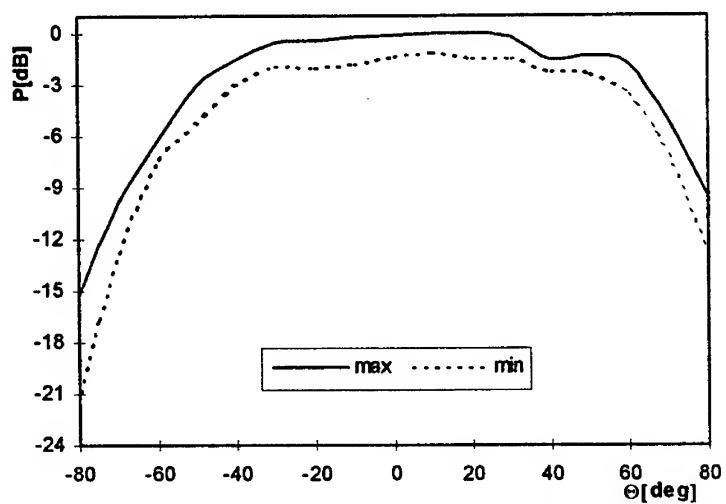


Fig. 6. Radiation pattern at 4.9 GHz

CHARACTERISATION OF SCHOTTKY DIODE PERFORMANCE BY NUMERICAL SIMULATION COUPLED WITH HARMONIC BALANCE.

J. Grajal*, V. Krozer⁺, E. González *, J. Gismero*, F. Maldonado*, C. Lin**, A. Simon**,
H. L. Hartnagel**

* U.P. Madrid, ETSIT, Ciudad Universitaria s/n, 28040 Madrid, Spain. Phone: 34-1-3367358, fax: 34-1-3367362,
e-mail: jesus@gmr.ssr.upm.es.

⁺ TU Chemnitz-Zwickau, Lehrstuhl für Hochfrequenztechnik, Reichenhainerstr. 70, D-09126 Chemnitz, Germany.
E-mail: krozer@egon.infotech.tu-chemnitz.de

** TH-Darmstadt, Institut für Hochfrequenztechnik, Merckstr. 25, D-64283 Darmstadt, Germany.

ABSTRACT

The electrical and RF performance characteristics of submillimetre-wave Schottky diodes are investigated using an accurate physical model which combines drift-diffusion current transport with thermionic and thermionic-field emission currents imposed at the Schottky contact. The model includes self-consistently image force effect, tunneling transport, and current dependent recombination velocity at the Schottky contact. This physical simulator has been coupled to a harmonic balance simulator as a non-linear element. The integrated device-circuit simulator has allowed to study in detail the limiting factors of varactor operation. The contribution of large-signal capacitance excitation is discussed. The influence of external loads at different harmonics, bias and power level is also analysed.

INTRODUCTION

Schottky-barrier diodes have been applied to heterodyne receivers in the frequency range up to a few THz, Peatmann and Crowe [1]. However, their RF performance is still not well understood and the optimization of the Schottky diodes for THz frequency range applications can only be accomplished with accurate physical models. The major current limitation in the design of submm-wave multipliers is the optimization of the diode structure for maximum breakdown voltage, maximum capacitance swing, and minimum transit time, as well as the appropriate choice of the load impedances for the multiplier circuit. We have developed a physical simulator coupled to a harmonic balance programme for the analysis of Schottky diode multiplier circuits.

This 1-D Schottky simulator accounts for the most important physical effects. It joins drift-diffusion transport through the semiconductor structure with thermionic and thermionic-field emission currents at the metal-semiconductor contact and heterojunction interfaces. Image force lowering of the metal-semiconductor barrier and tunnelling through the barrier are self-consistently implemented into the governing equations. The validation of the numerical simulator is performed by comparison with experimental results obtained from submm-wave Schottky diodes, Krozer and Grüb [2]. The DC and RF operational behaviour of the diodes is investigated with special emphasis on the diode breakdown and maximum capacitance swing.

This Schottky diode model has been included in a harmonic balance simulator. The integration of numerical simulators for submm-wave devices as a part of circuit simulators will avoid the need of equivalent circuit model extraction or tedious measurements. This new philosophy provides another degree of freedom to improve the performance of microwave circuits because they can be designed from both a device and a circuit point of view.

PHYSICAL MODEL

The model for the carrier transport throughout the bulk is based on the classical drift-diffusion (DD) formulation, Selberherr [3], and extended to include image force lowering. The governing equations are the Poisson's equation, and continuity equations for electrons and holes.

$$\nabla \cdot (\epsilon \nabla \varphi) = -q(N_d^+ - n + p) \quad (1)$$

$$\nabla \cdot J_n - q \frac{\partial n}{\partial t} = q(R - G) \quad (2)$$

$$J_n = -q\mu_n n \frac{d}{dx}(\varphi + \varphi_n) + kT\mu_n \frac{dn}{dx} \quad (3)$$

$$\varphi_n = \frac{\chi}{q} + \frac{kT}{q} \ln N_c + \frac{q}{16\pi\epsilon x} \quad (4)$$

where φ is the electrostatic potential, ϵ is the dielectric permivity, and n, p, N_d^+ are the electron concentration, the hole concentration, and the ionized impurity donor concentration, respectively, in (1). In (2), J_n, R , and G are the electron particle density current, the recombination rate -Schockey-Read-Hall model is assumed, and the generation rate -through which impact ionization is introduced in the model [3], respectively. Besides, μ_n, T, χ , and N_c represent the field-dependent electron mobility, temperature, affinity, and density of states in the conduction band, respectively.

Here image-force potential reduction is taken into account self-consistently (4) as opposed to previous attempts, Hjelmgren [4]. Similar equations also hold for holes.

BOUNDARY CONDITIONS

Dirichlet boundary conditions are imposed at the metal contacts for Poisson's and carrier continuity equations [3]. Thermionic and thermionic-field transport at the barrier is introduced through an interface condition at the maximum of the barrier x_m , Darling [5]. The position of the maximum is no longer at the Schottky contact because of the influence of the bias-dependent image force lowering. The transport condition developed by Darling, J_n , is based on the assumption that the carrier distribution can be modelled by a displaced Maxwellian.

$$J_n = qn(x_m)v_n - qn_0(x_m)v_r \quad (5)$$

Here $n(x_m)$ is the electron concentration at the maximum of the barrier. $n_0(x_m)$ accounts for the electrons in the metal with enough thermal energy to cross over the top of the barrier into the bulk. It represents a *quasi-equilibrium* density of electrons -the density which would be present at the top of the barrier if the electrons could be brought into thermal equilibrium without disturbing the potential distribution. v_r is the classical recombination velocity of the Crowell-Sze theory [6] $v_r = \sqrt{\frac{kT}{2\pi m_e}}$. v_n is the recombination velocity after assuming a displaced Maxwellian shifted by a drift velocity v_{drift} .

$$v_n = v_r \cdot F(\xi) = v_r [\exp(-\xi^2) - \sqrt{\pi}\xi \operatorname{erfc}(-\xi)] \quad (6)$$

$$\xi = v_{drift} \sqrt{\frac{m_e}{2kT}} \quad (7)$$

$$v_{drift} = \frac{J_{th}}{qn(x_m)} \quad (8)$$

This boundary condition prevents the unphysical effect of carrier accumulation at the interface, Nylander et al [7], Adams and Tang [8].

Tunnelling transport through the barrier is important for Schottky diodes with high doping in the epitaxial layer. The commonly employed WKB approximation [6] for tunnelling does not take into account the detailed structure of a given barrier below the penetrating carrier energy level, Lui and Fukuma [9], neglects quantum mechanical reflection, Ando and Itoh [10], and assumes a constant effective mass on either side of the interface. In our model, the time-independent Schrödinger equation is solved for arbitrary piecewise-linear potential barriers using the transfer matrix approach [10]. The solution is expressed as a linear combination of Airy functions [9]. The grid defined for Poisson's equation is also used for Schrödinger's equation and both are solved self-consistently. The new expression for the current density can be represented by a simple integration, Bhapkar and Mattauch [11],

$$J_n = \frac{AT}{k} \int_{E_{min}}^{\infty} T(E_n, V) [f_s(E_n, V) - f_m(E_n)] dE_n \quad (9)$$

where A is the Richardson constant, T is the temperature, $T(E_n)$ is the transmission coefficient for the tunnelling transport, E_n is the energy for the normal component of the carrier velocity, f_s , and f_m are the electron distributions in the semiconductor and the metal, respectively. We have assumed that f_s is a displaced Maxwellian distribution, and f_m is a Maxwell-Boltzmann distribution. If tunnelling is not considered, this equation is similar to that proposed by Darling [5].

HARMONIC BALANCE SIMULATOR

The harmonic balance method is the most common technique for the design of non-linear microwave circuits. Active devices are usually treated as lumped equivalent circuits in commercially harmonic balance codes as a trade-off between speed and accuracy in the solution. However, physical models are fundamental for the characterization of high-frequency and large-signal operation of active devices. Therefore, the coupling of harmonic balance circuit simulators and full time-dependent physical device models is necessary to accurately design high-frequency circuits from both a device and circuit point of view. There exist several algorithms for the harmonic balance method, Rizzoli and Neri [12], and Maas [13], some of them have been specifically designed to deal with physical device simulators, Tait [14]. The selected algorithm for this work is based on the optimization of the error function by using the Levenberg-Marquardt algorithm, Gismero and Pérez [15].

RESULTS AND DISCUSSION

Experimental and numerical results of fabricated submm-wave Schottky diodes at the university of Darmstadt, Germany, are presented below. The structure of these diodes is shown in Table I. Diodes with the labels *D1* and *D2* present abrupt transitions between the epi-layer and the buffer layer. On the contrary, *D3* has a linear doping profile from the metal contact to the buffer layer.

Darmstadt GaAs mm-wave Schottky diodes: $\phi_{Anode} = 6.7\mu m$				
Diode	Epi-layer		Buffer layer	
	Doping (cm^{-3})	Thickness (μm)	Doping (cm^{-3})	Thickness (μm)
D1-Abrupt	10^{17}	– 0.350	3×10^{18}	– 0.720
D2-Abrupt	2×10^{16}	– 0.400	3×10^{18}	– 0.720
D3-Linear	$2 \times 10^{16} \rightarrow 3 \times 10^{18}$		0.348	3×10^{18} – 0.720
Substrate (Doping: $2 \times 10^{18} cm^{-3}$ -Thickness: 100 μm)				

Figure 1 shows the different contributions to the forward current of diode *D1*. After including the image force lowering and tunnelling through the barrier, the agreement between simulations and measurements is very good. The contribution of the tunnelling current is more important at high doping concentration in active epi-layer. In fact, the contribution of tunnelling to the total current is negligible in *D2*. At high bias voltages, the dominant effect limiting current flow is the voltage drop across the neutral epi-layer. Figure 2 illustrates the evolution of the total resistance of the diode, $R_t + R_j$, with applied voltage. R_j accounts for the junction resistance, and R_t corresponds to the ohmic losses in the neutral regions, which is dominant at high voltages. Moreover, there exists an increase in this resistance due to the decrease of the mobility $\mu(E)$ with the electric field, Kollberg et al [16]. The developed model has also used to investigate the different performance of the diodes in table I. Figure 3 shows the currents at forward bias. The most interesting result is that the current for the diode with linear doping in the epi-layer, *D3*, is more than one order of magnitude than for the abrupt diodes, *D1* and *D2*. This is important for diodes working as mixers, where the non-linear conductance swing must be maximized with the minimum local oscillator level. The explanation for this feature is twofold. First, the barrier height for *D3* ($\Phi_b = 0.95$ eV) is significantly lower than the barrier height for the abrupt diodes ($\Phi_b = 1.0$ eV). Second, the abrupt transition between the epi-layer and the buffer layer creates an electric field against the movement of electrons towards the Schottky contact, figure 4. This field does not exist in *D3* because the transition between the doping of these layers is gradual. This performance is achieved at the expense of a decrease in the breakdown voltage: $BV_{D1} \approx -10V$, $BV_{D2} \approx -13V$, $BV_{D3} \approx -4V$.

Figure 5 illustrates a comparison between measured and simulated normalized junction capacitances versus the applied voltage. For high voltages our simulations predict a maximum and a subsequent decrease in the junction capacitance [4]. Classical models based on the depletion approximation predict an infinite capacitance at flat band conditions. The objective of these simulations is to select the diode with the largest swing of capacitance. This diode will be the best for varactor applications: frequency multipliers, for example. The agreement between measurements and simulations is not too satisfactory, maybe due to the technological

variations in the growing of the epilayer. However, the simulations correctly predict that *D1* is the most suitable diode because it maximizes the capacitance swing. The results of figures 1-5 show that this model is a useful tool for the analysis and optimization of the Schottky diode structures for radio-frequency applications.

Performances of active devices are defined not only by their inherent characteristics but also for the circuits where they are embedded. Therefore, this coupling can be taken into account by including the numerical physical model into a circuit simulator based on the harmonic balance method. We have focused on the study of the performance of *D1* working as a $2 \times 50\text{GHz}$ frequency multiplier. Several aspects are crucial for the maximization of the conversion efficiency in a multiplier: loads at different harmonics, bias, and power level [13], Rauscher [17]. The contribution of these design elements is studied in figures 6-8. Twelve harmonic are considered in these simulations, and the impedances of the higher harmonics (3rd-12th) have been set to $0.001\ \Omega$ for both the resistive and reactive components. The diode is always matched at the fundamental frequency. The bias voltage has been optimized to have a maximum voltage swing between breakdown voltage and the conduction voltage: $V_{DC} = -4.75\text{V}$.

Figure 6 shows the simulated conversion efficiency versus the second harmonic circuit impedance Z_2^{ckt} for an input power level of 7dBm. Only positive reactances have been considered, because the device is typically capacitive. Maximum conversion efficiency of 37% is achieved for $Z_2^{ckt} = 25 + j125\Omega$. Figure 7 displays the input-output power characteristic of the doubler, the conversion efficiency, and the DC diode current (Z_2^{ckt} is obtained from previous simulations). Both the output power and conversion efficiency increase with the input power level. A minimum loss of 3.6 dB occurs at an input level of 10 dBm. Above this input level, the output power level continues to rise, but the conversion loss also increases. The resistive junction begins to rectify the input power, as evidenced by the onset of DC current [13]. The DC power delivered by the diode comes from the RF input signal, so it represents a waste of available input power. Figure 8 depicts the variation of the input impedance of the diode at the fundamental frequency. As the input power level increases, the voltages and fields in the undepleted region increase, the mobility goes down and the resistance increases [16].

CONCLUSION

Coupling of accurate physical modelling for active devices and circuit simulators is fundamental for the design of RF applications working at hard conditions: high frequency applications based on non-linear operation modes.

References

- [1] W. Peatmann and T. Crowe. Design and fabrication of .5um GaAs Schottky barrier diodes for low noise terahertz applications. *International Journal Infrared and Milimeter Waves*, 11(3):355-365, March 1990.
- [2] V. Krozer and A. Grüb. A novel fabrication technique and process simulation by an analytical model for near-ideal epitaxial Pt/GaAs Schottky barrier diodes. *Solid-State Electronics*, 37(1):169-180, 1994.
- [3] S. Selberherr. *Analysis and Simulation of Semiconductor Devices*. Springer-Verlag, 1984.
- [4] H. Hjelmgren. Numerical modeling of hot electrons in n-GaAs Shottky-barrier diodes. *IEEE Transactions on Electron Devices*, 37(5):1228-1234, May 1990.
- [5] R. B. Darling. High field, nonlinear electron transport in lightly doped Schottky-barrier diodes. *Solid-State Electronics*, 31(6):1031-1047, 1988.
- [6] C.R. Crowell and S.M. Sze. Current transport in metal-semiconductor barriers. *Solid-State Electronics*, 9:1035-1048, 1966.
- [7] J. O. Nylander, F. Masszi, S. Selberherr, and S. Berg. Computer simulations of Schottky contacts with a non-constant recombination velocity. *Solid-State Electronics*, 32(5):363-367, 1989.
- [8] J. Adams and T. Tang. A revised boundary condition for numerical analysis of Schottky barrier diodes. *IEEE Electron Device Letters*, 7(9):525-527, September 1986.
- [9] W.W. Lui and M. Fukuma. Exact solution of the Schrödinger equation across an arbitrary one-dimensional piecewise-linear potential barrier. *Journal of Applied Physics*, 60(5):1555-1559, 1986.
- [10] Y. Ando and T. Itoh. Calculation of transmission tunneling current across arbitraty potential barriers. *Journal of Applied Physics*, 1(4):1497-1502, 1987.

- [11] U. V. Bhapkar and R. J. Mattauch. Numerical simulation of the current-voltage characteristics of heteroepitaxial Schottky-barrier diodes. *IEEE Trans. Electron Devices*, 40(6):1038–1046, June 1993.
- [12] V. Rizzoli and A. Neri. State of the art and present trends in nonlinear microwave CAD techniques. *IEEE Transactions on Microwave Theory and Techniques*, 36(2):343–365, February 1988.
- [13] S. A. Maas. *Nonlinear Microwave Circuits*. Artech House, 1988.
- [14] G. B. Tait. Efficient solution method for unified nonlinear microwave circuit and numerical solid-state device simulation. *IEEE Microwave and Guided Wave Letters*, 4(12):420–422, December 1994.
- [15] J. Gismero and J. Pérez. Comparison of algorithms for the simulation of nonlinear circuits through the harmonic balance method. In *1989 IEEE International Symposium on Circuits and Systems*, Portland, USA, May 1989.
- [16] E. L. Kollberg, T. J. Tolmunen, M. A. Frerking, and J. R. East. Current saturation in submillimeter wave varactors. *IEEE Transactions on Microwave Theory and Techniques*, 40(5):831–838, May 1992.
- [17] C. Rauscher. High-frequency doubler operation of GaAs field-effect transistors. *IEEE Transactions on Microwave Theory and Techniques*, 31(6):462–473, June 1983.

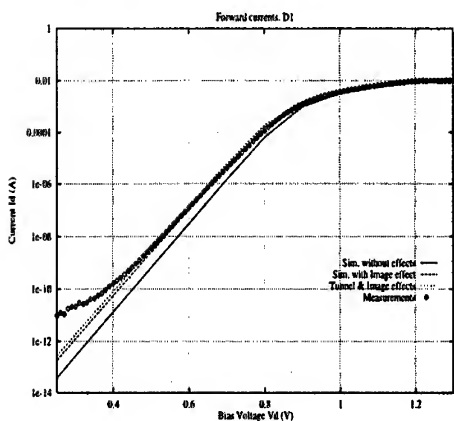


Fig.1: I-V Simulated and measured currents for $D1$. Different contributions.

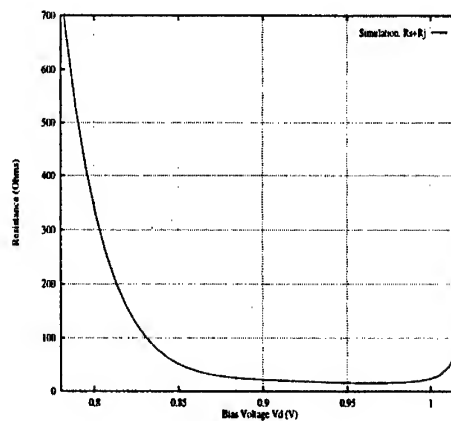


Fig.2: Simulations for the DC resistance of abrupt diode $D2$.

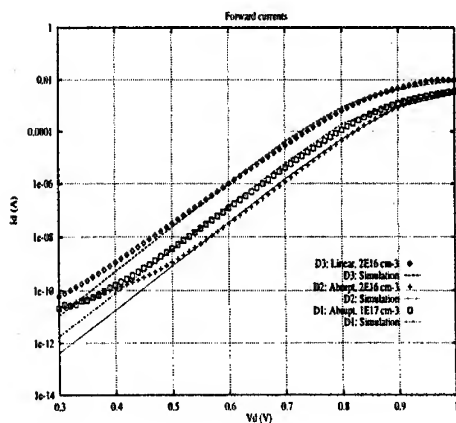


Fig.3: Simulated and measured I-V curves for structures of table I.

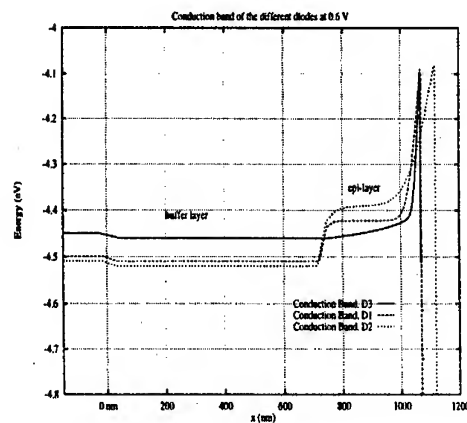


Fig.4: Conduction band for structures of table I at $V=0.6$ V.

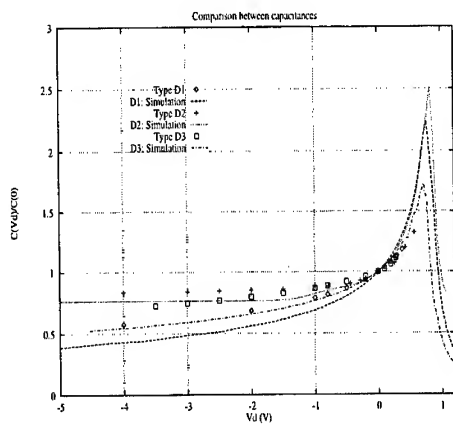


Fig.5: Simulated and measured normalized capacitances for the diodes of table I.

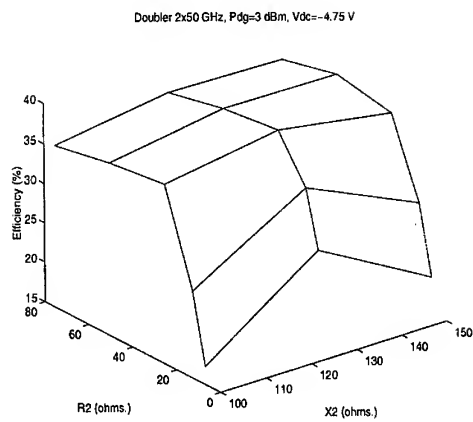


Fig.6: Conversion efficiency vs. second harmonic circuit impedances $P_{dg} = 7 \text{ dBm}$.

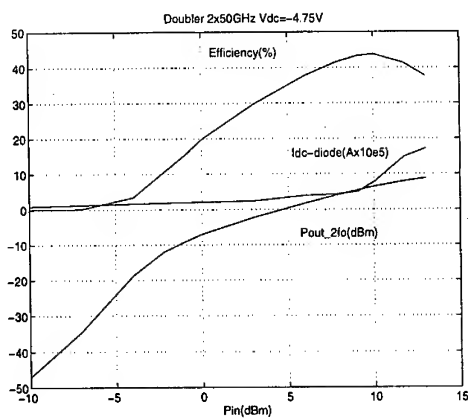


Fig.7: Output power, conversion efficiency and rectifier diode current for $2 \times 50 \text{ GHz}$ doubler.

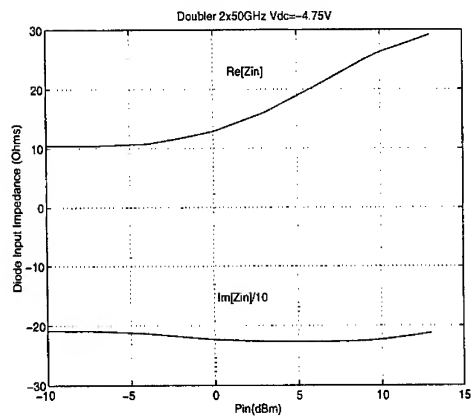


Fig.8: Diode input impedance at fundamental frequency vs. input power.

HTS/FERROELECTRIC CPW STRUCTURES FOR VOLTAGE TUNEABLE PHASE SHIFTERS

O. G. Vendik*, E. F. Carlsson, P. K. Petrov*, R. A. Chakalov, S. S. Gevorgian, and Z. G. Ivanov

Chalmers University of Technology, Göteborg, S 421 96, SWEDEN.

Phone: +46 (31) 772 1727, FAX: +46 (31) 16 45 13. E-mail: spartak@ep.chalmers.se

*Permanent address: Electrotechnical University, St.-Petersburg, 197376, RUSSIA.

Phone: +7 (812) 234 59 80, FAX: +7 (812) 234 48 09, E-mail: vendik@hollmann.usr.etu.spb.ru

ABSTRACT

Coplanar waveguides (CPW) based on single and multi-layered ferroelectric films with high- T_c superconducting (HTS) and golden electrodes have been investigated in the frequency range between 40 MHz and 40 GHz with the goal of designing voltage tuneable phase shifters operating at cryogenic temperatures. Tuneability and losses are investigated as function of temperature and voltage. The quality factor of a tuneable component K is introduced and discussed. The results obtained are promising for design of voltage controlled analog phase shifter.

INTRODUCTION

Ferroelectric film structures are very attractive for microwave engineers due to a field dependent dielectric permittivity ϵ . However the intrinsic microwave loss of these materials at room temperature (300 K) limits their applications. The initial success for HTS application at microwave frequencies lead to development of a new branch in microwave electronics operating at cryogenic temperature Vendik et al (1,2), Gevorgian et al (3,4). In this connection the (HTS)/ferroelectrics combination looks very promising for a realisation of tuneable microwave components such as phase shifters and delay lines. The most important characteristics of ferroelectric are the temperature and voltage dependence of the controllability ($\epsilon_{\max}/\epsilon_{\min}$) and dielectric loss. The most studied, and today most important for practical applications, are $\text{YBa}_2\text{Cu}_3\text{O}_{7-x}/\text{SrTiO}_3$ (YBCO/STO) and $\text{YBa}_2\text{Cu}_3\text{O}_{7-x}/\text{Ba}_x\text{Sr}_{1-x}\text{TiO}_3$ (YBCO/BSTO) structures. Pure bulk STO demonstrates a relatively low loss level and a large tuneability at low temperatures. Increasing the barium content in BSTO increase the controllability and operation temperature, but also the losses. In the present work the microwave properties of single and multi-layered structures based on SrTiO_3 , $\text{Ba}_{0.05}\text{Sr}_{0.95}\text{TiO}_3$ and YBCO thin films are examined. The quality factor of a tuneable component K should be used for the performance evaluation of the tuneable components obtained.

FILM PREPARATION AND DEVICE PATTERNING

The structures investigated were deposited by laser ablation (KrF , $\lambda = 248$ nm) on 5 mm^2 (001) LaAlO_3 or (100) MgO substrates. The STO and BSTO films were deposited from 1/2 inch in diameter stoichiometrical SrTiO_3 , and $\text{Ba}_{0.05}\text{Sr}_{0.95}\text{TiO}_3$ targets respectively in 0.4 mbar oxygen pressure with the substrate temperature $T_s = 740^\circ\text{C}$. The energy density of the laser spot (1 mm^2) was 1.0 J/cm^2 which yielded a growth rate of 0.45 \AA/pulse . The thickness of the films grown were 240, 400, 480, and 960 nm. After deposition the substrate heater was cooled down to room temperature by $20^\circ/\text{min}$ at pressure 0.9 atm of oxygen. Then the chamber was pumped down again and on the STO (or BSTO) film a 250 nm YBCO and 20 nm Au films were deposited "in situ". The YBCO film was manufactured from 1/2 inch diameter stoichiometric $\text{YBa}_2\text{Cu}_3\text{O}_{7-x}$ target at 0.4 mbar oxygen pressure and $T_s = 760^\circ\text{C}$. After deposition the substrate was cooled down to room temperature by $20^\circ/\text{min}$ at 0.9 atm of oxygen. The Au layer for the contact pads was deposited at $T_s = 50^\circ\text{C}$ with a pressure of $2 \cdot 10^{-5}$ mbar. The Au conductors ($1 \text{ }\mu\text{m}$) were fabricated by electron beam evaporation. Double layer STO films as $\text{Au/STO/CeO}_2/\text{STO}$ and Au/STO/MgO/STO were also deposited. For device patterning standard photolithography and ion milling were used.

The critical temperature T_c of the top YBCO was determined from ac ($f = 1 \text{ kHz}$) magnetic susceptibility measurements and the value of T_c was found to be in the range 88-89 K.

MEASUREMENTS

The microwave properties of the ferroelectric films are investigated using a cryogenic probe station in the temperature range from 20 to 300 K and in the frequency range from 40 MHz to 40 GHz. Four coplanar waveguide (CPW) phase shifters with different geometry are patterned on the each substrate. The strip and gap widths are chosen to give an impedance of 50 Ohm. This was verified by measuring the return loss, which was better than 10 dB, and typically 20 dB, for all phase shifters. The total length of the line (Fig. 1) is $L = 4$ mm with the active part $l = 3$ mm. The measurements are done using Wiltron 360B and HP 8510 vector network analysers. Fig. 2 illustrates the temperature dependence of the dielectric constant of STO and BSTO films measured with a capacitance meter at 1 MHz and extracted by means of conformal mapping techniques. The measurement of phase shift as a function of frequency makes possible to estimate the effective dielectric constant of CPW with a ferroelectric layer. For different samples the effective dielectric constant was found to be in the range 50 - 200 which is in a good agreement with theoretical estimations (3). Under the applied voltage 0 - 35 V the effective dielectric constant changes 1.5 times. Fig. 3 shows the dependence of the dielectric constant of a BSTO film on applied voltage. In the frequency range up to 100 GHz, there is no frequency dispersion in materials investigated. Fig. 4 and Fig. 5 present the frequency dependence of the CPW total losses in the samples of STO and BSTO for 0 and 35 V applied voltage.

QUALITY FACTOR OF A TUNEABLE COMPONENT

Let us consider a transmission line section filled with a tuneable dielectric. The phase velocity is a function of effective dielectric constant of the line:

$$v_{ph} = \frac{c_0}{\sqrt{\epsilon_{eff}(U)}}, \quad (1)$$

where c_0 is the light velocity in free space, U is the voltage applied to the tuneable dielectric. Thus, for two values of the voltage the phase shift given by the transmission line section is:

$$\Delta\varphi = \left(\frac{\omega}{v_{ph,1}} - \frac{\omega}{v_{ph,2}} \right) \cdot l, \quad (2)$$

where l is length of the section.

The averaged loss for two states of the phase shifter can be written as follows:

$$L_{dB} = -4.34 \cdot \frac{\omega}{c_0} \cdot l \cdot (\epsilon_1 \epsilon_2)^{1/4} (\tan\delta_1 \tan\delta_2)^{1/2}, \quad (3)$$

where loss tangent of the material should characterise not only the dissipation of microwave energy in the dielectric, but the dissipation in the conducting components of the line as well. Combining (1)-(3) one obtains

$$\frac{\Delta\varphi}{|L_{dB}|} = \frac{\epsilon_1^{1/2} - \epsilon_2^{1/2}}{4.34(\epsilon_1 \epsilon_2)^{1/4} (\tan\delta_1 \tan\delta_2)^{1/2}}. \quad (4)$$

Let us introduce the quality factor as:

$$K = \frac{4(\sqrt{n} - 1)^2}{\sqrt{n} \cdot \tan\delta_1 \tan\delta_2}, \quad (5)$$

where

$$n = \frac{\varepsilon_1}{\varepsilon_2} \quad (6)$$

is the tuneability of the ferroelectric material.
Thus we may write

$$\frac{\Delta\varphi_{deg\,rec}}{L_{dB}} = 6.6\sqrt{K} \quad (7)$$

The ratio presented by the equation (7) can be called phase shift/loss merit of the phase shifter. It is easy to show that for $n \leq 4$ the quality factor can be written as:

$$K = \frac{(n-1)^2}{n \tan\delta_1 \tan\delta_2} \quad (8)$$

For example, if $n = 2$, and $\sqrt{\tan\delta_1 \cdot \tan\delta_2} = 0.02$ one has the quality factor of the material $K = 1250$ and the phase shift/loss merit of the phase shifter:

$$\frac{\Delta\varphi_{deg\,rec}}{L_{dB}} = 240 \text{ deg rec/dB}$$

The quality factor in the form (8) can be obtained as a particular case from the known generalised formula Kawakami (5), Khizha et al (6):

$$K + \frac{1}{K} = \frac{r_1}{r_2} + \frac{r_2}{r_1} + \frac{(x_2 - x_1)^2}{r_1 r_2} \quad (9)$$

where x_1 , x_2 and r_1 , r_2 are series reactance and resistance of the circuit in two states.

The formula (9) is used for characterisation of the quality of $p-i-n$ diodes (5,6) and of switches based on S-N transition in superconductive microwave electronics Vendik et al (7).

DISCUSSION

The data from Fig. 2 and 3 are in a good agreement with the measurements of a ferroelectric film dielectric constant in the planar capacitor structure Galt and Price (8). The low temperature of the dielectric constant maximum of the pure STO film (Fig. 2) indicates a rather high crystallinity of the film. Fig. 4 and 5 show the losses as a function of frequency in a wide range of the frequency change. It is known that the dependence of the loss factor of ferroelectric is proportional to the frequency Vendik (9) and the surface resistance of the HTS film is proportional to the frequency squared Klein et al (10). One may see that experimental dependence in Fig. 4 exhibits the remarkable contribution of the power two, that should be followed by the conclusion that the losses in BSTO film CPW at $T = 75$ K are basically determined by the HTS films. At the same time Fig. 5 exhibits almost linear dependence of the loss against frequency. STO structure at low temperature can be characterised mainly by the loss in the ferroelectric film. Both Fig. 4 and 5 show the decrease of the loss factors under the applied dc voltage. That allows to conclude that the ferroelectric films contain the charged defects of a rather large density (9), Vendik and Platonova (11). Additional data are collected in the Table.

The quality factor introduced above should be used as a generalised characteristic of the dielectric layer with a tuneable dielectric constant. Let us take the quality factor $K = 120$ and characteristic of tuneability $n = 1.5$ which are typical for the effective dielectric constant of CPW with a ferroelectric layer. Using equation (8) the averaged value of loss tangent can be found:

$$\tan \delta_{\text{average}} = 0.03, \quad (10)$$

This result is the good enough for the frequency 20 GHz, but we are sure that the quality of the films will be improved in a high extend. The quality factor of $K = 120$ provides the phase shift/loss merit of the phase shifter 70°/dB. One can see from the Table that the quality factor of the samples are dispersed over a large area. One can find some samples which provides the phase shift/loss merit of the phase shifter up to 130 °/dB which can be considered as a very good result for the frequency 20 GHz. Admittedly, there is no considerable correlation between sizes and structures of the sample and their generalised characteristic - the quality factor. That confirms the supposition that the technological process of manufacturing the ferroelectric films is not stabilised enough and should be essentially improved.

CONCLUSION

The results obtained show the possibilities for practical applications of devices based on high- T_c superconductor/ferroelectric CPW structures at microwaves. At high frequency (20 GHz) certain samples of the CPW phase shifters exhibited high value of the quality factor. The phase shift of 100 degree with loss not higher than 1 dB has been provided. The method based on application of the quality factor for characterisation of the result of technological efforts seems to be fruitful. Further study aimed to increase the dielectric constant tuneability and decrease the dielectric loss of thin STO (BSTO) films should be carried out. For optimisation of the technological process of manufacturing the high- T_c superconductor/ferroelectric CPW structures the quality factor of the tuneable component can be used as a generalised characteristic of the component.

ACKNOWLEDGEMENT

The authors of the paper are grateful to E. Kollberg for interest to the problem and support of the Project. Some materials obtained in the Project have been presented at EUCAS'97 as well Carlsson et al (12).

REFERENCES

1. O. G. Vendik, L. T. Ter-Martirosyan, A. I. Dedyk, S. F. Karmanenko, R. A. Chakalov, "High- T_c Superconductivity: New Applications of Ferroelectrics at Microwave Frequencies". - *Ferroelectrics*, 1993, Vol. 144, No. 1-4, pp. 33-43.
2. O. G. Vendik, I. G. Mironenko, and L. T. Ter-Martirosyan, "Superconductors Spur Application of Ferroelectric Films", - *Microwaves & RF*, 1994, Vol. 33, No. 7, pp. 67-70.
3. S. S. Gevorgian, D. I. Kaparkov, O. G. Vendik, "Electrically Controlled HTSC/Ferroelectric Coplanar Waveguide", - *IEEE Proc.-Microw. Antennas Propag.*, 1994, Vol. 141, No. 6, pp. 501-503.
4. S. S. Gevorgian, E. Carlsson, S. Rudner, U. Helmersson, E. Kollberg, E. Wikborg, and O. Vendik, "HTS/Ferroelectric Devices for Microwave Applications" *IEEE Trans. on Appl. Supercon.*, 1996, Vol.7.
5. S.Kawakami "Lossless reciprocal transmission and synthesis of two state network" *IEEE Trans.*, Vol. CT-13, pp. 128 - 138, 1966.
6. G.S. Khizha, I.B. Vendik, E.A. Serebryakova "Microwave phase shifters and switches based on $p-i-n$ diodes" (In Russian), *Moscow, Publish. House "Radio I Svyas"*, 1984.
7. O.G. Vendik, M.M. Gaidukov, S.G. Kolesov, A.B. Kozyrev, A.Yu. Popov, "Microwave signal limiters and commutators based on superconducting films", *Proc. of 21st EuMC, Stuttgart, Microwave Exh. and Publ.* 1991, Vol. 1, pp.72-92.
8. Galt D., Price J.C. "Characterization of a tunable thin film microwave $\text{YBa}_2\text{Cu}_3\text{O}_{7.8}/\text{SrTiO}_3$ coplanar capacitor" // *Appl. Phys. Lett.* V. 63. № 22. P. 3078-3080 (1993).
9. O.G. Vendik, "Dielectric nonlinearity of the displacive ferroelectrics at UHF", *Ferroelectrics*, Vol. 12, pp.85-90 (1976).
10. N. Klein, U. Dähne, U. Poppe, N. Tellmann, K. Urban, S. Orbach, S. Hensen, G. Müller, and H. Piel, "Microwave surface resistance of epitaxial $\text{YBa}_2\text{Cu}_3\text{O}_{7.8}$ thin films at 18.7 GHz measured by a dielectric resonator technique", *J. Supercond.*, Vol. 5, No. 2, pp. 195-201, 1992.

11. O.G.Vendik, L.M. Platonova, "Influence of Charged Defects on Dielectric Properties of Ferroelectric Materials". *Fiz. Tverd. Tela (Leningrad)*, Vol. 13, No. 6, pp. 1617-1624 (1971). [*Sov. Phys. Solid State*, Vol. 13, No. 6, (1971)].
12. E.F. Carlsson, P.K. Petrov, R.A. Chakalov, P. Larsson, Z.G. Ivanov, S.S. Gevorgian, "Experimental study of thin film HTS/ferroelectric CPW phase shifter for microwave application", Proc. of EUCAS'97.

Table. Data for the CPW phase shifters at 20 GHz and 20 K

Characteristics of the samples		Layer thickness, nm				Quality factor
No	Geometry*	BSTO	STO	YBCO	Au	K
AYSL609	4/18	—	400	250	20	120
ASMSM620	6/15	—	2x240	—	1000	130
AY8SL621	6/25	—	8x50	250	20	100
YSL51**	6/15	240	—	240	20	375
YSL51**	14/28	240	—	240	20	145

*) Strip width(μm)/Gap width (μm)

**) measured at $T = 16\text{ K}$

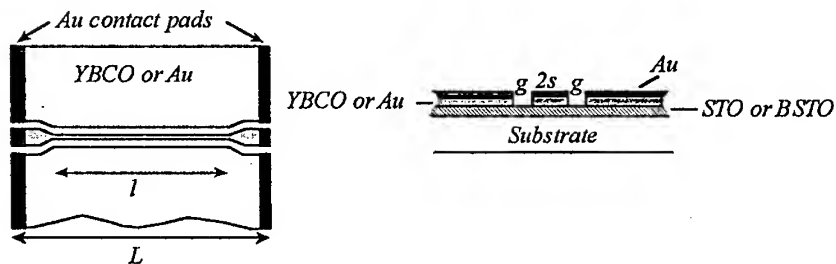


Fig. 1 Layout and cross-section of the thin film CPW

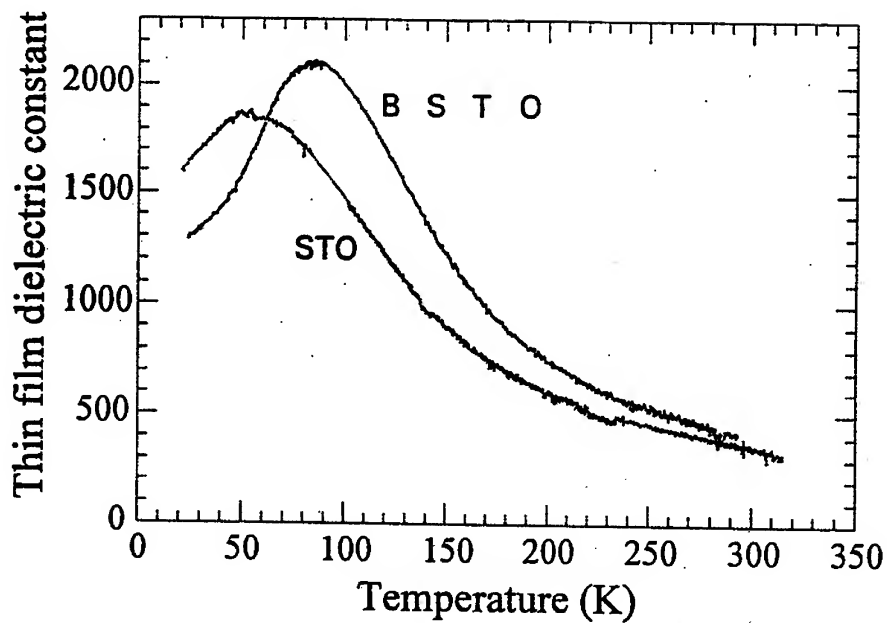


Fig. 2. Temperature dependence of BSTO and STO dielectric constant.

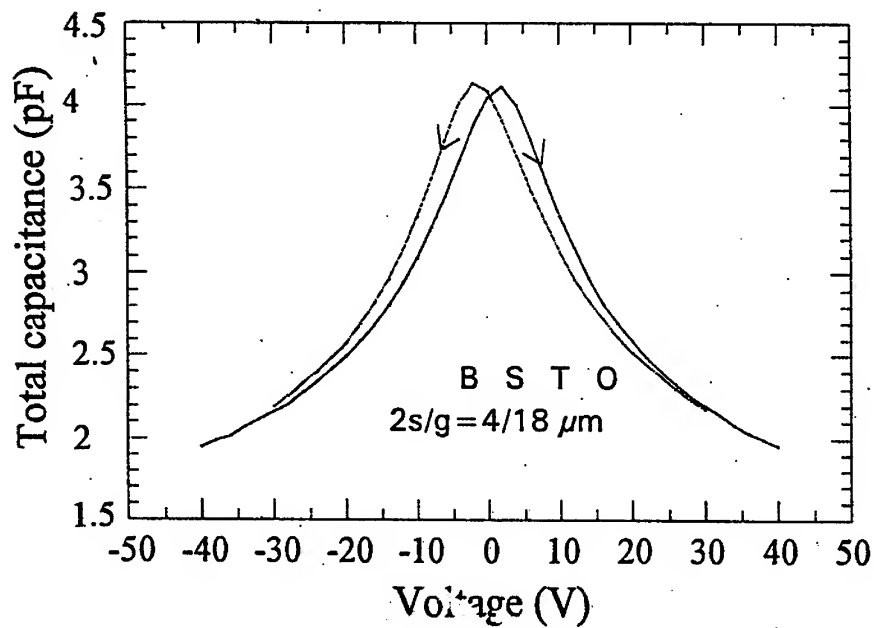


Fig. 3. Capacitance vs voltage for a BSTO sample measured at the temperature 80 K.

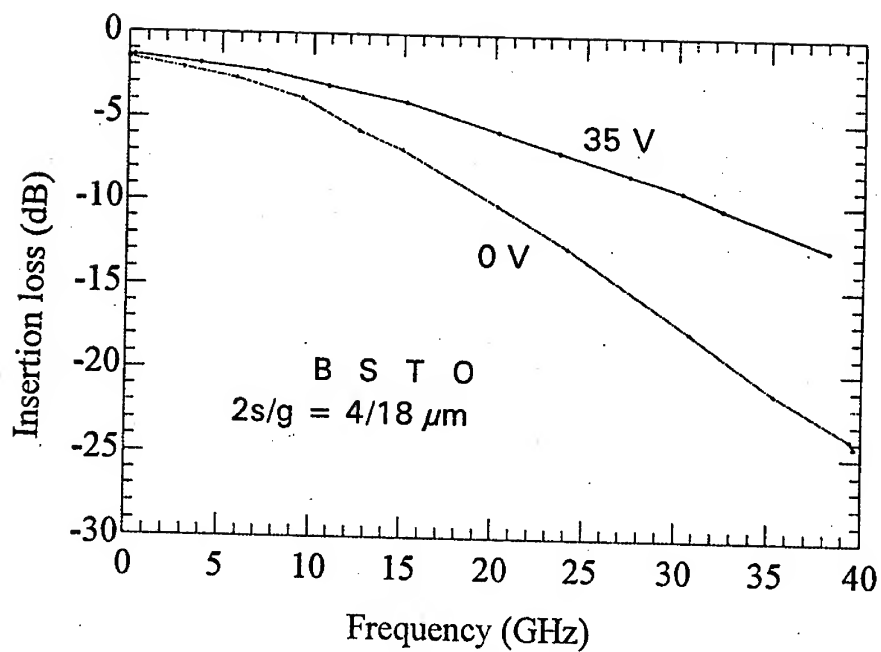


Fig. 4. Insertion loss for a BSTO CPW at two different voltages, $T=75\text{K}$.

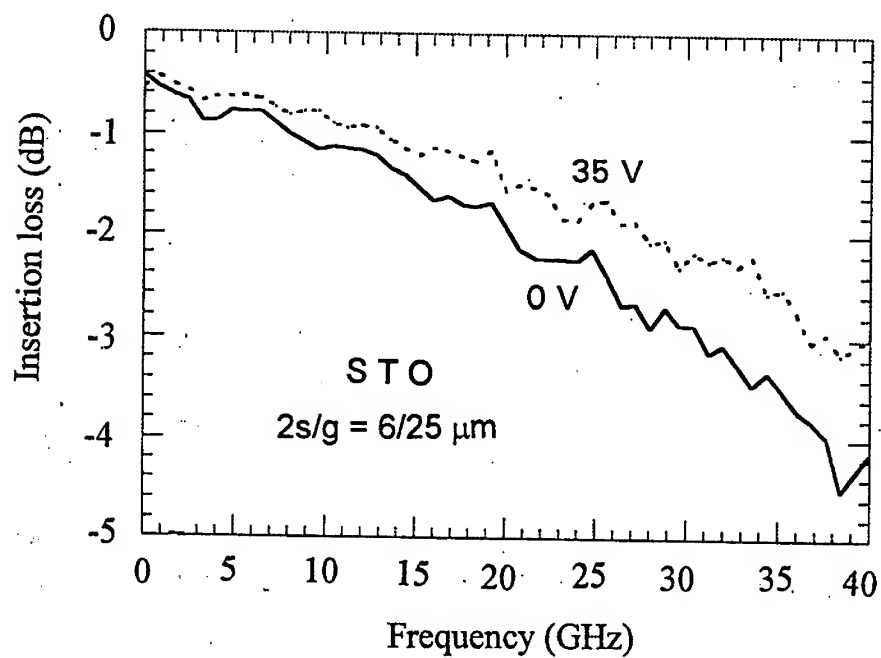


Fig. 5. Insertion loss for a STO CPW at two different voltages, $T=20\text{K}$.

Electromagnetic shielding effects using chiral and other complex materials

Ari Sihvola and Murat Ermutlu*

Helsinki University of Technology, Electromagnetics Laboratory,
FIN-02015 HUT, Finland

* Nokia Research Center, P.O. Box 45, 00211 Helsinki, Finland

ABSTRACT

The present study focuses on the attenuation analysis of spherical shell structures that are made of complex materials. An analysis will be presented which calculates the electric and magnetic fields within spherically layered structures in the quasistatic limit, in other words the wavelength of the field has to be smaller than the diameter of the shell. Due to the magnetoelectric coupling which is inherent in chiral and other novel complex materials, the electric and magnetic field problems cannot be treated separately. The newly developed six-vector formalism is used in the analysis. Numerical results are shown for the shielding effectivity of a chiral shell.

INTRODUCTION

Dielectric materials influence the behavior of electric fields, and magnetic materials interact with magnetic fields. The dielectric and magnetic properties of media can be exploited to protect equipment against excessive electromagnetic field densities. The present paper focuses on the low-frequency shielding effect of a simple geometry: a spherical shell. In spite of the basic canonical geometry of this structure, the problem is challenging because the shell is allowed to have complex material properties. In particular, the shell in the analysis is chiral, meaning that it has to be described in a more general way than those characterized by the ordinary dielectric permittivity and magnetic permeability. The analysis covers in fact all bi-isotropic materials, like non-reciprocal media, too. It can also be generalized to the bi-anisotropic regime.

In the study of fields inside a hollow sphere, the restriction to low frequencies means that the wavelength of the operating electromagnetic is larger than the diameter of the sphere. A practical limit for the diameter of the shell is one-fifth of the wavelength λ . This guarantees that one can concentrate on the Laplace equation instead of the full Maxwell equations. Note however, that this approach is well valid for microwave applications as long as the size limit is accounted for.

SHIELDING EFFICIENCY OF SIMPLE MATERIALS

The quasistatic solution of the electric field inside a dielectric shell is well known. The internal field \mathbf{E} is constant and its relation to the outside (constant) field \mathbf{E}_0 depends on the permittivity of the shell ϵ according to Sihvola and Lindell [1]:

$$\mathbf{E} = \frac{9\epsilon_0\epsilon}{(\epsilon + 2\epsilon_0)(\epsilon_0 + 2\epsilon) - 2\alpha(\epsilon - \epsilon_0)^2} \mathbf{E}_0 \quad (1)$$

where $\alpha = (a_2/a_1)^3$ and a_1 is the inner radius and a_2 is the outer radius of the shell. ϵ_0 is the permittivity of free space.

Analogously, the corresponding magnetic field ratio for a hollow sphere of material with permeability μ is according to Stratton [2]

$$\mathbf{H} = \frac{9\mu_0\mu}{(\mu + 2\mu_0)(\mu_0 + 2\mu) - 2\alpha(\mu - \mu_0)^2} \mathbf{H}_0 \quad (2)$$

These formulas can be used to design electric and magnetic shields. In addition to the thickness of the layer, the electric shielding magnitude depends on the permittivity of the shell, and the magnetic shielding depends on its permeability. This low-frequency decoupling into separate dielectric and magnetic problems does not hold anymore in the case of more complex materials, which is the focus in this study. In chiral materials, there exists magnetoelectric coupling.

ISOTROPIC CHIRAL MEDIA

Chiral media have received considerable attention in the microwave community in recent years (see Lindell et al [3]). These materials are intrinsically handed, *i.e.*, they differ from their mirror image. Handedness brings forth rotation of the polarization plane of a linearly polarized field, and at lightwave frequencies, this property of chiral materials has been known as "optical activity" (see, for example, Barron [4], Hegstrom and Kondepudi [5], or Applequist [6]).

Constitutive relations describe the effect of medium on the electric and magnetic quantities. The isotropic chiral medium obeys the following relations:

$$\mathbf{D} = \epsilon\mathbf{E} - j\kappa\sqrt{\mu_0\epsilon_0} \mathbf{H} \quad (3)$$

$$\mathbf{B} = \mu\mathbf{H} + j\kappa\sqrt{\mu_0\epsilon_0} \mathbf{E} \quad (4)$$

where \mathbf{E} is the electric and \mathbf{H} is the magnetic field, \mathbf{D} is the electric and \mathbf{B} is the magnetic flux density. In addition to the media parameters permittivity ϵ and permeability μ , there exists a dimensionless chirality parameter κ . Note that the isotropy (or, rather, bi-isotropy) assumption explains the scalar character of the material parameters in these relations. The free-space permittivity and permeability are ϵ_0 and μ_0 . These relations assume time-harmonic field dependence with the convention $e^{j\omega t}$.

Although most of the interest engineers are focusing on chiral materials deals with microwave and millimeter wave applications, like antennas, couplers, polarizers, *etc.*, applications may also be found at lower frequencies. The trend in chiral research is opposite to what radio engineers are used to in other branches of technology where progress means advancing towards higher frequencies. Chirality was first observed at optical frequencies, and only this century has seen man-made chiral materials which are active at microwaves. Today strongly chiral materials (although the bandwidth of these material samples is not very broad) are being produced at X

band. Perhaps in the near future materials are available which display strong chiral behavior at lower frequencies.

Note also that a fourth parameter can be added to the full bi-isotropic description of materials. This is the non-reciprocity parameter. The non-reciprocal bi-isotropic medium is often called as the "Tellegen material" and the recent literature contains much discussion about the possible existence of Tellegen materials (see Sihvola, Lakhtakia, and Weiglhofer [7]).

Leaving aside the Tellegen discussion, it is with this background of chiral media that the present study aims at generalizing the expressions (1) and (2). How does the electric and magnetic shielding effects depend on the three material parameters of the chiral medium which makes the spherical layer? And for more general materials with more medium parameters, what is the added effect of these?

SIX-VECTOR ANALYSIS

A powerful way to analyse electromagnetic problems involving chiral and bi-anisotropic structures is the so-called six-vector formalism (Lindell et al [8]). Six-vectors combine electric and magnetic quantities (that both have three components) into a single vector with six components. The electromagnetic six-vector field \mathbf{e} and six-vector flux density \mathbf{d} look like

$$\mathbf{e} = \begin{pmatrix} \mathbf{E} \\ \mathbf{H} \end{pmatrix} \quad (5)$$

$$\mathbf{d} = \begin{pmatrix} \mathbf{D} \\ \mathbf{B} \end{pmatrix} \quad (6)$$

and the constitutive relations can be written as a single equation:

$$\mathbf{d} = \mathbf{M} \cdot \mathbf{e} \quad (7)$$

where

$$\mathbf{M} = \begin{pmatrix} \bar{\bar{\epsilon}} & \bar{\bar{\xi}} \\ \bar{\bar{\zeta}} & \bar{\bar{\mu}} \end{pmatrix} \quad (8)$$

is the six-dyadic of the material parameters. It has a 6×6 -element matrix representation and the full medium description requires 36 parameters. For example, for chiral media,

$$\mathbf{M} = \begin{pmatrix} \epsilon \bar{\bar{\mathbf{I}}} & -j\kappa\sqrt{\mu_0\epsilon_0}\bar{\bar{\mathbf{I}}} \\ j\kappa\sqrt{\mu_0\epsilon_0}\bar{\bar{\mathbf{I}}} & \mu \bar{\bar{\mathbf{I}}} \end{pmatrix} \quad (9)$$

where $\bar{\bar{\mathbf{I}}}$ is the unit three-dyadic (i.e., such a dyadic that when it operates on any three-vector

(from either side), the result is the same vector). In fact, in the isotropic case where the material parameters are multiples of the unit dyadic, the six-vector analysis results are very often 2×2 -matrix expressions.

Using six-vectors and six-dyadics, it turns out that the electromagnetic field analysis can be kept formally on an as simple level as in the plain isotropic dielectric case; now only the shielding effects become matrices. Also the resulting formulas have the same appearance as in the isotropic case; one just has to remember to use inverses of matrices instead of divisions, and keep in mind that six-matrices do not commute in general.

As a result, the electric shielding component (the ratio between the absolute values of the internal and external electric fields) of a chiral layer is illustrated in the figure. The shell is assumed non-magnetic and its relative permittivity is ϵ_{r1} and chirality parameter κ_1 . The parameter $1/\delta = 0.9$ means that the volume of the hollow empty space to the volume of the whole sphere is 0.9. This corresponds to the ratio of the inner to outer radius of the shell of 0.965. Note the singularity in the shielding as the chirality parameter approaches the physical limit $\kappa_1 \rightarrow \sqrt{\epsilon_{r1}}$.

CONCLUSION

Using the newly developed six-vector formalism, many bi-anisotropic electromagnetic problems can be formulated in a simple way, which also helps to solve the desired quantities. The example of the present paper is the attenuation analysis of a spherical shell that can be made of a complex medium, like in the most general case a fully bi-anisotropic medium. The numerical result shows the shielding effect of a chiral shell which is a totally new result, and the six-vector formulation makes it possible to solve even more complex geometries and materials. These include, for example, ellipsoidal forms in terms of geometry, and several classes of anisotropic and bi-anisotropic materials.

REFERENCES

- [1] A. Sihvola and I. V. Lindell: Transmission line analogy for calculating the effective permittivity of mixtures with spherical multilayer scatterers. *Journal of Electromagnetic Waves and Applications*, Vol. 2, No. 8, p. 741-756, 1988.
- [2] J.A. Stratton: *Electromagnetic theory*, McGraw-Hill, New York, 1941, p. 265.
- [3] I.V. Lindell, A.H. Sihvola, S.A. Tretyakov, and A.J. Viitanen: *Electromagnetic Waves in Chiral and Bi-Isotropic Media*, Artech House, Norwood, Mass., 1994.
- [4] L.D. Barron: *Molecular light scattering and optical activity*, Cambridge University Press, 1982.
- [5] R.A. Hegstrom and D.K. Kondepudi: The handedness of the universe, *Scientific American*, Vol. 262, No. 1, pp. 108-115, January 1990.
- [6] J. Applequist: Optical activity: Biot's bequest, *American Scientist*, Vol. 75, pp. 59-67, 1987.

[7] A.H. Sihvola: Are nonreciprocal bi-isotropic media forbidden indeed? IEEE Trans. Microwave Theory Tech., Vol. 43, No. 9, Pt. I, pp. 2160-2162, September 1995. See also Comment and Reply, *ibid.*, Vol. 43, No. 12, pp. 2722-2724, December 1995.

[8] I.V. Lindell, A.H. Sihvola, and K. Suchy: Six-vector formalism in electromagnetics of bianisotropic media, J. of Electromagnetic Waves and Applications, Vol. 9, No. 7/8, pp. 887-903, 1995.

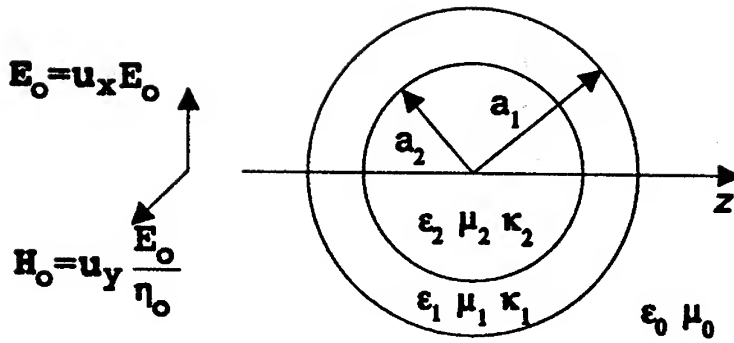


Figure 1. Geometry of the problem: a layered chiral sphere, with the core and shell characterized by three parameters; permittivity ϵ , permeability μ , and chirality κ .

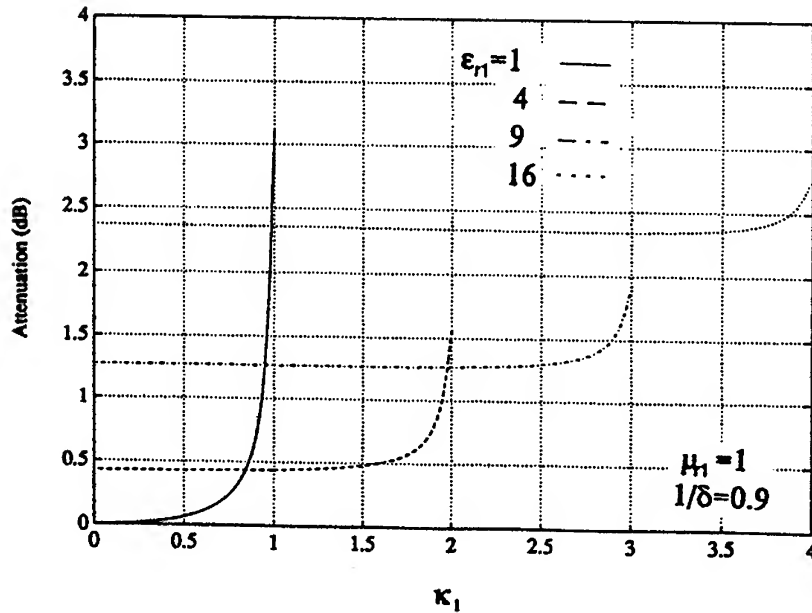


Figure 2. The electric shielding of chiral shell as function of the chirality parameter κ of the shell. The inner and outer radii of the layer satisfy $a_2^3/a_1^3 = 0.9$, the relative permeability is $\mu_r = 1$, and the relative permittivity varies.

MULTIFREQUENCY MODES AND OUTPUT SIGNAL MODULATION – TYPE BWTs

B.P. Yefimov, G.Ya. Levin, M.V. Milcho

Institute of Radiophysics and Electronics, National Academy of Sciences of Ukraine

12 Acad. Proskura st., 310085 Kharkov, Ukraine

Tel.: 38(572)44-11-05 Fax: 38 (0572) 44-11-05

Topic number : 6, Type of paper : scientific

Abstract

Physical principles of designing continuous action BWT type vacuum generators radiating microwave energy simultaneously at several carrier frequencies in a MMB are described. The control of the output level and frequency in every band are considered. The resonance properties of the sections of periodical structures and the focusing of electron beams in an inhomogeneous magnetic field are used in the generators. A description is given of how to excite the amplitude-modulated (AM) oscillations with a high modulation depth factor and small non-linear distortions. Moreover, the frequency deviation is insignificant. The operating characteristics and output device parameters are given.

Introduction

Diagnostic methods for the investigation of the plasma properties in thermonuclear machines of the type "TOKOMAK", "OGRA", "URAGAN" required that the new sources of electromagnetic oscillations should be provided in the MMB, i.e. in generators radiating microwave energy at several carrier frequencies to determine the distribution of the particle concentrations in plasma by changing the wave phase shifts in different parts of the MM-band. Earlier, according to this technique, several magnetron generators controlled by separate supply units have been used in diagnostics devices. Microwave energy localization in one beam was obtained by using a waveguide connecting device and a common electromagnetic horn.

The advantages of multibeam diagnostics were fully utilized in a new vacuum device - a multiwave resonance clinotron [1]. Such generators with a separating device on polyethylene waveguides radiating the microwave energy at wavelengths 16-8-4-2, 16-8-4, 8-4-2 and 8-4 were tested in the I.V.Kurchatov Institute of Atom Energy (Moscow) and showed positive results [2]. The measurements of the basic characteristics of transmitting channel components, the oscillatory systems of devices, loads, etc. can be obtained through the use of generators operating in AM - oscillation mode. The fundamental parameters of radio engineering devices are normally measured at a signal modulation frequency using the receive/transmit equipment, which results in the enhanced sensitivity of the method being used and in the reduced interference effect. In addition, these generators are widely employed in several fields of science and technology, particularly, in studies of plasma properties, in radiospectroscopy, etc.

1. The statement of the problem. The calculation of slow wave structures.

The basic requirements for multiwave generators are as follows: approximately the same level of microwave power at every wavelength, spread of carrier frequencies in the MMB of the octava order, continuous radiation of microwave energy, inertialess change of oscillation frequency power in every band, small power consumption.

Possible design versions of such sources are presented in Fig.1. The scale modeling technique for designing these generators is not suitable. Therefore in order to calculate them electrodynamic methods and experimental results obtained in the MMB at single frequency devices were used. The resonance properties of the sections of the periodical structures and focusing of thin electron flows (as compared to slow wavelength) were widely used in an inhomogeneous magnetic field.

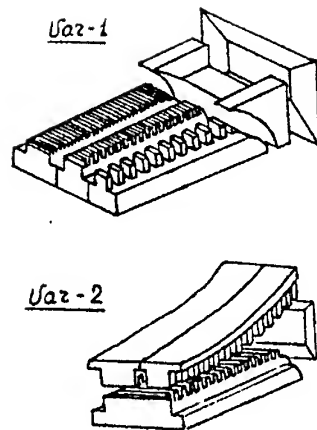


Fig. 1. Design versions of MMB multiwave generators.

The length (l) and width of the structure were experimentally chosen under the stationary condition of microwave power at every wave and with minimum starting conditions. Experimental dispersion dependencies for the three wave bands are given in Fig. 2.

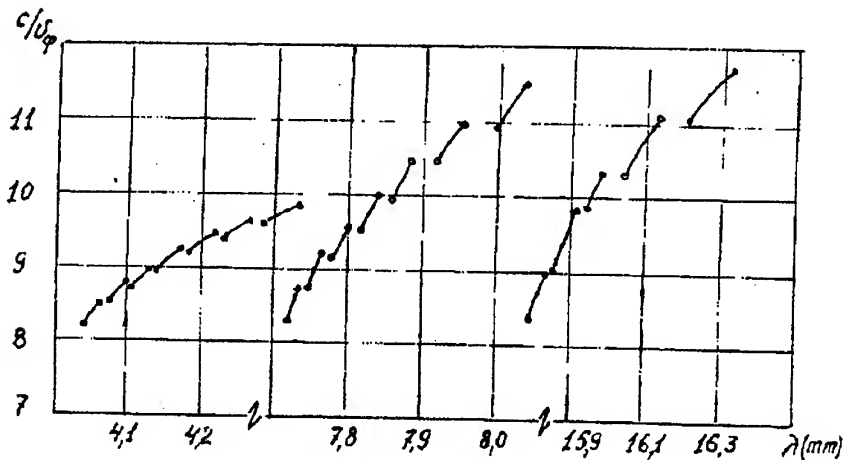


Fig. 2. Dispersion characteristics of a three-frequency generator

2. Influence of inhomogeneous focusing magnetic field on characteristics of MMB devices

An increase in the efficiency of the electron flow interaction with a wave field of the SWS in a inhomogeneous focusing magnetic field is usually observed in the EHF of the MMB and is accounted for by an increase in the effective length of electron transit in the presence of "a depleted layer" in the pulse electron flow. This phenomena is followed by a decrease in the starting current, and accordingly, an increase of microwave power.

The magnitude of the magnetic field inhomogeneity is negligible and amounts to $\frac{\Delta\beta}{\beta} = 0.0002$, and, therefore,

it is not necessary to measure it with a high degree of accuracy. Experimentally this magnitude is estimated indirectly according to the shift of the generator (in mm) from the magnet axis into the domain of the inhomogeneous filed. For this purpose an adjustment device which allows the magnet axis inclination to change to an accuracy of 2 to 3 is applied. The inhomogeneity of the stationary magnetic field is in general determined from the relation D/L (the pole shoes diameter to the value of the magnetic gap).

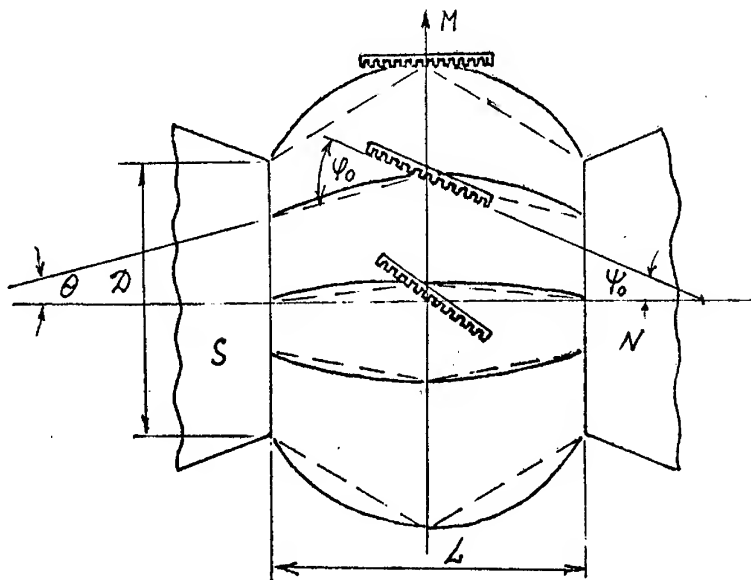


Fig.3. Change in the position of the periodic structure in an inhomogeneous magnetic field.

The behavior of varying the line curvature of the magnetic field and the location of the SWS (M) is shown in Fig.3. In terms of the angle constancy of the electron flow inclination to "the comb" φ , which is determined from the relation $\varphi = \arctg \frac{a}{l}$ ("a" is the flow thickness) it can be stated that $\varphi = \Psi_0 + \Theta$. Then the experimentally measured angle Ψ can be written as

$$\Psi\left(\frac{a}{l}, \frac{D}{L}, M\right) = \varphi\left(\frac{a}{l}\right) - \Theta\left(\frac{D}{L}, M\right)$$

The experiments showed that as the wavelength becomes shorter for the more effective operation of the tube, large field inhomogeneity is required, that is to say, it is necessary to increase the parameter (M).

3. Influence of reflections on the generator characteristics

With several "combs" being simultaneously current-excited there is a small probability that the microwave power maxima coincide in the MMB at all carrier frequencies because of the insignificant reflections in the waveguide. However, considerable reflections give rise to a number of effects which imply a decrease in the starting current, increased output power, stabilized frequency and device efficiency. At this point the discontinuity in frequency characteristics appears (in accordance with the phase generation modes) in well-defined places at an interval of $\Delta f = 150 \cdot \lambda / l \lambda_b$ (here l is the waveguide length, λ_b is the wavelength in the waveguide). This fact simplifies the problem of designing such generators since the possibility of occurring arbitrary discontinuities in the frequency characteristics is ruled out. In the device the reflection coefficient related to the electron gun " r_{II} " is equal to 0.7 whereas in the collector part it makes up $r_k \approx 1$. Thus, in the waveguide a standing field pattern is established. Displacement of the piston permits the location of the frequency zones and the output powers level to be controlled. Since the frequencies differ in octave, the period of frequency and power change is also different by a factor of 2. As the phase generation modes vary faster in going to the shorter wave bands (with the piston being displaced) one may expect that with its certain position an optimal case of meeting phase

conditions at all radiative frequencies is possible. The level of the microwave power on each carrier frequency amounted to several hundreds of milliwatts, which would suffice to conduct multichannel measurements.

4. Frequency responses of the GSWR.

As the generator is operated on an unmatched load the frequency "pulling" offers its specific characteristics involving the peculiarities of power output and load matching conditions. Generators like a magnetron, a klystron, etc. can operate in a stable mode when there is only high-quality matching. Otherwise, it gives rise to frequency hopping and failure of oscillations.

The variation in the generator frequency can be described by the following expression:

$$\Delta\omega_0 = -a \cdot \sin \psi / (\gamma + \cos \psi), \quad (1)$$

where $\gamma = (1 + k^2) / 2k$, $a = \alpha_T^2 y_0 \omega_0 / 2 y_{ok}$, k and ψ are the module and the phase of the reflection coefficient at the line input, α_T is the transformation ratio, y_0 is the characteristic admittance of the transmitting line, y_{ok} is the characteristic admittance of the oscillatory system. The maximum frequency deviation from the value that corresponds to the matched load can be written as

$$(\omega - \omega_0)_{\max} = 2ak / (1 - k^2). \quad (2)$$

As will be seen from expression (1) and (2) the frequency "pulling" is determined by the parameters of the generators oscillatory system as well as by the module and the phase of the load reflection coefficient. A decrease in the parameter a in expressions (1) and (2) is accounted for by an increase in external Q , since $a \sim Q_{ex}^{-1}$, which, in its turn, brings about a power decrease.

Based on the foregoing let us consider the operation of the GSWR (generator with a surface wave resonator) and compare its parameters to those of the extensively utilized devices. Fig.4 gives a schematic design of the device that comprises: 1 - a periodic comb-like structure; 2 - $5.5 \times 11 \text{ m}^2$ section of the prismatic waveguide; 3 - an electron beam of the basic electron gun; 4 - an electron beam of the second (supplementary) electron gun.

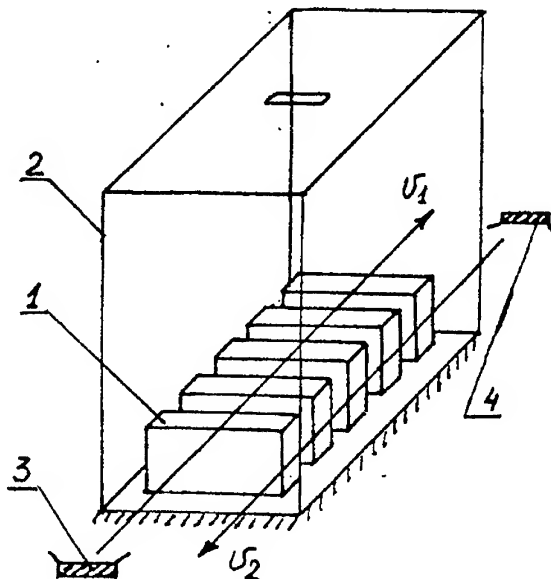


Fig 4 Design of AM - oscillation Generator with a Surface Wave Resonator (SWR)

The experiments that were made suggested that with an output power of several watts the generator frequency "pulling" quantity was small.

For instance, with the standing wave ratio (SWR) of the load being equal to 9 and a change in the phase of the wave reflection coefficient Ψ to π the frequency deviation accounted for 1 to 3 MHz at $f = 35,500$ MHz.

5. Generator Operation in a AM - oscillation mode.

As Fig.4 suggests the electron flux of the gun 3 brings about an excitation of the comb-like system 1 in a 8-mm band and at the same time interacts with - 1 slow space harmonic of the field.

To apply the modulation of the continuous radiation in amplitude into the interaction space an opposing low-power electron beam 4 is injected; this beam interacts with one of the spatial harmonics in a regenerative mode. The AM - oscillations are set up by amplifying or suppressing the oscillations induced at the expense of the basic electron flux [3]. Both of the electron fluxes are spatially separated. This stems from the need for adjustment of the device in a focusing magnetic field.

As far as the operative generator breadboard is concerned, the d.c. beam power was equal to 150-200W.

As will be apparent from Fig 5 the AM - oscillations can be set up provided that the accelerating voltage (whose variation obeys the law $U = U_0 + U_m \sin \omega t$) is applied to the electron gun 4. The point b estimated from the value of the potential U_0 is chosen on condition that minimum non-linear distortions occur. Thus, with $U_0 = 1500V$ and $U_m = 100V$ an amplitude of the high-frequency signal varies from point P_a to point P_c , which correlated with the modulation factor $m \approx 1$ if it is to be determined from the relation $m = (P_{max} - P_{min}) / (P_{max} + P_{min})$.

The frequency drifts (shown on the graph by the dotted line) for the given potentials are on the order of 1 to 3 MHz.

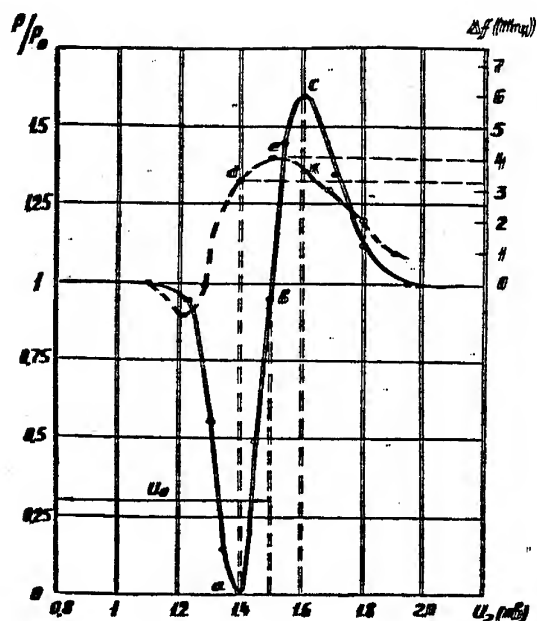


Fig.5 Variation in output power and frequency deviation with modulating voltage.

In actual practice the oscillations with $m=0.1$ to 0.3 can be applied to most of measuring circuits. In this case the AM - signal frequency drift is 0.1 to 0.3 MHz. Small frequency drifts can be achieved if the generator is fitted with a high - Q oscillatory system represented as an open or closed prismatic resonator [4].

Conclusion

The developed O-type MMB multiwave resonance generators operating in a mode of continuous coincided radiation were primarily utilized to detect the moving plasma and its radioscopy at many bands. These devices provided the basis for the development of diagnostic equipment: a multiband Doppler locator and a plasma radioscopy unit. In the first case it became possible to estimate the velocities and the laws of moving plasma

formations fronts of different concentrations. In the second case - the structure and gradients of plasma bunches. This made the information more reliable.

In conclusion, it should be pointed out that the MMB AM - oscillation generator featuring a new modulation method is distinguished by a small frequency deviation with great values of the modulation depth coefficient and by the level of the output power in the order of several watts. The generator was tested in diagnostic units to study the physical properties of plasma and shock waves. This principle can be used to develop the AM - oscillation generators in the short - wave portions of the MMW band.

References

1. A.C. No. 341113 (USSR) MKI. Backward-wave tube / G.Ya.Levin/ Discoveries and Inventions. 1972, No. 25, p.201.
2. Yefimov B.P., Kirilenko A.Ya., Kozorovitsky L.L., Rusanov V.D., Smirnov V.P. Consideration of the effects of multiple reflections from dielectric walls in microwave plasma sounding. Collection: Plasma diagnostics. Atomizdat, 1968, vyp. 2.
3. A.C.(author's certificate) #520840 (USSR). Resonance Backward-wave tube: B.P.Yefimov, A.P.Kas'yanenko, L.I.Korotun. Wish priority of 2.21.69.
4. A.C. #292820 (USSR). MMB-amplitude-modulated generator: B.P.Yefimov, A.P.Kas'yanenko, L.I.Korotun, B.Ya. Krivitsky, P.J.Mos'pan. Wish priority of 11.22.71.

Channel Dropping and Branching Filters Using NRD-guide for Millimeter-Wave Integrated Circuits

Tomohiro YAGINUMA, Takeshi YAMAGUCHI, Tadashi FUKUDA and Isao OHTOMO

Department of Electronic Engineering
Kogakuin University
1-24-2 Nishi-Shinjuku, Shinjuku-ku,
Tokyo 163 JAPAN

Tel. : +81-3-3342-1211
Fax. : +81-3-3348-3486
e-mail: ohtomo@cc.kogakuin.ac.jp

Abstract—As is generally known, dielectric waveguides have low-loss characteristics in the millimeter-optical-frequency range. The dielectric waveguide is necessary to be bent when it is used for a filter. However, it has radiation losses due to the bend. In order to lower the bending losses, nonradiative waveguides are being studied widely.

This paper describes applications of nonradiative dielectric waveguides to filters and presents the measured characteristics of newly designed filters. A comparison of the bending losses is also presented for three kinds of waveguides, namely dielectric waveguide, aluminum plated dielectric waveguide and nonradiative dielectric waveguide. As a result, 0.7 dB of insertion loss was obtained for a ring type channel dropping filter, and 0.5 dB for a periodic branching filter in 20 GHz band.

1. Introduction

The dielectric waveguide (D-guide) is very promising for millimeter-wave integrated circuits. A ring type and a periodic filters using the D-guides have been also reported^{[2],[3]}. However, it is difficult to obtain low bending loss and to build a small-sized filter, because a radiation loss caused by bending can not be ignored. On the other hand, nonradiative dielectric waveguide (NRD-guide^[1]) has low bending loss characteristics. Therefore, as components of a filter, it can be considered to use an NRD-guide which is a D-guide sandwiched by metal plates.

This paper describes characteristics of newly designed ring type channel dropping and periodic branching filters using NRD-guides, as well as fundamental characteristics of NRD-guides used for filters. In order to confirm effectiveness of NRD-guide, an aluminum foil plated waveguide (APD-guide) on the top and the bottom sides of a D-guide is also examined.

2. Strip Structure in NRD-guide

Figure 1 shows a strip structure of NRD-guide. The electromagnetic wave propagates along the dielectric strip. Theoretically, the radiated power completely disappears when a is less than half wavelength, where a is a gap between the two metal plates. NRD-guides are suitable for millimeter-wave integrated circuits because the higher the frequency is, the lower the conduction losses.

3. Basic characteristics of NRD-guide

In order to use NRD-guide for filters, fundamental characteristics of NRD-guide are investigated.

3.1. Transmission Loss of Straight NRD-guide

The transmission loss of straight NRD-guide was measured to be about 2 dB/m at 20 GHz. The parameters of this waveguide are:

Sizes: $a = 7$ mm and $b = 10$ mm
Metal Plates: Copper ($\sigma = 5.801 \times 10^7$)
Dielectric Strip: PTFE (Poly-Tetra-Fluoro-Ethylene,
 $\epsilon_r = 2.01$, $\tan \delta = 1.5 \times 10^{-4}$)

3.2. Bending loss

An undesired signal of LSE₁₀ transmission mode is generated when the NRD-guide is bent and it couples with the desired signal of LSM₁₀ transmission mode. Accordingly the bending loss increases. Figure 2 shows the relation between the strip width b and the radius of curvature R when the losses are zero and the maximum for 180° bend at 20 GHz^[1]. From Figure 2, the NRD-guide becomes lossless when $a = 7$ mm, $b = 10$ mm and $R = 44$ mm.

Figure 3 shows measured values of bending losses for three kinds of waveguides having the above sizes, namely D-guide, APD-guide and NRD-guide. The bends of dielectric strip of the three guides are 7 mm in height, 10 mm in width, 44 mm in radius of curvature and 180° in bend angle.

It is well known that the bending loss of D-guide decreases with the increase of frequency as is shown in Fig. 3. However, the losses of APD-guide and NRD-guide do not depend much on frequency. The loss characteristics of NRD-guide have spikes in the lower-frequency range. On the other hand, the loss is very low in the higher-frequency range. It is shown that the loss of NRD-guide is the lowest on comparing those of three kinds of waveguides.

3.3. Directional Coupler

Figure 4 shows structures of K-type and X-type couplers which are generally used for basic filter circuits and Figure 5 shows their measured and calculated coupling factors respectively. Close agreements between the measured and the calculated factors are obtained.

4. Ring Type Channel Dropping Filter

The structure of a two-cavity ring type filter using NRD-guides is shown in Fig. 7. The fabricated ring type filter is shown in Fig. 8. The filter is composed of two ring resonators and two straight waveguides for the line from the input to the output ports. The designed center frequency and 3-dB bandwidth of ring type filter are 20 GHz and 120 MHz. The other design parameters are; resonant index $N = 26$, ring resonator radius $R = 44$ mm, gap between the two metal plates $a = 7$ mm and dielectric strip width $b = 10$ mm. With these design parameters, the coupling factors of K-type and X-type couplers are calculated to be 1.5 dB and 6.0 dB, respectively.

Figure 9 shows the measured and calculated characteristics of the filter. The measured channel dropping loss was 0.7 dB at 20.21 GHz and 3-dB bandwidth was 140 MHz. On the other hands, the measured loss of the same type of filter using APD-guide which was designed with the same parameters was 4.8 dB and larger than that of filter using NRD guides.

5. Periodic Branching Filter

5.1. Structure

A periodic branching filter using ring resonators and connecting waveguides for phase adjustment has simple structure and can obtain amplitude characteristics nearly equal to that of a sixth- or seventh-order Maximally flat type filter^[3].

It is composed of three directional couplers, two connecting waveguides for phase adjustment and a ring resonator. Two of the three couplers are 3-dB hybrids which are used for the K-type coupler. The other is used to couple the resonator to one of the connecting waveguides. The coupling factor between them is required to be 0.26 dB^[3]. The equivalent circuit of this filter is shown in Fig. 10.

5.2. Design

All bend angles are designed to be 180° and the radius of each bend is 45 mm. Similarly with the ring type filter, the size of dielectric strip width is determined using the lossless condition as $a = 6.75$ mm and $b = 11.3$ mm. Other parameters are: resonant index $N = 60$, $l_0 = 388.1$ mm, $l_1 = 180.0$ mm, and $l_2 = 370.8$ mm. The fabricated periodic filter is shown in Fig. 11.

5.3 Characteristics of Periodic Branching Filter

The amplitude transmission characteristics of filter using NRD-guide is shown in Fig. 12. The measured branching losses are about 0.5 dB between ports ① and ③, and about 1.5 dB between ports ① and ④.

On the other hand, the losses of periodic branching filter using APD-guide with the same designed parameters, are about 3.5 dB between ports ① and ③, and about 6.0 dB between ports ① and ④. Therefore, it is evident that the loss of periodic branching filter using NRD-guide is much lower than that using APD-guide.

6. Conclusion

Two kinds of filters using NRD-guides, namely ring type channel dropping filter and periodic branching filter, are examined as well as the basic characteristics of NRD guides. It was shown that use of NRD-guides is effective in order to lower the bending loss. The experimental results show that the filters using NRD-guide have low losses of which values agree well with the designed values. As a result, low loss filters were obtained, i.e. 0.7 dB of insertion loss for a ring type channel dropping filter and 0.5 dB for a periodic branching filter in 20 GHz band.

It is possible to make the sizes of filters much small because their low bending loss characteristics. Therefore, filters using the NRD-guide can be easily applied to millimeter-wave integrated circuits.

References

- [1] T. Yoneyama and S. Nishida: "Nonradiative Dielectric Waveguide for Millimeter-Wave Integrated Circuits", IEEE Trans. Microwave Theory & Tech., MTT-29,11, pp.1188-1192 (Nov.1981)
- [2] T. Itanami and S. Shindo: "Channel Dropping Filter for Millimeter-Wave Integrated Circuits", IEEE Trans. Microwave Theory & Tech., MTT-26, 10, pp. 759-764 (Oct. 1978)
- [3] T. Itanami: "A Periodic Branching Filter for Millimeter-Wave Integrated Circuits", IEEE Trans. Microwave Theory & Tech., MTT-29, 9, pp.971-978 (Sep.1981)

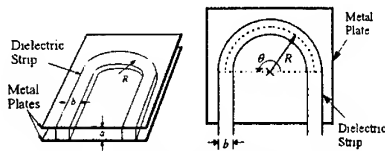


Fig. 1. Strip structure in NRD-guide.

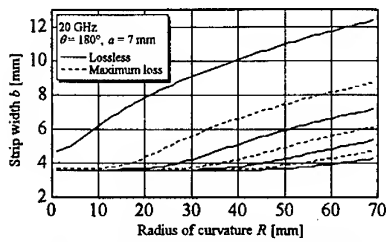


Fig. 2. The relation between strip width and radius of curvature.

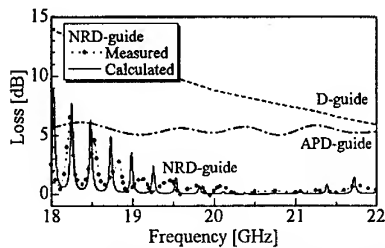


Fig. 3. Bending losses in three kinds of waveguides.

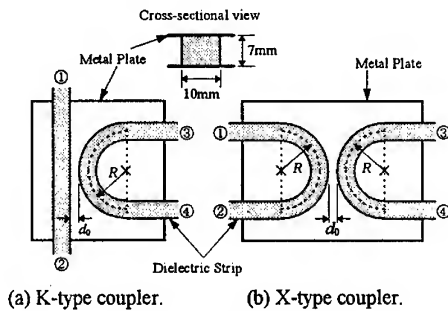


Fig. 4. Directional Coupler.

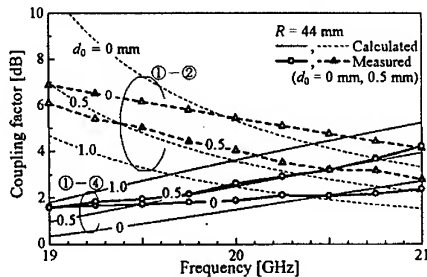


Fig. 5. Coupling factors of K-type coupler.

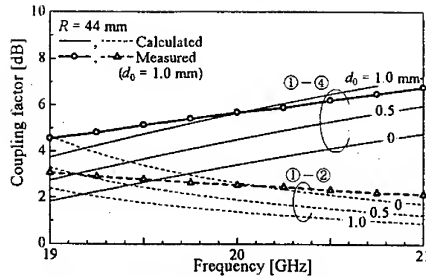


Fig. 6. Coupling factors of X-type coupler.

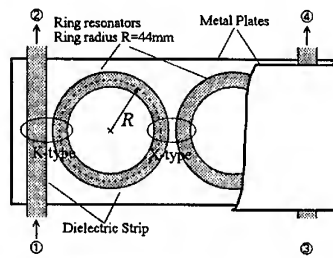


Fig. 7. Structure of two-cavity ring type filter.

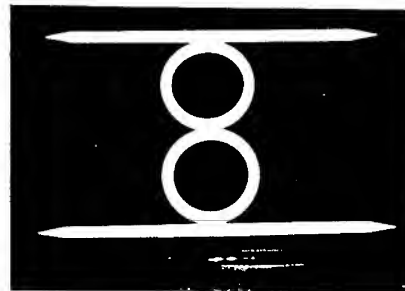


Fig. 8. Fabricated ring type filter (the metal plates removed).

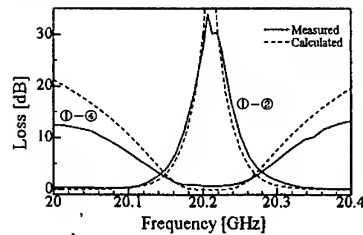


Fig. 9. Transmission characteristics of ring type filter.

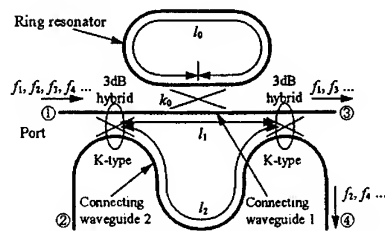


Fig. 10. The equivalent circuits for periodic branching filter.

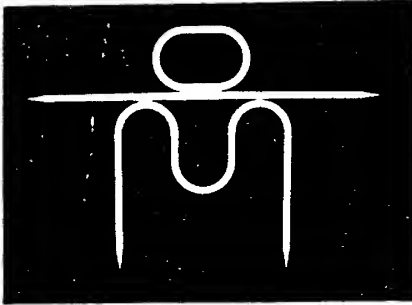


Fig. 11. Fabricated periodic branching filter (the metal plates removed).

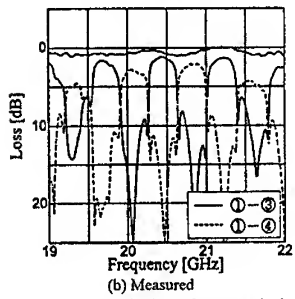
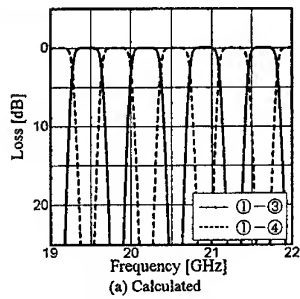


Fig. 12. Transmission characteristics of periodic branching filter.

Monolithic Artificial Transmission Line Balanced Frequency Doublers

P. Kangaslahti^{(1),(2)}, P. Alinikula⁽¹⁾, V. Porra⁽¹⁾

⁽¹⁾ Institute of Radio Communications, Electronic Circuit Design Laboratory, Helsinki University of Technology, Otakaari 5A, FIN-02150 Espoo, Finland
tel: +358-9-451 2279, fax: +358-9-451 2269, email: pek@clara.hut.fi

⁽²⁾ Ylinen Electronics, Kauniainen, Finland

ABSTRACT

Artificial transmission lines, realized using standard passive components of the foundry library, were utilized to design 180-degree baluns for millimetre wave frequency doublers. Monolithic integration of the complete doubler was achieved on extremely small chip area, 0.6mm². However, the performance of the frequency doubler was not sacrificed, since the operating frequency bandwidth was 30 %. These results show the suitability of this new technique for integration of several of the functions of a transmit/receive unit economically on a very small area on chip.

INTRODUCTION

A key issue in the development of cost effective high volume millimetre wave systems is the monolithic integration of several functions on a single chip. Due to the reduced total chip area required for the MMIC transmit or receive unit, the problems and costs of several millimetre wave interconnections can be avoided. To accomplish this single chip integration, we minimized the area required for the frequency multiplier. If traditional microstrip or coplanar transmission lines are used, the transmission line parts of the multiplier require very large area on the chip. To achieve a remarkable circuit area reduction, we used artificial transmission lines.

DESIGN OF THE BALANCED FREQUENCY DOUBLERS

Millimetre wave frequency doublers are normally designed using a single nonlinear device, or two nonlinear devices in balanced configuration [1]. A fundamental frequency quarter-wave stub is needed in single device doubler for the filtering of the unwanted harmonics [2,3]. When two nonlinear devices are connected in balanced configuration, the stubs are not needed. However, a traditionally large transmission line balun [4] or a special electromagnetically simulated balun [5,6] is required at the fundamental frequency.

The balanced configuration has potential for small-area monolithic integration, only if the balun area requirement can be decreased. We replaced the 180-degree transmission line balun in a frequency doubler by a 180-degree artificial transmission line (ATL), as shown in Figure 1. The ATL is a network of equal series inductors, L_s , and equal shunt capacitors, C_p . The characteristic impedance, Z_0 , and the propagation constant, γ , of the ideal, lossless ATL are

$$Z_0 = \sqrt{\frac{L_s}{C_p}} \quad (1)$$

$$\gamma = \omega \sqrt{L_s C_p} \quad (2)$$

Thus, we had the freedom to design the impedance and electrical length to the optimum by simply adjusting the parallel shunt capacitor, C_p , and series inductor, L_s , values in the ATL.

We used standard Philips D02AH foundry models of inductors and thin film capacitors. The simulation results of the ATL and, for comparison, the conventional microstrip balun are presented in Figure 2. The ATL had three shunt capacitors and short lines as series inductors. The values of C_p and L_s were selected to give $Z_0 = 25\Omega$ according to (1). The total area requirement for the ATL hybrid was only 0.1 mm². The electrically equivalent microstrip balun was 2.6 mm long and 266µm wide, requiring at least 1.3 mm² area, when folded. The loss and phase shift of the ATL are almost identical to the microstrip balun up to 23GHz. The ATL cut-off frequency is at 29GHz. The complete circuit was designed on a standard chip of a multi-user processing run as shown in Figure 3. The area requirement of the frequency doubler on this chip was only 0.6 mm². We used 0.2 x 90µm² depletion pHEMTs in the design. The pHEMTs were biased close to threshold voltage for maximum efficiency and reliability [1]. The simulations were performed using harmonic balance method to find the optimum matching networks.

To verify the applicability of the ATL design technique for different MMIC processes, a second ATL frequency doubler was processed at Fraunhofer Institut for Applied Physics (FhGIAF). In this completely planar circuit the active devices were 0.3x50µm² enhancement HEMTs. The circuit has high-Q airbridge spiral inductors and thin-film capacitors in the balun. The applied design methods were similar as for the D02AH circuit. Photograph of the chip is presented in Figure 4.

MEASUREMENT RESULTS

The processed circuits were measured directly on chip without any external filtering. The D02AH process balanced frequency doubler has operating bandwidth from 32GHz to over 42GHz. The FhGIAF process balanced frequency doubler operating bandwidth is also wide, covering the frequencies from 34GHz to 41GHz. The measurement and simulation results are shown in Figure 5. Correspondence between simulations and measurements is within a few desibels over most of the frequency range, which is good for nonlinear circuits. The processed FhGIAF circuits have smaller I_{ds} than the transistor models predict, so the second harmonic output power has also decreased.

CONCLUSION

A design technique for wideband, very small-size balanced frequency doublers was presented. The balancing hybrids in the doublers were artificial transmission lines, which reduce the balun size to 1/10 or less of the

conventional baluns. We used standard foundry library models for the design of frequency doublers in two different types of HEMT processes. Measured circuits had 7GHz to 11GHz operating bandwidth at 38GHz output frequency.

ACKNOWLEDGMENT

This study was supported by the Academy of Finland, the Finnish Technology Development Centre and Ylinen Electronics.

REFERENCES

- [1] Maas, S.A. *Nonlinear Microwave Circuits*. Norwood, MA 1988. Artech House, Boston, MA, USA. 469p.
- [2] Rauscher, C. High-Frequency Doubler Operation of GaAs Field-Effect Transistors. *IEEE Trans. on Microwave Theory and Techniques*, Vol. 31, No. 6, June 1983, pp. 462-473.
- [3] Kangaslahti, P., Alinikula, P., Kaunisto, R., Stadius, K., Pärssinen, A. and Porra, V. Monolithic Frequency Doublers for Millimetre Wave Signal Generation. *Proceedings ESA Workshop on Millimeter Wave Technology and Applications*, 5-7 December 1995, ESTEC, Noordwijk, The Netherlands. pp. 6.3.1-6.3.5.
- [4] Angelov, I., Zirath, H., Rorsman, N., Grönqvist, H. A Balanced Millimeter Wave Doubler Based on Pseudomorphic HEMTs. *Proceedings 1992 IEEE MTT-S International Microwave Symposium Digest*, 1-5 June 1992, Albuquerque, NM, USA. pp. 353-356.
- [5] Ogawa, H. and Minagawa, A. Uniplanar MIC Balanced Multiplier - A Proposed New Structure for MIC's. *IEEE Trans. on Microwave Theory and Techniques*, Vol. 35, No. 12, December 1987, pp. 1363-1368.
- [6] Abdo-Tuko, M., Bertenburg, R., Wolff, I. A Balanced Ka-band GaAs FET MMIC Frequency Doubler. *IEEE Microwave and Guided Wave Letters*, Vol. 4, No. 7, July 1994, pp. 217-219.

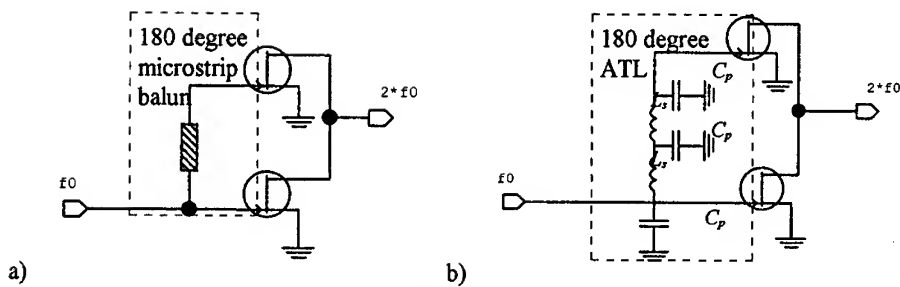


Figure 1. Balanced frequency doubler schematics. The conventional a) and the new ATL balanced frequency doubler b) are shown. The matching and bias networks have been omitted.

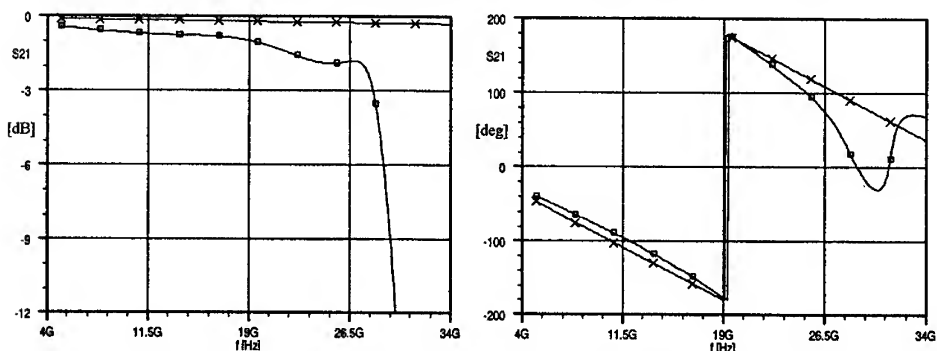


Figure 2. Simulation of S_{21} magnitude [dB] and phase [deg] for the microstrip (-x-) and ATL (-o-).

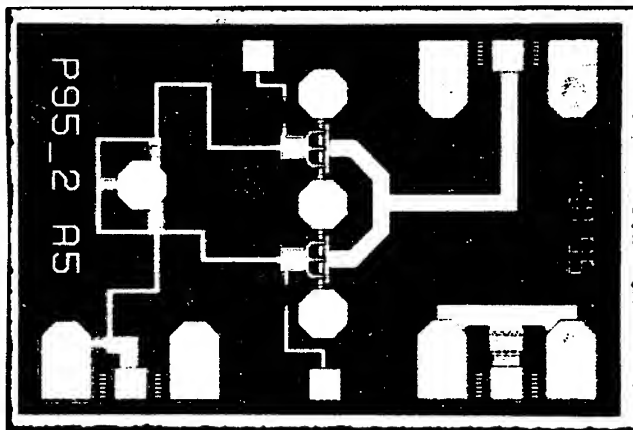


Figure 3. Photograph of the ATL balanced frequency doubler processed in D02AH process. The area of the circuit is 0.6 mm^2 on the standard multiuser process chip ($0.9 \text{ mm} \times 1.4 \text{ mm}$).

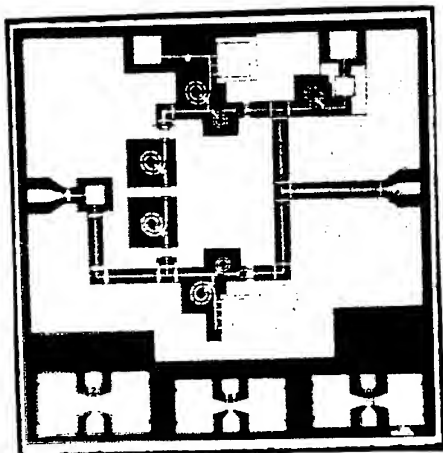


Figure 4. Photograph of the ATL balanced frequency doubler processed in FhGIAF process. Circuit area on chip is less than 1mm^2 . The chip dimensions are $1.4\text{mm} \times 1.4\text{mm}$.

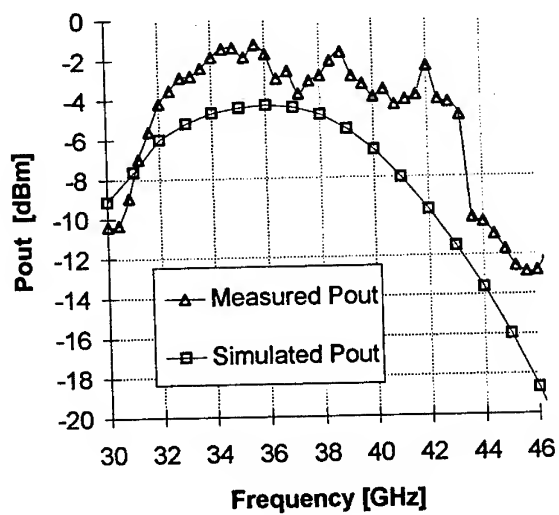


Figure 5. The measured and simulated results of the ATL balanced frequency doubler processed in Philips D02AH process. Second harmonic output power, P_{out} , is shown as a function of output frequency, when input power $P_{in} = +6\text{dBm}$.

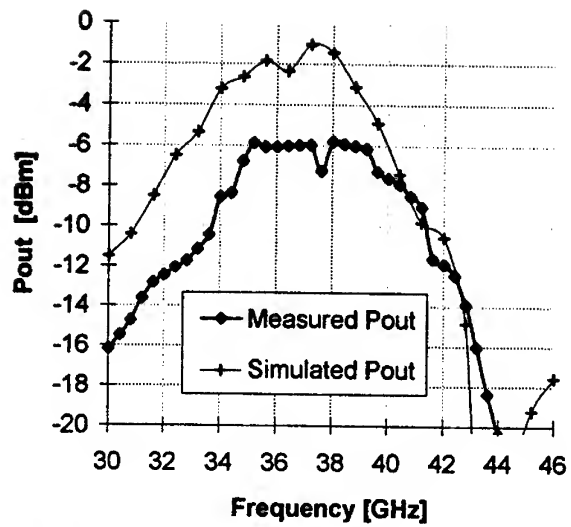


Figure 6. The measured and simulated results of the ATL balanced frequency doubler processed in FhGIAF process. Second harmonic output power, P_{out} , is shown as a function of output frequency, when input power $P_{in} = +6$ dBm.

Ka-BAND FET FREQUENCY QUADRUPLER WITH LOW GROUP DELAY VARIATION

Z. Nativ, A. Kadosh, S. Matarasso
Rafael, P.O. Box 2250, Haifa Israel
Tel: 972-4-8794112, Fax: 972-4-8792037

ABSTRACT

The Design of a 8GHz to 32GHz FET frequency quadrupler is described. Typical conversion loss of 9.5dB and low group delay variation of 2 nsec was measured over 2GHz output bandwidth, including the loss and dispersion of the MIC output filter. The design was based on the linear S-parameters of the chip device (including the bond wires), at the required operating frequencies and harmonics bandwidths.

INTRODUCTION

Frequency Multipliers using GaAs FETs find broad applications in Mm-wave modern electronic systems, providing improved design flexibility and capabilities. These include Mm-wave transceivers for applications in Mixer LO's, High frequency broadband synthesizers and phase-locked sources. Low group delay circuits are highly desirable in some modern high frequency radar systems.

A comprehensive study and an analytic large signal model of the FET frequency doubler is presented in [1], and the analysis of relative contributions of the various nonlinearities to harmonics generation is described in [2]. The majority of works published in the area of GaAs FET multipliers mainly deal with doublers, however, none of them address group delay response.

This paper presents the design and realization of a MIC Ka-band frequency quadrupler using a single HJ FET in a chip form.

The design of the input and output matching circuits was based on the linear S-parameters of the device, provided by the manufacturer.

The bias point of the device was chosen at $V_{gs}=0$ where it provides better RF conversion efficiency.

The measured group delay variation of the quadrupler was low, in the range of 2 nsec, over bandwidth.

QUADRUPLER CIRCUIT DESIGN

Simulations using a unilateral power FET model [3] have shown that the non-linearity which is the largest contributor to harmonic generation is the clipping of the I_{DS} waveform. This effect can be induced by biasing the FET at 0V just below the forward conduction point of the gate-source junction, which causes a half wave rectified sinusoidal output voltage. Since this sort of frequency multiplier is less sensitive to reactive terminations as compare to a varactor multiplier for instance, it promises lower group delay variation.

The design of an efficient FET Quadrupler requires proper matching and filtering of the pump and harmonic frequencies.

In order to optimize the harmonic generation of the frequency multiplier, attention must be paid to the terminations that are presented at the device output to the fundamental and its harmonics.

At the FET reference plane the input circuit must provide matching to the source at the pump frequency f_0 , and open (or short) circuit to its harmonic frequencies. The output circuit must provide matching to the load at the 4th harmonic, and open (or short) circuit to reject the pump frequency and its harmonics at $2f_0$ and $3f_0$.

The output network also includes a parallel coupled 3 sections bandpass filter with proper phasing, centered at the 4th harmonic. Figure 1 shows the circuit configuration of the 8/32GHz FET quadrupler.

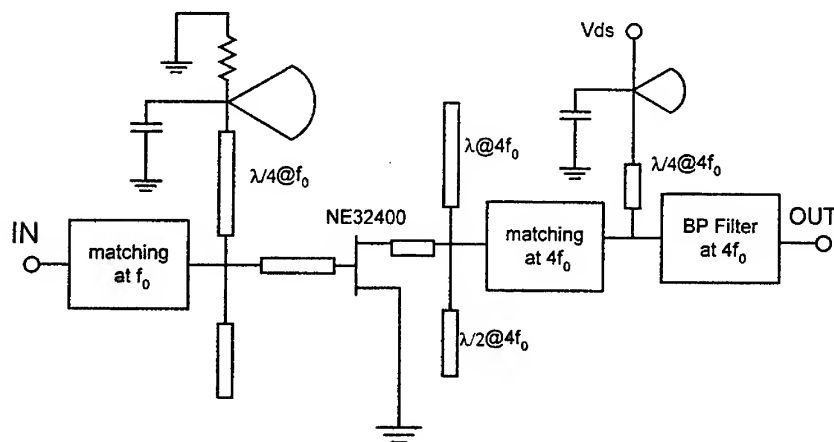


Fig 1 : Circuit configuration of the FET quadrupler

The circuit uses the NE32400 Pseudomorphic Hetero-Junction FET chip, and the design was based on the linear S-parameters of the device supplied by the manufacturer at $V_{DS}=2V$, $I_{DS}=20\text{ mA}$, in the 1-40 GHz band, which also include the bond wires.

The circuit was optimized and analyzed using EESOF (Libra), by taking into account all the requirements of matching at the operating frequencies and harmonics rejection over the required bandwidths.

The quadrupler circuit was fabricated on a 10 mil alumina substrate and has an area of 12×15 mm. The output of the microstrip circuit was terminated with a K-connector.

QUADRUPLER RESULTS

Measurements of P_{out} vs. P_{in} were performed for the two modes of operation: $V_{gs}=0$, and $V_{gs} = -V_T$. The $V_{gs}=0$ mode provides better RF conversion efficiency, as was found also in [4].

Since the quadrupler is operated under large signal conditions as compare to the given small signal S-parameters used in the design, Some adjustments of the input/output networks were required. The conversion efficiency prior to tuning was about 16dB. However, after tuning the circuit at the optimal bias voltages of $V_{ds}=2.5V$ and $V_{gs}=0$, the conversion loss results in 9.5dB at $P_{in}= +6dBm$, over 2GHz output bandwidth centered at 32.4GHz (Fig. 2).

The input return loss was about -10dB. The group delay variation of the quadrupler including the output band-pass filter was measured, using the HP Transition - analyzer [5]. As shown in Fig.2, a low group delay variation of about 2 nsec was obtained.

Since the previous measured group delay variation of a 3 sections band-pass filter of 2GHz bandwidth of this sort was about 1.5nsec, we conclude that the FET frequency quadrupler itself has low group delay variation.

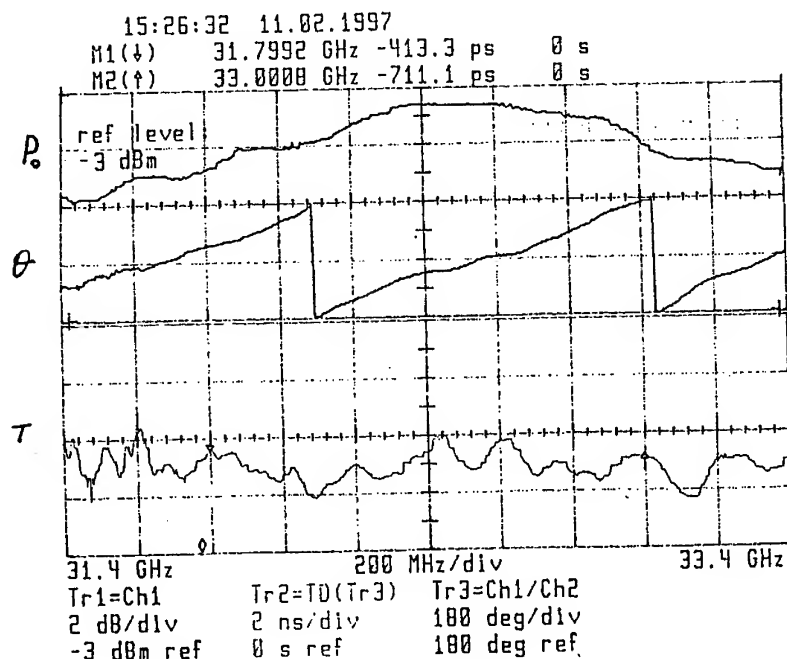


Fig.2 - Power output, phase, and group delay response of the quadrupler.

CONCLUSIONS

A broadband Ka-band Frequency quadrupler using an HJ FET chip has been demonstrated in microstrip. Its conversion loss was about 9.5dB, and low group delay variation of about 2 nsec was measured, over 2GHz bandwidth, including the output band-pass filter.

ACKNOWLEDGEMENT

The authors wish to thank Shimon Uliel, Gabi Lorber and Sonia Dammari for their helpful contribution in fabricating and testing of the circuit.

REFERENCES

- [1] C. Rauscher, "High-Frequency Doubler operation of GaAs Field - Effect Transistor", IEEE Trans Microwave Theory Tech., Vol. MTT-31, No. 6, June 1983, PP. 462-473.
- [2] A. Gopinath, and J.B. Rankin, "Single - Gate MESFET Frequency Doublers", IEEE Trans. Microwave Theory Tech., Vol. MTT-30, No. 6, June 1982, PP. 869-875.
- [3] E. Camargo, R. Soares, R.A. Perichon and M. Goloubkoff, "Sources of Non-Linearity in GaAs MESFET Frequency Multipliers", 1983 IEEE MTT-S Digest, PP. 343-345.
- [4] J. Geddes, V. Sokolov, and A. Contolatis, "W-Band GaAs MESFET Frequency Doubler", 1987 IEEE Microwave and Mm-Wave Monolithic Circuits Symposium, PP. 7-10
- [5] HP, "The Microwave Transition Analyzer..."
Product note 70820-1, 1991.

Analysis of Circular Waveguides with Azimuthally Magnetized Ferrite

Kamen P. Ivanov and Reinhold Pregla
Allgemeine und Theoretische Elektrotechnik,
FernUniversität, D-58084 Hagen, E-mail: R.Pregla@FernUni-Hagen.de
Topic numbers 5, 15 ; scientific

Abstract: Examined and interpreted are the transmission characteristics of the azimuthally magnetized ferrite-loaded coaxial waveguide – a canonical structure for digital remanent phaser designs, using the versatile and flexible Method of Lines. Emphasis is placed on TE_{01} mode exhibiting anisotropic effects of phase shifting and magnetically controlled cutoff dependent on the direction of remanent magnetization. A rigorous numerical analysis of field distribution over the guide cross-section, the eigenvalue spectrum and transmission characteristics is performed, giving a great deal of insight and essential quantitative information on propagation phenomena in the gyrotropic structure.

Introduction: The normal wave propagation in a cylindrical waveguide containing anisotropic ferrite magnetized azimuthally to remanence has been the subject of extensive study [1,2]. The propagation problem in case of rotationally symmetric TE mode has been integrated in terms of Kummer and Tricomi confluent hypergeometric functions of complex parameters and variable for propagation in gyrotropic structure. An extensive study of descriptive properties of these functions has been performed essential for computation of nonreciprocal characteristics of the structure under TE_{01} mode excitation. However, in case of azimuthally dependent TE_{mn} mode the solution of propagation problem leads to coupled differential equations for longitudinal components E_z and H_z , which cannot be separated. This paper aims at presenting the use of the Method of Lines (MoL)[3] – a special finite difference method for analysis of cylindrical waveguiding structures containing remanent ferrite magnetized azimuthally to remanence.

Formulation of the Problem: The geometry of the problem (Fig. 1) is an infinitely long, uniform coaxial waveguide of outer and inner radii r_0 and r_1 , with perfectly conducting walls completely filled with ferrite, with square hysteresis loop, magnetized azimuthally to remanence, propagating a monochromatic wave.

A cylindrical coordinate system (r, θ, z) with z -axis along the geometric axis is introduced. The remanent ferrite is characterized by a scalar permittivity $\epsilon = \epsilon_0 \epsilon_r$ assumed to be lossless and an asymmetric complex tensor permeability of the Polder form

$$\bar{\mu} = \mu_0 \begin{bmatrix} 1 & 0 & -j\alpha \\ 0 & 1 & 0 \\ j\alpha & 0 & 1 \end{bmatrix} \quad (1)$$

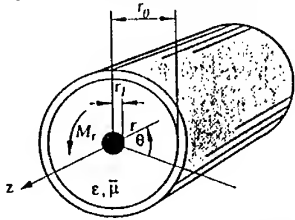


Figure 1: Circular waveguide with magnetized ferrite

where the off-diagonal element $\alpha = jM_r/\omega$, γ is gyromagnetic ratio, M_r -ferrite remanent magnetization, ω is the angular frequency of propagating wave, $\epsilon_0 = (1/36 \pi)10^{-9}$ F/m and $\mu_0 = 4\pi \cdot 10^{-7}$ H/m are permittivity and permeability in vacuo.

The problem at hand is to study the normal mode propagation along the gyrotropic circular waveguide. The uniform guide cross-section permits an assumption of $\exp(j(\omega t - \beta z))$ dependence of the fields on time and coordinate z , which accounts for $+z$ wave solution for a phase constant β .

Mathematical Treatment: A study of the expansion of Maxwell curl relationships excluding the transverse components of electric and magnetic field (E_r, E_θ) and (H_z, H_θ) reveals that the z -directed components satisfy the following second-order differential equations in the double connected ferrite region

$$\frac{1}{r_n} \frac{\partial}{\partial r_n} \left(r_n \frac{\partial}{\partial r_n} \right) E_{zn} - \frac{m^2}{r_n^2} E_{zn} + f_n^2 (1 - \epsilon_{ren}) E_{zn} - \alpha m \frac{f_n}{r_n} \tilde{H}_z = 0 \quad (2)$$

$$\frac{1}{r_n} \frac{\partial}{\partial r_n} \left(r_n \frac{\partial}{\partial r_n} \right) \tilde{H}_z - \frac{m^2}{r_n^2} \tilde{H}_z \frac{\partial^2 \tilde{H}_z}{\partial \theta^2} + f_n^2 \left(\mu_1 - \epsilon_{ren} - \alpha \frac{\sqrt{\epsilon_{ren}}}{r_n f_n} \right) \tilde{H}_z + \alpha m \frac{f_n}{r_n} E_{zn} = 0 \quad (3)$$

where the coordinates r, z and guide radius r_0 are normalized with the free space wavenumber $k_0 = \omega \sqrt{\epsilon_0 \mu_0}$ according to $\bar{r} = k_0 z, \bar{z} = k_0 z, \bar{r}_0 = k_0 r_0$; $\epsilon_{re} = \beta^2 / \kappa_0^2$ is the effective permittivity and $\mu_1 = 1 - \alpha^2$ the effective magnetic permeability of the ferrite. In addition the notations $r_n = \bar{r} / \bar{r}_0 = r / r_0, \epsilon_{ren} = \epsilon_{re} / \epsilon_r, f_n = \bar{r}_0 \sqrt{\epsilon_r} -$ normalized frequency, $E_{un} = \sqrt{\epsilon_r} E_u, u = r, \theta, z$, and $\tilde{H}_z = \eta_0 H_z$ are introduced with $\eta_0 = \sqrt{\mu_0 / \epsilon_0}$ – free space wave impedance. The azimuthal dependence of E_z and H_z components is assumed of the form $\sin(m\theta)$ and $\cos(m\theta)$, respectively (m – positive integer). The components E_r and H_θ (H_r and E_θ) have the same θ -dependence as E_z (H_z). As seen, the normalized electric and magnetic field components E_{zn} and \tilde{H}_z are coupled by the off-diagonal element α of permeability tensor.

Discretization: The coupled second order differential equations for longitudinal components are solved by the MoL using discretization on two different line systems

$$\begin{array}{ll}
 \text{e-line system} & \text{h-line system} \\
 E_{zn} \rightarrow \mathbf{E}_{zn} & \tilde{H}_z \rightarrow \tilde{\mathbf{H}}_z \\
 r_n \rightarrow \mathbf{r}_e & r_n \rightarrow \mathbf{r}_h \\
 D_r \rightarrow h_n^{-1} D_e = \bar{D}_e & D_r \rightarrow h_n^{-1} D_h = \bar{D}_h
 \end{array} \quad (4)$$

where $D_r = \partial/\partial r_n$ is differential operator with respect to r_n , \mathbf{E}_{zn} and $\tilde{\mathbf{H}}_z$ are onedimensional vectors, $\mathbf{r}_{e,h}$ are diagonal matrices of the discretized radii and the difference operators $D_{e,h}$ are matrices with bandwidth 2. In case $m = 0$ and TE_z modes D_h should satisfy the Neumann boundary conditions

$$\frac{\partial H_z}{\partial r_n} = \alpha f_n \sqrt{\epsilon_{ren}} H_z \quad (5)$$

at inner ($r = r_1$) and at outer guide radius ($r = r_0$). ($E_\theta(0) = 0$). The matrix form of discretized equations for longitudinal field components is

$$\begin{bmatrix} P_e^r + f_n^2(1 - \epsilon_{ren})I_e & -m\alpha f_n r_e^{-1} M_h \\ m\alpha f_n r_h^{-1} M_e & P_h^r + f_n^2(\mu_\perp - \epsilon_{ren})I_h - \alpha f_n \sqrt{\epsilon_{ren}} \bar{r}_h^{-1} \end{bmatrix} \begin{bmatrix} \mathbf{E}_{zn} \\ \tilde{\mathbf{H}}_z \end{bmatrix} = 0 \quad (6)$$

with

$$P_e^r = -r_e^{-1} \bar{D}_e^t r_h \bar{D}_e - m^2 r_e^{-2} \quad \text{and} \quad P_h^r = -r_h^{-1} \bar{D}_h^t r_e \bar{D}_h - m^2 r_h^{-2} \quad (7)$$

The matrices M_e and M_h are introduced to facilitate interpolation between the two discretization line systems, and the superscript t denotes transposed matrices $D_{e,h}$. The matrix form given by equ. (6) is an indirect eigenvalue system. Its determinant must be zero, resulting in a relation between the normalized propagation constant ϵ_{ren} and normalized frequency f_n with normalized guide radius \bar{r}_0 and off-diagonal component of permeability tensor α as parameters.

The discretized equations for transverse field components are given by the following matrix form

$$(1 - \epsilon_{ren}) f_n \begin{bmatrix} \mathbf{E}_{rn} \\ \mathbf{E}_{\theta n} \end{bmatrix} = \begin{bmatrix} -\sqrt{\epsilon_{ren}} \bar{D}_e & m r_h^{-1} \\ -m \sqrt{\epsilon_{ren}} r_e^{-1} & -\alpha f_n \sqrt{\epsilon_{ren}} M_h + \bar{D}_h \end{bmatrix} \begin{bmatrix} j \mathbf{E}_{zn} \\ j \tilde{\mathbf{H}}_z \end{bmatrix} \quad (8)$$

$$(1 - \epsilon_{ren}) f_n \begin{bmatrix} \tilde{\mathbf{H}}_\theta \\ \tilde{\mathbf{H}}_r \end{bmatrix} = \begin{bmatrix} -\bar{D}_e & m \sqrt{\epsilon_{ren}} r_h^{-1} \\ m r_e^{-1} & \alpha f_n M_h - \sqrt{\epsilon_{ren}} \bar{D}_h \end{bmatrix} \begin{bmatrix} j \mathbf{E}_{zn} \\ j \tilde{\mathbf{H}}_z \end{bmatrix} \quad (9)$$

Numerical Results: (i) *Field components.* A solution of the matrix forms of discretized equations for longitudinal and transverse components of electric and magnetic fields is performed by the MoL, yielding the values of all electromagnetic fields in the gyrotropic structure. As an illustrative example the distribution

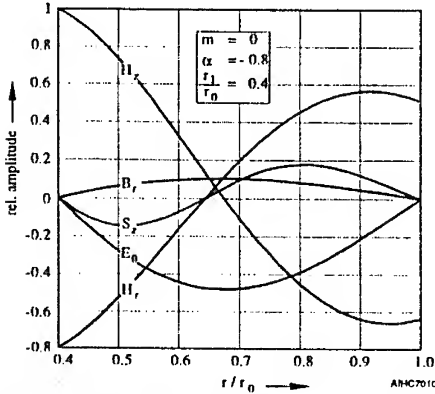


Figure 2: Distribution of field components across the cross-section of coaxial waveguide

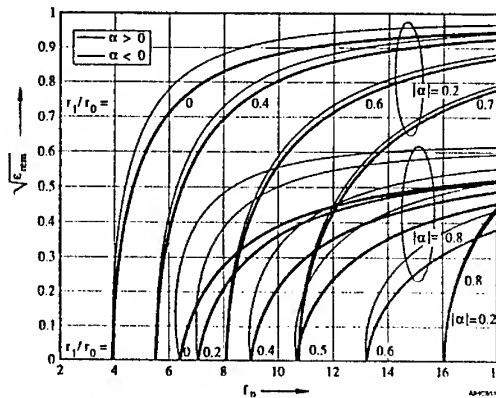


Figure 3: Normalized phase characteristics of coaxial gyrotropic waveguide

of E_θ , H_r and H_z of the TE_{01} mode in a coaxial guide with inner to outer radius ratio $\rho = r_1/r_0 = 0.4$ filled with azimuthally magnetized ferrite with $\alpha = -0.8$ is shown in Fig. 2 vs. reduced distance r/r_0 from

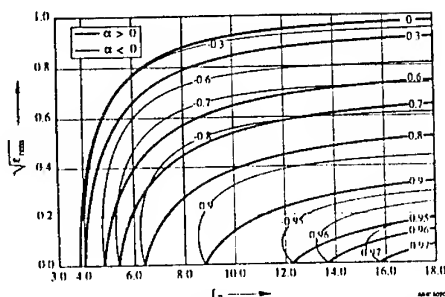


Figure 4: Normalized phase characteristics of circular gyrotropic waveguide

i.e. the integral of S_z over this region is negative. However, the total power defined by the integral of Poynting vector over the whole guide cross-section, propagates in $+z$ -direction.

(ii) *Normalized Phase Characteristics*: Using the discretized form of equations for longitudinal components E_z and H_z , the normalized phase constant $\bar{\beta} = \sqrt{\epsilon_{ren}}$ is computed as function of normalized frequency f_n . A representative set of theoretically calculated $\sqrt{\epsilon_{ren}} - f_n$ characteristics of gyrotropic coaxial guide for TE_{01} mode is plotted in Fig. 3 for $+M_r$ and $-M_r$ (thick and thin lines, resp.) parameterized with α for discrete values of inner to outer guide radius ratio. The graphs show that the structure exhibits substantially different normalized phase constants $\bar{\beta}_+$ and $\bar{\beta}_-$ corresponding to $+M_r$ or $-M_r$. A reversal of M_r produces a normalized phase shift of propagating TE_{01} mode $\Delta\bar{\beta} = \bar{\beta}_- - \bar{\beta}_+$ which can easily be computed from the curves. Fig. 4 is a plot of normalized phase characteristics vs. normalized radius of a circular guide of radius r_0 , completely filled with ferrite, magnetized azimuthally to remanence with α as parameter for both signs of M_r . Latching the ferrite between the two stable states of M_r provides a discrete differential phase shift. In general, the observed effect of increased α (strong anisotropy) is a substantial increase of $\Delta\bar{\beta}$.

(iii) *Near Cutoff Behavior*: Each pair of phase characteristics for given α and ρ in Figs. 3 and 4 intersect the horizontal axis at points $\bar{\beta}_{\pm} = 0$ defining the spectrum of cutoff frequencies of TE_{01} mode. In general the observed effect of increased α (M_r) is a reduction of normalized phase constant accompanied by a substantial increase of cutoff frequency. As seen from the curves in Figs. 3, 4 at the bifurcation points of each two branches of phase characteristics for given α , $\bar{\beta}_+ = 0$ while $\bar{\beta}_- \neq 0$, i.e. the structure can support TE_{01} mode at this point for negative remanent magnetization only. A reversal from $-M_r$ to $+M_r$ brings the guide from transmission state with $\bar{\beta}_- \neq 0$ into a state of cutoff ($\bar{\beta}_+ = 0$). Thus, the structure exhibits two states of transmission, depending on the direction of remanent magnetization. This nonreciprocal effect of magnetically dependent cutoff reveals additional potentialities of ferrite-loaded guide as a bistable ferrite switch geometry with two operation states (on and off positions). The structure could be adjusted in transmission state (with low losses) for incident wave and in a state of cutoff for reflected wave resulting in an exponential decay of its amplitude. A particularly interesting application of this nonreciprocal effect appears to be the design of an effective cutoff isolator.

Concluding Remarks: The application of the MoL for the first time to a gyrotropic waveguiding geometry allows a logical, systematic and precise treatment of its inherent nonreciprocity. Summarizing, the azimuthally magnetized ferrite-loaded circular guide turns out to be a suitable device geometry for phase shifting, switching and isolation, whose performance is readily described in terms of TE_{01} mode. The graphs presented could be used as design curves, by means of which wide class of specifications at microwave and millimeter frequencies could be translated into a suitable configuration with appropriate latching ferrite parameters, performing the intended device functions as phaser, cutoff switch or isolator. The problem leads to easy programming using MATLAB. The main part of the programme is about 2 - 3 pages long. The CPU time is of the order of seconds.

References

- [1] W. J. Ince and G. N. Tsandoulas "Modal inversion in circular waveguides. Part II: Application to latching nonreciprocal phasers", *IEEE Trans Microwave Theory Tech.*, vol. MTT-19, Apr. 1971, pp. 393-400.
- [2] K. P. Ivanov, "Propagation along azimuthally magnetized ferrite loaded circular guide" *Radio Sci.*, 1984, vol. 19, pp. 1305-1310.
- [3] R. Pregla and W. Pascher, "The Method of Lines", in T. Itoh, (editor), *Numerical Techniques for Microwave and Millimeter Wave Passive Structures*, J. Wiley Publ., New York, 1989, pp. 381-446.

UTD-BASED PATH LOSS PREDICTION WITH EXPERIMENTAL VALIDATIONS FOR MICRO-CELLULAR MOBILE RADIO COMMUNICATIONS

Wei Zhang¹ and Jaakko Lähteenmäki²

¹ Helsinki University of Technology, Institute of Radio Communications, Radio Laboratory, Otakaari 5A, FIN-02150 Espoo, FINLAND. TEL.: +358 9 451 2255, FAX: +358 9 451 2152, E-Mail: WZH@radio.hut.fi

² VTT Information Technology, P. O. Box 1202, FIN-02044 VTT, FINLAND. TEL.: +358 9 456 6547, FAX: +358 9 456 7013, E-Mail: Jaakko.Lahtenmaki@vtt.fi

ABSTRACT

The new work makes three UTD (uniform geometrical theory of diffraction) based path-loss prediction models and their experimental validations for urban micro-cellular mobile radio communications. The three models apply to the base station and mobile antennas much lower than the surrounding buildings and can be written in explicit forms for both vertical- and horizontal-polarization transmission and reception. Comparisons of their predictions with measurements at 900.5 and 1800 MHz in shadow zones of urban areas confirm the three models experimentally. The results demonstrate that fast two-dimensional (2-D) models which do not require a building height database can provide acceptable accuracy for micro-cellular mobile radio propagation predictions in urban environments. The methodology of this work is to determine in advance significant rays to use, from a particular geometry of the buildings in an urban area. It appears suitable here for 2-D modeling for parallel-street problem and irregular side-street problems. It has the potential to be used in practical design of micro-cellular mobile radio systems.

Indexing terms: 2-D UTD propagation model, Micro-cellular mobile radio, Multiple diffraction, Reflection

INTRODUCTION

The purpose of the new work is to investigate if propagation models with two-dimensional (2-D) building database can provide acceptable accuracy for micro-cellular mobile radio predictions in urban environments. The work itself contributes three UTD (uniform geometrical theory of diffraction) [1] based path-loss prediction models. The experimental validations are made by comparisons of the three models' predictions with measured data in shadow zones. Figure 1 shows an area in the center of Helsinki, Finland, where propagation measurements MAK62, MAK63 and MAK64 were performed. The base station (BS) and mobile station (MS), moving with a car, heights h_b and h_m , are much lower than buildings in the area.

The UTD model I, including more major diffraction rays, is an extension to path-loss models [2-5] for cellular mobile radio communications. The UTD model II solves a parallel-street problem represented by measurement MAK63, containing two major rays determined by modifications to the path-loss model in [5]. The UTD model III is derived from UTD models I and II for a site-specific case of measurement MAK62. The UTD formulae I and III are fast 2-D solutions to irregular side-street problems.

The methodology of these 2-D solutions is to find out, in advance, significant rays to use, in view of a particular geometry of the buildings in an urban area. It avoids a costly ray-search and is rather similar to the determination of a solution to an electromagnetic scattering problem from given boundary conditions. The salient points of the new work are described in the following.

THREE PATH-LOSS PREDICTION MODELS

The top views for UTD models I-III are shown in Figs 2 and 3. In the $O-xy$ coordinate system of Figs 1-3, BS and MS are at $BS(0,0)$ and $MS(x,y)$, respectively. The route of measurement MAK64 to which the UTD model I is applicable is along side streets, in the $-y$ direction. The route of measurement MAK63 is along a parallel street. The main street is in the x direction, as well as all parallel streets. All streets have a half width $y_0 = 7$ m.

The UTD model I is derived considering the buildings along side streets all in $\pm y$ directions as rows of knife edges with an equal spacing $d = 100$ m. This implies that reflections from the ground are ignored which have smaller amplitudes by UTD model I, as well as by UTD models II and III.

To compare with horizontal path length, vertical path length, i.e. the difference of $h_t - h_r$, is smaller and negligible. Since the height of the ground over the mean sea level varies in the measurement area, h_t is variable and the difference of $h_t - h_r$, where $h_r \approx 13.3$ m appears to be not critical. Because of the two reasons, 2-D simplification ($h_t - h_r \sim 0$) is taken for UTD models I-III. The MS height relative to the ground is 1.5 m.

The three models can be written in explicit forms for both vertical- and horizontal-polarization transmission and reception. Due to 2-D simplification, the depolarization effect (vertically polarized transmission to cause some horizontally polarized reception) is excluded from the three models. The vertically polarized transmission and reception practically applies to mobile radio communications [2, 6, 7], as well as to measurements MAK62, MAK63 and MAK64 at 900.5 and 1800 MHz. The cross-polarized reception is usually smaller, but the importance of the depolarization effects should be further investigated.

A. UTD I FOR IRREGULAR STREET CROSSINGS

Notations 1-4 in Fig 2 indicate four rays of UTD model I in the regions of $y > 0$. Let P_t and P_r be the radiated and received powers by isotropic antennas, respectively. The total path loss $L_t = -10 \log_{10}(P_r / P_t)$ in dB is derived as

$$L_t = L_0 + L_{1p} + L_{mfp} + L_{imp} \quad (1)$$

where L_0 , L_{1p} , L_{mfp} and L_{imp} are the losses due to free-space radio propagation, due to the diffraction by the local row (numbering n) of buildings, due to multiple diffraction by the intervening row of buildings and due to the interference between the rays, respectively. Losses L_{1p} , L_{mfp} and L_{imp} depend on the polarization of transmission and reception. The loss of $L_0 + L_{1p} + L_{mfp}$ is derived from UTD-based expression and models in [3-5]. The interference loss L_{imp} contributed by this work approximates the majority of multipath effects, like deep fading in the total received signal. The multipath effects are due to the diffraction and reflection of primary-diffracted fields from the surrounding obstacles, the primary diffraction itself and other multipath field components.

Existing at $y > 0$, the diffraction-reflection ray 4 disappears in the regions of $y < 0$. The reflection ray path length r_{24} from the diffraction point (x_n, y_n) to MS is derived as

$$r_{24} = [(2x_0 - x - x_n)^2 + (y - y_n)^2]^{1/2}. \quad (2)$$

As seen in Fig 2, $x_0 = 460$ m is the x position of a transverse church building at the end of main street and x_n is the x position of a local half screen at $(x_n, y > y_n)$. The diffraction-reflection angle β_4 is derived from

$$\tan \beta_4 = \frac{y - y_n}{2x_0 - x - x_n}. \quad (3)$$

Both r_{24} and β_4 are found from the image of MS, that would be at $(2x_0 - x, y)$ not indicated in Fig 2.

Three diffraction rays 1-3 in the entire y range of UTD model I are determined in four steps. First, let a plane wave from BS propagate across $n-1$ rows of and arrive at a local row of knife edges. The loss L_{mfp} is derived from the field ratio of $|E_{np} / E_0|$, where E_0 and E_{np} are the field magnitude of the incident plane wave and its corresponding total field at a local screen at $(x_n, y > y_n)$ or $(x_n, y < -y_n)$. Second, a spherical wave from BS is incident on this local screen. The corresponding diffracted field arrives at MS. The loss of $L_0 + L_{1p}$ is derived. The path loss for a primary-diffracted field of ray 1 is the sum of $L_0 + L_{1p} + L_{mfp}$. In addition, the step determines the diffraction-reflection ray 4 in the regions of $y > 0$. Third, a spherical wave from BS is incident on a knife edge at $(x_n, y > -y_n)$, modeling the transverse church building. This step determines the diffraction ray 2. Finally, similar calculations to steps 1 and 2 determine ray 3 and this step derives the interference loss L_{imp} .

In addition to the majority of diffraction, the interference loss L_{imp} in this work includes a diffraction-reflection ray 4. For the vertical polarization transmission and reception, it is written as

$$L_{imp} = -20 \log_{10} \left| 1 + \sum_{i=2}^4 \frac{E_{ir}}{E_{1r}} \right| \quad (4)$$

where E_{1r} , E_{2r} , E_{3r} and E_{4r} are the electric fields of rays 1-4, respectively, and E_{ir} / E_{1r} are the complex field ratios. Both E_{ir} / E_{1r} and E_{ih} / E_{1h} are explicitly written as

$$\frac{E_{2r,2h}}{E_{1r,1h}} = \frac{1}{|E_{nr,nh} / E_0|} \sqrt{\frac{r_1 r_2 (r_1 + r_2)}{r_{12} r_{22} (r_{12} + r_{22})}} \frac{D_{nr,nh}^{II}}{D_{nr,nh}} e^{-jk(r_{12} + r_{22} - r_1 - r_2)} \quad (5)$$

$$\frac{E_{3r,3h}}{E_{1r,1h}} = \sqrt{\frac{r_2 (r_1 + r_2)}{r_{23} (r_1 + r_{23})}} \frac{D_{nr,nh}^{III}}{D_{nr,nh}} e^{-jk(r_{23} - r_2)} \quad (6)$$

$$\frac{E_{4r,4h}}{E_{1r,1h}} = R_{1,4} \sqrt{\frac{r_3 (r_1 + r_2)}{r_{24} (r_1 + r_{24})}} \frac{D_{nr,nh}^{IV}}{D_{nr,nh}} e^{-jk(r_{24} - r_2)} \quad (7)$$

where k is the wave-number, $r_1 = \sqrt{x_n^2 + y_0^2}$ and $r_2 = [(x - x_n)^2 + (|y| - y_0)^2]^{1/2}$ are ray path lengths from BS to a diffraction point of local knife edges at $(x_n, |y| > y_0)$ and from the latter to MS, respectively, $r_{22} = [(x_0 - x)^2 + (y + y_0)^2]^{1/2}$ and $r_{23} = [(x - x_n)^2 + (|y| + y_0)^2]^{1/2}$ are ray path lengths from the diffraction points of knife edges at $(x_0, y > -y_0)$ and $(x_n, |y| > y_0)$ to MS for rays 2 and 3, respectively, and $r_{12} = (x_0^2 + y_0^2)^{1/2}$ is the ray path length from BS to the diffraction point of the knife edge at $(x_0, y > -y_0)$ for ray 2. Both $|E_{ns}/E_0|$ and $|E_{nh}/E_0|$ for multiple diffraction have been addressed in [3]. The UTD diffraction coefficients $D_{ns,nh}$, $D_{s,h}^H$, $D_{ns,nh}^H$ and $D_{ns,nh}^N$ for rays 1-4 are derived from the expressions in [1] for spherical-wave incidence. Specifically, $R_{\perp,\parallel}$ are reflection coefficients for perpendicular " \perp " and parallel " \parallel " polarization, written as

$$R_{\perp,\parallel} = \frac{\cos \beta_1 - a_{\perp,\parallel} \sqrt{\epsilon_r - \sin^2 \beta_1}}{\cos \beta_1 + a_{\perp,\parallel} \sqrt{\epsilon_r - \sin^2 \beta_1}} \quad (8)$$

where $a_{\perp} = 1$ and $a_{\parallel} = 1/\epsilon_r$ correspond to $R_{\perp,\parallel}$, respectively, and ϵ_r is the relative permittivity of concrete walls. By replacing β_1 with another angle, (8) applies to the calculation of the reflection coefficients for UTD models II and III. The ϵ_r values in the range of about 5-15 were used for calculating the reflections in the UHF (300 MHz-3 GHz) band. An appropriate value of $\epsilon_r = 5$ is selected in this work.

The UTD model I applies to MS in two shadow zones. In the regions of $y < 0$ where $E_{4s,4h} = 0$, $\beta > \alpha$, derived from $\alpha = \arctan(y_0/x_n)$ and $\beta = \arctan(|y| - y_0)/(x - x_n)$, and $\beta_2 > \alpha_2$, defined as $\beta_2 = \arctan[|y + y_0|/(x_0 - x)]$ and $\alpha_2 = \arctan(y_0/x_0)$, must be satisfied. Also, $\beta_1 > \alpha$ must be satisfied for $y > 0$. These are written as

$$y < -\max\{y_0 + (x - x_n) \tan \alpha, y_0 + (x_0 - x) \tan \alpha_2\}; \quad (9)$$

$$y > y_0 + (2x_0 - x - x_n) \tan \alpha. \quad (10)$$

This defines the applicable regions of UTD model I. The total path loss L_t for the horizontal polarization transmission and reception is also expressed by (1). Specifically, the polarization change can be made, replacing all UTD diffraction coefficients identified by subscript " s " by those identified by subscript " h ", as well as replacing R_{\perp} by R_{\parallel} . This also applies to UTD models II and III.

The knife edges are all along vertical (z) direction in the present work, whereas all knife edges are along a horizontal (e.g. y) direction in [3-5]. The hard and soft boundaries [1] correspond, respectively, to horizontally and vertically polarized electric fields now. This results in the major difference between the UTD-based expression of $L_0 + L_{1p} + L_{mfp}$ here and that of [3, 4], where the hard and soft boundaries correspond, respectively, to vertically and horizontally polarized electric fields.

B. UTD II FOR A PARALLEL-STREET

Notations 1 and 2 for UTD model II seen on the left of Fig 3 indicate a diffraction and a diffraction-reflection ray. The UTD-based expressions L_t of UTD model II are written in the form of (1) at $L_{mfp} = 0$. For vertical-polarization transmission and reception, L_{vp} is expressed as

$$L_{mv} = -20 \log_{10} \left| 1 + \frac{E_{2s}}{E_{1s}} \right| \quad (11)$$

$$\frac{E_{2s,2h}}{E_{1s,1h}} = R_{\perp,\parallel} \sqrt{\frac{r_2(r_1 + r_2)}{r_{22}(r_1 + r_{22})}} \frac{D_{s,h}^H}{D_{s,h}} e^{-jk(r_{22} - r_2)} \quad (12)$$

$$r_1 = (x_{n+1}^2 + y_1^2)^{1/2} \quad (13)$$

$$r_2 = [(x - x_{n+1})^2 + (y - y_1)^2]^{1/2} \quad (14)$$

$$r_{22} = [(x - x_{n+1})^2 + (2y_2 - y_1 - y)^2]^{1/2} \quad (15)$$

where $y_1 = x_{n+1} \tan \alpha$ and UTD diffraction coefficients $D_{v,h}$ and $D_{h,h}''$ for rays 1 and 2 are calculated at appropriate angles for spherical-wave incidence [1]. The reflection coefficients $R_{1,1}$ are calculated at

$$\beta_1 = \arctan \frac{x - x_{n+1}}{2y_2 - y_1 - y} \quad (16)$$

The applicable region of UTD II, that is naturally satisfied for the parallel-street problem, is given by

$$\beta = \arctan \frac{x - x_{n+1}}{y - y_1} > 0. \quad (17)$$

This solution is obtained from two key points formulating the problem. First, the direct spherical waves from BS are shadowed in the regions of $x > x_{n+1}$ and $y > y_1$, by side street walls at $(x_n, y > y_0)$ and $(x_{n+1}, y > y_0)$. Second, the majority of total received signal by MS should be generated by the power of the spherical wave incident direct on (x_{n+1}, y_1) .

The UTD model II considers that a spherical wave from an equivalent transmitter at $BS'(x_{n+1}, y_1 - r_1)$ is incident on (x_{n+1}, y_1) of a knife edge at $(x > x_{n+1}, y_1)$, as seen in Fig 3. This simplification and approximation remains the regions of $x > x_{n+1}$ and $y > y_1$ shadowed, as well as the same amount power of spherical wave incident direct on (x_{n+1}, y_1) . Rays 1 and 2 are thus determined by a derivation, similar to the second step determining rays 1 and 4 of UTD model I for $y > 0$.

C. UTD III FOR A SIDE STREET CLOSE TO BASE STATION

The UTD-based expressions L_i of UTD III can also be written in the form of (1) at $L_{mfp} = 0$. The UTD formulae III contain a total of six rays as shown on the right of Fig 3. Calculations similar to those for UTD I determine diffraction rays 1-4. The diffraction ray 4 by a knife edge at $(x_{14}, y > y_0)$ is shadowed by the knife edge at $(x_1, y < -y_0)$ and the fields $E_{1,4,h}$ of single diffraction vanish in the range of $y < y_{\min} = y_0 - (x - x_{14}) \tan \beta_{4m}$, where $\tan \beta_{4m} = 2y_0 / (x_1 - x_{14})$.

The single diffraction ray 5 by a knife edge at $(x > x_5, y_5)$ is added only in the regions of $y > y_5$. For the regions of $y < 0$, the reflection-diffraction ray 6 is determined, similar to the determination of ray 2 for UTD II. In other words, a spherical wave multiplied by $R_{1,1}$ at an appropriate angle from an equivalent source at $BS'(x_{6d} - r_{16}, y_6)$ is incident on a knife edge at $(x_{6d}, y > y_6)$, and the diffracted fields $E_{6,6,h}$ arrive at MS.

EXPERIMENTAL VALIDATIONS

Use an average error Δ_{av} and a root mean square (rms) error Δ_{rms} in dB as

$$\Delta_{av} = \frac{1}{N} \sum_{i=1}^N (L_{pi} - L_{mi}) \quad (18)$$

$$\Delta_{rms} = \sqrt{\frac{1}{N} \sum_{i=1}^N (L_{pi} - L_{mi})^2} \quad (19)$$

where L_{pi} and L_{mi} are predicted and measured path losses, respectively, and N is the number of predicted, or measured, path-loss data. Comparisons of its prediction with measurement MAK64 confirm UTD model I, see Fig 4 and Table 1. Good agreements of UTD model II prediction with measurement MAK63 are demonstrated in Fig 5 and Table 1. It is seen in Fig 6 and Table 1 that measurement MAK62 confirms UTD model III. The path-loss underestimate of UTD model III in the line-of-sight (LOS) region, around $y = 0$, may be caused by blockage of other obstacles (e.g. cars) during the measurements.

CONCLUSIONS

Three UTD-based path-loss prediction models are made for urban micro-cellular mobile radio communications. They are validated by comparisons of their predictions with measurements at 900.5 and 1800 MHz in shadow zones of urban areas. They apply to the BS and MS antennas much lower than the surrounding buildings and can be written in explicit forms for both vertical- and horizontal-polarization transmission and reception.

The results demonstrate that fast 2-D models which do not require a building height database can provide acceptable accuracy for micro-cellular mobile radio propagation predictions in urban environments. The methodology here appears suitable for 2-D modeling for parallel-street problem and irregular side-street problems. It has the potential to be used in practical design of micro-cellular mobile radio systems.

ACKNOWLEDGMENTS

This work was supported by the Academy of Finland, Helsinki Telephone Company Ltd., Technology Development Centre, Finland, Nokia Telecommunications, Telecom Finland Ltd. and VTT Information Technology. The authors would like to thank Prof. A. Räsänen, Associate Prof. P. Vainikainen and Prof. V. Porra for their encouragement. They would also like to thank Mr. H. Hakojärvi who helped in performing the propagation measurements.

REFERENCES

- 1 Kouyoumjian R G and Pathak P H, A uniform geometrical theory of diffraction for an edge in a perfectly conducting surface, 1974, Proc. IEEE, Vol 62, No 11, pp 1448-1461.
- 2 Walfisch J and Bertoni H L, A theoretical model of UHF propagation in urban environments, 1988, IEEE Trans. Antennas and Propag., Vol 36, No 12, pp 1788-1796.
- 3 Zhang W, A more rigorous UTD-based expression for multiple diffractions by buildings, 1995, IEE Proc.-Microw. Antennas Propag., Vol 142, No 6, pp 481-484.
- 4 Zhang W, A UTD-based propagation model for cellular mobile radio systems, 1995, Proc. of the 25th European Microwave Conf., pp 276-280.
- 5 Zhang W, A wide-band propagation model based on UTD for cellular mobile radio communications, 1997, accepted for publication in IEEE Trans. Antennas and Propagat.
- 6 Bertoni H L, Honcharenko W, Maciel L R and Xia H H, UHF propagation prediction for wireless personal communications, 1994, Proc. IEEE, Vol 82, No 9, pp 1333-1359.
- 7 Tan S Y and Tan H S, A microcellular communications propagation model based on the uniform theory of diffraction and multiple image theory, 1996, IEEE Trans. Antennas and Propagat., Vol 44, No 10, pp 1317-1326.

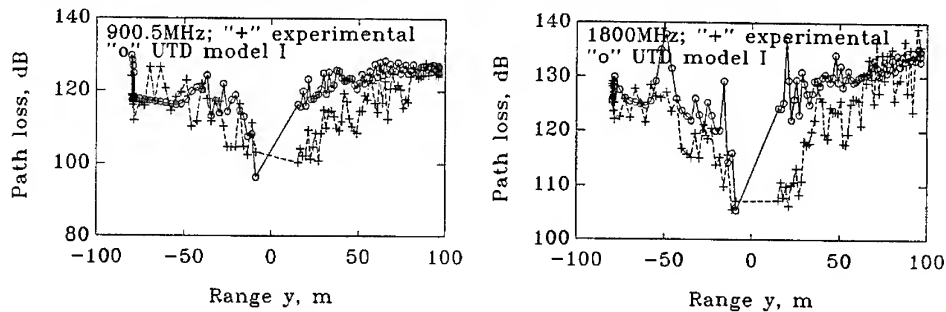


Fig 4: Path-loss predictions of UTD model I, valid with measurement MAK64

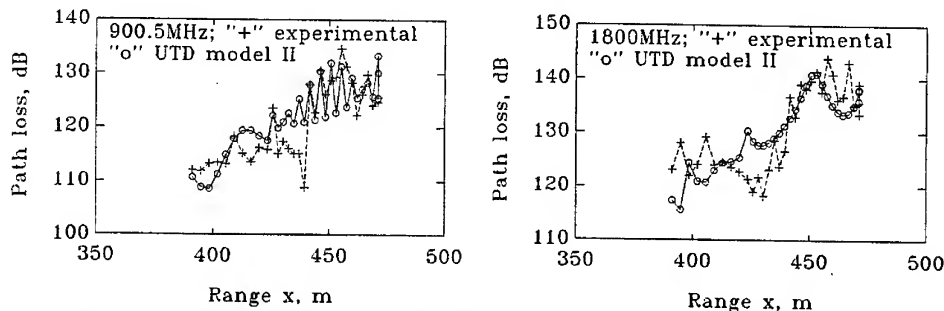


Fig 5: Path-loss predictions of UTD model II, valid with measurement MAK63

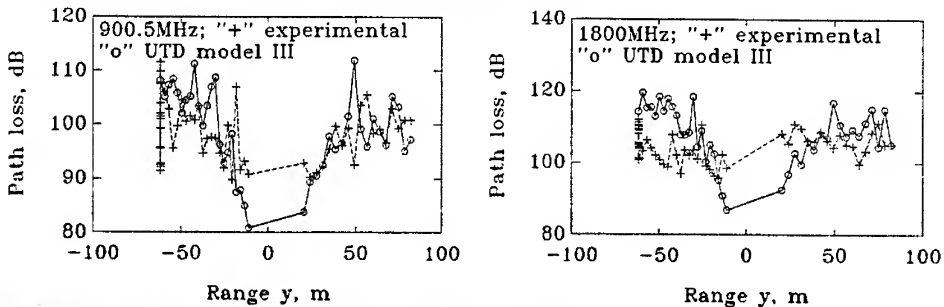


Fig 6: Path-loss predictions of UTD model III, valid with measurement MAK62

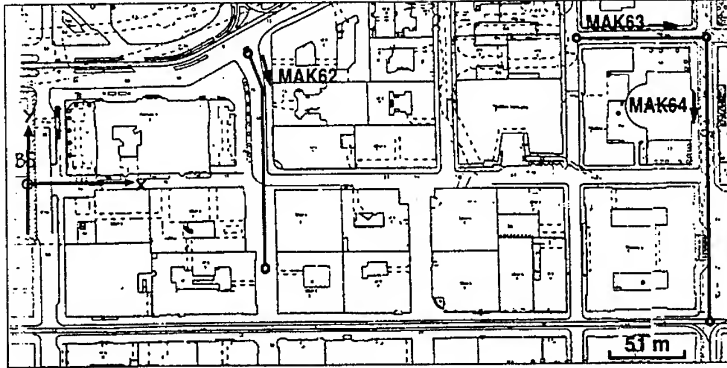


Fig 1: A Helsinki city center map showing an area where propagation measurements MAK62, MAK63 and MAK64 were performed, BS representing Base Station and O indicating its position, as well as initial and final measurement positions

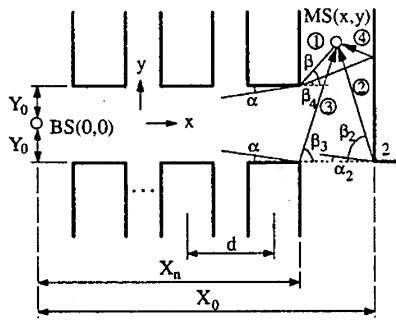


Table 1: Average and root mean square errors Δ_{av} and Δ_{rms} for comparisons of UTD path-loss model predictions with measurements MAK62, MAK63 and MAK64 at 900.5/1800 MHz

items	Δ_{av} (dB)	Δ_{rms} (dB)
MAK62	2.78/5.02	8.08/9.18
MAK63	1.35/-0.0331	4.69/5.27
MAK64	5.68/5.23	8.47/8.34

Fig 2: Top view geometry of UTD model I, applicable to measurement MAK64

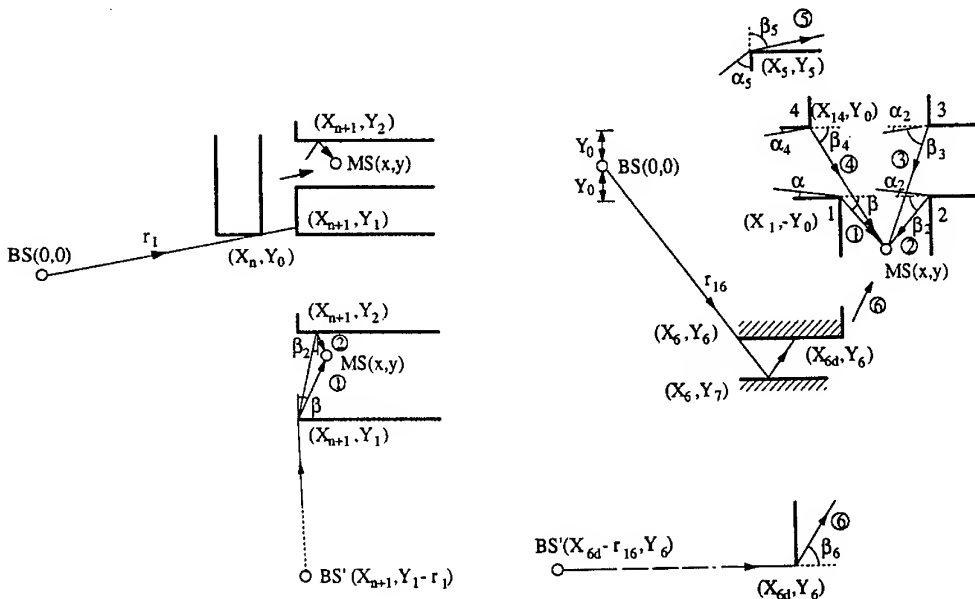


Fig 3: Top views of UTD models II and III, applicable to measurements MAK63 and MAK62

Regular Linearization Principle for Electronic Circuits

Yuri M. Bruck, IEEE member

Radioastronomical Institute, 4, Krasnoznamennaja St., Kharkov, UKRAINE. men@rian.kharkov.ua
Center Technological Education of Holon. Communication Dept. 52, Golomb St. Tel-Aviv, ISRAEL
Box 8629, Misgav St. 27/8, 21862, Carmiel, ISRAEL 100310.2246@compuserve.com

ABSTRACT

New methods are suggested for linearizing transfer functions TFs of nonlinear electronic circuits through inclusion of dual nonlinear circuits NDC that involve similar nonlinear, as well as linear elements. Linearizing methods are based on using of inverse functions IFs. A consistent procedure of circuit synthesis has been developed. The examples given to describe the synthesis of exponential and binomial function sets and the complete self-linearization of a binomial series. These functions will be used here in other papers for linearization of the opened and closed p-n junction.

INTRODUCTION

The processes of amplification and transmission of electrical signals in electron devices are nonlinear. Even very small deviations from linearity often may result in combination effects, greatly reducing the interference immunity and sensitivity of multicarrier telephony, short wave communication, radioastronomy et al. Therefore the problem of linearization is a special importance for the semiconductor amplifiers and switching elements.

Two main methods of linearization are known [1]:

- (i) -low level operation when the signal magnitude is less than nonlinear section of the characteristic and
- (ii)-compensation of the nonlinear effects by negative feedback, feedforward and predistortion linearization [1-4], harmonics suppression [5].

For a number of reasons, the potential of many methods has been nearly exhausted, and the necessity to further reduce combination effects stimulates the search for new ways. One is discussed in this paper. It seems promising to analyze the possibilities of linearizing nonlinear circuits through compensation of the nonlinearity by introduction of other nonlinear elements. It has been, believed, that such compensation is inefficient. The author's intention is to show this is not true and suggest a regular method for synthesizing compensation circuits that would involve identical nonlinear and/or linear elements.

There are two reasons in a foundation of our proposals.

FIRST ONE: All the circuits should consist of the identical nonlinear elements. It provides the small differences their parameters and high compensation stability especially at use of a modern technology.

SECOND ONE: It is possible to synthesize such pairs of the complementary circuits (which consists from identical elements !) which have the opposite signs of non-linearity. Further on we will name such circuits as nonlinear dual circuits NDC from the formal analogy between frequency dual linear circuits.

LINEARIZATION METHODS

Consider an analytical function $y=f(x)$ and its inverse function $x=s(y)$, specified by the Taylor expansions at $x = y = 0$, with $s(y) = f(x)^{\wedge}$ and $f(x) = s(y)^{\wedge}$, where symbol $[\wedge]$ denotes an IF. As is known,

$$f(x) = a*x + b*x^2 + c*x^3 + d*x^4 + e*x^5 + \dots, \quad s(y) = A*y + B*y^2 + C*y^3 + D*y^4 + E*y^5 + \dots \quad (1)$$

0

The coefficients a to e and A to E are related by the inversion equations.

$$A = 1/a; \quad B = -b/a^3; \quad C = (2*b^2 - a*c)/a^5; \quad \text{and so on [6].} \quad (2)$$

In what follows, we will perform summation and subtraction of expansions similar to (1) as this technique is based essentially on compensation of the nonlinear terms in the Taylor series for the circuit or element TF by the Taylor expansion of the symmetric and / or IF of the similar element or circuit.

Consider some of the properties shown by the expansions (1) with regard to summations, subtractions and scaling argument.

- 1 The r -th coefficient in the function s depends upon r coefficients of the function f and can assume any sign and magnitude, including zero. In other words, the nonlinear behavior of the F and IF is substantially different. If $r-1$ term of the expansion of f , except the first one, are all equal to zero, then the r -th term in the expansion of s has the opposite sign, each $r+1$ terms in r and f functions have the same signs. This suggests the possibility of synthesizing a circuit with an opposite kind of non-linearity, involving similar nonlinear elements. As a result, it would be possible to compensate the non-linearities in various synthesized circuits by using combinations of the response function involved.
- 2 The expansion coefficients of the function s all depend on a , i.e. the linear term of f . This implies the possibility of circuit linearization with the aid of linear elements. There is a practical importance the condition that the 3-th order term would be equal to zero. Equation (2) yields

$$C = 2*b^2 - a*c = 0. \quad (3)$$

- 3 Summation of different functions.

Let $f_1 \neq f_2$; $s_1 = f_1^{\wedge}$; $s_2 = f_2^{\wedge}$; $F = f_1 + f_2$; $S^{\wedge} = F$. Then $S \neq s_1 + s_2$, i.e. summation of the functions generates an IF with different nonlinear properties. The two particular cases of importance are:

Changing the sign of the argument.

If $f_2(x) = f_1(-x)$, then $F = f_1 - f_2$ is odd function and $F = f_1 + f_2$ an even function, non-analytical at $x = 0$, that will not be considered further.

Scaling of the argument or function.

The change from $f(x)$ to $f(h*x)$ or $h*f(x)$ from $s(y)$ to $s(h*y)$ or $h*s(y)$, where $h \neq 1$, allows eliminating any term (1), except the linear one.

The properties discussed give sufficient ground to the linearization technique and allow presenting the synthesis procedure for compensated circuits. To facilitate the understanding by circuit specialists, we will appeal freely to the concepts of parallel and series connections when describing summation of the f and s functions. The regular method should involve consecutive stages, the result of the k -th stage being generation of a pair dual functions DFs of NDC which characterized by odd TFs .

$$\begin{aligned} f1k(x) &= ak1*x + akr*x^r + ak(r+1)*x^{r+1} + \dots \\ f2k(x) &= bk1*x - bkr*x^r + bk(r+1)*x^{r+1} - \dots \\ s1k(y) &= Ak1*y - Akr*y^r + Ak(r+1)*y^{r+1} - \dots \\ s2k(y) &= Bk1*y + Bkr*y^r + Bk(r+1)*y^{r+1} + \dots \end{aligned} \quad (4)$$

In Eq(4), the expansion coefficients for all $1 < t < r$ are zeros, while the non-zero coefficients of the r -th order terms have opposite signs. This allows equating their magnitudes, by properly selecting the scale factors h and l at the $k + 1$ -th stage. By further summing the functions f and s , we shall arrive DFs of new NDC where the r -th order term would be zero :

$$\begin{aligned} f1k+1(x) &= f1k(h*x) + f2k(x), \\ f2k+1(x) &= [s1k(l*y) + s2k(y)]^{\wedge}. \end{aligned} \quad (5)$$

This ends up the $k + 1$ -th stage, and the linearization procedure can be followed on. But the initial stage which is different from the rest. The major distinction is that $f1(x)$ is a single function and it is not evident if it can be linearized by the method discussed. As has been mentioned above, the terms to be compensated in the series expansions of the dual functions $f1$ and $f2$ should be of different signs. Hence, the corresponding terms of the TF and IF should be of the same sign. Even order terms in the expansion of $f1$ can be easily eliminated through changing the sign of the argument, therefore the lowest order term to cancel is of order three. Then the linearizability conditions with account of (3) are the following.

$$(i) \quad b \neq 0; \quad (ii) \quad c > 0; \quad (iii) \quad a*c < 2*b^2 \quad (6)$$

If (6) is met for f_1 , then two different ways are possible for synthesizing the pair of DF: f_{11} and f_{21} .

* One is summing of symmetrical dual functions.

$$f_{11}(x) = f_1(x) - f_1(-x), f_{21}(x) = [f_1(x)^2 - f_1(-x)^2]^2. \quad (7)$$

* The second way is more complex.

First, the functions f_1 and $s_1 = f_1^2$ are to be transformed into new functions, f_{11} and s_{11} , such that the expansions of their IF, $s_{12} = f_{11}^2$ and $f_{12} = s_{11}^2$ should not involve third-order terms. This can be achieved, f. ex., by summing $f_1(x)$ and $s_1(y)$ with the respective linear functions $p \cdot x$ and $q \cdot y$, or by subtracting the scaled functions $f(-h \cdot x)$ [or $h \cdot f_1(-x)$] and $s_1(-w \cdot y)$ or $w \cdot s_1(-y)$ to meet the condition (3). The result would be the two sets of relations with $q = 1/p = 2 \cdot b^2 / c - a$,

$$\begin{aligned} 2 \cdot b^2 - (a + p) \cdot c &= 0, \\ 2 \cdot b^2 - (1/a + q) \cdot c &= 0. \end{aligned} \quad (8)$$

$$\begin{aligned} 2 \cdot (1 - h)^2 \cdot b^2 - (1 - h + h^2) \cdot a \cdot c &= 0, & \text{for } f_1(x) - f_1(-h \cdot x) \\ 2 \cdot (1 - h)^2 \cdot b^2 - (1 + h)^2 \cdot a \cdot c &= 0 & \text{for } f_1(x) - h \cdot f_1(-x) \\ 2 \cdot (1 - w)^2 \cdot b^2 - (1 - w + w^2) \cdot (2 \cdot b^2 - a \cdot c) &= 0. \end{aligned} \quad (9)$$

that should be used to determine either p and q , or h and w . Further, the pair of functions $f_1(x)$ and $f_2(x)$ are formed like in (5).

APPLICATION

To illustrate the method, we will consider three examples. Then they will be used to synthesize the p-n junction compensated circuits.

** Let $f_1(x) = e^x - 1$, $s_1(y) = \ln(1+y)$, $a = 1$, $b = 1/2$ and $c = 1/6$. Then Eq. (6) is satisfied, since $1/6 > 1/18$, and hence f_1 can be linearized. Then, similar to (7)

$$\begin{aligned} f_{11}(x) &= f_1(x) - f_1(-x) = 2 \cdot \text{sh}(x) = x^2 + x^4/3 + x^6/60 \dots, \\ f_{21}(x) &= [s_1(y) - s_1(-y)]^2 = \text{th}(x/2) = x/2 - x^3/24 + x^5/240 \dots, \end{aligned} \quad (10)$$

$$\begin{aligned} s_{11}(y) &= [f_1(x) - f_1(-x)]^2 = \text{Arsh}(y/2) = y/2 - y^3/48 + y^5/1280 \dots, \\ s_{21}(y) &= s_1(y) - s_1(-y) = 2 \cdot \text{Arth}(y) = y^2 + y^4/3 + y^6/5 \dots \end{aligned} \quad (11)$$

At the next step, (10) and (11) are scaled and added pair-wise, according to (5), in order to eliminate third-order terms. The result is the pair of DFs (12) to be further linearized:

$$\begin{aligned} f_2(x) &= f_{11}(x \cdot 0.333) + f_{21}(x \cdot 0.667) = x + x^5 \cdot 6.17 \cdot 10^{-4} + \dots \\ s_2^*(x) &= [s_{11}(y \cdot 0.885) + s_{21}(y \cdot 0.279)]^2 = x - x^5 \cdot 1.95 \cdot 10^{-3} + \dots \end{aligned} \quad (12)$$

The functions f_1 , s_1 , f_2 , s_2 are shown in Fig.1. As it can be seen, compensating one exponential function with three others has improved the linearity by 30 to 70 dB. Curves 3 and 4 are parallel to each other, which implies that attempted compensation of the fifth-order term at the next stage, through a 2dB change in the scale of one function, should be a success as well. In principle, the procedure could be repeated ad infinitum, however the number of exponential functions involved is doubled at each consecutive stage and the requirements as to the accuracy of compensation increase.

$$\text{** Let now } f_1(x) = \pm ((1+x)^{\pm m} - 1); (y) = \pm ((1+y)^{\pm m} - 1). \quad (13)$$

(i) with the "+" sign we have $a = m$; $b = m \cdot (m-1)/2$; $c = m \cdot (m-1) \cdot (m-2)/6$.

(ii) with the "-" sign we have $a = m$; $b = m \cdot (m+1)/2$; $c = m \cdot (m+1) \cdot (m+2)/6$.

The function f_1 meets the linearization condition (6), provided $m > 0.5$ in case (i) or $m > 0$ in case (ii).

COMPLETE LINEARIZATION

As an example, consider the function that is remarkable in many respects, namely the binomial series.

$$f_1(x) = x^*(1-x)^{-1} = x + x^2 + x^3 + \dots \quad s_1(y) = y^*(1+y)^{-1} = y - y^2 + y^3 - \dots \quad (14)$$

Let us start linearizing (14) with variation of its linear term. As can be found from (8), $p = q = 1$, and hence the new functions f_{11} and s_{11} are

$$f_{11}(x) = x + x^*(1-x)^{-1} = x^2 + x^2 + x^3 + \dots \quad s_{11}(y) = y + y^*(1+y)^{-1} = y^2 - y^2 + y^3 - \dots \quad (14.1)$$

Their IFs, $f_{12} = s_{11}^{\wedge}$ and $s_{12} = f_{11}^{\wedge}$ there are only even-order non-linearities.

$$f_{12}(x) = x/2 - 1 + (1+x^2/4)^{0.5} = x/2 + x^2/8 - x^4/32 + \dots, \quad s_{12}(y) = y/2 + 1 - (1+y^2/4)^{0.5} = y/2 - y^2/8 + y^4/32 - \dots \quad (14.2)$$

The equation roots used in (14.2) during inversion of (14.1) are only those that obey the conditions $f_{12}(0) = s_{12}(0) = 0$. By eliminating the even-order terms, like in (5), we arrive at the pair of linear functions $f_1 = f_{12}(x) - f_{12}(-x) = x$ and $s_1 = s_{12}(y) - s_{12}(-y) = y$. Thus, having applied Eq(3) for compensating the third-order term, we have also eliminated all other odd terms in the series (14) and achieved, unexpectedly, complete compensation of non-linearity. Note that the same result will be for any $f_1(x) = v*x*(1+v*x)^{-1}$. Certainly, this is only a special case, however so curious that we illustrate in Fig.2 all stages of the linearization procedure.

There is important consequence from this property. Let the nonlinear section of the expansion TF is a geometric series with the common factor v , up to the n -th order term, i.e.

$$y = a*x + \sum_{t=2}^n (v*x)^t + \sum_{t=n+1}^m at*x^t, \quad \text{with } m > n \text{ and } at \neq v, \text{ when } t > n \quad (15)$$

With a proper choice of v , this approximation may prove valid for many functions, from the point of view of analyzing some particular properties of coefficients in the IF expansions. Then we can rewrite (15)

$$y = x*(a-v) + v*x*(1-v*x)^{-1} - (v*x)^{n+1}*(1-v*x)^{-1} + \sum_{t=n+1}^n at*x^t \quad (15.1)$$

Owing to the property 1 of the IF, the third and fourth terms of Eq.(15.1) does not affect the first n terms of the series for y as its lowest degree is $n+1$. The IF of two first terms of Eq.(15.1) is

$$x = \{y + p - [p^2 + y^2 + 2*(2-p)*y]^{0.5}\} / (p-1)/2, \quad (15.2)$$

where $g = a/v$ and the n first terms are the corresponding terms of the y -series. With $p=2$ the IF of Eq.(15.2) contains only even-order nonlinear terms, such that subtraction of $x(-y)$ results in a complete linearization, $x(y) - x(-y) = y$. Since $p = 2$ implies $C=2*b^2 - a*c = 0$, all odd-order terms of the $y(x)$ series of lower order than n should vanish. It seems probable that the condition $C = 0$ may lead to a nearly total linearization of real functions too.

CONCLUSION

Nonlinear functions are linearized by a similar or slightly modified function, or even a linear one, which makes the method highly attractive. Like in any nonlinear problem, practical approaches greatly depend upon the specific form of the function. However, the examples given allow expect the method to be practically efficient especially by using a current technology.

ACKNOWLEDGMENTS

This investigations carried out in the frame of the new amplification system designing program for the UTR-2 decameter radio telescope and was supported by the National Academy of Science of Ukraine (project 1.20), State Committee for Science and Technology of Ukraine (grants 22/100 and 23/547), the European Southern Observatory (grant ESO A-01-041) and International Association of the European Community (grant INTAS 94-3097). I'd like to thank also Center Technological Education of Holon and Absorption Ministry of Israel for support of this investigation.

REFERENCES

- [1] O.V.Golovin and I.Hardon-Aguilard. Methods of increasing linearity of amplifiers of the professional short-wave receivers. / 1984, Radiotekhnika, No.1pp.8-13.
- [2] D.E.Norton. High dynamic range transistor amplifiers using lossless feed- back. / 1975, Microwave J., No.5, pp.53-56.
- [3] E.P.Abranin, and Yu.M.Bruck. Highly linear broadband amplifiers with loss-less feedback. Part 1. Theory / 1990, Int.J.Electr.,V.68,No.5,pp.743-756.
E.P.Abranin, Yu.M.Bruck and A.A.Konovalenko. Highly linear broadband amplifiers with lossless feedback. Part 2. Experience of development. / 1990, Int.J.Electr.V.69, No.3, pp.345-357.
- [4] S.Kumar. Power Amplifier Linearization Using MMICs. / 1992, Microwave J.No.4, pp.96-104.
- [5] J.C.Durec. Amplifier circuit having high linearity for canceling third order harmonic distortion. / 1996, Patent USA 5497123.
- [6] I.N.Bronshtein and K.A.Semendyaev. Handbook of Math. / 1986, Moscow Nauka Publ.Co. pp.544.

FIGURE CAPTIONS

Fig.1 Relative deviations dy in dB of $y = f(x)$ function from the linear one $y = x$: $dy = 20\log [f..(x)/x - 1]$
1- $f1(x)$; 2 - $s1(x)$; 3 - $f2(x)$; 4 - $s2(x)$

Fig.2 Linearization of $y = x/(1 - x)$ and $x = y/(1 + y)$
1 - $f1(x)$ and $s1(x)$ 2 - $f12(x)$ and $s12(x)$ 3 - $-f12(-x)$ and $-s12(-x)$ 4 - $f11(x)$ and $s11(x)$

Linearization of P-N Junctions by the Same P-N Junctions

Yuri M. Bruck, IEEE member

Radioastronomical Institute, 4, Krasnoznamennaja St., Kharkov, UKRAINE. men@rian.kharkov.ua
Center Technological Education of Holon., Communication Dept. 52, Golomb St. Tel-Aviv, ISRAEL.
Box 8629, Misgav St. 27/8, 21862, Carmiel, ISRAEL 100310.2246@compuserve.com

ABSTRACT

Linearized circuits are suggested and analyzed theoretically, where even- (2n) and odd- (2n+1) order (n > 0) non-linearity of opened or closed p-n junctions can be compensated by non-linearity of other P-N junctions. The effect is stable against scatter in the values of P-N junctions parameters. Linearized circuits with linear and non-linear compensation are compared.

INTRODUCTION

Communication [1] was dedicated to methods of compensating the non-linearity of p-n junctions with the aid of nonlinear dual circuits NDC that involved the junctions to be linearized and linear linearizing elements. Here we will consider non-linearity compensation with the aid of nonlinear symmetric and non symmetric NDC involving other p-n junction [2], and will analyze the relative effectiveness of the different linearization techniques. First, we analyze once again the linear compensating circuits that were considered in [1], however replacing the linear compensating elements with nonlinear ones. Then we will turn to the circuits where non-linearity are compensated by such of their DCs. The analysis will be limited, as before, to the case of quasi-static operation for which the complex (real plus imaginary) nature of the nonlinear element can be disregarded. The equations and figures of papers [1] and [2] will be referred to as (nn-[1] or [2]), respectively. Designation TF, IF, DC and NDC are quoted also from [2].

P-N JUNCTION IS OPENED

Following the logistics of this paper, we offer no explanations to Fig.1 showing (similar to Fig.1-[1]) NDC that involve opened p-n junctions (the junction to be linearized and the linearizing one). As can be seen in the Figure, the junctions are connected oppositely, i.e. in counter phase, and their bias currents are not equal. Following Eq.(1-[1]), the TFs of the circuits Fig.1a and 1b can be written as (as before [f^Λ] means IF of [f]).

$$\begin{aligned}j(h,u) &= e^u - 1 - h \cdot e^{-u} + h, \\j^\Lambda(h,i) &= \ln[(i+1-h)/2 + ((i+1-h)^2/4 + h)^{0.5}], \\v(w,i) &= \ln(1+i) - \ln(1-w \cdot i), \\v^\Lambda(w,u) &= (e^u - 1)/(w \cdot e^u + 1).\end{aligned}\tag{1}$$

Similar to [1,2], here and below $u=U_s/U_t$, $i=I_s/(I_1+I_{sat})$; $h=(1j+I_{sat})/(I_2j+I_{sat})=\exp(U_1j/U_t-U_2j/U_t) \neq 1$; $w=(I_1v+I_{sat})/(I_2v+I_{sat})=\exp(U_1v/U_t-U_2v/U_t) \neq 1$; where U_s , I_s , U_1, U_2 , I_1 , I_2 are the signal and bias voltages and currents, respectively; U_t and I_{sat} are the thermal potential and saturation current. The subscripts 1 and 2, j and v underline the difference of operation parameters of different p-n junctions in the NDC. We will be using Taylor expansions of the TF and IF involved in the analysis [3], and the series inversion algorithm of paper [4]. However in all the cases where possible, closed analytic expressions for the IFs will be also given as they would estimating the limits of validity for the Taylor series representations. Let us rewrite Eqs.(1) as

$$\begin{aligned}v(w,i) &= i \cdot (1+w) + i^2 \cdot (1-w^2)/2 + i^3 \cdot (1+w^3)/3 \dots \\j(h,u) &= u \cdot (1+h) + u^2 \cdot (1-h)/2 + u^3 \cdot (1+h)/6 \dots,\end{aligned}\tag{1.1}$$

According to the circuit synthesis procedure described in [2] it is necessary first to find such values of h and w that would nullify third-order terms in the expansions of $j^{\wedge}(h,i)$ and $v^{\wedge}(w,u)$. Making use of Eq.(9-[2]) we can obtain from Eq.(1.1) two equations to yield the desired magnitudes h and w .

$$\begin{aligned} 3*(1-h)^2 - (1+h)^2 &= 0, \\ 3*(1-w^2)^2 - 2*(1+w)*(1+w^3) &= 0. \end{aligned} \quad (2)$$

As it can be shown, Eq.(2) in fact is a single equation, $x^2-4*x+1=0$, whose two roots are mutually reciprocal, $x_1 = h_1 = w_1 = 0.26795$ and $x_2 = h_2 = w_2 = 3.73205$. This is a single solution reflecting the equivalence of the linearizing junction and the one to be linearized. However the condition allowing compensation of the fifth-order term is met solely by h_1 and w_2 . Substituting h_1 and w_2 into Eq.(1.1), let us perform inversion and then subtract the IFs for the forward- and inverse directions of u and i from one another. The result will be TFs for the symmetric NDC of Figs. 1c and 1d,

$$\begin{aligned} v(h_1,i) = j^{\wedge}(h_1,u_1) - j^{\wedge}(h_1,-u_2) &= i*0.423 - i^5*6.556e-5 + i^7*1.195e-6 ..., \\ j(w_2,u) = v^{\wedge}(w_2,i_1) - v^{\wedge}(w_2,-i_2) &= u*1.577 - u^5*8.763e-3 + u^7*1.043e-3.... \end{aligned} \quad (3)$$

Here and below, the series representations have been written explicitly to terms of the seventh order, to permit following the variations of the series coefficients in all transformations. The fifth-order terms are of the same sign, which suggests a possibility of their compensation by this technique. To do that it is necessary to invert one of the functions of Eq.(3) and add it to the other after changing the scale. Apparently, this can be done in two ways, the result being two TFs Eqs.(3.1) for the NDS shown in Figs.1e and 1f:

$$\begin{aligned} v(i) = v(h_1,i) + j^{\wedge}(w_2,s*i) &= i*0.834 - i^7*1.267e-7 ..., \\ j(u) = j(w_2,p*u) + v^{\wedge}(h_1,u) &= u*3.818 + u^7*2.412e-4 \end{aligned} \quad (3.1)$$

where s (0.64910) and p (0.94710) are the current and voltage scaling factors for one of these. Further linearization is not possible because of the different signs of seventh-order terms in the functions of Eq.(3.1). Fig.2 shows the level of odd-order nonlinear distortions as a function of the signal amplitude in the circuits of Fig.1, for the cases of total (h, w) and partial compensation ($0.95*h, 0.95*w$). The TFs Eq.(1) of symmetric non-linearized ($h=w=1$) circuits are also given for comparison and for demonstrating the linearization efficiency. Similar to [1], the normalized TFs have been calculated here to terms of the eleventh order. The normalization was performed through such a substitution that the numerical factor of the linear term in the expansion should be equal to 1. As is easy to see, the amount of non-linearity in the linearized NDC of appropriate order is not the same, however the gain in linearity is always high. The circuits are also different in other respects, e.g. details of the circuit design or the dynamic range (extent of the operating section on the I-V curve). Some of the characteristic dependencies are markedly different from straight lines (on the log - log scale). This is quite understandable, as the coefficients in front of nonlinear terms in the expansions of many functions are comparable in magnitude but different in sign, hence some of the complex zeros of such functions may lie close to the real axis.

Consider now the linearization procedure based on symmetric NDC. According to the example given in [2], the TF Eq.(1) satisfy the unlimited linearization condition Eq.(3-[2]). At the first stage of the synthesis procedure the TFs of the two initial symmetric NDC of Figs.3a and 3b, $j_{11}(u)$ and $j_{12}(u)$, and their IFs, $v_{11}(i)$ and $v_{12}(i)$ can be obtained from Eq.(1) with $h = w = 1$. They are

$$\begin{aligned} j_{11}(u) = 2*sh(u) &= u*2 + u^3/3 + u^5/60 + u^7*3.97e-4 ..., \\ j_{12}(u) = th(u/2) &= u/2 - u^3/24 + u^5/240 - u^7*4.22e-4 ..., \end{aligned} \quad (4)$$

$$\begin{aligned} v_{11}(i) = Arsh(i/2) &= i/2 - i^3/48 + i^5*2.3e-3 - i^7*3.5e-4..., \\ v_{12}(i) = 2*Arth(i) &= i*2 + i^3*2/3 + i^5*2/5 + i^7*2/7.... \end{aligned} \quad (5)$$

Next, these functions are used to derive, through scaling the variable (in practice, through changing the bias) and adding the functions themselves, a pair of new TFs (Eq.(6)) for the NDC of Figs.3c and 3d. Their third-order terms will be zeros,

$$\begin{aligned} j11(u) + j12(u^2) &= u^3 + u^5 * 0.150 - u^7 * 0.054..., \\ v11(i^{1/3}) + v12(i) &= i^3 * 3.587 + i^5 * 1.156 - i^7 * 0.848.... \end{aligned} \quad (6)$$

Quite similarly, the functions Eq.(6) are used at the next stage to generate the TFs, Eq.(7), of two new NDC (Figs. 3e and 3f), such that their fifth-order terms will be zeros,

$$\begin{aligned} j21(u) + j22(u * 3.0787) &= u^3 * 3.858 + u^7 * 0.0275 ..., \\ v21(i) + v22(i * 5.6223) &= i^3 * 5.462 + i^7 * 0.6019 \end{aligned} \quad (7)$$

Similar to circuits Fig.1 the parameters of linearized NDC of matching order are rather close and the gain in linearity is high. Other important characteristics of the circuits (dynamic range and details of the circuit design) are greatly different again. This diversity may prove useful in practical applications.

P-N JUNCTION IS CLOSED

Since formal linearization procedures and the corresponding synthesis methods are identical for the opened and closed junctions, differing only in the bias voltage polarity, we will refer, wherever convenient, to the figures and equations of the above section. Returning to Fig.1, we will assume it to show (like Fig.3 -[1]) NDC involving closed p-n junctions, specifically one to be linearized and the other as a linearizing element. The junctions are oppositely connected and their bias voltages and currents are not the same. The TFs of the circuits in Figs.1a,b are, according to Eq.(5-[1]), of the following form

$$\begin{aligned} j(h,u) &= u * (1 + h) - u^2 * (1 - h^2)/2 + u^3 * (1 + h^3) * 0.375 ..., \\ v(w,i) &= i * (1 + w) + i^2 * (1 - w^2)/2 + i^3 * (1 + w^3) * 0.125 \end{aligned} \quad (8)$$

Like in [1], $u = U_s / (U_1 + U_b)$, $i = I_s / I_1$; $h = (U_1 + U_b) / (u_2 + U_b) \neq 1$; $w = I_1 v / I_2 v \neq 1$; and $I_1 = Y_1 * (U_1 + U_b)$; $I_2 = Y_2 * (U_2 + U_b)$; where U_s , I_s ; U_1 , U_2 ; and I_1 , I_2 are the signal and bias voltages and currents, respectively; U_b is the p-n junction potential, and Y_1, Y_2 are the junction capacity admittances at $U=U_1$, $U=U_2$. The subscripts 1 and 2; j and v denote different operating modes of the different p-n junctions in the circuits. To determine h and w , we have two equations,

$$\begin{aligned} h^2 - 5 * h + 1 &= 0, \\ w^2 - 7/3 * w + 1 &= 0, \end{aligned} \quad (9)$$

whose each pair of solutions (i.e. $h_1 = 0.3394$, $h_2 = 1/h_1$; $w_1 = 0.4250$ and $w_2 = 1/w_1$) provides for compensation of the third-order expansion term in the TFs of the symmetric NDC of Figs.1c,d. Accordingly, the TFs derived in the similar way as Eq.(3) become

$$\begin{aligned} v(h_1, i) &= i * 1.655 - i^5 * 4.485e-3 + i^7 * 1.272e-4 ..., \\ j(w_1, u) &= u * 1.277 - u^5 * 6.436e-3 + u^7 * 1.249e-3.... \end{aligned} \quad (10)$$

The coincidence of signs of the fifth-order terms in these functions suggests a possibility of compensating them by the same technique. If necessary, Eq.(10) can be used like Eq.(3.1) to derive the pair of TFs, Eq.(10.1) for the two NDC of Figs.1e and 1f,

$$\begin{aligned} v(i) &= v(h_1, i) + j^s(w_1, s * u) = i * 2.632 - i^7 * 7.032e-4 ..., \\ j(u) &= j(w_1, p * u) + v^h(h_1, i) = u * 2.466 - u^7 * 9.906e-4 ..., \end{aligned} \quad (10.1)$$

where $s = 1.54382$ and $p = 1.57395$ are voltage scaling factors for one of the circuits. The coincidence of signs of the seventh-order terms in these functions suggests a possibility of compensating them by the

same technique. As before the level of nonlinear distortions for linearized NDC of the same order are close to Fig.2 and the gain in circuits linearity is high.

Consider now the linearization procedure with the use of symmetric NDC. Once again, according to the example in [2], the TF Eq.(5-[1]) satisfy the condition Eq.(2-[2]). At the first stage, the TFs of the initial two symmetric NDC (Figs. 3a,b), $j11(u)$ and $j12(u)$, and their IFs $v11(i)$ and $v12(i)$ are derived from Eq.(8) with $h = w = 1$. They are

$$\begin{aligned} j11(u) &= u^2 + u^3 * 7.50e-1 + u^5 * 5.47e-1 + u^7 * 4.51e-1 \dots, \\ j12(u) &= u/2 - u^3 * 1.56e-2 + u^5 * 1.71e-3 - u^7 * 2.52e-4 \dots, \end{aligned} \quad (11)$$

$$\begin{aligned} v11(i) &= i/2 - i^3 * 4.69e-2 + i^5 * 4.63e-3 - i^7 * 2.98e-4 \dots, \\ v12(i) &= i^2 + i^3 * 2.50e-1 + i^5 * 1.56e-2 + i^7 * 1.95e-3 \dots \end{aligned} \quad (12)$$

Then Eqs.(11) and (12) are scaled and added in a pair wise manner to yield two new TFs corresponding to the NDC of Figs. 3c and 3d, whose third-order terms are equal to zero,

$$\begin{aligned} j11(u) + j12(u * 3.634) &= u^3 * 8.2 + u^5 * 1.63 - u^7 * 1.66 \dots, \\ v11(i * 1.747) + v12(i) &= i^2 * 2.87 + i^5 * 6.00e-3 - i^7 * 7.93e-6 \dots \end{aligned} \quad (13)$$

Similarly, Eq.(13) is used at the second stage to generate another pair of transfer functions, Eq.(14), that would correspond to the new dual circuits of Figs. 3e and 3f and whose fifth-order terms would be zeros.

$$\begin{aligned} j21(u) + j22(u * 6.872) &= u^6 * 2.1 + u^7 * 3.41e-1 \dots, \\ v21(i * 2.577) + v22(i) &= i^3 * 3.55 + i^7 * 1.49e-2 \dots, \end{aligned} \quad (14)$$

Fig.4 shows the normalized level of odd-order nonlinear distortions as a function of the signal amplitude for the circuits of Figs.3a through 3f and third-order expansion term in the case of incomplete compensation (0.95h, 1.05w). As before the level of non-linear distortions for linearized NDC of the same order are close. Meanwhile, the circuits are greatly different with respect to the dynamic range and circuit structure and design.

CONCLUSION: COMPARISON OF LINEAR AND NONLINEAR COMPENSATION

We have completed the analysis of the compensation procedure for opened and closed p-n junctions, and it seems of interest to compare the effectiveness of the linear and nonlinear compensation techniques. This can be done by considering, as an example, circuits with a compensated third-order term in the transfer function expansion, since these are of the greatest practical importance. By confronting the data of paper [1] with this paper one can note a greater effect of the linear compensation. Some of the representative TF are shown in Fig.7. All of these data bring us to the conclusion that circuit linearization with the aid of a linear element (resistor or capacitor) in NDC results in a lesser level of fifth-order combinations. In addition, the compensated circuits involve only two p-n junctions against the four of nonlinear methods, with both junctions operating in similar modes. This is particularly important for thermal stabilization of the compensation conditions and for extending the linear section on the V-I curve, i.e. the dynamic range. Probably, it should be mentioned that the regular method of nonlinear compensation of non-linearity in symmetric NDC initially seemed the most effective. The possibility of compensating a non-linearity with the aid of a linear circuit element was discovered as a by-product and no practical importance was attached to it. Moreover, the effect seemed dubious. Currently the author believes this method to be most suitable for the majority of quasi-linear circuits. Whereas compensation with nonlinear elements apparently is better fit for parametric circuits. To conclude the paper, let us discuss briefly some of the tasks and practical applications for linearized circuits. First, it would be necessary to analyze their real advantages and limitations, especially those arising from the complexity of both p-n junctions and other circuit elements. Naturally, applications would call for synthesizing a broader variety of linearized circuits. It might prove advantageous to employ such circuits in HF switching devices, analog and digital attenuators and phase shifters, mixers and electronically tunable generators. The possibility of applying such linearization technique to transistor based circuits should be

investigated as a priority. Probably the most challenging task would be to implement the linearization techniques discussed in integrated circuits.

ACKNOWLEDGMENTS

This investigations carried out in the frame of the new amplification system designing program for the UTR-2 decameter radio telescope and was supported by the National Academy of Science of Ukraine (project 1.20), State Committee for Science and Technology of Ukraine (grants 22/100 and 23/547), the European Southern Observatory (grant ESO A-01-041) and International Association of the European Community (grant INTAS 94-3097). I'd like to thank also Center Technological Education of Holon and Absorption Ministry of Israel for support of this investigation and Dr. M.Haridim for useful discussion.

REFERENCES

- [1] Y.M.Bruck. Linearization of P-N Junction by Linear Elements. /1997, Proceedings of this Conference.
- [2] Y.M.Bruck. Regular Linearization Principle for Electronic Circuit. /1997, Proceeding of this Conference
- [3] I.N.Bronstein, K.A.Semendyaev. Handbook of Mathematics. /1986, Moscow Nauka Publ.Co.pp.544.
- [4] D.E.Knuth. The Art of Computer Programming /1969, Addison-Wesley Publ.Com.California. pp. 540

FIGURE CAPTIONS

Fig.1 Functional dual circuit diagrams for non-symmetric linearizing opened and closed p - n junctions: U_1, U_2, I_1, I_2 are the bias voltages and currents, respectively; u, i, i_1, u_2, i_1, i_2 are the signal voltages and currents, respectively;

- a - non-symmetric parallel third-order circuit; b - a non-symmetric series-connected third-order circuit;
- c - series symmetric fifth-order circuit with a common current i and different voltages u_1, u_2 ; $u=u_1+u_2$;
- d - parallel symmetric fifth-order circuit with a common voltage u and different currents i_1, i_2 ; $i = i_1+i_2$;
- e - symmetric series seventh-order circuit; f - a parallel symmetric seventh-order circuit.

Fig.2 The level of nonlinear distortions $[A(x) - x]/x$, normalized by the signal amplitude, as a function of the signal level in an opened p-n junction for non-symmetric linearizing technique:

- 1,3,5,7 - parallel symmetric circuits, $A(x)=i(u)$; 2,4,6,8 - series symmetric circuits, $A(x)=u(i)$;
- 1 - $h = 1$; 3 and 5 - $h = 3.732$; 7 - $h = 3.928$; 2 - $w = 1$; 4 and 6 - $w = 0.268$; 8 - $w = 0.255$.

Fig.3 Functional dual circuit diagrams for symmetric linearizing opened and closed p - n junctions: U_0, I_0 , and u, i are the bias and signal voltages and currents, respectively;

- a - symmetric parallel third-order circuit; b - a symmetric series third-order circuit;
- c - series, symmetric fifth-order circuit with a common current i and different voltages u_1, u_2 , $u=u_1+u_2$;
- d - parallel symmetric fifth-order circuit with a common voltage u and different currents i_1, i_2 , $i=i_1+i_2$;
- e - series, symmetric seventh-order circuit; f - a parallel, symmetric seventh-order circuit.

Fig.4 The levels of fifth-order nonlinear distortions with different types of non-linearity compensating circuits:

- 1,3,5 - series circuit, $A(x) = u(i)$; p-n junction is opened;
- 2,4,6 - parallel circuit, $A(x) = i(u)$; p-n junction is closed;
- 1 and 2 - compensation with linear elements; 3 and 4 - nonlinear symmetric compensation;
- 5 and 6 - nonlinear non-symmetric compensation.

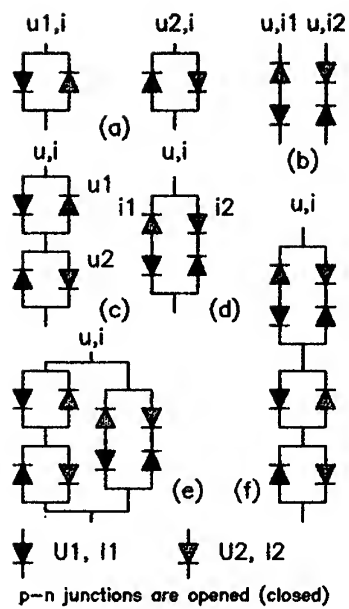


Fig. 1

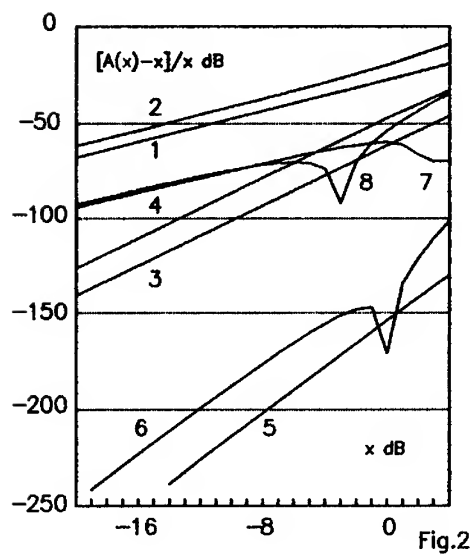


Fig. 2

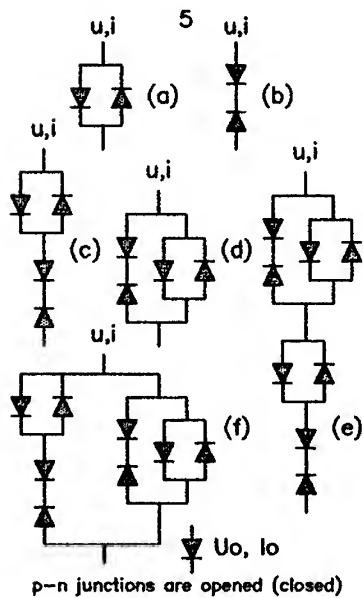


Fig. 3

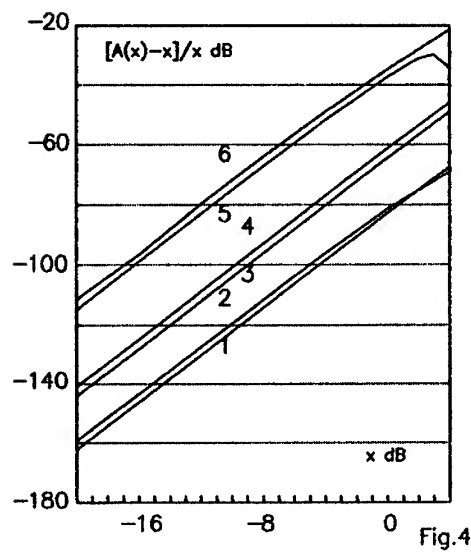


Fig. 4

Linearization of P-N Junctions by Linear Elements

Yuri.M.Bruck IEEE member

Radioastronomical Institute, 4, Krasnoznamennaja St., Kharkov, UKRAINE. men@rian.kharkov.ua
Center Technological Education of Holon. Communication Dept. 52, Golomb St. Tel-Aviv, ISRAEL;
Box 8629, Misgav St. 27/8, 21862, Carmiel, ISRAEL 100310.2246@compuserve.com

ABSTRACT

Linearizing circuits for opened and closed p-n junctions are suggested and analyzed theoretically, in which the third-order and all even-order non-linearities are totally cancelled by external linear circuit elements and using of the symmetrical nonlinear circuits. Higher-order non-linearities are also reduced by two to five orders of magnitude. The theory is corroborated by an experimentally investigated V-I curve of one version of the linearized opened P-N junction.

INTRODUCTION

For quite a long time attempts have been made to compensate transfer function non-linearities through the use of circuit elements with the same or opposite kind of non-linearity. Many of the methods currently in use are underlined by different principles, and nonlinear elements of the compensating circuits are greatly different from such of the circuits to be linearized. Therefore, the compensating circuits are structurally complex and require adjustment as to the signal phase and amplitude [1]. In paper [2] was suggested other principles, aimed primarily at the linearization of basic nonlinear elements by using the same nonlinear elements. An important result of [2] was the discovery that a function can be linearized by properly changing of its linear part. This apparently nontrivial technique is characterized by some advantages and certainly deserves special analysis. Therefore, the first considers linear compensation techniques. The analysis is restricted to the quasi-static mode, when the complex (i.e. real plus imaginary) nature of the nonlinear element may be disregarded. The equations quoted from [2] are referred to as (nn-[2]). Designations TF, IF and NDC are quoted also from [2].

P - N JUNCTION EQUATIONS

In what follows, we will make use of the simple equations to represent the TFs of nonlinear circuit elements. This should not have a strong effect on the result, since the linearization procedure is based on the same nonlinear elements. The opened p-n junction, can be described by TFs

$$i = e^u - 1 = u + u^2/2 + u^3/6 + \dots, \quad u = \ln(1+i) = i - i^2/2 + i^3/3 + \dots \quad (1)$$

Eq. (1) has been written, as is customary in the analysis of nonlinear circuits, in terms of dimensionless values. Here and after:

$I = I_s/(I_o + I_{sat})$ and $u = U_s/U_t$, $I_o = I_{sat} * e^{U_o/U_t}$ $U_o \gg U_t$; U_t -thermal potential; $I_o \gg I_{sat}$ ($I_{sat} = 10^{-6} \dots 10^{-7} A$); U_o, I_o -bias; U_s, I_s -signal. The dynamic resistance is $dU_s/dI_s = U_t/(I_o + I_{sat})$, while $du/di = 1$.

If a junction is closed, we will consider only the nonlinear capacitance $C(U)$. $C(U) = C_o * [1 + U_s/(U_o + U_b)]^{0.5}$ C_o is the capacitance at $U = U_o + U_b$, $U_s = 0$, U_b -junction potential. The signal current I_s can be obtained by differentiating the charge $Q = C(U) * U$. i.e. $I_s = dQ/dt = [U * dC(U)/dU_s + C(U)] * dU_s/dt$.

We denote: $I_o = \omega * C_o * (U_o + U_b)/2$, $C = \cos(\omega * t)$; $S = \sin(\omega * t)$; $U = U_s * S$; $dU/dt = U_s * C$, $i = I_s/I_o$, $u = U_s/(U_o + U_b)$. As $u(t) = u * S$ and $du/dt = u * C$, it can be shown

$$i(u, t) = u * C * (1 + u * S)^{-0.5} = \sum_{k=1}^{\infty} a_k * C * S^{k-1} * u^k, \quad (2.1)$$

$$du(i, t)/dt = \sum_{k=1}^{\infty} A_k * C * S^{k-1} * i^k.$$

$$u(i,t) = \sum_{k=1}^{\infty} A_k * S^{k-1} * i^k \quad (2.2)$$

with a_k and A_k are the Taylor's coefficients of the straight $u*(1+v)^{-0.5}$ and inverse $i*(1+i^2/4)^{0.5} + i^2/2$ functions and not depend from time. Then from Eqs.(2.1) and (2.2)

$$i(u,t) = u*C - u^2*C*S/2 + u^3*C*S^2/3/8 - \dots, \quad u(i,t) = i*S + i^2*S^2/2 + i^3*S^3/8 + \dots \quad (2.3)$$

To simplify expressions and to generalize consideration for opened and closed p-n junction, farther we will omit (i.e. put one) factors $C*S^{k-1}$ and S^k , which produce harmonics and combinations. If need, their real amplitudes are calculated on the basis of well known formulas for different U_s kinds (one, two or multiply carriers).

LINEARIZATION OF THE OPENED P-N JUNCTION

As follows from the example analyzed in [2], its TF (1) satisfies the condition of (3)-[2], which implies absence of limitations to its linearization by this technique. To do that, let us re-write Eq.(1), complementing the linear terms of the expansions involved with a conductivity, g , and resistance r , yet unknown; i_1, i_2, u_1, u_2 - currents and voltages in NDC.

$$\begin{aligned} i &= g*u_1 + e^{u_1} - 1 = u_1*(1+g) + u_1^2/2 + u_1^3/6 + \dots, \\ i &= g*u_2 + 1 - e^{-u_2} = u_2*(1+g) - u_2^2/2 + u_2^3/6 - \dots, \\ u &= r*i_1 + \ln(1+i_1) = i_1*(1+r) - i_1^2/2 + i_1^3/3 - \dots, \\ u &= r*i_2 - \ln(1-i_2) = i_2*(1+r) + i_2^2/2 + i_2^3/3 + \dots, \end{aligned} \quad (3)$$

Here and after the first and the second equation in similar pairs corresponds to the "+" and "-" signs, respectively in $I = I_s \pm I_o$ and $U = U_s \pm U_o$. According to [2], it is necessary at first to cancel third-order terms in the expansions of the IFs i^\wedge and u^\wedge , by properly selecting the magnitudes of g and r . Eq.(3-[2]) yields $g = 2$ and $r = 0.5$. To eliminate even-order terms, the equations governing the IFs have to be added pair-wise, which is equivalent to series and parallel connection of the corresponding initial NDC. The values involved in the TFs of the two resultant NDC obey.

$$\begin{aligned} i_{12} &= i_1 + i_2 = 4/3*u + 6.503e-4*u^5 + \dots \\ u_{12} &= u_1 + u_2 = 2/3*i - 1.016e-5*i^5 + \dots \end{aligned} \quad (4)$$

i.e. nonlinear terms up to the fourth order have vanished. The NDC corresponding to (3) and (4) are shown in Figs. 1a,b. Fig.2 shows the level of odd-order nonlinear distortions as a function of the signal amplitude. The IF function expansion coefficients up to eleven order were derived with the aid of the remarkable algorithm suggested by Bramhall and described in [3]. As can be seen, the linearity TF is high for such NDC.

LINEARIZATION OF THE CLOSED P-N JUNCTION

According to Eq.(3-[2]), its TFs (2.1) and (2.2) comply with the condition for unlimited linearization. Making use of (2.3), we will complement the expansions with yet unknown g and z .

$$\begin{aligned} i &= u_1*(1+g) - 1/2*u_1^2 + 3/8*u_1^3 - 5/16*u_1^4 + 35/128*u_1^5 - \dots, \\ i &= u_2*(1+g) + 1/2*u_2^2 + 3/8*u_2^3 + 5/16*u_2^4 + 35/128*u_2^5 - \dots \\ u &= i_1*(1+z) + 1/2*i_1^2 + 1/8*i_1^3 + 0*i_1^4 + 1/128*i_1^5 + \dots, \\ u &= i_2*(1+z) - 1/2*i_2^2 + 1/8*i_2^3 - 0*i_2^4 - 1/128*i_2^5 + \dots \end{aligned} \quad (5)$$

In (5), g and z are parameters of the constant linearizing capacitors, normalized to the junction capacitance magnitude. At this point it is necessary to select the values of g and z to cancel third order terms in the expansions of the IFs i^\wedge and u^\wedge . Eq.(8-[2]) yields $g = 1/3$ and $z = 3$. To cancel even-order

terms we add the IFs equations in a pair-wise manner, which is equivalent to series and parallel connections of their NDC. The TFs of two new NDC are

$$\begin{aligned} i_{12} &= i_1 + i_2 = 1/2 * u - 3.815e-6 * u^5 + \dots, \\ u_{12} &= u_1 + u_2 = 3/2 * i + 2.781e-3 * i^5 - \dots, \end{aligned} \quad (6)$$

i.e. all nonlinear terms, including those of the fourth-order, have been suppressed. The NDC corresponding to (5) and (6) are shown in Fig.3. Fig.4 shows the level of nonlinear distortions as a function of the signal amplitude. The gain in linearity is high in all cases. In fact, it is so high that it seems natural to analyze its stability against scatter in the circuit element parameters. Fig.2 and 4 show the level of third-order distortions for the cases when actual circuit impedances are equal to prescribed values (curves 3 and 4) and are not (curves 5 and 6). Apparently, $\pm 5\%$ deviations from the total compensation (when the third-order expansion term of the TF varies within 15%) are quite allowable for all the circuits considered here. This is evidence for a stable gain in the circuit linearity against scatter in the parameters and operating regimes, suggesting prospects for practical applications of such circuits.

EXPERIMENTAL TESTING

The linearization procedure based on selection of a linear parameter seems to be so simple and suspiciously efficient that it certainly demands experimental testing. The experiment was conducted with a DC circuit (see Fig.5) to exclude probable frequency-dependent errors. The p-n junctions investigated were the emitter-base junctions of the HF bipolar transistors KT 939-A. The transistors were selected so as to provide equal voltage drops with equal currents. The measured values U_t , was used to choose the resistance r , calculate the current I_0 and measure the voltage U_0 that served as a reference level against which the signal current and voltage increments I_s and U_s were counted and measured. The results are presented in Fig.6 shows V-I curves for a single junction and two oppositely connected non-linearized junctions, as well as for the entire linearized circuit. To the measurement accuracy, no non-linearity has been detected in the characteristic of the linearized circuit, even at $I_s > I_0$.

CONCLUSION

We have analyzed circuits where the p-n junction non-linearity is compensated with the aid of a linear element (resistor or capacitor), and found an unexpectedly high linearization efficiency. However such circuits suffer of a certain drawback. If the linear parameter is not adjusted in magnitude, a strict compensation is achieved only for the prescribed operation mode, although small deviations leave the third-order non-linearity insignificant. This might prove inadmissible for circuits where the p-n junction operation is dynamically controlled over a wide range. The author believes that the problem can be solved within linearization techniques employing nonlinear elements. Such circuits are discussed here in the next communication.

ACKNOWLEDGMENTS

This investigations carried out in the frame of the new amplification system designing program for the UTR-2 decameter radio telescope and was supported by the National Academy of Science of Ukraine (project 1.20), State Committee for Science and Technology of Ukraine (grants 22/100 and 23/547), the European Southern Observatory (grant ESO A-01-041) and International Association of the European Community (grant INTAS 94-3097). I'd like to thank also Center Technological Education of Holon and Absorption Ministry of Israel for support of this investigation and Dr.M.Haridim for useful discussions.

REFERENCES

- [1] N.Imai, T.Noijima, and T.Murase. "Novel Linearizer Using Balanced Circulators and its Application to Multilevel Digital Radio". / Aug. 1989, IEEE Trans. on Microwave Theory and Techniques, V.37, pp.1237-1243.
- [2] Y.M. Bruck. Regular Linearization Principle for Electronic Circuits. / 1997 Proceedings of this conference.

[3] D.N.Knuth. The Art of Computer Programming. Addison-Wesley Series Computer. vol.2 Seminumerical Algorithms. / 1969, Menlo Park, California. pp. 540.

FIGURE CAPTIONS

Fig.1 Functional dual circuit diagrams for linearizing opened p-n junction. U_0 , I_0 ; u , i are the bias and signal voltages and currents, respectively:

- a - parallel non-symmetric circuits; b - series non-symmetric circuits;
- c - symmetric series circuit with a common current i and different voltages, u_1 and u_2 , $u = u_1 + u_2$;
- d - symmetric parallel circuit with a common voltage u and different currents, i_1 and i_2 , $i = i_1 + i_2$.

Fig.2 The level of nonlinear distortions $[A(x) - x]/x$, normalized by the signal amplitude, as a function of the signal level in an opened p-n junction for non-symmetric linearizing technique for different values of the linearizing element parameters g and r :

- 1,3,5 - parallel symmetric circuits; $A(x) = i(u)$. 2,4,6 - series symmetric circuits; $A(x) = u(i)$.
- 1. $r = 0$; 3. $r = 0.5$; 5. $r = 0.525$. 2. $g = 0$; 4. $g = 2.0$; 6. $g = 1.9$.

Fig.3 Functional dual circuit diagrams for linearizing closed p-n junction. U_0 , I_0 ; u , i are the bias and signal voltages and currents, respectively:

- a - non-symmetric parallel circuits; b - series non-symmetric circuits;
- c - symmetric series circuit with a common current i and different voltages, u_1 and u_2 , $u = u_1 + u_2$;
- d - symmetric parallel circuit with a common voltage u and different currents, i_1 and i_2 , $i = i_1 + i_2$.

Fig.4 The level of nonlinear distortions $[A(x) - x]/x$, normalized by the signal amplitude, as a function of the signal level in a closed p-n junction for non-symmetric linearizing technique for different values of the linearizing element parameters g and z :

- 1,3,5 - parallel symmetric circuits; $A(x) = i(u)$. 2,4,6 - series symmetric circuits; $A(x) = u(i)$.
- 1. $z = 0$; 3. $z = 3.0$ 5. $r = 2.85$. 2. $g = 0$; 4. $g = 1/3$; 6. $g = 0.32$.

Fig.5 An experimental set for investigating of a parallel symmetric circuit with a p-n junction.

- 1- voltage stabilizer - is a current source I_0 ;
- 2- current stabilizer - is a current source I_s ;
- 3- digital voltmeter for measuring of U_s .

Fig.6 Measured V-I curves with $U_t = 42$ mV.

- 1,4 - are the branches of the function $I_s = 13.6 \cdot \exp(U_s/U_t) - I_0$ for the same opened p-n junction. $I_0 = 13.6$ mA.
- 2 - two oppositely connected P-N junctions: $s = 13.6 \cdot \text{sh}(U_s/U_t)$; $I_0 = 6.8$ mA.
- 3 - the linearized symmetric circuit, $I_s = U_s/3.1$; $I_0 = 10.0$ mA.

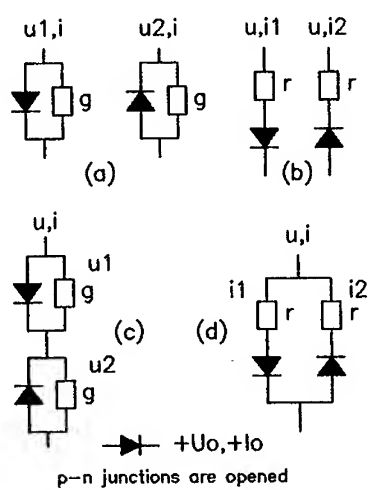


Fig. 1

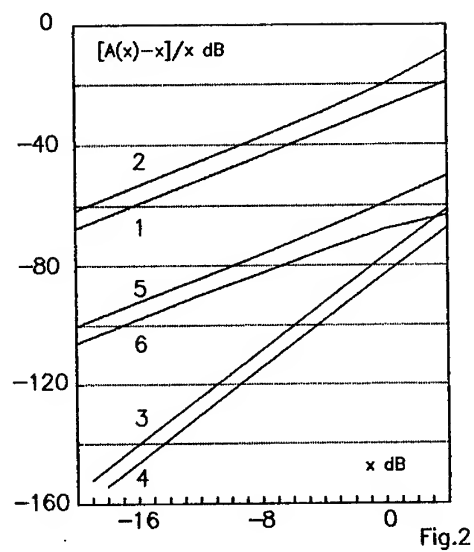


Fig. 2

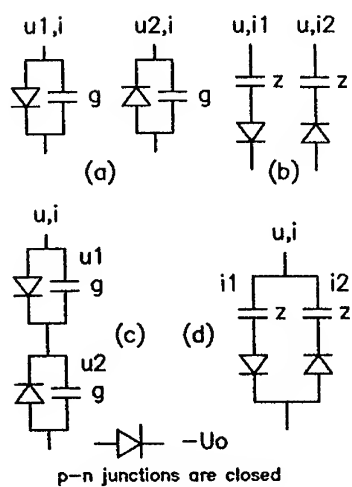


Fig. 3

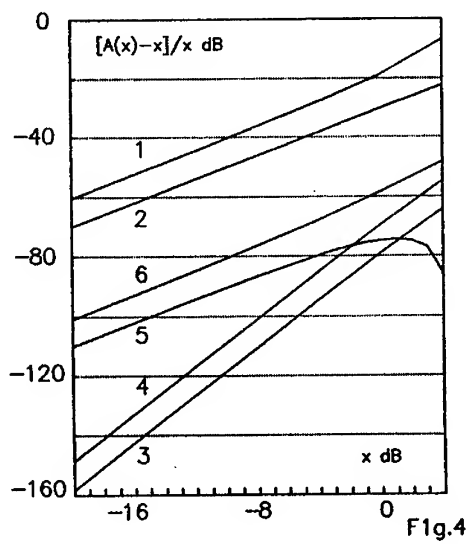


Fig. 4

DEVELOPMENT OF A 30 GHz, WIRELESS LAN TRANSMIT/RECEIVE MODULE

M.G. Stubbs, C. Glaser, H. Do Ky, C.J. Verver,
L. Shafai[#] and J.S. Wight[†]

Communications Research Centre, 3701 Carling Ave.,
P.O. Box 11490, Station H, Ottawa, Ontario, K2H 8S2, Canada

[#]University of Manitoba, Dept. of Electrical and Computer Engineering, Winnipeg, Canada

[†]Carleton University, Dept. of Electronics, Ottawa, Canada

ABSTRACT

Development of a transmit/receive module operating at 30 GHz is described. This module is intended for use in a broadband wireless, local area network (WLAN) demonstrator system and consists of monolithic microwave integrated circuits (MMICs) and miniature hybrid microwave integrated circuits (MHMICs) assembled together in a single housing together with four planar, leaky wave antenna elements. The antenna array is used in a switching mode, with an MMIC switching network, to direct the transmit or receive signals appropriately. The demonstrator module has a 90° coverage in the horizontal plane and can be extended to provide full 360° coverage, by grouping four such modules together.

INTRODUCTION

WLAN networks are an attractive means of interconnecting computers and associated equipment in modern office layouts, since they avoid the need to reroute wiring when office requirements and locations are changed. Recent research activities in this area have been focused at 2.4 and 17 GHz in Europe [1, 2] and 60 GHz in Japan and Australia [3,4] with the increased propagation loss at the higher frequencies offering the advantage of system isolation, while also accommodating the transmission of higher data rates. This paper discusses the development of a broadband WLAN system currently being investigated in Canada at 30 GHz. The system will demonstrate two way transmission of high data rate signals between a centrally located base station, mounted on a ceiling, and several remote terminals, either fixed or mobile. It was developed for the "Broadband Indoor Wireless Communications Project" of the Canadian Institute for Telecommunications Research and is expected to cover an in-building area with 50 m. radius.

The 30 GHz demonstrator system will initially be set up as a one way, 40 Mb/s, communications link between two personal computers in an indoor environment, evolving finally to a complete 160 Mb/s simplex communications system. This will allow unresolved questions such as the required power budget, multipath effects and switching algorithms to be investigated and the data to be compared with predicted results. This paper describes the development and results of the completed microwave transmit/receive module that is to be an integral part of the demonstrator system.

WLAN Module

The specifications for the base station and remote units are identical and are shown in Table 1. The final module will require a full 360° coverage but for the demonstration, full coverage is not necessary. The coverage of this prototype therefore consists of one 90° sector, considerably simplifying the number of switching networks required in the module between the antenna and the common up and down converters [5]. An indoor environment is very dynamic, from an RF signal's point-of-view, since people are constantly in motion changing the reflection and transmission characteristics of the propagation path. It is therefore very probable that an indoor communications link will be interrupted during transmission. As a result, the system must be designed to detect the loss of signal, stop transmission, identify a more appropriate communication path and start transmission once again. In the module described here, only one antenna element, out of a possible sixteen, is active at any one time on both the base station and remote units. The choice of antenna elements is made by determining which ones provide the maximum signal level transmitted between the two units.

MODULE COMPONENTS

Upconverter: In the transmit mode, the input signal to the transmit/receive module is a modulated 3.5 GHz IF signal which is translated to 30 GHz by an MHMIC upconverter containing a single, 0.2 µm x 150 µm, GaAs PHEMT active device (Fig. 1). The 26.5 GHz LO and 30 GHz RF signals are fed to, and extracted from, the drain terminal of the PHEMT via MIC parallel-coupled filters configured as a diplexer. The LO signal delivered to the upconverter is 5 dBm and is currently derived from a commercial Gunn oscillator source (the same signal is also used for the downconverter in the receive path of the module). The conversion loss of the upconverter is shown in Fig. 2 and is approximately 0 dB at 3.5 GHz, increasing to about 2 dB at 3.3 GHz and 3.9 GHz. The LO-RF isolation is 40 dB.

Power Amplifier: The 26.5 GHz LO signal is filtered out from the transmit path by the diplexer and the RF signal is amplified by two GaAs PHEMT MMIC chips connected together with short wirebonds. The operation of the module was first demonstrated with commercial MMIC power amplifier chips but these have since been replaced by chips designed at CRC and fabricated at an external foundry. The latter amplifiers are based on a 0.2 µm x 600 µm output stage PHEMT and can provide up to 24 dBm at 30 GHz. The chip dimensions are 5.15 x 1.3 mm² and the S₂₁ response is shown in Fig. 3.

Switching network: An MMIC switching network, consisting of four, low loss single pole double throw, PHEMT based, MMIC switches [5], interconnects the power amplifier and low noise receiver with the antenna arrays through 50 Ω microstrip lines. The switches are controlled by TTL logic that directs the signal to the appropriate antenna element.

Antenna array: Four novel, planar antenna arrays [6], each consisting of a crank shaped launcher, a reflector element and thirty passive directors are fabricated on Duroid ($\epsilon_r = 2.5$) material. The antenna operates in a leaky wave mode and was adopted from the Yagi Yuda design. The antenna has a gain of 16 dBi at 30 GHz and an input return loss of around 13 dB. The E and H plane radiation patterns of one of the antenna elements are shown in Fig. 4.

Low noise amplifier: In the receive mode, an MMIC LNA receives the signal from the switching network. The amplifier uses a two stage, 0.2 μ m GaAs PHEMT design and has a 4 dB noise figure and 17 dB gain at 30 GHz.

Downconverter: A diplexer, identical to the one used in the upconverter, is used in this component. In this case, however, the active downconverter is an MMIC chip (Fig. 5), measuring 2.5 x 1.4 mm², and is based on a GaAs PHEMT device. The RF and LO signals are applied to the gate of the PHEMT, producing less than 2 dB conversion loss over the band of interest (Fig. 6). The RF-LO and LO-IF isolations were found to be 35 and 75 dB respectively. The output signal is a modulated 3.5 GHz IF signal which is then fed to a demodulator.

MODULE RESULTS

The assembled module with four antenna arrays is shown in Fig. 7, together with the necessary switching control lines. To illustrate the RF performance of the module, a -15 dBm, swept IF signal was fed into the upconverter. The resultant swept RF response at the input to the antenna arrays is shown in Fig. 8. The output signal was found to be 15.5 \pm 2.5 dBm over the swept bandwidth. In a similar measurement of the receive path, an IF output level of -21 \pm 1 dBm between 2.6 - 4.45 GHz was achieved with an input level to the switching network of -25 dBm.

CONCLUSIONS

Details of an integrated MMIC/MHMC/MIC transmit/receive module for a WLAN demonstrator are presented. The module, integrated together with a novel microstrip, leaky wave antenna, provides 15 dBm output power at 30 GHz, which should be sufficient for a WLAN system capable of covering an indoor area of about 8000 m².

REFERENCES

1. L.M. Devlin et al, "A 2.4GHz Single Chip Transceiver", 1993, IEEE Microwave and Millimeter-wave Monolithic Circuits Symposium Digest, pp. 23-26.
2. S. Nam et al, "GaAs MMIC chipset for 17/18 GHz indoor radio LANs", 1996, Proc. 26th European Microwave Conference, Vol. 2, pp. 960-963.
3. Y. Takimoto and T. Ihara, "Research Activities on Millimeter Wave Indoor Communication Systems in Japan", 1993, IEEE MTT-S International Symposium Digest, Vol. 2, pp. 673-676.
4. R.A. Batchelor et al, "Australian Activities in Microwave Links for Wireless LANS", 1993, IEEE MTT-S International Symposium Digest, Vol. 2, pp. 677-680.
5. M.G. Stubbs et al, "MMIC switching network for an EHF in-building WLAN system", 1996, Proc. 26th European Microwave Conference, Vol. 2, pp. 945-948.
6. L. Shafai, "A Microstrip Line-Fed Leaky Wave Antenna for EHF Links", 1996, Wireless '96, pp. 222-228.

Antenna		Electronics	
Topology	16 radially oriented, planar	Power amplifier output	20 dBm
Construction	Flat, horizontal microstrip	LNA NF	3.5 dB
Number of beams	16	LNA gain	23 dB
Polarization	Horizontal	Switch loss	1 dB per stage
3 dB beamwidth, azim.	22.5°	RF bandwidth	28.5 - 31.5 GHz
3 dB beamwidth, elev.	35°	IF bandwidth	3.0 - 4.2 GHz
Antenna gain	17 dBi	LO frequency	25.5, 26.5, 27.5 GHz
Bandwidth	28.5 - 31.5 GHz	Construction	MMIC, MHMIC, MIC

Table 1. Transmit/receive module specifications

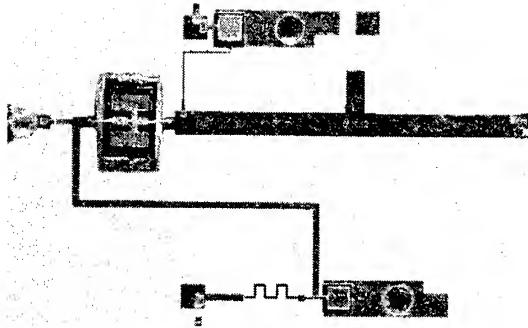


Figure 1. MHMIC 3.5/30 GHz upconverter

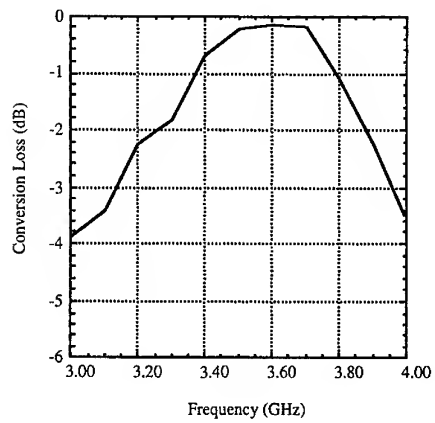


Figure 2. Conversion loss versus frequency of MHMIC upconverter

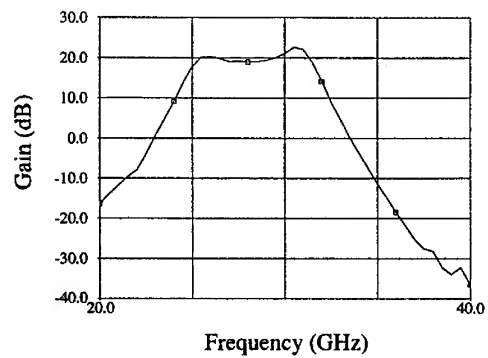


Figure 3. Transmission gain response of 30 GHz MMIC amplifier

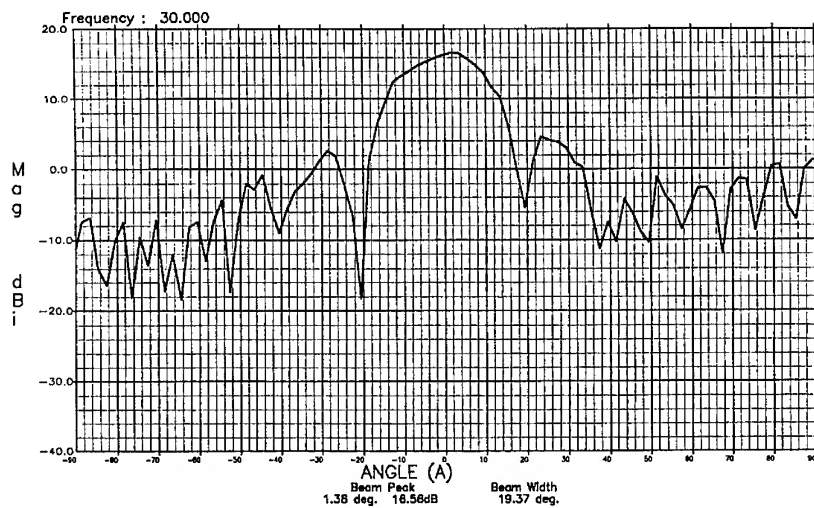


Figure 4(a)

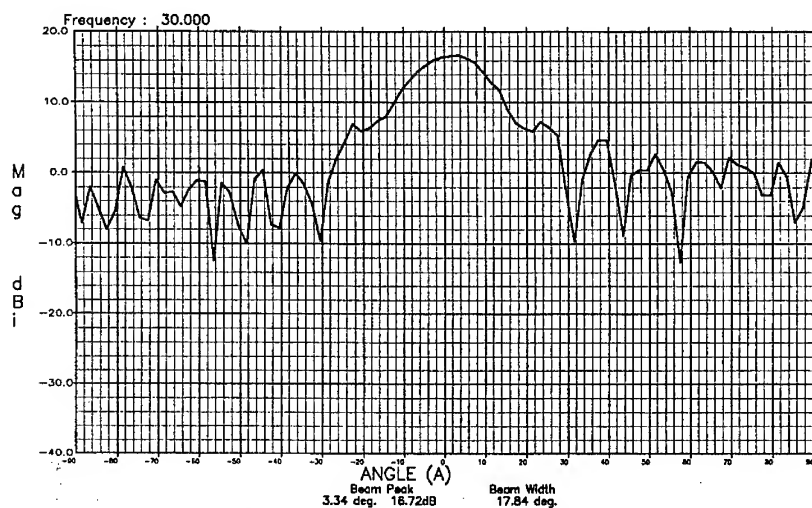


Figure 4(b)

Figure 4 Measured radiation patterns of the leaky wave antenna
(a) E-plane, (b) H-plane

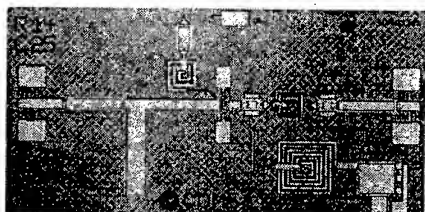


Figure 5. Photomicrograph of 30/3.5 GHz MMIC downconverter

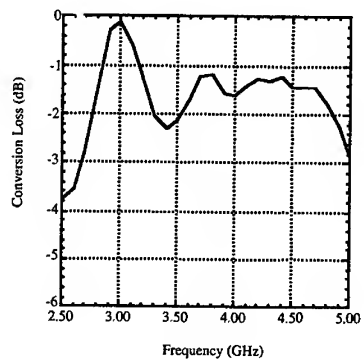


Figure 6. Conversion loss versus frequency of MMIC downconverter

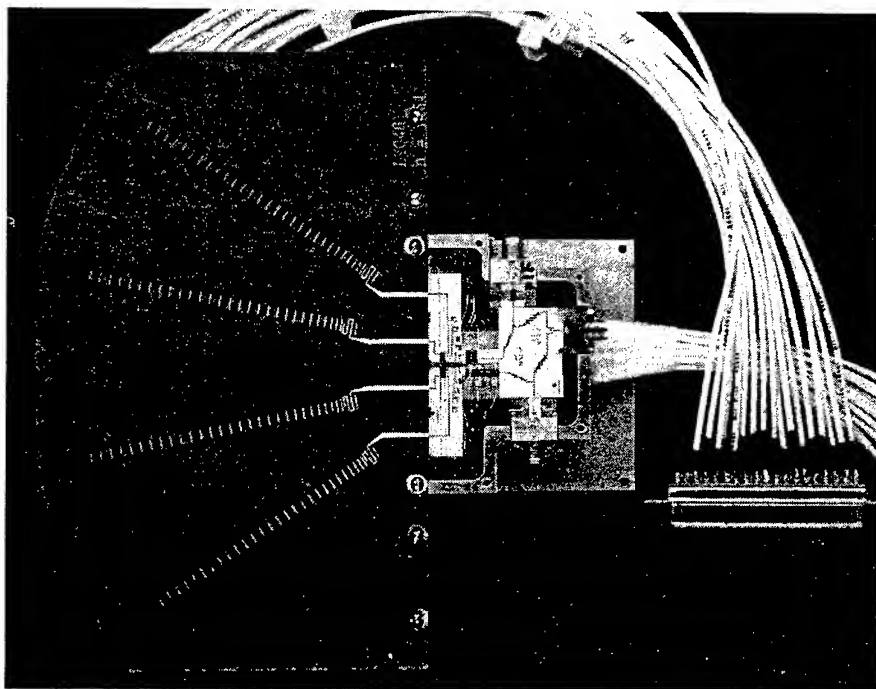


Figure 7. Integrated WLAN transmit/receive module together with leaky wave antenna arrays

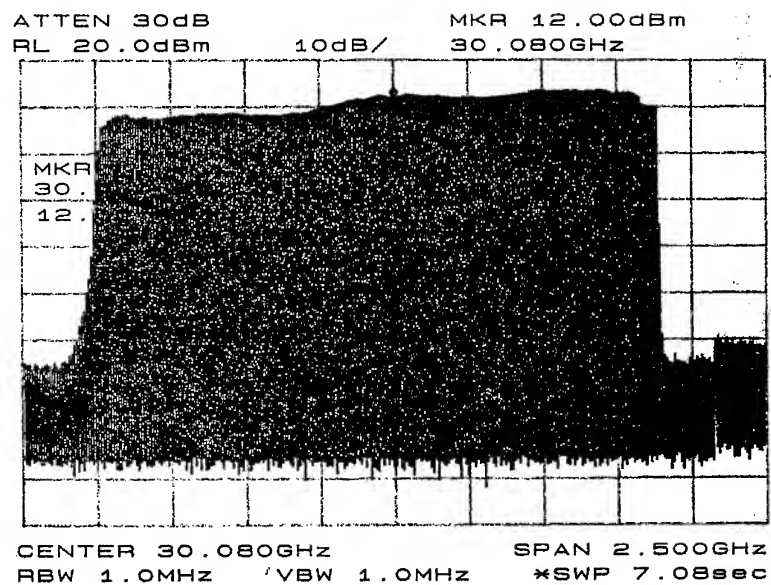


Figure 8. Module output power versus frequency with a swept IF input signal.
The plot shows a power level of 12 dBm at 30.12 GHz
and includes a cable loss of about 3 dB.

Frequency Tunable MESFET Active Patch Antenna/Oscillators

Wenzhang Wang and L. Wilson Pearson
Department of Electrical and Computer Engineering
Clemson University
Clemson, SC 29634-0915
USA

(864)656-3946 (voice & fax)

E-mail: wenzhaw@ces.clemson.edu, pearson@ces.clemson.edu

ABSTRACT

An integrated transistor-excited patch antenna/oscillator configuration that provides control of oscillation frequency and E-plane radiation pattern by way of an integral stub transmission line is presented. The configuration has been analyzed experimentally through six different models—three involving changing patch widths and three involving changing stub length. The latter three are characterized for the case when the stub end is shorted directly to the adjacent patch surface with a capacitor. This modification changes both the oscillating frequency and the radiation pattern of the structure. It is observed that the stub supports both microstrip and coplanar waveguide modes—a feature that potentially can be exploited because of the additional degree of freedom available.

Introduction

Spatial power combining proves to be a good way to generate high-power microwave and millimeter wave radiation fields, *e.g.*, Wiltse and Mink (1). One class of power combining structures employs an array of active patch antennas residing on a dielectric substrate as in Mortazawi, *et al.* (2). Of the variety of circuit configurations conceivable, transistor patch antennas can be classified into two categories: single-patch and dual-patch transistor-excited antennas. A single-patch transistor antenna usually consists of a patch antenna and a transistor microstrip oscillator (Erturk, *et al.* (3), Liao and York (4)). The oscillation frequency is determined by the oscillator while the patch serves simply as a radiating load to the oscillator. In a dual-patch transistor antenna, the gate and drain terminals of the transistors are connected to two patches or two halves of a patch with the source terminal either grounded (York and Compton (5)) or connected to a section of microstrip line sandwiched between the two patches (Wu and Chang (6,7)). The patches act both as radiation elements and as resonant circuits. Since a patch antenna is a narrow band device, it is difficult to incorporate it in tunable oscillator with a wide tuning range. The configuration discussed here incorporates a transmission line stub as the gate-feedback coupling element. Considerable control over antenna/oscillator operation is afforded through adjustment of this patch. Experiments indicate that this stub supports both a microstrip and a coplanar-waveguide mode, which may be terminated independently. Thus, in principle, three degrees of freedom for design control are associated with each of the two modes.

Figure 1 depicts the circuit configuration of the new MESFET active patch antenna/oscillator. It consists of two patch antenna and a transistor. A metal strip island is etched inside the lower patch. The upper and lower patches are connected to the drain and source terminals of the transistor, respectively. While the gate is connected to the microstrip line section, which may either be open ended or terminated. (However, a DC open circuit must be maintained in the terminated case because of bias considerations.) The presence of this microstrip stub introduced substantial flexibility into the design of the active radiator. In fact, the stub supports a microstrip mode against the ground plane below the substrate and a coplanar waveguide (CPW) mode relative to the adjacent patch. By influencing the standing wave in each of these modes, one may influence both the radiation field pattern and the resonant frequency of the antenna. Insertion of a varactor diode into the stub can provide voltage control of the oscillating frequency, by which, Both frequency modulation and phase modulation can be realized.

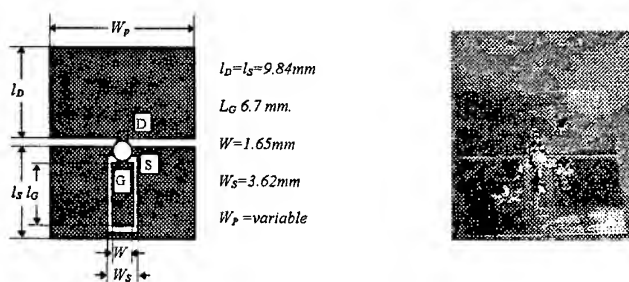


Figure 1. Circuit Configuration of the MESFET active patch.

Oscillation Frequency Experiments

Six active patch antennas with different patch width were designed and fabricated on 0.031" thick RT/Duroid 5870 substrate. Three antennas were fabricated with progressively wider patch width w_p . Change of patch width changes the radiation resistance of the antenna and hence the resistive loading of the oscillator. (One might also consider varying the length of the patch l_p , which directly influences the resonant frequency of the patch. This is relatively less interesting than the width variation.) The general dimensions of these three patches are listed on the right hand side of figure 1. The MESFETs used in the circuits are packaged Fujitsu FHX35LG.

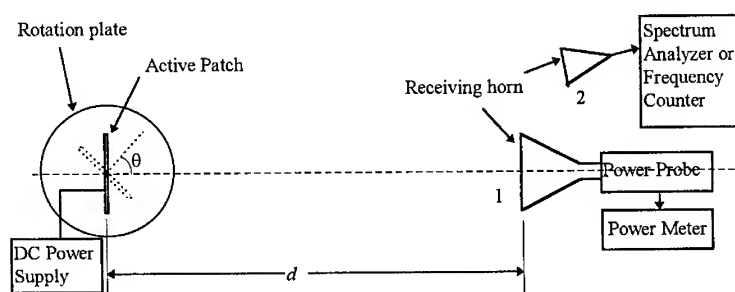


Figure 2. Measurement system setup.

Figure 2 shows the setup for the MESFET active patch/oscillator measurement system. It consists of a rotatable plate, two horn antennas, a power meter, a DC power supply and a frequency counter or a spectrum analyzer. The active patch antenna/oscillator to be measured is placed vertically on the rotatable plate. The receiving horn#1 is connected to a power meter for measuring the radiated power. The distance between the patch antenna and the horn#1 is d . The horn#2 is used for frequency and spectrum measurement.

The radiated power of the active patch antenna/oscillator is measured by effective isotropic radiated power, EIRP., which is equal to $P_0 G_0$. From the Friis transmission formula

$$EIRP = \frac{P_r}{G_r} \left(\frac{4\pi d}{\lambda} \right)^2$$

where

- P_r received power,
- G_r receiving antenna gain,
- λ signal wavelength,
- d distance between receiving and transmitting antenna.

Table 1. Oscillator frequency and EIRP as patch width is varied.

	CU-Patch#1	CU-Patch#2	CU-Patch#3
Patch Width	19.75mm	14.86mm	9.91mm
Frequency	8.05GHz	8.12GHz	7.85GHz
EIRP	17dBm	15dBm	14dBm

Table 1 lists the measured oscillation frequency and effective isotropic radiated power (EIRP) for the three MESFET active patch antenna/oscillators for which patch width was varied. One observes the expected increasing of the loaded Q (quality factor) as the patch narrows.

Table 2. Oscillation frequency, EIRP and estimated oscillator power as stub length is varied

	CU-Patch#4	CU-Patch#5	CU-Patch#6
Gate stub length	6mm	5mm	4mm
Osc. frequency	8.501GHz	9.041GHz	9.370GHz
EIRP	22.95dBm	24.4dBm	27.85dBm
Estimated Power	12.65dBm	13.5dBm	18.5dBm

Table 2 displays the measured oscillation frequency, the EIRP, and an estimate of the power produced by the oscillator for three MESFET active patch antenna/oscillators for three different stub lengths. We see that lengthening the stub decreases the frequency of oscillation and that resonance attains with stub lengths less than $\lambda/4$ for the microstrip mode. However, because of the dual-mode nature of the stub, no simple relationship between stub length and oscillating frequency is discernable.

The configurations of Table 2 were modified through the attachment of a 20 pf beam-leaded capacitor bridging from the open end of the stubs to the antenna patch surrounding the respective stubs, providing a low-impedance termination to the CPW mode on the stubs. The oscillation frequencies of the modified configurations are given in Table 3.

Table 3. Oscillation frequency, EIRP and estimated oscillator power as stub length of the capacitively terminated stub is varied

	CU-Patch#4	CU-Patch#5	CU-Patch#6
Gate stub length	6mm	5mm	4mm
Osc. frequency	11.7 GHz	11.18 GHz	5.66 GHz
EIRP	26.2 dBm	23.4 dBm	20.5 dBm
Estimated Power	10.6 dBm	10.4 dBm	12.36 dBm

Radiation Pattern

Two sequences of three patterns each are given in this section. The first three patterns are those of the MESFET patch with an open-circuited stub. The second sequence of three patterns is associated with antennas with capacitively terminated stubs. We call the reader's attention to the contrast in patterns of the first sequence and the second. The results suggest strongly that the open end of the stub is radiating in the first sequence, while the capacitor suppresses radiation in the second case.

Figure 3 to figure 5 plotted the measured radiation patterns for CU-Patch numbers 4, 5 and 6 with open-circuited stubs. These data were measured when the drain to source voltages $V_{DS}=4V$ and the drain current $I_{DS}=20-23mA$. One may observe that the E-plane pattern is asymmetric to a significant degree. The phenomenon is believed to be due to slot radiation from the gap at the open end of the stub, as subsequent data supports. The patterns are generally broad beamed, as one expects from microstrip patches.

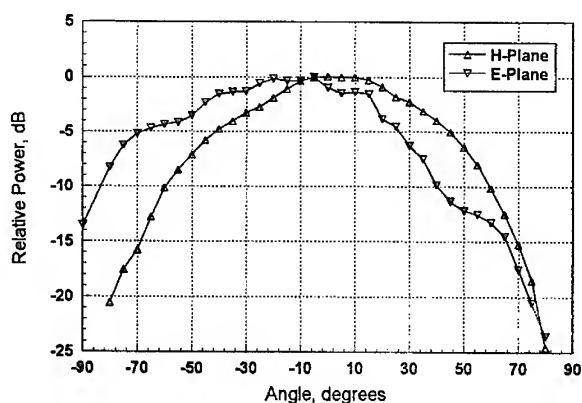


Figure 3. Measured Radiation Pattern for CU-Patch#4 with open stub.

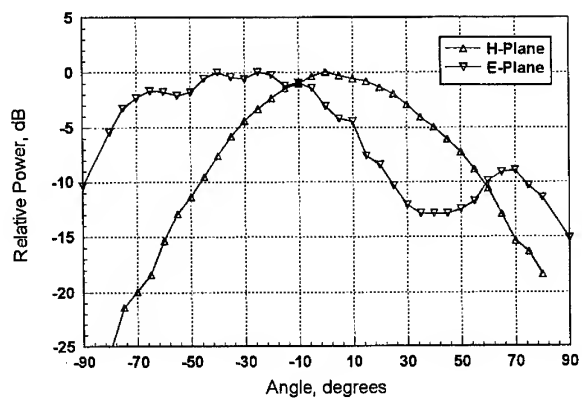


Figure 4. Measured Radiation Pattern for CU-Patch#5 with open stub.

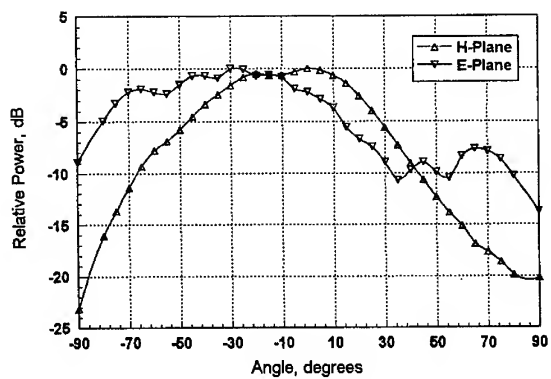


Figure 5. Measured Radiation Pattern for CU-Patch#6 with open stub.

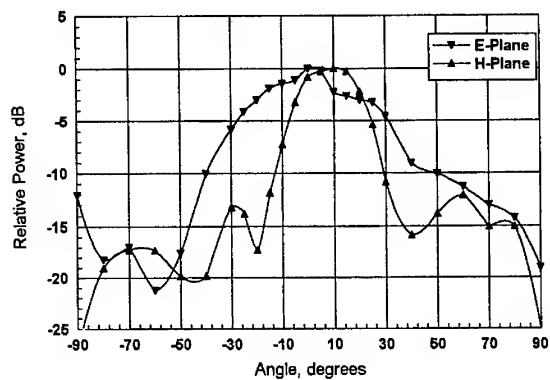


Figure 6. Measured Radiation Pattern for CU-Patch#4 with capacitive short at end of stub.

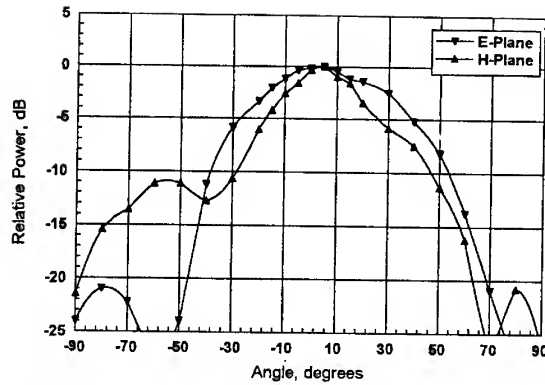


Figure 7. Measured Radiation Pattern for CU-Patch#5 with capacitive short at end of stub.

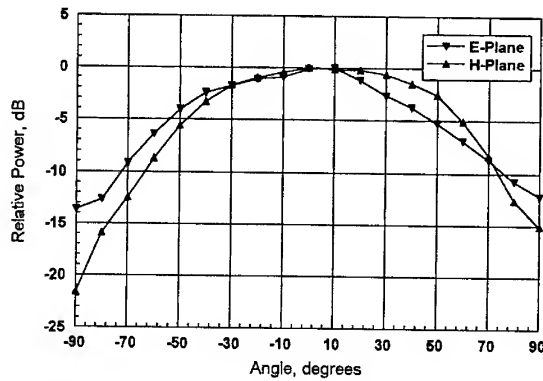


Figure 8. Measured Radiation Pattern for CU-Patch#6 with capacitive short at end of stub.

We note that the patterns shown in Figures 6-8 are more nearly symmetric than those in Figures 3-5. This leads us to conclude that the patterns of the configuration with the stub open circuited (Figures 3-5) manifest a component of radiation from the gap formed between the stub end and the adjacent portion of the patch surrounding the stub. When the capacitor is present, the charge build up around this gap is suppressed, and the gap radiation is not significant. Of course, the presence of the capacitor influences the oscillating frequency, as indicated in Table 3.

Oscillation Properties vs. Bias Voltage Both the oscillation frequency and the output power change with the applied drain to source voltage V_{DS} . Figure 9 shows the relationship between the oscillation frequency of the structure and the drain-to-source voltage for one patch model.

From the plot, one can find that in the range of $V_{DS}=2$ to $5V$, the output power increases as the applied voltage increases, while the oscillation frequency increases at first, when it reaches a maximum value, it decreases as the applied voltage increases. This suggest that in order to get higher power, one needs to increase the biasing voltage. When higher frequency stability is desired, one always need to select the applied voltage at which the maximum oscillation frequency occurs. On the other hand, if one wants to using the bias voltage to control the oscillation frequency, the operating point should be away from the maximum frequency point.

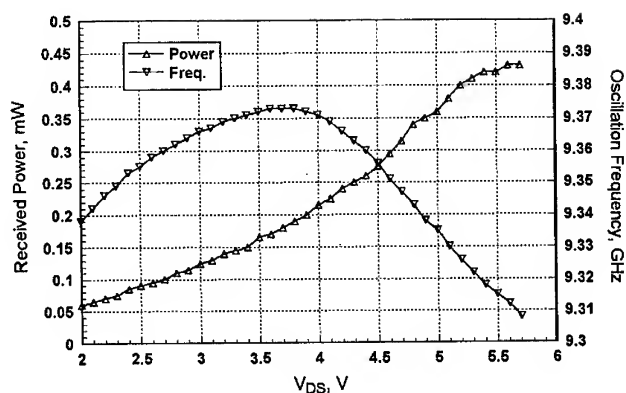


Figure 9. Oscillation Properties vs. Bias Voltage for CU-Patch#6.

References

1. J. C. Wiltse and J. W. Mink, "Quasi-Optical Power Combining of Solid-State Sources," *Microwave Journal*, No. 2, February 1992, pp. 144-156.
2. A. Mortazawi, H.D. Foltz, and T. Itoh "Aperiodic Second Harmonic Spation Power Combining Oscillator," *IEEE Trans. On Microwave Theory Tech.*, Vol. 40, no. 5, May, 1992, pp. 851-856.
3. V. B. Erturk, R. G. Rojas and P. Roblin, "Design/Analysis of an Active Integrated Antenna," 1996 IEEE Internat. Sympos. On Antennas and Propagat., July 1996, Baltimore, MD, pp. 1322-1325.
4. P. Liao and R. A. York, "A Varactor-Tuned Patch Oscillator for Active Arrays," *IEEE Microwave and Guided Wave Lett.*, Vol.4, No. 10, October 1994, pp. 335-337.
5. R. A. York and R. C. Compton, "Quasi-Optical Power Combining Using Mutually Synchronized Oscillator Arrays," *IEEE Trans. On Microwave Theory Tech.*, Vol. 39, No. 6, June 1991, pp. 1000-1007.
6. X-D Wu and K. Chang, "Novel Active FET Circular Patch Antenna Arrays for Quasi-Optical Power Combining," *IEEE Trans. On Microwave Theory Tech.*, Vol. 42, No. 5, May 1994, pp. 766-771.
7. X. D. Wu and K. Chang, "Dual FET Active Patch Elements for Spatial Power Combiners," *IEEE Trans. On Microwave Theory Tech.*, Vol. 43, No. 1, January 1995, pp. 26-30.

2 TO 18 GHz TRIPLE BALANCED MIXER FOR MMIC IMPLEMENTATION

A. MILANO

ELTA / ISRAEL AIRCRAFT INDUSTRIES, P.O.B. 330, ASHDOD, ISRAEL.

ABSTRACT

Multioctave Triple Balanced Mixers are circuits characterized by inherent ability to isolate the three signals for a very wide frequency range. Usually, this characteristic has been achieved by "suspended substrate" structures, on duroid or on alumina, involving double side mask alignment techniques, expensive assembly procedures and, consequently, high production costs. Moreover, two ring quads of diodes are requested to implement the circuits. At our knowledge, the only alternative proposal for such an item has been done by the author of this conference contribution few years ago, based on uniplanar technology on alumina.

But even this circuit was not completely uniplanar, as long as the IF output circuit was implemented in "bifilar line".

The MMIC circuit we intend to present is, on the contrary, fully uniplanar, that means the IF output circuit has been implemented on the same surface of the GaAs substrate of the other items. The circuit uses only four diodes, and shows much more performant electrical characteristics compared to the previous one implemented on alumina: this excellent result has been achieved thanks to LIBRA non linear simulation and SONNET e.m. analysis. The advantage in production costs and production reliability is pretty evident; the design is intended to be implemented in ELTA's GaAs foundry in the near future.

CIRCUIT DESIGN TOPICS

The equivalent circuit of the mixer is described in fig. 1). The lumped element power splitters and baluns have been implemented in the physical item, taking advantage of the circumstance that a coplanar waveguide has the ability of handling "even" and "odd" modes. Therefore, the MMIC circuit consists in a network of CPW, slot lines and planar coupled lines.

HARMONICS AND INTERMODULATION PRODUCTS

Following the symbolic vectors as depicted in fig. 1), and accordingly with a very well known geometric algorithm, (1), it is very easy to see the following topics:

- 1). L.O. even harmonics are recovered on the diodes;
- 2). L.O. odd harmonics are dissipated at the L.O. port;
- 3). R.F. even harmonics are recovered on the diodes;
- 4). R.F. odd harmonics are dissipated at the R.F. port;
- 5). $2*f/LO + 2*f/RF$, $2*f/LO - 2*f/RF$ are cancelled at I.F. port;
- 6). The following intermodulation products are cancelled at I.F. port:
 $2*n*f/RF \times 2*n*f/LO$, $(2*n+1)*f/RF \times 2*n*f/LO$,
 $2*n*f/RF \times (2*n+1)*f/LO$, $(2*n+1)*f/RF \times (2*n+1)*f/LO$.

Of course, the cancellation is as good as the four diodes are similar: in the MMIC implementation this circumstance is achieved beyond any doubt.

ISOLATION

The same geometric algorithm we used to prove the cancellation of several harmonics and intermodulation products, can be easily used to prove the inherent isolation among the ports of the mixer. Once again, the isolation in the physical item will depend on the ideality factor of the practical power splitters and baluns, beside the similarity among the diodes.

OUTPUT NETWORK *****

The last critical item is the I.F. output network. The ideal element is a theoretical balun, (fig. 2). It splits the input power at about 3.5 dB, with 9 dB return losses, (see fig.3 and fig. 4). The practical network we implemented for approaching the ideal balun presents similar power splitting with reasonable return loss, as depicted in fig. 5) and fig. 6).

ELECTRICAL PERFORMANCES *****

In fig. 7), 8), 9), are shown the typical performances. In the following we present the summary of them, for a typical channel:

R.F. freq. range = 2 / 18 GHz
 L.O. freq. range = 2 / 18 GHz
 I.F. freq. range = 4 / 8 GHz
 Conversion loss ~ 6 dB
 Ripple ~ +/- 0.7 dB
 R.F. matching ~ 9 dB
 L.O. matching ~ 9 dB
 I.F. matching ~ 13 dB
 RF/LO isolation ~ 25 dB
 RF/IF isolation ~ 25 dB
 RF/IF isolation ~ 30 dB

C). CONCLUSION *****

We have presented an original Triple Balanced Mixer for MMIC implementation. The MMIC technology offers several advantages: low production cost, improvements in electrical performances. The circuit has fully planar layout, so that the mixer is confined on only one side of the substrate. No plated holes are necessary, only air bridges will perform the function of "mode" filters.

BIBLIOGRAPHY

- (1). Ben R. Halford: "Trace phase states to check mixer design", Microwaves June 1980, pagg. 52, 60.

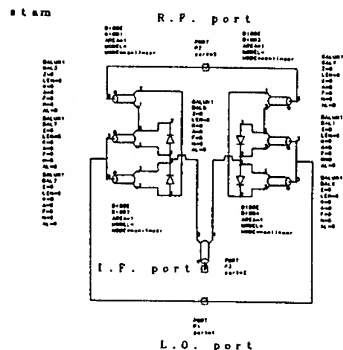


Fig. 1. Triple Balanced Mixer equivalent circuit.

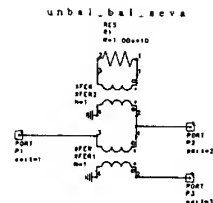


Fig. 2. Ideal Balun equivalent circuit.

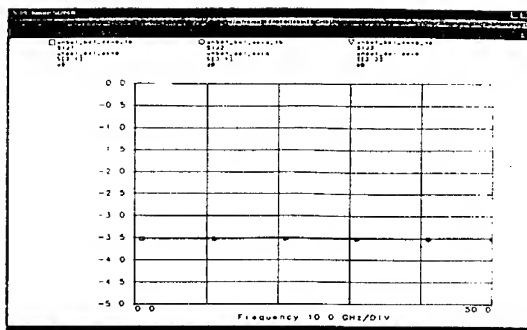


Fig. 3. Ideal Balun power division.

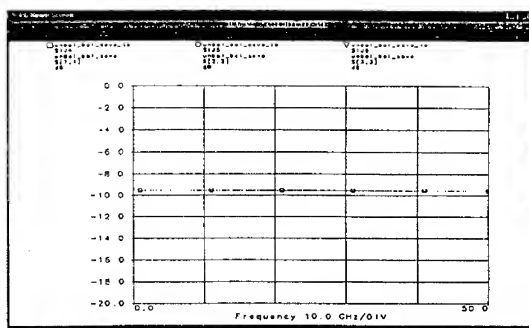


Fig. 4. Ideal balun input and output matching.

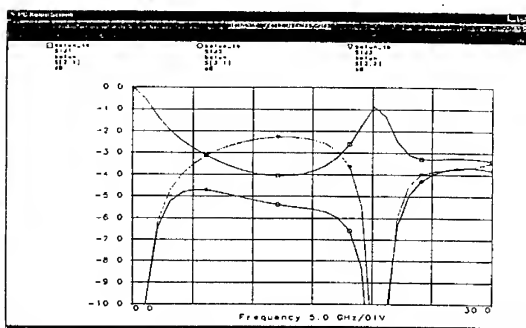


Fig. 5. Physical Balun power division.

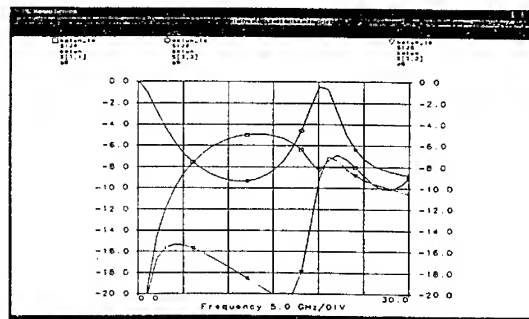


Fig. 6. Physical Balun input and output matching.

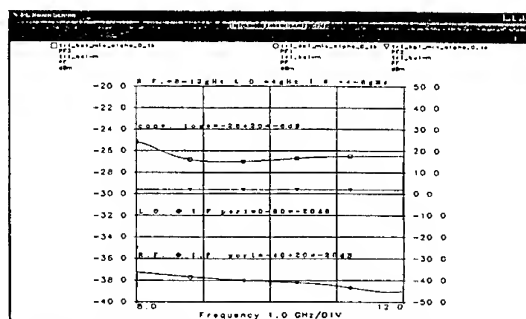


Fig. 7. I.F., L.O., R.F. @ output port.

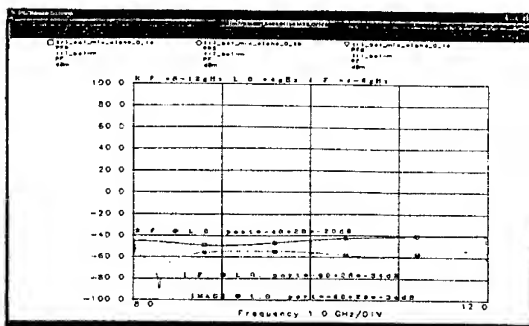


Fig. 8. I.F., R.F., Image @ L.O. port.

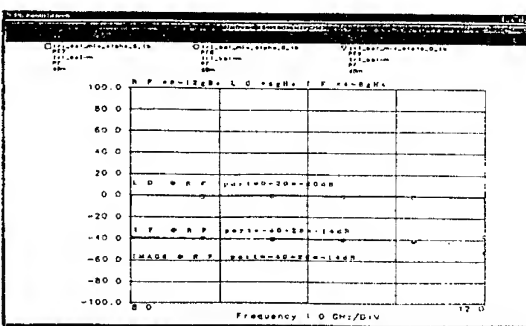


Fig. 9. I.F., L.O., Image @ R.F. port.

6 TO 18 GHz MMIC PHASE SHIFTER: A NEW HIGH PERFORMANCE SWITCH MESFET

A. MILANO, I. LEVIN, M. VERED

ELTA / ISRAEL AIRCRAFT INDUSTRIES, P.O.B. 330, ASHDOD, ISRAEL.

ABSTRACT

Multi-octave Phase Shifters are key items in E.W. systems. On the market only few MMIC items are available, whose performances are not good enough for some special application. The way how to improve the performances doesn't involve the circuit, which is pretty classical: improving the switching FET will lead to more significant achievements.

For the well known reasons, (1), we decided to use MESFET as switching elements. Therefore we designed together the Phase Shifter and its switching element, tailoring the two designs one on each other.

The main goals to the design were:

a). reduction of the "ON" resistances; b). reduction of "ON" capacitances.

We obtained the result at the expenses of the "OFF" state parameters, which exceeded the goal performances in the device we wanted to improve.

We performed the simulations using EESOF and SONNET C.A.D., for the circuits, and HELENA for MESFET simulations.

A). CIRCUIT DESIGN TOPICS

1). 180 DEG. BIT.

The circuit is based on two parallel branches, (fig. 1), switched in alternative by two couples of SPST switches. The two branches consist in two Lange couplers, whose outputs are loaded by two open circuits and two short circuits. The output signal comes from the reflection of each one of the two switched branches. The reference branch has been implemented with a second Lange coupler rather than a "PI" of transmission lines, (2), because of the easy implementation of the Lange coupler in MMIC technology. The simulation has been carried out taking in account the improved parameters of the new MESFET we designed. In fig 1) is shown the layout of the 180 degrees bit; in fig. 2), 3), 4), are depicted the electrical parameters of the same circuit.

2). 90 DEG., 45 DEG., 22 DEG., 11 DEG. BITS.

The basic circuit of all the mentioned bits is the same: a single Lange coupler, whose outputs are loaded by two reactive capacitive impedances.

Two SPST switches provide to connect and disconnect the capacitive load to the Lange outputs, so that the output signal comes from the reflection of the input signal, depending on the two states of the two SPST switches.

It has to be noticed that, disregarding the performances of the MESFET and the parasitic losses of the capacitors, the difference in transmission loss between the two states of each bit does depend on the phase shift; as a matter of fact, the highest difference in losses concerns the 90 degrees bit. It has also been noticed that the phase shift value and its precision do depend, both, on the value of the smaller capacitor, and the ratio between the bigger and the smaller capacitor. Therefore, in order to have a reliable and repeatable MMIC implementation, specific attention shall be paid to the capacitor layouts and their orientation on the GaAs substrate. Therefore we chose to implement the capacitors with the same orientation toward the anisotropic axes of the GaAs substrate. This way the fringing capacitances will be almost identical for the two components of the same bit, while the significant part of the capacitance will be proportional to its length.

In fig. 5),6),7), are shown the electrical characteristics of 90 deg. bit; fig. 8) shows the typical bit layout.

3). LINEAR PHASE, 0 / 7 DEG. BIT.

All the previous bit have constant phase versus frequency; the smallest bit has been designed as LINEAR PHASE versus frequency, in order to provide the possibility of correcting any reasonable cause of "unmonotonicity" of the Phase Shifter.

In fig. 9) we can see the schematic of the LINEAR PHASE bit; in fig. 10), 11), 12), are described the electrical performance of the same circuit.

B). STRUCTURE OF THE SWITCH MESFET.

Starting from an existing MESFET produced in ELTA's foundry, we studied the improvements specifically devoted to the switch application. The first choice has been the reduction of the gate length to 0.25 microns. As direct consequence we reduced the channel depth and length. It has been found that a double recess of the gate can improve the "ON" state resistances. In order to keep low the "gate lag", (3), the gate shall lay directly on the channel. Even though this condition is in contrast with the achievement of high breakdown voltage, a wide range of trade off solutions is available to the designer, (4). A buffer layer underneath the channel will provide high "OFF" resistance. In the following are summarized the main parameters of the MESFET we designed:

$t = 0.1 \mu\text{m}$; $Q_u = 2.3 \times 10^{12} / \text{cm}^2$; $N = 2.3 \times 10^{17} / \text{cm}^3$; $N_+ = 2 \times 10^{18} / \text{cm}^3$; $I_s = 310 \text{ mA/mm}$
 $IDSS = 200 \text{ mA/mm}$; $V_{\text{pinch off}} \sim 1.5 \text{ V}$; $V_{\text{br}} \sim 25 \text{ V}$.

C). CONCLUSION

We presented a multioctave Phase Shifter, intended to be more performant in comparison to the ones already available on the MMIC market. The major effort has been devoted to the design of a specifically devoted MESFET as switching element. The technological process of the MESFET is basically a "power process", but the vertical structure shall be dedicated to the specific application.

BIBLIOGRAPHY

- (1). Y. Ayasly: "Microwave switching with GaAs FET", Microwave Journal november 1982, pagg. 61, 74.
- (2). D. C. Boire et al.: "A 4.5 to 18 GHz Phase Shifter", IEEE MTT-S Digest 1985, pagg. 601, 604.
- (3). R. Yeats: "Gate slow transient in GaAs MESFET", IEEE-IEDM 1988, pagg. 842, 845.
- (4). S. H. Wimple: "Control of gate drain avalanche in GaAs MESFET", IEEE-TED june 1980, pagg. 1013, 1018.

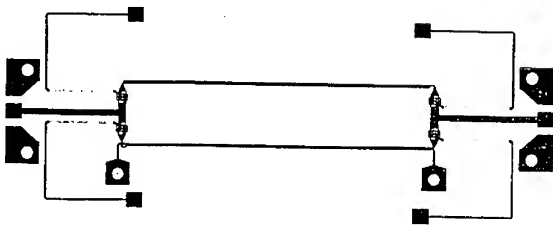


Fig. 1. 180 deg. BIT layout.

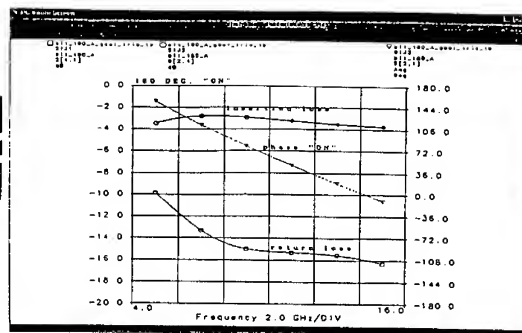


Fig. 2. 180 deg. BIT "ON" state: loss, phase, matching.

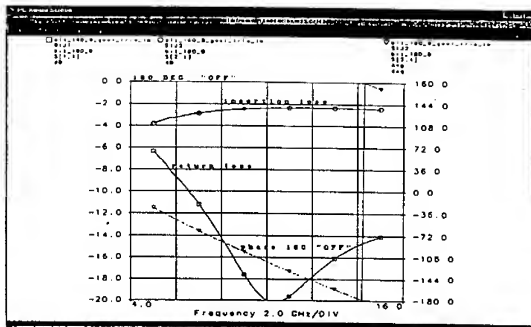


Fig. 3. 180 deg. BIT "OFF" state: loss, phase, matching.

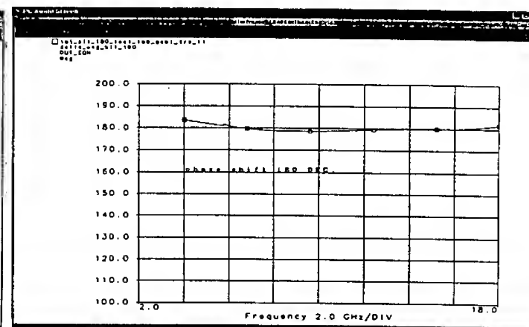


Fig. 4. 180 deg. BIT phase shift.

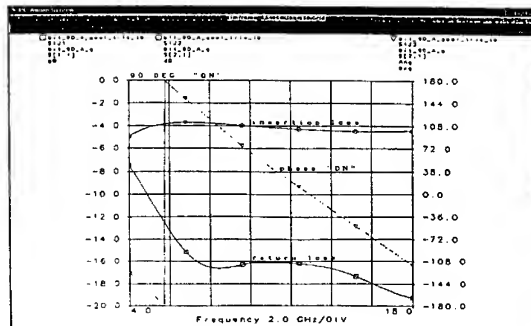


Fig. 5. 90 deg. BIT "ON" state: loss, phase, matching.

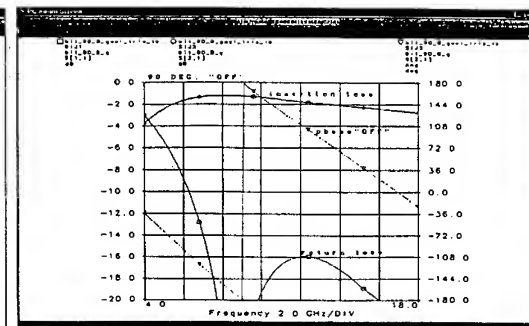
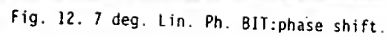
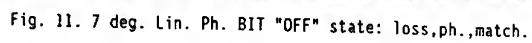
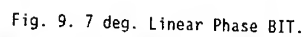
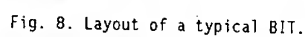
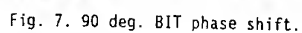


Fig. 6. 90 deg. BIT "OFF" state: loss, phase, matching.



Topic n/o 10 // application oriented // R. SHAVIT, BEN-GURION
UNIVERSITY, ISRAEL, tel. 07/6461508 fax. 07/6472949
D. GABBAY, M. GARZON, ELTA PO BOX 330 ASHDOD 77102 ISRAEL tel.
08/8572195, fax. 08/8572107.

Summation Topologies for High Power Amplifier based on MMIC Technology.

ABSTRACT—Implementation of Power Amplifiers, based on MMIC technology, requires a method for summing the power from several active devices like F.E.T's and H.B.T's.

This paper addresses the practical benefits and limitations of several in-phase summing topologies. The application for each power summing method is related to the device technology as well as to the performance goal. The decision strategy among the options yields a compromise among performance, size and circuit complexity.

The methodology is a function of the technological parameters of the specific chosen device, the manufacturing process, as well as the assets and limitations of the summing topology. The approach discussed in the paper has been developed in order to provide evaluation quality criteria for the required performance.

I. INTRODUCTION

The design of Power Amplifiers, based on MMIC, leads the designer to dedicate a lot of thought to the issue of power summation.

In this paper we present a brief description of few topologies to sum the power from which the designer can choose, depending on several parameters like frequency, power, power density, size of the active element, characteristics of the passive elements.

The topologies considered are:

- 1) Parallel Summation with a wide and long microstrip line connected in parallel to the outputs of the active devices on one side and on the opposite side the total output power is obtained as shown in Fig. 1.
- 2) Use of Microstrip Directional Coupler in which its two inputs are connected to two out of phase (90°) outputs from the active element.
At one of the coupler outputs the summed power is obtained while the other output is isolated [1] as shown in Fig. 2. Cascading few couplers achieves the power summation from all active elements outputs.
- 3) In case of unacceptable long microstrip lines in the previous topologies (1 & 2) there is a way to replace every microstrip by lumped elements [2]
Fig. 3 shows several topologies which the designer can choose from depending on biasing, DC blocking, level of the summation from the active element and the size of the coupler as shown in Fig. 4.

- 4) Use of equal-split Wilkinson power summation network [3] in microstrip form, which connects the output from the active element to one output which generates the summer power as shown in Fig. 5.
- 5) In case of unacceptable long line in the design of Wilkinson power summation network in the microstrip form, the lines can be replaced by lumped elements [4] as shown in Fig. 6.
- 6) A microstrip fanshape in which the active elements are connected to a radial shape line with one port output as shown in Fig. 7. At the output port, all inputs are summed with the same amplitude and phase.

II. DESIGN CONSIDERATIONS

The design considerations will be based on the size of the summation circuit and this will be directly dependent on the frequency.

In the lumped topology the consideration is on biasing the DRAIN's and blocking the DC from going out from the circuit.

the disadvantage of using lumped topology is the size of the passive elements but, even so, at certain frequency range the designed circuit will be smaller than the alternative which is the distributed one.

Another disadvantage to consider is the small bandwidth of the lumped circuit.

The advantage of using microstrip distributed circuit is its wide frequency range of response. Its disadvantage lies in the excessive length and width of the lines when designed at low frequency and high power.

Fig. 8 shows the concept of the size issue, when the circuit is designed with lumped elements.

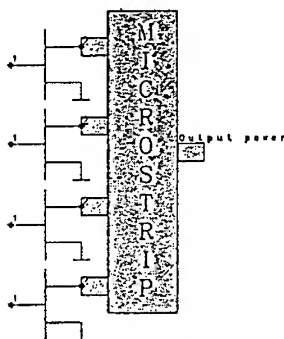


Figure 1: A parallel summation.

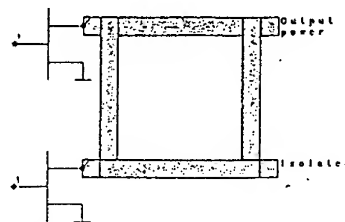


Figure 2: Directional coupler.

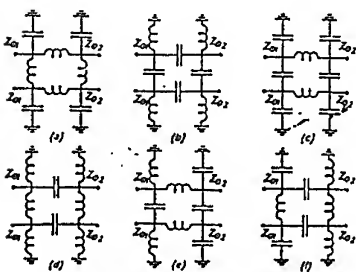


Fig. 3. Equivalent circuits of LE COD couplers.

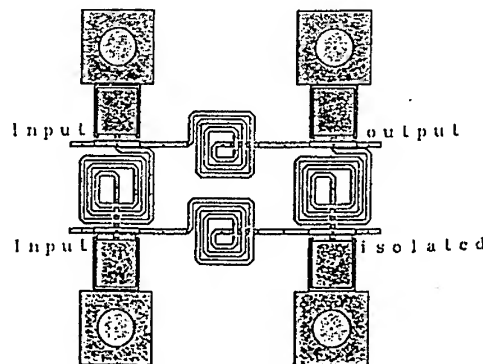


Figure 4: layout for lumped directional coupler.

III. DESIGN EXAMPLE

In this section we present an example of an amplifier designed in three configurations: 1) Wilkinson with lumped elements, 2) Parallel summation with a wide and long microstrip line, 3) Microstrip lines which connect two gates without any previous consideration.

The amplifier was designed for 15 GHz to 17GHz, and in Fig. 9 the reader should note that we present only the power summation part, and that all the configurations was match to the input and to the output with the same topologies for the output and for the input respectively.

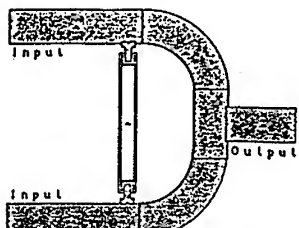


Figure 5: Equal split Wilkinson power summation

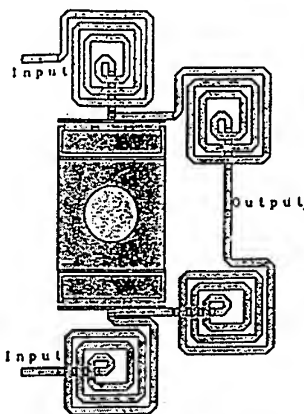


Figure 6: Wilkinson with lumped elements

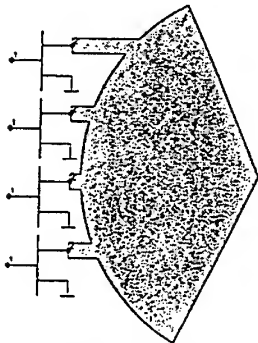


Figure 7: Fanshape summation.

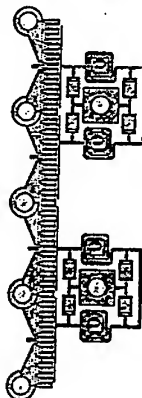


Figure 8: Power summation with lumped elements coupler.

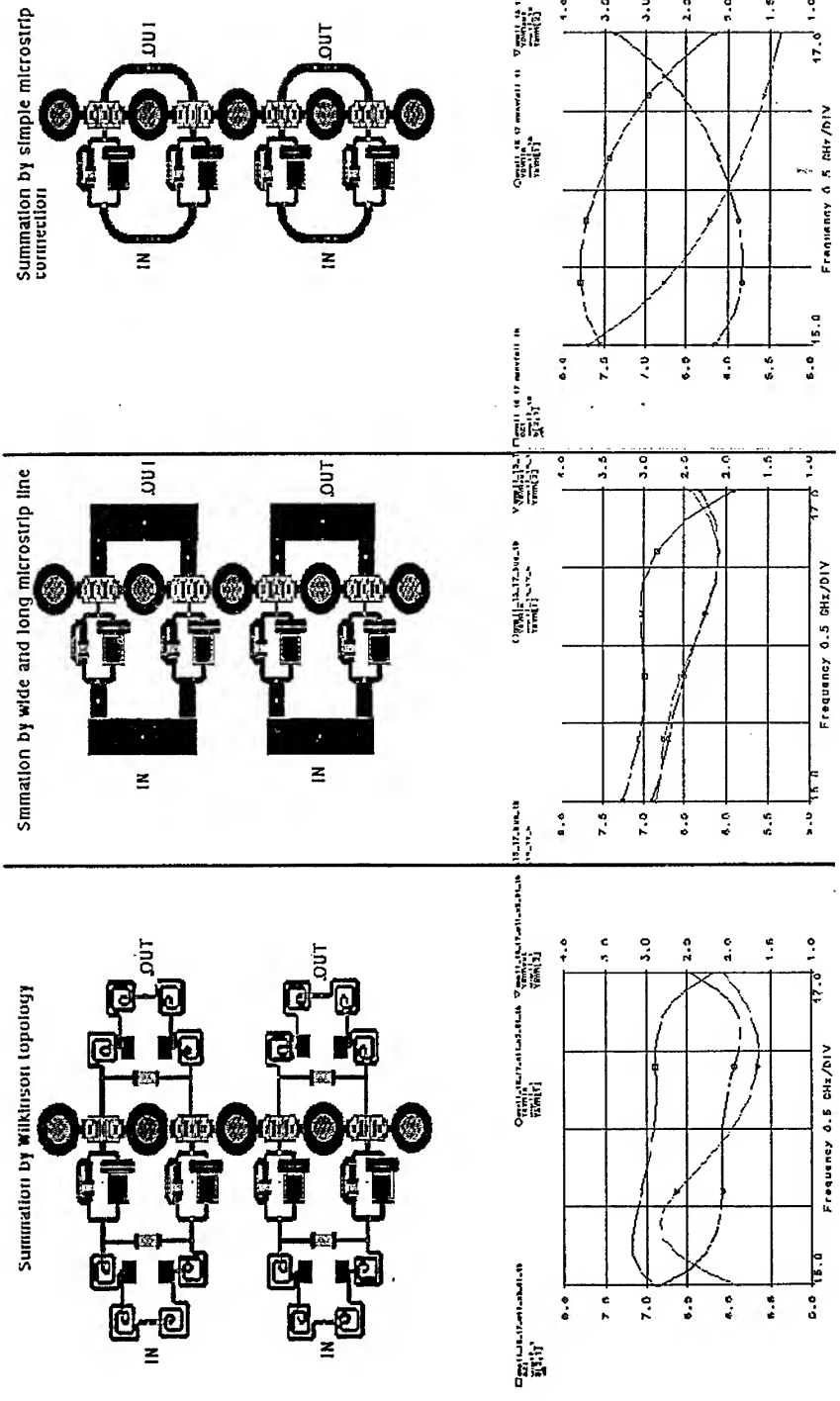


Fig. 9 Few topologies for an amplifier design example.

IV. CONCLUSION

Few topologies for Power Amplifier summation networks were presented. Advantages and disadvantages for each topology were discussed. The designer has several tools to realize the required performance of a Power Amplifier, based on critical parameters like frequency range, he can choose any of the presented topologies that will help his desired performance goal.

V. REFERENCES

- [1] D. M. Pozar, "Microwave engineering", Addison-Wesley Publishing Company., 1990.
- [2] R. W. Vogel, "Analysis and design of lumped-and lumped-distributed-element directional couplers for MIC and MMIC applications," IEEE Trans. Microwave Theory Tech. ,vol. 40, no. 2, pp. 253-262, Feb. 1992.
- [3] S. R. Mercer, "Linear simulator offer successful microstrip modeling for Wilkinson power-splitters," RF microstrip, pp. 38-48, Sep. 1996.
- [4] P. Vizmuller, "RF Design Guide: System, Circuit and Equations," Artech House., 1995.

AN AUTOMATED EMULATOR OF MOBILE SATELLITE LINK

César Briso, Rafael Herradon
Dpto. Ingeniería Audiovisual y
Comunicaciones
E.U.I.T. Telecomunicaciones.U.P.M.
Cra. Valencia Km 7 28031 Madrid
Tel: 34-1-336 77 98
FAX: 34-1 336 77 84
E-mail: Cbriso@diac.upm.es
E-mail: Rherradon@diac.upm.es

José I. Alonso
Dpto. Señales, Sistemas y
Radiocomunicaciones
E.T.S.I. Telecomunicaciones.U.P.M
Ciudad Universitaria s/n 28040 Madrid
Tel: 34-1-336 73 66 EXT. 481
FAX: 34- 1 336 73 62
E-mail: Ignacio@gmr.ssr.upm.es

ABSTRACT

This paper describes the specifications of an automated land mobile channel emulator developed. The system is able to reproduce most of the characteristics of the propagation channel between a real transmitter and receiver, allowing the study of mobile systems and the comprobation of propagation models in the laboratory. Fading, shadowing, doppler shift, noise increase, multipath and other effects like propagation delays and transponder non linearities can be emulated.

INTRODUCTION

Channel modelling and simulation is basic for the analysis and desing of mobile communications systems. On terrestrial communications, the radio mobile propagation channel has been widely studied, and there are many papers published about it, an example of which are (1)-(2). Also we can find some propagation models for satellite communications on (3)-(4) and their aplication to differents modulation schemas, (5)-(6). Those models has been applied to the development of channel simulators which allow the study of complete practical systems.

Normally systems analisys has been carried out by using propagation models for software simulation and confirmed with practical measurments. But now we propose the use of a channel emulator to analyze the especificacions of a system, appling the existing models. The behavior of a system can be study in different conditions and enviroments in the laboratory, without having to make measurements in a vehicle using the satellite.

The developed emulator is able to reproduce most of the characteristics of the propagation channel: fadding, shadowing, doppler shift, noise increase, multipath, and can also emulate satellite transponder effects as non linearities, phase noise and group delay, which is very important to analyze digital systems.

EMULATOR OPERATION

The equipment is designed to allow differents possibilities of use depending of the system we are working with. It permit to test from a mobil receiver to a full transmission system, and can be used in two different ways.

For example, if we are developing a mobile receiver to be used with an existing satellite, we can input the received signal from the satellite to the emulator, as can be seen on figure 1.a, and test the receiver in different conditions. Another possibility, fig. 1.b, is to use the system to emulate a transmit and receive system. In this case we need to emulate the up-link, satellite and down-link, which requires signal processing to reproduce the characteristics of the satellite as non linearities, group delay variation, phase noise and others.

SYSTEM DESCRIPTION

The system is composed of a RF Unit and a IF Processor, both controlled by a PC.

1.- RF Unit

This unit (Figure 3) basically is a down-converter followed by an up-converter where most of the propagation effects are added.

The down converter is a dual conversion receiver which converts the input signal from 850 to 1950 Mhz to an intermediate frequency centered on 9.5 Mhz with a bandwidth of 16 Mhz. This IF signal can be input to the IF Processor, to be sampled and processed, or can be connected directly to the up converter. The converter has an input attenuator to get the desired output IF level, and the reference frequency of the first local oscillator is generated with a DDS to get 1 Hz resolution.

The propagation effects of the channel are added in the up-converter. This module is a triple conversion circuit, which uses IF's of 9.5, 70 and 479 Mhz to get the final output in 850-1950 Mhz. The 70 Mhz stage is included to allow the use of a SAW filter to get a spurious free output. Finally phase variations and doppler shift are generated in the last frequency conversion using a local oscillator driven by a DDS which has 32 bits of frequency control and 12 bits of phase control. Fading is emulated using two variable attenuators and white noise is added to the output to get the desired noise figure.

All the circuits are controlled through the computer, using a parallel interface

2.- IF Processor

The signal processor basically is designed to reproduce the non linearities of the satellite and propagation delays of the channel. It uses a 12 bits A/D converter, which allows more than 60 dB of spurious free dynamic range, and processes 40Msp/s using a 10Mbit FIFO memory. The output of the FIFO goes to two RAM memories where the non linear characteristics of the satellite transponders are saved for the computer. Both RAM memories drive two 12 bits D/A converters, one for the IF output and the other to control a phase shifter to produce phase distortion.

With these characteristics the processor can generate: propagation delay from 1 to 250ms in 1ms steps, third order distortion (phase and amplitude) and group delay distortion. The schema of the processor can be seen on figure 4

3.-Personal Computer

All the system is controled through a 166 Mhz Pentium personal computer with software running under Windows.

The software generates all the calculations to reproduce the characteristics of the channel and programs the emulator through a paralell interface card. With this computer, is posible to get up to 1 Million changes per second, been most part of the time dedicated to produced random phase variations and fadding.

A propagation model is generaed with a file where the variations of attenuation, phase, frecuency and doppler shift are defined for their statistical models and distorsion and propagation delay are defined through equations..

MEASURMENTS

Some example of channel effects generated with the emulator are figure 5. where we can see Raileigh fadding, and figure 6 where we have uniform fase variations added to a carrier. On figure 7 we see the frecuency response of the 9.5 Mhz IF signal. This IF is sampled with the 12 bit A/D and so that it must be very flat and with very low distorsion (lower than 60 dB). Finally in Table 1 we have the principal characteristics of the system.

CONCLUSIONS

The emulator shown offers maximun flexibility to simulate satellite-to-ground transmission links and can be adecuated to every application. It can be easily integrated with other testing equipments to perform multipath fading emulation, BER testing and closed-loop validation of mobile transceiver. Also it can be adecuated to any other frecuency band using external up and down-converters.

AGREEMENTS

This work was supported by the proyects TIC96-0724-C06-01 and TIC96-1022-C02-02 of the national board of Cientific and Tecnological Research (CICYT)

BIBLIOGRAPHY

- [1] H.Suzuki "A statistical model for urban radio propagation,"
IEEE Trans. On Communications, vol. com-25, No. 7,pp 673-680, July 1977
- [2] T.Aulin, " A modified model for the fading signal ata a mobile radio channel",
IEEE Trans. On Vehicular Techn., vol. VT-28, No. 3, August 1979
- [3] Chun Loo, "A Statistical Model for land Mobile Satellite Link"
IEEE Trans. On Vehicular Techn., vol. VT-34, No. 3, August 1985
- [4] Chun Loo, "Digital Transmission Through a Land Mobile Satellite Channel"
IEEE Trans. On Comunications, vol. 38, No. 5, May 1990
- [5] Chun Loo, "Measurments and Models of a Land Mobile Satellite Channel and their Applications to MSK Signals". IEEE Trans. On Veh. Techn., vol.VT-35, No. 3, August 1987
- [6] Israel Korn. "GMSK with Limiter Discriminator Detection in Satellite Mobile Channel". IEEE Trans. On Comunications, vol. 39, No. 5, Jan. 1

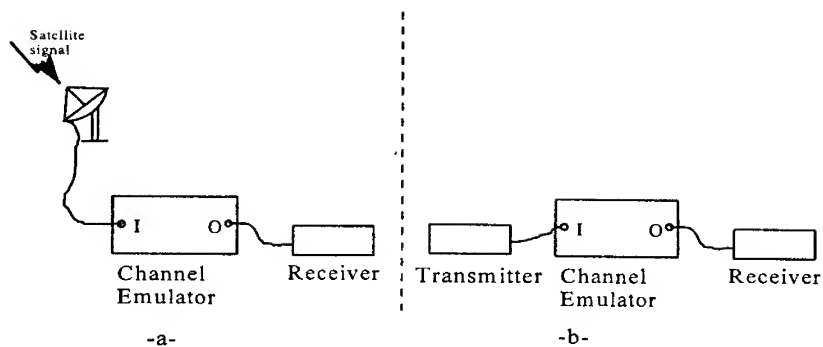


Figure 1. Emulator operation

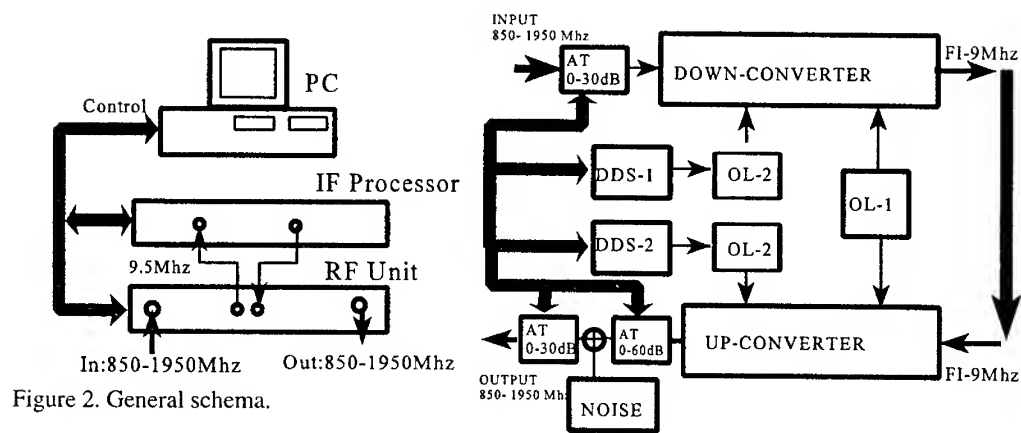


Figure 2. General schema.

Figure 3. RF unit.

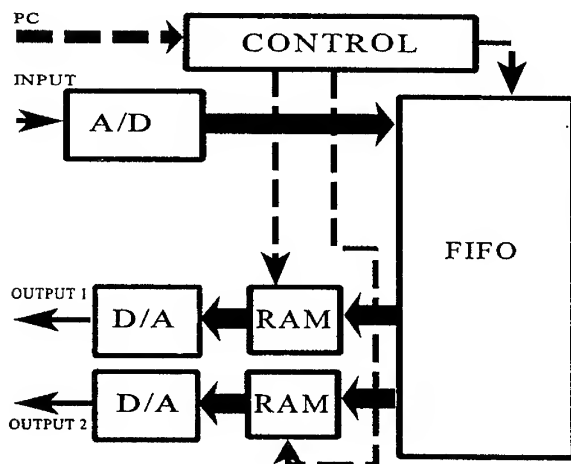


Figure 4. IF Processor.

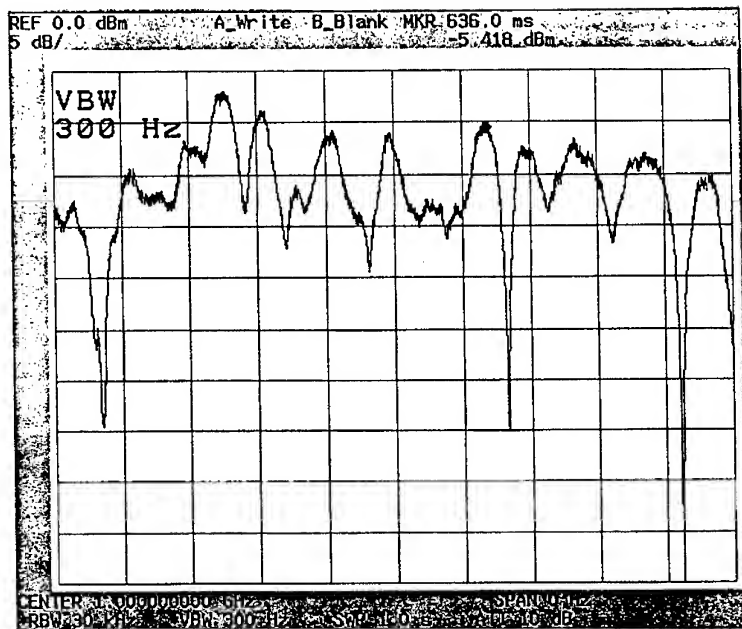


Figure 5. Raileigh fading generated with the emulator.

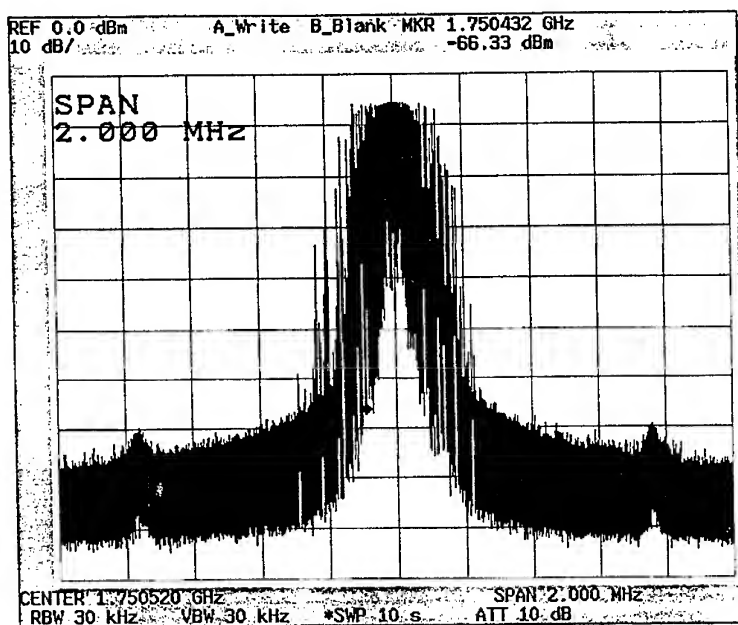


Figure 6. Phase variations added to a carrier, numerically generated with a DDS.

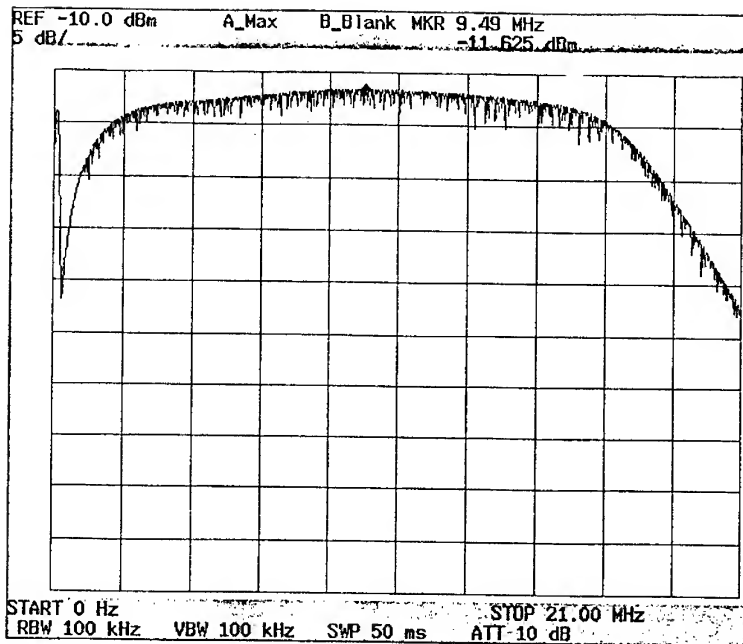


Figure 7. IF response of the emulator.

SPECIFICATIONS OF THE SATELLITE LINK EMULATOR	
- Input/output frequency range	850-1950Mhz
- Input/output bandwidth	16Mhz
- Fading	90dB
- Doppler shift	$\pm 10\text{Mhz}/1\text{Hz}$ steps
- Phase variation	360°
- Noise increase	30dB
- Propagation delays	1- 250ms /1ms steps
- Distorsion (phase and amplitud)	third order polinom
- Group delay	Programable

Tabla 1. Principal characteristics of the system.

Non-Linear Photonic Mixers For Up and Down-Converting Links Based on Mach-Zehnder Intensity Modulators.

J.M.Fuster, J. Marti, V. Polo

ETSI Telecomunicacion, Universidad Politecnica de Valencia
Camino de Vera s/n, 46071 Valencia (SPAIN)
Phone : 34-6-3877756, 34-6-3877307, Fax : 34-6-3877309
e-mail : jfuster@ddcom.upv.es, jmarti@ddcom.upv.es

Abstract :

Novel photonic mixer schemes for up and down-converting encounter a great number of applications in several areas of microwave-photonics interaction. Photonic mixers may be used for up and downconverting channels in subcarrier systems such as mobile communication signal distribution network, remote antenna fibre-optic links [Park et al (1)] as well as channel tuners in CATV systems [Gopalakrishnan et al (2)]. The novelty of the schemes presented in this work consists on requiring a RF source of a half, a third, a fourth, a fifth,... of the nominal frequency required for the up or down conversion. The approach is based on using the nonlinear behaviour at the modulator. We present the theoretical analysis, simulation and experimental demonstration of the approach in a remote antenna up-converting fibre-optic link application.

I. Introduction

The photonic mixer device is based on a Mach-Zehnder electro-optic modulator (MZ-EOM) configuration. MZ-EOMs have been studied previously as photonic mixers for up and down converting applications for quadrature bias (QB) [Lindsay et al (3), Gopalakrishnan et al (4)]. In this work, minimum transmission bias (MTB) is also considered, and non-linear effects occurring at the MZ-EOM are used for harmonic generation at the photonic mixer. In the QB case, the fundamental and odd harmonics of the local oscillator (LO) driving signal may be used for the up/down-conversion. Even order harmonics are employed in the MTB case. The use of LO harmonics eases LO frequency requirements. However, as the harmonic order increases, a higher LO power is required to drive the device to optimum performance. Moreover, optimum performance worsens slightly as higher harmonics of the LO driving signals are employed.

MZ-EOM based devices may be used as either electrical mixers (EM), using photonic technology for mixing electrical signals, or as hybrid electrical-photonic mixers (HEPM), for up/down-conversion of the electrical subcarriers carried onto the optical signal. Section II will cover modelling and parameter characterisation of EM devices, while HEPM devices will be discussed in section III. Section IV overviews a remote-antenna application which includes an HEPM for the up-conversion. A good agreement between theoretical and experimental results is obtained. Final conclusions are presented in section V.

II. EM analysis

Several mixing configurations may be considered for EM devices [4]. Figure 1 depicts a mixer scheme based on a single MZ-EOM. In this configuration, two electrical input signals enter the mixer through a laser diode and an external modulator, respectively. The electrical output signal is provided by the photoreceiver. This device may be considered as an electrical mixer black box, with two electrical inputs and one electrical output. Therefore, it may be characterised by current electrical parameters such as gain or noise figure. For the sake of simplicity, loads are supposed to be impedance matched to Z_0 .

Under these assumptions, the gain of the mixer is given by,

$$G_{mix} = GZ_0 k_{laser} \left(\frac{\Re P_{laser} J_n \left(\frac{\pi \sqrt{2P_{E,IN2} Z_0}}{V_\pi(f_{RF})} \right)}{4L_{EOM} L_{opt}} \right)^2 \quad (1)$$

where G is the photoreceiver amplifier gain, \Re is the photodiode responsivity, P_{laser} is the optical power launched by the laser diode, $k_{laser} = m_1^2/P_{E,IN1}$ is the laser diode response, $J_n(\cdot)$ is the n^{th} -order Bessel function of the first kind ($n = 1, 3, 5, \dots$ for QB and $n = 2, 4, 6, \dots$ for MTB), $V_\pi(f_{RF})$ is the half-wave voltage of the EOM at f_{RF} , L_{EOM} is the EOM insertion loss and L_{opt} is the optical loss due to connectors.

Figure 2 shows the dependence of the gain of the mixer as a function of the LO driving signal power level, both for QB and MTB, where n indicates the harmonic order of the LO source employed for the up/down conversion. As it can be observed from figure 2, the gain increases linearly as the LO power level, until the compression point is reached. Optimum performance occurs at the peak of the curve. As the harmonic order increases, the peak of the curve diminishes and the LO power level required for optimum performance augments.

The noise figure of the mixer is given by,

$$F_{mix} = \frac{N_{tot}}{kTB_{mix} G_{mix}} = \frac{N_{shot} + N_{ther} + N_{RIN}}{kTB_{mix} G_{mix}} = \frac{2qL_{EOM} L_{phot} \alpha}{kT k_{laser} \Re P_{laser} \left[J_n \left(\frac{\pi \sqrt{2P_{E,IN2} Z_0}}{V_\pi(f_{RF})} \right) \right]^2} + \frac{F_{phot} (4L_{EOM} L_{phot})^2}{k_{laser} Z_0 \left[\Re P_{laser} J_n \left(\frac{\pi \sqrt{2P_{E,IN2} Z_0}}{V_\pi(f_{RF})} \right) \right]^2} + \frac{RIN \alpha^2}{4kT k_{laser} \left[J_n \left(\frac{\pi \sqrt{2P_{E,IN2} Z_0}}{V_\pi(f_{RF})} \right) \right]^2} \quad (2)$$

where $n = 2, 4, 6, \dots$ and $\alpha = 1 - J_0 \left(\frac{\pi \sqrt{2P_{E,IN2} Z_0}}{V_\pi(f_{RF})} \right)$ for the MTB case and $n = 1, 3, 5, \dots$ and $\alpha = 1$ for the QB case.

F_{phot} is the photoreceiver amplifier noise figure, RIN is the laser diode relative intensity noise parameter and q is the electron charge.

Figure 4 shows the dependence of the mixer noise figure as a function of the LO power level. Optimum performance, that is minimum mixer noise figure, is achieved for the same LO power levels as at the former parameter.

As a conclusion, it may be pointed out that harmonic mixing is perfectly achievable with EM devices and allows the use of a LO source of lower frequency. However, the optimum performance worsens slightly and a higher LO power level is required.

III. HEPM analysis

The HEPM device performs signal mixing between a LO signal and an electrical signal modulated onto the optical carrier. These devices are normally used in fibre-optic links for up/down-converting subcarrier multiplexed signals previously modulated onto the optical carrier. They can not be characterised by electrical parameters, such as gain or noise figure. However, a couple of factors accounting for signal and noise contributions may be defined. The first factor (F1) is related with the signal power gain contribution and is given by the following expression,

$$F1 = \frac{J_n \left(\frac{\pi \sqrt{2P_{E,IN2} Z_0}}{V_\pi(f_{RF})} \right)}{L_{EOM}} \quad (3)$$

where $n = 1, 3, 5, \dots$ for QB and $n = 2, 4, 6, \dots$ for MTB. The second factor (F2) is related with the average optical power gain contribution and is given by,

$$F2 = \frac{1}{2L_{EOM}} \quad (4a)$$

$$F2 = \frac{1 - J_0 \left(\frac{\pi \sqrt{2P_{E,IN2} Z_0}}{V_\pi(f_{RF})} \right)}{2L_{EOM}} \quad (4b)$$

for QB and MTB, respectively.

Figure 5(a) and figure 5(b) show F1 and F2 as a function of the LO power level, respectively. F1 affects the up/down-converted signal level at the output of the link, while F2 affects the overall noise level of the fibre-optic link through the shot, RIN and EDFA contributions. A HEPM device with a high F1 and a low F2 will improve the overall carrier to noise ratio of the optical fibre link. F1 provides the same type of information in HEPM devices as gain does in EM devices. As it can be observed from figure 5(a), optimum performance occurs for certain values of the LO driving signal power level, and similar conclusions to those deduced for EM devices may be obtained. F2 is related with the input optical power at the photodetector. Figure 5(b) shows that the dependence of F2 with the LO power level is constant for the QB case, and mostly linear for the MTB case.

IV. Application

To demonstrate the proposed approach, an experimental setup for an up-converting fibre-optic link in a remote-antenna system using the HEPM structure is presented. The arrangement is shown in figure 6.

A 150 MHz subcarrier is used as the IF modulation signal of a tunable laser operating at 1550 nm whose optical power has been set to 0 dBm. An optical span of 46.2 Km SSMF and a 21 dB gain EDFA with a n_{sp} of 1.4 is employed. The MZ-EOM is driven by a RF synthesiser (HP83620A) whose frequency has been set to 1.65 GHz for the QB case and to 0.825 GHz for the MTB case. The upconverted RF signal at the receiver output is then at 1.8 GHz. For the MTB case the second harmonic generated by the nonlinear response of the MZ-EOM is selected.

The up-converted electrical signal power level (P_e) is given by,

$$P_{el} = \frac{GZ_L}{2} \left(\frac{\Re P_{laser} m_i G_{EDFA} F1}{2L_{fibre} L_{phot}} \right)^2 \quad (5)$$

where F1 is defined as in (3).

The noise modelling (including shot noise, thermic noise, RIN noise and EDFA noise) is based on the averaged incident optical power in the photodiode (P_a), which is given by,

$$P_a = \frac{2 \left(G_{EDFA} \frac{P_{laser}}{L_{fibre}} + (G_{EDFA} - 1) n_{sp} h f_0 \Delta \nu \right)}{L_{phot}} F2 \quad (6)$$

where F2 is defined as in (4a) for QB and as in (4b) for MTB.

Theoretical results and experimental measurements are shown in figure 7. Same detected power levels and signal to noise ratios are expected for a RF oscillator power level of 36 dBm both in QB and MTB cases, but with half the frequency requirements for the MTB case. This optimum RF oscillator power level may be lowered by using a EOM with a lower $V_{\pi}(\text{DC})$ parameter ($V_{\pi}(\text{DC}) = 19.1$ V in our experiment).

V. Conclusions

A novel scheme for microwave and mm-wave signal transmission through optical fibre links, based on the nonlinear behaviour of MZ-EOM based photonic mixers has been investigated. The upconverting techniques has been demonstrated for transmission of a subcarrier of 1.8 GHz along 46.2 km of standard fibre.

Acknowledgements

The authors would like to thank the Spanish Research Comission (CICYT) for funding the projects TIC96-0611 and TIC95-0859-C02-01.

References

- [1] Park J., Shakouri M.S., Lau K.Y.: 'Millimetre-wave electro-optical upconverter for wireless digital communications', *Electron. Lett.*, 1995, 31, 13, pp.1085-1086.
- [2] Gopalakrishnan G.K., Williams K.J., Moeller R.P., Howerton M.M., Burns W.K., Esman R.D.: 'Fibre-optic link architecture for microwave subcarrier transmission and reception', *Electron. Lett.*, 1995, 31, 20, pp. 1764-1765.
- [3] Lindsay A.C., Knight G.A., Winnall S.T.: 'Photonic mixers for wide bandwidth RF receiver applications', *IEEE Trans. Microwave Theory Tech.*, 1995, 43, 9, pp. 2311-2317.
- [4] Gopalakrishnan G.K., Burns W.K., Bulmer C.H.: 'Microwave-Optical Mixing in LiNbO₃ Modulators', *IEEE Trans. Microwave Theory Tech.*, 1993, 41, 12, pp. 2383-2391.

Figure Captions

Figure 1. Electrical mixer (EM) scheme

Figure 2. Hybrid electrical-photonic mixer (HEPM) scheme

Figure 3. Mixer gain versus LO power level in a EM device. n indicates the harmonic order of the LO driving signal employed for the mixing.

Figure 4. Mixer figure noise versus LO power level in a EM device. n indicates the harmonic order of the LO driving signal employed for the mixing.

Figure 5. F1 and F2 factors versus LO power level in a HEPM device. n indicates the harmonic order of the LO driving signal employed for the mixing.

Figure 6. Experimental setup for a remote-antenna fibre-optic up-converting link application

Figure 7. Detected power and system noise versus LO power in a fibre-optic upconverting link for a remote-antenna application. Circles and crosses correspond to experimental results and solid lines to simulation results.

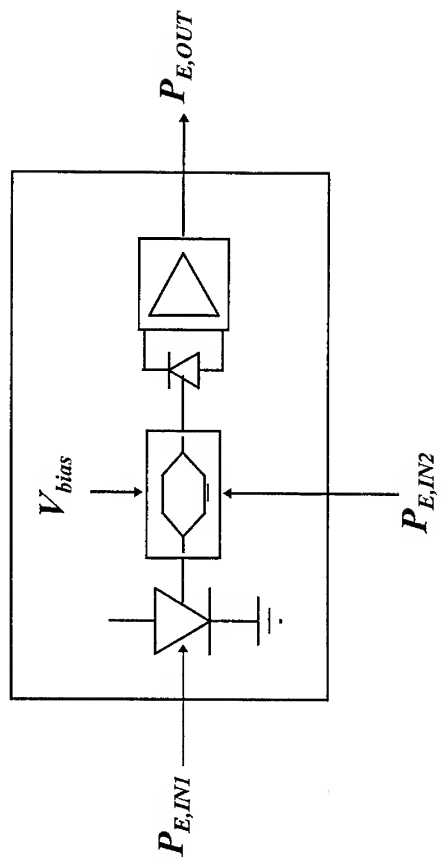


Figure 1

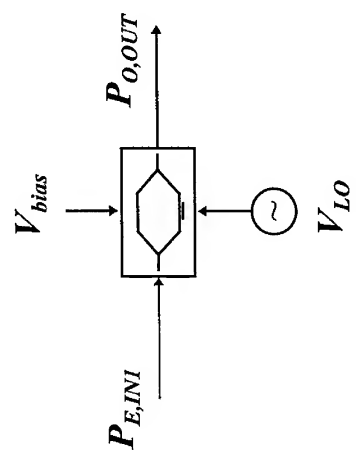


Figure 2

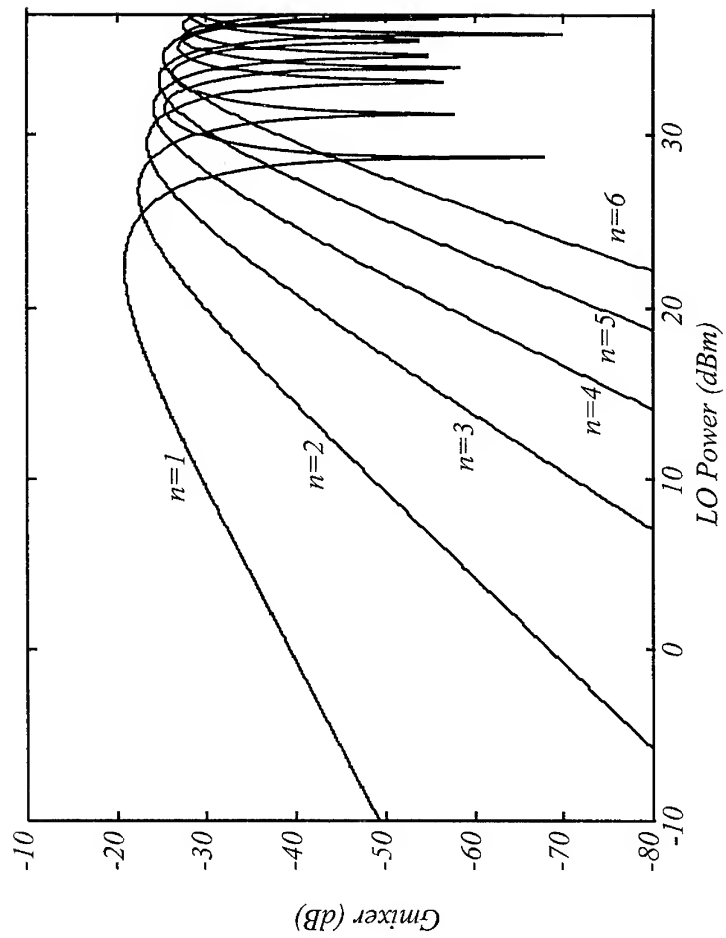


Figure 3

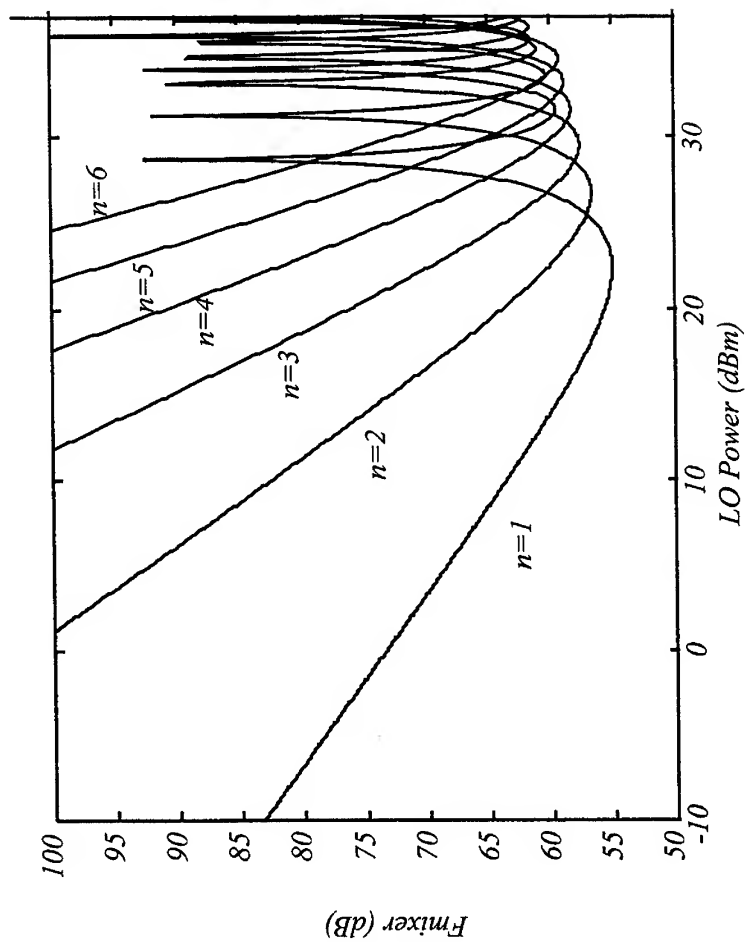


Figure 4

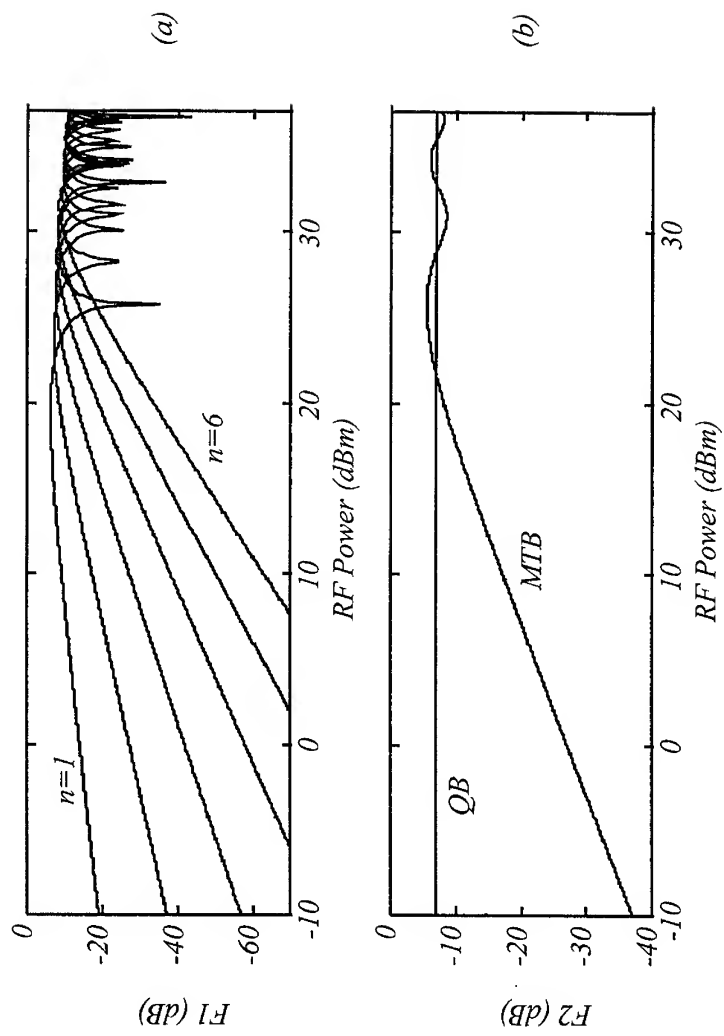


Figure 5

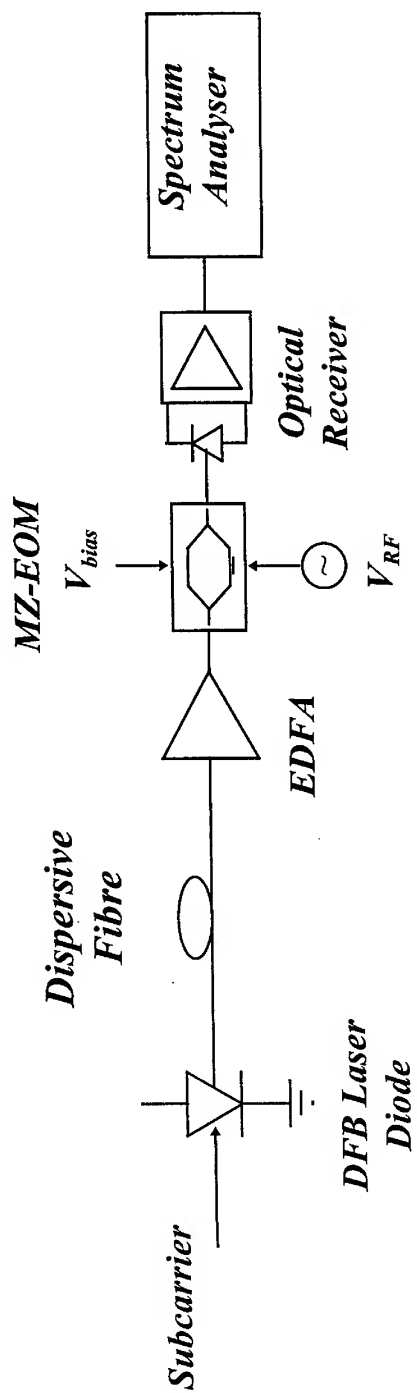


Figure 6

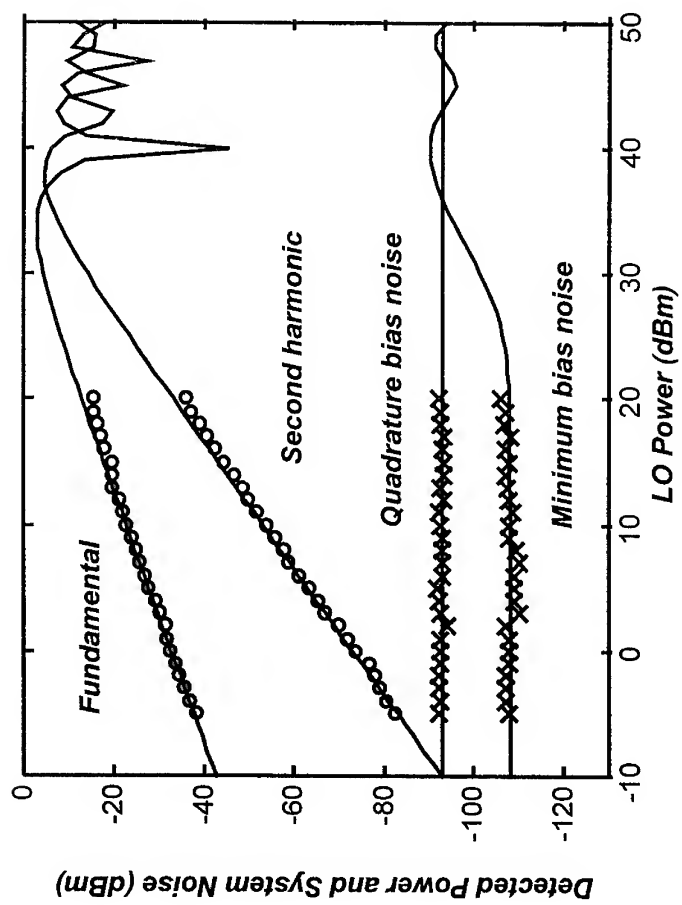


Figure 7

Efficient Determination of Nonlinear Microwave Circuits Operating Regions

I. Barbancho-Pérez and I. Molina-Fernández

Departamento de Ingeniería de Comunicaciones

E.T.S. Ingenieros de Telecomunicación, Universidad de Málaga

Málaga, Campus de Teatinos s/n, E-29071 Spain

Phone +34-5-2132587, Fax +34-5-2132027, e-mail: ibp@ic.uma.es

ABSTRACT

In this paper a direct method for obtaining the operating regions of nonlinear microwave frequency dividers in the frequency domain, is presented. This method is based on the enlargement of the Harmonic Balance system of equations with an additional equation which stands for the condition of turning and/or bifurcation points. This enlarged system of equations is solved in an efficient way by means of a suitable continuation technique. The proposed method has been applied to the analysis of a parametric frequency divider obtaining excellent results.

1. INTRODUCTION

Certain nonlinear microwave circuits, like frequency dividers and injection locked oscillators, can show different types of behavior: periodic, divided-periodic and quasi-periodic, depending on the amplitude and the frequency of the input signal. These circuits constitute an essential part of many communications systems, so the development of Computer Aided Design (CAD) tools able to analyze and predict the type of behavior that they are going to present is of fundamental importance Rizzoli and Neri (1). Particularly it is of great interest to develop methods to efficiently trace the circuit operating regions within already existing frequency domain based tools.

In this paper, efficient tracing of the operating regions of a microstrip parametric frequency divider Rizzoli and Lipparini (2) according to the amplitude and frequency of the input generator is performed by means of a direct frequency domain strategy. The aim of the method lies in that transition between different operating regions is determined by the appearance of turning and bifurcation points, that will be called from now on branch points, in the solution curves of the circuit depending on the interest parameters. This fact allows to enlarge the Harmonic Balance system of equations, that describes the circuit in the frequency domain, with a new equation which stands for the condition of turning and/or bifurcation points. Such enlarged system of equations, that directly describes the solution curve defined by the points where the circuit undergoes some change in its behavior, is solved in an efficient way by the application of a pseudoarclength continuation method Barbancho and Molina (3).

2. OPERATING REGIONS TRACING OF A NONLINEAR CIRCUIT

2.1 INDIRECT METHOD

A first approach to determine the operating regions of a nonlinear circuit, depending on the amplitude and the frequency of the input generator, consists in studying its behavior by means of tracing the solution curves according to only one parameter, like for example the power of the input generator, keeping the other parameter constant to a fixed value, for example fixing the generator frequency. This procedure has to be repeated for a certain set of frequency generator values in the rank of interest. This way of tracing the operating regions, that will be called indirect method, has been the most commonly used for the study of this type of circuits R. Quéré et al (4), J. Morales et al (5).

For tracing the circuit solution curves, the Harmonic Balance System of Equations (F_{HB}) describing the circuit in the frequency domain is formulated. This algebraic nonlinear system of equations can be written as

$$F_{HB}(X, \lambda = A_g) = 0 \quad (1)$$

where X stands for the Fourier coefficients of the N_x controlling variables and $\lambda = A_g$ is the generator amplitude, that is the parameter according to which the system (1) is solved. This system has $N = N_x(2N_H + 1)$ equations and N unknowns plus one parameter. The generator frequency ω_g is kept constant during the whole process.

While tracing this solution curve some typical phenomena of nonlinear dynamics, such as bifurcation or turning points, will appear. These points imply a change of the stability of the solution branch being followed, and so, they determine a possible jump between two different operating regions. Furthermore, the jacobian of the system of equations becomes singular at these points and this fact is an obstacle in the process of branch following. Continuation methods allow a solution curve depending on a parameter to be traced, locating and overcoming the obstacle presented for the appearance of a turning or bifurcation point in the solution curve. Different continuation methods, Rizzoli and Constanzo (6), Suárez et al (7), Hente and Jansen (8), (3), have been previously applied to overcome the appearance of turning points in nonlinear microwave circuit problems analyzed in the frequency domain. The switching parameter strategy, that is a local method consisting on interchanging the roles of the parameter and of one of the system unknowns in the neighborhood of the turning point, has been used to trace the solution curve of an injection-locked oscillator as a function of frequency (6) and to obtain the operating regions of a frequency divider (7). The pseudoarclength continuation method Keller (9), that is the one utilized in this paper, consists in adding a new equation and a new parameter so that in the solution curve according to the new parameter there is no turning point. With this equation, the new parameter $\lambda = s$ approximates the arclength along the solution curve. The introduction of this equation has two advantages:

in one hand it solves the problem of the turning points in a global way and in the other hand, as s contains information about the arclength along the solution curve, it gives invaluable information for the step-length control. This way, the new system of equations to be solved is

$$\begin{aligned} &F_{HB}(X, A_g) = 0 \\ &+ \\ &F_{par}(X, A_g, \lambda = s) = \left| \frac{dX}{ds} \right|^2 + \left(\frac{dA_g}{ds} \right)^2 - 1 = 0 \end{aligned} \quad (2)$$

where the generator amplitude has become an unknown. From (2), it has to be noticed that the parametrization equation involves the s -derivatives of X and A_g rather than these quantities themselves. This way the system of equations (2) has $N+1$ equations, $2(N+1)$ unknowns (the N Fourier coefficients, the generator amplitude and all their derivatives with respect to s) and one parameter. It follows that it will be necessary to approximate the s -derivatives in any way such that X and A_g become the unknowns and the resulting system of equations has only $N+1$ unknowns. Many approximations are possible and in Barbancho and Molina (10) some of them are presented. This method has been applied to analyze a tunnel-diode oscillator (8) and frequency dividers (3).

In figs.1-4, the solution curves of the frequency divider proposed in (2), traced depending on the amplitude of the input generator for a fixed frequency, are presented. The turning points (marked with **X**) that appear in the curves, were overcome by the continuation method without any difficulty. In the curves two types of branch points are found: I-type and D-type Kawakami (11). The I-type branch points, which correspond to bifurcation points (marked with **O**), establish the change from the periodic regime to the divided periodic regime (P-DP). With regard to the D-type branch points, even if all of them imply a change in the stability of the solution branch being followed and they involve a jump to other stable solution branch, not always this jump implies a change in the type of regime. As can be seen in figs.1-4, there are many turning points in which only jumps between divided periodic branch take place. When tracing the operating regions, the D-type branch points to be taken into account are those in which the jump between the divided-periodic and the periodic regime occurs. Such points has been labeled in the graphs as DP-P. It is worth to mention that when the dynamic of the circuits becomes complex and there are many simultaneous stable solution branches, the Harmonic Balance does not convey enough information to know exactly to which of the possible stable branches the circuit is going to jump. This fact makes sometimes necessary to resort to time domain simulations. Coming back to figs.1-4, if the point labeled as P-DP is considered, it can be observed that as the generator frequency is being modified, the generator amplitude for which the I-type branch point appears is changing, defining a curve in the generator frequency-amplitude plane. This curve establishes the change from the periodic regime to the divided periodic regime. The DP-P region can be analogously obtained, but further difficulties arise due to the great number of existing turning points, which make necessary a careful selection of the desired point to be followed. From previous comments it is clear that tracing the operating regions by means of the indirect method requires a large amount of solution curves, similar to those of figs.1-4, to be obtained for different values of the generator frequency. Note that this is a very inefficient procedure, from the numerical point of view, since for each figure to obtain one or two branching points all the intermediate points of the solution curve must be calculated. As it will be seen in the next section, the proposed method for tracing the operating regions avoids this unnecessary numerical overload by directly searching for the desired branching points.

2.2 DIRECT METHOD

An alternative method to calculate the branch points is to add to the Harmonic Balance system of equations another equation (F_{branch}) which stands for the condition of branch point, leading to an Enlarged Harmonic Balance system of equations (F_{EHB}). In this case, the generator amplitude is considered to be an unknown and the solution of such enlarged system will directly be the turning and bifurcation points. This new system of equations, with $N+1$ equations and $N+1$ unknowns can be written as

$$\begin{aligned} &F_{HB}(X, A_g) = 0 \\ &+ \\ &F_{branch}(X, A_g) = 0 \end{aligned} \quad -F_{EHB}(X, A_g) = 0 \quad (3)$$

With the system of equations (3), the generator amplitude values where a branch point appears can be calculated for each frequency value and in this case it is not necessary to calculate the whole solution branch. This method has two disadvantages: in one hand it needs a sufficiently good initial approach so that the Newton method converges, and in the other hand, as it was previously discussed, not all the branch points are relevant to obtain the circuit operating regions.

It must be noticed that, when solving (3) for different frequency values, the branch points are defining a solution curve in the frequency-amplitude plane, so the problem of calculating the branch points can be reconverted to a continuation problem and the F_{EHB} will be solved considering the generator frequency as a parameter, i.e.

$$F_{EHB}(X, A_g, \lambda = \omega_g) = 0 \quad (4)$$

The resolution of the system of equations (4) gives the generator amplitude values where a branch point appears, for each frequency value. From the numerical point of view, the problem of solving a system of equations depending on a parameter has to be faced again, so the same tool will be used: the pseudoarclength continuation method. In doing so equation (4) becomes

$$F_{EHB}(X, A_g, \omega_g) = 0 + F_{par}(X, A_g, \omega_g, \lambda = s) = \left| \frac{dX}{ds} \right|^2 + \left(\frac{dA_g}{ds} \right)^2 + \left(\frac{d\omega_g}{ds} \right)^2 - 1 = 0 \quad (5)$$

which is the system of equations to be solved for direct obtention of the circuit operating regions.

Going back to the branching equation (F_{branch}) of expression (3), it must be noticed that, in contrast to previously published methods in which a different equation is utilized depending on the type of branch point to be determined (7, 11), the direct method proposed in this communication uses the same equation to search for both kinds of branch points (I-type and D-type). In fact, the proposed branching equation looks for the singularity of the jacobian of the Harmonic Balance system of equations, using $\omega_g/2$ as the fundamental frequency, and it is imposed as

$$F_{branch}(X, A_g) = \frac{Min(SV)}{Max(SV)} = 0 \quad (6)$$

where $Min(SV)$ stands for the smallest singular value of the jacobian and $Max(SV)$ for the biggest. This way the system of equations (5) used for tracing the solution curves defined by both types of branch points is the same and only the initial solution (an I-type or a D-type point) for starting the continuation method needs to be changed.

From a practical point of view, obtaining the operating regions by means of equation (5) can only be fulfilled if an initial point of the desired solution curve is provided. However this can easily be done by following the next steps: i) fixed one of the two possible parameters to a constant value, the solution curve of the F_{HB} (2) according to the other parameter is traced and some branch points are obtained; ii) the points calculated in the previous step are used like initial values for the direct tracing of the branch solution curve solving the F_{EHB} (5). This is the technique that has been used in this paper. It should also be mentioned that all the sensibilities of the system of equations (5) are calculated in an analytical way Camacho and Martín (12), except for the ones of the branch equation (6), that are calculated in a numerical way. With this strategy, the jacobian of the system is calculated very efficiently.

3. OBTAINED RESULTS

The direct method for tracing the operating regions has been applied to the frequency divider proposed in (2). The frequency divider has been analyzed in a 800MHz band centered at 2.375GHz, frequency for which the divider was designed. Figs.5-6 show the solution curves determined by the I-type and D-type branch points, respectively, in the generator amplitude-frequency plane. Both curves has been directly traced applying the pseudoarclength continuation method to the enlarged Harmonic Balance system of equations F_{EHB} . Due to the fact that the circuit behavior changes considerably with the generator frequency and amplitude, it was not possible to trace the whole branching curves with only one initial solution, and it was necessary to calculate some intermediate points from which to restart the continuation method. Particularly, 5 starting points were needed for the I-type solution curve and 6 for the D-type one. In spite of that, the computational efficiency of the direct method for tracing the operating regions is clear if one takes into account that the computational effort needed for calculating only one branch point with the F_{HB} is comparable with the one needed for tracing the whole curve of branch points by means of the direct method.

Figs.7-10 clearly illustrate the reason why the direct method cannot trace the whole region in a single shot and some restarting points must be provided. In fig.7, obtained for a generator frequency $f_g=2.69$ GHz, a turning point (labeled $A_{2.69}$) exists in the divided periodic path which corresponds to a D-type branch point. When frequency is increased this points suddenly disappears and two new D-type turning points appear in a different part of the curve (labeled $C_{2.72}$ and $B_{2.72}$ in fig.8). As frequency is further increased (figs.9-10), these new points move gradually away. In fig.11 a magnified piece of the D-type solution curve of fig.6, corresponding to this frequency band, is shown and the previously mentioned A, B and C points are indicated. From this figure it becomes evident that it is not possible for the direct method to jump from the left side of the solution curve (which contains point A), to its right side (where the B and C points are located), and therefore it is necessary to search for a new starting point to follow with direct tracing of the curve.

On other hand, it can be seen in figs.5-6 that around $f_g=2.48$ GHz the direct method is not able to trace any branch curve. This fact can be

explained with the help of fig.12 in which complex behavior shown by the circuit in this part of the frequency band can be appreciated.

4. CONCLUSIONS

A novel direct method to efficiently trace the operating regions in a frequency divider, that is computationally more efficient than previously applied indirect methods, is presented. The proposed branching equation (F_{branch}), which looks for the singularity of the jacobian, allows to treat all types of branching points with a unique system of equations. This system of equations is then solved by means of a pseudoarc-length continuation method. This strategy has been applied to the analysis of a parametric frequency divider obtaining excellent results. To our knowledge, the advantages of using a continuation method for the direct obtention of microwave circuits operating regions, had not been exploited previously.

ACKNOWLEDGEMENTS

The authors acknowledge the financial support provided by the spanish Comisión Interministerial de Ciencia y Tecnología under Grant No.TIC96-1072-C04-04.

REFERENCES

- [1] V. Rizzoli, A. Neri, "State of the art and present trends in nonlinear microwave CAD techniques", 1988, IEEE Trans. Microwave Theory Tech., vol. 36, no. 2, pp. 343-365.
- [2] V. Rizzoli, A. Lipparini, "General stability analysis of periodic steady-state regimes in nonlinear microwave circuits", 1985, IEEE Trans. Microwave Theory Tech., vol.33, no. 1, pp. 30-37.
- [3] I. Barbancho-Pérez, I. Molina-Fernández, "Predictor strategies applied to nonlinear circuit analysis", 1996, 8th Mediterranean Electrotechnical Conf., vol. III, pp.1419-1422.
- [4] R.Quéré, E.Ngoya, M. Camiade, A. Suárez, M. Hessane, J. Obregón, "Large Signal Design of Broadband Monolithic Microwave Frequency Dividers and Phase-Locked Oscillator", 1993, IEEE Trans. Microwave Theory Tech., vol. 41, no. 11, pp. 1928-1938.
- [5] J. Morales, A. Suárez, E. Artal, R. Quéré, "Global stability analysis of self-oscillating mixers", 1995, 25th European Microwave Conf., pp.1216-1219.
- [6] V. Rizzoli, A. Constanzo, "Automatic generation of the solution path of a parametrized nonlinear circuit in the presence of turning points", 1994, Microwave and Optical Technology Lett., vol. 7, no. 6, pp. 271-274.
- [7] A. Suárez, J. C. Sarkissian, R. Sommet, E. Ngoya, R. Quéré, "Stability analysis of analog frequency dividers in the quasi-periodic regime", 1994, IEEE Microwave and Guided Lett., vol. 4, no. 5, pp. 138-140.
- [8] D. Hente, R. H. Jansen, "Frequency domain continuation method for the analysis and stability investigation of nonlinear microwave circuits", 1986, IEE Proc., vol. 133, no. 5, pp. 351-362.
- [9] H. B. Keller, "Numerical solutions of bifurcation and nonlinear eigenvalues problems", in "Applications of Bifurcation Theory" edited by P. H. Rabinowitz, 1977, Academic Press, pp. 359-384.
- [10] I. Barbancho Pérez, I. Molina Fernández, "Análisis de un divisor paramétrico de frecuencia en línea microstrip mediante reparametrización del sistema de ecuaciones", 1995, Actas del X Simposium Nacional de la U.R.S.I, pp. 969-972.
- [11] H. Kawakami, "Bifurcation of periodic responses in forced dynamic nonlinear circuits: Computation of bifurcation values of the system parameters", 1994, IEEE Trans. Circuits and Systems, vol. 31, no. 3, pp. 248-260.
- [12] C. Camacho-Peñalosa, E. Martín-Funke, "On the harmonic balance analysis of almost-periodic autonomous nonlinear circuits with dynamic nonlinear characteristics", 1992, IEEE Microwave and Guided Lett., vol. 5, no. 1, pp. 35-38.

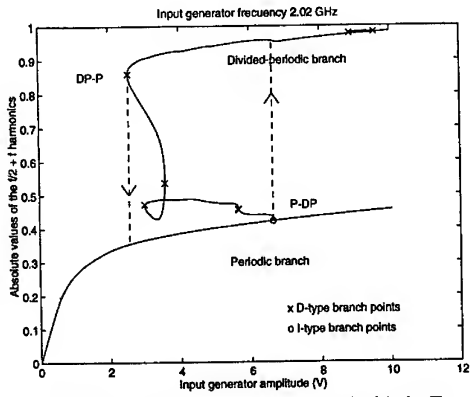


Fig.1. Solution curve for 2.02 GHz solved with the F_{HB} .

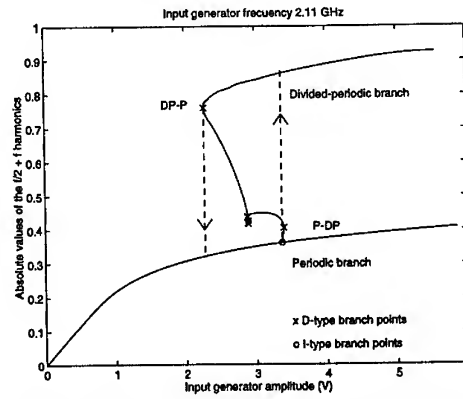


Fig.2. Solution curve for 2.11 GHz solved with the F_{HB} .

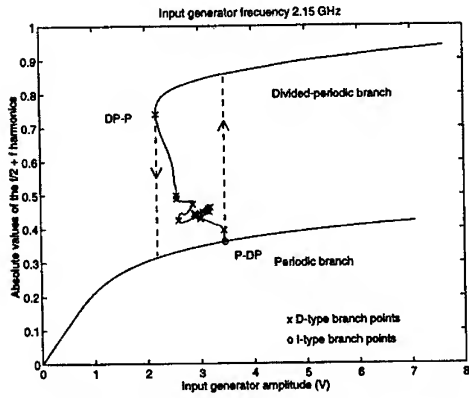


Fig.3. Solution curve for 2.15 GHz solved with the F_{HB} .

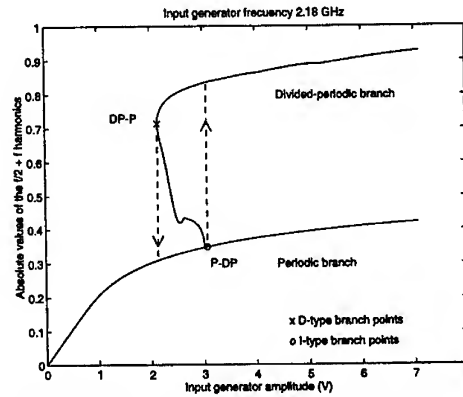


Fig.4. Solution curve for 2.18 GHz solved with the F_{HB} .

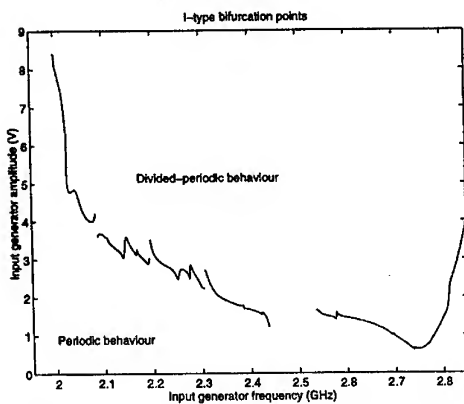


Fig.5. I-type branch points calculated with the direct method (F_{EHB}).

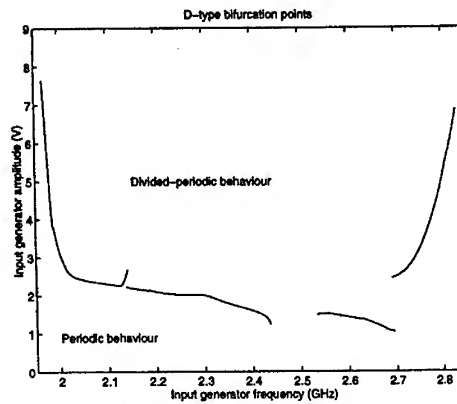


Fig.6. D-type branch points calculated with the direct method (F_{EHB}).

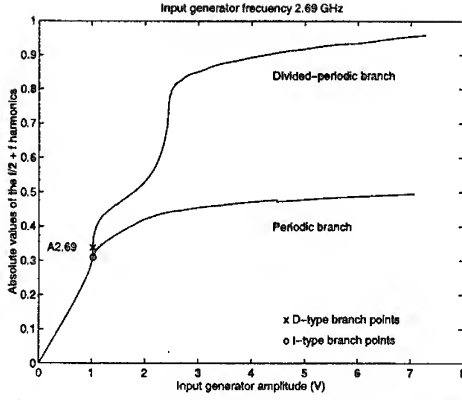


Fig.7. Solution curve for 2.69 GHz solved with the F_{HB} .

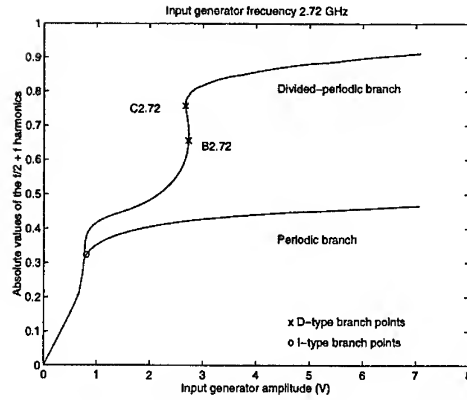


Fig.8. Solution curve for 2.72 GHz solved with the F_{HB} .

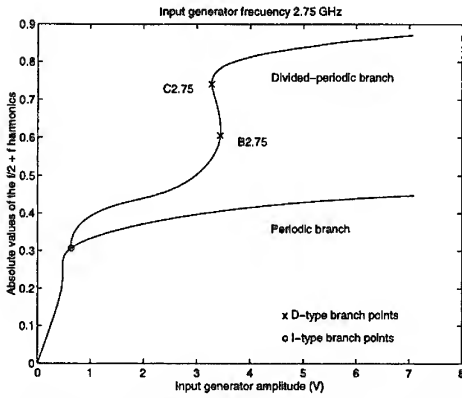


Fig.9. Solution curve for 2.75 GHz solved with the F_{HB} .

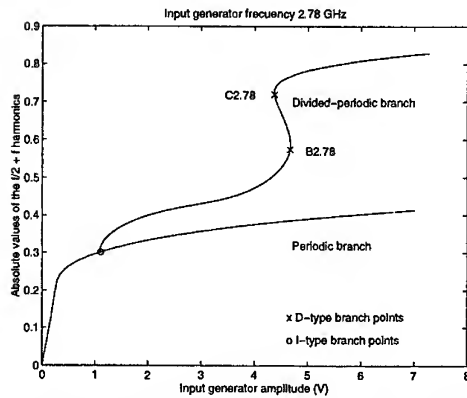


Fig.10. Solution curve for 2.78 GHz solved with the F_{HB} .

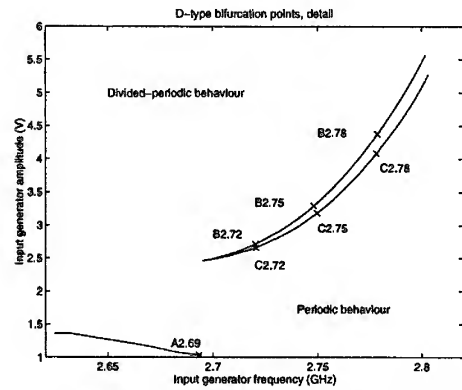


Fig.11. Detail of the D-type branch points curve calculated with the direct method (F_{HB}).

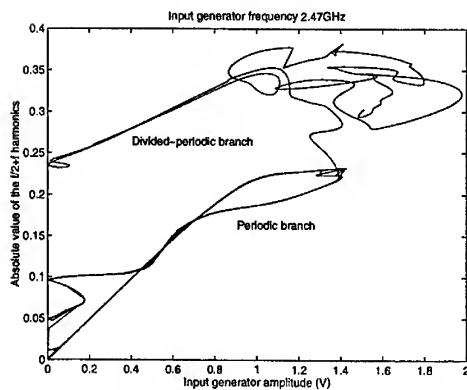


Fig.12. Solution curve for 2.47 GHz solved with the F_{HB} .

Wideband analytical model of an open-ended microstrip line under illumination

M. Serres, I. Huynen, A. Vander Vorst
Microwave Laboratory
Université Catholique de Louvain, Bâtiment Maxwell
B-1348 Louvain-la-Neuve, Belgium
Fax: +32 10 47 87 05; Tél: +32 10 47 40 20
serres@emic.ucl.ac.be

Abstract

This paper describes a new model for an open-ended microstrip line under illumination for the design of optically-controlled microwave devices. The model gives an analytical expression of the load impedance of the open circuit as a function of the line geometry and the electrical parameters of the substrate on which it is manufactured. Measurements are made to validate the model over a wide frequency range and show a very good agreement between modelling and experiment.

I. Introduction

Since the last fifteen years, optical control of microwave devices is a growing topic of research. These devices can be separated into two categories : the active and passive devices. In this work, we are interested in a passive device and more particularly, a microstrip open circuit (figure 1). This microwave element is widely used for building more complex microwave devices. Knowing the behaviour of this element should enable us to simulate and to design easily optically controllable microwave devices.

II. Description of the model

When the end region of the line is illuminated, electron/hole pairs are generated in the semiconductor substrate. The presence of these new free carriers modifies the microwave behaviour of the open circuit. The observable effect of the light penetration is the modification of the input reflection factor. It is reasonable to suppose that the line itself is not influenced by the illumination. The variation of the input reflection factor due to the illumination is thus modelled by a variable load placed at the end of the microstrip line. The importance of the phenomenon depends as well on the light beam as on the substrate characteristics. All these specifications have thus to be integrated in the model.

The calculation of the load impedance is based on the plasma theory which gives an expression of the complex permittivity as a function of the photogenerated carriers concentration present in the substrate. Thanks to this expression, the model takes into account all the parameters influencing the generation phenomenon.

The equations are derived in [1] and give :

$$\varepsilon_p = \varepsilon_r - \sum_i \frac{n_i q^2}{\varepsilon_0 m_i^*} \frac{\tau_i^2}{(1 + \omega^2 \tau_i^2)} - j \sum_i \frac{n_i q^2}{\varepsilon_0 \omega m_i^*} \frac{\tau_i}{(1 + \omega^2 \tau_i^2)}, \quad (1)$$

where $i = 0, h$ and e . The doping concentration is n_0 , while n_h and n_e are respectively the photogenerated hole and electron concentrations. The mean time between two collisions and the effective masse are denoted τ_h and m_h^* for holes and τ_e and m_e^* for electrons.

The expression of ε_p is then introduced in the displacement current equation to get an equivalent conductivity :

$$J = j\omega \varepsilon_0 \varepsilon_p E = \sigma E. \quad (2)$$

The load impedance can be found by integrating the conductivity in the volume where the electromagnetic fields exist :

$$\frac{1}{Z'} = \iint_S \sigma dS, \quad (3)$$

$$Z_{load} = \int_L Z' dl. \quad (4)$$

Making some assumptions on the carrier distribution the integration leads into an analytical expression. In this case, the concentration decays exponentially with depth and is considered as uniform over the surface :

$$n = n_{max} e^{-\frac{z}{z_0}}, \quad (5)$$

where z_0 is the diffusion length.

With this carrier distribution in the substrate, the load impedance reduces to :

$$Z_{load} = \frac{L}{C_1} + \frac{z_0}{C_1} \ln\left(\frac{C_1 + C_2 e^{-\frac{L}{z_0}}}{C_1 + C_2}\right), \quad (6)$$

where the expressions C_1 and C_2 are given in the appendix.

III. Validation of the model

A comparison with published measurements [2] has been made. Despite of the very narrow band of frequencies, it has shown good agreement between simulation and measurement. We have thus carried out measurements to validate the model over a wider band of frequencies.

A set of microstrip lines have been designed and manufactured on a silicon substrate to be measured by a network analyser. The TRL calibration fixes the reference planes at the middle of the “thru” element. The reference impedance is the characteristic impedance of the microstrip line but cannot be determined by the calibration procedure. An estimation of the complex characteristic impedance is calculated using the technique described in [3].

The measured scattering parameters S_{11} with and without illumination are depicted in figure 2. It is possible from these parameters to calculate the input impedance of the open-ended microstrip line. Figure 3 shows the change of the input impedance due to the illumination and suggests to modify the value of the reference impedance to bring the effect of the light to the fore. The scattering parameters computed from measured ones using a reference impedance of 20Ω are drawn in figure 4. The measured scattering parameters are not corrupted but simply differently presented. This representation let appear a shift in the phase of S_{11} already observed in [2] that was not visible in figure 2.

Finally, the figures 5 and 6 show the comparison between the simulation and the measurement with and without illumination. In the two cases the solid curve follows very closely the measurement points over the whole frequency band. The model gives thus a very good prediction of the open-ended microstrip line behaviour under illumination.

IV. Conclusion

We have presented an analytical model of the load placed at the end of an open-ended microstrip line on doped semiconductor substrate. This model will offer very interesting applications for the design of optically-controlled microwave devices. The first advantage of this model is the short calculation time even for a wide band of frequencies, due to its analytical expression. The second one resides in the fact that all the parameters of the model are physical. In addition, the measurements have shown that it is valid over a wide frequency range.

V. Appendix

$$C_1 = \pi R^2 \left[j\omega \epsilon_0 \epsilon_r + \frac{q^2 n_0 \tau_h}{m_h^* (1 + \omega^2 \tau_h^2)} - j\omega \frac{q^2 n_0 \tau_h^2}{m_h^* (1 + \omega^2 \tau_h^2)} \right]$$

$$C_2 = n_{\max} \pi R^2 q^2 \left[\left(\frac{\tau_h}{m_h^* (1 + \omega^2 \tau_h^2)} + \frac{\tau_e}{m_e^* (1 + \omega^2 \tau_e^2)} \right) - j\omega \left(\frac{\tau_h^2}{m_h^* (1 + \omega^2 \tau_h^2)} + \frac{\tau_e^2}{m_e^* (1 + \omega^2 \tau_e^2)} \right) \right]$$

VI. References

- [1] C. H. Lee, P. S. Mak and A. P. DeFonzo, "Optical control of millimetre-wave propagation in dielectric waveguides," *IEEE J. Quant. Electron.*, vol. 16, n°3, pp. 277-288, 1980.
- [2] H. Shimasaki and M. Tsutsumi, "Reflection characteristics of optically-controlled microwave through an open-ended microstrip line," *IEICE Trans. Electron.*, vol. E76-C, n°2, February 1993.
- [3] R. B. Marks and D. F. Williams, "Characteristic impedance determination using propagation constant measurement," *IEEE Microwave and Guided Wave Letters*, vol. 1, n°6, June 1991.

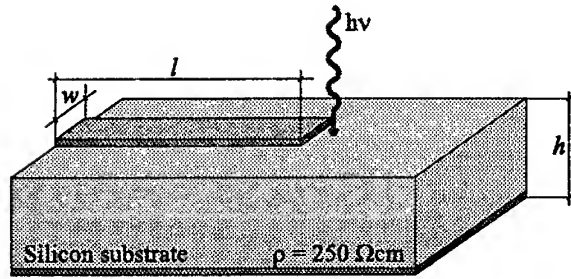


Figure 1 : View of the open-ended microstrip line under illumination. The dimensions are : $w = 400 \mu\text{m}$, $h = 280 \mu\text{m}$ and $l = 8.655 \text{ mm}$. The illumination power equals 20 mW at $\lambda = 685 \text{ nm}$.

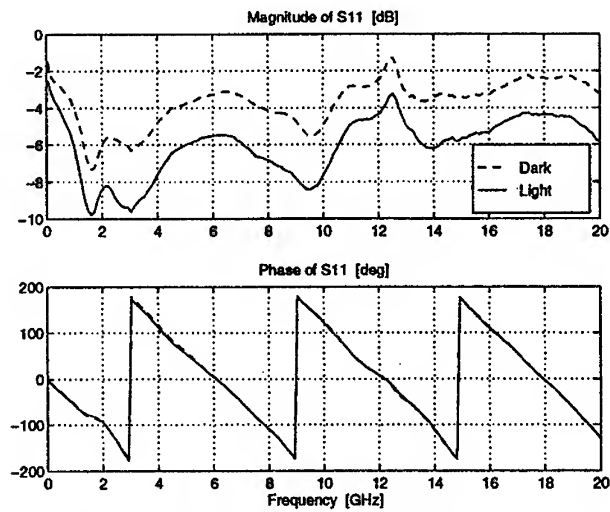


Figure 2 : Measured scattering parameter S_{11} of the open-ended line with and without illumination. The reference impedance equals the characteristic impedance of the microstrip line.

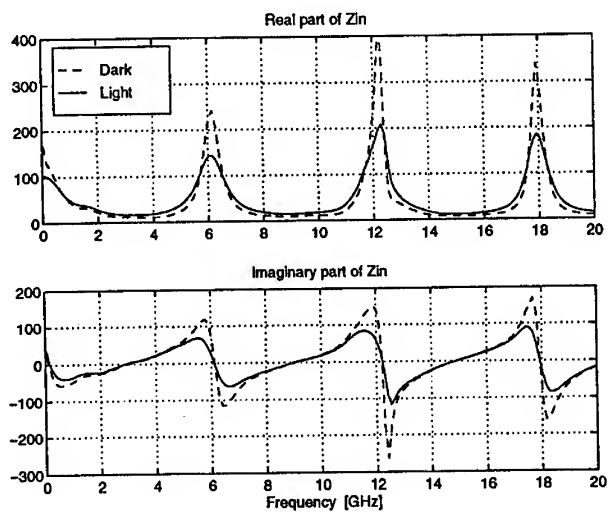


Figure 3 : *Input impedance of the open-ended line with and without illumination, extracted from measured scattering parameters.*

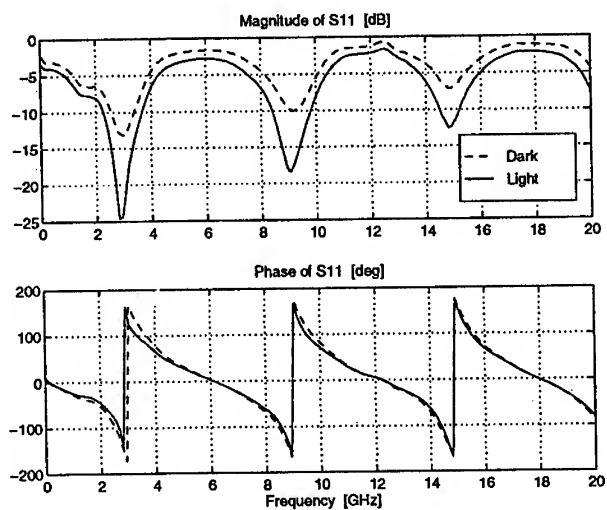


Figure 4 : *Measured scattering parameter S_{11} of the open-ended line with and without illumination. The reference impedance equals 20Ω .*

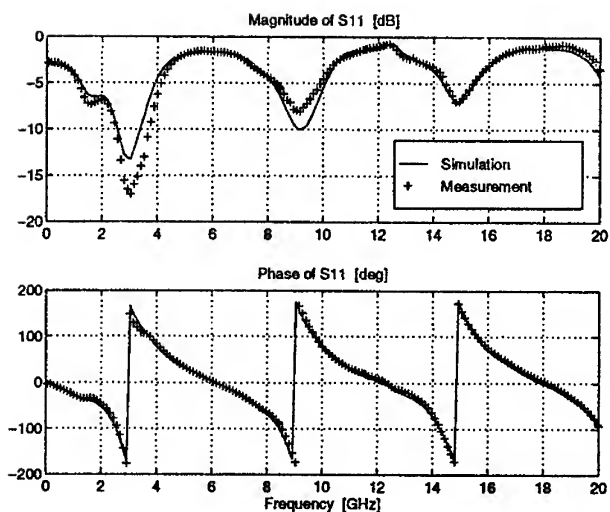


Figure 5 : Comparison of the simulated and the measured scattering parameters without illumination. The reference impedance equals 20Ω .

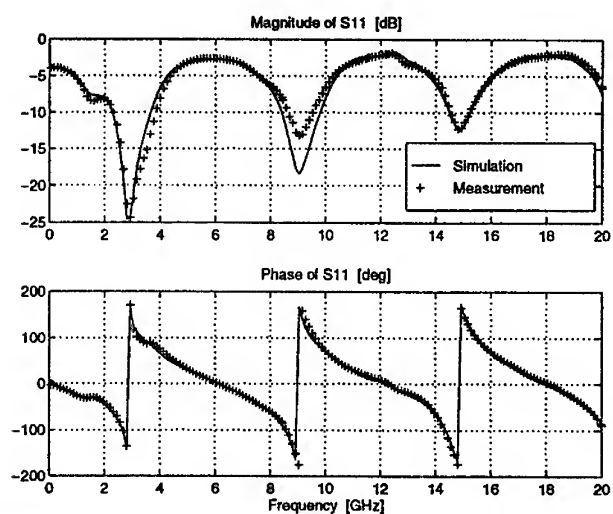


Figure 6 : Comparison of the simulated and the measured scattering parameters with illumination. The reference impedance equals 20Ω .

Noise and loss characteristics of microwave direct modulated optical links

I. Frigyes, I. Habermajaer, B.G. Molnár, A. Seeds*, F. Som
Budapest Technical University, Budapest, Goldmann Gy. tér 3, 1111;
phone: 361 463 3689 e-mail: t-frigyes@nov.mht.bme.hu

*University College of London, Torrington Place, London WC1E 7JE,
phone: 44713877050/3972; fax: 4471 387 4350, e-mail: a.seeds@eleceng.ucl.ac.uk

Abstract: *Loss and noise figure of optical links transmitting microwave signals - e.g. for remote antennas in wireless communications - is dealt with. Conditions are rather general, including arbitrary matching conditions, shot noise and laser relative intensity noise. It is shown, that - alike passive microwave systems - noise figure is not proportional to the loss and theoretically it can be less than the loss. Optical power should be as low as possible - this limit being mainly determined by the required dynamic range of the system.*

1. Introduction

The transmission of microwave signals via point-to-point and point-to-multipoint optical links becomes more-and-more common in wireless indoor and outdoor cellular/picocellular communications and elsewhere. In these applications the optical link serves as a passive or active microwave component. Its loss (or possibly: gain) and its noise figure, further dependence of the latter on the former is of basic importance in these applications *i.e. they are, of course, important in the design of optical microwave links but also important from the conceptual point of view). As it will be seen in the sequel, the behavior of optical/microwave links is much different from that of their purely microwave counterparts.

In *typical optical applications* (i.e. in links transmitting digital signals) noise figure of the total link is a non-existent parameter and therefore standard optical texts do not deal too much with this problem. There are, however a few papers and also books dealing with the theory of link noise figure such as [1,2,3,4]; further, loss or gain is closely related to the noise figure problem and some of the above references attacks this problem also. However, none of these deals with the problem and some of the above references attacks this problem also. However, none of these deals with the problem in general and sometimes the conclusion is not correct neither. As far as known by the authors, neither the referenced papers nor other ones take all of the noise sources into account. The intention of the present paper is to give such a general discussion.

To give a short review only on the above references, [1] and [4] do not take into account the (electrical) thermal noise generated at the photodetector end; [2] neglects the RIN and further matching conditions are not discussed; [3] does not deal with thermal noise at all.

electrical matching and on optical power. Further, also leading to theoretical limits on the loss and noise figure of these links.

The system to be discussed is shown in Fig. 1.

It is assumed that both the impedance of the laser diode and the admittance of the photodiode are real - eventually by adding an appropriate reactance and susceptance in series and in parallel, respectively. the real parts of the laser impedance r_L and the photodiode admittance, g_D can be adjusted virtually to any magnitude, via the transformers; these transformed magnitudes will be designated as R_L and G_D , respectively. Transformers shown in Fig.1 can represent any lossless matching circuit. The optical power can be detected either by a pin photodiode or by an APD (Avalanche Photo Diode). As in the present paper the optical link is regarded as a passive microwave component, no optical amplifier is assumed within this link. However, there is a post-photodetector electrical amplifier; characterised by it's optimal noise figure F_{AO} and the corresponding generator resistance R_{AO} . Note that the amplifier noise figure depends on the generator impedance - in the present case on the impedance of the photodiode. This may well be different from the noise matching impedance, which fact must be taken into account in any practical case.

2. Loss characteristics

Electrical loss L is defined as

$$L = \frac{P_a}{P_{out}} \quad (1)$$

with P_a the generator available power

P_{out} the power outputted to the postdetection amplifier

the (high frequency) current flowing through the laser diode is

$$i = \frac{2}{R + R_L} \sqrt{\frac{P_a R R_L}{r_L}} \quad (2)$$

with R the generator resistance, normally equal to the characteristic impedance of the connecting transmission line;

the high frequency component of the optical power generated in the laser

$$P_{opt} = \frac{h \cdot f}{e} \eta_L i \quad (3)$$

here h is Plank's constant; f is the optical carrier frequency; e the charge of the electron; η_L the quantum efficiency of the laser diode.

The micro wave component of the received optical power, inputted to the photodiode is

$$P_{opt,rec} = \frac{P_{opt}}{L_r} \quad (4)$$

with L_r the combined loss of the optical components, including coupling loss into and out of the optical fibre; the source current of the detected current

$$k = \eta_Q M \frac{e}{h f} P_{opt,rec} \quad (5)$$

with η_Q the quantum efficiency of the photodiode;
M the current multiplication factor of the (possible) APD at the microwave carrier frequency;

And the output (electrical) power is $P_{out} = k^2 \frac{1}{\left(1 + \frac{G_D}{G_A}\right)^2} \frac{G_D}{G_A g_D}$ (6)

here G_A is the amplifier input conductance.

So, finally, the total loss can be expressed as

$$L = b L_r^2 \quad (7)$$

with

$$b = \frac{R G_A}{4 \left(M \eta_L \eta_Q \right)^2} \left(1 + \frac{R_L}{R} \right)^2 \left(1 + \frac{G_D}{G_A} \right)^2 \frac{r_L g_D}{R_L G_D} \quad (8)$$

The fact, that laser impedance is in practical cases low while photodiode resistance is high can lead to a significant decrease of microwave loss, or, in principle, even to a microwave gain. If the matching circuits transforms these to the appropriate impedances, (i.e. $R_L = R$, $G_D = G_A$) we get

$$L_0 = \left(\frac{2 L_r}{M \eta_L \eta_Q} \right)^2 r_L g_D \quad (9)$$

If laser impedance r_L is equal to that of the generator and photo diode admittance g_D to the input impedance of the amplifier, and both input and output are matched, (i.e. $r_L = R = R_L$, $G_D = G_A = G_D$), the microwave power loss, designated as L_1 is (10)

$$L_1 = \left(\frac{2 L_r}{M \eta_L \eta_Q} \right)^2 R G_A$$

It can be regarded as the case of resistive matching, where transformers can be omitted and passive resistors are connected to the diodes to fulfill the matching conditions.

In the (idealised) case, in which both $r_L/R \ll 1$ and $G_D/G_A \ll 1$ with no transformers ($r_L = R_L$, $G_D = G_D$), when

$$L_2 = \left(\frac{L_r}{2 M \eta_L \eta_Q} \right)^2 R G_A \quad (11)$$

i.e. 12 dB less than in the above resistive matched case.

3. Noise figure of passive optical microwave links

Coming now to the evaluation of the noise figure, there are several noise sources, as shown in Fig. 2.

Mean square values of these, respectively, are:

generator noise, k_g :

$$k_g^2 = \frac{4 k_B T_0 B}{(R + R_L)} \cdot \left(\frac{\eta_L \eta_Q M}{L_r} \right)^2 \frac{R_L}{r_L} \frac{G_D}{g_D} \quad (12)$$

shot noise, k_s (denoting the diode dark current *and* detected current caused by optical background noise together by I_d):

$$k_s^2 = 2eB \left[(I_0 - I_{th}) F_M \frac{\eta_L \eta_Q M^2}{L_r} + I_d \right] \frac{G_D}{g_D} \quad (13)$$

intensity noise, k_i :

$$k_i^2 = (I_0 - I_{th})^2 RIN(\omega_c) \left(\frac{\eta_L \eta_Q M}{L_r} \right)^2 B \frac{G_D}{g_D} \quad (14)$$

thermal noise of the photodiode:

$$k_d^2 = 4k_B T_0 B G_D \quad (15)$$

and amplifier noise, reduced to the input of the amplifier as show in Fig. 2.

$$k_a^2 = 2(F_{A0} - 1) \frac{k_B T_0 B}{R_{A0}} \quad (16)$$

and

$$v_a^2 = 2(F_{A0} - 1) k_B T_0 B R_{A0} \quad (17)$$

where we assumed that the voltage and current sources are uncorrelated.

Here, apart from the quantities defined before

k_B is the Boltzmann-constant; e is the electronic charge;

B is the receiver band-width

$RIN(\omega_c)$ is the laser relative intensity noise measured at the microwave carrier angular frequency ω_c . It is assumed that B is low enough to take RIN being constant in this band - a not very important assumption;

I_0 the DC current of the transmitter laser diode

I_{th} the laser threshold current.

Note, that the noise temperature of the photodiode can be well different from T_0 ; for sake of simplicity T_0 was applied in (15); a deeper investigation of this problem is out of the scope of this paper.

Having noise sources in Equations (12)-(17) available, noise figure can be determined. As known, this is defined as

$$F = \frac{(S/N)_{in}}{(S/N)_{out}} \bigg|_{T_s=T_0} \quad (18)$$

with S/N the signal-to noise power ratio at the input and output, respectively.

As usual, it is reasonable to assume statistical independence of the noise sources. Thus the output noise power can be written as

$$N_{out} = k_N^2 \frac{1}{(1 + G_D / G_A)^2 G_A} \quad (19)$$

with

$$k_N^2 = k_g^2 + k_s^2 + k_i^2 + k_d^2 + k_a^2 + v_a^2 G_D^2 \quad (20)$$

Taking all these into account the noise figure can be written as a second order polynomial of optical loss

$$F = 1 + \frac{R_L}{R} + \frac{(R + R_L)^2 r_L}{RR_L} (a_0 + a_1 L_r + a_2 L_r^2) \quad (21)$$

with the coefficients of

$$a_0 = \frac{(I_0 - I_{th})^2}{4k_B T_0} \text{RIN}(\omega_c) \quad (22)$$

$$a_1 = \frac{e(I_0 - I_{th})}{k_B T_0} \frac{F_M}{\eta_L \eta_Q} \quad (23)$$

$$a_2 = \frac{1}{(\eta_L \eta_Q M)^2} \left[\frac{e}{k_B T_0} I_d + g_D + g_D \varphi (F_{A0} - 1) \right] \quad (24)$$

$$\varphi = \frac{1}{2} \left(R_{A0} G_D + \frac{1}{R_{A0} G_D} \right) \quad (25)$$

where F_M the APD noise figure; usually $2 \leq F_M \leq M$. Or applying (8) one can express the noise figure with the electric loss

$$F = 1 + \frac{R_L}{R} + \frac{(R + R_L)^2 r_L}{RR_L} \left(a_0 + \frac{a_1}{b} \sqrt{L} + \frac{a_2}{b} L \right) \quad (26)$$

4. Properties of Optical links

4.1. Link behaviour under ideal or near to ideal circumstances

In order to see the ultimate possibilities, let us make the following - of course, idealised - assumptions:

no dark current is assumed - $I_d=0$

no RIN is assumed - $\text{RIN}(\omega_c)=0$

no optical loss is assumed - $L_r = \eta_L = \eta_Q = 1$

PIN Photodiode is applied - $M = F_M = 1$

In this case the noise figure can be written as

$$F = 1 + \frac{R_L}{R} +$$

To idealise further

$$+ \frac{(R + R_L)^2 r_L}{RR_L} \left\{ \frac{e(I - I_{th})}{k_B T_0} + g_D [1 + (F_A - 1)\varphi] \right\}$$

let the shot noise also be very low - $I - I_{th} = 0$

(27)

and the amplifier ideal - $F_A = 1$.

In this over idealised case F can approach 1 (in contrast to some statements in the literature), i.e. if $R_L = R$ is chosen and both r_L and g_D are low. But this is the case in real situations: laser diodes have very low resistance (say 3-5Ω) while that of photodiodes is very high (in the order of kΩ-s). I.e.

$$F = 1 + \frac{r_L}{R} + g_D R (\approx 1)$$

(28)

On the other hand, if the laser diode is matched to the source resistance (i.e. $R_L = R$)

$$F = 2 + 4r_L g_D (\approx 2)$$

(29)

As seen, matching being optimal for minimising loss can be sub-optimal for minimising noise figure.

4.2 Comparison of electric and optical links at high attenuation

It is well known, that in a system containing only electrical components at reference temperature, the noise figure is always greater than or equal to the link loss. The question can arise whether it is true for the systems that contain optical elements and furthermore what noise figure can be achieved as a theoretical minimum in such a link. To get a first impression on this problem, assume the ideal situation that only the shot noise is taken into account. In this case we can conclude from (24) that a_2 vanishes, so at high link loss, the noise figure is proportional to the square root of the (electrical) loss, therefore above a certain link loss, the noise figure must be less than the loss.

Consequently, contradiction to electric circuits, the theoretical noise figure in an optical link can be less than the electric link loss.

Fig. 3 shows the result of a calculation in a ideal case where $\lambda = 1.55 \mu\text{m}$, $R = 1/G_A = 50\Omega$, $r_L = R_L \ll R$, $g_D = G_D \ll G_A$ and 1 mW for laser optical power were assumed. In the region of high attenuation:

$$F^{[dB]} \cong \frac{1}{2} L^{[dB]} + 3.8$$

(30)

In fact there are three regions where different causes are predominant as depicted in Fig. 4.

The noise figure is less than the link loss if

$$F_{A0} < 1 + \frac{\frac{1}{4} \left(\sqrt{\frac{G_A}{G_D}} + \sqrt{\frac{G_D}{G_A}} \right)^2 - 1}{\frac{1}{2} \left(R_{A0} G_D + \frac{1}{R_{A0} G_D} \right)}$$

(31)

condition is fulfilled, where the dark current is taken negligible for simplicity.

5. Measuring results and discussion

Unfortunately at the present stage to make preliminary measurements was only possible. In particular

- an optical/ microwave link of relatively high overall optical loss was only available - resulting in a rather high RF loss; this fact did not allow to verify that term of the noise figure formulae (23) which describe the effect of shot noise; further, overall noise figure was rather high;
- Only laser diodes and photodetectors of "resistive" matching were available, i.e. laser diode was matched with a series resistance (a 47Ω in series with the approximately 3Ω laser) and photo diode with a parallel resistance.

Measurements were made at 1300 nm optical wavelength. Radio frequencies were 700 and 1250 MHz. Laser threshold current was about 9 mA. RIN peak was about 1.5 GHz at 10 mA laser DC current and about 3.5 GHz at 20 mA - i.e. much above the measuring frequencies. RIN peak was less than 10dB higher only than its low frequency value. In the measurements laser DC current was 10 mA and 20 mA at the lower measuring frequency but only 20 mA at the higher one.

The validity of Formula (10) was checked first. According to this RF loss is by 6 dB higher than optical loss-squared; this was approximated with less than 1 dB difference, with a negligible difference at the two measuring frequencies only. In detail:

$$L_r/\eta_L=14.3 \text{ dB}$$

$$\eta_D=1.5 \text{ dB}$$

$$L_0=38.5 \text{ dB}$$

Dependence of noise figure on an inserted optical attenuation was measured next. Results are given in Fig. 5. Reference value for the noise figure ($\Delta F=0$) was taken the lowest measured value, i.e. that at 700 MHz, $I=0$ mA and no additional optical loss. Even this value was rather high, i.e. 61 dB

In spite of the rather limited experimental possibilities, measurements proved some of the theoretical predictions. So dependence of RF loss and noise figure on optical loss is fully proved. Further the role of intensity noise is also demonstrated; in particular the rather complicated dependence of noise figure on this characteristic, as stated in Formula (22) can be seen from the curve. By the way the following $RIN(\omega_c)$ values can be computed from the presented measurements:

$$RIN (700 \text{ MHz}) = -111 \text{ dB / Hz}; I - I_{th} = 11 \text{ mA}$$

$$RIN (700 \text{ MHz}) = -105 \text{ dB / Hz}; I - I_{th} = 1 \text{ mA}$$

6. Conclusions

Some rather interesting conclusions can be drawn from the present paper; these give also a summary of the new results of this paper.

Without resistive matching, applying extreme impedance, a loss of 12 dB lower can be achieved; in how far this can be approximated depends on practical factors; in particular on how well conditions $R_L \ll R$; $G_D \ll G_A$ can be fulfilled. Further, if laser reactance and photodiode conductance are low, very low loss or even gain can in principle be achieved.

Dependence of noise figure on loss is radically different from that of purely electrical systems; in particular it can be less than electrical loss. Under idealised conditions - i.e. if shot noise is the only noise source - noise figure is (nearly) proportional to the square-root of the electrical loss. If shot noise is also negligible, the idealised situation of F-1 can be realised. In the general case, besides of shot noise proportional to \sqrt{L} thermal noise is approximately proportional to electrical loss and RIN is loss-independent. Not also that there is no unique relationship between loss and noise figure.

Shot noise and laser intensity noise are proportional to the average optical power and its square, respectively. (or, as optical power is linearly related to the laser direct current the same laws are holding for current.) Thus the optical power must be chosen very carefully. If RIN is neglected, dynamic range (and relaxation oscillation frequency) are determining factors; then current should be chosen as low as possible, conditioned on these. (E.G. rather low dynamic range is required if digital signals of an angle-modulated - PSK or FSK - GEO satellite are to be transmitted.) But even if RIN can not be neglected - what is the usual case - low laser current (yielding appropriate dynamic range) is preferable, as this outperforms the increase of RIN close to threshold.

Acknowledgment

This work was partly sponsored by OTKA, the Hungarian Fund for Scientific Research project no. T7396. Their support is gratefully acknowledged.

References

- [1] Cox, Betts, Johnson: An analytic and experimental comparison of direct and external modulation in analog fiber-optic links, IEEE Trans on MTT, 38, No 5, pp. 501-509
- [2] Cox, Ackerman, Betts: Relationship between gain and noise figure in an optical analog link, IEEE MTT IMS Digest, Vol.3, pp.1551-54, San Francisco CA, June 1996
- [3] Rainee Simons: Optical control of microwave devices, Artech House, London etc, 1990
- [4] Som: Ph.D. Dissertation, 1996 (in Hungarian)

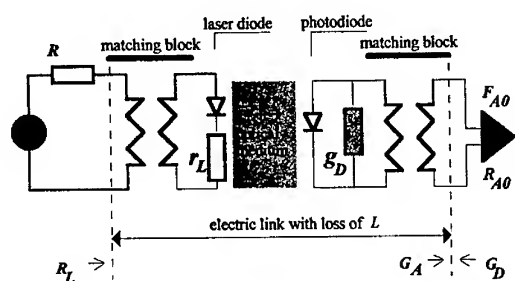


Fig. 1 Conceptual drawing of an optical microwave link

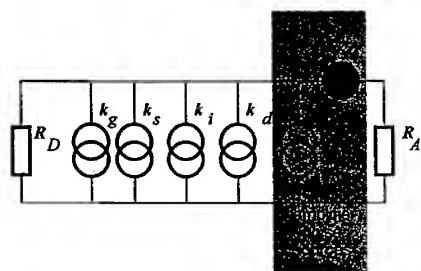


Fig. 2 Noise sources of optical microwave links

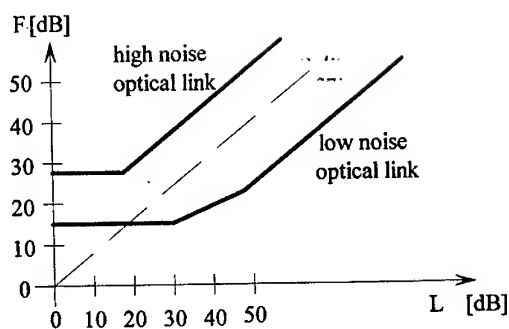


Fig. 4 Qualitative form of the noise figure as function of the link loss.

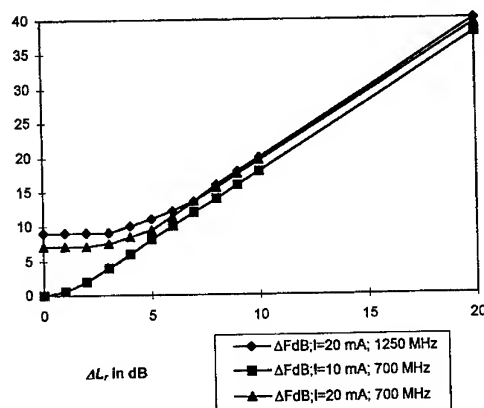


Fig. 5 Dependence of noise figure difference in dB on the inserted optical attenuation

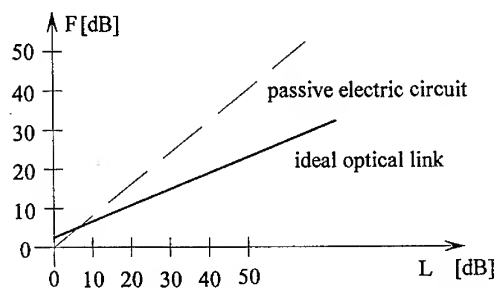


Fig. 3 The noise figure versus link loss in an ideal situation.

SIMULATION OF LINEAR AND NONLINEAR CHARACTERISTICS OF HIGH- T_c SUPERCONDUCTING RESONATORS AND FILTERS

O. Vendik, I. Vendik, D. Kaparkov*, M. Gubina*, V. Kondratiev*

Chalmers University of Technology, Göteborg, S 421 96, SWEDEN.

Phone: +46 (31) 772 1727, FAX: +46 (31) 16 45 13. E-mail: spartak@ep.chalmers.se

Permanent address: see below

*St. Petersburg Electrotechnical University, 5 Prof. Popov str. St.-Petersburg, 197376, RUSSIA,

Phone: +7 (812) 234 96 72, Fax: +7 (812) 234 48 09, e-mail: vib&mwgroup.mit.etu.spb.ru

ABSTRACT

A simple closed form model of linear and non-linear response of high- T_c superconducting resonators is proposed. The phenomenological model of the microwave surface impedance is improved by a minimization of the number of fitting parameters. The specified characteristic power is suggested to use as a fitting parameter for description of the non-linear microwave power dependence of the unloaded quality factor of planar resonators: microstrip, coplanar waveguide, and disk resonator. Application of the model to the planar filter design is discussed.

INTRODUCTION

For an accurate simulation of linear characteristics of high- T_c superconducting (HTS) resonators and filters it is necessary to use correct models of the planar line characteristics including microwave properties of HTS thin film. The simplified phenomenological model is proposed for the microwave surface impedance. That allows to predict microwave characteristics of HTS resonators versus frequency and temperature. The model of coupled planar lines is the basis for simulation of planar HTS filters. The characteristics of the filter can be obtained at any temperature. The non-linear phenomenological model of the HTS film surface resistance is used in a form of a series expansion with respect to the magnetic field in the resonator. The universal non-linear equation for unloaded quality factor Q is obtained. The only phenomenological parameter is used in the suggested non-linear model.

LINEAR MODEL OF HTS SURFACE IMPEDANCE

The simplified phenomenological model of the microwave surface impedance of HTS is proposed in a linear approach. The model is a further development of the model by Vendik and Kollberg (1), which describes surface impedance of HTS using 5 parameters: the transition temperature T_c , the normal conductivity $\sigma_n(T_c)$, the London penetration depth $\lambda_L(0)$, exponent γ in temperature dependence of $\lambda_L(T)$ and the residual resistance parameter α . Correlation between fitting parameters of the model $\lambda_L(0)$, α and γ allows to reduce the number of independent fitting parameters:

$$\lambda_L(0) = 0.13 \cdot 10^{-6} \cdot \exp(1.27 - 0.5\gamma) \quad (1)$$

$$\alpha = 10.263 + 119.9 \cdot \gamma^{-6.304} \quad (2)$$

The exponent γ varies in the range 1.5-2.5. It determines absolute value of $\lambda_L(0)$, the value of Z_{sur} near transition temperature, and residual resistance of the film at low temperatures. Thus, parameter γ may be considered as a measure of the HTS film quality.

The model was verified on numerous experimental data. As an example, the experimental results from Zaitsev et al (2) are shown in Fig. 1 in comparison with simulation data.

THE NON-LINEAR PHENOMENOLOGICAL MODEL OF PLANAR HTS RESONATOR

The surface resistance of the HTS film in resonators as a function of alternating field one may describe using the main idea of the model Vendik et al (3):

$$R_{\text{sur}}(\bar{r}, t) = R_{\text{sur},0} \cdot \left(1 + \frac{H_m^2 \cdot \cos^2(\omega t) \cdot f^2(\bar{r})}{H_0^2} \right), \quad (3)$$

where $R_{\text{sur},0}$ is the surface resistance of the film in the linear approach, H_m is the amplitude of the magnetic field in the resonator, \bar{r} is the coordinate, $f(\bar{r})$ is the function of the field distribution, H_0 is the phenomenological parameter which describes the nonlinearity.

The dissipated power in the resonator P_{diss} can be found upon integrating over the superconducting surface of the resonator and with respect to time over the period of the microwave oscillations:

$$P_{\text{diss}} = \int_S R_{\text{sur}}(\bar{r}, t) \cdot |\vec{H}(\bar{r})|^2 ds. \quad (4)$$

As a result

$$P_{\text{diss}} = P_{\text{diss},0} \cdot \left(1 + \frac{H_m^2}{H_0^2} \cdot \frac{\chi}{2} \right), \quad (5)$$

with χ as a geometric factor.

Let us use the definition of the unloaded Q-factor of the resonator as

$$Q_U = \frac{P_{\text{osc}}}{P_{\text{diss}}}, \quad (6)$$

where P_{osc} is the power of oscillations in the resonator. Using the relation

$$\frac{P_{\text{osc}}}{P_{\text{inc}}} = \frac{2 \cdot Q_E}{(1 + Q_E/Q_U)^2} \quad (7)$$

and the equation (6) one can find the effective unloaded Q-factor as a function of the input power P_{inc} in form of the nonlinear equation:

$$\frac{Q_U}{Q_{U,\text{eff}}} = 1 + \chi \cdot \frac{Q_E}{\left(1 + \frac{Q_U}{Q_{U,\text{eff}}} \right)^2} \cdot \frac{P_{\text{inc}}}{P_0}, \quad (8)$$

where Q_E is the external quality factor of the resonator determined by the coupling of the resonator with the external transmission lines, P_0 is the model fitting parameter which may be extracted from experimental data.

The parameter χ depends on the field distribution in the resonator. For the half-wave length microstrip line or coplanar waveguide HTS resonator with two coupling elements (Fig. 2)

$$\chi = \frac{9}{4\pi}. \quad (9)$$

For the disk resonator of radius R with TM_{010} mode (Fig. 3)

$$\chi = \frac{3}{2} \cdot \frac{\int_0^R J_1^4(k_r r) r dr}{\int_0^R J_1^2(k_r r) r dr} = 0.378, \quad (10)$$

where $J_1(k_r r)$ is the Bessel function.

P_0 is the effective oscillating power which would be in the resonator, if the magnetic field amplitude is H_0 :

$$P_0 = \frac{\omega \mu_0}{2} \cdot \int_V H_0^2 \cdot f^2(x) \, dv. \quad (11)$$

Here V is the resonator volume.

For the half-wave length resonator

$$P_0 = 60\pi \cdot H_0^2 \cdot \frac{2\pi}{\lambda_0} \cdot w \cdot h \cdot \ell. \quad (12)$$

For the disc resonator

$$P_0 = 120\pi^2 \cdot H_0^2 \cdot \frac{2\pi}{\lambda_0} \cdot R^2 \cdot h \cdot 0.595. \quad (13)$$

For a rough estimation of the model fitting parameter one may suppose that

$$H_0 = j_{c,vol} \cdot \lambda_L, \quad (14)$$

where $j_{c,vol}$ is the volume critical current density of the HTS film measured at dc, λ_L is the London penetration depth of the film. Since the values depend on the temperature, the model fitting parameter P_0 depend on the temperature as well. The better is the quality of the film, the higher is the model fitting parameter P_0 .

The equation (8) can be presented in the dimensionless form:

$$\frac{1}{z} = 1 + \chi \cdot \frac{A}{(1 + A/z)^2} \cdot p, \quad (15)$$

where

$$z = \frac{Q_{U,eff}}{Q_U}, \quad A = \frac{Q_E}{Q_U}, \quad p = \frac{P_{inc} \cdot Q_U}{P_0}. \quad (16)$$

The introduced notations have the following sence: z characterizes decreasing the $Q_{U,eff}$ under influence of the incident power; A is the measure of the coupling the resonator with the external circuit; p is the normalized incident power.

The parameter p is considered as the only fitting parameter of the nonlinear model. Fig. 4 shows the result of solution of the equation (15) for different coupling parameter A of the resonator with the external circuit. The weaker is the coupling, the lower is the power handling capability.

EXPERIMENTAL INVESTIGATION OF THE NONLINEAR CHARACTERISTICS OF THE PLANAR HTS RESONATORS

Fig. 5 shows the experimental unloaded Q-factor at $T = 60$ K on the normalized incident power p of the disk resonator with a high power handling capability Chaloupka et al (4) in comparison with the results of simulation using equation (15). The nonlinear response of the microstrip line resonator at $T = 77$ K was also investigated. Fig. 6 illustrates the resonator layout. Dependencies of the experimental and simulated unloaded Q-factor on the normalized incident power p are shown in Fig. 7. The parameter P_0 for the disk resonator is equal $0.21 \cdot 10^6$ W, for the microstrip resonator $P_0 = 2$ mW.

THE HTS FILTER SIMULATION

Model of the surface resistance of the HTS film and models of HTS transmission lines taking into account the non-homogeneous current distribution in the line cross section are used for HTS filter simulation. The filter characteristics may be simulated at any temperature considering contribution from kinetic inductance, change of surface resistance as well as temperature dependence of dielectric permittivity of substrate material. The simulated characteristics of 5-pole YBCO filter at two different temperature are presented in Fig.8. The non-linear characteristics of the filter can be found using the same approach (3), as it was used for the resonators. If the loaded Q-factor is determined by the frequency band $\Delta\omega_{res}$ for a resonator and $\Delta\omega_{filt}$ for a filter, the maximum current in the resonator as a function of the incident power will be $(\Delta\omega_{filt}/\Delta\omega_{res})^{1/2}$ times higher than in the filter. Hence the power handling capability of the filter is higher comparing with the resonator on the planar line with the same unloaded Q-factor.

CONCLUSION

The simple and accurate empirical model of linear and non-linear HTS resonators is derived and verified by comparison with experimental data. The model can be effectively used in a CAD of HTS devices with high power handling capability.

ACKNOWLEDGMENT

The authors are grateful to A.G.Zaitsev for YBCO films used in the investigations.

REFERENCES

1. O.Vendik, E.Kollberg, "Software models HTSC microstrip and coplanar lines", 1993, Microwave & RF, Vol. 32, pp. 118-121.
2. A. Zaitsev, R. Kutzner, and R. Wördenweber, "Growth of high-quality $\text{YBa}_2\text{Cu}_3\text{O}_{7-x}$ films on CeO_2 buffer layer of mixed (001)/(111) orientation on sapphire", 1995, Appl. Phys. Lett., Vol. 67, No. 18, pp. 2723-2725.
3. O.G.Vendik, I.B.Vendik, and T.B.Samoilova, "Non-linearity of superconducting transmission line and microstrip resonator", 1997, IEEE Trans. on MTT, Vol. 45, No. 2, pp. 173-178.
4. H.Chaloupka, M.Jeck, B.Gurzinski, and S.Kolesov, "Superconducting planar disk resonators and filters with high power handling capability", 1996, El. Lett., Vol. 32, No.18, pp. 1735-1737.

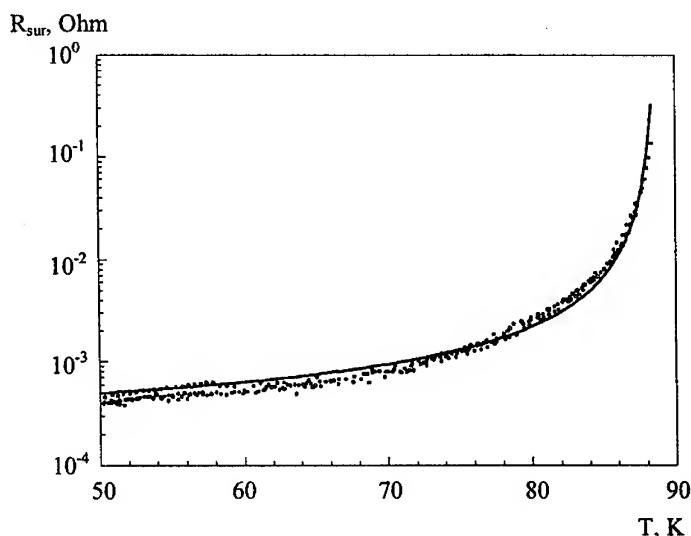


Fig. 1. Measured and simulated dependence of the surface resistance of the YBCO film on r-cut sapphire substrate on temperature ($f=18.7$ GHz, $d=0.25$ μm , $T_c=88.7$ K, $\sigma_n(1)=1 \times 10^6$ ($\text{Ohm} \times \text{m})^{-1}$, $\gamma=2.45$).

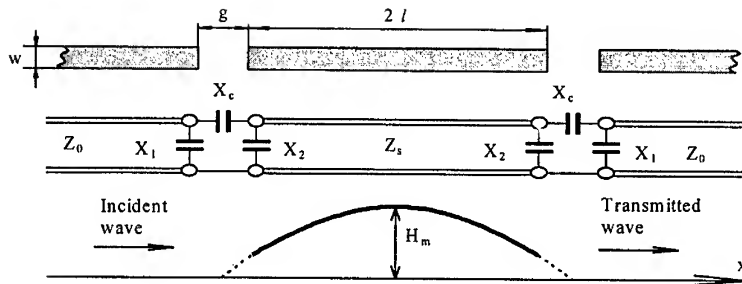


Fig. 2. Equivalent circuit of the half-wave length resonator.

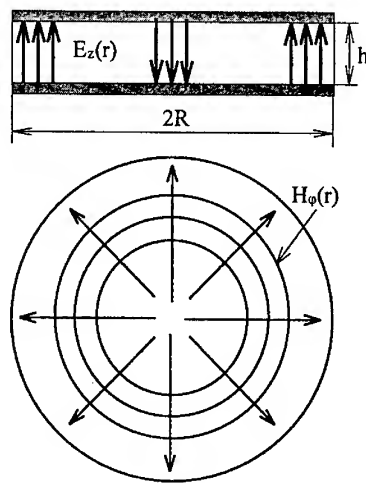


Fig. 3. Electrical and magnetic field distribution in the circular disk resonator for TM_{010} mode.

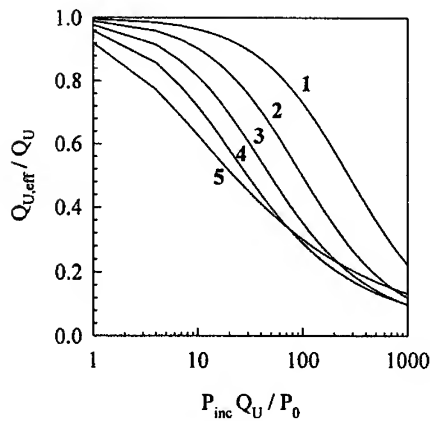


Fig. 4. Dependence of effective unloaded quality factor $Q_{U,eff}/Q_U$ on the normalized incident power p for different coupling factors: $A = 0.01$ (1), 0.03 (2), 0.07 (3), 0.25 (4), 0.75 (5).

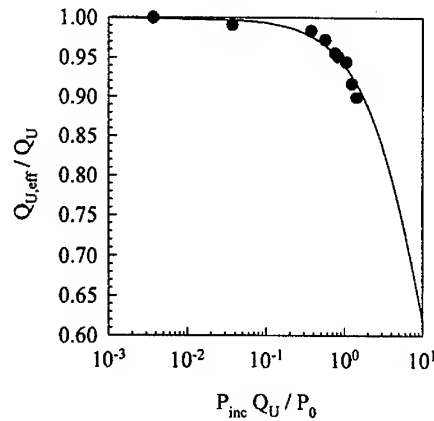


Fig. 5. Measured (points) (4) and calculated (solid line) unloaded Q -factor of the disk resonator as a function of the normalized incident power ($f = 3.5$ GHz).

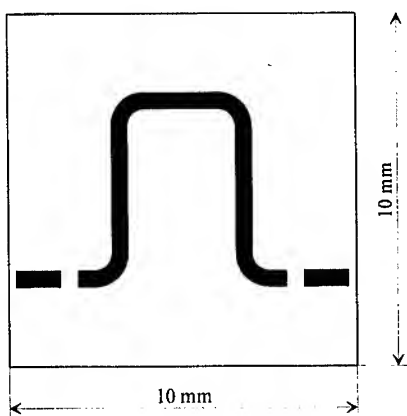


Fig. 6. Layout of the microstrip line resonator.

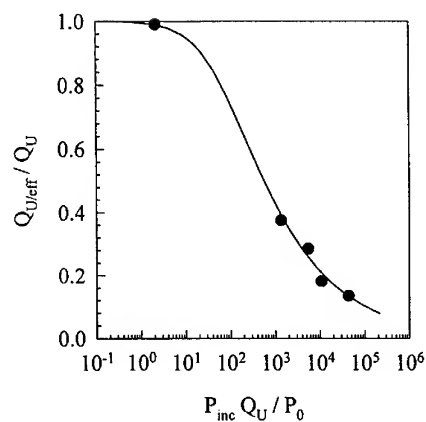


Fig. 7. Measured (points) and calculated (solid line) unloaded Q-factor of the microstrip line resonator as a function of the incident power ($f = 4$ GHz).

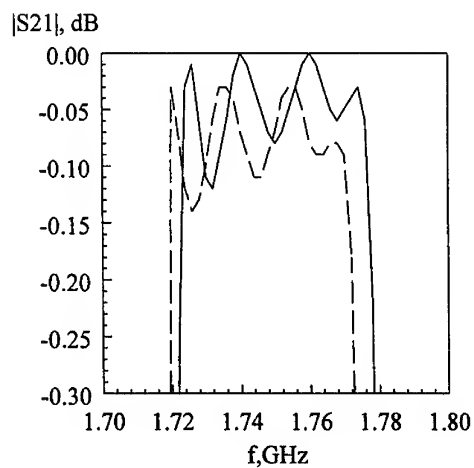
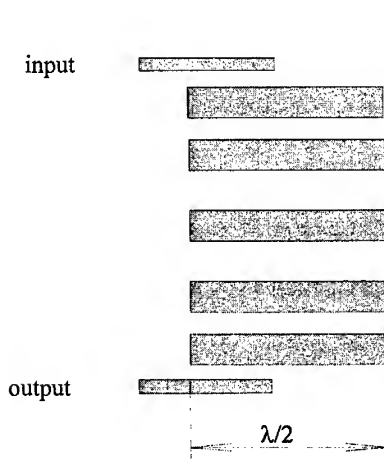


Fig. 8. Layout (a) and simulated transmission coefficient (b) of the 5-pole microstrip line filter at $T = 30$ K (solid line) and $T = 85$ K (dashed line). Parameters of the model of surface resistance: film thickness $d = 0.2 \mu\text{m}$, $T_c = 88.7$ K, $\gamma = 2.45$, $\sigma(1) = 1 \cdot 10^6 (\Omega \cdot \text{m})^{-1}$.

A Simplified Physics-based Quasi-static MSM Photodiode Model

Mustapha Djebbari, Günter Kompa, Armin Stolze

FG Hochfrequenztechnik, University of Kassel, Germany

D-34121 Kassel, Wilhelmshöher Allee 73

Tel: +49 561 804 6528, Fax: 6529

E-mail: musta@hfm.e-technik.uni-kassel.de

ABSTRACT

This paper presents a novel large-signal model of a MSM photodiode. Based on a network synthesis approach, the complex analytical frequency response function which characterizes the generation of electron-hole-pairs and the drift of carriers in the depletion layer of the device is equivalently described by a simple lumped-element RLC network. The values of the elements depend on the transit time of the electrons and holes, which can be extracted from measurements. The residual electrical performance of the device is FET-like modelled using nonlinear current and charge sources (e.g. Kompa [1]). It will be demonstrated that the derived lumped-element large-signal model is very easy to implement and to use for transient response analysis in common commercial CAD software programs.

INTRODUCTION

The GaAs metal-semiconductor-metal (MSM) photodiode is known as an ultrafast device which is attractive for high speed optoelectronic applications (Chou [2] and Jinwook [3]). Regarding the design of optical receivers, covering also high signal dynamics as in laser radar systems, an accurate nonlinear model of the photodiode is indispensable. In Fig. 1 the MSM photodiode is described as a 2-port which comprises an optical input and an electrical output port. $P_{opt}^i(t)$ and $P_{opt}^r(t)$ are the incident and the reflected modulated optical power signals at the optical port 1. The state functions at the electrical port 2 are $V_2(t)$ and $I_2(t)$. Fig. 2 shows the large-signal model proposed by Stolze [4]. It consists of a physics-based O/E-converter and an electrical network with nonlinear current and charge sources. The transfer function of the MSM photodiode converter can be derived as

$$H(\omega) = \frac{e^{-j\omega\tau_n} - 1}{-j\omega\tau_n} - \frac{e^{-j\omega\tau_n}(j\omega\tau_n + 1) - 1}{(\omega\tau_n)^2} + \frac{e^{-j\omega\tau_p} - 1}{-j\omega\tau_p} - \frac{e^{-j\omega\tau_p}(j\omega\tau_p + 1) - 1}{(\omega\tau_p)^2} \quad (1)$$

τ_n , and τ_p are the electron and hole transit times, which can be determined by measurement (Stolze [4]). As our experience has shown, the presentation in Fig. 2 is not very suited for the general use, in particular taking into account transient response analysis. In this paper we will show that using a synthesis approach (Unbehauen [5] and Budak [6]), the O/E-converter can equivalently be described by a simple RLC network. The derived modified lumped-element photodiode model can easily be implemented in common CAD software. Simulation based on the nonlinear model show very strong dependence of the pulse response as a function of the optical peak power.

MODEL DESCRIPTION

Eq. (1) can be reformulated as follows

$$H(\omega) = \frac{e^{-j\omega\tau_n} - 1}{(j\omega\tau_n)^2} + \frac{1}{j\omega\tau_n} + \frac{e^{-j\omega\tau_p} - 1}{(j\omega\tau_p)^2} + \frac{1}{j\omega\tau_p} \quad (2)$$

The exponential terms are expanded into Taylor series and truncated after the fourth power. This can be rewritten as follows

$$H(\omega) \approx 1 - 2\left(\frac{\tau_n + \tau_p}{12}\right)j\omega + 3\left(\frac{\tau_n + \tau_p}{12}\right)^2(j\omega)^2 + \frac{1}{48}(\tau_n - \tau_p)^2(j\omega)^2 \quad (3)$$

The last term in eq. (3) is very small and can be neglected. Thus eq. (3) reads after some reorganizing

$$H(\omega) \approx \frac{1}{\left[1 + \frac{1}{12}(\tau_n + \tau_p)j\omega\right]^2} \quad \text{with} \quad H(\omega) = \frac{I_i(\omega)}{V_i(\omega)} \quad (4)$$

As can be seen from Fig. 4, very good approximation is given for lower frequencies up to 25 GHz. A lumped-element RLC circuit can now be derived from eq.(4), with $L = 2(\tau_n + \tau_p)/k$ H, $C = (\tau_n + \tau_p)/2k$ F and $R = 1$ Ohm (k fitting parameter). The final new lumped model of the MSM is given in Fig. 5. For CAD implementation the optical input power is normalized to $V_1 = (P_{opt}^i/1A)$.

EXPERIMENTAL RESULTS

Figs. 6, 7, 8 show the nonlinear model elements as a function of optical input power P_{opt}^i and input bias voltage V_2 . The values have been extracted from measurements as described by Stolze [4]. The bias independent model elements are $L_p \approx 640$ pH and $C_p \approx 4$ fF.

Fig. 9 shows some simulated transient pulse response results (bias point: $P_{opt,DC} = 0$ mW, $V_2 = 8$ V) due to a triangular optical input pulse with $t_{rise} = 20$ ps and $t_{fall} = 50$ ps. Curve M1 is the result directly derived from the small-signal model in the used bias point. Curves M2, M3 and M4 are simulated results for different peak values of optical power (M2: 0.1 mW, M3: 2 mW, M4: 3 mW) based on the nonlinear model. It can be seen that M2, resulting from rather small signal input power of 0.1 mW, is in good agreement with the small signal simulation M1. With higher amplitude of optical stimulus significant change in the pulse shapeform can be observed which originates in the growing influence of the device nonlinearity. In Fig. 10 the measured and simulated pulse response are represented for an optical input pulse with $P_{peak} = 0.75$ mW, $t_{rise} = 24$ ps and $t_{FWHM} = 35$ ps. The pulse shape of the optical input pulse (inset of Fig. 10) was detected with a streak camera. For this measurement a double heterostructure injection laser and a MSM photodiode are used.

CONCLUSION

In this paper a new nonlinear quasi-static model for a MSM photodiode has been proposed. It has been shown that the physics-based O/E-converter, which describes the generation and transport of carriers in the depletion layer can simply be modelled by a lumped RLC low pass circuit. Based on the new model transient pulse response simulations have been performed. It has been shown that the nonlinearity of the MSM photodiode leads to severe pulse deformation. The measured pulse response is in excellent agreement with the corresponding simulated pulse. Only the following tail of the simulated pulse is somewhat shorter. We tentatively explain it by the chosen values of the electron and particularly of the hole transit times.

REFERENCES

- [1] G. Kompa: "Modelling of dispersive microwave FET devices using a quasi-static approach", International Journal of Microwave and Millimeter-Wave Computer Aided Engineering, Vol. 5 No. 3, 1995, pp. 173-194.

- [2] S. Y. Chou and M Y. Liu: "Nanoscale tera-hertz metal-semiconductor-metal photodetectors", IEEE Journal of Quantum Electronics, Vol. 28, No. 10, Oct. 1992, pp. 2358-2368.
- [3] B. Jinwook, I. Kerry, D.W. Woordard, J. W. Schaff, P. Mandeville, M. A. Jaspan, M. M. Gitin, and L. F. Eastman: "High-frequency, high-efficiency MSM photodetectors, IEEE Journal of Quantum Electronics", Vol. 31 No. 8 Aug. 1995, pp. 1504-1509.
- [4] A. Stolze and G. Kompa: "Nonlinear modelling of dispersive photodiodes based on frequency- and time-domain measurements", 26th European Microwave Conference Proceedings, 1996, Prague, P2.15, pp 379-382.
- [5] R. Unbehauen: "Netzwerk- und Filtersynthese", Aufl. 4, R. Oldenburg Verlag, 1993.
- [6] A. Budak: "Passive and active network analysis and synthesis", Houghton Misslin Company, USA, 1974.

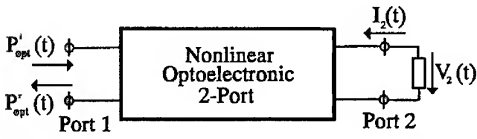


Fig.1: Two port representation of a photodiode

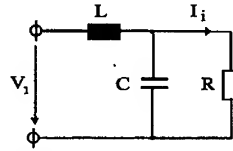


Fig. 3: Network synthesis of eq. (4)

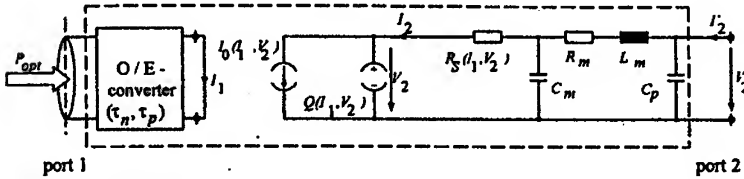


Fig. 2: Large signal model of a MSM photodiode (Stolze [3])

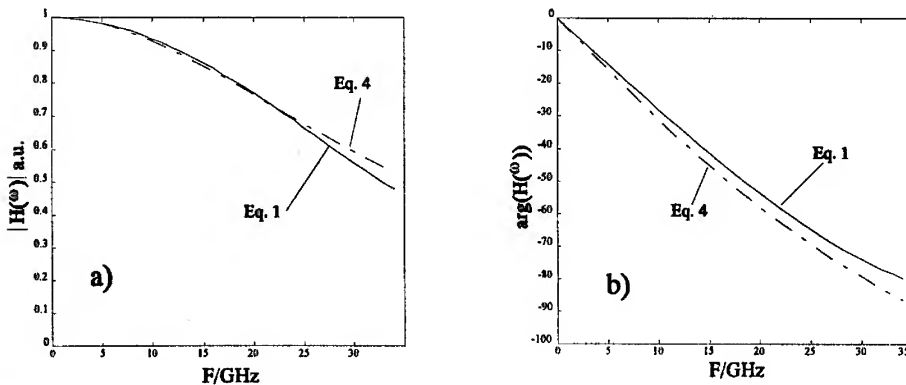


Fig. 4: Frequency response a) amplitude b) phase

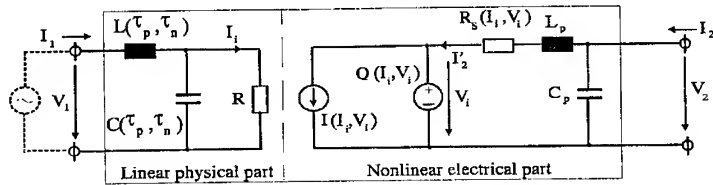


Fig. 5: The new circuit element based large signal model of a MSM photodiode

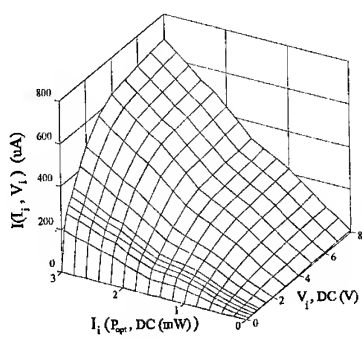


Fig. 6: Current source $I(I_1, V_1)$

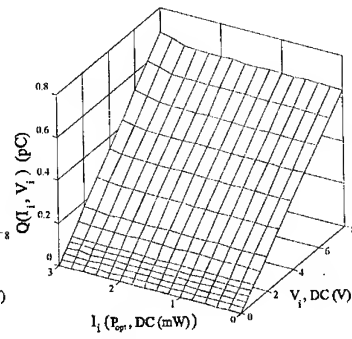


Fig. 7: Charge source $Q(I_1, V_1)$

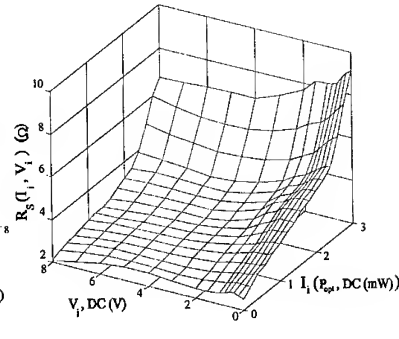


Fig. 8: Small signal series resistance $R_s(I_1, V_1)$

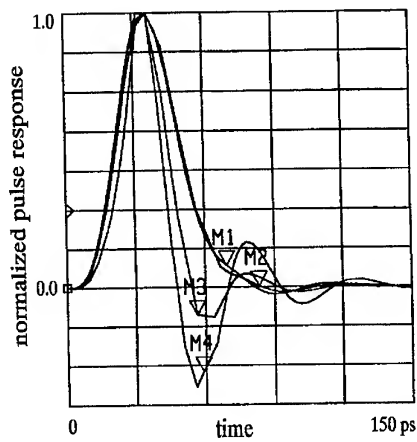


Fig. 9: Simulated transient pulse response for different optical peak power

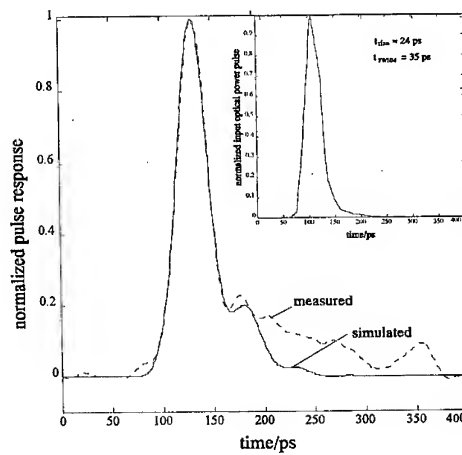


Fig. 10: The simulated and measured pulse response of the used MSM photodiode ($60 \times 60 \mu m$)

An improved physics-based nonquasi-static FET-model

Ingo Schmale, Günter Kompa

University of Kassel, Germany
Fachgebiet Hochfrequenztechnik
D-34121 Kassel, Wilhelmshöher Allee 73
Tel: +49-561-804-6535, Fax: -6529
E-mail: ingo@hfm.e-technik.uni-kassel.de

ABSTRACT

This paper presents a novel large-signal model for MESFETs and HEMTs derived from the physics-based topology known from small-signal modelling. It is easy to extract, implement, and use, and gives very accurate results even for non-linear applications. The model contains nonquasi-static charge source formulations, and includes low-frequency dispersion. The validity of the concept is demonstrated in the analysis of a 12/24 GHz MMIC frequency doubler.

INTRODUCTION

As large-signal applications such as oscillators or multipliers are evolving into higher frequency ranges, better and more complete models are required to ensure highest efficiencies. Nonquasi-static models, that include delay constants for the charge sources, have demonstrated to be good candidates [1,2], in that they give good fitting to measured S-parameters.

MODEL DESCRIPTION

Our advanced model is straightforwardly derived from the well-accepted small-signal equivalent circuit supported by device physics. In this symmetrical model (containing R_i and R_{gd}), the bias dependence of the intrinsic element values is obtained during the extraction process. The extrinsic circuit includes the resistances R_g , R_s , and R_d , as well as the parasitic capacitances and inductances.

The large-signal topology (Fig. 1) maintains the structure of the small-signal equivalent circuit. Two charge sources are used symmetrically to the gate incorporating the effect of the three capacitances. The charges are obtained by a path-independent integration [3] over the small-signal quantities, starting from an arbitrary vector (V_{gs0}, V_{ds0}) :

$$Q_{gs}(V_{gs}, V_{ds}) = \int_{(V_{gs0}, V_{ds0})}^{(V_{gs}, V_{ds})} C_{gs} dV_{gs} + \int_{(V_{gs0}, V_{ds0})}^{(V_{gs}, V_{ds})} C_{ds} dV_{ds} \quad (1)$$

$$Q_{gd}(V_{gs}, V_{ds}) = \int_{(V_{gs0}, V_{ds0})}^{(V_{gs}, V_{ds})} (-C_{ds} - C_{gd}) dV_{gs} + \int_{(V_{gs0}, V_{ds0})}^{(V_{gs}, V_{ds})} C_{gd} dV_{ds} \quad (2)$$

The symmetric topology is superior to the conventional one [1,2,4], where Q_{gs} and Q_{ds} are used, and is motivated by device physics. It allows to maintain the resistances R_i and R_{gd} in the circuit instead of using time-delay factors that do not occur in the small-signal circuit [5,6].

The drain current source is modelled as a DC- and an RF-source in parallel, to be able to take into account its low-frequency dispersion. While the low-frequency current I_{dsDC} represents the measured DC-IV-characteristic, the high-frequency current I_{dsRF} is obtained by integration:

$$I_{dsRF}(V_{gs}, V_{ds}) = \int_{(V_{gso}, V_{dso})}^{(V_{gs}, V_{ds})} G_m dV_{gs} + \int_{(V_{gso}, V_{dso})}^{(V_{gs}, V_{ds})} G_{ds} dV_{ds} \quad (3)$$

In this formula, V_{gs} stands indeed for $V_{gs}(t-\tau)$, with the time constant τ being variable, taking thus the G_m -delay into account. The implementation of the two current sources is improved with respect to that proposed by Root [1]:

$$I_{ds}(\omega) = \frac{1}{1 + j\omega} I_{dsDC}(\omega) + \frac{j\omega}{1 + j\omega} I_{dsRF}(\omega) \quad (4)$$

MODEL IMPLEMENTATION AND VALIDATION

The implementation of the model in the harmonic balance simulator MDS is direct and straightforward (Fig. 1). All elements are visible on the circuit pages; no hidden user-compiled sub-routines need to be developed. The model is implemented as a 6-port Symbolically-Defined Device, which permits to include time-domain expressions.

An MMIC frequency doubler (Fig. 2) for 12 to 24 GHz has been designed in a 0.3 μm HEMT technology and analysed with this new model. The agreement is far more precise than in [4], and due to better models for the passive components [7], the problem of the remaining frequency shift reported in [4] is now also resolved. Measurements and simulations were carried out for various fundamental frequencies and input-powers. All sweeps (Fig. 3) show excellent agreement for the fundamental, the desired doubled frequency and also the third harmonic, thus confirming the validity of this new modelling approach.

CONCLUSION

A new complete MESFET and HEMT-model has been implemented in a commercial harmonic balance simulator. This empirical large-signal model contains symmetrical charge sources delayed via loading resistors, and uses two current sources at the output to cover the low-frequency dispersion effect. All parameters are stored in 2-dimensional tables of data prepared for spline-interpolation. The accuracy of this approach has been demonstrated with an MMIC frequency doubler analysis, giving far more precise results than with conventional models [4].

REFERENCES

- [1] D. E. Root, S. Fan, J. Meyer, "Technology-independent large-signal FET models: a measurement-based approach to active device modelling", Proceedings of 15th ARMMS conference, Sept. 1991
- [2] Mónica Fernandez-Barciela et al., "A simplified nonquasi-static table based FET model", 26th EuMC Proceedings, 1996, Prague, pp. 20-23
- [3] G. Kompa, "Modelling of Dispersive Microwave FET Devices using a Quasi-static Approach", Int. J. of Microwave and Millimeter-Wave Comp.-Aided Engineering, vol. 5, no. 3, 1995, pp. 173-194
- [4] Ingo Schmale et al., "Dispersive table-based large-signal FET-model validated in analysis of MMIC frequency doubler", 26th European Microwave Conf. Proceedings, 1996, Prague, A4.3, pp. 260-263
- [5] R. H. Daniels et al., "A Nonquasi-Static, Large-Signal FET Model Derived from Small Signal S-parameters", 1991, Proceedings of the Int. Semiconductor Research Symposium, pp. 601-604
- [6] Mark C. Foisy, Paul E. Jeroma, Glenn H. Martin, "Large-signal relaxation-time model for HEMTs and MESFETs", IEEE MTT-Symp. Dig., 1992, IF1 D-2, pp. 251-254
- [7] W. Haydl et al., "Models of coplanar lines and elements over the frequency range 0-120 GHz", 26th EuMC proceedings, Sept. 1996, Prague, B11.5, pp. 996-1000

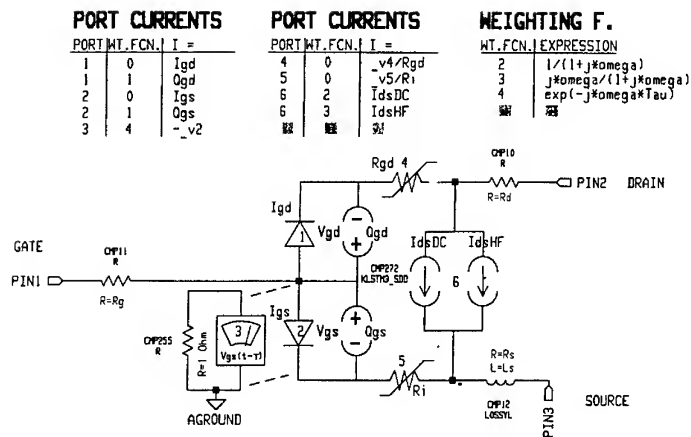


Fig. 1 Large-signal model implementation in MDS.

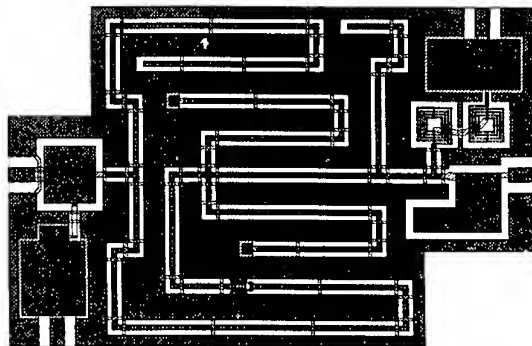


Fig. 2 MMIC 12/24GHz frequency doubler.

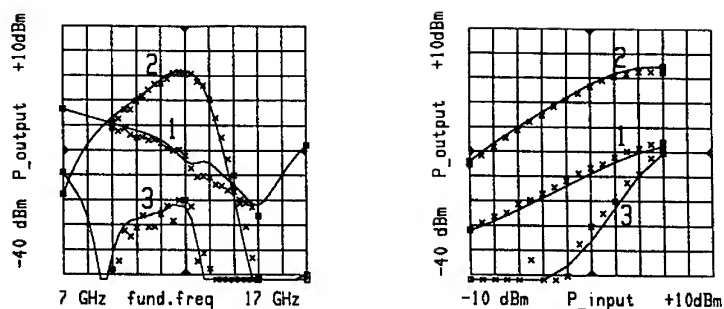


Fig. 3 Comparison of simulated data (lines) versus measured data (crosses); output power of fundamental (1), desired doubled (2) and tripled (3) harmonic (left: sweep versus fundamental frequency; right: sweep versus input power).

SIMULATION OF HIGH BIT RATE OPTICAL FIBRE COMMUNICATIONS LINK USING PHYSICS BASED LASER DIODE MODEL

Dr. Joseph Barnard, Barnard Microsystems Limited, 134 Crouch Hill, London N8 9DX
TEL: +44 181 341 0566 FAX: +44 181 341 0583
EMAIL: BML@CompuServe.COM

1. INTRODUCTION

Following extensive work on the development of the transmitting and receiving components of a 2.5 and 10 Gbit/sec optical fibre communications link (hereafter referred to as "the link"), we soon came to appreciate the value of being able to predict the bit error rate and other parameters for a complete optical fibre communications link into which we could "insert" our new components. We found that simply looking at waveforms on very fast sampling oscilloscopes and measuring component S parameters were insufficient to enable us to fully minimise the bit error rate of the link.

Another useful attribute of such a simulation capability related to the ease with which we could alter the nature of the circuitry between the laser diode driver chip and the laser diode transmitter module to measurably reduce the bit error rate of the link. An interesting aspect that came to light in our work was the importance of the interaction between the laser diode driver and the laser diode module, an interaction that some people minimise by placing the two components as close to each other as possible.

2. LINK COMPONENT PARTITIONING

The link was partitioned as discussed next to enable the user of the software to modify a few components in the overall link and observe the effects of those changes on the link parameters, such as the bit error rate.

input circuit for laser driver	passive microstrip network
laser diode driver	currently solved using linear simulator
inter-component circuit	passive microstrip network
passive circuit in laser diode package	passive microstrip/stripline network
embedded laser diode	linear or non-linear simulation
electrical-to-optical transformation	laser diode rate equation solution
dispersive optical fibre effects	time sliced optical signal with dispersion
receiving photodiode	current controlled current source with time delay, series resistance and parallel capacitance
transimpedance amplifier	currently solved using linear simulator
Thomson-Bessel filter	using ideal fourth order filter response equations for filter with bandwidth = 75% of bit rate

3. GENERAL SIMULATION PRINCIPLES

In general we predicted the S parameter response of a linear microwave network using our WaveMaker linear microwave circuit simulator and saved the response in the form of an S parameter data file. We then generated a 2,048 time sampled waveform that represented a 64 bit data stream with a user defined data content. The rising and falling edges of the waveform were defined using a modified Fermi Dirac equation (borrowed from semiconductor physics) for better matching of the waveform to reality, and had user defined rise and fall times. The waveform was transformed into the frequency domain using the Fast Fourier Transform (FFT), convolved with the real and imaginary parts of the linear circuit S21 response and then Inverse Fast Fourier Transformed (IFFT) to derive the prediction of the waveform emerging from the linear network. The assumption here is that the linear circuit sections see characteristic impedances at their ports.

We modified the FFT routine defined in the "Numerical Recipes In C", Second Edition by Press et al., Cambridge University Press, by replacing the floating point variables with double precision real variables together with some other minor changes. We verified the dynamic range of the FFT routine on a pure sine wave to be 325 dB, as expected when double precision variables are used on a 32 bit computer. This verification is necessary to define the FFT noise floor. The FFT routine is used with the addition of a simple scaling factor related to the number of samples in the spectral response to perform the IFFT.

Noise was included in the simulation through the addition of physically realistic noise to the waveform as detected at the photodiode. This conforms to the practice of referring the noise generated in the transimpedance amplifier to an equivalent noise level at the input to the amplifier in terms of pA per sqrt hertz or nV per sqrt Hertz. The noise itself consisted of impulses, the amplitude of which is determined by a biased random number generator where the higher amplitudes above and below a particular level (equivalent to room temperature) are exponentially less probable, and the angle of the impulse is determined by a second uniform random number. The impulse angle is then simply mapped to a vertical plane to determine both the signal polarity and multiplier value.

At any point in the link, we could visualise the electrical or optical waveform and the spectrum of that waveform. In the case of the optical waveform, we could also view the wavelength of the optical signal as a function of time to determine the optical signal chirp. The S parameter response of any of the linear circuit sections could also be displayed should the user wish to modify any of the linear circuit sections.

4. PREDICTING THE OPTICAL SIGNAL AMPLITUDE AND WAVELENGTH

input circuit for laser driver	passive microstrip network
laser diode driver	currently solved using linear simulator
inter-component circuit	passive microstrip network
passive circuit in laser diode package	passive microstrip/stripline network
embedded laser diode	linear or non-linear simulation

The laser diode driver equivalent linear circuit is constructed by matching the equivalent circuit response to the measured S parameters from the actual laser diode driver (eg. Fujitsu FMM 311). An example of such an equivalent circuit approximation for the Fujitsu FMM311 laser diode driver in netlist form is as follows:

CKT

```
IND 1 2 L=0.2609
VCCS 2 3 0 0 M=-0.01 A=0.0 R1=5000 R2=5000 F=100 T=0.0
SRC 2 0 R=10.50 C=1.517
PRC 3 0 R=267.6 C=1.515
SRC 3 0 R=220.9 C=8.611
IND 3 6 L=2.218
TLIN 6 10 Z=263.7 E=1.32 F=1.0
DEF2P 1 10 FMM311
```

The laser diode package equivalent circuit is derived from inspection of the contents of the laser diode package. Since the laser diode is always biased, we can use a linear circuit approximation for the non-linear electrical characteristics of the diode itself.

VAR

```
L1=3.5
```

CKT

```
MSUB ER=9.6 H=0.2 T=0.012 RHO=1 RGH=0.002 TAND=0.001
WIRE 1 2 D=0.35 L=L1 RHO=1 H=3
MLIN+ 2 3 4 W=0.608 L=3.3
IND 3 5 L=0.05
MLIN+ 5 6 4 W=0.608 L=2.1
IND 6 8 L=0.5
RES 8 9 R=18
IND 9 10 L=0.2
IND 10 11 L=0.2
CCCS 11 12 13 0 M=-0.027 A=0 R1=8.0 R2=5000 F=500 T=0
CAP 11 13 C=4.0
CAP 10 4 C=3.9
IND 13 4 L=0.2
WIRE 4 0 D=0.35 L=L1 RHO=1 H=3
WIRE 4 0 D=0.35 L=L1 RHO=1 H=3
DEF2P 1 12 HPLD
```

We must solve for the voltage across the linearised diode relative to the voltage applied at the input to the input circuitry in front of the laser diode driver. The voltage across the linearised laser diode is monitored through the use of a current controlled current source (CCCS) which monitors the current through the laser diode resistance (8 ohms in the above example). Remember that the laser diode resistance is made up of the dynamic resistance and the series parasitic contact and other resistances.

The electrical response of all the five components at the transmitting side of the optical fibre need to be simulated together since the impedances at the ports are usually not the characteristic impedances. The inclusion of the laser diode driver is most important if the performance of the communications link is to be correctly simulated.

Using the previously mentioned FFT/IFFT techniques and the predicted input circuit S21 transfer response, we can predict the waveform of the current into the laser diode. We then read the physical data for the laser diode being used (diode length, width, various relaxation times and so on) from a data file and solve the laser diode rate equations given the driving current waveform to predict both the amplitude of the light emitted from the laser diode, and the wavelength of the emitted light. We have verified the accuracy of our laser diode model through the use of fast optical waveform sampling and fast time resolved optical spectrometry. The laser diode model was derived from the work of Professor Ian White at the University of Bristol, with whom we will be working to refine the model to account for transient temperature effects appropriate to the laser being used in the absence of a Peltier thermoelectric cooler.

5. THE OPTICAL FIBRE AND THE OPTICAL RECEIVER

Rather than use the Fourier Transform, we have time sliced the optical waveform from the laser diode and applied the appropriate wavelength dispersion, average time delay and attenuation to each optical slice, and then recombined the slices appropriately at the end of the fibre. We did not account for any amplitude dispersion effects in the fibre since the incident transmitted optical power level was relatively low (few milliwatts).

At the receiver, we added a user defined amount of physically realistic noise and then passed the signal through the transimpedance amplifier circuit into the fourth order, flat phase (equal signal group delay) Thomson-Bessel filter with a -3dB cut off frequency of 75% of the bit rate.

6. BIT ERROR RATE DETERMINATION

We used the FFT based correlation capability to determine the relative time delay between the signal at the input circuit in front of the laser diode driver and the signal emerging from the Thomson-Bessel filter at the link output. The input signal is then delayed by the link delay and directly compared with the output signal, where we have taken care to remove any d.c. bias from the output signal. We compare the signal amplitudes at the middle of each bit period: any difference between the two signals is registered as a contribution to the bit error rate (BER).

Since we typically look at a very small bit length compared with that looked at by bit error rate test equipment (1024 bits rather than $2^{23} - 1$) we increase the noise level to induce a measurable BER. With a measurable BER of, for example, 100 in 1024 bits, we can investigate the relative reduction (or increase) in this ratio as a function of circuit element and drive level changes.

7. APPLICATION OF THIS APPROACH

One of the problems with the current generation of laser diode drivers is their high source impedance. This arises because the driver output consists typically of a direct connection to the drain of a GaAs MESFET or the collector of a bipolar transistor. Any reflected electrical signal from the laser diode package will encounter the high impedance of the laser diode driver and be reflected back to the laser diode package, so setting up a resonant situation in the microstrip line between the laser diode driver and the laser diode package. To reduce the source impedance of the laser diode driver, we found that by placing a 100 ohm resistance in series with a 1nF capacitance across the laser diode driver output to ground measurably reduced the BER from 150 in 1024 bits to 83 in 1024 bits. The 1nF capacitance should not be too small, otherwise bit pattern error effects will become evident.

We used the whole link simulation approach to help us in the design of a new 2.488 GBit/sec laser diode module including the design of the butterfly package itself. Since the laser diode model predicted such effects as optical resonance (increase relative optical intensity noise) we were able to minimise these effects through judicious choice of the components and bond wire lengths within the package itself. The beauty of this approach is that we could determine the effects of changing the length of a single bond wire within the laser diode package on the link BER and on any of the waveforms throughout the link.

We have included all of the above mentioned optical link simulation capability in our commercially available WaveMaker software as our COMMS software option. This software is currently being used by some of the optical communications component manufacturers to help them to design low bit error rate components for use in multi-Gigabit optical fibre communications links.

Currently, the most difficult aspect associated with this approach is the derivation of the models for the components, particularly:

the transimpedance amplifier	not so difficult
the laser diode driver	difficult
the laser diode itself	most difficult at the present time

Our current work involves simplifying the procedure used to derive the physical laser diode parameters for an arbitrary laser diode, initially unpackaged, followed by the extraction of the parameters for a packaged laser diode. Additionally, we have in the prototype stage as a result of our collaborative work with Professor Tom Brazil at University College Dublin, a non-linear simulator based on a heavily modified version of SPICE in which we can import S parameter data and solve for the current waveform through non-linear devices such as diodes. The use of this new time domain simulator with S parameter data import capability allows us to very accurately simulate the electrical behaviour of the laser diode driver and the non-linear laser diode in the laser diode package.

Linearization of Microwave Emitters using an Adaptive Digital Predistorter

Ernesto G. Jeckeln, Fadhel M. Ghannouchi and Mohamad Sawan

Department of Electrical and Computer Engineering
Ecole Polytechnique de Montréal
C.P. 6079, Succ. Centre Ville, Montréal, Canada H3C 3A7

Abstract

Adaptive digital predistortion for nonlinear power amplifier (PA) became one of the most robust linearization techniques that can be implemented in digital signal processors (DSP) environment. However, its precision compensation for AM-AM and AM-PM distortion is wasted when the quadrature modulator (QM) impairments are not to be considered. This paper presents a new digital predistorter for microwave emitters with real time modeling of both, PA and QM distortions, that can compensate for nonlinearity, gain imbalance, phase imbalance and DC offset. An improvement of 35 dB of out-of-band power is obtained in simulating with 10^5 complex input look-up table using 2D interpolation.

Introduction

Spectral efficiency and high power added efficiency became the important factors in Cellular and Personal Communication Services (PCS). To maximize these parameters, linear modulation methods and saturated power amplifiers have to be used. However, the fluctuating envelope of the resulted signal from linear modulation methods causes distortion and spectral spreading in the output of microwave emitters. A generic microwave emitter is constituted by a quadrature vector modulator and power amplifier (see Fig.1). In order to reduce these undesired effects and meeting both, power efficiency and spectral efficiency, linearization techniques must be introduced. In addition, quadrature modulator suffers from severe deficiencies Imai et al (1), such as gain imbalance, phase imbalance and DC offset. As a result, the residual intermodulation products in the output signal of the microwave emitter cause the BER degradation. Therefore, a compensation technique for these impairments must be included.

A variety of linearization methods have been reported and predistortion linearization, Imai et al (2) and Stapleton et al (3), is one of the techniques that can be chosen for an analog or digital implementation. This method uses a nonlinear element preceding the device to be compensated and its gain expansion characteristic cancels the gain compression of the amplifier. In the case of the digital implementation, one of the most important feature is that any function is easy to be performed by software and therefore, significant improvements can be obtained using inverse nonlinearities. The first successful work were presented by Nagata (4), using a two-dimensional look-up table technique with adaptive digital feedback at baseband and pulse shaping filter prior to predistortion. This technique has the advantage that any order of nonlinearity and any modulation format can be performed. Moreover, the use of two-dimensional look-up table permits also correction of PM-PM and PM-AM distortion generated in the QM of analog part. The disadvantage of this technique is that for an acceptable accuracy, the size of the look-up tables must be kept higher (two millions complex words). Therefore, the memory requirement becomes large and results in the slowly convergence each time when the tables are updated.

Several drawbacks of this technique have been improved, by Caver (5) and Faulkner (6), using one-dimensional table. It has made possible that less memory is needed and therefore, the convergence time is reduced. In this way, another successful approach were presented by authors in (7), using real time nonlinearity modeling, where the iterative algorithm and the convergence time have been eliminated. It is to be noted that the improvement in the last three techniques (5), (6) and (7) comparing to the one proposed by (4) is at the expense of the QM impairments.

Because of the DSP is expanding at high rate, the benefits of this technology have become available to RF and microwave community. The contribution in the last few years had permitted that the processing power required, which are not available on a single processor, is recently available by multiprocessing architecture. This technology can handle higher bandwidth signal and can perform more intensive processing.

Taking into account this potentiality, we propose in this paper a new adaptive digital predistorter with Real Time Modeling (RTM) of both, PA and QM distortions, that can supply correction for any order of non linearity, gain imbalance, phase imbalance and DC offset. This technique have been developed to be implemented with a digital signal multiprocessors, where the RTM of the all distortions generated in the forward path signal is performed to provide, using a two-dimensional lookup table technique, the predistorted signal.

The adaptive digital predistorter

Fig.1 shows a simplified block diagram of the proposed adaptive digital predistorter where, in addition to the digital domain, a dual DA/AD converters, a quadrature modulator and demodulator, a microwave coupler and a microwave power amplifier form the analog domain to complete the entire system. The spectrally efficient 16-QAM modulation method is used as a transmitted signal source, which is passed through a pulse shaping filter to ensure free Inter-Symbol-Interference (ISI). In the RTM algorithm, the input digital baseband signal and the output lowpass equivalent complex envelopes of the amplifier are sampled, scaled and updated into the lookup tables to provide the predistorted signal. These tables are configured to implement a mapping from the input (I,Q) to the output (Id,Qd) using 2D interpolation and according to the number of sampled pairs measured. Because of the random nature of the data measurement, unequal spacing between tables entries are used. An important feature to be considerate is the adaptability dedicated to drift correction. The predistorted signal over time-varying characteristics (AM-AM and AM-PM) requires that the predistorter adapt to this change. Adapting the predistorter to compensate this variation requires a feedback path through which the linearizer can be notified of this change. In this case, mean error criterion between the desired and the distorted feedback signals is used to perform adaptability. The feedback loop is used only to update the LUT. After each adaptation and during normal data transmission, the feedback loop is opened until new significant drifts have occurred and new data has to be entered in the LUT. In order to estimate the delay in the feedback loop, correlation between the predistorted signal and the feedback signals is performed, and the delay is compensated by the same amount in the predistorted signal.

Let the Emitter be considered as a zero memory system. Then, the input-output relationship of such system can be written as follows :

$$w(t) = T[z(t)], \quad (1)$$

where $z(t)$ and $w(t)$ represent the input digital baseband signal and the output lowpass equivalent complex envelopes of the emitter respectively. The complex transfer function is given by :

$$T[z(t)] = |T[z(t)]| e^{j\phi[z(t)]}. \quad (2)$$

Since $z(t)$ is complex-valued, $z(t) = I_d(t) + jQ_d(t)$, where $I_d(t)$ and $Q_d(t)$ are real values. Hence, $w(t)$ can be written as a complex-valued function of the real values $I_d(t)$ and $Q_d(t)$ as follows :

$$w(t) = I(I_d, Q_d) + jQ(I_d, Q_d), \quad (3)$$

where $I(I_d, Q_d)$ and $Q(I_d, Q_d)$ are real functions of the variables I_d and Q_d . Now, let the complex transfer function $T[z(t)]$ be analytic on a set S. Then, it is always possible to find a complex function $z(t) = P[w(t)]$

that satisfies $w(t) = T\{P[w(t)]\}$ and which is unique in that no other function has this properties. Then, $P[w(t)]$ become the inverse function of the $T[z(t)]$ and can be used as a complex predistortion transfer function. Thus,

$$z(t) = I_d(I, Q) + jQ_d(I, Q), \quad (4)$$

and the complex predistortion transfer function is given by :

$$P[w(t)] = |P[w(t)]|e^{j\phi[w(t)]}. \quad (5)$$

Simulations results

The global system has been built with Signal Processing WorkSystem (SPW) (8) environment and several important analysis results are presented here. The spectrally efficient 16QAM modulation method with a baud rate of 24.3 kHz is used as signal source. Hence, 16 different possible symbols form the signal-space diagrams where we have assumed equally likely signal set. The pulse shaping filter was a raised cosine having a roll off $\alpha=0.35$, and the oversampled rate was 16 samples/symbol. In addition to estimate the spectral magnitude, the signals have been multiplied by a blackman window function to smooth the signals frequency spectrum, then, Discrete Fourier Transform (DFT) have been obtained for each signal with $N=1024$ points. The Pin-Pout characteristics of a class AB power amplifier were modeled using cubic spline interpolation and stored in two look-up tables for simulation purpose. QM impairments were 5° of phase error, 2% of gain error and 5% of DC offset. From the time domain analysis, four constellation diagram is used to evaluate the distortion and the compensation. In fig.3(a), we can see a compression and an expansion in the real and imaginary part, respectively, where the vector signal will follow an offset elliptical trajectory. In real system, the PA nonlinearity and the QM impairments can be lumped together and modeled using 2D interpolation. Fig. 4(a) shows the distorted constellation diagram at the output of the emitter and Fig.5(a) shows that the distorted symbols are mapped back to the desired positions when the compensation is performed. A comparison of the spectral magnitude shows clearly a degradation in out of band emissions, Fig.4(b), and that the spectral magnitude floor is limited by the QM impairments, Fig.3(b). Note, in Fig.5(b), that an improvement of 35 dB of out-of-band power can be reached using 10^5 complex words in each table (real and imaginary part). A further reduction in spectral distortion can be achieved if the tables sizes are increased.

Conclusion

In this paper, a new method dedicated to Adaptive Digital Predistorter that can compensate for non linearity, gain imbalance, phase imbalance and DC offset of a microwave emitters is proposed and simulation results using SPW software are presented. The real time modeling of both PA and QM distortions was implemented to calculate the predistortion function using 2D interpolation. Two dimensional look-up tables were used with unequal spacing between table entries. The RTM algorithm has demonstrated to be a powerful tool for sounding the distortion during normal data transmission and supplying the knowledge of the nonlinearity to the predistorter. The major advantages of this technique in comparison with the predistorter presented by [6] is the reduced memory requirements, from 2 millions complex words to 200K complex words. In addition, the proposed adaptive linearization technique can be self corrected for any drift in the operating points and without any iterative procedure. It is noted that the ability of the RTM algorithm is in eliminating the need for complex convergence algorithms in the adaptation update step.

Acknowledgment

This work was supported by the "Programme Synergie" of the Quebec government through the AMPLI project in collaboration with Advantech Inc. and NSI Communications.

References

- [1] N. Imai, T. Nojima and T. Murase, "Novel Linearizer Using Balanced Circulators and Its Application to Multilevel Digital Radio Systems", August 1989, IEEE Transactions on Microwave Theory and Techniques, vol. 37, no 8, pp. 1237-1243.
- [2] N. Imai, T. Nojima and T. Murase, "Novel Linearizer Using Balanced Circulators and Its Application to Multilevel Digital Radio Systems", August 1989, IEEE Transactions on Microwave Theory and Techniques, vol. 37, No 8.
- [3] Stapleton S.; Costescu, C. "An Adaptive Predistorter for a Power Amplifier Based on Adjacent Channel Emissions", February 1992, IEEE T.V.T. vol. 41 No 1.
- [4] Y. Nagata, "Linear Amplification Technique for Digital Mobile Communications", 1989, in Proc. IEEE Veh. Technol. Conf., San Francisco, CA, pp. 159-164.
- [5] J. Cavers, "Amplifier Linearization Using a Digital Predistorter with Fast Adaptation and Low Memory Requirement", November 1990, IEEE Transactions on Vehicular Technology, vol. 39, no 4, pp 374-382.
- [6] M. Faulkner, T. Mattsson and W. Yates, "Adaptive Linearization Using Predistortion", 1990. in Proc. 40th IEEE Veh. Technol. Conf., pp. 35-40.
- [7] E.G. Jeckeln, F.M. Ghannouchi and Mohamad Sawan, "Adaptive Digital Predistorter for Power Amplifiers with Real Time Modeling of Memoryless Complex Gains", June 1996, IEEE MTT-S 1996 International Microwave Symposium, San Francisco, CA.
- [8] Signal Processing WorkSystem (SPW), Alta Groupe of Cadence Design System, Inc., 1996.

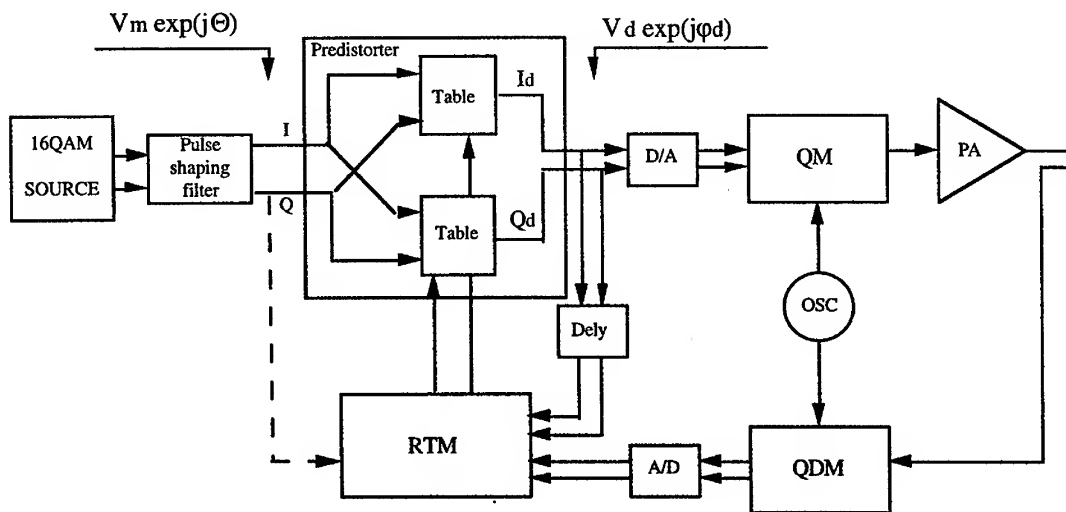
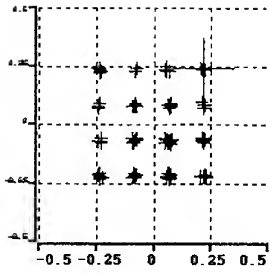
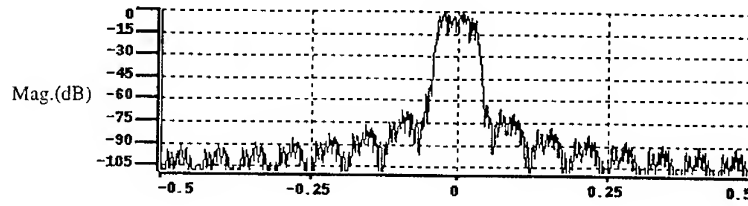


Fig. 1 Block diagram

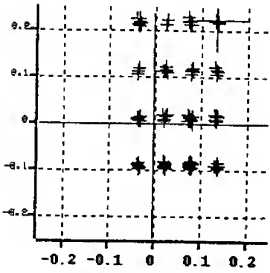


a)

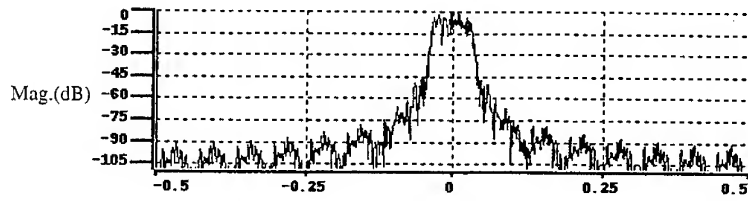


b)

Fig.2 The input signal. a) Scatter diagram. b) Spectral diagram

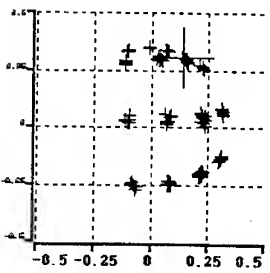


a)

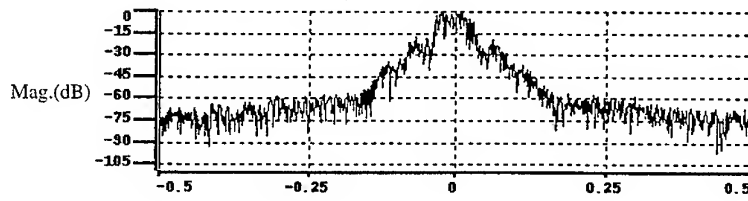


b)

Fig.3 The signal at the output of the QM. a) Scatter diagram. b) Spectral diagram

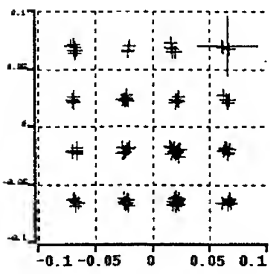


a)

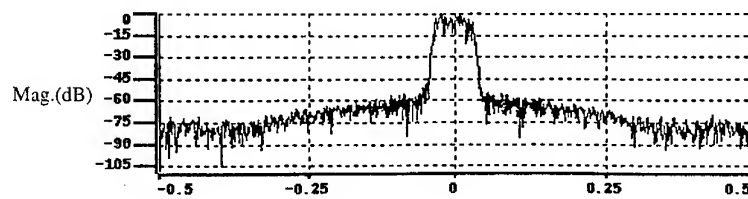


b)

Fig.4 The output signal without linearization



a)



b)

Fig.5 The output signal with linearization

Six-port Direct Conversion Receiver

Jari Hyyryläinen, Leonid Bogod,
Seppo Kangasmaa, Hans-Otto Scheck, Tommi Ylämurto

Nokia Research Center, P.O. Box 45, (Heikkiläntie 7), FIN-00211 Helsinki, Finland

ABSTRACT

The applicability of the known six-port receiver structure for mobile phones was studied. The six-port receiver is typically used in high frequency microwave analyzers where a wide bandwidth is required. In these applications the unperfections of the six-port structure can be canceled by using calibration. In direct conversion receivers a severe problem is to achieve the required AM suppression characteristics. This is known as a DC problem. Strong adjacent channel signals cause interference in the baseband through second order effects. To evaluate the suitability of a six-port receiver to achieve the required AM suppression level a discrete component six-port receiver operating at 2GHz frequency area was implemented and measured. The results were compared against traditional mixer structures.

FOREWORD

The ever increasing demand for wireless communication services has led to the situation where a mobile phone is a cheap mass-produced article. The multiple of different cellular systems and standards complicates the situation. The markets are separated into sections each having their own characteristics. Different systems use different frequency bands and modulation methods. This variety of systems creates also demand for multimode devices (e.g. GSM/DECT phone).

The traditional superheterodyne receiver architecture is the best solution in terms of electrical performance. Unfortunately it is not easily integrable and thus can not easily fulfill all future demands. Low power consumption, weight, size and cost can be achieved only by integration. Strict limitations in the tuning range and in the fixed channel filtering make superheterodyne receiver an inadequate choice for the multimode receivers. In the superheterodyne receiver the noise generated by the LNA is mixed into the IF band from both upper and lower sidebands. Therefore an additional bandpass filter is needed to suppress the noise from the unwanted sideband. So far it has been impossible to integrate the intermediate and image rejection filters. In the direct conversion receiver these bulky filters are unnecessary.

DIRECT CONVERSION RECEIVER

The direct conversion concept means a direct frequency translation from the radio frequency (RF) to the baseband. The channel filtering is performed at the baseband and the bandwidth can be defined by reconfigurable digital filters. The direct conversion principle has already been applied successfully in paging receivers and its applicability for narrow band TDMA systems like GSM are heavily studied.

Usually the direct conversion receiver is implemented by utilizing Gilbert-cell mixers. Direct conversion suffers from some unique problems. Main causes to these are insufficient LO-RF isolation and the unsymmetry in the receiver structure. Due to insufficient LO-RF isolation LO leakage from the receiver into the antenna may cause interference to other users. DC offset in the receiver is even more serious problem. There are three causes to the DC offset. The LO signal leaking to the RF port and reflecting back causes DC through self-mixing. This is not very harmful because the LO level is constant. Strong near-channel AM-modulated signals may leakage to the LO port of the mixer and then self-downconvert to DC. The generated DC signal is dynamic by nature and can not be filtered out. Any unsymmetry in the mixer structure generates also DC offset. However this can be minimized by good design. The DC generated by interfering signals is more problematic.

SIX-PORT BASICS

The idea of using a six-port structure to determine the phase of a microwave signal was first presented in 1964 by Cohn and Weinhouse (1). A six-port is a black box with two inputs and four outputs. The output ports are terminated with power detectors. When the relations between the input and output ports are known the relations between the two input signals (phase and amplitude) can be determined. The only requirements are that the six-port is linear and that the outputs are not linearly dependent on each other. From the four equations can be solved four unknowns. With a calibration procedure, the equations can be found very accurately. Therefore the six-port structure has been used in network analyzers. Analysis of the six-port structure can be found from Hoer and Roe (2).

In a six-port receiver the RF signal can be applied into one input port and the LO at the second. These are then summed up with different phases in the six-port correlator structure. The correlator can be formed by using one power splitter and three quadrature hybrids. Also more complicated implementations are possible. The power levels of the four other ports are measured and used to calculate the baseband I- and Q-signals. In the six-port receiver are used power detectors instead of mixers to get the baseband signals, see figure 1.

In a switching mixer, the LO signal must be high enough to switch a diode or a transistor from a conducting state to a non-conducting state. The power detectors require lower voltage swing. So the six-port receiver has potential for a very low voltage operation. Also the LO power consumption is low.

SIX-PORT DEMONSTRATOR

To study the applicability of the six-port structure as a handportable receiver a demonstration device was made. The designed phase correlator adds up the input signals (LO and RF) creating four different combinations. Every combination is a sum of the input signals with different phase shift (0° , 90° , 180° and 270°).

In the six-port demonstrator the baseband I- and Q-channel signals can be attained easily by subtracting the power readings from the appropriate correlator output ports, see figures 1 and 2. However the correlator outputs are not linearly independent. This means that the correlator is actually a five-port and it is not possible to calibrate it. One more independent output should be added in order to make the calibration. Originally the six-port was used in network analyzers where only one

frequency is used at time. The calibration is made at the frequency of interest to remove the unperfections caused by the six-port structure. When the six-port is used as a receiver, the channel filtering is performed after the power detectors. Signals at different frequencies pass through the preselection (duplex) filter and finally reach the power detectors. When the unwanted channels are detected in the square-law detectors, they cause DC component which can not be removed by the calibration process. Neighboring channel interfering signals can not be filtered out in a single correlator output channel (U1, U2, U3 or U4, figure 1). But the combining of the two correlator channels cancels the interfering signals.

The phase correlator was implemented with microstrip techniques. Two different microstrip correlator alternatives were designed and analyzed. The traditional correlator constructed from three branch-line hybrids and one power divider and a second one constructed with two ring hybrids, one branch-line hybrid and one power divider. Both correlators give the sum and the difference of its input signals. The correlators were implemented on a printed circuit board with high permittivity DiClad 810 (Arlon) substrate. The structures were optimized at 1.84GHz. The ring hybrid implementation was selected for the final receiver design because measurements gave better isolation between its input ports (40dB). The ring hybrid correlator is seen in the figure 2.

As power detectors were used commercial matched diode pairs to get optimal symmetry. To form a complete receiver front-end a LNA, a DCS 1800 duplex filter and 4th order active baseband filters with 10dB gain were added, see figure 3.

MEASUREMENTS

The total six-port receiver gain was 39dB and the noise figure 13dB. The 1dB compression point was -24dBm at the antenna input. The IQ-balance was adequate. The measured characteristics of the demonstration six-port receiver were compared to these of a Gilbert cell and FET ring mixers, see table 1. In the comparison it has to be kept in mind that the six-port is a complete I-Q demodulator whereas the mixer presents a single channel only. A comparable receiver configuration would consist of two mixers and two power splitters. The splitting of the input power into two branches in the six-port is taken into account in table 1.

In the direct conversion receiver both the modulated and continuous wave (CW) blocking tests give some response at the baseband due to the second order nonlinearities of the receiver. The CW test gives a constant DC offset at the baseband. In the DC offset measurements an unwanted signal with a 5MHz frequency offset to the LO frequency was applied at the input of the receiver. The wanted baseband signal and DC offset of the six-port receiver are seen in the figure 4.

The good LO-RF isolation of the ring hybrid correlator was severely deteriorated when the detectors were connected.

In (3) is specified the required AM suppression characteristics of the GSM receiver. With a direct conversion receiver these can be fulfilled when the IIP2 is in the order of 50dBm. The discrete component six-port demonstration receiver is missing about 20dB from this value.

CONCLUSION

The growth of cellular subscribers leads to more effective use of the spectrum which increases the interference in the future. The direct conversion receiver is especially sensitive to the spurious signals. On the other hand, the direct conversion method can offer a low-cost solution for the future handportable phones with the capability of smooth change between different systems and services.

The six-port direct conversion receiver seems to be a viable alternative for mobile terminals. The basic six-port structure operates with low supply voltages and low LO power is required, typically from -10dBm to 0dBm. Also voltage conversion gain in the order of a Gilbert cell mixer is achievable. The noise figure is comparable to a standard mixer. The main problem in a direct conversion receiver seems to be the DC offset caused by the second order effects. A symmetrical structure - mixer or six-port - combined with a high RF-LO isolation would make the life of a direct conversion receiver designer much easier.

References

- (1) S.B. Cohn and N.P. Weinhouse, "An automatic microwave phase measurement system", Feb. 1964, Microwave Journal, vol. 7, no. 2, pp. 49-56.
- (2) C.A. Hoer and K.C. Roe, "Using an arbitrary six-port junction to measure complex voltage ratios", December 1975, IEEE Trans. on MTT, vol MTT-23, no. 12, pp. 978-984
- (3) ETSI GSM 05.05, Digital cellular telecommunications system (Phase 2); Radio transmission and reception, January 1996

	Six-port	Gilbert cell	FET ring
Power conversion gain	-8.5dB ¹⁾	-2.5dB	-10dB
Voltage conv. gain	14dB / 9k ¹⁾	8dB / 1k	3dB / 2k
Noise Figure	22dB	23dB	10dB
IIP2	32dBm	24dBm	36dBm
G(1dB) input	-13dBm ¹⁾	-5dBm	1.5dBm
LO-RF isolation	> 23dB	50dB	48dB
LO power	-10dBm	-7dBm	+5dBm
Power consumption	2V 0.16mA	5V 1.6mA	-1.5V ~0mA

¹⁾ Results refer to a single branch of the six-port

Table 1. Comparison of six-port, Gilbert cell and FET ring mixer characteristics at 2GHz. The LNA is not included.

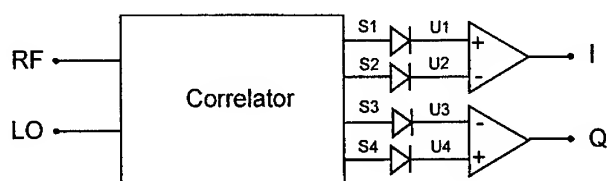


Figure 1. The basic six-port implementation

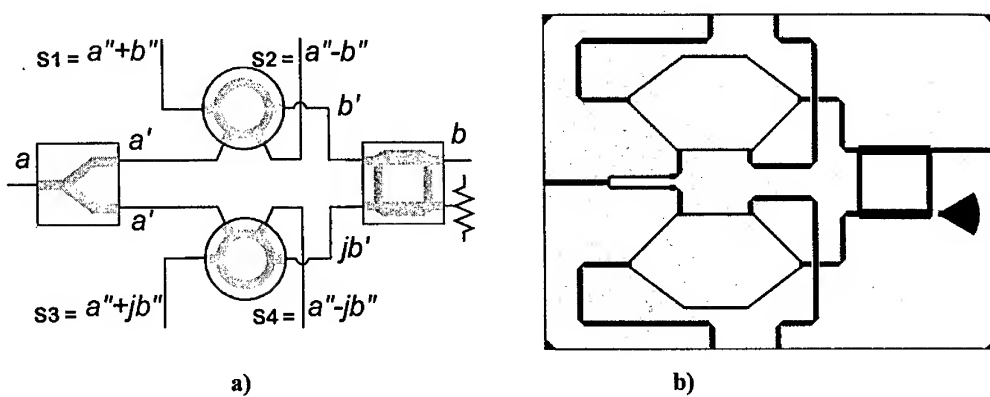


Figure 2. a) A six-port junction using ring hybrids. b) Ring hybrid implementation with microstrips.

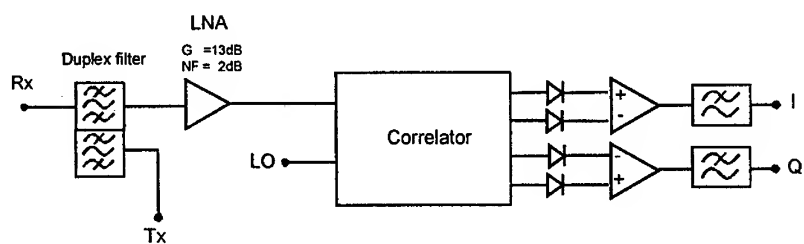


Figure 3. A six-port direct conversion receiver front-end.

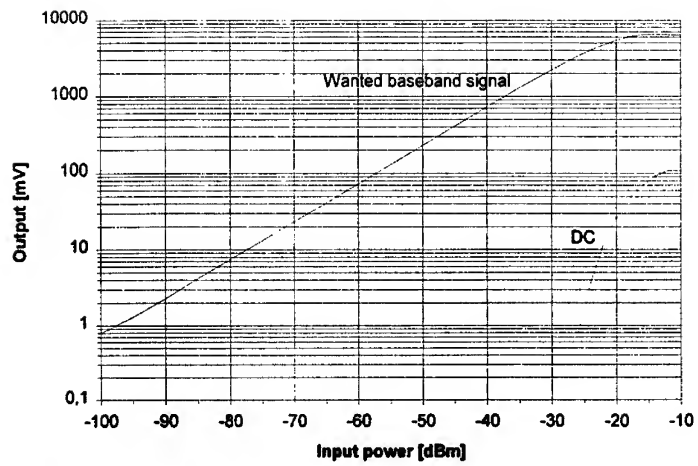


Figure 4. Wanted baseband signal and DC offset.

Modulation Imperfections in IS54 Dual Mode Cellular Radio

Avi Brillant B.Sc.-EE
Optomic Microwaves LTD.
Migdal Ha'Emek 10551
P.O.B 153
Tel :972-6-545440
Fax :972-6-545382

David Pezo B.Sc.-EE
Telrad Inc. LTD.
Lod-71100
P.O.B-50
Tel :972-8-9273229
Fax :972-8-9273164

A. Abstract

Non ideal I and Q calibration circuits on one hand, phase noise spurious response of the synthesizers and carrier leakage on the other hand, will affect the modulation quality by degrading Modulation parameters such as EVM, Spectral Mask and Residual AM. Transmitter's gain chain and its output power amplifier linearity and synthesizers phase noise will degrade the spectral purity of the transmitter and its Spectral Mask even further, consequently degrade system's performance - Bit Error Rate (BER).

This presentation will identify typical Modulation errors related to the RF and Digital sections of the Dual Mode[12,13] (TDMA/AMPS) Cellular phone front end, and develop calibration methods which will effectively minimize the modulator internal errors by analyzing the output signal. We will focus on $\pi/4$ DQPSK digital modulation imperfections, errors in synthetic base band I & Q signals used to generate FM modulated signal by a QPSK modulator, Non linear effects and a modulation scheme commonly used in cellular IS54 radios

B. Quadrature Modulators

Quadrature modulators were used for Single-Sideband transmission and in recent years for quadrature AM (QAM) and other digital modulation schemes in digital radios. In dual-mode cellular phone radios, the Modem is designed to use one modulator for both digital and analog mode transmissions. This is done in order to simplify the design and calibration of the RF section of the mobile unit.

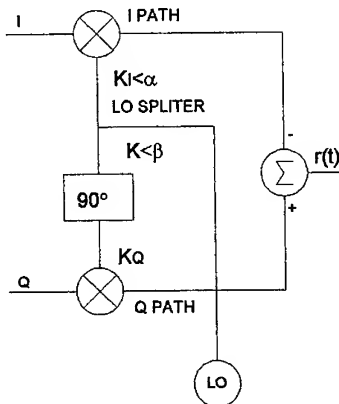


Figure-1: Quadrature Modulator

The block diagram of a quadrature modulator, consists of two mixers and a summation circuit to combine the mixers outputs. The inputs to the mixers are the information bearing baseband (low pass) signals $i(t)$ and $q(t)$ and a carrier of the local oscillator signal $\cos(\omega_c t)$ mixing with the I input, and $\sin(\omega_c t)$ mixing with the Q input. The transmitted signal is therefore [17]

$$(1) \quad r(t) = \sqrt{i^2(t) + q^2(t)} \cos\left(\omega_c t + \tan^{-1}\left(\frac{q(t)}{i(t)}\right)\right) = A(t) \cos(\omega_c t + \theta(t))$$

$$\text{or } (2) \quad A(t) e^{j\theta(t)} = i(t) + jq(t)$$

The later presentation of the QPSK modulator output signal implies that any complex modulation can be generated by properly chosen amplitudes and phases of I and Q. Moreover, since the I and Q signals have low pass characteristics, the low frequency modulation circuitry is usually easier to implement at the required accuracy. This is a major reason for the popularity of quadrature modulators.

C. Analog FM modulation impairments

C.1. Generating FM Using QPSK Modulators

To establish Frequency Modulated signal, the carrier's amplitude is held constant and the phase is varied. The FM transmitted signal is thus given by [17]:

$$(3) \quad r(t) = A \cos\left(\omega_c t + \Delta\omega \int_{-\infty}^t m(\tau) d\tau\right)$$

Where $\Delta\omega$ is the peak radian deviation and the peak magnitude of $m(t)$ is 1. $m(t)$ is the information bearing signal and the phase $\theta(t)$ is given by the integral of $\Delta\omega m(t)$.

From (3) it is concluded that the required baseband I and Q signals needed to generate an FM transmitted signal using a QPSK modulator are given by [17]:

$$(4) \quad i(t) + q(t) = A(t)e^{jq(t)} = A(t)e^{j\Delta\omega \int_{-\infty}^t m(\tau)d\tau}$$

$$= A(t) \left\{ \cos \left(\Delta\omega \int_{-\infty}^t m(\tau)d\tau \right) + j \sin \left(\Delta\omega \int_{-\infty}^t m(\tau)d\tau \right) \right\}$$

C.2. Residual AM of FM modulated signal

In case of an ideal modulation, $A(t)=A$. However in reality, there are several parameters that affect the amplitude A versus time like amplitude and phase imbalances between I and Q baseband inputs. These cause fluctuations in the magnitude A , known as **Residual AM**. Residual AM of an FM signal is defined as the amount of AM fluctuation on the FM signal amplitude. Residual AM is measured by AM Modulation Index $mi\%$ as defined by equation (5)

$$(5) \quad mi\% = \frac{m1 - m2}{m1 + m2} \times 100; m1 = \max|A(t)|; m2 = \min|A(t)|$$

In figure 2 the residual AM is plotted as a function of phase balance between I and Q, while the amplitude balance is a parameter.

It can be seen that the residual AM is more sensitive to the phase balance α rather than to the amplitude imbalance δ for high phase imbalance, but the amplitude imbalance correction is crucial for small phase errors. This is because that in the ideal case I and Q trajectory is a circle with a radius equal to $A_I=A_Q=A$. However in the non ideal case there is an amplitude imbalance between I and Q, phase imbalance α and DC offsets. The phase imbalance cause the projection of I on Q, I is decreased by $\cos\alpha$ while Q is increased by $1+\sin\alpha$. Hence the circle turns into an ellipse with offset axis due to the DC offsets caused by the carrier leakage.

D Digital $\pi/4$ QPSK Signal Impairments and Effects

Impairments types can be divided into two groups: Linear Impairments (like I and Q amplitude imbalance, phase imbalance, I and Q DC offset [14],[15],[16],[17] causing the carrier leakage), and Non linear Impairments (like AM to PM generally caused by the transmitter power chain, and LO Phase Noise affecting the phase imbalance by adding LO's $\pm\Delta\theta$ rms. to the phase error between I and Q). We will concentrate on the effects of linear impairments herein (non linear effects will be discussed in paragraph E).

Transmitter's modulation impairments will affect the constellation diagram of the transmitted signal, as described on Fig.3., and thus degrade the Error Vector Magnitude (EVM) and channel performance.

1. I and Q amplitude imbalance will affect the constellation symmetry and cause an ellipse-shaped constellation diagram, depending on either I or Q input is larger.
2. I and Q paths phase mismatch will cause constellation distortion in both directions X and Y. This is because the orthogonal projection of one component on the other is not zero. Such a phase error will rotate the constellation points from their original location.
3. The leakage of the carrier to modulators output, because of DC offset of the I/Q inputs, will affect the constellation origin offset. Since Carrier leakage consists of two perpendicular components related to the I path and the Q path of the QPSK modulator, the constellation origin is shifted both in X and Y axis direction respectively.

By applying Sine and Cosine to the I and Q inputs, the resultant modulated signal will be an SSB RF signal. Using these input signals, the modulator can be easily calibrated and checked for any malfunctioning and thus eliminating any constellation distortion and BER degradation.

D-1 I and Q Amplitude Imbalance

The side band suppression of a SSB signal is defined by [14,15,16,17]:

$$(6) \quad S[dBc] = 10 \log \left[\frac{\delta^2 + 2\delta \cos\alpha + 1}{\delta^2 - 2\delta \cos\alpha + 1} \right] \quad \text{Where } \alpha \text{ is the phase imbalance between the I path}$$

to the Q path and δ is the amplitude imbalance. (in dB or as a relative value).

The plot in Figure 4 shows the side band suppression as a function of amplitude balance between I and Q while the phase balance between I and Q is a parameter. It can be seen that phase imbalance α and amplitude imbalance δ limit side band suppression, so that for 30 dB of suppression, α should be below 3° and δ below 0.3 dB.

D-2 I and Q relative phase imbalance

The same reasoning of an SSB signal side band suppression, when I and Q transmission phases are not in perfect match, can be done by setting eq.(6) for constant amplitude error. Figure 5 shows the side band suppression as a function of phase balance between I and Q

while the amplitude balance between I and Q is a parameter.

It can be seen that up to 10% amplitude imbalance I and Q relative phase imbalance affects the side band suppression.

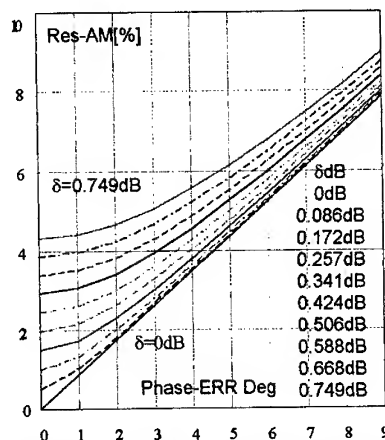
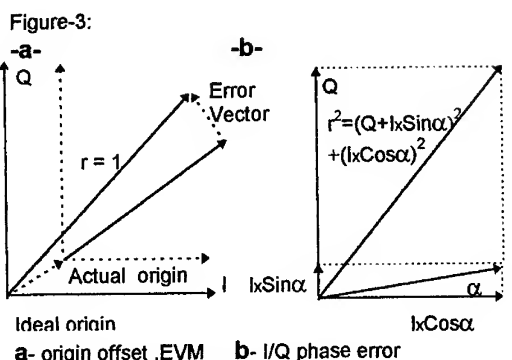


Figure 2: Residual AM vs. phase balance of a 1.004KHz FM modulated signal with 8 KHz peak deviation.



Phase errors over 3° limits the ability to calibrate the side band suppression and will require phase calibrating circuit. Hence for low phase errors only simple amplitude matching circuit is required. For 3° phase error and 0.3dB amplitude error the side band suppression will be 30dBc and thus the measured EVM was 4.5%.

D-3 I and Q DC offset calibration

The second calibration required is the DC offset between I and Q. This parameter affects the carrier leakage from the modulator. Carrier signal leaking to the antenna affects the Origin Offset of the constellation at the Base Station's receiver. The result might be poor BER performance. The carrier suppression is given by equation 7 [14],[15],[17].

$$(7) \quad S_{LO} [dBc] = 10 \log \frac{1/4 [1 + 2K\delta \cos(\beta - \alpha) + [K\delta]^2]}{D_{m1}^2 + 2K\delta D_{m1} D_{m2} \sin \beta + [K\delta D_{m2}]^2}$$

The potential Impairments of the modulator (Fig-1) and input baseband signals (I vs. Q) are as follows:

Dc1 DC offset error of the LO at the I input.

Dc2 DC offset error of the LO at the Q input

Dm1 DC offset error at the I input

Dm2 DC offset error at the Q input

α - Phase error between I and Q Inputs

β - Phase balance of the LO splitter within the modulator to quadrature

δ - Amplitude balance between I and Q inputs.

KI< α The I path mixer transfer function, including the phase error α between I and Q inputs.

KQ The Q path mixer transfer function, with zero phase

K Amplitude balance of the LO splitter within the modulator

Fig. 6 shows the carrier suppression as a function of DC Offset voltage where the phase quadrature error β of the LO divider is a parameter.

It can be seen that the carrier leakage is highly sensitive to DC Offset errors of I and Q inputs and thus offset of less than 20 mv are essential for carrier reduction of 30 dB and higher

By analyzing Eq.(6) for constant α and DC Offset, it can be shown that carrier suppression is only slightly affected by errors in LO quadrature (β) or LO amplitude imbalance factor (K).

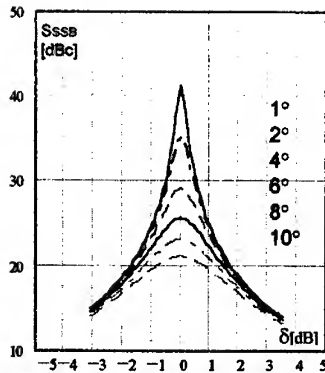


Figure 4: Side Band Suppression VS Amplitude Balance factor δ while Phase Balance between I/Q is a parameter

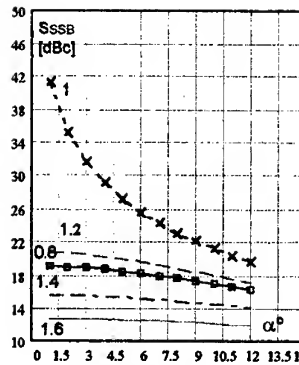


Figure 5: Side Band Suppression VS Phase Balance while the I/Q relative balance factor δ is a parameter

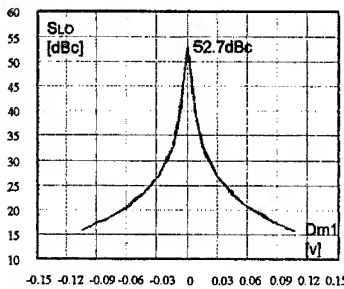


Figure 6: Carrier suppression as a function of the DC offset. I offset is between -150mV to +150mV. LO phase balance β is a parameter between 1° to 10° , I & Q phase balance $\alpha=1^\circ$, $\delta=1$, $K=1$ and Q offset is 2mV.

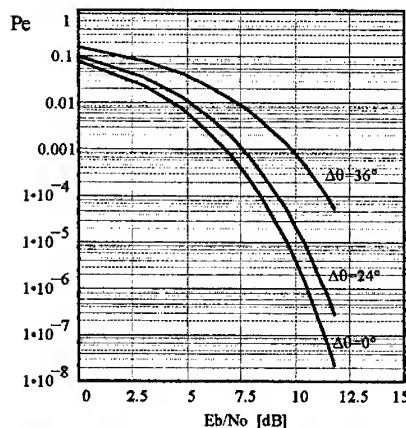


Figure 7: Bit error probability for coherently detected BPSK with constant phase errors [5]

E Non Linear Analysis

E-1 Frequency accuracy of the carrier

Frequency error cause a constant phase error offset $-\Delta\theta$ from the required phase of the symbol point. The result can be seen as constant rotation of $\Delta\theta$ radians of the constellation diagram around its center. A BPSK modulated signal is a simple example to describe the frequency error effect [9]. The E_b/N_0 of the modulated signal is reduces by $\cos^2\Delta\theta$ thus, it results in degradation of bit error probability of the system, so higher energy per bit to noise is needed to achieve the same error probability ratio (E_b/N_0). Figure 7 describes bit error probability for various phase errors values.

E-2 Phase Noise

A practical synthesizer implies random frequency fluctuations around its center frequency known as phase noise. There are several ways to define LO's phase noise. The common definition is Single Side Band (SSB) phase noise $\mathcal{L}(f)$ [dBc/Hz]. But with phase modulated signals, the LO's phase stability $\Delta\theta_{rms}$ as incidental Phase Modulation is used to describe the LO phase noise. With this last definition an indication on the total phase stability of the LO within the information BW is given. For a stable oscillator used for communication radios the phase noise will follow the relation [17]

$$(8) \quad 2 \int_{f_a}^{\infty} \mathcal{L}(f) df \ll 1 \text{ rad}^2 \text{ then } \Delta\theta_{rms} = \pm \sqrt{2 \int_{f_a}^{\infty} \mathcal{L}(f) df}$$

This phase error is a stochastic value, that exists in both I and Q vectors. As a result both I and Q would have the same phase error due to phase noise and the phase relationship between I and Q components is preserved when phase noise exists. Hence, $r(t)$ will be [17]:

$$(9) \quad r(t) = \sqrt{i^2(t) + q^2(t)} \cos\left(\omega_c t + \tan^{-1}\left(\frac{q(t)}{i(t)}\right) \pm \Delta\theta_{rms}\right) = A(t) \cos(\omega_c t + \beta(t) \pm \Delta\theta_{rms})$$

The bit error probability versus E_b/N_0 can be calculated analytically by:

$$(10) \quad P_e\left(\frac{E_b}{N_0}, \theta\right) = \int_{\theta} F_e\left(\frac{E_b}{N_0}, \theta\right) f(\theta) d\theta$$

Where: $F_e(E_b/N_0, \theta)$ is bit error probability, for the given modulation technique, as a function of E_b/N_0 and a random phase error θ . $f(\theta)$ is the distribution function of the phase noise θ . We assume a Gaussian distribution of mean zero and variance $\Delta\theta_{RMS}$.

The phase noise results in random rotations of the constellation diagram around its center point. Figure 8 describes a constellation diagram of a QPSK modulated signal when the RMS phase error is 5.75 Deg. Figure 9 describes bit error probability of a QPSK modulated signal for 3 $\Delta\theta_{RMS}$ phase error values. Phase noise results in a degradation of bit error probability. In an ideal communication system, BER goes to zero as E_b/N_0 goes to infinity. In presence of phase noise, the BER goes to a non zero value. As the phase noise power increases, the bit error increases thus we are limited in improving BER performance by increasing the E_b/N_0 .

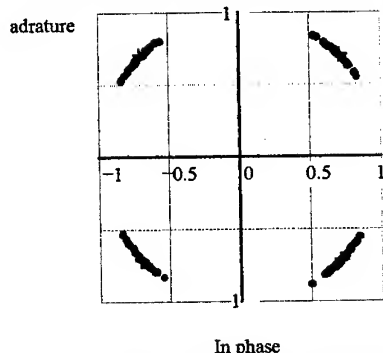


Figure 8: Constellation diagram for QPSK with phase noise of $\Delta\theta_{RMS} = 5.75^\circ$

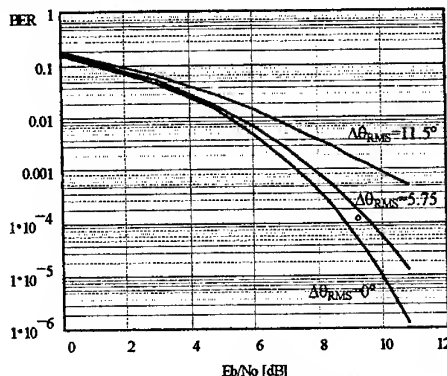


Figure 9: Bit error probability for coherently detected QPSK with phase noise [5]

E-3 Spurious Response

The effect of spurious from the synthesizer on modulated signal quality, depends on the frequency offset of the spurious from the synthesizer's frequency. Spurious within channel band, would shift the symbols position around their constellation target point, and will cause BER degradation. The shift radius of the symbols depends on the spurious to carrier power ratio. Figure 6 describes the constellation diagram of QPSK modulated signal while there is a spurious 20 dBc. Out of channel band spurious, contributes to the increment of the out-of-band emission.

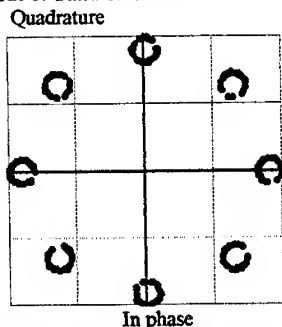


Figure 6: Constellation diagram for $\pi/4$ DQPSK with a spurious of 20 dBc within channel band

E-4 Power Amplifier Nonlinearities

In cellular portables, which are battery fed, it is important to design the transceiver for minimum power consumption. A lower power consumption PA is more efficient but is less linear. Non linearity of the PA results in AM to AM and AM to PM conversions. These conversions cause to degradation in modulation quality and consequently results to poor bit error probability and increases out of band emissions that reduces spectral efficiency. The nonlinear characteristics of the PA are represented by Eq 11:

$$(11) \quad s(t) = A(|g(t)|) e^{j\Phi(|g(t)|)} = A(|g(t)|) e^{j(\phi(t) + \Phi(|g(t)|)}$$

where:

- $|g(t)|$: The magnitude of the input signal to the PA
- $A(|g(t)|)$: The AM to AM conversion
- $\Phi(|g(t)|)$: The AM to PM conversion.
- $\phi(t)$: The phase of the input signal $r(t)$

The effect of the AM to AM and AM to PM of a PA results by out of band power emission known as Spectral Mask. The out of band power emission can be modeled by measuring $A(|g(t)|)$ and $\Phi(|g(t)|)$ functions, and by analyzing the power spectrum of the output signal when a baseband signal waveform function is applied to $A(|g(t)|)$ and $\Phi(|g(t)|)$.

An alternative way is to approximate $A(|g(t)|)$ and $\Phi(|g(t)|)$ by power series and then apply a power spectrum analysis [6],[10],[11] efficiency. Fig. 7 describes a power spectrum of a $\pi/4$ DQPSK modulated signal shaped by a SRC filter with $\alpha=0.35$ that feeds the approximated PA.

E-5 Thermal Noise

The transmitted symbols represented by the constellation diagram points, are corresponded by a "cloud of points" around each ideal target of the constellation, as described in Fig. 8. The Thermal noise results a modulation error that degrades bit error probability of the system. Another effect of the transmitted noise is desensitization of the receiver. Generally the transmission and the receiving channels within a transceiver are connected to the antenna through a Duplexer. A wide band PA injects high level broadband noise into the receiver and thus reduces its sensitivity. Thermal noise effect on receivers sensitivity can be minimized by properly design of the out-of-band transmitter's noise rejection.

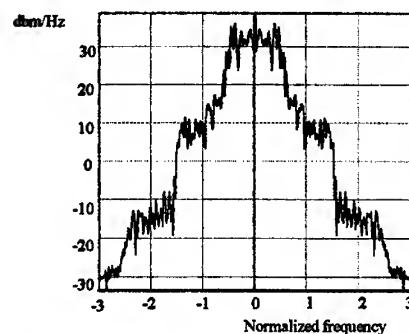


Fig. 7: Out of band emission for $\pi/4$ DQPSK modulated signal

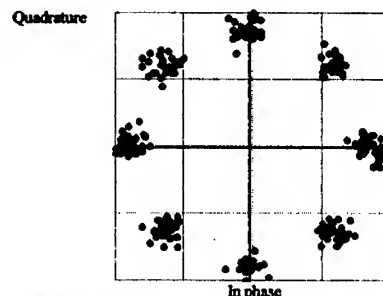


Fig. 8: Constellation of 20 dB SNR $\pi/4$ DQPSK modulated signal

F. Measured Results

Dual mode subscriber units containing radio cards with 440-450MHz and 825-850 MHz TX channels and 485-495MHz and 870-895 MHz RX channels were tested. Calibration methods and optimization based on the aforementioned analysis were used in the dual mode radio cards, achieving good agreement between the measurements and the calculated results

G. Conclusions

When designing a digital radio modulator and demodulator circuits, it is important to consider the effects of non-ideal Modulator and limited accuracy of its baseband interface network. The analytical approach to modulation impairments presented, can help in practical non-ideal modulation effects which are common to digital communication radios. Special attention should be given to I and Q signals amplitude and phase balancing if the QPSK modulator is used to generate analog FM signal. Special care should be given to I and Q inputs DC Offset balancing of the modulator to optimize carrier leakage (Origin Offset) problems. Optimizing the transmitter's power amplifier to an optimal biasing point and designing the synthesizers to a low phase noise and spurious would improve the spectral mask and the constellation performance of the radio's transmitter.

H. Acknowledgments

The authors thank Optomic Microwaves Ltd. Chief Engineer- Mr. Gideon Argaman for his encouragement, his guidance as well as his review of this paper.

Mr. Mark Kirzner and Mr. Florin Deligorgi the project development technicians from Optomic Microwaves LTD, who helped to carry out the project's tasks from the idea to its success.

Mr. Joseph Aharon from Telrad Inc. for his aid on tests.

I. References

- 1- Sean A. Lindsay, "Equations derive error-vector magnitude", *Microwaves & RF*, April 1995 pp. 158÷167.
- 2- Bill Law & Mike Groh, "Identifying RF related impairments in full service digital networks", *Microwave Journal* March 1996 pp. 88 ÷94.
- 3- Bob Buxton, "Measurement methods analyze digital modulation signals", *Microwaves & RF*, July 1995 pp. 67÷72.
- 4- Walter Joswick, "I/Q networks deliver various modulation formats", *Microwaves & RF* March 1995 pp. 81÷93.
- 5- Jonathan Y.C Cheah, "Analysis of phase noise in oscillators", *RF design*, November 1991 pp. 99÷104.
- 6- Joseph Bocuzzi, "Performance evaluation of non linear transmit power amplifiers for North American Digital cellular portables", *IEEE trans. on veh. tech.* Vol.44 no.2 May 1995 pp. 220÷228.
- 7- J. Proakis, "Digital Communication", 2nd ed. McGraw Hill 1989.
- 8- Edward A.Lee, David Messershmiddt, "Digital Communication", 2nd ed. 1994 Kluwer Academic Publishers.
- 9- J.J Stiffier, "Theory of synchronous communications" Prantice Hall Inc. 1971
- 10- J. Stevenson Kenny & Achankeng leke, "Power amplifier spectral regrowth for digital cellular and PCs application", *Microwave journal*, October 1995.
- 11- Seng-Woon Chen & William Panton & Robert Gilmore, "Effects of non linear communication systems", *IEEE trans. on microwave. theory & tech. vol 44 No 12*, December 1996.
- 12- Telecommunications Industry Association, Cellular System Dual Mode Mobile Station and Base Station compatibility Standard (EIA/TIA) IS54B. April 1992
- 13- TIA/EIA IS55 INTERIM STANDARD
Recommended Minimum Performance Standards of 800 MHz
Dual-Mode Mobile Stations
September 1993
- 14- Ruth Umsttdad: "Quadrature Modulators Part-1,
Assy Quadrature Modulators for PCS Applications"
MW&RF, Aug. 1993, pp90÷102.
- 15- Ruth Umsttdad: "Quadrature Modulators Part-2,
Assy Quadrature Modulators for PCS Applications"
MW&RF, Sept. 1993, pp129÷134.
- 16- Alex Margulis "Integrated Single Sideband Modulators Implemented on Soft Substrates"
MSN &CT, Sept. , 1985 , pp. 81÷90.
- 17- Spectrum Inversion Correction Simulation and Non Ideal Effects Corrections in a $\pi/4$ DQPSK Communication Channel
Optomic Microwaves LTD report Nov. , 1995 Doc No:1501- 2055.

A GaAs MMIC Digital Phase Modulator

G. Avitabile, A. Cidronali, C. Salvador, G. Manes

Dipartimento di Ingegneria Elettronica

Via S.Marta, 3 - I - 50139 - FLORENCE - ITALY

phone # +39.55.4796386 fax # +39.55.494569 E-Mail acidronali@ingfi1.ing.unifi.it

Abstract - The paper introduces a GaAs MMIC digital phase modulator based on a lumped quadrature hybrid. The quadrature coupler is implemented using two interleaved spiral inductors in a transformer-like configuration. The phase control is obtained electronically tuning two L-C resonators that load the coupled ports. The resulting phase modulator exhibits a continuous phase-shift capability of nearly 230°. The modulator can be digitally driven providing a 0°-180° or 0°-90° phase-shift, with constant insertion loss. Theoretical and experimental results are discussed.

Introduction - The growing interest in the personal communication (PC) field has stimulated the research of even more compact and integrated multifunction components. A critical block in PC systems is represented by the RF section, which is subjected to very stringent requirements in terms of cost and performance. A monolithic implementation is highly desirable for the RF section. In the low-microwave band (1-6 GHz), however, a monolithic approach requiring distributed elements [1], often results in large die area, owing to the dimension of the transmission lines. Many efforts have been spent in developing new circuit configurations based on a lumped element approach in order to decrease the die-area occupation.

A particularly critical circuit, requested in many applications, is the electronic phase-shifter, often implemented using a distributed-element approach with switching PIN diodes as control elements. This solution gives rise to hardly integrable circuits.

This paper introduces a new approach for the implementation of a phase shifter, based on a 90 degrees hybrid coupler, which allows the realization of digital phase modulators suitable for PC applications. The circuit is implemented in monolithic form and it is based on a lumped-element approach, resulting in a very compact and die-area saving realization. The hybrid topology is based on a general LE COD (lumped element codirectional) structure [2], which results particularly suitable for a monolithic implementation [3]. Sample prototypes have been designed and tested using GEC Marconi F20 process. A theoretical investigation of the new configuration is reported, along with experimental results.

Lumped element 90 degrees hybrid coupler - The ideal 3dB directional coupler is described in terms of S parameters by the symmetrical matrix S shows in (1).

$$S = \frac{1}{\sqrt{2}} \begin{bmatrix} 0 & 1 & 0 & j \\ 1 & 0 & j & 0 \\ 0 & j & 0 & 1 \\ j & 0 & 1 & 0 \end{bmatrix} \quad (1)$$

The matrix can be implemented on a lumped element basis, which results suitable for MMIC design (Fig.1).

The mutual inductance, M , became a design parameter that needs to be carefully evaluated performing an extracting procedure [4], either from measurements or from full-wave analysis. The components in Fig.1a are evaluated using the procedure described in [5], which relates the single components of the model to the symbolical Y -matrix elements and are expressed as a function of the coupling factor C , Z_0 and ω_0 by the relations:

$$\begin{aligned} L &= \frac{1}{c} \frac{Z_0}{\omega_0} & M &= \frac{Z_0}{\omega_0} \\ C_1 &= \frac{1}{\omega_0 Z_0} & C_2 &= \frac{c}{1+c} \frac{1}{Z_0} \end{aligned} \quad (2)$$

The proposed phase modulator is based on the configuration previously described where the ports 2 and 3 are terminated by reverse biased Schottky diodes connected in series to a proper inductance, in order to enhance the phase variation with voltage.

The following equation relates the transmission coefficient between ports 1 and 4 to the loading at the coupled ports 2 and 3

$$S_{41} = e^{j[\frac{\pi}{2} + \angle \Gamma(v)]} \quad (3)$$

in which $\Gamma(v)$ represents the reflection coefficient common to the ports 2 and 3.

Phase-shifter implementation - A phase-shifter prototype has been designed and implemented in the 5.8GHz ISM-band. The design parameters were evaluated using (2). The coupling factor, C , in (2) does not affect the phase-shift introduced by the hybrid, but it is relevant for the physical implementation of the circuit. In particular, higher values of C are related to closer conductors spacing, G , in Fig.1a. The value of C has been chosen on the basis of the minimum G allowed from the foundry rules.

The prototypes have been implemented on a GaAs substrate and the layout is represented in Fig.2. MIM capacitors have been used to compensate for the parasitic capacitances between the two interleaved inductances. The values of the circuit elements have been evaluated using a full-wave analysis based on the method of moments (MoM) [1-4].

The experimental results are shown in Fig.3, where the amplitude and phase of the transmission coefficient, S_{41} , are reported. A phase variation in excess to 200° is observed.

The amplitude transmission coefficient exhibits a 3dB variation in the 3V÷1V range with a maximum insertion loss of 4dB. When the circuit operates as a binary phase-shifter, a constant amplitude transmission coefficient can be easily achieved. As shown in Fig.3, a 90° or 180° relative phase-shift, with constant insertion loss is obtained, when the control voltage switches between V1 and V2 or V3 and V4, respectively (Fig.3).

Based on the previous observations, the proposed circuit can be used as the building block of the QPSK modulator represented in Fig.4, where two identical phase-shifters are cascaded. In this arrangements, the first section provides a phase shift of 126° @ -0.6V and 216° @ 0.2V, while the second provides 80° @ 0.5V and 260° @ -1.3V

phase-shift.

The transmission phase-shifts and the related binary control are reported in Table I. For the first unit, the low and the high levels are related to the V2 and V1 voltage in Fig.3 respectively, while, for the second unit, the voltages are V4 and V3.

Conclusions - The described MMIC hybrid design procedure [4] has proven to be accurate in predicting sample performances. A single chip implementation of the QPSK modulator is currently under development.

References:

- [1] Matthei, L. Young, E.M.T. Jones " Microwave filters, impedance-matching networks and coupling structures" Artech House Books, Dedham, MA.
- [2] Ali, A. Podell " A wide band GaAs monolithic spiral quadrature hybrid and its circuit application " IEEE - JSSC Vol. 26 nr.10 Oct 1991.
- [3] Ali, N.Mysoor " An analog MMIC phase modulator for X- band satellite transponder application " IEEE Microwave and Guided Wave Letters. Vol. 2 nr.11 Nov. 1992.
- [4] G. Avitabile, A. Cidronali, C. Salvador "Equivalent Circuit Model for GaAs MMIC Coupled Planar Spiral Inductors", to be published on Inter. Journal on MiMiCAE, vol.7 n.3, 1997.
- [5] G. Avitabile, A. Cidronali, C. Salvador "A Compact MMIC 90 Degree Coupler for ISM Applications ", 1997 IEEE - MTT-S Inter. Microwave Sym., Denver, Colorado, 8-13 June 1997.

Figures and Captions

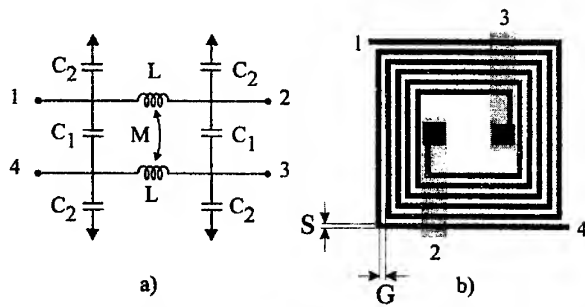


Fig.1: Concentric spiral inductors; a) Circuitual model; b) MMIC implementation.

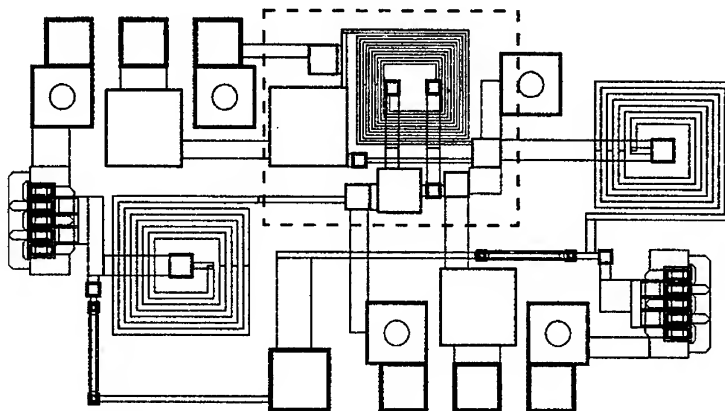


Fig.2: Layout of the MMIC phase modulator prototype, the dashed area includes the hybrid coupler

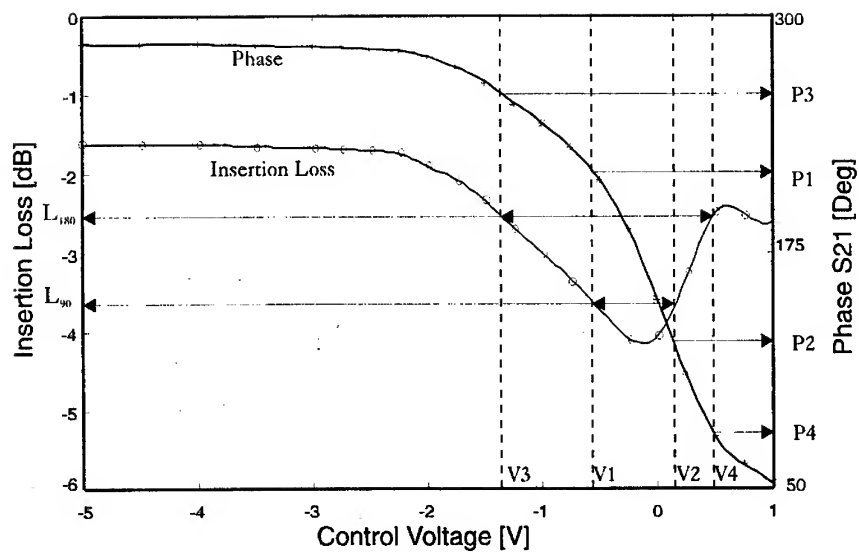


Fig.3. Measured response of the phase modulator prototype

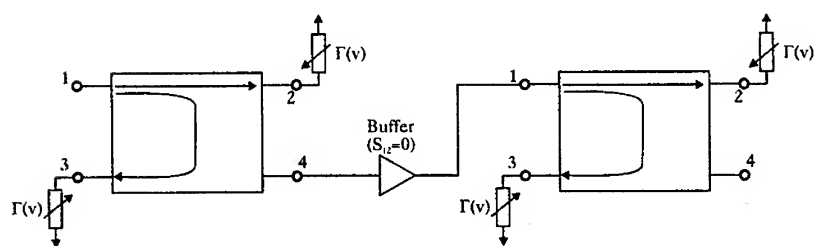


Fig.4. QPSK proposed structure composed of two identical phase shifter and an isolating buffer

LSB	MSB	Unit 1 In-out phase	Unit 2 In-out phase	Transmission Phase-shift
0	0	126°	80°	206°
1	0	216°	80°	296°
0	1	126°	260°	386°
1	1	216°	260°	476°

Table 1

Radiation From Directive Antennas Close to Human Tissue

Robert Leijon, Zvonimir Šipuš and Per-Simon Kildal

Antenna Group, Department of Microwave Technology
Chalmers University of Technology
S-412 96 Göteborg, Sweden
e-mail: leijon@nt.chalmers.se

Abstract

The possibility of reducing the radiation from mobile phones into the human body by using a directive antenna is studied. The antenna analyzed is a Huygen's source, that is, a theoretical directive antenna consisting of an incremental electric dipole perpendicular to an incremental magnetic dipole. The relative power absorption is calculated for three different models of the human head. The simplest head model is a lossy dielectric half space, a somewhat less rough model is an infinitely long lossy cylinder of circular cross section and the most exact head model is a homogeneous lossy dielectric sphere. A comparison with a Hertzian dipole, i.e. an incremental electric dipole, at the same positions is done. The different head models are used in order to investigate to what extent it is possible to simplify the model of the human head while still getting useful results.

The results show that the relative power absorption for the Huygen's source is substantially lower than that for a Hertzian dipole. When the antenna is placed 2 cm from a lossy dielectric homogeneous sphere of radius 10 cm, the relative absorption is 5 dB lower for the Huygen's source compared to a Hertzian dipole.

It is also shown that when the antenna is placed close to the head, the results for the different head models are fairly similar, especially when the antenna is a Hertzian dipole.

Introduction

When analyzing antennas for mobile phones it is of great importance to consider the presence of the phone user. Not only does he substantially affect the performance of the phone, but the radiation absorbed in his body is also a possible health hazard. Therefore, it is desirable to find antennas that are less sensitive to the user as well as reduce the energy deposition in the human body. A number of studies has been performed on this topic [1]-[3] but from the health hazards point of view few improved antenna concepts have been presented.

A possible way of reducing the absorbed power would be to use an antenna producing a directive radiation pattern. In this paper we study the Huygen's source, which is known to have 3 dB higher directivity in free space than a Hertzian dipole, i.e. an incremental electric dipole. The Huygen's source consists of a Hertzian dipole perpendicular to an incremental magnetic dipole excited by the same normalized amplitude and phase.

The most commonly used method when analyzing mobile phones radiating in the presence of a human is the Finite-Difference Time-Domain (FD-TD) method [4]-[5]. However, that method is very time consuming and needs large computer resources. Therefore, there is a need of more simple yet usable methods of modeling the antenna and human body. Previously, we have modeled the phone and the human hand holding it as rotationally symmetric [6] in order to reduce the problem to two dimensions and thereby lessen the computation time. In this paper we will model the human head in three different ways:

- As an infinite half-space (Fig. 1)
- As an infinitely long cylinder of circular cross section (Fig. 2)
- As a sphere (Fig. 3)

All structures are homogeneous and their relative permittivity is $20 - j5$, which is an estimated average value of the human head. The reason for using three different models is to find out how detailed the model of the head must be to obtain useful results.

For these three cases we will calculate the relative power absorption as a function of the distance between the antenna and the dielectric. For each case a comparison with a Hertzian dipole at the same location will be performed.

Method of calculation

Since the structures in this paper are one-dimensional, it is convenient to perform the analysis in the spectral domain. Doing that we Fourier transform the current at the antenna. The result for the planar case is an infinite current sheet with harmonic variations. For the cylindrical and spherical cases we get a current tube and a current shell, respectively. The fields are then given as a spectrum of one-dimensional solutions. Therefore, we call this approach the S1DS method [7]-[8].

A further advantage of this method is that the computer codes are very similar for all one-dimensional structures. Only a minor modification is needed [7].

Relative absorption

Let us consider an antenna placed at a distance d from an infinite lossy dielectric plane (Fig.1), an infinitely long dielectric cylinder (Fig.2) or a lossy dielectric sphere (Fig. 3). Then we write the total radiated power as $P_{tot} = P_{abs} + P_{rad}$, where P_{rad} is the power radiating to the far field and P_{abs} is the power absorbed by the structure. The computation of P_{rad} and P_{abs} are performed by means of the spectral domain Poynting vector normal to the boundaries of the structures.

Now we define the relative absorbed power as

$$T = \frac{P_{abs}}{P_{tot}}$$

Results

In Fig. 4 and Fig. 5 we have plotted the relative power absorption as a function of the distance between the antenna and the plane, cylinder and sphere, respectively. We see that the absorption for the Huygen's source is substantially lower compared to that for a Hertzian dipole. Although almost all radiated power is absorbed when the antenna is close to the dielectric, independently of the antenna type, we soon get much less absorption for the Huygen's source as the distance d is increasing. For the sphere, the Hertzian dipole has to be more than 2 cm away from the structure in order to decrease the absorption to -3 dB. For the Huygen's source, on the other hand, the

distance only has to be about 0,9 cm for a relative absorption of -3 dB. When the Huygen's source is positioned 2 cm from the sphere, which is a typical distance between a mobile phone antenna and the user's head, the absorption is as low as -8 dB.

Further, we note that when the antenna is close to the structure, the result does not differ very much for the three head models – especially not for the Hertzian dipole case. As one would expect, the absorption is highest for the half-space and lowest for the sphere. As the distance between the antenna and the structure becomes larger, the difference for the three models increases.

For all cases the radius of the sphere and cylinder is 10 cm, the relative permittivity of the material is $\epsilon_r = 20 - j5$ and the frequency 1,8 GHz. For the cylindrical case with Huygen's source, the magnetic dipole is z directed and the electric dipole ϕ directed.

Conclusion

We have shown that an antenna which produces a directive far field radiation pattern considerably reduces the absorption into the human head compared to an electric dipole, even when positioned very close to the body. When the head is modeled as a homogeneous lossy dielectric sphere and the distance between the antenna and the head is equal to 2 cm, which is a typical distance between a mobile phone antenna and the head of the user, the relative power absorption is 5 dB lower for the Huygen's source compared to a Hertzian dipole.

Although the Huygen's source is a theoretical antenna, the results are interesting as a general study of directive antennas radiating close to human tissue. The results indicate that antennas which are directive in the far field still have these directive properties when close to human tissue.

Finally, we have observed that for a Hertzian dipole or Huygen's source close to a human head, we can draw general conclusions about the radiation behavior even if the head is modeled as simply as a half-space or an infinitely long cylinder.

References

- [1] Raymond Luebbers, Li Chen, Toru Uno and Saburo Adachi, "FDTD Calculation of Radiation Patterns, Impedance and Gain for a Monopole Antenna on a Conducting box", *IEEE Trans. Ant. Propag.*, vol. 40, pp. 1577-1583, Dec. 1992.
- [2] Michael A. Jensen and Yahya Rahmat-Samii, "EM Interaction of Handset Antennas and a Human in Personal Communications", *Proc. IEEE*, vol. 83, pp. 7-17, Jan. 1995.
- [3] Michal Okoniewski and Maria A. Stuchly, "A study of the Handset Antenna and Human Body Interaction", *IEEE Trans. Microwave Theory Tech.*, vol. 44, pp. 1855-1864
- [4] Kane S. Yee, "Numerical Solution of Initial Boundary Value Problems Involving Maxwell's Equations in Isotropic Media", *IEEE Trans. Antennas Propagat.*, vol. AP-14, n0. 4, pp. 302-307, 1966
- [5] Karl S. Kunz, Raymond Luebbers, *Finite Difference Time Domain Method for Electromagnetics*, CRC Press, Boca Raton, 1993
- [6] Robert Leijon, Per-Simon Kildal and Ahmed Kishk, "Analysis of a Rotationally Symmetric Cellular Phone with a Monopole Antenna", *Proc. 26th European Microwave Conference*, Prague, 1996
- [7] Zvonimir Šipuš, Per-Simon Kildal, Robert Leijon and Martin Johansson, "An Algorithm for Calculating Green's Functions for Planar, Cylindrical and Spherical Multilayer Substrates", *Journal Manuscript submitted to the Applied Computational Electromagnetics Society Journal*.
- [8] P-S. Kildal, J. Sanford, "Analysis of conformal antennas by using spectral domain techniques for curved structures," COST 245 - ESA workshop on active antennas, Noordwijk, The Netherlands, 1996, pp. 17-26.

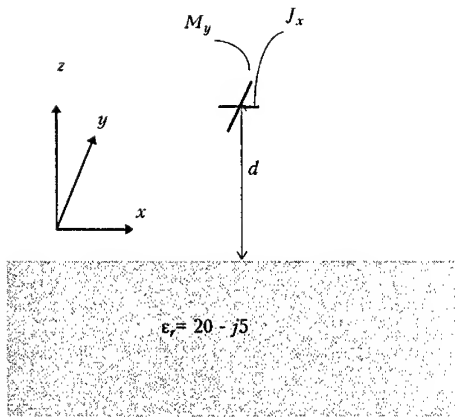


Fig. 1 A Huygen's source above a lossy half-space

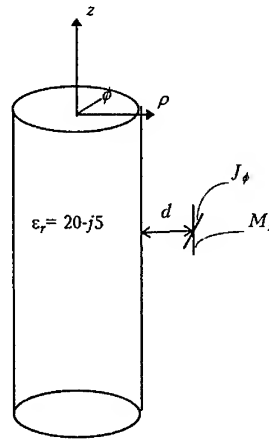


Fig. 2 A Huygen's source close to an infinite lossy cylinder

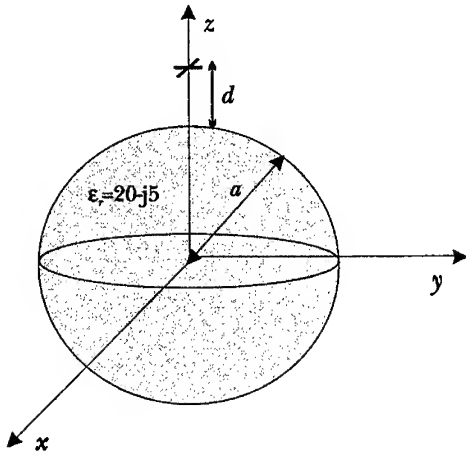


Fig. 3 A Huygen's source close to a lossy sphere

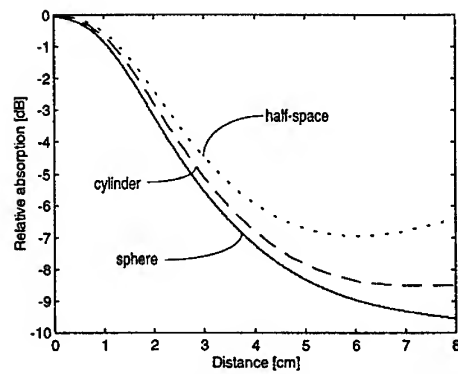


Fig. 4 Relative absorption for a Hertzian dipole above a half-space, infinite cylinder and sphere.

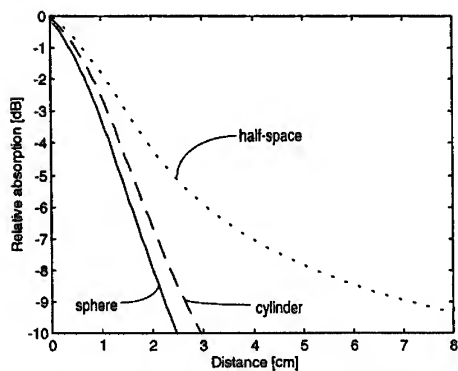


Fig. 5 Relative absorption for a Huygen's source above a half-space, infinite cylinder and sphere

IMPROVING OF HIGH-SPEED MODULES BY AN ADVANCED CHIP-IN-BOARD ASSEMBLY

Gerhard Hanke* and Wolf-Dieter Nohr†

Deutsche Telekom AG
Technologiezentrum Darmstadt
Am Kavalleriesand 3) - Agastraße 24)†
64 295 Darmstadt) - 12 489 Berlin)†
Germany

Phone: +49 6151 83 3526) - +49 30 6708 3591)†

Fax: +49 6151 83 4465) - +49 30 6708 2161)†

E-mail: hanke@ttd.telekom.de) - w.d.nohr@t-online.de)†

ABSTRACT

For an experimental ETDM fiber transmission systems working at 20 Gbit/s and an OTDM 40 Gbit/s system the electronic transmitter, receiver, and amplifier modules were developed. To guarantee reliable and error free operation unpackaged GaAs- and Si-chips on ceramic thinfilm substrates in combination with a sophisticated interconnection technology had to be used. We call this technology "Reverse Beam Lead"-technic. It uses self-supporting leads at the ceramic substrate which contact the semiconductor chips and it allows low impedance and rather reflection- and discontinuity-free connections even for millimeter-wave applications.

INTRODUCTION

The higher bit rates are needed for modern telecommunication use the more difficult become assembling and interconnecting technics. In contrast to small- and medium-band microwave and millimeterwave applications most of the digital signal processings have to be performed in the basic band and therefore need low cut-off frequencies down to DC. Problems like frequency dispersion of micro striplines, frequency dependence of parasitic impedances, transforming characteristics of any finite length of layer must be solved.

A good and meanwhile proved and reliable tool for multi-gigabit rates and millimeterwave interconnecting and assembling is the chip-in-board mounting of semiconductor circuits and components into ceramic substrates in combination with hybrid integrated technics and the "Reverse Beam-Lead"-interconnecting method. High-speed modules for optical fiber transmission systems working at 20 Gbit/s and a 40 GHz driver amplifier for an experimental optical time division multiplexing system working at 40 Gbit/s demonstrate the advantages of this technology.

EXPERIMENTAL OPTICAL 20 GBIT/S TRANSMISSION SYSTEM

The schematic circuit diagram of an experimental optical system is given in Fig. 1. Two data signals of 10 Gbit/s each, e.g. two STM-64-channels, are multiplexed synchronously in the transmitter module into one 20 Gbit/s output signal which after amplification by a driver circuit controls the optical modulator. The laser light is modulated by the 20 Gbit/s-signal in NRZ-format.

At the end of the fiber link the optical signal is reconverted into the original two 10 Gbit/s data streams. This is done by detecting the light in a PIN-photodiode and amplifying and demultiplexing the regenerated data signal into two 10 Gbit/s channels, which can be used for error rate measurements or SDH signal processing.

20 GBIT/S TRANSMITTER MODULE

For transmission experiments over fiber links and measurements of optical and electrical components the use of pseudo random sequences with maximum length is advantageous. Fig. 2. The two generators are synchronized in such a way, that the output signal of the slave is delayed by half the wordlength with respect to the master. In this case after multiplexing a sequence of maximum length can be obtained again. Each of the generators is realized by only one monolithic integrated Si-chip. The word lengths of their output patterns can be switched between $(2^{15}-1)$ bit and $(2^{23}-1)$ bit. The transmitter module consists of four GaAs-chips which are mounted on a ceramic thinfilm MIC and has the size of 2 by 2 square inches. The GaAs-chips are of NLG4000 (Mux and clock distributor) and C14600 (DFF and frequency divider) families from NEL. the 20 GHz power divider is a 3dB/180° ring coupler in micro stripline-technic. The output amplitude of the module is 1 V_{pp}, therefore an additional modulator driver is necessary to reach 6 V_{pp}.

20 GBIT/S RECEIVER MODULE

At the receiving end, Fig. 3, one needs a conventional TDM-receiver with clock recovery circuit, regenerator for both, amplitude and phase, and demultiplexer 1:2. The two 10 Gbit/s output signals then correspond to the two input data signals of the transmitter. The signal splitter is a resistive 6dB coupler, because a preamplifier with differential outputs is still under development as well as the decision circuit, which both will be monolithic integrated Si/Ge-circuits. The receiver module also has the size of 2 by 2 square inches: the DFFs, the clock distributor and the phase control are GaAs-chips. The 10 GHz clock phase for the DFFs is switched between 0° and 180° by means of a synchronization signal to get the same channel coordination as at the transmitting end.

40 GHz AMPLIFIER

As an example for applying the new mounting and interconnection technology to microwave circuits Fig. 6 shows the layout of a 40 GHz small band power amplifier (HP HMMC-5040) for use as clock driver in a 40 Gbit/s OTDM-system. Hybrid

integrated thinfilm bypass capacitors are used, the capacitance is about 5pF/mm^2 . Due to fabrication tolerances of the GaAs-chips the air gap between chip and ceramic substrate still has to be $50\mu\text{m}$. This air gap is the main reason for remaining reflections. Therefore we are experimenting with precision excimer-laser cuttings of chip edges and we are hopeful to reach less than $10\mu\text{m}$ of air gaps in the near future.

ASSEMBLING TECHNIC

To realize nearly lossless and non-reflecting interconnections between semiconductor-chips and microstrip lines working at up to 50 GHz, an advanced CIB (Chip-in-Board) technology is developed. For this purpose the microstrip line device is implemented on an Al_2O_3 thin-film ceramic substrate containing chip-sized openings provided with projecting leads for chip interconnecting as an extension of the microstrip lines. The dice can be inserted by face-down mounting with flip-chip bonding devices. The chips are to be mounted flush with the film circuit surface into the previously prepared chip-sized substrate openings and interconnected e.g. by soldering or ultrasonic welding. To produce the desired microstrip line device we use the photolithographic technic as well as sputtering and galvanic plating. In order to manufacture such a device equipped with integrated thinfilm bypass capacitors the basic electrodes are structured at first. Then we cover these electrodes with an overlapping dielectric layer. For this we use a photosensitive polyimide (PI). The next step is to realize top electrodes extending as leads which project into a chip-sized substrate opening. To receive such leads at first substrate openings are cut out with a laser and following filled with indium. Then the needed structure is realized. After removal of the indium filling in the case of solder interconnecting of chips the inner sides of the leads are plated with solder (e.g. indium). But solder-free techniques of lead-pad interconnection (e.g. ultrasonic welding or thermocompression bonding) are applicable, too.

Fig. 4 shows the technological process of the lead manufacturing. In Fig. 5 the principle of CIB face-down placing is given. Fig. 8 is a photograph of some leads projecting into a substrate opening. The mounted GaAs amplifier chip (widths of the pads: $50\mu\text{m}$) can be seen in Fig. 9. On the reverse side of the chip a heat sink is mounted. For this purpose we use a gold-plated deep-drawing sheet metal adhered with a silver-filled adhesive.

As an additional example in Fig. 7 the front side layout of the transmitter module with all 50Ω microstrip lines and with power supply layers for chip capacitors and some termination resistors is drawn. These layers are connected with the reverse side by metallized via holes and in case of the ground layers by the partly metallized chip cutoffs. The ground layer for the micro striplines and all power supply interconnections and hybrid integrated decoupling capacitors are on the reverse side of the substrate. Chip surfaces and substrate surface are on the same level, therefore wire bonds can be made as short and flat as possible. Where 50Ω lines cross each other the crossed line is bridged by a $250\mu\text{m}$ wide gold ribbon.

Due to thermal problems the distances between the chips are chosen as long as possible because the power dissipation of all chips together is about 9.6 W. The substrate is mounted to a large heat sink which must be cooled by air.

The first four circuits at the left hand side are working at 10 Gbit/s with the exception of the frequency divider. These chips are conventionally wire bonded. The selector and the D-flipflop, however, at the right hand side of the substrate (inside the circle line) are working at 20 Gbit/s. They are connected to the substrate layers by the above described reverse beam-lead technic. The extended part in Fig. 7 shows some details. The thinfilm gold-leads, which are connected to the chips by welding are of optimal shape to obtain lowest inductivities for the power supply and ground connections and to guarantee as perfect as possible impedance matching for the 50Ω microstrip lines. The advantages of this technic in comparison with bonded wires are remarkable. Nevertheless there are still some points to be improved. The next goal, e.g. is to reduce the gap width between substrate and chip to a minimum, because this gap is responsible for discontinuities of the line impedances and therefore causes reflections. This can be done by precise cutting of chips and substrate cutoffs or by filling the gap with a material with a suitable dielectric constant.

Furthermore we are working on hybrid integrated microwave capacitors basing on polyimide materials. These capacitors shall be used as coupling capacitors as well as bypass capacitors and we try to place them very close to the chips. First experiments with coaxial bypass capacitors inside the via holes show quite satisfactory results.

CONCLUSION

The paper describes two 20 Gbit/s modules and a 40 GHz amplifier for optical transmission experiments as examples for an advanced chip interconnection technic which is suitable for high-speed and microwave applications up to more than 50 GHz. We obtain nearly lossless and non-reflecting interconnections between semiconductor chips and micro striplines and also very low impedances of ground and power supply interconnections. By the aid of planar bypass-capacitors with polyimide dielectric, which are placed as close to the chips as possible, a nearly frequency independent decoupling of the power supply is obtained. Comparative measurements with conventional wire bonded circuits up to 50 GHz show the advantage of the new technology and will be given at the conference.

REFERENCES

- [1] Nohr, W.-D.; Hanke, G.: Reverse Beam-Lead Interconnections for Ultra High-Speed Multichip Applications. 5th International Conference & Exhibition on Multichip Modules, Denver / USA, 17.-19.04.1996
- [2] Hanke, G.; Nohr, W.-D.: A new Chip Interconnection Technic for Ultra High-Speed and Millimeterwave Applications. 1996 IEEE MTT-S International Microwave Symposium, San Francisco / USA, June 96
- [3] Nohr, W.-D., Lemanski, H., Meusel, E.: Simultaneous CIB Interconnection Technology for Ultra High-Speed Applications. Proc. of 11th European Microelectronics Conference, Venice / Italy, May 1997, pp. 558-561

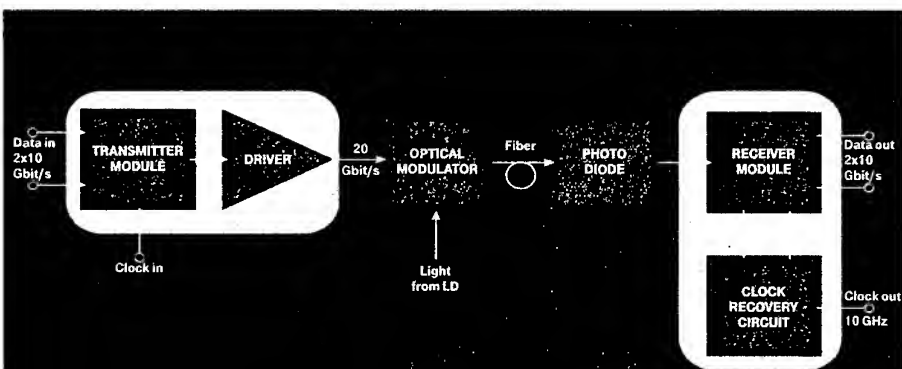


Fig.1 Schematic Circuit Diagram of the Experimental 20 Gbit/s Optical Transmission System with Electrical Time Division Multiplexing

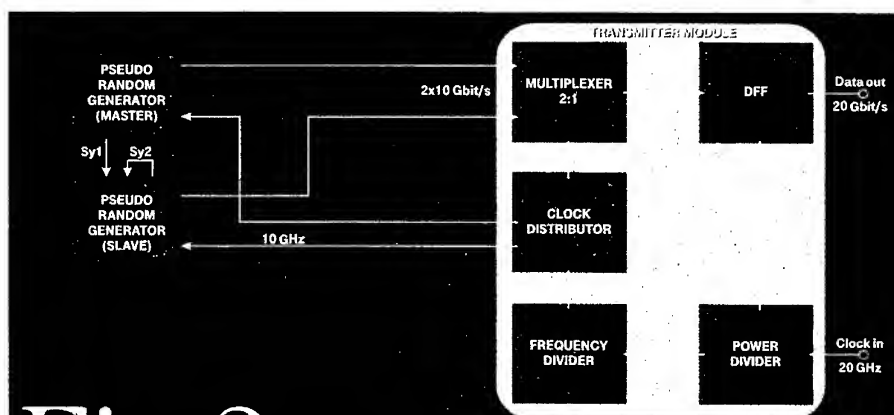


Fig.2 Transmitter Module and two Pseudo Random Generators for the 20 Gbit/s Optical System

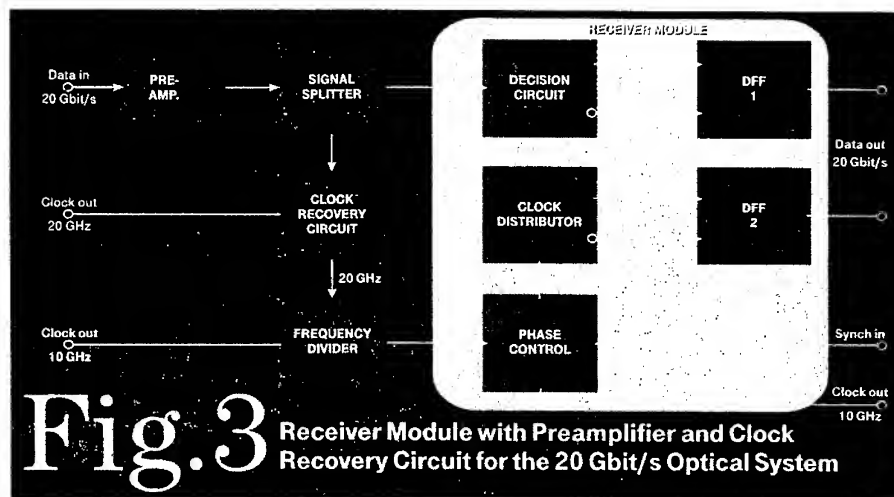


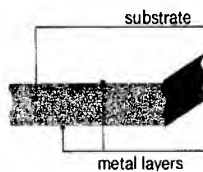
Fig.3 Receiver Module with Preamplifier and Clock Recovery Circuit for the 20 Gbit/s Optical System

Structuring of a "Reverse Beam Lead"- Device with Capacitor

Example: Microstrip-Circuit

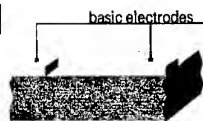
1. SUBSTRATE METALLIZATION

- * alumina (Al_2O_3)
- thin film ceramic (254 μm)
- double sided vacuum deposition: chromium/gold (Cr: 10 nm / Au: 0,2 μm ; e. g. by sputtering)



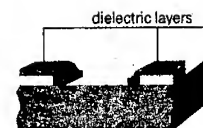
2. BASIC ELECTRODES

- * photolithography
- * galvanic gold plating (Au: 5 μm)
- * removal of top sputter layer



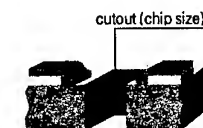
3. DIELECTRIC

- * photosensitive polyimide (PI: 5 μm)
- * photolithography



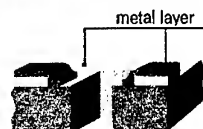
4. SUBSTRATE CUTOFF

- * cut by laser (e. g. Nd-YAG)



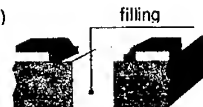
5. TOP SIDE METALLIZATION

- * chromium/ gold (Cr: 10 nm / Au: 0,2 μm ; e. g. by sputtering)



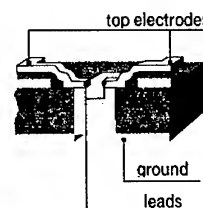
6. METAL FILLING

- * filling material: indium (In)



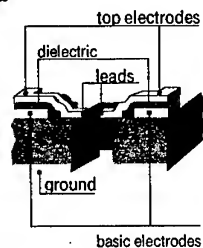
7. LEAD STRUCTURING / TOP ELECTRODES / GROUND

- * photolithography
- * galvanic gold plating (Au: 10 μm)
- * removal of sputter layer



8. COMPLETE CIRCUIT

- * filling removal
- * optional: solder covering of lead undersides by galvanic plating (e.g. Ni: 1 μm / In: 8 μm)



Technologiezentrum Darmstadt FZ 245

Fig. 4 Schematic technological steps to fabricate gold-leads for connecting fast semiconductor chips in „Reverse Beam Lead“-technic in combination with integrated capacitors

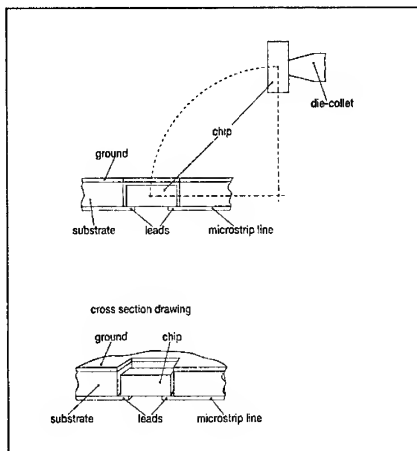


Fig. 5

Principle of the face-down mounting procedure. By the aid of a Fineplacer (Finetech, Berlin, Germany) the chip can be positioned within a tolerance of few micrometers. The Fineplacer projects both, the lead structure and the chip surface one upon the other. If both are non-overlapping, the chip can be lifted down.

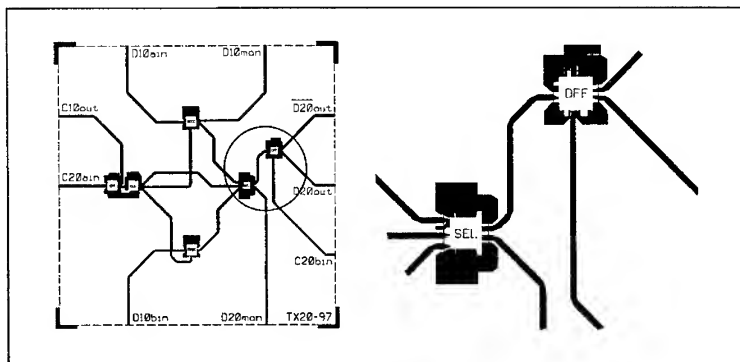


Fig. 7

Layout of the transmitter module. A 254 μm thick ceramic substrate has been used for the hybrid integration of the six GaAs chips. The 50 Ω microstrip lines are 250 μm wide, all power supply layers are on the reverse side of the substrate. Only the two circuits inside the circle are operated at 20 Gbit/s and therefore connected in Reverse Beam-Lead technic. Details of their layouts are given at the right hand side.

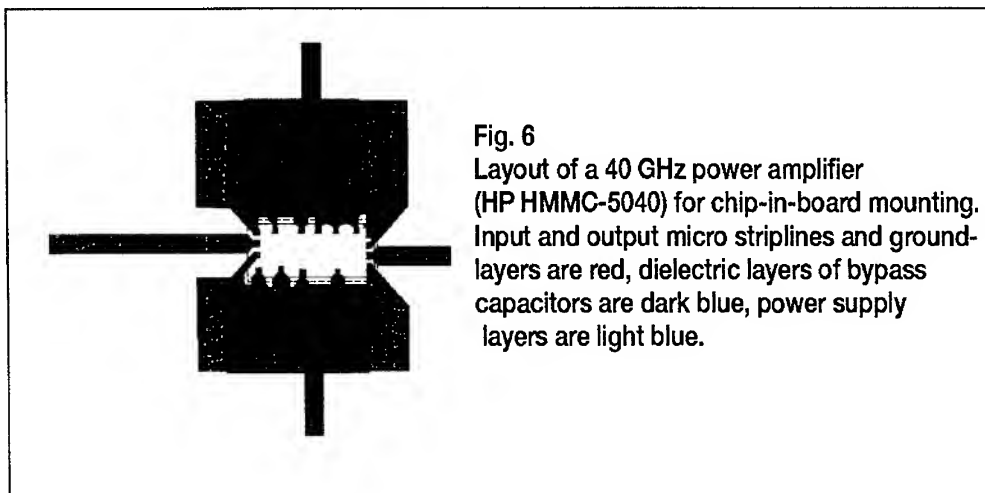


Fig. 6

Layout of a 40 GHz power amplifier (HP HMMC-5040) for chip-in-board mounting. Input and output micro striplines and ground-layers are red, dielectric layers of bypass capacitors are dark blue, power supply layers are light blue.

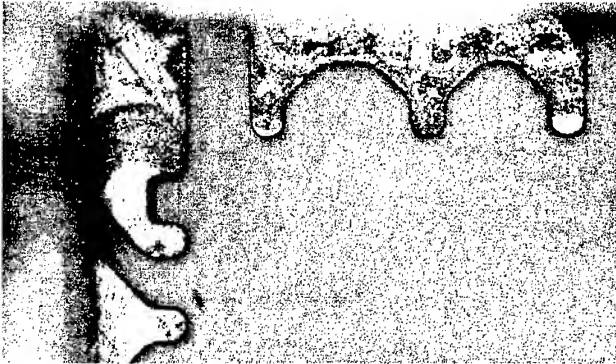


Fig. 8

Some of the finished gold-leads for the 40 GHz amplifier (upper right hand side corner of Fig. 6, seen from the rear side). The widths of the contacting areas are 50 μm , thickness of the layers is about 10 μm . The layers project about 100 μm into the cut out

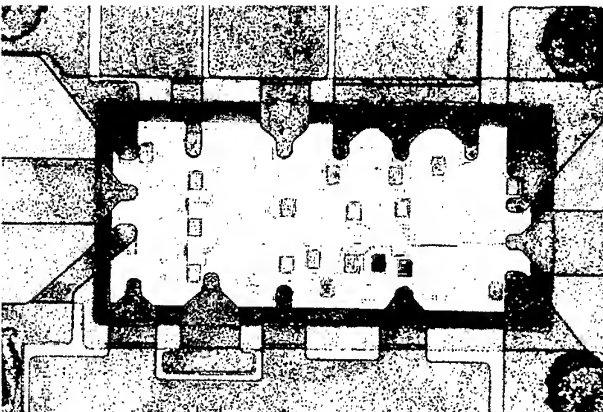


Fig 9

Photograph of the amplifier chip connected in "Reverse Beam Lead"-technic. There is still a too large gap between chip and substrate and also the capacitors must come closer to the chip

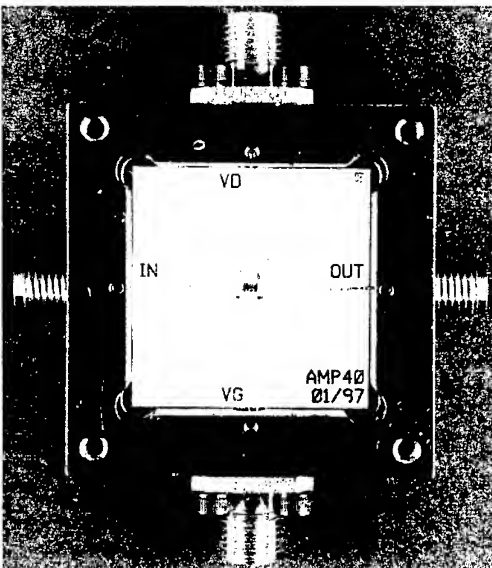


Fig. 10

The ceramic substrate (inner size 1" by 1") with the 40 GHz amplifier chip is built into a nickel-plated alumina microwave package. Input and output micro striplines lead to K-connectors. An additional heat sink is located at the rear side

RF and DC multilayer: The Multi Function Concept

P.Langlois

Hollandse Signaalapparaten BV

PO Box 42

Hengelo, The Netherlands

Tel: +31 74 2482774 / Fax: +31 74 2484058 / E-mail: langloisp@signaal.nl

Abstract:

Future beamforming radar, especially of the phase array type, have demanding requirements on integration of RF antenna, transmit and receive functions. This paper describes a novel type of printed circuit board (PCB), combining highly integrated analog and digital circuitry on one side, and on the other side both active (e.g. MMIC's) and passive RF antenna components (e.g. radiating elements). The paper addresses the requirements for such a board both from a performance point of view and from an industrial point of view. A complex multilayer board including a microstrip transmission line, stripline for RF and 4 DC layers is described. This paper indicates cost issues. Further developments of this type of board design and opportunities for application in telecom domain are identified. An example of the manufactured board will be demonstrated at the conference.

Key words: Microwave, multilayer, PCB, interconnection, radar

TMM® is a material from Rogers

Summary:

Future beamforming radar, especially of the phase array type, have demanding requirements on integration of RF antenna, transmit and receive functions. The main characteristics are:

- Lot of functional modules in the antenna (some hundreds to some thousands).
- More preprocessing in the antenna in order to reduce the high data rate between antenna and processing ($n \times 10$ Gbits/s).
- Distributed RF, IF & LO on one RF carrier for a group of modules.
- Radiating elements included in the same board as RF distribution.
- Less levels of interconnection and packaging between radiating elements and processing.
- MMIC's and MIC's as components for RF & IF multilayer structure.
- MIC's on ceramic with high density multilayer (LTCC, Thick film, photo imageable thick film...).
- Large PCB for RF, IF, LO, Control & Command (digital / analog) and Power Supply, for frequencies beyond X-band.
- Typically $\geq 125 \mu\text{m}$ space and width lines with local fine space for filters and couplers
- Lots of Surface Mounted Devices (especially plastic packages) and some Hybrids.
- Data transmission by Fibre Optic link between antenna and below deck processing.
- Less cabling, especially RF coax, which will simplify the structure of the antenna.

Signaal, as a specialist in Naval Combat System, and more specifically in radars & sensors, has started a complex new technology development. Concerning our PCB facility, our goal was to extend our possibilities in board manufacturing and to minimize the investments. We decided to combine our background in RF multilayers and in digital boards to develop a novel type of printed circuit board (PCB). Our approach was to put all the RF and part of the IF components on one side, and the low IF and the preprocessing on the other side. The interconnection between the control boards and the RF components would be realized with several plated through holes. The RF interconnections would be only between each stripline and the microstrip line, with blind via and special ground via around the transitions to avoid parasitic propagation. After a review of the type of components used we decided to include some cavities in the RF multilayers.

1. Bare board design

RF layout has been design in the HP environment (HFSS & MDS) and the DC layout in Cadence. The merging of the two layouts did create problems. These were solved manually for our test board, but dedicated software would be required, HP and Cadence are currently looking into a seamless approach (Intermediate File Format).

We have adapted existing filters in L and X band to the configuration. The program Filtsyn doesn't take in account the losses of the material, only its dimensions and dielectric constant, it generate the filter mechanical dimensions which are incorporated later on in MDS to generate the layout and the simulation. The requirements for the filters are:

L-band: $F_c = 1300$ MHz; $BW = 15\%$, rejection 50 dB at 500 and 2000 MHz

X-band: $F_o = 9.2$ GHz; $BW = 10\%$, rejection 50 dB at 5.2 GHz and at 13.2 GHz.

These filters are used as front end filtering. No steep filter is needed there, but the only important requirement is low loss (e.g. low receiver noise figure). Other filters would be IF filters at 1 GHz up to 3 GHz; more steep filters will be needed here, but implementation could easily be done with discrete ceramic SMD type filters.

Figure 1. CAD of the RF layers

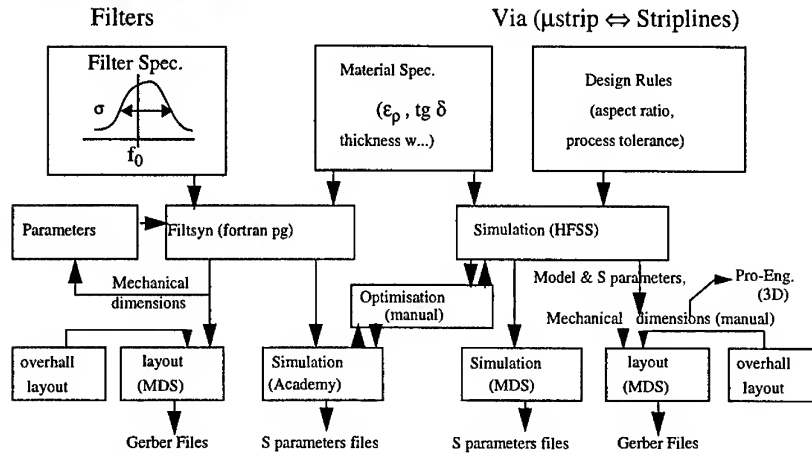
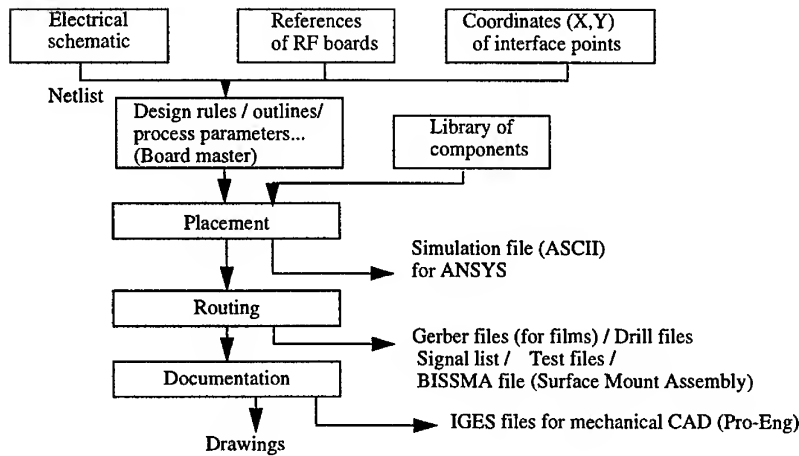
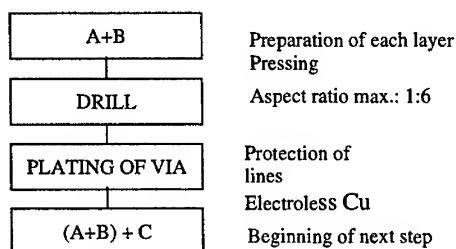


Figure 2. Flow chart of the DC multilayer



2. Bare board manufacturing

Due to the large number of blind via (interconnection between the two striplines and the microstripline, grounding around each transition, interconnection between the top and bottom layers), the production department has decided to use a sequential process (for the assembly of each layer and the plating of the via). This means that we plate through holes at each step and there are 5 sequences of assembly, drilling and plating, which is time consuming.



The finish has to be compatible with SMD assembly (SnPb joint), wire bonding (Au wedge bonding with a preheating at 150 °C) and with RF performance. We have decided to test two Au thicknesses, both compatible with SMD assembly and which don't increase significantly the RF losses up to 10 GHz.

Ni / Au (5 μm / 0.05 μm)

Ni / Au (5 μm / 0.5 μm)

We have used a high Tg FR4 (180°C) because of its better thermal stability, especially during multiple reflows (one per side and repair of components). The DC multilayer has been realized separately and then assembled with the RF part. We had two ground layers face to face, which allow us to use an epoxy prepeg as bonding film. This film can flow and fill the plated through holes, which avoid to entrap chemical residue during the final plating process (Ni/Au).

3. Electrical measurements:

The test vehicle is described in figures 3, 4 & 5. The 50 Ohms lines show good performance up to 14 GHz, beyond, the return losses becomes important. The losses of the transition microstrip to stripline 1 and microstrip to stripline 2 are respectively 0.4 dB @ 10 GHz, and 0.9 dB @ 10 GHz (per transition). The simulation and the measurements of the filters are in a very good accordance. The influence of the Ni Au finish is too small to be accurately measured with such small lines.

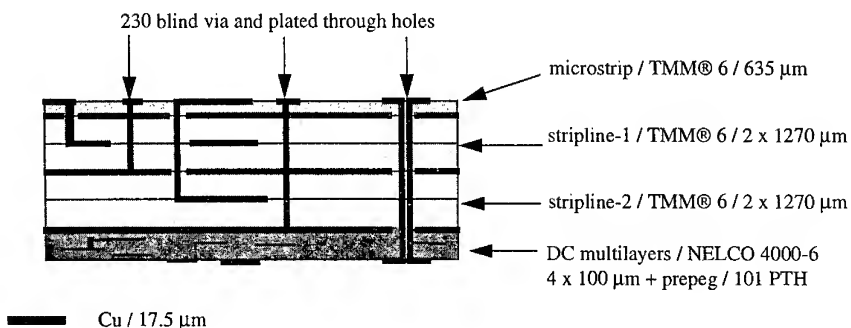


Figure 3: cross section view

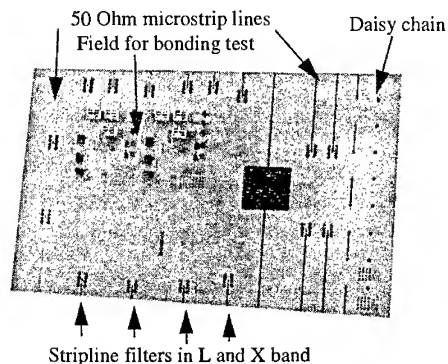


Figure 4: RF multilayer side

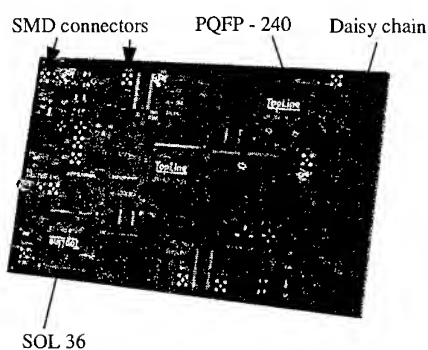


Figure 5: DC multilayer side

4. Thermo mechanical tests:

A group of bare boards has been tested in thermal shocks. The DC resistance of the daisy chain has been measured before and after the test. All of them have passed successfully the thermal shock (-40 °C / + 80 °C, cycle time 40 min, 20 min at each temperature, 100 cycles), with minor change in the resistance. Two boards have been tested in temperature cycling (-55 °C / + 125 °C, cycle time 1 hour, slow ramp, 100 cycles), one passed the test but for the other one, a failure occurs after 16 cycles, one of the 1.4 mm via was cracked, this was due to a local delamination because of the low Tg of the bonding film, this has been corrected in the next boards by changing the bonding film.

5. SMD assembly, Die assembly and wire bondability (IPC-TM 650 & MIL-STD-883):

SMD assembly has been done using a standard process: screen printing of the SnPb solder paste, reflow with a convection + IR furnace. The bare dies were glued on the boards. Au wire bonds have been realized with a Hughes 2470-III automatic wire bonder. A number of 400 wire-bonds per boards have been realized with the best parameters settings and the wire bonds have been tested by destructive pull-testing after ageing (150 °C / N₂ / 1500 h). The results are that ageing of the wire bonds does not affect too much the pull strength and only the top layer finish with thick gold (5 µm Ni / 0.5 µm Au) meets the requirements of the MIL-STD-883D. The assembly of SMD components with SnPb and the gluing of die imply to use a bonding film which withstand the high temperature, like a high Tg thermoplastic or a thermoset material. Both options have been tested successfully.

6. Cost comparison:

A cost comparison between a classical approach and the MFC for one of our projects has been conducted to determine the interest of introducing this new concept.

	Standard approach:	MFC approach	cost reduction ratio
NRE	NRE including the layout, documentation, test fixtures, tooling for each board.		60%
Bare board	1 RF board (1 microstrip layer in TMM®) 1 IF board (6 inner layer + 2 external layers for pads and conductors) in FR4 1 digital board for processing (6 inner layer + 1 external layer for pads and conductors) in FR4 + 2 analog board for SERVO drive and DC-DC converter (same technology as for IF board)	1 board with one RF layer incorporated in FR4 multilayer (IF / Processing / servo / DC-DC converter)	50%
Assembly	loading / unloading / references for each boards...		50%
Interconnection	1 RF and 6 DC cables or flex..., including connectors, cables assembly and tests)	Plated through holes between each function are included in the board	100%
test	Final test including the test program, loading, test fixture change, for each board.		40%

The assessment is positive, even if we include the development cost, because of the limited investment. For medium to large quantities the potential cost reduction is obvious to see, for small quantities, even though the cost reduction may not look as appealing, the potential benefit at system level can be massive in term of size, weight, reliability and maintainability.

7. Conclusion:

During that feasibility study we have detected several problems at each steps, from the design to production and tests. We have proven that the technology is feasible. We have been able to develop the design rules and the process to the status of ready for manufacturing. In parallel we made a market survey as an input for our make or buy policy. Now we have started the phase 2 of this project. We are testing 2 manufacturing process with 4 boards configurations. The production is shared between our internal facility and selected subcontractors. The first test vehicle has been modified to take in account some new requirements. As a spin off of this study, we are applying this new concept for some prototype of new products (a passive phase shifter with his radiating element and his control board, a TR module and a Ka band antenna). In parallel we are investigating a special version for power application. This concept is currently used in a simpler version for several consumer or professional products (e.g. telecom boards, remote control systems and radars).

Acknowledgments: I would like to thank all the members of the Front End Technology group and of the Multilayer Production department for their technical support, and especially Y.Maatman, F.Ros and H.Gierveld from production for their important contribution in this program. I am grateful to P.van Genderen and S.Singh for the valuable discussion which help me to write this paper.

AIR BRIDGE BASED PLANAR HYBRID TECHNOLOGY FOR MICROWAVE AND MILLIMETERWAVE APPLICATIONS

E. Wasige, G. Kompa, F. van Raay, I. Schmale, I.W. Rangelow*, W. Scholz*; F. Shi*, R. Kassing*, R. Meyer**, M.-C. Amann** and P. Hudek***.

FG Hochfrequenztechnik/AG Technische Physik*/FG Technische Elektronik**
University of Kassel
D-34121 Kassel, Wilhelmshöher Allee 73
Tel: +49-561-804 6364, Fax: +49-561-804 6529
E-mail: wasige@hfm.e-technik.uni-kassel.de

Slowak Academy of Sciences, Bratislava, Slowakei***

ABSTRACT

A new silicon based, planar hybrid technology is being developed to address limitations associated with packaging and interconnections. The approach combines the advantages of both hybrid and monolithic technologies. Microwave transistor chips (e.g. GaAs FETs) are glued with an epoxy resin in openings micromachined in a high resistivity silicon substrate with a vertical precision of better than 2 μm and lateral tolerances less than 10 μm . Air bridge technology and thin film techniques are then used to provide the necessary interconnections. Preliminary results show very promising high frequency properties of this assembly.

I. INTRODUCTION

Microwave and millimeterwave monolithic integrated circuits ((M)MMICs) are commonly implemented on semi-insulating III-V compound semiconductor substrates (GaAs or InP). Transistors and microwave circuits, e.g. MESFET and HEMT technologies, based on these substrates have demonstrated good results over the last 20 years and are consequently, well developed. Commercial HEMT chips covering frequencies beyond 60 GHz are available [9]. In spite of this, their cost remains too high and research on alternate low-cost technologies, mainly focusing on advanced hybrid technologies, continues. Generally, hybrid technologies have been used for many different applications as a good compromise between cost and performance e.g. [1], [3]. A promising alternative to significantly reduce cost are integrated circuits based on silicon substrate [2], [10], [13].

Typically, conventional hybrid integration or MICs contain a small number of discrete transistors and use transmission lines and other distributed elements fabricated on a microwave circuit board and/or lumped passive elements. The devices are typically wire bonded to the circuit board. Wire bonding has a large parasitic inductance that can change from bond to bond even in automated systems. This degrades and limits the circuit performance and bandwidth respectively. Flip-chip bonding has been used widely in industry recently to circumvent these limitations [1], [8], [14]. Flip-chip devices are manufactured with suitable bonding bumps allowing very short and repeatable interconnections. However, a large number of microwave devices, for example low-noise or low-power, do not have bump contacts and have to be bonded [3]. Planar interconnect technologies focusing specifically on low-power microwave devices have been reported [5], [6]. The proposed technologies also use very short interconnections which, however, are carried out in a bonding step.

This paper presents a novel hybrid technology whereby discrete GaAs FET devices are fixed in a silicon substrate in a planar position and interconnections made by using air bridge technology as in

monolithic circuits. The approach takes advantage of conventional silicon micromachining technology, thin film technology and, as active devices, uses commercially available GaAs FETs in chip form. The high resistivity silicon substrate serves as a basis for fabricating distributed passive coplanar components. In addition to repeatable, low parasitic interconnections, the approach allows a variety of technologies to be incorporated in a single circuit.

II. PLANAR HYBRID TECHNOLOGY

The proposed technology is based on two main steps, namely planar integration of the GaAs FETs in Si substrate and thin film/air bridge interconnections of the embedded chip to the rest of the circuit.

a) Planar Embedding Technique

This is the first and most important technological step. The aim here is to make an opening in a substrate and then glue an active device in it such that a plane surface between the active device and substrate results. This must be attained to guarantee for the successful subsequent processing associated with lithography and metallisation.

Grooves in silicon for housing the active devices may be micromachined either by wet or dry etching. Wet etching of silicon (with $\langle 100 \rangle$ crystal orientation) results in slanting sidewalls. The depth of the openings can be exactly controlled but the resulting gap between a mounted chip and silicon is impossible to planarize removing the possibility of fabricating planar interconnections [15]. On the other hand, dry etching with inductively coupled plasma and cryo-temperature of the substrate allows the etching of grooves with vertical sidewalls [12]. The depth of the grooves is however difficult to control without laser interferometry. A technique for planar integration of GaAs based active devices in silicon substrate utilizing openings micromachined by wet etching of Si and using a planarization adhesive film was therefore developed.

Fig. 1 shows a summary of the procedure developed for high precision mounting of chips in a substrate. First of all, openings corresponding to the size of the active devices are etched in a silicon substrate from the backside in KOH solution at the required positions. Next, an adhesive film is spanned with care to cover the opening on the front side. A chip is then introduced face down into the substrate and positioned on the adhesive film. The gaps between the chip and the substrate are filled out with an epoxy resin. After the glue dries up, the adhesive film is pulled away leaving a plane surface. A surface planarity of less than $2\text{ }\mu\text{m}$ has been achieved. A scan of the surface profile across an embedded chip and the surrounding substrate area is shown in fig. 2. Note that multi chip modules based on same principle have been found in the literature [4], [7], [11] and lend credence to the viability of the proposed technique. A typical low-noise microwave transistor chip has dimensions of the order $350 \times 400 \times 100\text{ }\mu\text{m}$ which calls for very fine handling. Besides, selection of the epoxy glue should be done carefully not only taking into account electrical isolation properties but also good thermal properties.

b) Interconnection Technology

The interconnections to the embedded active device are fabricated using air bridge technology. This technology offers low parasitic interconnect capacitance and inductance. Furthermore, it eliminates uncertainty that may be caused by the small non-planarity of the surface at the chip-silicon interface which could lead to cracks or total breakage of a connection. A cheaper technology based on aluminium rather than standard gold plated bridges has been developed. Fig. 3 depicts a schematic diagram of this air bridge fabrication technique.

First a thick layer of photoresist is spun on the substrate and patterned. After a careful bake of the resist for removing all solvents a 2 μm thick aluminium layer is evaporated under rotating/swaying motion of the substrate for uniform covering of the resist slopes/edges. Then a second layer of photoresist is spun on and patterned. The extra aluminium is etched away and finally the resist stripped leaving stable air bridges. Fig. 4 shows scanning electron micrographs of a GaAs MESFET (MGFC 1402 from Mitsubishi) with air-bridge interconnections. Design and fabrication of circuits using this technology is under progress.

III. CONCLUSIONS

A low-cost planar hybrid technology for microwave circuits has been described. GaAs FET devices have been integrated in a quasi-monolithic manner in silicon substrates. Planar, very short and reproducible interconnections complete the simple assembly with promising microwave performances at low-cost.

IV. REFERENCES

- [1] Baumann G., Ferling D. and Richter H.: Comparison of flip chip and wire bond interconnections and the technology evaluation on 51 GHz transceiver modules, *26th European Microwave Conference*, Sept. 1996, pp. 98-100.
- [2] Beisswanger F. et al: Microstrip and coplanar SiGe-MMIC oscillators, *26th European Microwave Conference*, Sept. 1996, pp 588-592.
- [3] Belohoubek E.: Miniature Microwave Circuits - Alternative to Monolithic Circuits, *RCA Review* 46, Dec. 1985, pp. 464-483.
- [4] Buschick K. et al: Multichipmodule auf der Basis von Einbettechniken, *VDI Berichte Nr. 960*, 1992, pp. 497-508.
- [5] Fathy A., Brown R., Belohoubek E.: Miniature gain Block for Satellite Communication Receivers, *IEEE MTT-S Digest*, 1987, pp 565-567.
- [6] Güngerich V., Schadel R., Ramisch R., Russer P.: A Process for Inserting Chips into Planar Microwave Structures on Semiconductor Substrates, *Microelectronic Engineering* 18 (1992) pp. 247-252.
- [7] Johnson R. W. et al.: Planar hybrid interconnection technology, *International Journal of Hybrid Microelectronics*, vol 10, no. 1, 1987, pp. 28-35.
- [8] Krems T., Haydl W., Massler H., Rüdiger J.: Millimeter-Wave Performance of Chip Interconnections Using Wire Bonding and Flip Chip, *IEEE MTT-S Digest*, 1996, pp. 247 - 250.
- [9] Lunden O.-P., Sipilä M and Jenu M.: A 60 GHz LNA using commercially available PM HEMTs for intersatellite and mobile communications, *IEEE MTT-S Digest*, 1994, pp. 1341-1344.
- [10] Luy J.-F. and Russer P. (Eds.): *Silicon-Based Millimeter-Wave Devices*, Berlin: Springer, 1992.
- [11] Müller H.G. et al.: Plane surface embedding technique for thin film hybrids, *Proc. 1st Conf. on Microsystems*, pp. 335-340, Berlin, 1990.
- [12] Rangelow I. W., Löschner H.: Reactive ion etching for microelectrical mechanical system fabrication, *J. Vac. Sci. Technol. B* 13(6), Nov/Dec 1995, pp.2394-2399.
- [13] Reyes A. C., El-Ghazaly S.M. et al: Coplanar Waveguides and Microwave Inductors on Silicon Substrates, *IEEE Trans. on Microwave Theory and Techniques*, MTT-43, No. 9, September 1995, pp. 2016-2022.
- [14] Sturdivant R.: On The Performance of GaAs MMIC Flip Chips, *IEEE MTT-S Digest*, pp 1591-1594, 1994.
- [15] Wasige E., Kompa G., van Raay F., Rangelow I.W., Shi F., Scholz W., Kassing R.: A New Silicon Micro-test-fixture Facilitates the Re-usability of Accurately Characterized Low-Power FET Devices, *26th European Microwave Conf.*, Sept. 1996, pp. 521-523.

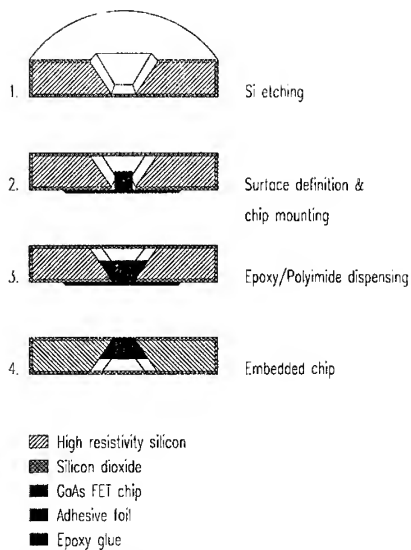


Fig. 1: Procedure for high precision integration of GaAs FETs in Si substrate.

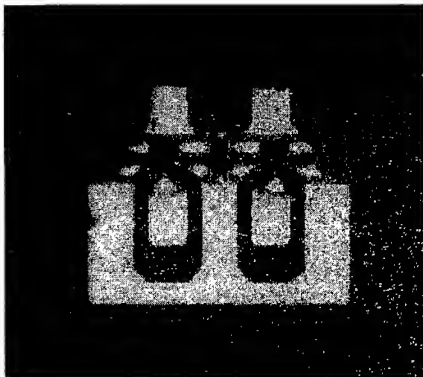


Fig. 2: (a) Top view of GaAs PHEMT chip mounted in a Si Substrate.

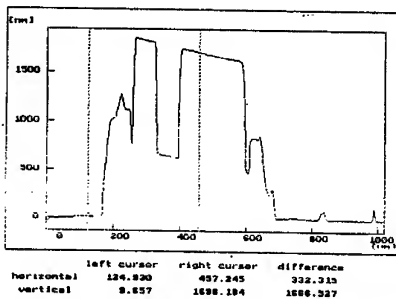


Fig. 2: (b) Profilometer scan of the chip in (a)

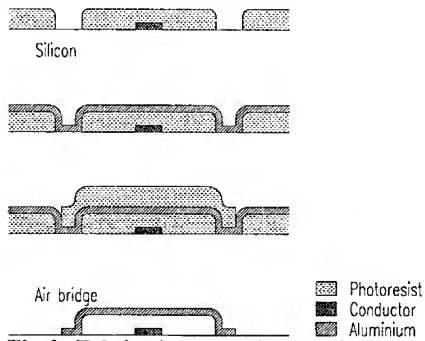


Fig.3: Fabrication steps for the air bridges.

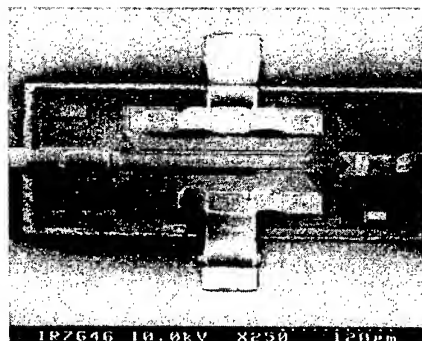
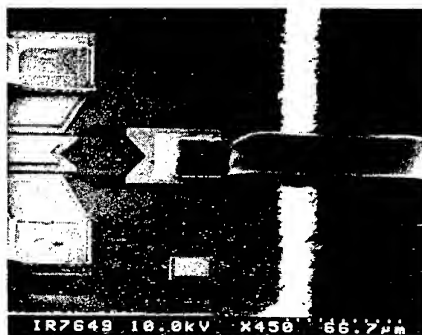


Fig. 4: Scanning Electron Micrographs (SEM) of air bridge interconnections between a GaAs FET (Mitsubishi MGFC 1402) and coplanar pads on a silicon substrate.

Scattering Parameters and Mode Conversion in Asymmetric CPW-Microstrip Overlap Transitions.

L. KADRI, P. PANNIER, F. HURET, P. PALECZNY, C. SEGUINOT, P. KENNIS.

Institut d'Electronique et de Microélectronique du Nord. U. M. R. CNRS 9929.
Avenue Poincaré, Domaine Scientifique et Universitaire de Villeneuve d'Ascq.
B. P. 69, 59652 Villeneuve d'Ascq Cedex, FRANCE.
Tel. : (+33) 3.20.19.79.58., Fax. : (+33) 3.20.19.78.83.
E.mail: fabrice.huret@iemn.univ-lille1.fr.

ABSTRACT:

In this communication, an asymmetric overlay transition between a microstrip and a CPW is studied. The mode conversion phenomenon is characterized by an efficient full-wave approach associated with the Matrix Pencil post-treatment.

INTRODUCTION:

Wavelengths at millimeter-wave frequencies, especially in conjunction with GaAs or alumina substrates, are rather small. Therefore, electromagnetic coupling between transmission line segments with absolute lengths of a fraction of a millimeter become compatible with the size of MMIC's [1] [2].

So, in this communication, a coplanar probe is investigated, and its electromagnetic interaction with the microstrip measured (without contact). The main idea could be to create a process to check the S-parameters of the microstrip circuits without damaging them. The process is to use an electromagnetic coupling between the probe and the circuit.

The problem of electromagnetic coupling from a coplanar to a microstrip line may find applications in the design of Millimeter-wave Monolithic Integrated Circuits. Indeed, since MMIC's are typically composed of a variety of different types of transmission lines, low loss connection between the different propagation media, i.e., CPW to slotline or CPW to

microstrip, is of considerable concern in the design of components like balanced mixers, multipliers, switches, etc.

In this communication, an overlay transition between a microstrip and a CPW is investigated [3] [4]. In this mind, a generalized full-wave model is used for the evaluation of the mutual electromagnetic coupling between the two transmission lines [5]. The boundary conditions on the slots and microstrip are applied to the structure, and the related spectral domain integral equations are solved using Galerkin's Method of Moments. Green's function for the stratified layer is calculated by applying a transmission line approach [5] [6].

RESULTS:

The transition shown in figure 1 has been already studied by Jing and Vahldieck and our results are in agreement with published data [4] (figure 2). However, to check possible tolerances with respect to the adjustment of top and bottom metallization, the influence of a lateral shift between the two planes (figure 1) has been investigated in this communication. When a lateral shift is taking into account, the discontinuity becomes asymmetric and the mode conversion between CPW coplanar and slotline modes have to be studied.

In this mind, given the magnetic current distribution on the slots and the electric current distribution on the microstrip line, the Matrix Pencil approach is employed to extract the modal amplitudes of all the modes [7]. In order to exhibit mode conversion, this multiport scattering is described by a generalized scattering matrix (figure 1) :

$$\begin{pmatrix} b_e \\ b_o \\ b_M \end{pmatrix} = \begin{pmatrix} \Gamma_{ee} & \Gamma_{eo} & T_{eM} \\ \Gamma_{oe} & \Gamma_{oo} & T_{oM} \\ T_{Me} & T_{Mo} & \Gamma_{MM} \end{pmatrix} * \begin{pmatrix} a_e \\ a_o \\ a_M \end{pmatrix} \quad (1)$$

Where the subscripts o and e stand for the odd slotline and even coplanar modes. The subscript M stand for the microstrip mode. For example, Γ_{oe} is the reflection coefficient of the CPW odd mode due to an incident CPW even mode of unit amplitude.

When scattering parameters between two modes with different field map are calculated, these values are highly sensitive to the definition used to obtain the characteristic impedance. For passive device, this difficulty has been overcome by using the reciprocity theorem.

Figure 3 shows the evolution of S-parameters versus the lateral displacement m . As expected, the coupling between the even coplanar and the microstrip modes is the most important and the better configuration is naturally obtained for $m = 0$. Nevertheless, a mode conversion occurs.

Concerning the mode conversion, we must notice that the parameter Γ_{oe} presents a very low value whatever the lateral displacement may be. It appears that tolerance requirements about the lateral shift can be determined neglecting the mode conversion in this studied transition.

From another point of view, the coupling between the CPW slotline (odd) mode and the microstrip mode can be neglected, specially for $m = 0$. This result can be explained easily because the two modes present a very different field map.

CONCLUSION:

In this communication an overlay transition between a microstrip and a CPW is investigated. The influence of a lateral shift between the two planes has been investigated. Theoretical results for the full 3x3 Scattering matrix of the discontinuity is presented and the mode conversion phenomenon is characterized.

REFERENCES :

- 1 J. J. BURKE, R. W. JACKSON: 'Surface-to-Surface Transition via Electromagnetic Coupling of Microstrip and Coplanar Waveguide', IEEE Trans. on M.T.T., Vol. MTT-37, No 3, March 1989, pp. 519-525.
- 2 G STRAUSS, W. MENZEL : 'A novel concept for mm-wave MMIC interconnects and packaging', IEEE Int. Micr. Symp. MTT-S, San Diego, 1994, pp. 1141-1144.
- 3 G STRAUSS, W. MENZEL : 'Millimeter-Wave Monolithic Integrated Circuit Interconnects Using Electromagnetic Field Coupling', IEEE Trans. on Comp., Pack., and Man. Tech., Vol. 19, No. 2, May 1996, pp. 278-282.

- 4 H. JIN, R. VAHLIDIECK : 'Full-Wave Analysis of Coplanar Waveguide Discontinuities Using the Frequency Domain TLM Method', IEEE Trans. on M.T.T., Vol. MTT-41, No 9, Sept. 1993, pp. 1538-1542.
- 5 M. KAHRIZI, T. SARKAR, Z. A. MARICEVIC : 'Analysis of a Wide Radiating Slot in the Ground Plane of a Microstrip Line', IEEE Trans. on M.T.T., Vol. MTT-41, No 1, Jan. 1993, pp. 29-37.
- 6 A. B. KOUKI, R. MITTRA, C. H. CHAN : 'Analysis of a thin slot discontinuity in the reference plane of a microstrip structure', IEEE Trans on M.T.T., Vol. MTT-41, No 8, August 1993, pp. 1356-1361.
- 7 Y. HUA, T. SARKAR : 'Matrix Pencil Method for Estimating Parameters of Exponentially Damped / Undamped Sinusoids in noise', IEEE Trans. A.S.S.P., Vol. 38, May 1990, pp. 814-824.

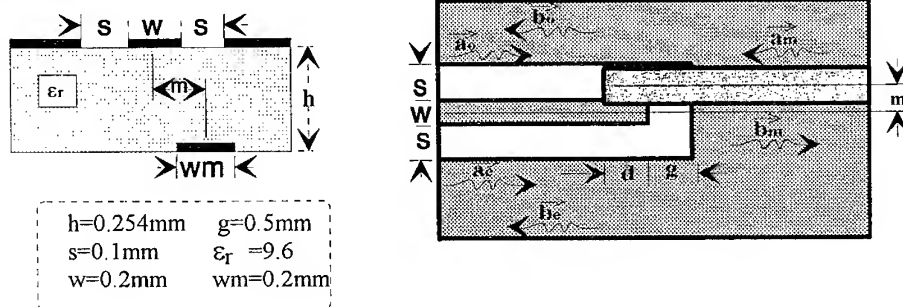


Figure1:CPW-microstrip overlap transition.

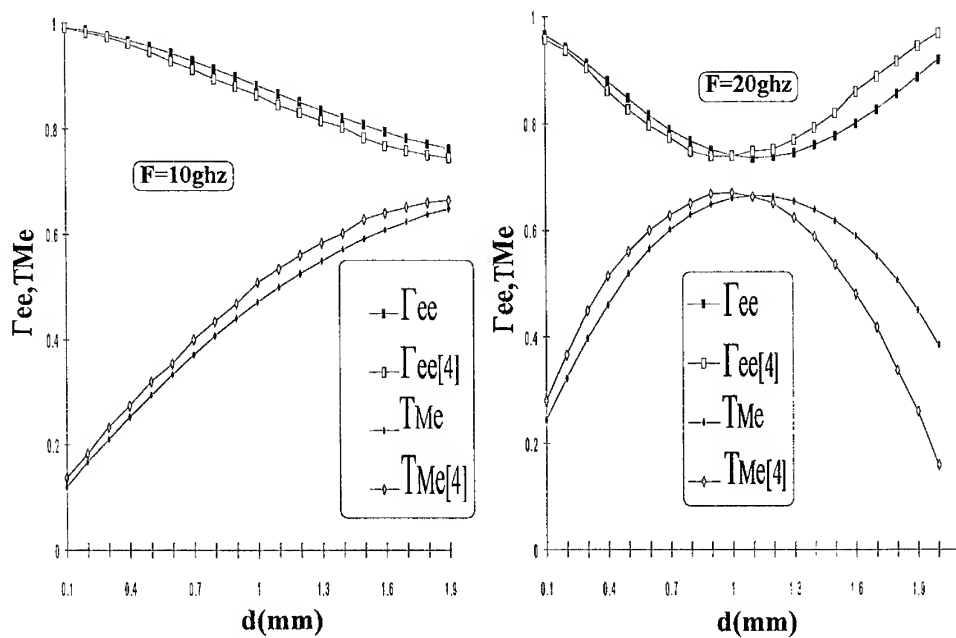


Figure2: Variation of the S-parameter versus the overlap length d of a CPW-microstrip transition for $m=0$

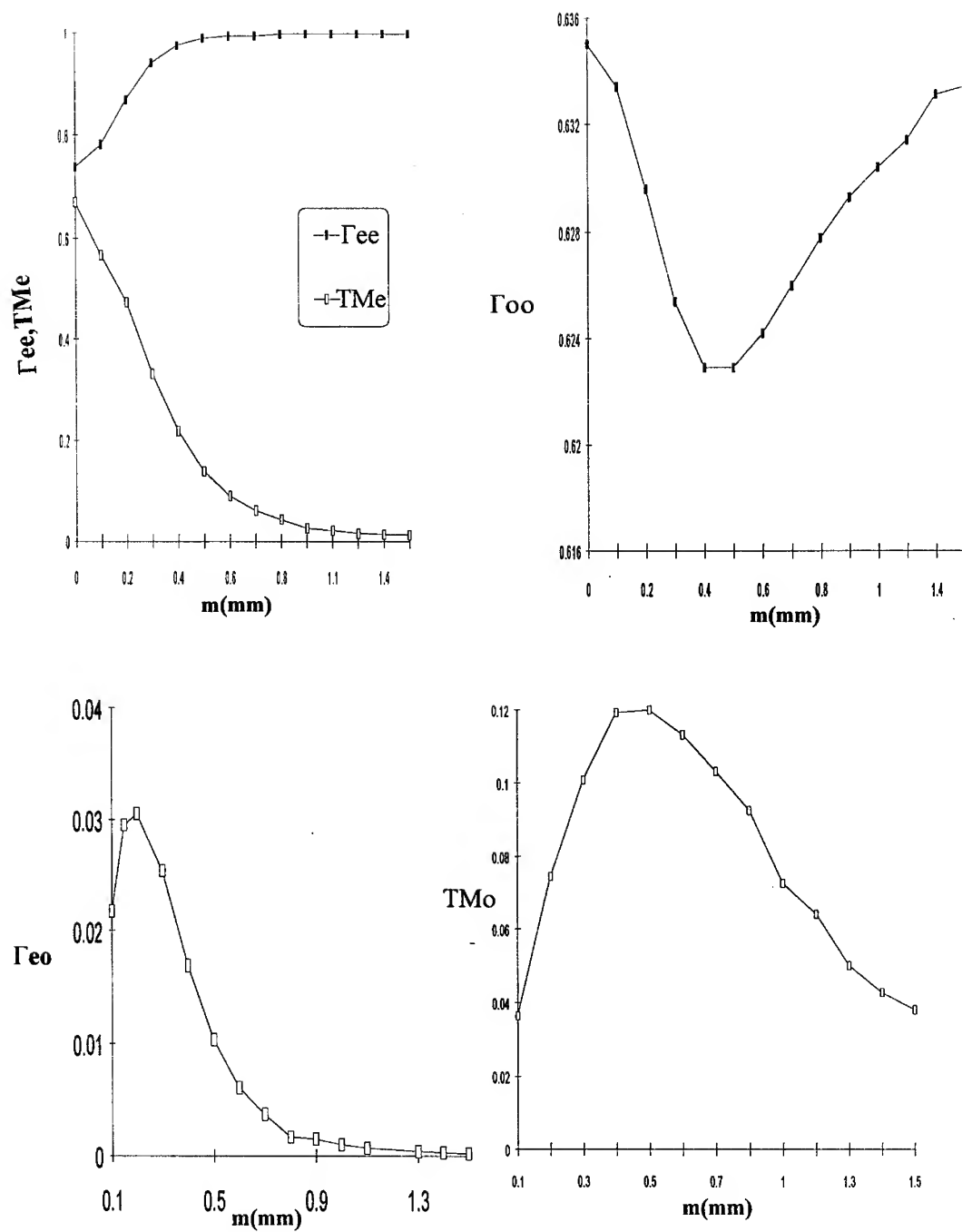


Figure3 :Variation of the S-parameter magnitudes versus lateral displacement m of the CPW-microstrip transition for $d=1$ mm and $F=20$ ghz.

ANALYSIS OF TRANSIENTS IN COUPLED TAPERED LOSSY AND FREQUENCY-DEPENDENT TRANSMISSION LINES USING SPICE

José I. Alonso ¹, José M. Gómez ²

¹ Dpto. Señales, Sistemas y Radiocomunicaciones. E.T.S.I. Telecomunicación.
Universidad Politécnica de Madrid. Ciudad Universitaria S/N. 28840 Madrid.
e-mail: ignacio@gmr.ssr.upm.es

² Dpto. de Teoría de la Señal y Comunicaciones. E.U. Politécnica.
Universidad de Alcalá. Crta. Madrid-Barcelona. Km 33,6. 28871 Alcalá de Henares. Madrid.
e-mail: tsjmgp@teose.alcala.es

ABSTRACT

A simple technique for implementing multiconductor nonuniform transmission lines, with lossy and frequency-dependent parameters, into SPICE program is presented. The technique proposed in this paper uses the *Analog Behavioral Modelling* option of SPICE and only requires to know the S-parameters of the multiconductor system. So that, the transient analysis of distributed nonuniform multiconductor system can be undertaken of a straightforward and efficient way.

I. INTRODUCTION

With the recent advances in electronic packaging design, interest on the subject of multiconductor nonuniform transmission lines has taken on a great importance. Usually, interconnections lines between the "chip" and the "exterior world" are nonuniform coupled tapered transmission lines. Several methods for modelling wavefront propagation along tapered multiconductor transmission lines have been proposed [1-5]. However, the aforementioned methods are not easy to combine with others popular general-purpose circuits simulators, such as SPICE.

In this paper, a simple technique for implementing nonuniform multiconductor transmission lines, with frequency-dependent parameters, into SPICE program is presented. The method proposed uses the *Analog Behavioral Modelling* option, avoids the problems of circuit synthesis and to develop sophisticated techniques for analysis of this kind of structures. The use of S-parameters as a starting point for obtaining the model permits greater generality to the technique because they are easier to measure or can be calculated with any CAD commercial program.

II. NONUNIFORM MULTICONDUCTOR TRANSMISSION LINES MODEL

II.1. Basic principles

The starting point of the developed model, consist of finding the functional relations between the S parameters of the n -conductor nonuniform transmission-line system and the input impedances, $Z_{ii}(s)$, and the frequency-dependent voltages sources, $F_{ij}(s)$, which form the model, as is shown in Fig.1.

In order to find these relations, we assume that the S-parameters of the nonuniform interconnection structure whit a total of n ports are known from measurements o from simulations. The $n \times n$ generalized scattering matrix S of this n -ports network, normalized whit respect the n impedances $Z_{N1}, Z_{N2}, \dots, Z_{Nn}$ is defined by means of the linear matrix equation

$$\mathbf{b} = \mathbf{S} \mathbf{a} \quad (1)$$

where S is a square matrix, and \mathbf{a} , \mathbf{b} are the n -vectors whose i th component a_i , b_i are, respectively, the generalized incident and reflected scattering variables. According to the definition of complex power waves,

[6], vectors \mathbf{a} and \mathbf{b} can be written in terms of \mathbf{V} and \mathbf{I} as follows:

$$\mathbf{a} = \mathbf{R}(\mathbf{V} + \mathbf{Z}_N \mathbf{I}) \quad (2)$$

$$\mathbf{b} = \mathbf{R}(\mathbf{V} - \mathbf{Z}_N^* \mathbf{I}) \quad (3)$$

In these equations \mathbf{V} and \mathbf{I} are n -vectors whose i th component V_i , I_i , are respectively, the voltage across and the current into port i th. \mathbf{R} and \mathbf{Z}_N are diagonal matrices whose i th elements are given by $1/2 [\text{Re}(Z_{Ni})]^{-1/2}$ and Z_{Ni} , respectively.

II.2. Generalized Method of Characteristics. S Parameters Formulation

The coupled nonuniform transmission line system can be described by the following characteristic formulation:

$$\mathbf{V} = \mathbf{Z}\mathbf{I} + \mathbf{E} = \mathbf{Z}\mathbf{I} + \mathbf{F}[\mathbf{V} + \mathbf{Z}_N \mathbf{I}] \quad (4)$$

where \mathbf{Z} is a diagonal matrix of impedances, whose elements, $Z_{ii}(s)$, are the input impedances in each port with the others ports matched, and \mathbf{E} is the vector which contains the frequency-dependent voltage waveform generators, as is shown in the model of Fig.1. On the hand, the matrix \mathbf{E} can be split in a diagonal matrix \mathbf{F} and vector $[\mathbf{V} + \mathbf{Z}_N \mathbf{I}]$. The matrix \mathbf{F} is a propagation matrix, whose elements, $F_{ij}(s)$, simulate the delay and attenuation of signal propagation between i th and j th ports. The elements of $[\mathbf{V} + \mathbf{Z}_N \mathbf{I}]$ vector are the incident voltage in j th port. The next step consist of finding the relationships between the S-parameters of multiconductor nonuniform system and the $Z_{ii}(s)$ and $F_{ij}(s)$ functions.

To obtain these relationships, we substitute (2) and (3) into (1), obtaining:

$$(\mathbf{R} - \mathbf{S}\mathbf{R})\mathbf{V} = (\mathbf{R}\mathbf{Z}_N^* + \mathbf{S}\mathbf{R}\mathbf{Z}_N)\mathbf{I} \quad (5)$$

If we split the matrix \mathbf{S} in a diagonal matrix \mathbf{S}_d and another matrix \mathbf{S}_r which contains the rest of elements, that is to say $\mathbf{S} = \mathbf{S}_d + \mathbf{S}_r$, the equation (5) is transformed to:

$$\{(\mathbf{1}_n - \mathbf{S}_d)\mathbf{R} - (\mathbf{S} - \mathbf{S}_d)\mathbf{R}\}\mathbf{V} = \{\mathbf{R}\mathbf{Z}_N^* + \mathbf{S}_d\mathbf{R}\mathbf{Z}_N + (\mathbf{S} - \mathbf{S}_d)\mathbf{R}\mathbf{Z}_N\}\mathbf{I} \quad (6)$$

Multiplying both sides of (6) by $\mathbf{R}^{-1}(\mathbf{1}_n - \mathbf{S}_d)^{-1}$, we obtain after an algebraical manipulation:

$$\{\mathbf{1}_n - \mathbf{R}^{-1}(\mathbf{1}_n - \mathbf{S}_d)^{-1}(\mathbf{S} - \mathbf{S}_d)\mathbf{R}\}\mathbf{V} = \{\mathbf{1}_n - \mathbf{S}_d\}^{-1}\mathbf{Z}_N^* + \{\mathbf{1}_n - \mathbf{S}_d\}^{-1}\mathbf{S}_d\mathbf{R}\mathbf{Z}_N\}\mathbf{I} + \{\mathbf{R}^{-1}(\mathbf{1}_n - \mathbf{S}_d)^{-1}(\mathbf{S} - \mathbf{S}_d)\mathbf{R}\mathbf{Z}_N\}\mathbf{I} \quad (7)$$

which can be reformulated in this way:

$$\mathbf{V} = \{(\mathbf{I}_n - \mathbf{S}_d)^{-1} [\mathbf{Z}_N^* + \mathbf{S}_d \mathbf{Z}_N]\} \mathbf{I} + \{\mathbf{R}^{-1}(\mathbf{I}_n - \mathbf{S}_d)^{-1}(\mathbf{S} - \mathbf{S}_d)\mathbf{R}\} \{\mathbf{V} + \mathbf{Z}_N \mathbf{I}\} \quad (8)$$

Therefore, if we compare the equation (4) with (8), we can obtain the values of matrices \mathbf{Z} and \mathbf{F} of the characteristic formulation in terms of scattering matrix \mathbf{S} and the normalization impedances matrix \mathbf{Z}_N . The following result are obtained:

$$\mathbf{Z} = (\mathbf{I}_n - \mathbf{S}_d)^{-1} [\mathbf{Z}_N^* + \mathbf{S}_d \mathbf{Z}_N] \quad (9)$$

$$\mathbf{F} = \mathbf{R}^{-1}(\mathbf{I}_n - \mathbf{S}_d)^{-1}(\mathbf{S} - \mathbf{S}_d)\mathbf{R} \quad (10)$$

The i th elements of the previous matrices are given by:

$$Z_{ii} = \frac{Z_{Ni}^* + S_{ii} Z_{Ni}}{1 - S_{ii}} \quad (11)$$

$$F_{ij} = \sqrt{\frac{\text{Re}(Z_{Ni})}{\text{Re}(Z_{Nj})}} \frac{S_{ij}}{1 - S_{ii}} \quad (12)$$

For measures in broadband, the normalizing impedances are, normally, $Z_{Ni} = Z_{0i} = 50 \Omega$, so the equations (11) and (12) are notably simplified.

Therefore, frequency-dependent input impedances, $Z_{ii}(s)$, and voltage controlled voltage sources $E_{ij}(s) = F_{ij}(s)[V_j + Z_{0j} I_j]$, whose gains and phases and dependent on the frequency, must be implemented, in accordance with [7].

In the proposed technique, the Analog Behavioral Modelling option is used to implement these controlled sources. That it why is necessary to calculated a frequency response table of functions $Z_{ii}(s)$ and $F_{ij}(s)$. This task can be easily done with any CAD commercial program of microwaves circuits, such as HP-EESOF or SUPERCOMPACT, taking into account the relationships provided by equations (11) and (12).

III. EXAMPLE

To illustrate the advantages and the effectiveness of this method we give a representative example. We consider two coupled lossy nonuniform copper lines, with a total length of 5 cm. The network configuration and geometry of coupled nonuniform microstrip lines are shown in Fig. 2. This reference example was introduced by G.- W. Pan et al. [8]. The lines are driven by a voltage source that generates a trapezoidal pulse with an amplitude of 1 V. and a width of 0.8 ns., with a rise and fall time of 0.1 ns. The S-parameters have been calculated in 512 frequency discrete points from DC to 204.4 Ghz using HP-EESOF. To calculate the S-parameters of the structure the coupled tapered lines have been divided into 20 coupled uniform sections. Fig. 3 shows the SPICE network resulting from the application of the developed technique to the simulation of two nonuniform coupled transmission lines.. Figures 4a. and 4b. illustrate the waveform of the active and passive lines at both near and far ends. In these figures the results obtained in the reference example (\square) and those computed with the technique proposed in this paper (Δ) are compared. As it is shown both approaches give identical results.

IV. CONCLUSIONS

A method with allows the implementation of nonuniform multiconductor transmission lines, whit frequency-dependent parameters, into a SPICE program has been proposed. The method uses the *Analogical Behavioral Modelling* option and only is necessary to know the S parameters of multiconductor nonuniform system, that can be calculated using any CAD commercial programs of microwaves circuits.

ACKNOWLEDGMENTS

This work was supported by the projects TIC96-0724-C06-01 and ESP95-0612 of the National Board of Scientific and Technological Research (CICYT).

REFERENCES

- [1] M. Mehalic and R. Mittra, "Investigation of Tapered Multiple Microstrip Lines for VLSI Circuits". 1990. IEEE T-MTT., n°11, pp.1559-1567.
- [2] O. A. Palusinski and A. Lee, "Analysis of Transient in Nonuniform and Uniform Multiconductor Transmission Lines". 1989. IEEE T-MTT, n° 1, pp.127-138.
- [3] F-Y. Chang, "Transient Simulation of Nonuniform Coupled Lossy Transmission Lines Characterized with Frequency-Dependent Parameters - Part I: Waveform Relaxation Analysis". 1992. IEEE T-CASI, n° 8, pp.585-603.
- [4] T. Dhaene et al., "Transient Simulation of Arbitrary Nonuniform Interconnection Structures Characterized by Scattering Parameters". 1992. IEEE T-CASI, n°11, pp.928-937.
- [5] J. F. Mao et al., "Analysis of the response of Nonuniform Multiconductor Transmission Lines with a method of Equivalent cascaded Network Chain". 1992. IEEE T-MTT, n° 5, pp.948-954.
- [6] K. Kurokawa, "Power Waves and the Scattering Parameters". 1965. IEEE T-MTT, n° 2, pp.94-202.
- [7] J. I. Alonso et al., "Simulation of arbitrary nonuniform frequency-dependent interconnections using SPICE". 1995. Electronics Letters, n° 4, pp.253-254.
- [8] G.- W. Pan et al., "Frequency-Domain Analysis of Coupled Nonuniform Transmission Lines using Chebyshev Pseudo-Spatial Techniques" IEEE T-MTT, n°11, pp.2025-2033.

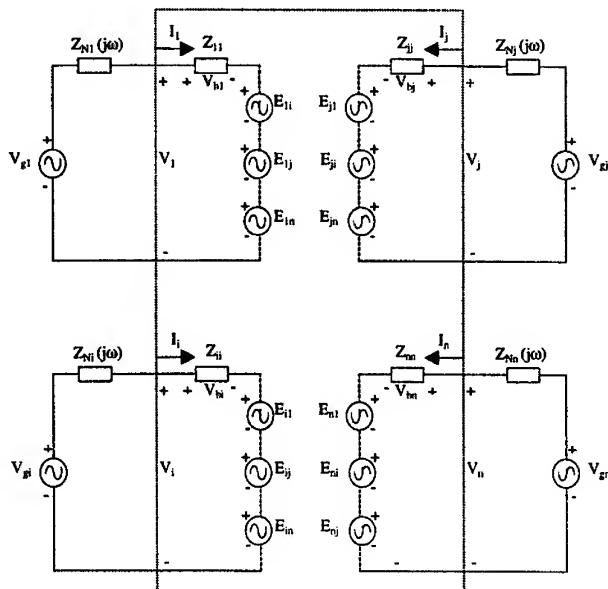


Figure 1. The generalized characteristics model of a multiconductor nonuniform coupled transmission line system.

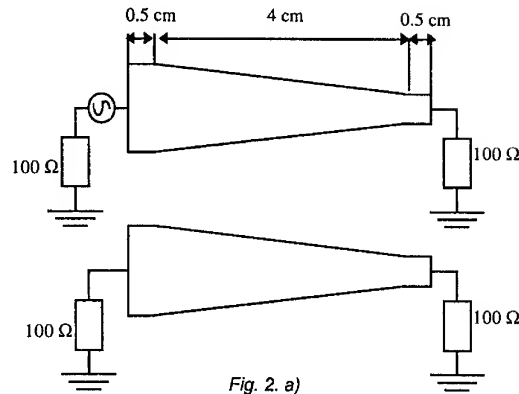


Fig. 2. a)

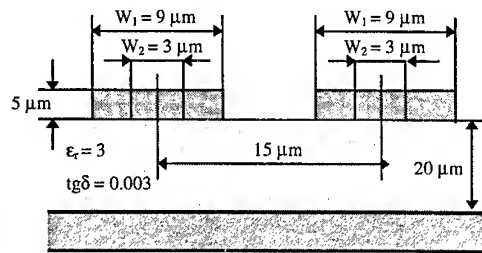


Fig. 2. b)

Figure 2. a) Network configuration of coupled nonuniform lines.

b) Cross section and geometry of microstrip lines.

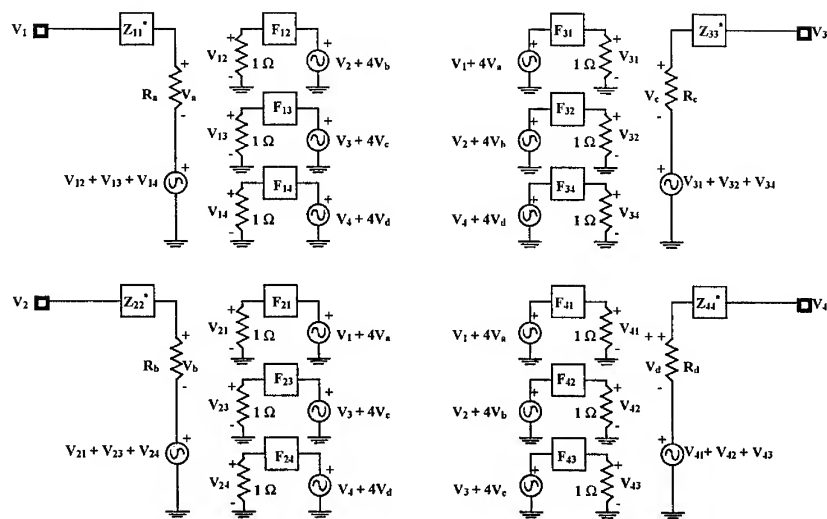


Figure 3. SPICE network for two nonuniform coupled lines.

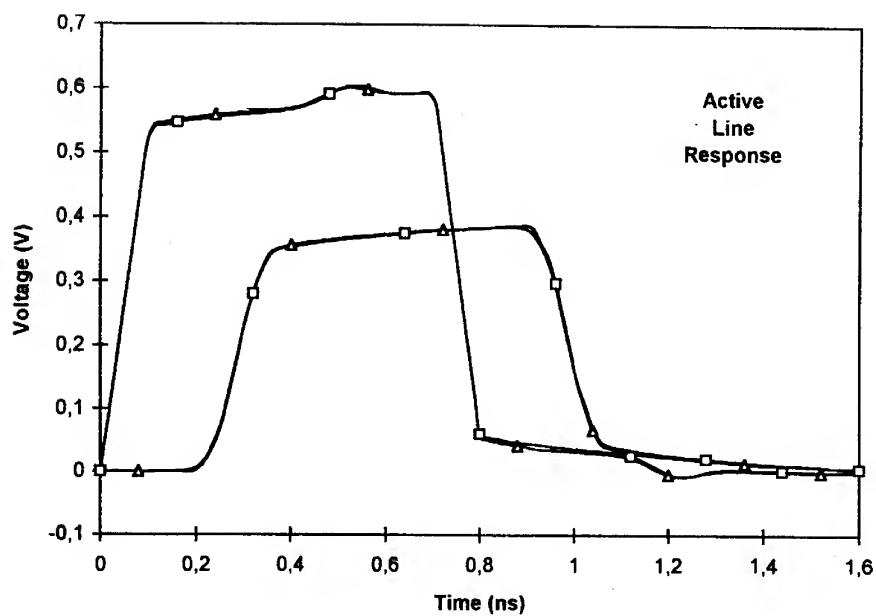


Figure 4 a)

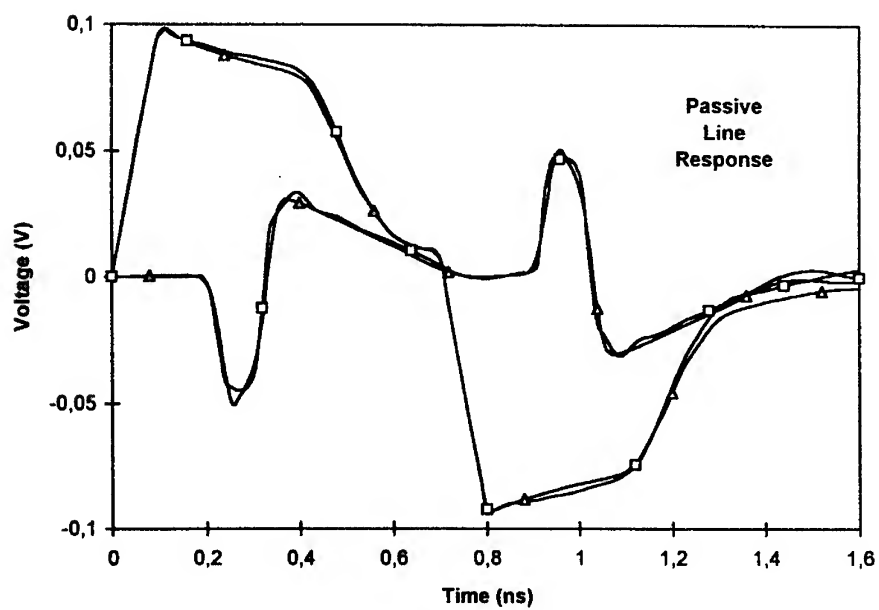


Figure 4 b)

Figure. 4. Simulation results of electrical response.
a) Response in the generator end.
b) Response at load end.

LOW-NOISE MICROWAVE ACTIVE FILTERS IN PLANAR REALIZATIONS

W. Menzel, W. Schwab*

Microwave Technique, University of Ulm, D-89069 Ulm, Germany

* now with Daimler-Benz Aerospace, Woerthstr. 85, D-89077 Ulm, Germany

ABSTRACT

Design and results of active filters based on low-loss suspended stripline filter resonators and MeSFET gain blocks realized in microstrip are presented. The coupling between filter resonators and microstrip gain blocks is performed electromagnetically acting, at the same time, as matching structures for input and output of the transistor. In this way, very low noise active filter circuits with a single gain stage and two stages at 10 GHz as well as a single stage 35 GHz active filter were realized.

INTRODUCTION

With decreasing bandwidth, passive filters - especially in planar integrated form - become more and more lossy, their edges are rounded, and the filter slopes become less steep.

Filters in the input of a front-end typically should suppress adjacent signals to avoid intermodulation products or even saturation of the input amplifier. Due to their position in the system, losses as low as possible and a low noise figure are of a major importance, while the form of the filter response is not as critical as losses or noise. On the other hand, sharp edges and a steep filter slope are of prime interest for signal separation in channelized receivers or for the reduction of noise bandwidth to a minimum. This mostly, however, is done after preamplification, therefore losses and especially noise figure are not as relevant.

To reduce filter losses by active elements, a number of efforts have been published, e.g. [1] - [11], with different types of filters and based on lumped elements or transmission line structures together with MeSFETs as discrete devices or even using monolithic circuits. As the active elements add noise to the filter circuit, noise figure might be considerably high - higher than the insertion loss of a respective passive circuit. In many papers, noise figure is not considered, or noise figures up to even 15 dB are reported. A detailed investigation of noise in active filters is presented in [8].

In this contribution, design and results of active band pass filters (or frequency selective amplifiers) is reported with prime attention to low noise figure, as it is necessary in the input of a receiver.

DESIGN OF THE FILTER

To achieve best performance of the low-noise active filter, a basic structure according to Fig. 1 was chosen. A first filter resonator does some preselection to reduce intermodulation problems, a gain block provides low-noise amplification, and a further resonator improves selectivity [12]. More gain blocks and resonators may be added in the same way [13]. For optimum performance, the following set-up was chosen:

- Suspended stripline as planar transmission line with lowest loss was employed for the resonators.

- Microstrip line with very short line segments was used for the gain block, resulting in easy via-hole realization and good thermal performance, as the microstrip part of the whole circuit can easily be placed on a metal block.
- Multilayer structures with electromagnetic coupling between filter resonators and gain blocks were chosen [14]. In this way, at the same time and with one coupling structure only, the inverter function, gain block input or output matching, and DC isolation are achieved with minimum loss. Furthermore, a capacitive load close to the transistor gate or drain will, in many cases, improve stability, especially at low frequencies.

The basic layout of such a filter with one gain block is shown in Fig. 2.

The multilayer transition between suspended stripline and microstrip (inset of Fig. 3) is calculated using spectral domain techniques [15]. The overlap d of both „hot“ conductors mostly determines the performance of the transition, while the gap width g between stripline and microstrip ground has a minor influence. As can be seen from Fig. 3, a wide range of coupling coefficients can be adjusted.

FILTER RESULTS

A first test filter according to Fig. 2 was realized for 10 GHz, using a MeSFET CFY25 (Siemens) with $0.5\mu\text{m}$ gate length and $6 \times 40\mu\text{m}$ gate width. The measured minimum device noise figure for several transistors ($I_{DS} = 0.3I_{DSS} = 10\text{ mA}$) was in the range from 1.9 to 2.2 dB; the maximal available gain about 12 dB. The filter was fabricated on a soft substrate of $254\mu\text{m}$ height and a dielectric constant of 2.22, mounted to a brass housing (channel dimensions $5\text{ mm} \times 5\text{ mm}$) with SMA coaxial connectors.

Two of these filters were fabricated, showing a maximal gain of 10.7 and 11.9 dB (Fig. 4) and noise figures of 2.3 and 2.0 dB, respectively, at center frequency. Compared to the device performance, only a slight degradation can be stated due to the filter and amplifier circuitry. As the circuit exhibits a considerable gain, the noise contribution of further components added to the output of the filter is reduced remarkably.

In a second step, a filter with two gain blocks and three filter resonators was designed (Fig. 5). The first transistor was biased for minimum noise figure, the second one for maximally gain ($I_{DS} = 0.5I_{DSS}$). This two-stage active filter exhibited a gain of 22.1 dB (Fig. 6), associated with an overall noise figure at center frequency of 3.2 dB. This noise figure is slightly higher than expected from cascading another gain block and another filter element to the structure according to Figs. 2 and 4; but with this filter, bandwidth was much lower than in the first example (100 MHz compared to 420 MHz) resulting in increased losses.

To demonstrate the performance of this type of active filter in the mm-wave range, a circuit according to Fig. 2 was designed at 35 GHz employing a pseudomorphic HEMT with $0.25\mu\text{m}$ gate length and $120\mu\text{m}$ gate width from the Daimler Benz Research Institute. The S-parameters of the resulting circuit are plotted in Fig. 7, showing a gain of 4.2 dB. In this case, however, the transistor performance was degraded, to some extent, while placing it into the circuit, therefore the gain was relative low, and the noise figure amounted to 4.0 dB only. Nevertheless, the operating principle could be demonstrated at this frequency, too.

REFERENCES

- [1] C. Rauscher: Microwave Active Filters Based on Transversal and Recursive Principles. IEEE Trans. on Microw. Theory Techn. MTT-33 (1985), pp. 1350-1360.
- [2] C.-Y. Chang, T. Itoh: Microwave Active Filters Based on Coupled Negative Resistance Method. IEEE Trans. on Microw. Theory Techn. MTT-38 (1990), pp. 1879-1184.
- [3] Y. Yamamoto, K. Kawasaki, T. Itoh: A MESFET-Controlled X-Band Active Bandpass Filter. IEEE Microw. and Guided Wave Letters, Vol 1, 1991, pp. 110-111.
- [4] R.R. Bonetti et al.: An MMIC Active Filter with 60 dB Rejection. IEEE Intern. Microw. Symp. 1992, Albuquerque, NM, pp. 1195-1198.
- [5] J. Lin, T. Itoh: IEEE Intern. Microw. Symp. 1992, Albuquerque, NM, pp. 921-924. Tunable Active Bandpass Filters Using Three-Terminal MESFET Varactors.
- [6] R.G. Arnold, S.P. Marsh: A Microwave Active Bandstop Filter with Tunable Centre Frequency. IEEE Intern. Microw. Symp. 1993, Atlanta, pp. 1313-1316.
- [7] U. Karacaoglu, L.D. Robertson, M. Guglielmi: Microstrip Bandpass Filters Using MMIC Negative Resistance Circuits for Loss Compensation. IEEE Intern. Microw. Symp. 1994, Sand Diego, Ca., pp. 613-616.
- [8] E.C. Krantz, G.R. Branner: Active Microwave Filters with Noise Performance Considerations. IEEE Trans. on Microw. Theory Techn. MTT-42 (1994), pp. 1368-1379.
- [9] U. Karacaoglu, L.D. Robertson: MMIC Active Bandpass Filter Using Negative Resistance Elements. IEEE Intern. Microw. Symp. 1995, Orlando, FL, pp. 135-138.
- [10] A. Brucher et al: Broadband and Tunable Negative Monolithic Circuits for Microwave Active Filters Compensation. IEEE Intern. Microw. Symp. 1995, Orlando, FL, pp. 745-748.
- [11] C. Rauscher, Microwave Channelized Active Filters - A New Modular Approach to Achieving Compactness and High Selectivity. IEEE Trans. on Microw. Theory Techn., MTT-44 (1996), pp. 122-132.
- [12] W. Schwab, W. Menzel: A Low-Noise Active Bandpass Filter. IEEE Microw. and Guided Wave Letters, Vol. 3 (1993), pp. 1-2.
- [13] W. Schwab, F. Boegelsack, W. Menzel: Multilayer Suspended Stripline and Coplanar Line Filters. IEEE Trans. on Microw. Theory Techn. MTT-42 (1994), pp. 1403-1407.
- [14] W. Schwab, W. Menzel: A Suspended Stripline to Microstrip Transistor Using Multilayer Techniques. 22nd European Microw. Conf. 1992, Helsinki, Finland, pp. 1181-1186.
- [15] W. Schwab, W. Menzel: On The Design of Planar Microwave Components Using Multilayer Structures. IEEE Trans. on Microw. Theory Techn., MTT-40 (1992), pp. 67-72.

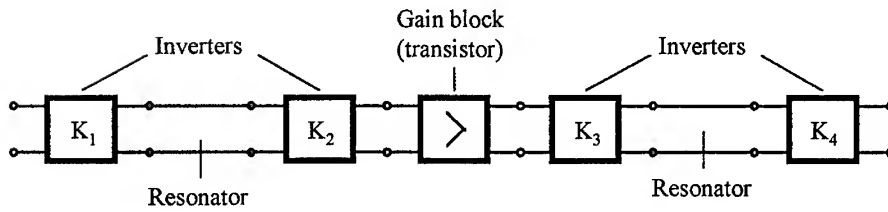


Fig. 1: Basic structure of active filter circuit.

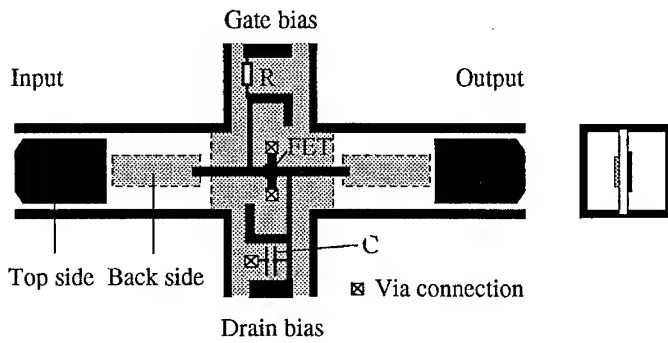


Fig. 2: Basic layout of active filter circuit.

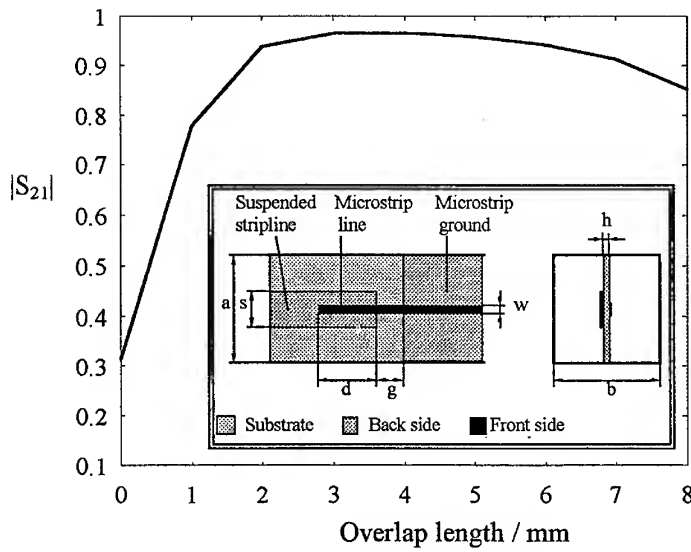


Fig. 3: Basic suspended stripline - microstrip coupling structure and coupling behavior as a function of coupling length ($f = 10$ GHz, $a = b = 5$ mm, $s = 1.75$ mm, $w = 0.76$ mm, $g = 1$ mm, $h = 0.254$ mm, $\epsilon_r = 2.22$).

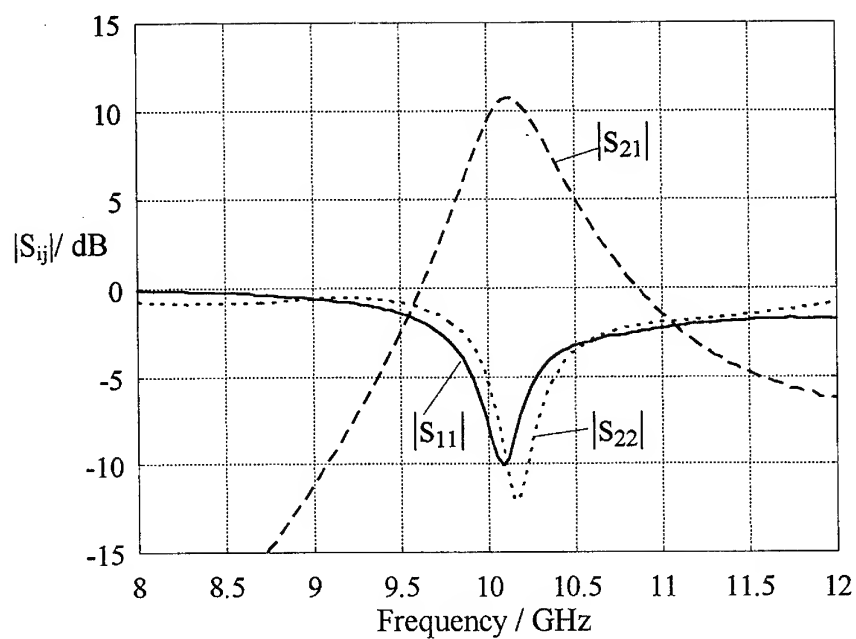


Fig. 4: Input and output return loss and gain of one stage active filter.

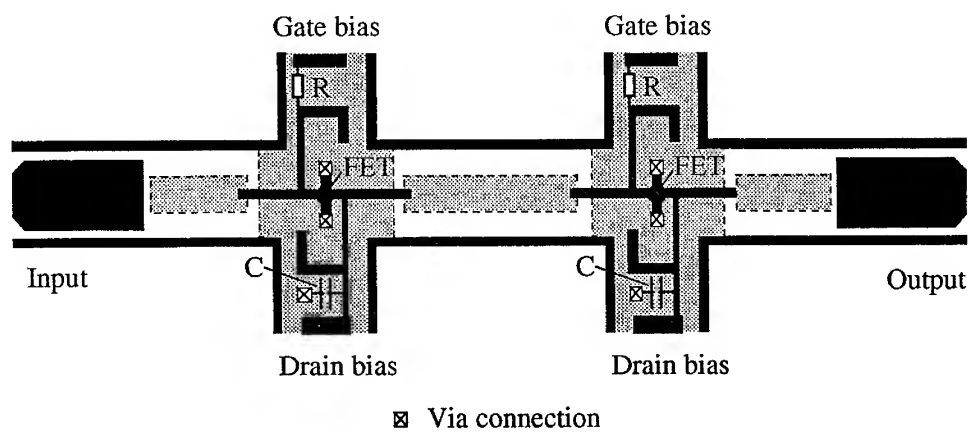


Fig. 5: Basic layout of two stage active filter circuit.

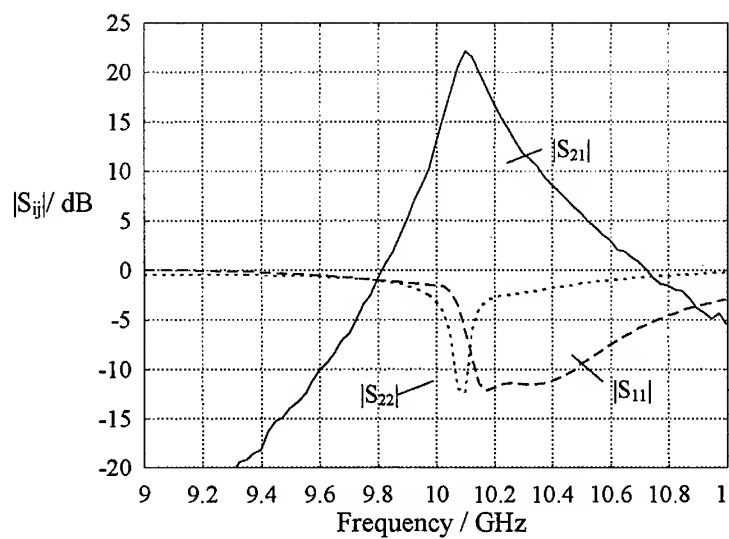


Fig. 6: Input and output return loss and gain of two stage active filter.

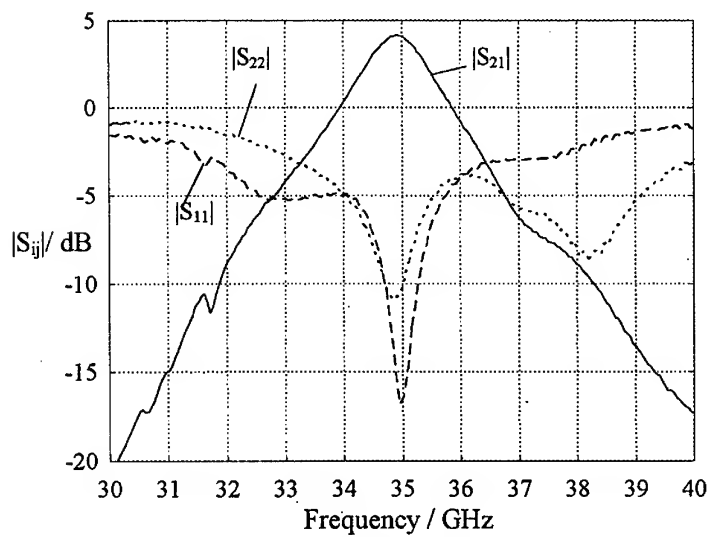


Fig. 7: Input and output return loss and gain of 35 GHz active filter.

Variety of Approaches to Designing Microwave Active Filters

Boris Yu.Kapilevich

Siberia State Academy of Telecommunications @ Informatics, Microwaves and Antennas Dept.
86 Kirov Str., 630102 Novosibirsk, Russia. Fax: +7-3832-222581, e-mail: boris@neic.nsk.su

Abstract

Microwave active filters continue to attract the attention of specialists because of their unique performance. The paper is targeted at providing microwave and RF designers with an introduction to the state of the art including both of current tendencies and unsolved problems. Emphasis is placed on a physical interpretation of general principles of design and practical realizations of microwave active filters.

1. Introduction

Major physical limitation inherent all passive microwave filters is the well known relationship between insertion loss and bandwidth, namely, their product is a constant for a given realization of a passive filtering structure. There is a promising way to overcome the limitation by using active elements to compensate for insertion loss. Based on this idea different configurations of microwave active filters (MAF) have been developed. The key features of MAFs are:

- gain control without distortion of the frequency response;
- wide frequency tuning capability;
- capability of a performance for specified poles to improve selectivity;
- simple adaptation to MIC & MMIC technology;
- small filter dimensions and little weight.

The paper presents a comprehensive overview of tendencies and the current state of the art concerning MAFs including estimates of achievements and unsolved problems which may certainly attract the attention of microwave specialists.

2. Basic MAF Configurations

A variety of MAF configurations can be subdivided into several groups depending on the type of active elements, schematic approaches and structure of passive filtering parts. Microwave diodes with negative resistance such as Gunn diodes, IMPATT diodes and tunnel diodes can be used as active elements. At present high-Q GaAs abrupt junction varactor diodes are available with a total capacitance ratio up to 5 or greater and a Q-factor about 4000 -7000. This allows a good performance of voltage tunable MAF filters to be achieved. The drawback of IMPATT diodes is a higher noise level which prevents their use for MAF intended to be applied in input cascades of low noise receivers, while tunnel diodes have a lower saturation level which limits the dynamic range of MAFs.

There are no universal recommendations regarding transistors to be applied in MAFs but GaAs FETs, HEMTs and bipolar transistors may be chosen depending on the operating frequency, noise level, power handling capacity and other specified requirements. Some MAF configurations involve both microwave diodes and transistors in order to obtain additional positive effects.

Different schematic MAF realizations are known at present. However, MAFs based on active loop configurations, active inductors and channelized structures can be recommended for typical applications, Hunter et al [1]. Any MAF configuration consists of passive and active components with resonant and non-

resonant properties. Non-resonant components, both lumped and distributed (R , L , C , directional couplers, sections of the transmission lines etc.) are needed to adjust input/output coupling coefficients and coupling coefficients between resonant units. Resonant components, mostly distributed, are used to provide a desirable frequency response of a MAF. They may have different structures, however, microstrip, stripline, slot or coplanar lines, Dib et al [2], Kulke et al [3], Sheinwald [4], Schwab and Menzel [14], dielectric resonators, Kajfez and Guillon [5], fin-lines, Solbach [6] or waveguides below cut-off (evanescent mode) , Kapilevich and Trubechin [7-9], Shunemann [10] can be recommended to be implemented into many MAF configurations. The resonant elements can also be realized without transmission line sections using high frequency inductance-simulating circuits , Sussman-Fort[11], Filinuk[12], Alinikula et al [13].

3. MAFs with Diodes as Active Elements

Microwave diode as an active element of MAF is preferable for waveguide configurations where direct maintaining transistor provides some problems. One of the example demonstrating this approach has been described by Kapilevich [15]. The MAF consist of an evanescent mode filtering structure to provide the required frequency response and a Gunn diode to compensate for dissipative losses. The passive filtering part of MAF is a quasi-periodic connection of dielectric slabs with relatively high and low permittivities positioned in rectangular waveguide operating below cut-off frequency. However, such structure is essentially lossy because of the energy dissipation from dielectric and conductor. To overcome the disadvantage an active element is introduced, Fig. 1. The waveguide width is chosen to obtain a propagating TE_{10} mode for sections with permittivity ϵ_{r1} and nonpropagating (evanescent) mode for sections with permittivity ϵ_{r2} . Hence, the condition $\epsilon_{r1} > \epsilon_{r2}$ must be satisfied. An active element needed to compensate for loss is placed on the center of a filter. It can be characterized by a complex admittance $Y = G + jB$ normalized to the system admittance.

Following a technique similar to that applied by [7] , a resulting transmission matrix A^{res} corresponding to Fig. 1 can be presented in the form

$$A^{res} = A_{in} * A_Y * A_{out} \quad (1)$$

where A_{in} and A_{out} are generalized resonance sections (GRSs)[8] consisting of lines with lengths l , t , $d/2$ at the input and output respectively . A_Y is a transmission matrix of the active element. The GRSs are determined as the product of transmission matrices of the above mentioned sections:

$$A_{in} = A_l * A_t * A_{d/2} \quad \text{and} \quad A_{out} = A_{d/2} * A_t * A_l \quad (2)$$

where

$$A_l = \begin{bmatrix} \cos \theta_l & jZ_l \sin \theta_l \\ j \sin \theta_l / Z_l & \cos \theta_l \end{bmatrix}, \quad A_t = \begin{bmatrix} \cosh \theta_t & jZ_t \sinh \theta_t \\ -j \sinh \theta_t / Z_t & \cosh \theta_t \end{bmatrix} \quad (3)$$

θ_l and θ_t are electric lengths of corresponding transmission lines, Z_l and Z_t are the impedances of the same lines. To determine the elements of $A_{d/2}$ a substitution of θ_l by $\theta_{d/2}$ must be carried out in eqn. 3. Finally, insertion loss L [dB] can be calculated using the S_{21} element of scattering matrix as follows

$$L = -20 \log |S_{21}| \text{ dB} \quad \text{with} \quad S_{21} = \frac{2}{2A_{11}^{res} + A_{12}^{res} + A_{21}^{res}} \quad (4)$$

The following passive filtering structure has been used to illustrate compensating effect: $\epsilon_{r1}=3.8-j0.02$, $\epsilon_{r2}=1$, $t/a=0.67$, $l/a=1.5$, $d/a=2.4$ and the width of a rectangular waveguide is $a = 9.65\text{mm}$. As an additional analysis

has shown the correct choice of G and B may provide zero loss, keeping the frequency response corresponding almost to that of original waveguide dielectric filter with a slight shift in its frequency response toward higher one. An experiment has confirmed the existence of the compensating effect predicted by theoretical model.

The two resonators MAF was fabricated with dimensions corresponding to the above mentioned example. An AA715D Gunn diode was used as the active element with proper bias circuit to control its gain. The measured values of insertion loss are plotted against frequency in Fig. 2 for $Y = 0$ (the line marked by \square) and for the maximum level of a loss compensation (the line marked by \blacksquare). The configuration of such MAF is useful for miniaturization of filters based on integrated waveguide technology and other monolithic waveguide dielectric components.

4. Varactor-tuned Resonators for MAF's Applications

Basically tunable MAFs include microwave transistors as active elements compensating for losses and varactor tuned microstrip resonators (VTMR) as passive resonant elements of tunable filters. Their tuning facilities depend on many factors: characteristics of transistors, varactors and transmission lines, configuration of resonators and coupling elements, etc. To ensure the best realization of such a resonator an optimum design must be carried out on the basis of an adequate circuit model.

There are different configurations of VTMR. Some of them were considered by Chandler et al [16], Jiao et al [17], Lin et al [18], Makimoto and Sagava [19] and other authors. Usually a single or double varactors are used in practice for unbalanced or balanced applications respectively. A single varactor configuration of VTMR is considered below to avoid difficulties related to microwave varactors identification needed for balanced applications.

One of the possible configuration of a single varactor VTMR suitable for active tunable filters is shown in Fig. 3, Kapilevich et al [20]. A varactor is represented by a two port network with a single normalized impedance Z_v (in a case of series connection) or normalized admittance Y_v (in a case of parallel connection).

Both VTMR's configurations have been studied. It was assumed that the normalized impedance of the coupling capacitor was $C=6$, providing the weak coupling coefficient needed for narrow-band applications. Fig. 4 shows the calculated insertion loss of VTMR as a function of electrical length t for different normalized varactor impedances (Fig. 4a, series connection) and admittances (Fig. 4b, parallel connection). The normalized impedance of the varactor circuit lines equals 1.5. Both series and parallel configurations exhibit odd and even resonances with different tuning behavior. For both configurations the lowest resonance is odd and nearest higher resonance is even resulting in a maximum current amplitude or maximum voltage amplitude in the center of the VTMR, accordingly. Therefore one of the above resonances must not always depend on varactor capacity, however the nearest other resonances are sensitive to it. This means that "fixed" and "tuned" resonant modes are natural phenomena belonging to the configurations of interest.

The tuning facilities of both configurations have been also investigated as a function of normalized varactor impedance or admittance for the first and second resonances. In both cases the frequency separation between adjacent resonances tends to be reduced when resonators are tuned towards higher frequencies. The phenomenon establishes the physical limit of tuning range for the VTMR itself and the MAFs based on such configurations.

Another problem takes place with odd and even resonances moving towards each other. They can produce a two-pole filter similar to coupled resonators. Fig. 5 illustrates this behavior for both configurations with the normalized impedance of a coupling capacitor $C=2$. In practice, the phenomenon discussed will restrict the available bandwidth of tunable MAFs. As an illustrative example, the calculated VTMR performances are shown in Fig. 6 for both configurations of Fig. 3. The results were obtained with following parameters:

- design frequency - 1.7 GHz;
- permittivity of substrate - 9.8 (Al_2O_3);
thickness of substrate - 1 mm;
- capacity of varactor - (0.5 - 2.5) pF;
series resistance of varactor - 2 Ohms;
- coupling capacitors - 0.3 pF;
- transmission line impedance - 80 Ohms;
- transmission line quality factor - 300;
- system impedance - 50 Ohms.

The tuning ranges are about 500 MHz for the first resonance in the series configuration and about 570 MHz for the second resonance in parallel configuration.

5. MAFs with Active Loops

Combining an active loop with a passive filtering structure is a simple and effective way to realize MAFs in practice. The most attractive feature here is the possibility of relatively independent design of both passive and active parts of a MAF. Indeed the frequency response is primarily determined by the passive filtering part of a MAF while the active part provides compensation for loss. Such an approach is valid if the coupling coefficient between the passive part and the active loop is small enough so that they can be designed independently, at least for initial stage. Otherwise, both parts of MAF interact with each other and the above decomposition is inadmissible. The other problem that should be taken into account is a match-to-phase loop property. Usually, it is impossible to support this condition covering a wide frequency band. Hence because of the above limitations a design of MAF based on an active loop approach may be recommended for narrow band applications with a moderate level of a loss to be compensated Kapilevich et al [21].

As the example, Fig. 7 shows the configuration of a two-sections tuned MAF for the 1.7 GHz operating frequency with capacitors as coupling elements between the VTRM and feed. The total phase-equalizing line is 270° with impedance $Z_{0e} = 65$ Ohms and $Z_{0o} = 50$ Ohms for sections of coupled lines. The termination resistors are connected at both ends of coupled lines to the ground. These lines determine a coupling coefficient between a passive resonator and an active loop. A design of the VTRM part has been carried out using the above described technique. The optimum loop impedance needed to avoid parasitic effects is 65 Ohms in the given configuration.

The frequency response of the two-sections MAF is shown in Fig.8 with a typical abrupt-junction silicon varactor diode for a maximum biasing voltage 50V. The frequency tuning range is between 1.65 - 2.2 GHz with almost loss compensation at whole. The transistor FHX04 has been used in the active part of the MAF.

Various types of dielectric resonator (DR) filters have been realized during two last decades [5]. Adding an active loop is a simple way to transform them to a lossless MAF. The idea was first suggested by M. Matsumura and Konishi [23]. They described bandstop and bandpass MAF configurations with an active loop that provided an increase of unloaded Q of the DR from 1500 to 37000 at a center frequency of 6.6GHz. Further development of the technique has been described by Mdrangeas[24,25], Delpino [26] and other authors. A typical schematic of a MAF with DR is shown in Fig. 9. The active loop consisted of a FET amplifier providing a fixed 10 dB flat gain over the 3.5-4.5 GHz bandwidth, an attenuating-phase shifting circuit composed of a Lange coupler, a Wilkinson combiner and two p-i-n diodes, so that independent phase and gain tuning were available. The three poles DR MAF had a 3 dB bandwidth of 24 MHz centered on 3.98 GHz with the gain of feedback active loop of 3.5 dB. The theoretical predictions and experimental data are in a good agreement. The major problem that a designer have to solve in practice of MAFs with the active loop is to provide a gain stability conditions for the configuration chosen avoiding an extremely high Q value of resonance circuit.

6. MAFs based on an active inductor

Two basic advantages are associated with active inductors:

- replacement of traditional spiral inductors by their active equivalents avoids a drastic degradation of Q-factor of inductance with increasing frequency;
- the area of an active inductor is much less compared to one of a spiral inductor so it is preferable for wide-band applications.

Physically, the existence of active inductors is determined by signal delay in a transistor. Due to the finiteness of the time for the non-equilibrium current carriers to move in the base of the transistor, the emitter current lags behind the voltage between the emitter and collector. The result is that the inductive nature of the total resistance Z_{ec} of emitter-collector circuits can be observed. More details illustrating the phenomenon may be found in Sussman-Fort [11], Filinuk [12], Chang and Itoh [22]. Both reciprocal and nonreciprocal MAFs can be realized in practice [12]. Also both band-pass and band-reject filters may be constructed using a concept of the active inductor.

Further development of the concept has been done by Hara et al [27] where new type of a girator circuit was proposed to realize low-loss or lossless characteristics. The goal has been achieved by replacement of the feedback resistor by GaAs FETs. Active inductors are composed of a common-source cascode FET and a feedback FET which is a common-gate FET or a common-gate cascode FET, Fig. 10. Modeling and experiments showed that a maximum Q factor of 65 is available at frequency about 8GHz because the resistor value is selected to make the active inductor stable. However, there is facility to realize an infinite Q factor by increasing the value of the output shunt resistor. For instance, a Q factor of more than 15000 has been measured with the active inductor described by Karacaoglu et al [28]. But the problem of unstable behavior of an active inductor will certainly provide a natural limit.

Bipolar transistor can be also used for the creation of active inductors. By virtue of the inherent base resistance it gives rise to a Q-enhancing effect. But the control of instability becomes more difficult. An example of a successful solution to the problem has been described by Kobayashi and Oki [29].

One of the problems in designing MAFs with active inductor is an undesirable phase delay inherent microwave amplifiers resulting in an unstable circuit. To avoid the phenomenon, low gain amplifiers with a smaller phase delay must be used. However, this causes a degradation of the Q factor. The contradiction is overcome with a MAF configuration proposed by Suwaki and Ohira [30]. It consists of two lowpass filters with transfer functions $T_1(s)$ and $T_2(s)$ connected to each other so that a negative feedback loop is formed. The first lowpass filter (LPF1) suppresses the high frequency signals resulting in the passing of only the low frequency signals. By virtue of the negative feedback loop formed with the second lowpass filter (LPF2), the bandpass features can be realized. The performance of the MAF discussed is simplified in practice because the transfer function of an amplifier may be approximated as follows

$$A(\omega) = A_0 / (1 + j\omega/\omega_c) \quad (5)$$

where A_0 is the amplifier gain at $\omega = 0$ and ω_c is a 3 dB roll-off frequency. Hence, the required transfer functions $T_1(s)$ and $T_2(s)$ are directly reproduced using (5). The variation of parameters A_0 and ω_c allows the obtaining of a variable filter to control the center frequency and Q factor. Varactors and varistors which are implemented in amplifiers can be used in practice for this aim.

7. Transversal and Recursive MAFs

MAFs with active loops and active inductors allow the realization of configurations used in narrow and moderated bandwidth applications. In contrast, the MAFs based on transversal and recursive principles

considered by Rauscher [31], Jutzi [32] and other authors have demonstrated an ability to achieve a wider bandwidth up to an octave with excellent selectivity near the band edges.

Recently new configuration called Microwave Channelized Active Filter (MCAF) has been described by Rauscher [33] as a modification of microwave transversal filter resulting in significant improving compactness and selectivity. This filter design approach requires that a considerable amount of RF components both active and passive must be taking into account to control interference among different signal branches in order to get highly selective filtering action. A simple MCAF configuration depicted in Fig.11 is used as an illustrative example to demonstrate its operation. Inner channel consisting of sections of transmission line *e* and active part *b* is needed to form pass-band property of a filter while external channels are added to reject a signal by means of creating proper transmission poles. They consist of sections of transmission lines *f* and *g* working as phase equalizers and attenuators which are required to get phase-amplitude equalizing and active parts *a* and *c* are used for a loss compensation. Sections *d* are quarter wave length matching transformers.

The first step in designing MCAF is to determine its active resonance parts which can have both lumped and distributed structures. For a simplicity of further analysis it is assumed that this part is based on half-wave resonator *e*, coupling reactances *d* and low noise amplifiers *f* to compensate an insertion loss, Fig.12. Assuming the 50 Ohms system impedance, transmission matrices of resonator $A1(\Theta)$, coupling reactances $A2(Z)$, and amplifiers $A3(q)$ can be written as follows:

$$A1(\Theta) := \begin{pmatrix} \cos(\Theta) & i \cdot \sin(\Theta) \cdot 50 \\ i \cdot \frac{\sin(\Theta)}{50} & \cos(\Theta) \end{pmatrix} \quad (6)$$

$$A2(Z) := \begin{pmatrix} 1 & i \cdot Z \\ 0 & 1 \end{pmatrix}$$

$$A3(q) := \begin{pmatrix} q+1 & 1-q \\ 1-q & q+1 \end{pmatrix}$$

where Θ is the electric length of a part *e*, *Z* is the impedance of a coupling element *d*, $q = S_{21} \cdot S_{12}$ depends on characteristics of amplifiers. The resulting transmission matrix A^{res} can be presented in the form:

$$A^{res}(q, Z, \Theta) = A3(q) \cdot A2(Z) \cdot A1(\Theta) \cdot A2(Z) \cdot A3(q) / 4S_{21}^2 \quad (7)$$

Finally, the insertion loss *L* in dB is calculated through S_{21} determined by (7). It should be noted that the term $A3(q)$ affects on changing an insertion loss only as a scalar multiplier.

Now, it is necessary to specify resonators for different MCAF signal branches. For configuration shown in Fig. 11 the resonator connected with the inner channel *b* is designed to operate at a center frequency. Both resonators used within external channels *a* and *c* should be designed to possess their resonance frequencies near desired poles. Fig. 12 illustrates this situation assuming that the center frequency is 10 GHz and poles are ± 0.4 GHz aside. The capacitance coupling 0.02 pF (element *d*), 13 dB low-noise FET amplifier (element *f*), $\Theta = 165^\circ$ (branch *a*) and $\Theta = 180^\circ$ (branch *c*) were supposed. In order to get better selectivity the resonance curves of branches *a* and *c* must be narrower compared to one in branch *b* that may be achieved by a proper choice of the coupling elements.

Phase and amplitude equalizing for signals propagating through inner and external channels is very important part of MCAF design. To obtain phase tuning, lines *f* and *g* with adjusted electrical lengths are used here. For illustrating aims the simple MCAF configuration shown in Fig. 11 has been studied. It is impossible to provide a symmetrical positions of attenuation poles if no measures undertake to get phase equalizing. Fig.13 illustrates

this fact when the electric lengths of sections f and g are the same ($\Theta = 80^\circ$ - curve 1 and $\Theta = 95^\circ$ curve 2). Asymmetrical responses with the only attenuation pole are observed in the both cases. By adjusting these lengths the symmetrical response can be achieved but the attenuation near poles is reduced significantly, Fig. 14 ($\Theta = 87^\circ$, curve 1). The response can be improved when proper phase equalizing is carried out, Fig. 14 ($\Theta = 102^\circ$ for the line f and $\Theta = 72^\circ$ for the line g , see curve 2). Typically, insertion losses of both external channels are different and amplitude equalizing must be done to avoid undesirable response distortion. According to Fig.12 the channel a has about 2.7 dB greater gain compared to the channel c . Hence, the insertion loss of attenuator which is used as an amplitude equalizer should be reduced properly for an equalizing purpose and obtaining quasi symmetrical frequency response. Fig. 15 shows calculated results corresponding to the following specifications of MCAF after amplitude equalizing:

d : impedance - 30.3Ω , electric length - 90° ; e : impedance - 60Ω , electric length - 87° ;
 f : impedance - 45Ω , electric length - 106° ; g : impedance - 45Ω , electric length - 75° ;
 attenuation - 4 dB for the channel c and 6 dB for the channel a .

Proper choice of phase and amplitude relations between different channels has provided significant selectivity improvement although basic resonance circuits had low Q .

8. Conclusion

Development of Microwave Active Filters is one of the promising ways to upgrade the selectivity of the wireless and radar equipment. The paper has presented a comprehensive review of potential facilities providing better performance of MAFs. Integration of passive and active microwave components together with MIC and MMIC technologies has allowed the realization of various filtering devices possessing unique characteristics which are not available from conventional microwave filters. There is no doubt that MAFs will find wide areas of application in new generations of mobile and space communications, radar and some other areas of Microwaves & RF.

9. Acknowledgments

Author would like to thank Prof. Peter A. Matthews for a critical reading and useful discussions during preparing particular sections of the paper manuscript.

10. References

1. Hunter J.C., Chandler S.R., Young D., Kennerly A: "Miniature microwave filters for communication systems", 1996, IEEE Trans., MTT-43, pp.1751-1757.
2. N.Dib, L.Katehi, G.Ponchak, and R.Simons, "Theoretical and Experimental Characterization of Coplanar Waveguide Discontinuities for Filter Applications" *IEEE Transactions on Microwave Theory and Techniques*, Vol.39, No.5, May, 1991, pp. 873-881.
3. R.Kulke, T.Sporkmann, D.Kother, I.Wolff, and P.Pogatzki, Coplanar Elements, Part 1: "Coplanar Elements Support Circuit Design to 67 Ghz", *Microwaves & RF*, Vol.33, no.13,1994, pp103-104,106,108-109,112-114
4. J. Sheinwald, "MMIC Compatible Bandpass Filter Design", *Microwave J.* Vol.37, No. 3, pp. 26, 28, 31, 35-36, 38, 41-2, March 1994.
5. D. Kajfez and P.Guillon, "Dielectric resonators", Vector Fields, 1990.
6. K.Solbach, "The Status of Printed Millimeter-Wave E-Plane Circuits", *IEEE Transactions on Microwave Theory and Techniques*, Vol.31, No.2, February 1983, pp.107-120.
7. B.Yu.Kapilevich and Ye.R.Trubechin, "Waveguide-Dielectric Filtering Structures" (Reference Book), Moscow, Radio & Swjaz, 1990 (in Russian).
8. B. Yu. Kapilevich and Ye. R. Trubechin, "Monolithic Waveguide-Dielectric Microwave Devices", *Radioelectron. Commun. Syst.*, Vol.33, no.10, 1990, pp.10-16.

9. B.Yu.Kapilevich and Ye.R.Trubechin, "Monolithic Dielectric Filters in Integrated Waveguide Technology", *Int. J. Electronics*, Vol.66, no.3, 1989, pp.449-456.
10. K.Shunemann, R.Knochel, G.Begemann, "Components for Microwave Integrated Circuits with Evanescent-Mode Resonators" *IEEE Transactions on Microwave Theory and Techniques*, Vol.25, No.12, December 1977, pp.1026-1032.
11. S.E.Sussman-Fort, "Design Concepts for Microwave GaAs FET Active Filters", *IEEE Transactions on Microwave Theory and Techniques*, Vol.37, No.9, September 1989, pp.1418-1424.
12. N.A.Filinuk, "Active UHF Filters Based on Transistor Immitance Converters", *Radio Eng. Electron Physics*, Vol.28, May 1983, pp.1-15.13. P.Alinikula, R.Kaunisto, and K.Stadius, "Integrating Active Resonators for Wireless Applications", *Microwave J.*, Vol.38, no.1, January 1995, pp.106,109,111-113.
14. W.Schwab and W.Menzel, "A low-Noise Active Bandpass Filter", *IEEE Microwave and Guided Wave Letters*, Vol.3, No.1, January 1992, pp.1-2.
15. Kapilevich B.Yu.: "Microwave active filter in integrated waveguide technology", 1996, *Electronics Letters*, vol. 33, no.19, pp.1789-1790.
16. S.R.Chandler, I.C.Hunter, and J.G.Gardiner, "Active Varactor Tunable Banpass Filter", *IEEE Microwave and Guided Wave Letters*, Vol.3, No.3, March 1993, pp.70-71.
17. X.H.Jiao, P.Guillon, B.Jary, and B. Madrangeas, "Microwave Frequency Agile Active Filters for MIC and MMIC Applications", *IEEE MTT-S Symp. Digest*, 1990, pp.503-506.
18. J. Lin, Chi-Yang Chang, Y.Yamamoto and T.Itoh, "Progress of a Tunable Active Bandpass Filter", *Annales des Telecommunications*, Vol. 47, no. 11-12, Nov.-Dec. 1992, pp.499 - 507.
19. M.Makimoto and M.Sagava, "Varactor Tuned bandpass filters using microstrip-line ring resonators", *IEEE MTT-S Symposium Digest*, 1986, pp.411-414.
20. B.Yu.Kapilevich, Tharek Abd.Rahman, and Kamarruddin Abd.Ghani, "Modeling Microwave Active Filters for Mobile Communication Systems", *Asia-Pacific Microwave Conf.*, 1995, Korea, Vol.2, pp.816 - 819.
21. B.Yu.Kapilevich, Kamaruddin Abd. Ghani, "Microwave Active Filters: strategies of development" *Int. Conf. on Advances in Strategic Technologies, Section: electronics and information technology*, 1995, pp.20-28, Malaysia.
22. C.Y. Chang and T.Itoh, "Microwave Active Filters based on Coupled Negative Resistance Method", *IEEE Transactions on Microwave Theory and Techniques*, Vol.38, No.12, December 1990, pp.1879-1990.
23. M.Matsumura and Y.Konishi, "An Active Microwave Filter with Dielectric Resonator", *IEEE MTT-S Digest*, 1979, pp.323-325.
24. B.Madrangeas, B.Jarry, P.Guillon, J.Larroque, B.Theron, D.Parise, "Three-poles Dielectric Resonators Bandpass Active Filter", *IEEE Proceedings-H*, Vol.139, no.2, Aprill 1992, pp.205-207.
25. --- the same authors--- "Theoretical and Experimental Analysis of Microwave Dielectric Resonators Active Filters", *20th European Microwave Conf. Proc.*, 1990, pp.928-933.
26. F. Delpino, V.Madrangeas, L. Billonnet, B. Jarry, P. Guillon, "Dual-Mode Dielectric-Resonator Microwave Active Filters", *Microwave and Optical Technology Letters*, Vol. 7, no. 7, May 1994, pp. 330 - 332.
27. S.Hara, T.Tokumitsu, and M.Aikawa, "Lossless Broad-Band Monolithic Microwave Active Inductors", *IEEE Transactions on Microwave Theory and Techniques*, Vol.37, No.12, December 1989, pp.1979-1984.
28. U.Karacaoglu, S.Lucyszyn, I.D Robertson, and M.Guglielmi, "GaAs MMIC Active Filters for L-Band Mobile Systems", *IEE Colloquium Digest*, no.062, 1993, pp.7/1-7/5.
29. K.Kobayashi and A.Oki, "A Novel Heterojunction bipolar Transistor VCO Using an Active Tunable Inductance", *IEEE Microwave and Guided Wave Letters*, Vol.4, No.7, July 1993, pp.235-237.
30. H.Suwaki and T.Ohira, "A very Small MMIC Variable Filter Based on a New Active Filter Design Concept", *12th Annual GaAs IC Symp. Digest*, 1990, pp.93-96.
31. C.Rauscher, "Microwave Active Filters Based on Transversal and Recursive Principles", *IEEE Transactions on Microwave Theory and Techniques*, Vol.33, No.12, December 1985, pp.1350-1360.
32. W.Jutzi, "Microwave Bandwidth Active Transversal Filter Concept with MESFET", *IEEE Transactions on Microwave Theory and Techniques*, Vol.19, No.9, September 1971, pp.760-767.
33. C.Rauscher "Microwave Channelized Active Filters - A New Modular Approach to Achieving Compactness and High Selectivity", *IEEE Trans. on Microwave Theory and Techniques*, January, 1996, Vol. 44, no.1, pp. 122 - 132.

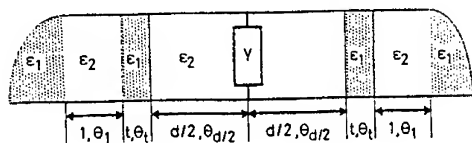


Fig. 1. Evanescent mode MAF configuration.

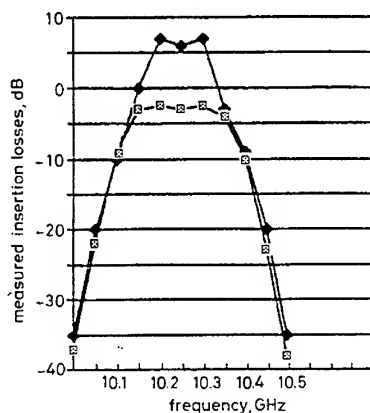


Fig. 2. Measured insertion losses against frequency for passive ($Y = 0$, $-\square-\square-$) and active ($G < 0$, $-\blacksquare-\blacksquare-$) states of the Gunn diode.

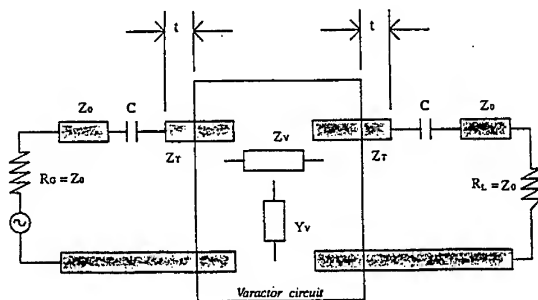
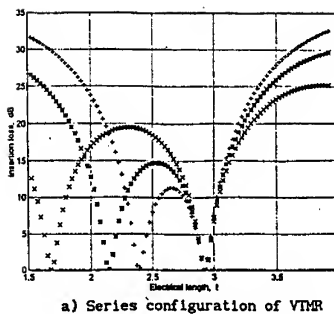
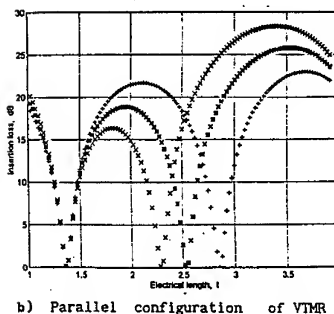


Fig. 3. Configuration of the varactor - tuned microstrip resonator (VTRM).

Fig. 5. Coupling effects for different VTRM configurations. The normalized varactor impedance and admittance are the similar to Fig. 4.

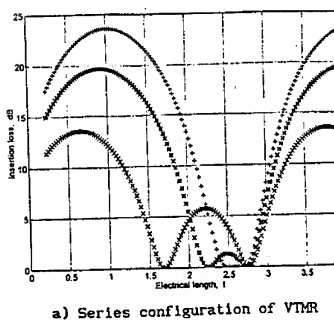


a) Series configuration of VTRM

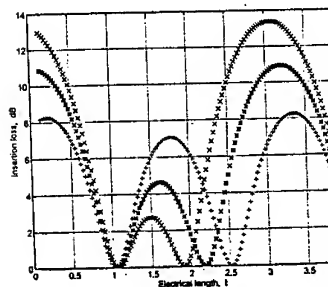


b) Parallel configuration of VTRM

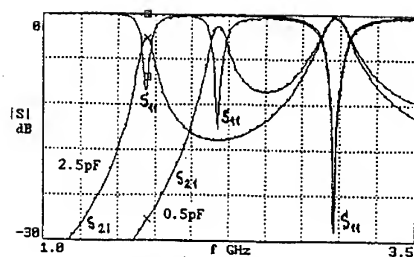
Fig. 4. Calculated insertion losses of VTRM as a function of an electric length l : (a) - normalized impedance is 1 ($\times \times \times$), 3 ($\blacksquare \blacksquare \blacksquare$) and 5 ($+++$); (b) - normalized admittance is 1 ($\times \times \times$), 0.55 ($\blacksquare \blacksquare \blacksquare$) and 0.1 ($+++$).



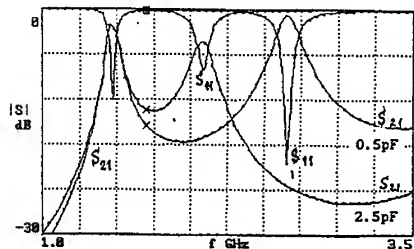
a) Series configuration of VTRM



b) Parallel configuration of VTRM



a) Series configuration of VTRM



b) Parallel configuration of VTRM

Fig. 6. Calculated VTRM's performances for series (a) and parallel (b) configurations.

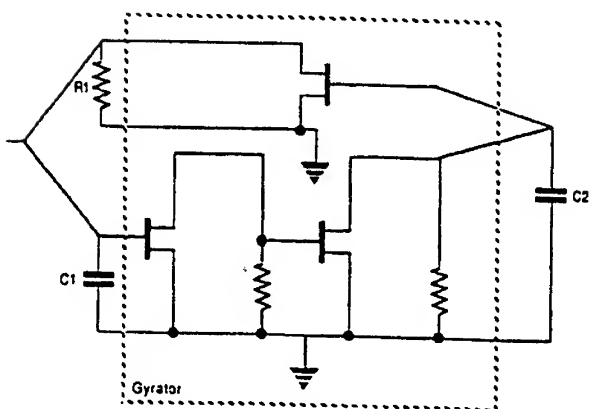


Fig. 7. The two-sections tuned MAF based on VTRM.

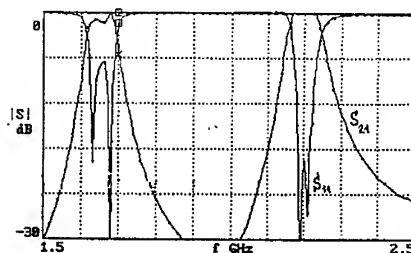


Fig. 8. The performance of the two sections MAF shown in Fig. 7.

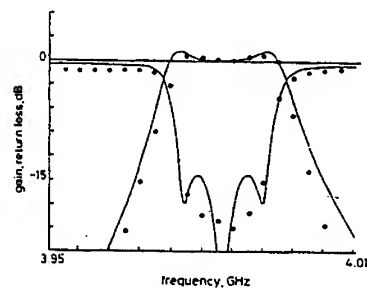
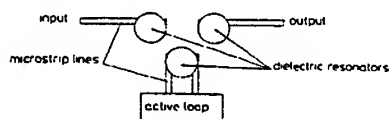
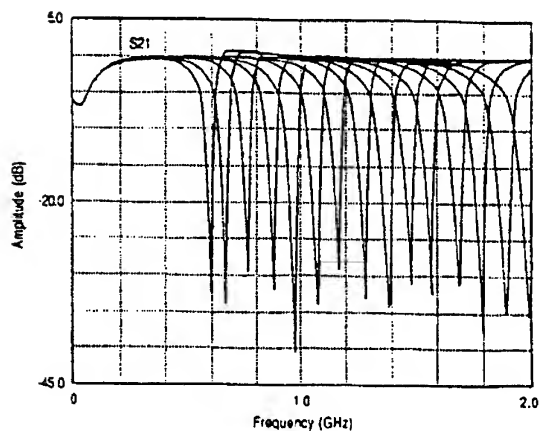


Fig. 9. Schematic and performance of the three-poles MAF with DR [24].

Fig. 10. Schematic circuit of a resonator based on an active inductor and its tuning characteristic by steps of 100 MHz [27].



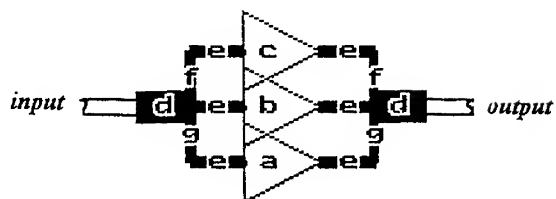


Fig. 11. Schematic diagram of a bandpass MCAF consisting of three branches **a**, **b** and **c** as low noise amplifiers, phase-amplitude equalizing lines **f** and **g**, connecting lines **e**.

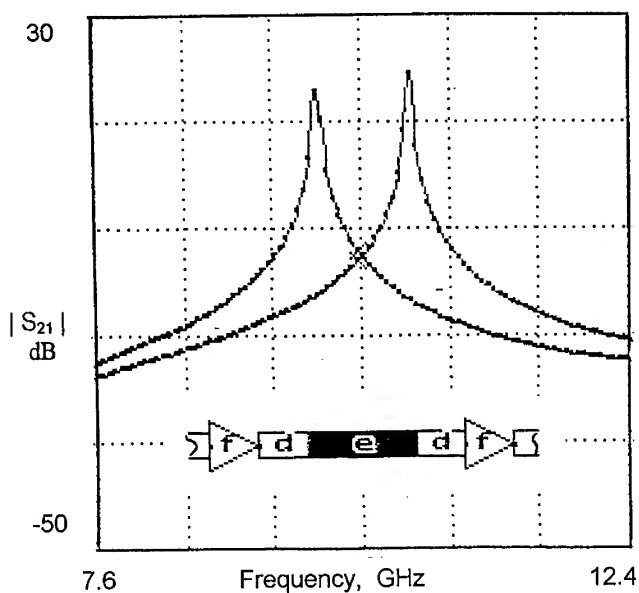


Fig. 12. A basic resonance unit of the MCAF and its frequency response for branches **a** and **c** where **e** is a half wave resonator, **d** is a coupling reactance, **f** is a low noise amplifier.

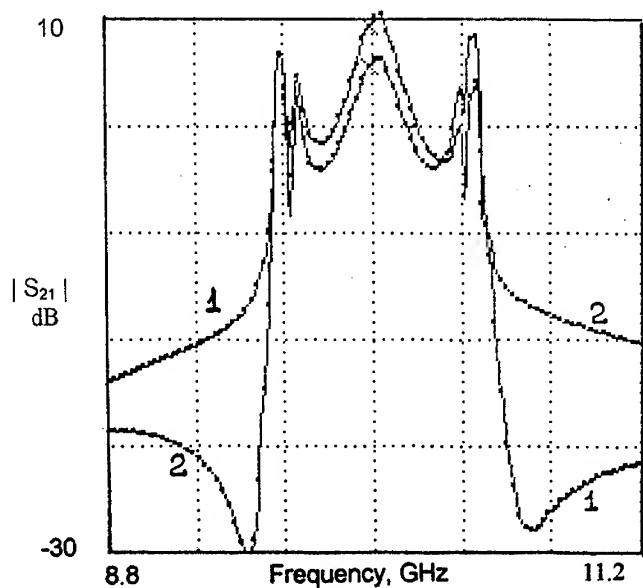


Fig. 13. Performance of the MCAF for the configuration of the Fig. 11 before equalizing procedures.

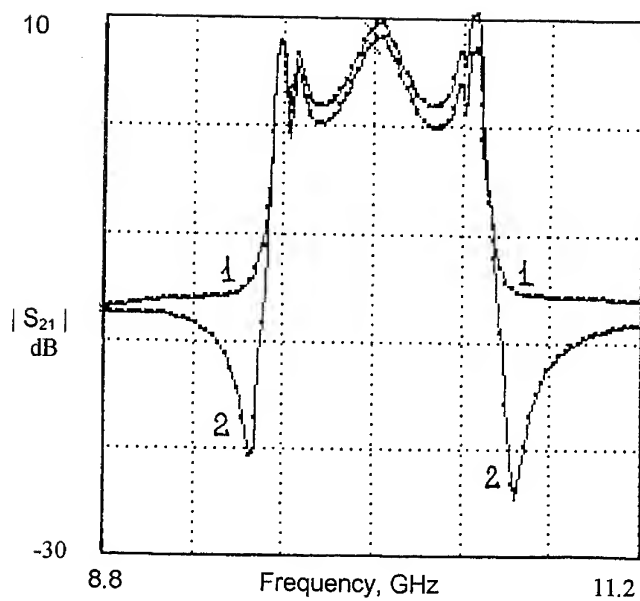


Fig. 14. Performance of the MCAF for the configuration of the Fig. 11 after phase equalizing.

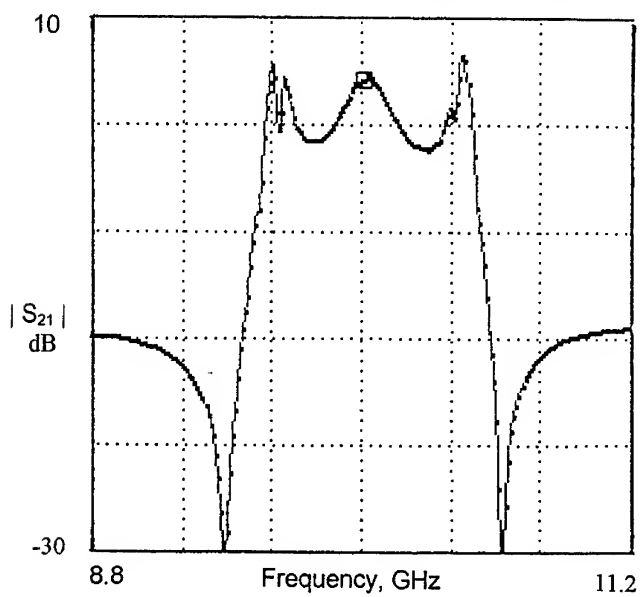


Fig. 15. Performance of the MCAF for the configuration of the Fig. 11 after amplitude equalizing.

MICROWAVE ACTIVE FILTERS FOR WIRELESS APPLICATIONS: SYSTEMS APPROACH

Petteri Alinikula¹ and Risto Kaunisto²

¹Nokia Research Center, P.O. Box 407, FIN-00045 Nokia Group, Finland

²Helsinki University of Technology, IRC/ECDL, Otakaari 5 A, FIN-02150 Espoo, Finland

ABSTRACT

The trends in wireless telecommunication terminals speak in favor of adjustable miniature microwave filters. The most potential integrated high-frequency active filter topologies, the active inductors and the loss compensated passive resonators, can be designed to reach the low microwave region. The dynamic range requirements for the cellular phones have proven to be still too demanding for the reported circuits. However, the less demanding filtering specifications of some applications, e.g., the wireless LANs, might be fulfilled with microwave active filters.

INTRODUCTION: TRENDS IN WIRELESS TERMINALS

Wireless communication systems are facing a new era. The expansion of digital cellular systems continues with an accelerated speed: in Nordic countries the penetration of mobile phones is expected to reach 40% this year. In the near future the voice-based cellular systems are complemented by wireless data communication systems enabling mobile multimedia. The next generation systems, the European UMTS and Japanese FPLMTS, are addressing the mobile multimedia market with adaptive capacity reaching up to 2 Mbit/s. Although these systems are targeted to be global, the trend is toward higher diversity of co-existing systems. As a result, terminals enabling access to several systems are needed. Already now some dual mode products are on the market: in the USA the DAMPS phones and in the urban areas of Europe the GSM/DCS1800 phones. The ultimate target is a world phone that is adaptive to all major systems and frequency bands. The main trends in developing the handheld terminals for the future needs are the multisystem/multiband capability and the continuous miniaturization.

The implementation of multisystem/multiband terminals can have different levels of parallel functions. Typically, the same baseband section is used whereas the RF sections for different systems remain separate. To simplify the RF section many active functions, such as variable-gain amplifiers and mixers, can be designed to cover multiple systems and multiple frequency bands. The passive filters, however, cannot be adjusted and the only feasible solution at the moment is to use selectable filters for each designated frequency band. As a result, the products become bulky and expensive. The alternative architectures for multimode transceivers are shown in Figure 1.

The second key trend for handheld terminals is the continuous drive toward higher miniaturization. The development of the size and component count of handheld digital cellular phones is shown in Figure 2. The significant improvements have been achieved by increasing the level of integration in the phone; currently, all active functions are integrated. In order to go further the main emphasis is on the packaging and interconnection technology. The chip scale packaging has already been applied in some products and the usage is rapidly increasing. Integrating the numerous discrete components and, in particular, the filters addresses a key challenge to the phone manufacturers. Improved transceiver architectures, e.g., the direct conversion, can be applied in some systems to remove the IF filters, but the RF filters are still needed. Currently, the RF filters are based on SAW, ceramic, and dielectric technologies, none of which is expected to offer suitable solutions for future multimode terminals.

High-frequency filter technologies are in a key position in finding implementation solutions for future miniaturized multimode terminals. Microwave active filters would enable the complete integration of the transceivers and offer the required adjustability. The objective of this paper is to analyze the applicability of

the microwave active filter structures for wireless applications, in particular, for cellular phones. The most promising active filter topologies are addressed and the required performance in various radio architectures is discussed.

INTEGRATED MICROWAVE ACTIVE FILTERS

Integrated filters at frequencies 1-2 GHz possess certain technological challenges. High-gain amplifiers needed in most active filter topologies are not available. Passive LC filters can be implemented with on-chip capacitors and inductors, but the Q-values are not acceptable for high selectivity and sufficiently low passband attenuation. Furthermore, the tolerances of integrated passive elements make accurate frequency controlling very difficult.

Several different integrated active filter topologies have been reported for the UHF band, e.g., transconductor-C and frequency selective feedback filters. The comparison of the topologies is outside the scope of this paper. Instead, the discussion is limited to two topologies that have shown to be applicable to 1-2 GHz frequencies: the gyrator-based LC filters and the passive LC filters with active loss compensation. Both of the topologies are suitable for integration.

The principle of the gyrator-based active inductors has been known for a long time but it wasn't until the early 1990's when the availability of the high-frequency IC technologies boosted new interest. Several new circuit topologies were reported with capabilities up to the GHz-region. In Figure 3 two gyrator-based active inductor circuits are shown: an early implementation with GaAs MESFET technology [1] and a modified circuit more suitable for low-voltage operation and less sensitive to parasitics [2].

Inherently the Q-values of the active inductor circuits are relatively low, but techniques for tuning the Q-value have been developed, e.g., in Reference [2]. In the Q-enhancing techniques the collapse of the Q-value is avoided by compensating the phase error occurring in a practical gyrator. Active resonators built using active inductors and passive capacitors can be used for implementing highly selective tunable filters. In Figure 4 a three-resonator HBT active filter is shown [3]. The filter is probably one of the most advanced circuits that have been implemented with this technique: the center frequency is tunable from 2.05 GHz up to 2.37 GHz as shown in Figure 5. The dynamic range characteristics are poor: the noise figure is 30 dB and the corresponding 1-dB-gain compression point is -41 dBm. The dynamic range difficulties are typical to the active inductor-based filters. The simple noise analysis reveals that the noise of an active inductor-based resonator is many times that of a lossy passive resonator with the same Q-value [4], [5]. With typical component values the noise figure degradation is 10-20 dB.

Microwave active resonator filters are usually constructed from multiple active resonators with loose capacitive coupling. This topology, whilst facilitating the design, inherently involves excessive voltage swings across the resonators and limits the upper end of the dynamic range. High system impedance levels will suppress the voltage peaking inside the filter but unavoidably increase the overall voltage level.

The dynamic range can be improved with an alternative filter topology where negative resistors are used for compensating the losses of passive resonators. The schematic diagram of a passive LC resonator with balanced loss compensation is shown in Figure 6 [6]. The simple noise analysis shows that the loss-compensated passive resonator is superior to active inductors with respect to the noise characteristics [5]. The balanced negative resistance circuit is insensitive to process variations and the resistance value can be tuned using the current source. Furthermore, the current consumption is much smaller than with active inductors, because high transconductance values are not needed for the desired functionality. Since the center frequency is mainly defined by the passive structures, the frequency tuning is difficult. Varactor tuning is applicable but then the low Q-value and the parasitics of the varactor deteriorate the performance. In Reference [6] a 2 GHz loss-compensated GaAs MMIC passive resonator was reported. The 1-dB-gain compression point was measured to be 9.5 dBm and the simulated noise figure was 12 dB. A remarkable improvement in the dynamic range compared to the active inductor-based filter can be noticed.

MICROWAVE ACTIVE FILTERS FOR CELLULAR PHONES

The analog section of a typical heterodyne transceiver for a cellular phone includes several RF and IF filters. The relative bandwidth of a signal channel is very small: only $200 \text{ kHz}/900 \text{ MHz} = 0.2\%$ for the GSM. As a result, the channel selection filtering is not possible at RF. Instead, the main function of the RF filters is to relax the dynamic range requirements of the following stages. Then, the dynamic range of the filter itself becomes a critical parameter. In this context five applications are considered: 1. Frequency-division-duplex (FDD) heterodyne receiver filters, 2. Time-division-duplex (TDD) heterodyne receiver filters, 3. Image-rejection filters, 4. TDD direct-conversion receiver filters, and 5. direct-modulation transmitter filters

1. In FDD systems the receiver and transmitter are both on at the same time. As a result, the first filter of the receiver, the duplexer, must be able to attenuate the transmitted signal having a power level of about 30 dBm. This corresponds to unacceptable stopband voltage swings for the active filter even with very low impedance level. The filter itself will compress and fail to function.

2. In TDD systems the transmitter is turned off when receiving. Then, the maximum signal strength is caused by the out-of-the-band blocking signals that can have a maximum power level of approximately 0 dBm in digital cellular systems. The out-of-the-band blocking signals need to be attenuated about 20 dB down to the level of the in-band blocking signals. In applying active filters for TDD duplexers the main issue is the noise. The noise specifications of the systems are quite demanding: the minimum detectable input signal is -102 dBm in GSM with a carrier-to-noise ratio requirement of about 9 dB. As a result the maximum system noise figure F_S of the receiver becomes

$$F_S < -102 + 174 - 10 \log(200 \text{ kHz}) - 9 = 10 \text{ dB} \quad (1)$$

The duplexers typically have a passband attenuation L_F of 3 dB and the corresponding maximum receiver noise figure F_{RX} de-embedded from the duplexer becomes

$$F_S > F_F + L_F(F_{RX} - 1) \Leftrightarrow F_{RX} < \frac{F_S - F_F}{L_F} + 1 \quad (2)$$

With passive filters F_F equals L_F and then $F_{RX} < F_S/L_F = 7 \text{ dB}$. While active filters can even have a slight gain ($L_F < 1$), the noise figure F_F is considerably higher resulting in an unrealistically low F_{RX} .

3. The second RF filter in heterodyne receivers is used mainly for the image rejection. Typically, the image band rejection requirements vary between 60-80 dB in different systems. The image filtering is distributed between the duplexer and the second RF filter, which might include extra poles for image trapping. If an image-rejection mixer with a 30 dB rejection is utilized and the duplexer provides an additional rejection of 15 dB, a reasonable 15-35 dB rejection is needed from the filter. The overall dynamic range of the signal is, however, too large for active filters: typically $-90 \dots -5 \text{ dBm}$ in digital cellular phones.

4. The direct-conversion transceiver is a simplified concept in which the modulation and demodulation are carried out directly at the carrier frequency. From filtering point of view, the direct conversion principle is desirable because neither IF nor image band filters are needed. The dynamic range requirements for the first filter in a TDD direct-conversion receiver are essentially the same as for the heterodyne receiver.

5. In the transmitter chain the last filter is used for cleaning up the spectrum before the transmission. The output filter cannot be active, because the transmitted power levels in cellular systems are high. The filter between the IQ-modulator and the power amplifier is used for filtering the modulator output signal from the leaking spurious frequencies and for attenuating the noise floor outside the transmit band. Now, the most

important specification of the filter is the noise contribution in the stopband. Unfortunately, with the microwave active filters the stopband noise figure easily exceeds the stopband rejection by 10-20 dB. Consequently, these filters cannot be applied to noise floor attenuation in the transmitter chain.

The only RF block of the mobile phone in which the dynamic range is quite limited is the synthesizer. In generating the LO signal in a direct modulator a problem will occur if the high-power output signal couples back to the oscillator chain. The coupling can be avoided if the LO signal is generated inside the modulator from two reference signals. Then, however, the generated LO signal has to be filtered prior to the mixers. If the filtering is carried out off-chip, the output signal might leak again through the package pins. Thus, on-chip LO filtering could provide improved performance and be the first application for microwave active filters in cellular phones. Still, the high noise floor caused by the active filter can couple to the signal path and degrade the noise of the modulator. The system architecture of the modulator with on-chip filtering is illustrated in Figure 7.

The RF specifications of the wireless LAN applications, e.g., for the 2.4 GHz ISM band, are quite different. CDMA FDD systems and TDMA TDD systems are widely used. The dynamic range requirement is more relaxed, e.g., 60 dB, and the blocking signal levels are relatively low. In heterodyne receivers, the image band problem is not as severe as with cellular systems since the signal levels in the image band are very low. For the complete transmitter chain a single passive filter after the output stage should be sufficient. There is clearly not as much need for filtering in wireless LANs as in cellular terminals and the microwave active filters could find some applications here. Still, it seems evident that the main RF filter would be a passive band selection filter.

If the performance of active filters were sufficient, there would be an additional inconvenience: the filter would require alternatively a closed-loop control or a calibration procedure for the center frequency control resulting in an increased component count and total cost.

CONCLUSIONS

The trends in wireless telecommunications indicate that multisystem/multiband terminals are becoming popular in the coming years. Furthermore, the miniaturization of all wireless products will continue. Tunable microwave active filters would provide an attractive solution addressing the needs of the future wireless terminals. The filtering specifications of the cellular terminals are, however, extremely demanding. The gap between the specifications and the performance of the reported integrated microwave active filters is still wide. In particular, the dynamic range capabilities of even the most potential active filter circuits are not sufficient for signal filtering in cellular terminals. In the synthesizer path and in wireless LAN applications the filter specifications are more relaxed; consequently, the microwave active filters might become feasible.

ACKNOWLEDGMENT

The authors would like to thank Hans-Otto Scheck from Nokia Research Center for helpful comments.

LIST OF REFERENCES

1. S. Hara, T. Tokumitsu, M. Aikawa; Broad-Band Monolithic Microwave Active Inductor and Its Application to Miniaturized Wide-Band Amplifiers; 1988; IEEE Trans. Microwave Theory Tech.: Vol. MTT-36; pp. 1920-1924.
2. R. Kaunisto, P. Alinikula, K. Stadius; Q-Enhancing Technique for High-Speed Active Inductors; 1994; in Proc. IEEE ISCAS; 735-738.
3. R. Kaunisto, P. Alinikula, K. Stadius, V. Porra; A Low-Power HBT MMIC Filter Based on Tunable Active Inductors; 1997; IEEE Microwave Guided Wave Lett.: accepted for publication.
4. A. Abidi; Noise in Active Resonators and the Available Dynamic Range; 1992; IEEE Trans. Circ. Sys.-I: Vol. CAS-39; pp. 296-299.
5. R. Kaunisto; Monolithic Radio Frequency Active Filters; 1997; Helsinki Univ. of Technology Licentiate Thesis.
6. R. Kaunisto, D. Webster, D. Haigh; Improved MMIC Active Filters Based on Passive LC Resonators with Active Negative Resistance Circuits; 1996; in IEE Colloquium on Advanced Signal Processing for Microwave Applications, London

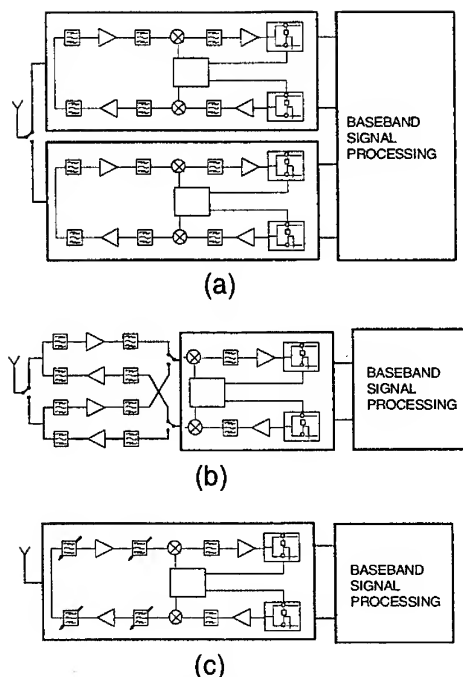


Figure 1. Multimode transceiver architectures: (a) parallel RF sections, (b) joint RF sections, (c) common RF with adjustable filters.

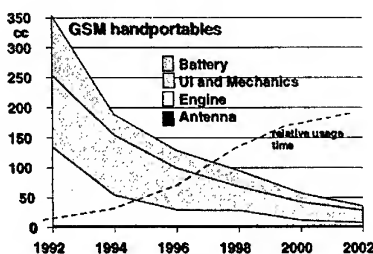


Figure 2. Development of the size and component count of the handheld terminals.

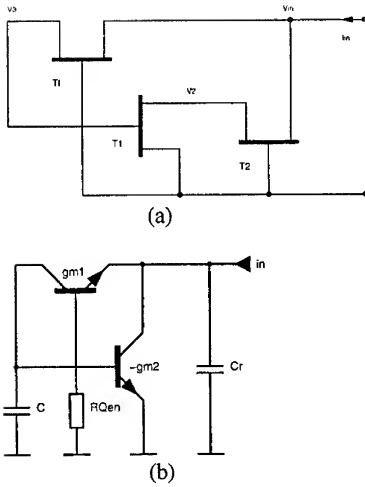


Figure 3. Gyrator-based active inductors: (a) GaAs MESFET implementation by Hara et al [1], (b) low-voltage modification by Kaunisto et al [2].

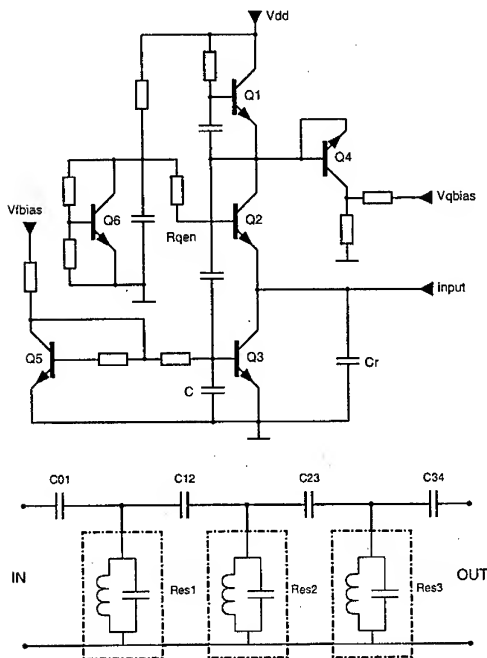


Figure 4. HBT filter based on tunable active inductors: schematic diagram of the applied active resonator and top-level schematic of the filter [3].

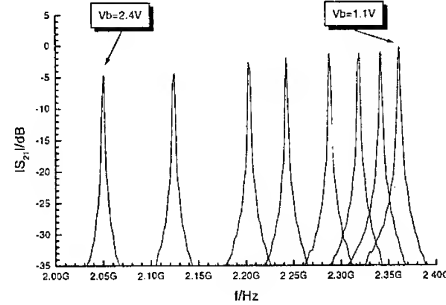


Figure 5. Tunable frequency response of the HBT filter [3].

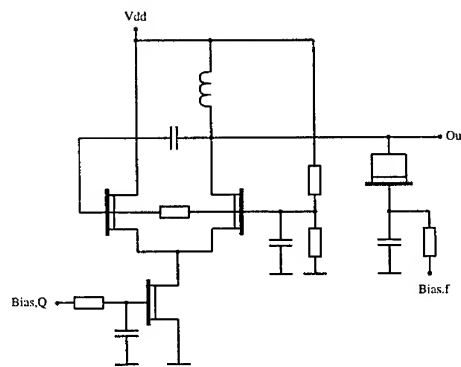


Figure 6. Passive LC resonator with negative resistance loss compensation [6].

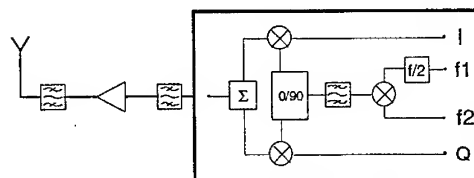


Figure 7. Direct modulator with on-chip LO generation.

A new simple extraction method for higher order components of channel current in GaAs MESFET

o.**Tae Moon Roh, *Youngsik Kim, ***Youngsuk Suh and *Bumman Kim

** Department of Electronic and Electrical Engineering
and Microwave Application Research Center, Pohang University of Science and Technology

** Samsung Electronics Co., LTD.

*** Electrical and Electronic Engineering Yeungnam University

Abstract—A simple new extraction method of the higher order channel current in GaAs MESFET has been developed. Low frequency (~ 60 MHz) two-tone signals are employed to measure the harmonic components. The measured data are fitted to the Volterra series analysis for extracting of Taylor series coefficients of the nonlinear channel current. This proposed parameter extraction procedure is simple and straightforward. The extracted current model is utilized successfully for intermodulation analysis.

I. INTRODUCTION

Volterra series analysis has been the common technique used for the prediction of distortion properties. This analysis is superior, in terms of conversion efficiency in numerical simulation, to the harmonic balance technique. Volterra series analysis is based on the Taylor series expansion of the channel current which is a major nonlinear component of MESFETs. Its form is given by Equation 1. In this equation, the higher order terms of channel current are dependent on the bias voltages.

$$\begin{aligned} I_{ds}(v_{gs}, v_{ds}) = & G_m v_{gs} + G_d v_{ds} + G_{m2} v_{gs}^2 G_{md} v_{gs} v_{ds} \\ & + G_{d2} v_{ds}^2 + G_{m3} v_{gs}^3 + G_{m2d} v_{gs}^2 v_{ds} \\ & + G_{md2} v_{gs} v_{ds}^2 + G_{d3} v_{ds}^3 \\ & + \dots \end{aligned} \quad (1)$$

Many works for the high order derivatives of $I_{ds}(v_{gs}, v_{ds})$ in Equation 1 have been reported. A parameter set for Equation 1 had been adjusted by a least-square fit to the measured S-parameters at several bias points [1] or to microwave two-tone test data [2]. These methods are inaccurate due to the measurement error and insufficient data in the fitting process. Recently, more advanced methods based on the low frequency harmonic measurements were proposed [3], [4]. These methods have merits that the

measurement errors are small and the coefficient in Equation 1 can be analytically extracted. However, Maas method [3] can not represent the cross terms of I_{ds} , i.e., a transconductance variation with v_{ds} and an output conductance variation with v_{gs} . Pedro [4] reported on the more accurate harmonic component measurement technique. But Pedro method is very complex, because the measurement system should have a high power source at the drain side and a very high performance diplexer to reject the leakage of harmonics generated from the large signal source. That is: this method has difficulties on the measurement of the intermodulation power from the drain side.

A new simple measurement system for the higher order channel current terms has been developed. This system shown in Figure 1 is composed of low frequency two-tone signals, power combiner, filter at the input port, and spectrum analyzer at the output port. In the equivalent circuit shown in Figure 2, $V_{s1}(\omega_1)$ and $V_{s2}(\omega_2)$ are low frequency two-tone signals around 60 MHz. Using the system, all harmonic output power terms can be measured. From the terms, the coefficients in Equation 1 can be accurately extracted.

II. EXTRACTION METHODOLOGY

Volterra series analysis [5] is used to calculate the harmonic distorted output power. The MESFET equivalent circuit is shown at Figure 2. At very low frequencies (~ 60 MHz), the C_{gs} is basically open circuit and its nonlinearity is not important. Therefore, the major nonlinear component is the drain-source channel current and the harmonic distorted output power can be expressed as a function of Taylor coefficients of the channel current in Equation 1. Comparing the calculated and measured harmonic output power; these Taylor coefficients are extracted.

The channel current is modeled as two dimensional Taylor series of v_{gs} and v_{ds} . Since all capacitance(

C_{gs} , C_{ds} and C_{dg}) of the equivalent circuit can be treated as open circuit in this low frequencies, the circuit is very simplified. From the simplified circuit, the relationships between (v_{gs} , v_{ds}) and V_s , I_n are given by

$$\begin{aligned} v_{gs} &= V_{s1} + V_{s2} + K_{gn}I_n \\ v_{ds} &= K_{ds}(\omega_1)V_{s1} + K_{ds}(\omega_2)V_{s2} + K_{dn}I_n \end{aligned} \quad (2)$$

$$\begin{aligned} K_{ds}(\omega) &= \frac{v_{ds}(\omega)}{V_s(\omega)}|_{I_n=0} = -G_m(R_s + Z_L(\omega)) \\ K_{gn}(\omega) &= \frac{v_{gs}(\omega)}{I_n(\omega)}|_{V_s=0} = -\frac{R_s}{1 + R_s G_m} \\ K_{dn}(\omega) &= \frac{v_{ds}(\omega)}{I_n(\omega)}|_{V_s=0} = -\frac{R_s + Z_L(\omega)}{1 + R_s G_m} \end{aligned} \quad (3)$$

In this equation, K_{ds} is linear voltage gain at C_{ds} terminals, and K_{gn} and K_{dn} are the transimpedance between I_{ds} and terminal voltages. I_n is the nonlinear current component, which is generated by the device nonlinearities.

From the Equation 2, the second order harmonic components $I_n(\omega_2 - \omega_1)$, $I_n(2\omega_1)$ and $I_n(2\omega_2)$ can be obtained as

$$\begin{aligned} I_n(\omega_2 - \omega_1) &= [G_{m2} + (K_{ds}(\omega_1)^* + K_{ds}(\omega_2))G_{md} \\ &\quad + K_{ds}(\omega_1)^* K_{ds}(\omega_2)G_{d2}] \frac{1}{2} V_{s1}^* V_{s2} \end{aligned} \quad (4)$$

$$\begin{aligned} I_n(2\omega_1) &= [G_{m2} + K_{ds}(\omega_1)G_{md} \\ &\quad + K_{ds}(\omega_1)^2 G_{d2}] \frac{1}{2} V_{s1}^2 \end{aligned} \quad (5)$$

$$\begin{aligned} I_n(\omega_1 + \omega_2) &= [G_{m2} + (K_{ds}(\omega_1) + K_{ds}(\omega_2))G_{md} \\ &\quad + K_{ds}(\omega_1)K_{ds}(\omega_2)G_{d2}] \\ &\quad \cdot \frac{1}{2} V_{s1} V_{s2} \end{aligned} \quad (6)$$

In the same way, the third order harmonic components $I_n(2\omega_2 - \omega_1)$, $I_n(3\omega_1)$, $I_n(2\omega_1 + \omega_2)$ and $I_n(3\omega_2)$ can be obtain. $I_n(3\omega_1)$ is given by

$$\begin{aligned} I_n(3\omega_1) &= \frac{1}{2} \{ 2G_{m2}K_{gn}(2\omega_1)I_n(2\omega_1)V_{s1} \\ &\quad + G_{md}[K_{gn}(2\omega_1)I_n(2\omega_1)K_{ds}(\omega_1)V_{s1} \\ &\quad + V_{s1}K_{dn}(2\omega_1)I_n(2\omega_1)] \\ &\quad + 2G_{d2}K_{dn}(2\omega_1)I_n(2\omega_1)K_{ds}(\omega_1)V_{s1} \} \\ &\quad + \{ G_{m3} + K_{ds}(\omega_1)G_{m2d} + K_{ds}(\omega_1)^2 G_{md2} \\ &\quad + K_{ds}(\omega_1)^3 G_{d3} \} \frac{1}{4} (V_{s1}^3) \end{aligned} \quad (7)$$

In Equation 7, the first term is generated by the second order nonlinear current and the later term from third order nonlinearity.

From the calculated harmonic currents components, the harmonic power is calculated from the load impedance ($Z_L(\omega)$) at each frequencies:

$$P_{no}(\omega) = \frac{1}{2} \text{Re} \left[Z_L(\omega) \left| \frac{I_n(\omega)}{1 + R_s G_m} \right|^2 \right] \quad (8)$$

From the measured and calculated the harmonic output power at each harmonic frequencies ($\omega_2 - \omega_1$, $2\omega_1$, $\omega_1 + \omega_2$, $2\omega_2 - \omega_1$, $3\omega_1$, $2\omega_1 + \omega_2$ and $3\omega_2$), the channel current Taylor series coefficients given at Equation 1 can be found.

III. RESULT

In this experiment, the general two-tone test shown at Figure 1 are performed to measure the harmonic output power terms. The source signals are $\omega_1 = 55$ MHz, $\omega_2 = 65$ MHz and $P_{in} = -13$ dBm. In this test, OKI KGF-1284 MESFET is used at the bias point $V_{ds} = 3.5$ V. To reduce the measurement system error, the harmonic power ratio with respect to the first order output power, instead of absolute harmonic powers, are used in extracting the coefficients. Measured and calculated harmonic powers are compared to extract the Taylor coefficients. The extracted second and third order harmonic channel current coefficients in Equation 1 are shown in Figure 3 - 5. With this extracted channel current coefficients and nonlinear capacitance model extracted from the measured bias dependent S-parameters, a Volterra series model for OKI KGF-1284 GaAs MESFET has been constructed. In order to verify this model, the two-tone test was carried out using automatic tuner system at 1.75 GHz. The simulated and measured results are shown in Figure 6. The simulation results predict very accurately the nonlinear behavior of MESFET.

IV. CONCLUSION

In this paper, we have proposed a very simple and straightforward method to measure higher order Taylor series coefficients of the channel current of GaAs MESFET. The low frequency harmonic measurement are performed using the general two tone signal test with the OKI-KGF1284. The MESFET model are constructed and the extracted model is verified by comparing the two tone power performance.

REFERENCES

- [1] Rodney S. Tucker, "Third-Order Intermodulation Distortion and Gain Compression in GaAs FET's." *IEEE Trans. Microwave Theory Tech.*, vol. MTT-27 pp. 400 - 408, May 1979.

- [2] Robert A. Minasian. "Intermodulation Distortion Analysis of MESFET Amplifiers Using the Volterra Series Representation." *IEEE Trans. Microwave Theory Tech.*, vol. MTT-28 pp. 1 - 8, Jan. 1980.
- [3] S. A. Maas and D. Neilson. "Modeling GaAs MESFET's for intermodulation distortion analysis." *Microwave Journal*, vol. 34, pp. 295 - 300, May 1991.
- [4] J. C. Pedro and J. Perez, "Accurate Simulation of GaAs MESFET's Intermodulation Distortion Using a New Drain-Source Current Model." *IEEE Trans. Microwave Theory Tech.*, vol. MTT-42 pp. 25 - 33, Jan. 1994.
- [5] S. A. Maas. "Nonlinear Microwave Circuits.", Buttlar, WI: Artech House. 1988.
- [6] G. Dambrine, A. Cappy, F. Helicore, and E. Playez. "A new method for determining the FET small-signal equivalent circuit," *IEEE Trans. Microwave Theory Tech.*, vol. MTT-36 pp. 1151-1159, July 1988.

Figure Captions

Figure 1. New measurement setup for output harmonic power

Figure 2. MESFET equivalent circuit for nonlinear analysis

Figure 3. Extracted G_m (\blacklozenge), G_{m2} (\blacktriangle) and G_{m3} (\square)

Figure 4. Extracted G_d (\blacklozenge), G_{md} (\blacktriangle) and G_{m2d} (\square)

Figure 5. Extracted G_{d2} (\blacklozenge), G_{md2} (\blacktriangle) and G_{d3} (\square)

Figure 6. Comparison of simulated (lines) and measured (points) results of two-tone test

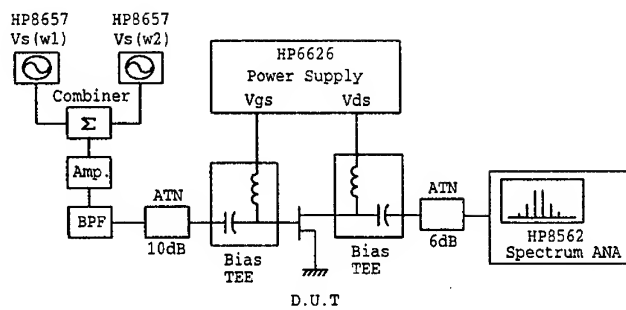


Figure 1. Measurement setup for output harmonic powers

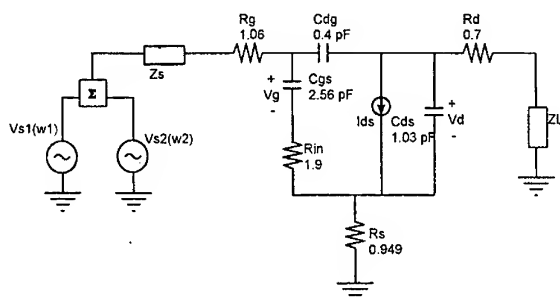


Figure 2. Equivalent circuit used for nonlinear analysis

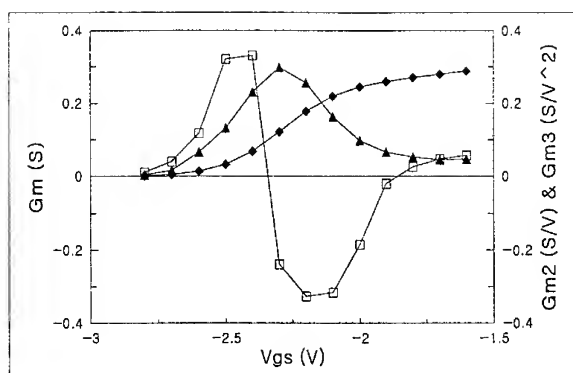


Figure 3. Extracted G_m (◆), G_{m2} (▲) and G_{m3} (□)

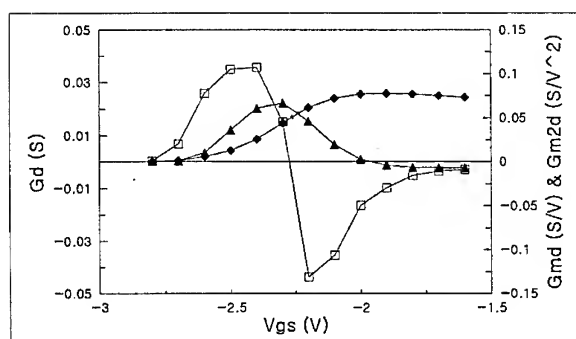


Figure 4. Extracted G_d (◆), G_{md} (▲) and G_{m2d} (□)

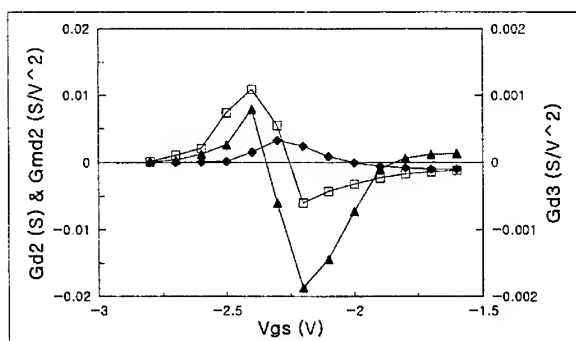


Figure 5. Extracted G_{d2} (\blacklozenge), G_{m2d} (\blacktriangle), and G_{d3} (\square)

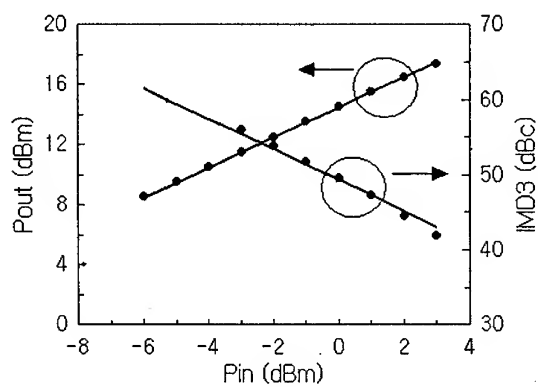


Figure 6. Comparison of simulated (lines) and measured (points) results of two-tone test

A Finite-Memory Nonlinear Model for microwave electron devices

Fabio Filicori

DEIS - Dipartimento di Elettronica, Informatica e Sistemistica, Università di Bologna,
Viale Risorgimento 2 - 40136 Bologna, Italy

Giorgio Vannini, Alberto Santarelli

DEIS - Università di Bologna and CSITE Research Center of the Italian National Research Council,
Viale Risorgimento 2 - 40136 Bologna, Italy

ABSTRACT

A technology-independent, mathematical approach is proposed for the look-up-table based nonlinear modeling of electron devices. The model allows for accurate large-signal performance prediction at high operating frequencies, even in the presence of important parasitic and low-frequency dispersive effects. All the nonlinear functions which characterise this black-box model are directly related to conventional measurements which can be carried out with automatic instrumentation. Preliminary experimental results are presented which confirm the validity of the approach.

INTRODUCTION

A number of mathematical approaches [1..7] has been recently proposed for the look-up-table based modelling of electron devices under nonlinear operating conditions. The basic aim of these methods is that of providing accurate large-signal performance prediction directly in terms of commonly available experimental data (i.e., DC characteristics and bias dependent small-signal AC measurements), without the need for technology-dependent analytical functions to describe the nonlinear device characteristics. These approaches should also provide a reliable, unambiguous and technology-independent predictive link between conventional measurements and CAD tools for circuit analysis and design. More precisely, possible uncertainties and non-uniqueness problems, arising in conventional parameter extraction procedures based on numerical optimisation techniques, should be avoided.

The Nonlinear Integral Model (NIM) proposed in [1,2] meets the above requirements, since it is directly derived, without any constraint on the physical device structure, by truncation of a Volterra-like integral series under the hypothesis of a "short duration" of nonlinear memory effects in voltage-controlled electron devices. Moreover, all the nonlinear functions which characterise this mathematical model are directly related to DC characteristics and bias/frequency dependent small-signal admittance parameters. This allows for easy, closed-form identification of the model, without the need for numerical optimisation procedures (with possible local minima problems) or potentially ambiguous computation of the nonlinear characteristics through numerical integration of differential parameters.

The validity of the Nonlinear Integral approach (i.e., the validity of the short-term memory hypothesis on the device behaviour) has been verified [1..4], with good results, by considering both accurate two-dimensional numerical device simulations and actual measurements on devices not affected by strong parasitics. However when, especially at very high operating frequencies, parasitic phenomena strongly affect the device behaviour, the dynamic response becomes much "slower" (w.r.t. the "intrinsic" device) so that the short-term nonlinear memory hypothesis may be not satisfied. Parasitic de-embedding does not always represent a sufficient solution to this problem, owing to uncertainties in parasitic identification procedures. In such conditions, when strongly nonlinear operation has to be considered, the errors of the NIM may become quite large. To overcome such a limitation, mainly arising from limited accuracy in parasitic modeling, a "Finite-Memory nonlinear Model" (FMM), following the same "philosophy" of the NIM but with important new concepts, is proposed.

In this new approach, the short duration of nonlinear memory effects is not only an "hypothesis" on device behaviour, but an "intrinsic feature" of the model, where a limitation on memory duration is forced by introducing a finite-time window function with sufficiently short width T_M . In this way, a family of convolution-based models is obtained where a single parameter T_M (i.e., the finite duration of memory) identifies a particular one of different models. For $T_M \rightarrow \infty$ the new FMM coincides with the NIM proposed in [1,2]. For $T_M \rightarrow 0$, instead, the FMM practically coincides with conventional quasi-static models where the currents are represented as the sum of static conductive terms and displacement ones defined as time derivatives of quasi-static charges.

In practice, by choosing a suitably small, yet finite, value of T_M , a non quasi-static model is obtained which can provide more accurate and more "robust" (w.r.t. measurement errors) results than the extreme cases mentioned above.

In the following, after introducing the FMM model and the associated identification procedures, considering also important parasitics and dispersive phenomena, some preliminary experimental results are presented.

THE FINITE-CONVOLUTION NONLINEAR MODEL

For simplicity only the modelling of a single-port electron device will be considered in this section. The model, however, can be directly extended to the case of multiport electron devices as shown in another section.

The time-domain current/voltage relationship of a single-port electron device can be expressed in the following form:

$$i(t) = \Psi \left[\left. v(t - \tau) \right|_{\tau=0}^{+\infty} \right] \quad (1)$$

where $\Psi[\cdot]$ is a suitable nonlinear functional or "line-function", according to the symbolism introduced by Volterra [8,9], which indicates the nonlinear dependence of the electron device current i at the generic instant t on the applied voltage $v(t - \tau)$ in a time-interval $0 \leq \tau \leq +\infty$.

By introducing the "dynamic voltage deviations":

$$e(t, \tau) \doteq v(t - \tau) - v(t) \quad (2)$$

which represent the difference between "past" values $v(t - \tau)$ of the applied voltage with respect to the present value $v(t)$, eqn. (1) can be rewritten as:

$$i(t) = \Psi \left[[v(t) + e(t, \tau)] \right]_{\tau=0}^{+\infty} \quad (3)$$

It must be emphasised that the above equation is a very general description of the nonlinear dynamic behaviour of an electron device, since (3) has been derived without any simplifying assumption. However, identification of a description like (3) is practically not feasible due to its great generality and complexity.

Usually, in an electron device, the memory effects have a practically finite, short duration. This important feature can be exploited to derive a simplified, practically usable electron device model. In particular, by limiting the functional dependence in eqn. (3) to a practically finite time T_M , we can introduce the "finite-memory-time model":

$$i(t) = \Psi \left[[v(t) + e(t, \tau)] \right]_{\tau=0}^{T_M} + \Delta i_M \quad (4)$$

where Δi_M represents the "memory truncation error"; clearly, $\lim_{T_M \rightarrow \infty} \Delta i_M = 0$.

The time-domain truncation of the memory effects can be more conveniently represented by introducing a rectangular time-windowing function $w(T_M, \tau)$ defined as follows:

$$w(T_M, \tau) = \begin{cases} 1 & \text{for } |\tau| \leq T_M \\ 0 & \text{otherwise} \end{cases} \quad (5)$$

By using the time-windowing function $w(T_M, \tau)$, we can rewrite eqn. (4) in the form:

$$i(t) = \Psi \left[[v(t) + w(T_M, \tau)e(t, \tau)] \right]_{\tau=0}^{+\infty} + \Delta i_M \quad (6)$$

The finite-memory-time model defined by the first term in the right hand of (6) is accurate enough when the memory truncation error Δi_M is negligible.

To allow for practically feasible model identification, further simplifications are necessary. The still high complexity of (6) can be substantially reduced under the hypothesis of a short-duration of the memory effects (i.e., small T_M). In fact, under such conditions, the dynamic deviations $e(t, \tau)$ can be small even in the presence of large signals $v(t - \tau)$. In particular, it can be shown [9] that, for a given signal v with fundamental frequency f_1 , the peak-to-peak amplitude of the dynamic deviations has an upper limit:

$$|e|_{max} \leq \min\{\rho T_M f_1 V_{pp}, V_{pp}\} \quad (7)$$

where V_{pp} is the peak-to-peak voltage amplitude and ρ is a derivative shape factor:

$$\rho \doteq \frac{\left| \frac{dv(t - \tau)}{d\tau} \right|_{max}}{f_1 V_{pp}} \quad (8)$$

which characterises the voltage waveform shape and is independent on its amplitude and frequency. For instance, for a sinusoidal voltage waveform $\rho = \pi$. Clearly, for a given shape factor ρ , the term $|e|_{max}$ can be small even in the presence of a large peak-to-peak signal amplitude V_{pp} , provided that $T_M \ll \frac{1}{f_1} = T$.

On this basis we can introduce the concept of a device (or system) with a relatively "short memory" (w.r.t. a given family of signals) under large-signal operation. For this class of devices, since the dynamic deviations are small, the nonlinear functional dependence on $e(t, \tau)$ in (6) can be linearised and described in terms of a linear convolution w.r.t. $e(t, \tau)$:

$$i(t) = F_{DC}[v(t)] + \int_0^{+\infty} w(T_M, \tau) g[v(t), \tau] e(t, \tau) d\tau + \Delta i_M + \Delta i_N \quad (9)$$

where F_{DC} is the DC characteristic of the device and $g[v(t), \tau]$ is the nonlinearly voltage controlled impulse response of the electron device. More precisely, the integral expression in (9) is the first term of a multidimensional integral series where the higher order terms have been neglected under the hypothesis of small dynamic deviations $e(t, \tau)$. So, the term Δi_N represents the "nonlinear series truncation error" due to the linearised approximation for small dynamic deviations. Clearly, $\lim_{T_M \rightarrow 0} \Delta i_N = 0$ since, when T_M approaches zero, the dynamic deviations $e(t, \tau)$ become vanishing small, and the convolution description becomes exact.

It is worth noting the strong analogy between (9) and the small-signal description of a device by means of the linear convolution integral. In fact, the short-term memory concept (i.e., small dynamic deviations) enables the description in

terms of a convolution integral with respect to the dynamic deviations to be adopted even under large signals, likewise the small-signal hypothesis allows for the description in terms of a convolution integral with respect to the small signals applied. The sum of the first two terms in the right hand of (9) represents a Finite-Memory Nonlinear Model which can correctly describe the behaviour of a given electron device provided that, for a given set of voltage signals v , suitable values of T_M can be found for which Δi_M and Δi_N are both small enough. This happens in small-signal (or mildly nonlinear) operating conditions, as the series truncation error Δi_N is certainly small, while Δi_M can be made small by simply choosing T_M large enough.

In strongly nonlinear operation, instead, in order to have a small Δi_N (which implies, according to eqn. (7), small $\epsilon(t, \tau)$ even with large v), a relatively small T_M (i.e., $T_M \ll \frac{1}{f_1}$) must necessarily be chosen. In such conditions, the actual duration of the memory effects within the device must be not too much longer than T_M , to have also small Δi_M . Both accurate physics-based simulations and experimental evidence [1.4] have shown that this normally happens for devices with small parasitic effects (e.g., "intrinsic devices") and negligible low-frequency dispersive phenomena. Otherwise, to achieve good accuracy in high-frequency strongly nonlinear operation, both parasitic and low-frequency dispersive effects should be dealt with separately in the model extraction procedure, as shown in the following.

When considering discrete-spectrum signals, the voltage v can be described as a sum of spectral components V_k by the Fourier series:

$$v(t) = \sum_{k=-\infty}^{+\infty} V_k e^{j\omega_k t} \quad (10)$$

so that, according to well-known properties of the Fourier transform, eqn. (9) can be expressed, after simple mathematical developments, in the Harmonic-Balance-oriented form:

$$i(t) = F_{DC}[v(t)] + \sum_{k=-\infty}^{+\infty} \tilde{Y}[T_M, v(t), \omega_k] V_k e^{j\omega_k t} + \Delta i_M + \Delta i_N \quad (11)$$

$$\text{with } \tilde{Y}[T_M, v(t), \omega] = G[T_M, v(t), \omega] - G[T_M, v(t), 0] \quad (12)$$

$$\text{and } G[T_M, v(t), \omega] = \mathcal{F}_\omega \{w(T_M, \tau)g[v(t), \tau]\} \quad (13)$$

\mathcal{F}_ω being the operator denoting the Fourier transform. In (11), \tilde{Y} is a nonlinearly voltage-controlled dynamic admittance, which describes only the purely dynamic phenomena since, according to (12), $\tilde{Y}[T_M, v(t), \omega] = 0$ for $\omega = 0$.

Equation (11) defines, for different values of the parameter T_M ranging from 0 to ∞ , a family of models among which a number of existing modelling approaches can be singled out as special cases of the FMM. For instance, for $T_M \rightarrow \infty$ eqn. (11) coincides with the NIM proposed in [1,2]. Instead, when $T_M \rightarrow 0$ a conventional quasi-static charge-controlled model is obtained. In fact, it can be shown that:

$$\lim_{T_M \rightarrow 0} \tilde{Y}[T_M, v, \omega] = j\omega C(v) \quad (14)$$

where $C(v)$ is a voltage-controlled capacitance corresponding to the derivative of a quasi-static voltage-controlled charge. Thus, as it is well-known that quasi-static models can provide acceptable (although sometime limited) accuracy for different types of devices, we can reasonably expect that, for the same devices and operating conditions, suitably small values of T_M can be found which make Δi_N negligible without introducing large Δi_M . According to these considerations the FMM should be regarded as a mildly non quasi-static model, since a small, but finite, T_M is adopted. It should be noted that when, for a given device and a given set of possible operating conditions, a suitable value of T_M has been chosen, the general-purpose technology-independent model (11) has been, in practice, "tailored" on the specific nonlinear dynamics of that device.

MODEL IDENTIFICATION

As far as model identification is concerned, the function F_{DC} can be directly measured, since it simply represents the DC characteristic of the device. The dynamic admittance \tilde{Y} , instead, can be easily identified on the bases of the following considerations.

Let us consider small-signal sinusoidal operation (so that the series truncation error $\Delta i_N \rightarrow 0$) around a bias condition V_B , and $T_M \rightarrow \infty$ (so that the memory truncation error $\Delta i_M \rightarrow 0$). Under such conditions, linearisation of eqn. (11), taking also into account eqn. (12), leads to:

$$Y[V_B, \omega] = g_{DC}[V_B] + \tilde{Y}_\infty[V_B, \omega] = g_{DC}[V_B] + G_\infty[V_B, \omega] - G_\infty[V_B, 0] \quad (15)$$

with

$$\tilde{Y}_\infty[V_B, \omega] \doteq \lim_{T_M \rightarrow \infty} \tilde{Y}[T_M, V_B, \omega]$$

$$G_\infty[V_B, \omega] \doteq \lim_{T_M \rightarrow \infty} G[T_M, V_B, \omega]$$

In (15) Y is the conventional small-signal bias/frequency dependent admittance and g_{DC} is the bias dependent DC differential conductance of the device.

Equation (15) can be rewritten as:

$$-424- \quad G_\infty[V_B, \omega] = Y[V_B, \omega] - g_{DC}[V_B] + G_\infty[V_B, 0] \quad (16)$$

The Fourier transform of the product $w \cdot g$ in eqn. (13) can be expressed as the convolution of the transformed functions in the form:

$$G[T_M, V_B, \omega] = \int_{-\infty}^{+\infty} W(T_M, \xi) G_\infty[V_B, \omega - \xi] d\xi \quad (17)$$

$$\text{where } W(T_M, \omega) = \mathcal{F}_\omega\{w(T_M, \tau)\}$$

which, taking into account (16) becomes:

$$G[T_M, V_B, \omega] = \int_{-\infty}^{+\infty} W(T_M, \xi) \{Y[V_B, \omega - \xi] - g_{DC}[V_B] + G_\infty[V_B, 0]\} d\xi \quad (18)$$

By substituting (18) in (12) we obtain the final result:

$$\tilde{Y}[T_M, V_B, \omega] = \int_{-\infty}^{+\infty} W(T_M, \xi) \{Y[V_B, \omega - \xi] - Y[V_B, -\xi]\} d\xi \quad (19)$$

which shows how model identification can be carried out on the bases of conventional small-signal bias/frequency dependent admittance parameters (obtained through simple transformations of scattering parameters which are more easily measured at microwave frequencies) by applying a simple frequency-domain linear convolution of measured parameters. It should be noted that the integral operator in (19) actually involves a "weighted" averaging of measured Y parameters, which also introduces a beneficial "smoothing" effect on noise-like errors in the frequency-domain measurements. Practically, in (19) a Gaussian-like windowing function $W(T_M, \omega)$ is adopted which has a limited frequency width so that the integration interval is finite.

Once the functions F_{DC} and $\tilde{Y}[T_M, V_B, \omega]$ have been identified on a suitable grid of bias conditions and in the frequency range of interest, eqn. (11) can be directly used to compute the FMM response in the framework of Harmonic-Balance tools for circuit analysis. To this end, suitable interpolation techniques are needed [13] to evaluate the functions F_{DC} and $\tilde{Y}[T_M, V_B, \omega]$ for each frequency and set of voltages occurring in the HB analysis.

MODELLING OF III-V FETs

For transistor modeling eqn. (6) must be considered as a two-dimensional nonlinear functional of the voltages v_1 and v_2 at the two ports. Moreover, in the case of III-V FETs, low-frequency dispersive effects, due to surface state densities and bulk traps, should be taken into account. Since these effects are characterised by slow dynamics, which would limit the validity of the simplifications based on the short-term memory concept, they must be dealt with separately. To this end, the functional (6) can be written in the following form:

$$\dot{\mathbf{i}}(t) = \underline{\Psi} \left[v_1(t) + w(T_M, \tau_1) e_1(t, \tau_1), v_2(t) + w(T_M, \tau_2) e_2(t, \tau_2), \underline{\mathbf{x}}(t) \right]_{\tau_1, \tau_2=0}^{+\infty} + \underline{\Delta i_M} \quad (20)$$

where $\dot{\mathbf{i}}$ is the vector of the port currents and e_1, e_2 , are the dynamic deviations, defined as in (2), relative to v_1 and v_2 , respectively. In (20), $\underline{\mathbf{x}}$ is the set of state variables (e.g., equivalent surface potentials, trap level filling, etc.) used to describe the "slow" dynamic phenomena associated with dispersive effects.

Since the slow dynamics associated with traps have been separately described through the dependence on $\underline{\mathbf{x}}(t)$, the simplifying assumption of small T_M can still be introduced. Thus, through a procedure similar to that previously described, and by dealing with the dispersive state variables $\underline{\mathbf{x}}$ in the same way as in [10], the following vectorial expression is obtained:

$$\begin{aligned} \dot{\mathbf{i}}(t) = & \underline{F}_{DC}[\underline{\mathbf{v}}(t)] + \underline{\tilde{g}}_{LF}[\underline{\mathbf{v}}(t)][\underline{\mathbf{v}}(t) - \underline{V}_0] + \\ & + \int_0^{+\infty} w(T_M, \tau) \underline{g}[\underline{\mathbf{v}}(t), \tau] \underline{\mathbf{e}}(t, \tau) d\tau + \underline{\Delta i_M} + \underline{\Delta i_N} + \underline{\Delta i_x} \end{aligned} \quad (21)$$

where $\underline{\Delta i_x}$ is the error due to the simplifications introduced [10,11] to describe the dispersive effects. These, according to the experimental and simulated results provided in [10,11], are quite small and almost negligible.

In (21), \underline{V}_0 is the vector of the mean values V_{1o} and V_{2o} of $v_1(t)$ and $v_2(t)$, respectively. The matrix $\underline{\tilde{g}}_{LF}$ is a low-frequency voltage controlled dynamic conductance matrix which describes the deviations due to traps from the DC static characteristics \underline{F}_{DC} ; the matrix $\underline{\tilde{g}}_{LF}$ can be identified as described in [10,11] on the basis of small-signal or pulsed measurements. The integral term, instead, describes only the deviations of high frequency dynamics w.r.t. low-frequency behaviour.

When considering discrete-spectrum signals, by applying well-known properties of the Fourier transform, eqn. (21) can be expressed, after simple mathematical developments, in the Harmonic-Balance-oriented form:

$$\dot{\mathbf{i}}(t) = \underline{F}_{DC}[\underline{\mathbf{v}}(t)] + \underline{\tilde{g}}_{LF}[\underline{\mathbf{v}}(t)][\underline{\mathbf{v}}(t) - \underline{V}_0] + \sum_{k=-\infty}^{+\infty} \tilde{Y}[T_M, \underline{\mathbf{v}}(t), \omega] \underline{V}_k e^{j\omega_k t} + \underline{\Delta i_M} + \underline{\Delta i_N} + \underline{\Delta i_x} \quad (22)$$

By applying the same procedure described above and assuming $\underline{\Delta i_x} \simeq 0$, we obtain:

$$\tilde{Y}[T_M, \underline{V}_B, \omega] = \int_{-\infty}^{+\infty} W(T_M, \xi) \{Y[\underline{V}_B, \omega - \xi] - Y[\underline{V}_B, -\xi] - \underline{\tilde{g}}_{LF}[\underline{V}_B]\} d\xi \quad (23)$$

which, analogously to eqn. (19), provides a simple model identification criterion.

MODEL IDENTIFICATION CONSIDERING IMPORTANT PARASITIC EFFECTS

In order to guarantee the existence of suitable values of T_M , such as to make the error terms in (11) negligible even when parasitics become very important in high-frequency, strongly nonlinear operating conditions, separate modelling of parasitic effects is needed, like in many other modelling approaches. This can be done by using the scheme in Fig.1 where parasitics have been described, according to conventional approaches, by series inductances and resistances, while a generic linear parasitic network \underline{Y}_P has been considered in parallel to the ports of the intrinsic transistor (which is described by the FMM). The latter, non-conventional feature, while enabling for better accuracy in the modeling of parasitics, does not add significant complexity since, owing to the parallel-like admittance-matrix-based formulation of the FMM, the parasitic matrix \underline{Y}_P simply corresponds to a linear additional term in the nonlinear equation (11). In fact, the complete model equation becomes:

$$\begin{aligned} \tilde{i}^{(e)}(t) = & \underline{F}_{DC}[\underline{v}(t)] + \tilde{\underline{g}}_{LF}[\underline{v}(t)][\underline{v}(t) - \underline{V}_0] + \\ & + \sum_{k=-\infty}^{+\infty} \left\{ \underline{Y}_P[\omega] + \tilde{\underline{Y}}[T_M, \underline{v}(t), \omega] \right\} \underline{V}_k e^{j\omega_k t} + \underline{\Delta i}_M + \underline{\Delta i}_N + \underline{\Delta i}_x \end{aligned} \quad (24)$$

where $\underline{V}_k = \underline{V}_k^{(e)} - \underline{Z}[\omega_k]I_k^{(e)}$

\underline{Z} being an impedance matrix corresponding to the three LR series branches. External parasitic parallel capacitances have not been considered since their contribution to the memory effects is less important and can be somehow taken into account by the parallel network \underline{Y}_P .

When the series parasitic resistances and inductances have been identified and de-embedded (through conventional approaches or special-purpose procedures which directly take into account the specific short-term memory requirements), the parallel matrix \underline{Y}_P can be easily determined by solving an over-determined set of linear equations which impose the constraint of minimum discrepancy between measured and computed small-signal behaviour at different bias points in the given operating region of the device. Alternatively and more easily, if good accuracy is required for operation around a given bias condition, \underline{Y}_P can be simply obtained by imposing an exactness constraint on the small-signal response at that bias.

PRELIMINARY EXPERIMENTAL RESULTS

Preliminary experimental validation was carried out by comparing the performance predicted by the above described modelling approach and small- and large-signal measurements on a $0.6\mu\text{m} \times 600\mu\text{m}$ GaAs MESFET.

In particular, DC characteristics and scattering parameters of the MESFET were measured on a grid of 200 bias points up to a frequency of 40GHz. After parasitic de-embedding, the voltage-controlled dynamic admittance matrix $\tilde{\underline{Y}}$ of the FMM was identified according to eqn. (23). The associated dynamic conductance matrix $\tilde{\underline{g}}_{LF}$, which accounts for low-frequency dispersive effects was identified according to the procedures described in [10,11]. In particular, the FMM model was identified by using both a windowing function with $T_M = \infty$ (this corresponds to the NIM model [1,2]) and $T_M = 10 \text{ psec}$ in (23).

Since no memory truncation is introduced with the NIM model, the small-signal device behaviour is exactly reproduced. However, under large-signal operations, the accuracy of the NIM was found to be not accurate enough. This is reasonably due to uncertainties in the parasitic de-embedding which leads to an intrinsic device where the memory effects are still important enough so that for $T_M = \infty$ the series truncation error $\underline{\Delta i}_N$ in (11) is so large to limit the model accuracy.

As previously said, the application of the FMM approach with a suitable, finite T_M should reduce the series truncation error $\underline{\Delta i}_N$, having at the same time small memory truncation error $\underline{\Delta i}_M$. For the GaAs MESFET considered, a value of $T_M = 10 \text{ psec}$ was easily found which satisfies the above condition. In particular, the good agreement shown in Fig.2 between measured and simulated small-signal scattering parameters, confirms that the memory truncation error $\underline{\Delta i}_M$ introduced is negligible, since the small-signal frequency response of the device is not substantially modified (good agreement was generally found for a large number of different bias conditions). Moreover, the accuracy of large-signal performance prediction of the FMM (the results in Fig.3 and Table 1 were obtained applying in nonlinear simulations the highly accurate interpolation techniques described in [13]) also indicates that the series truncation error $\underline{\Delta i}_N$ has been substantially reduced w.r.t. the NIM approach.

REFERENCES

- [1] F.Filicori, G.Vannini, "A mathematical approach to large-signal modelling of electron devices", Electronics Letters, Feb 1991.
- [2] F.Filicori, G.Vannini, V.A.Monaco, "A nonlinear integral model of electron devices for HB circuit analysis", IEEE Trans. on MTT, Jul 1992.
- [3] G.Vannini, "Nonlinear integral modeling of Dual-Gate GaAs MESFETs", IEEE Trans. on MTT, Jun 1994.
- [4] F.Filicori, G.Vannini, A.Santarelli, D.Torcolacci, V.A.Monaco, "Accurate prediction of intermodulation distortion in GaAs MESFETs", Proc. of 25th EuMC, 1995.
- [5] D.E.Root et al., "Technology independent large-signal non quasi-static FET models by direct construction from automatically characterised device data", Proc. of 21st EuMC, 1991.
- [6] R.Daniels, A.Yang, J.Harrang, "A universal large/small signal 3-terminal FET model using a nonquasi-static charge-based approach", IEEE Trans. on ED, Oct 1993.
- [7] T.Narhi, "Frequency-domain analysis of strongly nonlinear circuits using a consistent large-signal model", IEEE Trans. on MTT, Feb 1996.
- [8] V.Volterra, "Theory of functionals and of integral and integro-differential equations", Dover, 1959.

[9] D.Mirri, G.Iuculano, F.Filicori, G.Vannini, G.Pasini, G.Pellegrini, "A modified Volterra series approach for the characterisation of non-linear dynamic systems", IMTC 96, Brussels, Jun 1996.

[10] F.Filicori, G.Vannini, A.Santarelli, A.Mediavilla et al. "Empirical modeling of low-frequency dispersive effects due to traps and thermal phenomena in III-V FETs", IEEE Trans. on MTT, Dec 1995.

[11] C.Fiegna, F.Filicori, G.Vannini, F.Venturi, "Modeling the effects of traps on the IV-characteristics of GaAs MESFETs", Proc. of the 1995 IEDM.

[12] G.Vannini, F.Filicori, A.Santarelli, "Integral approaches to nonlinear modeling of electron devices", 1997 IEEE MTT-S, Workshop on Nonlinear Measurements and Modeling.

[13] F.Filicori, V.A.Monaco, G.Vannini, A.Santarelli, "Nonlinear microwave device modelling based on system and signal theory approaches", Workshop on Nonlinear Microwave Design, 27th EuMC, 1997.

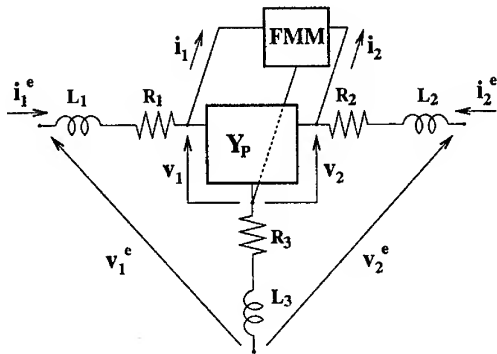


Figure 1: Equivalent scheme for parasitic modelling in the FMM.

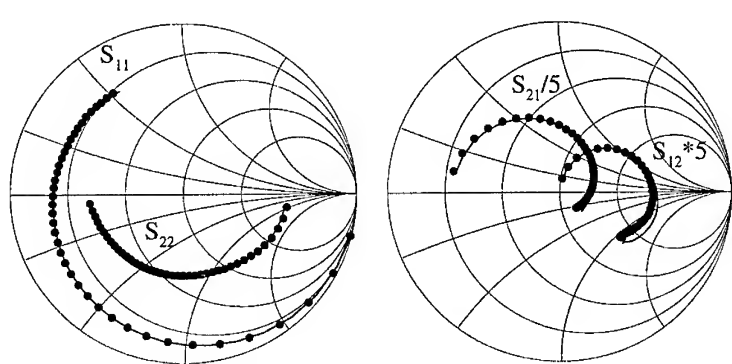


Figure 2: Comparison between S-parameters (1-40GHz) measured (•) and simulated (—) through the FMM for a GaAs MESFET, ($V_{GS} = -0.25V$, $V_{DS} = 2V$). The good agreement confirms that the memory truncation error introduced is negligible.

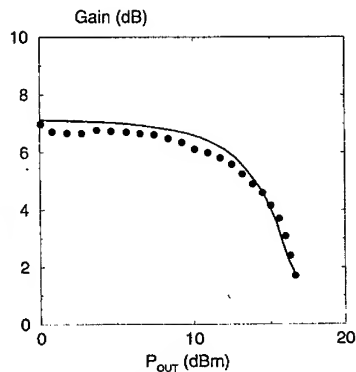


Figure 3: Power gain vs output power for a GaAs MESFET at 5GHz. The agreement between measurements (•) and the performance predicted through the FMM (—) is good.

$P_{IN}(dBm)$	Measured P_{OUT} (dBm)			FMM P_{OUT} (dBm)		
	$k = 1$	$k = 2$	$k = 3$	$k = 1$	$k = 2$	$k = 3$
0	6.6	-25.3	-36.6	6.8	-27.8	-38.8
5	11.0	-13.4	-22.7	11.3	-14.4	-23.0
10	14.5	-3.3	-12.0	14.5	-2.6	-12.6
15	16.7	2.0	-3.3	16.7	2.2	-3.6

Table 1: Comparison between harmonics of the output power measured and predicted by the FMM for a GaAs MESFET. The fundamental frequency is 5GHz.

Large Signal and Noise Modeling of HEMT Devices including Frequency and Temperature Effects

F. Sinnesbichler, T. Felgentreff*, G.R. Olbrich

Technische Universität München, Lehrstuhl für Hochfrequenztechnik
Arcisstraße 21, 80290 München, Germany
Phone: +49 (89) 2892 8390, Fax: +49 (89) 2892 3365
e-mail: olbrich@hft.e-technik.tu-muenchen.de

* Siemens AG, Public Communication Networks Group, Mobile Networks Development
Hofmannstr. 51, 81359 München

ABSTRACT

In this paper we present a novel physics based large signal HEMT model which describes the signal properties and the low and high frequency noise behavior in the frequency range from 1 Hz to 40 GHz. The modeling includes also dispersion and thermal effects of the active device which at this time are only considered in small signal models. The model is used in amplifier and oscillator applications. Calculation products are compared with measurement results.

INTRODUCTION

For oscillator and amplifier applications it is necessary to know the noise behavior and the large signal properties of the active device. In oscillators the low frequency noise contributions are upconverted to noise sidebands of the oscillator signal and in amplifiers the nonlinear behavior of the active devices causes harmonics and intermodulation distortions which limit the usable dynamic range.

In the first part of this paper we present a lumped element model which describes the large signal behavior of HFET devices. In this part we also consider the dispersion and give a correction formula for thermal effects. In the second part we will concentrate on the different noise contributions in AlGaAs/GaAs-HEMTs and describe the implementation of noise current sources in the model. The third part of the paper gives examples in which this HEMT model is used in amplifier and oscillator applications.

SMALL SIGNAL AND LARGE SIGNAL MODELING

The model is based on S-parameter measurements up to 40 GHz. The linear and not bias dependent extrinsic elements L_g , L_d , L_s and R_g , R_d , R_s are extracted from small signal S-parameters using hot and cold modeling techniques. To determine the nonlinear elements of the inner transistor (R_{gs} , R_{gd} , C_{gs} , C_{gd} , C_{ds} , G_m , G_{ds} , τ) we apply a deembedding procedure to the measured small signal S-parameter data of 200 different bias points [1,2]. This has to be done for all interesting frequencies. The nonlinear elements can be modeled either by analytical functions or by interpolation using look-up-tables [3]. The two dimensional look-up-tables contain the data of the nonlinear elements as a function of the two independent controlling voltages V_{gs} and V_{ds} at the intrinsic HEMT (Fig. 1). Both approaches are based on a quasistatic approximation. The nonlinear diode admittances G_{gs} and G_{gd} are given by their I/V-characteristics whereby the parameters have been determined by DC measurements. The gate resistor R_g which is given by the ohmic resistance of the gate finger and the resistance of the gate connection metallisation was determined using an approximation technique with $I_g \rightarrow \infty$ [1]. To model the channel current I_{ds} we use the DC I/V-characteristic and the dynamic output I/V characteristic we get by an integration of the differential small signal RF admittances G_m and G_{ds} (Fig. 1) with

$$I_{ds}(U_{gs}, U_{ds}) = \int_{U_{GS0}}^{U_{gs}} G_m(u_{gs}, U_{DS0}) du_{gs} + \int_{U_{DS0}}^{U_{ds}} G_{ds}(U_{gs}, u_{ds}) du_{ds} + I_{ds}(U_{GS0}, U_{DS0}). \quad (1)$$

So dispersion effects of G_{ds} caused by deep level traps [4] are included.

With growing drain source voltage the channel temperature is increased by self heating. This gives a decrease of the effective mobility and the saturation velocity of the electrons and therefore a smaller current density J_n . As a result of this thermal effect at high output voltages and currents a lowered differential output admittance can be observed which sometimes accepts negative values. The power dissipation in a large signal application is mainly different from the power dissipation which occurs during small signal measurements. The small signal measurement results therefore have to be compensated with the channel temperature during the measurement. In large signal applications on the other hand we have to consider the dynamic power dissipation and the resulting channel temperature in this case. The extracted results for I_{ds0} , G_{m0} and G_{ds0} from small

signal measurements have to be compensated with the temperature increase ΔT_{DC} caused by the power dissipation $P_d = U_{ds}^{DC} I_{ds}^{DC}$. In the case of large signal operation I_{ds} , G_m and G_{ds} have to be corrected with ΔT caused by P_d

$$P_d = \frac{1}{T} \int_0^T U_{ds}(t) I_{ds}(t) dt. \quad (2)$$

Therefore, we get the following correction formulas [5]

$$\begin{pmatrix} I_{ds}(T) \\ G_{ds}(T) \\ G_m(T) \end{pmatrix} = \begin{pmatrix} I_{ds0} \\ G_{ds0} \\ G_{m0} \end{pmatrix} \cdot \frac{1 + \frac{\Delta T_{DC}}{T_0}}{1 + \frac{\Delta T}{T_0}}. \quad (3)$$

NOISE MODELING

The high frequency noise performance of the HEMT device is described by the model given in [6,7] which uses three uncorrelated white noise current sources (I_{Nds} , I_{NRgs} , I_{NRgd}) allocated to the resistive elements of the intrinsic transistor (Fig. 2). The parameters of these noise sources are determined from noise parameter measurements using the correlation matrix method. Baseband noise measurements were done to determine the bias dependent low frequency noise power spectra (Fig. 3). The low frequency noise contribution is modeled as a noise current source I_{NF} , which includes the fundamental f_c noise source and the $g-r$ noise source showing an Lorentzian spectrum [8]. Besides the three white noise current sources I_{Nds} , I_{NRgs} and I_{NRgd} in the intrinsic HEMT, the large signal and noise model also includes noise sources for the shot noise of the Schottky diodes (I_{Ngs} , I_{Ngd}) and the thermal noise of the parasitic resistances (R_g , R_d , R_s). The noise source I_{Nds} describes the diffusion noise of the channel current I_{ds} (hot electrons).

In general the diffusion noise of the channel current dominates all other noise contributions. Usually, the Schottky noise of the diodes can be neglected. This is not applicable if the diodes show high leakage currents. The Nyquist noise of the resistances is responsible for the minimum noise figure of the HEMT and, therefore, we have to take it into consideration.

AMPLIFIER AND OSCILLATOR APPLICATIONS

Fig. 4 gives a complete presentation of the lumped element large signal and noise model we use in different applications. Calculation results of the fundamental signal and the 1st harmonic of a 10 GHz amplifier including dispersion and self heating effect are presented and compared with measurement results (Fig. 5 - datamod). The influence of dispersion and temperature effects (datamod without dispersion, datamod without thermal effects) on the calculated results are shown separately.

The model was also used for the simulation of planar oscillators. The calculated oscillator output power (datamod) is compared with measurement results and calculations using the Curtice model (Fig. 6). A parameter variation is used for model validation. Varying the gate voltage U_{gs} of the transistor, we measure output power and frequency of the oscillator. In Fig. 6, the measured output power is displayed versus frequency shift and compared with calculated results.

In Fig. 7 the equivalent circuit of the investigated 15-GHz-coplanar-oscillator is given.

In addition the large signal and noise model was used for oscillator phase noise calculations in time domain. The calculations agree within +/- 2dB with results of phase noise measurements.

CONCLUSION

The result of the investigations demonstrates in a clear manner that the presented large signal and noise model is well suited for amplifier and oscillator simulations in a wide range of linear and nonlinear applications.

ACKNOWLEDGEMENT

The investigations have been financially supported by the Deutsche Forschungsgemeinschaft (DFG/SFB348).

REFERENCES

- [1] Dambrine, G. et al: A new method for determining the FET small signal equivalent circuit. IEEE Trans. MTT, Vol. 36, 1988, No.7, pp. 1151-1159.
- [2] Berroth, M.; Bosch, R.: Broad band determination of the FET small signal equivalent circuit. IEEE Trans. MTT, Vol. 38, 1990, No.7, pp. 891-895.
- [3] Felgentreff, T.; Olbrich, G.; Russer, P.: A small signal databased HEMT model for nonlinear time domain simulation. -In: Simulation of Semiconductor Devices and Processes, Vol. 5, Eds.: S. Selberherr, H. Stippel, E. Strasser. Wien: Springer-Verlag Wien New York, 1993, pp. 269-272.
- [4] Canfield, P.C.; Lam, S.C.; Allstot, D.J.: Modeling of frequency and temperature effects in GaAs MESFETs. IEEE Journ. Solid State Circuits, Vol. 25, No. 1, Feb. 1990, pp. 300-306.
- [5] Felgentreff, T.: Großsignal- und Rauschmodellierung von Heterostruktur-Feldeffekttransistoren. Dissertation Technische Universität München, Hochfrequenztechnik, 1995, pp. 57.
- [6] Felgentreff, T.; Olbrich, G.; Russer, P.: Noise parameter modeling of HEMTs with resistor temperature noise sources. IEEE MTT-Symposium Digest 1994, pp. 853-856.
- [7] Pospieszalski, M.: Modeling of noise parameters of MESFETs and MODFETs and their frequency and temperature dependence. IEEE Trans. MTT, Vol.37, No.9, pp. 1340-1350.
- [8] Felgentreff, T.; Olbrich, G.: Modeling of Low Frequency Noise Sources in HEMTs. -In: IEEE MTT-Symposium Digest 1996, San Francisco, California, 17-21. Juni 1996, Vol. 3, pp. 1743-1746.

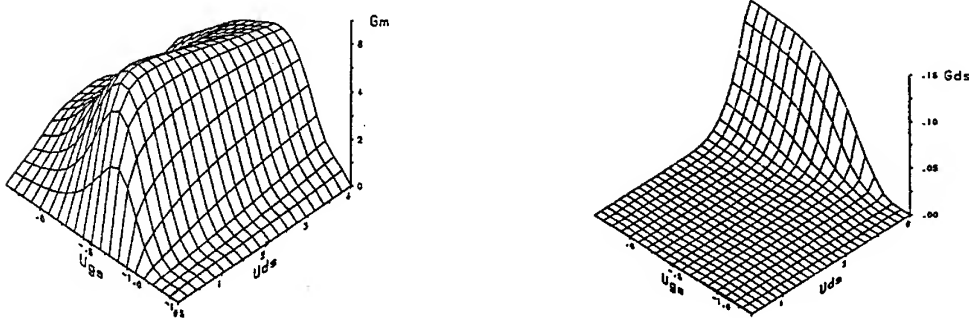


Fig. 1 Transconductance G_m and output admittance G_{ds}

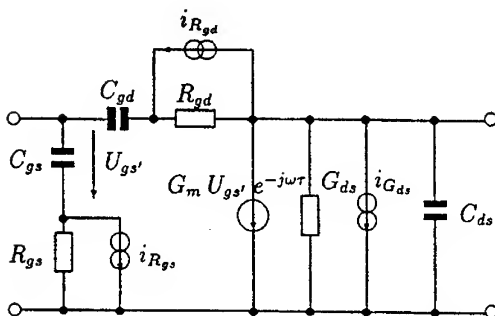


Fig. 2 Resistive elements with noise current sources of the intrinsic HEMT

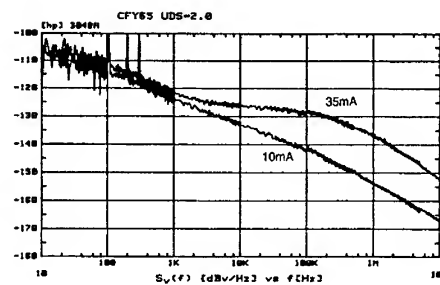


Fig. 3 Low frequency noise measurement results ($f^{-1/2}$ -noise and g-r-noise) at two different bias points ($I_{ds}=10mA$, $I_{ds}=35mA$)

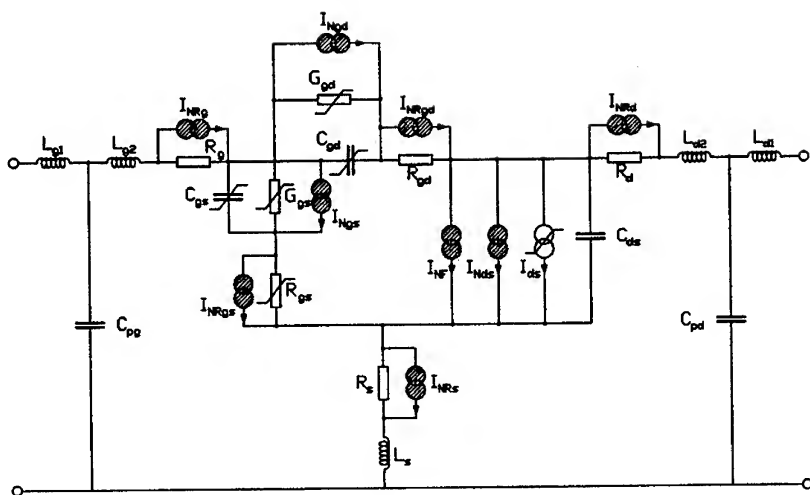


Fig. 4 Large signal and noise equivalent circuit of a HEMT device

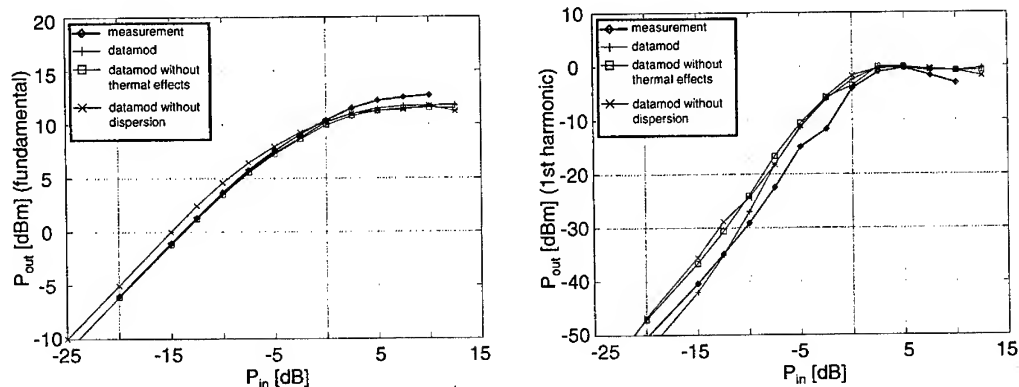


Fig. 5 Calculated and measured output power of the fundamental and 1st harmonic of an amplifier signal with $f_0=10$ GHz

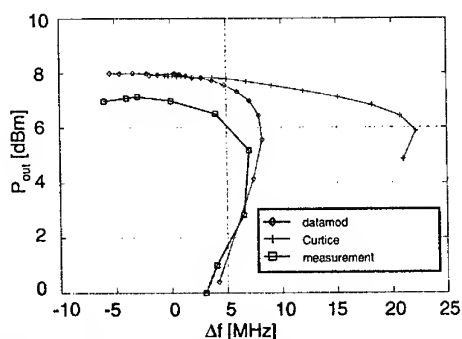


Fig. 6 Calculated and measured oscillator output power vs. frequency shift ($U_{ds}=2$ V, parameter = U_{gs}).

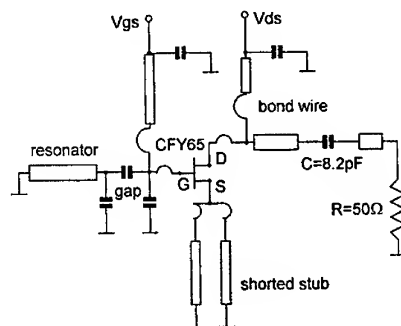


Fig. 7 Coplanar 15-GHz-HEMT-oscillator

Genetic Determination of Large-Signal HEMT Model

Kazuo Shirakawa and Naofumi Okubo

Fujitsu Laboratories Ltd.
Wireless Communication Systems Laboratory.
1015 Kamikodanaka, Nakahara-ku, Kawasaki 211, Japan
Tel: +81-44-754-2647
Fax: +81-44-754-2646
E-mail: nato@flab.fujitsu.co.jp

Abstract

This paper reports on a general approach to build a large-signal, neural network HEMT model using a genetic algorithm. By representing the configuration of a neural network model as the chromosome of a virtual creature, we looked for an optimum network configuration by simulating the evolution of a group of these virtual creatures (a population).

We successfully designed neural networks representing bias-dependent intrinsic elements of a HEMT's equivalent circuit. We also verified the reliability of this technique by searching for the optimum model from different initial conditions.

1. Introduction

In recent years, some authors have introduced the use of neural networks for active device modeling. This model is open to everyone and is capable of improving the drawbacks of conventional models without losing their advantages, but it is difficult to determine its proper configuration in return for its flexibility. As a result, the reported neural network models always employ a fixed three-layered configuration [1,2].

However, taking advantage of a user-defined model in commercial CAD software effectively, it is desirable to achieve minimal error using a neural network with as few as possible weighting factors irrelevant to the number of layers. Moreover, it is known that the simplest configuration also avoids the excessive training trap.

In this paper, we report on a technique to determine large-signal, neural network HEMT models. The configuration of a multi-layered neural network [3] describing bias-dependent intrinsic elements of a HEMT's equivalent circuit is represented as the chromosome of a virtual creature. We applied the concept of a genetic algorithm [4] to a group of these creatures and obtained an optimum neural network model.

We successfully determined a neural network Cgs model and a single neural network model simultaneously representing seven intrinsic elements, Cgs to Cds, in order to show the practicality of our approach. We also checked the reliability of our approach by determining the optimum configuration of a Cgs model under different initial conditions. As the genetic approach is a hands-off technique, it would be convenient for operators who have no neural network backgrounds.

2. Genetic Algorithm

A genetic algorithm [4] is an optimization technique based on a computer simulation of the virtual creatures' evolution in a particular habitat.

Each individual creature has its own chromosome and adaptability to the habitat (fitness). The i -th creature has chromosome G_i and fitness value f_i , defined as follows:

$$G_i = \{g_0^i, g_1^i, \dots, g_{Ng-1}^i\} \quad (1)$$

and

$$f_i = f(G_i), \quad (2)$$

where g_j^i ($j=0, \dots, N_g-1$) denotes a gene, and N_g is the number of genes in one chromosome. Function f in Eq. 2 is determined according to a particular problem.

Figure 1 is a flowchart of a genetic algorithm. First, we generate a population composed of N_p members and evaluate each creature's fitness relative to given conditions. We then remove $s\%$ of the current population from the creatures with the lowest fitness value. Third, from among the survivors, we select $N_c (= N_p \cdot s/100)$ pairs of parents and generate their offspring. So that creatures with higher fitness values should have more offspring, the parent individual is chosen according to the following probability:

$$P_i = \frac{f_i}{\frac{1}{N_p - N_c} \sum_{j=0}^{N_p - N_c - 1} f_j} \quad (3)$$

Here, the j -th gene of the offspring's chromosome is chosen from the j -th gene of one parent at the probability of p , or from the j -th gene in the other parent at the probability of $1-p$. Each offspring's gene also suffers from a mutation at a probability of $m\%$ to maintain variety.

We then replace the current populations by $N_p - N_c$ survivors and their N_c offspring to obtain the populations of the next generation.

Steps 2 to 4 are repeated until the populations adequately fit the conditions or the number of generations reaches N_{gen} (maximum number of generations).

3. Implementation

Figure 2 shows an abridged multi-layered neural network used to model the bias-dependent intrinsic elements of a HEMT's equivalent circuit.

We defined a gene as representing the number of neurons in each layer, and which takes multi-level integer values between 0 to N_n-1 . (N_n is the maximum number of neurons in each layer). A gene of zero indicates a null layer. For example, if the total number of neurons is limited to N , the maximum number of layers becomes $L = N/N_n$. And from the initial populations, we especially eliminated equivalent creatures to achieve a wider variety.

The class definitions of the multi-layered neural network and a population of virtual creatures are shown in Figure 3. The class of a neural network consists of a structural definition part and a data part. The vector *config* denotes the number of neurons in each layer. The actual memories for weighting factors, denoted as the pointer to matrix **weight*, are dynamically allocated when required according to *config* and the number of layers. The pointer to vector **input* indicates the input teaching signal for the neural network such as V_{gs} and V_{ds} . The pointer to vector **output* indicates a set of output teaching signals for the neural network such as C_{gs} .

The class of a population is composed of two parts. The first part describes neural networks, that is a pointer to class *neural_net*, **net* and some parameters. N_i is the number of the input node, N_o is the number of the output node, and N_h is the maximum number of neurons in each hidden layer. The second part describes the population. N_p and N_{gen} are the number of members in a population and the maximum number of generations. Pointers to vectors **G* and **f* indicate the chromosome and its fitness values. A pointer to vector **ev_parameters* indicates the parameters used for the evolution, such as the selection rate.

To determine the simplest configuration possible for a neural network that generates errors below a certain criterion, ϵ_0 , we defined the fitness value as follows:

$$f_i = \begin{cases} \frac{1}{\epsilon} & : \epsilon \geq \epsilon_0 \\ \frac{1}{\epsilon} \left(1 + \frac{N - N_a}{N} \right) & : \epsilon \leq \epsilon_0 \end{cases}, \quad (4)$$

where ϵ denotes the fitting error of the neural network corresponding to G_i , and N_a is the total number of active neurons.

We saved the weighting factors of every generation and used them as initial values to train a neural network having a chromosome equivalent to that of a former generation. This accelerates convergence.

4. Measurement

To demonstrate the usefulness of our approach, we first verified the convergence of populations for the Cgs model of a HEMT with $L_g = 0.25 \mu\text{m}$ and $W_g = 100 \mu\text{m}$. Figure 4 shows the average fitness in relation to the generations. In this figure, lines correspond to the cases: $(N_n, N_p) = (10, 50)$, $(7, 30)$, and $(5, 10)$, where N_p is the number of creatures. Regardless of different habitats, the populations converge to the same configuration. The determined neural network and its fitting results are shown in Figures 5 and 6. Error values less than 0.0002 (3.0 % of rms error) between the measured and calculated values can be achieved. The other parameters are $\epsilon_0 = 0.00075$, $N_{\text{gen}} = 50$, and $L = 3$.

A better configuration for seven intrinsic elements than that reported in Ref. 3 can also be obtained. Using parameters $\epsilon_0 = 0.0015$, $N_{\text{gen}} = 20$, $L = 4$, $N_n = 10$, and $N_p = 50$, we obtained the neural network model as shown in Figure 7. It generated a 0.0008 fitting error (2.8 % of rms error). The parameters $s = 40\%$, $p = 50\%$, and $m = 1\%$ are commonly used in both cases.

5. Conclusions

We have reported on a technique to determine a large-signal HEMT model. The bias-dependent intrinsic elements are described by a multi-layered neural network, and its configuration is represented as a chromosome of a virtual creature. We applied a genetic algorithm to these creatures and determined the optimum model configuration.

We verified the practicality of this technique by determining an optimum Cgs model. Regardless of different initial conditions, the same configuration model was obtained. We also established optimum neural networks for modeling seven intrinsic elements. These neural networks matched the actual data more closely than was determined experimentally.

References

1. A. H. Zaabab, Q. J. Zhang, and M. Nakhla, "A Neural Network Modeling Approach to Circuit Optimization and Statistical Design," IEEE Trans. MTT-43, pp. 1349-1358, Jun. 1995.
2. J. Rousset, Y. Harkouss, J. M. Collantes, and M. Campovecchio, "An accurate neural network model of FET for intermodulation and power analysis," Proc. 26th EuMC., pp. 16-19, Sept. 1996.
3. K. Shirakawa and Naofumi Okubo, "A neural network characterization of a HEMT," Proc. 26th EuMC., pp. 370-373, Sept. 1996.
4. R. S. Michalski, et. al, "Machine Learning Vol. 2," Morgan Kaufmann, 1986

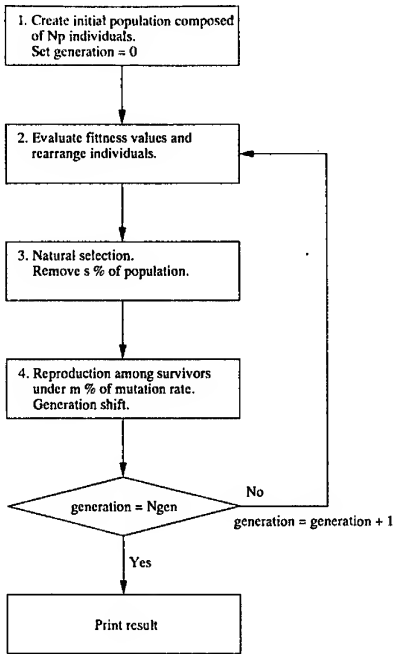


Fig. 1. Flowchart of a genetic algorithm

```

class neural_net
{
    int    number_of_layer;
    vector config;
    matrix *weight;

    int    number_of_data;
    vector *input,*output;
};

class population
{
    int    Ni,Nh,No;
    neural_net *net;

    int    Np,Ngen;
    vector *G;
    vector *f;
    vector *ev_parameters;
};
  
```

Fig. 3. Class definition of generalized multi-layered neural network, and a population of virtual creatures.

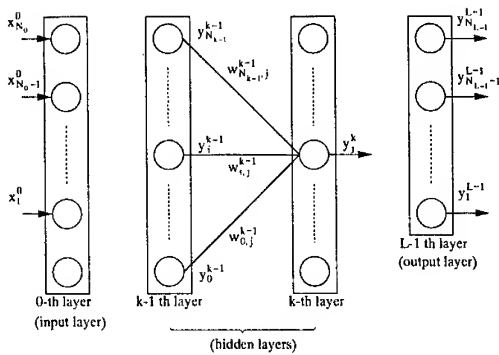


Fig. 2. Multi-layered neural network.

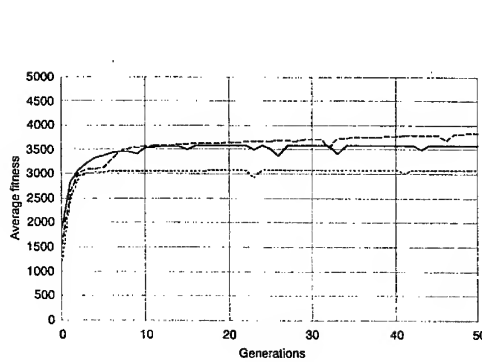


Fig. 4. Average fitness values against generation for Cgs model.
The solid line is case $(N_n, N_p) = (10, 50)$, the dotted line denotes $(7, 30)$, and the dashed line denotes $(5, 10)$.

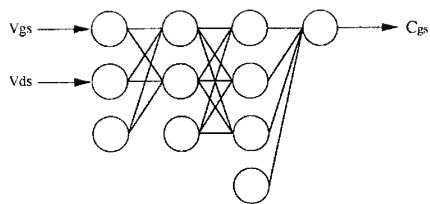


Fig. 5. Neural network model for C_{gs} .

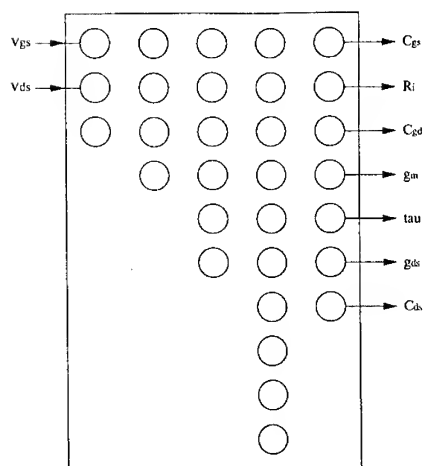


Fig. 7. Neural network model for C_{gs} to C_{ds} .

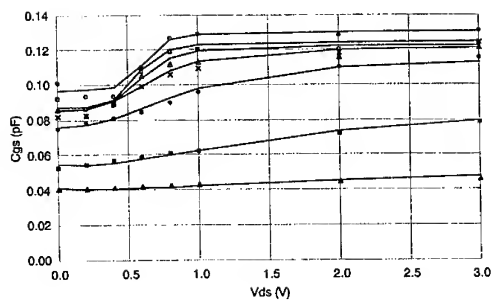


Fig. 6. Fitting results of C_{gs} .
Marks denote data and lines are calculations.

Monolithic Up / Down Converters for Millimeter-wave Wireless Networks

M. Madihan, L. Desclos*, K. Maruhashi, K. Onda, and M. Kuzuhara**

* Network Research Laboratory, C&C Research Laboratories, NEC Corporation, 4-1-1, Miyazaki, Miyamae-ku, Kawasaki 216 Japan
Tel: +81-44-856-2366, FAX: +81-44-856-2230, Email: madih@nwk.cl.nec.co.jp

** Kansai Electronics Research Laboratory, NEC Corporation, 2-9-1 Seiran, Otsu, Shiga 520 Japan.

Abstract

This paper describes CPW heterojunction FET (HJFET) down- and up- converter MMICs for millimeter-wave wireless networks. To realize a mixer featuring a simple structure with inherently isolated ports, and yet permitting independent port matching and low LO power operation, a "source injection" concept is utilized by treating the HJFET as a three-port device in which the LO signal is injected through the source terminal, the RF (or IF) signal, through the gate terminal, and the IF (or RF) signal is extracted from the drain terminal. With an LO power and frequency of 7dBm and 60.4GHz, both converters can operate for any IF frequency within 0.5 to 2GHz, with a corresponding conversion gain within -7 to -12dB. Chip size is 3.3mm x 2mm for the downconverter, and 3.5mm x 1.8mm for the upconverter.

Introduction

Development of low-cost small-size low-power fully monolithic transceiver modules with 1-2GHz IF frequencies, for facilitating 100-200Mbps transmission of data in a millimeter wave wireless local area network (LAN) system has been urged [1]-[4]. Frequency converters are key-elements in a transceiver module, and require rigorous design methods to achieve an optimum operation. Conventional FET converters employ either a "gate mixing" [5]-[6] or a "drain injection" [7]-[8] topology to produce a desired frequency component, by applying the LO signal to the gate terminal or drain terminal of the device, respectively. In such a structure, since LO signal shares the same port with RF (or IF) signal, independent port matching for each signal is impossible, and to achieve a sufficiently high isolation between LO signal and RF (or IF) signal, usually bulky hybrid circuits are required which totally increase the converter's circuit complexity. Introducing a "source injection" concept, and treating an FET as a "3-port device", the present paper describes V-band downconverter as well as upconverter MMICs for millimeter-wave wireless LAN applications.

Circuit Design

Equivalent circuits for the CPW V-band downconverter and upconverter MMICs are shown, respectively, in Figs. 1 and 2. The downconverter comprises an RF image rejection filter, a source injection down-mixer utilizing an HJFET as a mixing element, and an IF filter. RF signal, after passing through the image rejection filter and RF matching network, is applied to the HJFET gate terminal. LO signal is applied to the HJFET source terminal through the LO matching network. On the other hand, a resultant IF signal is

extracted from the HJFET drain terminal, after passing through the IF matching network. The LO matching network is essentially responsible to provide an unconditionally stable operation for the downconverter, both in the presence and absence of an LO signal. The upconverter comprises an IF filter, a source injection up-mixer, and an output filter to suppress LO signal and other unwanted frequencies. IF signal, after passing through the IF matching network, is applied to the HJFET gate terminal, and LO signal is applied to the HJFET source terminal through the LO matching network. On the other hand, a resultant RF signal is extracted from the HJFET drain terminal, after passing through the RF matching network and the filter. The LO matching network for the upconverter is the same as the one for the downconverter MMIC. Both small signal linear and large signal non-linear parameters of a discrete $0.15\mu\text{m} \times 100\mu\text{m}$ AlGaAs/InGaAs HJFET were applied in a harmonic balance circuit design for best port-matching, maximum conversion gain, unconditional stability, and rejection of undesirable frequencies, at 60GHz band frequency range.

Fabrication Process

The down- and up- converter MMICs were fabricated on a 3-inch undoped semi-insulating GaAs substrate. A CPW structure was used for transmission lines which permits chip size reduction and possibility of realizing transmission lines with different characteristics impedances without affecting the overall chip layout. The HJFET used in the converter MMICs has a gate length of $0.15\mu\text{m}$ and a total gate width of $100\mu\text{m}$ ($50\mu\text{m} \times 2$ fingers). Typical transconductance of 380mS/mm and f_T of 70GHz , both at a drain bias of 4V , and a reverse gate-drain breakdown voltage of 10V have been measured for the HJFETs. Measured pinch-off voltage for the HJFET is -1.6V . Chip size is $3.3\text{mm} \times 2\text{mm}$ for the downconverter, and

Microwave Performance

Figs. 3 and 4 show the chip photographs for the complete V-band CPW downconverter and upconverter ICs. Chip size is $3.3\text{mm} \times 2\text{mm}$ for the downconverter, and $3.5\text{mm} \times 1.8\text{mm}$ for the upconverter. On-wafer millimeter-wave probes were utilized to evaluate the chip performance. The FET gate bias was -1.6V , corresponding to the FET gate pinch-off voltage, and the drain bias was 0.7V . Figs. 5 and 6, respectively, show the return loss characteristics for the down- and up-converter chips. Measured downconverter's in-band return loss for the IF and RF ports is better than 15dB , and for the LO port is better than 8dB . On the other hand, measured upconverter's in-band return loss for the IF and RF ports is 8dB , and for the LO port is 5dB . Converters' behavior with respect to the input power, and conversion gain characteristics are summarized in Figs. 6 to 10. The downconverter has a small signal conversion gain of -7dB and -8.5dB at 61.4GHz and 62.4GHz , respectively. The upconverter has a small conversion gain of -9dB and -12dB for an IF frequency of 1GHz and 2GHz , respectively.

Downconverter LO suppression at RF and IF ports is better than 22dB , and RF suppression at IF port is better than 25dB . Upconverter LO suppression at RF and IF ports is better than 20dB , and RF suppression at IF port is better than 47dB . Measured pass-band and rejection-band insertion loss for the image rejection filter in the downconverter were, respectively, 7dB and 16dB . Conversion gain of the converters is dominated by the insertion loss of the corresponding filter.

Conclusions

Design consideration and performance results for CPW downconverter as well as upconverter MMICs incorporating source injection mixers and RF filters were described. In the circuit design, the FET was treated as a 3-port device in which the LO signal is applied to the source terminal. With an LO power and frequency of 7dBm and 60.4GHz, both converters can operate for any IF frequency within 0.5 to 2GHz, with a corresponding conversion gain within -7 to -12dB. The frequency converters reported in this paper are expected to find applications in millimeter wave wireless networks.

References

- [1] R. A. Pucel, D. Masse, and R. Bera, "Performance of GaAs MESFET mixers at X-band," IEEE Trans. Microwave Theory Tech., vol. MTT-24, p. 351, June 1976.
- [2] C. C. Penalosa and C. Aichison, "Analysis and design of MESFET gate mixer," IEEE Trans. Microwave Theory Tech., vol. MTT-35, p. 643, July 1987.
- [3] P. Bura and R. Dikshit, "FET mixer with the drain LO injection," Electron. Lett., vol. 12, no. 20, p. 536, Sept. 1976.
- [4] G. Tomassetti, "An unusual microwave mixer," Proc. Eur. Microwave Conf., p. 754, 1986.
- [5] V. Brady, T. Hsu, R. Reeves, and M. Vermeulen, "Development of a monolithic FET Ka-band single side band upconverter and image reject downconverter," 1989 IEEE GaAs IC Symp. Digest, p. 189, Oct. 1989.
- [6] W. R. Brinlee, A. M. Pavio, C. L. Goldsmith, and W. J. Thompson, "A monolithic multifunction EW broadband receiver converter," 1993 IEEE GaAs IC Symp. Digest, p. 207, Oct. 1993.
- [7] T. Hirota and M. Muraguchi, "K-band frequency up-converters using reduced-size couplers and dividers," 1991 IEEE GaAs IC Symp. Digest, p. 53, Oct. 1991.
- [8] A. Minakawa and T. Hirota, "An extremely small 26GHz monolithic image-rejection mixer without DC power consumption," IEEE Trans. Microwave Theory Tech., vol. MTT-41, p. 1634, Sept. 1993.

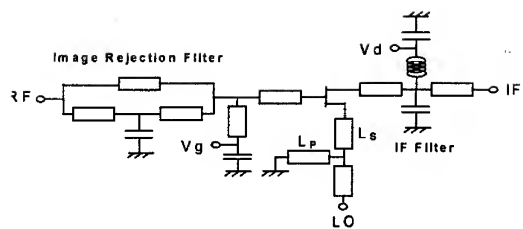


Fig. 1 V-band downconverter equivalent circuit.

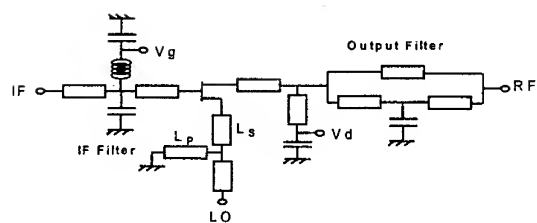


Fig. 2 V-band upconverter equivalent circuit.

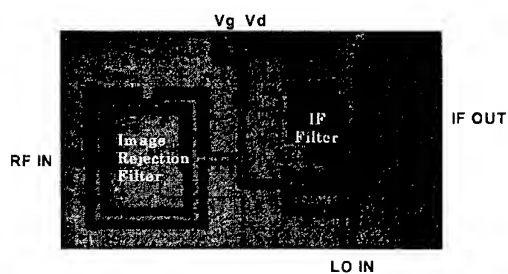


Fig. 3 Downconverter chip (3.3mm x 2mm).

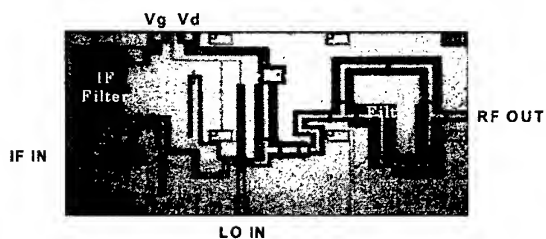


Fig. 4 Upconverter chip (3.5mm x 1.8mm).

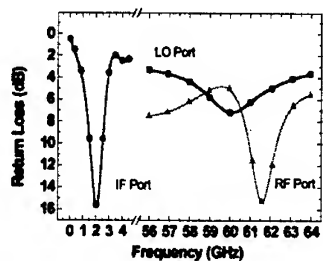


Fig. 5 Downconverter matching characteristics.

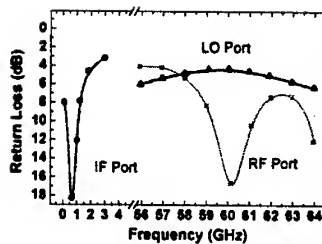


Fig. 6 Upconverter matching characteristics

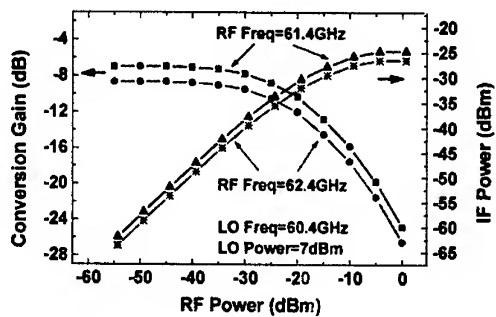


Fig. 7 Downconverter performance versus RF power.

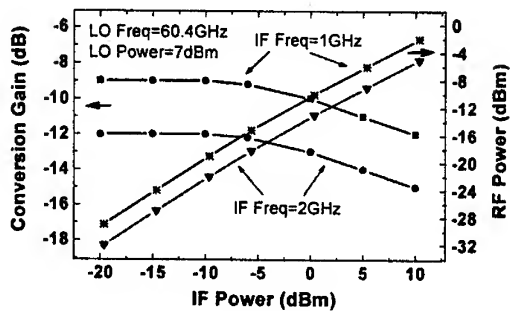


Fig. 8 Upconverter performance versus IF power.

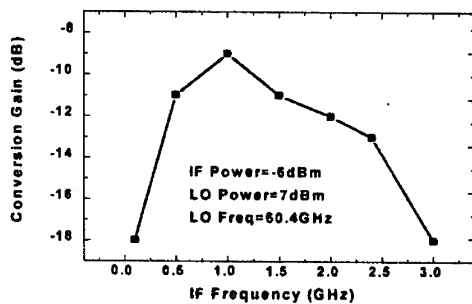


Fig. 9 Downconverter gain versus RF frequency.

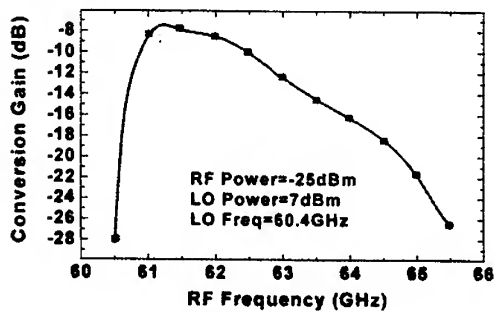


Fig. 10 Upconverter gain versus IF frequency.

Low-Loss High-Power Ka-Band Multipole Multithrow MMIC PIN Switch

M. Daly*, D. Whitefield, Z. Bogan, D. Bartle, J. Delconte
Alpha Industries, Inc. 20 Sylvan Road, Woburn, MA 01801

Abstract

A MMIC PIN multipole multithrow switch for Ka-band monopulse transceiver applications is presented. Incorporating multiple switch functions into a single MMIC topology yields substantial gains in system performance. The switch has a maximum insertion loss of 1.6dB in the critical antenna to LNA path and greater than 30dB of isolation between any two ports across the 29GHz to 37GHz frequency range. The switch is fabricated using a MMIC GaAs PIN process having a minimum breakdown voltage of 70V, resulting in high power handling PIN diodes. Additionally, the MMIC switch provides greater than 16dB of passive isolation when in an inactive mode.

Introduction

Monopulse front end modules require switches exhibiting low loss and high isolation between the transmit and receive paths. Insertion losses in the front end of a receiver contribute directly to the noise figure of the system, which places critical importance on maintaining low loss in all components preceding the low noise amplifier. High isolation as well as the ability to handle large signal levels are also necessary requirements in order to provide protection of the front end components. A multipole multithrow switch which has low insertion loss, high isolation, and multi-watt power handling capabilities has been designed and fabricated.

The MMIC PIN switch presented incorporates the functionality of multiple switches into a single GaAs chip. This single chip solution greatly improves system performance by significantly reducing the insertion loss in the critical path, while providing the necessary isolation. The chip allows three separate PIN switch chips and two LNA's to be replaced with the multi-function PIN switch and a single LNA circuit. Figure 1 illustrates the system advantage in terms of consolidation and reduction in the number of chips used, corresponding to an improvement in reliability and a decrease in assembly complexity required to achieve the same functionality. Additionally, utilization of a single MMIC chip ensures repeatable and predictable phase and amplitude insertion contributions, making it an ideal solution for multi-channel monopulse system applications.

Circuit Fabrication

The circuit is processed using Alpha Industries standard MMIC GaAs PIN process. The epitaxial PIN structures are grown on LEC semi-insulating GaAs substrates with two

mesa etch steps to define the active diode. The first mesa defines the cross sectional area of the diode. The second defines the N+ ohmic contact in addition to providing electrical isolation from the other components in the monolithic circuit. Low resistance ohmic contacts are made by evaporated Pt:Ti:Pt:Pt:Pt and Ni:Pt:Pt:Pt:Pt films alloyed into the P+ and N+ terminals respectively. Circuit transmission lines, metal layers of MIM capacitors, and dc bias lines are defined by a Ti:Pt:Pt:Pt:Pt evaporation and lift off process. An electroplating process is used to fabricate low parasitic air-bridge connections to the P+ terminal of the diode. The plating layer also provides the bulk of the metalization for low resistance transmission lines. The insulating layer of the MIM capacitors and diode passivation are provided by PECVD of Si_3N_4 . After lapping and polishing the substrate to a thickness of 100 μm , via holes are fabricated by reactive ion etching from the backside of the wafers. Finally the ground plane is provided by the backside metalization step. A GaAs PIN diode with an intrinsic layer thickness of 3 μm provides a reverse breakdown voltage between 70V and 80V measured at a leakage current of 10 μA . The typical 50 μm diameter diode has a junction capacitance of 65fF at -5V reverse bias and series resistance of 1.5 Ω at +30mA forward bias.

Circuit Design

The multipole multithrow switch layout circuit schematic is shown in Figure 2, and its circuit schematic in Figure 3. The seven I/O ports of the switch, as labeled in the illustration, are the Rx(LNA), Tx, Σ port, Δ port, and BIT/Cal port as well as two external 50 Ω terminations. The integrated chip topology allows for four active modes of operation: Δ port to LNA, Σ port to LNA, Tx to antenna (Σ), and BIT/Cal to LNA. An incoming signal from either antenna port can be directed to the LNA port during the receive mode. Switching the non-through path to an external load ensures that both antennas are always presented with VSWRs of less than 1.5:1. The switch is also used to direct a transmitted signal out the appropriate antenna port while providing protection to the components in the receiver front end. The final operating mode allows a calibration signal (BIT/Cal) to be injected to the receiver.

The circuit contains eight shunt PIN diodes which are either forward biased to a low resistance state, or reverse biased to a high impedance state. High impedance shunt transmission lines are used to provide bias to the diodes and MIM capacitors are used as DC blocks. The multipole multithrow switch circuit design is based on measured two port small signal scattering parameters of a nominal shunt diode. An

*M. Daly is currently with Lockheed-Sanders, Nashua, New Hampshire

all shunt design was selected in order to keep the losses minimal. The device data in conjunction with standard modeling techniques was used to optimize the circuit design for minimum loss between the antenna and LNA ports. A bias truth table for the four modes of operation is shown in Table 1. The truth table outlines the appropriate bias for each of the four modes of operation discussed previously. A "1" indicates that the particular diode is forward biased while a "0" signifies a reverse bias is applied to the diode. Note that diodes D1 and D2 are biased with a single control voltage, therefore turn on and off together.

In order to operate in the first mode listed, Δ antenna to LNA, an incoming signal is received when a reverse bias is applied to the shunt diodes labeled D3 and D8, while the remaining diodes (D1, D2, D4, D5, D6, D7) are forward biased. Shunt diode D3 presents a high impedance to the through transmission path, thereby allowing the signal to pass. The forward biased diodes D1, D2, D4, D5, D6, and D7 are biased to their low impedance state which, when rotated a quarter wave length away, present high impedances at the junctions labeled a, b, d, c and e. This high impedance, in turn, isolates the arms from the incoming signal flow. Reverse biasing the diode labeled D8 directs the sum port to a load, thereby ensuring a matched situation is present.

Diode D7 is used to provide isolation when the transmit path is not being used. When transmitting a signal out the sum antenna diode D7 is reverse biased allowing through signal flow while diodes D6 and D8 are reverse biased in order to present a high impedance at the cross junction. Additionally D5 is reverse biased with D3 and D4 forward biased which presents a matched load at the delta antenna port. D1 and D2 are also forward biased in order to prevent any leaked signal from reaching the Bit/Cal Port. Diodes D1 and D2 are reverse biased only when the BIT/Cal function is used, otherwise they are forward biased and present high impedances at junctions a and b, respectively.

An additional feature of significant merit is the switch's ability to protect the front end receiver components against extraneous radiation when it is not in active operation. When all of the diodes are left unbiased, D2 shorts an incoming RF signal to ground, providing greater than 16 dB isolation to the LNA port. During active receive and transmit modes this diode is forward biased, thereby presenting an open at junction b, contributing a minimal amount to the insertion loss.

Results

On-wafer small signal measurements were performed on the multipole multithrow switch from 20GHz to 40GHz in the four active modes of operation as well as in the passive mode. The measurements shown use a forward bias current

of 10 mA and a reverse bias of -3.5V. It may also be noted that there is very good agreement between the measured and predicted performance of the switch in all of its various modes of operation. The modeled and measured on-wafer performance of the critical parameters of Antenna to LNA insertion loss and isolation are shown in Figure 6. Less than 1.6dB of insertion loss is measured in the Antenna to LNA receive path across the 29GHz to 37GHz frequency band with an insertion loss of less than 2dB maintained across the entire Ka frequency band. Isolation of greater than 35dB will be provided to the alternate antenna path. VSWRs of less than 1.5:1 are presented to the antennas and LNA during all modes of operation.

Figure 5 depicts the insertion loss and isolation of the transmit to sum antenna path. The switch degrades the transmit signal power by less than 1.6dB. The high isolation of 32dB to 35dB across the entire band, provided by the switch, protects the LNA from RF leakage from the transmitter, rendering additional receive protect circuitry unnecessary.

The switch also provides a BIT/Cal path for system calibration. Figure 6 depicts the small signal performance of the switch BIT/cal port. Less than 1 dB of insertion loss and greater than 30dB of isolation are measured for this path. The passive isolation of the switch was measured with all of the diodes unbiased. The switch provides greater than 16dB across the 29GHz to 37GHz frequency range with a maximum of 38dB within the frequency band, as shown in Figure 7.

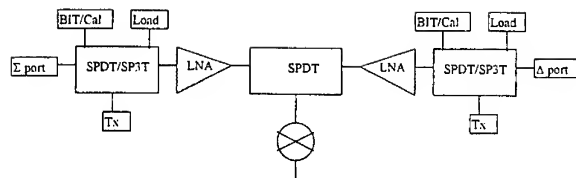
The power handling of this switch was not measured due to equipment limitations. However, a MMIC SPDT design utilizing the same diameter Alpha diodes has been shown to handle greater than 38dBm pulsed and 35dBm CW power, which were the maximum power ratings of the test equipment.¹ A minimum breakdown voltage of 70V was measured for the PIN devices in this multipole multithrow design. This high breakdown voltage corresponds to a calculated power handling of 12W in a 50 Ω system.

Conclusion

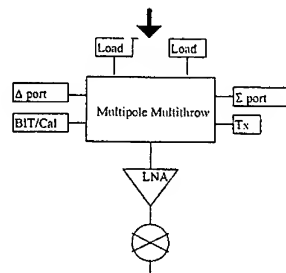
A single multifunction MMIC PIN switch has been fabricated which has exceptional performance reducing the system noise figure as well as the system component count. These reductions not only result in improved system performance but also account for substantial cost saving due to less components and their corresponding assembly cost. The consolidation of multiple functions into a single MMIC chip demonstrates the advantages of MMIC technology.

References

1. J. V. Bellatori, D. C. Bartle, D. Payne, G. McDermott, S. Bandla, R. Tayrani, and L. Raffaelli, "A MONOLITHIC HIGH POWER Ka BAND PIN SWITCH", IEEE 1989 Microwave and Millimeter-Wave Monolithic Circuits Symposium, pp 47-50.



a. Conventional Dual Channel Implementation



b. Dual Channel Configuration With Multi-Function PIN Chip

Figure 1. MultiPole MultiThrow Switch System Equivalent

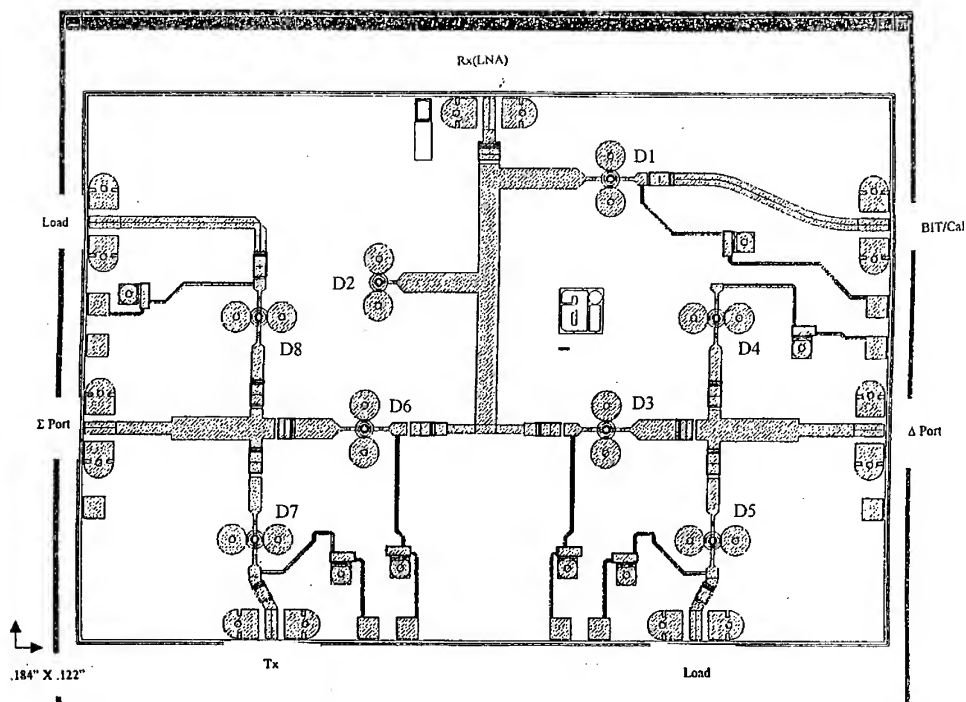


Figure 2. Multipole Multithrow Switch Layout

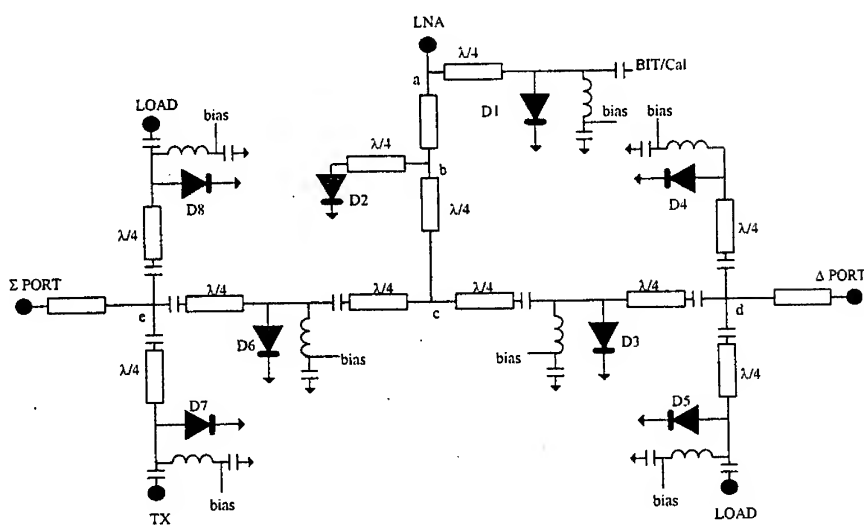


Figure 3. Multipole Multithrow Switch Schematic

	D1	D2	D3	D4	D5	D6	D7	D8
Δ Antenna to LNA	1	1	0	1	1	1	1	0
S Antenna to LNA	1	1	1	1	0	0	1	1
Tx to S Antenna	1	1	1	1	0	1	0	1
BIT/Cal to LNA	0	0	1	1	0	1	1	0

1= Diode ON, Forward Bias

0= Diode OFF, Reverse Bias

* Note: Diodes D1 and D2 are biased together.

Table 1. Multipole Multithrow Switch Bias Truth Table

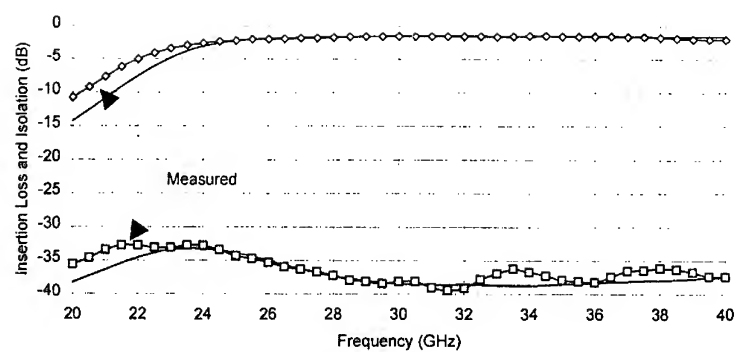


Figure 4. Antenna to LNA Path Measured and Modeled Insertion Loss and Isolation

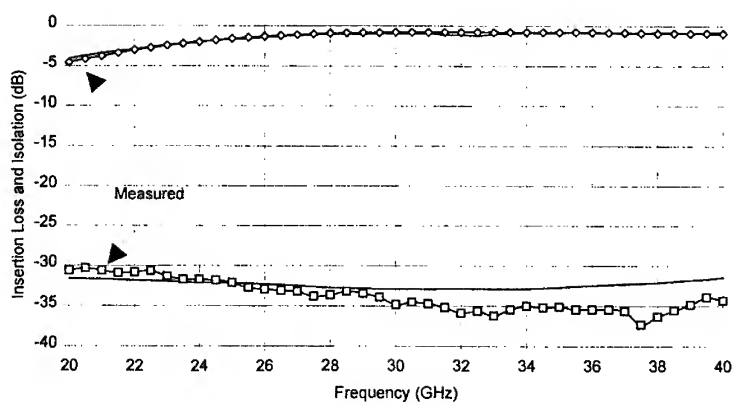


Figure 5. Transmit to Antenna Path Measured and Modeled Insertion Loss and Isolation

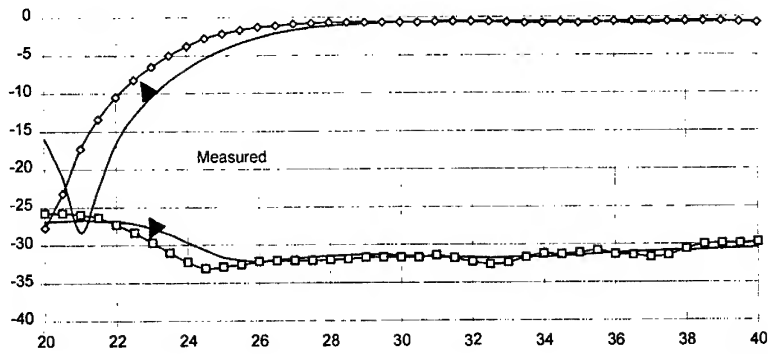


Figure 6. BIT/Cal to LNA Measured and Modeled Insertion Loss and Isolation

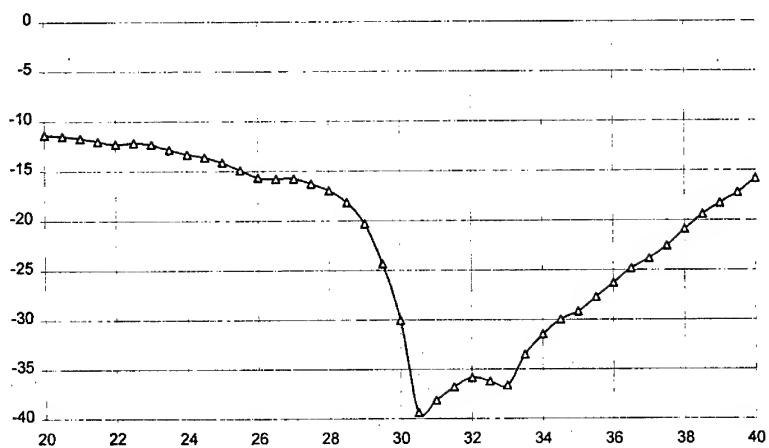


Figure 7. Passive Isolation of Multipole Multithrow Switch

Coplanar Switches in PHEMT Technology from X- to W-Band

K. Züfle, W. Haydl, H. Massler, R. Bosch, J. Schneider

Fraunhofer Institute for Applied Solid State Physics (IAF)

Tullastrasse 72, D-79108 Freiburg, Germany

phone +49-761-5159-442, fax +49-761-5159-565

e-mail: zuefle@iaf.fhg.de

Abstract

AlGaAs/InGaAs/GaAs PHEMT switching elements, combined with coplanar waveguide technology have been investigated to realize switches from X-band through W-band. Experimentally determined models, which apply over a range of 1-120 GHz, were used for the coplanar lines and elements. Several switch topologies, compatible with the active MMIC technology, have been designed and analyzed. With two different concepts for the X-band switches, we achieved insertion losses of 1.3/1.7 dB and isolations of 30/45 dB at 10 GHz. At W-band we obtained 2.9/3.2 dB insertion losses and isolations of 22/16 dB at 76 and 94 GHz, respectively.

Introduction

Over the past years the potential of coplanar wave guide technology (CPW) combined with PHEMTs has been successfully demonstrated. Excellent results for amplifiers, mixers, oscillators and other key components for communication and radar systems have been achieved [1, 2].

In high frequency electronics, particularly in radar applications, low loss and high isolation RF-switches play an important role since they are used to control transmit/receive (T/R) signal flow. Hence, up to W-band, p-i-n diode switching elements integrated with microstrip technology are commonly used [3, 4]. On the other hand, competing transistor switches offer fabrication advantages and are therefore preferable for monolithic integration. Outstanding results for single pole double throw (SPDT) and single pole single throw (SPST) PHEMT switches have been reported in Q- and W-band [5, 6].

To reduce system cost, the complete integration of coplanar transmit/receive modules is an important goal. In order to meet the requirements of monolithic fabrication processes and exploit the advantages of CPW over Micro Strip, coplanar transistor switches are in the center of interest for T/R MMICs. Additionally, monolithic integration avoids RF interconnections which can reduce system performance. As an example, system engineers must add at least 1 dB insertion loss and 0.5 mm² extra chip area for a compensated bond interconnection at W-band [7]. First coplanar X-band switches based on MESFETs were reported in [8] and achieved an insertion loss < 1.5 dB and an isolation > 20 dB. For SPDT transistor switches, results in W-band have not reported to date.

To investigate the feasibility and application of CPWs combined with PHEMT technology for switches up to W-band, we have designed and fabricated different coplanar monolithic SPDT switch topologies at two microwave bands of special interest. In this paper, we present a study of the different concepts and on-wafer measured results of the T/R switches.

Device Models

The circuits have been designed using characteristic impedances of 30, 50 and 67 Ω for CPW lines and elements. For simulation purpose they were described by physical transmission lines, including frequency dependent values for ϵ_{eff} and the attenuation constant α . All element parameters were extracted from passive test structures using on-wafer S-parameter measurement. The models are validated over the entire frequency range from 1-120 GHz [9].

The X-band FETs were modeled using simple equivalent circuits for the transistor ON- and OFF-state. The ON-state is represented by the channel resistance and the OFF-state by the drain-source capacitance. Transmission lines were added to account for the distributed effects of the gate.

Since the W-band switching HEMTs use the same standard layout and technology, we used the transistor small signal equivalent circuit model and set transconductance g_m to zero [8, 10].

For the ON- and OFF-state bias points, device parameters were extracted from on-wafer S-parameter measurements for the series and shunted HEMT-model.

All circuits have been developed, utilizing HP Microwave Design System with implemented user defined models.

X-Band-Switches

X-band switch A features a series and a shunt PHEMT in each branch. Figure 1 shows a simplified schematic of the switch.

Open gate resistors prevent the DC-control voltage ($V_{g1} = -3$ V and $V_{g2} = 0$ V) from taking effect on the RF-signal. They also prevent leakage through capacitive shunting paths between the transistors, which improves isolation performance. An inductor of 1.6 nH is placed at the switch junction to obtain a small return loss at port 1. The chip layout, realized for 2-port measurements, is internally matched with a 50 Ω load at Port 3 to provide realistic switch operation conditions and is shown in figure 2.

Simulated and measured performances of the switch agree well and are shown in figures 3 and 4. Within the desired band, the return loss is less than 16 dB. The insertion loss in ON-state is 1.3 dB and the isolation in switch OFF-state is 30 dB at 10 GHz.

The second SPDT switch B, shown in figures 5 and 6, uses an additional shunt transistor in each branch to achieve higher isolation. We measured an improved isolation of 45 dB and insertion loss of 1.7 dB at 10 GHz. Good agreement with predicted results is demonstrated in figure 7 and figure 8.

The switches were realized, using 100 μ m ground to ground spacing CPWs on GaAs and PHEMTs with conventional two finger gates of 0.3 μ m length and total gate width of 300 μ m.

W-Band-Switches

Both W-band switches were realized with PHEMTs, using e-beam-lithography to define the 0.15 μ m two finger T-gates with total gate width of 60 μ m. The ground to ground spacing of the CPWs is 50 μ m and the DC control voltage is $V_{g1} = -1$ V and $V_{g2} = 0$ V.

The topology of the W-band switches differs from that of the X-band versions since only shunt PHEMTs were used in order to reduce the insertion loss. Figures 9 and 10 show a schematic and a chip photo of W-band switch A.

The low impedance, presented by the pair of the shorted HEMTs, is transformed through the quarter-wavelength section to a high impedance at the switch junction. The characteristic impedances and lengths of the transmission lines are adjusted to give lowest insertion loss and highest isolation. This concept also uses open gate resistors. No additional inductor to compensate the drain-source-off-capacitance was used as in [6].

During measurement, the second branch was open. Thus, there is a deviation between measured and predicted data for isolation. Figures 11 and 12 illustrate the properties of the switch from 70-120 GHz. At 76 GHz the insertion loss is 2.9 dB and despite the incorrect termination we achieved 22 dB of isolation. For a monolithically integrated and properly matched switch, we expect at least 20 dB isolation over the entire W-band. The return loss of the circuit is less than 15 dB up to 90 GHz.

The second W-band switch B uses the same topology as the former, but instead of open gate resistors, quarter-wave-length gate transmission lines shorted by capacitors at the ends were used. For the RF-path they provide the same function as resistors. A schematic is shown in figure 13 and a chip photo in figure 14. The MMIC includes a 50 Ω NiCr resistor as termination for the second branch.

With the fourth switch we obtained 3.2 dB insertion loss at 94 GHz. Isolation is higher than 15 dB over the whole W-band. Additionally, return loss is smaller 20 dB over a 10 GHz bandwidth. Figures 15 and 16 depict the on-wafer measured S-parameters versus frequency.

Conclusion

The application of coplanar technology to switches at X-band and W-band has been investigated using different switch topologies. The active switching elements were PHEMTs with 0.3 μ m conventional and 0.15 μ m T-gates. We obtained good agreement between simulation and measurement.

References

- [1] M. Schlechtweg, W. H. Haydl, A. Bangert, J. Braunstein, P. J. Tasker, L. Verweyen, H. Massler, W. Bronner, A. Hülsmann, W. Reinert, and K. Köhler, "Coplanar Millimeter-Wave IC's for W-Band Applications Using 0.15 μm Pseudomorphic MODFET's," *IEEE J. Solid-State Circuits*, vol. 31, pp. 1426-1434, 1996.
- [2] M. Schlechtweg, W. H. Haydl, J. Braunstein, P. J. Tasker, A. Bangert, W. Reinert, L. Verweyen, H. Massler, K. Züfle, W. Bronner, T. Fink, A. Hofmann, G. Kaufel, K. Köhler, B. Raynor, and J. Schneider, "110 GHz Amplifiers Based on Compact Coplanar W-Band Receiver Technology," presented at IEEE GaAs IC Symp., pp. 214-217, 1995.
- [3] E. Alekseev, D. Pavlidis, J. Dickmann, and T. Hackbarth, "W-band InGaAs/InP PIN Diode Monolithic Integrated Switches," presented at IEEE GaAs IC Symp., pp. 285-288, 1996.
- [4] J. Putman, M. Fukuda, P. Staecker, and Y.-H. Yun, "A 94 GHz Monolithic Switch with a Vertical PIN Diode Structure," presented at IEEE GaAs IC Symp., pp. 333-336, 1994.
- [5] D. L. Ingram, K. Cha, K. Hubbard, and R. Lai, "Q-Band High Isolation HEMT Switches," presented at IEEE GaAs IC Symp., pp. 289-292, 1996.
- [6] H. Takasu, F. Sasaki, H. Kawasaki, H. Tokuda, and S. Kamihashi, "W-Band SPST Transistor Switches," *IEEE Microwave and Guided Wave Letters*, vol. 6, pp. 315-316, 1996.
- [7] T. Krems, W. Haydl, L. Verweyen, M. Schlechtweg, H. Massler, and J. Ruediger, "Coplanar Bondwire Interconnections for Millimeterwave Applications," presented at 4th Topical Meeting on Electrical Performance of Electronic Packaging, Portland, OR, pp. 178-180, 1995.
- [8] R. Tempel, "A Coplanar Line Technique used with Transistor Switches for MMIC-Applications," *Microwave Journal*, vol. 39, pp. 274-278, 1996.
- [9] W. H. Haydl, A. Tessmann, K. Züfle, H. Massler, L. Verweyen, and J. Schneider, "Models of coplanar lines and elements over the frequency range 0-120 GHz," presented at 26th EuMC - European Microwave Conference, pp. 996-1000, 1996.
- [10] M. Berroth and R. Bosch, "Broad-Band Determination of FET Small-Signal Equivalent Circuit," *IEEE Transactions on Microwave Theory and Techniques*, vol. 38, pp. 891-895, 1990.

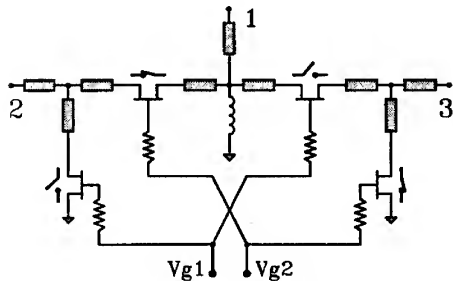


Fig. 1: Topology of SPDT X-band-PHEMT switch A with 1k Ω resistors in the gate bias lines.

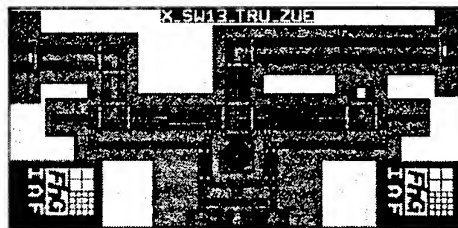


Fig. 2: X-band-PHEMT switch A (1.9x0.9 mm²).

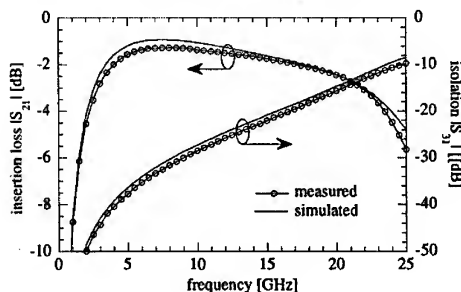


Fig. 3: Insertion loss and isolation of X-band-PHEMT switch A shown in figure 1.

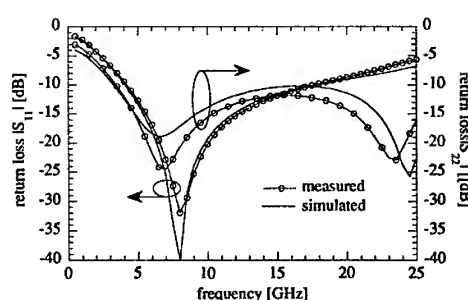


Fig. 4: Return loss of X-band-PHEMT switch A shown in figure 1.

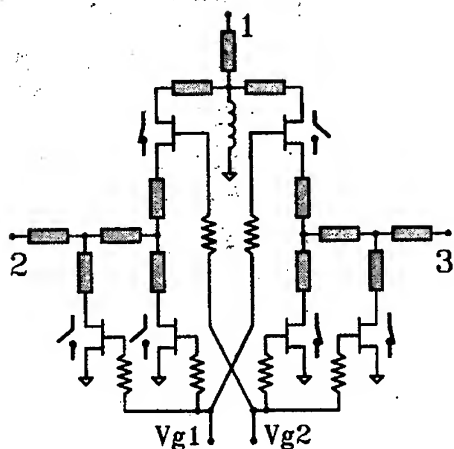


Fig. 5: Topology of SPDT X-band-PHEMT switch B with $1\text{k}\Omega$ resistors in the gate bias lines.

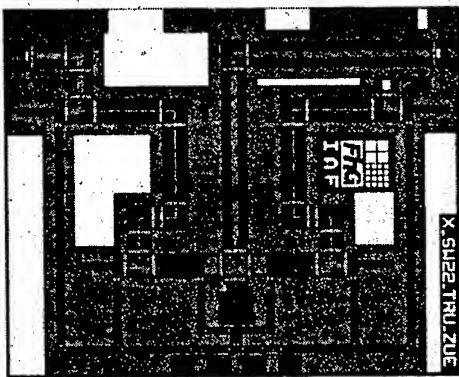


Fig. 6: X-band-PHEMT switch B ($1.9 \times 1.6 \text{ mm}^2$).

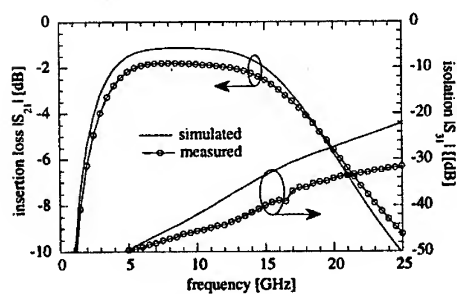


Fig. 7: Insertion loss and isolation of X-band-PHEMT switch B shown in figure 5.

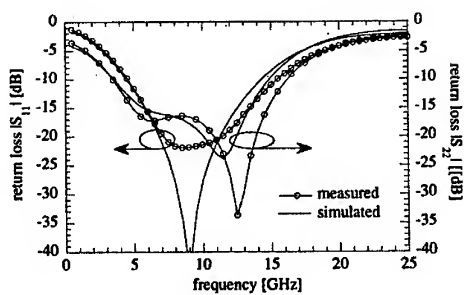


Fig. 8: Return loss of X-band-PHEMT switch A shown in figure 5.

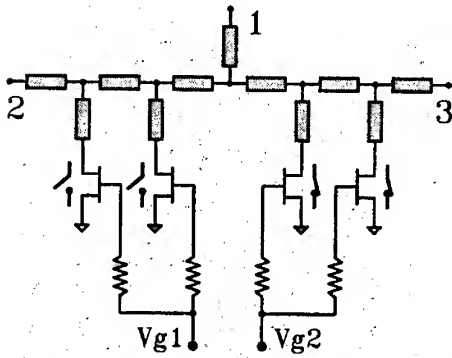


Fig. 9: Topology of SPDT W-band-PHEMT switch A with $1\text{k}\Omega$ resistors in the gate bias lines.

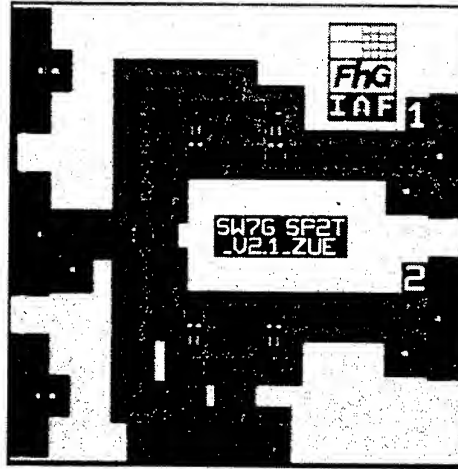


Fig. 10: W-band-PHEMT switch A ($1.4 \times 1.4 \text{ mm}^2$).

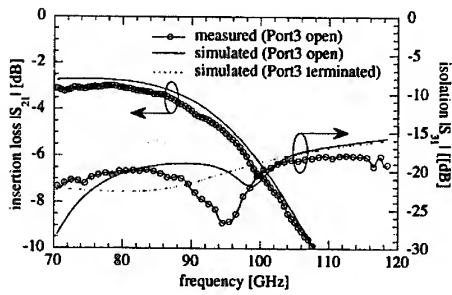


Fig. 11: Insertion loss and isolation of W-band-PHEMT switch A shown in figure 9.

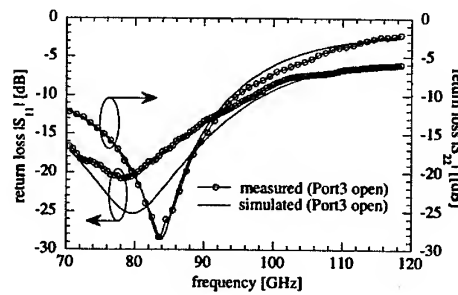


Fig. 12: Return loss of W-band-PHEMT switch A shown in figure 9.

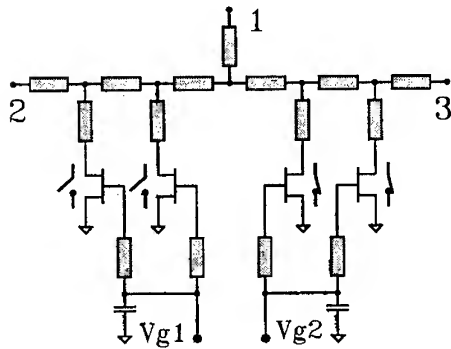


Fig. 13: Topology of SPDT W-band-PHEMT switch B with RF shorted $\lambda/4$ - gate bias lines.

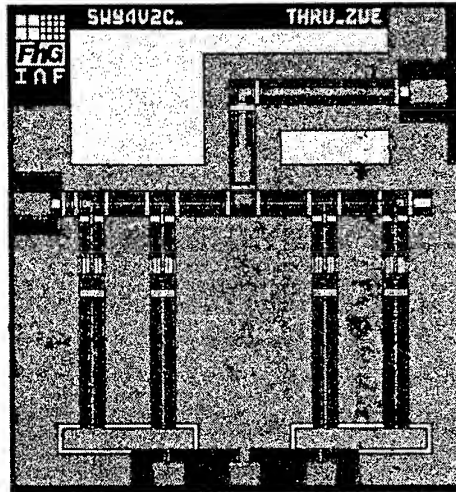


Fig. 14: W-band-PHEMT switch B ($0.9 \times 0.9 \text{ mm}^2$).

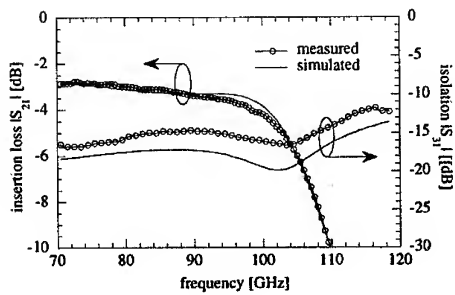


Fig. 15: Insertion loss and isolation of W-band-PHEMT switch B shown in figure 13.

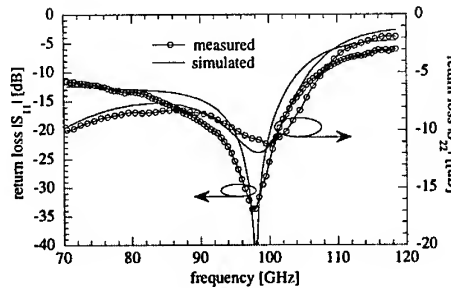


Fig. 16: Return loss of W-band-PHEMT switch B shown in figure 13.

A Novel Multi Chip Module Unifying Transmitter and Receiver at 51 GHz

Naoki Yakuwa, Makoto Akaishi, Tomoya Kaneko, Tomoaki Saryo

NEC Corporation

4035, Ikebe-cho, Tsuzuki-ku, Yokohama 224, JAPAN

TEL +81-45-939-2107

FAX +81-45-939-2109

E-mail : yakuwa@dvs.msc.yh.nec.co.jp

ABSTRACT

NEC has successfully developed a compact multi chip module for video and data communications. The transmitter (TX) and receiver (RX) are unified using high density packaging technology which is newly developed in consideration of reliability, e.g. hermetic seal and thermal management, and of low insertion loss RF I/O structure. Pseudomorphic Hetero Junction FETs (P-HJ-FET) are employed for LNA and power amplifier (PA) MMICs to achieve a low noise figure of 6.6 dB and high output power of 19 dBm. And the module also realized an excellent S/N of 60 dBp-p/rms for the NTSC VIDEO signal transmission.

I. INTRODUCTION

The conventional millimeterwave modules were composed of dielectric resonator oscillator (DRO) and waveguide structure, so they had disadvantages such as high cost, mechanical complexity and heavy weight[1]. The tendency of the market requirements needs compact size, light weight and portable equipment. Recently, there have been several reports about MMIC to oscillate directly in millimeterwave[2][3]. However, these MMICs are not suitable for the VIDEO signal transmission from the view point of $1/f$ noise. To achieve an excellent performance, compact size and cost reduction, it is necessary to optimize the LO -multiplier chain, and to integrate the transmitter and receiver in one MIC package with microstrip-to-waveguide transducer. Fundamental technology realizing the MIC is based on the metal package, the multi chip MMICs, thermal management, and the hermetic sealed microstrip-to-waveguide transducer. This paper discusses means of the newly developed packaging technology at millimeterwave and performance of the T/R module.

II. PACKAGE FOR MILLIMETERWAVE

In order to design the T/R module package, we considered of reliability, e.g. hermetic seal, thermal radiation from MMICs, low insertion loss at RF I/Os, electromagnetic shield and high isolation between TX and RX. Fig. 1 shows the external view of the T/R module with the lid removed. The T/R module size is only $38 \times 19.6 \times 3 \text{ mm}^3$. In order to achieve high isolation between TX and RX at 51 GHz, the cross section of the package mounting MMIC was designed to have high cut off frequency, that was 60 GHz. The block diagram of the T/R module is shown in Fig. 2.

1 THERMAL MANAGEMENT

It is suitable for package material to employ CuW if only thermal radiation is taken into consideration. However, CuW is

much more expensive than Kovar as material and takes long time processing at production, and the casting or injection molding of CuW is difficult. Therefore, the complex structure like a microstrip-to-waveguide transducer can not be made easily and cheaply. We employed Kovar for the package and CuW as a heat spreader. Fig. 3 shows the thermal radiation structure for the P-HJ-FET PA MMIC. Fig. 4 shows the estimated channel temperature of various thickness of CuW heat spreader. By using the 200 μ m thickness CuW heat spreader which has high thermal conductivity mounted under the MMIC directly, we can suppress the $T_{ch\ max}$ at 130°C even if the environmental temperature at 50°C.

2 MICROSTRIP-TO-WAVEGUIDE TRANSDUCER AND THE HERMETIC SEAL

Fig. 5 shows the cross-sectional view of the transducer. The alumina substrate is brazed to Kovar base plate with Ag. The insertion loss is 0.2 dB except the alumina substrate loss. The insertion loss and bandwidth are degraded by increasing the thickness of alumina substrate. On the other hand, the thickness of the alumina substrate is required more than 0.15mm in order to stand the pressure of 4 atm at the helium leak test procedure. By using the alumina substrate we couldn't find out the solution which satisfied the excellent insertion loss and mechanical strength. So, we brought in to use a low $\tan \delta$ material for the hermetic seal. Finally, the insertion loss of 0.25 dB and less than 10^{-8} atm·cc/sec leak rate are realized simultaneously.

III. PERFORMANCE OF THE T/R MODULE

1 TRANSMITTER

The transmitter consists of a 800 μ m P-HJ-FET 12.75GHz to 25.5GHz doubler, 400 μ m P-HJ-FET 25.5GHz to 51.0GHz doubler, two chips of two stage 400 μ m P-HJ-FET 51GHz PA MMICs, attenuator (i.e. PIN diode) and detector diode. Fig. 6 shows the TX power as a function of LO power and frequency. A saturated output power of 19 dBm at 51 GHz is obtained in condition of 15 dBm LO power. The operated output power is controlled within 14 dBm by the outer circuit.

2 RECEIVER

The receiver consists of a 200 μ m P-HJ-FET LNA and subharmonically pumping mixer where the 25.5 GHz LO is branched from transmitter. Fig. 7 shows the conversion loss as a function of LO power. Fig. 8 shows the conversion loss and NF as a function of frequency. A minimum conversion loss of 1.8 dB and a noise figure of 6.6dB at 51GHz are obtained in condition of 15 dBm LO power.

IV. VIDEO SIGNAL TRANSMISSION

In order to achieve an excellent S/N and modulation linearity, LO -multiplier chain is optimized. The LO is a 12.75 GHz VCO using a Si Bipolar Junction Transistor with the microstripline resonator. Fig. 9 shows the phase noise of the VCO as a function of offset frequency from carrier. The phase noise of the VCO is 104 dBc/Hz at 100kHz off carrier. The T/R module achieved a very high S/N of 60 dBp-p/rms for NTSC VIDEO signal transmission at 51 GHz. Fig. 10 shows the photograph of the T/R module.

V. CONCLUSION

We had investigated the millimeterwave package in terms of hermetic seal, thermal management of bare chips, low insertion

loss of RF I/Os and electromagnetic shield. Therefore, we integrated transmitter, receiver and microstrip-to-waveguide transducers in one package which volume is 1.55 cc successfully. The developed module achieved excellent RF performance and high reliability simultaneously.

ACKNOWLEDGMENT

The authors would like to thank Mr. Sachiro Fukuda and Mr. Eiji Nagata for their useful suggestions during this work. The authors also wish to thank Mr. Kenzo Wada for his technical advice and the engineers of the Product Engineering Department for their technical supports.

REFERENCE

- [1] K. Ogawa et al., "A 50-GHz Compact Communication System for Video Link Fabricated in MIC," 1988 IEEE MTT Symposium Digest, pp.1023-1024.
- [2] T. Inoue et al., "60GHz dielectrically stabilized monolithic voltage controlled oscillator," 1995 European Microwave Conf. Proc., pp281-284.
- [3] K. Ohata et al., "Sixty-GHz-Band Ultra-Miniature Monolithic T/R Modules for Multimedia Wireless Communication Systems," IEEE Trans. MTT., vol. 44, no. 12, Dec. 1996, pp.2354-2360.

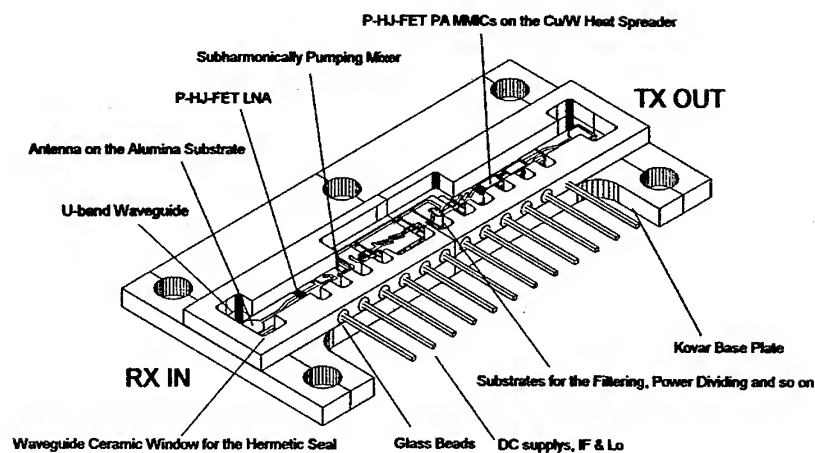


Fig. 1 External View of the T/R Module. Package Size is 38mm x 19.6mm x 3mm.

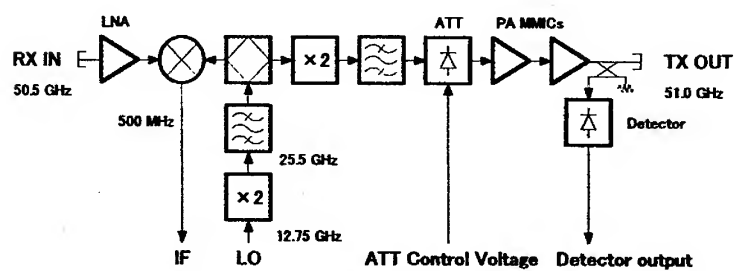


Fig. 2 Block Diagram of the T/R Module

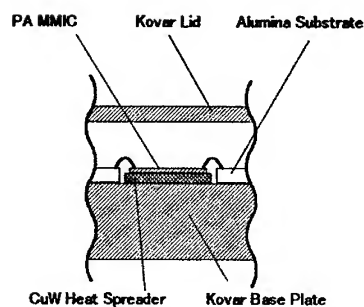


Fig. 3 Thermal Radiation Structure of the P-HJ-FET PA MMIC.

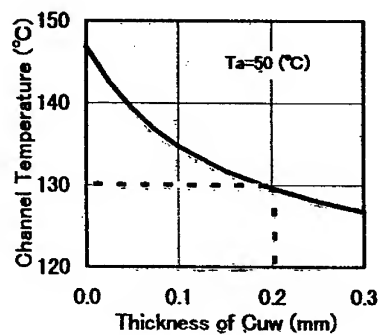


Fig. 4 Calculated Channel Temperature of the P-HJ-FET PA MMIC.

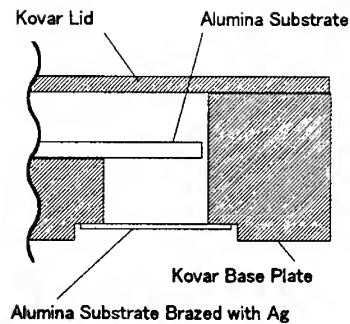


Fig. 5 Cross Sectional View of the Transducer.

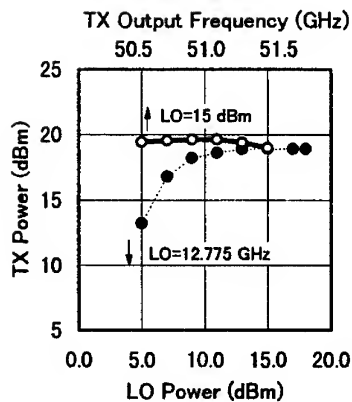


Fig. 6 TX Power as a Function of LO Power and Output Frequency.

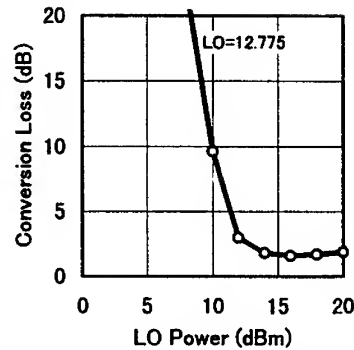


Fig. 7 Conversion Loss as a Function of LO Power.

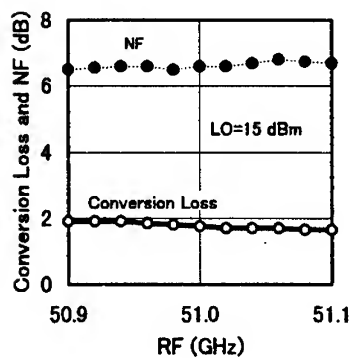


Fig. 8 Conversion Loss and NF as a Function of Frequency.

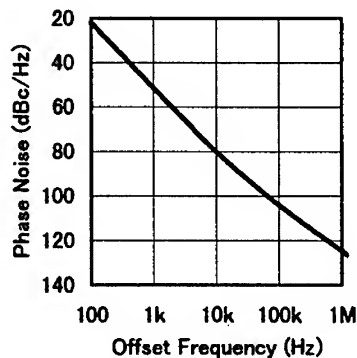


Fig. 9 Phase Noise of LO.

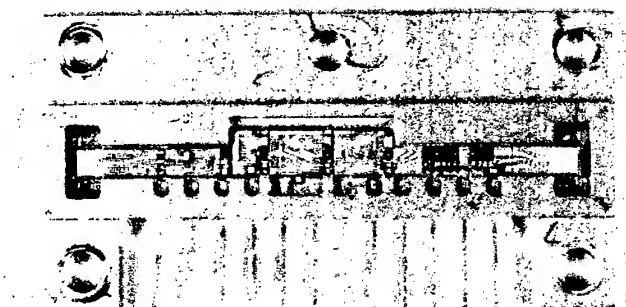


Fig. 10 Photograph of the T/R module.

MICRO-MACHINED GCPW RESONATORS AND FILTERS FOR APPLICATIONS AT MILLIMETRIC WAVE FREQUENCIES

S. J. Spiegel and Y. Nemirovsky¹

Rafael - Electronic Division Systems
P.O.Box. 2250, 31021, Haifa, Israel

¹Dept. of EE, Technion - Israel Institute of Technology
Technion City, 32000, Haifa, Israel

ABSTRACT

S-parameter results of 93Ω micro-machined ground coplanar waveguide resonators and filters at millimetric wave frequencies are presented. The loaded and unloaded quality factors are approximately 118 and 356 respectively at Ka-band. The GCPW resonators and filters were fabricated on a thin SiO_2 membrane (suspended membrane) over an air-cavity defined in the silicon wafer. The importance of micro-machined circuits is verified in low loss circuits at millimetric and sub-millimetric wave frequencies as filters and power combiners as well as oscillators with low phase noise spectrum.

1. INTRODUCTION

High performance and low cost transmission lines are required for applications at millimetric wave (MMW) and sub-millimetric wave (SMMW) frequencies. Modern military and civil communication systems demand, for instance, high-Q oscillators in order not to degrade the phase noise and high output power at MMW and SMMW frequencies. The first entails high-Q resonator circuit while the latter requires low loss combiners/splitters which can not be achieved with conventional substrates such as GaAs, Al_2O_3 and Duroid due to the high radiation and conductor losses at these frequencies. For applications at MMW and SMMW frequencies where the losses are a paramount issue, the solutions have been based on waveguides. In

practical terms, the choice between waveguides and printed circuits relies on a compromise between the size and the losses of a system.

Recently, millimetric and sub-millimetric waves planar transmission lines using micro-machining techniques have been demonstrated as a potential candidate for high performance transmission lines (1,2). Fig. 1 shows the cross-section of the micro-machined ground coplanar waveguide (GCPW) structure. The air-cavity under the thin membrane reduces the radiation and the dielectric losses as well as the dispersion (3). At MMW and SMMW frequencies, the radiation loss is an important, if not the dominant contributor to the overall loss of strip-like transmission lines printed on conventional substrates. The dielectric loss is negligible compared to the conductor and radiation losses for high resistivity substrates.

In this paper, the fabrication process and the measured results of several micro-machined GCPW resonators at frequencies above 30GHz are presented. The resonators were printed on a $200\mu\text{m}$ thick $\langle 100 \rangle$ -oriented silicon wafer. The characteristic impedance of the resonators is 93Ω . The micro-machined fabrication process can be integrated into MMIC circuits.

2. FABRICATION

The GCPW resonators and the coupled line filter of Fig. 2 were printed on a $200\mu\text{m}$ silicon wafer. A 5000Å layer of SiO_2 was thermally grown at 950°C by dry oxidation. Via-holes areas were

defined on the SiO₂ layer at front-side of the wafer by using photo-lithography techniques. The 5000Å SiO₂ layer was etched with B.O.E. - 13:2 mixture. The gold metal was electroplated on a sputter gold layer of 1000Å on the front-side surface of the wafer. The thickness of the gold layer equals 3µm is more than 6 times the skin depths at frequencies above 30GHz. A thin gold layer is first deposit on the wafer back-side. On the selected areas, i.e., the areas selected for the air-cavity, the gold layer was removed using Lift-off techniques. The wafer back side surface was then etched in a EDP solution. The anisotropic etching rate is 1.6µm/min. The 5000Å SiO₂ layer acts as etch stopper for the EDP. In order to avoid overetching, the depth of the air-cavity was constantly monitored. An angle of 57° was formed between the bottom plate and the air-cavity side walls, as shown in Fig. 1. The deposition of gold metal on the via-holes and on the cavity side walls was done through a thin metal mask attached to the back side of the wafer.

3. RESULTS

Figs. 3, 4 and 5 show the simulated insertion and return losses of the microstrip coupled line filter and the 93Ω GCPW resonators of Figs. 2a and b. The aspect ratio $s/(s+2w)$ of the GCPW resonators equals 0.389 ($s=318\mu\text{m}$ and $w=250\mu\text{m}$), where s and w are defined in Fig. 1. The gap between the feed lines and the $\lambda/2$ resonators equals 40µm. Table 1 summarizes the simulated values of the loaded (Q_L) and the unloaded (Q_U) quality factors of the resonators. Q_L and Q_U are expressed by (4,5)

$$Q_L = \left[\frac{w}{2(R+Z_o)} \frac{\partial X}{\partial w} \right]_{w=w_0} \quad (1)$$

$$Q_U = \frac{Q_L S_{21_{MAG}}}{1 - S_{21_{MAG}}} \quad (2)$$

where Z_o is the characteristic impedance, w_0 is the resonant frequency and $Z_{in}=R+jX$ is the series impedance. For high Q circuits, Q_L can also be expressed by (5)

$$Q_L = \frac{f_o}{BW_{3dB}} \quad (3)$$

where $f_o = w_0/2\pi$ and BW_{3dB} is the 3dB bandwidth.

The micro-machined GCPW lines presents an inherent higher the mechanical resistance in comparison with the micro-machined microstrip lines. The mechanical resistance of the membrane is increased in GCPW lines due to ground planes. i.e., the area of the SiO₂ membrane not covered by gold metal is smaller for GCPW than for microstrip lines.

4. CONCLUSIONS

Results of micro-machined GCPW resonators at millimetric wave frequencies were reported. The micro-machined resonators are potentially attractive to low phase noise MMIC oscillators at millimetric wave frequencies due to the easy fabrication process and the compatibility with the standard MMIC process.

ACKNOWLEDGE

The authors gratefully acknowledge the contribution of A. Shai to the processing and technology of fabrication.

5. REFERENCES

1. L.P.B. Katehi and G.M. Rebeiz, "Novel micromachined approaches to MMICs using low-parasitic, high-performance transmission media and environments" *IEEE Microwave Theory and Techniques Symposium Digest*, pp. 1145-1148, 1996.
2. H. Cheng, J.F. Whitaker, T.M. Weller and L.P.B. Katehi "Terahertz-bandwidth characteristics of coplanar transmission lines on low permittivity substrates" *IEEE Trans. Microwave Theory and Techniques*, vol. 42, no. 12, pp. 2399-2406, December 1994.

3. Z. Ma, A. Miyata and E. Yamashita, "Comparative studies of three types of coplanar waveguide structures for millimetric-wave applications" *European Microwave Conference*, pp. 986-990, 9-12 September 1996.
4. C. Chi and G. M. Rebeiz, "Conductor-loss limited stripline resonator and filters" *IEEE Trans. Microwave Theory and Techniques*, vol. 44, no. 4, pp. 626-630, April 1996.
5. J.M. Drozd and W.T. Jones, "Determining Q using S parameter data", *IEEE Trans. Microwave Theory and Techniques*, vol. 44, no. 11, pp. 2123-2127, Nov. 1996.

applications" *European Microwave Conference*, pp. 986-990, 9-12 September 1996.

Table 1: Simulated values of the loded and unloaded quality factors of GCPW resonators

	Frequency	Length	Simulated	
			Loaded-Q	Unloaded-Q
Resonator 1	28.096 GHz	5000 μm	211	315
Resonator 2	30.410 GHz	4600 μm	183	335
Resonator 3	33.126 GHz	4200 μm	134	310
Resonator 4	36.365 GHz	3800 μm	118	356
Resonator 5	45.210 GHz	3000 μm	89	706

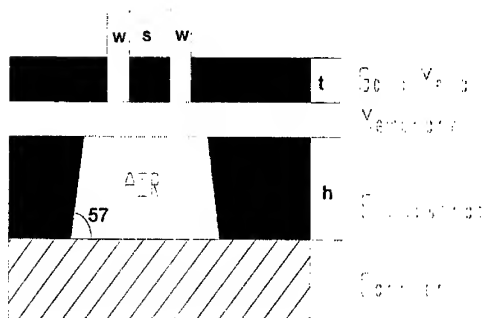


Fig. 1- Cross-section of the micro-machined GCPW structure

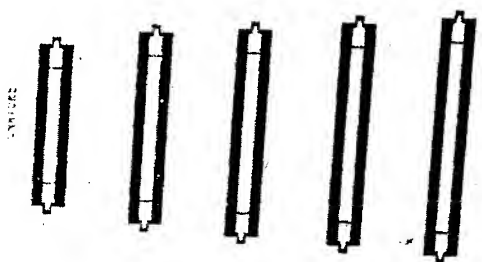


Fig. 2a - Microphotograph of the GCPW resonators.

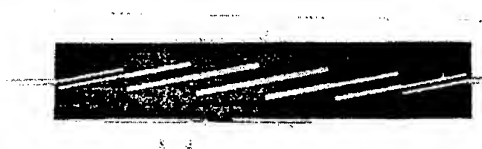
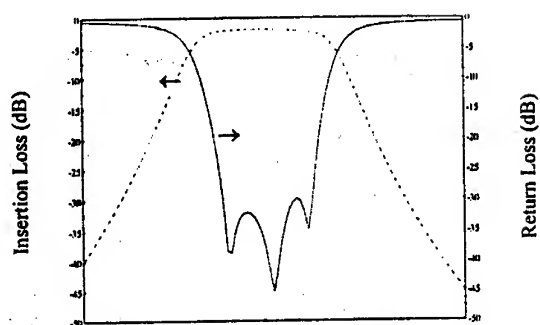


Fig. 2b - Microphotograph of the microstrip coupled line filters.



Ka - Band

Fig. 3 - Insertion and return losses of the Ka-band micro-machined coupled line filter.

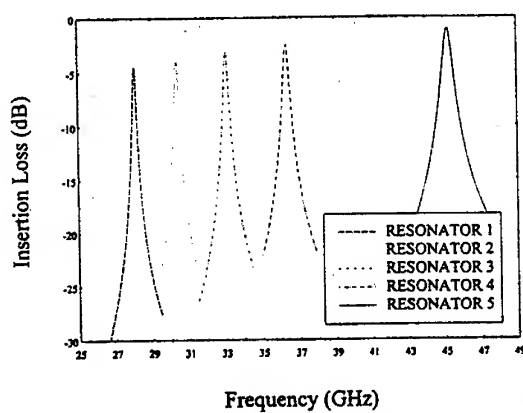


Fig. 4 - Insertion loss of GCPW resonators.

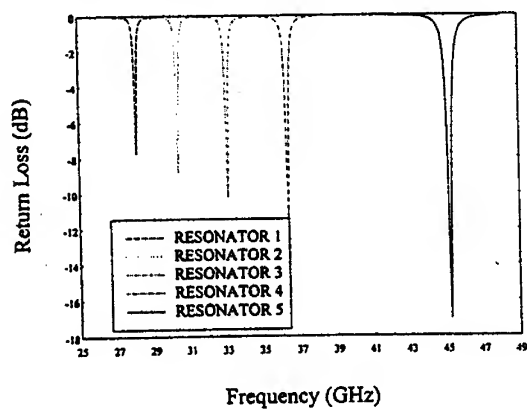


Fig. 5 - Return loss of GCPW resonators.

Wideband Indoor Radio Channel Measurements at 5.3 GHz

Jarmo Kivinen, Pertti Vainikainen
Helsinki University of Technology,
IRC / Radio Laboratory, P.O. Box 3000, FIN-02105 HUT, Finland

ABSTRACT

This paper describes a wideband radio channel complex impulse response measurement system with 5.3 GHz carrier frequency. The sounder uses crosscorrelation method. The first measurements have been performed using sliding correlator principle. Delay resolution of 20 ns and dynamic ranges over 25 dB have been achieved for the wideband impulse response measurement. Statistical radio channel parameters, like rms delay spread and pathloss for an office environment have been measured for empirical radio channel characterization purposes.

1 INTRODUCTION

There has been a rapid increase in radiocommunications area during the last decade. Several mobile phone systems are available and new systems are developed using high data rates and, therefore, larger bandwidths are required. Radio channel modeling is needed for system design. Empirical channel models use statistical characterization of the channel. Rms delay spread is the critical parameter when the high bit-rate radio LAN systems are designed. HIPERLAN (High Performance Local Area Network) has 23.5294 Mbit/s capacity in asynchronous mode. Therefore, rms delay spread values of the indoor radio channel are critical for the system reliability together with the pathloss values. The delay dispersion of the received signal can be compensated by means of adaptive equalisation to some extent [1]. Propagation simulations with ray-tracing algorithms are generally used in channel modeling (e.g. [1]). In the simulations, simplifying assumptions about propagation environment have to be made, and therefore propagation measurements have to be performed. Measurements with 5.3 GHz carrier frequency and 53.85 MHz 3 dB signal bandwidth are suitable for modeling of the 5.1–5.25 GHz HIPERLAN propagation environment.

2 IMPLEMENTATION OF THE MEASUREMENT SYSTEM

In this paper, the wideband radio channel has been measured at 5.3 GHz using a wideband channel sounder [2], which was developed at the Institute of the Radio Communications at the Helsinki University of Technology. The block diagram of the 5.3 GHz extension of the system is given in Figure 1. In the transmitter of the sounder, a pseudonoise sequence with 53.85 MHz chip frequency f_{chip} modulates the 5.3 GHz carrier signal. In the receiver, the crosscorrelation $R_{xs}(\tau)$ between the received signal and the replica of the original sequence is obtained yielding the channel complex impulse response (IR) $h_{ch}(\tau)$ the following way:

$$R_{xs}(\tau) = h_{ch}(\tau) \otimes h_{sys}(\tau) \otimes R_x(\tau), \quad (1)$$

where $h_{sys}(\tau)$ is the measurement system impulse response and $R_x(\tau)$ the autocorrelation of the used waveform. The dynamic range and delay resolution of the IR measurement are dictated by the autocorrelation properties of the signal. For m-sequences of length L , dynamic range $D=20\log L$ and resolution $\Delta\tau=1/f_{chip}$ are the given limits [2], though it is stated that delay resolution can be improved by measurement data post processing [3]. In that case, the delay resolution is seen to be limited to the reciprocal of the measurement system bandwidth, i.e. by $h_{sys}(\tau)$.

The sliding correlator (SC) detector presented in [4] is used in the measurements presented in this paper. In the SC, the replica has a slightly slower chip rate, which results in bandwidth compression eliminating the need for rapid A/D-conversion of the wideband signal. In the sliding correlator measurements, the difference between the clock frequencies deteriorates the dynamic range. Typical dynamic range achieved with the SCs is usually about 25 dB. To verify the dynamic range of the measurement with the delay/bandwidth scaling factor $K=2154$, the measured setup was tested in an anechoic chamber. The resulting impulse response is shown in Figure 2a. The 3 dB width of the IR is about 20 ns and the spurious-free dynamic range is over 25 dB. Each measured IR component is a time average over coherent integration time in the crosscorrelation process, which is given by K/f_{chip} .

Antennas used in the measurements were omnidirectional vertically polarized disc antennas. The measured gain of these antennas is 1.3 dB and the 3 dB beamwidth in the vertical plane is 108°. The measured radiation patterns in vertical plane including the co- and crosspolarisations of the disc antenna are shown in Figure 2b.

The automatic gain control, which is realized by three digital step attenuator stages, allows pathloss measurements with ± 1 dB uncertainty. In this paper, antenna gains are included in the announced pathloss results, i.e. the antennas are seen as parts of the propagation channel.

The pathloss calibration is done by connecting the TX and RX with a cable and an attenuator. To estimate the link budget, the thermal noise is assumed to be Gaussian distributed with variance σ^2 , and it is accepted that a noise peak is detected as a signal component with 0.1 % probability, which equals to 3σ . With this assumption the transmitted power +30 dBm and the receiver 3 dB noise figure give maximum EIRP pathloss of 113 dB with 25 dB IR dynamic. In this pathloss value the coherent integration in the crosscorrelation process is included. It is estimated to give +27 dB processing gain. To evaluate the range of the measurement system tentatively in indoor environment, the log-distance path loss model can be used [5]. Assuming path loss exponent value 4, free space propagation to distance of 5 m and pathloss peak to peak variation of 20 dB only 63 m range is given, although free space pathloss gives 2.5 km range.

3 INDOOR PROPAGATION MEASUREMENTS

The measurements were performed at the Department of Electrical and Communications Engineering at Helsinki University of Technology. The floor plan of the location is shown in Figure 3. Measurements were done in the corridors and in the rooms. The corridor measurements were continuous, the receiver was moving with 0.35 m/s average speed. The main parameters of these measurements are given in Table 1.

The measured time-variant complex impulse response $h(t, \tau)$ is expressed the following way:

$$h(t, \tau) = \sum_i h_i(t) \delta(\tau - \tau_i(t)) \quad (2)$$

where h_i is the complex amplitude of a signal arriving via discrete propagation path which has an excess delay τ_i . The rms delay spread S , which affects on the maximum capacity of uncompensated and uncoded channel [6, 7], is defined as:

$$S = \sqrt{\frac{\sum_{k=1}^M (\tau_k - D)^2 |h(\tau_k)|^2}{\sum_{k=1}^M |h(\tau_k)|^2}} \quad (3)$$

where D is the average delay of the power delay profile (PDP):

$$D = \frac{\sum_{k=1}^M \tau_k |h(\tau_k)|^2}{\sum_{k=1}^M |h(\tau_k)|^2} \quad (4)$$

It should be noted that the measured rms delay spread depends on the dynamic range of the IR. In the statistical analysis of the rms delay spread along a track with thousands of samples the dynamic range had to be reduced to 20 dB to prevent system noise peaks to be interpreted as signal components. This may happen when many equally strong distinguishable propagation paths exist in the channel. By assuming exponentially decaying PDP, it can be calculated that 20 dB dynamic range gives 11 % smaller measured rms delay spread values than actual. By summing large amounts of IR's to a single PDP, it was deduced that our measurement environment obeys the exponential law statistically. Therefore the measured statistical values of rms delay spread presented are considered smaller than what e.g. corresponding simulations with actually infinite dynamic range would give. The minimum measurable rms delay spread is 7 ns with described measurement setup. This is basically caused by the bandwidth limitation of the signal.

The Fourier transform of (2) is the delay-Doppler function [8]. Thus the delay-Doppler spectrum $X(\tau, \nu)$ of successive IR's measured at period T can be written as:

$$X(\tau, \nu) = \left| \int_{t-\frac{T}{2}}^{t+\frac{T}{2}} h_i(t, \tau) e^{-j2\pi\nu\tau} d\tau \right|^2, \quad (5)$$

where ν denotes the Doppler frequency. Generally the Doppler spectrum information is included in the digital radio system simulations. The Doppler shift can be considered to have a negligible effect on the performance of the HIPERLAN system, when the moving speed is relatively slow. This holds if the change of a propagation path in wavelengths is small during a data packet transmission time. The Doppler domain can also be used to create a synthetic aperture to locate individual scatterers. The resolution in the Doppler domain $\Delta\nu$ is the reciprocal of the integration time T :

$$\Delta\nu = \frac{1}{T}. \quad (6)$$

The uncertainty of the Doppler frequency measurement σ_ν is determined by the Allan variance σ_y^2 of the primary standard the following way:

$$\sigma_\nu(T) = \sqrt{2} \cdot f_c \cdot \sigma_y(T), \quad (7)$$

where f_c denotes the carrier frequency and the $\sqrt{2}$ is for the quadratic summing of the TX and RX primary standards. The $\sigma_y(T)$ is announced $3 \cdot 10^{-11} \cdot \sqrt{T}^{-1}$ for each primary standard, giving 0.22 Hz std for 1 s successive sets of IR's in equation (7). Thus, in practice, integration times of a few seconds only can be used in equation (5). The longer integration time causes the measurement uncertainty to be greater than the resolution.

It is obvious that the equations for optimum integration time T in (5) can be derived for having maximum angular resolution. The accurate solution is beyond the scope of this paper. In these measurements, 24 IR's at maximum is transformed in one set which is estimated to give 17° angular resolution when the location of the scatterer is perpendicular to the direction of motion. It must be noted that the direction of arrival is ambiguous, and that in indoor environment the ambiguity is three-dimensional. Therefore the resolved angle tells only the angular deviation from the direction of motion.

4 THE MEASUREMENT RESULTS

The absolute value of a typical impulse response of the channel in the northern corridor is presented in Figure 4a. Here the transmitter is TX1 in Figure 3, and the receiver RX1 moves along the corridor towards the TX1. In the measurement of Figure 4a, the RX1 is situated 10 m from the north end of the corridor. The size of the corridor was $31 \cdot 2.0 \cdot 2.2 \text{ m}^3$ ($l \cdot w \cdot h$). The sidewalls were made of brick, the floor was concrete covered with linoleum floor tiles and the ceiling was concrete covered with various metal structures. The north end of the corridor was a glass window and the south end a fire door (glass with wire mesh with 13 mm grid). In this simple case, the scatterers causing the impulse response components can be easily traced. The first component ($\tau=20 \text{ ns}$) is the line of sight signal (LOS). The next peak ($\tau=90 \text{ ns}$) is the reflection from the window at the end of the corridor. This is confirmed by the Doppler analysis of the subsequent IR's (Figure 4b): the direction of arrival of this signal is opposite to that of the LOS signal. The third ($\tau=130 \text{ ns}$) component is the backlobe of the TX, caused by objects outside of the corridor itself, and fourth ($\tau=230 \text{ ns}$) component is the twice reflected signal. The fifth ($\tau=300 \text{ ns}$) component is reflected three times from the corridor ends.

The LOS signal fades very abruptly along the corridor. The peak to peak variation of the LOS component was 25 dB with average over 12 samples ($\approx 0.15 \text{ m}$) analyzed from IR's with TX and RX distances 16–30 m. This causes also large variations in the rms delay spread. It can be concluded from the parallel and perpendicular reflection coefficients that the fading is mainly caused by the reflections from the walls, the floor and the ceiling. These reflections can not be resolved with the current measurement setup. The later signal components are not fading so steeply. They seem to decay exponentially relative to the distance from the reflection end, which implies that the propagation of reflected signals in the corridor is analogous to waveguide structures. The attenuation constant is estimated to be 0.3 dB/m in this case.

The rms delay spread along the corridor evaluated from the envelope of $|h(\tau)|$ and its cumulative distribution function (CDF) are presented in Figures 5a and 5b. The total number of IR's analyzed was 1500. The median value of about 20 ns can be evaluated, and 90 % of the values are less than 44 ns. The use of the envelope de-emphasizes weak paths compared to simulations with the same dynamic range, where the length of each IR component is limited by Dirac function as in Equation (2). Figure 6 shows the received power vs RX and TX distance in the corridor. Here the relative received power is the power sum of all received signal components exceeding the 20 dB dynamic of the measurement. The scatterplot of Figure 7 describes the received power vs. rms delay spread

which as expected are correlated. This happens because the large delay spread values result from the fading of the LOS signal. From this kind of figure bit error rates or outage estimates for the radio relay could be deduced as in reference [1].

In total, measurements were performed in various corridors and rooms (34 separate measurements) of the environment. Rms delay spread median values were in all measurement sets between 12–25 ns, the 90 % values of the CDF 28–44 ns and the largest rms delay spreads were near 70 ns. In the rooms, the rms delay spread seemed to be dependent on the room size. In some cases propagation paths existed outside of the building which is easily understood from Figure 3. A summary of the measured rms delay spread values is presented in Table 2.

6 CONCLUSIONS

In this paper, a measurement system for evaluating wideband radio system performance at 5.3 GHz frequency range is presented. Measurements can be done for moderate ranges with reasonable TX power, and no cable connection between RX and TX is needed. Some of the first measurement results are given. The rms delay spread values are more than 50 % smaller than has been published using simulations only [1], although the measurement errors caused by limited dynamic range are taken into account. This can be explained as well by the difference of the environments as by limited accuracy of modeling assumptions in simulations. It is shown, that the measurement device described is capable of providing information required in predicting wideband radio system performance in various environments. Obviously the results are useful for radio system design.

REFERENCES

- [1] A. R. Nix, G. E. Athanasiadou, J. P. McGeehan, "Predicted HIPERLAN Coverage and Outage Performance at 5.2 and 17 GHz Using Indoor 3-D Ray-Tracing Techniques," *Wireless Personal Communications*, 1996, no. 3, pp. 365-388.
- [2] J. Kivinen, T. Korhonen, J. Hubach, P. Vainikainen, "Fast sounding of broadband radio channel at 2 GHz frequency range," *Proceedings of the Nordic Radio Symposium 1995*, 24-27 April 1995, Saltsjöbaden, Sweden, pp. 121-126.
- [3] T. Manabe, H. Takai, "Superresolution of Multipath Delay Profiles Measured by PN Correlation Method," *IEEE Transactions on Antennas and Propagation*, vol. 40, no. 5, May 1992, pp. 500-509.
- [4] D. C. Cox, "Delay Doppler Characteristics of Multipath Propagation at 910 MHz in a Suburban Mobile Radio Environment," *IEEE Transactions on Antennas and Propagation*, vol. 20, no. 5, September 1972, pp. 625-635.
- [5] T. S. Rappaport, "Wireless Communications," Prentice Hall Inc., Upper Saddle River, NJ, 1996, 641 p.
- [6] J. C-I. Chuang, "The Effects of Time Delay Spread on Portable Radio Communications Channels with Digital Modulation," *IEEE Journal on Selected Areas in Communications*, vol. 5, no. 5, June 1987, pp. 879-889.
- [7] Yue Chen, J. C-I. Chuang, "The Effects of Time Delay Spread on Unequalized TCM in a Portable Radio Environment," *IEEE Transactions on Vehicular Technology*, vol. 46, no. 2, May 1997, pp. 375-380.
- [8] P. A. Bello, "Characterization of randomly time-variant linear channels," *IEEE Transactions on Communication Systems*, vol 11, Dec. 1963, pp. 360-393.

Table 1. Main parameters of the corridor measurements.

average velocity	0.35 m/s
average Doppler range	±6 Hz
IR dynamic range	20 dB
recorded IR's/second	24.4
recorded IR's/wavelength	4
measured delay window	1 µs
samples/delay window	205
antenna heights	1.8 m

Table 2. Summary of the measured rms delay spreads.

transmitter	receiver	number of IRS	CDF(50 %)	CDF(90%)
TX1	RX1	1500	20 ns	44 ns
TX2	RX2	1300	12 ns	28 ns
TX2	RX2'	2000	25 ns	40 ns
TX1, TX2	ROOMS1-10	34	22 ns	34 ns

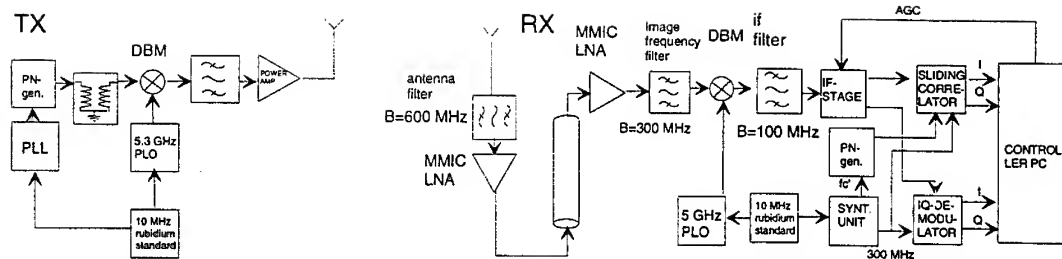


Figure 1. Block diagram of the 5.3 GHz measurement system. In the receiver, two options are included: the sliding correlator and DSP receiver, in which the received signal is downconverted to the baseband and sampled with 2·125 Ms/s sample rate.

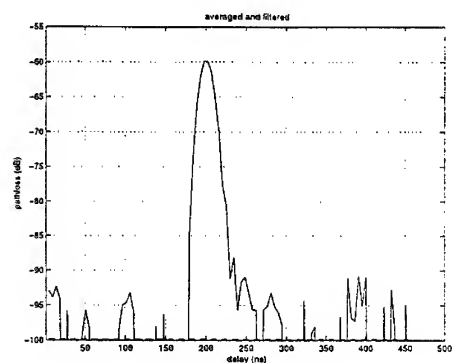


Figure 2a. The measurement system response in the anechoic chamber. The distance between transmitter and receiver was 5.7 m.

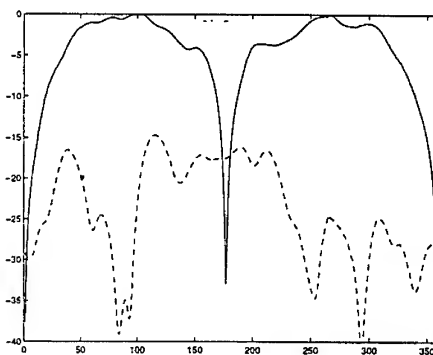


Figure 2b. Measurement antenna direction patterns in the vertical plane with co- and crosspolarisations.

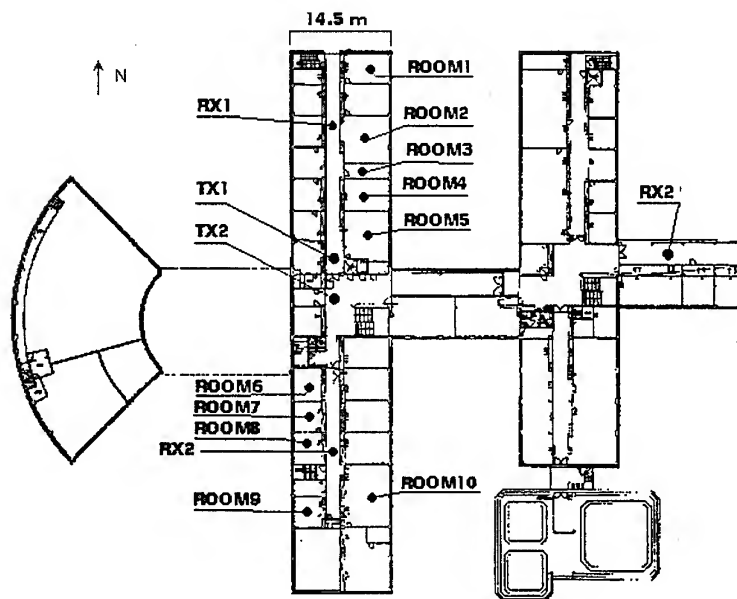


Figure 3. The floor plan of the measurement site (3rd floor).

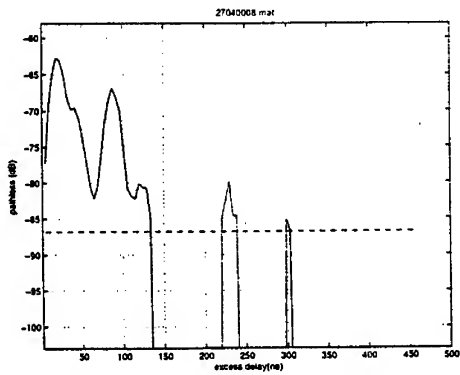


Figure 4a. Typical impulse response amplitude in the north corridor. The dotted line is the smallest detectable signal of the measurement. Rms delay spread is 36 ns.

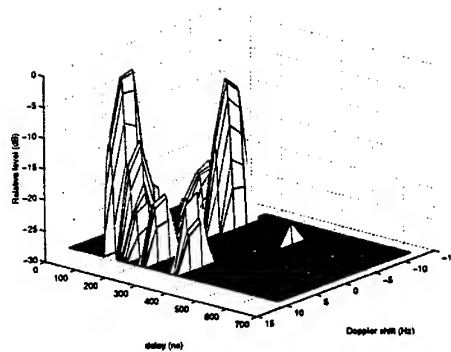


Figure 4b. The delay-Doppler spectrum integrated from 12 successive IR's.

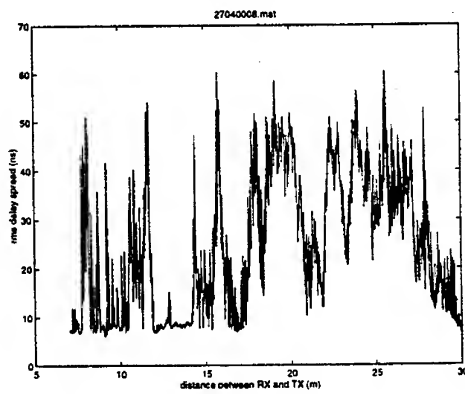


Figure 5a. The rms delay spread vs RX and TX distance in the north corridor.

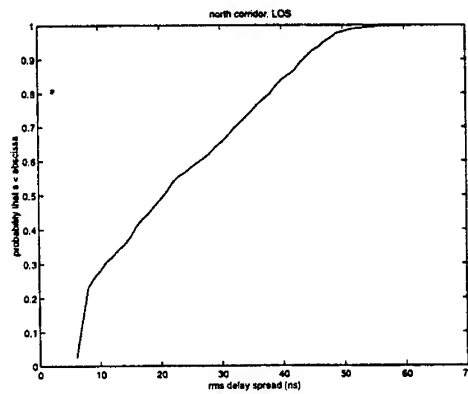


Figure 5b. The CDF of the rms delay spread in the north corridor.

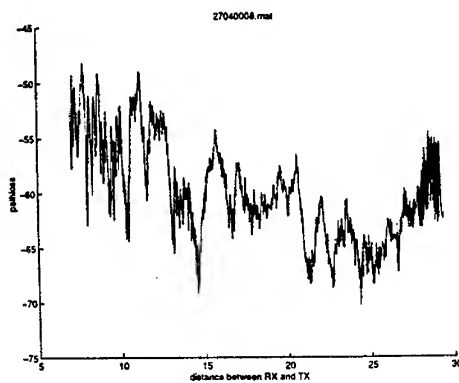


Figure 6a. Received power relative to transmitted power vs RX and TX distance in the north corridor.

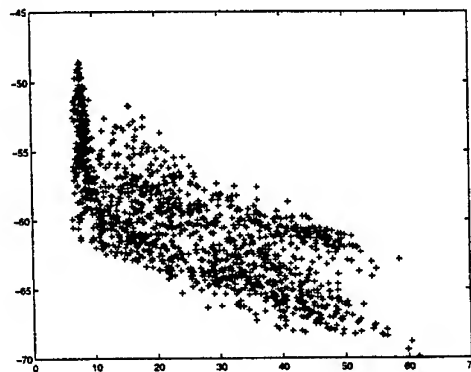


Figure 6b. Received power vs rms delay spread.

Time Domain Antenna Measurements: Implementation and Verification of a Novel Technique

R. V. de Jongh, M. Hajian, L. P. Ligthart

Delft University of Technology, Department of Electrical Engineering
International Research Centre for Telecommunications-transmission and Radar (IRCTR)
Mekelweg 4, 2628 CD Delft, The Netherlands
Phone: +31-15-2782496 Fax: +31-15-2782496
E-mail: R.V.deJongh@et.tudelft.nl

Abstract

The results of an experimental study in which time domain pulses are used to measure the far-field characteristics of an antenna are presented. Pulses with duration and rise times in the order of 50 ps are generated in order to characterize the behavior of an antenna in the frequency range 1-18 GHz. An X-band Standard Gain Horn (SGH) has been used to verify the overall performance of the measurement system. An excellent agreement between the time domain and the frequency domain measurements has been observed. This novel antenna measurement technique offers advantages over the traditional techniques for wideband measurements in frequency domain in reducing the measurement time and has great potentials. The paper describes the Antenna Time Domain Measurement (ATDM) system, including the potentials of time gating and summarizes the error sources, advantages and disadvantages of such a measurement technique.

I. Introduction

The increasing demanding performance required of today's antennas necessitate higher accuracy measurement techniques. Much attention has been given to the far- and near-field antenna measurements in the frequency domain. A new approach in antenna measurements is to determine the antenna characteristics in the time domain. Recently, the Antenna Time Domain Measurement (ATDM) technique has received considerable attention, Miller (1), Hansen, Yaghjian (2,3) and Dominek, Shamansky (4). The work described herein is motivated by the fact that the measurement times associated with conventional frequency domain techniques can be excessively long for electrically large and or sophisticated antennas, phased array antennas, and multi-beam antennas in radar. Such antenna systems have to be tested over the whole frequency band. Dramatic reduction in duration of antenna measurements can be achieved by using ATDM. The ATDM method enables the use of new error correction algorithms to increase the accuracy in antenna measurements. Also for antenna diagnosis can the ATDM technique become advantageous. The ATDM set-up incorporates a pulse generator, a sampling oscilloscope and a sampling unit. The Antenna Under Test (AUT) is excited with a short time pulse and the probe output signal is registered and processed to obtain the antenna characteristics over a broad bandwidth. This paper presents an introduction to the method, and discusses the unique hardware implementation at IRCTR.

II. Advantages and disadvantages of ATDM

The ATDM technique offers advantages over the classical antenna measurement technique in the frequency domain. The main advantages of ATDM are:

- **Direct gating:** A source of error in antenna measurements are reflections. Reflections are caused by mismatching and reflections of walls and nearby objects. These reflections are separated in time from the direct antenna signal and can thus be removed using time domain gating. The time gating in ATDM is applied directly upon each signal (figure 1).
- **Reduction of measurement time:** The frequency response of an antenna, including gating, can be determined from a single measurement. Dramatic reduction factors in

measurement time can be achieved for wide-band antennas, especially for time consuming measurements like near-field scanning.

- **Removal of scan plane errors in near-field measurements:** In planar near-field measurements a scan plane with finite size is used. This results in a scan plane error. Hansen and Yaghjian (2,3) have shown that the scan plane error can be removed by using time gating.
- **Simple measurement set-up:** ATDM is less complex than comparable frequency domain equipment and therefore commercially attractive.
- **Antenna diagnosis:** The performance of the antenna can be analyzed using the time response of the antenna. Reflections inside the antenna network can be easily observed from the measured time response. This feature of ATDM can be used in antenna diagnosis.

The main disadvantage of the ATDM method is:

- **Reduction in S/N for higher frequencies:** The spectrum of the measurement pulse decays with frequency, while the noise level remains constant. The resulting reduction of S/N ratio causes a lower measurement accuracy on higher frequencies.

III. Basic principles of time domain antenna measurements

The AUT is excited with short duration time pulses. Two important aspects of these pulse signals in antenna measurements are the pulse spectrum and pulse energy. The pulse spectrum determines the distribution of the energy of the time signal over each individual spectral component. The S/N ratio of spectral components is directly proportional to the energy of each component. The larger the S/N ratio, the more accurate are the measurements. The pulse energy and the pulse spectrum are related to the pulse signal by the following equations.

$$E_p = \int_{-\infty}^{\infty} |p(t)|^2 dt \quad (1)$$

$$P(f) = \int_{-\infty}^{\infty} p(t) e^{-j2\pi ft} dt \quad (2)$$

For short time pulses, the pulse energy is distributed over a large number of frequency components. In order to obtain sufficient energy per spectral component, the amplitude of the pulse should be increased. For pulse generators it is observed that maximum amplitude and minimum pulse width is a contradictory demand. A trade-off in the set-up is required.

The time domain antenna response is measured directly at the output of the probe antenna. To measure the high frequency signal, a stroboscopic receiver is used.

IV. Error sources in ATDM

For antenna measurements the error budget is important. By introducing a new technique, knowledge on the dominant error sources is required. This section overviews the error sources specific in ATDM. The error sources in the time domain measurements are divided into two groups: the short-term and long-term error sources.

Short-term error sources: These fast variations are uncorrelated from one measurement to another. Three types of short-term error sources can be distinguished in ATDM; thermal noise, jitter and quantization noise. Only jitter is discussed here, because this error source is specific for ATDM. Jitter is the non-deterministic variation in sample position. The time error distribution is considered to be Gaussian. If the signal slope is locally constant, then the voltage error distribution is simply the jitter distribution times the slope. In this case the

voltage error is also Gaussian. If the slope is not constant, then the analysis of the errors caused by the jitter is more complicated, Rahman, Sarkar (5) and Gans (6).

Long-term error sources: Long-term variations are due to changes in the position and shape of the measurement pulse. These long term variations are mainly caused by effects of the measurement environment and imperfections in the system. The variations in the pulse shape result in amplitude variations. The variations in the pulse position ('drift') result in phase errors. Long-term variations can be corrected using a reference signal.

V. Practical measurement set-up

In the IRCTR laboratory there is a moderately sized anechoic chamber called DUCAT (Delft University Chamber for Antenna Tests). DUCAT has over the years successfully been used for far-field measurements of electrical small antennas, near-field measurements of electrical large antennas and radar cross section measurements. The standard measurement equipment in DUCAT consists of an HP 8510B network analyzer, an HP 8341 B synthesized sweeper (RF source), and an HP 8350/HP 83592 B sweep oscillator (LO source). This equipment is controlled by an HP 9000/320 computer.

The time domain measurement system K2-63 has been developed and integrated in DUCAT in a cooperative project between RTI, Moscow and IRCTR. The DUCAT-ATDM system is shown in figure 2 and consists of the K2-63-1 sampling oscilloscope, the K2-63-2 pulse generator and the K2-63-3 sampling unit. The main characteristics of the equipment are given in table 1 and 2.

VI. Measurement results

To demonstrate the characteristics of the ATDM equipment, the far field radiation patterns of an X-band Standard Gain Horn were measured and compared with measurements using the standard frequency domain equipment.

The pulse shown in figure 3 excites the linear polarized SGH. The transmitted signal is received by a second (identical) SGH and recorded with the sampling oscilloscope. The separation between the two SGH is approximately 3.5 m (sufficient for the antenna far-field). In figure 4 the time domain antenna response on the main axis is shown. The antenna response is determined with 1024 samples and a sampling time of 4.0 ps. The time response is averaged over 256 observations.

For the main axis signal, the S/N ratio of this particular set-up is measured and shown in figure 5. The S/N ratio is determined from the statistical properties of 100 consecutive measurements. The frequency spectrum is determined using a DFT transformation of the time signal. The DC offset of the pulse is compensated and a raised cosine windowing function is used. The S/N ratio is an indication for the measurement accuracy of the SGH patterns in X-band for this particular measurement set-up.

To determine the radiation patterns, the AUT is rotated from -90° to $+90^\circ$ with a step size of 1.0° . In each rotation point a 1024 point time signal is measured with a sampling time of 4.0ps and an averaging of 256. To compare the time domain measurements with the frequency domain the signal is transferred to the frequency domain using a DFT transformation. The DC-offset of the signal is compensated and a raised cosine windowing function is used. Figures 6 and 7 compare the results of the time domain measurements with CW measurements done with the HP equipment. Comparison patterns of the SGH at 11.23 GHz, in *E*-plane and *H*-plane, are shown respectively. Note that the time and frequency domain measurements are done on consecutive days for an identical antenna set-up.

VII. Conclusions

A novel customized antenna time domain measurement technique has been presented as an alternative to the classical frequency domain techniques. This configuration is practical, accurate, uses less equipment, less time for measurement over a wide frequency band, and is capable of measuring the antenna patterns in the far- and near-field. This paper is an introduction to the ATDM far-field measurement concept, including the unique hardware implementation at IRCTR and, what is most important, it shows measured results. An SGH in X-band was used to check the overall performance of the system. Direct comparison with a traditional frequency domain measurement yielded excellent agreement for each frequency component. In future, the near-field time domain measurement technique will be implemented.

VIII. References

- [1] E.K. Miller, 'Time-Domain Measurements in Electromagnetics', Van Nostrand Reinhold Company, New York, 1986.
- [2] T.B. Hansen, A.D. Yaghjian, 'Planar Near-field Scanning in the Time Domain, Part 1: Formulation', IEEE Transactions on Antennas and Propagation, Vol. 42, No.9, September 1994.
- [3] T.B. Hansen, A.D. Yaghjian, 'Planar Near-field Scanning in the Time Domain, Part 2: Sampling Theorems and Computation Schemes', IEEE Transactions on Antennas and Propagation, Vol. 42, No.9, September 1994.
- [4] A. Dominek, H. Shamansky, 'Planar, Time Domain, Near-Field Scanning Measurements', 1996 AMTA Conference, pp. 92-96, Seattle, Washington, USA, 1996.
- [5] J. Rahman, T.K. Sarkar, 'Deconvolution and Total Least Squares in Finding the Impulse Response of an Electromagnetic System from Measured Data', IEEE Trans. on Antennas and Propagation, Vol 43, No. 4, pp 416-421, April 1995.
- [6] W.L. Gans, 'The Measurement and Deconvolution of Time Jitter in Equivalent-Time Waveform Samplers', IEEE Trans. on Instrumentation and Measurement, Vol IM-32, No. 1, pp 126-133, March 1983.

List of figures:

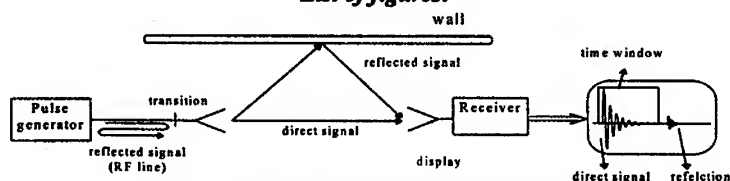


Figure 1: The application of time gating in ATDM

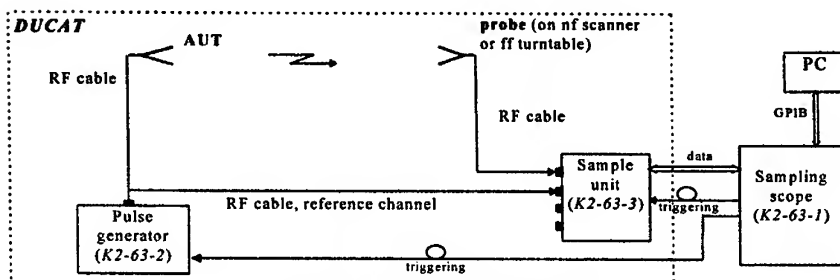


Figure 2: ATDM set-up in DUCAT

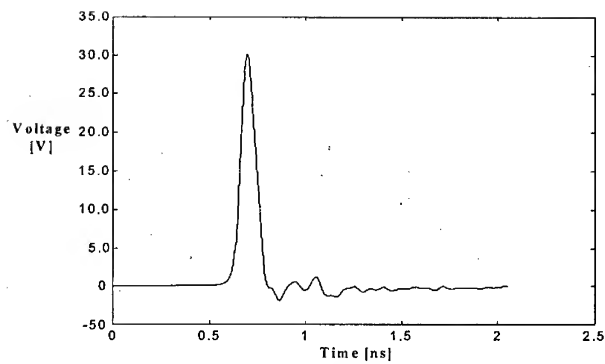


Figure 3: Time signal delta pulse with shaper 1

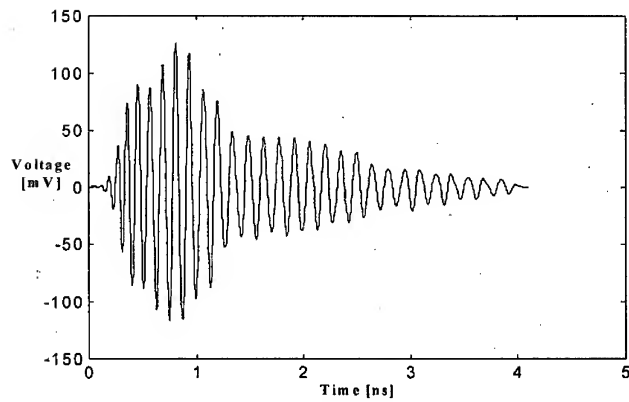


Figure 4: The time domain response of the SGH

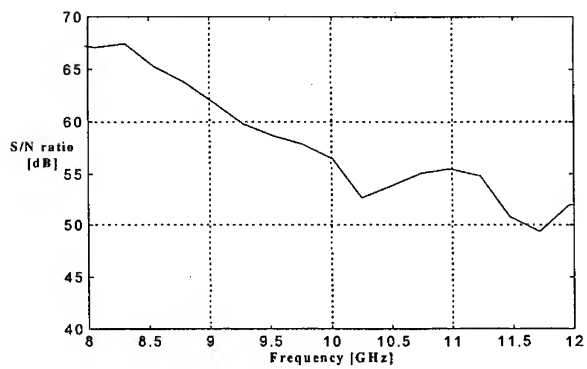


Figure 5: The S/N ratio of the antenna response

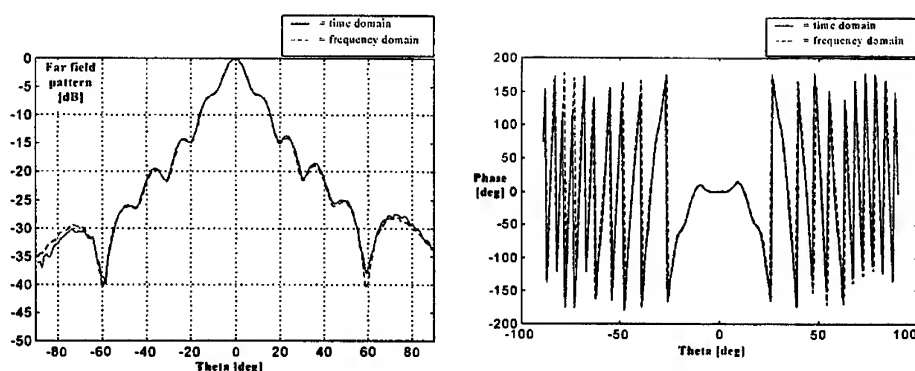


Figure 6: Comparison far-field pattern for a time and frequency domain measurement at 11.23 GHz; E-plane

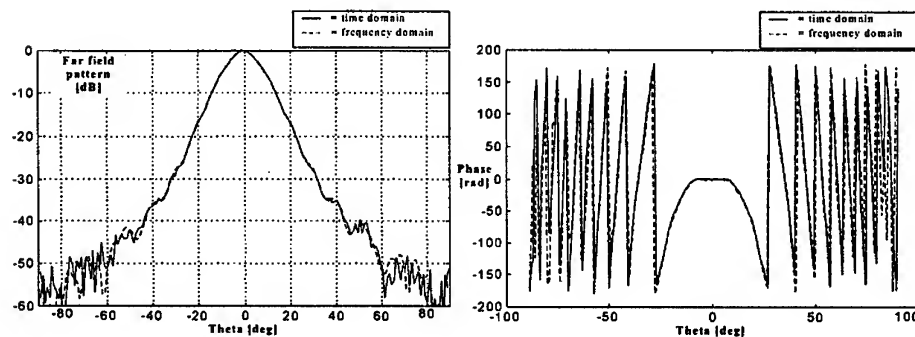


Figure 7: Comparison far-field pattern for a time and frequency domain measurement at 11.23 GHz; H-plane

List of tables

Table 1: Characteristics sampling oscilloscope

Parameter	Value
Number of channels	4
Bandwidth	2 x(1+6 GHz) 2 x(1+18 GHz)
Noise (RMS)	≤ 1.0 mV (1+6 GHz) ≤ 4.0 mV (1+18 GHz)
Max. input voltage	± 1.0 V
Measurement accuracy	$\pm(0.02 V_x + 0.002)$ V
A/D converter	12 bits
Number of samples	256, 512, 1024, 2048
Max. averaging	256
Minimum sampling time	0.1 ps
Jitter	≤ 2.0 ps
Measurement range	10.0 ps \div 10 μ s

Table 2: Characteristics pulse generator

Parameter	Value
Type 1 ('step pulse')	
Amplitude (controllable)	15+30 V
10%-90% rise time	60 ps
Type 2 ('block pulse')	
Amplitude	40 V
50% pulse width	190 ps
Type 3 ('delta pulse'+shaper 1)	
Amplitude	30 V
50% pulse width	85 ps
Type 4 ('block pulse'+shaper 2)	
Amplitude	-5 V
50% pulse width	30 ps
Pulse repetition rate	10 \div 100 kHz

A MILLIMETER-WAVE FREQUENCY EXTENDER FOR MICROWAVE NETWORK-ANALYZERS

B. Geck, J. Marquardt
Institut für Hochfrequenztechnik, University of Hannover
Appelstr. 9A, 30167 Hannover, Germany
Tel.: #49 511 762 5163, FAX #49 511 762 4010
E-Mail: geck@mbox.hft.uni-hannover.de

ABSTRACT

A new principle of a mm-wave frequency extender, suitable for commercial available network analyzers, is presented and the main features of the modified network analyzer are discussed. A system realization in W-band is described. The system performance is proved by measurements in the frequency range 89-100 GHz.

INTRODUCTION

The increasing industrial interest into the use of mm-wave systems for communication and sensor applications results in an increasing demand for measurement equipment in this frequency range. Unfortunately, complex measurement systems which operate in the mm-wave range, for example network analyzers (NA), are very expensive. In the past some alternative, low cost network analyzer systems like homodyne NA presented by Geck and Marquardt [1] or sixport systems published by Neumeyer [2] have been developed, but no commercial success of such systems is known. On the other hand in most laboratories a NA covering the microwave range already exists. In 1985 Hartmann [3] presented a W-band frequency extension for a NA but due to the analog NA this system was rather complicated and no full two port error correction was possible.

With the frequency extender (FE) presented in this paper, error corrected two port measurements are possible. The FE converts the original frequency range of a microwave NA into the mm-wave range and makes extensive use of the NA hard- and software. Display and data processing tools like averaging etc. can be used as usual. Because only a few mm-wave components are needed for the frequency extender, which is connected to the NA only via the test port cables, this system is not much expensive but very easy to use.

PRINCIPLE

A block diagram of the frequency extender is shown in fig. 1. The sweep signal ($f_{START} \leq f_{s,\mu W} \leq f_{STOP}$) generated by the NA (Port 1 of the Test-Set) is mixed in a double balanced mixer with a mm-wave LO-signal (f_{LO}). The lower sideband- and the carrier-signal is suppressed by the band-pass filter BP1, therefore only the upper sideband signal, covering the frequency range $(f_{START} + f_{LO}) \leq f_{s,mmW} \leq (f_{STOP} + f_{LO})$, is present at test port A of the FE. Depending on the position of switch S, the transmitted or the reflected signal reaches the second mixer and is converted into the original frequency range of the NA. Because the up- and down-conversion process is accomplished with the same LO-signal, no phase synchronization between the LO and the signal source of the NA is necessary. The second band-pass gives a further improvement in the suppression of the unwanted sideband.

Because the transmitted and the reflected measuring signal is always delivered to Port 2 of the NA Test-Set, the standard definition of \underline{S}_{11} has to be changed to:

$$\underline{S}_{11} = \left. \frac{\underline{b}_2}{\underline{a}_1} \right|_{\text{Switch-Position 1}}$$

This can be reached with the standard firmware of modern NA like HP 8510C or Wiltron 360B. In the same way the frequency offset due to the mixing with f_{LO} can be taken into account. Therefore one port measurements can be realized under software control of the NA firmware. Only a standard calibration-kit is needed.

Two port measurements are a little bit more complicated, because the NA needs the uncalibrated reflection and transmission measuring data of the DUT for the error correction of each S-Parameter. Until now the mechanical waveguide switch S is not under software control of the NA, so the switch position has to be changed manually while the NA stops measuring. Therefore a small C++ program running on a PC has been developed, which takes control over the whole measuring process via IEEE 488 bus. After the error correction the S-parameters are written back into the NA memory and occur on the display. The change of system settings like frequency offset and redefinition of S-parameters is also done by this software. Nevertheless, all well known features of the NA firmware like averaging etc. are still available and accessible via the NA front panel.

SYSTEM REALIZATION AND MEASUREMENTS

The W-band was chosen for a practical system realization based on a HP8510 C network analyzer with a HP 8514 Test-Set (upper frequency limit 20 GHz). As shown in fig. 1 waveguide components are used for the FE. The LO is a free running Gunn-oscillator ($P_{LO} = 15$ dBm, $f_{LO} = 87,5$ GHz). The temperature drift of the LO-frequency is -3 MHz/ $^{\circ}$ C and therefore sufficient for most applications. A higher frequency stability can be accomplished by phase synchronisation between LO and NA. A Rat-Race-coupler is used as power divider for the LO-signal. An additional waveguide LO-Test-port at the rear side of the FE allows the measurement of the LO frequency before the begin of S-parameter measurements. Then the actual LO-frequency is used for frequency setting. Because the high-power signal is delivered by the Gunn-oscillator, the microwave signal can be small signal. Therefore it's possible to connect the FE and the NA only via the test-port cables and no hardware changes at the NA are needed.

Until now the frequency range of our demonstrator is mainly restricted by the pass-band of the waveguide filters to 89-100 GHz. Due to the conversion loss of the mixers and the attenuation of the other mm-wave components the signal power in the IF-range is rather low and the dynamic range of the NA is reduced. A low noise amplifier placed at the IF-port of the second mixer improves the system performance for high attenuation measurements.

The calibration of the whole system is possible with the well known TMSO-method (Thru, Match, Short, Offset short), so any commercial available calibration-kit is suitable for this task.

To prove the system performance, test measurements in the frequency range 89-100 GHz have been carried out. Fig. 2 shows the reflection of a waveguide (length 30 mm) terminated with a short. In fig. 3, a waveguide filter was used for comparison of measured results taken from a HP 8510C with the commercial Option

75-110 GHz and the system as described above. This figure makes quite clear that the useful bandwidth of the FE is not only limited by the band-pass filters BP 1 and 2 (fig. 1), because also the increasing mixer conversion loss reduces the system performance at higher frequencies. Fig. 4 gives a good impression of the dynamic range for transmission measurements. The measured $|S_{21}|$ of a precision attenuator for different settings of attenuation is shown. Obviously the dynamic range of the NA is reduced, due to the conversion loss of the FE. Fig. 5 shows the reflection of a horn antenna. The solid lines show the results directly after calibration and the dotted lines 6 hours later. During this time the change of temperature was about 2.5°C, so the system stability is quite good.

CONCLUSION

A low cost frequency extender for commercial network analyzers is presented. Test measurements show a good quality of the measuring system. The dynamic range and the band-width is mainly limited by the band-pass filters and the mixers. Until now the measuring speed is slow, due to the mechanical switch inside the FE. A replacement of this component by a PIN-switch is planned.

REFERENCES

- [1] GECK, B.; MARQUARDT, J.: "A homodyne network analyser with parallel mixers for the millimetre wave range", Proc. 24th EUMC, pp. 922-927, Cannes 1994
- [2] NEUMEYER, B.: Impedanzmessung im mm-Wellen-Bereich ohne Frequenzumsetzung, Dissertation, Fakultät für Elektrotechnik und Informationstechnik, Technische Universität München, 1989
- [3] HARTMANN, TH.: A W-Band Network Analyzer System Using Up-Conversion, Proc. 15th EUMC, pp.489-494, Paris, 1985

FIGURES

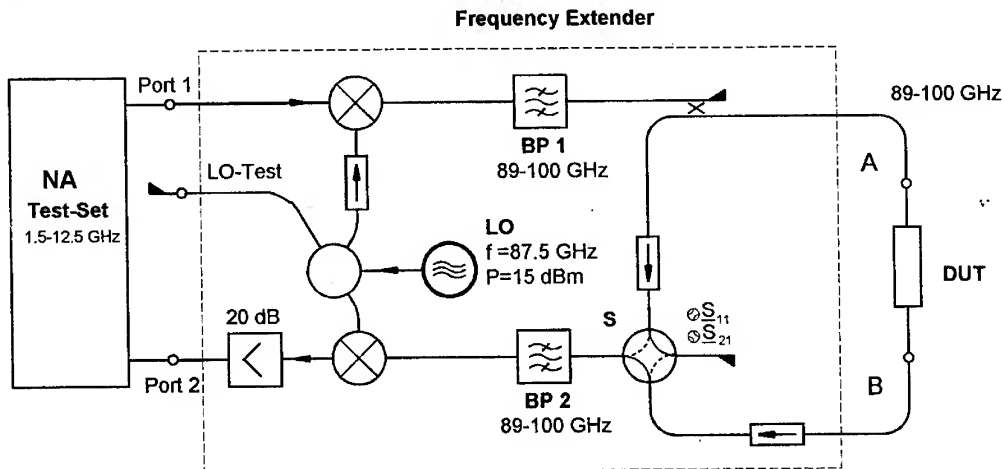


Fig. 1: Block diagram of the frequency extender

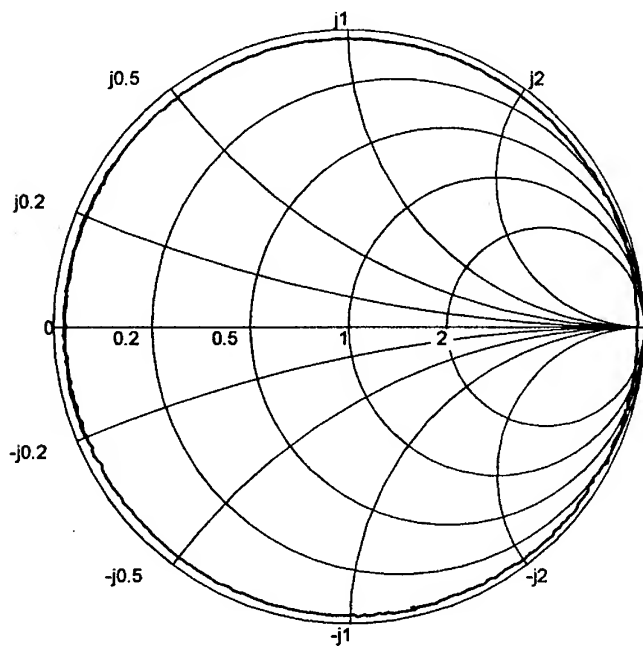


Fig. 2: Reflection of an offset short (length=30mm)

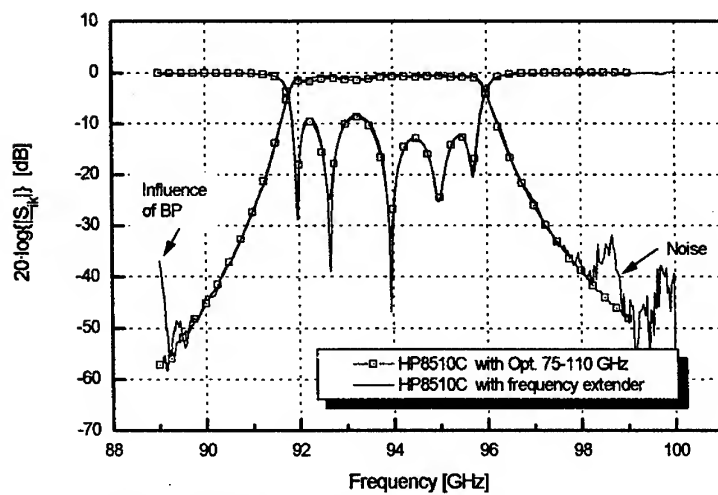


Fig 3: Comparison of measurements

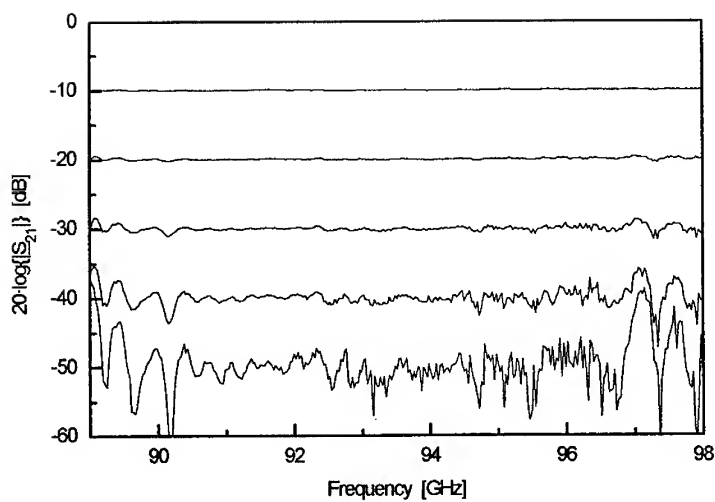


Fig. 4: Measurement of an attenuator

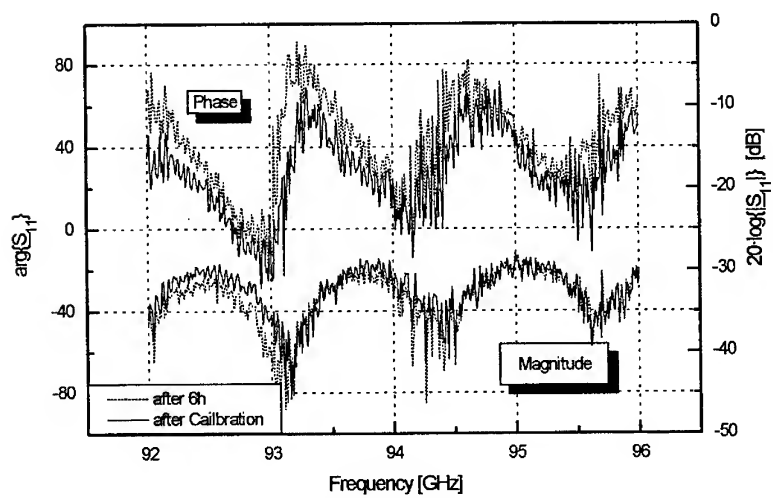


Fig 5: S_{11} of a waveguide horn antenna directly after calibration and after 6 hours

A Membrane Probe for Testing High Power Amplifiers at mm-Wave Frequencies

Saswata Basu, Pat Nussbaumer*, and Eric Strid
Cascade Microtech, Inc., Beaverton, OR
*TRW, Redondo Beach, CA

ABSTRACT

Traditional coaxial-needle probe cards have difficulty in incorporating combiner structures and generally have poor bypassing capability at high frequencies. In this paper, we will demonstrate how membrane probes can incorporate these features with minimal parasitic effects and conduct accurate and fast testing of power amplifiers at Ka-band.

Introduction

There are two principal problems that traditional coaxial-needle probes face with high power amplifier chips tested on-wafer. One is the difficulty of implementing off-chip matching networks on coaxial probes due to significant parasitics associated with assembly at high frequencies. The other problem is the inability to provide an RF short for the DC lines close to the probe tip. Besides these shortcomings conventional coaxial-needle technology is mechanically not as robust; it requires careful handling and is ill-suited for a production type environment. We will show how a membrane probe [1] can integrate combiners with minimal parasitic effects and conduct accurate and fast testing of Ka-band power amplifiers.

The power amplifier is a two-stage PHEMT device designed and fabricated by TRW. The device has two 50 ohm inputs and four 36 ohm outputs. The testing specifications for this chip require a 2-by-1 splitter at the input and a 4-by-1 combiner at the output with current carrying capability of 2 A.

Probe Description

The layout of the probe is shown in Figure 1. It consists of an input circuit on the left and an output circuit on the right with symmetrically located DC bias lines on the top and bottom. The input circuit has a Wilkinson splitter with its legs having a characteristic impedance of 72 ohms to match the 50 ohms at the tip. The microstrip lines have a solid ground backing unlike the output circuit where it is meshed. The solid ground plane is removed at the resistor pad locations to keep the characteristic impedance close to 50 ohms. The resistors are thin film resistors on alumina substrate and have 20 x 6 mils physical dimension. At the edge of the layout the microstrip goes through a CPW transition to interface the center rectangular ring of the probe card. The transition between the probe and the card is iterated to insure a controlled impedance of 50 ohms over 50 GHz.

The output circuit unlike the input is based on meshed ground because the RF lines need to accommodate 2 A of DC current. The meshed microstrip line can be represented

by an inductor and capacitor network. The areas of the line with no ground bar underneath are inductive whereas the portions with the ground bar component of the mesh under the line are capacitive. Because of the apparent fragmentation of the ground, signal lines can be made wider without any change in the characteristic impedance while accommodating larger amounts of current. The width of the lines for this specific design are derived from subsequent measured results on test structures.

The output circuit has a 4-by-1 combiner with its front legs (closest to the tip) having characteristic impedances of 60 ohms to match the tip impedances of 36 ohms. The bias networks consist of two quarter-wave lines at the center frequency. The ground mesh is removed from the first line to increase its characteristic impedance, and the radial stub has a ground plane to maximize its capacitance. A DC blocking cap is mounted at the edge of the output RF line; the ground underneath the mounting pad is removed to eliminate any parasitic capacitive effect on the transmission line.

The other DC bias lines are made wide to lower their characteristic impedance. The 150 pF bypass capacitors are mounted close to the tip of the probe to provide a good RF short. An equivalent circuit looking into one of the DC lines would see a pi circuit with the short transmission line capacitance, the ribbon inductance, and the 150 pF. By controlling the width of the lines and the distance of the bypassing capacitor, stray inductances can be lowered to less than 0.5 nH. This bypassing capability is lower by a factor of 20 relative to conventional needle card technology.

The input and output circuit of the probe is characterized using a custom impedance standard substrate (ISS). The ISS was laid out to accommodate load and short

standards for the input and the output circuit at Ka-, Q-, and V- band for TRW's respective PHEMT amplifiers. The load standard is made to match the footprint of the probe bumps and the impedances of the input and output circuit. The characterizations of the circuits are made by calibrating up to the coaxial cable, attaching it to the probe, and then measuring three known standards such as open, short and load. Considering these three measurements and the assumption that $S_{21}=S_{12}$ the three s-parameter unknowns can be determined. One such characterization is that of the output circuit as shown in Figure 2. The return and insertion losses are below 10 dB and 5 dB, respectively, in the 32-34 GHz range. Most of the circuit losses are in the membrane probe and are predominantly conductor losses.

Results

There are various different calibration schemes that can be used to test the TRW Ka-band chips on-wafer. The simplest and most efficient one chosen was a response thru calibration to determine the insertion gain of the amplifier. This was an adequate measurement criterion for the production testing of these chips for known good die. We fabricated a custom matching thru between the input and output circuit on membrane and mounted it on a glass slide. The loss and delay of the thru were measured and calculated independently with a pair of ACP probes and entered into the calibration. The comparison between probe and fixtured data is shown in Figure 4. The two curves correspond quite well showing the viability of on-wafer testing scheme using this membrane probe. The curves seem to be shifted in frequency by about 0.5 GHz. This is attributed to the difference in parasitics of bond wires in the fixtured set-up relative to the bumps and lines at the tip of the probe. We will investigate this testing

scheme further for higher frequency applications such as in the Q and V band.

Acknowledgments

This work was supported in part by DARPA under Mafet-C contract BAA 95-06. We greatly appreciate the help of Vickie Van Syckel, David Hogue, Art Schiaroli, Martin Koxxy, and Dave Lockman on this project.

Conclusions

We have shown the viability of integrating combiner circuits in the membrane probes for testing power amplifier chips at Ka-band at on-wafer level. Such integration reduces parasitics that are significant at very high frequencies and enable fast production level testing.

References

1. Ken Smith, Reed Gleason, and Eric Strid, "Membrane Probe Speeds Digital and RF IC Testing," *Microwaves and RF*, Jan 1995, pp. 135-139.

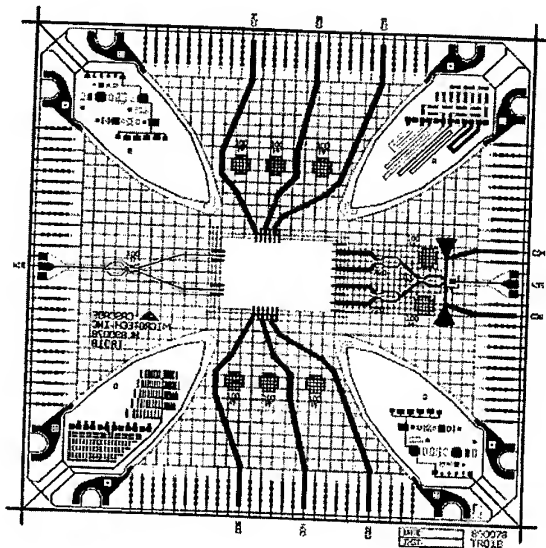


Figure 1: A Ka-band membrane probe for testing PHEMT amplifiers with two inputs and four outputs at non-50 ohm impedances.

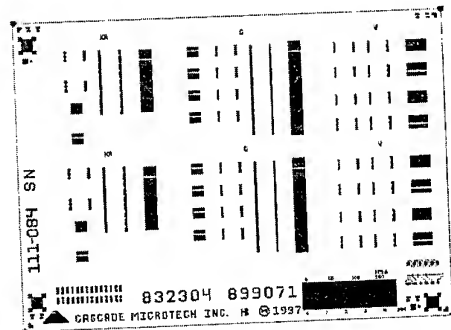


Figure 2: An impedance standard substrate (ISS) designed to calibrate the membrane probe in Figure 1.

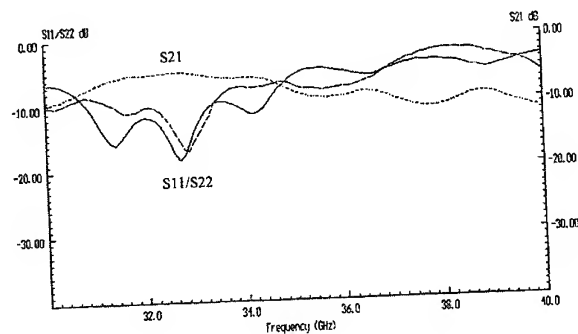


Figure 3: S-parameter responses of the output circuit of the membrane probe in Figure 1.

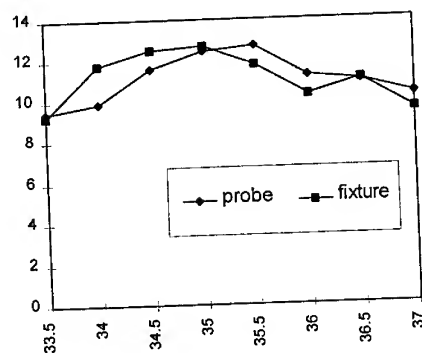


Figure 4: Comparison of measured responses between membrane probe and fixtured set-up of the TRW Ka-band amplifier.

ANALYTICAL AND FULL-WAVE CHARACTERIZATION OF MULTIMODE WAVEGUIDE DISCONTINUITIES

Ph. PANNIER, E. PALECZNY, C. SEGUINOT, F. HURET, P. KENNIS

« Institut d'Electronique et de Microélectronique du Nord »

IEMN, BP 69, Université de LILLE, 59655 Villeneuve D'Ascq cedex, FRANCE

phone: (33) 3 20 19 79 63, fax: (33) 3 20 19 78 83, E-mail: Seguinot@iemn.univ-lille1.fr

ABSTRACT

The derivation of multimode S parameters of a multiconductor waveguide discontinuity is investigated using an analytical quasi TEM model. Analytical and full wave results are compared. On the basis of the proposed methodology, precise and simple equivalent circuits can be derived. Such analytical models can be implemented in CAD libraries.

INTRODUCTION

Nowadays, Computer Aided Design offers a convenient and rapid way of prototyping MMICs. CAD tools libraries have been improved to include most of the active or passive components required in monolithic and microwaves technologies. Nevertheless, as soon as multiple mode problems have to be considered, analytical models are generally no longer available. In these cases, 3D EM simulations appears as the only solution. This is encountered for example with interconnections involving two different types of waveguides as well as multiconductor transmission lines discontinuities [1], [2].

The aim of this communication is to present a simple methodology leading to the determination of an analytical model accounting for multiple mode propagation. We will first present the investigated multimode network, and the proposed quasi TEM model. Then, the conversion between multimode S and Z parameters will be detailed. Finally, analytical and full wave results will be compared.

STUDIED STRUCTURE

The studied structure is presented figure 1. This is a simple two coupled strips transmission line discontinuity. The asymmetry of this one-port implies that the two fundamental quasi TEM modes will be propagated in the incoming waveguide. For example, if a generator is connected such as only the even mode is excited, one part of the power will be reflected on this mode while generally one another part will be guided by the odd reflected mode.

In order to characterize this effect, we have analyzed this one-port using a simple quasi TEM model described below. Such a model is based on the low frequency behavior of the network. It must be considered as a basic model which can be improved and optimized by comparison to rigorous simulations such as those provided by full-wave analysis. We have considered that the multiconductor section (before the reference plane) was connected to two lines of length $l=0$ and $l=d$. It was also found that more precise scattering parameters were found if open end effects were taken into account on both conductors. The conventional (single line) microstrip open end model has been used. Further improvements of the model have not been investigated

yet. Starting from the impedances seen in the reference plane, scattering parameters can be computed as describe in the next section.

CONVERSION FROM Z PARAMETERS TO MULTIMODE S PARAMETERS

We will assume that the quasi TEM approximation can be made. In a waveguide, EM fields can be described by fields of modes and related complex wave amplitudes. We define waves amplitudes column vectors A_k and B_k with

$$\begin{aligned} A_k^t &= (a_{k,1} \quad a_{k,2} \quad \dots \quad a_{k,N_k}) \\ B_k^t &= (b_{k,1} \quad b_{k,2} \quad \dots \quad b_{k,N_k}) \end{aligned} \quad (1)$$

N_k being the number of TEM or quasi TEM modes propagated in the waveguide k . We assume that all modes incident fields are normalized with

$$\frac{1}{2} \int_{S_k} (\vec{e}_{k,i}^+ \wedge \vec{h}_{k,j}^+) \cdot d\vec{s} = \delta_{ij} \quad (2)$$

The generalized reciprocity normalized scattering matrix S is used to relate all the reflected wave amplitudes to the incident wave amplitudes

$$[B] = S [A] = \begin{bmatrix} B_1 \\ B_2 \end{bmatrix} = \begin{bmatrix} S_{11} & S_{12} \\ S_{21} & S_{22} \end{bmatrix} \begin{bmatrix} A_1 \\ A_2 \end{bmatrix} \quad (3)$$

We will now relate analytically voltages and currents to wave amplitudes of EM fields. If (N_k+1) conductors are encountered, N_k TEM modes propagate. Conductor 0 is the voltage reference conductor (ground). We define vector conductor voltage (V_k) and current (I_k) in waveguide k by:

$$\begin{aligned} V_k^t &= (v_{k1}, v_{k2}, \dots, v_{kN_k}) \\ I_k^t &= (i_{k1}, i_{k2}, \dots, i_{kN_k}) \end{aligned} \quad (4)$$

Where scalar v_{kj} (i_{kj}) denotes the RMS voltage (current) associated to conductor j in waveguide k . In waveguide k we also note $v_{ok,ij}$ ($i_{ok,ij}$) the voltage (current) induced by unit amplitude wave m_{kj} (or mode j) on conductor i . This is used to define reference wave voltage and current matrices:

$$V_{ok} = [v_{ok,ij}] \quad I_{ok} = [i_{ok,ij}] \quad (5)$$

As TEM modes are orthogonal (2), and fields of reference waves have been normalized, we can derive the orthogonality of reference voltages and currents matrices

$$V_{ok}^t I_{ok} = [I] \quad (6)$$

In order to characterize two-ports, we now define V_o and I_o

$$V_o = \begin{pmatrix} V_{o1} & 0 \\ 0 & V_{o2} \end{pmatrix} \quad I_o = \begin{pmatrix} I_{o1} & 0 \\ 0 & I_{o2} \end{pmatrix} \quad (7)$$

At this point, we must observe that each port is associated to one block of block diagonal matrices V_o and I_o . Thus, our work can be easily extended to multiport networks by simply adding blocks to V_o and I_o . In the same way, multimode one-ports can be considered by retaining only one block in V_o and I_o . We use the orthonormality of V_o and I_o (6) to define a normalization impedance matrix Z_o [3]

$$Z_o = V_o (I_o^{-1})^t = (V_o)^2 = (I_o^t)^{-2} \quad (8)$$

Equation (8) is derived using Maxwell equations the TEM assumption and the reciprocity principle. It is similar to $M_o M_o^t = [I]$ or related expressions derived from transmission line equivalent circuits and sometimes found in the literature [3], [4]. The voltage and current vector in waveguide K are found to be related to wave amplitude by

$$\begin{pmatrix} V_k \\ I_k \end{pmatrix} = \begin{pmatrix} V_{ok} & V_{ok} \\ I_{ok} & -I_{ok} \end{pmatrix} \begin{pmatrix} A_k \\ B_k \end{pmatrix} \quad (9)$$

Using this, we now relate S and Z matrix:

$$S = (Zm - [I])(Zm + [I])^{-1} \\ Zm = \sqrt{Z_o}^{-1} Z (\sqrt{Z_o}^{-1})^t \quad (10)$$

Where the square root of matrix Z_o is equal to V_o (8). We must point out that (10) is valid for any multiports having TEM ports. If a one-port is considered, as in the present case, S in (10) reduces to the reflection coefficient ($Z=Z_{11}$, $S=S_{11}$). Furthermore, if single mode waveguide are considered, Z_o is a diagonal matrix (multiport) or a single scalar (single mode one-port) and (10) reduces to well known conventional formulas.

RESULTS

The above procedure was applied to the multimode discontinuity of figure 1. Z_o was evaluated using a quasi TEM model. As only one port and two quasi TEM mode are considered, the S matrix reduces to a 2*2 reflection coefficient

$$S = \Gamma = \begin{bmatrix} \Gamma_{ee} & \Gamma_{eo} \\ \Gamma_{oe} & \Gamma_{oo} \end{bmatrix} \quad (11)$$

In (11), lowerscript *e* and *o* refer to *even* and *odd* mode. For example Γ_{eo} is the reflection of the even mode with respect to the excitation of the odd mode. Analytical results are compared to multimode S parameters obtained using a full-wave analysis [5] associated to a matrix pencil method [6] (figure 2). For small line length difference (*d*), Γ_{ee} and Γ_{oo} are close to +1 (linear) which indicate that the one-port behave like an open circuit for the two modes, as could have been expected. In this situation, no coupling is found between the odd and even mode ($\Gamma_{oe} = \Gamma_{eo} = 0$). For d/λ_0 close to 0.1, the line length difference (*d*) is close to a guided wavelength. The conversion from one mode to the other is high and close to 0 dB. This indicates that all the incident power carried by one mode is reflected back by the other mode. Consequently, Γ_{eo} and Γ_{oe} are close to 0 (-15 dB).

CONCLUSION

We have derived the multimode scattering parameters of a simple multiconductor discontinuity. The proposed method can be extended to derive analytical model for multiconductor waveguides transitions. Such models are based on low frequency behavior and quasi TEM approximations, so we suggest that their domain of validity (frequency range for example) have to be improved. This can be provided by optimizing models using rigorous full-wave analysis. The present method yields simple models which are well suited to be implemented in CAD software.

RÉFÉRENCES

- [1] L. KADRI, Ph. PANNIER, F. HURET, E. PALECZNY, C. SEGUINOT, « *Scattering parameters and mode conversion in asymmetric CPW-microstrip overlap transition* », current issue
- [2] M. Wu, S. Deng, R. Wu, P. Hsu, « *Full-wave characterization of the mode conversion in a coplanar waveguide right-angled bend* », IEEE Trans. on MTT, Vol 43, n°11; nov. 1995, pp 2532-2538
- [3] C. R. Paul, « *Decoupling the multiconductor transmission line equations.* », IEEE Trans. on MTT, Vol 44, n°8; aug.1996, pp 1429-1440
- [4] L.A. Hayden, V.K. Tripathi, « *characterization and modeling of multiple line interconnections from time domain measurements* », IEEE Trans. on MTT, Vol 42, n°9; sep. 1994, pp 1737-1743
- [5] P. Pannier, L. Kadri, J.F. Carpentier, F. Huret, P. Kennis, « *Full-wave spectral domain analysis of coplanar discontinuities using numerically matched loads.* », Microwave and Optical Technology Letters, vol. 10, n°6, dec. 1995, pp 350-353
- [6] Y. Hua, T.K. Sarkar, « *Generalized pencil of function method for extracting poles of an EM system from its transient response* », IEEE Trans. on Antennas and Propagat., Vol AP-37, feb. 1989, pp 229-234

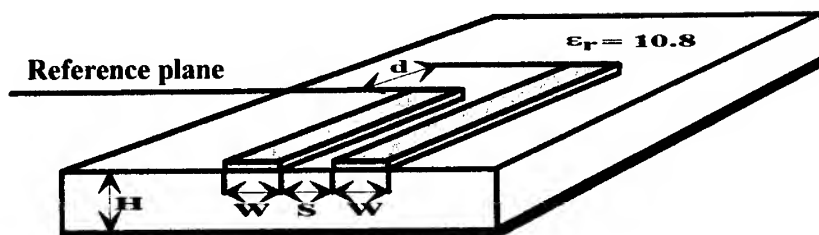


Figure 1: Studied multimode structure

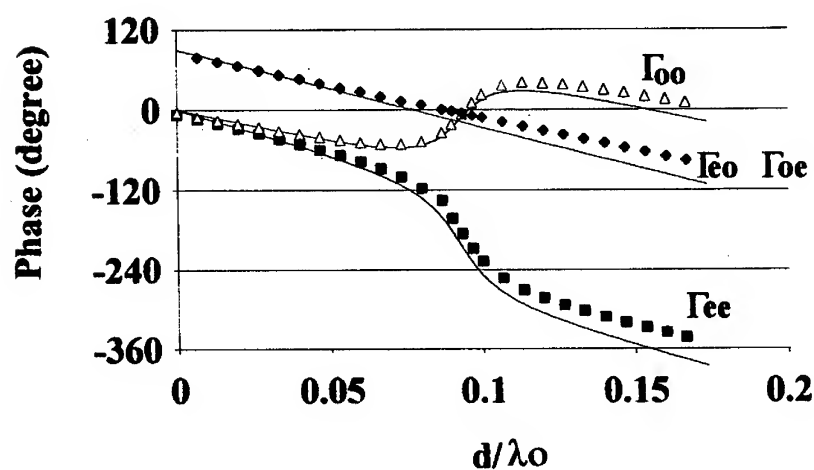
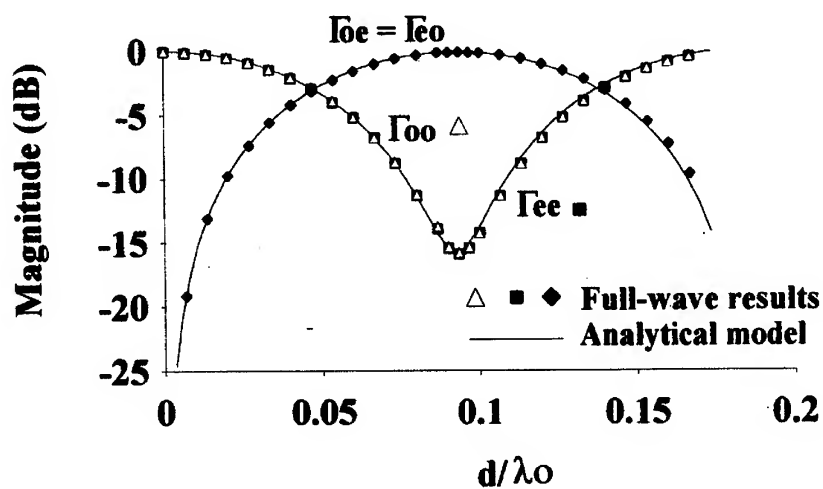


Figure 2: Scattering parameters of the studied one-port

A Matrix Decomposition Technique for the Efficient Analysis of Complex Waveguide Networks

Ferdinando Alessandri and Roberto Sorrentino

Istituto di Elettronica, Università di Perugia, Italy

Abstract

A method for fast and rigorous analysis of complex waveguide networks of any topology is presented. A modal analysis based on the generalized admittance matrix representation of discontinuities and components is employed leading to a linear set of equations in the internal voltages. A special L*U decomposition is introduced that exploits the specific features of the coefficient matrix, namely: symmetry, block banded and stepped structure. The high numerical efficiency of this approach is shown at the example of a 4x4 Butler matrix.

Introduction

The mode matching method is a very efficient technique for the analysis of waveguide components. In recent years the method has been extensively used for the analysis and optimization of very complex components and networks [1]. For optimization purposes however the technique must be implemented with the highest numerical efficiency since hundreds or thousands analyses may be required [2]. The efficiency issue is extremely critical when complex waveguide networks have to be designed, as in the case, for instance, of beam forming networks for high performance satellite antennas. In this paper we present a numerical approach to the solution of the linear system of equations arising from the application of modal analysis to the modelling of complex waveguide networks. The method consists of a proper matrix decomposition technique that exploits the typical features of the system matrix, in such a way as to reduce the computational cost of the solution process by one order of magnitude. A 4X4 Butler matrix is used as an example to demonstrate the validity of the proposed approach.

Theory

The application of the mode matching technique to the analysis of a complex microwave structure requires the latter to be divided into elementary cells or buildings blocks [3]. (To avoid confusion, the term "elementary cell" rather than "building block" will be used throughout this paper). Each elementary cell corresponds to a discontinuity or a junction or, in some instances, to an entire component of the network

By way of the microwave network formalism, each elementary cell is represented as a multiport network. Although the most commonly used representation is the generalised scattering matrix (GSM), the generalised admittance matrix (GAM) has proved to be more efficient for lossless structures as it can be evaluated analytically with no matrix inversion [4]. Since the losslessness hypothesis can be assumed for the analysis of waveguide components in most practical cases, the GAM approach has been adopted here.

Once each cell has been characterized as a multiport, the analysis of the overall microwave network is reduced to the analysis of the equivalent network resulting from the connection of the GAM's of the elementary cells. By combining the GAM descriptions of the elementary cells with the topological equations expressing the equalities between voltages and (apart from the sign) currents at the connected ports, the analysis of the overall network is reduced to the solution of the following set of equations:

$$\mathbf{A}\mathbf{V}_i = \mathbf{B}\mathbf{V}_e \quad (1)$$

$$\mathbf{I}_e = \mathbf{C}\mathbf{V}_i + \mathbf{D}\mathbf{V}_e \quad (2)$$

where \mathbf{V}_i and \mathbf{V}_e are vectors representing the voltages at the internal and external ports, respectively, \mathbf{I}_e is the vector of the currents at the external ports. \mathbf{A} , \mathbf{B} , \mathbf{C} , \mathbf{D} are known matrices that are expressed in terms of the GAM's of the elementary cells.

For a given excitation \mathbf{V}_e at the external ports, the internal voltage distribution can be computed first by solving the linear system (1). The current distribution \mathbf{I}_e at the external ports is then evaluated through (2). In this manner, the admittance matrix of the entire network is obtained.

It could be observed that the solution process could also be developed along different lines, e.g. by sequentially cascading the various GAM's of the elementary cells. This strategy, however, besides leading to numerical instabilities, is such that the information on the internal voltage (and current) distribution is lost. This information, on the contrary, is necessary when circuit optimization has to be performed [7] as well as for high-power check purposes.

It is noted that the key step of the entire is the solution of (1), i.e. the solution of a linear system of $N_i \times N_i$ equations. The associated numerical effort is obviously strictly related to the structure of the coefficient matrix \mathbf{A} , provided that a suited solution algorithm is adopted to fully exploit its typical features. Depending on the numbering adopted to identify the internal ports of the network, different matrix structures are obtained.

By adopting a proper port numbering, a banded block matrix \mathbf{A} with minimum bandwidth can be obtained [5], the band having a block structure. Because of the different dimensions of the blocks and to the presence of null blocks within the band, the latter has a stepped structure (skyline).

As shown in this paper, the specific structure of the coefficient matrix \mathbf{A} can be exploited to reduce dramatically the computer effort, in such a way as to make affordable the fullwave analysis and optimization of very complex waveguide networks. More specifically, we first exploit the symmetry of the coefficient matrix by adopting the following decomposition:

$$\mathbf{A} = \mathbf{U}^T \boldsymbol{\lambda} \mathbf{U} \quad (3)$$

where \mathbf{U} is a upper triangular matrix with unit elements on the diagonal and $\boldsymbol{\lambda}$ is a diagonal matrix. The elements of $\boldsymbol{\lambda}$ and \mathbf{U} can be computed by the following formulas:

$$\begin{aligned} \lambda_i &= a_{i,i} - \sum_{k=1, i-1} \lambda_k u_{i,k} \\ u_{i,j} &= (a_{i,j} - \sum_{k=1, i-1} u_{k,i} \lambda_k u_{k,j}) / \lambda_i \quad \text{for } j=1, i-1 \\ u_{i,i} &= 1 \end{aligned} \quad (4)$$

As can easily verified the \mathbf{U} matrix has the same stepped-banded structure with minimum bandwidth as the \mathbf{A} matrix. This allowed us to develop a very efficient solution algorithm, that

not only exploits the block banded structure of the matrix, but takes advantage of the presence of the nulls in the band in such a way as to minimize the overall computational effort to solve the system (1).

The approach is illustrated in the next Section, at the specific example of a 4x4 Butler matrix.

Results

The geometry of 4x4 Butler matrix is shown in Fig.1 The structure consists of 6 branch guide couplers and 4 phase shifters. Each phase shifter consists of two H-plane symmetrical steps and a cascade of five symmetrical E-plane stubs. For analysis purposes the overall structure has been divided into 18 elementary cells corresponding to: 6 six branch guide couplers, 4 cascades of 5 E-plane stubs, 8 H-plane steps.

The reference planes of the elementary cells, shown in Fig.1, are placed at half distances between two discontinuities so as to minimize the number of modes to be taken into account at each physical port.

The structure of the coefficient matrix **A** resulting from the analysis described in the previous section is shown in Tab.1. It is a symmetrical matrix partitioned into 20x20 blocks. Only the numbering of the internal ports is shown in Fig.1, since the structure of the matrix does not depend on the numbering of the external ports. Each block of the **A** matrix corresponds to a block of the admittance matrix of an elementary cell. The apex indicates the corresponding elementary cell (shown in Fig.1), while the indices correspond to the port numbers. The blocks of the main diagonal (e.g. $Y_{C11}^{C} + Y_{D11}^{D}$) are the sum of the admittance matrices of the elementary cells (C and D).

The port numbering has been optimized in such a way as to minimize the block bandwidth. In the present example, the block bandwidth is five. The actual bandwidth of the coefficient matrix depends on the number of modes used at the reference planes (connected ports), since these numbers correspond to the dimensions of the GAM's. The actual bandwidth BW can be computed by the formula:

$$BW = \max_{(for\ j=1,20)} \left[\sum_{i=j, \min(j+5,20)} mode(i) \right] \quad (5)$$

where $mode(i)$ is the number of modes at port i .

In addition to being block banded the matrix **A** is seen to have zeros within the band. Such a stepped-banded structure can be exploited to further reduce the computational effort required to solve the system (1). Observe that a conventional banded solver involves a computation time proportional to $N_i \cdot BW^2$. For a stepped banded matrix, by taking advantage of the presence of null blocks located at the band border, the same expression can be used assuming an average bandwidth BW_{eff} . In the present example, an average bandwidth of $BW_{eff} = 0.8 \cdot BW$ has been found, so that a further reduction of more than one third of the computation time has been achieved.

Fig.2 shows the computed response of the 4x4 Butler matrix of Fig.1. Using the presented approach, the analysis of the Butler matrix required less than one second for frequency point by using a 486 PC 50MHz. The same analysis required 11 seconds per frequency point using a conventional solver, showing a computer time saving exceeding one order of magnitude.

Conclusions

A method for fast and rigorous analysis of complex waveguide networks of any topology has been presented. The method is based on the exploitation of the specific features of the coefficient matrix arising in the mode matching analysis of the segmented microwave structure. This has led to a considerable increase of the computational efficiency. For a 4x4 Butler matrix, used as a test case, a CPU time reduction of more than one order of magnitude has been demonstrated in comparison with conventional solvers.

References

- [1] T. Sieverding, F. Arndt, "Field Theoretic CAD of Open Aperture Matched T-junction Coupled Rectangular Waveguide Structures", IEEE Trans. Microwave Theory and Tech., Vol. MTT- 40, n.2, pp.353-362, Feb. 1992
- [2] J.W. Bandler and R.E. Seviara, "Current trends in network optimization," IEEE Trans. Microwave Theory and Tech., Vol. MTT-18, n.12, pp.1159-1170, Dec. 1970
- [3] T.Sieverding, U. Papziner, T. Wolf and F. Arndt, "New Mode-Matching Building Blocks for Common Circuit CAD Programs", Microwave Journal, Dec. 1993, pp. 66-79.
- [4] F. Alessandri, M. Mongiardo, R. Sorrentino, "Computer-Aided Design of Beam Forming Networks for Modern Satellite Antennas", IEEE Trans. Microwave Theory and Tech., Vol. MTT- 40, pp.1117-1127, June 1992
- [5] L.Tarricone, M.Dionigi, R. Sorrentino, "A strategy for the efficient fullwave description of complex waveguide networks", Int. Journal of Microwave and MM-Wave Computed Aided Engineering, vol.6, N. 3, pp.183-195, 1996.
- [6] W.H. Press, B.P. Flannery, S.A. Teukolsky, W.T. Vetterling, *Numerical Recipes*, Cambridge University Press, 1986, pp.31-38.
- [7] F. Alessandri, M. Dionigi, R. Sorrentino, "A full-wave cad tool of waveguide components using a high speed direct optimizer", IEEE Trans.Microwave Theory and Tech., Vol. 43, pp.2046-2052, Sept. 1995

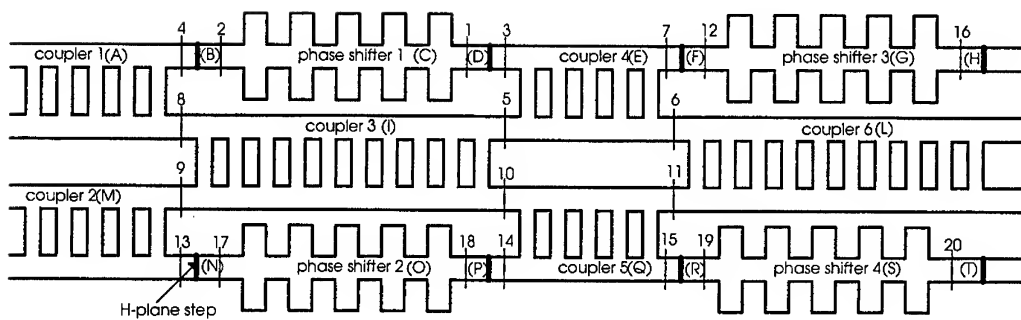


Fig.1, A 4x4 Butler matrix. Numbers identify internal ports.
Letters identify elementary cells

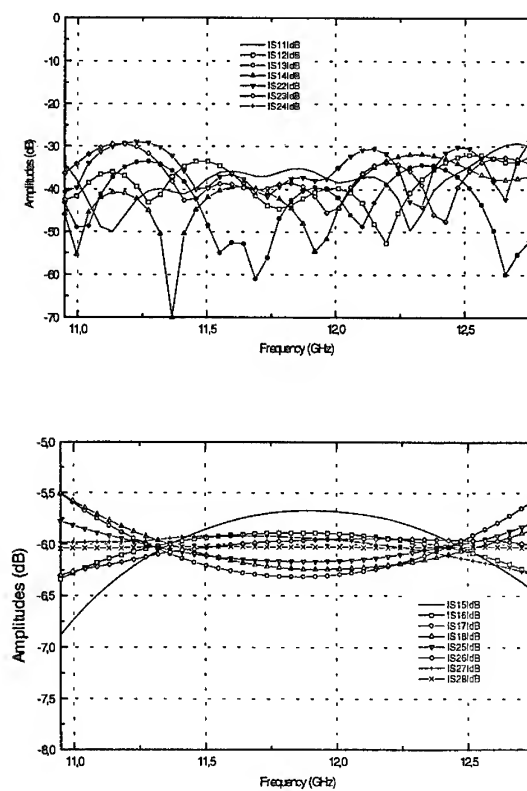


Fig. 2. Response of the Butler matrix of Fig. 1

Tab.1 : the upper half band of the matrix of the unknown coefficients.

SCATTERING OF TE_{11} MODE FROM TWO ASYMMETRIC RIDGES OF FINITE THICKNESS IN A CIRCULAR WAVEGUIDE

Smain Amari¹, Rüdiger Vahldieck² and Jens Bornemann¹

¹Department of Electrical and Computer Engineering
University of Victoria, B.C., Canada V8W 3P6

²Institute für Feld Theorie und Höchstfrequenztechnik
Swiss Federal Institute of Technology
Gloriastrasse, 35, 8092 Zürich, Switzerland

Abstract

The scattering properties of the TE_{11} mode from two asymmetric ridges of finite thickness in a circular waveguide are determined using the Coupled-Integral-Equations Technique (CIET). Two vector coupled integral equations for the transverse electric field at the two discontinuities are derived and then solved by the moment method. The eigenmodes of the ridged section, in terms of which the kernels of the integral equations are expressed, are themselves determined using the CIET where basis functions with the proper edge conditions are used.

1 INTRODUCTION

Ridged structures are important components in modern microwave communication systems such as dual-mode filters and polarizers whose frequency response is primarily determined by the dimensions and positions of the ridges. Accurate prediction of the response functions of these devices is contingent upon an efficient and precise determination of the scattering properties of their ridged sections.

The first step in determining the scattering properties of ridged sections in waveguides consists in solving for the cutoff frequencies and eigenmodes of the corresponding infinitely

long ridged structures. In this work, this first and important step is carried out through the Coupled-Integral-Equations Technique (CIET) where a set of coupled integral equations for the tangential electric field are solved by the moment method using basis functions which include the proper edge conditions at all the metallic wedges [1].

The second step consists in the analysis of the scattering of incident modes of the empty waveguide at the different discontinuities of the ridged sections. In this work, we establish sets of coupled vector integral equations for the transverse electric field at the different discontinuities. More specifically, we are concerned with the scattering of the fundamental modes of a circular waveguide, TE_{11} , with arbitrary polarization, by a finite section of an asymmetric double ridge structure. Instead of following the Mode-Matching Technique (MMT) and determining the scattering matrix by cascading the scattering matrices of the two discontinuities, we determine the scattering matrix of the section directly. This alternative approach allows us to concentrate directly on the dominant physics of the problem which takes place at the discontinuities and also take advantage of the fact that the coupling between the modes of the empty waveguide and those of the ridged waveguide are identical at both discontinuities. In addition, by solving the vector integral equations for the electric field at both discontinuities simultaneously, we eliminate the arbitrariness in determining what is commonly referred to as accessible modes between the two interacting discontinuities.

We purposely limit the analysis to the fundamental mode as it is the only propagating mode in the uniform regions between the different ridged sections as long as these are not too closely located. It is, however, worth mentioning that the analysis is straightforwardly extended to handle the case where modes other than the fundamental are propagating.

2 THEORY

The cross section of the ridged waveguide is shown in figure 1a. We assume that all metallic walls are lossless and that the ridges fit into the polar system of coordinates.

The eigenmodes of the structure can be divided into TE and TM modes whose cutoff frequencies are determined from the solution of Helmholtz equation. The electric and magnetic potentials are expanded in modal series in each of the subregions of figure 1a. A set of coupled integral equations for the electric field at the interfaces between the different regions are derived from the continuity of the magnetic field [1]. These are solved by the moment method using basis functions which include the edge conditions at the metallic wedges of the two ridges. The details can be found in reference [1].

To determine the scattering of the fundamental mode from a ridged section of finite length L , as depicted in figure 1b, we again derive two coupled vector integral equations for the

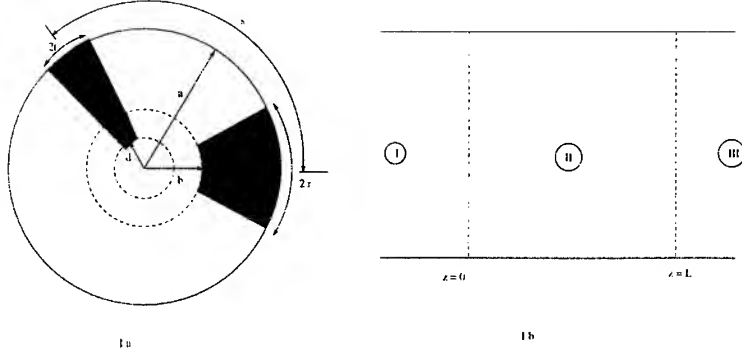


Figure 1: Cross section of asymmetric ridged circular waveguide (a) and ridged section of finite length (b)

transverse electric field at the two discontinuities at $z = 0$ and $z = L$ [2]. Let us assume that the transverse electric field at the two discontinuities are given by two unknown vector functions \mathbf{Z} and \mathbf{W} . Using the orthogonality properties of the normal modes in the boundary conditions of the transverse electric field, the modal expansion coefficients are eliminated in favour of the vector functions \mathbf{Z} and \mathbf{W} . Substituting the resulting expressions in the continuity condition of the transverse magnetic field at the two discontinuities, we obtain two coupled integral equations in these two vector functions. A moment method solution is applied to determine \mathbf{Z} and \mathbf{W} after which the reflected and transmitted waves follow straightforwardly. More precisely, we get the following coupled integral equations

$$\begin{aligned}
 \sum_m -\frac{\omega\epsilon_0}{k_{zm}^{TM I}} \left[\frac{\int_{S_2} \mathbf{Z} \cdot \nabla \Phi_m^{TM I} ds}{\int_{S_1} \nabla \Phi_m^{TM I} \nabla \Phi_m^{TM I} ds} \right] \mathbf{a}_z \times \nabla \Phi_m^{TM I} + \sum_m \frac{k_{zm}^{TE I}}{\omega\mu_0} \left[\frac{\int_{S_2} \mathbf{Z} (\mathbf{a}_z \times \nabla \Phi_m^{TE I}) ds}{\int_{S_1} \nabla \Phi_m^{TM I} \nabla \Phi_m^{TE I} ds} \right] \nabla \Phi_m^{TE I} \\
 - j \sum_m \frac{\omega\epsilon_0}{k_{zm}^{TM II}} \cot(k_{zm}^{TM II} L) \left[\frac{\int_{S_2} \mathbf{Z} \cdot \nabla \Phi_m^{TM II} ds}{\int_{S_2} \nabla \Phi_m^{TM II} \nabla \Phi_m^{TM II} ds} \right] \mathbf{a}_z \times \nabla \Phi_m^{TM II} \\
 + \sum_m j \frac{\omega\epsilon_0}{k_{zm}^{TM II}} \frac{1}{\sin(k_{zm}^{TM II} L)} \left[\frac{\int_{S_2} \mathbf{W} \cdot \nabla \Phi_m^{TM II} ds}{\int_{S_2} \nabla \Phi_m^{TM II} \nabla \Phi_m^{TM II} ds} \right] \mathbf{a}_z \times \nabla \Phi_m^{TM II} \quad (1) \\
 + \sum_m j \frac{k_{zm}^{TE II}}{\omega\mu_0} \cot(k_{zm}^{TE II} L) \left[\frac{\int_{S_2} \mathbf{Z} \cdot (\mathbf{a}_z \times \nabla \Phi_m^{TE II}) ds}{\int_{S_2} \nabla \Phi_m^{TE II} \nabla \Phi_m^{TE II} ds} \right] \nabla \Phi_m^{TE II} \\
 - \sum_m j \frac{k_{zm}^{TE II}}{\omega\mu_0} \frac{1}{\sin(k_{zm}^{TE II} L)} \left[\frac{\int_{S_2} \mathbf{W} \cdot (\mathbf{a}_z \times \nabla \Phi_m^{TE II}) ds}{\int_{S_2} \nabla \Phi_m^{TE II} \nabla \Phi_m^{TE II} ds} \right] \nabla \Phi_m^{TE II} = 2 \sum_m j k_{zm}^{TE I} D_m^I \nabla \Phi_m^{TE I}
 \end{aligned}$$

and

$$\begin{aligned}
& \sum_m -\frac{\omega\epsilon_0}{k_{zm}^{TMI}} \left[\frac{\int_{S_2} \mathbf{W} \cdot \nabla \Phi_m^{TMI} ds}{\int_{S_1} \nabla \Phi_m^{TMI} \nabla \Phi_m^{TMI} ds} \right] \mathbf{a}_z \times \nabla \Phi_m^{TMI} + \sum_m \frac{k_{zm}^{TEI}}{\omega\mu_0} \left[\frac{\int_{S_2} \mathbf{W} (\mathbf{a}_z \times \nabla \Phi_m^{TEI}) ds}{\int_{S_1} \nabla \Phi_m^{TMI} \nabla \Phi_m^{TEI} ds} \right] \nabla \Phi_m^{TEI} \\
& -j \sum_m \frac{\omega\epsilon_0}{k_{zm}^{TMII}} \cot(k_{zm}^{TMII} L) \left[\frac{\int_{S_2} \mathbf{W} \cdot \nabla \Phi_m^{TMII} ds}{\int_{S_2} \nabla \Phi_m^{TMII} \nabla \Phi_m^{TMII} ds} \right] \mathbf{a}_z \times \nabla \Phi_m^{TMII} \\
& + \sum_m j \frac{\omega\epsilon_0}{k_{zm}^{TMII}} \frac{1}{\sin(k_{zm}^{TMII} L)} \left[\frac{\int_{S_2} \mathbf{Z} \cdot \nabla \Phi_m^{TMII} ds}{\int_{S_2} \nabla \Phi_m^{TMII} \nabla \Phi_m^{TMII} ds} \right] \mathbf{a}_z \times \nabla \Phi_m^{TMII} \quad (2) \\
& + \sum_m j \frac{k_{zm}^{TEII}}{\omega\mu_0} \cot(k_{zm}^{TEII} L) \left[\frac{\int_{S_2} \mathbf{W} \cdot (\mathbf{a}_z \times \nabla \Phi_m^{TEII}) ds}{\int_{S_2} \nabla \Phi_m^{TEII} \nabla \Phi_m^{TEII} ds} \right] \nabla \Phi_m^{TEII} \\
& - \sum_m j \frac{k_{zm}^{TEII}}{\omega\mu_0} \frac{1}{\sin(k_{zm}^{TEII} L)} \left[\frac{\int_{S_2} \mathbf{Z} \cdot (\mathbf{a}_z \times \nabla \Phi_m^{TEII}) ds}{\int_{S_2} \nabla \Phi_m^{TEII} \nabla \Phi_m^{TEII} ds} \right] \nabla \Phi_m^{TEII} = -2 \sum_m j k_{zm}^{TEI} C_m^{III} \nabla \Phi_m^{TEI}
\end{aligned}$$

The evident symmetry of these two integral equations in \mathbf{Z} and \mathbf{W} should be fruitfully exploited in the numerical solution by the moment method.

3 RESULTS

The present approach is applied to compute the reflection coefficient of the fundamental mode of arbitrary polarization at a ridged section of lengths $L = 10mm$ as a function of frequency. Figure 2 shows the reflection coefficients polarization S_{11cc} , S_{11cs} , and S_{11ss} as a function of frequency. The notation S_{11sc} stands for the reflection of the since polarization when only the cosine polarization is incident at port 1, the other terms follow by analogy. The dependence of the coupling between the two polarizations shows a substantial sensitivity to the frequency as exhibited by the dip at 9.80 GHz which corresponds to a phase of approximately 90 degrees for the lowest mode in the ridged section.

4 REFERENCES

1. S. Amari, S. Catreux, R. Vahldieck and J. Bornemann, "Application of a coupled-integral equations technique to circular ridged waveguides," to appear in IEEE Trans. Microwave Theory Tech.
2. S. Amari, J. Bornemann and R. Vahldieck, "Accurate analysis of scattering from multiple waveguide discontinuities using the coupled-integral- equations technique," Journal of Electromagnetic Waves and Applications, Vol. 8, No. 12, pp. 1642-1655, 1996.

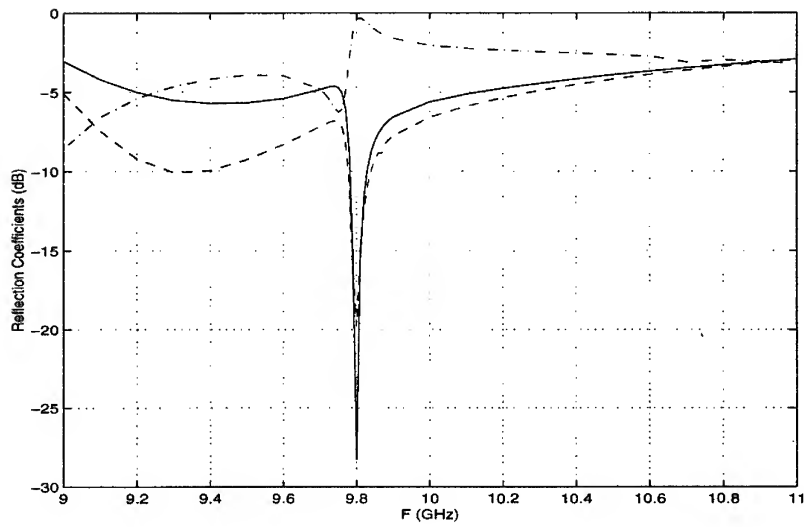


Figure 2: Reflection coefficients S_{11cc} (solid line), S_{11ss} (dashed line) and S_{11sc} (dotted-dashed line) versus frequency of a ridged section of length $L = 10$ mm. $r = t = 3^\circ$, $s = 135^\circ$, $b = 0.5a$ and $d = 0.4a$ and $a = 10$ mm

DESIGN OF MULTILAYER TYPE 2-POLE BAND PASS FILTER WITH ADDITIONAL POLES USING CLOSED LOOP RESONATOR

Heon-Jin Hong*, Dong-Phil Jang*
In-Seon Kim**, Chul-Soo Kim***
Min-Ho Chung***, Dal Ahn***

* Electronics and Telecommunications
Research Institute, R.O.Korea

** 5th R&D Center, Agency for Defense
Development, R.O.Korea

*** Dept. of Electronics,
Soonchunhyang Univ., P.O.Box 97
Asan, Chungnam, R.O.Korea
Email: rfmwlab@electra.sch.ac.kr

Abstract

This paper presents the design method of BPF using closed loop resonator, analyzed on the basis of TEM mode [1] and broadside coupled lines. The closed loop resonator has been analyzed with many different methods; magnetic wall method, numerical solution, field solution and so on. However, these methods take large amounts of calculations due to using field theories and it is difficult to build application circuits including other elements[2]. But the analysis method given in this paper is more simple and faster and the analysis of other elements in resonator is possible.

The BPF using closed loop resonator is possible to put the number of additional poles equal to the number of closed loop resonator by assigning resonance frequency of each closed loop resonator differently. By taking advantage of the presented design method, the BPF containing good attenuation slope and wide rejection band characteristics can be realized by proper assignment of poles.

In this paper, the 2-pole, 3-pole BPFs have been designed with the presented design method and the 2-pole BPF has been realized on 1.72 ~ 1.75 GHz frequency band.

Theory and Design Method

In case of the 2-pole BPF is shown in Fig.1 [3]. It consists of the closed loop resonator and In/Output broadside coupled lines. Fig.2 shows the equivalent circuit of coupled lines which has one port open. n, Z_1 and Z_2 are defined as follows[4].

$$\begin{aligned} n &= \frac{Z_{oe} + Z_{oo}}{Z_{oe} - Z_{oo}} \\ Z_1 &= \frac{Z_{oe} + Z_{oo}}{2} \\ Z_2 &= Z_1(n^2 - 1) \end{aligned} \quad (1)$$

The equivalent circuit of 2-pole BPF can be expressed as shown in Fig. 3. Another equivalent circuit like Fig. 4. is obtained by eliminating transformer and impedance conversion from Fig. 4. the closed loop resonator in Fig. 4 is converted with π -network as transmission line equivalent circuit. Thus, Fig. 4 can be converted to Fig. 5. Susceptances in Fig. 5 are expressed as eq. (2), (3).

$$jB_a = jn^2 \left\{ Y_4 \tan(\phi_1/2) + Y_1 \frac{Y_3 \tan(\phi_2/2) + Y_1 \tan \theta_1}{Y_1 - Y_3 \tan(\phi_2/2) \tan \theta_1} \right\} \quad (2)$$

$$jB_b = -jn^2 \left\{ Y_4 \csc \phi_1 + \frac{Y_1^2 Y_3}{\sin \phi_2 (Y_1^2 \cos^2 \theta_1 - Y_3^2 \sin^2 \theta_1) + Y_1 Y_3 \sin 2\theta_1 \cos \phi_2} \right\} \quad (3)$$

The structure of general 2-pole BPF using admittance inverter can be expressed in Fig. 6. So, eq. (4), (5) are derived from equivalence between Fig. 5 and Fig. 6.

$$jB_r = j(B_a + B_b) + jwC_t \quad (4)$$

where $C_t = (C_p n^2 + C_t^e)$

$$j_{01} = \sqrt{\frac{Y_0 B_{r1}(w_2)}{w_1 g_0 g_1}}$$

$$J_{12} = \sqrt{\frac{B_{r1}(w_2) B_{r2}(w_2)}{(w_1 g_1)(w_2 g_2)}} \quad (5)$$

$$J_{23} = \sqrt{\frac{Y_0 B_{r2}(w_2)}{w_1 g_2 g_3}}$$

C_1 , lumped capacitor between In/Output port and closed loop resonator, can be expressed by J-inverter as follows:

$$C_1 = \frac{J_{01}/w_0}{\sqrt{1 - (J_{01}/Y_0)^2}} \quad (6)$$

$$C_1^e = \frac{C_1}{1 + (w_0 C_1/Y_0)^2} \quad (7)$$

If we apply resonance condition, $B_r(w_0) = 0$ to eq. (6), we can obtain eq. (8).

$$C_t = -\frac{(B_a + B_b)}{w_0} \quad (8)$$

Shunt capacitor, C_p can be derived by eq. (4) and eq. (8).

$$C_p = \frac{C_t - C_1^e}{n^2} \quad (9)$$

We can obtain the characteristics of 2-pole BPF with J-inverter by using the above equations and closed loop resonator as Fig. 1.

Simulation and Measurements

The 2-pole BPF using one closed loop resonator is designed with presented method in this paper and fabricated with 3-layer substrates. Each substrates were used 31 mil-thick Teflon ($\epsilon_r=2.2$). The total electrical length of this BPF is 360° at 1.84 GHz and the electrical length of $(2\theta_1 + \phi_2)$ and ϕ_1 are 293° and 67° respectively. The passband is 1.72 GHz to 1.75 GHz. Fig. 7, 8 show simulated, measured result respectively, and show two attenuation poles at 1.84 GHz and 1.476 GHz. the insertion loss characteristic in pass-band and attenuation slope in stop-band are excellent.

The 3-pole BPF using two closed loop resonators is designed with extension of equations given in this paper for another application. The passband of 3-pole BPF is 2.30 to 2.33 GHz and resonance frequencies of closed loop resonators are selected as 2.372 GHz, 2.395 GHz respectively to get the rejection band of 2.37 to 2.40 GHz. Fig.9 shows simulated results of designed BPF. The attenuation of about 50 dB above overall rejection band was obtained by assigning resonance frequency of each closed loop resonator differently. the substrate was used same one for simulation.

Conclusions

Firstly, analysis method based on TEM mode for closed loop resonator was presented. It is possible analyze efficiently with π - type network as transmission line equivalent circuit without requiring special numerical treatments. Second, the design method of BPF adjusting rejection and easily with the proper assignment of poles of closed loop resonator was suggested. The usefulness of this design method was verified through 2-pole and 3-pole BPF having simple geometry design. This method is available to the implementation of BPF or duplexer in handset of mobile communication system which require high performance such as high attenuation and compact size.

Reference

- [1] Dal Ahn, I.S.Kim, Y.K.Shin, K.Y.Kang, S.Y.Lee, "A New Analysis of The Ring Resonator Based on TEM Mode Analysis", Microwave Conference Proceeding of Kite, vol. 18, No. 1, pp. 28~31, 1995.
- [2] J.A.Navaro, Kai Chang, "Varactor-tunable Uniplanar Ring Resonators", MTT Trans., Vol. 41, No. 5, pp. 760~765, May 1993.
- [3] Dal Ahn, J.S.Lim, I.S.Kim, Y.K.Shin, K.Y.Kwang, "Design of 2-pole Band Pass Filter Using Closed Loop Resonator and Coupled Lines", MTT-S, vol.3 pp. 1643~1646, June 1996.
- [4] J.A.G.Malherbe, "Microwave Transmission Line filter", Artech house, pp. 11~24, 1970.

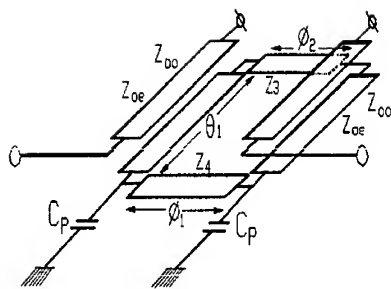


Fig. 1 The structure of 2-pole BPF

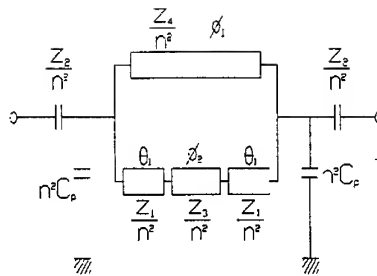


Fig. 4 2-pole BPF of which transformer has been eliminated by impedance conversion

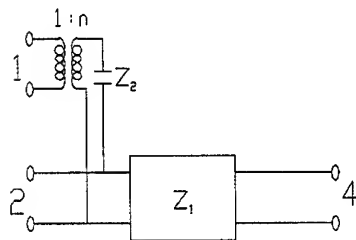


Fig. 2 The equivalent circuit of coupled line

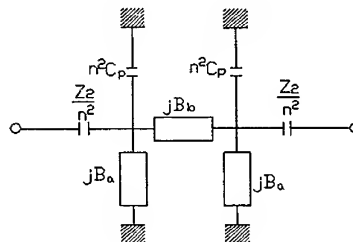


Fig. 5 \$\pi\$-network as transmission line equivalent circuit

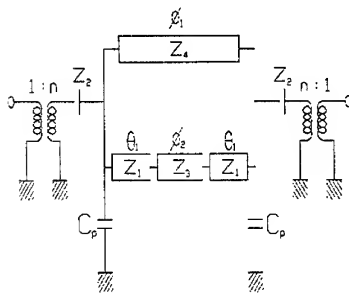


Fig. 3 The equivalent circuit of Fig. 1

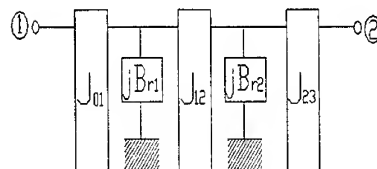


Fig. 6 2-pole BPF using admittance inverter

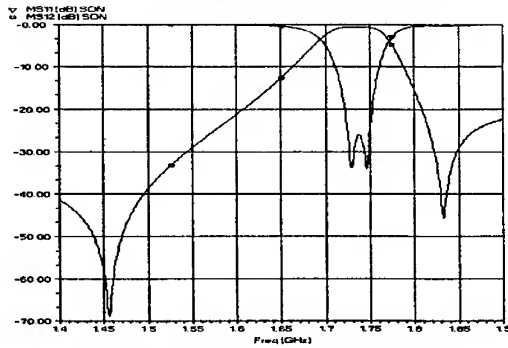


Fig. 7 The simulation results of 2-pole BPF

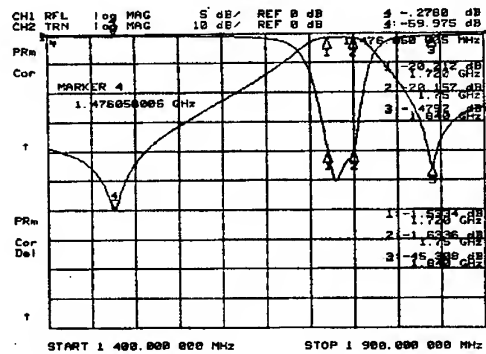


Fig. 8 The measured results of 2-pole BPF

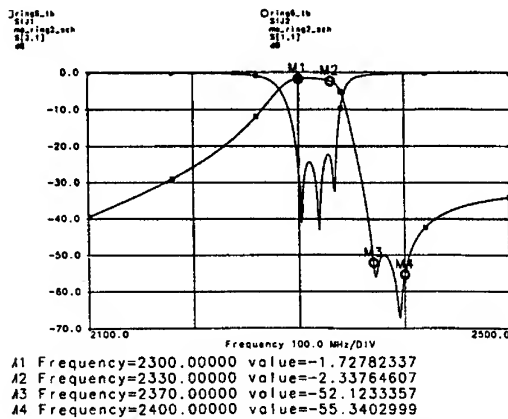


Fig. 9 The simulation results of 3-pole BPF

ANTENNAS ANALYSIS USING EDGE ELEMENTS AND SPHERICAL MODES EXPANSION

E. RICHALOT, M.F. WONG, V. FOUAD-HANNA, H. BAUDRAND*

France Télécom CNET DMR/RMC, 38-40 rue du général Leclerc, 92794 Issy-les-Moulineaux cedex 9, France
Tel. : +33 01 45 29 47 71 Fax : +33 01 45 29 41 94

*Laboratoire d'Electronique, ENSEEIHT, 2 rue C.Camichel, 31071 Toulouse cedex, France
richalot@issy.cnet.fr, wong@issy.cnet.fr, victor.fouad@issy.cnet.fr, baudrandh@len7.enseeiht.fr

Abstract - We present here a rigorous method for analysing antennas, using the finite element method inside a sphere and an expansion of fields in spherical harmonics in the exterior domain. The studied structure, represented as a multipole, can be entirely determined by its scattering matrix at the interfaces. The radiating pattern and input impedances obtained for an axisymmetric feedhorn and for a microstrip antenna are presented and compared to those obtained with other methods.

I-INTRODUCTION

The Finite Element Method presents the advantage of being able to characterise precisely structures having complex geometries and to take into account dielectric losses. It applies usually to bounded domain, therefore it has to be modified to study open structures. Several methods are proposed to achieve this goal (1). Absorbing Boundary Conditions are often applied, but they give approximate results, which eliminate one great advantage of the FEM, also they increase the domain to be studied because the ABC surface must be far enough from the studied radiating structure. We can also couple the FEM to an integral method or a boundary element method. The system to be solved in this case is partly full and partly sparse, which represents a numerical disadvantage. To preserve two great advantages of the FEM which are its precision and its sparse system to be solved, we have chosen to expand the fields in the open region in spherical harmonics. Moreover this rigorous treatment allows to characterise fully and economically the radiating structure as a network. The associated scattering matrix contains all the information that enable to determine the interesting features of the structure, mainly its radiating pattern and its input impedance.

II-METHOD OF ANALYSIS

1-Delimiting the FEM domain

We know that in order to characterise open structures using finite element analysis, the studied domain has to be bounded. The spherical harmonics can well describe the physical phenomenon of propagation in free space. As the basis of spherical modes is discrete, we easily express the fields as an expansion on spherical harmonics. Therefore, the domain is bounded by a spherical surface. The FEM is applied inside it and the fields are decomposed on edge elements.

2-The spherical modes

A complete and orthogonal set of spherical modes TE_{mn} and TM_{mn} is employed to express the fields in the open region:

$$\vec{E}(r, \theta, \varphi) = \sum_{\substack{n=1 \\ m=0}}^{\infty} \left[a'_n k_0 r h_n^{(1)}(k_0 r) + b'_n k_0 r h_n^{(2)}(k_0 r) \right] \vec{e}_{TE_{mn}}^{\varepsilon, o}(\theta, \varphi) + \sum_{\substack{n=1 \\ m=1}}^{\infty} \left\{ a''_n \left[k_0 r h_{n-1}^{(1)}(k_0 r) - n h_n^{(1)}(k_0 r) \right] + b''_n \left[k_0 r h_{n-1}^{(2)}(k_0 r) - n h_n^{(2)}(k_0 r) \right] \right\} \vec{e}_{TM_{mn}}^{\varepsilon, o}(\theta, \varphi) \quad (1)$$

$$\vec{H}(r, \theta, \varphi) = j \sum_{\substack{n=1 \\ m=0}}^{\infty} \left\{ a'_n \left[k_0 r h_{n-1}^{(1)}(k_0 r) - n h_n^{(1)}(k_0 r) \right] + b'_n \left[k_0 r h_{n-1}^{(2)}(k_0 r) - n h_n^{(2)}(k_0 r) \right] \right\} \vec{h}_{TE_{mn}}^{\varepsilon, o}(\theta, \varphi) - j \sum_{\substack{n=1 \\ m=1}}^{\infty} \left[a''_n k_0 r h_n^{(1)}(k_0 r) + b''_n k_0 r h_n^{(2)}(k_0 r) \right] \vec{h}_{TM_{mn}}^{\varepsilon, o}(\theta, \varphi) \quad (2)$$

The index 1 and 2 of the Hankel spherical functions indicate inward and outward travelling waves respectively.

The radiated fields can, in principle, contain an infinity of modes, but for r larger than n/k , we can truncate the expansion of series representation of spherical waves functions. A sufficient number of terms is given by the empirical rule (2):

$$N = [kr_0] + n_1 \quad (3)$$

where r_0 is the radius of the minimum sphere, the square brackets indicate the largest integer smaller or equal to kr_0 , and n_1 , integer, depends on the size of the sphere delimiting the domain and on the accuracy required. Typically we take $n_1 = 10$.

3-Network representation

In our method, the space outside the sphere is explicitly considered as a spherical waveguide, in which the propagation takes place in the radial direction. Concepts as orthogonal modes, cut-off, propagation and evanescence can then be defined as in conventional cylindrical waveguides. The studied structure is represented as a network, its constant section waveguides and the bounding spherical waveguide are considered to have ports excited by several modes (fig. 1). It can be shown (3) that in order to determine the scattering matrix for this network, the impedance matrix or admittance matrix can be calculated by imposing the magnetic or electric fields on the ports, and converted into a scattering one. The system to be solved is always sparse.

III-PARTICULAR GEOMETRIES

1-Axisymmetry

As many closed or open microwave devices like dielectric resonators or antenna feeds and horns exhibit a rotational symmetry, it is computationally interesting to benefit from this axisymmetry to reduce the computational domain. In this case, the field can be expanded in Fourier series. As Fourier mode are decoupled, they can be studied separately, and the studied domain can be reduced to a 2D one in the meridian plane (4). For example a circular waveguide excited by the TE_{11} mode imposes a φ dependence in $\cos \varphi$ for E_r and H_φ , and in $\sin \varphi$ for E_φ and H_r . The spherical modes to be excited have to follow the same φ dependence and are then the TE_{1n}^c and the TM_{1n}^s spherical modes.

2-Microstrip antennas

The spherical modes defined in the half space also form a complete and orthogonal set of modes. Therefore we can study microstrip antennas by delimiting the open region where they radiate with a half-sphere.

We consider that the ground plane of the antenna coincides with the plane $z=0$. The spherical modes taken into account follow the electric wall conditions on the plane $z=0$, and are of the form $TE_{mn}^{e,o}$ with $(n+m)$ even, and $TM_{mn}^{e,o}$ with $(n+m)$ odd.

IV-APPLICATIONS

1-Axisymmetric feedhorn

The circularly polarised primary feedhorn operating in the Ku band (14.-14.5 GHz) like that shown in fig. 2 was developed in (5) as a primary feed radiating a sectoral pattern on a $\pm 70^\circ$ angular width for a satellite payload. Its excitation is performed through a circular waveguide having the TE_{11} mode as the fundamental operating mode.

The radiation pattern at 14.25GHz (fig. 3) and the input impedances (fig. 4) have been determined using our formulation and compared to the results obtained using an integral equation method (6). A very good concordance of the results can be noticed.

2-Microstrip antenna

The microstrip antenna shown in fig. 5 is characterised using our proposed combination of the FEM and spherical modes expansion. The radiation pattern at the first anti-resonance frequency 6.647GHz (fig. 6) and at the second resonance frequency 11.48GHz (fig. 7) are compared to those obtained using the FDTD (Finite Difference Time Domain) method using PML (Perfect Matched Layer) condition (6). A relatively good concordance of the results is noticed.

V- CONCLUSION

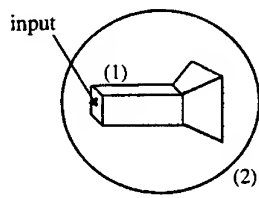
The presented method for analysing antennas, using the finite element method and an expansion on spherical modes, benefits from the advantages that presents the finite elements method, mainly : precision, capacity of characterising complex geometries containing different materials, and having a sparse system to solve.

Our proposed analysis permits to characterise entirely the studied structure by its scattering matrix in terms of modes of the structure and spherical modes applied on an equivalent network. This matrix representation allows to characterise entirely both off transmitting and receiving antennas.

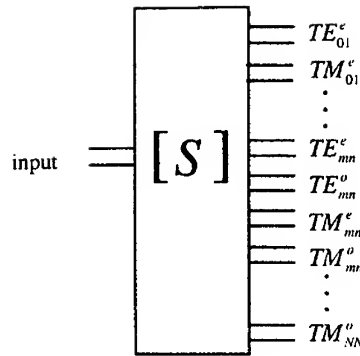
The adaptability of our formulation for characterising complex structures has been demonstrated through the determination of the radiation patterns and input impedances for different types of antennas.

References

- (1) J. Jin, "The Finite Element Method in Electromagnetics", 1993, John Wiley&Sons, New York.
- (2) J.E. Hansen, "Spherical near-field antenna measurements", 1988, London.
- (3) M.F. Wong, O. Picon, V. Fouad Hanna, "Three-Dimensional Finite Element Analysis of N-Port Waveguide Junctions using Edge-Elements", 1993, Int. Jour. Microwave and Millimeter-Wave CAE, Vol. 3, No. 4, pp. 442-451.
- (4) M.F. Wong, M. Prak, V. Fouad-Hanna, "Axisymmetric Edge-Based Finite Element Formulation For Bodies Of Revolution: Application To Dielectric Resonators", 1995, IEEE Microwave-Symposium MTT-S, Orlando.
- (5) P. Brachat, "Sectoral Pattern Synthesis with Primary Feeds ", April 1994, IEE Trans. On Antennas and Propagation, vol. 42, No. 4.
- (6) A. Reinex, B. Jecko, "Application de la méthode de résolution par différences finies transitoires à l'étude des antennes plaquées", 1987, Ann. Telecommun., 42, No. 9-10.



(a)



(b)

Fig 1: (a) Studied FEM domain

(1) Studied structure, (2) Spherical bounding domain

(b) Structure network representation

One input port (excited by its fundamental mode), outputs ports (excited by spherical modes, $TE_{mn}^{e,o}$ and $TM_{mn}^{e,o}$ for $1 \leq n \leq N$ and $0 \leq m \leq n$).

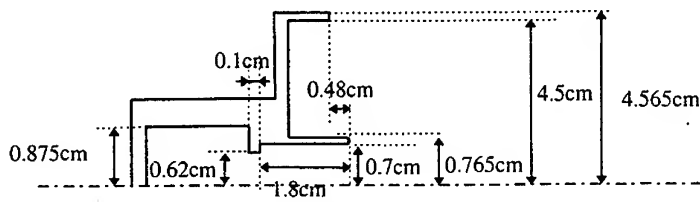


Fig 2 : Half-meridian plane of the feedhorn

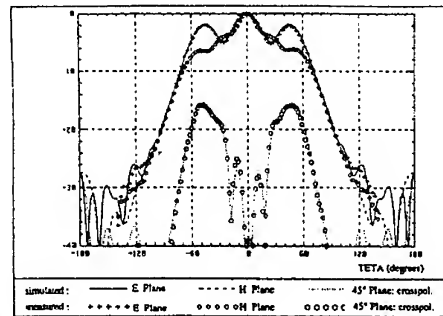
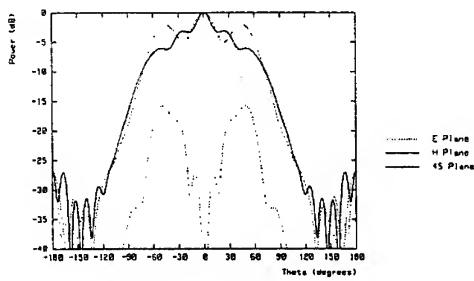


Fig. 3

(a) : Radiation pattern at 14.25GHz using the FEM spherical modes expansion

(b) : Radiation pattern at 14.25GHz using an integral equation method

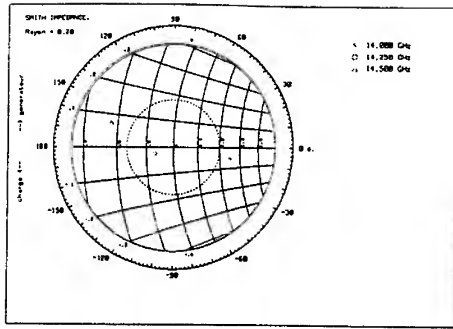
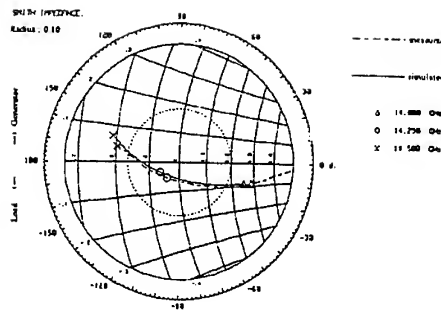


Fig. 4

a): Normalized input impedances using the FEM and spherical modes expansion



(b): Normalized input impedances using an integral equation method

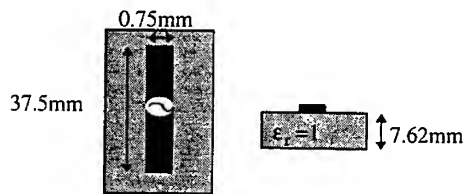


Fig 5 : Microstrip antenna

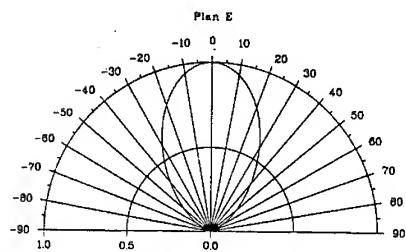
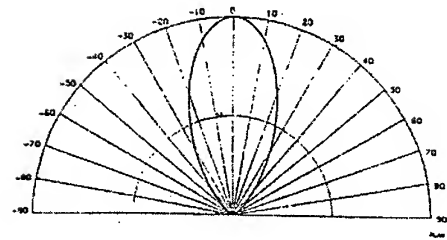
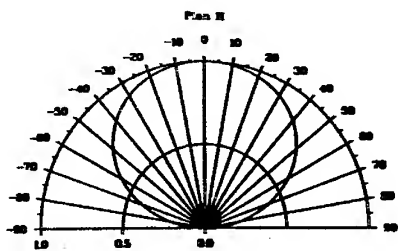


Fig. 6

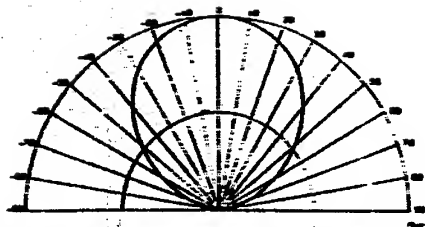
a) : Radiation pattern in the E-plane at 6.647GHz using the FEM and spherical modes expansion



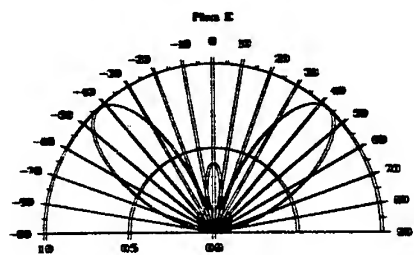
(b) : Radiation pattern in the E-plane at 6.647GHz using the FDTD



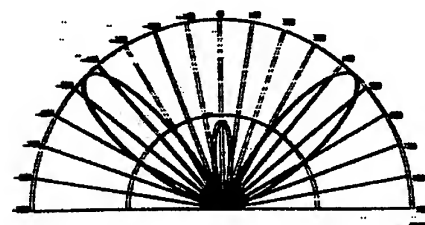
(c) : Radiation pattern in the H-plane at 6.647GHz using the FEM and spherical modes expansion.



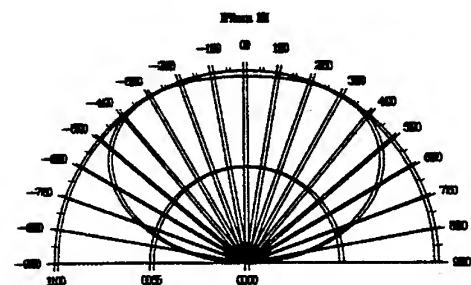
(d) : Radiation pattern in the H-plane at 6.647GHz using the FDTD.



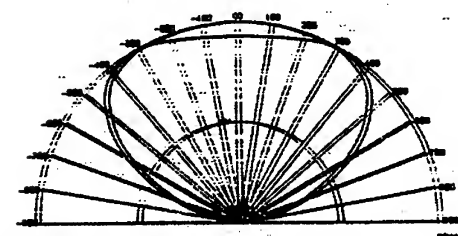
(a) : Radiation pattern in the E-plane at 11.48GHz using the FEM and spherical modes expansion.



(b) : Radiation pattern in the E-plane at 11.48GHz using the FDTD.



(c) : Radiation pattern in the H-plane at 111.48GHz using the FEM and spherical modes expansion.



(d) : Radiation pattern in the H-plane at 111.48GHz using the FDTD.

POLARIZATION TRANSFORMER CONSTRUCTED FROM CHIRAL SLAB AND SOFT AND HARD SURFACE

Perttu P. Puska, Ari J. Viitanen
Electromagnetics Laboratory
Helsinki University of Technology
P.O.Box 3000 FIN-02015 HUT
Finland

Abstract

Plane wave reflection from soft and hard surface coated with chiral material is analyzed for the normal incidence. The fields inside the chiral slab are presented with circularly polarized eigenwaves. The eigenwaves are not coupled at the soft and hard surface, the coupling occurs at the interface between free space and chiral medium. Reflection coefficients are calculated and the polarization properties of the reflected field are studied. The soft and hard surface coated with chiral medium can be used for applications, such as polarization transformers and twist reflectors.

1 INTRODUCTION

Chiral materials have recently been achieving attention because they can be used to build novel microwave devices and structures [1]–[4]. They can be utilized to change the plane of polarization of the electromagnetic field in lens antennas [5], or to construct polarization transformers [6], [7]. Chiral materials are realizations of the chiral medium, which is the most general reciprocal isotropic medium, its eigenfields being right hand and left hand circularly polarized fields. When constructing devices using chiral materials one evidently has to cope with the behavior of the eigenfields at boundaries and interfaces. In the applications exhibiting air-chiral or conductor-chiral interfaces one observes that the eigenfields couple at the interfaces, which usually is a rather undesirable phenomenon. However, there is an anisotropic surface that does not have this coupling property: the soft and hard surface (SHS) [8],[9], usually realized as a corrugated surface. Now, since the eigenpolarizations of the chiral medium are 'compatible' with the soft and hard surface, it might be interesting to investigate the possibility of constructing a polarization transformer from these materials, and indeed, in this paper we give the essential parameters for building such a transformer. Obviously we have to begin by analyzing the reflection of the plane wave that is normally incident upon the chiral slab backed with the soft and hard surface.

2 ANALYSIS OF THE FIELDS AT THE INTERFACE

Assuming $e^{j\omega t}$ time dependency the constitutive relations of the chiral medium become

$$\mathbf{D} = \epsilon \mathbf{E} - j\kappa \sqrt{\mu_0 \epsilon_0} \mathbf{H}, \quad \mathbf{B} = \mu \mathbf{H} + j\kappa \sqrt{\mu_0 \epsilon_0} \mathbf{E},$$

where ϵ and μ are the permittivity and permeability, respectively, and κ is the chirality parameter of the chiral medium. Inserting these constitutive relations into the sourceless Maxwell equations the fields in the chiral medium

can be obtained. The plane wave solution of the Maxwell equations consists of two partial waves, + and - waves, which are the right hand and left hand circularly polarized eigenwaves, respectively,

$$\mathbf{E}_{\pm}(\mathbf{r}) = \mathbf{E}_{\pm} e^{-jk_{\pm}z},$$

where the corresponding propagation factors are $k_{\pm} = \omega \sqrt{\mu_o \epsilon_o} (\sqrt{\mu_r \epsilon_r} \mp \kappa)$. In this case the plane wave is coming normally to the slab as shown in Figure 1. The fields inside the chiral slab can be written as combinations of the eigenwaves [4]

$$\begin{aligned} \mathbf{E}(\mathbf{r}) &= E_+ \mathbf{a}_r e^{-jk_+z} + E_- \mathbf{a}_l e^{-jk_-z} + E_+^r \mathbf{b}_r e^{jk_+z} + E_-^r \mathbf{b}_l e^{jk_-z}, \\ \mathbf{H}(\mathbf{r}) &= \frac{1}{\eta} \mathbf{u}_i \times [E_+ \mathbf{a}_r e^{-jk_+z} + E_- \mathbf{a}_l e^{-jk_-z}] + \frac{1}{\eta} \mathbf{u}_r \times [E_+^r \mathbf{b}_r e^{jk_+z} + E_-^r \mathbf{b}_l e^{jk_-z}], \end{aligned}$$

where

$$\mathbf{a}_r = \mathbf{u}_z \times \mathbf{v} + j\mathbf{v}, \quad \mathbf{a}_l = \mathbf{u}_z \times \mathbf{v} - j\mathbf{v}, \quad \mathbf{b}_r = -\mathbf{u}_z \times \mathbf{v} + j\mathbf{v}, \quad \mathbf{b}_l = -\mathbf{u}_z \times \mathbf{v} - j\mathbf{v}, \quad (1)$$

are the circularly polarized eigenvectors for the two waves propagating in the positive ($\mathbf{a}_{r,l}$) and negative z direction ($\mathbf{b}_{r,l}$). The unit vector \mathbf{v} indicates the direction of the corrugation on the soft and hard surface. The unit vector $\mathbf{u}_i = \mathbf{u}_z$ is the propagation direction of incoming plane wave and the unit vector $\mathbf{u}_r = -\mathbf{u}_z$ is the propagation direction of the reflected plane wave. The boundary conditions at the soft and hard surface, $z = 0$, are [8]

$$\mathbf{v} \cdot \mathbf{E} = 0, \quad \mathbf{v} \cdot \mathbf{H} = 0.$$

These equations lead to the conditions relating the coefficients of the reflected part and the propagating part of the total field

$$E_+^r = -E_+, \quad E_-^r = -E_-.$$

This means that the two circularly polarized eigenmodes are not coupled at the soft and hard surface [9]. Because the soft and hard surface does not couple the two eigenmodes propagating in the chiral medium the total fields can be written inside the chiral slab as

$$\begin{aligned} \mathbf{E}(\mathbf{r}) &= E_+ [\mathbf{a}_r e^{-jk_+z} - \mathbf{b}_r e^{jk_+z}] + E_- [\mathbf{a}_l e^{-jk_-z} - \mathbf{b}_l e^{jk_-z}], \\ \mathbf{H}(\mathbf{r}) &= j \frac{E_+}{\eta} [\mathbf{a}_r e^{-jk_+z} - \mathbf{b}_r e^{jk_+z}] - j \frac{E_-}{\eta} [\mathbf{a}_l e^{-jk_-z} - \mathbf{b}_l e^{jk_-z}]. \end{aligned}$$

Here we have also applied relations (1). The total field in the free space outside the chiral slab consists of the incident and reflected field

$$\mathbf{E}_o(\mathbf{r}) = \mathbf{E}^i e^{-jk_o z} + \mathbf{E}^r e^{jk_o z}, \quad \mathbf{H}_o(\mathbf{r}) = \frac{1}{\eta_o} \mathbf{u}_z \times [\mathbf{E}^i e^{-jk_o z} - \mathbf{E}^r e^{jk_o z}].$$

By using the natural coordinates $\mathbf{v}, \mathbf{u}_z \times \mathbf{v}$ the incident and reflected fields can be written as

$$\mathbf{E}^i = E_v^i \mathbf{v} + E_{\perp}^i \mathbf{u}_z \times \mathbf{v}, \quad \mathbf{E}^r = E_v^r \mathbf{v} + E_{\perp}^r \mathbf{u}_z \times \mathbf{v},$$

and the continuity conditions of the tangential fields at $z = -d$ become

$$E_v^i e^{jk_o d} + E_v^r e^{-jk_o d} = -2E_+ \sin k_- d + 2E_- \sin k_- d, \quad (2)$$

$$E_{\perp}^i e^{jk_o d} + E_{\perp}^r e^{-jk_o d} = 2E_+ \cos k_- d + 2E_- \cos k_- d, \quad (3)$$

$$\frac{\eta}{\eta_o} [E_{\perp}^i e^{jk_o d} - E_{\perp}^r e^{-jk_o d}] = j2E_+ \cos k_- d - j2E_- \cos k_- d, \quad (4)$$

$$\frac{\eta}{\eta_o} [E_v^i e^{jk_o d} - E_v^r e^{-jk_o d}] = j2E_+ \sin k_- d + j2E_- \sin k_- d. \quad (5)$$

After eliminating the coefficients E_+ and E_- in the above equations the reflected field can be given as a function of the incident field $\mathbf{E}^r = \bar{\bar{R}} \cdot \mathbf{E}^i$.

3 REFLECTION DYADIC

The continuity of the tangential field leads to the expression for the reflection dyadic

$$\bar{\bar{R}} = R_{vv} \mathbf{v} \mathbf{v} + R_{v\perp} \mathbf{v} (\mathbf{u}_z \times \mathbf{v}) + R_{\perp v} (\mathbf{u}_z \times \mathbf{v}) + R_{\perp\perp} (\mathbf{u}_z \times \mathbf{v}) (\mathbf{u}_z \times \mathbf{v}).$$

This can be obtained by solving the coefficients E_+ and E_- from the equations (2) - (3) and inserting these coefficients into the equations (4) - (5). The reflection coefficients, when written in \mathbf{v} , $\mathbf{u}_z \times \mathbf{v}$ coordinates, read

$$R_{vv} = e^{j2k_o d} \left[\frac{\frac{\eta}{\eta_o} + j \frac{\cos(k_+ - k_-)d - \cos(k_+ + k_-)d}{\sin(k_+ + k_-)d}}{\left[\frac{\eta}{\eta_o} + j \frac{\cos(k_+ - k_-)d + \cos(k_+ + k_-)d}{\sin(k_+ + k_-)d} \right] - \frac{\sin^2(k_+ - k_-)d}{\sin^2(k_+ + k_-)d}} \right]$$

$$\left[\frac{\frac{\eta}{\eta_o} + j \frac{\cos(k_+ - k_-)d - \cos(k_+ + k_-)d}{\sin(k_+ + k_-)d}}{\left[\frac{\eta}{\eta_o} - j \frac{\cos(k_+ - k_-)d + \cos(k_+ + k_-)d}{\sin(k_+ + k_-)d} \right] + \frac{\sin^2(k_+ - k_-)d}{\sin^2(k_+ + k_-)d}} \right]$$

$$R_{\perp\perp} = e^{j2k_o d} \left[\frac{\frac{\eta}{\eta_o} - j \frac{\cos(k_+ - k_-)d - \cos(k_+ + k_-)d}{\sin(k_+ + k_-)d}}{\left[\frac{\eta}{\eta_o} - j \frac{\cos(k_+ - k_-)d + \cos(k_+ + k_-)d}{\sin(k_+ + k_-)d} \right] - \frac{\sin^2(k_+ - k_-)d}{\sin^2(k_+ + k_-)d}} \right]$$

$$\left[\frac{\frac{\eta}{\eta_o} + j \frac{\cos(k_+ - k_-)d - \cos(k_+ + k_-)d}{\sin(k_+ + k_-)d}}{\left[\frac{\eta}{\eta_o} - j \frac{\cos(k_+ - k_-)d + \cos(k_+ + k_-)d}{\sin(k_+ + k_-)d} \right] + \frac{\sin^2(k_+ - k_-)d}{\sin^2(k_+ + k_-)d}} \right]$$

$$R_{v\perp} = R_{\perp v} = \frac{j2 \frac{\eta}{\eta_o} \frac{\sin(k_+ - k_-)d}{\sin(k_+ + k_-)d} e^{j2k_o d}}{\left[\frac{\eta}{\eta_o} + j \frac{\cos(k_+ - k_-)d - \cos(k_+ + k_-)d}{\sin(k_+ + k_-)d} \right] \left[\frac{\eta}{\eta_o} - j \frac{\cos(k_+ - k_-)d + \cos(k_+ + k_-)d}{\sin(k_+ + k_-)d} \right] + \frac{\sin^2(k_+ - k_-)d}{\sin^2(k_+ + k_-)d}}$$

For the isotropic slab, $k_+ = k_- = k$, and the crosspolarized reflection coefficients vanish whereas the copolarized reflection coefficients are

$$R_{vv} = e^{j2k_o d} \frac{\frac{\eta}{\eta_o} + j \cot kd}{\frac{\eta}{\eta_o} - j \cot kd}, \quad R_{\perp\perp} = e^{j2k_o d} \frac{\frac{\eta}{\eta_o} - j \tan kd}{\frac{\eta}{\eta_o} + j \tan kd}.$$

Thus there is no change of the polarization in the reflection, but the copolarized field components are shifted in phase. But for the chiral slab, $k_+ \neq k_-$, and the crosspolarized reflection coefficients remain. The expressions for the reflection coefficients do not reduce to a simple form except in some special cases considered in the next section. In those special cases there is a phase shift between the copolarized and crosspolarized reflection coefficients and hence the polarization will be changed.

4 POLARIZATION TRANSFORMER

By choosing suitable values for the parameters and thickness of the slab we can construct a polarization transformer (Fig. 2). In the polarization transformer the incident linearly polarized field is changed to an elliptically polarized one in the reflection. The suitable values might be chosen as follows

$$(k_+ + k_-)d = \frac{3\pi}{2}, \quad (k_+ - k_-)d = \frac{\pi}{2}, \quad (6)$$

that is $k_+d = \pi$, $k_-d = \frac{\pi}{2}$, and the expressions for the reflection coefficients reduce to

$$R_{vv} = R_{\perp\perp} = -e^{j2k_0d} \frac{1 - \left(\frac{\eta}{\eta_0}\right)^2}{1 + \left(\frac{\eta}{\eta_0}\right)^2}, \quad R_{v\perp} = R_{\perp v} = -je^{j2k_0d} \frac{2\frac{\eta}{\eta_0}}{1 + \left(\frac{\eta}{\eta_0}\right)^2}.$$

The helicity vector \mathbf{p} can be utilized to determine the polarization state of the field. For the electric field \mathbf{p} is [4],[10]

$$\mathbf{p} = \frac{\mathbf{E} \times \mathbf{E}^*}{j\mathbf{E} \cdot \mathbf{E}^*}.$$

The helicity vector is a real valued vector and the magnitude of the helicity vector is $-1 \leq p \leq 1$. When $p = 1$, the field is right hand circularly polarized, when $p = -1$, field is left hand circularly polarized, and when $p = 0$, the field is linearly polarized. In other cases the field is elliptically polarized. Let us then consider the case where the incident field is linearly polarized

$$\mathbf{E}^i = E_0[\cos \alpha \mathbf{v} + \sin \alpha \mathbf{u}_z \times \mathbf{v}] e^{-jk_0z}. \quad (7)$$

Then the reflected field is

$$\mathbf{E}^r = E_0 e^{jk_0z} \{ [R_{vv} \cos \alpha + R_{v\perp} \sin \alpha] \mathbf{v} + [R_{\perp v} \cos \alpha + R_{\perp\perp} \sin \alpha] \mathbf{u}_z \times \mathbf{v} \}$$

The helicity vector of the reflected field is

$$\mathbf{p} = \frac{\mathbf{E}^r \times \mathbf{E}^{r*}}{j\mathbf{E}^r \cdot \mathbf{E}^{r*}} = -\frac{4\frac{\eta}{\eta_0}[1 - \left(\frac{\eta}{\eta_0}\right)^2]}{[1 + \left(\frac{\eta}{\eta_0}\right)^2]^2} \cos 2\alpha \mathbf{u}_z.$$

In a general case the reflected field is elliptically polarized. The ellipticity and handedness depend on the impedance η/η_0 and the angle α . The performance of the transformer is optimal when all the values in the range $-1 \leq p \leq 1$ can be reached as the angle α changes. One obtains this optimal situation when $\eta/\eta_0 = \sqrt{2} \pm 1$. The helicity vector of the reflected field becomes now $\mathbf{p} = \pm \cos 2\alpha \mathbf{u}_z$, and all polarization states can be obtained from linearly polarized incident field by rotating the soft and hard surface. A resembling polarization transformer that changes the polarization of the transmitted field is presented in [6]. However, the transformer presented in [11] is also worth mentioning, for it can be thought of being a dual to our transformer.

In the chiral case when the thickness of the slab is chosen as in (6), and choosing the impedance of the chiral

medium as $\eta/\eta_0 = 1$. the copolarized reflection coefficients vanish and the crosspolarized ones reduce to the form

$$R_{v\perp} = R_{\perp v} = -j e^{j2k_0 d}.$$

The linearly polarized incident field (7) remains linearly polarized in the reflection, but is twisted by an angle $\varphi = 90^\circ - 2\alpha$. The electric field that is parallel or perpendicular to the direction of the corrugation is twisted 90° in the reflection. Also the ellipse for elliptically polarized incident field is twisted in reflection while for circularly polarized incident field there is a phase shift in the reflection.

5 CONCLUSION

We can construct a reflector polarization transformer from the chiral slab and from the soft and hard surface by choosing the thickness of the slab and the impedance of the chiral medium properly. The use of the chiral material is essential, for one can not achieve the polarization altering effects we described by substituting a nonchiral isotropic slab in the place of the chiral slab.

References

- [1] S. Bassiri, N. Engheta, C.H. Papas, "Dyadic Green's function and dipole radiation in chiral media," *Alta Frequenza*, No. 2, pp. 83-88, March-April, 1986.
- [2] D.L. Jaggard, X. Sun, N. Engheta, "Canonical sources and duality in chiral media," *IEEE Trans. Antennas Propagat.*, Vol. AP-36, No. 7, pp. 1007-1013, July, 1988.
- [3] J.C. Monzon, "Radiation and scattering in homogeneous general biisotropic regions," *IEEE Trans. Antennas Propagat.*, Vol. AP-38, No. 2, pp. 227-235, February, 1990.
- [4] I.V. Lindell, A.H. Sihvola, S.A. Tretyakov, A.J. Viitanen, *Electromagnetic Waves in Chiral and Bi-Isotropic Media*, Artech House, Norwood, NY, 1994.
- [5] I.V. Lindell, A.H. Sihvola, A.J. Viitanen, S.A. Tretyakov, "Geometrical optics in inhomogeneous chiral media with application to polarization correction of inhomogeneous microwave lens antennas," *Journal of Electromagn. Waves and Applic.*, Vol. 4, No. 6, pp. 533-548, 1990.
- [6] A.J. Viitanen, I.V. Lindell, "Uniaxial chiral quarter-wave polarization transformer," *Electronics Letters*, Vol. 29, No. 12, pp. 1074-1075, June, 1993.
- [7] A.J. Viitanen, I.V. Lindell, "Plane-wave propagation in an anisotropic chiral medium with isotropic permittivity and permeability," *Microwave and Opt. Tech. Letters*, Vol. 7, No. 8, pp. 344-348, June 5, 1994.
- [8] P-S. Kildal, "Artificially soft and hard surfaces in electromagnetics," *IEEE Antennas Propagat.*, vol. 38, no. 10, pp. 1537-1544, October, 1990.
- [9] I.V. Lindell, P.P. Puska, "Reflection dyadic for the soft and hard surface with application to depolarising corner reflector," *IEE Proc. Microwave Antennas Propag.*, Vol. 143, No. 5, October, 1996, pp. 417-421.
- [10] I.V. Lindell, *Methods for Electromagnetic Field Analysis*, Oxford: Clarendon Press, 1992.
- [11] A.J. Viitanen, "Conductor-backed uniaxial slab as polarization transformer," *Microwave and Optical Technology Letters*, Vol. 12, No. 2, pp. 107-111, June, 1996.

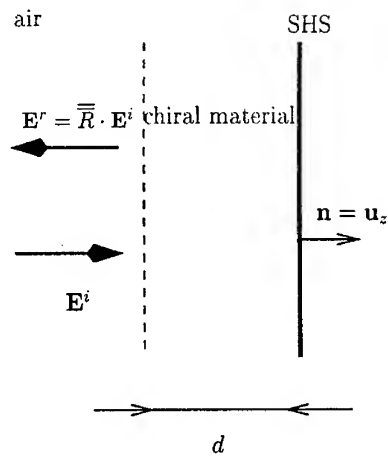


Figure 1. Plane wave reflection from soft and hard surface coated with chiral slab.

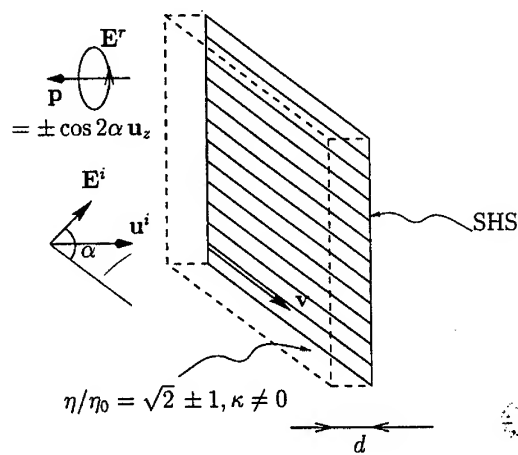


Figure 2. Polarization transformer.

Microwave Ferroelectric Superconducting Phase Shifter

Farhat Abbas, J C Gallop and C D Langham

National Physical Laboratory
Teddington Middlesex TW11 0LW UK

Abstract

This study provides the possibility of developing tunable microwave components based on the dielectric substrate nonlinearity, with the conducting surfaces made of a superconductor. It is shown that with a ferroelectric film thickness of 140 nm, phase shifts in the order of tens of degrees per cm can be obtained with bias voltages of tens of millivolts at 4 K for a frequency of 10 GHz.

INTRODUCTION

The particular property of ferroelectric materials of having a relative dielectric constant (ϵ_r) that can be altered by ambient temperature and externally applied electric field has been explored Vendik and Ter-Martirosyan (1), Varadan, et al (2), Jackson, et al (3) and Takemoto-Kobayashi, et al (4). There is potential to exploit the use of the nonlinearity of ferroelectric materials with superconducting surfaces for tunable microwave device applications. Ceramic phase shifters employing ferroelectric materials are distinguished by their high power handling capacity, great speed, low drive power, high radiation resistance, low cost and the simplicity with which they can be incorporated into integrated circuits Vendik and Ter-Martirosyan (1) and Varadan, et al (2). Such tunable microwave phase shifters based on the dielectric nonlinearity by using high temperature superconductors (HTS) and ferroelectric thin-films are promising for the development of phased antenna arrays with large numbers of elements. In this case a phase shifter is usually subject to additional requirements: low energy loss in the control circuits and (for use in phased antenna arrays) a low noise figure. Ferrite phase shifters have been used presently for phased arrays because of their high operational speed, and their small weight and size, but their high unit cost and complexity have prevented their widespread use Varadan, et al (2). PIN diode phase shifters are cheaper than ferrite phase shifters but the high insertion loss of PIN diode phase shifters limits their usefulness Varadan, et al (2). Also, the figure of merit of the PIN diode and HTS/ferroelectric/HTS phase shifters is same order of magnitude but the former are not as fast as the latter ones, since the switching time of the diode is determined by the time of diffusion of the minority carriers in the I-region. The switching time for a PIN diode is of the order of 10^{-7} to 10^{-8} s whereas for the ferroelectric phase shifters the switching time is 10^{-9} – 10^{-10} s Vendik and Ter-Martirosyan (1). Another recently proposed cooled discrete phase shifter based on superconducting switches can provide the same parameter values as ferroelectric phase shifters [Vendik and Ter-Martirosyan (1), and references therein]. The control element is a superconductor switch made in the form of a lumped element in the shape of a meander. In principle, with a control current (dc or pulsed) the switch is converted from the superconducting to the normal state, with its resistance abruptly increasing, in a transition time of no more than 10^{-10} s. When the superconducting technology develops to enable such switches to be optimized, it will be necessary to compare the phase shifters based on switched superconducting and ferroelectric phase shifters for use in cooled microwave integrated circuits. Ferroelectric/superconductor tunable microwave components are advantageous because of their power handling capability Jackson, et

al (3) compared to superconducting types based on the use of rf SQUIDs Takemoto-Kobayashi, et al (4). Non-linearity can occur in a transmission line when the rf voltage becomes comparable to the dc control voltage Jager (5). Power for a microstrip is given by $P = V^2/Z$, and for the minimum 5 volts bias, and a 1 ohm impedance, 25 watts (i.e. > 40 dBm) could be handled before distortion occurs. This is an under estimate, and without a non-linear analysis, it is not an over estimate to expect that even higher powers might be used. These high powers will determine the microstrip linewidth requirement to insure that the critical current carrying capacity of the line is not exceeded.

DISCUSSIONS AND RESULTS

Tunable microwave components based on dielectric nonlinearity by using HTS/ferroelectric/HTS thin-films shown in figure 1 can be described by the penetration depth λ_r and the normal conductivity σ_r of the superconductors, the dielectric constant ϵ_r of the dielectric, and the thicknesses d and l_r of the dielectric and the superconductors. The temperature dependence of penetration depth λ and the normal

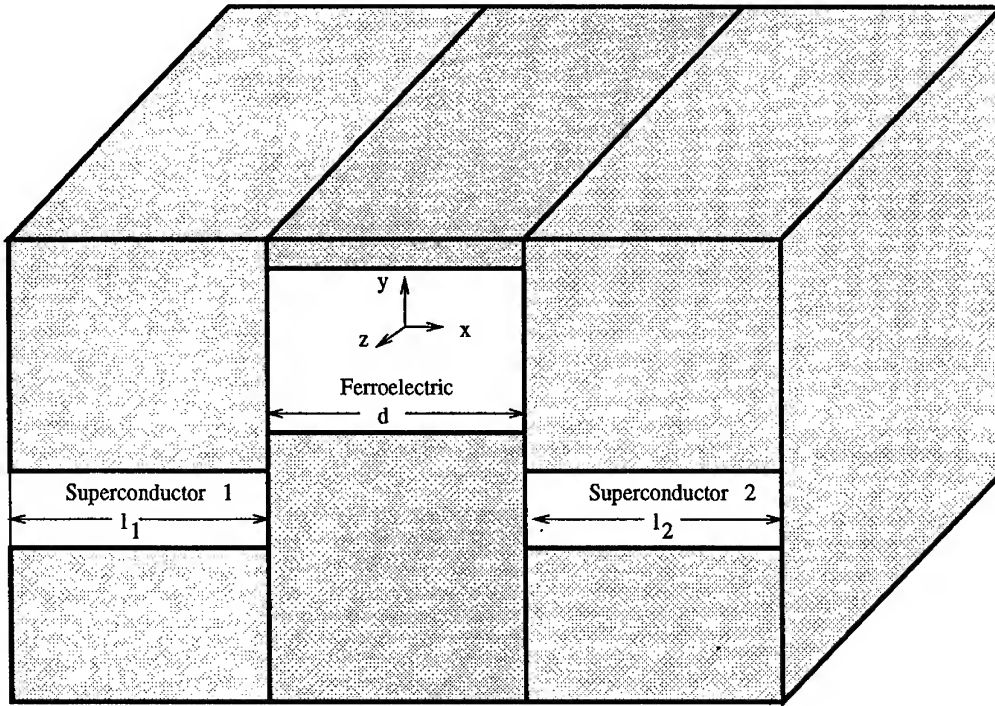


Figure 1: Configuration of tunable microwave structure investigated.

conductivity σ of a superconductor can be described using any one of several models outlined in the Ref. Abbas, et al (6). Any of those models for complex conductivity can be used in our analysis. Nonlinearity of the dielectric constant ϵ_2 due to the variations of the temperature T (K) and the dc bias electric field E (kV/cm) can be approximated using, Sawaguchi, et al (7) and Barrett, et al (8) $\epsilon_2 = M/[(T_1/2) \coth(T_1/T) - T_0]$ or $\epsilon_2 = -429E^2 + 12992$ where $M = 9 \times 10^4$ K, $T_0 = 38$ K and $T_1 = 84$ K. The above equation is obtained by using the MATLAB polyfit routine which fits the data

Sawaguchi, et al (7), in a least-squares sense. Also, equations in Ref. Abbas, et al (6). give the expression for the phase shift

$$\Delta\phi = L\omega\sqrt{\mu_o\epsilon_o}\left[\sqrt{\epsilon_2(E=0)} - \sqrt{\epsilon_2(E)}\right]\sqrt{[1 + \lambda_1/d_2 \coth(l_1/\lambda_1) + \lambda_2/d_2 \coth(l_2/\lambda_2)]}$$

where L is the length of the line. Different experimental combinations for the layers of HTS/ferroelectric/HTS have been reported in the literature Vendik and Ter-Martirosyan (1), Varadan, et al (2), Jackson, et al (3) and Takemoto-Kobayashi, et al (4), and the derived expressions can be used for any combination of superconductors and dielectric to describe the tunability. Let us consider an example in which superconductors are taken to be thin films of YBCO, and ferroelectric (dielectric) is taken to be Strontium Titanate (SrTiO_3). The parameters for these materials are taken from the references Vendik and Ter-Martirosyan (1), Varadan, et al (2), Jackson, et al (3), Takemoto-Kobayashi, et al (4), Sawaguchi, et al (7) and Scott (9). The value for penetration depth used for the high quality thin films of YBCO is 140 nm.

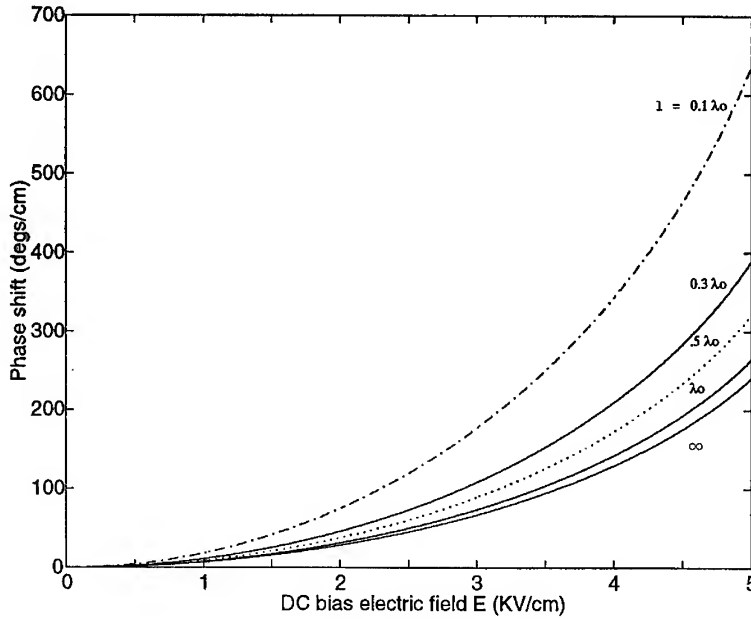


Figure 2: Computed phase shift per cm versus dc bias electric field for different thickness of HTS at 10 GHz.

In Figure 2, phase shifts are plotted versus dc bias electric field E (KV/cm) for different thickness ($l/\lambda_o = \infty, 1, 0.5, 0.3$ and 0.1) of YBCO (HTS) films at $T/T_c = 0.05$ by using above and in Abbas, et al (6) equations. The dielectric thickness d is taken equal to 140 nm and the temperature variation of λ is according to the two-fluid model of Gorter and Casimir. The phase shift can be tuned by a dc bias electric field E (KV/cm) as shown in Figure 2. It is also clear from Figure 2 that the thinner the (HTS) YBCO films, the more the phase shift.

In Figure 3, phase shifts are plotted versus electric field E (KV/cm) for different separations ($\lambda_o/d = 1, 2, 5, 10, 50$) of identical infinite superconducting planes at $T/T_c = 0.05$. It is clear in the electric field range shown in Figure 3 that the thinner ferroelectric material gives more tunability, i.e. phase shift.

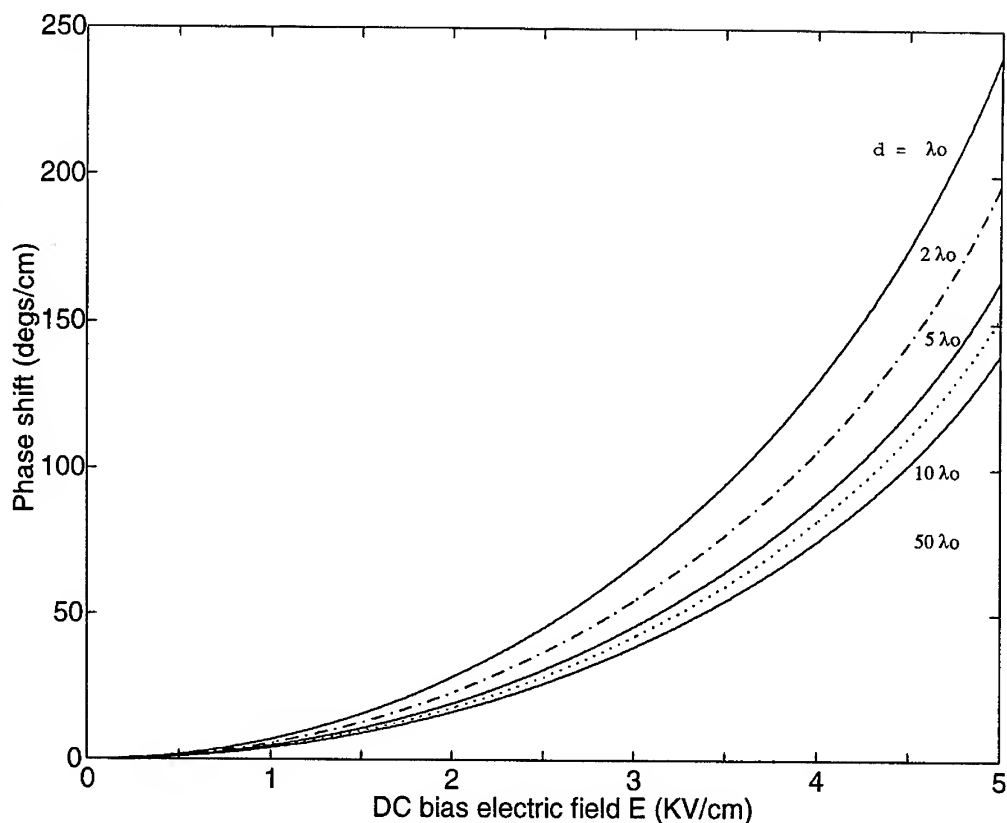


Figure 3: Phase shift per cm versus dc bias electric field for different separation d at 10 GHz.

CONCLUSIONS

An analysis has been completed which provides the possibility of developing tunable microwave components based on the dielectric nonlinearity of ferroelectrics with conducting surfaces made of a superconductor as shown in figure 1. A sinusoidal wave solution is found for a planar superconducting transmission line using the displacement vector, the dipole moment, polarization, polarizability, susceptibility and relative permittivity concepts for ferroelectrics, and for superconductors the Gorter and the Casimir two-fluid model, London's equations, and the classical skin effect for the normal component of the current. The use of Bose statistics for the superconductor gives very similar results. The solution gives expressions for the phase velocity and attenuation coefficient which are used to characterize the tunability of microwave components. The variation of the relative phase velocities and phase shifts, with reduced temperature and dc bias electric field has been computed for YBCO and SrTiO_3 . From this example, it may be concluded by using thinner ferroelectric and superconducting films a larger variation of phase shift with voltage can be obtained, i.e. increased tunability.

References

- [1] I B Vendik and L T Ter-Martirosyan, "Use of high-temperature superconducting structures in cooled microwave phase shifter," *Tech. Phys.*; vol. 38, no. 12, pp. 1090-1093, Dec. 1993.
- [2] V K Varadan, D K Ghodgaonkar, V V Varadan, J F Kelly and P Glikerdas, "Ceramic phase shifters for electronically steerable antenna systems," *Microwave J.*; vol. 35, pp. 116-127, Jan. 1992.
- [3] C M Jackson, J H Kobayashi, A Z Kain, A Lee, C L Pettiette-Hall, J F Burch and R Hu, "Novel monolithic phase shifter combining ferroelectric and superconductors," *Integrated Ferroelec.* vol. 4, pp. 121-129, 1994.
- [4] J H Takemoto-Kobayashi, C M Jackson, C L Pettiette-Hall and J F Burch, "High T_c superconducting monolithic phase shifter," *IEEE Trans. Applied Superconduct.*; vol. 2, pp. 39-44, 1992.
- [5] D Jager, "Slow-wave propagation along variable Schottky-Contact microstrip line," *IEEE Trans. Microwave Theory Tech.* vol. MTT-24, pp. 566-573, Sept. 1976.
- [6] Farhat Abbas, L E Davis and J C Gallop, "Field solution for a thin-film superconducting parallel-plate transmission line," *Physica C*, vol. 215, pp. 132-144, 1993.
- [7] E Sawaguchi, A Kikuchi and Y Kadera, "Dielectric constant of strontium titanate at low temperature," *J Phys. Soc.*; vol. 17, pp. 1666-1667, 1962.
- [8] J H Barrett, "Dielectric constant in perovskite type crystals," *Phys. Rev.* vol. 86, pp. 118, 1952.
- [9] J F Scott, "Ferroelectric memories," *Physics World*, vol. 8, pp. 46-50, Feb. 1995, and references therein.

**SUSCEPTIBILITY ANALYSIS OF ARBITRARILY SHAPED 2-D DIELECTRIC SCREENS
USING THE GENERALIZED SCATTERING MATRIX METHOD**

J. V. Balbastre (Member), L. Nuño (Member), M. Bort and E. de los Reyes (Sr. Member)

Departamento de Comunicaciones
E.T.S.I. Telecomunicación

Universidad Politécnica de Valencia
Cno de Vera s/n 46071 Valencia

Phone: 34-6-3877306

FAX: 34-6-3877309

e-mail: lnuno@dc.com.upv.es

ABSTRACT

The EMS inside slotted screens has been studied by using a hybrid technique. The screen is characterized, using the FEM, by a generalized admittance or impedance matrix, from which the scattering matrix can be straightforwardly obtained. The scattering matrix is then combined with a modal solution to compute the fields inside and outside the envelope. This circuital approach provides a systematic procedure for the analysis of very complex open structures.

1. INTRODUCTION

Electronic devices are generally covered by some kind of envelope or screen. One important property of those covering structures is the way they protect the enclosed circuit from external electromagnetic interference. When the envelope is slotted, environmental electromagnetic fields can originate an important field inside the envelope, which may affect the electrical performance of the enclosed devices or circuits. In this case, the knowledge of the internal field distribution and polarization can help the designer to choose the best place and orientation for the most sensitive devices. Moreover, the electromagnetic behavior of the screens depends on the electromagnetic properties of the materials they are made of (usually lossy dielectric materials).

The analysis of arbitrarily shaped screens made of lossy dielectric is a quite difficult problem, so it is necessary to carry it out by numerical methods [1-4]. The Finite Element Method (FEM) is a very good tool for the electromagnetic analysis of complex structures, but it can not deal with open problems. In this paper the study of cylindrical dielectric envelopes of arbitrary cross section has been accomplished by combining a modal analysis in free-space and a circuital representation of the screen obtained with the FEM. The proposed method is used in this paper for the analysis of several screens, in order to show its possibilities.

2. SCREEN CHARACTERIZATION

The structure to be analyzed, which is invariant in z , is enclosed by two circles, named access or ports, as is shown in figure 1. The analysis will be presented for TM^z waves, but the same procedure is directly applicable to TE^z waves. In $\rho \geq \rho_1$ the electric field can be expanded in terms of Bessel functions of the first kind and Hankel function of the second kind [5], as is stated in eq. (1), while in the region $\rho \leq \rho_2$, the electric field is written in terms of Hankel functions of the first and second kind [5], as in eq. (2). The superscripts + and - in eq. (1) and (2) stand for waves propagating towards and from the coordinate origin. In eq. (1) the limit of the series is taken $N_1 \cong k_0 \rho_1$, in order to account only for propagating waves in the $\rho \geq \rho_1$ region [6], while in eq. (2) the value of N_2 depends on the problem, and it will be discussed later.

$$E_z^+ = \sum_{n=-N_1}^{N_1} b_{1n} J_n(k_0 \rho) e^{jn\phi} \quad \rho \geq \rho_1 \quad (1-a)$$

$$E_z^- = \sum_{n=-N_1}^{N_1} a_{1n} H_n^{(2)}(k_0 \rho) e^{jn\phi} \quad \rho \geq \rho_1 \quad (1-b)$$

$$E_z^+ = \sum_{n=-N_2}^{N_2} b_{2n} H_n^{(1)}(k_0 \rho) e^{jn\phi} \quad \rho \leq \rho_2 \quad (2-a)$$

$$E_z^- = \sum_{n=-N_2}^{N_2} a_{2n} H_n^{(2)}(k_0 \rho) e^{jn\phi} \quad \rho \leq \rho_2 \quad (2-b)$$

The first step of the analysis is to characterize the screen by a generalized admittance matrix. To do so, the magnetic fields $H_{\phi,n}^l \big|_{\rho=\rho_k}$, with $k=1,2$ and $l=1,2$, must be computed by solving via the FEM the vector wave equation

$$\nabla \times (\epsilon_r^{-1} \nabla \times \vec{H}_n^l) - k_0^2 \mu_r \vec{H}_n^l = 0 \quad (6)$$

with the boundary conditions

$$E_{z,n} \Big|_{\rho=\rho_l} = e^{jm\phi} \quad (7)$$

and $E_{z,n} = 0$ at the other port, with $-N_l \leq n \leq N_l$.

The FEM discretization of the problem described by eqs. (6) and (7) using first order triangular edge elements leads to $2(N_l + N_2 + 1)$ systems of equations of the form:

$$[A]\{\dot{H}_n^l\} = \{C_n^l\} \quad (8)$$

where $\{\dot{H}_n^l\}$ is the value of the transverse magnetic field at the edges of the FEM mesh. In eq. (8) $[A]$ is a very sparse matrix which depends only on the differential operator which is being analyzed, so it is independent of the excitation terms given by the boundary conditions (7). This matrix can be factorized once, and then, after computing each excitation vector $\{C_n^l\}$, the corresponding magnetic field can be computed by backsubstitution, leading to a very efficient procedure. After computing the tangential magnetic field on each port for all the excitation terms, the admittance parameters are defined as:

$$H_{\phi,n}^l \Big|_{\rho=\rho_k} = \sum_{m=-N_k}^{N_k} Y_{nm}^{kl} e^{jm\phi} \quad (9)$$

Using the orthogonality property of the complex exponentials, the admittance parameters can be straightforwardly computed:

$$Y_{mn}^{kl} = \frac{1}{2\pi} \int_0^{2\pi} H_{\phi,n}^l \Big|_{\rho=\rho_k} e^{-jm\phi} d\phi \quad -N_k \leq m \leq N_k \quad -N_l \leq n \leq N_l \quad (10)$$

From these admittance parameters, the scattering matrix relating the amplitudes of the cylindrical harmonics in eq. (1)-(2) can be derived [7]:

$$\begin{Bmatrix} \{a_1\} \\ \{b_2\} \end{Bmatrix} = \begin{bmatrix} [S_{11}^{TM}] & [S_{12}^{TM}] \\ [S_{21}^{TM}] & [S_{22}^{TM}] \end{bmatrix} \begin{Bmatrix} \{b_1\} \\ \{a_2\} \end{Bmatrix} \quad (11)$$

This approach permits to make use of well-known circuital techniques, developed for closed problems, but which can be straightforwardly extended to open problems (8). So, the study of complex open problems can be carried out in a very systematic way.

3. NUMERICAL RESULTS

To show the possibilities of the proposed method, it has been applied to the study of different structures. First, we have computed the electric field inside the dielectric circular shell of figure 2, with $R_1=0.45$ m, $R_2=0.5$ m, and $\epsilon_r' = 1.25$, when a TM^z wave of the form $\vec{E} = e^{-jkx} \hat{z}$, with $k=6$ m⁻¹, incides over the structure. Since the incident field is a plane wave, we have:

$$b_{1m} = e^{-jm(\frac{\pi}{2} + \phi_0)} \quad (12)$$

being ϕ_0 the angle of incidence. To compute the coefficient vectors $\{a_1\}$, $\{b_2\}$ and $\{a_2\}$ we need another condition, which may be derived from the fact that the harmonics propagating towards the origin cannot be absorbed nor reflected at $\rho = 0$, and hence $\{a_2\} = \{b_2\}$ [1]. So, (2) leads to a convergent series of Bessel functions of the first kind for the total field in the $\rho \leq \rho_2$ region. In this case, the value $N_2 \cong k_0 \rho_1$ has been found to be a good limiting criterion. In figure 2 we plot the amplitude of the computed E_z field inside the envelope at $y = 0$ for different values of the loss tangent. It can be seen how the electric field decreases exponentially inside the lossy material, and when $\text{tg } \delta$ increases, the field penetration into the material decreases, as can be expected from the skin effect theory. Moreover, as the material approaches to a perfect electric conductor (which means that $\text{tg } \delta \rightarrow \infty$), the electric field tangent to the envelope surface vanishes.

When the envelopes are made of perfect conductor, it has been shown [1,3,4] that they present resonances at the cut-off frequencies of the modes in the corresponding waveguides. This behavior holds when the envelope is made of a lossy material. To show that, we have analyzed the slotted square envelope of figure 3, taking $\epsilon_r = 1 - j2 \cdot 10^6$. A TE^z incidence of the form $\vec{H} = e^{jky} \hat{z}$ is assumed. Since it is also an empty screen, the analysis is carried out in the same way as described for the previous example. In figure 4 we present the computed magnetic field near and inside the screen when the frequency of the incident wave matches the cut-off frequency of the TE_{10} mode in the square waveguide. As it was pointed out in [3] for the perfect conductor screen, the field inside the envelope corresponds to the TE_{10} mode field pattern. However, when the frequency of the incident wave does not correspond to the cut-off frequency of any mode in the waveguide, no significant field is excited inside it. This behavior can be seen in figure 5, where we have used $k=4$, which does not match any cut-off wavenumber of the square waveguide.

Finally, we have analyzed the slotted coaxial structure of figure 6, where $R=0.25$ m and the square envelope has the same dimensions of that of figure 3. The $\rho \leq R$ region is a perfect conductor, while the envelope is made of a conductor material with conductivity σ . In this case, the analysis can be solved using the circuital model of figure 7. The coefficients $\{b_i\}$ are those given by eq. (12), while the other coefficients can be computed as:

$$\{a^1\} = \left[[S_{11}] + [S_{12}][S_L][I] - [S_{22}][S_L] \right]^{-1} [S_{21}] \{b^1\} \quad (13)$$

$$\{a^2\} = [S_L][I] - [S_{22}][S_L]^{-1} [S_{21}] \{b^1\} \quad (14)$$

$$\{b^2\} = \left[[I] - [S_{22}][S_L] \right]^{-1} [S_{21}] \{b^1\} \quad (15)$$

where $[S_{11}]$, $[S_{12}]$, $[S_{21}]$, $[S_{22}]$ are the submatrices of the scattering matrix characterizing the envelope, $[I]$ is the identity matrix and $[S_L]$ is the scattering matrix which characterizes the shielded conductor. For a perfect conductor of circular shape, $[S_L]$ is a diagonal matrix with:

$$[S_L]_{n,n} = -\frac{H_n^{(2)}(k_0 R)}{H_n^{(1)}(k_0 R)} \quad -N_2 \leq n \leq N_2, \quad N_2 \cong k_0 R \quad (16)$$

for the TM^z case [5].

The induced current in the inner conductor is given by:

$$I = R \int_0^{2\pi} (\hat{\rho} \times \vec{H}) \cdot \hat{z} \Big|_{\rho=R} d\phi \quad (17)$$

Due to the modal coupling described in the previous examples, there will be peaks of current at the cut-off wavenumbers of the corresponding coaxial waveguide [1,4]. Because of the particular symmetry of this waveguide, an taking into account eq. (17) the peaks are expected to occur only at the cut-off frequencies of the ϕ -invariant modes. However, another peaks will appear due to the unsymmetry of the induced field, as it will be discussed later.

In figure 6 we have plotted the induced current in the inner conductor, as a function of the wavenumber, when a TM^z wave of the form $\vec{E} = e^{jky} \hat{z}$ incides over structure when the envelope is made of a material with $\sigma = 1000 \Omega^{-1}$. The graphic shows two peaks. The first peak corresponds to the first TM mode of the coaxial, which is a ϕ -invariant mode with $k_c = 10.04 \text{ m}^{-1}$. The second peak correspond to the sixth TM mode, which has $k_c = 14.26 \text{ m}^{-1}$. This mode is not ϕ -invariant, but the induced field exhibits some degree of unsymmetry (the so-called *banana modes* [1]) which is the responsible of this induced current. This behavior is strongly dependent on the particular modal field pattern. In fact, the induced current at $k_c = 10.48 \text{ m}^{-1}$ and $k_c = 13.19 \text{ m}^{-1}$, corresponding to the forth and fifth modes, is nearly negligible. Finally, the second and third modes, both with $k_c = 10.19 \text{ m}^{-1}$, do not present a separate resonance. This is due to the high mode density near $k = 10 \text{ m}^{-1}$. (in fact, the peak of current near this frequency is due not only to the first mode, but also to the second and third modes).

Finally, to study the effect of the conductivity in the induced current, the same structure of figure 6 has been analyzed, but considering now an envelope conductivity of $\sigma = 5 \Omega^{-1}$, and the induced current is shown in figure 8. We can see that the basic behavior of the current holds, even for very low conductivity values. However, there are some evident differences. The first one is that the resonant peak widths is bigger when the conductivity drops, because the modal coupling phenomenon is less frequency-selective. The second is that the values of the induced current are smaller when the conductivity decreases. The reason to this behavior is found to be the value of the induced field inside the envelope. In fact, if for a $\sigma = 1000 \Omega^{-1}$ the maximum value of the induced field at $k_c = 10.04 \text{ m}^{-1}$ was $|E_z| = 12.3 \text{ Vm}^{-1}$, and $|E_z| = 6.44 \text{ Vm}^{-1}$ at $k_c = 14.26 \text{ m}^{-1}$, this values drop to $|E_z| = 2.17 \text{ Vm}^{-1}$ and $|E_z| = 2.96 \text{ Vm}^{-1}$, respectively, when the conductivity is $\sigma = 5 \Omega^{-1}$.

4. CONCLUSIONS

A very powerful tool for studying the electromagnetic susceptibility in arbitrarily shaped screens made of lossy dielectric materials has been developed. The proposed method is based on a circuital characterization of the structure with a generalized admittance matrix, via the FEM, which is then combined with a modal expansion to compute the field inside and outside the envelope. The versatility of the FEM allows the application of the method to any bi-dimensional envelope, no matter it has more than one slot, or it contains different dielectric parts. The analysis has been carried out for both TM^z and TE^z waves. The proposed scheme is a very helpful tool for circuit designers, since it permits to chose the best location and orientation for the most sensitive devices and the optimal shape and material for the screen at a given frequency.

5.- REFERENCES

- [1] R. W. Ziolkowski and J. B. Grant, "Scattering from Cavity-Backed Apertures: The Generalized Dual Series Solution of the Concentrically Loaded E-Pol Slit Cylinder Problem", *IEEE Trans. Antennas Propagat.*, vol. AP-35, pp.504-528, May 1987.
- [2] E. H. Newman and M. Kragalott, "Moment Method Analysis of the Electric Shielding Factor of a Conducting TM Shield at ELF", *IEEE Trans. Electromagn. Compat.* vol 37, Aug. 1995, pp 400-407.
- [3] J. V. Balbastre and L. Nuño, "Susceptibility Analysis of Arbitrarily Shaped 2-D Slotted Screens Using a Hybrid Modal-Finite Element Technique", 5th Topical Meeting on Electrical Performance of Electronic Devices, Napa (California), Oct. 28-30 1997, pp 220-222.
- [4] J. V. Balbastre, L. Nuño and Miguel Ferrando, "Susceptibility Analysis or Arbitrarily Shaped 2-D Slotted Screens using a Hybrid Generalized Scattering Matrix-Finite Element Method", submitted to the *IEEE Trans. Electromagn. Compat.* for evaluation, MS #96-109.
- [5] C. A. Balanis, "Advanced Engineering Electromagnetics", John Wiley, N. Y. 1982.
- [6] S. K. Chang y K. K. Mei, "Application of the Unimoment Method to Electromagnetic Scattering of Dielectric Cylinders", *IEEE Trans. Antennas Propagat.*, vol. AP-24, pp 35-42, Jan. 1976.
- [7] J. V. Balbastre, "Solución de problemas electromagnéticos cerrados y abiertos mediante el método de los elementos finitos, incluyendo materiales anisótropos e inhomogéneos", Ph.D. Dissertation, Departamento de Comunicaciones, Universidad Politécnica de Valencia, July 1996.
- [8] A. Valero, "Solución de problemas electromagnéticos complejos mediante análisis circuital generalizado", Ph.D. Dissertation, Departamento de Comunicaciones, Universidad Politécnica de Valencia, June 1997.
- [9] Luis Nuño, J. V. Balbastre and H. Castañé, "Analysis of General Lossy Inhomogeneous and Anisotropic Waveguides by the Finite Element Method Using Edge Elements", *IEEE Trans. Microwave Theory Tech.*, vol. 45, pp. 446-449, March 1997.

LIST OF CAPTIONS

FIGURE 1: General dielectric slotted screen

FIGURE 2: Electric field amplitude inside a lossy closed dielectric screen for different values of $\text{tg}\delta$

FIGURE 3: Square slotted screen.

FIGURE 4: Magnetic field amplitude inside the square dielectric screen when the frequency of the incident wave matches that of the TE_{10}^z mode of the corresponding square waveguide.

FIGURE 5: Magnetic field amplitude inside the square dielectric screen when the frequency of the incident wave matches that of the TE_{20}^z mode of the corresponding square waveguide.

FIGURE 6: Induced current in a circular perfect conductor of radius $R = 0.25$ m screened by the dielectric envelope of figure 4 with $\sigma = 1000 \Omega^{-1}$.

FIGURE 7: Schematic representation of the Generalized Circuit Model of a conductor covered by an arbitrary dielectric screen.

FIGURE 7: Induced current in a circular perfect conductor of radius $R = 0.25$ m screened by the dielectric envelope of figure 4 with $\sigma = 5 \Omega^{-1}$.

TABLE 1: Cut-off wavenumber for the first six TM^z modes in the waveguide formed by one circular perfect conductor of radius $R = 0.25$ inside a square waveguide of $1 \text{ m} \times 1 \text{ m}$ cross-section, computed following the procedure described in [9].

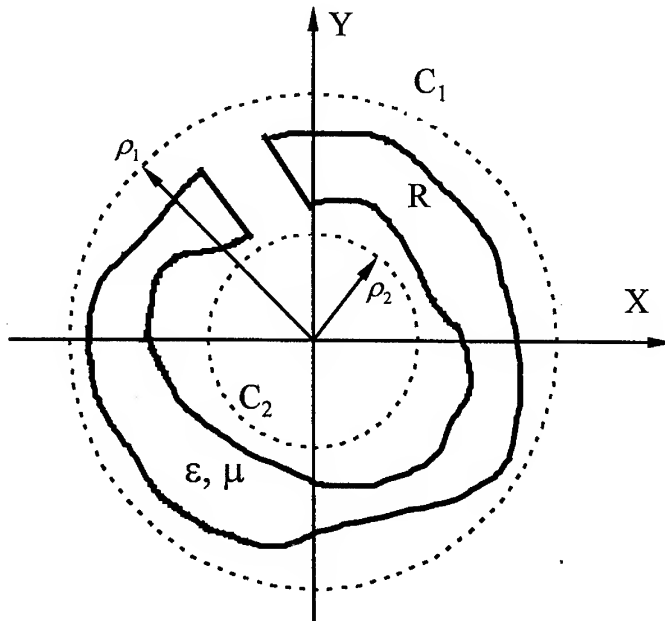


FIGURE 1

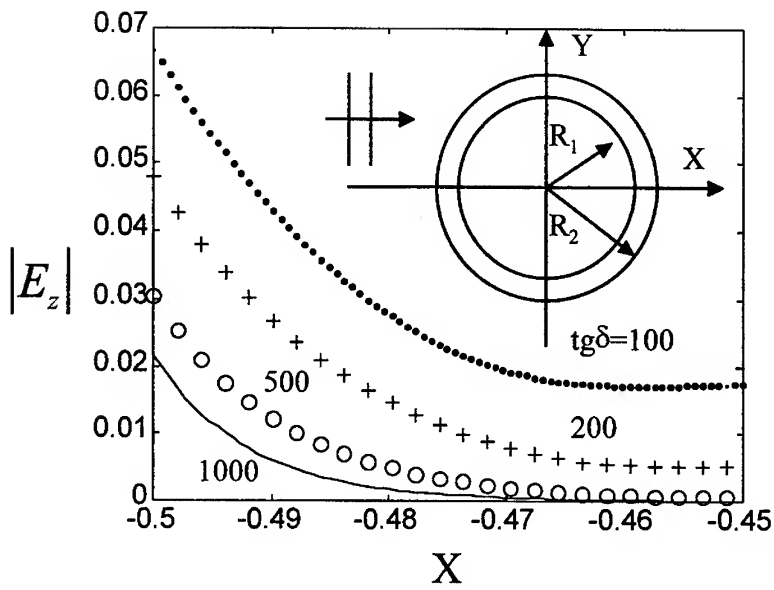


FIGURE 2

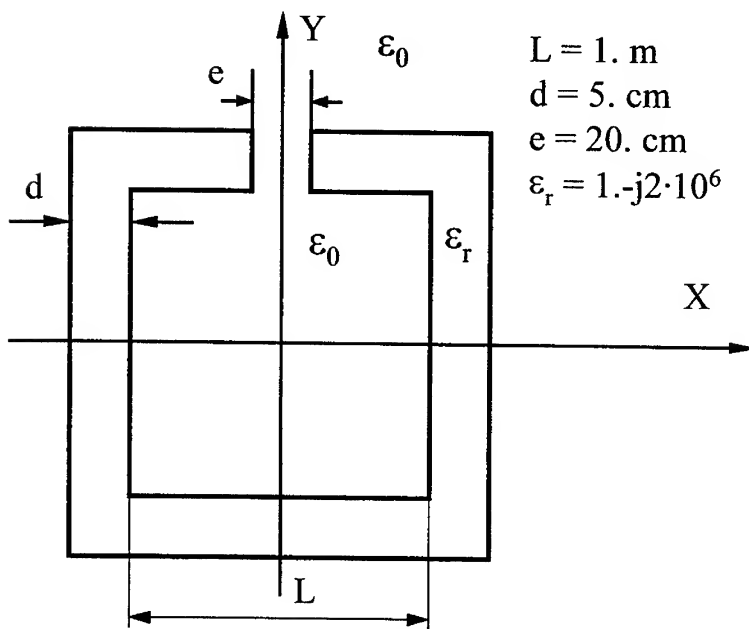


FIGURE 3

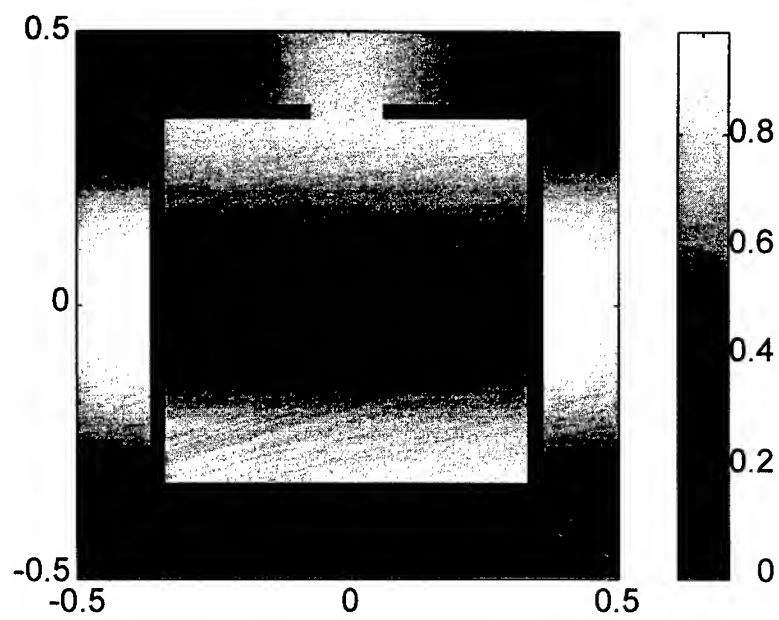


FIGURE 4

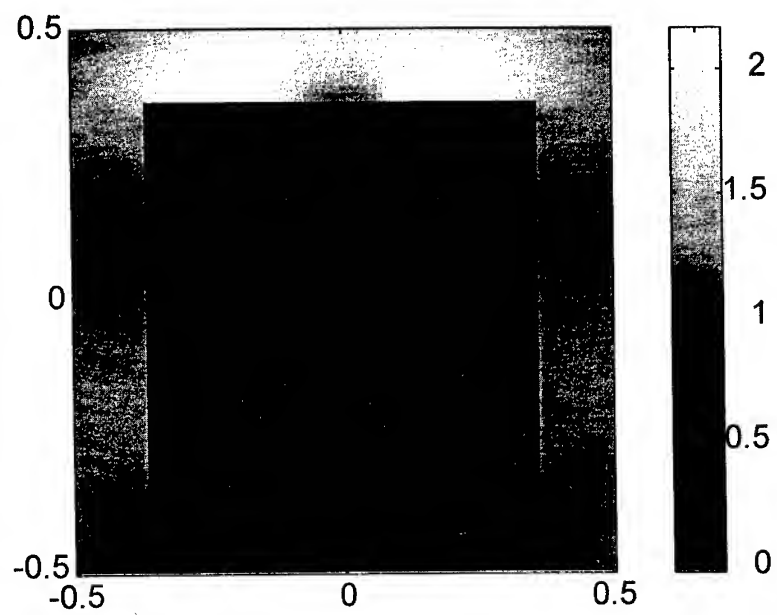


FIGURE 5

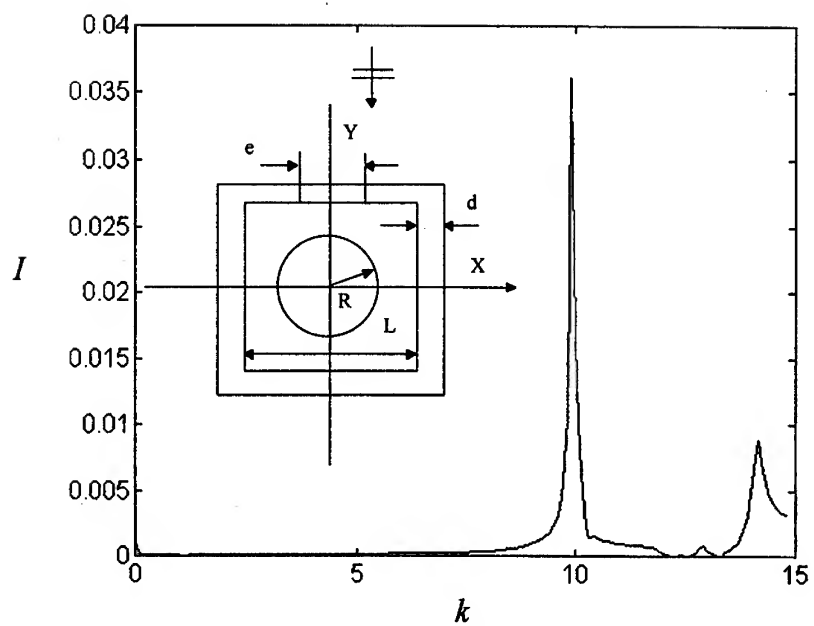


FIGURE 6

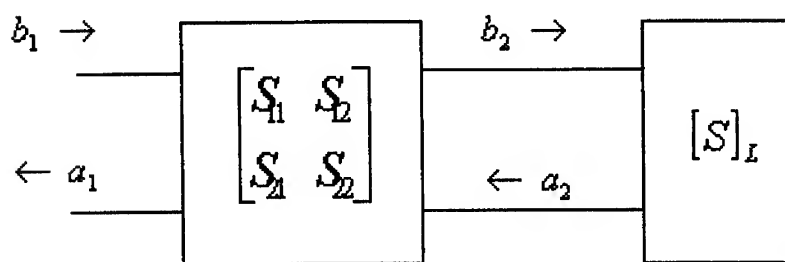


FIGURE 7

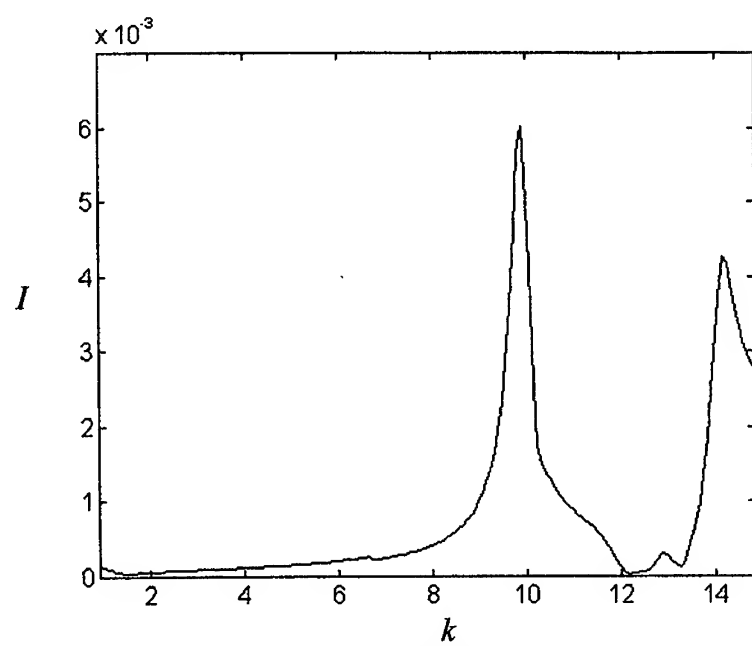


FIGURE 8

$k_c (m^{-1})$
10,04
10,19
10,19
10,48
13,19
14,26

TABLE I

Conductive Substrate Losses in Coplanar and Microstrip Transmission Lines

William H. Haydl

Fraunhofer Institute for Applied Solid State Physics (IAF),
Tullastr. 72, D-79108 Freiburg, Germany
Tel: +49 761 5159 554, Fax: +49 761 5159 565, e-mail: haydl@iaf.fhg.de

Abstract

The effect of a conductive substrate, such as silicon, on the attenuation of microstrip (MS) lines has been investigated in the past. No such treatment exists for coplanar (CPW) lines, and experimental data on the additional attenuation due to a finite conductivity of the substrate is extremely scarce. Using basic transmission line theory, simple expressions have been derived for the losses caused by a conductive substrate for both the coplanar and the microstrip lines. For microstrip lines, good agreement is obtained with previously published theoretical and experimental data on conducting silicon substrates.

In contrast to the case for microstrip lines, where the conductive substrate losses are independent of the line impedance, a dependence is found for coplanar lines.

Introduction

Silicon is an attractive substrate material for microwave and millimeter wave transmission lines and packaging applications, because of the more advanced and costeffective technology. Present and future microwave and millimeter wave systems in the areas of communication and data transmission, radar, imaging, etc. are driven primarily by cost. With the development of low loss interconnection techniques [1, 2], it is more efficient to place passive circuit elements and transmission lines not on the substrate containing the active high performance circuits, but on different inexpensive substrates in close proximity. Silicon (Si), because its mature state of technology, which allows incorporation of elements such as resistors and capacitors, as well as active devices, meets the above criteria. In contrast to most III–V material substrates, which have a typical resistivity of 10^6 – $10^7 \Omega\cdot\text{cm}$, the upper limit of the resistivity of Si substrates is in the range 10^3 – $10^4 \Omega\cdot\text{cm}$. The effect of this finite conductivity on the wave propagation in coplanar and microstrip transmission lines is treated below.

The properties of microstrip transmission lines on substrates such as gallium arsenide (GaAs) and silicon (Si) have been studied extensively in the past [3, 4, 5, 6]. Recently, coplanar transmission lines however have been used increasingly in the microwave and millimeter wave frequency range [7, 8]. There is extensive theoretical and experimental data available on the ohmic losses in coplanar transmission lines [9, 10]. However, little is known for coplanar transmission lines [11] about the additional attenuation of conducting substrates.

Following the classical quasistatic approach for coplanar lines [12], and applying fundamental transmission line theory [13], simple expressions for the substrate conductance and the resulting attenuation of coplanar lines have been derived below. Similarly, expressions have also been developed for microstrip lines for the conductive substrate losses.

Transmission line losses

The total losses of a transmission system are the sum of ohmic losses due to the rf currents in the resistive metalisation (skin effect) α_{ohmic} [9, 10], radiation losses α_{rad} , losses due to conversion of energy into undesired modes α_{modes} [14], losses due to substrate polarization effects ($\tan \delta$) $\alpha_{\text{sub-pol}}$, and losses due to a conducting substrate $\alpha_{\text{sub-cond}}$. Thus,

$$\alpha_{\text{total}} = \alpha_{\text{ohmic}} + \alpha_{\text{rad}} + \alpha_{\text{modes}} + \alpha_{\text{sub-pol}} + \alpha_{\text{sub-cond}} \quad (1)$$

Ohmic losses in microstrip lines have been treated extensively in the past [3, 6]. Recently, such data has also become available for coplanar lines up to millimeter wave frequencies [9, 10]. Losses due to radiation and conversion of energy into other modes, will not be discussed here. They have been treated by numerous authors in the past [14, 15].

A) Substrate polarization losses, $\alpha_{\text{sub-pol}}$:

If an rf field at frequency ω is applied to a dielectric, polarization and displacement lag behind, resulting in a complex dielectric constant

$$\epsilon(\omega) = \epsilon'(\omega) - j\epsilon''(\omega), \quad (2)$$

where the loss angle δ is defined by

$$\tan \delta(\omega) = \frac{\epsilon''(\omega)}{\epsilon'(\omega)} \quad (3)$$

The resulting energy loss is [16]

$$L_p = \frac{\omega}{8\pi} E^2 \epsilon''(\omega) \quad (4)$$

where E is the electric field. The energy loss is proportional to ω and $\sin \delta$, the loss factor. For small δ , $\sin \delta \approx \tan \delta$. Values for $\tan \delta$ are scarce, but typically in the 10^{-4} to 10^{-3} range. These dielectric losses become significant at millimeter wave frequencies for $\tan \delta \leq 10^{-3}$.

B) Losses due to a conducting substrate, $\alpha_{\text{sub-cond}}$:

The additional losses for microstrip lines caused by conductive silicon substrates have been treated in the past [3, 5, 6, 17].

Because of the less mature nature of the coplanar line however, neither theoretical nor experimental data is available for this type of transmission line.

Below, we present simple analytical expressions which describe these additional conductive substrate losses for coplanar and microstrip lines.

a.) Coplanar line:

Only ohmic and conductive substrate losses are considered in the following treatment.

From transmission line theory, for the case when losses are low, the attenuation may be approximated by [13, p. 250]

$$\alpha = \alpha_{\text{ohmic}} + \alpha_{\text{sub-cond}} \approx \frac{R'}{2Z_0} + \frac{G'Z_0}{2}, \quad (5)$$

where the first term is due to the ohmic losses in the conductors, and the second term represents the losses in the substrate due to its finite conductivity. Here, R' and G' are the rf resistance and conductance per unit length, and Z_0 is the line impedance.

Analogous to quasi-static calculations of the capacitance of coplanar lines [12, p. 349], we can express the conductance per unit length G' of a coplanar line, on a substrate of finite resistivity ρ , as

$$G' = \frac{2}{\rho} \frac{K(k)}{K(k')} \quad (6)$$

$$\text{where } k = \frac{w}{d} \quad (7)$$

$$\text{and } k' = \sqrt{1 - k^2} \quad (8)$$

Here, $K(k)$ and $K(k')$ are the elliptic integrals of the first kind [12, p. 371], w is the width of the center line, and d is the spacing between ground planes (see Insert of Fig. 2).

For ρ in $[\Omega\text{-cm}]$ and α in $[\text{dB/mm}]$, the conductive substrate losses are

$$\alpha_{\text{sub-cond}} = 8.68 \frac{Z_0}{10\rho} \frac{K(k)}{K(k')} \quad (9)$$

The impedance Z_0 for various w/d ratios for coplanar lines on silicon is shown in Fig. 1. The values of $\alpha_{\text{sub-cond}}$ obtained from equation (9) are illustrated in Fig. 2 for different values of w/d .

b) Microstrip line :

If we follow a similar approach for microstrip lines, we obtain

$$G' = \frac{1}{\rho} \left(1 + \frac{w}{h} \right) \quad (10)$$

$$\alpha_{\text{sub-cond}} = \frac{Z_0}{2\rho} \left(1 + \frac{w}{h} \right) , \quad (11)$$

where w is the width of the microstrip line, and h the substrate thickness.

For ρ in [$\Omega\text{-cm}$] and α in [dB/mm],

$$\alpha_{\text{sub-cond}} = 8.68 \frac{Z_0}{20\rho} \left(1 + \frac{w}{h} \right) \quad (12)$$

The values of the attenuation $\alpha_{\text{sub-cond}}$ as derived from this expression, are shown in Fig. 3 and agree well with values published previously [3, 5, 6, 17], as shown in Fig.4.

Summary :

Simple equations have been developed which predict the losses of coplanar and microstrip transmission lines on conductive substrates. Whereas the theoretical predictions presented agree well with published theoretical and experimental data for microstrip lines, they remain to be verified by experimental data for coplanar lines.

References

- [1] T. Krems, W. Haydl, H. Massler, J. Rüdiger, "Millimeter-wave performance of chip interconnections using wire bonding and flip chip", 1996 IEEE MTT-S Digest, pp. 247-250, June 1996.
- [2] G. Baumann, H. Richter, A. Baumgärtner, D. Ferling, R. Heilig, D. Hollmann, H. Müller, H. Nachansky, M. Schlechtweg, "51 GHz frontend with flip-chip and wire bond interconnections from GaAs MMICs to planar patch antenna", 1995 IEEE MTT-S Symposium Digest, pp. 1639-1642, June 1996.
- [3] T. M. Hyltin, "Microstrip transmission on semiconductor dielectrics", IEEE Trans. Microwave Theory Tech., vol. MTT-13, pp. 777-781, Nov. 1965.
- [4] R. A. Pucel, D. J. Masse, C. P. Hartwig, "Losses in microstrip", IEEE Trans. Microwave Theory and Techniques, vol. MTT-36, pp. 342-350, June 1968.
- [5] H. Sobol, M. Caulton, "The technology of microwave integrated circuits," Advances in Microwaves, vol. 8, pp. 11-66, Academic Press, 1974.
- [6] A. Rosen, M. Caulton, P. Stabile, A. M. Bombar, W. M. Janton, C. P. Wu, J. F. Corboy, C. W. Magee, "Silicon as a millimeter-wave monolithically integrated substrate-a new look", RCA Review, vol. 42, pp. 633-660, Dec. 1981.
- [7] W. H. Haydl, W. Heinrich, R. Bosch, M. Schlechtweg, P. Tasker, J. Braunstein, "Design data for millimeter wave coplanar circuits", 23 rd European Microwave Conference, pp. 223-228, Sept. 1993.
- [8] W. H. Haydl, L. Verweyen, T. Jakobus, M. Neumann, A. Tessmann, T. Krems, M. Schlechtweg, W. Reinert, H. Massler, J. Rüdiger, W. Bronner, A. Hülsmann, T. Fink, "Compact monolithic coplanar 94 GHz front ends", 1997 IEEE MTT-S International Microwave Symp. Digest, pp. 1281-1284, June 1997.

- [9] W. H. Haydl, J. Braunstein, T. Kitazawa, M. Schlechtweg, P. Tasker, L. F. Eastman, "Attenuation of millimeterwave coplanar lines on gallium arsenide and indium phosphide Microwave Symp. Digest, pp. 349-352, June 1992.
- [10] W. Haydl, "Experimentally observed frequency variation of the attenuation of millimeter wave coplanar transmission lines with thin metallization," IEEE Microwave and Guided Wave Letters, vol. 2, pp.322-324, Aug. 1992.
- [11] G. E. Ponchak, A. N. Downey, L. P. B. Katehi, " High frequency interconnects on silicon substrates", 1997 IEEE Radio Frequency Integrated Circuits Symposium Digest, pp. 101-104, June 1997.
- [12] R. K. Hofmann, Handbook of Microwave Integrated Circuits, Artech House, 1987.
- [13] S. Ramo, J. R. Whinnery, T. VanDuzer, Fields and Waves in Communication Electronics, J. Wiley, 1984.
- [14] T. Krems, W. H. Haydl, H. Massler, J. Rüdiger, " Advantages of flip-chip technology in millimeter-wave packaging", 1997 IEEE MTT-S Digest, pp. 987-990, June 1997.
- [15] H. Shigesawa, M. Tsuji, A. A. Oliner, "Conductor-backed slot line and coplanar waveguide: dangers and full-wave analyses", IEEE MTT-S Digest, pp. 199-202, June 1988.
- [16] A. J. Dekker, Solid State Physics, Prentice-Hall, Inc., 1962, pp. 148.
- [17] M. I. Aksun, H. Morcroc, "GaAs on Si as a substrate for microwave and millimeter-wave monolithic integration", IEEE Trans. Microwave Theory Techn., vol. 36, pp. 160-162, Jan. 1988.

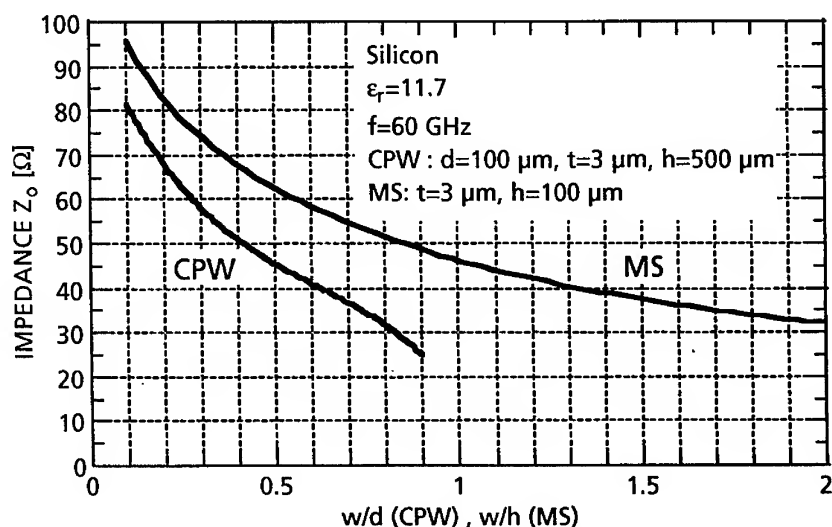


Fig. 1

Typical impedance values for coplanar (CPW) and microstrip (MS) transmission lines on silicon.

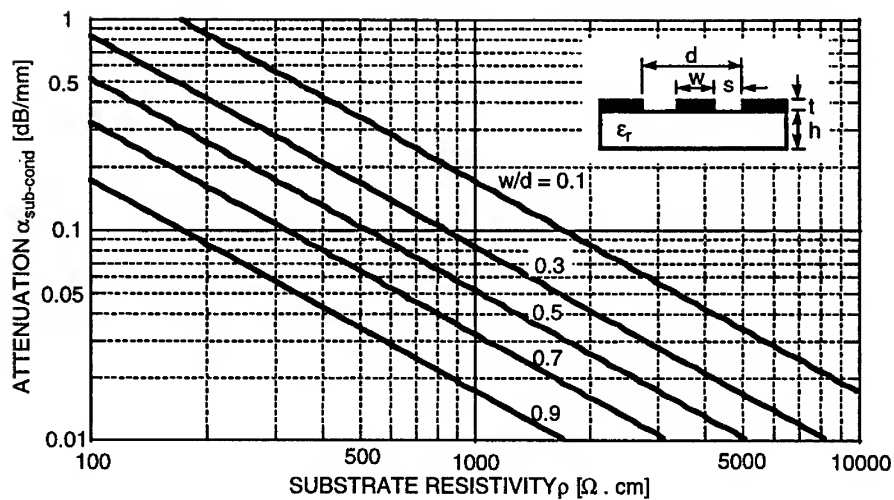


Fig. 2

The additional attenuation caused by a conductive substrate of finite resistivity, for coplanar (CPW) transmission lines, as determined from this theory (Equ. 9).

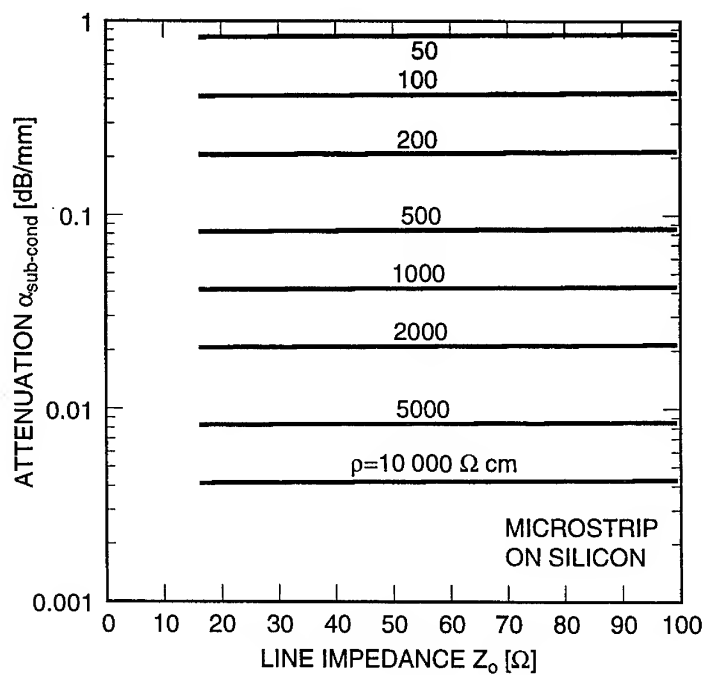


Fig. 3

The additional attenuation caused by a conductive substrate of finite resistivity ρ for microstrip (MS) transmission lines on Si, as determined from this theory (Equ. 12).

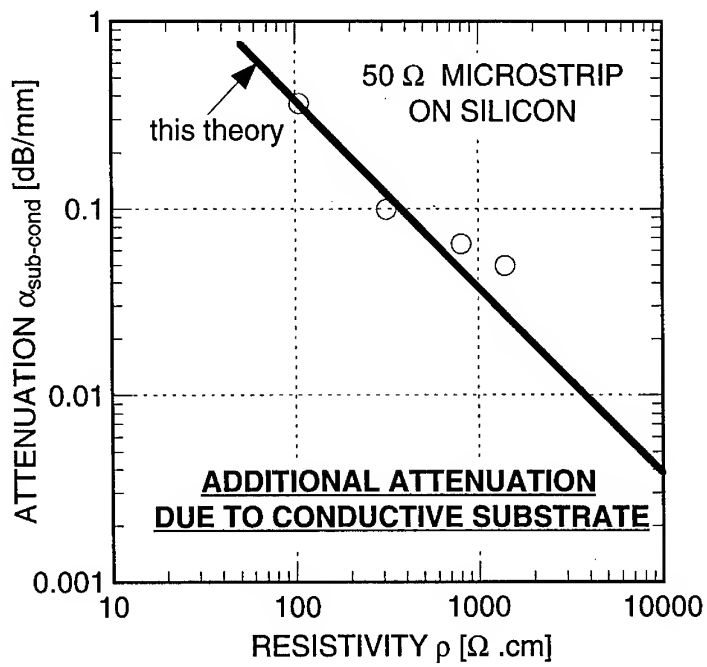


Fig. 4

The additional attenuation caused by a conductive substrate of finite resistivity ρ for 50 Ω microstrip (MS) transmission lines on Si substrates. The circles are published data [3, 5, 6, 17], the solid line represents this theory (Equ. 12).

MODELING OF MULTICHIP MODULE INTERCONNECTIONS BY THE TLM METHOD AND SYSTEM IDENTIFICATION

T. Mangold, P. Russer

Institut für Hochfrequenztechnik, University of Technology, Munich,
Arcisstraße 21, D-80333 München, Germany

Abstract

We present a method for computer aided generation of lumped element equivalent circuits for linear reciprocal distributed microwave circuits. The method is based on a field theoretical analysis of the distributed multiport circuit by the three-dimensional Transmission-Line-Matrix method. It allows to generate the topology as well as the parameters of the lumped element equivalent circuit. System identification techniques are used for the extraction of approximated admittance parameters describing the essential multiport characteristics. By Foster decomposition of the admittance matrices canonical equivalent circuit models are generated. Two examples are given to verify the proposed method and demonstrate their application to the modeling of multichip module (MCM) interconnections.

1 INTRODUCTION

In recent years, the Transmission-Line-Matrix (TLM) method [1] and the Finite Difference Time Domain method (FDTD) [2] have proven their ability to handle general structures. Due to the high numerical effort the application of electromagnetic full-wave analysis is restricted to small substructures of the circuits. Usually only the critical distributed circuit elements are modeled by full-wave analysis, and the complete circuit modeling is performed using network-oriented methods. There are different ways to incorporate the models of the distributed circuits into the network-oriented overall circuit simulation as for example by description of the distributed circuits by look-up tables, by general methods of system identification or by equivalent circuit models. When modeling circuits containing nonlinear and active devices, two generally different approaches are possible. One way is to include the nonlinear behavior into the electromagnetic field simulation [3]. This method suffers from a high computational effort and is not optimum if the nonlinear and active parts of the circuit may be treated as lumped element subcircuits. A circuit consisting of several electrically large interconnect structures with many active devices can be modeled in an optimum way by separating distributed linear and lumped nonlinear parts. The incorporation of distributed subcircuit models into network-oriented nonlinear time-domain circuit simulation has already been demonstrated in [4], where the distributed linear subcircuits have been represented by their pulse response functions and have been incorporated into the computation via a convolution procedure. Substituting distributed subcircuits by lumped element equivalent circuits with reduced complexity is another possible method. Equivalent circuit models exhibit the advantage of compactness, easy implementation in existing circuit simulators, applicability in frequency domain as well as in time domain, and exact representation of some fundamental circuit properties as for example passivity, stability and reciprocity. However, usually it requires a lot of creativity to find an appropriate lumped element equivalent circuit that models a certain distributed circuit within a specified interval of frequency.

This work presents a general method for the generation of lumped element equivalent circuits for linear passive reciprocal multiports.

2 MODEL GENERATION

Starting with a three-dimensional electromagnetic full-wave analysis of a distributed multiport we obtain the impulse response functions for reflection and transmission between the ports. For this we use the time

domain TLM scheme with Symmetrical Condensed Nodes [1]. To reduce the computational effort an irregularly graded mesh is used [5]. This TLM scheme is completely implemented in a distributed computation simulation package, which is realized within the Parallel Virtual Machine (PVM) environment [6].

In order to establish a lumped element equivalent circuit for a symmetrical four port MCM microstrip crossing two single simulation runs are necessary (plus two short time reference simulations). Time responses $s(n)$ are separated from spurious parts by utilizing system identification techniques. Applying an augmented UD identification (AUDI) algorithm [7] to reference simulation data an IIR Filter describing the dispersive transmission lines at the ports can be set up. A time shifting of all input signals with this filter structure results in a complete deembedding of the analyzed discontinuity from its connecting transmission lines.

After this preprocessing of simulation results the locations of multiport admittance function poles are extracted by a steepest-ascent search algorithm. Therefore the Laplace transforms of the complete set of time domain scattering signals has to be calculated numerically. The scattering parameters for a certain frequency point p are given by

$$S_{ij}(p) = \frac{\sum_{n=1}^N s_{i(n)out} e^{-pnT}}{\sum_{n=1}^N s_{j(n)in} e^{-pnT}} \quad (1)$$

Simulated time domain scattering signals are well suited for numerical transformations, because they are as well bandwidth as time length limited. Even lossless structures result in short time series due to the loading of resonant structures by their connecting transmission line impedances. The multiport admittance matrix $\mathbf{Y}(p)$ can be determined from its corresponding scattering matrix $\mathbf{S}(p)$.

$$\mathbf{Y}(p) = (\mathbf{q} + \mathbf{S}(p)\mathbf{q})^{-1} \cdot (\mathbf{q}^{-1} - \mathbf{S}(p)\mathbf{q}^{-1}) \quad (2)$$

\mathbf{q} is a diagonal matrix containing the square roots of all port impedances. Reasonable starting values for a gradient based pole extraction working on single elements of $\mathbf{Y}(p)$ can be taken from contour plots of the admittance function Laplace transforms. Choosing all local maximums in the Fourier transform ($\text{Re}(p) = 0$) of all admittance functions $y_{ij}(p)$ within the specified frequency range results in the extraction of all dominant poles. Any additional poles and trial solutions converging towards them can be found easily. Knowing the location of a number of N poles α_n of a linear reciprocal lossless multiport a Foster equivalent circuit model may be specified directly. We extend this method also to lossy linear reciprocal multiports. Their admittance matrix $\mathbf{Y}(p)$ may be represented by

$$\mathbf{Y}(p) = \mathbf{A}^{(0)} + \sum_{n=1}^N \underbrace{\left(\frac{A_0^{(n)}}{p - \alpha_n} + \frac{A_0^{(n)*}}{p - \alpha_n^*} \right)}_{\mathbf{Y}^{(n)}} \cdot \mathbf{A}^{(n)} + \mathbf{A}^{(\infty)} p \quad (3)$$

where the $\mathbf{A}^{(n)}$ are real, symmetric and positive semidefinite matrices. The proof is given for two-ports in [8] and holds also for multiports. In order to describe a passive multiport all poles must be stable and the contained parameters must fulfill the following conditions:

$$|A_0^{(n)}| = 1 \quad , \quad \text{Re} \{A_0^{(n)}\} > 0 \quad , \quad \text{Re} \{A_0^{(n)} \alpha_n^*\} < 0 \quad (4)$$

In [9] Cauer has shown that every matrix $\mathbf{A}^{(n)}$ can be realized by a network of ideal transformers and $M \leq \dim(\mathbf{A}^{(n)})$ one-port admittances. Each of the matrices $\mathbf{A}^{(n)}$ may be decomposed into a sum of real symmetric matrices of rank 1. For example:

$$\begin{aligned} \mathbf{A}^{(n)} = & K_1^{(n)} \cdot \begin{pmatrix} 1 & k_{11} & k_{12} \\ k_{11} & (k_{11})^2 & k_{11}k_{12} \\ k_{12} & k_{11}k_{12} & (k_{12})^2 \end{pmatrix} + \\ & K_2^{(n)} \cdot \begin{pmatrix} 0 & 0 & 0 \\ 0 & 1 & k_{21} \\ 0 & k_{21} & (k_{21})^2 \end{pmatrix} + K_3^{(n)} \cdot \begin{pmatrix} 0 & 0 & 0 \\ 0 & 0 & 0 \\ 0 & 0 & 1 \end{pmatrix} \end{aligned} \quad (5)$$

$$Y_i^{(n)} = \frac{G_i^{(n)} + pC_i^{(n)}}{p^2 L_i^{(n)} C_i^{(n)} + p(G_i^{(n)} L_i^{(n)} + R_i^{(n)} C_i^{(n)}) + 1 + R_i^{(n)} C_i^{(n)}} = K_i^{(n)} Y^{(n)} \quad (7)$$

These matrices of rank 1 in combination with their admittance function $Y^{(n)}$ contribute multiport elements as depicted in Fig.(3) consisting of R, G, L, C and ideal transformers. Connecting these compact n-port elements according to eq.(5) results in full rank M-port elements as depicted in Fig.(5).

All matrix elements $a_{ij}^{(n)}$ associated with the amplitudes of the poles can be calculated by fitting eq.(3) to the supposed admittance values obtained in eq.(2). Solving these $(N + 2)$ dimensional optimization problems has to be done with respect to the valid parameter space. Due to the special function structure in eq.(3) (a sum of highly localized subfunctions) the global minimum of the used error function can be found without any convergence problems. After computing all parameters in eq.(3) and decomposing all matrices according eq.(5) the parameter values of the equivalent lumped element circuit can be determined. The turns ratios of the transformers in Fig.(5) can be expressed by the following relationships:

$$\begin{aligned} k_{11} &= -\frac{n_{11}}{n_{12}} \quad , \quad k_{12} = -\frac{n_{21}}{n_{23}} \quad , \quad k_{13} = -\frac{n_{31}}{n_{34}} \\ k_{21} &= -\frac{n_{22}}{n_{23}} \quad , \quad k_{22} = -\frac{n_{32}}{n_{34}} \quad , \quad k_{31} = -\frac{n_{33}}{n_{34}} \end{aligned} \quad (6)$$

The parameter values of R, G, L and C are defined by a comparison of the coefficients in eq.(7) and eq.(3). This leads to

$$\frac{1}{L} = 2\text{Re}\{\gamma\} \quad , \quad C = \frac{2\text{Re}\{\gamma\}}{\frac{1}{LC}} \quad (8)$$

with

$$\frac{1}{LC} = |\alpha_n|^2 - \frac{RG}{L} \quad (9)$$

$$\frac{R}{L} = \frac{\text{Re}\{\gamma\alpha_n^*\}}{\text{Re}\{\gamma\}} - 2\text{Re}\{\alpha_n\} \quad (10)$$

$$\frac{G}{C} = \frac{\text{Re}\{\gamma\alpha_n^*\}}{\text{Re}\{\gamma\}} \quad (11)$$

$$\gamma = A_0^{(n)} K_i^{(n)} \quad (12)$$

in general or even simpler formulas for special cases like $\alpha_n = 0$.

3 EXAMPLES

As a verification example we have modeled a microstrip spiral inductor which was analyzed and measured by Becks in [10]. Its structure with stair-case approximated boundaries is shown in Fig.(6). We used nine poles for the generation of the equivalent circuit model shown in Fig.(2). A comparison of the simulation results, the measurement data taken from [10] and the scattering parameters of the generated equivalent lumped element circuit are depicted in Fig.(7). An acceptable agreement between all curves can be seen over the whole frequency range. A minimization of admittance error functions doesn't minimize the approximation error for scattering parameters and explains the general deviation between model and simulation results.

As a second example we modeled a MCM transmission line crossing. This four port structure is shown in Fig.(4). It is placed on a ceramic MCM substrate ($\epsilon_r = 9.8$) carrying a dielectric polyimide layer ($10\mu\text{m}$, $\epsilon_r = 3.3$), a structured ground metalization, another $25\mu\text{m}$ polyimide layer and a signal layer. We took three poles for model generation and the resulting equivalent circuit consists of a shunt connection of three elementary four port sections depicted in Fig.(5). A comparison of admittance parameters is shown in Fig.(8). Increasing the number of poles up to six doesn't enhance the complexity of the model. Due to the symmetry of the structure, a mayor part of the matrices $\mathbf{A}^{(n)}$ reduces to rank one or two. In our first approach, which includes only three poles, this reduction doesn't take place and consequently undermodels this microstrip crossing.

4 CONCLUSION

We have presented a method for generation of lumped element equivalent circuits for distributed microwave components based on time domain scattering signals. It can be applied to linear reciprocal multiports and produces topology as well as parameters of a model, which is restricted to a user specified range of frequencies. Equivalent lumped element circuits for two and four port circuits have been extracted from TLM simulation data. A comparison between generated models, simulation and measurement results demonstrates the ability of our method to approximate signal transmission characteristics within the range of resonant frequencies.

Acknowledgement:

This work has been financially supported by the German Ministry of Education, Science, Research and Technologie.

References

- [1] W.J.R. Hoefer. The transmission line matrix (tlm) method: Theory and applications. *IEEE Trans. Microwave Theory Tech.*, 33:882–893, 1985.
- [2] K.S. Yee. Numerical solution of boundary value problems involving maxwell's equations in isotropic media. *IEEE Trans. Antennas and Propagation*, 14(5):302–307, May 1966.
- [3] P. Russer, P. M. So., and W. J. R. Hoefer. Modeling of nonlinear active regions in tlm. *IEEE Microwave and Guided Wave Letters*, 1(1):10–13, 1991.
- [4] M. Schwab. Determination of the steady state of an oscillator by a combined time-frequency method. *IEEE Trans. Microwave Theory Tech.*, 39:1391–1402, 1991.
- [5] D.A. Al-Mukhtar and J.E. Sitch. Transmission-line matrix method with irregularly graded space. *Proc. IEE, part H*, 128(6):299–305, 1981.
- [6] B. Isele, T. Mangold, R. Weigel, and P. Russer. A novel subgridding scheme for the distributed tlm modelling of thin layers. *Proc. PIERS 97, Hong Kong*, 1997.
- [7] S. Nui, D.G. Fisher, and D. Xiao. An augmented ud identification algorithm. *International Journal of Control*, 56(1):193–211.
- [8] Rolf Unbehauen. *Synthese elektrischer Netzwerke und Filter*. R. Oldenbourg Verlag, München, 3 edition, 1988.
- [9] W. Cauer. Ideale transformatoren und lineare transformationen. *Elektr. Nachr. Techn.*, 9:157–174, 1932.
- [10] T. Becks and I. Wolf. Analysis of 3-d metallization structures by a full-wave spectral domain technique. *IEEE Trans. Microwave Theory Tech.*, 40(12):2219–2227, 1992.

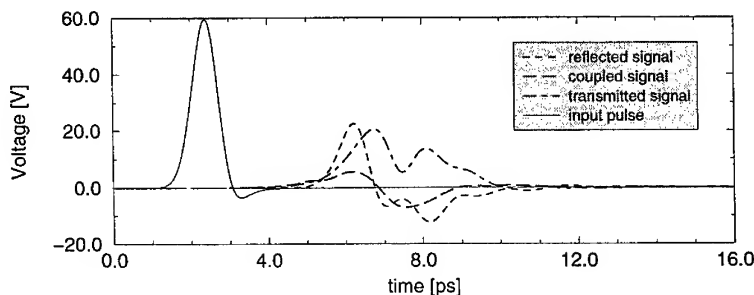


Figure 1: Microstrip crossing: signals for Gaussian excitation at port 1

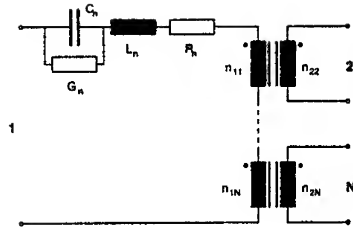


Figure 3: A compact rank 1 n-port element

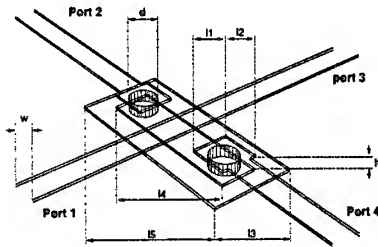


Figure 4: A symmetrical MCM microstrip crossing: $w=64\mu\text{m}$, $h=25\mu\text{m}$, $d=60\mu\text{m}$, $l1=l2=80\mu\text{m}$, $l3=184\mu\text{m}$, $l4=322\mu\text{m}$, $l5=402\mu\text{m}$, all metalizations $=5\mu\text{m}$

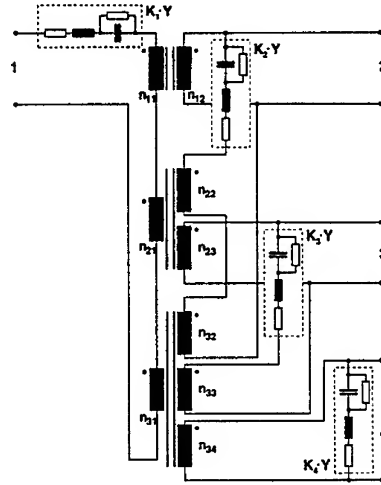


Figure 5: A four port section

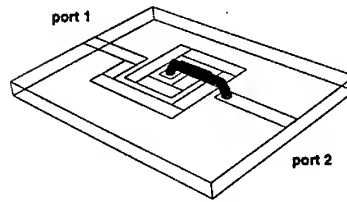


Figure 6: Microstrip spiral inductor

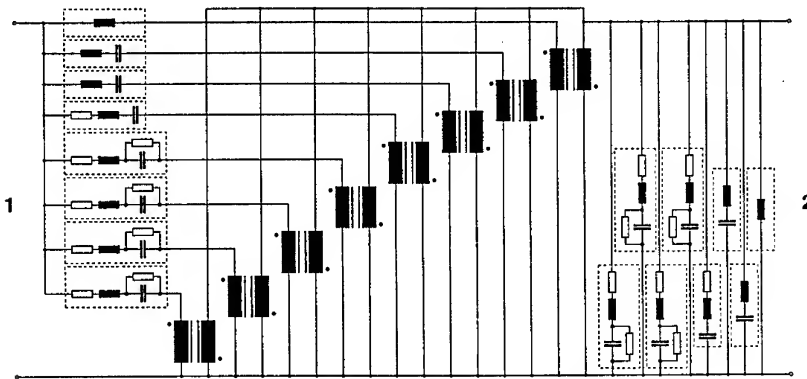


Figure 2: Equivalent lumped element circuit of the microstrip spiral inductor shown in Fig.(6)

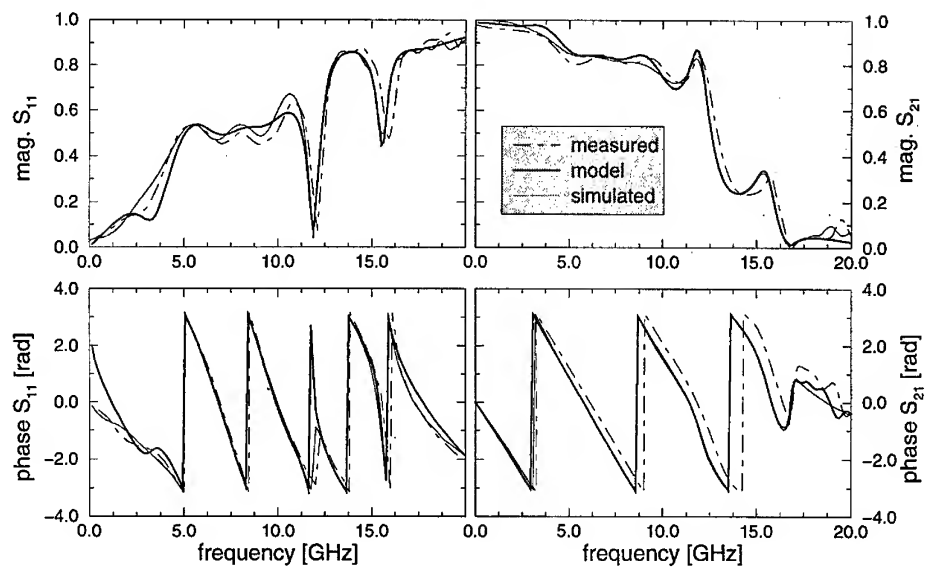


Figure 7: Scattering parameters for a microstrip spiral inductor (Fig.(6)); measurement data were taken from [10]

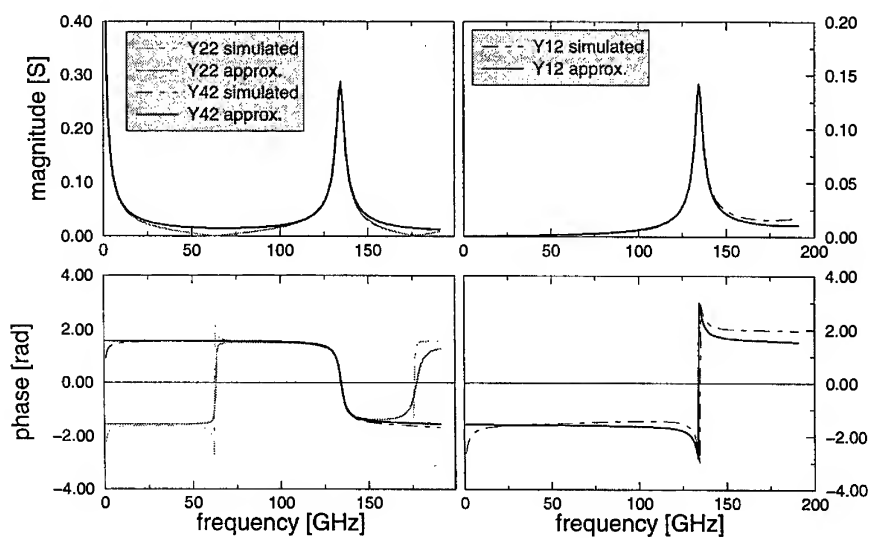


Figure 8: Admittance parameters of a MCM microstrip crossing (Fig.(4))

MONOLITHIC FILTERS AND FREQUENCY-SEPARATION DEVICES BASED ON THE CERAMIC RESONATORS

V.G.Tsykalov¹, A.G.Belous², O.V.Ovchar², Y.D.Stupin²

¹Kyiv Technical University of Ukraine (KPI), 37 Prospekt Pobedy, 252056 Kyiv, Ukraine.

Phone.: +38 044 441-14-01

²Institute of General and Inorganic Chemistry, 32/34 Palladina avenue, 252680 Kyiv 142, Ukraine ;

Phone/Fax: +38 044 444 2211

e-mail: belous@olinet.isf.kiev.ua

ABSTRACT

The series of band-pass, band-reject, and diplexer filters, and also the frequency-separation devices with excellent features were designed on the base of coaxial dielectric resonators (CDR). The dielectric materials used for the CDRs manufactory were distinguished by low dielectric loss and adjustable temperature stability covering the wide range of dielectric constant values (from 3 to 90). The electric MW parameters of the developed devices were measured at the frequency range of 100 MHz to 5 GHz. Some advice for improving the filters' design and quality were adduced.

INTRODUCTION

The development of air and cable broadcasting, communication systems, the increasing number of sets, and effective utilization of frequency ranges lead to more stringent requirements for the quality of microwave transmissions and for noise level. One of the ways to tackle the tasks of improving the information transmission quality is to improve the technical characteristics of filtering and oscillatory communication systems. The use of monolithic coaxial dielectric resonators (CDR) allows the reduction of weight/dimensional parameters and production costs of microwave devices. In some cases, it is possible to manufacture systems which operate under special conditions, e.g. under strong vibrations and impacts, which is difficult to effect on other mechanical principles. At the recent time MW filters and frequency- separation devices realized on CDRs' base were applied in the frequency ranges below 1 GHz for the low amplitude and power levels. As a basis for CDRs manufacture ceramic materials with a high dielectric constant values (from 40 to 90) are usually employed. The research of possible application of the devices mentioned above under conditions of high power and amplitude levels, and also in the frequency ranges above 1 GHz are insufficient.

In this connection our efforts were directed to developing the requirements for ceramic materials as well as for the design of coaxial dielectric resonators (CDRs) for the applications in filtering and frequency-separation devices which are employed in the frequency range of 1-10 GHz. The present work was devoted to developing band-pass (BP), band-reject (BR) filters, diplexer filters, and frequency- separation devices based on the single monolithic CDRs, which operate over the wide ranges of power and amplitude values at the frequencies from 100 MHz to 5 GHz as well as to researching their MW electric parameters.

The following activities have been executed to study this problem:

- 1) the research of ceramic materials with low and temperature stable dielectric constant;
- 2) the development of CDRs design to meet requirements of operating over the wide ranges of power and amplitude values;
- 3) the study of oscillatory modes distribution in the CDRs, which were made on the base of ceramics differed by dielectric constant values;
- 4) the development and research of the microwave devices based on CDRs.

MATERIALS

In the present work the ceramic dielectrics over the wide spectrum of dielectric constant, and based on single- or multi-phase systems were developed and investigated to obtain materials with temperature stable dielectric constant and low dielectric loss tangent ($\text{tg } \delta$) in the microwave range.

When investigating multiphase systems, a high temperature stability of electrophysical properties was achieved by effecting volume temperature compensation, which consists in the simultaneous existence of chemically not interacting phases, which are distinguished by the different character of the temperature dependence of ϵ . When developing dielectrics with low ϵ value (less than 15) we suggested composite of silicates and aluminates such as Mg_2SiO_4 , MgAl_2O_4 , ZnAl_2O_4 , and magnesium titanates (MgTiO_3 , Mg_2TiO_4) to be employed as a basic phases possessing low ϵ and positive temperature coefficient of ϵ (τ_ϵ). Dielectrics with ϵ value about 20 were based on the magnesium and zinc titanates. CaTiO_3 and ZnTiO_3 were chosen as phases with negative τ_ϵ . A possibility of free varying of the correlation between above mentioned compounds allowed us to obtain in a material controllable τ_ϵ on both the positive and negative sides from 0. Ceramics with dielectric constant of 35-40 were based on barium tetratitanates (BaTi_4O_9) differed by reagents grade to obtain various Q-factor in the ceramics retaining ϵ value.

When developing MW dielectrics with ϵ value of 60-90 based on single-phase systems, a great attention was given to the elucidation of the influence of aliovalent substitution in cationic sublattice on the electrophysical properties of perovskite-like complex oxides. This substitution leads to lattice distortions and structure channel and vacancy formation, permitting one to influence the phonon spectrum. The subjects of investigation were rare-earth elements titanates. Among rare-earth elements titanates (Ln_2O_3 - TiO_2), perovskite structure is formed only at a Ln_2O_3 : TiO_2 ratio of 1:3 ($\text{Ln}_2\text{O}_3 \cdot 3\text{TiO}_2$ - $3\text{Ln}_{2/3}\text{TiO}_3$) and is unstable.

When rare-earth ions are substituted by alkaline-earth ions, e.g. barium ions, according to the scheme

$\text{Ln}_{2/3-x}\text{Ba}_{3/2x}\text{TiO}_3$, at $x=1/6$ barium lanthanide tetratitanates, $\text{BaLn}_2\text{Ti}_4\text{O}_{12}$ are formed, which have higher ϵ values ($\epsilon = 70 - 90$) and a high temperature stability of properties ($\tau_\epsilon = +10 \cdot 10^{-6}\text{K}^{-1}$). The A sublattice vacancies in compounds lead to electromagnetic energy absorption, resulting in an increase in dielectric loss tangent ($\text{tg } \delta$). Our investigations showed that the partial substitution of rare-earth ions by alkali metal ions according to the scheme $\text{BaLn}^{3+}_{2-x}\text{M}^{1+}_{3x}\text{Ti}_4\text{O}_{12}$ within the confines of single-phase compositions ($0 < x < 1/6$) makes it possible to decrease $\text{tg } \delta$ by a factor of two in the microwave range due to a decrease in vacancy concentration. We also investigated barium-lanthanide titanates with various starting oxides ratio, and those partially substituted of Mg^{2+} , Ca^{2+} , Pb^{2+} ions for Ba^{2+} ions.

CDR DESIGN

Figure 1a shows a rectangular CDR design with the cylindrical central electrode. Unlike the known CDR designs and devices based on them, the coupling elements in our design (coupling and aligning capacitors) are constructed as plane electrodes on the open end. Figure 1a shows coupling electrodes (2), fine alignment (1) and coarse alignment (3) electrodes. Figure 1b shows an equivalent circuit of such a CDR. The coupling and aligning elements that are located on CDR allow one to control the coupling of the resonator with the load over a wide range and to change (to decrease) the resonant frequency by up to 10%. The absence of external additional coupling elements allowed us to extend the range of application of CDR's.

The resonance frequency of such CDR's was determined from the relation (for TEM wave):

$$\frac{1}{2\pi \cdot f_p \cdot C_\Sigma} = Z_0 \cdot \text{tg } \beta \cdot l \quad (1),$$

where $\beta = \frac{2 \cdot \pi \cdot f_p}{C} \sqrt{\epsilon}$, and l is the resonator length.

The capacitor capacity $C_s = C_A + C_C$, where C_A is the total capacity of aligning capacitors and C_C the total capacity of coupling capacitors.

The characteristic impedance (Z_0) of a cylindrical CDR was determined from the formula:

$$Z_0 = \frac{60}{\sqrt{\epsilon}} \cdot \ln \frac{D_o}{D_i}, \quad (2)$$

where D_o and D_i are the outer and inner diameters respectively. For a rectangular CDR, Z_0 was calculated from the formula:

$$Z_0 = \frac{60}{\sqrt{\epsilon}} \cdot \ln \frac{1.0787 A}{D_i}, \quad (3)$$

where A is the side length of the rectangular resonator cross-section. To calculate Z_0 , formula (2) may be used, in which $D_o = 1.27A$.

The critical wavelength, at which higher modes arise, was determined from the formula:

$$\lambda_{hp} = \frac{\pi \cdot D}{\sqrt{\epsilon}} \cdot \left(1 + \frac{D_o}{D_i}\right) \quad (4)$$

At the ratio $\frac{D_o}{D_i} \approx 3.3$, which is optimal in Q-factor, the following ratio was obtained, taking into account that no higher modes must be excited up to $f = 3f_p$, for calculating the dimensions of a homogeneous CDR operating under monofrequency conditions (up to $3f_p$):

$$\frac{l_p}{D_o} \geq \frac{10}{\epsilon} \quad (5)$$

We used this type of discrete CDR with cross-sectional dimensions of 5x5 mm to 25x25 mm as a base design in developing filters, frequency division systems and stabilizing circuits. CDR of such a type has a Q-factor of 500-1500.

At high frequencies (above 2000 MHz), resonance phenomena are observed in lumped coupling elements (capacitors, inductors), which lead to a decrease in the operating efficiency of CDR. To retain the single-mode monofrequency system of CDR's operating at frequencies above 2000 MHz, the following measures can be taken:

1. To decrease the ϵ value of ceramic from 90 to 4.
2. To reduce the cross-section of CDR's to the optimal one in terms of manufacturability and their Q-factor.
3. To use distributed couplings.

THE RESEARCH OF CDRs MODES SPECTRUM

The research of CDRs modes spectrum was carried out in the frequency range of 10^9 – $5 \cdot 10^9$ Hz inducing the natural oscillations spectrum in the resonator. Resonance modes were determined at the minimums of VSWR. It was applied inductive and capacitive coupling with resonator to reveal all oscillations, moreover the coupling rate was less than crucial one. Results of the tests are shown in Table 2, where f_1 is the lowest frequency corresponding to the basic TEM oscillation in quarter-wavelength resonator with one short-circuited end.

Data in the Table 2 clearly shows thinning out the modes spectrum of a resonator due to its diminishing and lowering ϵ in its material in the frequency range of 1 – $5 \cdot 10^9$ Hz. Q-factor in CDRs is in proportion to their cross-section, and tends to decrease when dielectric constant in material increases [1]. Therefore, lowering ϵ in

CDRs material at the frequencies above 10^9 Hz allows simultaneously suppression of undesirable modes and increase of Q-factor in CDRs as well as reproducibility of electrical parameters in CDRs based devices.

Due to the fact that CDR is almost screening resonance system, the overall dimensions of CDRs based devices are less in comparison with the similar ones based on the open dielectric resonators, e.g. with H_{10d} oscillations. A decrease in ϵ of the dielectric loading of CDR leads to an increase in higher mode excitation frequency. The reduction of CDR cross-section deteriorates the electrical characteristics of devices based on CDR's. However, by changing simultaneously the dimensions and ϵ one can optimize the electrical properties of CDR's and decrease the effect of higher modes.

Taking into account that the resonator modes spectrum is being thinned out when ϵ decreasing, filters based on the CDRs with low ϵ are preferable for the applications at the frequencies above 10^9 Hz in comparison with the similar ones based on the CDRs with ϵ value of 40-80. Moreover, utilization of low ϵ material in CDRs facilitates filters tuning and fabrication of coupling electrodes.

Monolithic block of resonators (MBR) was designed as a three-dimensional ceramic bar, in which holes were made during pressing. The bar and holes were covered by a high-conductivity coating. Coupling with the outer resonators is brought about through coupling capacitors, which are set up on MBR or attached as interconnection elements. The main purpose of MBR is band filters, which are produced in quantity. MBR's are promising designs for the quantity production of MW filters, including «chips», due to their monolithic design, the higher Q-factor of the resonators in them and the possibility of the automatic adjustment of filters.

We also developed CDR's which are combined into «quasi-monolithic» blocks, and a distributed coupling (of inductive or capacitive character) is formed between individual CDR's. In the design developed, it is possible to control couplings over a wide range on rectangular CDR's, which can be easily combined into blocks (fig.2) by soldering or cementing.

MW MONOLITHIC DEVICES

The characteristic feature of developed CDRs BP was that they were designed with the use of single CDRs and composed of 2 to 8 circuits with coupling units (capacitors), which were filled on the open end face of the quarter-wavelength rectangular resonator. Such design allows the easy adjustment of filter parameters: Center Frequency (F_c), Bandwidth (BW), Rectangularity Coefficient (C_r), V S W R, Insertion Loss, Attenuation out of BW. It also allows the choice of weight/dimensional parameters, provides high reliability, environmental durability, protection against strong vibration and impacts. The CDRs employed in filters were designed for the frequencies from 100 MHz to 5 GHz with cross-section dimensions from 25*25 mm to 6*6 mm.

All the filters were intended for purposes of TV systems signal processing, duplex communication systems, mobile and cellular phones, DRO systems.

1. Input BP Filters.

The relative BW of input BP filters composed of 3 to 5 CDRs was from 0.5% to 10%. Insertion loss in BW were in the range from 0.4 to 2 dB, rectangularity coefficient at 30/3 dB levels was from 1.5 to 3. For the input duplex filters attenuation at the transmitter frequencies attained more than 90 dB.

2. Transmitter Filter for duplex communication.

The transmitter filters for duplex communications (TDF) were designed on the 2-3 circuits base. Insertion loss for such design was from 0.5 to 1 dB, and attenuation at receiver frequencies was not less than 60 dB at the relative duplex BWs of 0.8% to 15 %. To provide the rise of steepness of the filters' slopes and to reduce insertion loss in BW the additive units formed attenuation poles were connected and settled at the relative distance of 1-10% from F_c . Such filters were designed for the VHF and UHF ranges for the power levels of 0.1 to 100 W. For example, parameters of TDF filter for mobile phone comprised 2 resonators with cross-section of 6*6 mm at $F_c = 814$ MHz were: BW = 25 MHz; insertion loss in BW was less than 0.8 dB; attenuation at transmitter frequency (904 MHz)- more than 50 dB. For the TDF filter designed on the base of 2 resonators with cross-section of 25*25 mm at the $F_c = 130$ MHz parameters were: BW = 1.5 MHz; Insertion loss - less than 0.8 dB; attenuation at 134 MHz - more than 50 dB.

3. Frequency-separation devices

Frequency-separation devices (FSD) were designed as BP filters connected with the mutual input (output) using the passive matching unit (MU). MU contained inductive circuits and capacitors, or quarter-wavelength cable segments and matching capacitor. The use of such a unit allows the stability of the filter parameters. For example, in the systems for TV transmitter signals addition of 24, 27, 30, 33 channels for the power level of up to 20 W the filters were designed on the base of CDRs with cross-section of 13*13 mm. The ceramic materials selected for CDRs manufacture possessed dielectric constant $\epsilon=38$ and low $\text{tg } d$.

In such filters, which consist of 4 circuits the following parameters were attained: insertion loss in BW - less than 1 dB; attenuation between the neighbor channels - not less than 45 dB; attenuation between the distant channels - more than 60 dB. Such FSDs allows the simultaneous transmission of 2 to 6 TV channels using single antenna with the VHF-transmitters distribution over the channel (8 MHz) or more for the transmitted power of up to 100 W. The developed FSDs help to avoid reciprocal influence both for the transmitters and for the receivers.

With the use of high CDRs' dielectric constant values (more than 60) and large CDRs cross-section dimensions at the frequencies above 1 GHz it is possible to expect a stimulation of a number of higher modes. In this case we can not attain high Q-factor for such CDRs without employment of special methods for the higher modes suppression. That is why the utilization of the dielectric materials with low dielectric constant (from 3 to 20) is preferable for the manufacture of CDRs, which are intended for the applications at the frequencies above 1 GHz. The use of low ϵ CDRs provides high quality of filter parameters without essential increase of filter weight and dimensions. To process the signals of VHF transmitters with transmitted power of up to 200 W the new antenna reject-band filters were designed. The attenuation of TV signal in BW for such filters was less than 0.5 dB, and intermodulation signals for them were rejected over 6.5 or 5.5 MHz to the level of 50 dB.

Table 1. Dielectric properties of sintered ceramics.

Material based on the systems:	ϵ	$\tau_f^* 10^{-6} \text{ K}^{-1}$	Q at 10 GHz
MgO-CaO-ZnO- Al_2O_3 - TiO_2	12	-10 -- +10	3000
MgO-CaO- TiO_2 - SiO_2	15	-10 -- +10	5000
MgO- TiO_2 -CaO	20	0 -- +5	5000
ZnO- TiO_2	22	0 -- +5	2000
Ba Ti_4O_9	38	+20	6000
Ba Ti_4O_9	38	+20	3000
BaO- Na_2O - Nd_2O_3 - Sm_2O_3 - TiO_2	80	0 -- +5	1200
BaO-CaO- Sm_2O_3 - TiO_2	80	0 -- +5	1200
BaO-PbO- Nd_2O_3 - Sm_2O_3 - TiO_2	90	0 -- +5	600

Table 2. CDR modes spectrum.

CDR cross-section, mm	ϵ	$\text{tg } \delta \cdot 10^4$ at 10^{10} Hz	Frequencies of the modes in CDR, MHz								
			f_1	f_2	f_3	f_4	f_5	f_6	f_7	f_8	f_9
13*13	22	7-8	1340	2810	4050	4190	4600	4850	4970		
13*13	20	2-3	1320	2780	3930	4170	4580	4830	4960	--	--
10*10	20	2-3	1452	3400	3590	4302	--	--	--	--	--
8*8	20	2-3	1335	3880	4060	--	--	--	--	--	--
13*13	38	2	1664	2440	2588	3395	4222	4428	4516	4680	4900
10*10	38	2	1446	2760	2850	4091	4500	4860	--	--	--
8*8	38	2	1430	3343	3416	4152	--	--	--	--	--
8*8	38	3-4	1394	3373	3438	4200	4918	5010	--	--	--
8*8	80	9-10	1496	2760	2850	4091	4500	4860	--	--	--

Table 3. Q-factor values of CDR's at the fundamental frequency (f_0) of TEM wave.

1	Crossection, mm^2	ϵ value	$\text{tg } \delta \cdot 10^4$	Measurement frequ-ency range (MHz)	Q_0 value
1.	6x6	80	4	600-900	450-500
2.	8x8	80	4	1400-1500	450-500
3.	8x8	38	2.5	1400-1500	450-500
4.	10x10	40	2.5	1600-1800	480-500
5.	10x10	20-21	2-3	1300-1400	900-980
6.	8x8	20-21	2-3	1300-1400	580-600
7.	13x13	20-22	2-2.5	1300-1400	1000-1050
8.	16x16	38	2.5	600-800	1000-1100
9.	20x20	38	2.5	600-800	1200-1250
10.	25x25	38	2.5	600-800	1350-1400

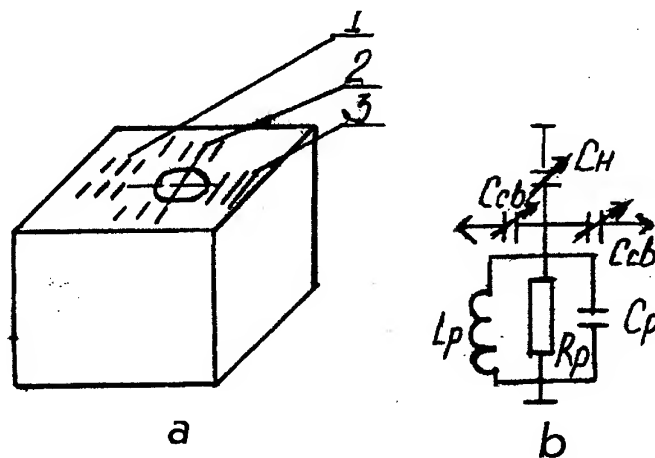


Figure 1. The Design of CDR (a), and its equivalent circuit (b).

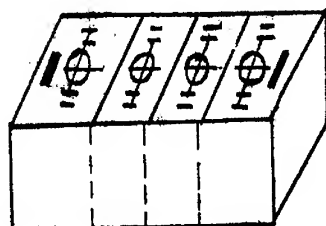


Figure 2. The design of quasi-monolithic block of resonators.

Transient Analysis of Printed Circuit Board Layouts using a Time Domain Solution of Kirchoff's Network Equations

Charlene S. L. Goh and Chris J. Railton

Centre for Communications Research, Faculty of Engineering, University of Bristol,
Bristol, BS8 1UB, England

ABSTRACT

With the clock speeds and data rates greater than 1GHz being used on digital Printed Circuit Boards, it is now essential that the electromagnetic effects of crosstalk, reflection and pulse distortion be taken into account in the design. Unfortunately the size and complexity of a typical PCB is so great that a full-wave electromagnetic analysis is not practicable and a more pragmatic approach, such as the derivation of equivalent passive electrical circuits to represent the actual structure, must be considered. In this contribution a novel time domain technique is presented for analysing such equivalent circuits in a computationally efficient and accurate manner. Results are presented for example structures showing the computational speed and accuracy achieved.

INTRODUCTION

As the clock speeds and component densities on digital Printed Circuit Boards increase, it becomes essential to take account of the electromagnetic effects of crosstalk, reflection and pulse distortion at the design stage. One technique for doing this involves the derivation of an equivalent passive electrical circuit which is analogous to the PCB under investigation based on a quasi-static analysis[1]. In addition similar techniques can be used for IC packages and other associated structures [2][3].

Once the equivalent circuit has been derived, it is then necessary to perform a circuit analysis in order to calculate the properties of the structure under investigation. Due to the complexity of the equivalent circuit, standard circuit solvers such as Spice are not appropriate and algorithms which are specialised and optimised to this type of circuit must be used. In [1] the analysis was done in the frequency domain, however there are many advantages to solving in the time domain:

1. For digital PCBs it is the time domain properties, such as pulse shape and peak crosstalk levels which are of most interest.
2. The effects of non-linear components are readily included.
3. It is easier to take advantage of the special topology of the equivalent circuits in a time domain algorithm. Indeed, if interactions are considered to be confined to a specified "radius of influence" then the computational resources can be made just linearly dependent on the number of unknowns in the formulation.
4. Once the system matrices are set up, no further matrix inversion is required.

In addition, even if frequency domain data is required, it is often faster to perform a transient analysis using a time domain algorithm and to use the Fourier transform than to use a frequency domain algorithm directly.

THE TIME DOMAIN ALGORITHM

Following [1], each track on the PCB is divided into segments, each of which is represented by an inductor and a capacitor. Mutual coupling is assumed to exist between each pair of inductors and capacitors. For example, the equivalent circuit of 2 parallel PCB tracks is shown in Figure 1. There is clearly a trade off between segment size and accuracy with a commonly used rule of thumb being that the segment size is chosen to have a magnitude approximately one tenth of a wavelength at the maximum frequency of interest.

Using Kirchoff's laws and applying a central difference approximation to the time derivatives the modelling equations for current and voltage taking into account mutual inductance and capacitance, are as follows :

$$I_b^{i\delta t} = I_b^{(i-1)\delta t} + \delta t \sum_m L_{bm}^{-1} (V_{n1(m)}^{(i-0.5)\delta t} - V_{n2(m)}^{(i-0.5)\delta t}) \quad (1)$$

$$V_n^{(i+0.5)\delta t} = V_n^{(i-0.5)\delta t} + \delta t \sum_m C_{nm}^{-1} (I_{b1(m)}^{i\delta t} - I_{b2(m)}^{i\delta t}) \quad (2)$$

where the vectors I and V are the currents flowing through each inductor and the voltages across each capacitor respectively, the matrices C and L are the capacitance and inductance matrices respectively, the functions $n1(m)$ and $n2(m)$ return the two nodes to which branch m is connected and the functions $b1(m)$ and $b2(m)$ return the branches which are connected to node m .

The voltage and current values are updated in a leap-frog manner at every time step increment until a specified maximum time is reached. The size of the time step is limited by the stability condition which has been found to be the minimum value of:

$$dt < dx\sqrt{LC}$$

where dx is the distance between consecutive nodes, L and C is the self inductance and self capacitance per unit length of the segment.

It can be seen that, once the inverse inductance and capacitance matrices have been calculated using, for example the methods of [1], no further matrix inversions are necessary. This contrasts with frequency domain methods where the system matrix must be inverted at every frequency point. Moreover if specified interactions, such as those between widely separated segments, can be assumed negligible, the corresponding terms in the summations of equations (1) and (2) can simply be omitted with a corresponding saving in computation time.

RESULTS

In order to demonstrate the efficiency of the technique, three examples are chosen:

1. Coupled parallel printed circuit tracks, 2. A stepped impedance microstrip filter, 3. Interconnections within an IC package and a PCB track

Example 1 has been previously analysed using both the Spectral Domain method [4] and the FDTD method [5]. Example 2 has been previously analysed in [1] in which there are measured and calculated results. Example 3 illustrates the use of the time domain technique in conjunction with different static analysis tools in order to model a complicated three dimensional structure.

Example 1 - coupled microstrip lines

For this example, the microstrip lines were on a substrate of permittivity 9.7 and thickness 1.5mm and had widths of 1.5mm and separation between centres of 4.5mm. The modelling parameters were as follows : segment size = 1.5 mm, no. of iterations = 300, width of excitation pulse = 100 picoseconds. Figure 2 shows the time domain responses obtained by the 3 methods on the sense line at a point 80mm from the position of excitation. From the results, it can be concluded that this approach produces results of similar accuracy to those produced by other existing methods and but the run time taken is significantly shorter. The time taken to run the time domain algorithm, taking into account all possible interactions, was 2 mins on a 133MHz Pentium.

Example 2 - Stepped impedance low-pass filter

This method was also applied to a microstrip low pass filter [1, p100]. The plan of the filter is shown in Figure

3 and the results obtained using this method are compared to measurement. Good agreement has been obtained. The time taken to run the new algorithm was 20 mins on a 133MHz Pentium whereas the time quoted in [1] using the frequency domain method was 90 mins for 100 frequency points on a Sun SparcStation 2. It is noted that, to obtain time domain results by applying the fourier transform, many more than 100 frequency points would be required, also all the couplings were included in the time domain model. If a "radius of influence" were defined then it is expected that the computer time would decrease by a factor of between 5 and 10.

Example 3 - interconnections within an IC package

The geometry for this example is shown in Figure 5. Here a ceramic integrated circuit containing a silicon chip is placed on a printed circuit board. The interconnect consists of a transmission line on the chip, a bond wire which includes a sharp bend, a pin and the PCB track to which it is connected. It can be seen that a number of discontinuities exist in this structure which would be expected to cause reflections and pulse distortion. In the simulation, a 1nS digital pulse having a risetime of 100ps [6] is applied at the chip and the resulting waveform at the PCB is examined. The chip transmission line and the PCB track are both assumed to be connected to matched loads.

In order to ascertain the equivalent circuit for this structure, the IC package and the PCB were treated as two separate modules which interact only through the intentional connection. In order to gain greatest accuracy and computational efficiency, the IC package was modelled using FASTCAP and FASTHENRY whereas the printed circuit board was modelled using techniques described in [1]. The outputs of these programs were then combined and used as input to the time domain analysis program.

In Figure 6 the calculated transmitted and reflected signals are shown together with the input pulse. It can be seen that, for this example the pulse suffers slight distortion and there is a reflected signal of approximately 600mV peak.

CONCLUSION

This contribution shows that the time domain response of PCB tracks and associated structures can be accurately and efficiently modelled using a time domain method based on a discretisation of circuit equations derived from Kirchoff's laws. This approach has advantages over other existing methods in terms of computational efficiency and, in particular, that the computation time can be made linearly dependent on the number of unknowns.

REFERENCES

1. K. J. Scott, "Practical Simulation of Printed Circuit Boards and Related Structures", Wiley and sons, 1994.
2. "K. Nabors, S. Kim and J. White, "Fast Capacitance Extraction of General 3D Structures", IEEE Trans MTT-40, July 1992, pp. 1496-1506
3. M. Kamon, M.J. Tusk and J.K. White, "FASTHENRY: A Multipole-accelerated 3D Inductance Extraction Program", IEEE Trans MTT-42, Sept. 1994, pp. 1750-1758
4. J.P. Gilb and C.A. Balanis, "Pulse Distortion on Multilayer Coupled Microstrip Lines", IEEE Trans. MTT-37 pp. 1620-1628, 1989
5. N.M. Potheary and C.J. Railton, "Analysis of Cross-talk on High-speed Digital Circuits using the Finite Difference Time Domain Method", Int. J. of Numerical Modelling: Electronic Networks, Devices and Fields, Vol 4, pp. 225-240, 1991
6. "Standard for Heterogeneous InterConnect(HIC)" IEEE Standard P1355, 1996.

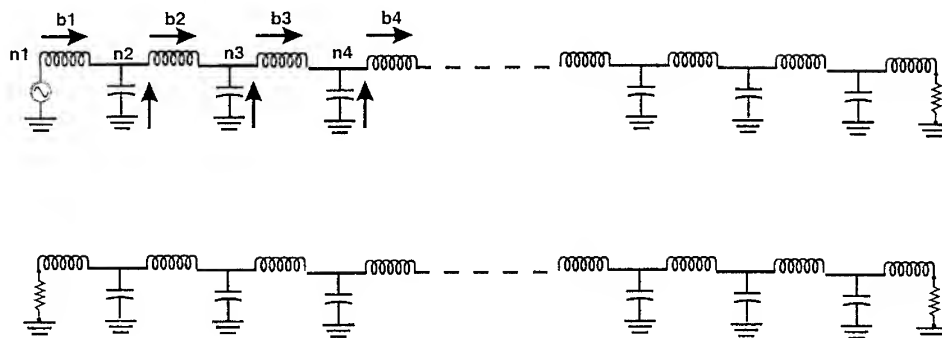


Figure 1 - Equivalent circuit for coupled microstrip lines

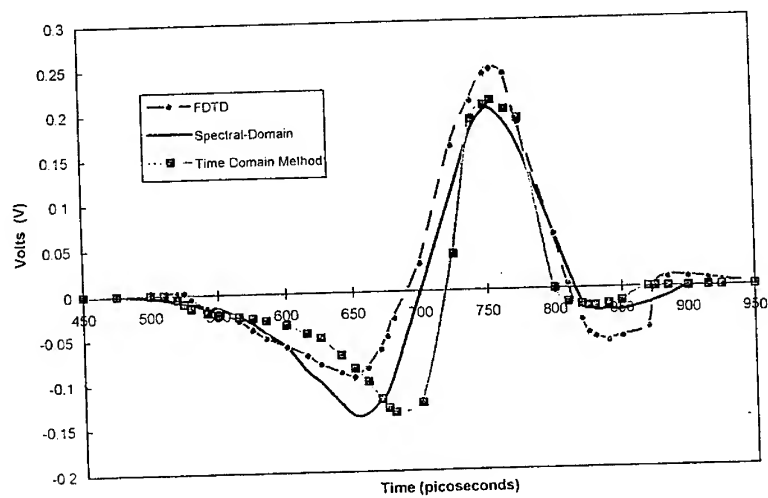


Figure 2 - Calculated crosstalk level on a coupled microstrip line

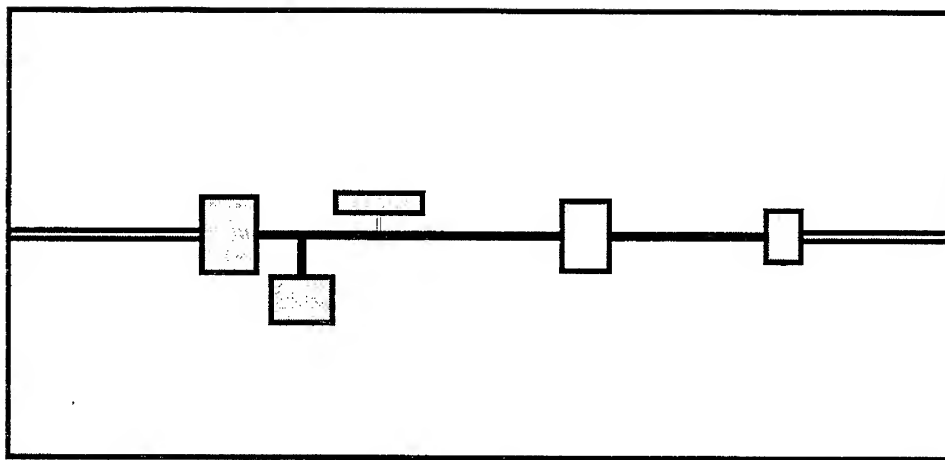


Figure 3 - The plan of the stepped-impedance low-pass filter

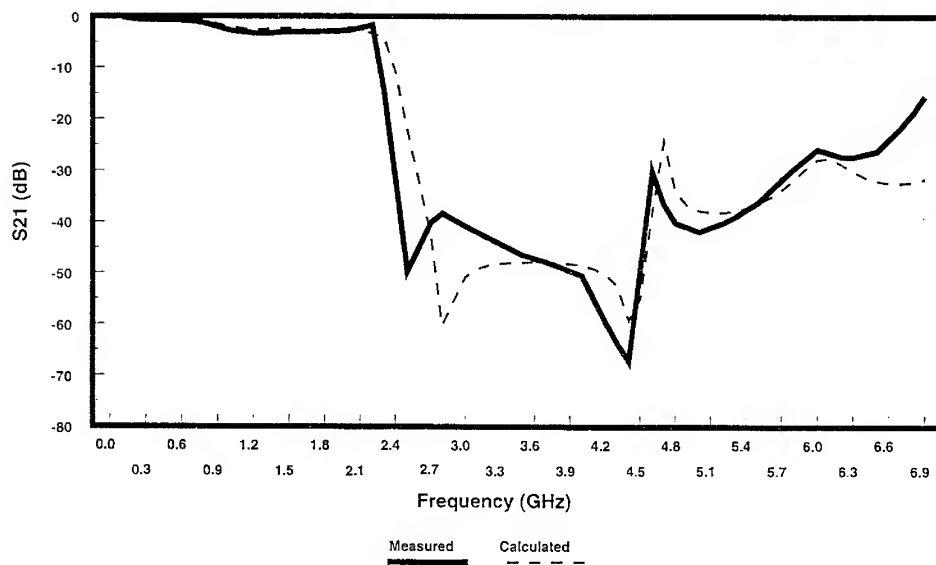


Figure 4 - Calculated and measured results for the stepped-impedance low-pass filter

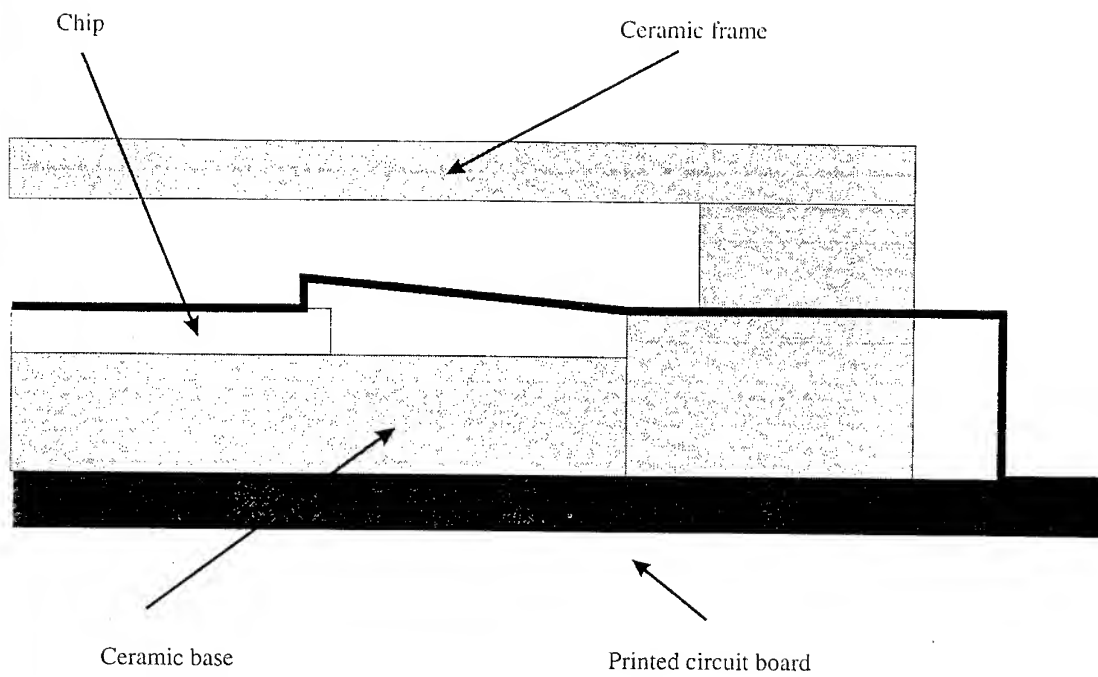


Figure 5 - The geometry of the interconnect within the chip package

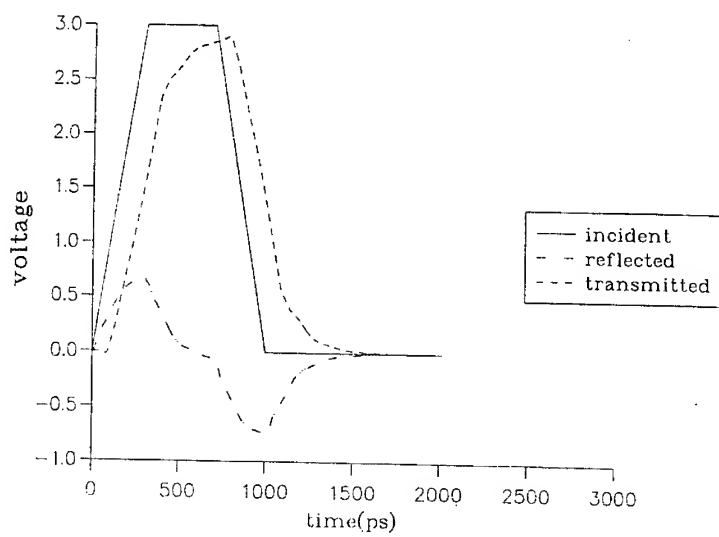


Figure 6 - Predicted waveforms on the interconnect in the chip package

MULTIPLE PROBE NEARFIELD SCANNING FOR EMC-INVESTIGATIONS

H.-O. Ruoss¹, J. Christ² and F. M. Landstorfer¹

¹Institut für Hochfrequenztechnik, University of Stuttgart, Pfaffenwaldring 47, 70550 Stuttgart (Germany)

²Bosch Telecom GmbH, Dept. UC-ON/ERA, 71520 Backnang (Germany)

ABSTRACT

Antennas such as log-periodic arrays are often used to quantify the emission of electromagnetic radiation from a test object. The calibration of such relatively large antennas is a challenging task with conventional farfield measuring sites, while nearfield scanning offers an advantageous alternative. From basic electromagnetic theory it is well-known that correct farfield data from a nearfield to farfield transformation can only be obtained if the nearfield is measured on a *closed* surface around the antenna under test. The consequence of sequentially scanning on a closed envelope is that measurement time becomes considerable, which cannot be accepted if these measurements involve test persons. To overcome these drawbacks, a new *multiple probe scanning technique* is proposed.

INTRODUCTION

Emission measurements of radiation in EMC applications are using the so-called *antenna factor* (AF) of a calibrated receiving antenna. As the conventional methods (e.g. as defined in [1]) to determine this antenna factor suffer from some significant disadvantages, the nearfield technique can be applied to overcome these drawbacks.

In mobile communications, a rapidly growing market for handsets and the public concern about possible radiation hazards necessitates the investigation of antennas of portable hand-held transceivers. Here, nearfield scanning is an efficient method to determine radiation performance and efficiency of the antenna, as well as absorption factors of the biological tissue.

NEARFIELD SCANNING

The essential advantages of nearfield scanning - due to the small distance between the antenna under test and the probe (which is typically 1 to 2 m) - are an improved signal-to-noise ratio, the reduction of reflections caused by the environment, as well as a significant reduction of space requirements [2]. Conventional nearfield scanning is carried out on planar, cylindrical or spherical surfaces as shown in **Figure 1**. Any of these techniques suffers from certain drawbacks as outlined in [2], [3] and [4]. While spherical scanning is usually accomplished by rotation of the antenna under test round two orthogonal axes, which for obvious reasons is not a procedure to be carried out if test persons are involved - such as is the case when measuring handsets under realistic operating conditions - the two remaining techniques do not take the entire radiating power into account and cause systematic errors in the nearfield-farfield transformation particularly with antennas of low directivity. To overcome these drawbacks, scanning along modified surfaces such as the biconical and the bicylindrical technique was suggested in [3] and [4]. Unfortunately, sequential scanning on a closed envelope requires a lot of measurement time when using a single probe. In the following a way to overcome the drawbacks of single probe nearfield scanning is presented.

MULTIPLE PROBE SCANNING

A drastic reduction of measurement time can be achieved by using *multiple probes* which are scanned by means of RF switches as shown in **Figure 2**. Hence, in the spherical case, a single-axis turntable is sufficient for azimuth scanning. To guarantee "identical performance of all probes", for any test frequency a *calibration* of the system (magnitude and phase) is necessary to take into account the different signal paths and the mutual coupling of the probes as well as manufacturing tolerances. In practice this is realized by scanning all probes with a calibration antenna to get the calibration factors, with which any following nearfield measurement can be corrected.

Carrying out nearfield measurements by multiple probe scanning makes no difference to the transformation algorithm and the basic ideas of conventional nearfield technique can be applied as presented in [2].

MEASURING THE ANTENNA FACTOR

In principle, all calibration methods to get the antenna factor use the measurement geometry shown in **Figure 3** (*two antenna method* acc. to ANSI, see [1]), requiring very large measurement sites (distance R up to 30 m) with flat and homogeneous ground planes as well as large and expensive linear axis positioners (height h_{2max} up to 6 m). On the other hand, the antenna factor of any antenna depends on its radiation characteristic which can be described by the so-called spherical transmitting coefficients (see [2] and [4]) as e.g. used in a nearfield to farfield transformation. These transmitting coefficients can be exploited not only to calculate the farfield results, but also to simulate the measurement set up shown in **Figure 3** with an identical receiving antenna and an image antenna representing the ground plane. Thus, the appropriate antenna factors can be determined for any separation distance R or any polarization of the antenna with only one measurement, using simple (low-cost) positioning systems. In addition, to reduce the significant measurement time for a broadband determination of the *AFs*, one can take advantage of the spherical multiprobe scanning as presented in this paper.

MEASURING THE ABSORPTION FACTOR OF HANDSET ANTENNAS

Measurement principle

The schematic picture of **Figure 4** defines the essential parameters and the situation describing the interaction between the antenna of a handset and its user. The single parameters are:

$$\begin{aligned} f &= 1800 \text{ MHz} \\ a \times b \times c &= 2 \times 6 \times 12 \text{ cm}^3, R = (r + d, 0, 1) \text{ cm}, d \rightarrow 0 \\ h &= \lambda_0 / 4 \approx 4 \text{ cm}, \rho = 0.5 \text{ mm} \\ F &= (r + d + a/2, 0, 1) \text{ cm} \end{aligned}$$

For *free space* measurement (index f), the entire radiated power P_t^f propagates through a closed envelope around the hand-held set ($P_t^f = P_{ff}^f$), whereas with the presence of *biological tissue* (index b) a part of the radiated power is absorbed: $P_t^b = P_{ff}^b + P_{abs}$.

The *absorption factor* of the lossy biological tissue is given by

$$\Gamma_{abs} = \frac{P_{abs}}{P_t^b} = \frac{P_t^b - P_{ff}^b}{P_t^b} \stackrel{P_t^b = P_t^f}{=} \frac{P_{ff}^f - P_{ff}^b}{P_{ff}^f} \quad (1)$$

assuming that the antenna is matched in both cases. If P_{t0} is the available power of the RF source, the radiated power depends on the matching of the antenna and is given by

$$P_t = (1 - |\Gamma|^2) \cdot P_{t0} \quad (2)$$

with Γ representing the reflection coefficient of the antenna. If the matching of the antenna deteriorates in the case of the presence of biological tissue ($P_t^b \neq P_t^f$), a "normalized" radiated power has to be introduced in order to assure comparability:

$$P_{t, norm}^b = P_t^b / (1 - |\Gamma_b|^2) \quad (3)$$

So, in the case of $|\Gamma_b| \neq 0$, equation (1) has to be modified to

$$\Gamma_{abs} = 1 - \frac{1}{1 - |\Gamma_b|^2} \cdot \frac{P_{ff}^b}{P_{ff}^f} \quad (4)$$

Measurement results

The absorption caused by DCS-1800 transceivers was investigated. The measurements were carried out with different test persons, applying the multiple-probe scanning as shown in **Figure 5**. In order to find out the *worst case of absorption*, the persons held the antenna in an upright position close to their head. **Figure 6** shows the spread of measured absorption factors; the average absorption factor is about 68%. This value decreases to 50% (see **Figure 7**) if the antenna is held with an inclination of about 60° out of the upright position as is customary when telephoning. **Figure 8** demonstrates that a reduction of the absorption losses can also be observed when increasing the distance between the antenna and the head.

REFERENCES

- [1] ANSI: *American National Standard for Calibration of Antennas used for Radiated Emission Measurements in Electromagnetic Interference (EMI) Control*; June 1988, ANSI C63.5
- [2] J. Christ: *Korrektur prinzipbedingter und durch die Meßumgebung verursachter Fehler bei der Nahfeld-Fernfeld-Transformation*; 1995, Dissertation, University of Stuttgart (Germany)
- [3] H.-O. Ruoss, J. Christ, and F.M. Landstorfer: *EMC-investigation of hand-held mobile telephones using a double-cone nearfield to farfield transformation*; 1996, 26 European Microwave Conference, Prague (Czech Rep.), 9.-12.9.1996, pp. 795-798
- [4] J. Christ, F.M. Landstorfer: *Overcoming the typical limitations of the cylindrical near-field to farfield transformation*; 1995, 25th Europ. Microwave Conf., Bologna (Italy), pp. 1245-1250

FIGURES

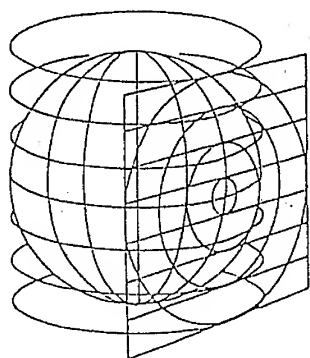


Figure 1: Conventional nearfield scanning surfaces

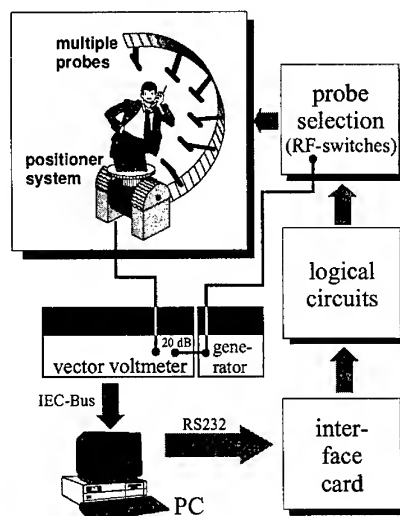


Figure 2: Principle arrangement of multiple probe scanning

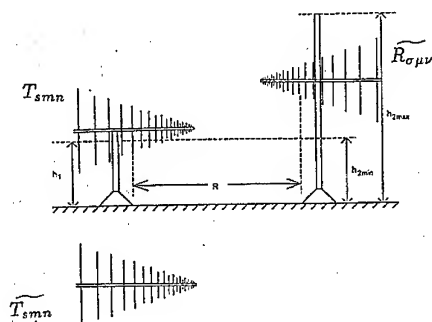
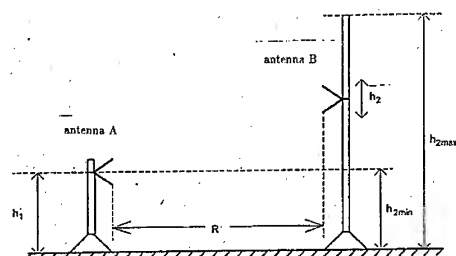


Figure 3: Typical measurement geometry acc. ANSI C63.5 (left) and: Simulation of the ANSI measurement (right)

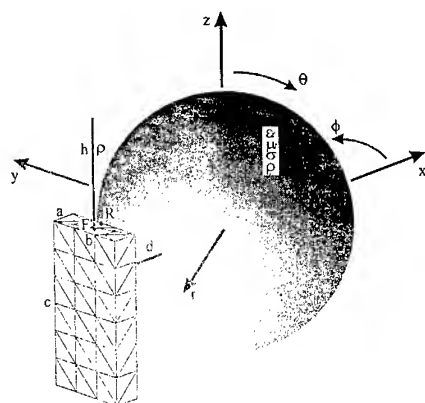


Figure 4: Principle situation

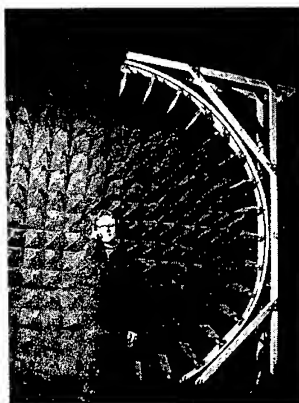


Figure 5: Measurement situation

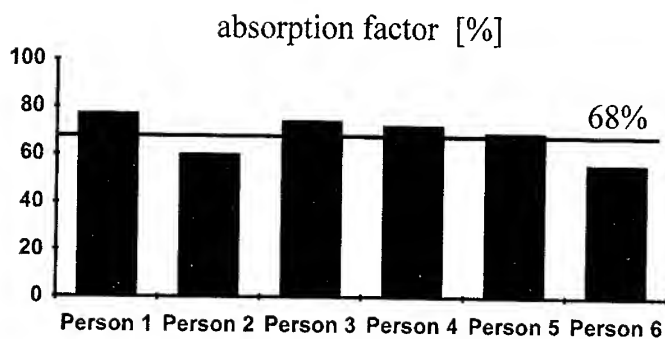


Figure 6: Measurement series 1: Worst case situation

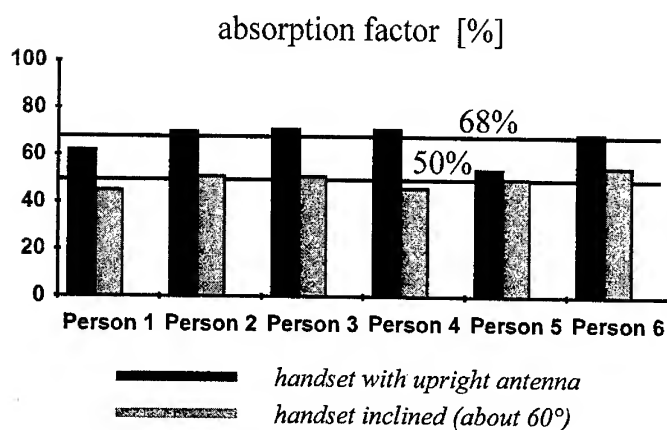


Figure 7: Measurement series 2: Influence of the inclination of the handset

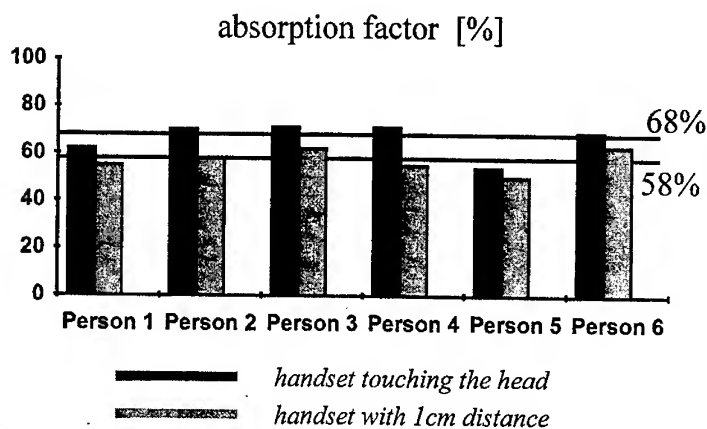


Figure 8: Measurement series 3: Influence of the distance between head and handset

TEM-Modes in Slot-Coupled Waveguides

A.S. Omar¹, C. Rieckmann¹ and A. Jöstingmeier²

¹ Technische Universität Hamburg-Harburg
Arbeitsbereich Hochfrequenztechnik
Postfach 901052, D-21071 Hamburg, Germany

² Deutsches Elektronen-Synchrotron DESY
Notkestr. 85, D-22609 Hamburg, Germany

Abstract

TEM-modes which are usually expressed in terms of a scalar electric potential ϕ are shown to be derivable from a scalar magnetic potential ψ if the supporting transmission line can be considered a slot coupled waveguide with more than one coupling slot. The magnetic potential must jump at the coupling slots in order to give rise to the axial electric current on the strips separating these slots. The advantage of this formulation is its compatibility to the numerically efficient generalized spectral domain technique which has been successfully applied for the analysis of planar transmission lines. Several multi-slot planar transmission lines have been analyzed using this formulation. Excellent agreement with the results obtained by other methods have been achieved with extremely low cpu-time and storage requirements.

I. Introduction

The numerically efficient generalized spectral domain (GSD) technique is the generalization of the conventional one-dimensional spectral domain technique [1],[2]. It has been applied to the analysis of both guiding and resonance structures (see e.g. [3]–[5]). This technique is based on subdividing the structure to be analyzed into well-defined regions which are coupled by apertures. The latter are next short-circuited and the non-vanishing tangential electric field there is restored by inserting surface magnetic currents at both sides of the introduced short circuit. This procedure has the advantage of separating the structure into subregions which are independently analyzed. This gives the method its modular feature. Details of the GSD method can be found in the above mentioned references.

In order to include the analysis of the TEM-modes in the GSD technique, it is necessary to describe these modes in terms of a scalar magnetic rather than the conventional electric potential. The existence of the axial electric current enforces the magnetic potential to be multi-valued, which gives rise to numerical difficulties. In this contribution it is shown that an equivalent alternative to the multi-valued feature in a class of slot-coupled transmission lines is to let the magnetic potential jump across the coupling apertures. Except there the magnetic potential remains well-behaved and single-valued.

II. Basic Formulation

We will now consider the double-slot-coupled waveguides shown in Fig. 1. Extending the analysis to arbitrary number of coupling slots will be done later. The two waveguides with cross sections $S^{(1)}$ and $S^{(2)}$ are considered to be slot-coupled by the composite slot C_0 ($C_0 = C_{01} \cup C_{02}$). The two unit vectors \hat{n} and $\hat{\tau}$ are normal and tangential to C_0 , respectively. Because of the metal strip separating C_{01} from C_{02} the waveguide supports a TEM-mode. For the analysis of this mode we will essentially follow the method presented in [5], which has already been applied to the computation of TE- and TM-modes of slot-coupled waveguides.

Let $h_{zn}^{(i)}$ and $e_{zn}^{(i)}$ ($i=1,2$) be the complete sets of axial magnetic and electric fields characterizing the TE- and TM-modes, respectively, in the individual waveguides (1) and (2). The scalar fields $h_{zn}^{(i)}$ and $e_{zn}^{(i)}$ which correspond to cutoff wavenumbers $k_{nh}^{(i)}$ and $k_{ne}^{(i)}$, respectively, are real functions of the transverse coordinates and satisfy the orthogonality relations [6]:

$$\int_{S^{(i)}} h_{zn}^{(i)} h_{zm}^{(i)} dS = P_{nh}^{(i)} \delta_{nm}, \quad \int_{S^{(i)}} e_{zn}^{(i)} e_{zm}^{(i)} dS = P_{ne}^{(i)} \delta_{nm}, \quad (1 \text{ a-b})$$

where δ_{nm} is the Kronecker delta.

Let ∇_t and \hat{k} be the transverse component of the del-operator and the unit vector in the axial direction, respectively. The sets $\{\nabla_t e_{zn}^{(i)}\}$ and $\{\hat{k} \times \nabla_t h_{zn}^{(i)}\}$ are complete with respect to curl-free and divergence-free transverse electric fields, respectively, which can exist in the i th waveguide. The two sets $\{\nabla_t e_{zn}^{(i)}\}$ and $\{\nabla_t e_{zn}^{(i)} \times \hat{k}\}$ have the same properties with respect to transverse magnetic fields.

Let e and h be the electric and magnetic field, respectively, of the TEM-mode in the composite waveguide with the z -dependence $e^{-jk_0 z}$ being dropped out, where k_0 denotes the free space wavenumber. Each of these fields can be written as

$$f = \begin{cases} f^{(1)} & \text{on } S^{(1)} \\ f^{(2)} & \text{on } S^{(2)} \end{cases} \quad (2)$$

The composite coupling slot C_0 is next short-circuited and the non-vanishing tangential electric field there is restored by sandwiching this short circuit between two surface magnetic currents \mathbf{m}_s (in waveguide (1)) and $-\mathbf{m}_s$ (in waveguide (2)) which are given by

$$\mathbf{m}_s = m_{sz} \hat{\mathbf{k}} = \hat{\mathbf{n}} \times \mathbf{e}|_{C_0} \quad (3)$$

The continuity of the tangential electric field across C_0 is then guaranteed. Maxwell's equations in the individual waveguides are then reduced to

$$\nabla_t \times \mathbf{e}^{(i)} = \mp m_{sz} \delta(n - n_0) \hat{\mathbf{k}}, \quad \nabla_t \times \mathbf{h}^{(i)} = 0, \quad \mathbf{e}^{(i)} = Z_0 (\mathbf{h}^{(i)} \times \hat{\mathbf{k}}), \quad (4 \text{ a-c})$$

where Z_0 is the free space intrinsic impedance, $\delta(n - n_0)$ is the Dirac delta function, n is the coordinate normal to the slot C_0 ; and n_0 corresponds to the location of the slot. The term $\delta(n - n_0)$ is necessary because the currents entering Maxwell's equations are volume and not surface distributions. The upper (lower) sign in (4 a-c) and the subsequent analysis corresponds to $i = 1$ ($i = 2$).

Before we go ahead with the analysis, it is worthy noting that due to short circuiting the coupling slot C_0 , the two waveguides (1) and (2) can be treated independently. In particular, the domain of definition of $f^{(i)}$ in (2) is $S^{(i)}$ which means that any derivative of $f^{(i)}$ with respect to n (i.e., normal derivative of any order) at $n = n_0$ is defined as that at n_0^- and n_0^+ for $i = 1$ and $i = 2$, respectively. On the other hand the normal derivative of f in (2) at $n = n_0$ is not defined.

A) The scalar magnetic potential

Due to (4b) $\mathbf{h}^{(i)}$ can be written as the transverse gradient of a single-valued scalar magnetic potential $\psi^{(i)}$:

$$\mathbf{h}^{(i)} = \nabla_t \psi^{(i)} \quad (5)$$

Substituting (5) into (4) results in

$$\nabla_t^2 \psi^{(i)} = \pm \frac{1}{Z_0} m_{sz} \delta(n - n_0) \quad (6)$$

with Neumann's boundary condition.

The two magnetic potentials $\psi^{(1)}$ and $\psi^{(2)}$ are next expanded with respect to the sets $\{h_{zn}^{(1)}\}$ and $\{h_{zn}^{(2)}\}$, respectively:

$$\psi^{(i)} = \sum_n \frac{a_n^{(i)}}{\sqrt{P_{nh}^{(i)}}} h_{zn}^{(i)} \quad (7)$$

The expansion coefficients are easily shown to be given by

$$a_n^{(i)} = \frac{1}{\sqrt{P_{nh}^{(i)}}} \int_{S^{(i)}} \psi^{(i)} h_{zn}^{(i)} dS = \mp \frac{1}{Z_0} \frac{1}{k_{nh}^{(i)2} \sqrt{P_{nh}^{(i)}}} \int_{C_0} m_{sz} h_{zn}^{(i)} dl \quad (8)$$

It is worthy noting that the H_{00} -mode must be included in (7) (see, e.g., [5]). This mode corresponds to $n = 0$ (with $k_{0h}^{(i)} = 0$ and $h_{z0}^{(i)} = \text{constant}$). $a_0^{(i)}$ in (8) remains however finite, because the line integral of m_{sz} along C_0 vanishes.

Let us now expand m_{sz} with respect to a suitable set of basis functions $\{\eta_k\}$, which satisfy the edge condition at the slot edges:

$$m_{sz} = \sum_k U_k \eta_k \quad (9)$$

Since the composite slot C_0 is composed of C_{01} and C_{02} , a part of the basis functions η_k must be defined over C_{01} and vanishes on C_{02} while the other part is defined the other way round. Following the standard procedure presented in [5] the matrices $[C^{(i)}]$ and the column vectors $\mathbf{D}^{(i)}$ are defined with the following elements:

$$C_{nk}^{(i)} = \frac{1}{\sqrt{P_{nh}^{(i)}}} \int_{C_0} h_{zn}^{(i)} \eta_k dl; \quad n \neq 0, \quad D_k^{(i)} = \frac{1}{\sqrt{P_{0h}^{(i)}}} \int_{C_0} \eta_k dl \quad (10 \text{ a-b})$$

This results then in

$$\mathbf{a}^{(i)} = \mp \frac{1}{Z_0} [\Lambda^{h(i)}]^{-1} [C^{(i)}] \mathbf{U}, \quad \mathbf{D}^{(i)T} \mathbf{U} = \mp Z_0 (k_{0h}^{(i)})^2 a_0^{(i)} = 0 \quad (11)$$

where $\mathbf{a}^{(i)}$ is a column vector with elements $a_n^{(i)}$ ($n \neq 0$), $[\Lambda^{h(i)}]$ is a diagonal matrix with elements $k_{nh}^{(i)2}$ ($n \neq 0$) and \mathbf{U} is a column vector with elements U_k .

B) Continuity of the tangential magnetic field

The fact that the surface magnetic currents in waveguides (1) and (2) are equal in magnitude and opposite in direction leads automatically to the continuity of the tangential electric field across the composite coupling slot C_0 . In order to determine the unknown expansion coefficients of the surface magnetic current (U_k), the continuity of the tangential magnetic field across the slot has to be enforced. Referring to (5), the continuity of the tangential magnetic field across C_0 leads to

$$\left. \frac{\partial \psi^{(1)}}{\partial \tau} \right|_{C_0} = \left. \frac{\partial \psi^{(2)}}{\partial \tau} \right|_{C_0} \quad (12)$$

The above equation tells us that the tangential derivatives of $\psi^{(1)}$ and $\psi^{(2)}$ must be equal at the slot C_0 . This does not necessarily mean that the two potentials $\psi^{(1)}$ and $\psi^{(2)}$ must be equal at C_0 . Equation (12) indicates that a possible difference between $\psi^{(1)}$ and $\psi^{(2)}$ must be constant along C_0 . Due to the composite nature of C_0 ($C_0 = C_{01} \cup C_{02}$) the above statement should be reformulated: The difference between $\psi^{(1)}$ and $\psi^{(2)}$ at C_{01} and C_{02} must be constant along C_{01} and C_{02} , respectively. These two constants must however be different as is shown in the following:

Let us integrate the transverse magnetic field along the closed contour \bar{C} as shown in Fig. 2:

$$\begin{aligned} \oint_{\bar{C}} \mathbf{h} \cdot d\mathbf{l} &= \int_{P_a}^{P_b} \mathbf{h}^{(2)} \cdot d\mathbf{l} + \int_{P_c}^{P_d} \mathbf{h}^{(1)} \cdot d\mathbf{l} = (\psi^{(2)}(P_b) - \psi^{(2)}(P_a)) + (\psi^{(1)}(P_d) - \psi^{(1)}(P_c)) \\ &= (\psi^{(1)}(P_d) - \psi^{(2)}(P_a)) - (\psi^{(1)}(P_c) - \psi^{(2)}(P_b)) = I \end{aligned} \quad (13)$$

where I is the current on the metal strip separating C_{01} from C_{02} . Equation (13) tells us that at least one potential difference (jump) must exist; either between P_d and P_a or between P_c and P_b (or both). In addition, the potential differences across C_{01} and across C_{02} must be different, otherwise, the current on the strip will vanish. However, one of the two potential jumps can be put equal to zero without loss of generality.

C) Multi-strip Transmission Lines

In this section we will consider the multi-strip transmission line shown in Fig. 3. The composite slot C_0 is now composed of the simple slots $C_{00}, C_{01}, \dots, C_{0M}$ ($C_0 = C_{00} \cup C_{01} \cup C_{02} \cup \dots \cup C_{0M}$). As mentioned before, the magnetic-potential jump at one of the slots is arbitrary. We will set the potential jump across C_{00} equal to zero. The potential jump across any other slot is then the algebraic sum of the axial currents on all strips below this slot. Let us denote the potential jump across the m th slot by α_m . We have then

$$\psi^{(2)}|_{C_{0m}} - \psi^{(1)}|_{C_{0m}} = \alpha_m, \quad m = 0, 1, \dots, M; \quad \alpha_0 = 0. \quad (14)$$

It is easily shown that the axial current I_m on the m th strip (which separates the $(m-1)$ st slot from the m th one) is given by

$$I_m = \alpha_m - \alpha_{m-1}; \quad m = 1, 2, \dots, M. \quad (15)$$

The two column vectors \mathbf{I} and $\boldsymbol{\alpha}$ with elements I_m and α_m ($\alpha_m \neq 0$), respectively, are then related by a linear transformation according to

$$\mathbf{I} = [\mathbf{T}] \boldsymbol{\alpha}, \quad (16)$$

where the elements of $[\mathbf{T}]$ are either $(+1)$, (-1) or zero. Note that $[\mathbf{T}]$ is non-singular and can be inverted.

Because the composite slot C_0 is now composed of $(M+1)$ slots, the matrices $[C^{(i)}]$ and the column vectors $\mathbf{D}^{(i)}$ and \mathbf{U} have to be subdivided into submatrices and subvectors, respectively.

$$\begin{aligned} [C^{(i)}] &= \begin{bmatrix} [C_0^{(i)}], [C_1^{(i)}], \dots, [C_m^{(i)}], \dots, [C_M^{(i)}] \end{bmatrix}, \quad \mathbf{U} = \begin{pmatrix} U_0^t, U_1^t, \dots, U_m^t, \dots, U_M^t \end{pmatrix}^t, \\ \mathbf{D}^{(i)} &= \frac{1}{\sqrt{P_{0h}^{(i)}}} \begin{pmatrix} D_0^t, D_1^t, \dots, D_m^t, \dots, D_M^t \end{pmatrix}^t = \frac{\mathbf{D}}{\sqrt{P_{0h}^{(i)}}}. \end{aligned} \quad (17 \text{ a-c})$$

where the submatrices $[C_m^{(i)}]$ and the subvectors \mathbf{D}_m and \mathbf{U}_m correspond to the m th slot according to (10 a-b) and (9), respectively.

Testing (14) with the same set of basis functions $\{\eta_k\}$ (Galerkin's procedure) results in

$$\left(\frac{a_0^{(2)}}{\sqrt{P_{0h}^{(2)}}} - \frac{a_0^{(1)}}{\sqrt{P_{0h}^{(1)}}} \right) \mathbf{D} + [C^{(2)}]^t \mathbf{a}^{(2)} - [C^{(1)}]^t \mathbf{a}^{(1)} = \begin{pmatrix} 0 \cdot \mathbf{D}_0^t, \alpha_1 \cdot \mathbf{D}_1^t, \dots, \alpha_m \cdot \mathbf{D}_m^t, \dots, \alpha_M \cdot \mathbf{D}_M^t \end{pmatrix}^t = \mathbf{X}. \quad (18)$$

Substituting (11a) into (18) leads to

$$A_0 \mathbf{D} + [\mathbf{Y}] \mathbf{U} = \mathbf{X}, \quad (19)$$

where

$$A_0 = \frac{a_0^{(2)}}{\sqrt{P_{0h}^{(2)}}} - \frac{a_0^{(1)}}{\sqrt{P_{0h}^{(1)}}}, \quad [\mathbf{Y}] = \frac{1}{Z_0} ([C^{(2)}]^t [\Lambda^{h(2)}]^{-1} [C^{(2)}] + [C^{(1)}]^t [\Lambda^{h(1)}]^{-1} [C^{(1)}]). \quad (20 \text{ a-b})$$

Note that the size of $[Y]$ is not affected by the number of eigenmodes in the individual waveguides. The dimension of $[Y]$ is rather determined by the number of expansion functions η_k . The unknown constant A_0 can be eliminated by making use of (11b):

$$A_0 = \mathbf{D}^t [Y]^{-1} \mathbf{X} / \mathbf{D}^t [Y]^{-1} \mathbf{D} \quad (21)$$

Because a potential is not affected by adding a constant, $a_0^{(1)}$ can be put equal to zero. The unknown surface magnetic current is finally determined in terms of \mathbf{U} which is obtained by combining (19) and (21):

$$\mathbf{U} = [Y]^{-1} \left(\mathbf{X} - \frac{\mathbf{D}^t [Y]^{-1} \mathbf{X}}{\mathbf{D}^t [Y]^{-1} \mathbf{D}} \mathbf{D} \right) \quad (22)$$

D) Determination of the characteristic-impedance matrix $[Z_c]$

Referring to Fig. 3, the voltage of the m th strip (referred to the external shielding) is easily shown to be given by

$$V_m = - \sum_{j=0}^{m-1} \int_{C_{0j}} m_{szj} dl = - \sum_{j=0}^{m-1} \mathbf{D}_j^t \mathbf{U}_j \quad (23)$$

Inserting (17 a-c) into (20 a-b) the matrix $[Y]^{-1}$ can be partitioned as

$$[Y]^{-1} = \begin{bmatrix} [Z_{00}] & [Z_{01}] & \cdots & [Z_{0M}] \\ [Z_{10}] & [Z_{11}] & \cdots & [Z_{1M}] \\ \vdots & \vdots & \ddots & \vdots \\ [Z_{M0}] & [Z_{M1}] & \cdots & [Z_{MM}] \end{bmatrix} \quad (24)$$

Making use of the above partitioning, (22) can be decomposed into

$$\mathbf{U}_j = \sum_{l=0}^M (\alpha_l - A_0) [Z_{jl}] \mathbf{D}_l, \quad (25)$$

where $\alpha_0 = 0$ and A_0 is given by (21) which can be rewritten as

$$A_0 = \left(\sum_{l=1}^M \alpha_l \left(\sum_{j=0}^M \mathbf{D}_j^t [Z_{jl}] \right) \mathbf{D}_l \right) / \left(\sum_{l=0}^M \sum_{j=0}^M \mathbf{D}_j^t [Z_{jl}] \mathbf{D}_l \right) \quad (26)$$

Combining (23), (25) and (26) results in expressing V_m 's in terms of α_l 's

$$V_m = \sum_{l=1}^M R_{ml} \alpha_l; \quad m = 1, 2, \dots, M, \quad (27)$$

where

$$R_{ml} = \frac{1}{\sum_{j=0}^M \sum_{k=0}^M \mathbf{D}_j^t [Z_{jk}] \mathbf{D}_k} \cdot \left(\left(\sum_{j=0}^M \sum_{k=0}^M \mathbf{D}_j^t [Z_{jk}] \mathbf{D}_k \right) \cdot \left(\sum_{j=0}^{m-1} \mathbf{D}_j^t [Z_{jl}] \mathbf{D}_l \right) - \left(\sum_{j=0}^{m-1} \sum_{k=0}^M \mathbf{D}_j^t [Z_{jk}] \mathbf{D}_k \right) \cdot \left(\sum_{j=0}^M \mathbf{D}_j^t [Z_{jl}] \mathbf{D}_l \right) \right); \quad \left\{ \begin{matrix} m \\ l \end{matrix} \right\} = 1, 2, \dots, M. \quad (28)$$

Equation (27) can be written in a matrix form

$$\mathbf{V} = [\mathbf{R}] \boldsymbol{\alpha}, \quad (29)$$

where \mathbf{V} and $[\mathbf{R}]$ are a column vector and a matrix with elements V_m and R_{ml} , respectively. Combining (16) and (29) results in the transmission-line-characteristic-impedance matrix $[Z_c]$:

$$\mathbf{V} = [\mathbf{R}] [\mathbf{T}]^{-1} \mathbf{I} = [\mathbf{Z}_c] \mathbf{I}. \quad (30)$$

For a given voltage (current) distribution (represented by the column vector $\mathbf{V}(\mathbf{I})$), $\boldsymbol{\alpha}$ is first determined by making use of (29) ((16)). The column vector \mathbf{X} is then determined according to (18). A_0 is given by (21). Next \mathbf{U} can be determined in terms of \mathbf{X} by using (19). The expansion coefficients $a_n^{(i)}$ ($n \neq 0$) and hence the magnetic potentials $\psi^{(i)}$ are then determined using (11a), which completes the determination of the field distribution.

III. Numerical results

The performance of the GSD technique can significantly be improved if the basis functions satisfy the edge condition [7] which reads $m_{sz} \propto r^{-\frac{1}{2}}$ for a 360° edge where m_{sz} and r denote the axial surface magnetic current and the distance from the edge, respectively. In most cases, three basis functions which fulfill the edge condition are sufficient even if high accuracy is required which leads to a very small characteristic system of equations.

Each element of the characteristic matrix contains however a doubly infinite sum over the eigenmodes of the individual waveguides. For these matrix elements as well as for the field series it has been found that the summation over the index corresponding to the direction normal to the surface magnetic current has a closed-form expression [8]. This increases the numerical efficiency of the presented method significantly. In order to validate the suggested method a coplanar slotline with three slots is analyzed. This structure supports two TEM-modes. In Fig. 4 the electric (solid line) and magnetic (dashed line) field lines are presented for both TEM-modes which have been defined by having a potential of unity on one of the two strips, and zero potential on the other one.

In Fig. 5 the axial surface magnetic current (solid line) is compared with the field component E_y in the plane of the slots (dashed line) for both TEM-modes. They should be equal because of (3). This is in good agreement with the plots.

Next a coplanar slotline which is symmetric with respect to $y = b/2$ where b is the height of the waveguide is analyzed. One even and one odd TEM-mode which are orthogonal to each other can be defined. The even (odd) mode is characterized by a magnetic (electric) wall at $y = b/2$. This is confirmed by Fig. 6, where the electric (solid line) and magnetic (dashed line) field lines the two TEM-modes are shown. The electric field lines of the even (odd) mode are parallel (orthogonal) and the magnetic field lines are orthogonal (parallel) to $y = b/2$. Note that not only for symmetric transmission lines but for all transmission lines an orthogonal set of TEM modes can be defined.

In order to check the results of the suggested method, a reference method has been implemented [9]. It is based on expressing TEM-modes in terms of a scalar electric potential ϕ which is excited by the electric currents on the strips. Again the performance of the reference method is improved by using basis functions of the electric currents which satisfy the edge conditions [7]. Enforcing ϕ to be constant on the strips and zero on the fins yields a characteristic matrix equation, the unknown of which are the expansion coefficients of the electric currents. In Fig. 7 results for the symmetric transmission line according to Fig 6 are presented. The electric current on the strips and fins, computed by the reference method are compared to the difference of the of the tangential magnetic fields at the plane of the slots computed by the suggested method. Both should be equal by definition. This is in good agreement with the plots.

Conclusions

A new method for the computation of TEM-modes in multi-strip transmission lines has been derived. The supporting transmission line has been treated as a slot-coupled waveguide with more than one coupling slot. Applying the GSD technique, all field components have been expressed in terms of a scalar magnetic potential that must jump at the coupling slots. Enforcing the continuity of the tangential magnetic fields at the coupling slots, the surface magnetic currents and consequently all field components have been determined. Furthermore the characteristic impedance matrix of the transmission line has been derived. This algorithm has been applied to coplanar slot lines and compared to the results of other methods.

References

- [1] R. H. Jansen, "The spectral-domain approach for microwave integrated circuits," *IEEE Trans. Microwave Theory Tech.*, vol. MTT-33, pp. 1043-1056, 1985.
- [2] Q. Zhang and T. Itoh, "Spectral-domain analysis of scattering from E-plane circuit elements," *IEEE Trans. Microwave Theory Tech.*, vol. MTT-35, pp. 268-275, 1987.
- [3] A. Jöstingmeier and A. S. Omar "Analysis of inhomogeneously filled cavities coupled to waveguides using the VIE formulation," *IEEE Trans. Microwave Theory Tech.*, vol. MTT-41, pp. 1207-1214, 1993.
- [4] A. Jöstingmeier and A. S. Omar "Analysis of the scattering by dielectric bodies using the SIE formulation," *IEEE Trans. Microwave Theory Tech.*, vol. MTT-42, pp. 471-480, 1994.
- [5] A. S. Omar, A. Jöstingmeier, C. Rieckmann, and S. Lütger "Application of the GSD technique to the analysis of slot-coupled waveguides," *IEEE Trans. Microwave Theory Tech.*, vol. MTT-42, pp. 2139-2148, 1994.
- [6] R. E. Collin, *Foundations for Microwave Engineering*. New York: McGraw-Hill, 1966.
- [7] R. E. Collin, *Field Theory of Guided Waves*, New York: IEEE Press, 1991.
- [8] J. A. Cochran, "Unusual identities for special functions from waveguide propagation analysis," *IEEE Trans. Microwave Theory Tech.*, vol. MTT-36, pp. 611-614, 1988.
- [9] A. S. Omar and K. Schünemann, "Analysis of waveguides with metal inserts," *IEEE Trans. Microwave Theory Tech.*, vol. MTT-37, pp. 1924-1932, 1989.

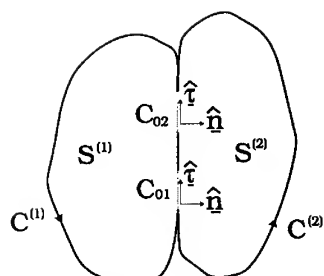


Fig. 1: Double-slot-coupled waveguides

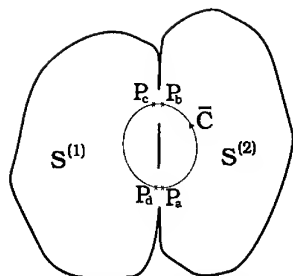


Fig. 2: Contour integral of the magnetic field.

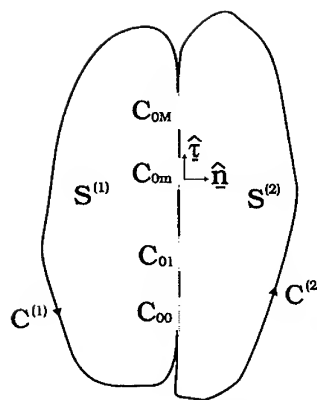


Fig. 3: M-strip transmission line.

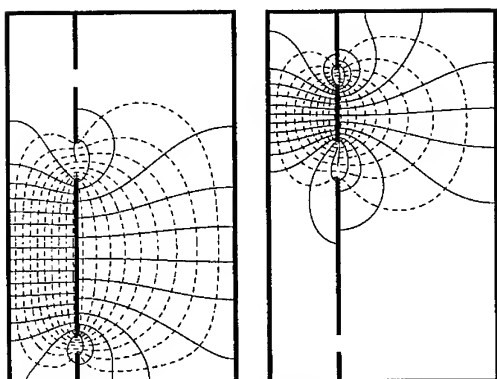


Fig. 4: Electric (—) and magnetic (---) field lines for the two TEM-modes of a three-slot coplanar slot line

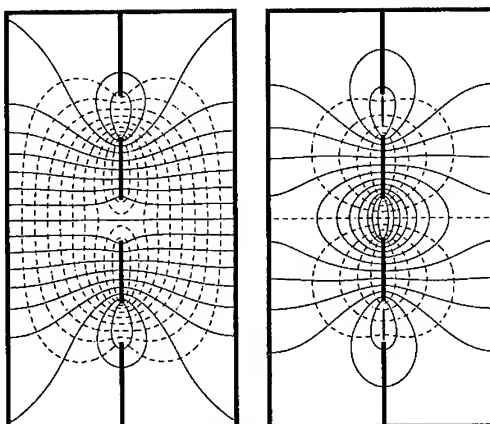


Fig. 6: Electric (—) and magnetic (---) field lines for the even and the odd TEM-modes of a symmetric three-slot coplanar slot line

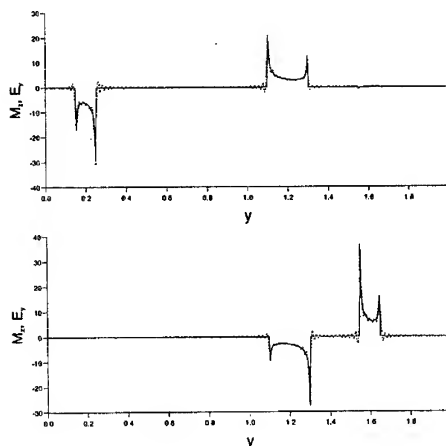


Fig. 5: Comparison between the slot tangential electric fields (---) and the axial surface magnetic current (—) for the two TEM modes shown in Fig. 4.

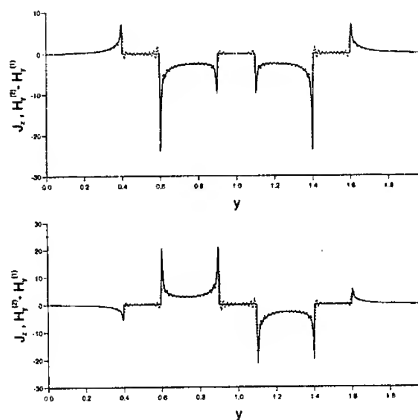


Fig. 7: Comparison between the jump of the slot tangential magnetic fields (---) and the axial surface electric current (—) corresponding to the two TEM-modes shown in Fig. 6. The first one is computed by the suggested method; the latter one by a reference method.

ENHANCED GAIN PATCH ANTENNAS AT MILLIMETER WAVES

Vladimir Rojansky, B. Sc. & Mark Winebrand, Ph. D.

RADAR & ELECTRO-OPTICS DEPT., MBT DIVISION, ISRAEL AIRCRAFT INDUSTRIES LTD., YEHUD, INDUSTRIAL ZONE, P.O.Box 105, ISRAEL 56000.

ABSTRACT

A study of a rectangular patch, with a dielectric plate installed in front of the patch at a "resonant" distance, has been performed at the upper Ka frequency band. For this purpose three antennas have been designed, analyzed, built and measured. These antennas are: a "conventional" rectangular patch; an enhanced gain rectangular patch (a "conventional" patch with a dielectric plate in front of it); and an "equivalent" 2x2 array of "conventional" patches with the beamwidth nearly the same as that of the enhanced gain patch antenna. A significant increase in the gain of the enhanced gain patch antenna as compared with the "conventional" one, was initially predicted theoretically based on the analysis, and then, confirmed by the measurements. In addition, it was shown that the enhanced gain patch antenna exhibits a larger gain and essentially lower sidelobes than the "equivalent" array.

1. INTRODUCTION

The idea to increase the gain of common radiating elements, such as a slot or dipole, by placing the element between two reflecting planes, one of which is perfect reflector and the other a semi-reflector, was proposed in the late 1970th and implemented by R. G. Immell and B. H. Sasser [1] to improve the performance of single slot and slot array antennas operating at X-band. Later, the idea received further attention in conjunction with the development and wider implementation of microstrip antennas. To overcome the low gain problem, a gain enhancement method relying on substrate-superstrate resonance has been proposed in several papers by N. G. Alexopoulos et. al. (see [3] for a list of references), where asymptotic formulas and a moment method solution have been derived for the enhanced gain printed dipole antennas. The solution for the enhanced gain rectangular patch antenna has been derived, first, by G. Qasim and S. S. Zhong in [2], and then by Xiao-Hai Shen et. al. in [3], where thorough moment method solution has been given for a rectangular patch operating at X-band. However, to our knowledge, there are no up-to-date references in the technical literature describing this method as applied to millimeter wave problems, and the only measurement results available, which confirm the method's feasibility at X-band, are contained in [1].

Note, that the problems, such as gain limit in microstrip arrays, feeder conductor losses, manufacturing tolerances, etc., are much more critical at millimeter waves, and significantly restrict the implementation of printed antennas. Therefore, any noncontact technology, particularly, the enhancement gain method, may simplify design and production and, therefore, reduce the price of millimeter wave printed antennas.

In this paper, the single square patch operated at upper Ka band is analyzed using the Finite Element Method (FEM). Then, the dielectric plate is added in front of the patch at the "resonant" distance and the renewed enhanced gain patch antenna is analyzed once again. The prototype of the patch has been built and measured with and without the "resonant" plate, and the results are compared with the theory. In addition, the performance of the enhanced gain patch antenna is compared with a 2x2 printed array built on the basis of the single square patch.

2. MODEL DESCRIPTION AND ANALYSIS

Usually, microstrip antenna design begins with the choice of material for substrate/ superstrate layers. When considering the materials available, frequency band, low loss and an impedance match requirements, it can be derived that only a few of materials can be used for substrate/ superstrate layers of the patch antenna operating at upper Ka band. The “RT/duroid” 5880 with dielectric constant $\epsilon_1 = 2.2$, and thickness 0.25 mm was found to be most suited for the substrate material of the patch (See P. Bhartia et. al , Chapter 3 in [4]), and the “RT/duroid ” 6010 with dielectric constant $\epsilon_2 = 10.5$, and thickness 0.64 mm is very well suited for the dielectric “resonant” plate. These materials were used in the manufacturing of the antenna prototypes, and their properties were accounted for in the analysis of the antennas.

The basic geometry of the enhanced gain patch antenna is shown in Fig. 1. The radiating element is an approximately $0.48 \lambda_g$ mm square patch fed by a microstrip line from an edge of insert, designed to match the impedance of the patch to that of the microstrip line. The patch element is placed in the bottom of the rectangular metallic box with area $2.5\lambda_0 \times 2.5\lambda_0$ mm.

The top of the box is covered by a superstrate “resonant” plate. The separation D between the patch and “resonant” plate is chosen to be around $0.5\lambda_0$ mm. The FEM analysis using μ WaveLab software by ANSOFT has been performed for two models: a “conventional” square patch antenna (a radiating element without metallic box and superstrate “resonant” plate), and an enhanced gain patch antenna. The results of the analysis are presented in Figs. 2-6. In Fig. 2 the E-plane patterns of the “conventional” patch are presented for the frequency band. The effect of the insert and microstrip line on pattern symmetry is clearly seen. The gain and return loss of the two models are presented in Figs. 3,4. In Fig. 3 one can see the significant increase of the gain of the enhanced gain patch antenna as compared with the “conventional” patch. In Fig. 4 one can recognize the drift of the resonant frequency of the enhanced gain patch antenna to the lower region as compared with the original resonant frequency - f_0 . The calculated difference, Δf , is about 3.5% off.

Going back to Fig. 3, one can see, that the gain peaks are at frequencies, which are in the vicinity of resonance for both antennas. Note, that the resonant frequency drift obtained earlier in [3] is only 1.78% i.e., twice less than shown in Fig. 4. Such a deviation may be explained by the difference in the models considered in [3] and in the paper, namely, that the model considered in [3] is an infinite plane-parallel structure, whereas the model presented in our paper is like a closed volume cavity. It is worth noting, that the gain data presented in Fig. 3 may exceed the realistic values. The reason for this is the introduction of the infinite ground plane into the models. This ground plane limits the volume involved in calculations by FEM and is necessary for software operation.

In Figs. 5,6 the E- and H- plane patterns of the enhanced gain patch antenna are presented for the frequency band. Note, that the patterns do not have a typical lobe pattern structure. The first saddle point in E-plane is at -15 dB below the peak and the effect of the insert and the feeding line is still noticeable, producing pattern asymmetry. The H-plane pattern saddle point is at -25 dB below peak.

3. MEASUREMENT RESULTS

In order to validate the method, the prototypes of the antennas discussed in Section 2 have been built and tested at the upper Ka frequency band. The measurement results of the “conventional” patch are presented in Figs. 7,8. The measured return loss of the “conventional” patch in Fig. 7 shows that the resonant frequency and impedance beamwidth (VSWR 2:1) - 2.7% of the prototype coincide, in general, with the theory. The prototype gain and H- plane patterns for frequency band are shown in Fig. 8, from which one can recognize a 6.3 dBi peak gain of the “conventional” patch.

A special device, which enabled holding the "resonant" plate in front of the patch and regulating the distance D between the patch and the plate, has been designed and constructed. The "resonant" plate has been installed at the required distance, and antenna pattern, gain and return loss measurements have been done. The E- and H - plane patterns are shown in Figs. 9,10. As predicted in Section 2, the patterns do not have an explicit lobe pattern structure and saddle point levels in Figs. 9,10 coincide with theory. The pattern oscillations at far angles in Fig.10 are noisy, and are explained by measurement difficulties at upper Ka band. The discrepancy in the peaks of E- and H - plane patterns is a consequence of misalignment of the positioning equipment to the measurement range boresight. Even so, the 13.2 dBi gain peak has been registered and is shown in Fig. 10. The relative prototype gain reduction as compared with the predicted value in Section 2 value is explained by the absence of the metallic walls around the patch circumference in the enhanced gain prototype antenna. In Fig. 11 the return loss measurements show a drift of resonant frequency, Δf , of 1.8% to the lower region, i.e. the measured drift is closer to the results of [3] than of Section 2. The reason for this may be the same as for prototype gain reduction. Finally, the 2x2 array of the "conventional" patches, designed to provide nearly the same beamwidth as in Fig. 10, has been built. The measured H - plane pattern is presented in Fig. 12. Comparing Fig. 10 and 12 one can see that the performance of the enhanced gain patch antenna supersedes that of the 2x2 array in gain and sidelobe behavior.

4. CONCLUSIONS

The validity of the enhanced gain method at upper Ka frequency band has been confirmed theoretically by using FEM, and by measurements of the three prototype antennas. The agreement between theory and experiment proves the quality of the measurements. The gain of the enhanced gain patch antenna may reach 13.2 dBi (measured) or more (according to theory). That is more than twice as large as the gain of a "conventional" patch, 6.3 dBi. In addition, the patterns of enhanced gain patch antenna do not possess a typical lobe pattern structure, but are smoother. This is one more advantage of the enhanced gain patch antenna, confirmed experimentally when comparing the enhanced gain patch antenna with a 2x2 "equivalent" array of "conventional" patches. The former surpasses the latter in gain and sidelobe behavior, and may replace the 2x2 elements in the array designs.

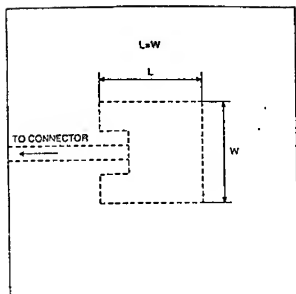
5. ACKNOWLEDGEMENTS

The authors wish to thank the management of MBT for their encouragement and continuous support of this work. We also would like to thank J. Helzinger and M. Markish for their enthusiasm and creativity during the prototype manufacturing and measurements.

6. REFERENCES

1. R. G. Immell and B. H. Sasser. A Highly Thinned Array Using The Image Element Antenna. 1979, September. Third Annual Antenna Application Symposium. Robert Allerton Park, IL.
2. G. Qasim and S.S. Zhong. Radiation Characteristics of Microstrip Patch Antennas With Dielectric Covers. In Proc. IEEE Antennas Propagat. Soc. Int. Symp., Chicago, 1992, pp. 2208-2211.
3. Xiao-Hai Shen, Guy A. E. Vandenbosch, Antonie R. Van de Capelle. Study of Gain Enhancement Method For Microstrip Antennas Using Moment Method. IEEE Trans. on Antennas and Propagat., Vol. 43, NO. 3, pp. 227-231, March, 1995.
4. P. Bhartia, K.V.S. Rao, R.S. Tomar. Millimeter-Wave Microstrip and Printed Circuit Antennas. Artech House, 1991.

TOP VIEW



SIDE VIEW

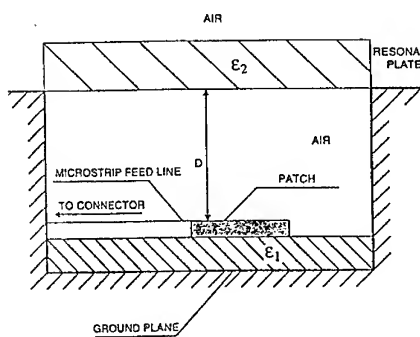


FIG. 1. BASIC GEOMETRY

E-Plane (Without Resonant Plate)

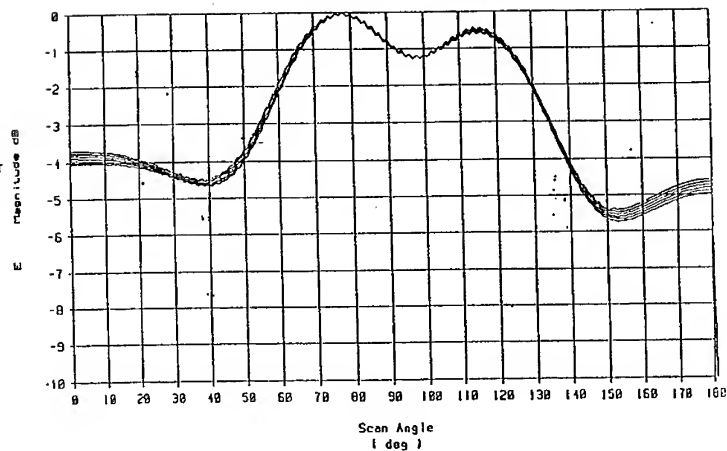


FIG. 2.

GAIN OF THE PATCH WITH (---) and WITHOUT (---) RESONANT PLATE

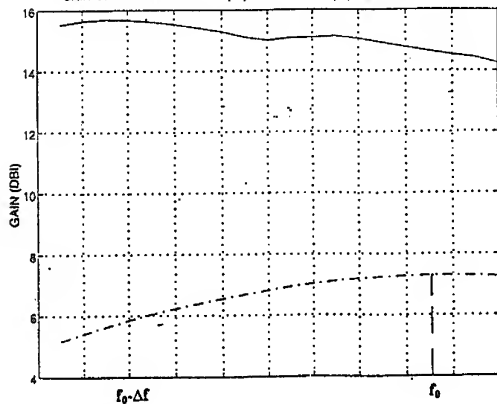


FIG. 3. GAIN

S11 OF THE PATCH WITH (---) and WITHOUT (---) RESONANT PLATE

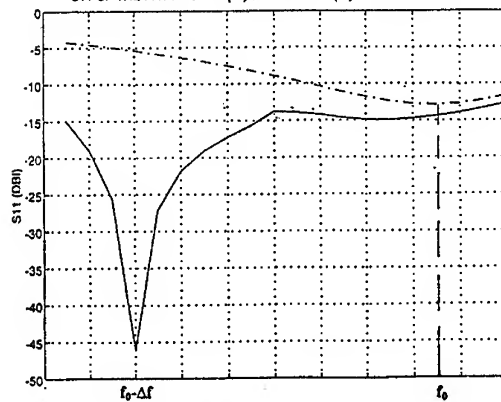


FIG. 4. RETURN LOSS

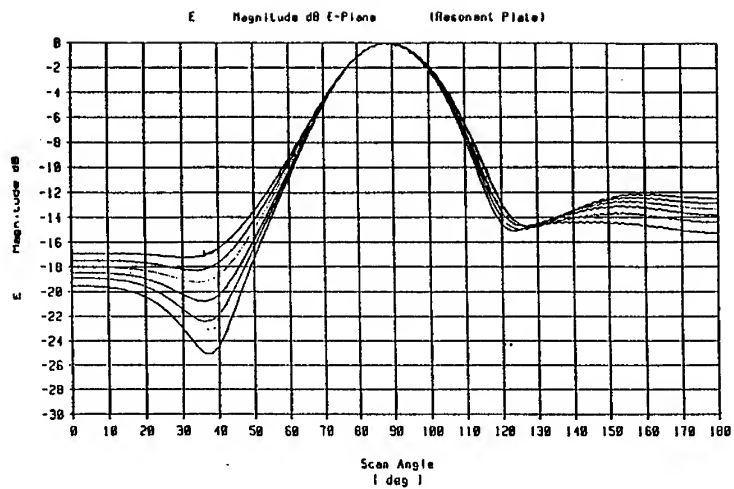


FIG. 5.

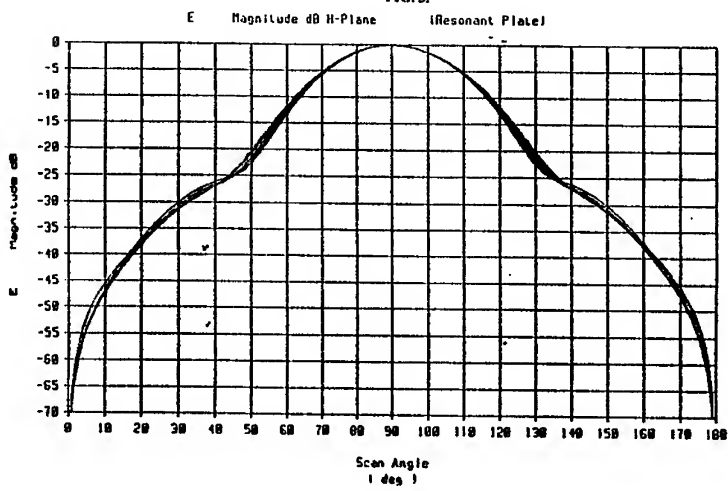


FIG. 6.

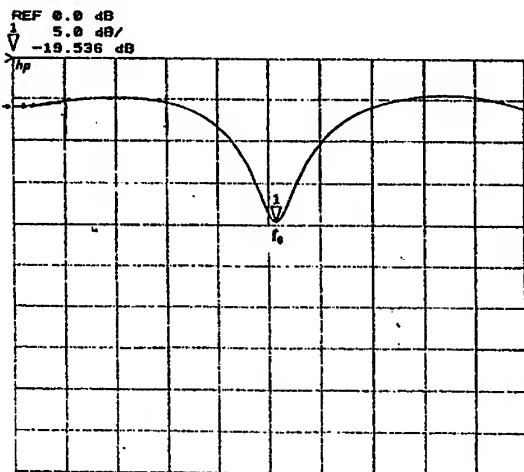


FIG. 7. MEASURED RETURN LOSS OF "CONVENTIONAL" PATCH.

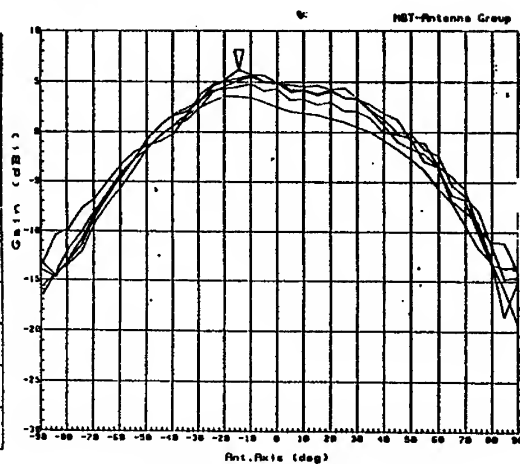


FIG. 8. MEASURED H-PLANE PATTERN OF "CONVENTIONAL" PATCH.

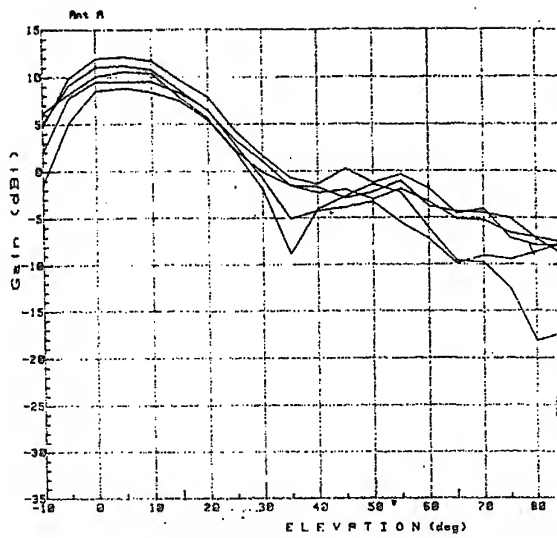


FIG. 9. MEASURED E-PLANE PATTERN OF ENHANCED GAIN PATCH ANTENNA.

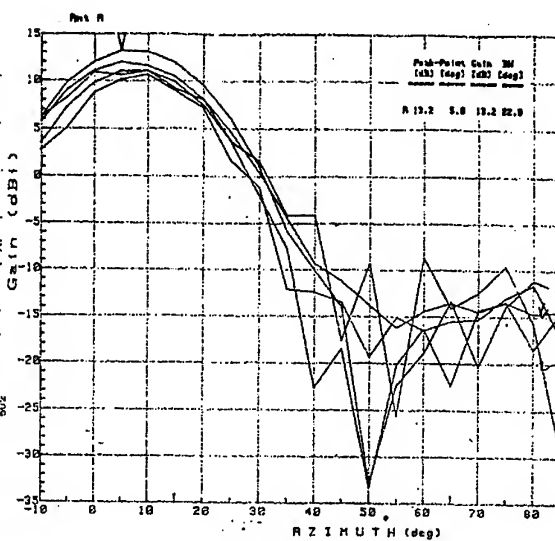


FIG. 10. MEASURED H-PLANE PATTERN OF ENHANCED GAIN PATCH ANTENNA.

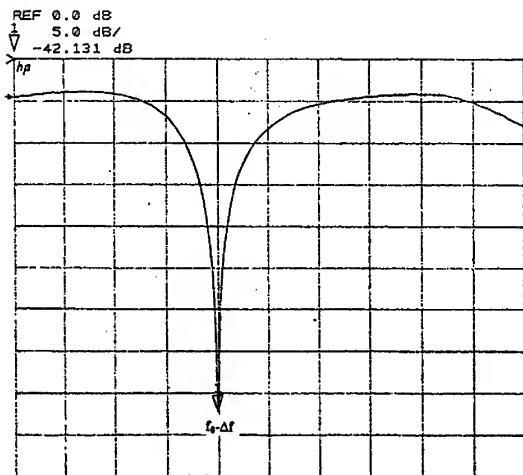


FIG. 11. MEASURED RETURN LOSS OF ENHANCED GAIN PATCH ANTENNA.

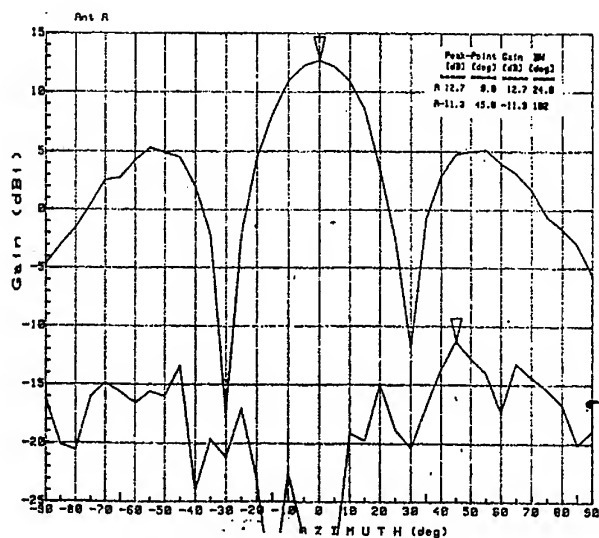


FIG. 12. MEASURED H-PLANE PATTERN OF 2x2 ARRAY OF "CONVENTIONAL" PATCHES

SYNTHESIS OF CIRCULARLY POLARISED RADIAL LINE SLOT ARRAY

Manuel Sierra P.¹, María Vera Isasa², Antonio G. Pino², Manuel Sierra C.¹

¹Universidad Politécnica de Madrid. E.T.S.I. Telecomunicación. Ciudad Universitaria
28040 Madrid (Spain). Phone: +3415495700 Fax: +3414532002. E-mail: manolo@gr.ssr.upm.es

²Universidad de Vigo. E.T.S.I. Telecomunicación.
36200 Vigo (Spain). Phone: +3486812117 E-mail: mirentxu@tsc.uvigo.es

ABSTRACT

In previous articles, an easy way to analyse a slot array fed through a radial line was presented. The analysis was based on a circuit approach where circuit parameters have been estimated using the first propagation mode in the radial line and the far field theory. Here we study the design of a particular application for circularly polarised broadside antenna. The design defines the length, position and orientation of the slots in the antenna surface. The final analysis of the antenna gives a good behaviour in field diagrams and gain.

INTRODUCTION

Antennas based on narrow slots directly coupled to a radial line have been used previously in Direct Broadcast Satellite (DBS) receivers [1] and mobile communications [2]. One of the most important features for such antennas is their low cost and low loss feeding line. This paper shows a synthesis method to define the length, position and orientation of slots on the antenna surface. The basic model is based on the assumption that fundamental TEM mode keeps its original structure over the radial line, except for the attenuation due to the slot power coupling. Changes in phase in the coupled field due to the slot resonance must be taken into account to obtain an uniform phase aperture field. Finally second order effects like the change in the field phase or field reflections must be included in the design process. The antenna final analysis using the equivalent circuit analysis method developed by the authors [3], [4] give a good behaviour of the antenna.

ANTENNA BASIC STRUCTURE: FIRST DESIGN

The radial line is a parallel plate structure, fed at its centre by the penetration of the inner conductor of a coaxial probe. The space between the plates (h) is less than half wavelength, so only the TEM mode can propagate between them. The slots are placed on the upper plate of the radial line. Figure 1 shows the antenna structure and the design variables for each slot: slot length (L_i), tilt angle between the slot and the radial line (α_i) and slot position referred to the feeding point (ρ_i , ϕ_i). Other parameters are considered as constants: slot width (w), metal thickness (t) or dielectric inside the waveguide (ϵ). The original field inside the radial line can be considered as an ideal TEM mode with symmetry of revolution, and far from the coaxial probe can be written like :

$$\vec{E}(\rho) = \sqrt{\frac{2}{\pi k \rho}} \left[E_1 e^{-j(k\rho - \frac{\pi}{4})} \right] \hat{z} \quad (1)$$

$$\vec{H}(\rho) = -\frac{1}{\eta} \sqrt{\frac{2}{\pi k \rho}} \left[E_1 e^{-j(k\rho - \frac{\pi}{4})} \right] \hat{\phi} \quad (2)$$

TWIN SLOTS FOR CIRCULARLY POLARISED FAR FIELD

The slots are narrow and close to resonance, so we can assume uniform field in the narrow dimension and cosine in the resonant dimension, giving a linearly polarised radiated field. To obtain the circular polarisation we must combine at least two slots as shown in figure 2. The relative field in the slots must satisfy the condition :

$$R = \left| \frac{E_1 \cdot L_1}{E_2 \cdot L_2} \right| = 1 \quad (3)$$

$$Phase\left(\frac{E_1}{E_2}\right) = -k_g \Delta r = \pm \theta \quad (4)$$

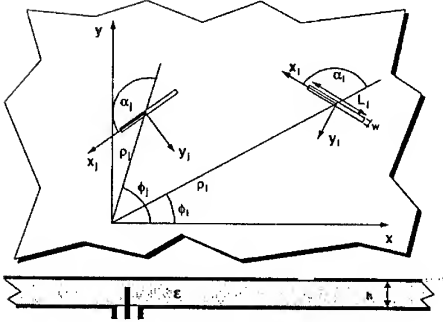


Figure 1. Antenna basic structure

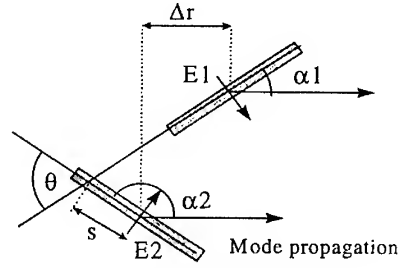


Figure 2. Twin slots angles

The field phase can be obtained moving the slots along the radial direction (Δr). The sign of previous equation depends on the desired polarisation. The parameter “s” is a final free parameter defining the relative position of the slots, and has been adjusted to minimize the coupling effect on the radiated field polarisation.

APERTURE PHASE: SLOT POSITION

Keeping constant the slot radial tilt angle (α), the far field phase from each slot twin depends on its orientation and must be compensated through the distance to the feeding point. This condition gives the position of slots over an spiral. To keep the space between slot pairs constant, an iterative formula is applied :

$$\rho_{i+1} = \rho_i \pm \frac{d}{\sqrt{1 \pm \frac{2\pi d}{\lambda_g} + \left(\frac{2\pi \rho_i}{\lambda_g}\right)^2}} \quad (5)$$

$$\phi = \pm \frac{2\pi \rho}{\lambda_g} - \alpha + \gamma_0 = \pm \frac{2\pi \rho}{\lambda_g} + \phi_0 \quad (6)$$

where γ_0 is a constant and d is the distance from slot pairs. Figures 3 shows the relative slot position obtained in the case of $\alpha = \pi/4$, $d = \lambda_g/2$ and $\gamma_0 = 0$.

APERTURE MAGNITUDE: SLOT LENGTH

The coupled field to slots depends on the slot position, tilt angle and length. Keeping constant the angle, the field inside the guide spreads and attenuates in previous slots and the slot length must grow from the centre to the antenna border. Assuming each slot turns as a coupling element and the field attenuation is uniform (keeping the symmetry), a closed formula for the slot coupling can be developed as :

$$\eta_p(\rho_k) = \frac{2\rho_k}{\frac{\rho_{max}^2 - \rho_{min}^2}{1-t} - (\rho_k - \rho_{min} - 0.5\lambda_g) \frac{(\rho_k + \rho_{min} - 0.5\lambda_g)}{\lambda_g}} \quad (7)$$

where ρ_{max} and ρ_{min} are the maximum and minimum distances from the feeding point, and t is the power fraction over the final load. Figure 4 shows the coupling versus distance from the centre for a 6λ antenna radius. The slot coupling depends on the slot length like a resonant cavity and can be computed from an equivalent circuit like shown in figure 5. Not always is possible to reach the estimated coupling and the maximum is assumed for the last slots.

PHASE CHANGE DUE TO SLOT RESONANCE

The slot field phase changes from the ideal field inside the guide due first to the slot resonance and second to field phase changes when coupled to previous slots. In general these changes are lower than $\pi/4$ but add with the same sign and can lower the antenna efficiency as much as 3dB. To compensate them, the slots are moved toward the centre of the antenna. This change in slot position allows reducing the wavelength in the guide keeping the grating lobes under control, without

using any dielectric. The phase change due to the slot resonance is shown in figure 6. In figure 7 we present the change in phase and amplitude of the wave after a ring of several slots. Both graphics can be written depending on the parameters of the circuit approach.

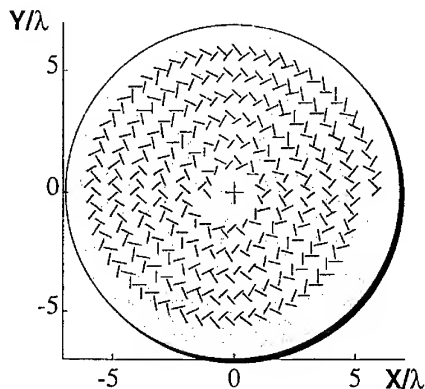


Figure 3. Initial slot position for antenna.

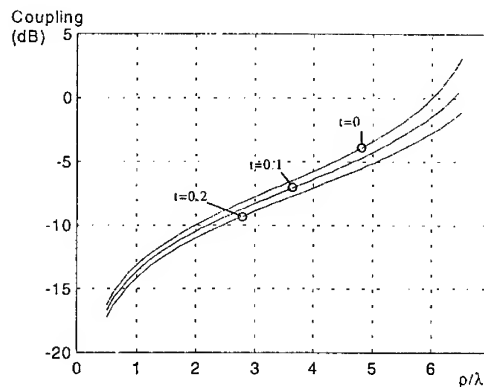


Figure 4. Theoretical coupling vs. Radius

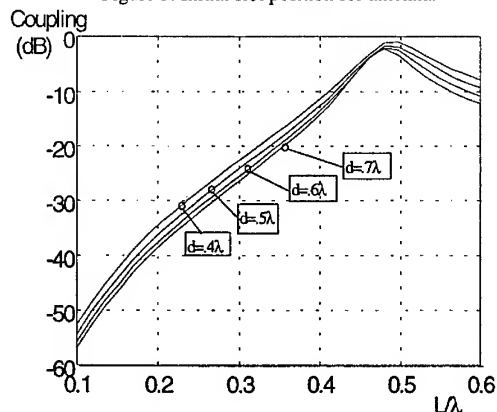


Figure 5. Coupling vs. Slot length

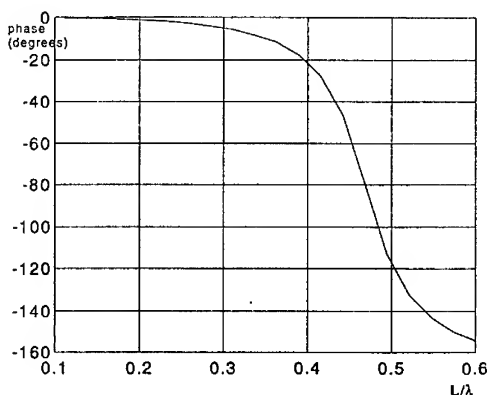


Figure 6: Change of phase in radiation field

These changes of phase produce a change in the position of the slots, that can be written as:

$$\Delta\rho = \frac{\lambda_s}{2\pi}(\phi_r + \phi_c) \quad (8)$$

FIELD REFLECTION

The field reflected in the slots creates an incoming mode that is not absorbed by the coaxial probe and propagates outward. This mode can be described as a TEM mode with a spiral phase front like:

$$\vec{E}_R = E_1 \Gamma \sqrt{\frac{2}{\pi k \rho}} e^{j\left(\frac{\pi}{4}\right)} e^{-j(k\rho)} e^{j2(\phi - \phi_0)} \quad (9)$$

where Γ is a reflection coefficient that depends on the slot coupling. This field adds to the main field mode and creates an asymmetry in the aperture field, reducing the aperture efficiency and rising the lateral lobes. The asymmetry is more important in small antennas, where slot coupling is larger. To avoid the influence of the reflected mode, the slots are moved again from its previous position but now in a non symmetric way. They are moved a small fraction of the wavelength in a random way. This displacement changes slightly the phase of the reflected field and it influence in the final slot field, although does not avoid the reflection.

After considering all these effects we can calculate the field over each slot with the analysis method described in [4]. In figure 8 we present the magnitude and phase of the field over each slot for a 275 slots antenna.

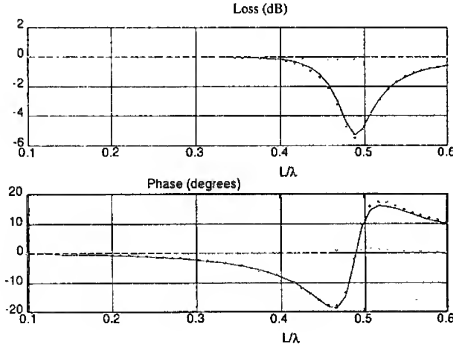


Figure 7: Change of phase after a ring of slots

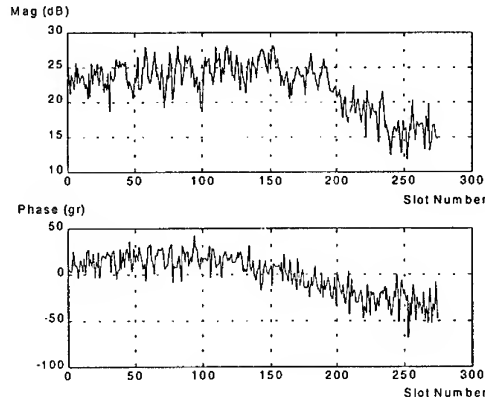


Figure 8. Final field over the slots

ANALYSIS

We designed an antenna based on this philosophy to be used for the reception of DBS with the Spanish Satellite HISPASAT. The frequency band was 12.1 – 12.5 GHz, left circular polarisation. We imposed a maximum diameter of 300 mm. The best design we could get with these limits were:

- Slot width: 1,5 mm
- Metal plate thickness: 0,1 mm
- Distance between metal plates: 8 mm
- The radial guide is finished in a short-circuit.
- Dielectric material: $\epsilon = 1,1$ (honeycomb)
- Coaxial probe: SMA (50 ohm and 0,65 mm)
- Gain = 29,5 dBi
- SLL better than -13,5 dB in the frequency band
- S11 better than -17 dB in the frequency band
- Beamwidth = 5°

MULTIPROBE FEED: SECOND DESIGN

The effects of the reflection field can be eliminated if we place the slots in concentric rings. That means we have to generate a cilindric wave, whose phase fronts are Archimedes spirals instead of generating a radial wave with the slots placed forming a spiral.

DESIGN OF THE COAXIAL PROBES

This is got if you excite the antenna with four coaxial probes, and you feed each one with phase changes of 90°. The purity of the spiral wave front depends on the separation of the four probes. The mode is better when the probes are closer, but the impedance bandwidth is perturbed when the probes are very close. We got an optimum value for a separation of 4 mm from the centre of the antenna to each probe. An scheme of the coaxial probes is shown in figure 9. With this value we estimate the impedance of each element in figure 10. In figure 11 and figure 12 we show the amplitude and phase of the electric field 81 mm from the centre of the antenna.

The equivalent circuit of the four probes is calculated as a four ports multipole where the mutual impedances follow the next formula:

$$z_{ij} = \frac{-\eta \cdot k}{4 \cdot h} \cdot G_i \cdot G_j \cdot \frac{\sqrt{2}}{k \cdot \pi \cdot \rho_{ij}} \cdot e^{-j\left(k\rho_{ij} - \frac{\pi}{4}\right)} \quad (10)$$

$$G_i = \frac{\cos(k\delta L_i) - \cos(k(L_i + \delta L_i))}{\sin(k(L_i + \delta L_i))} \quad (11)$$

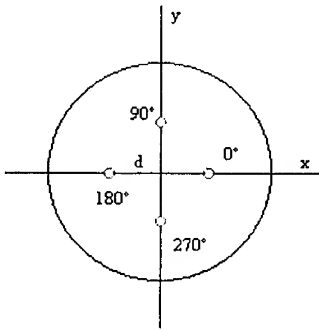


Figure 9: Situation and excitation of the probes

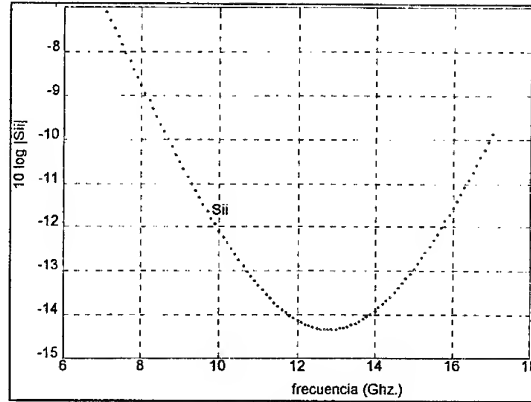


Figure 10: S11 of each probe

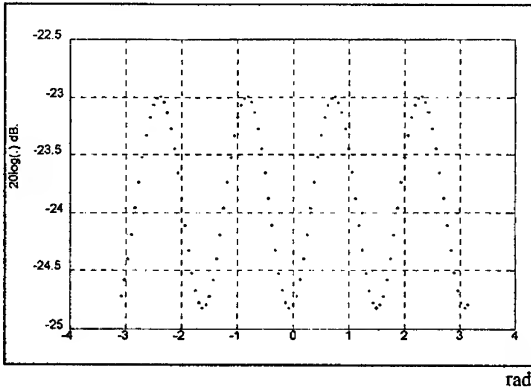


Figure 11: Amplitude in $r = 81$ mm

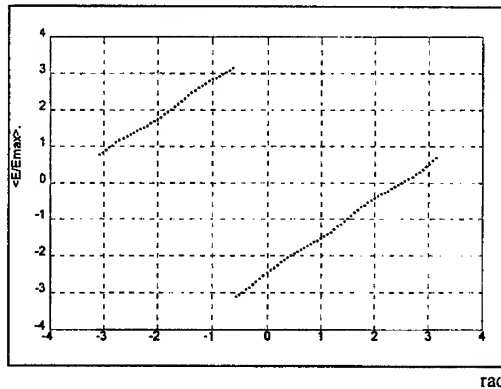


Figure 12 : Phase in $r = 81$ mm

The excitation circuit must be very simple in order to minimize the final cost of the product. We designed a serial circuit, where we adapt each probe varying the width of the microstrip lines. The circuit is composed by three $\lambda_g/4$ microstrip lines.

DESIGN OF THE SLOTS

We have the same design we had in the previous section in several aspects. We calculate the position of the two slots to get the circular polarisation, the slot length and width and we apply the corrections due to the resonance of the radiant and incident field in the same way we did before. The only difference is we generate now a wave whose phase front is a spiral.

If we want to get a circular polarised antenna we do not have to modify that phase with the different position of the slots. That means we can place the couple of slots in concentric rings, where each ring is separated λ_g of the previous one, in order to add in phase the radiated field of each slot.

When we place the slots in concentric rings the reflected field does not depend on the angle, so we are going to have an uniform field. The position of the first ring is going to fix the effect of the reflected field over the total field.

The position of the short circuit we placed at the end of the antenna is different too. That short circuit has to be placed $\lambda_g/4$ from the centre of the last slot. In the first design it had to be an Archimedes spiral but now it is a circumference,

much easier to manufacture. The reflected field on that short-circuit will no depend on the angle, so the design will be easier to optimise. In this case the electric field in the guide is shown in Ec. 12.

$$E_{in} \propto \frac{1}{\sqrt{k\rho}} e^{j\phi} e^{-jk\rho} \quad (12)$$

An scheme of the array is shown in figure 13. Figure 14 shows the radiated field (copolar and crosspolar) obtained with a five-turns circular array of 9.4-10.2 mm. slots, analyzed at 12.1 GHz. This means a 30 cm. antenna diameter with good characteristics to receive satellite communications.

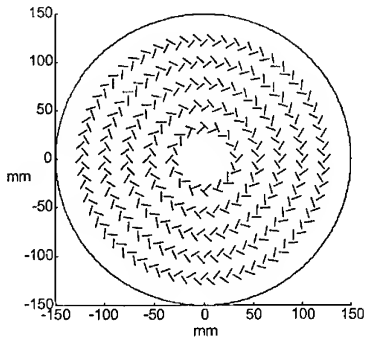


Figure 13. Circular array antenna

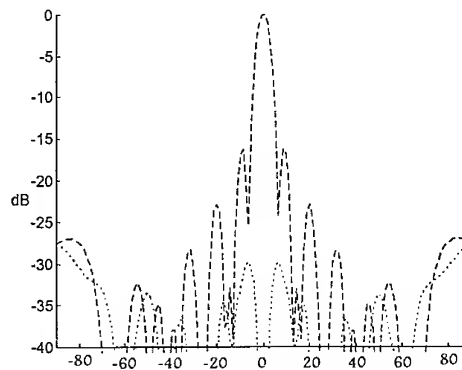


Figure 14 : Copolar-Contrapolar radiation pattern

CONCLUSIONS

This paper describes the way to design the antenna, giving the slot position and angle to get a radial line slot antenna having circular polarisation and broadside main beam. We show two different techniques ; with the first one the excitation is very simple, only the coaxial probe, while the position of the slots and the final short-circuit is complicate. This design generates a reflected field that depends on the angle. To solve this problem we complicate the excitation of the antenna (four coaxial probes with one microstrip circuit), but the antenna is perfectly symmetrical. This technique can also be extended to other kind of antennas and it is specially interesting for small arrays.

REFERENCES

- [1] Ando M. "New DBS Receiver Antennas ", 1993, Proc. 23rd EuMC, pp. 84-92.
- [2] Takada J., Tanisho A., Ito K., Ando M., "Circularly polarized conical beam radial line slot antenna", 1994, Electronics Letters, vol. 30, n°21, pp.1729-1730.
- [3] M. Sierra, J. Redoli, M. Vera, A.G. Pino, "Design and analysis of slot array antennas on a radial feed line", 1995, Proc. IEEE AP-S, vol. 1, pp. 362-365.
- [4] M.P.Sierra, M.Vera, A.G.Pino, M.S.Castañer, "Analysis of slot antennas on a radial transmission line", International Journal of Microwave and Millimeter-Wave Computer-Aided Engineering. vol.6, n°2, pp.115-127, Feb. 1996.
- [5] Vera M. "Diseño de Antenas de Ranuras sobre Guía Radial". Doctoral Disertation. Universidad de Vigo. 1996.
- [6] Ando M., Sakurai K., Arimura K., Ito Y. "A Radial Line Slot Antenna for 12 GHz Satellite TV Reception". IEEE Trans. Antennas and Prop. Vol AP-33, pp.1347-1353, 1985.
- [7] Sasazawa H., Oshima Y., Sakurai K., Ando M., Goto N. "Slot Coupling in a radial line slot antenna for 12 GHz Band Satellite TV Reception". IEEE Trans. on Antennas and Propagation. Vol. 36 n.9, 1988.
- [8] Natori M., Ando M., Goto N. "A Design of Coaxial to Radial Line Adaptors in Radial Line Slot Antennas". Trans. of the IECE". Vol. E73, n. 11 Nov. 1990

MICROSTRIP PATCH ARRAY FOR THE MOBILE TERMINAL ANTENNA OF A MOBILE COMMUNICATION SYSTEM

Tomasz Rutkowski and Custódio Peixeiro

Przemystowy Instytut Telekomunikacji
Ul. Gen. J Hallera, 13
Gdansk
Poland

IT/DEEC - Instituto Superior Técnico
Av. Rovisco Pais, 1
1096 Lisboa Codex
Portugal

ABSTRACT

The present paper describes a microstrip patch antenna array to be used in the mobile terminal of a mobile communication system at 2 GHz. The array can be used in two frequency sub-bands has an almost omnidirectional radiation pattern and provides a vertical plane shaped beam.

FRAMEWORK

The work described in this paper has been carried out in the frame of a research project entitled "ITCOM - Integration of Technologies for Mobile Communications" and TEMPUS project JEP 7403-94. The main objective of the research project is the integration of optical millimetric and microwave technologies for the implementation of mobile communication systems. The integration is focused in providing an optimum balance among some important features such as high performance, reliability, miniaturisation and low cost. A demonstrator for image transmission is under implementation. It is composed of two main subsystems:

- a cellular outdoor subsystem formed by one mobile terminal (MT) and two base stations (BS) connected to a central node by an optical fiber link;
- a wireless indoor subsystem formed by two infrared LAN cells interconnected via a wired Ethernet backbone.

The two systems are interconnected by an interconnection subsystem providing inter working functions.

INTRODUCTION

Microstrip patch antennas have some well known typical advantages, particularly important in mobile communication system applications, such as, small size, lightweight, low profile and low cost. Moreover they are suitable for planar and non-planar array configurations. Due to such important advantages the microstrip patch radiator has been selected as the basic element of the mobile communication system MT array antenna.

The antenna will operate in the two frequency sub-bands 1910-2000 MHz (up link) and 2110-2200 MHz (down link). The demonstration scenario is an elongated rectangular street cell with 10×400 m. The BS antenna is mounted in the middle of the rectangle narrow side at 10 m height

To allow the MT to move freely within the cell, an omnidirectional radiation pattern is required. To try to compensate the free-space attenuation (FSA) along the elongated cell and provide a power flux variation as small as possible a vertical shaped beam is used.

For the two extreme MT antenna locations shown in figure 1, below the BS antenna and at the end of the elongated cell, the FSA variation is 33.5 dB.

A total compensation of the FSA would require the cosec^2 radiation pattern, Sanford et al (1). That is not possible with the simple array configuration used here. Moreover the need to compensate the FSA can also be taken into account in the BS antenna specifications, Armogida and Peixeiro (2). Therefore only a decrease of the 33.5 dB FSA variation along the cell is envisaged.

ARRAY BASIC PATCH ELEMENT

To provide the dual frequency band the multilayer configuration of electromagnetically coupled patches, shown in figure 2, has been chosen as sub-array elements. A tuning stub has been included to compensate the modelling inaccuracy and fabrication tolerances. Both driven and parasitic patches are printed on a Duroid 5880 substrate separated by an air gap.

The sub-array elements are fed with semi-rigid coaxial cables. They have been designed with the help of the software package ENSEMBLE (3). Conventional photolithography printing circuit technology has been used in the fabrication. The input return loss is shown in figure 3.

ARRAY CONFIGURATION

Four patches have been mounted on the side walls of the truncated pyramid shown in figure 4. The side walls are tilted approximately 45° . The elements are fed with equal amplitude and phase by a cheap commercially available 4 -way power divider. Photos of the array are shown in figures 5 and 6. The array will provide vertical polarisation. Due to the relatively large dimensions and considerable weight the array is conceived for vehicular applications, not portable terminals.

ARRAY EXPERIMENTAL RESULTS

The amplitude of the experimental input reflection coefficient of the array prototype is shown in figure 7. As expected the required double resonance has been achieved providing an input return loss less than -10 dB in the two specified frequency sub-bands.

Preliminary radiation pattern experimental results have been obtained in an anechoic chamber far field facility. As expected the radiation pattern is almost omnidirectional with a maximum gain around 6 dBi and a ripple less than 3 dB. The vertical plane beam shaping provides a decrease of about 10 dB in the variation of the power flux along the rectangular street cell.

CONCLUSION

A small array of microstrip patches has been presented to be used as the mobile terminal antenna of a mobile communication system at 2 GHz. A multilayer structure of electromagnetically coupled microstrip patches provides the dual, up and down link, frequency bands. Four such sub-arrays have been mounted on the 45° tilted side walls of a truncated pyramid. An almost omnidirectional radiation pattern with beam shaping in the vertical plane is obtained. As the mobile terminal moves freely within the rectangular street cell a decrease of about 10 dB is obtained in the power flux dynamic range. An antenna prototype has been designed, fabricated and tested. The good agreement obtained between theoretical predictions and experimental results has allowed the validation of the design/fabrication procedure.

REFERENCES

1. Sanford, J. R., J.-F. Zürcher and S. Robert, "Optimized Antenna for Mobile Communication Base Stations", *Proc. European Microwave Conference*, pp. 780.786, Stuttgart, Germany, September 1991.
2. Armogida, A. and C. Peixeiro, "Microstrip Patch Antenna Array for a Mobile Communication System Base Station", *Proc. IEEE AP-S Int. Symposium*, Montréal, Canada, July 1997.
3. ENSEMBLE Design, Review, & 1D Array Synthesis. User's Guide. Boulder Microwave Technologies, Inc., Version 4.02, February 1996

ACKNOWLEDGMENTS

The authors want to thank the Portuguese National Research Council (JNICT) and the European Union for the partial funding, of projects ITCOM and TEMPUS JEP 7403-94, respectively.

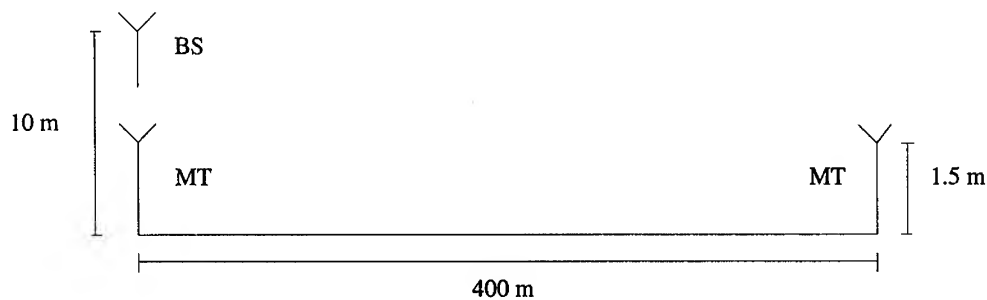


Figure 1: MT antenna located below BS antenna or at the end of the cell.

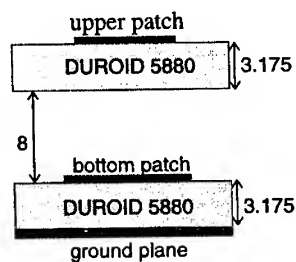


Figure 2: Sub-array configuration (dimensions in mm).

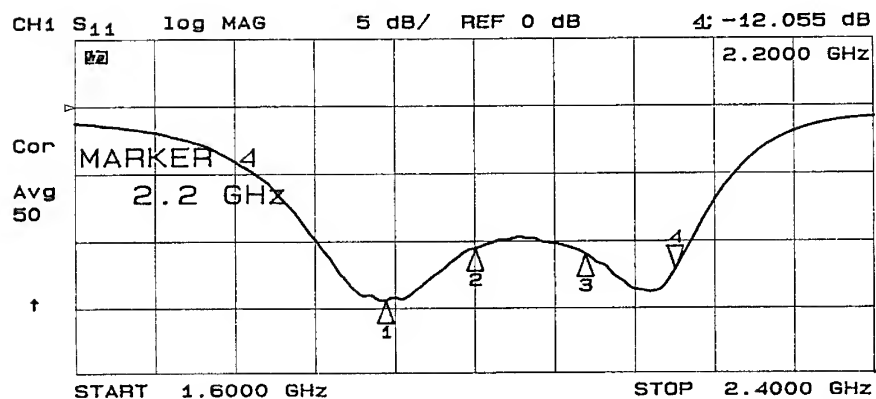
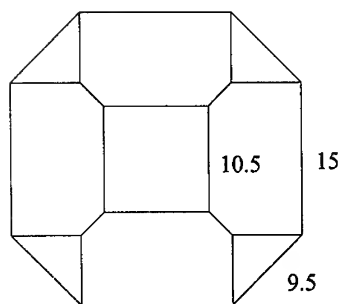
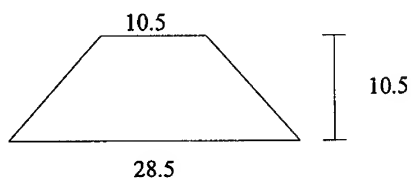


Figure 3: Input return loss of the array basic patch element.



a) Top view



b) Side view

Figure 4: Truncated pyramid for mounting of the array (dimensions in cm).

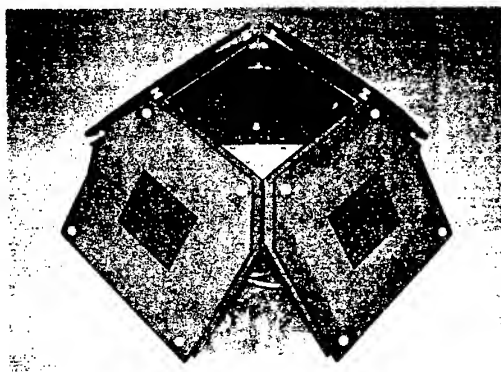


Figure 5: Photo of the array prototype.

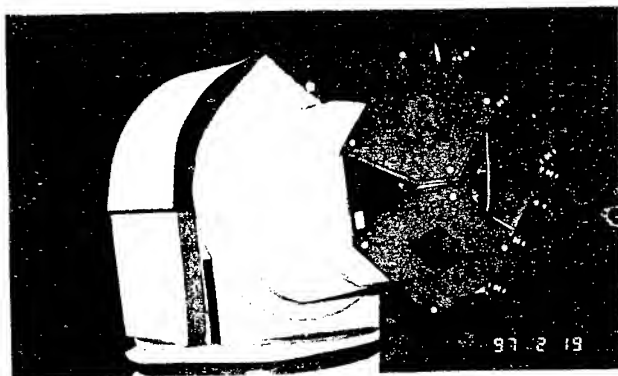


Figure 6: Photo of the array prototype mounted on the test positioner.

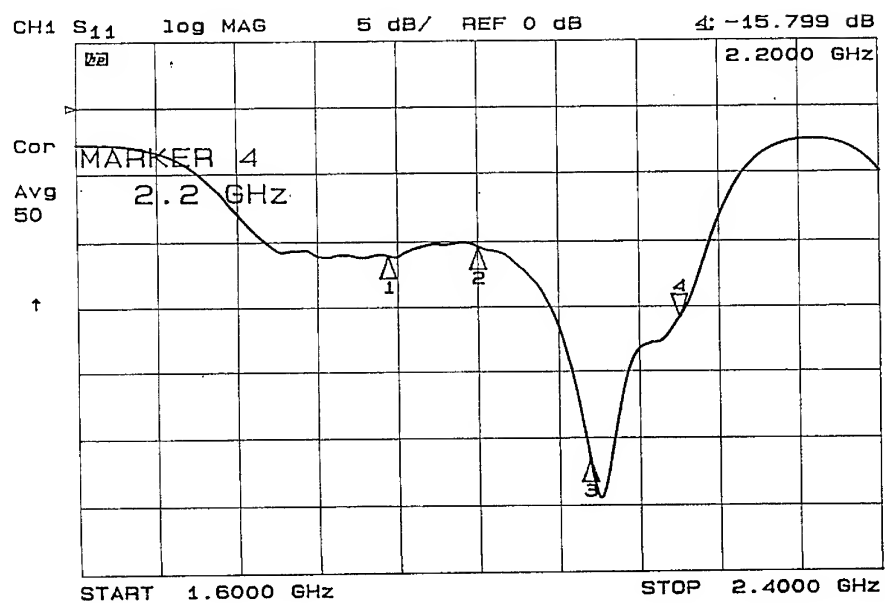


Figure 7: Array experimental input return loss

PROFILE INVERSION OF STRATIFIED DIELECTRIC MEDIA USING THE TWO-STEP RECONSTRUCTION

V.A. Mikhnev* and P. Vainikainen**

* Institute of Applied Physics, Skoriny 16, 220072 Minsk, Belarus

**Helsinki University of Technology, Radio Laboratory, Otakaari 5 A, 02150 Espoo, Finland

ABSTRACT

A novel two-step reconstruction approach for one-dimensional permittivity profiles in the frequency domain is presented. At the first step, the profile is reconstructed as a stack of homogeneous layers using minimax criterion for the modulus of the reflection coefficient. This method yields accurate reconstruction of simple layered profiles. In other cases, it provides good starting conditions for another method, based on application of the Newton-Kantorovich iterative procedure to the Riccati equation describing the reflection of electromagnetic wave from an inhomogeneous half-space. Thus, a computation time is considerably reduced without using *a priori* information. The convergence and the stability of solution are improved due to handling the problem in terms of an optical path length rather than in spatial coordinate. This is explained by a better accuracy of the integral equation derived to obtain the next iterates to the profile. The approach is valid for the inversion of discontinuous and highly contrasted profiles and retains a good stability with respect to the noise in the simulated data.

INTRODUCTION

Most of the imaging techniques that exist in literature are devoted to the two- and three-dimensional reconstruction because of their better orientation to the practical applications. Nevertheless, some new approaches are easier to find in the one-dimensional case due to its relative simplicity. Moreover, existing solutions to the one-dimensional inverse scattering problem are not ideal especially when the discontinuous profiles of high contrast are to be reconstructed. In particular, the Born-type approximation does not take into account multiple reflections and therefore is valid for weakly scattering objects (Bolomey *et al* (1), Cui and Liang (2)). Another class of inversion algorithms aims to obtain reconstructions by using solution of exact equations. Jaggard and Olson (3), Frangos and Jaggard (4) used the Gel'fand-Levitan-Marchenko theory. Iterative numerical methods based on the exact integral equations had been applied to the one-dimensional inverse scattering by Uno and Adachi (5), Habashy *et al* (6), Zhuk and Batrakov (7). Unfortunately, these approaches do not give reliable results for discontinuous profiles of high contrast. In many cases the convergence of the solution is strictly dependent on actual contrast values and initial guess used as a starting point for the reconstruction. That is why an importance of *a priori* knowledge of the object under investigation is usually emphasized.

In this work, two new complementary methods are proposed which yield accurate reconstruction of the discontinuous profiles of high contrast without using *a priori* information. One of them utilizes successive reconstruction of the dielectric interfaces and homogeneous layers. The second method is based on application of the Newton-Kantorovich iterative scheme to the inversion of the Riccati equation.

DISCRETE RECONSTRUCTION

The inhomogeneous half-space can be represented as a stack of homogeneous layers and treated using a concept employing 2x2 scattering matrices (Azzam and Bashara (8)). Accordingly, the scattering matrix of the stratified half-space is given by:

$$S = I_{01} L_1 I_{12} L_2 I_{23} \dots \quad (1)$$

where

$$I_{i(i+1)} = \frac{1}{1+r_{i(i+1)}} \begin{pmatrix} 1 & r_{i(i+1)} \\ r_{i(i+1)} & 1 \end{pmatrix} \quad (2)$$

is the matrix of interface between two adjacent layers numbered i and $i+1$,

$$\mathbf{L}_i = \begin{pmatrix} e^{j\beta_i} & 0 \\ 0 & e^{-j\beta_i} \end{pmatrix} \quad (3)$$

is the matrix of homogeneous layer with the number i , and

$$r_{i(i+1)} = \frac{n_i - n_{i+1}}{n_i + n_{i+1}}; \quad \beta_i = k d_i n_i, \quad (4)$$

where $k = 2\pi f/c$ is the free space wavenumber, f denotes frequency, n_i and d_i denote the refractive index and the thickness of layer with the number i , respectively. The medium in the observation domain is assumed to be a free space with $n_0=1$. The reflection coefficient is calculated from the formula (1) as

$$R = S(2,1)/S(1,1). \quad (5)$$

This formulation is valid not only for step-like profiles because any continuous profile can be represented with the desired accuracy by a large enough number of homogeneous layers.

The inversion principle valid for the lossless step-like profiles is based on the behavior of the maximum of modulus of the reflection coefficient of a normally incident electromagnetic wave. It can be shown, that an addition of one more step to the step-like multilayered profile results in increasing the maximum of modulus of the reflection coefficient in the infinite frequency range, and the increase is the larger, the higher is the step. Hence, the principle of reconstruction can be formulated as follows: the parameters of the layers are to be chosen successively one after another to ensure minimization of the maximum of modulus of the reflection coefficient for the remaining region in the frequency band of operation. A corresponding formula derived using the scattering matrices concept can be written in the form

$$\max |R_{i+1}(f)| = \max \left| \frac{R_i(f) \exp(2jk d_i n_i) - \frac{n_i - n_{i+1}}{n_i + n_{i+1}}}{1 - R_i(f) \exp(2jk d_i n_i) \frac{n_i - n_{i+1}}{n_i + n_{i+1}}} \right| \rightarrow \min, \quad i=0,1,2, \dots \quad (6)$$

where $R_i(f)$ is the reflection coefficient from the layered medium with i first interfaces being excluded. $R_0(f)$ is the given reflection coefficient from the whole inhomogeneous half-space.

At the first step of reconstruction the distance between the first layer and the reference plane d_0 and the refractive index of the first layer n_1 (case $i=0$) are obtained from (6). Consequently, the unknowns d_1 and n_2 , d_2 and n_3 etc. can be calculated by solving the optimization problem (6) repeatedly. The procedure is stopped at step p when the reflection coefficient $R_p(f)$ becomes zero at all frequencies, or when its maximum does not go down any more.

The method yields exact reconstruction for lossless layered profiles, if the reflection data are given in a wide enough frequency band. In other cases, the reconstruction is approximate because the frequency of maximal reflection can be outside the given frequency band. However, a discrepancy between the given profile and the reconstructed one is usually small. Therefore, this approach if does not cope with the reconstruction by itself, creates ideal starting conditions for the optimization method described below.

CONTINUOUS RECONSTRUCTION

Another way to calculate the reflection of electromagnetic wave from the inhomogeneous medium of unknown refractive index profile $n(x)$ is based on solution of the Riccati differential equation for the reflection coefficient:

$$\frac{dr(k,x)}{dx} = 2jkn(x)r(k,x) + \frac{1-r^2(k,x)}{2n(x)} \frac{dn(x)}{dx}. \quad (7)$$

The problem of interest is to find the refractive index profile from a knowledge of the reflection coefficient $r(k,0)$ given over some frequency band.

Introducing a new variable, optical path length

$$z = \int_0^x n(x') dx', \quad (8)$$

equation (7) can be rewritten in the form:

$$\frac{dr(k,z)}{dz} = 2jkr(k,z) + \frac{1-r^2(k,z)}{2n(z)} \frac{dn(z)}{dz}. \quad (9)$$

Since the solution to this nonlinear equation in closed form with subsequent inversion is impossible, some optimization technique is to be applied. In this work, an iterative Newton-Kantorovich procedure (e.g., Zhuk and Batrakov (7), Roger (9)) is used. The initial profile $n^*(z)$ is obtained by the method given above. Accordingly, the inversion process can be summarized as follows:

- step 1 solution of a forward problem for the initial profile $n^*(z)$. The numerical integration of the equation (9) from $z = 0$ to some depth z_0 with initial conditions given by the measured or simulated reflection coefficient data, yields the reflection coefficient $r^*(k,z)$; z_0 must be larger than the total electromagnetic path length in the inhomogeneous part of half-space
- step 2 derivation of a linear integral equation relating a small change of the medium profile $\Delta n(z)$ and corresponding change of the reflection coefficient $\Delta r(k, z_0)$:

$$\int_0^{z_0} \frac{e^{f(k,z)-f(k,z_0)}}{n^*(z)} jk [1+r^{*2}(k,z)] \Delta n(z) dz + \frac{1-r^{*2}(k,z_0)}{2} \frac{\Delta n(z_0)}{n^*(z_0)} = \Delta r(k, z_0), \quad (10)$$

where

$$f(k,z) = -2jkz + \int_0^z \frac{r^*(k,z')}{n^*(z')} \frac{dn^*(z')}{dz'} dz'. \quad (11)$$

First-order estimation of the function $\Delta n(z)$ eliminating a discrepancy between calculated and given reflection coefficient, by solving integral equation (10) with $\Delta r(k, z_0) = -r^*(k, z_0)$.

The equation (10) is solved by a commonly used technique, including expansion of the unknown $\Delta n(z)$ by some basis functions and transformation of the integral equation into a matrix equation to find the expansion coefficients. The standard Tikhonov regularization is employed to improve the stability of solution

- step 3 updating the profile function $n^{(1)}(z) = n^*(z) + \Delta n(z)$
- step 4 go to step 1 as long as $\|r^*(k, z_0)\|$ is larger than an acceptable error
- step 5 otherwise, stop the iterative procedure and return to the geometrical distance in the final profile using the equation (8).

The convergence and the stability of solution are improved considerably by handling the equations in terms of the optical path length. It can be explained by a better accuracy of the linear integral equation to calculate the iterates to the profile. Indeed, if the derivation of equation (10) is accomplished using the equation (7) as

a starting point, the second order term $2jk\Delta r(k,z)\Delta n(z)$ among others is to be neglected. When the coordinate transformation (8) is applied before, this term is absent.

A comparison of reconstructions performed using described approach and its analog derived using spatial coordinate, demonstrated apparent advantage of the proposed formulation with regard to the convergence and the stability of solution, i.e. the effect of ill-posedness of the problem is considerably reduced. The reconstruction depth z_0 can be chosen to a certain extent arbitrarily. Naturally, it must be larger than the optical path length in the inhomogeneous slab. However, it must not be too large to avoid loss of resolution.

NUMERICAL EXAMPLES

The capabilities of the proposed approach are demonstrated for multilayered profiles of high contrast using simulated reflection coefficient data calculated in the frequency range of 0.5 to 10 GHz with the use of formulas (1)-(5).

Fig.1 represents a two-layered lossless profile on a substrate. The Newton-Kantorovich procedure converges to the final reconstructed profile shown in Fig.1 in six iterations when started from a constant initial guess with $n=3.5$ (the best choice from the convergence viewpoint). The effect of measurement errors is estimated by adding to the real and imaginary parts of the reflection coefficients a random signal distributed uniformly over the interval $[-0.02 \text{ } +0.02]$. The solution retains a good stability as seen from Fig. 1. By using the discrete reconstruction method, the inversion of the same profile is performed exactly in a few seconds of microcomputer time.

A more complicated highly contrasted three-layered profile on a substrate is shown in Fig.2. An approximate reconstruction is obtained in this case by the discrete reconstruction method. Although an accuracy of the reconstruction is not good, a discrepancy between the exact profile and the reconstructed one is not too large. Using this profile as initial guess, the Newton-Kantorovich method completes the reconstruction in eight iterations.

CONCLUSIONS

A new two-step inverse scattering method valid for the discontinuous profiles of high contrast has been proposed. The fast convergence of the solution and its stability are achieved due to handling the inverse problem for the Riccati equation in terms of optical path length instead of the usual spatial coordinate. The initial profile needed for the optimization procedure is calculated using discrete reconstruction method based on application of the minimax criterion to the modulus of reflection coefficient in the frequency band of operation. Therefore, a lot of computation time is saved without using any *a priori* information.

REFERENCES

1. J.-C. Bolomey, D. Lesselier, C. Pichot and W. Tabbara, "Spectral and time domain approaches to some inverse scattering problems," 1981, *IEEE Trans. Antennas Propagat.*, 29, 206-212.
2. T.J. Cui and C.H. Liang, "Reconstruction of the permittivity profile of an inhomogeneous medium using an equivalent network method," 1993, *IEEE Trans. Antennas Propagat.*, 41, 1719-1726.
3. D.L. Jaggard and K.E. Olson, "Numerical reconstruction for dispersionless refractive profiles," 1985, *J. Opt. Soc. Am. A*, 2, 1931-1936.
4. P.V. Frangos and D.L. Jaggard, "The reconstruction of stratified dielectric profiles using successive approximations," 1987, *IEEE Trans. Antennas Propagat.*, 35, 1267-1272.
5. T. Uno and S. Adachi, "Inverse scattering method for one-dimensional inhomogeneous layered media," 1987, *IEEE Trans. Antennas Propagat.*, 35, 1456-1466.
6. T.M. Habashy, E.Y. Chow, and D.G. Dudley, "Profile inversion using the renormalized source-type integral equation approach," 1990, *IEEE Trans. Antennas Propagat.*, 38, 668-682.
7. N.P. Zhuk and D.O. Batrakov, "Inverse scattering problem in the polarization parameters domain for isotropic layered media: solution via Newton-Kantorovich iterative technique," 1994, *J. Electromagn. Waves Appl.*, 8, 759-779.
8. R.M. Azzam and N.M. Bashara, "Ellipsometry and polarized light," 1977, New York: North Holland.
9. A. Roger, "Newton-Kantorovich algorithm applied to an electromagnetic inverse problem," 1981, *IEEE Trans. Antennas Propagat.*, 29, 232-238.

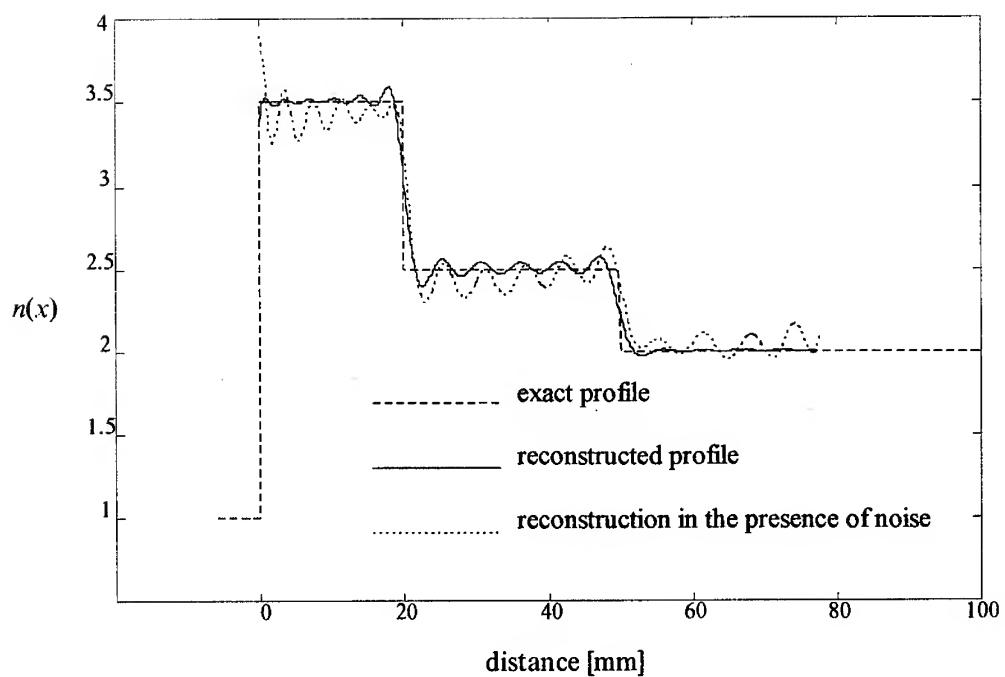


Fig. 1. Reconstruction of a two-layered profile for exact and noisy simulated data.

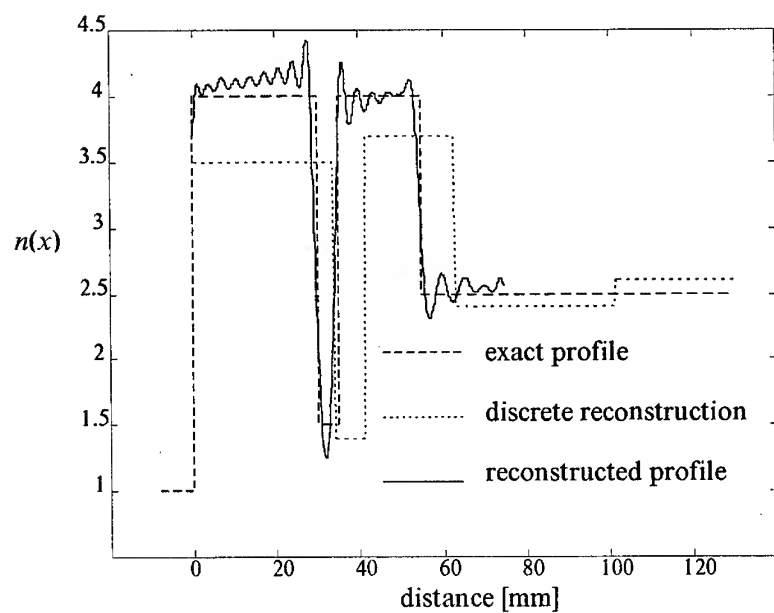


Fig. 2. Reconstruction of three-layered profile on a substrate using the two-step approach.

The Shielding Effects of Lossy Dielectric Material for Three Layered Elliptical Human Model

S.NISHIZAWA O.HASHIMOTO Member, IEEE
DEPARTMENT OF Electrical and Electronic Engineering
Graduate School of Science and Engineering
Aoyama Gakuin University

Setagayaku Chitosedai 6-16-1, 157 Tokyo, Japan
Tel : (+81)-3584-1111(Ex.322) , Fax : (+81)-3584-1121
E-mail: s-nishi@ee.aoyama.ac.jp, hasimoto@ee.aoyama.ac.jp

Abstract

In this paper, we discuss the shielding effects of lossy dielectric materials located in front of the human body. Using the Method of Moment, we investigate the shielding effects by calculating the 'whole average SAR' and 'local SAR' for a three layered elliptical model of the human body, which simulated the skin, fat and muscle tissues.

Two dielectric shield constants at a high frequency range of 1.3 GHz are selected for the shielding investigation and the results are presented for several thickness and gap values (between the human model and shield). This paper presents an interesting viewpoint on the high frequency shielding properties of these materials, and implementations for protecting the human body from possibly damaging electromagnetic effects.

1. Introduction

Recently, the marked increase in use of electromagnetic devices has raised concerns as to the possible damaging effects of the emitted electromagnetic waves on the human body.

Much research has been done on this field and the specific absorption rate (SAR) criteria, has been used to obtain the dosimetric data and to gain further understanding of the biological tissue absorption characteristics [1][2].

It is worth nothing however, that there has been little published research on the electromagnetic shielding of the human body[3].

In our research, we focused on the shielding effects on a homogeneous human model. Because of the resonance phenomena in the gap between the shield and the human model, we found out that a low loss material shield, located in front of the human model, at a frequency of 300 [MHz], actually increased the SAR values compared with the unshielded values[4].

Later we investigated a three-layered elliptical model and found that a an elliptical axis ratio choose to that of a human (b/a equal to 1.6), the resonance between the layers of skin, fat and muscle (layering resonance) occurred at the 1.3 [GHz]

frequency region and increased the SAR values compared to those calculated for the homogeneous human model[5].

In this paper, we focus on the shielding effect, of a lossy dielectric shield placed in front of a three-layered human model. The results are presented for several shield thickness, gap values, covered shielding range. During our research, we found out that at the frequency range of 1.3 [GHz] which the layering resonance occurred, a large shielding effect was achieved using low loss shield materials.

2. Formulation

As shown in Fig. 1, the incident plane wave E^i (TM Wave) which has the power density P of 1 [mW / cm²] and pointed in the Z axis, is travelling in the positive X direction and is incident on the 3-layered human model.

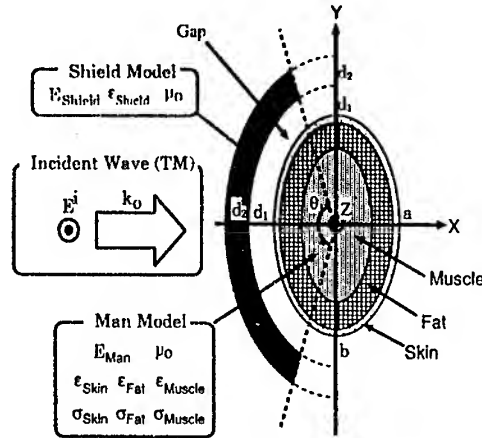


Fig 1: Analysis Model

The elliptical human model, which is infinite in the Z direction, has an ellipse axis ratio, b/a , equal to 1.6, with a permittivity(ϵ_{Skin} , ϵ_{Fat} , ϵ_{Muscle}), conductivity(σ_{Skin} , σ_{Fat} , σ_{Muscle})[6] and free space permeability μ_0 .

$$\begin{aligned}\epsilon_{Skin} &= 73.3f^{-0.0720} \\ \epsilon_{Fat} &= 10.5f^{-0.0827} \\ \epsilon_{Muscle} &= 90.0f^{-0.0849} \\ \sigma_{Skin} &= 2.55 \times 10^{-3} f^{0.864} \\ \sigma_{Fat} &= 5.51 \times 10^{-3} f^{0.405} \\ \sigma_{Muscle} &= 0.364 f^{0.190}\end{aligned}$$

Unit: f (MHz)

The shield is positioned in front of the human model and the shielding range is depicted as a function of the angle θ , with a permittivity and permeability of ϵ_{shield} and μ_0 respectively. The gap distance between the shield and the human model is d_1 [cm] and the thickness of the shield is d_2 [cm].

Using this model, we calculated the electric field inside both the human model and shield, $E_{man}(n)$ and $E_{shield}(n)$, using the Method of Moment [7][8]. We calculated the local SAR and the whole average SAR using the following equations:

$$Local\ SAR(n) = \frac{\sigma |E_{man}(n)|^2}{2\delta}$$

$$Average\ SAR = \sum_{n=1}^N (Local\ SAR(n)) / S$$

Where σ , δ , S are the conductivity, specific weight of the human body and the cross section area of the human model, respectively.

The specific weight of the human body are used $1000.67[kg/m^3]$ and the electro-magnetic constants are used the value which is written in [6]. The parameters used for the computations are as follows:

- (a) For an axis ration, b/a , equal to 1.0, the radius of the human cylindrical model was set to 11.28 [cm], by maintaining the same cross sectional area, the axis ratio, b/a , was changed from 1.0 to 1.6.
- (b) The gap distance d_1 , between the human model and shield, varied from 0.8 to 2.0 [cm] and the shield thickness d_2 varied from 0.5 to 3.0 [cm].
- (c) Shield angle range, θ , was set to 180° .

For the shield material, we assumed a carbon fiber reinforced plastic material (CFRP) and rubber sheets mixed with carbon fiber/particles[9]. The material constants which were used are, for a low loss shield $E_{shield} = (10-j5)\epsilon_0$ and for a higher loss shield $E_{shield} = (20-j20)\epsilon_0$.

3. Numerical Results

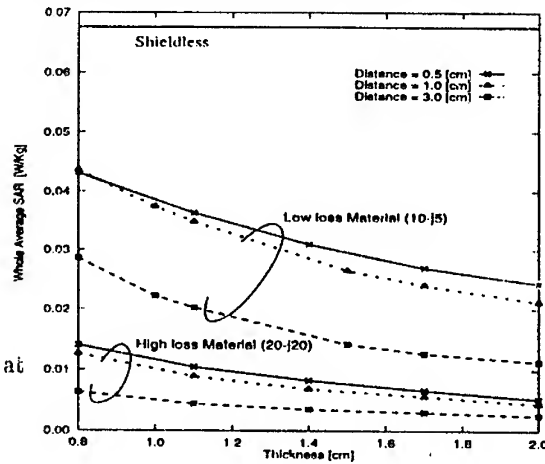
3.1 Whole average SAR

Fig.2 shows the whole average SAR as a function of shield thickness for a fixed gap distance, coverage angle, θ , of 180° and an axis ratio, b/a , of 1.6. The shield permittivity values for low loss material is used $(10-j5)\epsilon_0$ and for high loss material shield $(20-j20)\epsilon_0$. The x, Δ and * symbols represent the calculated SAR values for a gap distance, d_1 , of 0.5, 2.0 and 3.0 [cm], respectively. From this result, we found that by low loss material shield $(10-j5)$, compared to 300[MHz], the resonance phenomena between the gap[4] didn't occur and the SAR is reduced. Also by high loss material shield $(20-j20)$, an improved shielding effect was achieved. Because of

large reduction of transmission wave, using high loss material shield, there wasn't big variation of SAR by changing the distance (d_1), and thickness (d_2), compared to low loss material shield (10-j5).

Fig.2 :

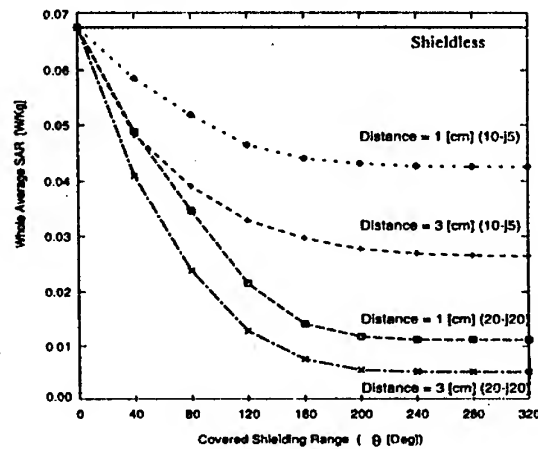
Calculated whole average SAR at 1.3[GHz]



In Fig.3 shows the calculated whole average SAR for low (10-j5) and high (20-j20) material shield, as a function of shield coverage angle θ from 0° to 320° . The calculation is done for shield thickness 0.8 [cm] and distance for 1 and 3 [cm]. From these plots, it is found that the whole average SAR were large reduced by extending the shield range to the back side of the model. However, the local SAR value hardly changes at angle θ above 200° .

Fig.3 :

Whole average SAR as a function of covered shielding range



3.2 Local SAR

Fig. 4 displays the unshielded local SAR distribution (a) and the sectional view (b) at $Y=0.0$ [cm]. From this distribution, it is found that the large local SAR value concentrated in the front of skin layer.

Fig. 5 and 6 show the shielded local SAR distribution and the sectional view for low (10-j5) and high (20-j20) material shield respectively. The shield thickness, distance and covered range (θ) is set to 2[cm], 3[cm] and 180° , respectively.

In the case of locating low loss material shield in front of the model (Fig.5), the SAR value decreased in comparison with unshielded values. But the large local SAR value, still appeared in front of the model.

Otherwise, by locating high loss material shield (Fig.6), large reduction of SAR value was appeared to the whole model, because of the shielding effect.

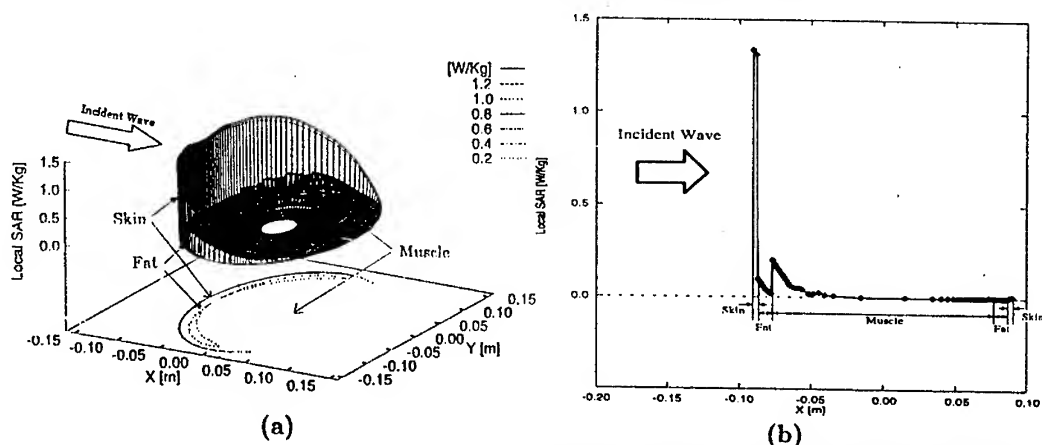


Fig.4 : Distribution of shieldless Local SAR and the sectional view at $Y=0.0[\text{cm}]$

3.3 Shielding effect and frequency characteristics

In the investigation of [4], we found out that by using low loss material ($10-j5$) at the frequency 300[MHz], because of the resonance phenomena between the gap, SAR values was higher compared to unshielded SAR values. On the other hand, a large reduction of SASR was achieved 1.3 GHz.

To know the relation between frequency and the shield effect, we investigated the frequency characteristics (100 to 2000[MHz]) of shielding effect using low loss material shield. In Fig.4, the shield range, θ , is set to 180° and the calculation is done for shield thickness 0.8 and 2.0 [cm]. The +, \square and X symbols represent the calculated SAR values for a gap distance, d_1 , of 0.5 1.0 and 3.0 [cm], respectively. The solid line shows an SAR value of unshielded human model.

As a result, we found out that by large value of shield thickness, the frequency range was narrower which the SAR values was higher compared to unshielded SAR values. And also a large shielding effect was achieved at the frequency range of 1.3 [GHz] which the layering resonance occurred in the three layered human model.

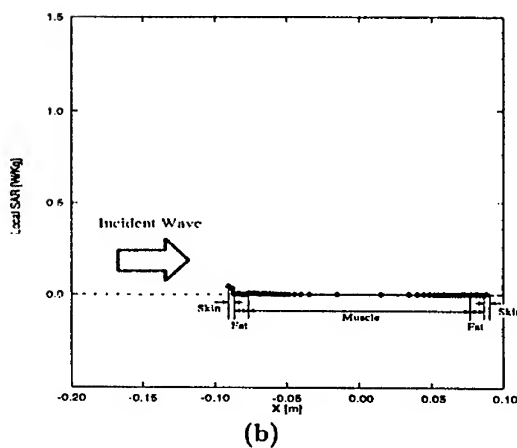
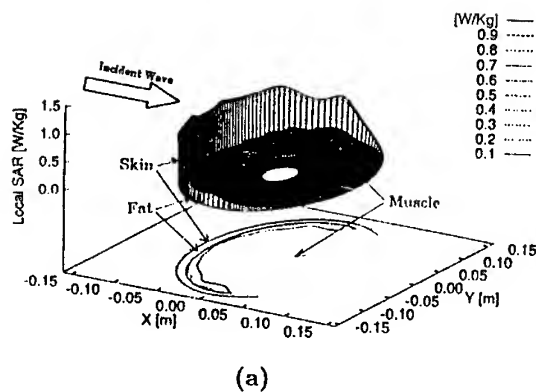


Fig.6 : Distribution of shielded Local SAR and the sectional view at $Y=0.0[\text{cm}]$ (In the case of $\epsilon_{\text{shield}} = (20 - j20)\epsilon_0$)

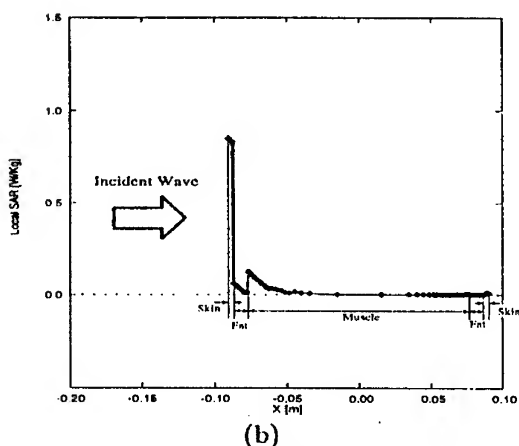


Fig.5 : Distribution of shielded Local SAR and the sectional view at $Y=0.0[\text{cm}]$ (In the case of $\epsilon_{\text{shield}} = (10 - j5)\epsilon_0$)

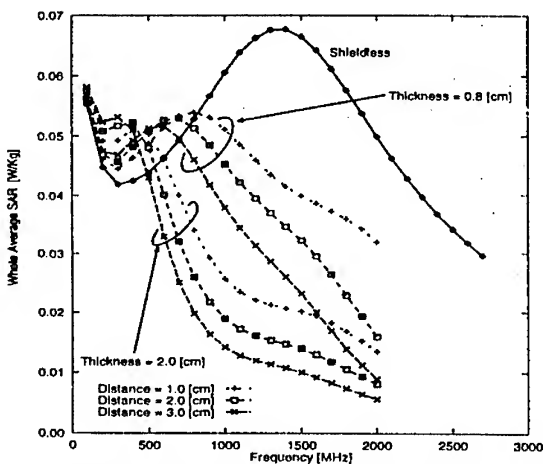
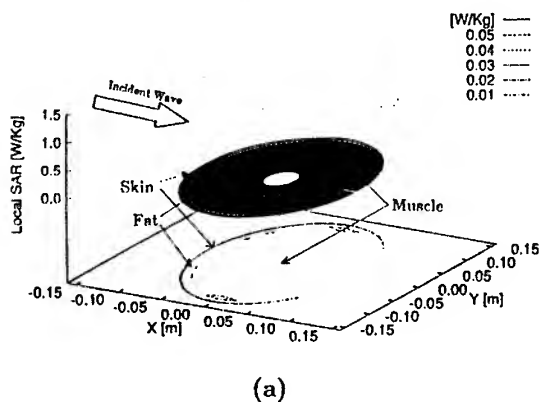


Fig 3: Frequency characteristics of whole average SAR for low loss material shield

4. Conclusion

The shielding effects of several dielectric materials covering parts of human body are investigated through the calculation of the average SAR. The following conclusions are drawn.

1. At the frequency 1.3[GHz], an improved shielding effect was achieved for both low and high loss material shield. Also, there wasn't big variation for shielding effect by changing the value of the gap and shield thickness for high loss material shield.
2. By extending the shield range to the back side of the human model, up to the coverage angle 200 °, the SAR value was large reduced. However, above this angle, the SAR value hardly changed.
3. A large local SAR value concentrated in the front of the skin layer, in comparison to fat and muscle layer.
4. Through the calculation of the frequency characteristics for shielding effect by using low loss material shield, we found out that the frequency range which the SAR value was higher compared to unshielded SAR values is going smaller by increasing shield thickness values. And also a large shielding effect was achieved in the frequency range which the maximum SAR values appeared.

Future research will include the calculations of the SAR for three dimensional model and experimental investigation.

5. Reference

- 1 M Taki "Safety Guidelines on Human Protection from Electromagnetic Field Exposure," Proceedings of the Institute of Electrostatics Japan, Vol 20, No 4 pp 219-224 (April 1996).
- 2 Carl H Dunney "electromagnetic Dosimetry for Models of Humans and Animals A review of Theoretical and Numerical Techniques," Proceedings of the IEEE, Vol 68, No 1, pp 33-40 (Jan 1980).
- 3 T Nakamura, S Tokumaru "Reduction of SAR in Human Body by Perfect Conducting Shield," IEICE Trans, Vol J78-B-II, No 3, pp 200-207 (March 1995)
- 4 S Nishizawa, O Hashimoto, W Tsuchida "Numerical study of reducing SAR of human body by lossy material shield" Asia Pacific Microwave Conference, Medical Application, Vol 1, pp 47-50 (Dec 1996)
- 5 O Hashimoto, T Setsu "SAR calculation of three-layered cylindrical human model with elliptical cross section based on point matching method," Asia Pacific Microwave Conference, Medical Application, Vol II, pp 333-336 (Dec 1994)
- 6 A Sokino, K Kodubun "Numerical Analysis of Microwave Energy Absorption in a Multi-layered Cylindrical Human Model," Technical Report of IEICE, EMCJ89-91, pp 15-20 (March 1990).
- 7 R F Harrington: "Field Computation by Moment Methods", New York, Macmillan (1968)
- 8 J H Richmond "Scattering by a dielectric cylinder of arbitrary cross-section shape," IEEE Trans Antennas Propagate, vol AP-13, pp 334-341, (May 1965).
- 9 O Hashimoto, Y Shimizu "Reflecting Characteristics of Anisotropic Rubber Sheets and Measurement of complex Permittivity Tensor," IEEE Trans NITT-34, No. 11, pp 1202-1207 (Nov 1986).

LOW POWER MICROWAVE EFFECTS ON ERYTHROCYTE MEMBRANES

Sajin George*, Rusu Ion*, Kovacs Eugenia**, Savopol Tudor**, Dinu Alexandru**,
Sajin Maria***

*) National Research Institute for Microtechnology, Str. Erou Iancu Nicolae 32 B, 72 996 Bucharest, Romania.

**) "Carol Davila" Medical University, Biophysical Research Department, P.O. Box 15 205, Bucharest, Romania.

***) "Carol Davila" Medical University, Chair of Morphopathology, Spl. Independentei 99 - 101, Bucharest.

Abstract -This work presents the results obtained by further experiments consisting in irradiation of human blood samples with high frequency low power density electromagnetic waves (2.45 GHz / 0.025...10 mW/cm²). The effect was studied by measuring the induced hemolysis of the exposed erythrocytes compared to controls. As a general result one confirm the observations and the conclusions of [1] indicating that the hemoglobin loss from the microwave irradiated cells is due to the membrane permeabilisation of the exposed erythrocytes rather than to their lysis

INTRODUCTION

The purpose of the present study was to examine the effects of long - term exposure of human blood to 2.45 GHz CW radiation at low power densities which are supposed not to induce thermal effects. Following the discussions carried out at 25 EuMC, Bologna, Italy (1995) (see [1]), a different microwave setup was used, with the possibility of measuring the effective power absorbed by the load. The microwave frequency of 2.45 GHz has been chosen for this study due to its extensively use in domestic, industrial and medical applications. The effects on the erythrocyte membrane have been characterized by measuring hemoglobin loss before and after irradiation at different power levels for both the irradiated samples and the controls.

EXPERIMENTS

The experimental setup (see Fig.1) permits simultaneous irradiation with different power levels the blood samples collected from the same single donor at the beginning of the experience, usually in the morning.. The microwave generator (1) was a R&S SLRD 41004 power generator able to provide 2.45 GHz CW in a power range up to 5 W. This power is applied via the isolator (2) to a series of directional couplers (3) with the coupling of 10 dB that allows simultaneous irradiation of three sets of blood samples. The variable attenuator (5) allows power adjustment for the irradiating system. The group built by the dual directional coupler (6), the two synchronized microwave switches (7) and the powermeter (9) with its detector (8) allows the measurement of incident and reflected powers from the applicator (11). The effective power level introduced in the applicator (11) is obtained as difference between these incident and reflected powers. These are the power levels indicated in Tables 1 and 2.

The microwave radiation is applied to the blood samples through the applicators made of the coaxial to R32 waveguide adapters. The aliquots containing blood were made in polystyrene

($\epsilon = 2.5$). Their dimensions were chosen so that 10 aliquots occupy the whole inner space of a R32 waveguide used as microwave irradiating chamber (13). The whole aliquots ensemble was practically made in a polystyrene block (13) with the dimensions $72 \times 34 \times 8 \text{ mm}^3$ in which 10 holes with 5 mm diameter and 32 mm depth were made. These holes were filled with human blood up to approx. 3/4 of their height (25 mm). The polystyrene block so prepared is introduced in the waveguide (12) that follows to the applicator (11). The blood quantity contained in each aliquot is approx. 0.5 ml and in all 10 aliquots there are approx. 5 ml of blood. A second R32 waveguide to coaxial adapter (14) close this irradiation chamber.

By means of a second powermeter (15) HP 436 with the detector (16) HP 8481, the emergent power from the irradiation chamber is measured. The difference between this power and the incident power gives an indication on the power effectively absorbed by the blood in aliquots. This measurement was performed for the maximum incident power density of 10 mW/cm^2 in order to see if the microwave power effectively absorbed by the blood modifies or not its temperature. The input power level was adjusted for a value $P_{\text{in}} = 245.6 \text{ mW}$ that means an incident power density of 10 mW/cm^2 on the surface of R32 waveguide aperture. The output power level from the irradiating chamber was measured as $P_{\text{out}} = 118.4 \text{ mW}$. One estimates that the power absorbed by the polystyrene volume is approx. 10 mW. It follows that the 10 aliquots containing blood samples absorb a power $P_{\text{abs}} = 117.2 \text{ mW}$ that corresponds to a microwave power density of approx. 5.5 mW/cm^2 calculated for the effective surface of blood samples.

It is well known from literature [4] that for biological 1 micrometer sized entities (like cells) that heating induced by power densities below 10 mW/cm^2 is of the order of $10^{-5} \text{ }^\circ\text{C}$. We think that for a power density of 10 mW/cm^2 in the irradiation chamber aperture, the effect of raising the hemoglobin relaxation from red cells is always a nonthermal effect. As an additional safety element, the whole irradiating chamber was maintained at the temperature of $+4 \text{ }^\circ\text{C}$.

The methods used to investigate the interaction of human erythrocytes with non-thermal power level densities of $0.025 \dots 10 \text{ mW/cm}^2$ of 2.45 GHz radiation were:

- hemoglobin release measurements for irradiated blood at different power densities and for the controls;
- Coulter Counter control of irradiated blood;
- measurement of the kinetics of irradiation induced hemolysis at different power levels in parallel to the measurement of the radiation induced osmotic fragility of the cells.

After irradiation, the free hemoglobin of both control and irradiated samples were measured. For this purpose the suspension from each test tube was homogenized and resedimented by centrifugation ($450\text{g} / 4 \text{ }^\circ\text{C} / 0.5 \text{ hour}$). The relative content of free hemoglobin from the supernatant was established by a spectrophotometric technique, measuring the corresponding absorption at 420 nm (the point of maximum hemoglobin absorption, characteristic of the Soret band). The remaining sediment of the irradiated samples (integral erythrocytes and fragments of plasmatic membrane) was weighted and totally hemolysed by adding 1 ml

distilled water, with 10 min. repose at room temperature and centrifugation (8000g/ 4 °C/ 0.5 hour). The total hemoglobin content of the supernatant was estimated by spectrophotometry. Except the kinetic measurements, time of irradiation was 60 hours. The degree of hemolysis was determined spectrophotometrically as the ratio of the optical absorbency of the supernatant from each sample at 420 nm to the mediated absorbency of a control samples totally hemolysed by osmotic shock. The main results are indicated in Tables 1 and 2.

Table 1. The hemolysis degree of 6 blood units exposed for 60 hours at different power densities

Blood unit	Controls	Microwave power density (mW/cm ²)			
		0.025	0.050	0.100	0.250
1	1.97 ± 0.12	---	2.33 ± 0.15	---	---
2	1.25 ± 0.14	---	1.39 ± 0.09	---	---
3	1.92 ± 0.15	1.97 ± 0.12	---	---	2.09 ± 0.07
4	2.01 ± 0.14	2.61 ± 0.25	---	---	3.00 ± 0.19
5	1.33 ± 0.16	---	1.44 ± 0.13	---	---
6	2.00 ± 0.15	---	---	2.29 ± 0.09	---

Blood unit	Microwave power density (mW/cm ²)				
	0.500	1.000	2.500	5.000	10.000
1	2.88 ± 0.19	---	---	3.45 ± 0.25	---
2	1.63 ± 0.11	---	---	2.07 ± 0.10	---
3	---	---	2.39 ± 0.07	---	---
4	---	---	4.61 ± 0.23	---	---
5	1.69 ± 0.13	---	---	2.09 ± 0.18	---
6	---	2.77 ± 0.15	---	---	3.71 ± .025

Table 2: Percentual increase of hemolysis degree of irradiated blood samples compared to controls

Blood unit	$\alpha (\%) = (A - A_0)/A_0 \times 100$								
	Microwave power density (mW/cm ²)								
	0.0250	0.050	0.100	0.250	0.500	1.000	2.500	5.00	10.00
1	---	18.27	---	---	46.19	---	---	75.12	---
2	---	11.2	---	---	30.4	---	---	65.6	---
3	2.6	---	---	8.85	---	---	24.5	---	---
4	29.8	---	---	49.25	---	---	129.3	---	---
5	---	8.2	---	---	27	---	---	57.1	---
6	---	---	14.5	---	---	38.5	---	---	85.5

In Table 2: A = hemolysis degree of irradiated blood samples measured at 420 nm wavelength;
A₀ = spontaneous hemolysis degree of control blood samples;

It was found that, at the mentioned power level densities irradiation induces a significant hemoglobin loss due to transient permeabilisation of irradiated erythrocytes rather than to their lysis. The microwave induced hemoglobin loss by irradiated erythrocytes is up to 80 % of the spontaneous hemoglobin loss by the controls. The rate of the increase of hemoglobin loss with the increased power density was found to be highly dependent on the initial level of spontaneous hemolysis. It seems that the membrane is as more sensitive to the microwave radiation as it was leakier at the start.

Kinetics of hemolysis degree at three different power densities was studied. While at low power densities ($0.8...1.36 \text{ mW/cm}^2$) there is a quasi-linear increase of the hemolysis degree with the time of irradiation, at higher density (5 mW / cm^2) this tendency seems to reverse after first 10 hours of irradiation. The only reasonable explanation for this seems to be that the spontaneous hemoglobin loss of controls increases faster than that of the exposed samples. It appears like long term irradiation would exert a protective action against spontaneous hemolysis caused by cells aging.

This observation is paralleled to the results of kinetic measurements of the osmotic resistance of irradiated erythrocytes showing a progressive increase of the osmotic resistance with time of irradiation at exposure levels of 5 mW / cm^2 (cf. [3]).

CONCLUSIONS

Summarizing our observation it may be found that:

- the microwave induced increase of hemoglobin loss by irradiated erythrocytes is up to 80 % of the spontaneous hemoglobin loss by the controls;
- the microwave induced increase of the hemoglobin loss reaches saturation below 10 hours for irradiation with 5.00 mW/cm^2 .
- the rate of increase of hemoglobin loss with the increasing power density is highly dependent on the initial level of spontaneous hemolysis. It looks like the membrane is as more sensitive to the radiation power as it was leakier at the start.

REFERENCES

- [1] George Sajin et al.: 2.45 GHz microwave radiation effects in nonthermal damaging of the human erythrocyte membrane. *25 - th European Microwave Conference, Bologna, Italy, 04 - 08 Sept. 1995*, p. 845.
- [2] Tudor Savopol et al.: Membrane damage of human red blood cells induced by low power microwave irradiation. *Electro-- and Magnetobiology*, 14(2), (1995), p 99.
- [3] Savopol T. et al.: *Bioelectrochemistry and Bioenergetics*, (4), 1996, pp. 171 - 173.
- [4] Keillman F.: Experimental RF and MW Resonant Nonthermal Effects, in *Biological Effects and Dosimetry of Nonionizing Radiation*, Grandolfo M., Michelson S. M., Rindi A., editors., Plenum Press, New York and London, 1983.

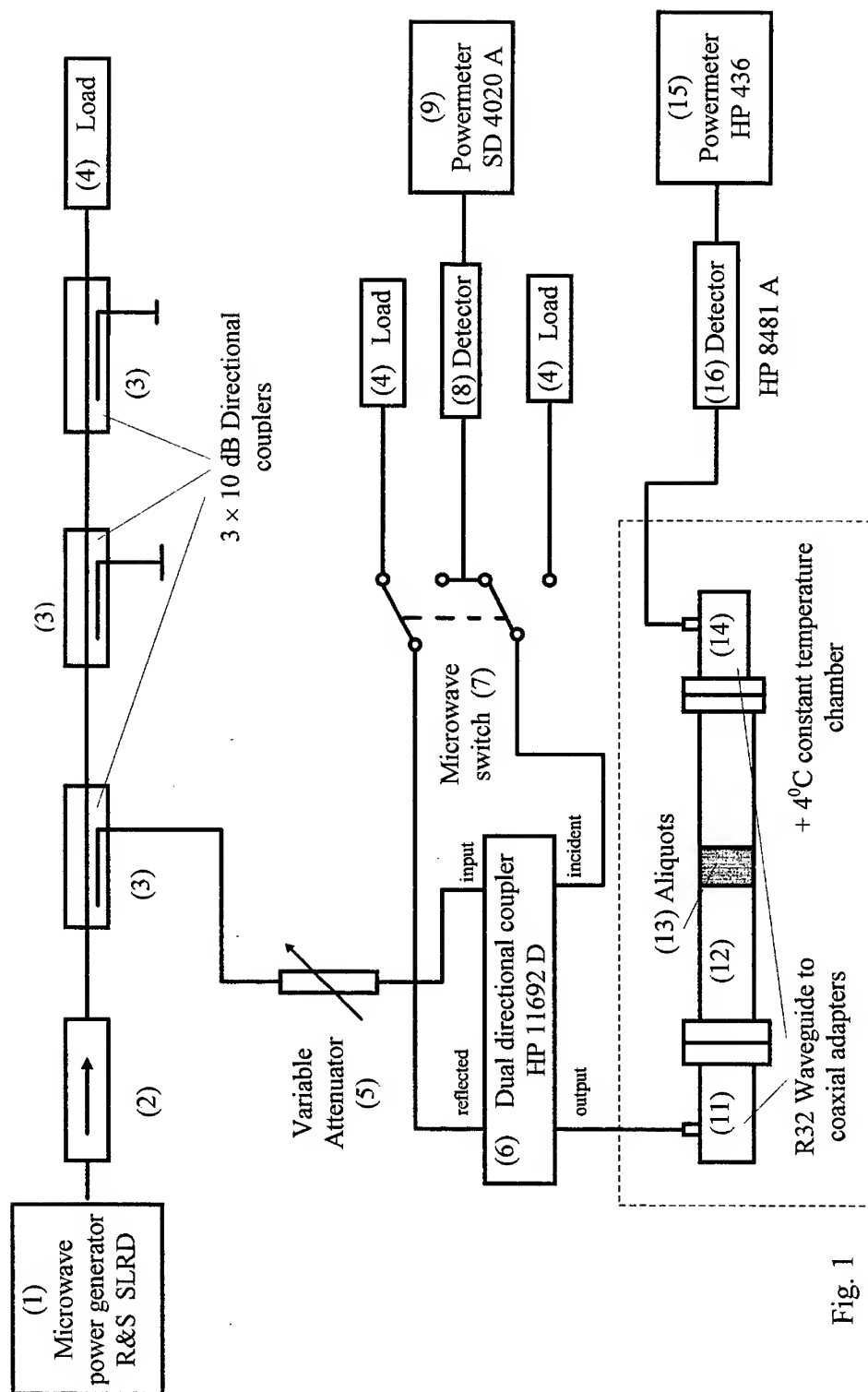


Fig. 1

A Laser Radar for precise 2D- and 3D-Object Imaging

Andreas Biernat, Günter Kompa

FG Hochfrequenztechnik, University of Kassel, Germany

34121 Kassel, Wilhelmshöher Allee 73

Tel: +49-561-8046528, Fax: +49-561-8046529

Email: andreasb@hfm.e-technik.uni-kassel.de

ABSTRACT

A high resolution laser radar useful for object scanning, profile measurements and level control has been set up. The distance measurement uncertainty is less than 300 μ m, the spot size, which defines the lateral resolution, is less than 1mm. Powerful picosecond laser pulses are used to scan also surfaces with low reflectance. Although the pulse repetition frequency (PRF) is relatively high (40kHz), eye-safety laser condition class 1 is fulfilled. Scanned objects can be drawn as a 3D-wireframe (useful for 3D-modelization) and as a 2D-contour plot.

I. INTRODUCTION

As is known, microwave radars generally exhibit a relatively large divergence of transmitted beam. This makes them less suited for precise imaging purposes. Operating at optical frequencies, the beam divergence angle can be made very small resulting in high angular resolution (e.g. Rodriguez et al [1]).

Fig. 1 gives a schematic view of a laser radar configuration for 3D-imaging, Höfler et al [12]. The focussed laser beam from the laser transmitter is directed toward the target via scanning mirrors. There the signal is reflected back to the scanning mirrors and then collected and focussed by the receiver optics onto the photodetector.

The following problems generally occur in the design of a 3D laser radar system for commercial use: Class 1 laser condition [2] should be fulfilled, which means that the laser emission is totally eye-safe. The radar system should be strictly cost-effective, including the laser source. Because of fast measurement response time, the PRF should be as high as possible. This requirement generally collides with the class 1 condition. Spatial measurement uncertainty in the x-, y- and z-direction at distances up to some meters should be less than 1mm. Reliable detection of targets with low reflectance require sufficiently high optical peak power of the transmitted pulses. Scanning of hot targets (e.g. 1200K) is difficult due to high background radiation which may significantly decrease the SNR, Kompa [4].

There are two fundamental limitations in the design of high resolution imaging systems. High optical power, which is needed for the detection of low-reflecting targets, can be obtained by using laser diodes with large emitting areas. However, as is known from the Lagrange-relation (Meyer-Arendt [3]), it is very difficult to image commonly used large apertures to sufficiently small laser spot sizes in the desired measuring reference plane. Alternatively, stacked laser diodes are being used for providing higher optical power (e.g. [4]). However, in this case a problem occurs regarding very fast current pulse modulation, the delay time between pumping and lasing is different for the cascaded diodes. This leads to optical pulses with stepped leading pulse edges and isolated spikes (see Fig. 2), which make unique and precise time interval measurements impossible. In a particular case the difference in delay time for the laser diodes is significantly large, so that a burst of a few single pulses can evolve. The number of pulses is then equal to the number of diodes in the stack.

The following sections describe the laser radar system and the laser transmitter. A novel pumping current modulation technique is proposed which exhibits extremely improved emission characteristics. It can generally be applied to any weakly index guiding laser structure such as single-quantum well ridge-waveguide (Eliseev et al [5]) and single heterostructure (SH) lasers. Results for investigated SH laser diodes will be given.

II. LASER RADAR SYSTEM SETUP

Fig. 3 shows a block diagram of the pulsed laser radar system. The concept is similar to that given in Fig. 1. In this case, both the reference and reflected signal are directed onto the same photodetector. This is used to eliminate temperature drift and various jitters of the laser transmitter and the photodiode. Sampling technique is used for economic time interval measurement, Kompa [8]. With knowledge of the mirror positions, a complete image of the target can be obtained. Ranging errors of several millimeters are observed with high received signal dynamics, which originate from the nonlinearities of the used photodiode, Stolze and Kompa [9]. However, knowing accurate nonlinear photodiode models, error-correction can be performed.

III. PUMPING CURRENT MODULATION TECHNIQUE

Mainly AlGaAs-GaAs SH laser diodes have been investigated. In Fig. 4 the energy band diagram under forward bias (a) and the real part of the complex refractive index (b) are shown. Under normal operating conditions, i.e. at moderate pumping currents, the concentration of the injected carriers in the center p-layer will not remarkably change the index profile of the asymmetric optical waveguide. In this case, at room temperature, an emission wavelength of about 904nm is expected for the investigated laser diodes. However, as is indicated by the dashed line in Fig. 4b, very strong carrier injection attributes to a considerable negative contribution to the real part of the refractive index, so that the commonly observed laser mode is weakened or even nearly suppressed. Regarding the dynamics, this operating condition can only be attained if the starting phase of the carrier injection is sufficiently fast, so that the index profile is considerably changed within the normal delay time of lasing being about 2.5ns. Typical rise time of the used pumping current is about 2ns and FWHM=3.4ns, as can be seen in Fig. 5. Then, still keeping up carrier injection gives rise to a further increase of the gain in the laser active area. Theoretical models using a quasi-static approach show, that due to these changes in the complex refractive index the threshold of the next higher order transversal mode is reached. After an additional delay time of roughly 1.5ns the laser radiates a very powerful and short single pulse at shorter wavelengths. The optical field of this pulse is both index- and gain-guided. A more detailed understanding using a full time-dependent approach is expected from further investigations.

Laser pulses with an optical peak power of 128W and pulse duration of 32ps have been obtained with a $2.032\mu\text{m} \times 76.2\mu\text{m}$ emitting area, which exceeds the rated optical power by a factor of 55. A laser diode with an emitting area twice as large delivers 253W and a FWHM of 44ps. The pulses in Fig. 6 have been measured with a 60GHz photodetector. These lasing characteristics are the most advanced values reported so far for commercially available single chip laser diodes with comparable emitting areas.

Preliminary simulation of the laser diodes is based on the drift-diffusion model for electrons and holes under steady state condition (Gel'mont et al [6], Sola [7], Volpe [13]). A more profound understanding of the physical effects are expected from numerical simulations involving the time-evolution of the strong carrier injection process, Biernat et al [14].

IV. EXPERIMENTAL RESULTS

Fig. 7 shows the attained measurement uncertainty at a distance of 1.5 meters. An uncertainty of less than $\pm 300\mu\text{m}$ has been obtained using averaging over 16 measurements for each grid point.

Fig. 8 and 9 show the scanned image of a standard plug for a wall-socket as reflectance image and 3D-wireframe, respectively. For the reflectance image the difference in intensity of the reflected and the reference pulse is coded into a color table from black (maximum difference) to white (minimum difference) for each pixel. Because of the fact that the scanning mirrors can be moved very accurately in very small steps, the pixel size can even be somewhat smaller than the spot size of the laser beam. For the 3D-wireframe the difference calculated from the time separation of the reflected and reference pulse of each raster point is plotted in the xy-plane.

The distance data can also be coded into a color table. The result is shown in Fig. 10a, which also contains the reflectance image of the same object (Beethoven's head, Fig. 10c). After calculating the (in this example horizontal) derivative of Fig. 10a, a gradient image is obtained as can be seen in Fig. 10b. The effect of a virtual light source from the left can be observed. The derivative of the distance uncertainty is very much larger than the uncertainty itself, so in this case the gradient image creates the impression of a stone texture on the object. To reduce this effect, various methods of filtering can be done. Using a low-pass filter (e.g. a spline approximation with constant weight factors), a certain amount of edge-smoothing occurs. This can be circumvented by using a Medianfilter which does not calculate an average value, but which sorts the distance values of the actual pixel and the neighbouring ones. The value in the middle of the linear array is used as the filtered distance. This does not smooth sharp edges in the image, only the noise is reduced. Image processing in general can enhance the resolution and reduce the distance-uncertainty of the scanned pictures.

V. CONCLUSIONS

A fundamentally new modulation technique has been developed for weakly index-guiding laser diode structures. It has been shown that the application to well-known SH laser diodes exhibits extremely improved lasing characteristics never observed before. The new modulation scheme based on a fast 'superinjection' of carriers into the active region of the device leads to powerful single laser spikes which are very useful for laser radar applications.

A high PRF eye-safe laser radar for precise 3D imaging has been set up. The attained measurement uncertainty is less than $300\mu\text{m}$, the spot size is less than 1mm. Other applications such as quality assurance of hot workpieces (Kompa [10]), precise velocity measurement and identification of vehicles are under investigation (Kompa [11]).

REFERENCES

- [1] A. Rodriguez, A. Comeron, A. Elias, E. Gonzales, J.L. Montesino-Espartero, and G. Rodriguez, "Low-power coherent laser radar velocimeter", Conf. Proc. of 25th European Microwave Conf. EuMC'95, pp. 485-489
- [2] CENELEC, "Radiation Safety of Laser Products, Equipments, Classification, Requirements and User's Guide", European Standard EN 60825, Brussel, 1991
- [3] J.R. Meyer-Arendt, "Introduction to classical and modern optics", Englewood Cliffs, NJ:Prentice-Hall, 1989
- [4] G. Kompa, "Optical short range radar for level control measurement", IEE Proceedings, Vol. 131, Part H, No. 3, pp. 159-165, June 1984

- [5] P.G. Eliseev, G. Beister, A.E. Drakin, G. Erbert, V.P. Konyaev, and J. Maeger, "Study of strained-layer InGaAs/GaAs/SQW RW lasers including analysis of internal coupling of modes and antiguiding effects", SPIE's Int. Symp. OE/LASE'94, Los Angeles, USA, Paper 2146-23, published in SPIE Vol. 2146, pp. 185-194, 1994
- [6] B.L. Gel'mont, V.A. Elyukhin, G.G. Zegrya, E.L. Portnoi, and M.K. Ebanoidze, "Threshold characteristics of an injection laser with one lightly doped heterojunction", Sov. Phys. Semicond. 20 (11), pp. 1289-1291, 1994
- [7] J. Sola, "Generation of optical pulses with single heretrostructure laser diodes for radartype sensors", diploma thesis, University of Kassel, 1994 (available only at HFT, University of Kassel)
- [8] G. Kompa, "Extended time sampling for accurate optical pulse reflection measurement in level control", IEEE Trans. Instrumentation and Measurement, Vol. IM-33, No. 2, pp. 97-100, June 1984
- [9] A. Stolze and G. Kompa, "Nonlinear modelling of dispersive photodiodes based on frequency- and time-domain measurements", Conf. proc. of 26th European Microwave Conf. EuMC'96, pp. 379-381
- [10] G. Kompa, "Pulsed laser radar for 3D-quality assurance of hot workpieces", Proc. 2nd Congress for Optical Sensor Technology, measuring Techniques and Electronics (OPTO 96), Leipzig, Germany, Sept. 1996, Paper 4.2
- [11] G. Kompa, "Powerful picosecond-pulsed laser radar with micrometer ranging resolution", Conf. Proc. of 26th European Microwave Conf. EuMC'96, pp. 147-152
- [12] H. Höfler, N. Dimopoulos, B. Metzger, R. Müller, H. Wölfelschneider, and E. Wagner, "Distance measurement by phase shift evaluation - system conceptualisation and applications", Proc. 2nd Congress for Optical Sensor Technology, Measuring Techniques and Electronics (OPTO 96), Leipzig, Germany, Sept. 1996, Paper 4.1
- [13] F. Volpe, "Generation of powerful optical picosecond pulses from semiconductor lasers used for near-field ranging with submillimeter accuracy", doctoral thesis (in German), University of Kassel, 1994
- [14] A. Biernat, G. Ridinó, and G. Kompa, "Numerical Transient Simulation of SH Laser Diodes under Strong and Highly Dynamic Carrier Injection", Conf. Proc. of Int. IEEE Workshop "Experimentally based FET device modelling and related nonlinear circuit design", 17.-18. July, University of Kassel, Germany

FIGURES

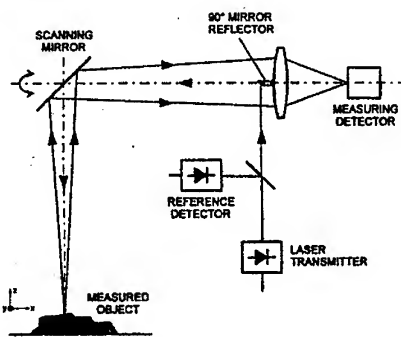


Fig. 1: Laser radar arrangement for 3D imaging (after Ref. [12])

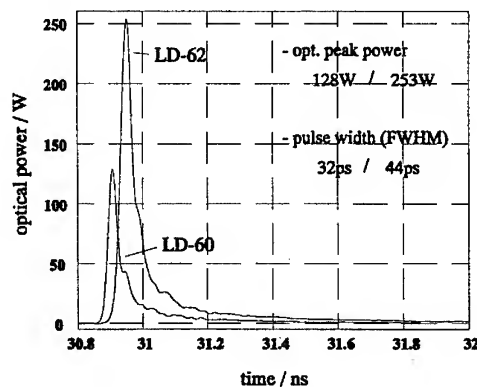


Fig. 6: Measured laser pulses of two different diodes

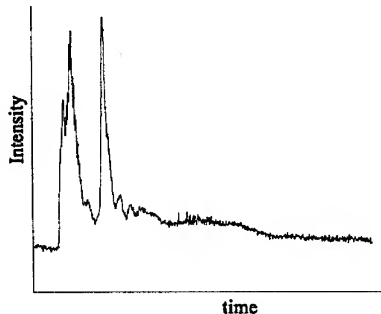


Fig. 2: Optical output of a 3-stack laser diode

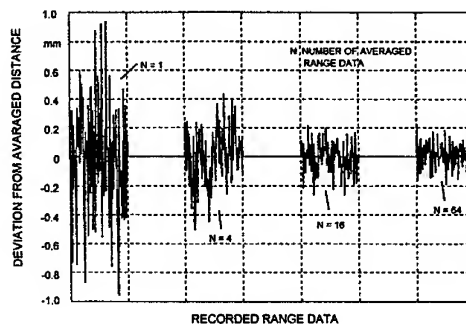


Fig. 7: Attained measurement uncertainty as a function of the number of averaged range data. N=16 has been used for imaging

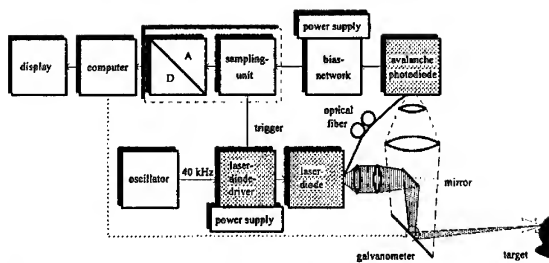


Fig. 3: Block diagram of the realized pulse laser radar

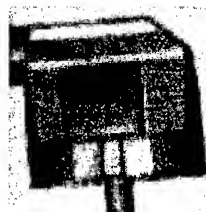


Fig. 8: Imaged standard plug for a wall-socket (contour). The size is 45 mm x 45 mm.

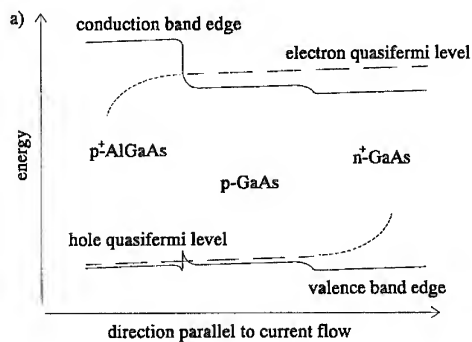


Fig. 4: Band structure and refractive index profile

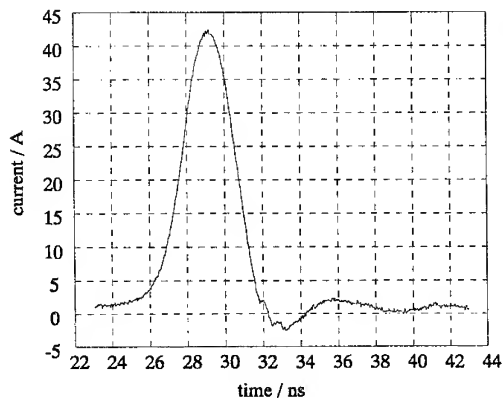


Fig. 5: Typical current pulse of the laser diode driver

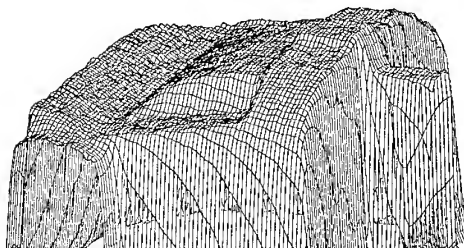


Fig. 9: Wireframe of the imaged plug viewed from the lower left corner of Fig. 8

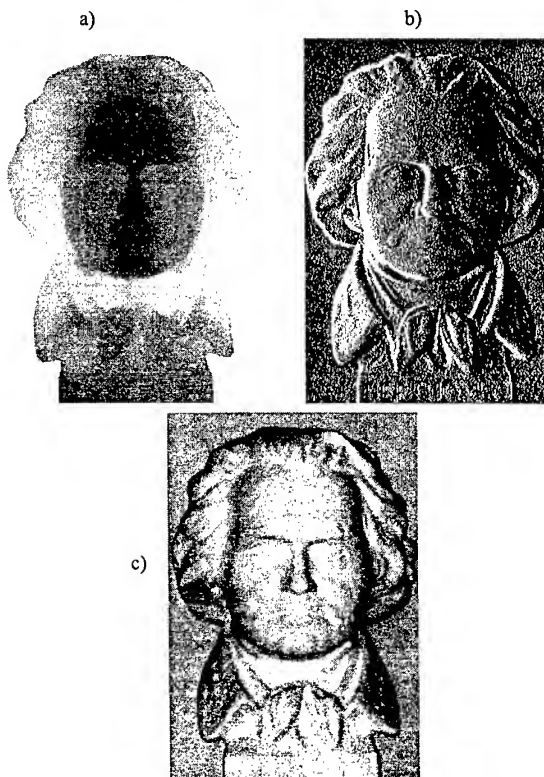


Fig. 10: Scanned image of Beethoven's head (130x190mm)
a) depth information
b) horizontal gradient of Fig. 10a
c) reflectance image

SCAN-OPTIMIZED INTEGRATED LENS ANTENNAS

M.J.M. van der Vorst, P.J.I. de Maagt* and M.H.A.J. Herben

Eindhoven University of Technology, Faculty of Electrical Engineering P.O. Box 513,
5600 MB Eindhoven, The Netherlands, e-mail: M.J.M.v.d.Vorst@ele.tue.nl

* European Space Agency ESTEC, P.O. Box 299, 2200 AG Noordwijk, The Netherlands

Abstract

In this paper the scan properties of integrated lens antennas with a quarter-wavelength matching layer are analyzed. For beam scanning on and within a cone, optimum feed positions are determined. It appears that for beam scanning on a cone the elliptical lens is the best choice if a small scan angle is required while the extended hemispherical lens should be used in case of a large scan angle. For beam scanning within a cone it is recommended to select an elliptical lens if a large average directivity is required while the extended hemispherical lens appears to be the best choice if a small variation in the directivity is important.

1 Introduction

In recent years the advancement of photo-lithographical and micromachining techniques has resulted in a very reliable and repeatable process for creating planar structures on dielectric substrates. This emergence of planar technology now allows millimeter-wave system components to be accurately produced in large numbers at low cost. Consequently, planar integrated antennas become a viable alternative for classical waveguide-based designs at these high frequencies [1]. Many commercial applications are already known in the low millimeter-wave range and can for example be found in the field of diagnostics, autonomous aircraft landing systems, car collision avoidance and traffic management.

It is obvious that with planar integrated technology extremely compact receivers can be made and that the technology is quite suitable for imaging antenna arrays (single lens or fly's eye) which are of great interest for spaceborne radio astronomy and atmospheric research. Particularly, in radio astronomy most of the spectral line emitting regions are usually spatially extended over many observing beams in the sky, and mapping is required to astrophysically understand the regions under study. In atmospheric research multi-beams allow to make pushbroom measurements in limb-sounding experiments.

A disadvantage of the integrated lens antenna is the large amount of power (typical 20-30%) that is reflected at the lens surface, especially for the high dielectric-constant materials as Alumina and GaAs [2]. These internal reflections degrade the performance of the antenna [3] and therefore a matching layer should be applied, which reduces the reflection losses to about 5%. The radiation properties of laterally-defocused extended hemispherical lens antennas without matching layer lens were studied by Filipovic et al. [4]. In the present paper we will investigate scan-optimized single lens antenna systems with a quarter-wavelength matching layer and an elliptical or extended hemispherical lens. The choice of this type of matching layer instead of a layer with an optimized thickness is mainly because of the ease of fabrication. Moreover, in Ref. 2 it is shown that the performance of both type of layers is quite similar. As feed element a double dipole with backing reflector (b.r.) [5,6] will be used. Of course the same analysis can be performed for double-slot feeds, but the results will not differ significantly because the main reason for beam scanning is the modification of the phase of the incident field at the lens surface due to the feed displacement.

2 Geometry and modeling of the lens antenna

A two-dimensional cross-section of the integrated lens antenna with matching layer and a laterally-defocused planar feed are depicted in Figure 1. Actually, this feed represents a double-dipole with backing reflector, but the ground plane is not shown here. The orientation of the double dipole is along

the z -axis, which means that the cross-section is in the H-plane.

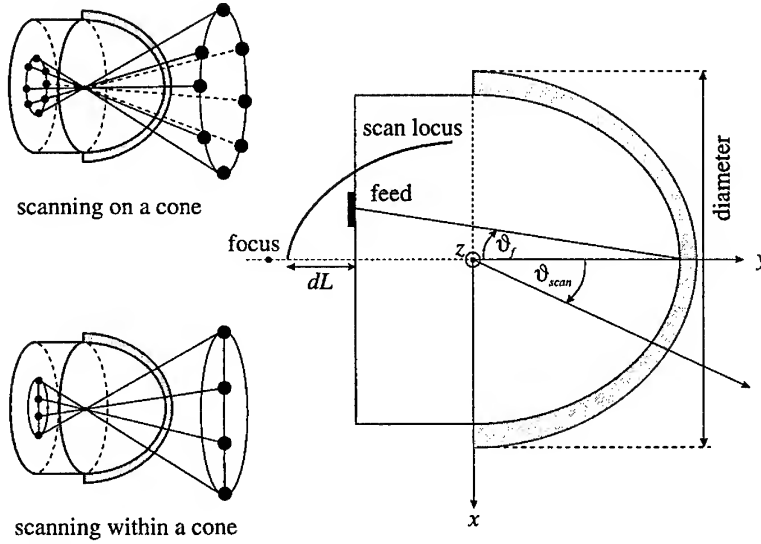


Figure 1: Geometry of integrated lens antenna with scanned beams.

The length of the double dipole equals $0.5\lambda_d$ while the distance between the elements is $0.4\lambda_d$, resulting in a nearly rotationally symmetric feed pattern. The backing reflector is placed $0.25\lambda_d$ behind the double-dipole feed in order to improve its directivity towards the lens surface. It should be noted that λ_d denotes the wavelength in the dielectric. For the electromagnetic modeling of the planar feed a cosine current distribution is assumed over each dipole element. This is justified because the width over length ratio of planar dipole elements is generally very small. For the calculation of the field within the dielectric the influence of the metal backing reflector is accounted for by introducing two image dipole elements which are 180° out of phase with the real dipole elements. Typical radiation patterns of this type of planar feed are shown in Ref. 5 for various lens materials. The scan locus shown in Figure 1 indicates the feed positions which yield maximum directivity for scanned beams. The axial displacement dL denotes the distance between a certain scan plane (perpendicular to the y -axis) and the intersection point of the scan locus with the y -axis.

3 Off-axis displacement from focus

As an example the far-field patterns of two elliptical lens antennas are calculated for an H-plane off-axis feed displacement of 10% of the lens radius (7.5 mm) at a frequency of 250 GHz. In Figure 2 the H-plane power patterns are depicted for an Alumina ($\epsilon_r = 9.8$) and a GaAs ($\epsilon_r = 12.8$) lens material and it is seen that a certain off-axis feed displacement results in a larger scan angle when the lens is made of GaAs instead of Alumina. This follows from a simple ray optics analysis, which shows that the central ray is refracted as:

$$\sin \vartheta_f = \frac{\sin \vartheta_{scan}}{\sqrt{\epsilon_r}} \quad (1)$$

where ϑ_f denotes the angle of the central ray with the y -axis.

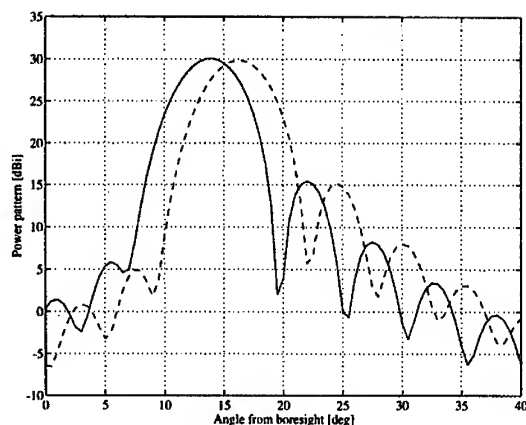
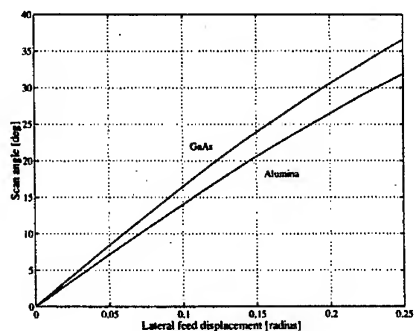


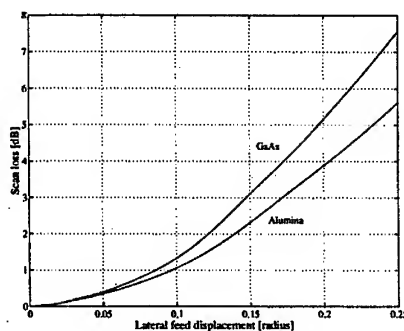
Figure 2: *H*-plane power patterns for two elliptical lens antennas, illuminated by a double-dipole feed with b.r. at 250 GHz (solid: Alumina and dashed: GaAs).

Obviously, the scanned patterns are not just shifted versions of the focused patterns. This would be the case if a feed displacement would introduce only a linear phase aberration. However, also higher order phase aberrations occur, resulting in pattern distortions.

In Figure 3a the scan angles are given as a function of the off-axis feed displacement, while 3b shows the corresponding scan loss curves. For feed displacements up to 25% of the lens radius it appears that the relation between scan angle and off-axis displacement is almost linear, which is in agreement with Equation (1) for small ϑ_f . From combining Figures 3a and 3b it can be concluded that, given a certain scan angle, the scan losses are slightly higher for Alumina than for GaAs lenses due to the larger feed displacements required. Consequently, in multi-beam operation (e.g. in a pushbroom system) a GaAs lens will have the advantage of a higher directivity. However, a disadvantage of GaAs with respect to Alumina is the possibility of having larger mutual couplings between the different double-dipole feed elements as a result of the higher packing density.



(a)



(b)

Figure 3: Scan angle (a) and scan loss (b) as a function of the *H*-plane off-axis displacement.

4 Maximum-directivity scan locus

The previous scan angle curves were computed for an off-axis feed displacement in the H-plane. Like in reflector antennas, the unwanted phase aberrations introduced by a feed displacement in the (lateral) x -direction can partly be reduced by also tolerating a feed displacement in the (axial) y -direction [7]. This results in a less distorted pattern with a higher directivity. Figure 4a shows the maximum-directivity scan curves for both lens materials and for two lens shapes, i.e. elliptical (ell) and extended hemispherical (hem). It appears that the scan loci for the elliptical lenses do not exactly start in the focus. This is explained by the fact that for a very small axial feed displacement towards the lens surface the increase of the spillover and transmission efficiency dominates the decrease in phase efficiency [8]. For an axial feed displacement of approximately 0.4% of the lens radius, with the focus as a reference, the directivity is at its maximum.

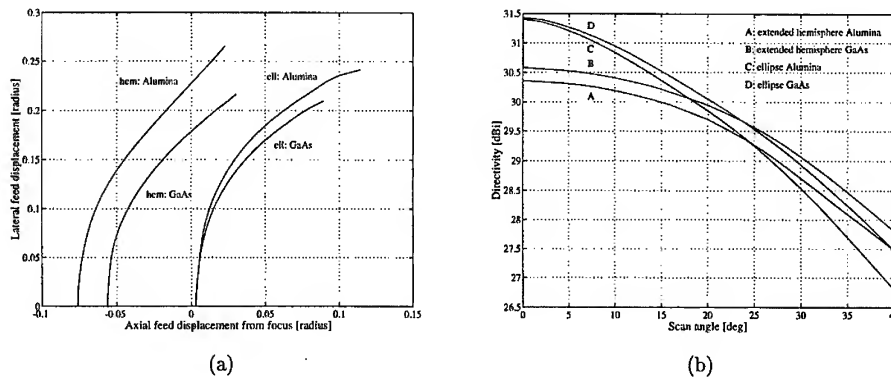


Figure 4: *H-plane scan loci (a) and corresponding directivity curves (b).*

Figure 4a also shows that as a result of the larger refractive index of GaAs compared to Alumina the scan loci are longer for the latter. Another remark is that for high dielectric-constant materials the elliptical lens can be accurately synthesized by an extended hemispherical lens, and this is the reason why the scan loci for GaAs are more alike than those for Alumina. Figure 4b shows the directivity as a function of scan angle for the four integrated lens antennas considered. Comparing Figures 3 and 4 clearly demonstrates that the directivity can be increased substantially by an additional feed displacement in the y -direction. Another conclusion that can be drawn from Figure 4 is that for scan angles up to 24-25° it is better to use an elliptical lens if a large directivity is required while for larger scan angles the extended hemispherical antenna performs better.

If the scan loci of Figure 4a are rotated around the y -axis, scan surfaces are obtained. The intersection of such a scan surface with a plane perpendicular to the y -axis gives a ring on which the feed elements should be placed if beam scanning on a cone is required. However, when beam scanning within a cone is needed the optimum feed positions are not located on a plane but on a curved surface. Because such an antenna system cannot be realized in practice, it is necessary to find an optimum scan plane.

5 Optimum scan plane

The optimum scan plane for beam scanning within a cone will be defined as the plane that is perpendicular to the y -axis and gives the highest average directivity of all possible scanned beams within that cone. The distance of this plane to the maximum directivity feed position (zero scan angle) is denoted by dL , as can be seen in Figure 2. In Figure 5a the displacement dL is given as a function of the maximum scan angle for the four lens antenna designs considered. The corresponding average directivities are depicted in Figure 5b, and it is seen that the elliptical lenses give the best results.

For some scanning applications it is important that the variation of the directivity is small. Therefore, the differences between the maximum and the minimum directivity are plotted in Figure 5c. It should be noted that these directivity variations are calculated by subtracting the maximum and minimum directivity in dB, while Figure 5b was obtained by calculating the average of the true linear (so not in dB) directivity values. Figure 5c clearly shows that the extended hemispherical lens antenna appears to be a better option if a small directivity variation is required. This agrees with wide-angle beam scanning with reflector antennas where the spherical reflector performs better than the parabolic reflector [9].

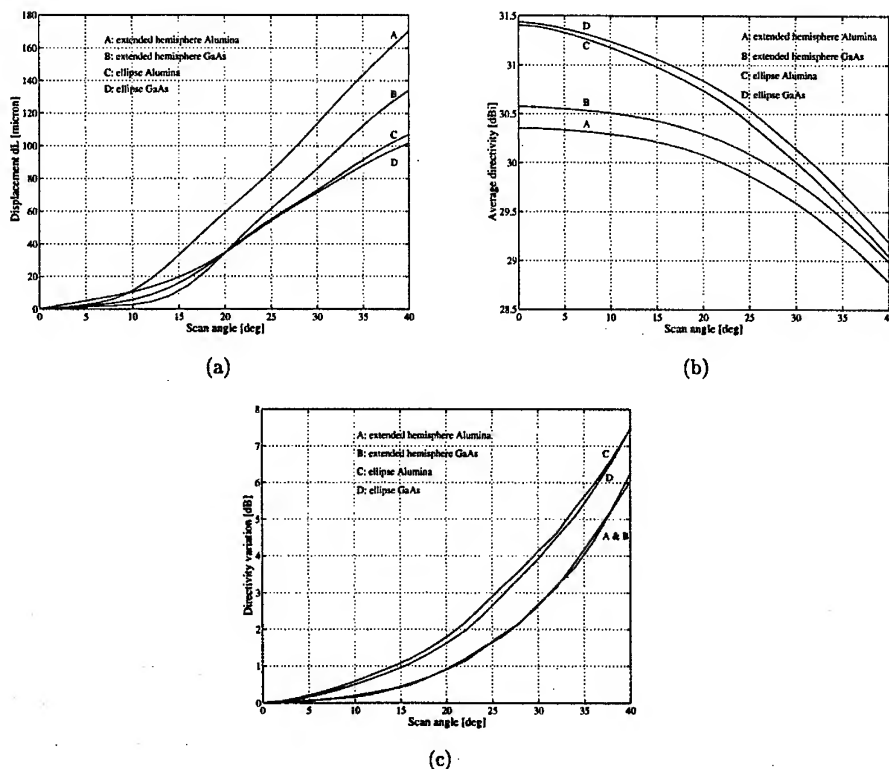


Figure 5: Displacement dL (a), average directivity (b) and directivity variation (c) in optimum scan plane.

6 Conclusions

For scanning applications, which require a scanning beam on or within a cone, the integrated lens antenna with quarter-wavelength matching layer can be used in a single lens imaging antenna configuration. However, there appears to be a substantial difference between an elliptical and an extended hemispherical lens. To obtain a good performance for scanning (small scan angles) on a cone an elliptical lens should be chosen, while for larger scan angles the extended hemispherical lens shows the highest directivities.

On the other hand, if a certain application requires scanning within a cone then the criterion of a high average directivity or a small directivity variation results in an antenna system with an elliptical or an extended hemispherical lens, respectively.

References

- [1] Rebeiz, G.M., *Millimeter-wave and terahertz integrated circuit antennas*, Proceedings of the IEEE, vol. 80, pp. 1748-1770, 1992.
- [2] van der Vorst, M.J.M., P.J.I. de Maagt and M.H.A.J. Herben, *Matching layers for integrated lens antennas*, Proceedings of the International Symposium on Antennas (JINA '96), pp. 511-515, Nice, France, 1996.
- [3] van der Vorst, M.J.M., P.J.I. de Maagt and M.H.A.J. Herben, *Influence of internal reflections on the far-field pattern of integrated lens antennas*, Proceedings of the International Symposium on Antennas and Propagation (ISAP '96), pp. 1225-1228, Chiba, Japan, 1996.
- [4] Filipovic, D.F. et al., *Off-axis properties of Silicon and Quartz dielectric lens antennas*, IEEE Trans. on Antennas and Propagat., vol. 45, pp. 760-766, 1997.
- [5] van der Vorst, M.J.M., *Design and analysis of integrated lens antennas*, Graduation report, Faculty of Electrical Engineering, Eindhoven University of Technology, 1995.
- [6] Skalare, A., Th. de Graauw and H. van de Stadt, *A planar dipole antenna with an elliptical lens*, Microwave and Optical Technology Letters, vol. 4, pp. 9-12, 1991.
- [7] Herben, M.H.A.J. et al., *Geometrical optical characteristics of the Schwarzschild scanning antenna (comparison with Cassegrain antenna)*, IEE Proceedings, Pt. H., vol. 129, pp. 315-320, 1982.
- [8] de Maagt, P.J.I., M.J.M. van der Vorst and M.H.A.J. Herben, *Internal reflections of and matching layers for integrated lens antennas*, Proceedings of the seventh International Symposium on Space Terahertz Technology, pp. 282-287, Virginia, USA, 1996.
- [9] Love, A.W., *Reflector Antennas*, Part VII and IX, New York: IEEE Press, 1978.

Mutual Coupling between Transverse Slots in Cylindrical Structures

Johan Wettergren
Saab Ericsson Space AB
SE-405 15 Göteborg, Sweden

E-mail: johan.wettergren@space.se
Phone: +46 31 3354034, Fax: +46 31 3359520

ABSTRACT

We compute the mutual coupling between transverse slots in cylindrical structures. The coupling is included in the slot antenna analysis and the waveguide scattering parameters are determined. Results agree well with measured S parameters. A proposed SAR antenna structure, that cannot be analyzed with the conventional infinite ground plane couplings is used as an example of possible applications of this work.

1 INTRODUCTION

Traditionally, the outer structures of waveguide slot antennas have been assumed to be infinitely large ground planes. It was pointed out early, however, that this restriction might be a serious restriction [1]. As the need of dual-polarized antennas, for instance for SAR applications, has been pronounced lately [2, 3], it is time to remove this restriction. In the dual-polarized slot antennas there is not room for both transverse and longitudinal slots if grating lobes are to be avoided. Instead, the antennas need to be corrugated [2, 3], like the one in Fig. 1.

The proposed dual-polarized antennas [2, 3] have outer structures of cylindrical shapes. We therefore try to predict the mutual couplings between slots in such geometries, in order to include them in the overall slot antenna analysis. It is of great advantage to restrict the analysis to infinitely long cylindrical structures, rather than to treat arbitrary geometries, since the Fourier transform can be used along the structure to reduce the complexity of the analysis. Previously, we have analyzed longitudinal slots [4, 5] and now we consider transverse slots.

For slots in infinite ground planes, there is no need to distinguish between longitudinal and transverse slots, since they amount to the same thing. There is no preferred direction. In cylindrical geometries, however, the analysis of longitudinal and transverse slots are different. Longitudinal slots is the simpler case, since the analysis is restricted to the TE polarization. Transverse slots excite generally polarized fields. The longitudinal slots also have a longer extent in the longitudinal direction. This gives a narrower spatial spectrum, when the Fourier transform is used to simplify the analysis.

2 THEORY

In rigorous analyses of slot antennas [6], the structure is divided into canonical regions. The field problems of the regions are solved separately and then matched together using the moment method. This gives rise to a matrix equation. For instance, the antenna in Fig. 1 is described by

$$Y \begin{bmatrix} A_{1q} \\ A_{2q} \\ A_{3q} \\ A_{4q} \end{bmatrix} = \begin{bmatrix} i_{1p} \\ i_{2p} \\ 0 \\ 0 \end{bmatrix} \quad (1)$$

where A_{bq} are the coefficients of the basis functions in the apertures between the regions. In this case there are four regions: The interior of the waveguide, the cavities at the slot between the inner and outer surfaces of the waveguide and the cylindrical exterior region. The incident field reactions, i_{bp} , are the incident field in the waveguide weighted with the moment method weighting functions. Both the basis and weighting functions are chosen as a trigonometric expansion. The admittance matrix,

$$Y = \begin{bmatrix} y_{I pq}^{11} + y_{III pq}^{11} & y_{I pq}^{12} & -y_{III pq}^{13} & 0 \\ y_{I pq}^{21} & y_{I pq}^{22} & 0 & -y_{III pq}^{24} \\ -y_{III pq}^{31} & 0 & y_{III pq}^{33} + y_{IV pq}^{33} & y_{IV pq}^{34} \\ 0 & -y_{III pq}^{42} & y_{IV pq}^{43} & y_{III pq}^{44} + y_{IV pq}^{44} \end{bmatrix} \quad (2)$$

consists of the mutual couplings, y_{apq}^{bc} , between the apertures. The couplings in the exterior region, $y_{IV pq}^{44}$, represent the novelty of this work. Instead of using the conventional infinite ground plane couplings, we solve the field problem in an arbitrary cylindrical structure [7].

The external mutual couplings are computed in the spectral domain. A Fourier transform along the structure is utilized to reduce the dimensionality of the analysis. In the transformed domain, an integral equation has been formulated [8] with the induced currents on the structure as unknowns. These currents are directly related to the magnetic field, which in turn is part of the mutual coupling calculation. The integral equation was semi-decoupled to allow determination of one current component at the time [8]. This reduces

computer storage space and CPU time. The integral equations to solve are

$$\tilde{E}_z^i = \frac{ik_p^2\eta}{k} \int_C \tilde{J}_z \tilde{G} dl' + \frac{k_z\eta}{k} \int_C \frac{\partial \tilde{J}_l}{\partial l'} \tilde{G} dl' \quad (3)$$

$$\tilde{E}_l^i + \frac{ik_z}{k_p^2} \frac{\partial \tilde{E}_z^i}{\partial l} = ik\eta l \cdot \int_C \tilde{J}_l \tilde{G} dl' + \frac{ik\eta}{k_p^2} \frac{\partial}{\partial l} \int_C \frac{\partial \tilde{J}_l}{\partial l'} \tilde{G} dl' \quad (4)$$

where \tilde{E}_z^i and \tilde{E}_l^i are the longitudinal and transverse components of the incident tangential electric field on the surface. The sources of the incident fields are the electric fields or equivalent magnetic currents at the slots. The unknown induced electric current components, \tilde{J}_z^i and \tilde{J}_l^i , are computed with the moment method using the free space Green's function \tilde{G} . Subsectional basis functions in the form of triangles for \tilde{J}_l^i and pulses for \tilde{J}_z^i are used. The pulses and triangles are placed in correspondence to each other in order to produce an efficient solution [8].

The mutual couplings are computed in the transformed domain and inverse Fourier transformed numerically, since the spectral magnetic field was determined numerically. For an arbitrary cylindrical structure there are no closed form solutions. The numerical inverse transformation has a discretization and truncation according to

$$y_{IVpq}^{44}(z_0) \approx \frac{\Delta k_z}{2\pi} \left[\tilde{y}_{IVpq}^{44}(0) + 2 \sum_{n=1}^N \tilde{y}_{IVpq}^{44}(n\Delta k_z) \cos(n\Delta k_z z_0) \right] \quad (5)$$

where Δk_z is the sampling interval and z_0 is the longitudinal displacement between the slots. The discretization introduces a periodic array of slots, which is known as aliasing. We have used $\Delta k_z = k/20$, which corresponds to an array with 20λ between the slots. The truncation is done at $N = 400$ ($k_z = 20k$), which is at a fairly high value of the spectral wavenumber. This is necessary due to the broad spectrum of the transverse slots.

3 RESULTS

The antenna of Fig. 1 was fabricated in order to perform measurements as verification of the computations. The results are shown in Fig. 2. The two $30mm \times 3mm$ slots are centered in the broad wall of a $50.80mm \times 25.40mm$ waveguide. The waveguide wall is $1.625mm$ thick and the trough size is $45.8mm \times 23.5mm$. The distance between the slots, z_0 , is $16mm$.

The solid curve in Fig. 2 shows the computed scattering parameter S_{11} and the dashed curve shows S_{12} . The dotted curves show measurements of all four scattering parameters. The agreement between the computations and measurements is very good.

4 CONCLUSION

Transverse slots in cylindrical structures were analyzed with good agreement to measured scattering parameters. The considered geometry where two transverse slots radiate from the side wall of a trough cannot be analyzed with the conventional infinite ground plane methods.

5 ACKNOWLEDGMENT

I would like to thank Jiro Hirokawa, Per-Simon Kildal and Peter Slättman for discussions and advice to the work.

The work was supported by The Swedish National Board for Industrial and Technical Development (NUTEK), and reported to COST245 on "Phased array and array-fed antennas".

References

- [1] A. F. Stevenson. Theory of slots in rectangular wave-guides. *Journal of Applied Physics*, 19:24–38, January 1948.
- [2] Lars Josefsson and C. G. M. van't Klooster. Dual polarized slotted waveguide SAR antenna. In *IEEE AP-S Symposium*, pages 625–628, July 1992.
- [3] A. G. Derneryd, R. N. O. Petersson, and P. Ingvarson. Slotted waveguide antennas for remote sensing satellites. In *PIERS*, July 1994.
- [4] Johan Wettergren and Per-Simon Kildal. Admittance of a longitudinal waveguide slot radiating into an arbitrary cylindrical structure. *IEEE Transactions on Antennas and Propagation*, AP-43:667–673, August 1995.
- [5] Johan Wettergren and Anders Derneryd. Mutual coupling between longitudinal slots in cylindrical structures. In *European Microwave Conference*, pages 377–380, Bologna, Italy, September 1995.
- [6] T. Vu Khac and C. T. Carson. Coupling by slots in rectangular waveguides with arbitrary wall thickness. *Electronic Letters*, 8(18):456–458, September 1972.
- [7] Johan Wettergren. *Cylindrical Waveguide Slot Antenna Analysis*. PhD thesis, Chalmers University of Technology, January 1997. Technical Report No. 298.
- [8] Johan Wettergren and Peter Slättman. An electric field integral equation for cylindrical structures. *IEE Proceedings—Microwaves, Antennas and Propagation*, 143(2):147–151, April 1996.

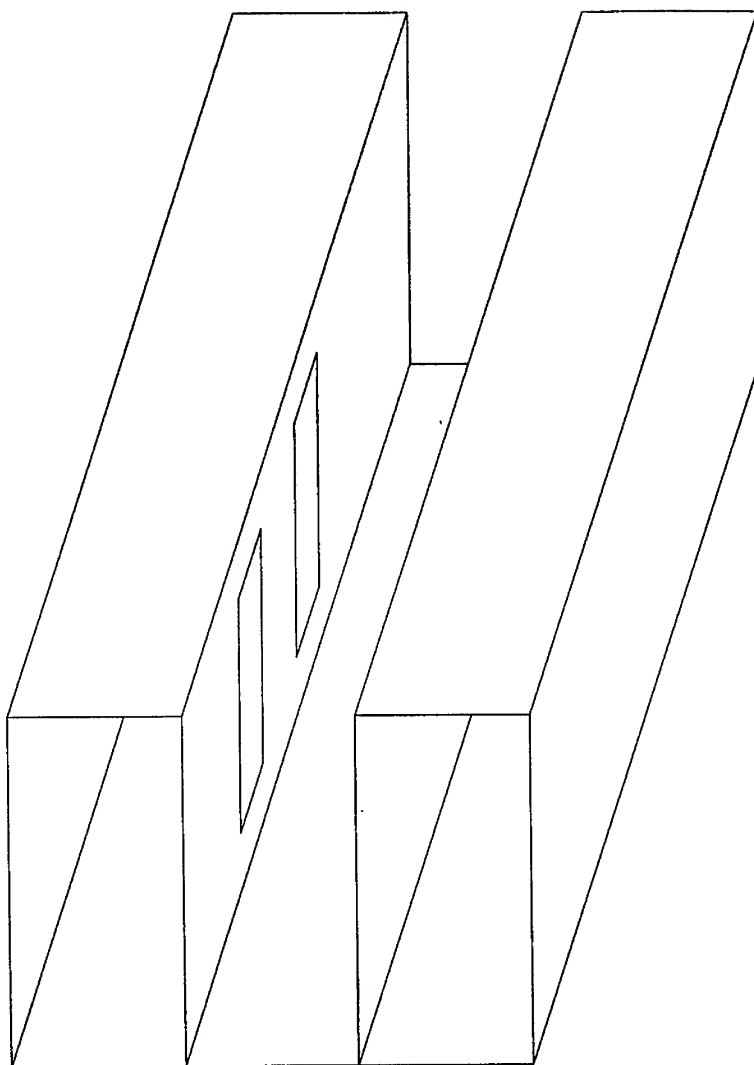


Figure 1: Two transverse waveguide slots radiating into a trough. The antenna can be made dual-polarized by adding longitudinal slots in the bottom of the trough.

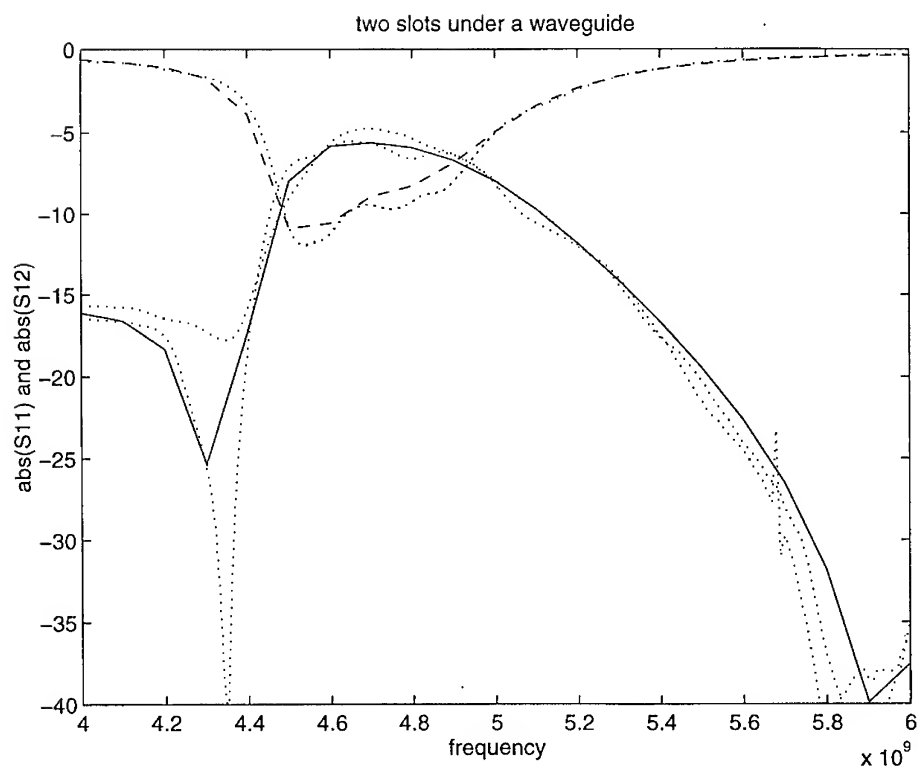


Figure 2: The magnitude in dB of S_{11} (solid) and S_{12} (dashed) for the waveguide slot antenna of Fig. 1 with two transverse slots in one waveguide. The dotted lines show measurements of all 4 scattering parameters.

A Simple Approach to a Statistical Path Loss Model for Indoor Communications

Constantino Pérez-Vega and Jose Luis García García.
Communications Engineering Department
University of Cantabria
Av. de los Castros s/n. 39005 -Santander, Spain

Abstract

Path-loss in indoor environments is investigated at 1.8 GHz, using a power-law model where the exponent of the distance is the descriptive random variable. The model is extremely simple and easily applicable in practice by working engineers who need only make a few measurements to get a knowledge of path loss sufficient for many applications. The model fits well experimental data in various environments under different propagation conditions, including cross polarization, and the observed behavior of the exponent suggests the possibility of using only one distribution function to statistically characterize path loss.

1. Introduction

A complete channel description requires a good knowledge not only of path loss, but also of delay spread, angle of arrival distribution, etc. However, in many engineering applications where the main objective is to define the required transmitted power, necessary to cover a specific service area for a given signal to noise ratio of the received signal, a simple statistical path loss model is a useful tool which allows to estimate the fade margins with which a system must operate in a particular indoor environment. The model investigated is statistical and does not require a detailed knowledge of environment topography. However, its application requires of measurements in order to get the statistical parameters, i.e., mean and standard deviation, to be used in a particular propagation environment. The descriptive parameter in this path loss model is the exponent of the distance; i.e. the received power can be expressed as:

$$P_r = \frac{P_{RAD}}{d^n} \left(\frac{\lambda}{4\pi} \right)^2 \quad (1)$$

where P_{RAD} is the radiated power; d , the distance in meters between transmitting and receiving antennas, and λ the wavelength. n is the exponent of the distance and is assumed a random variable in this model. In small or local areas a few wavelengths in radius, n varies randomly, its mean and standard deviation being larger at distances up to about 20λ from the transmitting antenna. At larger distances, the local means tend to be nearly constant in a given environment under the same propagation conditions. This characteristic in the behavior of n was observed for various propagation conditions in different buildings: line-of-sight (LOS), shadowing (NLOS) and total obstruction between the transmitting and receiving antennas by walls and floors (OBS), and suggests that, in the range of distances encountered in indoor communications, only one type of statistics can be used to describe path loss.

2. Theory

In (1) the received power, P_r , can be assumed random and expressed as:

$$\langle P_r \rangle = P_{r0} \langle \alpha_p \rangle \quad (2)$$

Where P_{r0} is the free space value of the received power and $\langle \alpha_p \rangle$ is an attenuation (or gain) factor, dependent on propagation mechanisms which, in general, are not possible to quantify individually, and include directive gains of antennas, reflection, diffraction, etc. The bracket notation is used to stress the random nature of the variable. From (1) it can be seen that:

$$\langle \alpha_p \rangle = \frac{1}{d^{(n)-2}} \quad (3)$$

is the excess attenuation referred to free space conditions. Using dB form, the path loss can now be written as:

$$L_{dB} = 10\langle n \rangle \log(d) + K \quad (4)$$

where K is the free space attenuation at 1 m. The value of n can be obtained directly as:

$$\langle n \rangle = \frac{P_{RAD} - \langle P_R \rangle - K}{10 \log(d)} \quad (5)$$

where, in actual conditions, P_{RAD} is known and the samples of the received power, $\langle P_R \rangle$ are obtained through measurements in the particular environment. The model given by equation (4) is formally equal to other models previously reported in the literature [1]-[3], the main difference is that here, the exponent of distance is treated as a random variable and no further variables are introduced, nor assumptions made about its statistical behavior.

3. Experimental procedure

Various experiments were made in different buildings of the University of Cantabria, Spain. One of them, of simple geometry with open areas and straight aisles. The other, of complex geometry, with narrow aisles occasionally curved, and with numerous obstructions by walls, columns and furniture. Measurement environments were chosen for well differentiated propagation conditions: line-of-sight (LOS), non line of sight (NLOS), mainly shadowing, and total obstruction between transmitter and receiver (OBS). Additionally the effect of depolarization was also measured. All experiments were made with a 10 dBm unmodulated carrier at 1.8 GHz using an RF signal generator as transmitter and a spectrum analyzer as receiver at distances ranging between 1 and 32 m. Transmitting and receiving antennas were $\lambda/4$ vertical monopoles at 2 m and 1.5 m height respectively. A $\lambda/2$ rotatable dipole was also used for reception, thus the copolar and crosspolar powers of the received signal could be easily measured at the same sampling points. The measurement procedure was mainly manual, and devised in order to make it easily applicable in practice, bearing in mind that it is essential that signal measurements should be made in a manner that permits the basic parameters to be extracted with an appropriate level of accuracy [4]. Thus, the sampling interval, i.e. the distance between individual samples, distance between local areas, and minimum number of samples per local area, must be properly defined. An empirical approach was followed with this purpose. Local areas were defined as squares of maximum area of 1 m², with a minimum separation between them of 20λ and several sets of measurements were taken over the same local areas, with sampling intervals of 1, 2.5 and 5 cm. Differences in the mean received power were within ± 1.5 dB for 1 and 2.5 cm intervals, and in the order of ± 5 dB for 2.5 and 5 cm intervals. A maximum sampling interval of 2.5 cm was considered adequate for practical purposes.

In order to establish the minimum number of samples required per local area, a similar approach was followed. Various sets of measurements were made over the same local areas in LOS and NLOS conditions, taking first 500 samples, then 100 and finally several sets of 50 samples. In all cases, the errors in the mean values of the exponent were less than 5%, and of 7.5% in the standard deviations. As a consequence, a minimum value of 50 samples per local area was considered sufficient. Such figure is in good agreement with the criteria suggested by other authors [5], [6], and with those drawn theoretically [7]. The distance between samples, as well as the number of samples per local area, results in a very simple measurement procedure to be used by practicing engineers who need to make only a few measurements in order to extract the basic parameters to get good idea of path loss behavior, and who do not need to have a deeper knowledge of channel dynamics. Such knowledge is sufficient in many practical applications where the main

objective is to dimension the power of a communications system and provides reliable information about the fading margins required in a practical design.

LOS measurements were performed in corridors and open areas, at distances between 1 and 32 m. NLOS, between perpendicular corridors, corridors into open areas and open areas partially obstructed by clutter at distances up to 25 m and, finally OBS measurements were made with the transmitter inside a closed room and the receiver in separated rooms and corridors at distances up to 18 m from the obstructing wall. Measurements with transmitter and receiver in different floors were also performed. In all cases, transmission was vertically polarized, and the transmitter kept fixed for each set of measurements while moving the receiver. Finally, polarization measurements were made taking, at each measurement point, two samples of the received power, one with the receiving antenna vertical and then, rotating it to an horizontal position. Measurements were made in 73 local areas in the various environments and for the propagation conditions already mentioned.

4. Statistics of the exponent

The statistical behavior of either received power, envelope amplitude, or path loss can always be described by unimodal and asymmetrical probability density functions (pdf), and it is assumed that the statistics of the exponent of distance should behave in the same way. However, since the relationship between n and the power is not linear, the function that best describes n will not, necessarily be the same as that of the power, and it cannot be assumed *a priori* that n will follow distributions such as Rayleigh, Rice or log-normal. Fitting of n to these functions was investigated with acceptable results, however, large deviations were observed in a significant number of cases, particularly at the tails. Such deviations would lead to very pessimistic predictions of fade margins, unless some corrections are introduced. Several empirical corrections were attempted to obtain better fittings to actual data, however, no general rule was found for a correction that worked in all cases. Therefore, fitting to other distributions was investigated, in particular gamma [8], Weibull [9] and Nakagami [10], with remarkably better results. In most cases, differences in fitting to these functions were only marginal, with the gamma distribution producing smaller errors and higher correlation coefficients between the theoretical function and the distribution of the samples. It must be said that the particular distribution functions used to fit the experimental data were used only as mathematical tools capable of describing the exponent behavior, and no attempt was made to establish a relationship between their parameters and the physical process. Fitting of data to probability density functions used the mean and standard deviation of the samples as input variables; the resulting cumulative distributions (cdf) being easily obtained from them. Goodness of fit was measured in terms of the rms error in pdf's between the theoretical function and experimental data, cdf's, and correlation coefficients in each case. Fitting errors with gamma distribution were in the order of 0.025 to 0.1 for pdf's, and between 0.01 and 0.068 for cdf's, whereas correlation coefficients were between 0.75 and 0.99 for pdf's and between 0.975 and 0.9995 for cdf's. Similar figures were observed with Weibull and Nakagami distributions.

In all cases investigated, two distinct regions of exponent behavior can be identified. At distances up to about 20λ from the transmitter in LOS and OBS conditions, and from the scattering edge in NLOS, means and standard deviations are higher and decay, approximately, in exponential form to nearly constant values, with small fluctuations, at distances greater than, approximately, 20λ . Typical values for LOS conditions in corridors are shown in Table 1.

Table 1

In the near region ($d < 20\lambda$), values of n as high as 8.4 and as low as 0.2 were observed in local areas at 2 m distance, with standard deviations about three times as large as those observed in the distant region ($d > 20\lambda$), where maximum and minimum values of n were 4.1 and 1.2 respectively. The terms *near region* and *distant region* used before are arbitrary, and not necessarily related with the concepts of near (induction) field and far (Fraunhofer) field and must not be confused with them. No attempt is made here to relate the observed multipath effects with such concepts. It can be said that the measurements made at distances

smaller than 20λ from the transmitting antenna do not reflect actual propagation conditions in large area, and from a practical point of view, if values of the exponent in this region are considered, a pessimistic coverage prediction will result. However, attention must be paid to NLOS (shadowing) cases where, in the vicinity of diffracting corners, the received power follows a similar behavior than that in the neighborhood of the transmitting antenna. In practical situations these conditions must be properly evaluated for particular cases. In Table II, the statistical parameters of the exponent are presented for the various experimental cases. Such values correspond to samples in the distant region defined before.

Table 2

Mean values of the exponent are in reasonable agreement with those reported by others [11], [12]. Standard deviations are environment-sensible, being higher where the amount of furniture, columns and objects is larger. This effect has direct consequences on the fade margin as can be seen in figure 1, where the gamma cumulative distribution for two LOS cases in corridors in different buildings is shown. The mean values of the exponent are almost equal (1.96 and 1.97), however the standard deviation is larger in building 1. From the figure it seems clear that the second building offers better LOS propagation conditions. For the cases shown in figure 1, 99% of values of the exponent will be below 3.75 for building 1, and below 2.6 for building 2 and, for a distance of, say, 100 m, the excess path loss with respect to free space conditions will be 22.8 dB for the first building and 7.8 dB for the second. The differences in the expected path losses in worst conditions (99% of values of the exponent in this example), are due only to the different standard deviations, since mean values are approximately equal.

Figure 1

Similar plots can be produced for other environments and propagation conditions. As mentioned before, the gamma distribution function fits very well in general, to experimental data, and equation (4) can be easily used to describe the statistical behavior. Since the mean value of the exponent is assumed constant in the range of distances of interest, there is no need to specifically describe the large area behavior with this model. Furthermore, all sets of samples under the same propagation conditions in a given environment can be grouped in a larger set whose parameters adequately describe the path loss behavior. A remark must be made for the case of total obstruction (OBS) between antennas: a total obstacle introduces a fixed attenuation which, in general, is not known and causes that the exponent *after* the obstacle be distance-dependent. Such dependence has not been found significant in the range of distances of the experiments, except at short distances from the obstacle. However, in this situation, the following expression can be used for the exponent:

$$\bar{n}(d) = \bar{n}_0 + \frac{\bar{L}_{OBS}}{10 \log(d)} \quad (6)$$

where $\bar{n}(d)$ is the mean value of the exponent after the obstacle, \bar{n}_0 is its value in the region before the obstacle, \bar{L}_{OBS} is the mean of the attenuation introduced by the obstacle, and d is the distance from the obstacle to the measurement point. \bar{L}_{OBS} can be easily obtained with the above expression, through measurements in the regions before and after the obstacle.

Polarization effects [13]. In the indoor propagation environment, electromagnetic waves suffer depolarization as a consequence of multiple scattering. The amount of depolarization was measured, as described in Section 3, in most of the experiments performed in building 2, and the statistical behavior of the exponent for copolar and crosspolar components analyzed. The results are resumed in Table 3 in terms of the exponent values, as well as path loss difference between copolar and crosspolar components.

Table 3

Values in Table 3 suggest that the amount of depolarization depends strongly on clutter in the environment, being greater when LOS and OBS conditions prevail. Crosspolar components can also be characterized with the gamma distribution function, and it is interesting to notice that, in the experiments performed, observed standard deviations are very similar for copolar and crosspolar components. In the worst conditions observed, the received crosspolar component was higher than the copolar in about 35% of the samples, which strongly suggests the convenience of polarization diversity in such in such circumstances.

6. Conclusions

A very simple model in which the exponent of distance is considered a random variable has been investigated to statistically characterize path loss at 1.8 GHz in indoor environments. Such model can be used by working engineers who, through a few measurements, can obtain the basic information needed to estimate the power budget of communications systems in a particular environment, and who do not require a deeper knowledge of channel dynamics. The exponent can be described with a gamma distribution function through which, the necessary information about fading can be extracted. Since the behavior of the exponent is fairly constant in large areas, only one distribution function is necessary to characterize it. Polarization effects were also measured and strong depolarization was observed in cases of shadowing (NLOS), and total obstruction in the signal path, suggesting the convenience of polarization diversity in such cases.

References

1. Motley A.J. & Keenan, J.M.P. "Personal communication radio coverage in buildings at 900 MHz and 1700 MHz". Electron Lett. Vol 24, N° 12, pp. 763-764, June 1988.
2. Radiowave propagation model document. COST231 TD(93)/13. Barcelona, January 19-22, 1993.
3. Rappaport, T.S. - *Wireless Communications. Principles and Practice*. IEEE Press - Prentice Hall PTR. 1996.
4. "Measurements and modeling recommendations". IEEE Trans. on Vehic. Techn. Vol. VT- 37, N° 1, pp. 45-46, Feb. 1988. Special Issue on Mobile Communications.
5. Lee, W.C. "Estimate of local average power of a mobile radio signal". IEEE Trans. on Vehic. Techn. Vol. VT-34, N° 1, pp. 22-27, Feb. 1985.
6. Parsons, J.D. *The Mobile Radio Propagation Channel*. Pentech Press. London. 1992.
7. Kendall, M. & Stuart, A. *The Advanced Theory of Statistics. Vol 1. Distribution Theory*. 4th. Ed. Charles Griffin & Co. Ltd. 1977.
8. CCIR Report 1007-1.
9. Ireson, W.G. *Reliability Handbook*. McGraw Hill Book Co. New York, 1966.
10. Nakagami, M. "The *m*-distribution-A general formula of intensity distribution of rapid fading". Pergamon Press. Symposium Publications Division. London, 1960.
11. Alexander, S.E. "Characterising buildings for propagation at 900 MHz". Electron. Lett. Vol. 19, N° 20. p. 860. Sept. 1983.
12. Bach Andersen J., Rappaport, T. & Yoshida, S. "Propagation measurements and models for wireless communications channels". IEEE Comm. Mag. Jan 1995. pp. 42-49.
13. Perez-Vega C. and García García J.L. "Polarisation behaviour in the indoor propagation channel". Electron. Lett. Vol 33, N° 10. pp. 898-899, May 1997.

Table 1. Typical values of the exponent (n) and its standard deviation (σ_n) for LOS conditions in corridors.

<i>distance</i>	2	4	8	16	32
n	2.49	2.21	1.94	1.96	2.05
σ_n	1.26	0.81	0.47	0.46	0.38

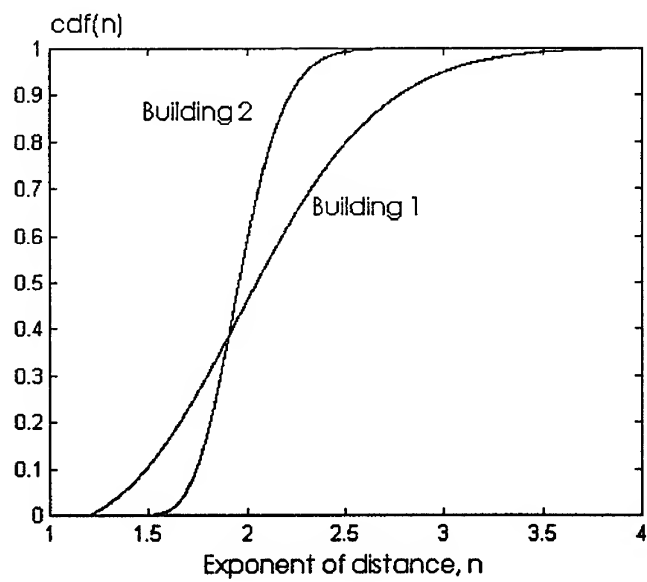
Table 2. Statistical parameters of the exponent in various environments.

Case	Building 1		Building 2	
	n_{mean}	σ_n	n_{mean}	σ_n
LOS				
Corridors	1.96	0.453	1.97	0.187
Open areas	2.05	0.535	2.07	0.528
NLOS				
Corridors	3.1	0.347		
Corridors into open area			2.6	0.235
Open area with partitions			3.79	0.45
OBS				
One wall	2.54	0.53		
Three walls			4.35	0.28
Five walls + stairs			4.93	0.54
Adjacent floors			4.28	0.286

Table 3. Statistical parameters of exponent and path loss difference for copolar and crosspolar components.

Environment	Polarization T-R	n_{mean}	σ_n	$L_{\text{H-V}}$ (dB)	σ_L (dB)
LOS - Open areas and aisles. Small clutter.	V-V	2.07	0.53		
	V-H	3.79	0.65	15.6	7.0
NLOS - Open areas. Heavy clutter and metallic objects	V-V	3.8	0.24		
	V-H	4.38	0.18	8.05	4.25
NLOS - Aisles and open areas. Mild obstructions	V-V	2.6	0.45		
	V-H	3.21	0.40	6.6	6.3
OBS - Thick brick walls	V-V	4.35	0.53		
	V-H	5.05	0.45	6.6	6.0
OBS - Concrete walls and areas with heavy clutter	V-V	4.93	0.26		
	V-H	5.03	0.23	1.44	3.7

Figure 1. Gamma cumulative distributions for LOS conditions in corridors in two different buildings.



Analytical analysis of antennas in the presence of a multilayered dielectric sphere with application to hand held terminals

Ilan Shtrikman, Norbert Henze, Henning Fruechting and Herbert Lindenborn
RF-Techniques and Communication Systems, University of Kassel, 34121 Kassel, Germany
E-mail: shtrikma@hfk.e-technik.uni-kassel.de

I. ABSTRACT

The problem of a herzian dipole in the presence of a dielectric sphere is solved by expanding the electromagnetic field in the vector spherical harmonics and imposing the appropriate boundary conditions. The solution is generalized to a N-layered sphere. The algorithm is programmed as the RAME (Radiation Analysis by Multipole Expansion) code by means of Matlab. Specific choice of the location of the dipole gives short computation time. The output includes near- and far-field plots and efficiency. The results have been compared with static solutions when applicable and good agreement was found. The analysis is extended to the arc antenna which is otherwise only numerically solvable. The theory of RAME is presented, followed by results for testing the program. Finally RAME results relevant to personal communications are presented.

II. THEORY, REALIZATION AND VERIFICATION OF RAME

The geometry of a dipole in front of a sphere is depicted in figure 1. Similar problems have been analyzed in [2] and [3]. Both authors solve the problem by inserting the fields radiated by the dipole in free space and solving for the scattered fields. They both deal with a homogeneous sphere only. In the present work the source is inserted as a boundary condition. This enables straightforward insertion of other sources and multilayered spheres. In RAME, the electromagnetic fields are expanded in the vector spherical harmonics [1]. The source is expanded in the same functions and the appropriate boundary condition is imposed, thus creating a matrix equation for the coefficients of the fields. Following the general solution to the Maxwell equations in spherical coordinates ([1], 16.46), the electromagnetic fields in the three regions are given by:

$$\vec{H}_1 = \sum_{\substack{-l \leq m \leq l \\ 1 \leq l \leq L}} -a_{E1}(l, m) j_l(k_1 r) \vec{X}_{lm} + \frac{i}{\omega \mu_1} a_{M1}(l, m) \nabla \times j_l(k_1 r) \vec{X}_{lm} \quad (1)$$

$$\vec{E}_1 = \sum_{\substack{-l \leq m \leq l \\ 1 \leq l \leq L}} \frac{i}{\omega \epsilon_1} a_{E1}(l, m) \nabla \times j_l(k_1 r) \vec{X}_{lm} + a_{M1}(l, m) j_l(k_1 r) \vec{X}_{lm} \quad (2)$$

$$\vec{H}_2 = \sum_{\substack{-l \leq m \leq l \\ 1 \leq l \leq L}} -a_{E2h}(l, m) h_l^1(k_0 r) \vec{X}_{lm} + \frac{i}{\omega \mu_0} a_{M2h}(l, m) \nabla \times h_l^1(k_0 r) \vec{X}_{lm} \\ - a_{E2j}(l, m) j_l(k_0 r) \vec{X}_{lm} + \frac{i}{\omega \mu_0} a_{M2j}(l, m) \nabla \times j_l(k_0 r) \vec{X}_{lm} \quad (3)$$

$$\vec{E}_2 = \sum_{\substack{-l \leq m \leq l \\ 1 \leq l \leq L}} \frac{i}{\omega \epsilon_0} a_{E2h}(l, m) \nabla \times h_l^1(k_0 r) \vec{X}_{lm} + a_{M2h}(l, m) h_l^1(k_0 r) \vec{X}_{lm} \\ + \frac{i}{\omega \epsilon_0} a_{E2j}(l, m) \nabla \times j_l(k_0 r) \vec{X}_{lm} + a_{M2j}(l, m) j_l(k_0 r) \vec{X}_{lm} \quad (4)$$

$$\vec{H}_3 = \sum_{\substack{-l \leq m \leq l \\ 1 \leq l \leq L}} -a_{E3}(l, m) h_l^1(k_0 r) \vec{X}_{lm} + \frac{i}{\omega \mu_0} a_{M3}(l, m) \nabla \times h_l^1(k_0 r) \vec{X}_{lm} \quad (5)$$

$$\vec{E}_3 = \sum_{\substack{-l \leq m \leq l \\ 1 \leq l \leq L}} \frac{i}{\omega \epsilon_0} a_{E3}(l, m) \nabla \times h_l^1(k_0 r) \vec{X}_{lm} + a_{M3}(l, m) h_l^1(k_0 r) \vec{X}_{lm} \quad (6)$$

Where the vector spherical harmonics are given by:

$$\vec{X}_{lm}(\theta, \phi) \cdot \hat{x} = \frac{\sqrt{(l-m)(l+m+1)} Y_{l,m+1}(\theta, \phi) + \sqrt{(l+m)(l-m+1)} Y_{l,m-1}(\theta, \phi)}{2\sqrt{l(l+1)}}$$

$$\begin{aligned}\vec{X}_{lm}(\theta, \phi) \cdot \hat{y} &= \frac{\sqrt{(l-m)(l+m+1)}Y_{l,m+1}(\theta, \phi) - \sqrt{(l+m)(l-m+1)}Y_{l,m-1}(\theta, \phi)}{2i\sqrt{l(l+1)}} \\ \vec{X}_{lm}(\theta, \phi) \cdot \hat{z} &= \frac{mY_{lm}(\theta, \phi)}{\sqrt{l(l+1)}}\end{aligned}\quad (7)$$

The Y_{lm} are the scalar spherical harmonics :

$$Y_{lm}(\theta, \phi) = \sqrt{\frac{2l+1}{4\pi} \frac{(l-m)!}{(l+m)!}} p_l^m(\cos\theta) e^{im\phi} \quad (8)$$

and p_l^m are the associated Legendre polynomials, j_l and h_l^1 are the spherical Bessel functions and spherical Hankel functions of the first kind, respectively. Note that one has to pay attention when making use of the expressions ([1], 16.46), since they are only valid in free space and their form in a given media is not given simply by replacing the wave number in free space with the relevant wave number but one must rewrite the expressions so that they satisfy the Maxwell equations.

The above procedure is implemented for elementary electric and magnetic dipoles as well as for an arc antenna, whereby the source expansion is analytical. For a radial elementary dipole the boundary condition is derived by extending ([1], 16.73) to time harmonic dependence.

For an electric dipole close to a small dielectric sphere, a static solution is valid. The simulation results for this case as long with the static solution are shown in figure 3 and very good agreement is found. One notices from the static solution that the radiated power of the L 'th multipole is singular for

$$\epsilon_1 = \frac{-(L+1)}{L} \epsilon_0 \quad (9)$$

These resonance can easily be seen in the figure 4 where $l_{max} = 5$ and therefor only 5 resonance are seen. These are the plasma resonances.

The RAME results for the impedance of a loop antenna in free space are compared to [5] in figure 5 and very good agreement is found.

The results of RAME were further checked for many different problems and good agreement with MAFIA was found. The near field results were sometimes slightly different. A canonical problem was defined by Luc Martens [4], as follows. An homogeneous dielectric sphere with radius $a = 10$ cm is situated at the center of the coordinate system. The sphere is filled with brain tissue with properties: $\rho = 1.0510^3 \text{ Kg/m}^3$, $f = 900 \text{ MHz}$; $\epsilon_r = 43$; $\sigma = 0.83 \text{ S/m}$. An elementary herzian dipole source is placed on the x-axis at $x = 11.5 \text{ cm}$ and is oriented along the z-axis. Since again the far field results showed exact correspondence, only the near field comparison is shown. Fig 6 shows the comparison between RAME, MAFIA and Luc Marten's analytical results for this case. Good agreement is seen, though there is a slight difference close to the surface of the sphere away from the source. RAME has been further generalized to include a multilayered sphere by imposing the appropriate boundary conditions, see fig 2.

III. APPLICATION OF RAME TO ANTENNAS FOR HAND HELD MOBILE TELEPHONES

In this section RAME is applied to antennas for hand held mobile telephones, the source is situated on the x-axis at $x = 12 \text{ cm}$. A 3-layered model was used, see table I :

The convergences of the solutions for 900 MHz and 1800 MHz are depicted in figures 7 and 8 respectively. It is noted that the convergence is much faster for the radiated power, ($l=7$), while the loss converges slower ($l=20$ for the electric and magnetic dipoles, $l=10$ for the arc antenna). The convergence for the arc antenna is faster, this is due to the fact that its series representation decays much faster than that of the point sources which are delta functions and cover the whole spherical harmonics spectra.

The near field results in terms of the SAR (Specific Absorption Rate) are seen in figures 9 and 10 for 900 MHz and 1800 MHz respectively. The plots are normalized to the maximum value for each source. For the arc antenna the decay of the field into the head is slower. A peak in the SAR is noticed at the CSF layer. The far field plots for 900 MHz and 1800 MHz are depicted in figures 11 and 12 respectively. It is noted that the magnetic source is much less influenced by the head. The results of this section are summarized in table II. The highest SAR is found for the electric dipole. It is also seen that the magnetic source could theoretically be a good choice at 900 MHz due to the high efficiency compared to the two other sources investigated.

IV. CONCLUSION

An analytical algorithm for the solution of Maxwell Equations in a multilayered spherical media has been derived and implemented in the code RAME under MATLAB. The program was successfully tested and applied to antennas for hand held mobile telephones. The program is a premium design tool for the portable radio engineer, providing the radiation characteristics of the dipole or arc antenna in the presence of a multilayered spherical model of the head. Plots of radiation patterns as well as plots of efficiency as a function of different parameters, ie. frequency or distance of the source to the model of the head are obtained within a matter of a few minutes on a Sun ultra-1 workstation. The near- and far-field results presented for the 3-layered head model are of important value for evaluating the user - mobile interaction. They show that a magnetic antenna has advantage in terms of electromagnetic compatibility at 900 MHz, reducing the losses by a factor of 2 as compared to the electric dipole.

V. REFERENCES

- [1] John David Jackson, Classical Electrodynamics, John Wiley and Sons, Inc.
- [2] Amemiya and Uenbayashi, The distribution of Absorbed Power Inside a Sphere Simulating Human Head in the Near Field of a $\frac{\lambda}{2}$ Dipole Antenna, Trans. IEIC Japan, J66-B, 9, pp.1115-1122, Sep.1983.
- [3] Butler and Keshavamurthy, Analysis of a Wire Antenna in the Presence of Sphere, IEEE Transactions on Electromagnetic Compatibility, Vol. EMC-22, pp. 113-118, May 1980.
- [4] Luc Martens et al., Proposal for Herizian Dipole Exercise within the COST244 WG3 Numerical Program.
- [5] A. Richtscheid, Calculation of the Radiation Resistance of Loop Antennas with Sinusoidal Current Distribution, IEEE Transactions on Antennas and Wave Propagation, Vol. AP-24, pp. 889-891, November 1976.

Tissue	Frequency [MHz]	ϵ_r	σ [S/m]	ρ [10^3 Kg/m^3]
Brain $r \leq 9 \text{ cm}$	900	43	0.83	1.04
	1800	41	1.14	
CSF $9 \text{ cm} < r \leq 9.5 \text{ cm}$	900	81	2.1	1.01
	1800	79	2.5	
Skull $9.5 \text{ cm} < r \leq 10 \text{ cm}$	900	17	0.25	1.81
	1800	16	0.50	

TABLE I
Tissue properties for the layered model of the head

Source	Frequency [MHz]	Total power (normalized to same source in free space)	Far field Front-back ratio [dB]	Efficiency [%]	Maximal SAR ptot=1W [W/Kg]
Infinitesimal elec. dipole (tangential)	900	0.710	5.9	32.6	1.79
	1800	0.838	12.5	66.3	15.61
Infinitesimal mag. dipole (tangential)	900	2.722	2.9	67.4	1.26
	1800	1.658	1.1	66.8	6.60
Arc antenna (tangential)	900	0.607	5.8	36.5	0.61
	1800	0.883	13.5	63.3	8.69

TABLE II
RAME comparison of antennas in front of a layered spherical model of the head

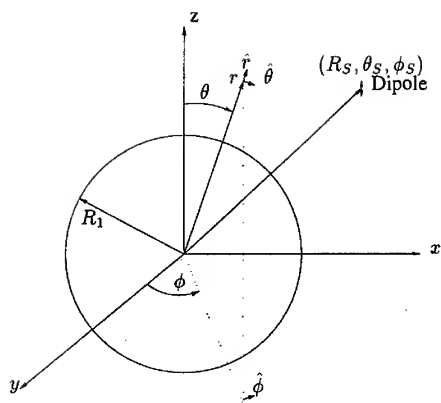
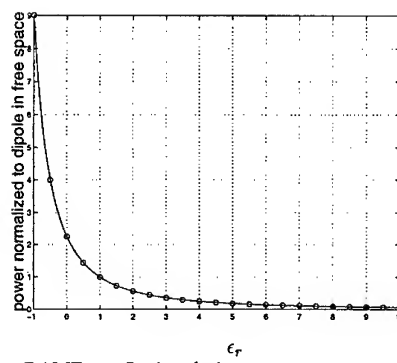


Figure 1: Herizian dipole in front of a sphere



RAME: —, Static solution: o

Figure 3: Radiated power from a dipole near a small dielectric sphere

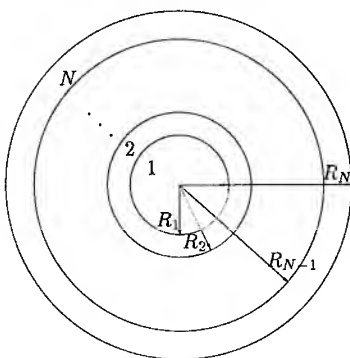


Figure 2: N-layered sphere

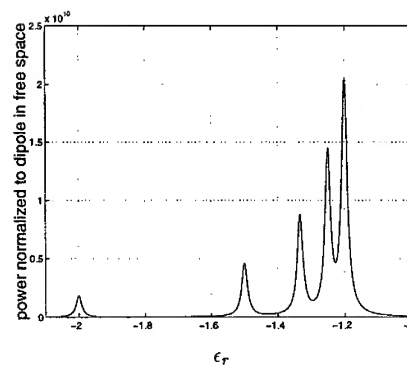
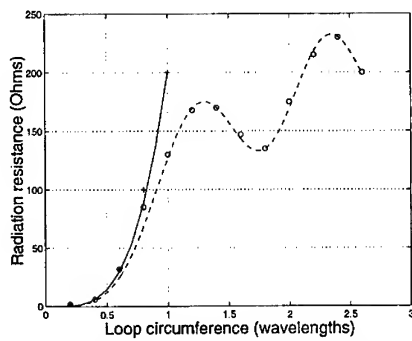
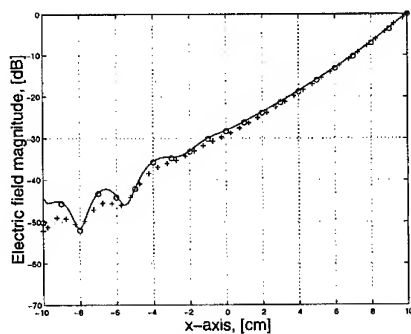


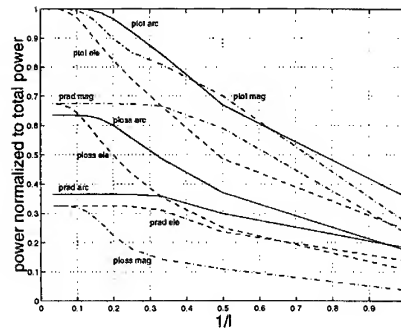
Figure 4: Dipole near a small dielectric sphere, the Plasma resonances



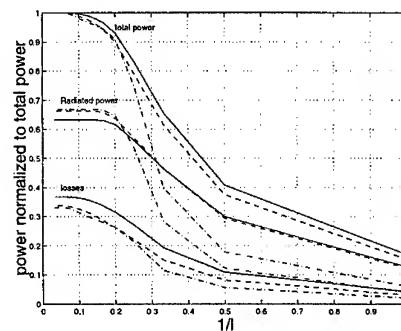
Sinusoidal current: RAME --, Vector potential solution o
Constant current: RAME —, Vector potential solution +
Figure 5: Radiation resistance of a circular loop with constant and with sinusoidal current distributions, RAME versus the vector potential solution



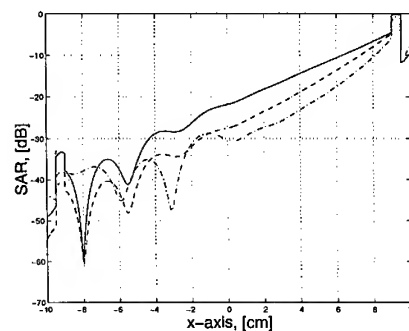
RAME: —, MAFIA: +, Luc Martens: o, $f = 900\text{ MHz}$
 $R_1 = 10\text{ cm}$, $R_S = 11.5\text{ cm}$, $\epsilon_1 = 43$, $\mu_1 = 1$, $\sigma_1 = 0.83$
Figure 6: Near field comparison for the canonical problem



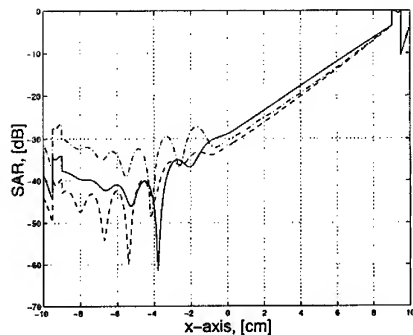
electric tangential --, magnetic tangential --., arc antenna —
Figure 7: Convergence of the RAME solution for the layered model of the head at 900 MHz



electric tangential --, magnetic tangential --., arc antenna —
Figure 8: Convergence of the RAME solution for the layered model of the head at 1800 MHz



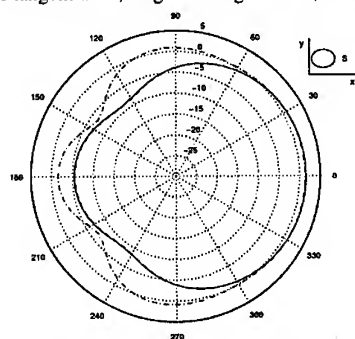
electric tangential --, magnetic tangential --., arc antenna —
Figure 9: SAR inside layered model of the head at 900 MHz



electric tangential --, magnetic tangential --, arc antenna —

Figure 10: SAR inside layered model of the head at 1800 MHz

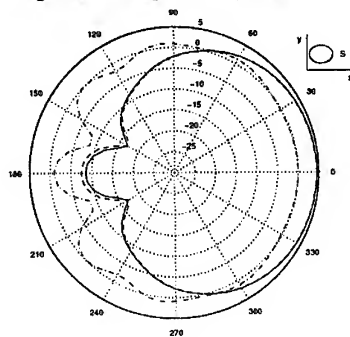
electric tangential --, magnetic tangential --, arc antenna —



Only the relevant component is shown, θ for ele. tang. and arc antenna, ϕ for mag. tang., other component is negligible

Figure 11: Far Field, layered model of the head, 900 MHz, electric field, [dBi]

electric tangential --, magnetic tangential --, arc antenna —



Only the relevant component is shown, θ for ele. tang. and arc antenna, ϕ for mag. tang., other component is negligible

Figure 12: Far Field, layered model of the head, 1800 MHz, electric field, [dBi]

A LOW LOSS PHASE SHIFTER FOR DIELECTRIC WAVEGUIDE USING ASYMMETRICAL GUIDES

P. R. Young, R. J. Collier and P. G. G. Bianconi,
Electronic Engineering Laboratories,
University of Kent,
Canterbury, Kent CT2 7NT, UK.
Tel: 01227 764000/Fax: 01227 456084

Abstract

This paper presents a phase shifter for dielectric waveguide. Phase shifting is achieved by varying the distance between the waveguide and a block of dielectric. By calculating the propagation constants of a coupled dielectric slab waveguide an approximate expression for the phase shift is given and is shown to be in good agreement with experimental results.

INTRODUCTION

There has been a renewed interest in dielectric guiding structures for the millimeter/submillimeter range in recent years. Automatic vehicle guidance systems and other radar applications all require low loss guiding structures in the millimeter/submillimeter range. Waveguides that rely on metallic planes such as microstrip, coplanar and conventional rectangular waveguide suffer from increased losses as frequency increases due to the skin effect and surface roughness. This has caused interest in guiding structures that do not require any conductors such as layered ridge dielectric waveguide [1] and dielectric ribbon waveguides [2]. Furthermore, dielectric waveguides can be made flexible at the higher frequency ranges making them ideally suitable for systems that require some movement. However, for dielectric structures to replace guiding structures that use conducting planes, waveguide components such as attenuators and phase shifters are required. This paper presents a design method for a low loss phase shifter for dielectric waveguide.

Existing phase shifters for dielectric waveguide [3-5] use a conducting plane in order to change the phase velocity of the propagating modes. By varying the distance between the dielectric waveguide and the conducting plane a varying phase shift is achieved. However, as we shall see, metallic plane phase shifters can become very lossy due to losses in the image. Furthermore, resistive losses in the metallic plane will increase with at least the square root of frequency due to the skin effect. This paper will present a low loss phase shifter for dielectric waveguide that uses an arbitrary piece of dielectric placed a distance $2D$ from the waveguide. By varying this distance the phase velocity of the propagating mode is changed and therefore the phase. It is shown that even at X band, phase shifters using a dielectric as the phase shifting material have less attenuation than existing metallic plane phase shifters. It is further envisaged that the difference in attenuation at higher frequencies will be even more prominent due to the skin effect.

THEORY

The basic configuration of the phase shifter can be seen in Figure 1. The structure consists of a dielectric waveguide with cross sectional dimensions $2a$ by $2d$ and relative permittivity ϵ_a . A piece of dielectric with cross sectional dimensions $2b$ by $2d$, of length L and relative permittivity ϵ_b is situated parallel to the waveguide at a distance $2D$. Both materials are assumed loss less and are surrounded by loss less dry air.

The phase shift of this structure is then given by

$$\Phi(2D) = [k_z - k'_z(2D)]L \quad (1)$$

where k_z is the longitudinal propagation constant of the isolated waveguide and k'_z is the propagation constant of the coupled dielectric waveguide which is formed by the piece of dielectric situated a distance $2D$.

We therefore need to evaluate the function $k'_z(2D)$. However, accurate evaluation of the propagation constants for dielectric waveguides is very difficult due to the rectangular geometry of the problem. We therefore use the simple effective index method as described by Chiang [6]. Firstly, we solve the TE (TM) coupled slab structure exactly in a method similar to Marcuse [7]. This gives us an effective permittivity $\epsilon_{eff} = (k_x/k_o)^2$. We then solve a TM (TE) slab structure of width $2d$ with a permittivity ϵ_{eff} . The propagation constant we calculate for this second structure is then a good approximation of the coupled dielectric waveguide in Figure 1.

If $k'_z(2D)$ is known then the phase shift in equation (1) can be calculated for the given structure. However, the composite structure can in general support more than one mode. This makes phase shift calculations more difficult since we then require the absolute amplitude of all of the modes. Furthermore, if the coupled guide supports two modes (an odd and even) then depending on the asymmetry the energy will transfer back and forth between the main waveguide and the dielectric with a beat length equal to $L = \pi/[k_{z(e)} - k_{z(o)}]$. Where $k_{z(e)}$ and $k_{z(o)}$ are the propagation constants of the even and odd modes, respectively. However, if the dielectric is much smaller than the waveguide then the composite structure can be made to propagate only a single mode, thereby preventing the energy from transferring to the dielectric. Furthermore, radiation and reflection from the discontinuities at $z=0$ and $z=L$ are reduced if the dielectric is small in comparison with the main guide.

RESULTS

Figure 2(a) shows experimental and theoretical results for a dielectric phase shifter operating at 8 GHz and 12 GHz. The results show E^y mode solutions for a PTFE dielectric waveguide of relative permittivity $\epsilon_r = 2.07$ [8] and dimensions $2a = 10.9$ mm by $2d = 22.9$ mm. The phase shifting dielectric is also PTFE with dimensions $2b = 3.4$ mm by $2d = 22.9$ mm and is of length $L = 180$ mm.

Figure 2(b) shows the attenuation of this structure. As can be seen the attenuation is less than 1 dB for both frequencies. If the phase shifter is operated for $2D > 10$ mm then the attenuation is reduced to less than 0.1 dB. This will of course reduce the maximum phase shift to less than 20 degrees. However, if the longitudinal length is increased then from equation (1) we see that the phase shift is also increased. Furthermore, increasing L has no effect on the attenuation (assuming the dielectric is loss less) because the losses are only due to the discontinuities at $z=0$ and $z=L$. The losses can be decreased further if the b dimension of the dielectric is reduced.

For the purpose of comparison a phase shifter using a metallic wall in place of the dielectric is given in Figure 3. The longitudinal length L is again 180 mm and results for both 8.0 GHz and 12.0 GHz are given. As can be seen the attenuation for the metallic phase shifter is far greater than that of the dielectric, especially in the low frequency case.

CONCLUSIONS

In summary, a low loss phase shifter for use with dielectric waveguide has been presented. Phase shifting is achieved by using a movable dielectric block, which forms an asymmetrical coupled waveguide. By introducing the appropriate asymmetry the coupled structure remains monomode, thereby eliminating coupling. The phase shifter has been shown to have a much lower insertion loss than existing phase shifters that rely on conducting planes. Furthermore, the phase shifter is expected to far outperform metallic phase shifters at higher frequency bands.

ACKNOWLEDGEMENTS

The Authors would like to thank the Engineering and Physical Sciences Research Council (EPSRC) for the support of P R Young.

REFERENCES

- [1] A. G. Engel, Jr. And L. P. B. Katehi, "Low-Loss monolithic transmission lines for the submillimeter and terahertz frequency applications," *IEEE Trans. Microwave Theory Tech.*, pp. 1847-1854, Nov. 1991.
- [2] C. Yeh, Fred I. Shimabukuro, J. Chu, "Dielectric ribbon waveguide: An optimum configuration for ultra-low-loss millimeter/submillimeter dielectric waveguide," *IEEE Trans. Microwave Theory Tech.*, pp. 691-701, June 1990.
- [3] R. J. Collier and M. F. D'Souza, "Phase shifters for dielectric guides," *IEE Proceedings-H*, Vol. 139, No. 2, pp. 202-204, April 1992.
- [4] R. J. Collier and M. F. D'Souza, "A multistate reflectometer in dielectric guide for the frequency range 75-140 GHz," *IEEE MTT-S Digest*, pp. 1027-1030, 1991.
- [5] J. W. Tao, B. Chan, H. Baudrand, J. Atechian, "Novel type of electrically-controlled phase shifter for millimeter-wave use: Theory and experiment," *IEEE MTT-S Digest*, pp. 671-674, 1991.
- [6] Kin Seng Chiang, "Effective-index method for the analysis of optical waveguide couplers and arrays: An asymptotic theory," *Journal of Lightwave Tech.*, Vol. 9, No. 1, pp. 62-72, Jan. 1991.
- [7] D. Marcuse, "Directional couplers made of nonidentical asymmetric slabs. Part I: Synchronous couplers," *Journal of Lightwave Tech.*, Vol. LT-5, No. 1, pp. 113-118, Jan. 1987.
- [8] M. N. Asfar, "Precision Dielectric Measurements of Nonpolar Polymers in the Millimeter Wavelength Range," *IEEE Trans. Microwave Theory Tech.*, Vol. MTT-33, No. 12, pp. 1410-1415, December 1985.

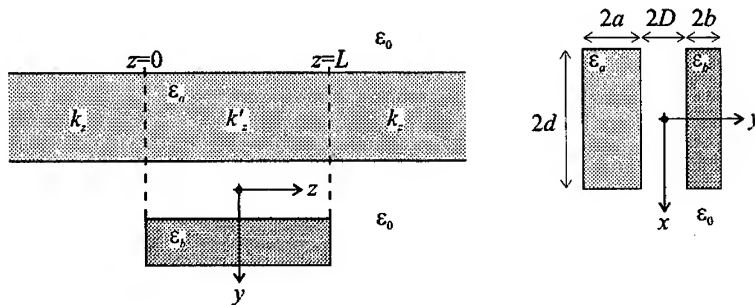


Figure 1. Geometry of dielectric waveguide phase shifter.

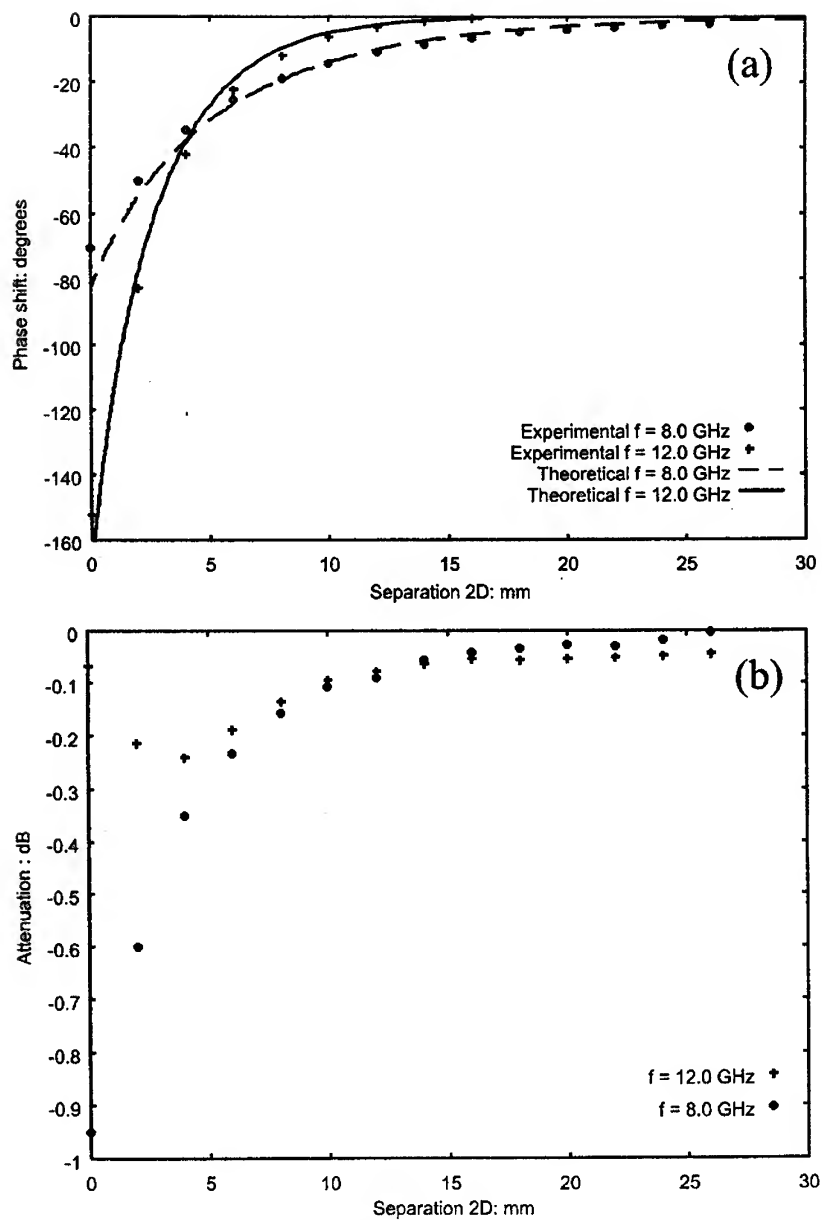


Figure 2. Phase shift (a) and attenuation (b) for dielectric phase shifter. $2a=10.9$ mm, $2b=3.4$ mm, $2d=22.9$ mm, $L=180$ mm and $\epsilon_a=\epsilon_b=2.07$.

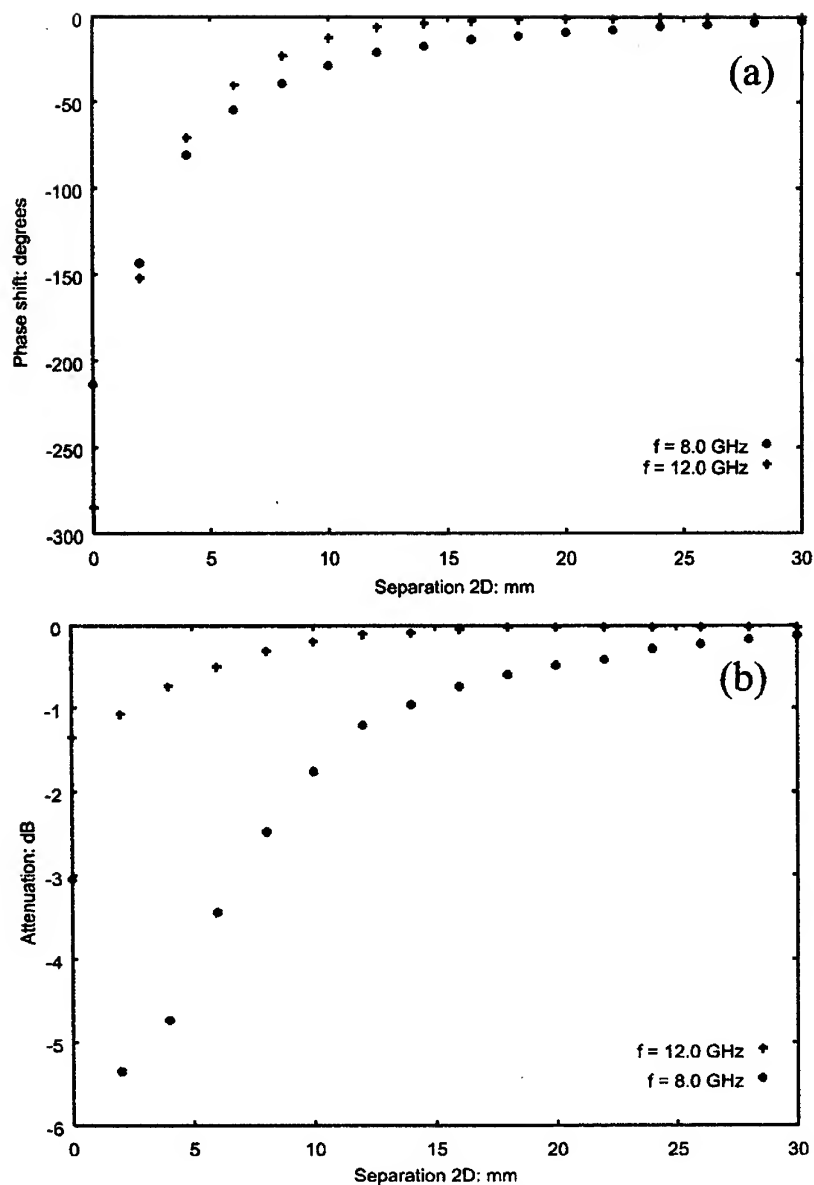


Figure 3. Phase shift (a) and attenuation (b) for metallic wall phase shifter of length $L=180$ mm.

OPTICAL SYNTHESIS OF MICROWAVE SIGNALS

A. J. Seeds

Department of Electronic and Electrical Engineering,
University College London, Torrington Place, London, WC1E 7JE, England.
a.seeds@eleceng.ucl.ac.uk, <http://www.ee.ucl.ac.uk>

ABSTRACT

Microwave signals can be generated by the photo-detection of multiple optical signals. This approach has potential for the generation of signals having characteristics not readily obtainable by other means, such as fast tuning over multi-octave ranges, low dispersion and non-linearity penalties in millimetre-wave over fibre transmission and compact millimetre-wave local oscillator generation. Obtaining the spectral purity required for practical applications is however a significant challenge. This paper describes techniques for the optical synthesis of microwave signals, focusing on optical heterodyne generation techniques and including recent results for a high spectral purity optical injection phase lock loop.

1. INTRODUCTION

Quantum efficient depletion layer photodetectors having 3dB bandwidths in excess of 100GHz were first reported several years ago [1]. For operation well within the 3dB bandwidth a simple current generator model for the photodiode can be used. Consider two monochromatic optical signals having polarisation matched electric fields

$$E_1 = \hat{E}_1 \cos(\omega_1 t + \phi_1) \quad (1)$$

and

$$E_2 = \hat{E}_2 \cos(\omega_2 t + \phi_2) \quad (2)$$

where ω is the signal frequency and ϕ the signal phase. For $\omega_1 \approx \omega_2$ and perfect wavefront overlap the photodiode output current is given by

$$i \propto \hat{E}_1 + \hat{E}_2 + 2\hat{E}_1\hat{E}_2 \cos(\omega_1 - \omega_2 + \phi_1 - \phi_2) \quad (3)$$

Using the relationship

$$\hat{E}^2 = 2 \frac{Z_o P}{A} \quad (4)$$

where A is the photodiode area, P the optical power and Z_o the characteristic impedance of the medium where the power is measured, the photodiode current can be written as

$$i = R[P_1 + P_2 + 2\sqrt{P_1 P_2} \cos(\omega_1 - \omega_2 + \phi_1 - \phi_2)] \quad (5)$$

where R is the photodiode responsivity. Note that a signal is generated at the difference frequency between the two optical signals and that the microwave power generated is proportional to the product of the powers of the incident optical signals. The analysis extends naturally to multiple frequency optical inputs. Note also that the spectral purity of the generated signal depends on the correlation of noise between the two inputs.

In this paper correlation of the noise by optical phase lock loop will be considered followed by a description of a locking technique that greatly eases the realisability of systems using semiconductor lasers; the optical injection phase lock loop (OIPLL). A conclusion section discusses applications of the techniques described and suggests avenues for further work.

2. OPTICAL PHASE LOCK LOOP

The simplest heterodyne microwave generation scheme would comprise two polarisation matched lasers with overlapped wavefronts incident on a suitable photodiode. Laser diode pumped Nd:YAG lasers have been used in this way and can offer a beat linewidth in the kHz region [2]. Tuning is by crystal heating and PZT applied stress giving maximum rates of order 1 GHz/ μ s. Semiconductor lasers can offer much higher tuning rates, > 100 GHz/ns, and are less bulky and expensive, but have much wider linewidths, typically in the 3 MHz - 50 MHz range. The emission frequency is also a strong function of temperature and current, values of 30 GHz/K and 3 GHz/mA being typical of distributed feedback (DFB) lasers operating at a wavelength of 1,550 nm. Whilst semiconductor lasers can be stabilised by locking their frequency to a cavity resonator, such as a Fabry-Perot etalon, the system is complex and wideband suppression of phase noise is not possible [3]. Figure 1 shows an alternative technique, the optical phase lock loop (OPLL). Samples of the outputs from the two lasers are combined, photo-detected and the resulting heterodyne signal compared with a microwave reference to derive an error signal which controls the frequency of one laser to lock the heterodyne frequency to the supplied reference.

The main difficulty in implementing OPLLs arises from the wide linewidth typical of semiconductor lasers which requires a very wide bandwidth, short propagation delay control loop. Figure 2 shows the dependence of the mean time to cycle slip on loop propagation delay for lasers of combined linewidth 8 MHz [4]. It is clear that to obtain reliable operation delays of less than 0.35 ns are required, corresponding to a free space path length of less than 105 mm. Considering that this includes delay in both optical and electronic components of the system the difficulties in OPLL construction become clear.

Optical injection locking (OIL), in which light from a modulated master laser is injected into a slave laser to lock its output frequency [5], does not present the loop delay restriction and the level of phase noise can be controlled by the amount of light injected into the slave laser cavity. However, the OIL locking range can be severely reduced due to instabilities occurring in the locking process above critical levels of injection [6].

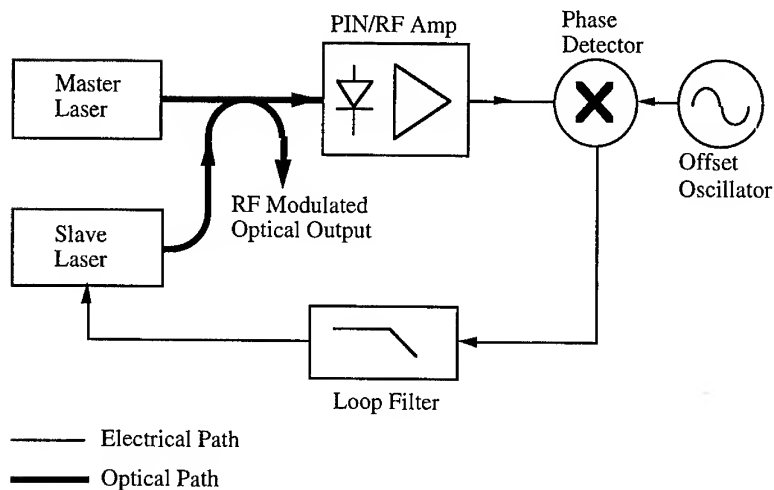


Figure 1: Optical phase lock loop

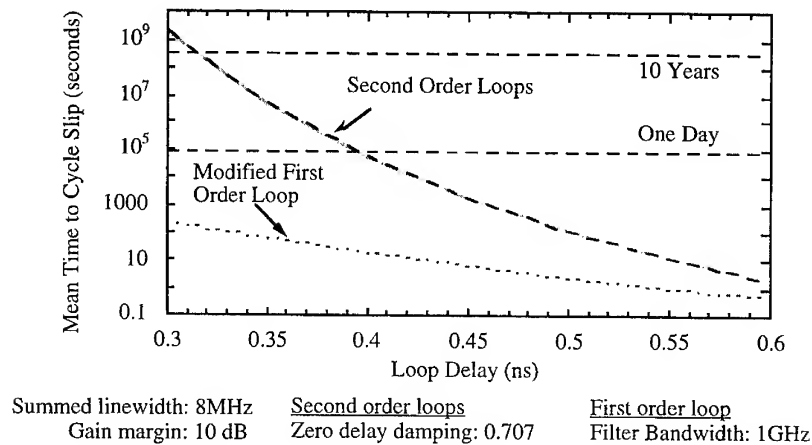


Figure 2: Mean time to cycle slip as a function of loop propagation delay for first and second order optical phase lock loops.

3. OPTICAL INJECTION PHASE LOCK LOOP

We have developed a new loop architecture, combining OPLL and OIL techniques, the optical injection phase-lock loop (OIPLL) [7]. This system allows low phase error variance to be achieved for loops using wide linewidth lasers and having significant loop propagation delay, offering improved performance over either OPLL or OIL systems used individually. An experimental homodyne OIPLL using lasers of summed linewidth 36 MHz achieved a phase error variance of less

than 0.006 rad^2 in measurement bandwidth 500 MHz and had a stable tuning range exceeding 26 GHz, limited only by saturation of the loop filter electronics [8].

Figure 3 shows an experimental heterodyne OIPLL. Part of the light emitted by the master laser is injected into the slave laser cavity. The other part is combined with the slave laser output light and photodetected. The resulting electrical signal is compared with the microwave reference signal in the phase detector. The loop filter includes an integration stage to give a second order type II loop response.

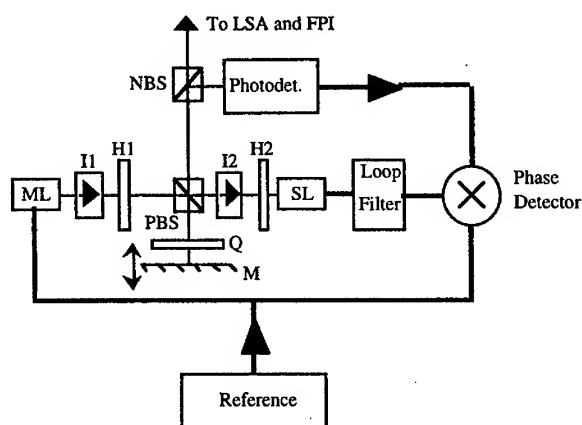


Figure 3 - Heterodyne OIPLL experimental set-up. ML: master laser; SL: slave laser; I: isolator; H: half-wave plate; Q: quarter-wave plate; PBS: polarising beam splitter; NBS: non-polarising beam splitter; M: mirror, LSA: lightwave signal analyser, FPI, Fabry-Perot interferometer.

The reference signal is also used to modulate the master laser so as to produce FM sidebands at harmonics of the reference frequency. The slave laser can be locked to the chosen harmonic by adjusting its bias current. Since phase comparison takes place at both the slave laser and the phase detector an adjustable mirror is used to match the path lengths and so avoid competition between the two locking processes.

Figure 4 shows the detected modulated output for a reference frequency of 8 GHz and lasers of summed linewidth 36 MHz. The noise power spectral density is -94 dBc/Hz at 10 kHz offset, within 1 dB of the phase noise level of the microwave synthesiser used as a reference and the phase error variance is 0.003 rad^2 in a bandwidth of 100 MHz (limited by lightwave signal analyser noise floor). The hold-in range was greater than 24 GHz.

Harmonic locking was also shown to be possible with the OIPLL system. Since modulation of the master laser results in both intensity modulation (IM) and frequency modulation (FM), multiple side frequencies are generated. The hold-in range was 4 GHz. The hold-in range is lower than for fundamental locking because the injection ratio for the 16 GHz sideband is smaller at -37 dB resulting in reduced loop gain.

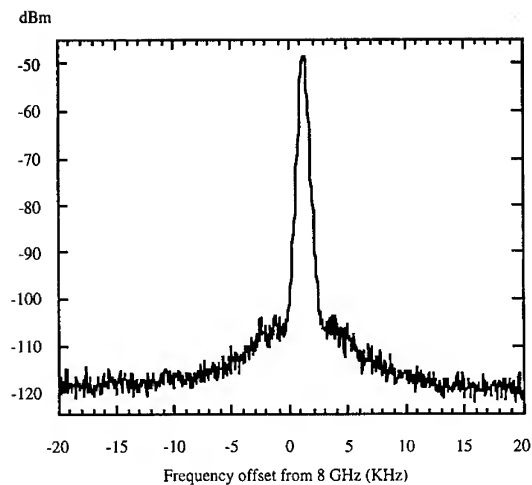


Figure 4: Heterodyne OIPLL spectrum. Injection ratio: -30 dB. Span = 200 MHz, resolution bandwidth = 3 kHz.

In contrast an OIL system using the same conditions had a stable tuning range of less than 2 GHz and it was not possible to achieve OPLL operation with the parameters used here.

4. CONCLUSIONS

The OIPLL and related heterodyne techniques offer several attractions in microwave over fibre transmission systems. First, it is possible to apply baseband modulation to one of the laser outputs only and then combine master and slave laser outputs for transmission through fibre. This enables a modulator of modest bandwidth to be used, with the up-conversion to the required microwave frequency taking place at the receiver photo-detector. Further, since modulation is applied to one laser output only, dispersion effects are reduced, since they affect only the baseband signal for narrow linewidth sources. Second, where the heterodyne frequency and laser linewidths are substantially greater than the Brillouin linewidth [9] (20 MHz at a wavelength of 1.55 μm) the power that can be launched into an optical fibre link can be raised above the Brillouin limit for a conventionally modulated system, thus allowing an improvement in received signal to noise ratio. Third, the chirp characteristic of directly modulated sources can be avoided using the heterodyne technique, thus increasing the dispersion limited transmission distance. In practice the main limitation comes from the dispersion induced decorrelation of the phase noise on the two laser outputs and polarisation mode dispersion [10].

More generally, approaches based on laser heterodyning can be used for signal generation at frequencies limited only by the bandwidth of the photodetector used. They are thus attractive for local oscillator generation at the higher millimetre-wave frequencies where compact and efficient

conventional electronic sources are difficult to realise. The development of kHz linewidth semiconductor lasers [11] also makes practical optical heterodyne swept frequency sources of tuning speed and range much greater than YIG tuned oscillators. A further development that could offer wide bandwidth, uniform tuning response is the use of the quantum confined Stark effect for semiconductor laser tuning [12].

The main disadvantage of the heterodyne approach using semiconductor lasers is its complexity and the need for milli-Kelvin precision temperature control of the source lasers due to their high temperature tuning sensitivity. Work by Braun et al [13] on the integration of two DBR lasers has produced a source having a free running heterodyne temperature stability of better than 10 MHz/K, offering the possibility of widespread application of the techniques described above to microwave and millimetre-wave systems.

ACKNOWLEDGEMENT

The author would like to thank his academic and industrial colleagues for their many contributions to the work described here. Work at University College London has been supported by the United Kingdom Engineering and Physical Sciences Research Council, the United States Air Force Office of Scientific Research and the United States Army Research Office. DFB lasers for the OIPLL work were supplied by Dr. D. Wake, BT Research Laboratories, Martlesham Heath.

REFERENCES

1. D. G. PARKER, P. G. SAY and A. M. HANSOM, *Electron. Lett.* **23** (1987) 527.
2. T. J. KANE and E. A. P. CHENG, *Opt. Lett.*, **13** (1988) 970.
3. M. OHTSU, M. MURATA and M. KUROGI, *IEEE J. Quantum. Electron.*, **QE26** (1990) 231.
4. R. T. RAMOS and A. J. SEEDS, *Electron. Lett.* **26** (1990) 389.
5. L. GOLDBERG, H. F. TAYLOR, J. F. WELLER, and D. M. BLOOM, *Electron. Lett.* **19** (1983), 491.
6. O. LIDOYNE, P. GALLION, C. CHABRAN and G. DEBARGE, *IEE Proc.* **137**, Pt. J (1990) 147.
7. R. T. RAMOS, P. GALLION, D. ERASME, A. J. SEEDS and A. C. BORDONALLI, *Opt. Lett.* **19** (1994) 4.
8. A. C. BORDONALLI, C. WALTON, and A. J. SEEDS, *IEEE Photon. Tech. Lett.*, **8**, (1996) 1217.
9. A. R. CHRAPLAVY, in T. Li (ed.), *Topics in Lightwave Transmission Systems*, (1991) San Diego, Academic Press 267.
10. R. HOFSTETTER, H. SCHMUCK and R. HEIDEMANN, *IEEE Trans. MTT-43* (1995) 2263.
11. M. OKAI, T. TSUCHIYA and N. CHINONE, in *Proc. CLEO'91*, Baltimore (1991), CPDP40.
12. X. HUANG A. J. SEEDS and J. S. ROBERTS, *Appl. Phys. Lett.*, **71**(6) (1997).
13. R. P. BRAUN, R. KAISER, D. ROHDE, R. STENZEL, D. TROMMER, H. HEIDRICH, and G. GROSSKOPF, in *Proc. 21st ECOC*, Brussels (1995), Th.B.3.5., vol. 3, 1023.

Millimeter Wave Fiberoptic Links

Peter R. Herczfeld
Center for Microwave - Lightwave Engineering
Drexel University
Philadelphia, PA. 19104, USA

Abstract

This paper is concerned with the use of fiberoptic links in millimeter wave systems. Two approaches are discussed. The first is an optically fed W-band transceiver. The second describes a mode-locked microchip laser to be used in optical generation and distribution of millimeter wave signals in wireless communication.

Introduction

The transmission of microwaves over fiber is now a common practice. Its advantages, often described in detail, include low loss, immunity to interference, small size and weight. However the transmission of millimeter wave signals over fiber is still in the experimental stages although impressive gains have been recorded. As communications and remote sensing applications advance to higher frequencies, into the millimeter wave region of the spectra, optical transmission of these signals becomes more desirable because conventional techniques such as coaxial cables and waveguides are more problematic. The main difficulty in producing high quality millimeter wave fiberoptic links has been the optical transmitters and receivers, more specifically the modulators and detectors.

Optical transmitters operating in the microwave region employ either direct modulation of semiconductor lasers or external modulators like the Mach-Zehnder interferometer. However, semiconductor can not be directly modulated at millimeter waves, because their relaxation oscillation frequencies are typically limited to thirty GHz or lower. Although external modulators can operate in the millimeter wave range [1], their performance, particularly high driving voltage and insufficient linearity, poses problems.

Optical heterodyning is an effective alternate way of generating millimeter waves [2]. In this case two laser lines are combined in a high speed photodetector generating a millimeter wave beat frequency. If one of the laser lines is tunable then the resulting beat frequency is, naturally, variable. Both semiconductor and solid state lasers can be employed in heterodyning. Another technique that is gaining considerable popularity is injection locking [2] or mode-locking lasers [3]. Although all these approaches are continually improving and in many instances excellent results have been obtained, the relative complexity of these techniques is of concern and may be an impediment to many applications.

PIN photodetectors with very good responsivity up to the 40GHz range and beyond are commercially available. Traveling wave photodetectors operating in the hundreds of GHz have been demonstrated in several laboratories [4]. The microwave HBT, which has a built in PIN diode, is a promising detector, with gain at millimeter wave frequencies [5].

Use of alternate components and techniques is usually governed by the particular application. In the subsequent sections two approaches, emphasizing simplicity and reliance on established microwave methods, will be presented.

Fiberoptic link for a W-band transceiver

The particular application of concern is a W-band Doppler radar. The function of the optical distribution is to provide a transmitter signal as well as a local oscillator signal for the W-band transmit/receive (transceiver) module [6]. The schematic diagram of the system is depicted in Fig.1. The optical link is configured at the Ku-band frequency, and reliable, low cost microwave monolithic integrated circuits (MMIC) frequency multipliers at the output of the optical link obtain the required millimeter wave transmit and local oscillator signals. For the radar application the key design parameter is the phase noise, which must be kept to a minimum.

Referring to Fig. 1, the optical link is configured to be compatible with the direct frequency synthesizer which provides a common reference signal to the transmitter, and to the receiver local oscillator. On the transmit side the Ku-band reference signal generated by the synthesizer is transmitted via the fiberoptic link. The received optical signal is detected, amplified multiplied by two, amplified again and multiplied by three. The resultant W-band signal is once more amplified and transmitted. On the receiver side the Ku-band signal is amplified and multiplied by three. The upconverted Q-band signal is subharmonically mixed with the received signal. The design and performance of the MMIC chips were reported earlier. The system can change frequencies rapidly since no phased lock loops with voltage controlled oscillators are used.

The Ku-band optical link comprises of commercially available components, a solid state laser, a Mach-Zehnder modulator and a PIN photodetector. The diode-pumped solid-state non-planar YAG ring laser provides for 8-mW output power at 1319nm. The laser was coupled to a Mach-Zehnder modulator with a half wave modulator voltage (V_{π}) of 13.5 volts, an optical loss of 3.74dB, and a modulation loss of 3dB. The PIN diode photo detector employed was terminated internally with an ac coupled 50-ohm resistor for matching. The measured responsivity was 0.45 A/W at 15-16 Ghz.

The externally modulated laser system was chosen for its low noise capability compared to a direct modulated system. This system reduced the relative intensity noise (RIN) to about -135 dBc at 1-MHz offset frequency. The noise then falls off to within 2dB of the shot noise limit for offset frequencies greater than 20MHz. Since the offset frequency is Ku-band, this noise is insignificant.

The residual phase noise of the optical link was determined using a low noise source consisting of a 640-MHz crystal output signal followed by a step recovery diode. A filter was fabricated to pick the 24th harmonic for Ku-band output. Fig. 2 illustrates the measured phase noise at Ku band. The noise floor is -145dBm/Hz and the measured signal level at the PIN diode optical detector is -26.2dBm. The noise floor is then -171.2dBm. The calculated noise floor is -172dBm/Hz taking into account both thermal noise and shot noise. The phase noise at W-band will increase $20 \log(6) = 15.6$ dB over the Ku-band phase noise due to the multipliers.

This experiment proves that a proper balance between the optical and microwave components can lead to a high performance system. Specifically, the use of millimeter wave domain up and down conversions employing MMICs, a mature and cost effective technology, can significantly reduce the requirements on the fiberoptic links.

Millimeter wave signal generation with a microchip laser

Applications, like fiberoptic feed of wireless communications, require the generation and transmission of high fidelity millimeter wave carriers. Diode pumped solid state lasers have no chirp and are inherently less noisy than their semiconductor

counterpart, making them exceptionally good candidates for fiberoptic communication links. In the subsequent paragraphs we describe a new laser which has two novel attributes. First, the host material, LiNbO_3 , is electrooptic, which means that it can be directly modulated for mode locking. Second, the device is embedded in a millimeter wave cavity which enhances interaction between the crystal and the microwave field and provides for compact packaging as well.

The microchip laser was fabricated by depositing dielectric mirrors on the surface of the Neodymium doped Lithium Niobate ($\text{Nd}:\text{LiNbO}_3$) crystal to form the optical cavity. The length of the laser cavity, 3.48mm, corresponds to a round-trip time of 50psec yielding an axial mode spacing of 20GHz. Thus, an applied microwave signal at 20GHz (or its multiples) will phase lock the modes thereby generating an optical and a millimeter wave carrier.

The laser was mounted in the gap of a 20GHz reentrant microwave cavity where most of the electric field is concentrated [7], and the driving field was applied along the z axis in order to effectively interact with the crystal. The pump beam from a laser diode was collimated and coupled to the $\text{Nd}:\text{LiNbO}_3$ laser using free-space optics.

The output signal was analyzed in the optical, time and microwave domains. Optical domain measurements revealed six modes, 20GHz apart, with a linewidth of ~30kHz (or ~10-6 Å). Time domain measurements showed the emergence of the pulse train when the microwave field locked the modes. With a 12.6dBm microwave signal applied to the microwave cavity an 8.6dB increase of the peak output at 20GHz is noted on the spectrum analyzer. The signal becomes very stable with a bandwidth of 84 kHz. Furthermore, the microchip laser was also mode-locked at 40GHz which corresponds to the second harmonic of the cavity. With an input microwave power of 30dBm, a 7.2dB increase in the millimeter wave signal was obtained, as depicted in Fig. 5.

A maximum of 95.6% modulation index was measured. The residual phase noise at 1kHz offset was -110dBc/Hz and the amplitude noise was less than -150dBc/Hz. These results imply that this particular laser source can meet the most stringent noise requirements of most applications. In a separate experiment the output of the mode-locked microchip laser, with the 20GHz modulation envelope, was fed into an external modulator where information signals were superimposed on the carrier verifying the viability of the method for communications.

Theoretical calculations predicted a temperature variation of $-0.8\text{MHz}/^\circ\text{C}$ of the output implying that a simple temperature controller would provide good stability. Experimentation proved this assertion correct.

A few comments are in order:

- i. this technique can be extended to higher frequencies by properly scaling the dimensions of the laser and the reentrant cavity. In fact our models predict that the laser should work as well or better at frequencies up to about 100GHz.
- ii. the simplicity of the approach signified by the fact that only four terminals are needed for the entire packaged unit: two optical (one for pumping and one for the laser output), one for the microwave input for the mode locking and one for the temperature controller.

- iii. employing Erbium doped LiNbO_3 lasing and mode-locking can be achieved at the important $1.55\mu\text{m}$ wavelength. New crystal growing and processing techniques are reducing the cost of the microchip lasers.

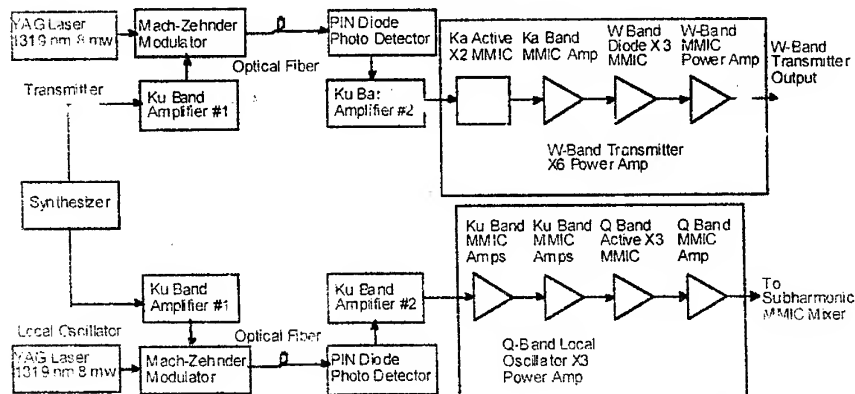
Summary

Two alternate approaches were presented for millimeter wave fiberoptic links. The first emphasized the proper balance between millimeter wave and optical components to achieve good results at a moderate cost. The second approach discussed the use of mode-locked microchip lasers in millimeter wave applications.

References

- [1] K. Noguchi *et al.*, "75 GHz broadband Ti:LiNbO_3 optical modulator with ridge structure", *El. Letters*, 1994, 30, pp. 949-951.
- [2] R. P. Braun *et al.*, "Microwave Generation and Transmission Using Optical Heterodyning or Upconversion Technique", *MWP'96*, Kyoto, Japan, 1996, Tech. Digest, pp. 53-55.
- [3] D. Novak *et al.*, "Locking range of a hybrid mode-locked monolithic DBR semiconductor laser at millimeter wave frequencies", *IEEE Micro. & Guided Wave Letters*, vol. 6, Sept. 1996.
- [4] J. Bowers, "Devices for Microwave Photonics", *MWP'96*, Kyoto, Japan, 1996, Tech. Digest, pp. 29-32.
- [5] L. E. M. de Barros Jr. *et al.*, "Demonstration of enhanced performance of HBT as photodetector", to be presented in this conference.
- [6] E. C. Niehenke *et al.*, "A planar 94-GHz Transceiver with Switchable Polarization", 1993 IEEE MTT-S International Microwave Symposium Digest, pp. 167-170, June, 1993.
- [7] O. P. Gandhi, "Microwave Engineering and Applications," Pergamon Press, New York, 1981.

Figure 1. W-Band Optical Link.



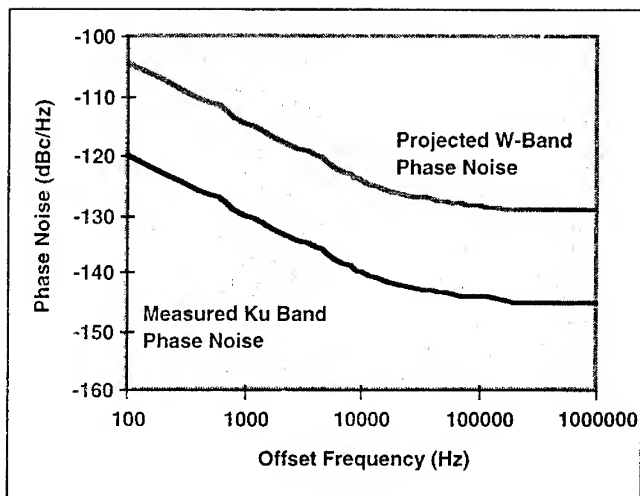


Figure 2. Measured Ku-Band Phase Noise and Projected W-Band Phase Noise.

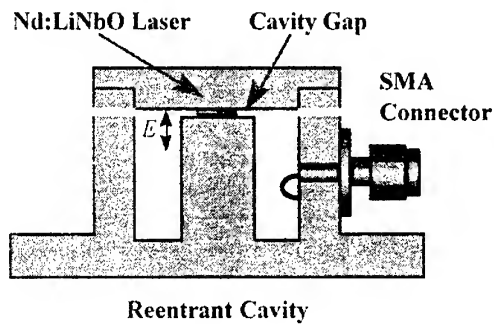


Figure 3 - The mode-locked microchip Nd:LiNbO₃ microchip laser. The laser is mounted in the gap of the reentrant microwave cavity where the driving electric field is polarized along the z-axis of the crystal.

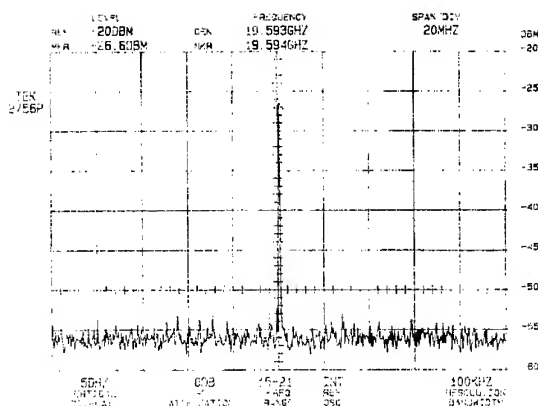
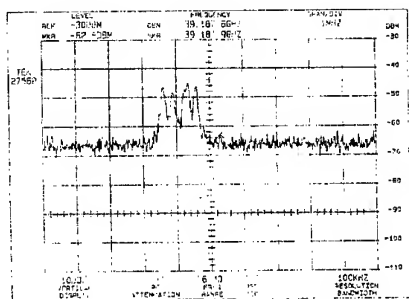
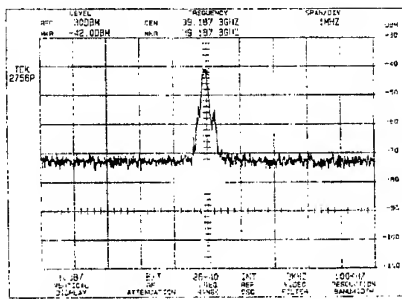


Figure 4 - Microwave spectrum intensity of the laser output at 20GHz.



(a)



(b)

Figure 5 - Microwave spectrum intensity of the laser output at 40GHz for (a) free-running and (b) mode-locked operation.

INTERCONNECTS AND PACKAGING FOR MMIC'S

Wolfgang Menzel

Microwave Techniques, University of Ulm, D-89069 Ulm, Germany

ABSTRACT

This contribution reviews a number of aspects relevant for interconnects and packaging of monolithic integrated millimeter-wave circuits, possibly combined with hybrid or even waveguide circuits. Topics are packaging and front-end architecture, package materials, and standard interconnects to microstrip or coplanar MMIC's. Following this, a special interconnect technique based on electromagnetic field coupling is presented. Finally, as a system application, the front-end of a 77 GHz automotive radar is described.

INTRODUCTION

In recent years, great efforts have been undertaken to develop mm-wave monolithic integrated circuits (MIMICs) which now are being introduced into radar [1], [8] and communication equipment [2]. Especially for low cost civil systems, however, there is still a lack of suitable and affordable techniques for interconnects and packaging of MIMICs, possibly together with hybrid integrated circuits or even waveguide. Packaging of micro- and mm-wave MICs, MMICs, components or subsystems has to provide protection against mechanical stress, environmental loads like moisture and chemicals, and, in some cases, against electromagnetic interferences (EMI). In addition, the complete assembly must operate in a wide temperature range, and it must allow the removal of heat generated in its interior [3] - [7]. Equally, packaging includes interconnects between different circuits (possibly between different types of transmission lines, too), feed-through elements into and out of the package, choice of materials, or front-end architecture. With increasing mass applications like phased arrays [4], [8] or traffic applications [1], packages have to be fabricated and assembled easily and quickly based on reliable processes at reasonable cost. All these problems are increasingly relevant for applications at mm-wave frequencies. Therefore, this contribution will address topics like front-end architecture for mm-wave circuits based on different transmission line media, package materials, and different techniques for circuit interconnects and feed-through elements.

PACKAGING AND FRONT-END ARCHITECTURE

While at lower frequencies, single devices or single MMICs are placed into a package, this mostly is not effective at millimeter wave frequencies. Even a single MIMIC is no longer small compared to wavelengths resulting in package resonance problems, and the cumulating effects of the interconnects from the MIMIC to the package feed-through, out of the package and from one packaged component to the other will add to high insertion and return losses. Therefore, carefully designed assemblies of MIMICs, passive components, radiating structures and other elements have to be combined to subsystems or "supercomponents" and will be placed together on a metal or dielectric carrier, shielded by a single package with special precautions against package resonances. The combination of components will be determined by good functionality, short interconnects for low noise figure or low loss in transmitter power paths, low number of package feed-through elements, limitation of interferences between single components, limitation of gain within one package (feedback prevention), sufficient removal of heat generated by active devices, separation of power and low noise elements etc. Typical topics to be considered are package materials, carrier plate material, or choice of transmission line types.

PACKAGE MATERIALS

Metal as material for at least part of a package shows optimal properties concerning thermal conductivity, electromagnetic shielding, mechanical and thermal stability. For thermal expansion, best match to semiconductor and ceramic materials can be achieved with molybdenum, tungsten, or special composites like kovar. These,

however, exhibit a medium thermal conductivity only and are difficult to machine and therefore expensive. Copper tungsten or copper molybdenum provide an improved thermal conductivity and a thermal expansion coefficient matched to semiconductor materials combined with high stability. Standard metals with good electrical and thermal conductivity like aluminium or brass (mostly plated with a less corrosive layer), are cheaper for these applications, but special precautions have to be taken due to their higher thermal expansion. Fabrication of metal package parts may be done using standard machining procedures or injection casting; new techniques like metal powder sintering and metal injection moulding may pave the way for reduced production cost.

Ceramic materials are applied both as parts of the package as well as for substrates carrying RF transmission lines. To this end, and to provide electromagnetic shielding, these materials (partly) have to be metallized. Beryllia (poisonous), aluminium nitride, or aluminium silicon carbide show best thermal conductivity and are therefore applied in high power applications, while alumina is well known from standard microwave applications. These materials show a low thermal expansion sufficiently matched to semiconductors. Ceramic parts typically are fabricated from fine powder, pressed to the required form and sintered at high temperatures. The sintering leads to a considerable shrinking of the dimensions which has to be taken into account during the design. In some applications, even *quartz* [12] with its relatively low dielectric constant or *silicon* which can be formed with micromachining techniques [13] are used.

Plastic materials are cheapest in material and production cost; pure plastic provides, however, a number of challenges concerning mechanical and thermal stability and thermal expansion. Even as substrate material, PTFE is enforced by fillings like glass fiber or ceramic powder. At lower frequencies, leadframes are used as stabilizing elements [6]. As a relative stable material for packages, polymers with special fillings of ceramic powder, glass or carbon fibers or even metal powder have been investigated [5]. These *composite materials* are engineered for high stability and low thermal expansion, they can withstand temperatures up to 200° C, and they may be easily fabricated employing powder or metal injection techniques. Metal inserts are used to remove heat from active areas. Liquid crystal polymers with their anisotropic behaviour may be of interest for a low thermal expansion in one plane [5]. Special care has to be taken using plastic materials with respect to hermeticity; in most cases, a metallisation will be used to keep penetration of vapour low enough; this improves, at the same time, the electromagnetic shielding of the package.

PACKAGE FEED-THROUGH ELEMENTS

A package feed-through structure has to provide an electrical interconnect into or out of the package maintaining a good seal and mechanical as well as thermal stability. With increasing frequencies, the width of a package wall, especially in conjunction with a material of high dielectric constant like ceramic, is no longer small compared to wavelength. Regarding possible discontinuities of the interfaces at the package wall edges, strong reflections may occur, and some compensation has to be included. For measurement purposes, coaxial cables and connector systems have been pushed into the mm-wave frequency region. Consequently, efforts are made to extend these systems to packaging techniques. The coaxial systems, however, require very stringent tolerances (a few mm only), and above 40 GHz, they pose severe problems with the transition to planar circuits within the package. Using planar lines on a carrier substrate serving, at the same time, as package carrier, the lines could easily be extended out of the package. Suitable compensating and matching structures have to be included to compensate the involved discontinuities [9], [10]. In addition, attention has to be paid to possible resonances of the feed-through structure [9]. For a compact integration of microwave and mm-wave front-ends, multilayer structures are used as carrier substrates which can support a complex interconnect network [6], [19]; a possible material for such substrates is low temperature cofired ceramic (LTCC), [20].

CIRCUIT INTERCONNECTS

At mm-wave frequencies, interconnects between different MIMIC chips or to an additional substrate with either hybrid circuits or interconnect lines behave more and more as strong discontinuities. Dye bonding as well as the interconnects themselves require tight tolerances, but in spite of this, the respective production processes should be easy and low cost. Therefore, the choice of the best interconnect technique, a good model for the microwave (and possibly thermal) behaviour, and a tolerance oriented optimisation is necessary. Equivalent circuit models as well as full wave calculations of different types of interconnects therefore are investigated.

A. Galvanic Interconnects to Microstrip MMIC's

A great part of the present MMICs are based on microstrip. Therefore, an interconnect between two chips or between one chip and a hybrid circuit placed side by side is of great importance. Due to tolerances in chip size, non-regular edges of the chips, and thermal expansion, some gap must remain between the two substrates, and the bonding structure must include some kind of loop. This, however, leads to a pronounced low pass behaviour of the interconnect (Fig. 1) resulting in increased difficulties with increasing frequencies. As bonding elements, one or two wires (at the edges of the lines), bond tapes, or special tapes integrated on thin dielectric carriers (TAB: tape automated bonding, [7]) are employed. At mm-wave frequencies, however, some compensation of the low pass performance of such transitions is necessary. One proposal is based on a theoretical model of bond wire interconnects [14] and a flexible compensation network. Depending on the gap between two circuits, the lateral distance between two bonds is modified such that a good transmission performance is maintained [5], Fig. 1. The distance between the chips is monitored by a camera, and by a suitable algorithm, bond wire positions and loop height are adjusted and controlled automatically. Up to 100 GHz, a return loss of better than 20 dB is predicted theoretically including reasonable ranges of gap widths as well as dye and loop bonding tolerances.

For some applications, microstrip MMICs may favourably be placed on top of a carrier substrate using coplanar interconnect lines. The ground planes of both circuits then are in the same plane, and as the microstrip substrate height typically is relatively small, a galvanic interconnect from the microstrip line to the coplanar line is feasible. A photograph and experimental results are shown in Figs. 2 and 3.

B. Interconnects for Coplanar MMIC's

As coplanar circuits are gaining increasing interest, great efforts are done developing effective interconnect techniques for this type of transmission line, too. Placing two coplanar circuits side by side ends up in even more severe problems compared to microstrip, as the ground plane has to be bonded together, too [15]. Therefore, flip-chip techniques have been introduced consisting of bumps fabricated (with galvanic processes) on top of the circuit metallisation. The MMIC - or even a single device like a FET - then is placed top down and bonded to an equivalent coplanar transmission line structure on a carrier substrate. The same technique can be used to remove the heat of active elements via bumps placed directly at the FET source region [8]. The height of the bumps should be about three times the coplanar slot width (or equal to the ground-to-ground distance) to prevent interactions with the carrier substrate; typical values are 30...75 μm . At mm-wave frequencies, some concern has to be made about the inductance of the bumps [16], but in any case, flip-chip mounting provides an effective and economical interconnect technique in the mm-wave range [2], [15], [17].

INTERCONNECTS AND FEED-THROUGH ELEMENTS USING ELECTROMAGNETIC FIELD COUPLING

While at mm-wave frequencies, the performance of standard interconnects is deteriorating, and tolerance requirements for bonding techniques get more and more critical, quarter-wave structures on GaAs, on the other hand, for electromagnetic field coupling measure only a few tenths of a mm being compatible with the size of MMICs. Fig. 4 shows some possible configurations suitable as feed-through elements, Fig. 5 structures for chip interconnects.

A first example given here is a novel transition from microstrip to waveguide [11] which is sketched in Fig. 6. From the microstrip line, the power is fed via a slot to a patch radiating into the waveguide. In this way, no waveguide structure is necessary on top of the planar circuit which, therefore, can extend independently of the transition. Results around 75 GHz for two transitions placed back to back, connected by 21 mm of microstrip line are given in Fig. 7. Taking into account a microstrip loss of 0.8 dB/cm, an insertion loss of about 0.3 dB per transition results in this frequency range. A second example is a transition from a microstrip line on a MMIC to a carrier substrate with a coplanar line. The microstrip circuit (chip) must have a gap in the ground metallisation in the coupling area; this, however, should not be any problem as some back side structuring is done anyway to enable dye separation. As an example of this technique, the results of two cascaded transitions from a coplanar line on a carrier substrate to a microstrip line on a GaAs substrate (and back) with electromagnetic coupling (including some small matching structure on the carrier substrate) is presented in Fig. 8.

SYSTEM EXAMPLE

To demonstrate some packaging technologies, a 76.5 GHz automotive radar front-end [1] realized within a research project in Germany is described in this section. Its general block diagram is shown in Fig. 9. In this pulse radar, the oscillator based on a 38 GHz voltage controlled oscillator (VCO) together with a frequency doubler serve both as transmitter and local oscillator (LO). To enable some imaging of the street in front of the car, three waveguide feed horns for three different antenna beam angles alternatively illuminate a dielectric lens. All circuits are realized as MMICs, placed side by side on a carrier plate made from a plastic compound. The mm-wave interconnects are done by compensated bonds [5], the transitions from microstrip to waveguide according to [11] and Fig. 6. The heat generated by the active elements is removed by a metal insert in the carrier plate. A photograph of this arrangement is shown in Fig. 10.

ACKNOWLEDGMENT

Part of the work described in this contribution was funded by the German Ministry of Research. Thanks are due, too, to Daimler-Benz Aerospace and the Daimler-Benz Research Institute, Ulm, for providing photographs and results of their work.

REFERENCES

- [1] Daembkes, H., Luy, J. F.: Millimetrewave components and systems for automotive applications. *Microwave Engineering Europe* (Dec.-Jan. 96), 43 - 48.
- [2] Baumann, G. et al.: 51 GHz Frontend with Flip Chip and Wire Bond Interconnections from GaAs MMICs to a Planar Patch Antenna. *IEEE Intern. Microw. Symp. MTT-S*, 1995, Orlando, USA, 1639 - 1641.
- [3] Berson, B.: Strategies for microwave and millimeter wave packaging today. *IEPS, Proc. Of the tech. Program, 9th Annual Intern. Electronics Packaging Conf.*, San Diego, USA, 1989, Vol. 1, 697 - 720.
- [4] Bierman, H.: Designers strive for low cost packages. *Microw. J.*, Sept. 1992, 100 - 106.
- [5] Boheim, M., Goebel, U.: Low Cost Packages for Micro- and Millimeterwave Circuits. *24th European Microw. Conf.*, 1994, Cannes, France, 122 - 132.
- [6] Nagy, C. et al.: Advanced Manufacturing and Packaging Technologies for Military and Commercial Markets. *Microw. J.*, Aug. 1995, 22 - 36.
- [7] Reichel, H.: Packaging aspects of single and multichip modules. *EuPac '94, 1st European Conference on Electronic Packaging Technology & 7th Intern. Conf. on Interconnection Technology in Electronics*, 1994, 6 - 9.
- [8] L. M. Felton: High yield GaAs Flip-Chip MMICs Lead to Low Cost T/R Modules. *IEEE Intern. Microw. Symp. MTT-S*, 1994, San Diego, USA, 1707 - 1710.
- [9] Rittweger, M. et al.: 3D FDTD Analysis Applied to the Investigation of the Resonant Behavior of Ceramic Feedthrus. *IEEE Intern. Microw. Symp. MTT-S*, 1994, San Diego, USA, 1719 - 1722.
- [10] Christ, A.: S-parameter calculations using three-dimensional finite differences for microwave chip interconnects (in German), PhD Thesis, Tech. Univ. Darmstadt, Germany, 1988.
- [11] Grabherr, W.; Huder, B.; Menzel, W.: Microstrip to waveguide transition compatible with mm-wave integrated circuits. *IEEE Trans. on MTT*, September 1994, 1842-1843.
- [12] Shih, Y. C. et al.: A High Performance Quartz Package for Millimeter-Wave Applications. *IEEE Intern. Microw. Symp. MTT-S*, 1991, Boston, USA, 1063 - 1066.
- [13] Robertson, S. V. et al.: Micromachined Self-Packaged W-Band Bandpass Filter. *IEEE Intern. Microw. Symp. MTT-S*, 1995, Orlando, USA, 1543 - 1546.
- [14] Alimenti, F. et al.: Quasi Static Analysis of Microstrip Bondwire Interconnects. *IEEE Intern. Microw. Symp. MTT-S*, 1995, Orlando, USA, 679 - 682.
- [15] Krems, Th., Haydl, W., Massler, H., Ruediger, J.: Millimeter-Wave Performance of Chip Interconnections Using Wire Bonding and Flip Chip. *IEEE Intern. Microw. Symposium MTT-S*, 1996, San Francisco, 247 - 250.
- [16] Jin, H. et al.: Rigorous Field Theory Analysis of Flip-Chip Interconnections in MMICs Using the FDTLM Method. *IEEE Intern. Microw. Symp. MTT-S*, 1994, San Diego, USA, 1711 - 1714.
- [17] Sakai, H. et al.: A novel millimeter-wave IC on Si substrate using flip-chip bonding technology. *IEEE Intern. Microw. Symp. MTT-S*, 1994, San Diego, 1763 - 1766.
- [18] Strauß, G., Menzel, W.: Millimeter-Wave Monolithic Integrated Circuit Interconnects Using Electromagnetic Field Coupling. *IEEE Trans. on CPMT, Pt. B*, Vol. 19, May 1996, 278 - 282.

[19] Session on High Density Microwave Packaging Program. Proc. of IEEE Intern. Microw. Symp. MTT-S, 1995, Orlando, USA, 169 - 184.

[20] Brown, R. L., Polinski, P. W., Shaikh, A. S.: Manufacturing of microwave modules using a low-temperature cofired ceramics. IEEE Intern. Microw. Symp. MTT-S, 1994, San Diego, 1727 - 1730.

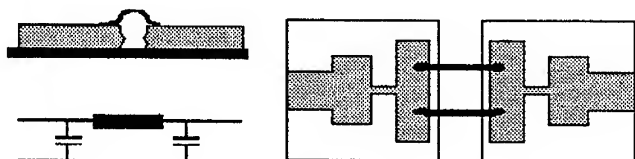


Fig. 1: Microstrip - microstrip bonding, equivalent circuit and compensated bonding interconnect.

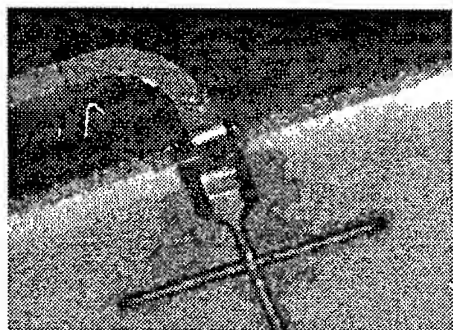


Fig. 2: Transition from a microstrip chip to a coplanar line on a carrier substrate (courtesy of Daimler-Benz Research Institute, Ulm).

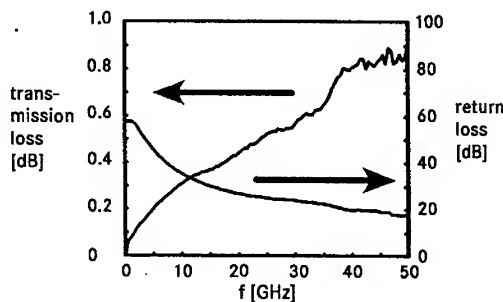


Fig. 3: Return and transmission loss of a double transition from a microstrip chip to a coplanar line on a carrier substrate (courtesy of Daimler-Benz Research Institute, Ulm).

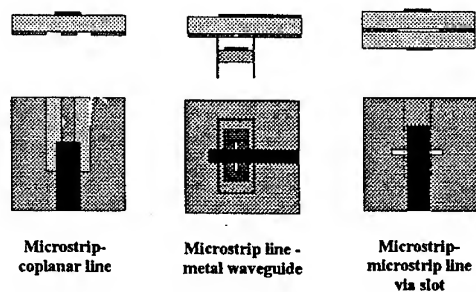


Fig. 4: Possible configurations for feed-through structures from the interior of a package to the outside using electromagnetic field coupling.

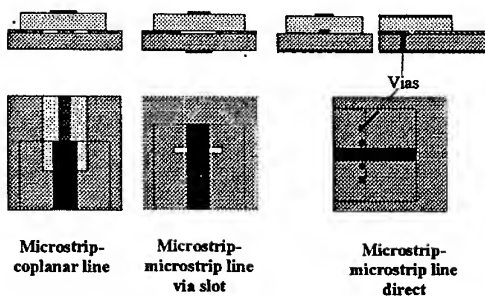


Fig. 5: Possible configurations for the electromagnetic field coupling from a microstrip line on a MMIC to a carrier substrate.

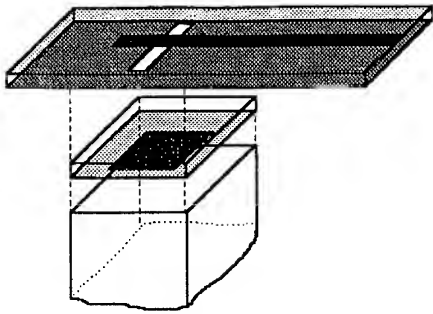


Fig. 6: Patch-coupled microstrip to waveguide transition.

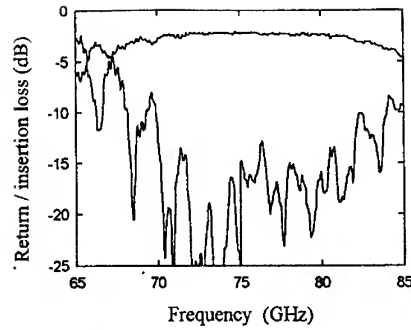


Fig. 7: Return and insertion loss of two cascaded microstrip to waveguide transitions (Fig. 6) placed back to back and connected by a 21 mm microstrip line.

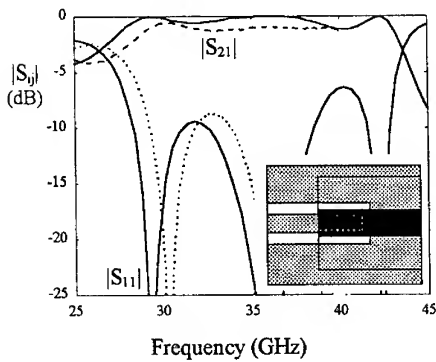


Fig. 8: Scattering parameters of two cascaded transitions from coplanar line to microstrip using electromagnetic field coupling.

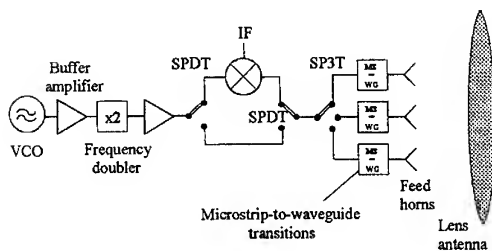


Fig. 9: Block diagram of automotive radar front-end [1].

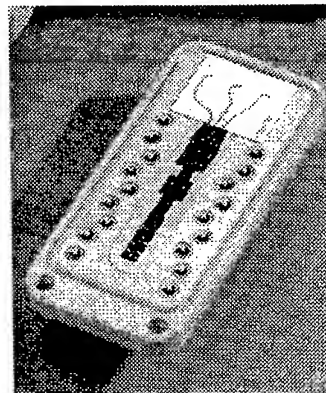


Fig. 10: Photograph of automotive radar front-end [1] (courtesy of Daimler-Benz Aerospace, Ulm).

MMIC GaAs FOUNDRY IN ISRAEL

Dr. ITZCHAK LEWIN

ELTA Electronics Industries

ISRAEL

levin@is.elta.co.il

ABSTRACT

The increase demand for MMIC based systems in ISRAEL, coupled with the long lead time between specification, design and chip fabrication/realization, led us here in ISRAEL to decide and build a National MMIC Foundry. The Fab which is part of ELTA Electronics Industries, was funded both by ELTA and the Government of ISRAEL.

The 4 year project started in 1994 and has as a goal to achieve a list of different device technology. Several processes are currently being developed, among them are the 0.5 micron Ion Implantation POWER MESFET and 0.25 micron e_{beam} lithography Power P-HEMT

The ISRAELI MMIC fab is tailored for the Companies in Israel. The FAB has 750 sq.-m of clean room class 100-1000, capable of running 2000-3000 wafers per year. There wasn't any know-how in ELTA or Israel of MMIC processes, or how to run a MMIC fab, We had to develop everything from the beginning.

This paper will review, the sequence of events that led us to build the MMIC FAB, our first MMIC prototype, type of equipment we use, the process we develop, examples of results in terms of design, technology and measurements will be described.

Obstacles encounter in the development and their solutions will be presented, as well as unsolved problems.

INTRODUCTION

In order to start an MMIC operation in Israel, most of the Microwave system houses joined together in a Consortium of seven companies including ELTA. Six of them are learning how to design MMIC according to ELTA design rule book, while ELTA has to build it's own fabrication facility.

In starting a new GaAs MMIC fab, one has to consider the following issues:

- Types of systems to be produced.
- Types of MMIC's that will be needed to satisfy those requirements?
- Are the fab going to be profitable?
- Should it be?
- Decide about the technology to develop for the active element - Mesfet, P-HEMT, or HBT, Gate - length, Power, Low-noise, High gain or Switch. Passive elements that are needed, Via-holes, Thinning, etc.

Taking in consideration the above, a decision about the equipment should be made, keeping in mind all the process steps that has to be done.

This paper will go through all these consideration, give example of problem and discuss the solutions.

DEFINITION OF PROCESSES

From system point of view, we decided to develop the following processes:

- 0.5 micron Power Mesfet
- 0.25 micron Power P-HEMT
- Schottkey diode
- PIN diode
- HBT

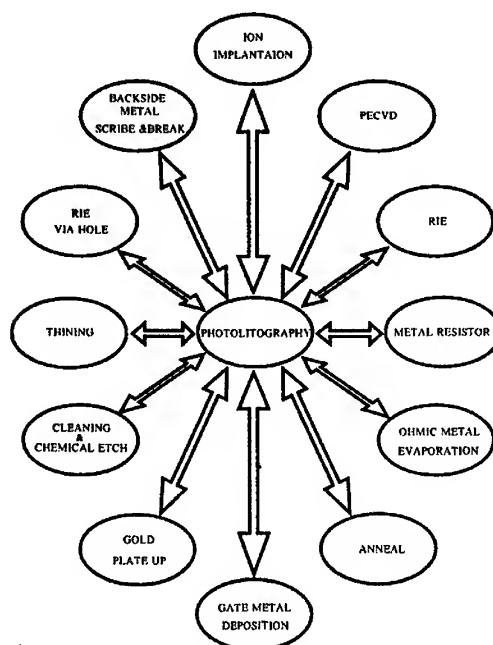
The first process is double selective Ion Implantation with contact lithography. We choose a process of gate and air-bridge gold plate-up, because of similarity to the MIC process which "run" parallel to the MMIC.

We try to keep the difference between processes to a minimum and made our P-HEMT process similar to the MESFET one with changes only in the necessary stages of gate recess and deposition.

Consideration in Equipment

To be able to develop all the above processes with the amount of wafers per year, we do need automatic equipment only for specific stages in the process, this will become clear in

Fig. 1
MMIC Infrastructure



Since all the processes have to pass through the lithography, the lithography step should be an automatic one.

For example: processing 4 wafers per day, in a process cycle of two weeks long, will put 40 wafers per day through the lithography and only 4 wafers per day through the process like the Thinning Evaporation or the Measurements.

This ratio of 1:10 put a lot of pressure on the lithography to be accurate, reliable, with minimum of breakage - Operator free stations. All other steps can be manually handled, with an automatic process.

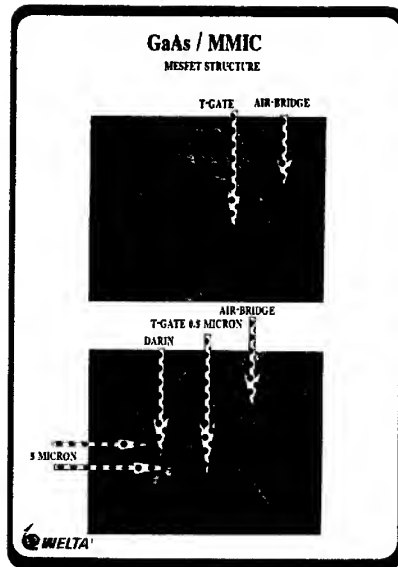
Steps in Development

The following steps should be taken in order for the fab to be qualified:

- Definition of process steps.
- Generate layout for all the passive and active elements.
- Define the layout design-rules.
- Develop all the process steps and verify repeatability.
- Generate S-Parameters and electrical models for both the passive and active elements.
- Verify the repeatability of the process through the electrical model and S-Parameters.
- Decide about automatic connections between the Layout and the electrical model.
- Transfer all the information to the MMIC Designer, and verify that the loop is working without any loop-holes.
- A decision should be made on the sequence of events: First to develop the best performance fet, or to establish a stable ground and confidence between the fab and the designers with less performance fet? Both steps should be done. They cannot be done together, so a choice has to be made.

Fig. 2 shows an example of the Mesfet that was developed at ELTA:

Fig 2.



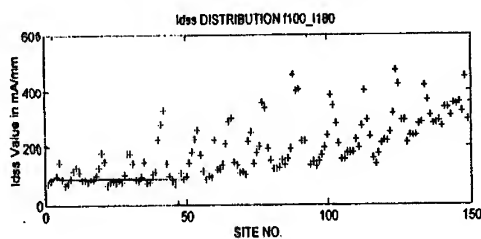
Problems and Solutions

Developing the process, we run into different types of problems. Most of the problems can be avoided, using the right equipment. Entering into the business late, mean that our equipment is more advanced and we might have less problems. Equipment is not everything, good manpower is crucial for the success of the operation.

Running wafers we started to have problems.

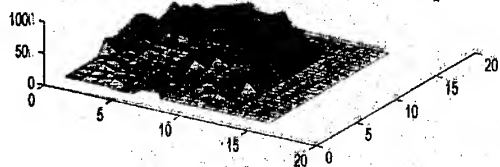
One example of a problem, was the distribution of I_{dss} across the wafer. Starting to run the process, we knew that we have to check the distribution of I_{dss} , but nothing really prepared us for the results shown here in Fig 3.

Fig 3.



The lack of any correlation between the points, at the end of the process was very discouraging. This graph explain how difficult it is to find the source of the problem. This problem can arise from Ion-Implantation, Anneal process or the gate recess. It is very difficult to decide which one of them is responsible and try to rectify it. Fig. 4 shows the same results in a different way, using MATLAB to connect every point to it's corresponding X-Y position on the wafer, we got the following result:

Fig 4.



From this picture, it is clear that we have a smooth change in value of I_{dss} from the major flat to the opposite side. The changes are very smooth and can easily be attributed to problem of inhomogenous in the recess. One can imagine the operator hand moving the wafer in and out from the acid bath.

Changing the recess to automatic top spray with tight control on time - without changing the equipment we have - solved the problem immediately

Another problem that we faces - like every other MMIC fab anywhere, was the e_beam gate and recess process development. It is very difficult to view the PMMA using SEM. Knowing the result of the "writing" is crucial for the decision whether or not to keep processing the wafer as well as understand the end result. It is impossible to decide using an optical microscope.

First issue involve etching down to the right plane at a known distance from the 2-D channel. Using a stopping layer, we believed it will stop at this plane without any problem.

Fig 5.

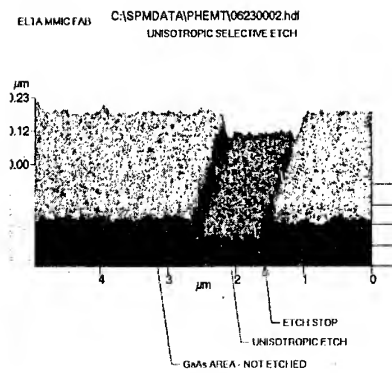
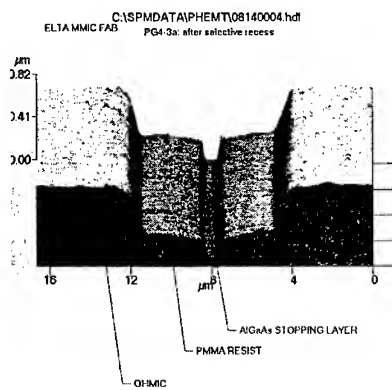


Fig 5. Shows how does a stopping layer look like after etching and how the plane really look like.

Fig 6. Shows how it looks after we “saw” the problem and fixed it.

Fig 6.

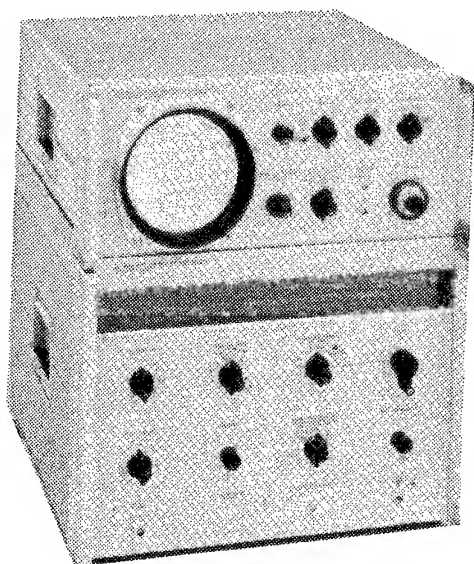


Summary

Building the Israeli MMIC fab was an exciting job, today we are facing a bigger and more challenging task of polishing the processes and introducing devices into systems. The major task of a fab is establishing good connection between designers and technology. The confidence of the designers in the process is crucial for the success of the fab, maintaining the process, getting repeatable results, will serve as a positive feedback for the designers and the system engineers in their decision to introduce the MMIC devices into their systems.

Acknowledgments

Thanks are due to many individuals at ELTA, who participated in the building of the fab, but particular thanks are due to Mr. M. Vered and the technological staff for preparing and discussing of the AFM pictures, and participating in building the fab with the author.



**IN 1964,
HP MADE HIGH QUALITY
SPECTRUM ANALYZERS
AT AN AFFORDABLE PRICE.**

**TODAY,
HP STILL PRODUCES THE BEST QUALITY
MICROWAVE PRODUCTS IN MANY CATEGORIES:**

- ★ VECTOR NETWORK ANALYZERS**
- ★ SCALAR NETWORK ANALYZERS**
- ★ MICROWAVE SOURCES**
- ★ POWER METERS**
- ★ SPECTRUM ANALYZERS**
- ★ MICROWAVE ACCESSORIES**
- ★ COMPUTER AIDED DESIGN**
- ★ EMC SYSTEMS**

** HEWLETT
PACKARD - SOME THINGS NEVER CHANGE**